

Alexander V. Kolobov
Junji Tominaga

Two-Dimensional Transition-Metal Dichalcogenides

Springer Series in Materials Science

Volume 239

Series editors

Robert Hull, Charlottesville, USA

Chennupati Jagadish, Canberra, Australia

Yoshiyuki Kawazoe, Sendai, Japan

Richard M. Osgood, New York, USA

Jürgen Parisi, Oldenburg, Germany

Tae-Yeon Seong, Seoul, Republic of Korea (South Korea)

Shin-ichi Uchida, Tokyo, Japan

Zhiming M. Wang, Chengdu, China

The Springer Series in Materials Science covers the complete spectrum of materials physics, including fundamental principles, physical properties, materials theory and design. Recognizing the increasing importance of materials science in future device technologies, the book titles in this series reflect the state-of-the-art in understanding and controlling the structure and properties of all important classes of materials.

More information about this series at <http://www.springer.com/series/856>

Alexander V. Kolobov · Junji Tominaga

Two-Dimensional Transition-Metal Dichalcogenides



Springer

Alexander V. Kolobov
Nanoelectronics Research Institute, AIST
Tsukuba, Ibaraki
Japan

Junji Tominaga
Nanoelectronics Research Institute, AIST
Tsukuba, Ibaraki
Japan

ISSN 0933-033X ISSN 2196-2812 (electronic)
Springer Series in Materials Science
ISBN 978-3-319-31449-5 ISBN 978-3-319-31450-1 (eBook)
DOI 10.1007/978-3-319-31450-1

Library of Congress Control Number: 2016936988

© Springer International Publishing Switzerland 2016

This work is subject to copyright. All rights are reserved by the Publisher, whether the whole or part of the material is concerned, specifically the rights of translation, reprinting, reuse of illustrations, recitation, broadcasting, reproduction on microfilms or in any other physical way, and transmission or information storage and retrieval, electronic adaptation, computer software, or by similar or dissimilar methodology now known or hereafter developed.

The use of general descriptive names, registered names, trademarks, service marks, etc. in this publication does not imply, even in the absence of a specific statement, that such names are exempt from the relevant protective laws and regulations and therefore free for general use.

The publisher, the authors and the editors are safe to assume that the advice and information in this book are believed to be true and accurate at the date of publication. Neither the publisher nor the authors or the editors give a warranty, express or implied, with respect to the material contained herein or for any errors or omissions that may have been made.

Printed on acid-free paper

This Springer imprint is published by Springer Nature
The registered company is Springer International Publishing AG Switzerland

*This book is dedicated to the bright memory
of Boris T. Kolomiets, Stanford R. Ovshinsky,
Radu Grigorovici and other pioneers of
chalcogenide semiconductors*

Foreword

We live in a digital age. The revolution of data processing and storage technologies, of signal detection and high speed communication impacts our lives as much as the industrial revolution did for our ancestors, but this impact is faster and more global. Materials science is the driving force behind these changes. It started with silicon semiconductors thanks to the special properties of silicon oxide. Materials science quickly diversified, each branch developing novel devices. I experienced the beginning of the field of semiconducting chalcogenide glasses ushered in by the discoveries of Boris T. Kolomiets and Stan Ovshinsky more than 55 years ago. An exciting novel feature was the presence of a band gap in disordered chalcogenides. Moreover, some Te-based compositions exhibited rapid and reversible transition between the amorphous and crystalline phases of some Te-based compositions. The large property contrast between the two phases led to their wide use in optical memories and rewritable DVDs. The chalcogenide glasses revealed, moreover, a rich trove of new science: a unique defect chemistry in the form of valence alternation pairs with negative correlation energy. Furthermore, many optically induced effects, such as optical anisotropies and optically induced changes in density, viscosity and electrical and optical properties were observed.

During the past several years an entirely new and promising field emerged in solid-state physics called topological insulators. These have a bulk energy gap but a conducting surface layer with properties very different from other one-dimensional or two-dimensional electronic systems. The key is strong spin-orbital coupling leading to band inversion. At the same time, transition-metal dichalcogenides emerged as post-graphene two-dimensional materials, where the existence of a direct gap in monolayers, co-existing with the very large exciton energies and strong spin-valley coupling offer exciting opportunities for novel devices. Chalcogenide elements are again major components of these materials.

Two-dimensional transition-metal dichalcogenides quickly became one of the hottest subjects of solid-state research with extremely rich physics and great promise for applications. The field is expanding with unprecedented pace with several papers published almost daily and several topical reviews appearing during the past

years. Yet there is no single-cover reference covering the whole rich field opened by these materials.

The stunning monograph by A.V. Kolobov and J. Tominaga closes this gap. They have written a must-have reference book for all scientists and engineers working in this field and an essential resource for graduate students interested in the forefront of materials science. The authors are highly qualified for writing this much needed book. They have been major contributors to the physics and the technology of chalcogenide semiconductors and their work led to our present understanding of the unique properties of the phase-change chalcogenide alloys. We are fortunate that they got caught by the exciting new physics and possible applications of this new class of chalcogenides. This outstanding volume represents a valuable source of reference starting from the chemistry of chalcogenide and transition metals and describing in detail various facets of their rich physics, laying the groundwork for understanding their two-dimensional manifestations, the main topic of the book. This ambitious book is pedagogically outstanding. It highlights the areas that are not yet understood, stimulating research and suggesting avenues for further discoveries.

Materials science continues to evolve in unexpected ways.

Hellmut Fritzsche
Professor Emeritus
The University of Chicago
Tucson, AZ, USA

Preface

Transition-metal dichalcogenides (TMDCs) are relatively old materials. The structure of one of the best studied materials, MoS₂, was determined back in 1923. Being layered materials, they share similarities with graphite and, as graphite, MoS₂ was mainly used as a dry lubricant, although it also had some ‘electronic’ applications, e.g. as an anode in lithium-ion batteries. Group IV TMDCs were a platform to study charge-density waves in low-dimensional solids, which still remains a very challenging research topic.

The situation changed after the discovery of graphene, for which in 2010 K.S. Novoselov and A.K. Geim were awarded the Nobel Prize. The success of graphene generated explosive interest in other two-dimensional materials, where the use of different elements opens novel opportunities for the exciting new physics and ultimately thin devices. Among them, TMDCs, which can be easily produced as monolayers, moved to the forefront of solid-state research due to their unique band structure featuring a large bandgap with degenerate valleys and non-zero Berry curvature. Two-dimensional TMDCs are often referred to as ‘next-generation graphene’ and ‘wonder materials’, which clearly demonstrates their place in modern science and technology.

The field has been developing at a fascinating pace. While in 2010 only two papers were published with ‘MoS₂’ and ‘monolayer’ as key words, in 2014 the number of papers exceeded 600. The interest in two-dimensional TMDC, triggered by the observation of a direct gap in monolayer MoS₂, rapidly spread to other TMDCs, especially semiconducting materials. Numerous topical reviews were published in the past couple of years, but they cover specific aspects of TMDCs and so far there is no single source of reference for this class of materials.

The present monograph, which originated from the personal notes taken by one of the authors (AK), closes the existing gap by presenting under a single cover the current status of progress in two-dimensional graphene-like monolayer and few-layer structures of TMDCs. Semiconducting monolayer TMDCs, due to the presence of a direct gap, significantly extend the potential of low-dimensional nanomaterials for applications in nanoelectronics and nano-optoelectronics as well as flexible

nanoelectronics with unprecedented possibilities to control the gap by external stimuli. Strong quantum confinement results in extremely high exciton binding energies, which forms an interesting platform for both fundamental studies and device applications. Breaking of spacial inversion symmetry in monolayers results in strong spin–valley coupling potentially leading to their use in valleytronics.

Starting with the basic chemistry of chalcogens and transition metals, the reader is introduced to the rich field of TMDCs. After a chapter on three-dimensional crystals and a description of top-down and bottom-up fabrication methods of few-layer and single-layer structures, the fascinating world of two-dimensional TMDCs structures is presented with their unique atomic, electronic, and magnetic properties. Particular features associated with decreased dimensionality such as the phase-stability of monolayers, the appearance of a direct gap, large binding energy of two-dimensional excitons and their dynamics, Raman scattering associated with decreased dimensionality, extraordinary strong light–matter interaction, layer-dependent photoluminescence properties, new physics associated with the destruction of the spatial inversion symmetry of the bulk phase, spin–orbit and spin–valley coupling are all covered in detail. The monograph is concluded by chapters on engineered heterostructures and device applications. It is richly illustrated with almost 400 figures, most of which are in colour, and contains a list of over 1000 references.

The authors did their best to make a complete coverage of the results available to date, but were limited by several factors. First, this book has been written by experimentalists and for experimentalists. As a consequence, some of the theoretical papers are covered in less detail. Second, considering the vastness of the field and the very fast pace with which it is developing, it is inevitable that some of the publications have not been included in this volume. Since the authors of different original papers use somewhat different terminology and notations, the present authors had to make a choice between preserving the original terminology and making the terminology unified throughout the volume; both approaches having their own advantages and drawbacks. We have adopted the former approach, i.e. preserved the original terminology, providing some comments where it was necessary. Finally, the results obtained by different groups are occasionally contradictory; we tried to add cross-references wherever possible.

Considering the explosive interest in physics and applications of two-dimensional materials, this book will be a valuable source of information for materials scientists and engineers working in the field as well as for the graduate students majoring in materials science.

The authors are very grateful to Paul Fons and Yuta Saito for careful reading of the manuscript and a number of useful suggestions. AVK is also thankful to Ritsuko Iwamoto for her dedicated help.

Tsukuba, Japan

Alexander V. Kolobov
Junji Tominaga

Contents

1	Introduction	1
	References	4
2	Chemistry of Chalcogenides and Transition Metals	7
2.1	Chemistry of Chalcogenides	7
2.1.1	Lone-Pair Semiconductors.	8
2.1.2	Valence Alternation Pairs	11
2.1.3	Dative Bonds.	13
2.1.4	sp^3 -Hybridization of Chalcogens	14
2.1.5	Multicenter Bonds	14
2.1.6	Transition-Metal Dichalcogenides.	15
2.1.7	Ubiquitous Chalcogenides	16
2.2	Transition Metal Chemistry	17
2.2.1	Valence Bond Theory.	18
2.2.2	Crystal-Field Theory.	20
2.2.3	Ligand-Field Theory.	23
2.2.4	Band Structure Calculations.	23
	References	26
3	Bulk TMDCs: Review of Structure and Properties	29
3.1	Atomic and Electronic Structure.	29
3.1.1	Structure of Individual Triple Layers	29
3.1.2	Bulk Structural Polymorphs.	31
3.1.3	Distorted Structures	34
3.1.4	Charge Density Waves	36
3.1.5	Van der Waals Interlayer Bonding	37
3.1.6	Group Theory Analysis.	39
3.1.7	Electronic Structure	42
3.2	Optical Properties of Bulk TMDCs	45
3.2.1	Optical Absorption.	45
3.2.2	Raman Scattering and Infra-Red Spectroscopy	45

3.3	Magnetism	57
3.3.1	Magnetism in MoS ₂	57
3.3.2	Non-saturating Magnetoresistance in WTe ₂	57
3.4	TMDC as Weyl Semimetals	59
3.5	Pressure-Induced Transformations	61
3.5.1	Pressure Effect on Physical Properties of MoS ₂	61
3.5.2	Pressure Effect on Extremely Large Magnetoresistance in WTe ₂	63
3.5.3	Pressure-Induced Structural Changes.	66
	References	71
4	From 3D to 2D: Fabrication Methods	79
4.1	Top-Down Methods	79
4.1.1	Mechanical Exfoliation	79
4.1.2	Liquid Exfoliation	81
4.1.3	Electrochemical Exfoliation	84
4.2	Bottom-Up Techniques	85
4.2.1	Synthesis via Metal Chalcogenisation	86
4.2.2	Thermolysis of Thiosalts.	90
4.2.3	Vapour Pressure Reaction of Transition Metal and Chalcogen Precursors	91
4.2.4	Growth of TMDC Alloys	93
4.2.5	Van der Waals Epitaxy	93
4.3	Layer Transfer	97
4.4	Analysis of 2D TMDC Layers	98
4.4.1	Comparison of Exfoliated and CVD-Grown TMDCs	98
4.4.2	Thickness Determination.	100
4.4.3	Domain Orientation	102
	References	102
5	Structure and Physico-Chemical Properties of Single Layer and Few-Layer TMDCs	109
5.1	Structure of Single Layers	109
5.1.1	2H-Phase	110
5.1.2	1T-Phase.	110
5.2	2H-1T Phase Transition	119
5.2.1	Phase Stability	119
5.2.2	Atomistic Details of the 2H to 1T Phase Transition	121
5.2.3	Local Phase-Patterning	125
5.2.4	Stability of CDW States and Gate-Tunable Phase Transitions in nm-Thick 1T-TaS ₂	126

5.3	Defects, Dislocations, and Grain Boundaries	128
5.3.1	Point Defects	129
5.3.2	Dislocations and Grain Boundaries	133
5.3.3	Grain Boundary Migration	138
5.4	Doping 2D TMDCs	141
5.5	Order-Disorder Phase Transitions in TMDC Alloys	142
5.6	Properties of Two-Dimensional TMDCs	142
5.6.1	Mechanical Properties	142
5.6.2	Thermal Expansion	145
5.6.3	Thermal Conductivity	146
5.6.4	Thermoelectric Properties	147
5.6.5	Optical Properties	148
5.6.6	Electrical Transport	150
5.6.7	Stability	151
5.7	Structures with Lower Dimensionality	153
5.7.1	TMDC Nanotubes	153
5.7.2	Nanoribbons	155
5.7.3	Quantum Dots	156
	References	156
6	Electronic Band Structure of 2D TMDCs	165
6.1	Theoretical Studies	165
6.1.1	Indirect-to-Direct Gap Transition	166
6.1.2	Monolayers Versus Bi-Layers	169
6.1.3	Spin-Orbit Splitting	171
6.1.4	Band Gap Tuning	174
6.1.5	Monolayer-Bilayer Boundary	181
6.1.6	Band Structure of the 1T-MoS ₂ Phase	181
6.1.7	Strong Light-Matter Coupling and Band Nesting	183
6.1.8	Excitonic Effects and Band Gap Renormalization	189
6.1.9	Van der Waals Interaction	192
6.1.10	Gapless MoS ₂ Allotrope	196
6.2	Experimental Studies	198
6.2.1	Optical Gap	198
6.2.2	Electronic Gap	203
6.2.3	Spin-Orbit Coupling	205
6.2.4	ARPES Measurements	207
6.2.5	Band Gap Renormalization	211
	References	218
7	Raman Scattering of 2D TMDCs	227
7.1	Symmetry of Odd- and Even-Layer Structures	227
7.1.1	2H-Polytype	227
7.1.2	1T-Polytype	229
7.1.3	Raman Tensors	230

7.2	Non-resonant Raman Scattering	231
7.2.1	Unusual Behaviour of the E_{2g}^1 and A_{1g} Modes	231
7.2.2	Davydov Splitting	236
7.2.3	Low-Frequency Modes	236
7.2.4	Peaks Associated with Decreased Dimensionality	240
7.3	Laser Power Effects	249
7.3.1	Temperature Dependence of Raman Scattering	249
7.3.2	Photogating	252
7.4	Effect of Carrier Concentration	254
7.5	Effect of Substrate	255
7.6	Effect of Pressure and Strain on Raman Scattering	255
7.6.1	Uniaxial Strain	255
7.6.2	Hydrostatic Pressure	259
7.7	Twisted and Folded Structures	262
7.8	Helicity-Resolved Raman Scattering	262
7.9	Resonant Raman Scattering	265
7.9.1	MoS_2	266
7.9.2	WS_2	269
7.9.3	Raman Excitation Profiles	271
7.10	Thickness Determination	273
7.11	Raman Scattering of Specific Materials	276
7.11.1	Raman Modes of the $1T'$ -Phase	276
7.11.2	Rhenium Dichalcogenides: A 2D Response from 3D Samples	276
7.11.3	Raman Signatures as a Fingerprint of VdW Interaction in Heterostructures	279
7.11.4	Raman Scattering in 2D Group IVB TMDCs	283
7.11.5	TMDC Alloys	286
	References	289
8	Luminescence of 2D TMDC	295
8.1	Intrinsic PL from Monolayers Versus Few-Layer Structures	295
8.1.1	Effect of the Number of Layers	295
8.1.2	Effect of Interlayer Coupling (Twisted Layers)	298
8.1.3	Band Nesting Effects	300
8.2	Defect-Related Photoluminescence	304
8.2.1	Defect-Enhanced PL Yield	304
8.2.2	Quantum Light Emission	306
8.3	PL Tuning by External Stimuli	309
8.3.1	Pressure and Strain Effects	309
8.3.2	Electrical Gating	311
8.3.3	Effect of Doping	313
8.3.4	Substrate Effects	313

8.4	Electroluminescence	315
8.5	PL from TMDC Alloys	316
	References	317
9	Excitons	321
9.1	Excitons in 2D	321
9.1.1	Exciton Binding Energy	322
9.1.2	Non-Rydberg Excitonic Series	326
9.1.3	'Dark' Excitonic States	330
9.1.4	Excitonic Collapse	334
9.1.5	Effect of Surrounding Dielectric Media	334
9.1.6	Intra-Excitonic Transition	337
9.2	Exciton Dynamics	339
9.2.1	Exciton–Exciton Interaction	342
9.2.2	"Excitons in a Mirror"	345
9.3	Excitons and Trions	347
9.4	Excitons in Heterostructures	354
	References	359
10	Magnetism in 2D TMDC	365
10.1	Ferromagnetism Associated with Crystal Imperfections	365
10.1.1	Magnetic States at Edges	365
10.1.2	Magnetism at Grain Boundaries	370
10.1.3	Vacancy-Induced Magnetism	372
10.1.4	Disorder-Induced Magnetism	374
10.2	Doping-Induced Magnetism	374
10.2.1	Magnetism Due to Magnetic Dopants	375
10.2.2	Magnetism of Non-metal Adsorbates	378
10.3	Controlling Ferromagnetic Easy Axis	378
10.4	Strain-Induced Tunable Magnetism	379
10.5	Magnetism Associated with the 2H-1T Phase Transition	382
10.6	Non-saturating Magnetoresistance in WTe ₂	386
	References	386
11	Spin-Valley Coupling	389
11.1	Valley Degree of Freedom	389
11.1.1	Optical Control of Valley Polarization	391
11.1.2	Electrical Control of Valley Polarisation	395
11.1.3	Valley Coherence	396
11.2	Zeeman-Type Splitting by an Electric Field	397
11.3	Magnetic Control of Valley Pseudospin in Monolayers	398
11.4	Valley Hall Effect	403
11.4.1	Nonlinear Valley and Spin Currents	405
11.5	Spin-Valley Physics in Bi-Layers	405
11.5.1	Electrical Control of Valley Magnetic Moment	405
11.5.2	Spin-Layer Locking	406

11.6	Spin Polarisation in Inversion-Symmetric Structures	409
11.7	Optical Stark Effect	412
11.8	Valley Depolarisation Dynamics	417
	References	417
12	Miscellaneous Phenomena	421
12.1	Second Harmonic Generation	421
12.1.1	SHG from Odd- and Even-Layer Structures	421
12.1.2	SHG and Edge States	425
12.1.3	Resonant SHG	425
12.1.4	Excitonic Effects	426
12.1.5	SHG in Twisted Bi-layers	426
12.1.6	Electrical Control of SHG	428
12.1.7	SHG Dynamics	431
12.2	Piezoelectricity in Monolayer MoS ₂	432
12.3	Quantum Spin Hall Effect	435
12.4	Burstein–Moss Effect	437
12.5	Gate-Tuned Superconductivity	439
12.6	Strong Light-Matter Coupling and Polaritons	442
	References	443
13	TMDC Heterostructures	447
13.1	Vertical Heterostructures	448
13.1.1	Lattice-Matched Simulations	448
13.1.2	Minimized-Strain Calculations	452
13.1.3	Single Layer Vertical Heterostructures	457
13.1.4	Re-Stacked TMDCs	457
13.1.5	Heterostructures with Vertically Aligned Layers	458
13.1.6	Experimental Studies	458
13.2	Lateral Heterostructures	462
13.2.1	Theoretical Studies	462
13.2.2	Experimental Results	463
13.3	Heterostructures Containing TMDC	466
13.3.1	TMDC/2D Heterostructures	466
13.3.2	Miscellaneous TMDC-Based Heterostructures	467
	References	468
14	Emerging Applications of 2D TMDCs	473
14.1	Transistors	473
14.1.1	Single- and Few-Layer Field-Effect Transistors	474
14.1.2	Ambipolar Transistors	479
14.1.3	Vertical Heterostructure Devices	480
14.2	Integrated Circuits	482
14.2.1	Amplifiers	482
14.2.2	Logic Circuits	483

14.3	Optoelectronic Devices	484
14.3.1	Photodetectors and Solar Cells	485
14.3.2	Light-Emitting Devices	487
14.4	Valleytronics	490
14.5	Memory Devices	490
14.6	Contacts for 2D TMDC Devices	492
14.6.1	Basic Principles	494
14.6.2	Role of Metal Contacts: Experiments	496
14.6.3	Ways to Better Contacts	498
14.7	Miscellaneous Applications	501
14.7.1	Sensors	501
14.7.2	Nanomechanical Systems	502
14.7.3	Catalysis and Energy Application	503
14.7.4	Biomedical Applications	504
	References	504
15	The Neverending Story	513
	References	526
16	Chalcogenides Nanoelectronics: Hype and Hope	529
	References	530
	Index	533

Chapter 1

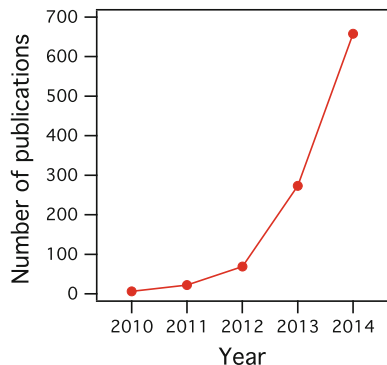
Introduction

Transition metal dichalcogenides (TMDCs) are old; the oldest known samples of MoS₂ date over 2.9 billion years [1]. A comprehensive, even though somewhat outdated, review about structure and properties of three-dimensional TMDCs can be found in [2]. Despite rather similar structure, TMDCs cover a wide spectrum of properties ranging from insulators, to semiconductors, to metals. This diversity of properties is a consequence of the existence of non-bonding *d* bands and the degree to which they are filled with electrons. It is also interesting to note that one of the first reports on monolayer TMDC was published in the mid 1980s [3] while few-layer-thick MoS₂ single crystals were reported even earlier [4] but these publications remained largely unnoticed.

These old materials experienced a renaissance after the discovery of unique electronic properties of graphene, for which K.S. Novoselov and A.K. Geim were awarded the Nobel Prize in 2010. In single-layer graphene's band structure, the linear dispersion at the *K* points gives rise to novel phenomena, such as the anomalous room-temperature quantum Hall effect, and opened up a new category of Fermi-Dirac physics. Graphene is a fantastic electronic and thermal conductor, and graphene-based materials have been proposed for a host of applications ranging from high-speed electronic and optical devices, energy generation and storage, hybrid materials, chemical sensors, and even DNA sequencing, and a variety of proof-of-concept devices have been demonstrated.

The success of graphene generated explosive interest in other two-dimensional materials, where use of different elements opens novel opportunities for the exciting new physics and ultimately thin devices. Two-dimensional TMDCs [5], which can be easily exfoliated [4] and present very interesting electrical and optical properties, became one of the most intensely studied areas of solid state physics and technology. Among these materials, semiconducting TMDCs are of special interest since the possibilities of gap engineering by varying the number of layers makes them exciting candidates for device applications. Figure 1.1 shows the number of publications per year found in the Web of Knowledge with the key words “MoS₂” and “monolayer”, which clearly indicates an exponential increase in interest in the past several years.

Fig. 1.1 The number of publications found by the Web of Knowledge with the search key words “MoS₂” and “monolayer”



The band structure of those compounds dramatically changes from bulk to single-layer samples, going from indirect gap in bulk materials to direct gap in monolayers, underscoring the important role of interlayer coupling. In addition, their electronic properties are very sensitive to external conditions such as temperature, pressure or strain.

The presence of boundaries, vacancies and/or adatoms in the samples can lead to interesting magnetic properties. Strong spin-orbit interaction in TMDCs alongside with the coupling of the spin, valley and layer degrees of freedom open unprecedented possibilities from both fundamental and applied perspectives. This possibility is especially interesting in single layers where the spin-orbit coupling lifts the spin degeneracy of the energy bands due to the absence of inversion symmetry. Furthermore, reduced dielectric screening in monolayer and few-layer samples of TMDCs makes excitonic effects exceptionally strong.

These and other properties of two-dimensional TMDCs are the subject of this volume. There have been numerous reviews published on this topic [6–21] as well as an edited volume on MoS₂ [22] and the interested readers can check them for details that may be missing here.

The TMDCs are about sixty in number; two-thirds of these assume layered structures. Most of these layered materials are synthetic but some exist naturally, e.g. natural MoS₂ crystals with the 2H and 3R phases (see Sect. 3.1.2 below for the explanation of the symbols) are quite common. The structure of this mineral, molybdenite, was first determined in 1923 [23]. Bulk TMDC crystals are conventionally grown using the chemical vapor transport method [24–26], where purified dichalcogenide material in the form of powder is mixed with the transport agent, usually bromine or iodine and sealed in a quartz ampoule. The quartz ampoule is introduced into a zone electric furnace, with a temperature gradient formed along the tube [27, 28]. Pure component materials, for example W and Se for the growth of WSe₂ can also be used.

The Periodic Table shows the following color coding for transition metals:

- Orange:** Ti, Cr, Mn, Fe, Co, Ni, Cu, Zn, Ga, As, Sb, Te, Ru, Rh, Pd, Ag, Cd, In, Sn, Pb, Bi, Po, At.
- Pink:** Sc, V, Cr, Mn, Fe, Co, Ni, Cu, Zn, Ga, As, Sb, Te, Ta, Hf, Os, Ir, Pt, Au, Hg, Tl, Uut.
- Blue:** Ti, Cr, Mn, Fe, Co, Ni, Cu, Zn, Ga, As, Sb, Te, Ru, Rh, Pd, Ag, Cd, In, Sn, Pb, Bi, Po, At.

Chalcogen atoms (S, Se, Te) are highlighted in orange. Hydrogen is also highlighted in orange.

Fig. 1.2 The transition metals and the three chalcogen elements that crystallise into layered structures are highlighted in the Periodic Table. The transition metals that crystallise into layered structures with some chalcogens but not with others are framed. The columns in the Periodic Table show both ‘old’ and new labels, i.e. chalcogen atoms can be referred to as either group VIA or group 16 elements

In Fig. 1.2 the Periodic Table of elements is shown with the transition metals that form layered structures highlighted in different colours; those metals that form layered structures with some chalcogens but not with others are colour-framed, e.g. while NiTe_2 has a layered structures, NiS_2 possesses a three-dimensional pyrite structure. Chalcogen atoms are highlighted in orange. Also shown in the Figure are the “old” and “new” notations for the columns, thus chalcogen atoms will be referred to as either group VIA or group 16 elements. Later in this volume the old and new notations are used interchangeably, following the original publications.

As can be seen from Fig. 1.2, group 4–7 metals are predominantly layered while some of the group 8–10 metals form three-dimensional crystals. Recent interest is mainly associated with semiconducting TMDCs, which form the main body of this volume. At the same time, we would like to mention that there are also reports on other materials, such as noble-transition-metal (Pt and Pd) dichalcogenides [29, 30] and tin disulphide [31], the latter being indirect-gap semiconductors.

The present monograph is organised as follows. In Chap. 2, the readers are introduced to chemistry of chalcogenides and transition metals, which is followed by Chap. 3, where the structure and properties of bulk TMDCs are briefly reviewed. Chapter 4 describes the major fabrication methods to produce two-dimensional TMDCs. In Chaps. 5 and 6, atomic and electronic structures of monolayer and few-layer TMDCs are discussed in detail. Raman scattering, which evolved into a major method of TMDCs characterisation, is the subject of Chap. 7. Luminescence from 2D TMDC and exciton behaviour are subsequently discussed in Chaps. 8 and 9, followed by Chaps. 10 and 11 dedicated to magnetism and spin-valley coupling in 2D TMDCs.

Chapter 12 is dedicated to miscellaneous phenomena observed in 2D TMDC, that are too short to be the subject of dedicated chapters, e.g. second-harmonic generation. Engineered heterostructures based on 2D TMDCs are described in Chap. 13, followed by the conclusive Chap. 14 that discusses emerging applications of 2D TMDCs in nanoelectronics.

References

1. J. Golden, M. McMillan, R.T. Downs, G. Hystad, I. Goldstein, H.J. Stein, A. Zimmerman, D.A. Sverjensky, J.T. Armstrong, R.M. Hazen, Rhenium variations in molybdenite (MoS_2): evidence for progressive subsurface oxidation. *Earth Planet. Sci. Lett.* **366**, 1 (2013)
2. J. Wilson, A. Yoffe, The transition metal dichalcogenides discussion and interpretation of the observed optical, electrical and structural properties. *Adv. Phys.* **18**(73), 193 (1969)
3. P. Joensen, R. Frindt, S.R. Morrison, Single-layer MoS_2 . *Mat. Res. Bull.* **21**(4), 457 (1986)
4. R. Frindt, Single crystals of MoS_2 several molecular layers thick. *J. Appl. Phys.* **37**(4), 1928 (1966)
5. H.S.S.R. Matte, A. Gomathi, A.K. Manna, D.J. Late, R. Datta, S.K. Pati, C.N.R. Rao, MoS_2 and WS_2 analogues of graphene. *Angew. Chem.* **122**(24), 4153 (2010)
6. M. Xu, T. Liang, M. Shi, H. Chen, Graphene-like two-dimensional materials. *Chem. Rev.* **113**(5), 3766 (2013)
7. S.Z. Butler, S.M. Hollen, L. Cao, Y. Cui, J.A. Gupta, H.R. Gutierrez, T.F. Heinz, S.S. Hong, J. Huang, A.F. Ismach et al., Progress, challenges, and opportunities in two-dimensional materials beyond graphene. *ACS Nano* **7**(4), 2898 (2013)
8. A. Kuc, Low-dimensional transition-metal dichalcogenides. *Chem. Modell.* **11**, 1 (2014)
9. M. Chhowalla, H.S. Shin, G. Eda, L.J. Li, K.P. Loh, H. Zhang, The chemistry of two-dimensional layered transition metal dichalcogenide nanosheets. *Nat. Chem.* **5**(4), 263 (2013)
10. W. Zhao, R.M. Ribeiro, G. Eda, Electronic structure and optical signatures of semiconducting transition metal dichalcogenide nanosheets. *Acc. Chem. Res.* **48**(1), 91 (2015)
11. H. Zeng, X. Cui, An optical spectroscopic study on two-dimensional group-vi transition metal dichalcogenides. *Chem. Soc. Rev.* **44**, 2629 (2015)
12. X. Zhang, X.F. Qiao, W. Shi, J.B. Wu, D.S. Jiang, P.H. Tan, Phonon and raman scattering of two-dimensional transition metal dichalcogenides from monolayer, multilayer to bulk material. *Chem. Soc. Rev.* **44**(9), 2757 (2015)
13. Q. Ji, Y. Zhang, Y. Zhang, Z. Liu, Chemical vapour deposition of group-VIB metal dichalcogenide monolayers: engineered substrates from amorphous to single crystalline. *Chem. Soc. Rev.* **44**, 2587 (2015)
14. D. Jariwala, V.K. Sangwan, L.J. Lauhon, T.J. Marks, M.C. Hersam, Emerging device applications for semiconducting two-dimensional transition metal dichalcogenides. *ACS Nano* **8**(2), 1102 (2014)
15. Q.H. Wang, K. Kalantar-Zadeh, A. Kis, J.N. Coleman, M.S. Strano, Electronics and optoelectronics of two-dimensional transition metal dichalcogenides. *Nat. Nanotech.* **7**(11), 699 (2012)
16. D. Voity, A. Mohite, M. Chhowalla, Phase engineering of transition metal dichalcogenides. *Chem. Soc. Rev.* **44**(9), 2702 (2015)
17. H. Wang, H. Yuan, S.S. Hong, Y. Li, Y. Cui, Physical and chemical tuning of two-dimensional transition metal dichalcogenides. *Chem. Soc. Rev.* **44**(9), 2664 (2015)
18. C. Tan, H. Zhang, Two-dimensional transition metal dichalcogenide nanosheet-based composites. *Chem. Soc. Rev.* **44**(9), 2713 (2015)
19. N. Zibouche, A. Kuc, J. Musfeldt, T. Heine, Transition-metal dichalcogenides for spintronic applications. *Ann. Phys. (Berlin)* **526**(9–10), 395 (2014)

20. D. Lembke, S. Bertolazzi, A. Kis, Single-layer MoS₂ electronics. *Acc. Chem. Res.* **48**(1), 100 (2015)
21. H. Yu, X. Cui, X. Xu, W. Yao, Valley excitons in two-dimensional semiconductors. *Nat. Sci. Rev.* **2**(1), 57 (2014)
22. Z.M. Wang, MoS₂: *Materials, Physics, and Devices* (Springer, Heidelberg, 2013)
23. R.G. Dickinson, L. Pauling, The crystal structure of molybdenite. *J. Am. Chem. Soc.* **45**(6), 1466 (1923)
24. A. Al-Hilli, B. Evans, The preparation and properties of transition metal dichalcogenide single crystals. *J. Cryst. Growth* **15**(2), 93 (1972)
25. H. Schäfer, *Chemical Transport Reactions* (Academic Press Inc., Cambridge, 1964)
26. A. Ubaldini, E. Giannini, Improved chemical vapor transport growth of transition metal dichalcogenides. *J. Cryst. Growth* **401**, 878 (2014)
27. L. Brixner, Preparation and properties of the single crystalline AB₂-type selenides and tellurides of niobium, tantalum, molybdenum and tungsten. *J. Inorg. Nucl. Chem.* **24**(3), 257 (1962)
28. R. Nitsche, The growth of single crystals of binary and ternary chalcogenides by chemical transport reactions. *J. Phys. Chem. Solid.* **17**(1), 163 (1960)
29. P. Miró, M. Ghorbani-Asl, T. Heine, Two dimensional materials beyond MoS₂: Noble-transition-metal dichalcogenides. *Angew. Chem. Int. Ed.* **53**(11), 3015 (2014)
30. N. Zibouche, A. Kuc, P. Miró, T. Heine, Noble-metal chalcogenide nanotubes. *Inorganics* **2**(4), 556 (2014)
31. Y. Huang, E. Sutter, J.T. Sadowski, M. Cotlet, O.L. Monti, D.A. Racke, M.R. Neupane, D. Wickramaratne, R.K. Lake, B.A. Parkinson et al., Tin disulfide an emerging layered metal dichalcogenide semiconductor: materials properties and device characteristics. *ACS Nano* **8**(10), 10743 (2014)

Chapter 2

Chemistry of Chalcogenides and Transition Metals

The lone-pair electrons of chalcogen atoms and the presence of *d*-orbitals of transition metal atoms determine the rich chemistry of transition-metal dichalcogenides. This Chapter presents a brief overview of the fundamental concepts that are needed to understand the chemistry of these materials.

2.1 Chemistry of Chalcogenides

Chalcogenides are materials that contain chalcogen species. The term ‘chalcogen’ refers to group VI elements such as sulphur, selenium, and tellurium. While oxygen and polonium are also, strictly speaking, chalcogens they will not be considered in this book. According to Wikipedia, the word chalcogen is derived from the Greek $\chi\alpha\lambda\kappa\sigma$ meaning ‘copper’ and the latinised Greek word *genes*, meaning ‘borne’ or ‘produced’. Why the group VIA elements are called after ‘copper’ may seem a puzzle. Its etymology has been investigated in [1, 2] and below we provide the explanation following [1].

According to this publication, around 1930, Wilhelm Blitz of the Institute of Inorganic Chemistry at the University of Hannover, Germany, and his colleagues were investigating the relationship between the physical properties of chemical elements and their position in the Periodic Table. It became useful to refer to certain groups of elements by characteristic names. However, the group of the elements O, S, Se, and Te lacked such a name. In about 1932, one of W. Blitz’s co-workers proposed the term ‘chalcogens’ for these elements and ‘chalcogenides’ for their compounds using the analogy with the well-known terms ‘halogens’ (‘salt formers’) and ‘halogenides’ for the neighboring elements in the Periodic Table; the majority of halogenides being salts and chalcogenides being ores.

Subsequently, the International Union of Chemistry (later IUPAC) for the Reform of the Nomenclature of Inorganic Chemistry recommended that “the elements

© Springer International Publishing Switzerland 2016

7

A.V. Kolobov and J. Tominaga, *Two-Dimensional Transition-Metal Dichalcogenides*, Springer Series in Materials Science 239,
DOI 10.1007/978-3-319-31450-1_2

oxygen, sulfur, selenium and tellurium may be called chalcogens and their compounds chalcogenides” [3].

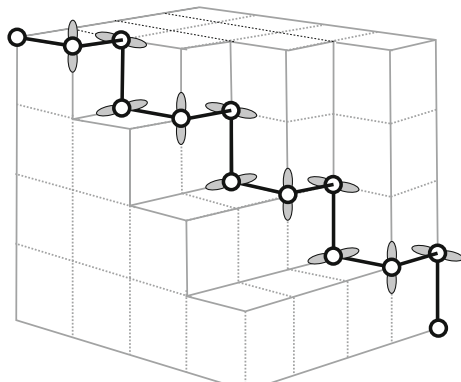
2.1.1 Lone-Pair Semiconductors

The electron configuration of chalcogens in the highest (valence) shell is $ns^2 p^4$ or $ns^2 p_x^1 p_y^1 p_z^2$, i.e. there are two electrons located on the atomic s -orbital, and two of the three p -orbitals possess unpaired electrons while the third one is occupied by a pair of electrons. The latter are usually called lone-pair (LP) electrons and *usually*—but not always—do not participate in the formation of covalent bonds. The s -electrons are also chemically inactive *in most cases*. This electron configuration is the source of the extreme structural richness of chalcogenides as briefly described below.

When chalcogen atoms are involved in chemical bonding, the atomic electronic configuration changes depending on other chemical species present in the compound. In the ideal case, each chalcogen atom forms two covalent bonds with its neighbours as in the case of elemental sulphur, selenium and/or tellurium, where sulphur typically forms rings, selenium can form rings or chains, and tellurium forms chains. In all these cases, only the two unpaired p -electrons are involved in the formation of covalent bonds, the pair of s -electrons and the p -orbital LP remain inert. Since p -orbitals are orthogonal, the bonding angle subtended by chalcogen atoms is rather close to 90° with the LP electrons occupying the orbital directed perpendicular to the plane formed by the p_x and p_y orbitals. The structure of selenium can be thus viewed to a zeroth approximation as nearly cubic (Fig. 2.1).

Depending on the dihedral angle sign sequence (sense of rotation), the Se atoms can either form extended Se_N chains (for $-,-,-,-,-$, etc. and $+,+,+,+,+,+$, $+,+,+,$, etc.) or eight-membered rings (for $+, -, +, -, +, -, +, -$) as illustrated in Fig. 2.2. The former modification is called trigonal (or hexagonal) selenium and the latter is monoclinic selenium. Bonding within a chain/ring is covalent. Bonding between the chains/rings is much weaker and is generally considered to be of a van der Waals (vdW) nature although in several publications it has also been referred to as

Fig. 2.1 Schematics of a selenium zig-zag chain in a simple cubic lattice. To obtain the real structure, intrachain atom distances have to be decreased and interchain atom distances increased with a concomitant increase in the bond angle



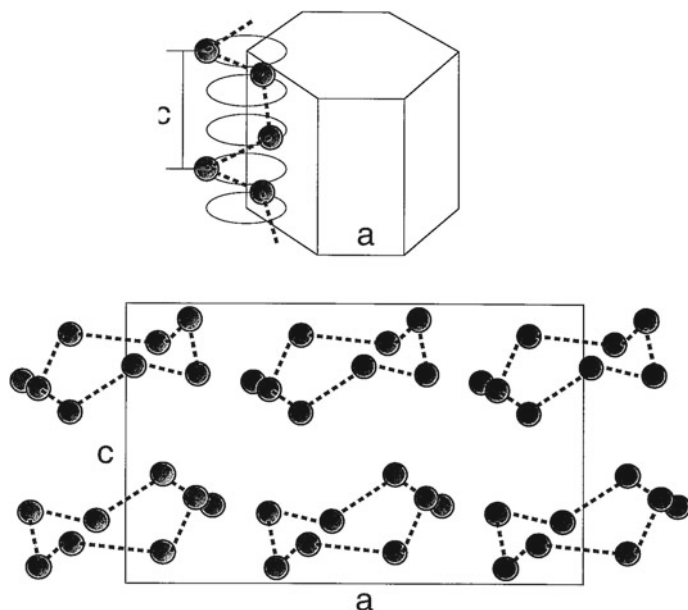


Fig. 2.2 Trigonal (top) and monoclinic (bottom) phases of selenium

resonant [4, 5]. It should be noted that even though the intermolecular interaction is significantly weaker, it is this interaction that is responsible for the long-range order in crystalline selenium. It may also be of interest to note that although sulphur, selenium and tellurium atoms have the same electronic configuration in the outer shell, the lighter sulphur atoms tend to form rings while the heavier tellurium atoms favour chains. It is also interesting to note that the ratio of the nearest distances between the chalcogenide atoms within the same chain and between chains decreases as one goes from S and Se to Te, indicating the presence of a stronger covalent component in the latter case.

Kastner was the first to point out [6] the important role of LP electrons in the chemistry of chalcogenides. In particular, he noted that while in tetrahedrally bonded semiconductors such as Si or Ge the hybridised sp^3 orbitals split into bonding (σ) and antibonding (σ^*) molecular states that are subsequently broadened into the valence and conduction bands, respectively, in the solid, in chalcogens (S, Se, Te), the s states lie well below the p states and need not be considered. Because only two of the three p orbitals can be utilised for bonding, one normally finds chalcogens in two-fold coordination, leaving behind one nonbonding electron pair (LP). In a solid, these unshared, or LP, electrons form an LP band near the original p -state energy. The bonding (σ) and antibonding (σ^*) bands are split symmetrically with respect to this reference energy. Both the σ and LP bands are occupied. As a result, the bonding band is no longer at the top of the valence band; this role is played by the LP band (Fig. 2.3). To account for this rather special situation Kastner suggested to use the term ‘LP semiconductors’ when referring to chalcogenides [6, 7].

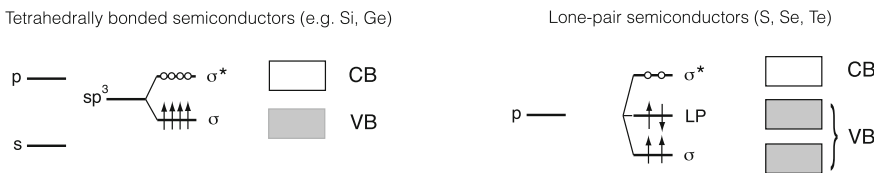


Fig. 2.3 Bonding in tetrahedrally bonded (*left*) and LP (*right*) semiconductors

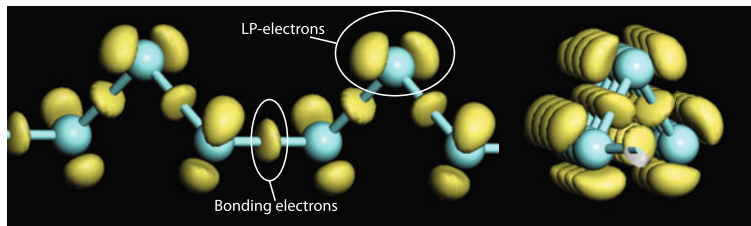


Fig. 2.4 A Se chain in two projections. CDD isosurfaces demonstrate the formation of covalent bonds as well as the presence of LP *p*-orbitals

In Fig. 2.4 we show an individual Se chain, where in addition to atoms shown as balls and covalent bonds shown as sticks, charge density difference (CDD) isosurfaces are also shown. As the name implies, CDD is the difference in electron density between the structure in question and isolated quasiatoms [8]. Hence, the appearance of a CDD cloud midway between two atoms is a signature of a covalent bond. In the example of a selenium chain above, alongside the CDD clouds located mid-way between atoms that are signatures of covalent bonds one can also see the CDD clouds corresponding to non-bonding *p*-orbitals (LP electrons).

Sometimes the two *s*-electrons are also referred to as LPs. In what follows we shall use this term with respect to both non-bonding *p*-electrons and also the *s*-electrons. In case of ambiguities we shall explicitly specify the orbital on which the LP is located.

Typical examples of materials in which chalcogen atoms have such an electronic configuration, apart from elemental chalcogens, are chalcogenide glasses and $A_2^{V\text{VI}}B_3^{\text{VI}}$ and $A^{\text{IV}}B_2^{\text{VI}}$ crystals such as As_2S_3 or GeS_2 . In these materials all elements satisfy their valence requirements and the covalent coordination number of constituent elements satisfy the so-called 8 – N rule. Valence in this context is defined to mean the number of single (σ -type) covalent bonds necessary for the atom to complete, via the shared electrons comprising the bonds, its outer shell of *s* and *p* electrons. Since the complete shell contains 8 electrons, the atoms generally obey the “8 – N” rule when $N > 4$, where N is the number of valence electrons and the coordination number is given by $8 - N$. For example, in the case of As_2Se_3 this means that all arsenic atoms are threefold coordinated and selenium atoms are twofold coordinated. The 8 – N rule was proposed for chalcogenides glasses in order to account for the observation that chalcogenide glasses were insensitive to doping. The 8 – N rule is often referred to as the Mott rule [9].

2.1.2 Valence Alteration Pairs

Deviations from the 8 – N rule give rise to topological defects in the continuous random network of glasses. The most straightforward kind of a topological defect would be atoms with unsatisfied, or broken, or dangling bonds. Thus any open S₈ ring will generate two dangling bond defects. Extended chains that are the building blocks of selenium also possess two dangling bonds at their ends. Each dangling bond contains one electron and is electrically neutral. Such defects should be present in large quantities in an amorphous network consistent with the fact that the Fermi level in chalcogenide glasses is pinned near the middle of the gap [10]. At the same time, in amorphous chalcogenides a dark electron spin resonance (ESR) signal is usually not observed whereas a large concentration of defect states has been demonstrated by various experimental techniques. This inconsistency suggested that dangling bonds, while easy to imagine, do not form the major kind of topological defects in amorphous chalcogenides.

To account for the above controversy, P.W. Anderson postulated [11] that, due to a strong electron-phonon coupling, electron pairing becomes energetically favourable despite the endothermic cost in energy required to place two electrons on one site. Such defects are called negative correlation energy, or negative-*U*, centres. This model was applied by Street and Mott to a case example of an elemental chalcogen [12]. They argued that the majority of defects in chalcogens are pairs of positively and negatively charged dangling bonds:



where *D* stands for a dangling bond and the superscripts describe the charge. The resulting system is diamagnetic (i.e. all electrons are paired), which explains the absence of an ESR signal.

In the model subsequently put forward by Kastner et al. [13], usually known as the *valence-alternation pair* (VAP) model or Kastner–Adler–Fritzsche model, the formation of over-coordinated defects through involvement of LP electrons was suggested. The essence of this idea is that an empty orbital of a positively charged dangling bond interacts with LP electrons of a neighbouring chain, forming a three-fold coordinated defect and thus lowering the energy of the system:



where *C* stands for chalcogen, the subscripts describe the coordination, and the superscripts correspond to the charge. The process of the VAP formation is illustrated in Fig. 2.5.

The gain in energy due to the formation of an extra bond was considered to be the driving force for compensating the energy cost for creation of the doubly occupied site at the negatively charged dangling bond. The energy levels of various defect configurations that may exist in a-Se are schematically shown in Fig. 2.6. Within

Fig. 2.5 Configuration-coordinate diagram depicting the formation of valence-alternation pairs in chalcogenide glasses. Dots indicate LP electrons

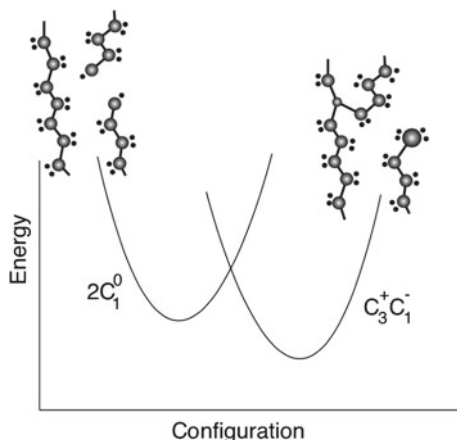
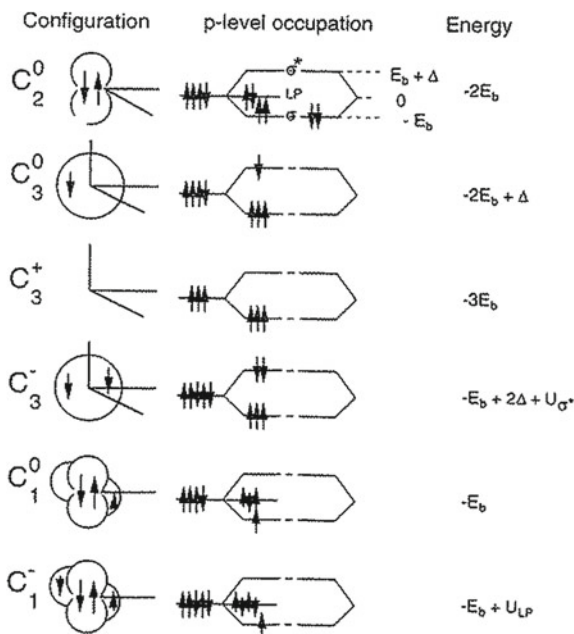


Fig. 2.6 Configurations and energy levels for coordination defects in selenium. In configurations, straight lines represent bonding (σ) orbitals, lobes represent the LP orbitals, and large circles represent the antibonding (σ^*) orbitals. Arrows represent electrons. Energies are given using LP energy as zero [13]. Copyright 1976 by the American Physical Society. Reprinted with permission



this model, the most stable defects are pairs consisting of triply coordinated positive sites and singly coordinated negative sites, i.e. $C_3^+ C_1^-$ pairs. The energy of this VAP defect is almost the same as the energy of two atoms within a chain ($2C_2^0$). If the two atoms are located in immediate proximity of each other, the defect pair is called an intimate valence-alternation pair.

As regards neutral defects, a triply coordinated atom (C_3^0) was found to be the most stable suggesting that under certain circumstances chalcogen atoms can adopt

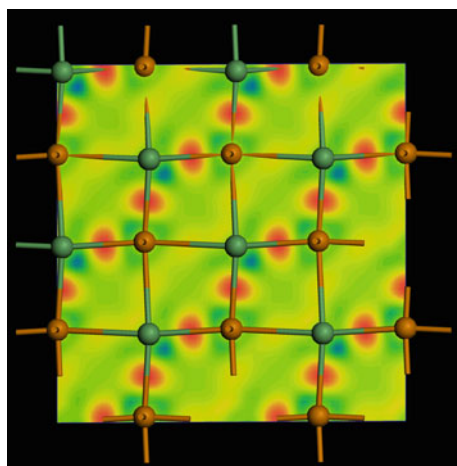
a coordination number of three, although subsequent experiments demonstrated that neutral dangling bonds are more stable [14, 15].

2.1.3 Dative Bonds

In IV-VI crystals (and the corresponding amorphous phases), the bonding is yet different. For the case of GeTe, examination of the electronic structure of Ge ($4p_x^1 p_y^1 p_z^0$) and Te ($5p_x^1 p_y^1 p_z^2$) shows that these two elements, when interacting between themselves, can form two kinds of covalent bonds, that differ in the electron source. Indeed, in addition to the formation of conventional covalent bonds when both Ge and Te atoms each provide one electron, there is an alternative possibility to form a two-electron two-orbital bond by using p -orbitals provided one each by Ge and Te atoms and *sharing two Te LP electrons*. This kind of bonding is called dative (or donor-acceptor, or coordinate) and its importance in GeTe-based alloys has been described in [16, 17]. Dative bonds are created in addition to the conventional covalent bonds (both Ge and Te can form two conventional covalent bonds) so that each Ge and Te atom forms two conventional covalent bonds and one dative bond. Once formed, all Ge-Te bonds are indistinguishable. As a result, both Ge and Te are three-fold coordinated in violation of the 8 – N rule.

At low temperature, GeTe crystal possesses a rhombohedral structure with three shorter and three longer Ge-Te distances. While often referred to as resonantly bonded distorted cubic, it should be noted that there is a very strong bonding energy hierarchy along the shorter and longer interatomic distances (Fig. 2.7) [18] demonstrating that any resonance that might exist is only partial.

Fig. 2.7 CDD for the rhombohedral GeTe phase demonstrating a strong bonding energy hierarchy between the shorter and longer Ge-Te distances with a large CDD pile-up along the shorter Ge-Te bonds [18]. Reprinted by permission from Macmillan Publishers Ltd., copyright (2011)



In IV-VI crystals with heavier metal elements, i.e. SnTe and PbTe, all metal-chalcogen distances are equal [19], i.e. all atoms are properly octahedrally coordinated, although recently there were several reports on distortions emerging at higher temperatures [20, 21]. Considering equal distances on any two opposite sides of each participating atom, referring to Sn(Pb)-Te bonds as resonant (using both lobes of the *p*-orbitals) is well justified.

Resonant bonds are also formed by chalcogens located inside quintuple layers and group V elements in topological insulators, such as Sb₂Te₃ or Bi₂Te₃, where these elements are octahedrally coordinated. At the same time, the chalcogen atoms located at the outermost planes of quintuple layers are three-fold coordinated. The bonding between quintuple layers is described as vdW.

2.1.4 *sp*³-Hybridization of Chalcogens

It is further possible that *s*- and *p*-orbitals of chalcogen atoms hybridise. In this case, such as in II-VI crystals, chalcogen atoms are *sp*³-hybridised and form tetrahedrally bonded zinc-blend structures. In some cases, such as Ga₂Te₃, the average structure is also zinc blend but due to the presence of 1/3 of intrinsic cation vacancies the structure acquires strong local distortions and the chalcogen atoms are in fact three-fold coordinated possessing a LP of electrons on an *sp*³ hybridised orbital.

2.1.5 Multicenter Bonds

Finally, LP electrons of chalcogens, may serve to form multicenter bonds, such as three-center four-electron bonds. An example of such a bond can be found in Sb-doped GeTe. While in the ideal rhombohedral GeTe phase all atoms are three-fold covalently coordinated as shown in the upper and lower-left panels of Fig. 2.8 (considering the very strong asymmetry along the shorter and longer GeTe distances in the rhombohedral phase, we describe the structure as layered [8, 18]), doping by group-V elements such as antimony results in the formation of vacancies with the Te atoms surrounding the vacancies being two-fold coordinated and possessing *p*-orbitals with LP electrons (lower right panel) [8].

The Te LP electrons may interact with Ge atoms in the neighbouring layer, which results in the formation of three-center four electron (3c-4e) Te-Ge-Te bonds (Fig. 2.9) with the Ge-Te distances on both sides of the Ge atom being equal. Such 3c-4e bonds are weaker than the two-center bonds but stronger than the interaction between GeTe layers in the ideal rhombohedral structure.

Resonant bonds that connect five aligned atoms in topological insulators such as Sb₂Te₃. Thus a Te-Sb-Te-Sb-Te fragment may be considered as multi-center bonds, where 5 bonds are formed using 4 electrons. Multicenter electron deficient bonds are usually weaker than conventional two-center two-electron covalent bonds.

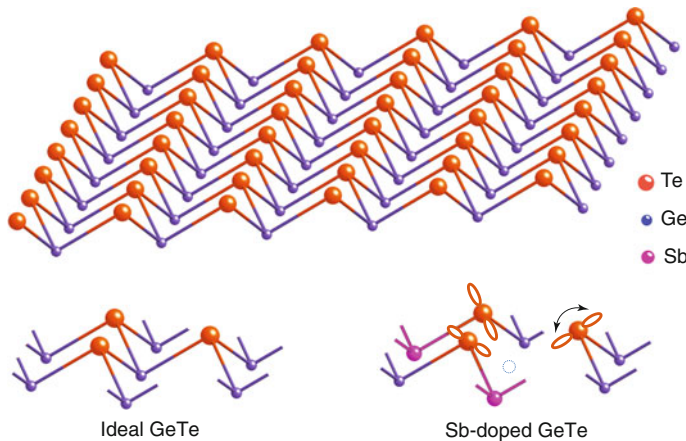


Fig. 2.8 *Top panel* a single buckled layer of the ideal GeTe. *Lower panel (left)* shows a smaller fragment of the layer including three Te atoms covalently (two conventional covalent bonds and one dative bond) bonded to Ge atoms. Both Ge and Te atoms are three-fold coordinated and no LP electrons exist. As a result of Sb doping (Sb atoms are shown in magenta) and different responses to the rupture of conventional covalent and dative bonds (see text), the Te atoms become two-fold coordinated and possess p -orbitals with LP electrons, directed along the broken Ge-Te bonds (*left right-hand panel*). The vacant Ge site is indicated by a dotted circle. Because of the low coordination numbers, the Te atoms can rather easily move in the directions indicated by the double-ended arrow [8]. Copyright 2013 by the American Physical Society. Reprinted with permission

2.1.6 Transition-Metal Dichalcogenides

Finally, we consider the class of materials called transition metal chalcogenides with the general formula of MX_2 , where M stands for a (six-fold coordinated) transition metal and X represents chalcogens, the latter are three fold coordinated (as also in the case of IV-VI crystals). While in transition metal complexes bonding is usually considered between empty orbitals of the metal and LPs of ligands, in TMDCs, the metal atoms provide four electrons to fill the bonding states and the transition metal and chalcogens can be ascribed a formal charge of +4 and -2, respectively [22]. The LP electrons of chalcogen atoms, located on sp^3 -hybridised orbitals, terminate the surfaces. As a result, the coordination around chalcogenides is lopsided, which leads to the marked cleavage properties perpendicular to the hexagonal/trigonal symmetry axis [23]. The absence of dangling bonds makes the surfaces very stable and non reactive.

While it is sometimes considered that chalcogen atoms utilise pure p -orbitals to form three bonds, CDD isosurfaces obtained from DFT simulations demonstrate that the chalcogen atoms are, in fact, sp^3 -hybridised, with LP electrons pointing into the vdW gap (see Fig. 3.2).

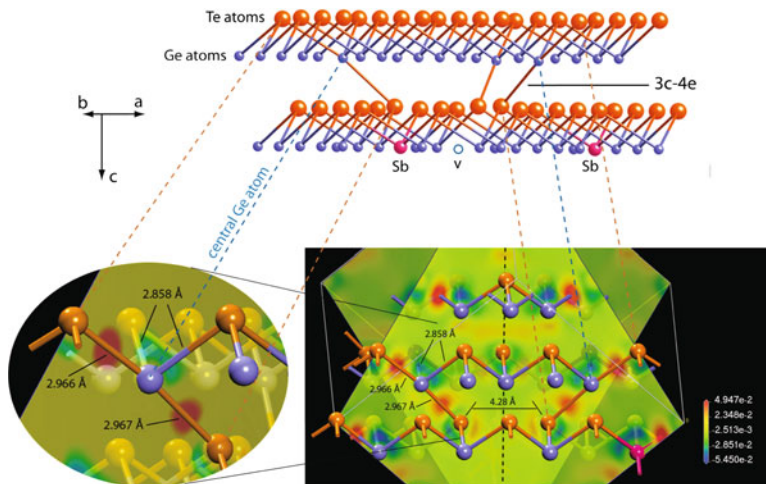


Fig. 2.9 Schematic of the formation of three-centre four-electron Te-Ge-Te bonds (*upper panel*) utilising Te LP electrons of the two-fold coordinated Te atoms located around a Ge vacancy. Te atoms are shown in *orange*, Ge atoms—in *blue*, Sb atoms—in *magenta* and the Ge-site vacancy is shown as an empty circle. The colour of the covalent bonds represent the origin of the bonding electrons (see text for more detail). The *lower panel* shows the result of a simulation of the three-center Te-Ge-Te bond complexes. Two CDD slices—separated by a *black dashed line*—one for each of the two 3c-4e bonds, are shown on the right. The *oval-shaped* image on the left zooms into one of the three-centre four-electron bonds. The CDD is projected onto a plane going through the atoms participating in the three-centre bonds with the atoms in front of the slice being brighter in colour than those behind the slice; the *red* spots of similar size and colour midway between the Ge and Te atoms in the CDD map indicate covalent(-like) interaction of similar strength on both sides of the central Ge atom along the Te-Ge-Te bond direction. Note that, because of the 2D nature of the CDD maps, the charge distribution along the two other Ge-Te bonds (centered on the same Ge atoms) that are not contained within the slices used to visualise the CDD for the 3c-4e bonds, is not shown [8]. Copyright 2013 by the American Physical Society. Reprinted with permission

2.1.7 Ubiquitous Chalcogenides

One can see from the above brief description that chalcogen atoms can form a very broad variety of bonding configurations, which results in a wide spectrum of chalcogenides with very different, often exotic, properties. In the past 60 years, chalcogenides experienced several booms. The first boom started in the mid 1950s after the discovery by N.A. Goryunova and B.T. Kolomiets, that chalcogenide glasses, which are disordered materials, are semiconductors. This discovery was very unusual because the presence of a semiconducting gap is usually associated with the presence of long-range order, which is obviously absent in glasses, and started a new field in solid state physics, *viz.*, amorphous semiconductors.

The interest to chalcogenides spiked again with the report in the 1960s by S.R. Ovshinsky that certain, mainly Te-based alloys, possess a very large property contrast between the crystalline and amorphous phases, which opened a possibility

to use these materials for memory applications. Chalcogenides used for memory applications are usually called phase-change alloys. Re-writable DVDs, whose production started in the 1990s are the best known example and recently electronic non-volatile phase-change random access memory (PC-RAM) has been commercialised by Samsung and Micron.

During the first decade of the 21st century, solid state physicists became excited by the new class of solids called topological insulators. These materials possess a bulk gap in the density of states but have quantum-mechanically protected metallic states on the surface. The best three-dimensional topological insulators are Sb_2Te_3 and Bi_2Te_3 and some other materials from the same *chalcogenide* family.

Finally, following the great success of graphene, the search for other 2D materials started and the transition metal dichalcogenides emerged as most promising candidates. Due to weak vdW bonding between the MX_2 layers, individual layers can be easily prepared, opening an unprecedented possibility to fabricate atomically small devices. Once again, chalcogenides become placed at the cutting edge of solid state research. In this monograph, we concentrate on two-dimensional transition metal dichalcogenides. The interested reader may find information relevant to other classes of chalcogenides in recent monographs [24–26].

2.2 Transition Metal Chemistry

We now proceed to bonding chemistry of transition metals. We start by briefly discussing electronic structure of transition metals, alternatively called *d*-elements. According to the IUPAC definition [27], a transition metal is ‘an element whose atom has a partially filled *d* sub-shell, or which can give rise to cations with an incomplete *d* sub-shell’. In reality, this term is often used to refer to any element in the *d*-block of the Periodic Table (i.e. groups 3 to 12 of the table). Transition metals have the following general electronic configuration: $(n - 1)d^{1-10}ns^2$. As one goes across the row from left to right in the Periodic Table, electrons are *generally* added to the $(n - 1)d$ shell that is filled according to the aufbau principle, which states that electrons fill the lowest available energy levels before filling higher levels, and Hund’s rule. At the same time, because the $(n - 1)d$ and ns shells are rather close in energy and half-filled and/or filled shells are characterised by an increased stability, occasionally, an electron is transferred from the s -shell into the *d*-shell, e.g. the atomic configuration of copper is $3d^{10}4s^1$ rather than $3d^94s^2$. The *d*-block transition metals have *s*, *p*, and *d* orbitals and those with *n* electrons in the *d*-orbitals are termed ions with a d^n configuration. For example, Ti^{3+} is a d^1 ion, and Co^{3+} a d^6 ion.

One of the most important properties of metallic elements is their ability to act as Lewis acids that form complexes with a variety of Lewis bases. A metal complex consists of a central metal atom or ion that is bonded to one or more neighbours, called ligands (from the Latin *ligare*, meaning ‘to bind’), which are ions or molecules that contain one or more pairs of electrons that can be shared with the metal.

Metal complexes can be neutral, such as $\text{Co}(\text{NH}_3)_3\text{Cl}_3$, positively charged, such as $[\text{Nd}(\text{H}_2\text{O})_9]^{3+}$, or negatively charged.

The coordination number of transition metals is determined by the size of the central metal ion, the number of d electrons, and/or steric effects arising from the ligands. Complexes with coordination numbers between 2 and 9 are known. In particular, 4–6 coordinations are the most stable electronically and geometrically and complexes with these coordination numbers are the most numerous. Because it is the six-fold coordination of the transition metals that is encountered in TMDCs, we shall only consider here this case.

When six ligands coordinate to a central metal, octahedral (O_h) coordination is the most stable geometry and the majority of such complexes assume this structure. The octahedral structure may show tetragonal (D_{4h}), rhombic (D_{2h}), or trigonal (D_{3h}) distortions caused by electronic or steric effects.

Six ligating atoms can also assume a trigonal prismatic coordination. Although this coordination is seen in some compounds, few metal complexes with this coordination structure are known because octahedral coordination is sterically less strained. At the same time, it has long been known that the bonding mode of chalcogen atoms around a metal is often trigonal prismatic in solid-state TMDCs such as MoS_2 and WS_2 (see Fig. 3.1). The stability of the trigonal prismatic configuration in TMCDs is determined by their electronic band structure, as is discussed in detail later (Sect. 3.1.7).

Properties of coordination complexes are determined not only by the chemical nature of the ligands but also by their spatial arrangement around the transition metal. An example is $\text{Co}(\text{NH}_3)_3\text{Cl}_3$, where the Co metal is coordinated by two kinds of ligands with the *cis*-isomer being blue while the *trans*-isomer has red colour.

We now proceed to the discussion of bonding in transition metals complexes, which is slightly different from usual covalently bonded solids. Recent developments of the density functional theory made it an ideal tool to analyse the atomic and electronic structure of solids. However, we believe that knowledge of qualitative chemical approaches would be very useful to understand the underlying physics and chemistry of the bond formation and the resulting properties and we discuss them briefly below.

2.2.1 Valence Bond Theory

This is the simplest theory accounting for the formation of covalent bonds. It assumes that covalent bonds are formed when atomic orbitals overlap and that the strength of a covalent bond is proportional to the amount of overlap. It further assumes that atomic orbitals hybridise in order to maximize the overlap with adjacent atoms. An example of such hybridization is sp^3 hybridization of Si or Ge in the corresponding crystals, where each atom is four-fold covalently coordinated. In a transition metal, a set of six s , p and d -orbitals can be hybridised similar to the sp^3 hybridization to generate six equivalent orbitals directed to the vertices of an octahedron.

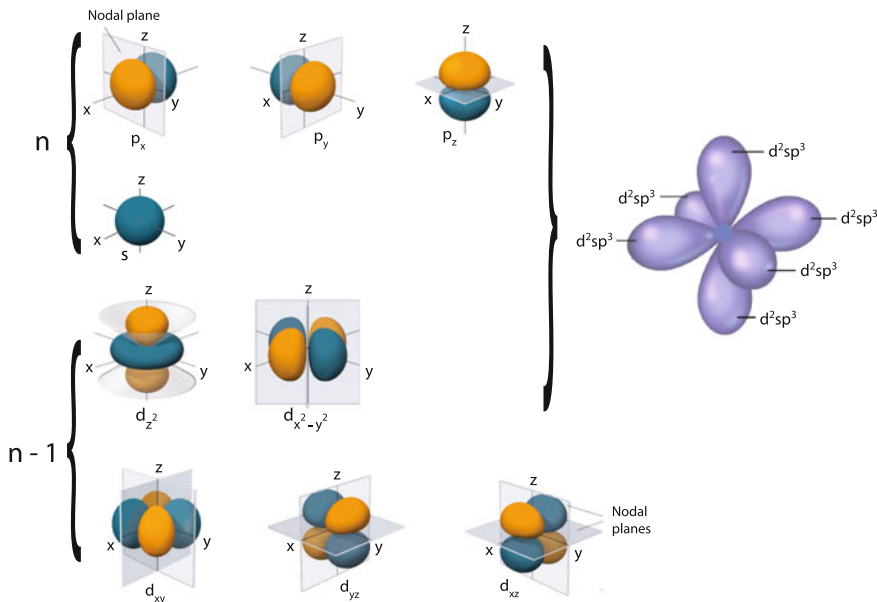


Fig. 2.10 Atomic s , p , and d -orbitals of a transition metal (left) (reproduced from [28]) and the corresponding set of d^2sp^3 -hybridised orbitals (right) that allow for an octahedral bonding geometry of the metal

While it is easy to visualise s -orbitals as spheres and p -orbitals as dumbbells, visualisation of d -orbitals is more complex. There are five d -orbitals referred to as d_{z^2} , $d_{x^2-y^2}$, d_{xy} , d_{yz} , and d_{xz} . When an octahedral bonding geometry is considered, the d_{xy} lobes lie in-between the x and the y axes, d_{xz} lobes lie in-between the x and the z axes, d_{yz} lobes lie in-between the y and the z axes, $d_{x^2-y^2}$ lobes lie on the x and y axes and, finally, the d_{z^2} (sometimes also denoted as $d_{3z^2-r^2}$) is represented by two lobes along the z axes and a donut-shape ring that lies on the xy plane around the other two lobes. These orbitals are shown in Fig. 2.10.

In order to form six-fold coordinated geometry, either d^2sp^3 or sp^3d^2 hybridization is required. The difference between the two is whether the d -electrons are characterised by the same quantum number n as the s - and p -electrons (sp^3d^2) or by the preceding number ($n - 1$), in which case it is d^2sp^3 (Fig. 2.11). Complexes using the sp^3d^2 hybridization are sometimes called outer-orbital complexes and those using the d^2sp^3 orbitals are called inner-orbital complexes.

While covalent bonds are typically formed between pairs of atoms each of which contributes one electron per bond, bonding in transition metal complexes is usually between vacant d - s - p -mixed (or hybridised) orbitals of the metal and LP electrons of ligands (Fig. 2.11, upper panel) giving rise to bonding and antibonding orbitals with σ symmetry around the metal-ligand bond axis. The resulting covalent bond is a dative bond, also called a coordinate covalent bond. For this reason, the transition metal complexes are often called coordination complexes.

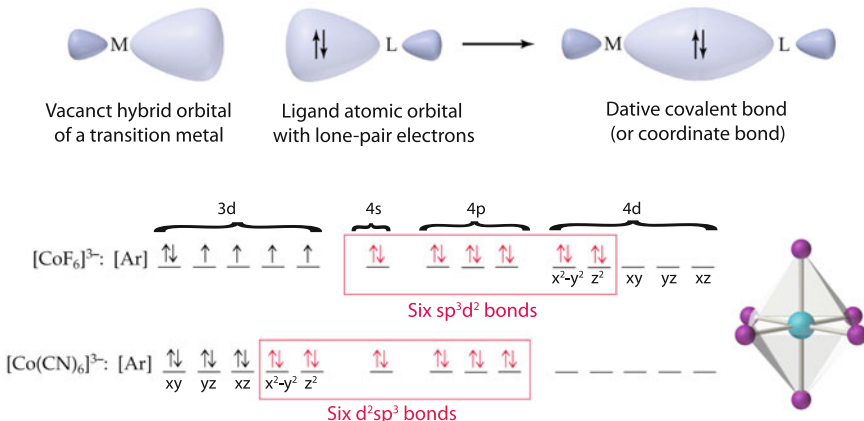


Fig. 2.11 *Top* schematic of the formation of a dative (coordination) bond between a vacant hybridised orbital of a transition metal and LP electrons of ligands. *Bottom* schematic of electrons involved in the formation of octahedrally coordinated complexes $[\text{CoF}_6]^{3-}$ and $[\text{Co}(\text{CN})_6]^{3-}$, using sp^3d^2 and d^2sp^3 hybridizations, respectively. The electrons are shown as arrows, where the opposite arrows correspond to opposite spins. The electrons provided by ligands are shown in red

The valence bond theory allows one to make certain predictions about complex properties. Let us consider cobalt as a case example to explain its magnetic properties. If an outer complex is formed, the $3d$ electrons remain undisturbed, i.e. four electrons will be unpaired and CoF_6^{3-} should be paramagnetic and it is (Fig. 2.11). On the other hand, if an inner complex is formed, the d -electrons are redistributed to provide two vacant orbitals for the coordination bond formation with ligands. As a result, all Co d -electrons become paired and $[\text{Co}(\text{CN})_6]^{3-}$ is expected to be diamagnetic, as it is observed experimentally. At the same time, while the valence bond theory produces two correct alternatives for the number of unpaired electrons, being too simplified it fails in making the choice between them.

2.2.2 Crystal-Field Theory

Additional understanding of transition metal complexes comes from the crystal-field theory. We remind the reader that initially the five d -orbitals are degenerate. If six negative charges are uniformly distributed over the surface of a sphere, the d orbitals remain degenerate, but their energy will be higher due to repulsive electrostatic interactions between the spherical shell of negative charge and electrons in the d -orbitals.

At the same time, when the six negative charges associated with LP electrons of the ligands are brought near the metal atom (ion) in an octahedral array along

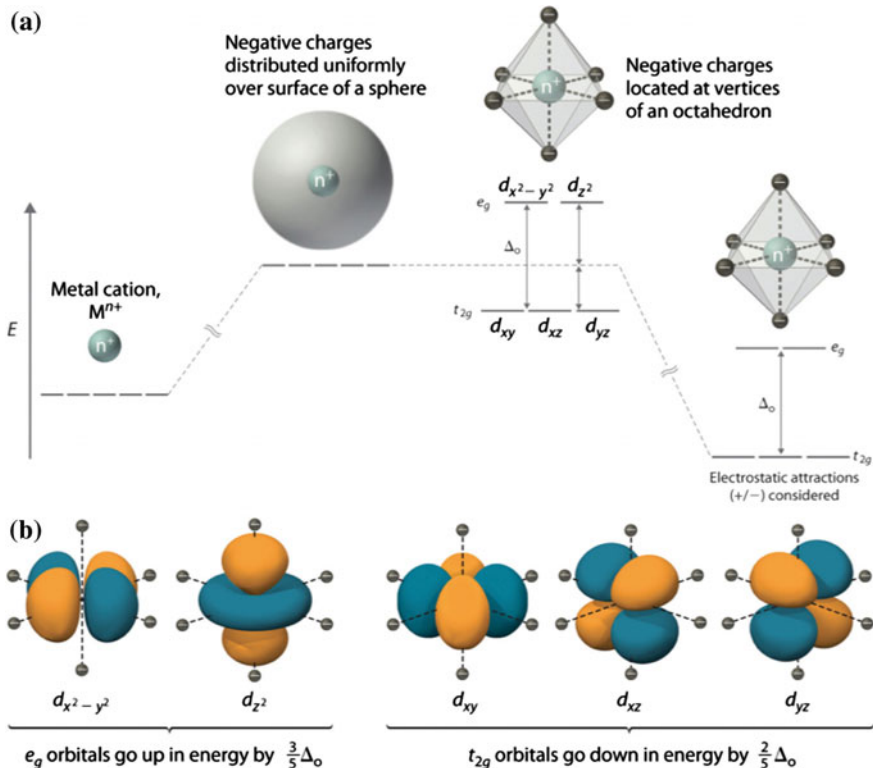
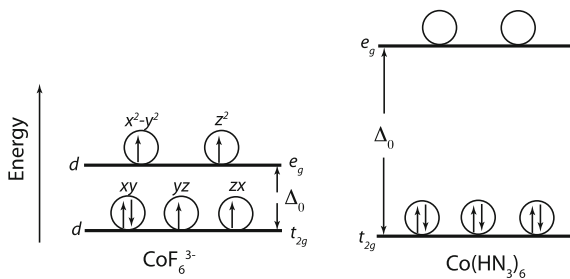


Fig. 2.12 Crystal field splitting of d -orbitals. Reproduced from [28]

the three principal axes, the average energy of the d -orbitals remains unchanged but the degeneracy is lifted. In particular, the d_{z^2} and $d_{x^2-y^2}$ orbitals are most affected because they point directly into the charges. Hence, electrons in these two orbitals have higher energies than those in the d_{xy} , d_{yz} , and d_{xz} orbitals. The net result of this is that the initially five degenerate d -orbitals split into two energy levels separated by a crystal-field splitting energy, Δ_o , as illustrated in Fig. 2.12. The lower level is called the t_{2g} level and the higher level is called the e_g level. The names come from group theory and are associated with the symmetry of the states. The magnitude of the splitting depends on the charge of the metal ion, the position of the metal in the Periodic Table, and the nature of the ligands. Because the splitting of the d orbitals in a crystal field does not change the total energy of the five d -orbitals: the two e_g orbitals increase their energy by $0.6 \Delta_o$, whereas the three t_{2g} orbitals go down in energy by $0.4 \Delta_o$.

In the previous description, only the effect of repulsive electrostatic interaction between electrons in the d orbitals and the six negatively charged ligands was

Fig. 2.13 Strong (left) and weak (right) ligands produce high-spin and the low-spin complexes, respectively



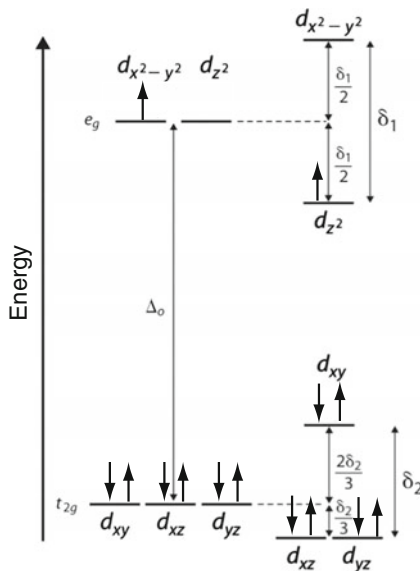
considered, which results in an increase in the total energy of the system and splits the d orbitals. Interactions between the positively charged metal ion and the ligands results in a net stabilization (lowering of the energy) of the system, which decreases the energy of all five d orbitals leaving the splitting unaffected (Fig. 2.12, right).

The crystal-field energy is crucial in determining properties of a complex. Thus, if the splitting energy Δ_o is larger than the correlation energy required to place two electrons with opposite spins onto the same orbital, u_p , the more stable electron configuration for metal ions with the d^n ($n \geq 4$) configuration is the one with the electrons filling the three lower orbitals. Conversely, if $\Delta_o < u_p$, as few electrons as possible will be paired. The relative magnitudes of Δ_o and u_p thus determine the total spin of the system. The former case is referred to as a high-spin complex and the latter case is a low-spin complex (Fig. 2.13). The stronger the electrostatic field created by the ligand, the greater the splitting is. For a series of complexes of metals from the same group in the Periodic Table with the same charge and the same ligands, the magnitude of Δ_o typically increases with increasing principal quantum number: $\Delta_o(3d) < \Delta_o(4d) < \Delta_o(5d)$. On the other hand, for a series of chemically similar ligands, the magnitude of Δ_o decreases as the size of the donor atom increases.

For metal ions that have electron configurations with an odd number of electrons in the e_g orbitals, the single electron (or the third electron) can occupy either one of two degenerate e_g orbitals, i.e. they have a degenerate ground state. According to the Jahn–Teller theorem [29] such systems are not stable. As a consequence, they undergo a distortion that decreases the symmetry and splits the degenerate states. Because the orbital that is pushed up in energy is empty, the net result of this splitting is a decrease in the energy of the system as illustrated in Fig. 2.14. The distortion and resulting decrease in energy are collectively referred to as the Jahn–Teller effect. Note that for systems with an even number of electrons the Jahn–Teller distortion is generally energetically unfavourable.

Finally it should be noted that the crystal-field theory views bonding in complexes as the result of purely electrostatic interactions and considers the effect of ligand charges on energies of metal ion d -orbitals but it does not consider covalent bonds.

Fig. 2.14 The Jahn–Teller Effect. Because the state that moves up in energy due to splitting is empty, the net result is a decrease in the total energy of the system



2.2.3 Ligand-Field Theory

Another step forward is to combine the valence bond theory with the crystal-field theory. Within this approach, called the ligand-field theory, the nine metal orbitals are combined with the six ligand orbitals to produce six bonding orbitals and six antibonding orbitals. The d_{xy} , d_{yz} , and d_{xz} orbitals have a different symmetry that does not combine with σ -like ligand orbitals. These orbitals do not change their energy and are called non-bonding. Electrons, or electron pairs, located in these orbitals are not involved in bonding the metal and ligands.

The corresponding energy diagram is shown in Fig. 2.15 for the example of $\text{Co}(\text{NH}_3)_6^{3+}$. The six bonding orbitals are filled with electron pairs (LPs provided by the ligands). The upper four orbitals are always empty in the ground state. The material's properties are determined by the electron population of the non-bonding level, t_{2g} , and the lowest antibonding level, e_g . It may be interesting to note that while in the crystal-field theory these split orbitals are a result of electrostatic repulsion, in the ligand-field theory this splitting is a consequence of how the molecular orbitals are prepared.

2.2.4 Band Structure Calculations

Electronic band structure of bulk TMDCs was first calculated using augmented spherical wave (ASW) method [30, 31]. The results were found to be in good agreement

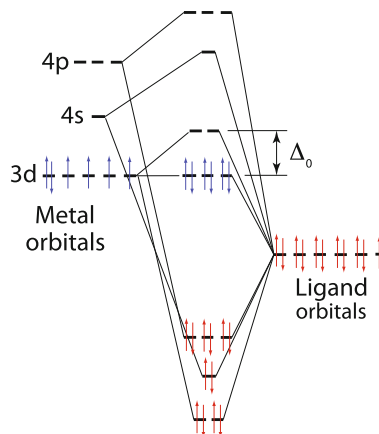


Fig. 2.15 Atomic orbitals of a transition metal and ligands and the corresponding molecular orbitals within the ligand-field theory. The shown electron configuration corresponds to a $\text{Co}(\text{NH}_3)_6^{3+}$ ion

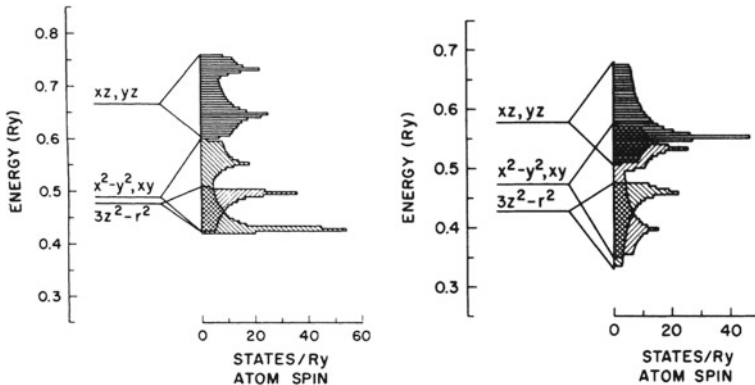


Fig. 2.16 Ligand-field levels and LCAO density-of-states curves for unhybridized d bands in 1T-TaS₂ (left) and 2H-MoS₂ (right) [32]. Copyright 1973 by the American Physical Society. Reprinted with permission

with angle-resolved photoelectron spectroscopy performed by the same authors. It was concluded that MoS₂, MoSe₂, WSe₂ are indirect gap semiconductors with the top of the valence band at Γ and the bottom of the conduction band halfway between Γ and K points. These conclusions are in good agreement with later simulations (see Chaps. 3 and 6).

Finally we mention the relationship between the ligand-field levels and the bands obtained from band structure calculations. It is important to emphasize that the ligand-field levels correspond to the centers of gravity of the appropriate d sub-bands in the periodic crystal and not to the band energies at $k = 0$ [32]. This is illustrated in Fig. 2.16, where the augmented plane-wave (APW)-LCAO¹ results for the tantalum

¹LCAO = linear combination of atomic orbitals

$5d$ bands in $1T\text{-TaS}_2$ are shown alongside with the ligand-field levels relationship to the density-of-states curves for the corresponding d sub-bands, neglecting interband hybridization. Similar APW-LCAO results for the d bands in $2H\text{-MoS}_2$ are shown in Fig. 2.16, where, again, the histograms joining the various ligand-field levels represent the density-of-states curves for the individual molybdenum $4d$ sub-bands, neglecting interband hybridization and interlayer interactions.

2.2.4.1 Density Functional Theory

In order to be able to reproduce the experimental results and possess predictive power, computer simulations should be based on first principles quantum mechanics, i.e. be independent of any empirical parameters, hence the name ab-initio, or first principles, simulations.

An exact ab-initio solution of the Schrödinger equation for a many-body system comprising nuclei and ions is virtually impossible. In order to study such systems with realistic computational costs, a range of approximations has been introduced [33]. One of the most successful approaches based on the single particle approximation is the density functional theory (DFT). Using this theory, the properties of a many-electron system can be determined by using functionals, i.e. functions of another function, which in this case is the spatially dependent electron density. DFT is among the most popular and versatile methods currently available in condensed-matter computational physics and chemistry.

The major problem with DFT is that the exact functionals for exchange and correlation are not known except for the free electron gas. However, approximations exist which permit accurate calculations of certain physical quantities. In physics the most widely used approximation is the local-density approximation (LDA), where the functional depends only on the density at the coordinate where the functional is evaluated:

$$E_{XC}^{LDA}[n] = \int \epsilon_{XC}(n) \cdot n(\mathbf{r}) d^3r \quad (2.3)$$

An extension of LDA is the generalised gradient approximation (GGA) which additionally takes into account the gradient of the density at the same coordinate:

$$E_{XC}^{GGA}[n] = \int \epsilon_{XC}(n, \nabla n) \cdot n(\mathbf{r}) d^3r \quad (2.4)$$

Using the latter (i.e. GGA), very good results for molecular geometries and *ground-state* energies (band structures) were achieved.

Use of DFT simulations allows one to determine contributions from different electrons into any particular band. For example, the orbital character of different bands for $2H\text{-MoS}_2$ were studied in [34], where it was demonstrated that the valence and conduction bands are made by hybridization of the $d_{3z^2-r^2}$, d_{xy} , and $d_{x^2-y^2}$ orbitals of the transition metal, and the p_x , p_y and p_z orbitals of the chalcogen atoms.

Very similar results were obtained in [35], where it was further noted that the conduction band minimum at the K -point, as well as the valence band maximum at the Γ -point are primarily composed of the Mo d_{z^2} and S p_z states, while the conduction band minimum along $K - \Gamma$ and the valence band maximum at the K -point are dominated by Mo $d_{x^2-y^2}$, d_{xy} and S p_x/p_y states. The Mo d_{xz}/d_{yz} states are located far off the Fermi energy.

One problem relevant to TMDCs is that standard DFT calculations do not describe the vdW interaction. The problem in describing the vdW interactions is that DFT conventionally applies local approximations, while the vdW interaction is a non-local correlation effect. Ways to empirically include vdW interaction into DFT simulations are described in more detail elsewhere (see Sect. 6.1.9).

References

1. W. Fischer, A second note on the term “chalcogen”. *J. Chem. Ed.* **78**(10), 1333 (2001)
2. W.B. Jensen, A note on the term “chalcogen”. *J. Chem. Ed.* **74**(9), 1063 (1997)
3. W. Jorissen, H. Bassett, A. Damiens, F. Fichter, H. Remy, Rules for naming inorganic compounds: report of the committee of the international union of chemistry for the reform of inorganic chemical nomenclature, 1940. *J. Amer. Chem. Soc.* **63**(4), 889 (1941)
4. G. Lucovsky, R. White, Effects of resonance bonding on the properties of crystalline and amorphous semiconductors. *Phys. Rev. B* **8**(2), 660 (1973)
5. K. Shportko, S. Kremers, M. Woda, D. Lencer, J. Robertson, M. Wuttig, Resonant bonding in crystalline phase-change materials. *Nat. Mater.* **7**(7), 653 (2008)
6. M. Kastner, Bonding bands, lone-pair bands, and impurity states in chalcogenide semiconductors. *Phys. Rev. Lett.* **28**(6), 355 (1972)
7. M. Kastner, H. Fritzsch, Defect chemistry of lone-pair semiconductors. *Philos. Mag. B* **37**(2), 199 (1978)
8. A.V. Kolobov, P. Fons, J. Tominaga, S.R. Ovshinsky, Vacancy-mediated three-center four-electron bonds in GeTe-Sb₂Te₃ phase-change memory alloys. *Phys. Rev. B* **87**, 165206 (2013)
9. N. Mott, Electrons in disordered structures. *Adv. Phys.* **16**(61), 49 (1967)
10. N.F. Mott, E.A. Davis, *Electronic Processes in Non-Crystalline Materials*, 2nd edn. (Clarendon Press, Oxford, 1979)
11. P. Anderson, Model for the electronic structure of amorphous semiconductors. *Phys. Rev. Lett.* **34**(15), 953 (1975)
12. R.A. Street, N.F. Mott, States in the gap in glassy semiconductors. *Phys. Rev. Lett.* **35**(19), 1293 (1975)
13. M. Kastner, D. Adler, H. Fritzsch, Valence-alternation model for localized gap states in lone-pair semiconductors. *Phys. Rev. Lett.* **37**(22), 1504 (1976)
14. A. Kolobov, M. Kondo, H. Oyanagi, R. Durny, A. Matsuda, K. Tanaka, Experimental evidence for negative correlation energy and valence alternation in amorphous selenium. *Phys. Rev. B* **56**(2), R485 (1997)
15. A. Kolobov, M. Kondo, H. Oyanagi, A. Matsuda, K. Tanaka, Negative correlation energy and valence alternation in amorphous selenium: an *in situ* optically induced ESR study. *Phys. Rev. B* **58**(18), 12004 (1998)
16. M. Krbał, A.V. Kolobov, P. Fons, J. Tominaga, S.R. Elliott, J. Hegedus, T. Uruga, Intrinsic complexity of the melt-quenched amorphous Ge₂Sb₂Te₅ memory alloy. *Phys. Rev. B* **83**(5), 054203 (2011)
17. M. Xu, Y. Cheng, H. Sheng, E. Ma, Nature of atomic bonding and atomic structure in the phase-change Ge₂Sb₂Te₅ glass. *Phys. Rev. Lett.* **103**(19), 195502 (2009)

18. A.V. Kolobov, M. Krbal, P. Fons, J. Tominaga, T. Uruga, Distortion-triggered loss of long-range order in solids with bonding energy hierarchy. *Nat. Chem.* **3**(4), 311 (2011)
19. R. Bate, D. Carter, J. Wrobel, Paraelectric behavior of PbTe. *Phys. Rev. Lett.* **25**, 159 (1970)
20. K.V. Mitrofanov, A.V. Kolobov, P. Fons, M. Krbal, T. Shintani, J. Tominaga, T. Uruga, Local structure of the SnTe topological crystalline insulator: Rhombohedral distortions emerging from the rocksalt phase. *Phys. Rev. B* **90**, 134101 (2014)
21. E.S. Božin, C.D. Malliakas, P. Souvatzis, T. Proffen, N.A. Spaldin, M.G. Kanatzidis, S.J. Billinge, Entropically stabilized local dipole formation in lead chalcogenides. *Science* **330**(6011), 1660 (2010)
22. M. Chhowalla, H.S. Shin, G. Eda, L.J. Li, K.P. Loh, H. Zhang, The chemistry of two-dimensional layered transition metal dichalcogenide nanosheets. *Nat. Chem.* **5**(4), 263 (2013)
23. J. Wilson, A. Yoffe, The transition metal dichalcogenides discussion and interpretation of the observed optical, electrical and structural properties. *Adv. Phys.* **18**(73), 193 (1969)
24. K. Tanaka, K. Shimakawa, *Amorphous Chalcogenide Semiconductors and Related Materials* (Springer Science & Business Media, Berlin, 2011)
25. S. Raoux, M. Wuttig (eds.), *Phase Change Materials: Science and Applications* (Springer Science & Business Media, Berlin, 2010)
26. A.V. Kolobov, J. Tominaga, *Chalcogenides: Metastability and Phase Change Phenomena* (Springer Science & Business Media, Berlin, 2012)
27. IUPAC, Compendium of Chemical Terminology (the “Gold Book”), 2nd ed. (1997)
28. B. Averill, P. Eldredge, *General Chemistry: Principles, Patterns, and Applications* (adapted by the Saylor Foundation (<http://www.saylor.org/books>) under a Creative Commons Attribution-NonCommercial-ShareAlike 3.0 License, 2011)
29. R. Englman, *The Jahn-Teller Effect in Molecules and Crystals* (Wiley-Interscience, New York, 1972)
30. R. Coehoorn, C. Haas, R. De Groot, Electronic structure of MoSe₂, MoS₂, and WSe₂. II. the nature of the optical band gaps. *Phys. Rev. B* **35**(12), 6203 (1987)
31. R. Coehoorn, C. Haas, J. Dijkstra, C. Flipse, R. De Groot, A. Wold, Electronic structure of MoSe₂, MoS₂, and WSe₂. I. band-structure calculations and photoelectron spectroscopy. *Phys. Rev. B* **35**(12), 6195 (1987)
32. L. Mattheiss, Band structures of transition-metal-dichalcogenide layer compounds. *Phys. Rev. B* **8**(8), 3719 (1973)
33. R.M. Martin, *Electronic Structure: Basic Theory and Practical Methods* (Cambridge University press, Cambridge, 2004)
34. E. Cappelluti, R. Roldán, J. Silva-Guillén, P. Ordejón, F. Guinea, Tight-binding model and direct-gap/indirect-gap transition in single-layer and multilayer MoS₂. *Phys. Rev. B* **88**(7), 075409 (2013)
35. Y. Cheng, Z. Zhu, U. Schwingenschlögl, Role of interlayer coupling in ultra thin MoS₂. *RSC Advances* **2**(20), 7798 (2012)

Chapter 3

Bulk TMDCs: Review of Structure and Properties

Bulk (or 3D) TMDCs have been known and used for a very long time, but most of the older applications (i.e. as solid lubricants) were related to their unique mechanical properties determined by the presence of van der Waals bonding between the layers. It is only recently, following the success of graphene, that TMDCs moved to the forefront of solid state research, with main interest being concentrated on mono and few-layer structures. At the same time, the interest to 3D TMDCs also acquired momentum. In this chapter we describe the structure and properties of 3D TMDCs, placing accent on (i) those issue that are important to understand 2D TMDCs and (ii) the latest results that were not reviewed previously.

3.1 Atomic and Electronic Structure

Layered TMDCs have the generic formula MX_2 , where M stands for a metal and X represents a chalcogen. The interatomic interaction within layers is covalent in nature, while the layers are held together by weak van der Waals (vdW) forces. The presence of the latter allows the crystals to cleave easily similar to graphene. The vdW forces across the gap are stronger in proportion in tellurides than in the sulphides [1]. One can see here an analogy with the relative shortening of the interchain distances with respect to the intrachain distances in trigonal Te compared to trigonal Se [2].

3.1.1 Structure of Individual Triple Layers

The structure of a typical layered TMDC is shown in Fig. 3.1. In this structure, each layer consists of three atomic planes with a typical thickness of 6–7 Å with a hexagonally packed plane of metal atoms sandwiched between two planes of chalcogen

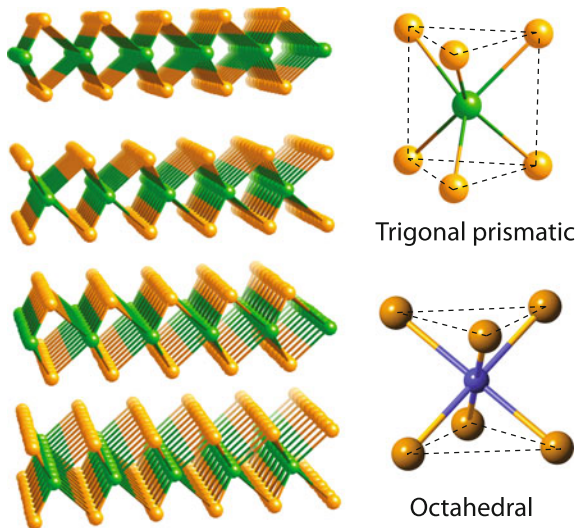


Fig. 3.1 Left a three-dimensional representation of a typical layered MX_2 structure, with the metal atoms shown in *green* and the chalcogen atoms shown in *orange*. The local coordination of the metal species can be of the two types shown in the right panel, viz., trigonal prismatic (*top*) and octahedral (*bottom*)

atoms. In some cases, the hexagonal in-plane geometry of metal ions is distorted and the layers are not planar (see Sect. 3.1.3 below). Depending on the context, and following the original publications, we shall sometimes refer to such layers as triple layers, or sandwiches, but in most cases they will be called monolayers (or single layers).

While in transition metal complexes bonding is usually considered between empty orbitals of the metal and lone-pairs of ligands, in TMDCs, the metal atoms provide four electrons to fill the bonding states and the transition metal and chalcogens can be ascribed a formal charge of +4 and -2, respectively [3]. As a result, the coordination around chalcogenides is lopsided, which leads to the marked cleavage properties perpendicular to the hexagonal/trigonal symmetry axis [1]. The absence of dangling bonds makes the surfaces very stable and non reactive. The distribution of the valence electrons in a TMDC is schematically shown in Fig. 3.2a. While in a simplified picture, the non-bonding electrons may be considered to be located on the s -orbital, with chalcogen pure p -orbitals participating in making the metal-chalcogen bonds, CDD isosurfaces generated using DFT theory suggest that the lone-pair electrons of chalcogen atoms, are in fact located on sp^3 -hybridised orbitals (Fig. 3.2b).

Metal atoms within a triple layer are six-fold coordinated and their bonding geometry can be either trigonal prismatic or octahedral, as illustrated in the right panel of Fig. 3.1. Note that in the trigonal prismatic arrangement the two chalcogenide planes forming a slab are stacked directly above each other, while in the octahedral arrangement they stagger.

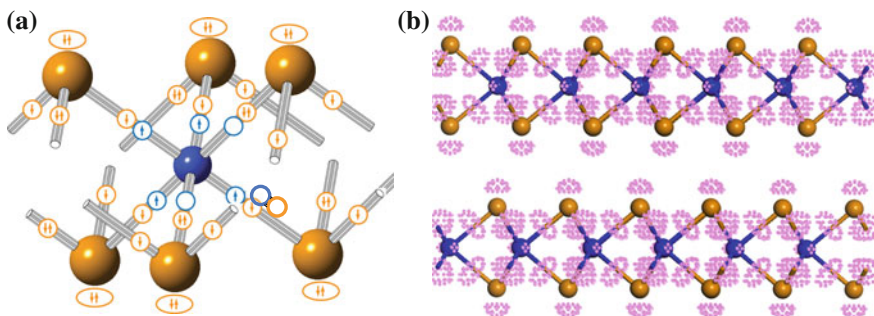


Fig. 3.2 **a** A fragment of an octahedral TMDC structure demonstrating the distribution of valence electrons. The metal atom is shown in *blue* and the chalcogen atoms are shown in *orange*. The electrons provided by each species are shown as *arrows* of a matching *colour* using the following convention. Unpaired electrons used for covalent bonding are shown as a single arrow in a *circle*. Lone-pair electrons used to form dative (coordinate) bonds are shown as two arrows of opposite directions in a *circle*, non-bonding lone-pair electrons are shown as two arrows in an *oval*. Finally, vacant orbitals are shown as empty *circles*. Note that the transition metal atom provides four bonding electrons plus two vacant orbitals. **b** DFT-relaxed structure of MoTe₂ and CDD isosurfaces (*pink*) demonstrating charge accumulation in the vdW gap, associated with *sp*³-hybridization of chalcogen atoms

The preferred phase adopted by TMDCs depends predominantly on the *d*-electron count of the transition metals, although a certain dependence on the relative size of the atoms plays a role. Group 4 (or Group IVB) metals all have octahedral structures. Most of group 5 metals also have octahedral structures, while some have trigonal-prismatic structures; the reverse is true for the group 6 metals. In group 7 one finds again octahedral structures, although in this case they are distorted. Finally, group 10 TMDCs are all in octahedral structure. The physico-chemical reasons for the choice of the coordination will be discussed below (see Sect. 3.1.7). It is also interesting to note that alkali metal intercalation induces phase changes in some TMDCs. For example, Li intercalation in 2*H*-MoS₂ results in it being transformed to 1*T*-MoS₂, while the opposite (1*T*–2*H*) transformation has been observed in TaS₂. The observed destabilisation of the original phase is usually attributed to the *d*-electron count as will be discussed in more detail later (see Sects. 3.1.7 and 5.1.2 below).

3.1.2 Bulk Structural Polymorphs

TMDCs are usually found in three polymorphs called 1*T*, 2*H* and 3*R*. Here the numbers stand for the number of layers in the unit cell and the letters indicate symmetry (*T*—trigonal, *H*—hexagonal, and *R*—rhombohedral). These polymorphs are schematically shown in Fig. 3.3. The unit cell is defined with the *c* axis perpendicular to the layers, and the *a* and *b* axes along the minimal chalcogen–chalcogen distance. Due to the hexagonal chalcogen packing and the compact interlayer stacking only octahedral and tetrahedral interstitial sites are present in the vdW gap.

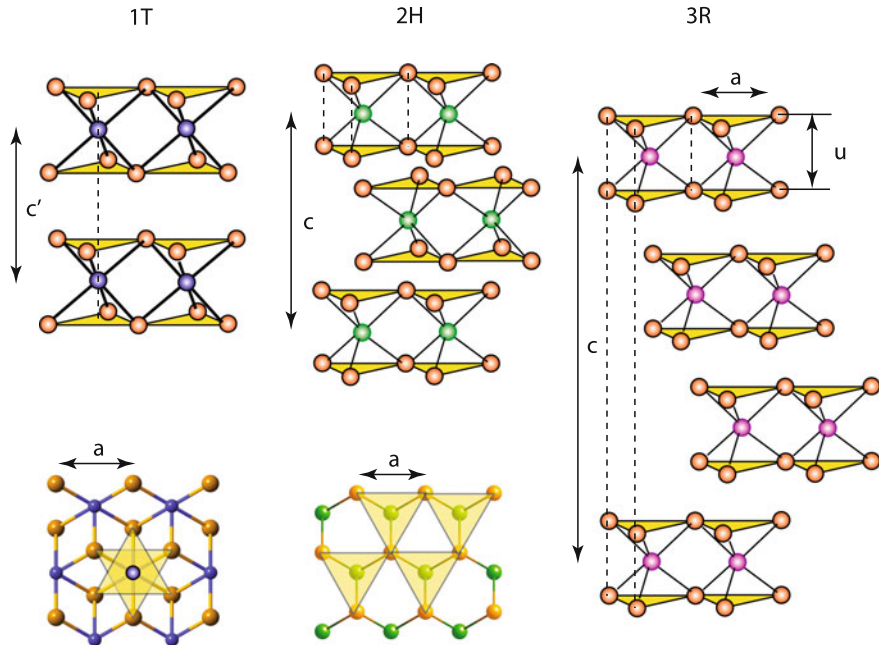


Fig. 3.3 Schematics of the structural polytypes of TMDC from *left to right* 1T (tetragonal symmetry, one layer per repeat, octahedral coordination of the metal), 2H (hexagonal symmetry, two layers per repeat, trigonal prismatic coordination) and 3R (rhombohedral symmetry, three layers per unit cell, trigonal prismatic coordination). The yellow-filled triangles highlight the spatial position of the chalcogen atoms. For the 1T and 2H polytypes, top views are additionally shown. Note that in these images the yellow triangles highlight spatial positions of the chalcogen species *within just one layer*

While these polymorphs are most common, other polymorphs also exist, as shown in Fig. 3.4, which shows side views of 11 different polymorphs [4]. Note, that the 2H polymorph can exist in three different modifications, with $2H_a$ and $2H_c$ being most common. These two forms have different stacking symmetries. In $2H_a$ (AbA CbC) stacking, transition metal atoms in one layer are located on top of transition metal atoms of the neighbouring layer. This polytype is reported to occur in NbSe_2 , NbS_2 , TaS_2 , and TaSe_2 crystals. The $2H_c$ polymorph is characterised by the CaC AcA stacking, i.e. any transition metal atom is located on top of two chalcogenides atoms of the subsequent layer. This polytype occurs in MoS_2 , WS_2 , MoSe_2 , and WSe_2 crystals. The $2H_b$ polytypes are obtained for the nonstoichiometric compounds $\text{Nb}_{1+x}\text{Se}_2$ and $\text{Ta}_{1+x}\text{Se}_2$, with the excess metal atoms intercalated in the vdW interlayer gap. It should be noted that the notations for different 2H polytypes are not unique, which can sometimes be confusing (see e.g. different notations used in [5]). Experimental lattice parameters of selected TMDCs are summarised in Table 3.1.

Sometimes, the same TMDC can be found in multiple polymorphs. For example, natural MoS_2 is usually found in the 2H phase, while synthetic MoS_2 often

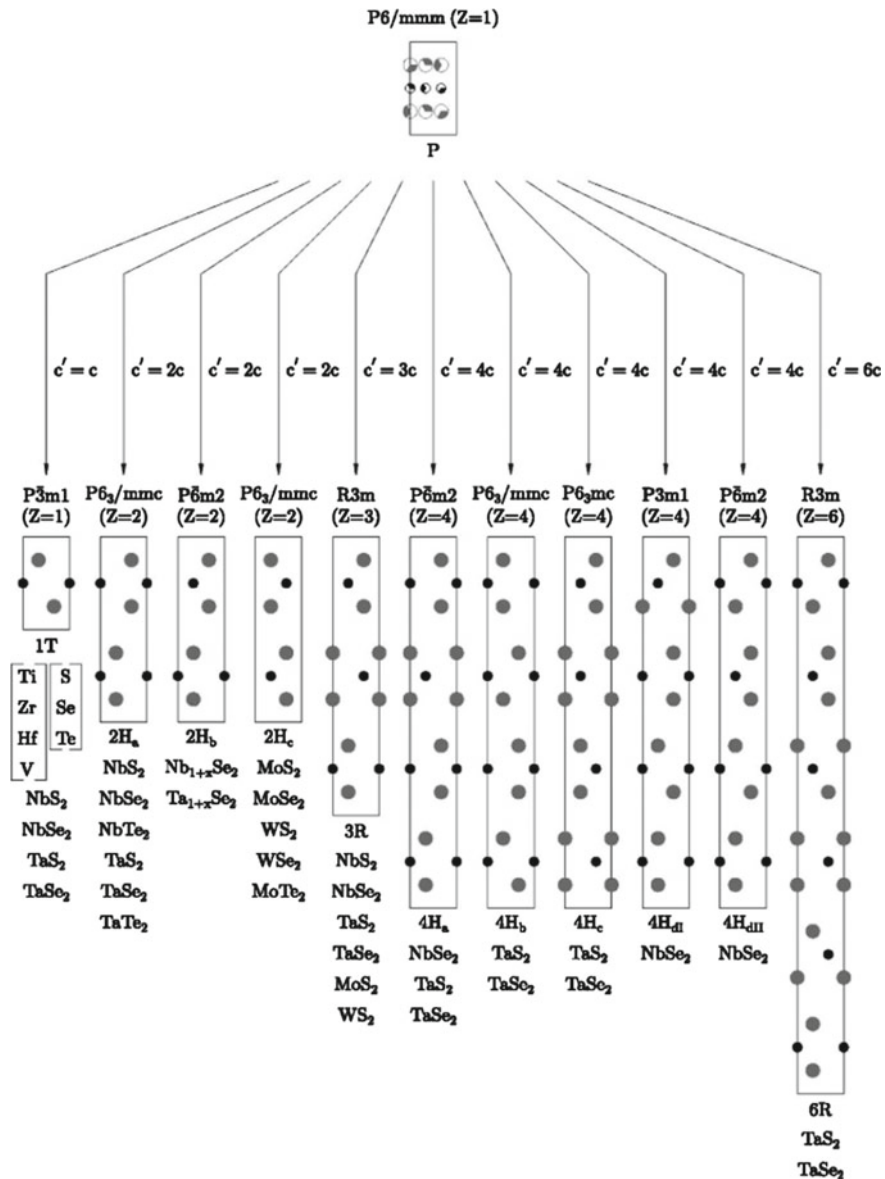


Fig. 3.4 Ordering mechanisms leading to the formation of the 11 polytype structures observed in TMDC materials. The polytypes are shown as $(11\bar{2}0)$ projections of their hexagonal structures. Small circles represent the metal atoms and large circles the chalcogens. The partial filling of the circles for the P structure indicates the positional occupancy [4]. Copyright 2004 by the American Physical Society. Reprinted with permission

contains the *3R* phase [3]. The latter is generally formed at high pressure and temperature (above 40 kbar and 1500 °C for MoSe₂ [7]). It should be noted that in both cases the metal coordination is trigonal prismatic underlying the fact that the metal coordination within sandwiches is not affected by the stacking sequence.

3.1.3 Distorted Structures

Some TMDCs develop a periodic distortion of the crystal lattice through the formation of chains of metal atoms, similar to charge-density waves. An example of TMDCs with a distorted octahedral structure is WTe₂, whose structure is shown in Fig. 3.5. with W atoms forming zig-zag chains. In a sense, this structure can be described as one-dimensional. Different from other group-VI TMDCs that are semiconductors, WTe₂ is a layered semimetal [8]. It is interesting to note that a very

Table 3.1 Experimental lattice parameters for some TMDCs after [6]

Material	<i>a</i> , Å	<i>c</i> , Å
MoS ₂	3.162	12.29
MoSe ₂	3.288	12.93
WS ₂	3.162	12.37
WSe ₂	3.286	12.99

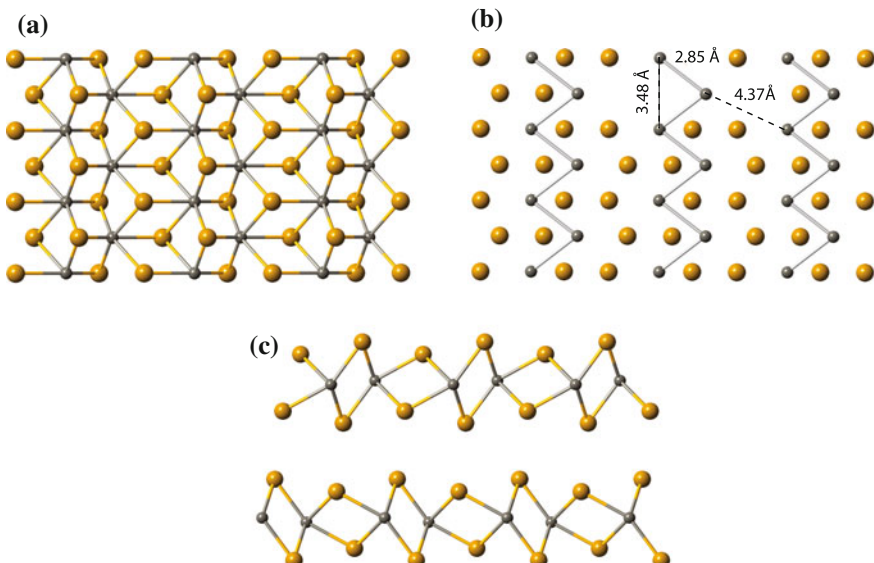


Fig. 3.5 The WTe₂ structure, Te atoms—orange, W atoms—gray. **a** A top view on a single layer with W-Te covalent bonds shown, **b** the same view demonstrating the W-W zig-zag chains with W-W distances shown; note that some of the Te atoms were made invisible in order to indicate the distances, **c** a side view of the bulk material (two layers are shown) with W-Te bonds shown

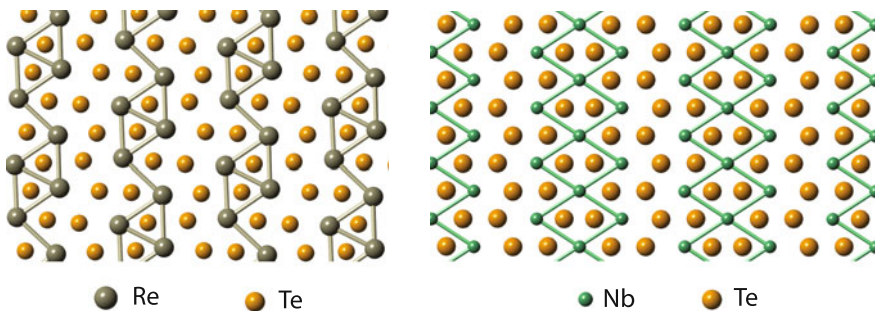


Fig. 3.6 Top views of ReTe_2 (left) and NbTe_2 (right), demonstrating the formation of metal–metal chains of different configuration. The metal–chalcogen bonds are not shown

similar structure is acquired by MoTe_2 (whose low-temperature phase is trigonal prismatic) at temperatures exceeding $900\text{ }^\circ\text{C}$ [9].

Different kinds of metal-ion clustering exist in ReSe_2 , ReTe_2 and NbTe_2 . The metal–metal chains for these structures are shown in Fig. 3.6. Thus, ReSe_2 and ReTe_2 crystallize in the triclinic system, with four formula units per unit cell and the bulk space group $P\bar{1}$. The structure was determined by X-ray diffraction and consists of one-dimensional chains or ribbons of rhenium atoms arranged in linked Re_4 “lozenge” or “diamond” shapes within the plane [10–12]. This arrangement can be considered as a distortion of the metal ions away from their ideal octahedral sites and the driving force for this distortion is usually discussed in terms of Peierls or Jahn–Teller distortions [13, 14]. Interestingly, the metal–metal distances in the resulting Re_4 units are comparable to, or smaller than, those in bulk rhenium metal. The one-dimensional arrangement of rhenium atoms leads to highly anisotropic properties in the layer plane, as revealed by studies of optical transmission and reflection normal to the layer plane and by electron transport [15–17]. A different kind of metallic chain is formed in NbTe_2 (Fig. 3.6, right panel). At the same time, the chalcogenide sheets slightly buckle to accommodate these distortions. This effect can play a role if ReSe_2 or ReTe_2 triple layers are used as a component of multilayer heterostructures.

In group IVB TMDCs, the structures are often distorted with the formation of charge density waves. This issue will be discussed later in a dedicated section. Regarding the issue of the distortion mechanism in group IVB TMDCs, Kertesz and Hoffman [13] provide the following arguments related to ReTe_2 . It was pointed out that the splitting at small distortion values does not occur at the Fermi level, although close to it. But the level splitting is large enough to move the Fermi level, whose exact position is not essential for the actual distortion to occur.

This is in contrast to other distortions which are known as Peierls distortion and periodic lattice distortions coupled to charge-density. In this case, the periodicity of the distortion is related to the particular dimensions and forms at the Fermi surface, which is often not commensurate with the periodicity of the lattice. These instabilities are most easily visualized in the language of energy band theory: the existence of large parallel ‘nesting’ regions of the Fermi level separated by a single wave vector

$2k_F$ leads to a strong scattering of the electrons with momentum $\pm k_F$, splitting their energy strongly. Thus, an energy gap opens up and the system is stabilized. The periodicity of the potential, and thus that of the periodic lattice distortion, is tied in this picture to the particular k_F [13]. It was concluded that the case of ReSe_2 is different in that neither the shape of the Fermi level nor its energy is determining the particular ‘clustering’ distortion of this semiconductor [13].

3.1.4 Charge Density Waves

Charge-density waves (CDWs) in low-dimensional solids are a rather old but still very challenging research topic. It is now some 40 years since CDWs in the TMDC were discovered and this class of layered crystals initiated the popularization of the concept of a CDW [18–21].

As an example we consider CDW states in $1T\text{-TaS}_2$. Near $T_{c0} = 550\text{ K}$, it forms an incommensurate (IC) CDW with an associated lattice distortion. Upon cooling, these modulations sharpen to form star-shaped polaron clusters (Fig. 3.7a). Their ordering is thought to be responsible for a variety of phases, causing a transition to a nearly commensurate (NC) state for $T < T_{c1} = 350\text{ K}$, and a hysteretic first-order transition to a gapped commensurate (C) phase near $T_{c2} = 183\text{ K}$. Upon heating, the system develops a triclinic (T) stripe-like ordered state around 223 K , which reverts to the NC state at $T = 283\text{ K}$ [22]. In the C-CDW, thirteen atoms form a star of David, constructing a triangular superlattice and leading to band reconstruction, whose half-filled band is stabilised by developing Mott insulator state. In the NC-CDW state such stars organise into local C-CDW domains. The transitions between different CDW states can be thickness and gate-controlled [23, 24].

Although much has been learnt about the structural and electronic properties of TMDC and about the nature of their various CDW phases and some important aspects of the CDW phase transition in these materials are captured qualitatively by models discussed in terms of Peierls instability, giant Kohn anomaly, Fermi level band nesting, Jahn–Teller effect or excitonic insulator states, profound understanding of how and why the CDWs in these systems are formed is still missing. In some of the recent work, the important role of strong electronic coupling was stressed [25–28] and a preformed excitonic liquid route was also explored [29, 30]. Some insights were also obtained from time-domain classification of charge-density wave insulators [31] where time-resolved ARPES was used to access relative contributions of electron-electron and electron-phonon interactions to electronic order in momentum space. For a recent review on the origin of CDW in select TMDCs the interested reader is referred to [32].

It is interesting to note that exposure of $1T\text{-TaS}_2$ to a femtosecond laser pulse can induce a transition into a “hidden” state with much lower resistance [33], that was associated with a different kind of clustering (Fig. 3.7b). The original C-CDW phase could be recovered by annealing. Switching between different conductivity states in $1T\text{-TaS}_2$ can also be achieved electronically [34].

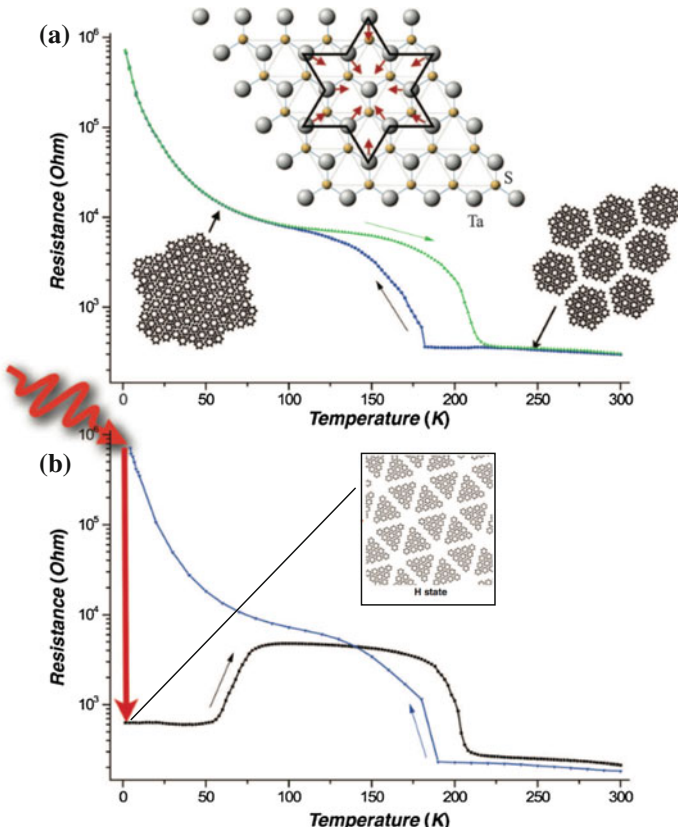


Fig. 3.7 Resistivity switching of 1T-TaS₂ by a 35-fs laser pulse at 800 nm. **a** Temperature dependence of the four-probe resistance on temperature cycling; blue and green curves are measured on cooling and warming, respectively. The sketches show the lattice distortions associated with an individual polaron (top) and their ordering in the NC (high T) and C (low T) states. **b** The drop of resistance at 1.5 K after a single pulse (red arrow); the blue curve is the resistance measured on cooling. Upon heating, the resistance reverts between 60 and 100 K (black curve) [33]. Reprinted with permission from AAAS

3.1.5 Van der Waals Interlayer Bonding

We would like to start by reminding the reader that in physical chemistry the term ‘vdW interaction’ is typically used to describe the sum of the attractive or repulsive forces between molecular entities (or between groups within the same molecular entity) other than those due to bond formation or to the electrostatic interaction of ions or ionic groups with one another or with neutral molecules. The term includes: dipole–dipole, dipole–induced dipole and London (instantaneously induced dipole–induced dipole) forces. The term is sometimes used loosely for the totality of non-specific attractive or repulsive intermolecular forces [35]. Hence, in most cases the

term ‘van der Waals bonding’ has no further meaning than the bonding between the triple layers being not covalent and significantly weaker than the covalent intralayer bonds. Zallen et al. [36] note that “the assumption of vdW forces is usually made in the absence of better information and is an admission of ignorance about the detailed nature of the intermolecular interaction”. The experimental evidence for the much weaker interlayer bonding compared to intralayer bonds comes from Raman scattering (see e.g. [37, 38]) and, of course, from the fact that these materials can be easily exfoliated.

The vdW energy, i.e. the energy required to exfoliate layered crystals, or the cost of removing a single layer from the surface of the bulk compound, has been estimated from both experiments [39, 40] and simulations [41, 42]. Experimental values for MoS₂, WS₂ and MoTe₂ obtained from techniques such as inverse gas chromatography were in a range of 45–120 mJ/m⁻² [39, 40] being comparable to the surface energy of graphene. This can be compared with the simulation results obtained using advanced calculation techniques, where the interlayer energies for various TMDCs were found to be in a rather narrow range of 13–21 meV/Å² [43]. ($1\text{J} = 6.24 \times 10^{18} \text{ eV}$) It was further found that the exfoliation energy is very close to the interlayer binding energy. Distribution of binding energies for various vdW compounds is shown in Fig. 3.8 (left). It should also be noted that the exfoliation energy depends on the thickness of the “bulk” phase (Fig. 3.8 (right)). Similar results, both qualitatively and quantitatively, were also obtained in [44–46].

It may be interesting to note that while computer simulations give very similar interlayer bonding energies for MoS₂ and MoTe₂, the experimental surface energies are significantly larger for the latter, which is reminiscent of the stronger interchain

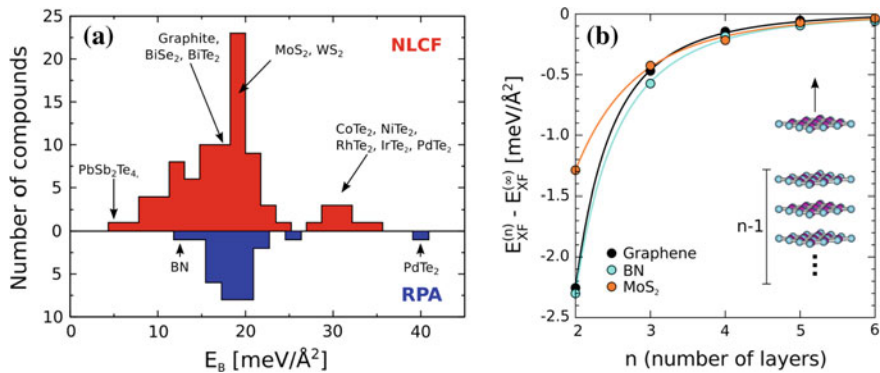


Fig. 3.8 **a** Distribution of binding energies of TMDCs estimated using two different methods (NLCF and RPA, see the original paper for details). The vast majority of the compounds fall in the interval 13–21 meV/Å². Some particular compounds are marked. **b** Energy required for exfoliation of a single layer from a multilayer structure as a function of the number of layers n as shown schematically in the inset [43]. Copyright 2012 by the American Physical Society. Reprinted with permission

interactions in trigonal Te versus Se [47]. It is also interesting to note [40] that the experimental values of the surface energy are lower than the simulation predictions.

There are some indications that interlayer coupling may be weaker in structures with metal chains and consequently buckled chalcogen sheets. Thus comparison of the interlayer energy in MoS₂ and ReS₂ using DFT simulations showed that the interlayer bonding is significantly (about an order of magnitude) weaker in ReS₂ [48]. While the authors used the GGA-PBE functional that does not include vdW interaction (see Sect. 6.1.9 below), the observed difference is very large and may be real.

It is interesting to note that despite the presence of vdW bonds TMDCs typically possess a very high melting point exceeding 1000 °C, e.g. $T_{\text{MoS}_2}^m = 1185^\circ\text{C}$, and then only with decomposition [1]. This is in stark contrast to other chalcogenide materials with vdW bonds. For example, Se, whose structure consists of covalently bonded chains (trigonal Se) or rings (monoclinic Se) held together by weak vdW forces, melts at 220 °C. As a result of melting, the interchain interaction is broken but the chains—and the semiconducting properties—persist above the melting point. The issue of the controversy between the presence of vdW bonds alongside with the very high melting point was addressed in [38] but no definitive explanation was given.

3.1.6 Group Theory Analysis

Group theory provides a valuable theoretical tool that can be used to understand the selection rules for optical transitions, to find the eigenvectors for lattice vibrations, and to identify the lifting of degeneracies due to external symmetry-breaking perturbations [49, 50]. Group theory has been used to describe the structure of TMDCs in the bulk form for different polytypes [1, 4], and in the few-layer 2H_c polytype for zone center phonons (at the Γ point of the Brillouin zone) [5, 51, 52] as well as for the electronic structure at the Γ and K points [53], as well as for a more detailed understanding of nonlinear optical processes [54]. A detailed group theory analysis of both bulk TMDCs and few-layer structures for the 2H and 1T polymorphs has been performed in [55] and below we present the main results of this work.

3.1.6.1 Real Space Symmetry

2H Polytype

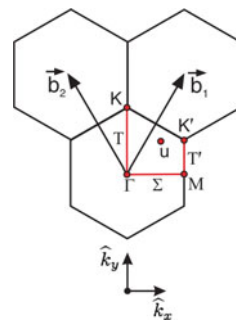
As mentioned above, the 2H bulk polytype can assume two major forms with different stacking symmetries: 2H_a (or /AbA CbC/ stacking), and 2H_c (/CaC AcA/ stacking). Both polytypes belong to the nonsymmorphic hexagonal space group $P6_3/mmc$ [1] (or D_{6h}^4 in Schönflies notation). The primitive unit cell for the bulk has six atoms. The Wyckoff positions for the 2H bulk polytypes, as well as the number of structural formulas Z in the unit cell are given in Table 3.2. The symmetry operations of odd and even layer structures for 2H TMDCs are described in Chap. 7.

Table 3.2 Number of structural formulas (Z) in the unit cell and Wyckoff positions for the 2H and 1T polytypes

Polytype	2H _a	2H _c	1T
No. of structural formulas, Z	2	2	1
Wyckoff positions	M(2b) X(4f)	M(2c) X(4f)	M(1a) M(1d)

One structural formula comprises one transition metal (M) and two chalcogen atoms (X₂)

Fig. 3.9 The Brillouin zone symmetries: Γ , K , K' , and M are high-symmetry points; T , T' , and Σ are high-symmetry lines, and u denotes the symmetry for a generic point. \vec{b}_1 and \vec{b}_2 denote the in-plane reciprocal lattice vectors [55]. Copyright 2014 by the American Physical Society. Reprinted with permission



1T Polytype

The 1T polytype is constructed by piling up single layers, where each subsequent layer is exactly the same as the previous one, with one transition metal atom (or chalcogen atom) located on top of another transition metal atom (or chalcogen atom), in an octahedral coordination. In bulk TMDC, the stacking of the 1T polytype is /AbC/AbC (see Fig. 3.3) and it belongs to the $P\bar{3}m1$ (or D_{3d}^3) symmorphic space group. The unit cell comprises three atoms. The Wyckoff positions for the 1T polytype TMDCs are given in Table 3.2.

Different from the 2H polytype where symmetry in few layer structures depend on the number of layers (odd vs. even), in the 1T polytype, because all layers are identical, the symmetry operations do not change by increasing the number of layers.

3.1.6.2 Group of the Wave Vector

The reciprocal space high-symmetry points and directions for the 2H and 1T polytypes are shown in Fig. 3.9. Considering that \vec{a}_1 and \vec{a}_2 are the primitive vectors of the real 2D lattice described by 3.1, the reciprocal lattice vectors \vec{b}_1 and \vec{b}_2 are described by 3.2 and shown in Fig. 3.9.

$$\vec{a}_1 = \frac{a}{2}(\sqrt{3}\hat{x} + \hat{y}); \quad \vec{a}_2 = \frac{a}{2}(-\sqrt{3}\hat{x} + \hat{y}) \quad (3.1)$$

$$\vec{b}_1 = \frac{2\pi}{a} \left(\frac{\sqrt{3}}{3} \hat{k}_x + \hat{k}_y \right); \quad \vec{b}_2 = \frac{2\pi}{a} \left(-\frac{\sqrt{3}}{3} \hat{k}_x + \hat{k}_y \right) \quad (3.2)$$

Knowledge of the group of the wave vector is important because the invariance of the Hamiltonian under symmetry operations usually leads to degeneracies at the high-symmetry points or directions in the Brillouin zone. The differences between the space groups D_{3h}^1 and D_{3d}^3 when the number of triple layers is odd or even define different symmetries for the group of the wave vectors at each high-symmetry point or direction of the reciprocal space.

Table 3.3 shows groups that are isomorphic to the group of wave vectors for all the high-symmetry points and axes in the Brillouin zone for 2H and 1T polytypes. The reader interested in more details of the group theory analysis of TMDCs is referred to the original publication [55].

Raman Tensors

For the nonsymmorphic space group for the bulk 2H polytype, the Raman tensors are [56]:

$$\begin{aligned} \Gamma_1^+(A_{1g}) &: \begin{pmatrix} a & 0 & 0 \\ 0 & a & 0 \\ 0 & 0 & b \end{pmatrix}, \\ \Gamma_5^+(E_{1g}) &: \begin{pmatrix} 0 & 0 & 0 \\ 0 & 0 & c \\ 0 & c & 0 \end{pmatrix}, \begin{pmatrix} 0 & 0 & -c \\ 0 & 0 & 0 \\ -c & 0 & 0 \end{pmatrix} \\ \Gamma_6^+(E_{2g}) &: \begin{pmatrix} 0 & d & 0 \\ d & 0 & 0 \\ 0 & 0 & 0 \end{pmatrix}, \begin{pmatrix} d & 0 & 0 \\ 0 & -d & 0 \\ 0 & 0 & 0 \end{pmatrix} \end{aligned}$$

For the 1T bulk crystal (D_{3d}^3 group of the wave vector for the Γ point), the Raman tensors are [56]:

Table 3.3 Space group and group of the wave vector for the high-symmetry points and directions in the Brillouin zone for 2H and 1T polytypes

Polytype	Space group	Γ	$K(K')$	M	$T(T')$	Σ
2H	D_{6h}^4 ($P6_3/mmc$)	D_{6h}^4 ($P6_3/mmc$)	D_{3h}^4 ($P62c$)	D_{2h}^{17} ($Cmcm$)	C_{2v}^{16} ($Ama2$)	C_{2v}^{14} ($Amm2$)
1T	D_{3d}^3 ($P\bar{3}m1$)	D_{3d}^3 ($P\bar{3}m1$)	D_3^2 ($P321$)	C_{2h}^3 ($C2/m$)	C_2^3 ($C2$)	C_s^{xz} (or C_s^3 , Cm)

$$\Gamma_1^+(A_{1g}) : \begin{pmatrix} a & 0 & 0 \\ 0 & a & 0 \\ 0 & 0 & b \end{pmatrix},$$

$$\Gamma_3^+(E_g)_{(1)} : \begin{pmatrix} c & 0 & 0 \\ 0 & -c & d \\ 0 & d & 0 \end{pmatrix}, \Gamma_3^+(E_g)_{(2)} : \begin{pmatrix} 0 & -c & -d \\ -c & 0 & 0 \\ -d & 0 & 0 \end{pmatrix}$$

3.1.7 Electronic Structure

We now get back to the issue of why some structures possess octahedral bonding geometry while others acquire trigonal prismatic geometry following the simple but insightful arguments of Kertesz and Hoffmann [13]. These authors simulated a generic band structures for the two different geometries using ReSe_2 as an example. The resulting band structures are shown in Fig. 3.10. There are several common features in the two band structures. Namely, the p -bands lie between -10.5 and -16.5 eV. The resonance with $\text{Re } 5d$ levels, located at 12.66 eV, is strong as is the overlap between Re and its six Se neighbours. Consequently, there is a substantial $\text{Re}-\text{Se}$ interaction splitting the $\text{Re } d$ -electron levels, i.e. the crystal field at Re is large with the $\text{Re } d$ -electron levels split into a three-below-two pattern, for both the octahedral and the trigonal prismatic cases.

As a result, for a d^0 electron count, bands 1 through 8 in Fig. 3.10 are filled and there is little difference between the two cases. The differences show up at higher

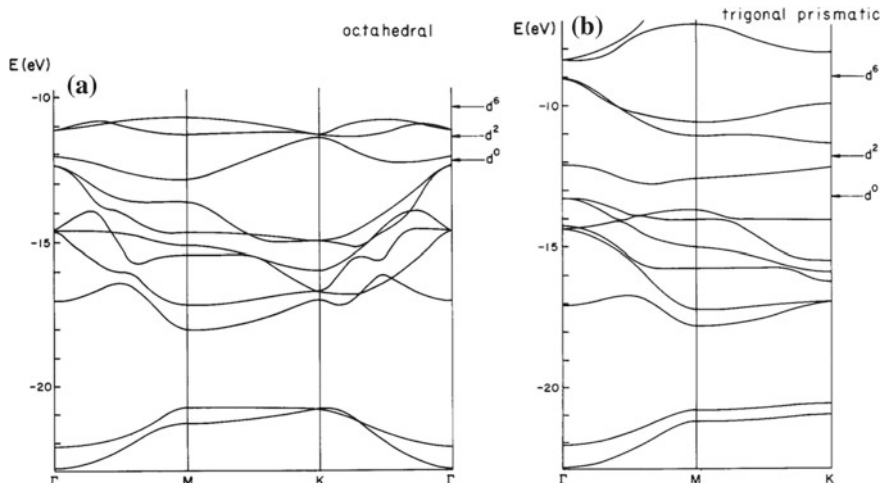


Fig. 3.10 Band structures simulated for ReSe_2 assuming octahedral (*left*) and trigonal prismatic (*right*) bonding geometries of the transition metal [13]. Copyright 1984 American Chemical Society. Published with permission

electron counts. There are pronounced differences at the Γ and K points. At the Γ point, bands 10 and 11 are shifted up for the trigonal prismatic structure, at the K -point band 9 goes down and band 11 goes up relative to the octahedron. It is argued that the energy gap at d^2 at the K point, which is larger for the trigonal prismatic case, plays an important role in determining the stability of the two structures.

As the higher bands are gradually filled, first the trigonal prismatic geometry becomes relatively more stable due to the downward shift of band 9 at the K -point. This effect reaches maximum around d^2 , when an opposite trend starts, where the upward shift of bands 10 and 11 at the Γ -point makes the octahedral structure more stable [13].

The electronic structure of TMDCs strongly depends on the coordination geometry and the d -electron count. In both $2H$ and $1T$ cases the nonbonding d -bands of the TMDCs lie between the bonding (σ) and anti-bonding (σ^*) bands as shown schematically in Fig. 3.11. In octahedrally coordinated structures (with D_{3d} symmetry) two degenerate orbitals are formed, namely, e_g (that contains d_{z^2} and $d_{x^2-y^2}$ orbitals) and t_{2g} (d_{xy} , d_{yz} , and d_{xz} orbitals) that can together accommodate up to 6 d -electrons. In the trigonal prismatic configuration (D_{3h}), on the other hand, the orbitals split into three groups: namely, d_{z^2} (a_1), $d_{x^2-y^2} + d_{xy}$ (e) and $d_{yz} + d_{xz}$ (e') [57].

The different electronic properties of TMDCs are a result of progressive filling of these bands. If the highest orbitals are partially filled, the material is a metal, when the bands are fully occupied, the materials become semiconductors. While the chalcogen atoms also have an effect on properties (the d -bands broaden with a concomitant decrease in the band gap), this effect is minor compared to the effect of the transition metal.

It should also be mentioned that based on pronounced differences in reflectivity spectra of group IVB and group VIB TMDCs, it was argued that there is a relationship between the ionicity of the bond and the metal coordination, the octahedral

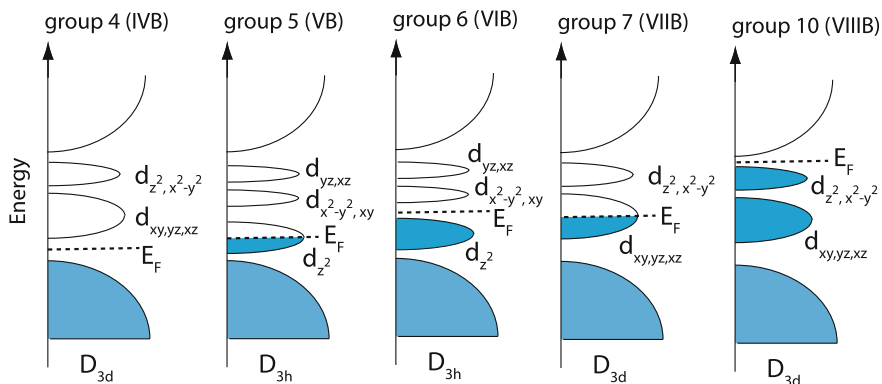


Fig. 3.11 Schematic DOS of layered TMDCs from different groups of the Periodic Table. Note different d -orbital splitting in structures with octahedral and trigonal prismatic geometry of transition metals. The symbols under DOS describe the symmetries of the structures

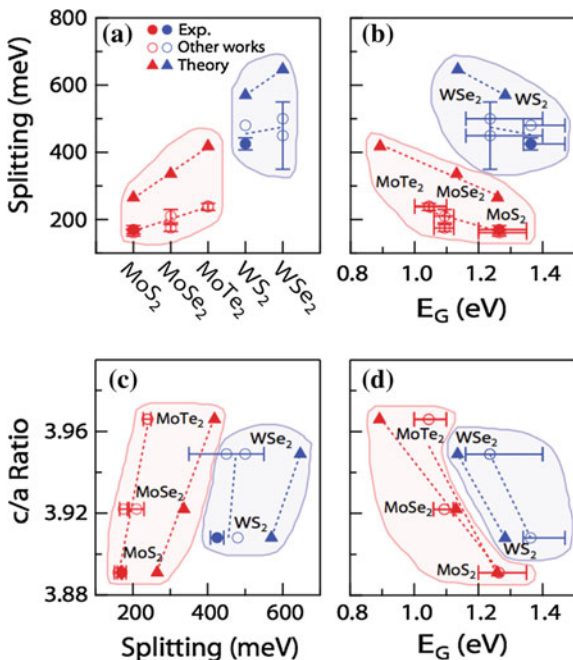
coordination being related to ionic bonds, while trigonal prismatic was associated with covalent bonding [6].

As already mentioned, intercalation with alkali metals may induce phase transformation in some TMDCs. For example, Li-intercalated MoS₂ changes from 2H to 1T, while the reverse change was reported for TaS₂. These changes can be explained by considering the effective change in the *d*-electron count through the transfer of an electron from the alkali metal to the transition metal.

The band structure of bulk semiconducting TMDCs have been simulated using DFT theory and experimentally measured by angle resolved photoelectron spectroscopy (ARPES) [58]. The details of the band structure are not discussed here because they are discussed in detail later (see Chap. 6) with respect to the band structure evolution upon decreasing the number of layers.

Electronic structure, spin-orbit coupling, and interlayer interaction in bulk MoS₂ and WS₂ was recently studied [59] through measurements of the electronic band structure using ARPES, with focus on the energy splittings in the valence bands at the *K* point of the Brillouin zone. Experimental results were interpreted in terms of parallel first-principles computations. It was found that interlayer interaction only weakly contributes to the splitting in bulk WS₂. Additionally it was found that across a range of TMDCs, the band gap generally decreases with the valence-band splitting, molecular mass, or the ratio of the out-of-plane to in-plane lattice constant (Fig. 3.12).

Fig. 3.12 **a** Magnitude of valence-band splitting at the *K*-point for bulk TMDCs **b** Magnitude of the splitting versus band gap E_G for bulk TMDCs. Ratio of out-of-plane to in-plane lattice constant, c/a , versus **c** magnitude of valence-band splitting and **d** band gap [59]. Copyright 2015 by the American Physical Society. Reprinted with permission



3.2 Optical Properties of Bulk TMDCs

3.2.1 Optical Absorption

A detailed summary of optical absorption in various TMDCs is given in [1]. In all cases the absorption spectra are characterised by strong excitonic peaks marked *A* and *B*. In some cases there is a subsequent absorption peak marked *C*. The same notations are preserved for excitons in single- and few-layer TMDC and are used later in this volume. (Several characteristic absorption spectra of bulk TMDCs are shown in Fig. 5.32 in comparison with those for monolayers).

It is interesting to note that even in 3D TMDCs, excitons are confined to single layers (Fig. 3.13) [60, 61] which was ascribed to a large interlayer distance preventing the wave function from spreading to other layers [61].

Detailed photocurrent spectroscopy of cleaved group VIB TMDCs has been performed in [62]. Thin films of MoS₂ exhibited polarization dependent optical absorption [63], which is expected from a highly anisotropic crystal.

3.2.2 Raman Scattering and Infra-Red Spectroscopy

3.2.2.1 Group-Theoretical Analysis

In this section we discuss infrared absorption and Raman scattering of bulk crystals. Application of Raman scattering to few- and single-layer TMCDs is a subject of a dedicated chapter (see Chap. 7). Infrared and Raman studies of long-wavelength optical phonons in TMDCs, primarily, MoS₂, were studied by various groups [38, 64–70]. Raman spectra were also measured for group IVB TMDCs [71] and metallic layered compounds such as NbSe₂ [72].

A group-theoretical analysis of the Γ -point lattice modes for the 2H-MoS₂ structure was given in [6, 64, 65]. There are six atoms per unit cell, which gives rise

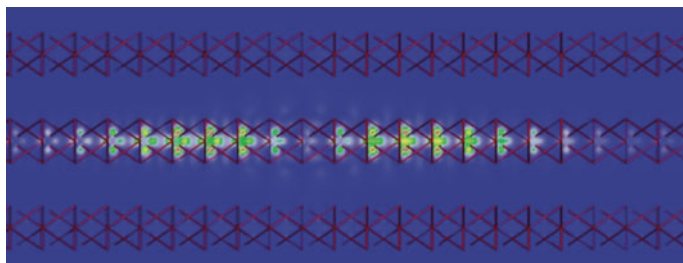


Fig. 3.13 Lateral view of the exciton *A* in bulk MoS₂. The hole has been placed on the Mo atom in the center of the figure [61]. Copyright 2013 by the American Physical Society. Reprinted with permission

to 18 vibrational modes, which decompose into irreducible representations at the Brillouin-zone center as follows [6]:

$$\Gamma = 2A_{2u} + B_{2g}^1 + B_{2g}^2 + B_{1u} + A_{1g} + 2E_{1u} + E_{2g}^1 + E_{2g}^2 + E_{2u} + E_{1g} \quad (3.3)$$

Hence, there are four first-order Raman active modes in MoS₂. All of the first-order bands are a result of vibrational modes within the S-Mo-S layer, except for the E_{2g}^2 (32 cm^{-1}) band, which is due to the vibration of the adjoining rigid layers [69].

For the 1T-TiS₂ structure, there are three atoms per unit cell and the decomposition into irreducible representations at the Γ point is given by

$$\Gamma = A_{1g} + E_g + 2A_{2u} + 2E_u \quad (3.4)$$

The mode motions for the infrared- and Raman-active optic vibrations are shown in Fig. 3.14 and infrared and Raman vibrational frequencies of the 2H polytypes of MoS₂, MoSe₂, and MoTe₂ are summarised in Table 3.4.

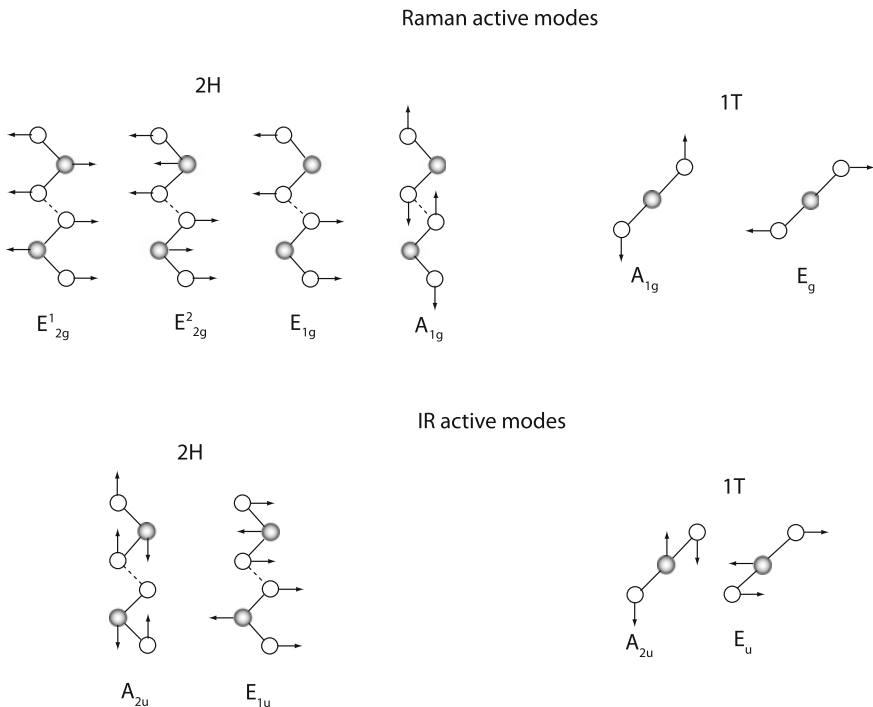
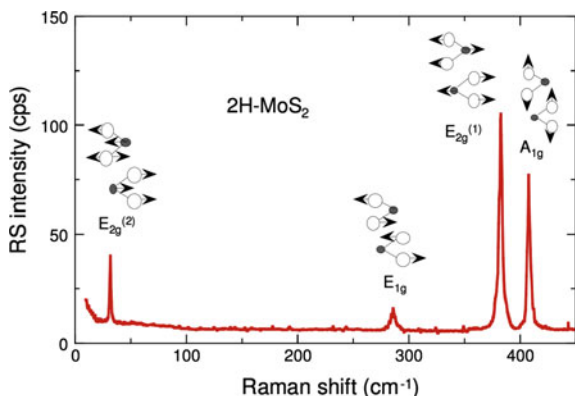


Fig. 3.14 Displacement vectors for the infrared- and Raman-active modes in the 2H and 1T polytypes. Adapted after [6]

Table 3.4 Infrared and Raman vibrational frequencies (in cm^{-1}) of 2H polytypes of MoS_2 , MoSe_2 , and $\alpha\text{-MoTe}_2$, after [66]

Symmetry of vibrations	MoS_2 [38, 65]	MoSe_2	MoTe_2
A_{2u}	470	350 [6]	
A_{1g}	409	243.1 [66], 361 [73–75]	171.4 [66], 321 [73–75]
E_{2g}^1	33.7	26.9 [66], 112 [73–75]	25.4 [66], 108 [73–75]
E_{1u}	384	286 [66], 277, 283 [73–75]; 288 [6], 286.9 [76]	234.5 [66], 240 [73–75]
E_{2g}^2	383	283 [66], 285 [73–75]	232.4 [66], 237 [73–75]
E_{1g}	287	168.8 [66], 217 [73–75]	116.8 [66], 207 [73–75]

Fig. 3.15 Raman scattering spectrum of 2H- MoS_2 single crystal showing the anisotropic character of the vibrational modes. The interlayer shear mode observed at 33.5 cm^{-1} is typical of the trigonal prismatic structure. Reproduced from [77]



3.2.2.2 Non-resonant Raman Scattering

A Raman scattering spectrum of pristine molybdenite recorded at ambient temperature is shown in Fig. 3.15 along with the associated mode assignments [77] (note that the atomic motions for the E_{1g} mode are different in Figs. 3.14 and 3.15). The A_{1g} mode at 407 cm^{-1} is an intralayer mode involving the motion of S atoms along the c axis. The E_{2g}^1 mode at 383 cm^{-1} is an intralayer vibrational mode involving motion of Mo+S atoms in the basal plane. The peak at 286 cm^{-1} with weak intensity and E_{1g} symmetry is observed, which involves S atoms in the basal plane. In addition, a rigid-layer mode E_{2g}^2 at 32 cm^{-1} , is present, which is of interlayer type involving rigid motion of neighboring layers in anti-phase [69, 78]. In layered crystals, the frequency of the rigid-layer mode provides direct information on the strength of the interlayer forces in these crystals, since for such rigid-layer motions the restoring forces are provided entirely by layer-layer interactions [78]. From the fact that interlayer shear force constant is much smaller than the intralayer force constants it was concluded that the interlayer interaction is of a vdW nature in MoS_2 [37, 38]. A similar result was obtained for WS_2 [79].

In [80] the dispersion of phonons on the (0001) surface of MoS₂ was measured by high-resolution electron-energy-loss spectroscopy along the $\Gamma - K$ and $\Gamma - M$ directions and it was found that the surface phonons have lower energies than the corresponding bulk phonons, indicating that the bonding interactions of the surface atoms are different from those of the bulk, even in a layer-lattice compound.

The effect of grain boundaries on Raman scattering was reported in [81]. While the E_{2g}^1 and A_{1g} modes were observed both on the surface and at the grain boundaries, these modes do not display any significant differences in peak position or height. However, an additional peak developed at ca. 282 cm⁻¹ only at grain boundaries which was attributed to the E_{1g} mode (Fig. 3.16). In principle, the latter mode is forbidden when the sample is oriented with the surface normal of the basal layers pointing in the opposite direction to the incoming laser, therefore, enhancement in the E_{1g} peak is related to the misorientation of the basal planes.

3.2.2.3 Polarised Raman Scattering

The two-dimensional nature and strong asymmetry of the crystal structure result in pronounced polarisation dependence of Raman scattering. Polarised Raman spectra for MoS₂ [65] and MoSe₂ [37] are shown in Fig. 3.17. Note that the appearance (or non-appearance) of certain peaks is also associated with the experiment geometry, e.g. the E_{1g} peak is not allowed in a back-scattering geometry.

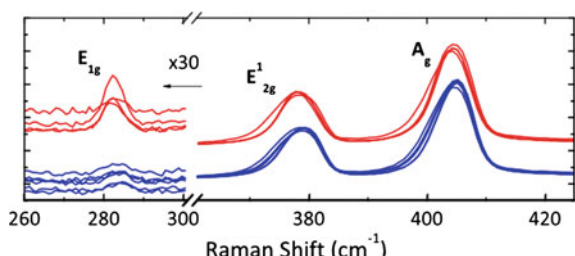
To describe polarised Raman scattering, Porto notations [82] are usually used of the type $x(ab)y$, where the symbols before and after parentheses are the direction of the incident and scattered light, respectively, and the two symbols in the parentheses represent polarization directions for the incident and scattered light, respectively. The backscattering geometry is thus referred to as $\bar{z}(xy)z$.

3.2.2.4 Resonant Raman Scattering

In resonant Raman measurements numerous additional peaks appear [67, 83], that are analysed in terms of second-order scattering due to the coupling of phonon modes of nonzero momentum with an electronic transition associated with excitonic states. Figure 3.18 shows a resonant Raman spectrum [83] of a MoS₂ single crystal. Second-

Fig. 3.16 Raman spectrum taken on the surface (blue) and at the grain boundaries (red) of MoS₂ [81].

Reprinted with permission.
Copyright 2012 by the
American Institute of
Physics



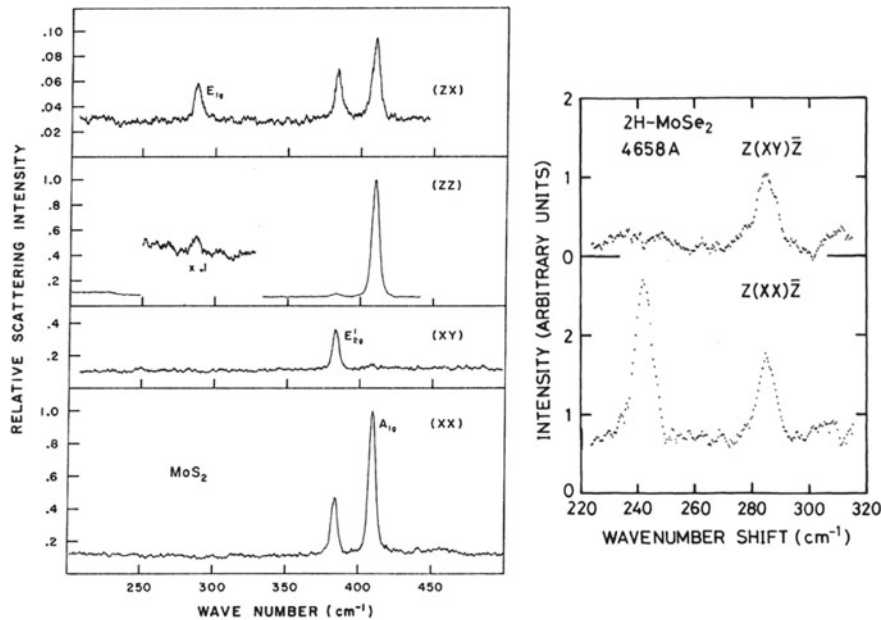
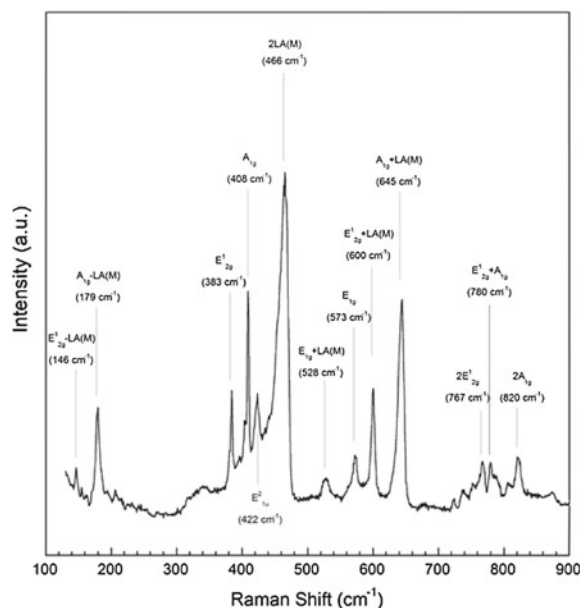


Fig. 3.17 *Left* polarized Raman spectra of $2\text{H}-\text{MoS}_2$ at room temperature. The (zx) and (xy) spectra are normalized to the (zz) and (xx) spectra, respectively [65]. Copyright 1971 by the American Physical Society. Reprinted with permission. *Right* polarised Raman spectra for MoSe_2 [37]. Reproduced with permission from the Physical Society of Japan

Fig. 3.18 Resonant Raman spectrum of MoS_2 recorded using 632.8 nm excitation [83]. Reproduced with permission from Springer



order Raman scattering of MoS_2 was also studied in detail in [69] and data for WS_2 can be found in [79, 84]. The temperature and pressure dependence of the Stokes and anti-Stokes Raman spectra of a single crystal of $2H\text{-MoS}_2$ was studied in [85] where the authors made use of the fact that the energies of the A_1 and B_1 excitons can be fine-tuned by varying temperature and pressure to resonate with the excitation laser. Increased interest in TMDCs monolayers and few-layers resulted in renewed interest to Raman scattering of the bulk phases with several recent publications [86, 87], challenging some of the existing peak assignments.

In particular, in [87] it is noted that the characteristic high energy cut-off shape of the 465 cm^{-1} peak in the MoS_2 spectrum closely resembles the shape of a higher-order scattering peak at 643 cm^{-1} . The authors assign the latter peak to a combined process involving the 465 cm^{-1} phonon and a phonon of energy 180 cm^{-1} (to which they refer as XA). They propose that the XA phonon is related to the transverse acoustic (TA) and/or out-of-plane acoustic (ZA) mode, noting that the dispersion of both modes flattens at the border of the Brillouin zone near the high-symmetry M point, leading to a substantial increase in the phonon density of states at 180 cm^{-1} .

At the high-energy end of the spectrum (Fig. 3.19a, b) a series of three similar features can be observed at energies 929.5 , 1107.5 , and 1289.5 cm^{-1} , which were

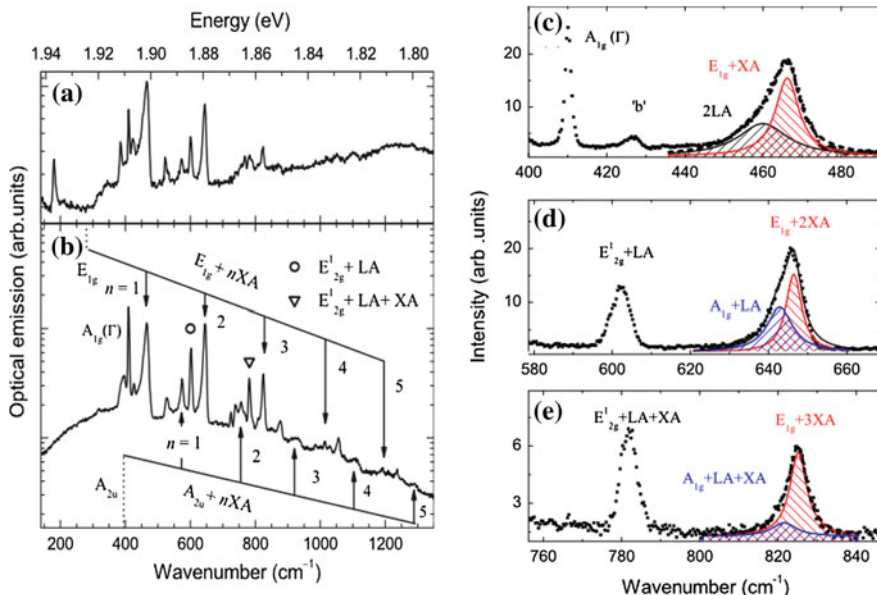


Fig. 3.19 Optical spectrum of MoS_2 resonantly excited at room temperature (a) and at low temperature ($T = 4.2\text{ K}$) (b). Details of the optical spectra of bulk MoS_2 measured at low temperature (c–e). The broadened peaks were deconvoluted to show Lorentzian wave-form contributions. The energy scales of consecutive panels are shifted by 178.6 cm^{-1} for more clarity. The attributed phonons originate from M point of the Brillouin zone unless stated otherwise [87]. Reprinted with permission. Copyright 2014 by the American Institute of Physics

attributed to the three-, four-, and five-XA(M) phonon replica of the $A_{2u}(M)$ phonon, proposing that the peak at 574 cm^{-1} also belongs to this series. The linear fit to these four energies allowed the authors to determine the energy of the XA(M) phonon as 178.6 cm^{-1} and the energy of the $A_{2u}(M)$ mode as 394.2 cm^{-1} .

It was argued [87] that the energy of the XA(M) phonon well explains the similarity of the peaks observed at low temperature at 466 and 645 cm^{-1} (Fig. 3.19c, d). The line shape analysis of these peaks as well as of the peak at 825 cm^{-1} (Fig. 3.19e) suggests that each peak is composed of two peaks of similar energies. The stronger components of those peaks were attributed to XA(M) phonon replicas of the $E_{1g}(M)$ mode, namely: $E_{1g}(M) + \text{XA}(M)$ at 466 cm^{-1} , $E_{1g}(M) + 2\text{XA}(M)$ at 646.5 cm^{-1} , and $E_{1g}(M) + 3\text{XA}(M)$ at 825 cm^{-1} and their weaker counterparts to $2\text{LA}(M)$ at 460 cm^{-1} , $A_{1g}(M) + \text{LA}(M)$ at 643 cm^{-1} , and $A_{1g}(M) + \text{LA}(M) + \text{XA}(M)$ at 82 cm^{-1} . From this attribution the energy of the $E_{1g}(M)$ mode as 289 cm^{-1} was determined. Introducing the XA(M) phonon into the picture the peak at 782 cm^{-1} was related to a replica of the previously identified $E_{2g}^1(M) + \text{LA}(M)$ mode at 602.5 cm^{-1} [88] (compare (Fig. 3.19e) as a peak due to a combined process: $E_{2g}^1(M) + \text{LA}(M) + \text{XA}(M)$ [87].

Resonant Raman spectra for two other common TMDCs, WS_2 and WSe_2 , are shown in Fig. 3.20 [86].

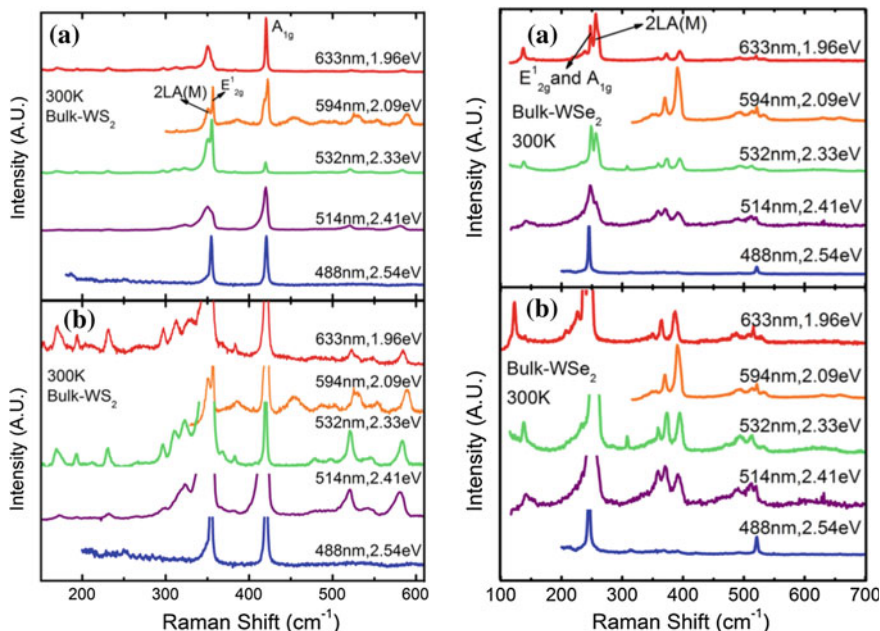


Fig. 3.20 Raman spectra of bulk WS_2 (left) and WSe_2 (right) measured at five excitation wavelengths. Panels (b) show the same spectra as in (a) with magnified intensities [86]. Reprinted with permission. Copyright 2014 by the American Institute of Physics

3.2.2.5 Raman Scattering from Alloys

In [89] mixed layered $\text{Mo}_{1-x}\text{W}_x\text{S}_2$ crystal were studied using Raman spectroscopy. To accurately determine the position of the E_{2g}^1 and A_{1g} modes as well as the second-order Raman band located in the vicinity of E_{2g}^1 of the tungsten containing samples, polarization dependent measurements in the back-scattering configuration were carried out.

Figure 3.21b represents the Raman spectra of $\text{Mo}_{1-x}\text{W}_x\text{S}_2$ in the range from 250 to 450 cm^{-1} (for comparison, in panel (a) Raman spectra for single-metal TMDCs are shown). The peaks are marked based on the polarized Raman measurements and the notations are obvious from the figure. With increasing W composition, peak I moves to higher wavenumber. In contrast, peak II shifts to lower wavenumber with a reduction of peak intensity. At the same time, with an increase of W content, two additional peaks, III and IV, appear on the lower wavenumber side of the Raman spectra of $\text{Mo}_{1-x}\text{W}_x\text{S}_2$. Both of them demonstrate a blue shift and become dominant peaks at higher x values. In addition, an alloy disorder-related peak located in between peaks II and III was observed for the mixed samples.

The composition dependence of the Raman-active modes of $\text{Mo}_{1-x}\text{W}_x\text{S}_2$ layered mixed crystals are shown in Fig. 3.21c. The A_{1g} mode exhibited a one-mode behavior, while for the E_{2g}^1 mode, a two-mode behavior was observed, which was interpreted on the basis of the atomic displacements for each mode; for the A_{1g} mode only sulfur atoms vibrate and this gives rise to a one-mode type behavior for the mixed crystals. For E_{2g}^1 mode metal atoms also vibrate as well as sulfur atoms. It was proposed that the significantly different atomic masses of tungsten and molybdenum causes the two-mode type behavior of the E_{2g}^1 mode [89], noting that such a behavior of the composition dependences is often seen in the Raman spectra of solid solutions with no ordered distribution of the constituent atoms.

As the composition of W increases, the disorder effect increases and, concomitantly, the intensities of the modes related to $2H\text{-MoS}_2$ decrease, while the $2H\text{-WS}_2$ associated modes become stronger. This finite periodicity in the mixed crystals relaxes the $q = 0$ Raman selection rule leading to the broadening and asymmetry of the Raman line shape. The low-wavenumber side half-width (Γ_{low}) is larger than the high-wavenumber side half-width (Γ_{high}). The ratio $\Gamma_{low}/\Gamma_{high}$ shows a maximum at $x = 0.5$, which indicates that the mixed crystal disorder effect is the main source for the Raman line shape change as a function of composition.

3.2.2.6 Raman Scattering from Group IVB TMDCs

Raman spectroscopy was also applied to group IVB TMDCs that form CDWs at lower temperatures such as TaS_2 , TaSe_2 and VSe_2 [71]. It was noted that three symmetry-related CDWs were found, under appropriate conditions, in the basal plane of the above compounds, resulting in observable shifts of metal ions. The distortions were periodic with a periodicity that can be commensurate or incommensurate with the

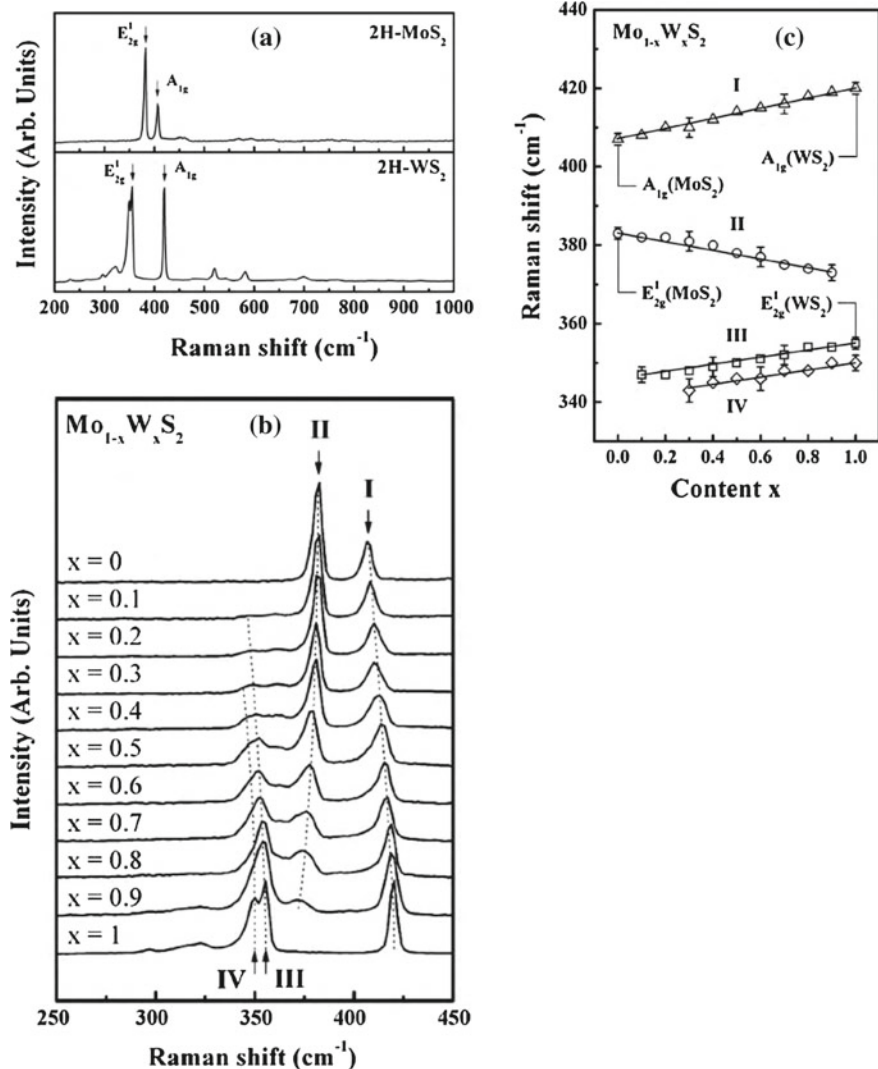


Fig. 3.21 Raman spectra of **a** 2H-MoS₂ and 2H-WS₂ layered crystals in the range between 200 and 1000 cm⁻¹, showing the prominent E_{2g}^1 and A_{1g} modes as well the second-order bands, **b** Raman spectra of $\text{Mo}_{1-x}\text{W}_x\text{S}_2$ layered mixed crystals in the range between 250 and 450 cm⁻¹. The *dotted lines* to guide the eyes show the position dependence of the peaks with W compositions x . **c** The variation of peaks I, II, III and IV as a function of W composition x of $\text{Mo}_{1-x}\text{W}_x\text{S}_2$ layered mixed crystals [89]. Reprinted with permission from Elsevier

undistorted lattice. In general the commensurate phase exists in the lowest temperature range, the incommensurate phase at intermediate temperatures, and the CDWs are not stable at the highest temperatures.

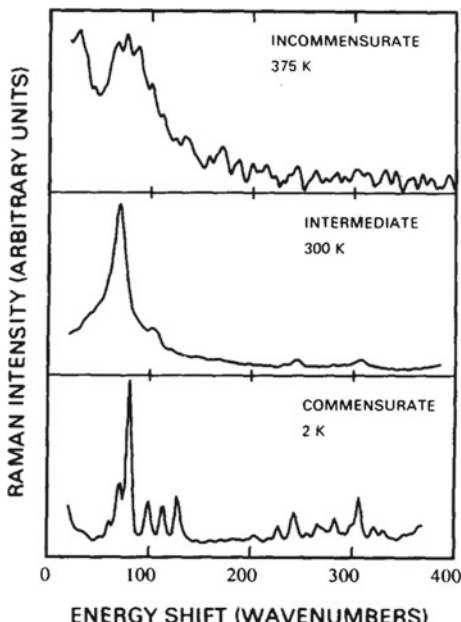
The effect of the imposition of a commensurate superlattice on the lattice is to reduce the size of the Brillouin zone, folding the dispersion curves of the various propagating excitations back into the center of the zone. This folding results in a greater number of zone center modes than are present in an undistorted structure.

In the case of incommensurate distortions, the translational symmetry of the lattice is destroyed and the components of momentum parallel to the incommensurate distortions are no longer good quantum numbers. Under these conditions the restriction of the first order Raman scattering to zone center phonons is relaxed, and all of the vibrational modes of the material can take part in first order Raman scattering.

This is exemplified by Fig. 3.22 showing the Raman spectra of $1T\text{-TaS}_2$ measured at three different temperatures. In the incommensurate CDW phase, the Raman spectrum is essentially a continuum (and very much weaker than that of the commensurate phase), indicating a lack of translational symmetry in the structure. At the same time, the commensurate phase is characterised by well resolved peaks, whose number is much larger than that expected from the undistorted structure [71].

In [90], microscopic description of the Raman scattering and infrared absorption of transition-metal dichalcogenides in the CDW state was developed in terms of the hybridization and multiphonon processes in which the condensed phonons participate.

Fig. 3.22 Raman spectra of different phases of $1T\text{-TaS}_2$ [71]. Reprinted with permission from Elsevier



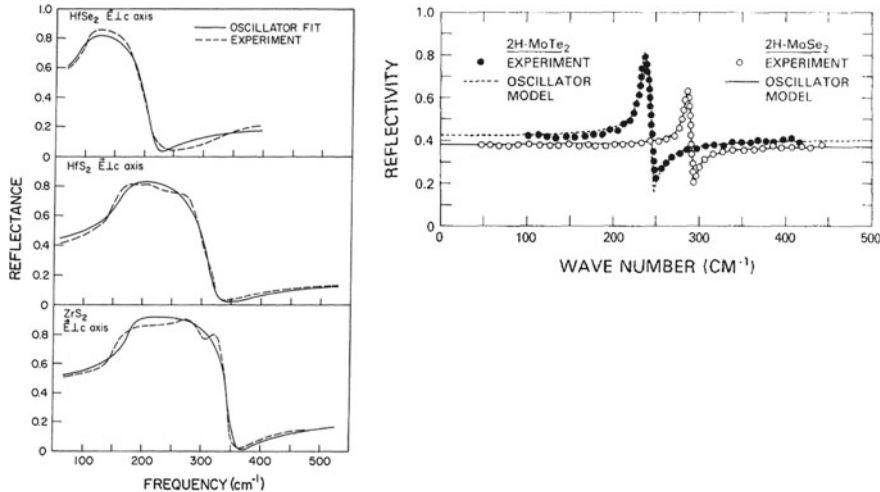


Fig. 3.23 Left reflectivities for $E \perp c$ of HfSe_2 , HfS_2 , and ZrS_2 [6]. Copyright 1973 by the American Physical Society. Reprinted with permission. Right reflectivities of 2H-MoSe_2 and 2H-MoTe_2 at room temperature [66]. Reprinted with permission from Elsevier

3.2.2.7 Infrared Spectroscopy

From infrared reflectance measurements (Fig. 3.23), the real and imaginary parts of the dielectric constant obtained for 2H-MoS_2 , 2H-MoSe_2 and 2H-MoTe_2 were obtained through Kramers–Kronig analyses of the reflectivity data [65, 66] as shown in Fig. 3.24. The obtained results are in agreement with the earlier data of [6]. In [6], group IVB TMDCs such as TiS_2 , HfSe_2 , and HfTe_2 were also studied. It was found that in group IVB TMDCs, there was a rather large difference between the LO and TO phonon frequencies (Fig. 3.25) compared to those in group VIB TMDCs, which was interpreted as a signature of larger charges arising from ionic bonding in group IVB materials, as opposed to covalently bonded group VIB TMDCs.

Considering the differences in the infrared spectra between group IVB and VIB TMDCs it should also be noted that the resonance Raman data of MoS_2 and WS_2 exhibit numerous additional peaks in comparison to HfS_2 , demonstrating strong electron coupling to phonons of nonzero momentum [67].

3.2.2.8 Brillouin Scattering

Studies of Brillouin scattering, i.e. scattering of light by long wavelength acoustic phonons, are rather limited. The results for 2H-WSe_2 , 2H-TaSe_2 , 2H-WSe_2 can be found in [91–93].

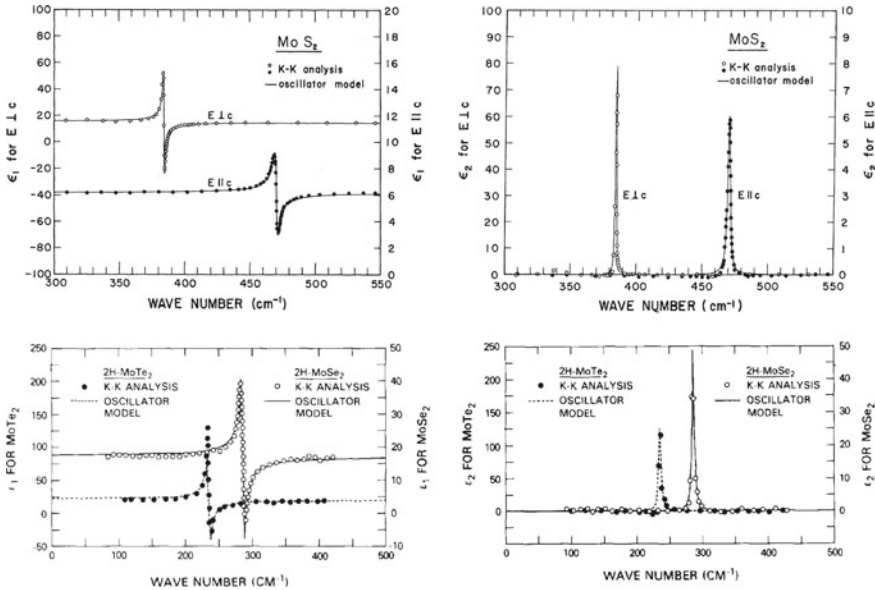


Fig. 3.24 Upper panel real (left) and imaginary (right) parts of the dielectric function for 2H- MoS_2 [65]. Copyright 1971 by the American Physical Society. Reprinted with permission. Lower panel 2H- $MoSe_2$ and 2H- $MoTe_2$ [66]. Reprinted with permission from Elsevier. The oscillator models for the two compounds are compared with the results of Kramers–Kronig analyses. For MoS_2 , results for two different polarisations are shown

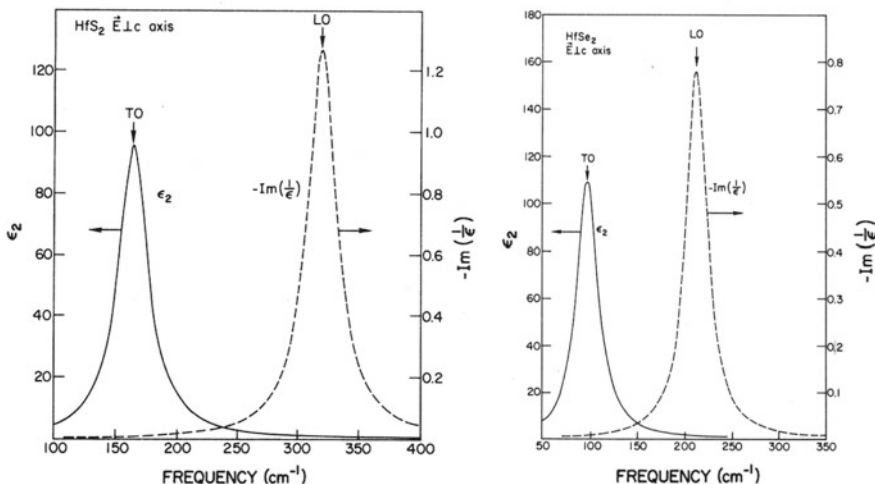


Fig. 3.25 Frequency dependence of ϵ_2 , the imaginary part of the dielectric constant, and $-\text{Im}(1/\epsilon)$, the energy loss function for HfS_2 (left) and $HfSe_2$ (right). The arrows indicate the TO- and LO-phonon frequencies [6]. Copyright 1973 by the American Physical Society. Reprinted with permission

3.3 Magnetism

3.3.1 Magnetism in MoS₂

Magnetism is not expected in the *ideal* bulk MoS₂ but has been observed in real samples, which is associated with the presence of grain boundaries, crystal imperfections etc. (see also Chap. 10).

3.3.2 Non-saturating Magnetoresistance in WTe₂

Magnetoresistance is the change in a material's electrical resistance in response to an applied magnetic field. Large magnetoresistance is an uncommon property, mostly of magnetic compounds. In [94], an extremely large positive magnetoresistance of up to 452,700 % at 4.5 K in an applied field of 14.7 T was observed in WTe₂ when the current direction was along the tungsten chains (*a* axis) and the magnetic field was applied perpendicular to the dichalcogenide layers, along the *c* axis. The magnetoresistance was still increasing at 60 T, the highest field in the reported measurements, where it had a value of 13,000,000 %. There was no indication of resistivity saturation even at these high applied fields, an indication of the unique character of WTe₂. The effect was very anisotropic: with current flowing along the chain direction it is maximized when the field was applied perpendicular to the WTe₂ layers, and decreased by more than 90 % when the magnetic field was applied in other directions. The effect became significant at temperatures below 150 K; the temperature of the ‘turn on’ increased with the magnitude of the applied magnetic field. The temperature-dependent resistivity under various applied magnetic fields ($\mu_0 H$ up to 14.7 T) is shown in Fig. 3.26. Electron diffraction patterns taken at low temperatures indicated that the origin of the observed effect was not linked to the onset of a CDW or a Peierls-like distortion.

The issue of the mechanism of the magnetoresistance in WTe₂ was further addressed in [95], where it was shown that tiny electron and hole pockets of equal size form the electronic basis for the unusual transport properties of WTe₂ at low temperatures. It was proposed that the extremely large magnetoresistance emerges from the resulting charge compensation, which was shown to be temperature dependent, apparently approaching perfect compensation at very low temperatures. The pronounced anisotropy of the magnetoresistance was concluded to be associated with the highly anisotropic character of the Fermi level and the proximity of the electron and hole pockets in momentum space along the direction of the metallic chains in this quasi-one-dimensional material. Finally, a flat band lying below the Fermi level has been recognized as the source of the turn-on temperature behavior of the magnetoresistance.

High resolution angle-resolved photoemission spectroscopy on WTe₂ was performed by several groups [95–97]. The results obtained are slightly contradictory.

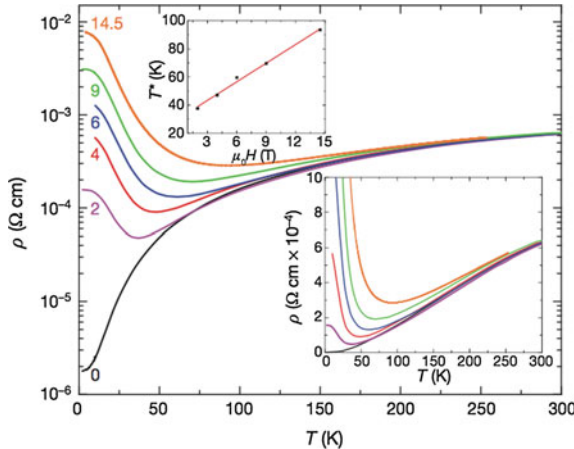


Fig. 3.26 The temperature and field dependence of the magnetoresistance in WTe_2 , for I parallel to a and H parallel to c . Plots of resistivity against temperature; numbers against graphs are field strengths in Teslas. *Lower* inset plot of resistivity against temperature, showing the effect turning on. T^* is defined as the temperature at which the resistivity is a minimum—an approximation of the temperature at which the magnetoresistance is turned on. *Upper* inset linear dependence of T^* on magnetic field; the slope is 4.4 K/T [94]. Reprinted by permission from Macmillan Publishers Ltd., copyright (2014)

Thus, one group found a pair of hole and electron pockets with comparable size along the $\Gamma - X$ direction [95]. In a subsequent study, two pairs of electron and two pairs of hole pockets along the $X - \Gamma - X$ direction were found [97]. In a later work, a yet more complex Fermi surface topology with nine Fermi pockets was revealed, namely, two pairs of hole and electron pockets on each side of the Γ point along the $\Gamma - X$ direction [96], alongside with a hole pocket at the Γ point. In [98], where the electronic structure was studied by ab-initio simulations, it was noted that a very small electron pocket does emerge at the Γ point by shifting the Fermi level with respect to the position required to match the experimental observations, which would lead to a total number of nine Fermi-surface sheets. It was further found that the geometry of the Fermi surface is very sensitive with respect to small displacements of the Fermi level (on the order of 20 meV), which is comparable to the experimental resolution of ARPES, and the distinction among the ARPES results was attributed to the different resolution in different setups [98].

It was further found that increasing temperature has a pronounced effect on the electronic structure, namely, it enhances the electron pockets and finally leads to the disappearance of the hole pockets at 160 K, which was associated with a Lifshitz transition [97]. Some interesting conclusions were drawn from studies of WTe_2 under pressure [99]. The results of these studies are described in more detail below in this chapter.

A remarkable photoemission intensity inversion between the right-circularly polarized and left-circularly polarized light data was observed [96], suggesting that

the orbital angular momentum varies with Fermi momentum, which is an evidence for the presence of strong spin-orbital coupling. The role of spin-orbit coupling and evolution of the electronic structure of WTe₂ was also studied in [98] using Shubnikov-de Haas oscillations, where it was additionally found that the effective masses in WTe₂ are renormalized by a magnetic field, increasing considerably as the field increases. It was concluded that the electronic structure of WTe₂ evolves due to the Zeeman effect.

In [100], temperature-dependent three-dimensional anisotropy of the magnetoresistance in WTe₂ was studied. Among other results, it was found that WTe₂ is electronically a 3D material with a small mass anisotropy, which varies with temperature and follows the magnetoresistance behavior of the Fermi liquid state. Raman scattering was also used to study the observed extremely large magnetoresistance in WTe₂ [101] but no definitive conclusions were drawn.

Optical properties of perfectly compensated WTe₂ were studied in [102]. It was found that a low-frequency plasma edge develops in the reflectance at low temperature where this material is a perfectly compensated semimetal. First-principles electronic structure calculations revealed that the low-lying optical excitations are due to direct transitions between the bands associated with the electron and hole pockets.

In [103], ultrafast transient reflectivity measurements on WTe₂ as a function of pump fluence and temperature were performed. It was found that below 50 K, an unusual decrease of the recombination time sets in, which was attributed to an electronic structure change. It was proposed that this change might play a key role in promoting the large magnetoresistance in WTe₂.

At the moment of writing there have been no experimental evidence that large and non-saturating magnetoresistance can be observed in mono- and few-layer WTe₂ but theoretical studies suggested this might be possible [104].

3.4 TMDC as Weyl Semimetals

The Weyl semimetal is a topological semimetal [105, 106] in which bands disperse linearly in three-dimensional (3D) momentum space through a node called a Weyl point. The appearance of Weyl points is only possible in a material if the product of parity and time-reversal is not a symmetry of the structure [107] and the Weyl point acts as a monopole with fixed chirality, a source or a sink of the Berry curvature. Similar to those of a topological insulator, topologically protected surface states exist on the surface of a Weyl semimetal. Topologically different from ordinary Fermi surfaces, these surface states present unclosed Fermi surfaces, called Fermi arcs, which connect the surface projections of Weyl points with opposite chirality [105].

The transport properties of Weyl semimetals are predicted to show many exotic phenomena including the negative magnetoresistance due to the chiral anomaly known from quantum field theory, non-local transport and quantum oscillations where electrons move in real space between opposite sides of a sample surface [108].

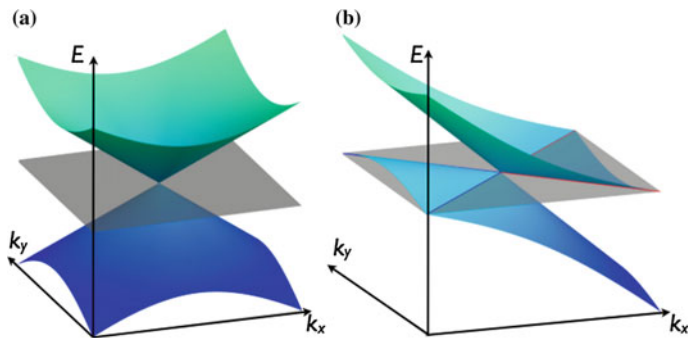


Fig. 3.27 Possible types of Weyl semimetals. **a** Type-I with a point-like Fermi surface. **b** A type-II Weyl point appears as the contact point between electron and hole pockets. The grey plane corresponds to the position of the Fermi level, and the blue (red) lines mark the boundaries of the hole (electron) pockets [107]. Reprinted by permission from Macmillan Publishers Ltd., copyright (2015)

Shortly after the theoretical prediction, the first Weyl semimetal was experimentally discovered but so far, the TaAs class of four iso-electronic compounds remained to be only experimentally realized Weyl semimetals [109, 110]. Recently several group addressed the issue of Weyl semimetals with respect to TMDCs.

While usually Weyl semimetals (type I) possess a point-like Fermi surface at the Weyl point (Fig. 3.27) (left panel), to contrast them a new type of the Weyl point (type II) was suggested in [107], that exist at the boundary of electron and hole pockets, as illustrated in the right panel of Fig. 3.27. This node, although still a protected crossing, has an open, not point-like, Fermi surface, suggesting that physical properties may be different from that of standard Weyl points. It was argued that an established material, WTe₂, is an example of this novel type of topological semimetals [107] but the reported separation between Weyl nodes was too small to be observed experimentally. In [108], it was argued that 2 % Mo doping of WTe₂ is sufficient to stabilize the Weyl semimetal state not only at low temperatures but also at room temperatures, where the momentum space distance between the Weyl nodes and hence the length of the Fermi arcs can be continuously tuned from zero to ca. 3 % of the Brillouin zone size via changing Mo concentration.

Subsequently, orthorhombic MoTe₂ was also predicted to be a Weyl semimetal [111]. From first-principles simulations it was shown that it exhibits four pairs of Weyl points lying slightly above (~ 6 meV) the Fermi energy in the bulk band structure. The spacing between each pair of Weyl points was found to be as large as 4 % of the reciprocal lattice. When projected onto the surface, the Weyl points were connected by Fermi arcs. It was noted that these arcs should be easily accessed by angle-resolved photoemission spectroscopy due to the large Weyl point separation. In addition, it was argued that the correlation effect or strain can drive MoTe₂ from a type-II to a type-I Weyl semimetal.

At the moment of writing there has been no experimental reports of Weyl semimetal from TMDC family.

3.5 Pressure-Induced Transformations

3.5.1 Pressure Effect on Physical Properties of MoS₂

The large vdW interlayer gap raises the prospects of strong chalcogen–chalcogen interlayer interactions under axial compression that might lead to an electronic phase transition and a semiconductor-metal transition under application of pressure has been suggested theoretically [112–114] and confirmed experimentally by high-pressure measurements using a diamond anvil cell with a hydrostatic pressure medium [115].

The elastic constants determine the relationship between strain (deformation) of a material and the stress/pressure applied to it. In a hexagonal material such as MoS₂ there are five independent elastic constants. An experimental determination was reported in [116] based on combining neutron data and linear compressibilities and the obtained numbers were $c_{11} = 238 \text{ GPa}$, $c_{12} = -54 \text{ GPa}$, $c_{13} = 23 \text{ GPa}$, $c_{33} = 528 \text{ GPa}$, and $c_{44} = 19 \text{ GPa}$. The elastic properties were also investigated theoretically, but there were substantial differences between the experimental values and theoretical calculations [117–119]. Also there is a disagreement between simulations using different functionals. Recently, the issue was revisited [120], using semiempirical Grimme D2 correction [121] that includes vdW interactions.

The pressure dependence of the lattice constants, compressibilities, phonon energies and their pressure derivatives, and interlayer and intralayer shear force constants and their pressure derivatives obtained from high-pressure measurements can be found in [122].

In-situ electric conductivity measurements at room temperature using standard four-point metallic contacts revealed a gradual decrease in resistivity with pressure up to 10 GPa (Fig. 3.28a), which was interpreted in the context of pressure-activated carrier transport. Between 10–19 GPa an abrupt decrease by about three orders of magnitude was observed. This result was reproduced by theoretical simulations with a predicted transition at ca. 20 GPa (Fig. 3.28a, inset), where the conductivity decreased to essentially zero. The semiconductor-metal transition was further confirmed by the negative temperature coefficient of resistivity at 10 GPa below the transition for the semiconducting state, whereas a positive temperature coefficient of the resistivity was observed at 34 GPa for the metallic state (Fig. 3.28b).

The effect of pressure on electrical properties was also studied in [123], where it was concluded that the semiconductor-metal transition occurs at a higher pressure (above 28 GPa) in the $2H_a$ phase when the phase transition is complete. The phase at 60 GPa was metallic. The observed changes were reversible.

Applied pressure also has a pronounced effect on the photoconductivity of MoS₂ as illustrated in Fig. 3.29 [115]. While at lower pressures, where the material is semiconducting, a photocurrent is generated upon exposure to light (2.3 eV), the

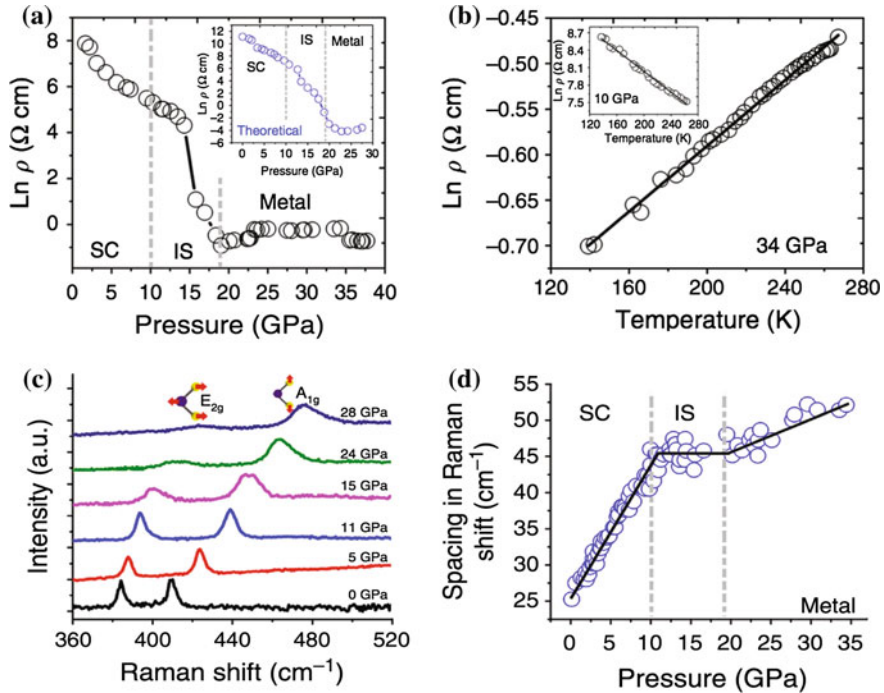


Fig. 3.28 **a** Pressure-dependent electrical resistivity of MoS₂. Three characteristic regions have been identified: semiconducting (SC), intermediate state (IS) and metallic regions. Inset: theoretically calculated pressure-dependent electrical resistivity. **b** Temperature-dependent resistivity of MoS₂ in the metallic state. Inset the experimental temperature-dependent semiconducting behaviour of MoS₂. The solid lines serve as visual guides. **c** Raman spectra at representative pressure points. The inset is an illustration of the in-plane and out-of-plane vibrations of the two key modes E_{2g} and A_{1g} , respectively. **d** The difference in Raman frequencies between the A_{1g} and E_{2g} modes as a function of pressure flattens out in the IS state and rises at a smaller slope in the metallic region. The solid black line is a visual guide [115]. Reprinted by permission from Macmillan Publishers Ltd., copyright (2014)

metallic high-pressure phase shows no photoresponse. It may be interesting to note that the photoresponse disappears at 10 GPa, i.e. the transient phase that still has a non-zero band-gap is already insensitive to light. No explanation of this result was proposed.

The evolution of different gaps of the band structure under applied hydrostatic pressure was theoretically studied in [120] with vdW corrections included in the simulations; the result is shown in Fig. 3.30.

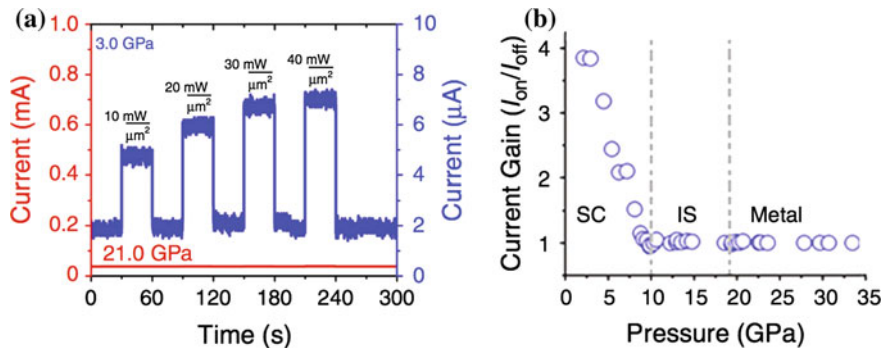
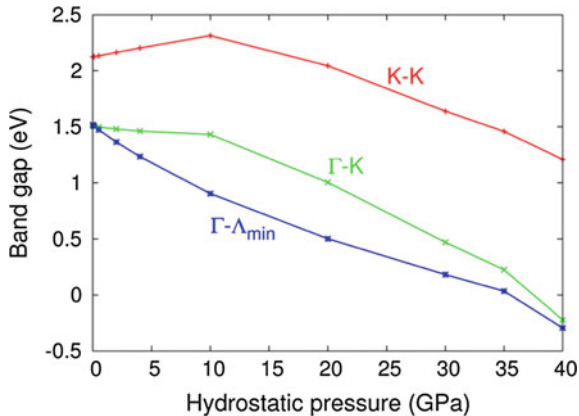


Fig. 3.29 **a** Optical switching behaviour before (blue lines at 3.0 GPa) and after (red line at 21.0 GPa) the semiconductor-metal transition with various laser intensities. **b** Current gain (defined as I_{on}/I_{off} ratio) as a function of pressure when exposed to a 532 nm (2.3 eV) laser light with an intensity of 40 W m^{-2} [115]. Reprinted by permission from Macmillan Publishers Ltd., copyright (2014)

Fig. 3.30 Evolution of the different band gaps of MoS₂ as a function of hydrostatic pressure [120]. Copyright 2014 American Chemical Society. Published with permission



3.5.2 Pressure Effect on Extremely Large Magnetoresistance in WTe₂

The perfect balance between electron and hole populations that is responsible for the extremely large magnetoresistance in WTe₂ should be very sensitive to tuning parameters such as doping and pressure. Pressure effects on the extremely large magnetoresistance were studied in [99]. Figure 3.31a presents the magnetoresistance up to 14.5 T at various temperatures. At 0.3 K Shubnikov-de Haas (SdH) oscillations are clearly observed. With increasing temperature, the magnetoresistance decreases rapidly and the oscillations disappear. The SdH oscillations are often used to detect the Fermi surface topology [124]. In Fig. 3.32a, the oscillatory magnetoresistance is analyzed by employing fast Fourier transform (FFT) for various temperatures from

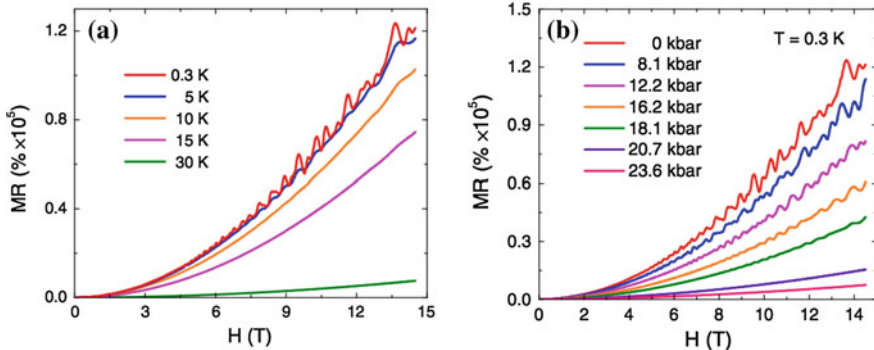


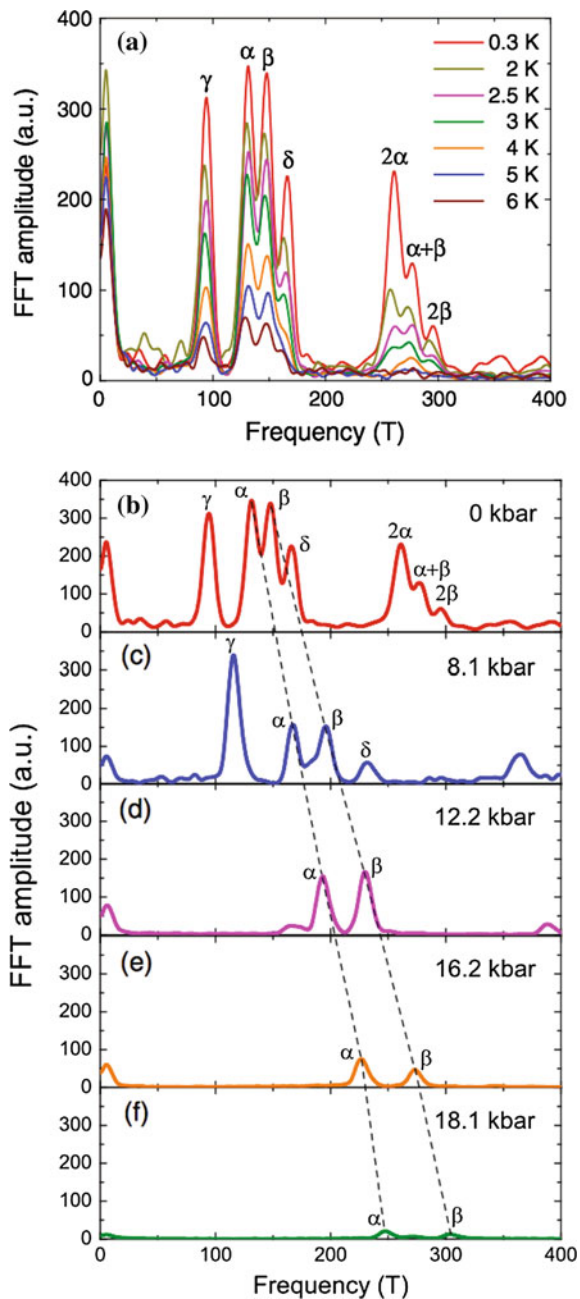
Fig. 3.31 **a** The magnetoresistance up to 14.5 T at various temperatures, with a magnetic field applied along the c -axis direction. There are clear Shubnikov-de Haas oscillations below 5 K. **b** The magnetoresistance of a WTe₂ single crystal under various pressures up to 23.6 kbar, measured at $T = 0.3$ K [99]. Copyright 2015 by the American Physical Society. Reprinted with permission

0.3 to 6 K. The FFT spectrum shows four major peaks at 94.7, 132, 148, and 166 T oscillation frequency, labeled as γ , α , β , and δ . Rather similar frequencies of quantum oscillations were also reported in [125].

Figure 3.31b shows the magnetoresistance of a WTe₂ single crystal under various pressures up to 23.6 kbar, measured at $T = 0.3$ K. With increasing pressure, the magnetoresistance is strongly suppressed and the oscillations also gradually disappear. In order to find out the cause of this strong suppression of magnetoresistance, the authors examined the evolution of its Fermi surfaces with pressure [99]. They identify the four Fermi pockets obtained at ambient pressure, by comparing with the two ARPES results [95, 96]. While one ARPES group found a pair of hole and electron pockets with comparable size along the $\Gamma - X$ direction [95], in a later work, another ARPES group revealed a more complex Fermi surface topology with two pairs of hole and electron pockets [96]. Two pairs of electron-like and hole-like pockets were also reported in [125], where each pair was found to be concentric with identical structure like a set of Russian dolls. The observed anisotropy was much smaller “than one would naively expect in a layered system” [125]. The number and sizes of the Fermi pockets obtained in [99] were consistent with the Fermi surface topology of WTe₂ revealed in [96, 125].

Figure 3.32b–f show the FFT spectra from ambient pressure to 18.1 kbar. (Above 18.1 kbar, the oscillations were too weak to give a reliable FFT spectrum). One can see that both α and β peaks persist all the way to the highest pressure. With increasing pressure, the absolute sizes of α and β pockets increase because of the shrinking of the lattice. The evolution of the relative size α and β pockets was found to correlate with the pressure dependence of magnetoresistance, which confirms the importance of the perfect balance between the electron and hole populations to the extremely large magnetoresistance in WTe₂ [99].

Fig. 3.32 **a** The FFT of the oscillatory magnetoresistance shows four major peaks, labeled as γ , α , β , and δ . The second harmonics were also observed. **b-f** The FFT spectra of the oscillatory magnetoresistance under various pressures up to 18.1 kbar. The α and β peaks persist to high pressure, which are identified as the pair of electron and hole pockets in (a). From (b) to (f), the dashed lines are guides to the eye to show that the sizes of electron and hole pockets become increasingly different [99]. Copyright 2015 by the American Physical Society. Reprinted with permission



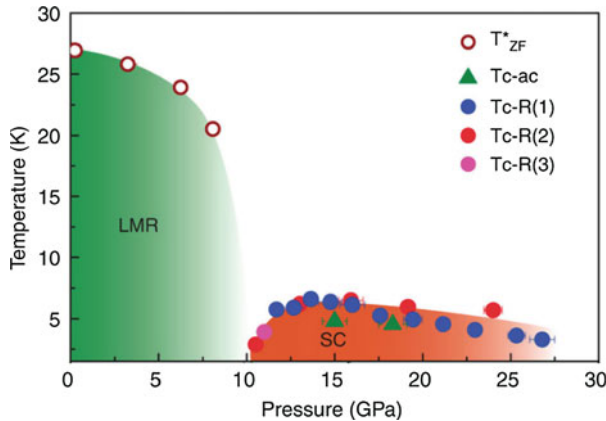


Fig. 3.33 Pressure-temperature phase diagram of WTe₂ and pressure-dependent Hall coefficient. **a** The T_{ZF}^* and T_c versus pressure. The red, pink and blue solid circles represent T_c extracted from different runs of electrical resistance measurements, and the green triangles represent the T_c determined from the a.c. susceptibility measurements. **b** Hall coefficient (R_H) as a function of pressure measured at 10 K and 1 Tesla, displaying a sign change from the positive to the negative at the critical pressure of 10.5 GPa. Solid purple circles and pink squares represent the R_H obtained from different runs. The inset shows the second derivative of the Hall coefficient, the maximum of which corresponds to the sign change of Hall coefficient. The shaded area indicates the pressure range where the superconductivity emerges and the sign of R_H changes. Reproduced from [126]

As mentioned above, the large magnetoresistance effect originates from a perfect balance of hole and electron carriers, which is sensitive to external pressure. In [126], suppression of the large magnetoresistance (LMR) and emergence of superconductivity (SC) in pressurized WTe₂ was reported based on high-pressure synchrotron X-ray diffraction, electrical resistance, magnetoresistance and alternating current magnetic susceptibility measurements. It was found that upon increasing pressure, the positive large magnetoresistance effect was gradually suppressed and turned off at a critical pressure of 10.5 GPa, where superconductivity accordingly emerged (Fig. 3.33).

No structural phase transition was observed under the pressure investigated. In-situ high-pressure Hall coefficient measurements at low temperatures demonstrated that elevating pressure decreased the population of holes but increased that of electrons. At the critical pressure, a sign change of the Hall coefficient was observed [126].

3.5.3 Pressure-Induced Structural Changes

3.5.3.1 X-Ray Diffraction Studies

The nature of the structural evolution was studied by x-ray diffraction and Raman scattering. The measured x-ray diffraction data over the entire pressure range could

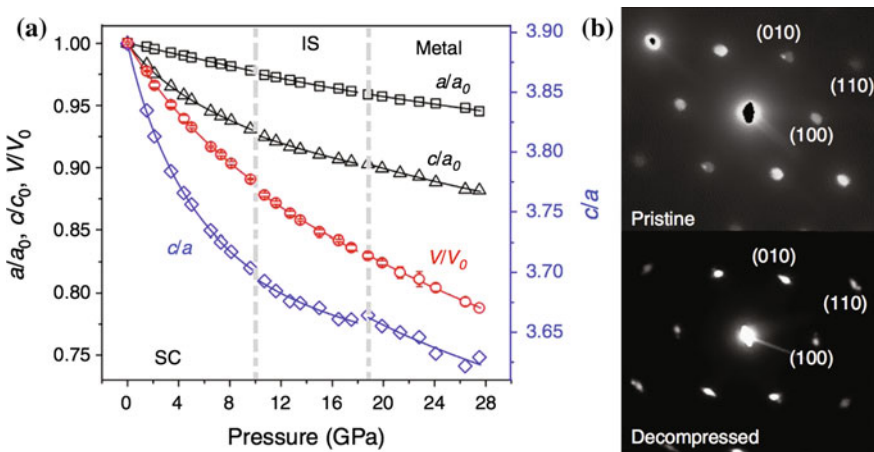


Fig. 3.34 Structural lattice parameters in multilayered MoS₂. **a** Experimental pressure dependence of the lattice parameters of MoS₂. The volume uncertainty bars are within 1 % of the data. **b** The experimental selected area diffraction patterns of both pristine and decompressed MoS₂. The patterns show that the single-crystal structure with the hexagonal symmetry was not significantly affected by high pressures and can be recovered back to its original crystal structure [115]. Reprinted by permission from Macmillan Publishers Ltd., copyright (2014)

be refined to the hexagonal *P63/mmc* structure using the Rietveld refinement suggesting that there is no structural transition in this pressure range. The pressure dependence of the lattice parameters of MoS₂ is shown in Fig. 3.34. The small discontinuity observed at ca. 19 GPa was attributed to a weak distortion of the structure. It is interesting to note that in a layered Sb₂Te₃ topological insulator, which also has a layered structure with vdW bonds between covalently bonded quintuple layers, several structural phase transitions were observed in the same pressure range [127], which may be an indication of the difference between the six-fold coordination achieved in the latter through ‘resonant’ *p*-orbital bonding as opposed to proper, and hence stronger, six covalent bonds in TMCDs that are formed through $4d^2sp^3$ hybridization.

The issue of pressure-induced transformations in MoS₂ using x-ray diffraction measurements was also addressed [123, 128], where structural data up to 81 GPa were collected, and somewhat different conclusions were drawn. All the Bragg peaks shifted to larger angles, showing the shrinkage of the MoS₂ lattice. Upon compression to 26.5 GPa, there were several changes in the XRD patterns in the number, shape, and intensity of the peaks. Upon Rietveld refinement, it was found that both the low-pressure and high-pressure patterns could be described by the single $2H_c$ and $2H_a$ phases, respectively, while the XRD patterns in the pressure range of 26–36 GPa were the superposition of these patterns in one sample [123, 128]. Upon decompression, the transition was reversible, but there was a small hysteresis [123].

The refined lattice parameters and the unit cell volume of different samples of MoS₂ upon both the compression and decompression runs as a function of pressure

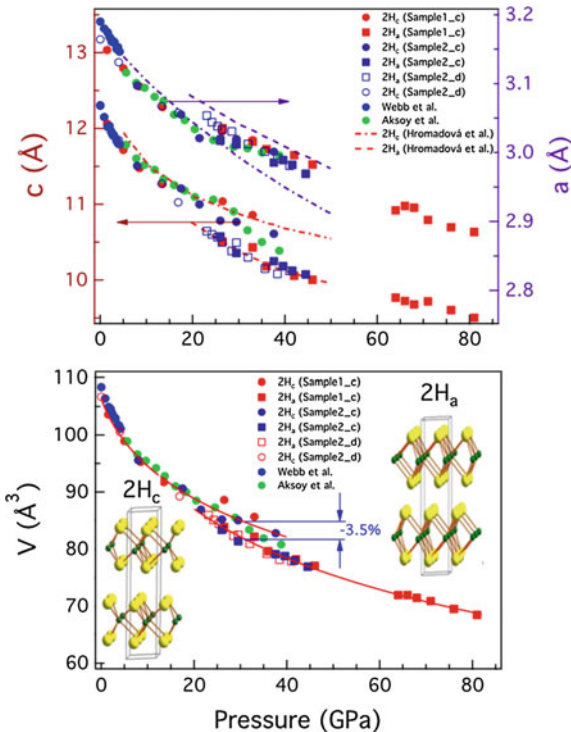


Fig. 3.35 Pressure dependence of the lattice parameters (*upper panel*) and volume per formula unit (*lower panel*) of two MoS_2 samples in both $2H_c$ and $2H_a$ phases in both the compression (denoted by ‘c’) and decompression (denoted by ‘d’) runs. The experimental data points from [130, 131], and the theoretical results of [132] are plotted for comparison. The arrows in the *upper panel* indicate the corresponding axes. The solid lines demonstrate the fitting data with respect to the equation of states of $2H_c$ and $2H_a$. The insets illustrate the atomic arrangement of the $2H_c$ and $2H_a$ structures where Mo is represented by small spheres and S by large spheres [123]. Copyright 2014 by the American Physical Society. Reprinted with permission

are shown in Fig. 3.35 together with experimental data obtained by other groups. The Birch-Murnaghan equation of state [129] provides a good description of the volume-pressure relationship in both phases. Fitting the data points in the $2H_c$ phase, the ambient-pressure bulk modulus K_0 of ≈ 47.65 GPa was obtained, while $K_0 \approx 57.86$ GPa, was obtained for the $2H_a$ phase. The structural transition from $2H_c$ to $2H_a$ due to MoS_2 layer sliding results in the contraction of the unit cell of about 3.5 % at 30 GPa.

3.5.3.2 Raman Scattering

Pressure effects in MoS_2 were initially studied in [122, 130, 133] in a rather limited pressure range of up to 15 GPa. This subject has been recently revisited due to the

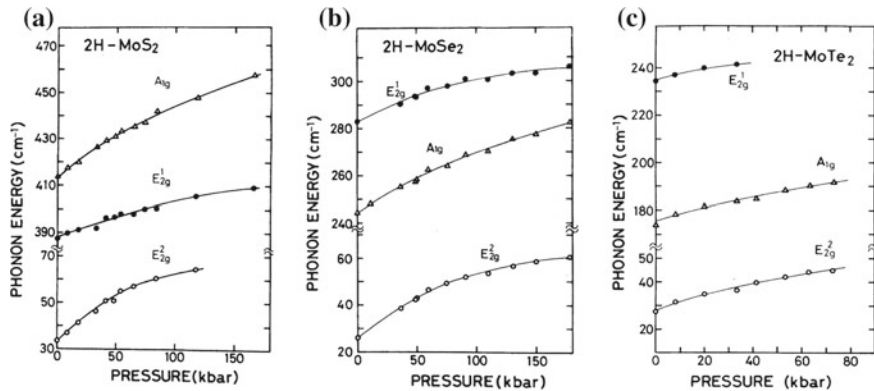
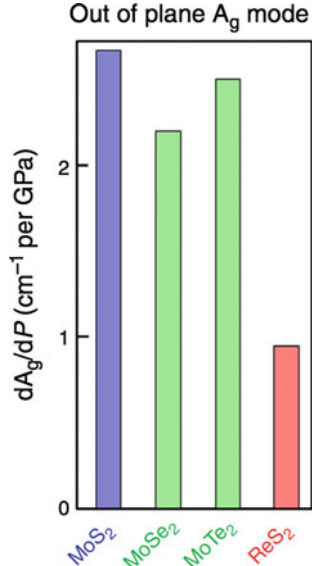


Fig. 3.36 Pressure-dependent phonon energies of the A_{1g} and E_{2g}^1 modes in 2H-MoS₂ (a), 2H-MoSe₂ (b), and 2H-MoTe₂ (c) [122]. Copyright 1982 by the American Physical Society. Reprinted with permission

Fig. 3.37 Comparison of pressure coefficients of the A_{1g} Raman mode of different TMDCs [48]. Reprinted by permission from Macmillan Publishers Ltd., copyright (2014)



interest in 2D TMDC, and high-pressure measurements were re-done over a significantly larger pressure range [115, 123]. Early results for MoS₂, MoSe₂, and MoTe₂ are shown in Fig. 3.36.

While the Raman peaks in MoX₂ shift in approximately very similar manner, the pressure-induced changes in Raman spectra of ReS₂ are much weaker (Fig. 3.37), which was attributed to a much weaker vdW interaction between the layers in this material [48] resulting from strong structural distortions.

More recently, Raman measurements were conducted *in situ* to probe vibrational changes in multilayered MoS₂ under high pressure [115]. Analyses of the high-pressure Raman spectra revealed (Fig. 3.28c) that the A_{1g} mode shows three distinct regions: (i) significantly increasing Raman shift up to about 10 GPa, (ii) nearly invariant shift with pressure between 10 and 19 GPa and (iii) pressure-dependent Raman shift above 19 GPa. An evaluation of the difference between the E_{2g}^1 and A_{1g} peak positions (Fig. 3.28d) also reveals three distinct regions with the maximum intensity ratio observed in the metallic region. It should be noted that this result is in disagreement with an earlier work [122], where a monotonic increase in the A_{2g} peak frequency was observed up to ca. 17 GPa. The DFT simulations suggested [115] that with increasing pressure, the contribution to the conduction band minima from S- p_x and S- p_y orbitals decreases, while the contribution from S- p_z orbitals increases. Similarly, there was a reduction with increasing pressure in contributions from Mo- p orbitals, while the contribution from Mo- d_{z^2} increased.

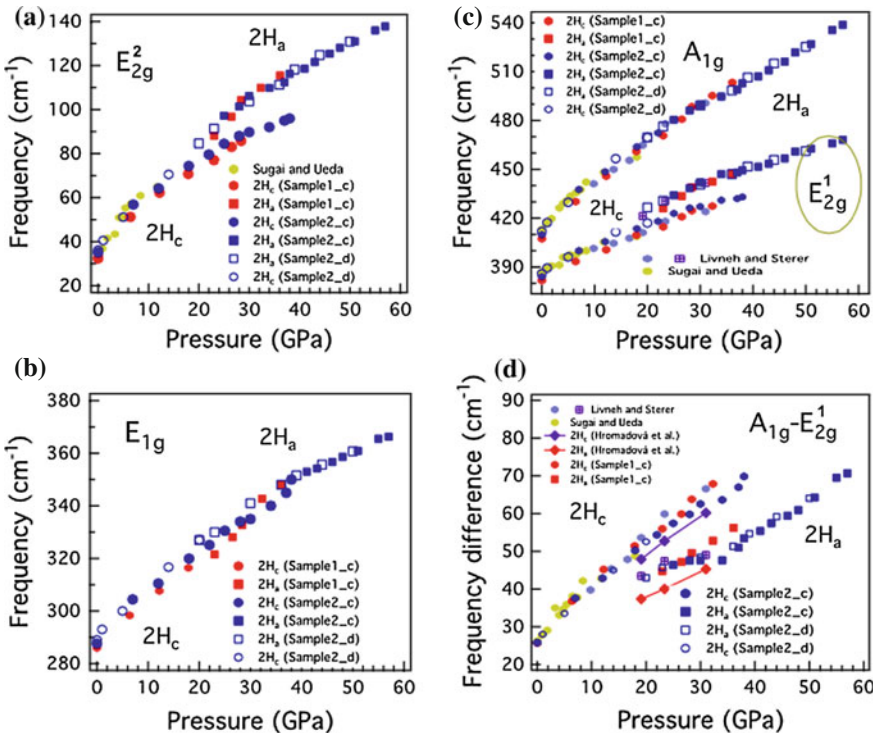
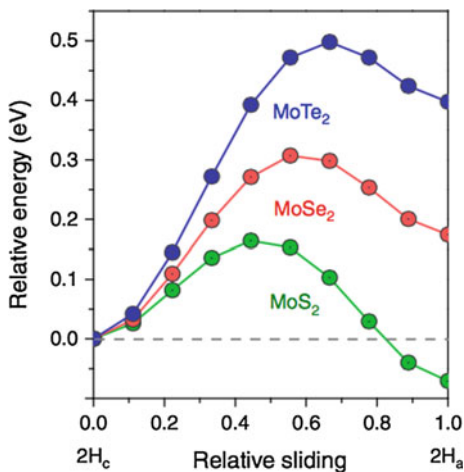


Fig. 3.38 Phonon frequencies of MoS₂ as a function of pressure with in-plane E_{2g}^2 (a), E_{1g} (b), and E_{2g}^1 modes and the out-of-plane A_{1g} mode (c) and the frequency differences (d) with respect to the corresponding modes. The solid and open symbols are the data for compression (denoted by ‘c’) and decompression (by ‘d’) run, respectively. The experimental [122] and theoretical [132] data points are shown for comparison. $2H_c$ and $2H_a$ are the low-pressure and high-pressure phases, respectively [123]. Copyright 2014 by the American Physical Society. Reprinted with permission

Fig. 3.39 The total energy of MoS_2 , MoSe_2 and MoTe_2 as a function of relative sliding from $2H_c$ to $2H_a$. The total energies of $2H_c$ structures are set to be zero as references, marked by the broken line. Reproduced from [134]



Raman scattering in a larger pressure range was studied in [123]. Figure 3.38 shows the pressure dependence of the vibrational frequencies and their differences for MoS_2 together with the data from other work [122, 132]. Consistent with these previous experiments, the E_{2g}^2 , A_{1g} , and E_{2g}^1 modes of both $2H_c$ and $2H_a$ phases increased with pressure. In addition, high-pressure behavior of the rigid layer mode E_{2g}^2 was observed. This mode first increased very rapidly, as it mostly involves weak interlayer vdW bonds, and then this rapid increase gradually slowed down approaching the transition, followed by the splitting of the peak. Clear Raman anomalies through the transition were observed for E_{2g}^1 and E_{2g}^2 , which involve lateral atomic motion, while almost no anomaly is seen for the A_{1g} mode, which was consistent with a radical change in the interlayer stacking and bonding evidenced by structural changes and discontinuities in lattice parameters [123].

Similar studies conducted on MoSe_2 demonstrated that the structural evolution proceeds without the $2H_c - 2H_a$ structural transition [134], which was attributed to different energy evolution during the relative layer sliding (Fig. 3.39). While the energy barrier was the lowest for MoS_2 and the $2H_a$ phase had a lower energy than the $2H_c$ phase, for MoSe_2 and MoTe_2 , the energy barrier was higher and the $2H_a$ phase had a higher energy than the $2H_c$ phase.

References

1. J. Wilson, A. Yoffe, The transition metal dichalcogenides discussion and interpretation of the observed optical, electrical and structural properties. *Adv. Phys.* **18**(73), 193 (1969)
2. M.A. Popescu, *Non-Crystalline Chalcogenides* (Kluwer Academic Publ, Dordrecht, 2000)
3. M. Chhowalla, H.S. Shin, G. Eda, L.J. Li, K.P. Loh, H. Zhang, The chemistry of two-dimensional layered transition metal dichalcogenide nanosheets. *Nat. Chem.* **5**(4), 263 (2013)

4. H. Katzke, P. Tolédano, W. Depmeier, Phase transitions between polytypes and intralayer superstructures in transition metal dichalcogenides. *Phys. Rev. B* **69**(13), 134111 (2004)
5. M. Yamamoto, S.T. Wang, M. Ni, Y.F. Lin, S.L. Li, S. Aikawa, W.B. Jian, K. Ueno, K. Wakabayashi, K. Tsukagoshi, Strong enhancement of raman scattering from a bulk-inactive vibrational mode in few-layer MoTe₂. *ACS Nano* **8**(4), 3895 (2014)
6. G. Lucovsky, R. White, J. Benda, J. Revelli, Infrared-reflectance spectra of layered group-IV and group-VI transition-metal dichalcogenides. *Phys. Rev. B* **7**(8), 3859 (1973)
7. L.C. Towle, V. Oberbeck, B.E. Brown, R.E. Stajdohar, Molybdenum diselenide: rhombohedral high pressure-high temperature polymorph. *Science* **154**(3751), 895 (1966)
8. C.H. Lee, E.C. Silva, L. Calderin, M.A.T. Nguyen, M.J. Hollander, B. Bersch, T.E. Mallouk, J.A. Robinson, Tungsten ditelluride: a layered semimetal. *Sci. Rep.* **5** (2015). doi:[10.1038/srep10013](https://doi.org/10.1038/srep10013)
9. B.E. Brown, The crystal structures of WTe₂ and high-temperature MoTe₂. *Acta Cryst.* **20**(2), 268 (1966)
10. H.J. Lamfers, A. Meetsma, G. Wiegers, J. De Boer, The crystal structure of some rhenium and technetium dichalcogenides. *J. Alloys Compd.* **241**(1), 34 (1996)
11. J. Wildervanck, F. Jellinek, The dichalcogenides of technetium and rhenium. *J. Less Common Metals* **24**(1), 73 (1971)
12. N. Alcock, A. Kjekshus, The crystal structure of ReSe₂. *Acta Chem. Scand.* **19**(1), 79 (1965)
13. M. Kertesz, R. Hoffmann, Octahedral versus trigonal-prismatic coordination and clustering in transition-metal dichalcogenides. *J. Amer. Chem. Soc.* **106**(12), 3453 (1984)
14. C. Fang, G. Wiegers, C. Haas, R. De Groot, Electronic structures of, and in the real and the hypothetical undistorted structures. *J. Phys. Cond. Matter* **9**(21), 4411 (1997)
15. C. Ho, P. Liao, Y. Huang, T. Yang, K. Tiong, Optical absorption of ReS₂ and ReSe₂ single crystals. *J. Appl. Phys.* **81**(9), 6380 (1997)
16. C. Ho, Y. Huang, K. Tiong, P. Liao, Absorption-edge anisotropy in ReS₂ and ReSe₂ layered semiconductors. *Phys. Rev. B* **58**(24), 16130 (1998)
17. C. Ho, Y. Huang, K. Tiong, In-plane anisotropy of the optical and electrical properties of ReS₂ and ReSe₂ layered crystals. *J. Alloys Compd.* **317**, 222 (2001)
18. J. Wilson, F. Di Salvo, S. Mahajan, Charge-density waves in metallic, layered, transition-metal dichalcogenides. *Phys. Rev. Lett.* **32**(16), 882 (1974)
19. J.A. Wilson, F. Di Salvo, S. Mahajan, Charge-density waves and superlattices in the metallic layered transition metal dichalcogenides. *Adv. Phys.* **24**(2), 117 (1975)
20. W. McMillan, Landau theory of charge-density waves in transition-metal dichalcogenides. *Phys. Rev. B* **12**(4), 1187 (1975)
21. K. Motizuki, *Structural Phase Transitions in Layered Transition Metal Compounds* (Reidel, Dordrecht, 1986)
22. R.E. Thomson, B. Burk, A. Zettl, J. Clarke, Scanning tunneling microscopy of the charge-density-wave structure in 1T-TaS₂. *Phys. Rev. B* **49**(24), 16899 (1994)
23. M. Yoshida, Y. Zhang, J. Ye, R. Suzuki, Y. Imai, S. Kimura, A. Fujiwara, Y. Iwasa, Controlling charge-density-wave states in nano-thick crystals of 1T-TaS₂. *Sci. Rep.* **4** (2014). doi:[10.1038/srep07302](https://doi.org/10.1038/srep07302)
24. Y. Yu, F. Yang, X.F. Lu, Y.J. Yan, Y.H. Cho, L. Ma, X. Niu, S. Kim, Y.W. Son, D. Feng et al., Gate-tunable phase transitions in thin flakes of 1T-TaS₂. *Nat. Nanotech.* **10**(3), 270 (2015)
25. L.P. Gor'kov, Strong electron-lattice coupling as the mechanism behind charge density wave transformations in transition-metal dichalcogenides. *Phys. Rev. B* **85**(16), 165142 (2012)
26. D. Shen, B. Xie, J. Zhao, L. Yang, L. Fang, J. Shi, R. He, D. Lu, H. Wen, D. Feng, Novel mechanism of a charge density wave in a transition metal dichalcogenide. *Phys. Rev. Lett.* **99**(21), 216404 (2007)
27. J. Dai, E. Calleja, J. Alldredge, X. Zhu, L. Li, W. Lu, Y. Sun, T. Wolf, H. Berger, K. McElroy, Microscopic evidence for strong periodic lattice distortion in two-dimensional charge-density wave systems. *Phys. Rev. B* **89**(16), 165140 (2014)
28. A.C. Neto, Charge density wave, superconductivity, and anomalous metallic behavior in 2d transition metal dichalcogenides. *Phys. Rev. Lett.* **86**(19), 4382 (2001)

29. S. Koley, M. Laad, N. Vidhyadhiraja, A. Taraphder, Preformed excitons, orbital selectivity, and charge density wave order in 1T-TaS₂. *Phys. Rev. B* **90**(11), 115146 (2014)
30. S. Koley, N. Mohanta, A. Taraphder, The unusual normal state and charge-density-wave order in 2H-NbSe₂. *J. Phys. Cond. Matter* **27**(18), 185601 (2015)
31. S. Hellmann, T. Rohwer, M. Kalläne, K. Hanff, C. Sohrt, A. Stange, A. Carr, M. Murnane, H. Kapteyn, L. Kipp, et al., Time-domain classification of charge-density-wave insulators. *Nat. Commun.* **3** (2012). doi:[10.1038/ncomms2078](https://doi.org/10.1038/ncomms2078)
32. K. Rossnagel, On the origin of charge-density waves in select layered transition-metal dichalcogenides. *J. Phys. Cond. Matter* **23**(21), 213001 (2011)
33. L. Stojchevska, I. Vaskivskyi, T. Mertelj, P. Kusar, D. Svetin, S. Brazovskii, D. Mihailovic, Ultrafast switching to a stable hidden quantum state in an electronic crystal. *Science* **344**(6180), 177 (2014)
34. M.J. Hollander, Y. Liu, W.J. Lu, L.J. Li, Y.P. Sun, J.A. Robinson, S. Datta, Electrically driven reversible insulator-metal phase transition in 1T-TaS₂. *Nano Lett.* **15**(3), 1861 (2015)
35. A.D. McNaught, A. Wilkinson, *IUPAC Compendium of Chemical Terminology*, 2nd edn. (Blackwell Science, Oxford, 1997)
36. R. Zallen, M. Slade, A. Ward, Lattice vibrations and interlayer interactions in crystalline As₂S₃ and As₂Se₃. *Phys. Rev. B* **3**(12), 4257 (1971)
37. T. Sekine, M. Izumi, T. Nakashizu, K. Uchinokura, E. Matsuura, Raman scattering and infrared reflectance in 2H-MoSe₂. *J. Phys. Soc. Jpn.* **49**(3), 1069 (1980)
38. J. Verble, T. Wietling, P. Reed, Rigid-layer lattice vibrations and van der Waals bonding in hexagonal MoS₂. *Solid State Commun.* **11**(8), 941 (1972)
39. A.P. Gaur, S. Sahoo, M. Ahmadi, S.P. Dash, M.J.F. Guinel, R.S. Katiyar, Surface energy engineering for tunable wettability through controlled synthesis of MoS₂. *Nano Lett.* **14**(8), 4314 (2014)
40. G. Cunningham, M. Lotya, C.S. Cucinotta, S. Sanyito, S.D. Bergin, R. Menzel, M.S. Shaffer, J.N. Coleman, Solvent exfoliation of transition metal dichalcogenides: dispersibility of exfoliated nanosheets varies only weakly between compounds. *ACS Nano* **6**(4), 3468 (2012)
41. K. Weiss, J.M. Phillips, Calculated specific surface energy of molybdenite (MoS₂). *Phys. Rev. B* **14**(12), 5392 (1976)
42. J.W. Jiang, H.S. Park, A gaussian treatment for the friction issue of Lennard-Jones potential in layered materials: application to friction between graphene, MoS₂ and black phosphorus. *J. Appl. Phys.* **117**, 124304 (2015)
43. T. Björkman, A. Gulans, A.V. Krasheninnikov, R.M. Nieminen, van der Waals bonding in layered compounds from advanced density-functional first-principles calculations. *Phys. Rev. Lett.* **108**(23), 235502 (2012)
44. H. Mirhosseini, G. Roma, J. Kiss, C. Felser, First-principles investigation of the bulk and low-index surfaces of MoSe₂. *Phys. Rev. B* **89**(20), 205301 (2014)
45. T. Bučko, S. Lebègue, J.G. Ángyán, J. Hafner, J. Chem., Extending the applicability of the Tkatchenko-Scheffler dispersion correction via iterative Hirshfeld partitioning. *J. Chem. Phys.* **141**(3), 034114 (2014)
46. H. Peelaers, C.G. Van de Walle, First-principles study of van der Waals interactions in MoS₂ and MoO₃. *J. Phys. Cond. Matter* **26**(30), 305502 (2014)
47. A.V. Kolobov, J. Tominaga, *Chalcogenides: Metastability and Phase Change Phenomena* (Springer Science & Business Media, Berlin, 2012)
48. S. Tongay, H. Sahin, C. Ko, A. Luce, W. Fan, K. Liu, J. Zhou, Y.S. Huang, C.H. Ho, J. Yan et al., Monolayer behaviour in bulk ReS₂ due to electronic and vibrational decoupling. *Nat. Commun.* **5** (2014). doi:[10.1038/ncomms4252](https://doi.org/10.1038/ncomms4252)
49. H.J. Conley, B. Wang, J.I. Ziegler, R.F. Haglund Jr., S.T. Pantelides, K.I. Bolotin, Bandgap engineering of strained monolayer and bilayer MoS₂. *Nano Lett.* **13**(8), 3626 (2013)
50. Y. Wang, C. Cong, C. Qiu, T. Yu, Raman spectroscopy study of lattice vibration and crystallographic orientation of monolayer MoS₂ under uniaxial strain. *Small* **9**(17), 2857 (2013)
51. Y. Zhao, X. Luo, H. Li, J. Zhang, P.T. Araujo, C.K. Gan, J. Wu, H. Zhang, S.Y. Quek, M.S. Dresselhaus et al., Interlayer breathing and shear modes in few-trilayer MoS₂ and WSe₂. *Nano Lett.* **13**(3), 1007 (2013)

52. X. Luo, Y. Zhao, J. Zhang, M. Toh, C. Kloc, Q. Xiong, S.Y. Quek, Effects of lower symmetry and dimensionality on Raman spectra in two-dimensional WSe₂. *Phys. Rev. B* **88**(19), 195313 (2013)
53. A. Kormányos, V. Zólyomi, N.D. Drummond, P. Rakytá, G. Burkard, V.I. Fal'ko, Monolayer MoS₂: trigonal warping, the Γ valley, and spin-orbit coupling effects. *Phys. Rev. B* **88**(4), 045416 (2013)
54. L.M. Malard, T.V. Alencar, A.P.M. Barboza, K.F. Mak, A.M. de Paula, Observation of intense second harmonic generation from MoS₂ atomic crystals. *Phys. Rev. B* **87**(20), 201401 (2013)
55. J. Ribeiro-Soares, R. Almeida, E. Barros, P. Araújo, M. Dresselhaus, L. Cançado, A. Jorio, Group theory analysis of phonons in two-dimensional transition metal dichalcogenides. *Phys. Rev. B* **90**(11), 115438 (2014)
56. R. Loudon, The Raman effect in crystals. *Adv. Phys.* **13**(52), 423 (1964)
57. R.L. Chu, G.B. Liu, W. Yao, X. Xu, D. Xiao, C. Zhang, Spin-orbit-coupled quantum wires and Majorana fermions on zigzag edges of monolayer transition-metal dichalcogenides. *Phys. Rev. B* **89**(15), 155317 (2014)
58. T. Böker, R. Severin, A. Müller, C. Janowitz, R. Manzke, D. Voß, P. Krüger, A. Mazur, J. Pollmann, Band structure of MoS₂, MoSe₂, and α -MoTe₂: angle-resolved photoelectron spectroscopy and ab initio calculations. *Phys. Rev. B* **64**(23), 235305 (2001)
59. D. Latzke, W. Zhang, S. Tongay, T.R. Chang, H. Lin, H.T. Jeng, A. Suslu, J. Wu, A. Bansil, A. Lanzara, Electronic structure, spin-orbit coupling, and interlayer interaction in bulk MoS₂ and WS₂. *Phys. Rev. B* **91**, 235202 (2015)
60. J.A. Schuller, S. Karaveli, T. Schiros, K. He, S. Yang, I. Kymmissis, J. Shan, R. Zia, Orientation of luminescent excitons in layered nanomaterials. *Nat. Nanotech.* **8**(4), 271 (2013)
61. A. Molina-Sánchez, D. Sangalli, K. Hummer, A. Marini, L. Wirtz, Effect of spin-orbit interaction on the optical spectra of single-layer, double-layer, and bulk MoS₂. *Phys. Rev. B* **88**(4), 045412 (2013)
62. K. Kam, B. Parkinson, Detailed photocurrent spectroscopy of the semiconducting group VIIB transition metal dichalcogenides. *J. Phys. Chem.* **86**(4), 463 (1982)
63. Y. Tan, R. He, C. Cheng, D. Wang, Y. Chen, F. Chen, Polarization-dependent optical absorption of MoS₂ for refractive index sensing. *Sci. Rep.* **4** (2014). doi:[10.1038/srep07523](https://doi.org/10.1038/srep07523)
64. J. Verble, T. Wieting, Lattice mode degeneracy in MoS₂ and other layer compounds. *Phys. Rev. Lett.* **25**(6), 362 (1970)
65. T. Wieting, J. Verble, Infrared and Raman studies of long-wavelength optical phonons in hexagonal MoS₂. *Phys. Rev. B* **3**(12), 4286 (1971)
66. T. Wieting, A. Grisel, F. Levy, Interlayer bonding and localized charge in MoSe₂ and α -MoTe₂. *Physica B+C* **99**(1), 337 (1980)
67. A. Stacy, D. Hodul, Raman spectra of IVB and VIIB transition metal disulfides using laser energies near the absorption edges. *J. Phys. Chem. Solids* **46**(4), 405 (1985)
68. T. Sekine, K. Uchinokura, T. Nakashizu, E. Matsuura, R. Yoshizaki, Dispersive Raman mode of layered compound 2H-MoS₂ under the resonant condition. *J. Phys. Soc. Jpn.* **53**(2), 811 (1984)
69. J. Chen, C. Wang, Second order Raman spectrum of MoS₂. *Solid State Commun.* **14**(9), 857 (1974)
70. T. Wieting, Long-wavelength lattice vibrations of MoS₂ and GaSe. *Solid State Commun.* **12**(9), 931 (1973)
71. J. Smith, J. Tsang, M. Shafer, Raman spectra of several layer compounds with charge density waves. *Solid State Commun.* **19**(4), 283 (1976)
72. C. Wang, J. Chen, Raman spectrum of metallic layered compound NbSe₂. *Solid State Commun.* **14**(11), 1145 (1974)
73. O.P. Agnihotri, H.K. Sehgal, Fundamental infrared lattice vibration spectrum and the laser-excited raman spectrum of MoSe₂. *Philos. Mag.* **26**(3), 753 (1972)
74. O.P. Agnihotri, H.K. Sehgal, A.K. Garg, Laser excited Raman spectra of Gr. VI semiconducting compounds. *Solid State Commun.* **12**(2), 135 (1973)

75. A.K. Garg, H.K. Sehgal, O.P. Agnihotri, Infrared optical properties of MoSe₂. Solid State Commun. **12**(12), 1261 (1973)
76. S.I. Uchida, S. Tanaka, Optical phonon modes and localized effective charges of transition-metal dichalcogenides. J. Phys. Soc. Jpn. **45**(1), 153 (1978)
77. C. Ramana, U. Becker, V. Shutthanandan, C. Julien, Oxidation and metal-insertion in molybdenite surfaces: evaluation of charge-transfer mechanisms and dynamics. Geochem. Trans. **9**(1), 8 (2008)
78. R. Zallen, M. Slade, Rigid-layer modes in chalcogenide crystals. Phys. Rev. B **9**(4), 1627 (1974)
79. T. Sekine, T. Nakashizu, K. Toyoda, K. Uchinokura, E. Matsuura, Raman scattering in layered compound 2H-WS₂. Solid State Commun. **35**(4), 371 (1980)
80. P. Bertrand, Surface-phonon dispersion of MoS₂. Phys. Rev. B **44**(11), 5745 (1991)
81. S. Tongay, S.S. Varroosfaderani, B.R. Appleton, J. Wu, A.F. Hebard, Magnetic properties of MoS₂: existence of ferromagnetism. Appl. Phys. Lett. **101**(12), 123105 (2012)
82. T.C. Damen, S. Porto, B. Tell, Raman effect in zinc oxide. Phys. Rev. **142**(2), 570 (1966)
83. B.C. Windom, W. Sawyer, D.W. Hahn, A Raman spectroscopic study of MoS₂ and MoO₃: applications to tribological systems. Tribology Lett. **42**(3), 301 (2011)
84. C. Sourisseau, F. Cruege, M. Fouassier, M. Alba, Second-order raman effects, inelastic neutron scattering and lattice dynamics in 2H-WS₂. Chem. Phys. **150**(2), 281 (1991)
85. T. Livneh, E. Sterer, Resonant Raman scattering at exciton states tuned by pressure and temperature in 2H-MoS₂. Phys. Rev. B **81**(19), 195209 (2010)
86. J.H. Fan, P. Gao, A.M. Zhang, B.R. Zhu, H.L. Zeng, X.D. Cui, R. He, Q.M. Zhang, Resonance Raman scattering in bulk 2H-MX₂ (M = Mo, W; X = S, Se) and monolayer MoS₂. J. Appl. Phys. **115**(5), 053527 (2014)
87. K. Gołasa, M. Grzeszczyk, P. Leszczyński, C. Faugeras, A. Nicolet, A. Wysmołek, M. Potemski, A. Babiński, Multiphonon resonant Raman scattering in MoS₂. App. Phys. Lett. **104**(9), 092106 (2014)
88. G.L. Frey, R. Tenne, M.J. Matthews, M. Dresselhaus, G. Dresselhaus, Raman and resonance Raman investigation of MoS₂ nanoparticles. Phys. Rev. B **60**(4), 2883 (1999)
89. D. Dumcenco, K. Chen, Y. Wang, Y. Huang, K. Tiong, Raman study of 2H-Mo_{1-x}W_xS₂ layered mixed crystals. J. Alloys Compd. **506**(2), 940 (2010)
90. N. Nagaoso, E. Hanamura, Microscopic theory of the Raman and infrared spectra of transition-metal dichalcogenides in the charge-density-wave state. Phys. Rev. B **29**(4), 2060 (1984)
91. C. Muratore, V. Varshney, J. Gengler, J. Hu, J. Bultman, T. Smith, P. Shamberger, B. Qiu, X. Ruan, A. Roy et al., Cross-plane thermal properties of transition metal dichalcogenides. Appl. Phys. Lett. **102**(8), 081604 (2013)
92. K. Akintola, G. Andrews, S. Curnoe, M. Koehler, V. Keppens, Raman and Brillouin scattering studies of bulk 2H-WSe₂. J. Phys. Cond. Matter **27**(39), 395401 (2015)
93. R. Harley, P. Fleury, Surface Brillouin scattering from layered metals and semimetals. J. Phys. C: Solid State **12**(22), L863 (1979)
94. M.N. Ali, J. Xiong, S. Flynn, J. Tao, Q.D. Gibson, L.M. Schoop, T. Liang, N. Halldorarachchige, M. Hirschberger, N. Ong et al., Large, non-saturating magnetoresistance in WTe₂. Nature **514**(7521), 205 (2014)
95. I. Pletikosić, M.N. Ali, A.V. Fedorov, R.J. Cava, T. Valla, Electronic structure basis for the extraordinary magnetoresistance in WTe₂. Phys. Rev. Lett. **113**(21), 216601 (2014)
96. J. Jiang, F. Tang, X. Pan, H. Liu, X. Niu, Y. Wang, D. Xu, H. Yang, B. Xie, F. Song et al., Signature of strong spin-orbital coupling in the large non-saturating magnetoresistance material WTe₂. Phys. Rev. Lett. **115**, 166601 (2015)
97. Y. Wu, N.H. Jo, M. Ochi, L. Huang, D. Mou, S.L. Bud'ko, P. Canfield, N. Trivedi, R. Arita, A. Kaminski, Temperature-induced Lifshitz transition in WTe₂. Phys. Rev. Lett. **115**(16), 166602 (2015)
98. D. Rhodes, S. Das, Q. Zhang, B. Zeng, N. Pradhan, N. Kikugawa, E. Manousakis, L. Balicas, Role of spin-orbit coupling and evolution of the electronic structure of WTe₂ under an external magnetic field. Phys. Rev. B **92**, 125152 (2015)

99. P. Cai, J. Hu, L. He, J. Pan, X. Hong, Z. Zhang, J. Zhang, J. Wei, Z. Mao, S. Li, Drastic pressure effect on the extremely large magnetoresistance in WTe₂: quantum oscillation study. *Phys. Rev. Lett.* **115**(5), 057202 (2015)
100. L. Thoutam, Y. Wang, Z. Xiao, S. Das, A. Luican-Mayer, R. Divan, G. Crabtree, W. Kwok, Temperature-dependent three-dimensional anisotropy of the magnetoresistance in WTe₂. *Phys. Rev. Lett.* **115**(4), 046602 (2015)
101. W.D. Kong, S.F. Wu, P. Richard, C.S. Lian, J.T. Wang, C.L. Yang, Y.G. Shi, H. Ding, Raman scattering investigation of large positive magnetoresistance material WTe₂. *Appl. Phys. Lett.* **106**(8), 081906 (2015)
102. C.C. Homes, M.N. Ali, R.J. Cava, Optical properties of the perfectly compensated semimetal WTe₂. *Phys. Rev. B* **92**(16), 161109 (2015)
103. Y. Dai, J. Bowlan, H. Li, H. Miao, S. Wu, W. Kong, Y. Shi, S. Trugman, J.X. Zhu, H. Ding et al., Ultrafast carrier dynamics in the large-magnetoresistance material WTe₂. *Phys. Rev. B* **92**(16), 161104 (2015)
104. H.Y. Lv, W.J. Lu, D.F. Shao, Y. Liu, S.G. Tan, Y.P. Sun, Perfect charge compensation in WTe₂ for the extraordinary magnetoresistance: from bulk to monolayer. *Europhys. Lett.* **110**(3), 37004 (2015)
105. X. Wan, A.M. Turner, A. Vishwanath, S.Y. Savrasov, Topological semimetal and Fermi-arc surface states in the electronic structure of pyrochlore iridates. *Phys. Rev. B* **83**(20), 205101 (2011)
106. A. Burkov, L. Balents, Weyl semimetal in a topological insulator multilayer. *Phys. Rev. Lett.* **107**(12), 127205 (2011)
107. A.A. Soluyanov, D. Gresch, Z. Wang, Q. Wu, M. Troyer, X. Dai, B.A. Bernevig, A new type of Weyl semimetals. *Nature* **527**, 495 (2015)
108. T.R. Chang, S.Y. Xu, G. Chang, C.C. Lee, S.M. Huang, B. Wang, G. Bian, H. Zheng, D.S. Sanchez, I. Belopolski, et al. Arc-tunable Weyl fermion metallic state in Mo_xW_{1-x}Te₂. arXiv preprint [arXiv:1508.06723](https://arxiv.org/abs/1508.06723) (2015)
109. S.Y. Xu, I. Belopolski, N. Alidoust, M. Neupane, G. Bian, C. Zhang, R. Sankar, G. Chang, Z. Yuan, C.C. Lee et al., Discovery of a Weyl fermion semimetal and topological Fermi arcs. *Science* **349**(6248), 613 (2015)
110. S.Y. Xu, I. Belopolski, D.S. Sanchez, C. Zhang, G. Chang, C. Guo, G. Bian, Z. Yuan, H. Lu, T.R. Chang et al., Experimental discovery of a topological Weyl semimetal state in TaP. *Sci. Adv.* **1**(10), 1501092 (2015)
111. Y. Sun, S.C. Wu, M.N. Ali, C. Felser, B. Yan, Prediction of Weyl semimetal in orthorhombic MoTe₂. *Phys. Rev. B* **92**(16), 161107 (2015)
112. S. Bhattacharyya, A.K. Singh, Semiconductor-metal transition in semiconducting bilayer sheets of transition-metal dichalcogenides. *Phys. Rev. B* **86**(7), 075454 (2012)
113. P. Johari, V.B. Shenoy, Tuning the electronic properties of semiconducting transition metal dichalcogenides by applying mechanical strains. *ACS Nano* **6**(6), 5449 (2012)
114. E. Scalise, M. Houssa, G. Pourtois, V. Afanasev, A. Stesmans, Strain-induced semiconductor to metal transition in the two-dimensional honeycomb structure of MoS₂. *Nano Res.* **5**(1), 43 (2012)
115. A.P. Nayak, S. Bhattacharyya, J. Zhu, J. Liu, X. Wu, T. Pandey, C. Jin, A.K. Singh, D. Akinwande, J.F. Lin, Pressure-induced semiconducting to metallic transition in multilayered molybdenum disulphide. *Nat. Commun.* **5** (2014). doi:[10.1038/ncomms4731](https://doi.org/10.1038/ncomms4731)
116. J. Feldman, Elastic constants of 2H-MoS₂ and 2H-NbSe₂ extracted from measured dispersion curves and linear compressibilities. *J. Phys. Chem. Solids* **37**(12), 1141 (1976)
117. L. Wei, C. Jun-fang, H. Qinyu, W. Teng, Electronic and elastic properties of MoS₂. *Physica B* **405**(10), 2498 (2010)
118. T. Todorova, V. Alexiev, R. Prins, T. Weber, Ab initio study of 2H-MoS₂ using Hay and Wadt effective core pseudo-potentials for modelling the (10 $\bar{1}$ 0) surface structure. *Phys. Chem. Chem. Phys.* **6**(11), 3023 (2004)
119. V. Alexiev, R. Prins, T. Weber, Ab initio study of MoS₂ and Li adsorbed on the (10 $\bar{1}$ 0) face of MoS₂. *Phys. Chem. Chem. Phys.* **2**(8), 1815 (2000)

120. H. Peelaers, C.G. Van de Walle, Elastic constants and pressure-induced effects in MoSe₂. *J. Phys. Chem. C* **118**(22), 12073 (2014)
121. S. Grimme, Semiempirical GGA-type density functional constructed with a long-range dispersion correction. *J. Comput. Chem.* **27**(15), 1787 (2006)
122. S. Sugai, T. Ueda, High-pressure raman spectroscopy in the layered materials 2H-MoS₂, 2H-MoSe₂, and 2H-MoTe₂. *Phys. Rev. B* **26**(12), 6554 (1982)
123. Z.H. Chi, X.M. Zhao, H. Zhang, A.F. Goncharov, S.S. Lobanov, T. Kagayama, M. Sakata, X.J. Chen, Pressure-induced metallization of molybdenum disulfide. *Phys. Rev. Lett.* **113**(3), 036802 (2014)
124. D. Shoenberg, *Magnetic Oscillations in Metals* (Cambridge University Press, Cambridge, 1984)
125. Z. Zhu, X. Lin, J. Liu, B. Fauqué, Q. Tao, C. Yang, Y. Shi, K. Behnia, Quantum oscillations, thermoelectric coefficients, and the Fermi surface of semimetallic WTe₂. *Phys. Rev. Lett.* **114**(17), 176601 (2015)
126. D. Kang, Y. Zhou, W. Yi, C. Yang, J. Guo, Y. Shi, S. Zhang, Z. Wang, C. Zhang, S. Jiang, et al., Superconductivity emerging from suppressed large magnetoresistant state in WTe₂. *Nat. Commun.* **6** (2015). doi:[10.1038/ncomms8804](https://doi.org/10.1038/ncomms8804)
127. J. Zhao, H. Liu, L. Ehm, Z. Chen, S. Sinogeikin, Y. Zhao, G. Gu, Pressure-induced disordered substitution alloy in Sb₂Te₃. *Inorg. Chem.* **50**(22), 11291 (2011)
128. N. Bandaru, R.S. Kumar, D. Sneed, O. Tschauner, J. Baker, D. Antonio, S.N. Luo, T. Hartmann, Y. Zhao, R. Venkat, Effect of pressure and temperature on structural stability of MoS₂. *J. Phys. Chem. C* **118**(6), 3230 (2014)
129. F. Birch, Finite elastic strain of cubic crystals. *Phys. Rev.* **71**(11), 809 (1947)
130. A. Webb, J. Feldman, E. Skelton, L. Towle, C. Liu, I. Spain, High pressure investigations of MoS₂. *J. Phys. Chem. Solids* **37**(3), 329 (1976)
131. R. Aksoy, Y. Ma, E. Selvi, M.C. Chyu, A. Ertas, A. White, X-ray diffraction study of molybdenum disulfide to 38.8 GPa. *J. Phys. Chem. Solids* **67**(9), 1914 (2006)
132. L. Hromadová, R. Martoňák, E. Tosatti, Structure change, layer sliding, and metallization in high-pressure MoS₂. *Phys. Rev. B* **87**(14), 144105 (2013)
133. A. Bagnall, W. Liang, E. Marseglia, B. Welber, Raman studies of MoS₂ at high pressure. *Physica B+C* **99**(1), 343 (1980)
134. Z. Zhao, H. Zhang, H. Yuan, S. Wang, Y. Lin, Q. Zeng, G. Xu, Z. Liu, G. Solanki, K. Patel, et al., Pressure induced metallization with absence of structural transition in layered molybdenum diselenide. *Nat. Commun.* **6** (2015). doi:[10.1038/ncomms8312](https://doi.org/10.1038/ncomms8312)

Chapter 4

From 3D to 2D: Fabrication Methods

Two-dimensional TMDCs can be fabricated using two types of approaches: the top-down approach, where the bulk forms are exfoliated into a few-layer structures and monolayers (MLs), and the bottom-up approach using growth methods such as chemical vapour deposition (CVD) or molecular epitaxy. Work already focusing on scale-up to large area arrays is in progress [1–10]. The present chapter describes the progress achieved along these two routes.

4.1 Top-Down Methods

The top-down techniques include micromechanical cleavage using the Scotch-tape method, liquid and chemical exfoliation, intercalation by ionic species, ultrasonication, and others. After successful application to produce graphene, the mechanical exfoliation has been extended to other inorganic materials, such as MoS₂ and other TMDCs.

4.1.1 Mechanical Exfoliation

To date, mechanical exfoliation is the most efficient way to produce the cleanest, highly crystalline and atomically thin nanosheets of layered materials. In a typical mechanical exfoliation process, appropriate thin TMDC crystals are first peeled off from the bulk crystal by using an adhesive Scotch tape (Fig. 4.1, top panel). These freshly cleaved thin crystals on the Scotch tape are brought into contact with a target substrate and rubbed to further cleave them. After the Scotch tape is removed, single-layer and multilayer TMDC nanosheets are left on the substrate (Fig. 4.1, bottom panels a–d). While this method produces single-crystal flakes of high purity and cleanliness that are suitable for fundamental characterisation and even for fabrication

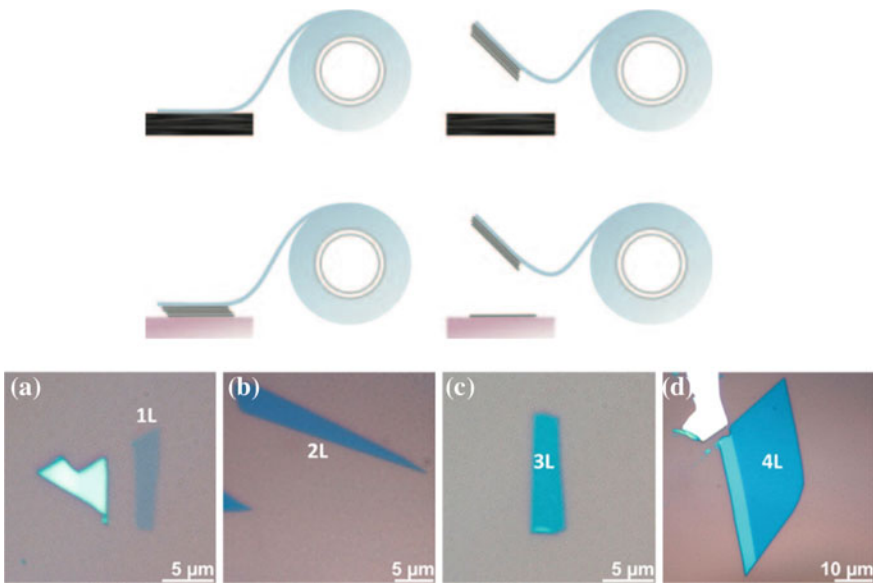


Fig. 4.1 *Top:* Schematic of micromechanical cleavage technique (the Scotch tape method) for producing few-layer structures. *Top row* adhesive tape is used to cleave the top few layers from a bulk crystal. *Bottom left* the tape with removed flakes is then pressed against the substrate of choice. *Bottom right* some flakes stay on the substrate, even on removal of the tape [12]. Copyright 2011 by the American Physical Society. Reprinted with permission. *Bottom:* Mechanically exfoliated single- and few-layer MoS₂ nanosheets on 300 nm SiO₂/Si. Optical microscopy (a–d) [13]. Copyright 2014 American Chemical Society. Published with permission

of individual devices, it is not scalable and does not allow systematic control of flake thickness and size. Therefore, this technique is not feasible for large-scale production of TMDCs monolayers for technological applications.

As a way to exfoliate large-area monolayers, it was proposed to make use of chemically enhanced adhesion. The use of chemical affinity of sulphur atoms that can bind to a gold surface more strongly than to neighbouring layers, single layers of various vdW bonded chalcogenides, such as MoS₂, WSe₂ and Bi₂Te₃ with lateral sizes of several hundreds of microns were successfully exfoliated [11].

Nanomechanical cleavage of MoS₂ was studied *in situ* using transmission electron microscopy and layers with thicknesses varying from a monolayer to 23 layers were successfully cleaved [14]. Thermal annealing and evaporative thinning using a focused laser spot were also used for layer-by-layer thinning of MoS₂ down to monolayer thickness by thermal ablation with micrometer-scale resolution [15–17].

Controlled MoS₂ layer etching using CF₄ plasma was reported in [18]. The damage and fluorine contamination of the etched MoS₂ layer could be effectively removed by exposure to H₂S.

4.1.2 Liquid Exfoliation

Liquid exfoliation by direct ultrasonication, that was successfully used earlier to disperse graphene, was also employed to fabricate single-layer and multilayer nanosheets of a number of layered TMDCs, such as MoS₂, WS₂, MoSe₂, NbSe₂, TaSe₂, MoTe₂, MoTe₂ and others [19, 20], where the authors initially sonicated commercial powders in a number of solvents with varying surface tensions; the resultant dispersions were centrifuged. Successful solvents were those with dispersive, polar, and H-bonding components of the cohesive energy density within certain well-defined ranges. Some of the more promising solvents were N-methyl-pyrrolidone and isopropanol. Using this method, the exfoliated nanosheets have to be stabilized against re-aggregation either by solvation or by steric or electrostatic repulsion due to the adsorption of molecules from solution. This method allowed the authors to prepare films of BN, MoS₂, and WS₂ by vacuum filtration or spraying, with thicknesses ranging from a few nanometers to hundreds of micrometers.

A number of layered crystals were also exfoliated in water. The nanosheets were dispersed by ultrasonication in an aqueous solution of the surfactant sodium cholate, which coats the sheets, preventing their re-aggregation. Since such direct ultrasonication techniques depend on the solvent or surfactant to overcome the cohesive energy between the neighbouring layers, solvents must be chosen to have surface energies comparable to those of the exfoliated crystal [7]. It may be worth noting that dispersibility of exfoliated nanosheets varied only weakly between different TMDCs [21]. The main challenge is to enhance the yield of the monolayers and to maintain the lateral dimensions of the exfoliated sheets.

Ion intercalation, such as lithium-intercalation or ultrasound-promoted hydration, is another approach, allowing fabrication of single-layer materials. The intercalation of TMDCs by ionic species [22, 23] allows the layers to be exfoliated in liquid. The typical procedure involves submerging bulk TMDC powder in a solution of a lithium-containing compound such as *n*-butyllithium for a relatively long time (days) to allow lithium ions to intercalate, which is followed by exposure of the intercalated material to water. The water reacts with the lithium between the layers; the process results in the formation of H₂ gas, which serves to separate the layers [22, 24]. Such chemical exfoliation methods allows one to produce significant quantities of submicrometre-sized monolayers [25], but the resulting material differs structurally and electronically from the source bulk. In particular, the electronic structure of exfoliated MoS₂ changes from semiconducting to metallic, and the Mo coordination changes from trigonal prismatic (2H-MoS₂) to octahedral (1T-MoS₂) (see Sect. 5.1.2 below). Annealing at 300 °C can revert the phase change from 1T-MoS₂ to 2H-MoS₂, restoring the trigonal prismatic coordination of Mo atoms and the corresponding semiconducting bandgap of the pristine material. Lithium-based chemical exfoliation has been demonstrated for various TMDCs, in particular MoS₂, WS₂, MoSe₂ and SnS₂ [26, 27]. This method was also used to exfoliate topological insulators such as Bi₂S₃ and Bi₂Te₃ [28].

An effective method for mass production of exfoliated TMD nanosheets is the ultrasound-promoted hydration of lithium-intercalated compounds. One well-known class of intercalants is the organolithium compounds. MoS_2 can be intercalated with lithium to give the reduced Li_xMX_n phase ($\text{X} = \text{Se}, \text{S}$, and so on) with expanded lattice, this can be exfoliated in a second step into single-layer sheets by ultrasound-assisted hydration process [23, 25, 29]. An important step in the lithium intercalation process is the formation of the Li_xMS_2 compound and this reaction can be tuned to control the yield of monolayers. The degree of lithiation also has implications on the amount of $1T$ phase present in MX_2 (see Sect. 5.1.2 below). The lithiated solid product can then be retrieved by filtration and washed with hexane to remove excess lithium and organic residues from *n*-butyl lithium. The extracted product can be readily exfoliated by sonication in water.

TMDC nanosheets can also be exfoliated by thermal cycling, such as rapid freezing (30 s in a liquid nitrogen bath) and heating (20 min in an oil bath at 60 °C), of hydrated TMDC powder in water [30].

An alternative method of lithiation that uses an electrochemical cell with a lithium foil anode and TMDC-containing cathode was demonstrated in [31, 32] (Fig. 4.2). Because the intercalation occurs while a galvanic discharge is occurring in the electrochemical cell, the degree of lithiation can be monitored and controlled. The resulting Li-intercalated material is exfoliated by ultrasonication in water as before, yielding monolayer TMDC nanosheets. The method was first demonstrated for MoS_2 , WS_2 , TiS_2 , TaS_2 , ZrS_2 and graphene [31], and then extended for BN, NbSe_2 , WSe_2 , Sb_2Se_3 and Bi_2Te_3 [32]. Another advantage of this method is that it only requires several hours for Li intercalation, compared with more than a day for the *n*-butyl-lithium method.

During the whole experimental process, the lithium ions fulfill several important functions. First, the Li^+ ions are inserted into the interlayer space of the layered bulk material, which expands the interlayer distance and weakens the vdW interactions between the layers. Second, the inserted Li^+ ions are subsequently reduced to Li by accepting electrons during the discharge process. The metallic Li can react with water to form LiOH and produce H_2 gas (apparently, bubbles were observed during the experiments). The generated H_2 gas pushes the layers further apart. Under vigorous agitation by sonication, well-dispersed 2D nanosheets can be thus obtained [32].

The intercalation of lithium into layered molybdenum disulphide may be described as an ion-electron transfer topotactic reaction. In most reported papers, organolithium reagents were used as intercalating agents because of its solubility in a wide range of solvents and the formation of stoichiometric LiMoS_2 ternary products [22]. Compared with Li ions, other alkali ions such as Na or K were less commonly used in exfoliation chemistry. At the same time, the ionic radii of Na and K are several times larger than that of Li ions, which means that in principle these ions can expand the lattice in the *c*-axis direction to a larger extent. Also, Na and K intercalation compounds react more violently with water than Li compounds, implying that single-layer TMDCs should be exfoliated more efficiently. Motivated by these potential advantages, naphthalenide adducts of Li, K and Na were compared from the

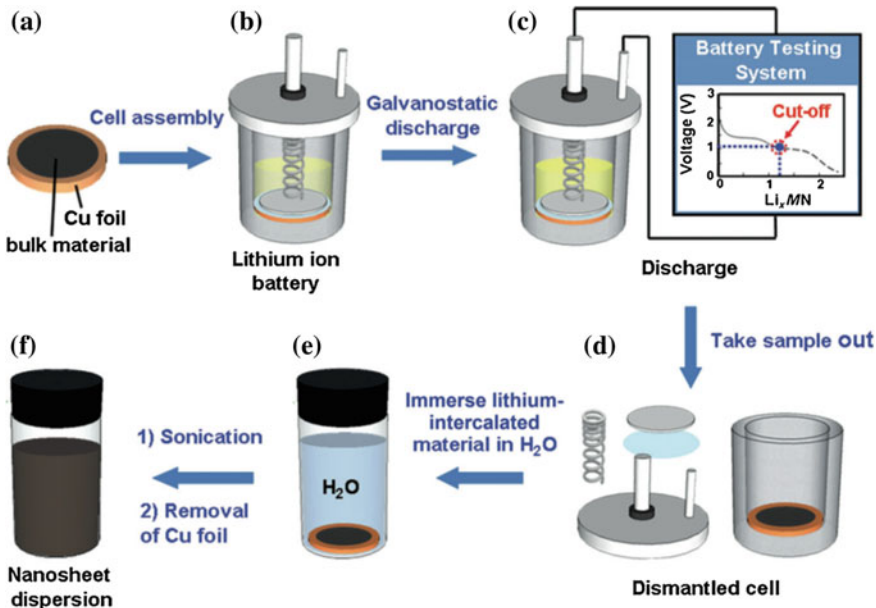


Fig. 4.2 The electrochemical lithium intercalation process to produce 2D nanosheets from the layered bulk material ($\text{MN} = \text{BN}$, metal selenides, or metal tellurides in $\text{Li}_x \text{MN}$) [32]. Reproduced with permission from Wiley-VCH Verlag GmbH

perspective of the exfoliation efficiency and high quality single-layer MoS₂ sheets were generated [33].

Figure 4.3 shows the schematic diagram of the processing steps involved in obtaining well-dispersed samples of LTMDs. First, bulk MoS₂ crystals (or powders) are expanded by reacting with hydrazine (N_2H_4) in hydrothermal condition (panel a). The expansion mechanism was explained by a redox rearrangement model in which part of the N_2H_4 is oxidized to N_2H_5^+ upon intercalation. The latter is unstable and decomposed to N_2 , NH_3 and H_2 upon heating the intercalated MoS₂ films at high temperature. Decomposition and gasification of intercalated N_2H_4 molecules expands the MoS₂ sheets by more than 100 times compared to its original volume. In a second step, the expanded MoS₂ crystal is intercalated by alkali naphthalenide solution (panel b). Finally the intercalated MoS₂ was exfoliated by dipping in ultrasonicated water operated at low power to avoid fragmentation of the sheets. This method was tested successfully on a wide range of TMDCs [33].

A tandem molecular intercalation was proposed for producing single-layer TMDCs from multi-layer colloidal TMDC nanostructures in solution phase, where short ‘initiator’ molecules first intercalate into TMDCs to open up the interlayer gap, and the long ‘primary’ molecules then bring the gap to full width so that a random mixture of intercalates overcomes the interlayer force [34]. With the appropriate

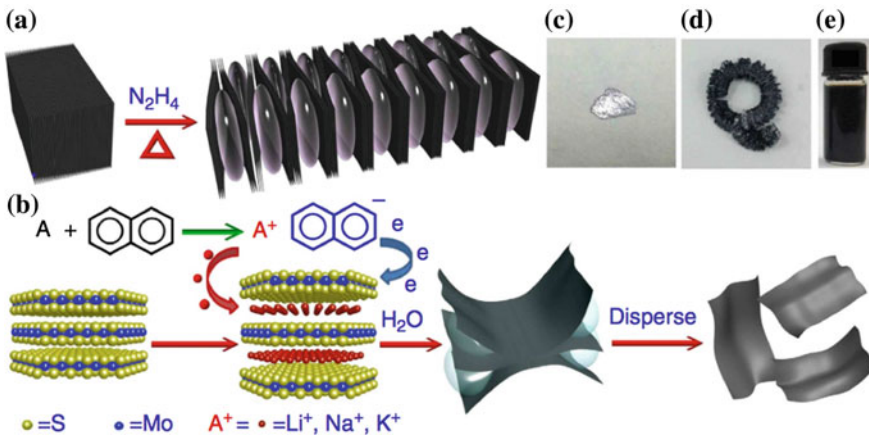


Fig. 4.3 **a** Bulk MoS₂ is pre-exfoliated by the decomposition products of N₂H₄. **b** Pre-exfoliated MoS₂ reacts with A⁺C₁₀H₈ to form an intercalation sample, and then exfoliates to single-layer sheets in water. **c** Photograph of bulk single-crystal MoS₂, **d** photograph of pre-exfoliated MoS₂, **e** photograph of Na-exfoliated single-layer MoS₂ dispersion in water [33]. Reprinted by permission from Macmillan Publishers Ltd., copyright (2014)

intercalates, single-layer nanostructures of group IV (TiS₂, ZrS₂), group V (NbS₂) and VI (WSe₂, MoS₂) TMDCs were successfully generated.

4.1.3 Electrochemical Exfoliation

A setup for the electrochemical exfoliation of bulk MoS₂ crystals is shown in Fig. 4.4a. A DC bias was applied between MoS₂ and the Pt wire for the electrochemical exfoliation, starting with a low positive bias to wet the bulk MoS₂ followed by a larger bias to exfoliate the crystal. As a result, many MoS₂ flakes dissociated from the bulk crystal and became suspended in the solution (panels b and c).

The mechanism of electrochemical exfoliation of bulk MoS₂ crystals is described as follows [6] (Fig. 4.4e). First, by applying a positive bias to the working electrode, the oxidation of water produces -OH and -O radicals assembled around the bulk MoS₂ crystal. The radicals and/or SO₄²⁻ anions insert themselves between the MoS₂ layers and weaken the vdW interactions between the layers. Second, oxidation of the radicals and/or anions leads to a release of O₂ and/or SO₂, which causes the MoS₂ interlayers to greatly expand. Finally, MoS₂ flakes are detached from the bulk MoS₂ crystal by the erupting gas and are then suspended in the solution.

A major problem here is that bulk MoS₂ should be oxidized during electrochemical exfoliation, which may affect the exfoliated MoS₂ nanosheets, unless the conditions are optimised [6].

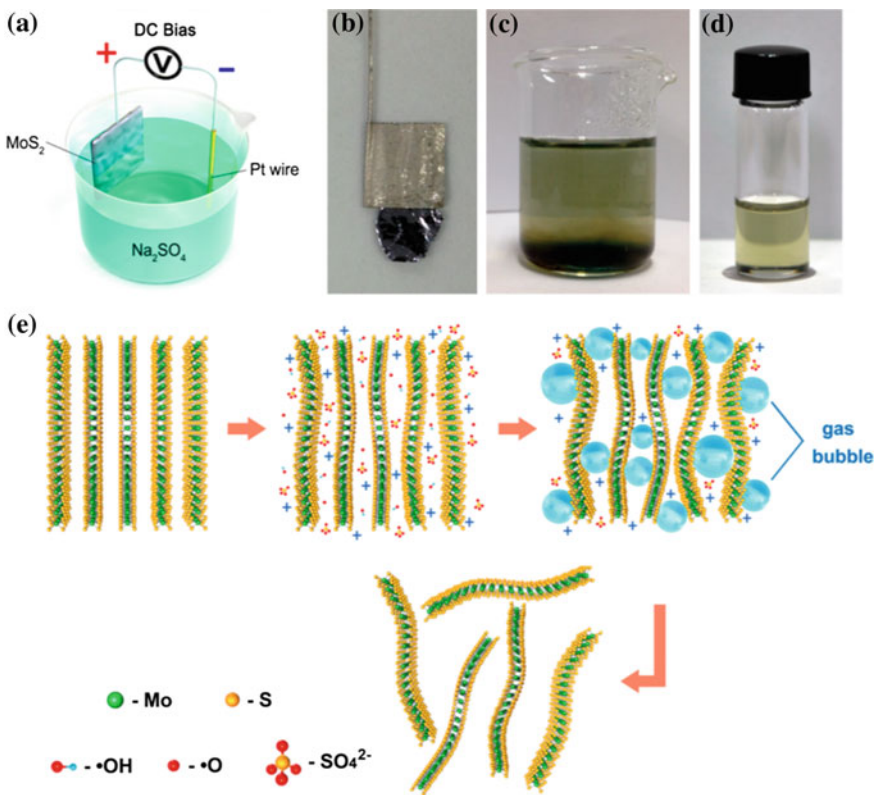
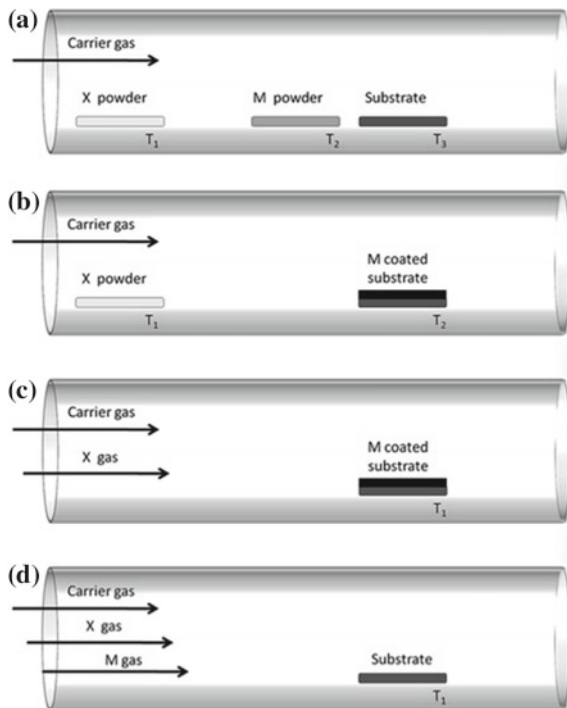


Fig. 4.4 **a** Schematic illustration of experimental setup for electrochemical exfoliation of bulk MoS₂ crystal. **b** Photograph of a bulk MoS₂ crystal held by a Pt clamp before exfoliation. **c** Exfoliated MoS₂ flakes suspended in Na₂SO₄ solution. **d** MoS₂ nanosheets dispersed in solution. **e** Schematic illustration for mechanism of electrochemical exfoliation of bulk MoS₂ crystal [6]. Copyright 2014 American Chemical Society. Published with permission

4.2 Bottom-Up Techniques

Developing methods for synthesizing large-area and uniform layers is an important step for applications. As previously CVD deposition of graphene was a breakthrough that has enabled the fabrication of large area sheets [5], CVD is also seen as a technique of choice for production of other layered materials such as TMDCs. Since most of the research was originally focused on MoS₂, most of the CVD growth efforts also concentrated on this material. Interested readers are referred to topical reviews [35, 36]. The latter review provides a nice summary of the growth conditions, precursors etc. For a detailed review of available precursors the interested reader is referred to [37].

Fig. 4.5 Schematics of the most common methods used to deposit TMDC from vapour phase. **a** Metal (M) and chalcogen (X) powders. **b** Metal or metal oxides deposited on substrate and chalcogen powders. **c** Metal or metal oxides deposited on substrate and chalcogen supplied as gaseous precursors. **d** Metal and chalcogen compounds supplied by gaseous precursors [37]. Reproduced by permission of the Royal Society of Chemistry



The CVD synthesis of monolayer MoS₂ has to date been performed by one of the following two routes. One is a two-step growth route, in which Mo-based precursors are initially deposited and then sulphurised/decomposed into MoS₂. The second process is considered as a one-step growth, wherein gaseous Mo and S feedstocks are simultaneously introduced and react to form MoS₂ on a substrate. These two approaches are schematically illustrated in Fig. 4.5.

4.2.1 Synthesis via Metal Chalcogenisation

An example of a two-step process is shown in Fig. 4.6a where a nm-thick Mo layer was first deposited onto SiO₂/Si substrates using *e*-beam evaporation, and then vapour-phase sulphurised at 750 °C in the CVD system [10]. The reaction mechanism can be understood as a direct chemical reaction. Therefore, the size and thickness of the pre-deposited Mo film determine the thickness and size of the obtained MoS₂ thin film. In this way, large-area MoS₂ with only a few layers in thickness could be synthesized, with the sample size only limited by the size of the growth substrate. However, because of the high melting point (2610 °C) of Mo, the migration of Mo atoms is effectively suppressed at the growth temperature. Consequently, Mo-based

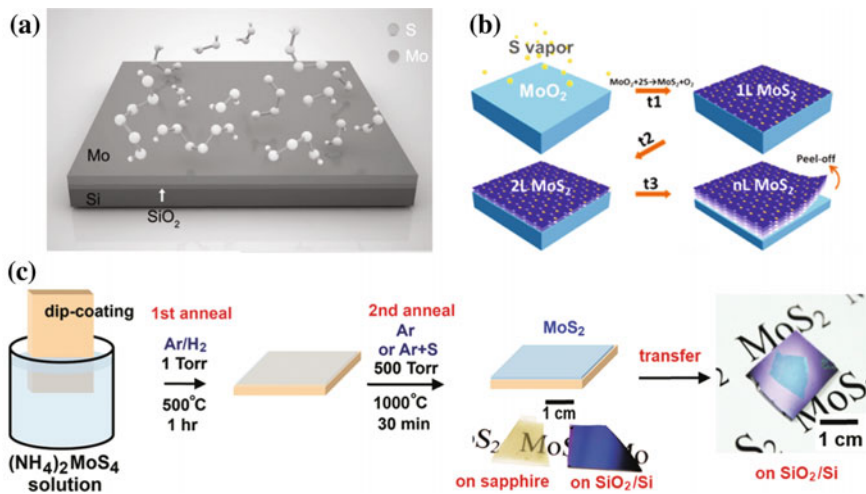


Fig. 4.6 CVD growth of MoS₂. **a** Sulphurisation of a Mo thin film was pre-deposited on a SiO₂ substrate [10]. Reproduced with permission from Wiley-VCH Verlag GmbH. **b** Schematics for the synthesis and cleavage of MoS₂. MoO₂ microplates were synthesized by reduction of MoO₃ and then used as template to grow MoS₂ by layer-by-layer surface sulfurization. The obtained MoS₂ coating was separated from MoO₂ and transferred to another substrate with the top layer facing up for further characterizations. 1L, 2L, and nL indicate single layer, bilayer, and n-layer, respectively. For simplicity, the growth of MoS₂ on the four sides of MoO₂ was not shown in this schematic [38]. Copyright 2013 American Chemical Society. Published with permission **c** schematic illustration of the two-step thermolysis process for the synthesis of MoS₂ thin layers on insulating substrates. The precursor (NH₄)₂MoS₄ was dip-coated on SiO₂/Si or sapphire substrates followed by the two-step annealing process. The as-grown MoS₂ film can be transferred onto other arbitrary substrates [39]. Copyright 2012 American Chemical Society. Published with permission

precursors with a low evaporation temperature are preferable in terms of improving the domain size and thickness uniformity of MoS₂ layers.

At the same time, facile substrate-scale growth of mono- and few-layer MoS₂ on Mo oils was reported in [40].

Interestingly, vertically aligned MoS₂ and MoSe₂ layers (Fig. 4.7) can also be produced by a rapid sulfurization/selenization process at 550 °C [41]. Smooth and uniform TMDC edge-terminated films with densely packed, strip-like grains can be produced on various substrates including glassy carbon, quartz and oxidized silicon. It was suggested that the distinction between vertical and in-plane growth of TMDCs could be due to different sulfurization/selenization conditions. The formation of the vertically aligned TMDC layers is proposed to be driven by a kinetic process, where at a high temperature the transition metal thin film converts to sulfide/selenide much faster than the diffusion of sulfur/selenium. Thus the sulfur/selenium diffusion limits the growth process. On the other hand, the anisotropic structure of TMDC layers makes it much faster for sulfur/selenium species to diffuse along the vdW gaps. Therefore, the TMDC layers naturally orient perpendicular to the film, exposing vdW

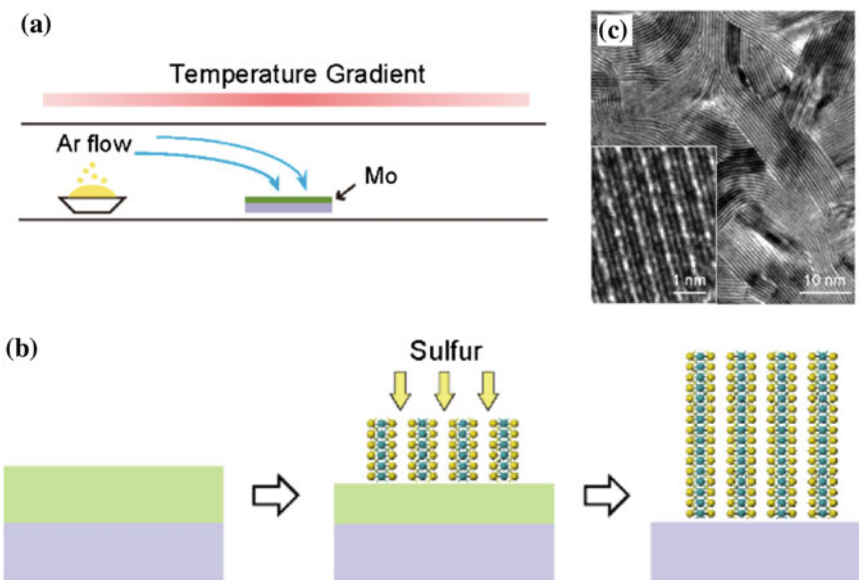


Fig. 4.7 **a** Schematic of the synthesis setup in a horizontal tube furnace; **b** Schematic of the proposed synthesis mechanism. The sulfurization/selenization reaction requires the diffusion of sulfur/ selenium into the film and converts it into sulfide/selenide. Mass transport along the layers through van der Waals gaps is much faster than across the layers in MoS₂/MoSe₂. Consequently, the layers tend to be perpendicular to the substrate, with exposed van der Waals gaps for fast reaction; **c** TEM image of a MoSe₂ film produced by rapid selenization showing exposed edges. Corresponding high-resolution TEM image (inset) reveals individual layers consisting of Se-Mo-Se atomic planes [41]. Copyright 2013 American Chemical Society. Published with permission

gaps for fast reaction [41]. These TMDC layers with predominately exposed edges exhibit a high surface energy and are thought to be metastable which may serve for diverse catalytic reactions. Using this approach, vertically aligned molecular layers of MoSe₂ and WSe₂ could also be grown on curved and rough surfaces [42].

Molybdenum trioxide (MoO₃) was selected as an alternative precursor for MoS₂ growth on the basis that it has an evaporation temperature of ca. 700 °C [43]. MoO₃ was first deposited onto *c*-face sapphire substrates using thermal evaporation, forming a uniformly thin layer suitable for sulphurisation. Using this synthesis method, wafer-scale MoS₂ thin films were successfully prepared on sapphire substrates (Fig. 4.8), wherein the film thickness (2-3 layers) was found to depend on the amount of deposited MoO₃.

In a different work, crystalline MoO₂ microcrystals were evolved on SiO₂/Si substrates under a weak reducing atmosphere of sulphur at 650–850 °C [38]. These MoO₂ microplates were then sulphurised to MoS₂ at 850 °C (Fig. 4.6b), with varied numbers of layers depending on the annealing duration.

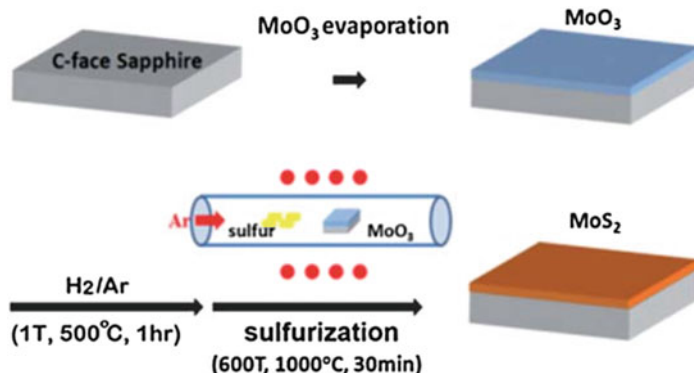


Fig. 4.8 Schematic illustration for the synthesis of MoS₂ layers by MoO₃ sulfurization. A layer of MoO₃ (ca. 3.6 nm) was thermally evaporated on the sapphire substrate. The MoO₃ was then converted to a MoS₂ by a two-step thermal process [43]. Reproduced by permission of the Royal Society of Chemistry

Under certain conditions, heating MoO₂ thin films in vapor sulphur atmosphere can result in the formation of MoS₂ nanoflowers with tens to hundreds petals self-assembles within a single nanoflower [44].

Of special interest is screw-dislocation-driven growth of pyramidal structures, demonstrated for WSe₂ [45] and MoS₂ [46, 47]. In such a case, the stacking sequence is different from the usual 2H stacking, which results in an increased second harmonic generation [47] and photoluminescence [46] intensities.

It should be noted that while CVD growth of sulphides and selenides was developed rather easily, until very recently, MoTe₂ layer were only produced using exfoliation methods. There are several difficulties in growing stoichiometric MoTe₂ layers compared to other TMDCs. At high temperatures, instead of evaporating as a compound, MoTe₂ decomposes and loses Te as a vapor. These properties make it challenging to directly obtain atomically thin MoTe₂ films by physical vapor deposition, and there is very often a Te deficiency in as-prepared MoTe₂. A second feature distinguishing MoTe₂ from other TMDCs is the very small energy difference between the 2H and 1T' phases, which complicates controllable synthesis of a pure MoTe₂ crystal phase¹.

Consequently, CVD growth of MoTe₂ was reported relatively late [48, 49]. It was found that the chemical composition of the Mo precursor was crucial for the CVD growth of MoTe₂. The resulting MoTe₂ phase and the efficiency of the tellurization were both strongly dependent on the oxidation state of the Mo precursor. Namely, it

¹In [48] another reason was mentioned. Namely, it was argued that “the electronegativity difference between Te and Mo is rather small (0.3 eV). Therefore, the bonding energy of Mo-Te bonds is quite small, which translates to a weaker tendency for the material to form”. This statement is not clear since homopolar bonds, i.e. bonds with zero electro-negativity difference, can be very strong.

was found that MoO_3 reacts more easily with Te and forms $2H\text{-MoTe}_2$ while, Mo and MoO_x ($x < 3$) precursors tend to form $1T'\text{-MoTe}_2$ under the same conditions [48]. It was further noted that Te vapor should be maintained during the growth of both the $2H$ and $1T'$ phases to avoid Te deficiency in the as-grown film because MoTe_2 is unstable and sublimes at high temperature [48].

An interesting observation was made for a Mo tellurisation process [49]. It was found that initially the $1T'\text{-MoTe}_2$ was formed and was converted gradually to $2H\text{-MoTe}_2$ over a prolonged growth time under a (excessive) Te atmosphere. Further annealing under a lower partial pressure of Te at the same temperature, followed by a rapid quenching, led to the reverse phase transition from $2H\text{-MoTe}_2$ to $1T'\text{-MoTe}_2$. It was further found that orientation of the $2H\text{-MoTe}_2$ phase was determined by the tellurization rate, namely, slow tellurization resulted in a highly oriented film over the entire area, while fast tellurization led to the formation of a $2H\text{-MoTe}_2$ film with a randomly oriented c -axis, the result being in agreement with an earlier observation [41].

4.2.2 Thermolysis of Thiosalts

As a variation of this process, a thermolysis process was also used for deposition of MoS_2 sheets by first dip-coating in ammonium thiomolibbdates $[(\text{NH}_4)_2\text{MoS}_4]$ and converting to MoS_2 by annealing at $500\text{ }^\circ\text{C}$ in Ar/H_2 flow to remove the residual solvents, NH_3 molecules and other by-products dissociated from the precursors. This was followed by sulphurisation in sulphur vapour at $1000\text{ }^\circ\text{C}$ (Fig. 4.6c) [39]. It should be noted that while the thermolysis of ammonium thiomolybdate produces a high quality of MoS_2 thin film, synthesis of large area TMDCs by this method is still challenging due to the technical limitations of uniform and ultra-thin ammonium thiomolybdate film preparation and as-synthesized films are polycrystalline.

The reported results show that MX_2 synthesis via the sulphurisation/decomposition of pre-deposited metal-based precursor layers is an effective means of preparing large-area MX_2 thin layers. At the same time, it has several limitations, for example, it is hard to control the thickness of pre-deposited metal oxide or metal thin film, which limits the wafer-scale uniformity. To obtain a high-quality TMDC with the desired number of layers, the thickness of metal oxides needs to be precisely controlled. Attempts were made to improve the synthetic process by depositing metal oxide layers via atomic layer deposition [50]. Using this method, atomically thin TMDC nanosheets with good thickness controllability and uniformity could be achieved.

4.2.3 Vapour Pressure Reaction of Transition Metal and Chalcogen Precursors

The direct reaction of simultaneously introduced gaseous metal and chalcogen precursors, was also realized in CVD systems. In one such setup, sulphur and MoO₃ powders were successively placed in the reaction chamber, with a SiO₂/Si substrate mounted face-down above the MoO₃ [4]. Pre-treating this substrate by spin-casting graphene-like aromatic molecules was found to be preferable for inducing effective nucleation and layered growth of MoS₂.

This method allowed to produce near triangular MoS₂ sheets of 1–3 monolayers. Planar aromatic molecules were also used as seeding promoters to grow MS₂ (M = Mo, W) on different substrates [51, 52] as shown in Fig. 4.9. It should be noted that the one-step CVD produced regularly triangular shaped MoS₂ flakes with a typical domain size larger than 1 μm.

It was subsequently demonstrated that aromatic molecular seeds were not essential for initializing the layered growth of MoS₂ and triangular monolayer MoS₂ flakes were successfully grown on bare SiO₂/Si substrates [53] with a typical edge length of ca. 10 μm. The grown films were single crystal domains. It was argued that the limiting factor for MoS₂ growth on bare SiO₂/Si was due to the nucleation process [53], where the triangular domains preferably nucleated at edges, scratches, dust particles etc.

The choice of starting materials for Mo and S source is crucial and different sources have different effects on the morphology of MoS₂ films. In [54] CVD growth of MoS₂ with two precursors MoO₃ and MoCl₅ was compared. It was found that while the MoO₃ source gave a triangular shaped MoS₂ monolayer, the use of MoCl₅ allowed to achieve uniform MoS₂ without triangles. The mechanism of the absence of geometric shapes when using MoS₂ was not revealed in this work.

Using ambient-pressure CVD, near-triangular MoS₂ flakes were fabricated (Fig. 4.10) with the longest edge length so far of ca. 120 μm [55] and in a setup in which a small quartz tube sealed at one end and used as the container for the precursors and the substrate (Fig. 4.11) triangular WS₂ monolayers with an edge length of up to 178 μm was realised [56].

MoS₂ monolayer flakes can also be produced on insulating substrates (such as a Si wafer and sapphire) by simple physical vapour transport of MoS₂ powder in an inert environment [57]. This method allowed the authors to produce high optical quality MoS₂ monolayers with near-unity valley polarisation (see Chap. 11).

Graphite was also proposed as an effective substrate. Thus, CVD-grown monolayer WS₂ on graphite gives rise to a single photoluminescence peak width a symmetric Lorentzian profile and very small peak width values of 21 meV at room temperature and 8 meV at 79 K (as opposed to 48 meV for the case of the SiO₂/Si substrate) [58]. It was argued that compared with WS₂ on sapphire and SiO₂/Si substrates, the WS₂ grown on graphite is less affected by charged impurities and structural defects.

Both these routes can conceivably be extrapolated to obtain various MX₂ layers: WS₂ [59, 60] MoSe₂ [41, 61–63] WSe₂ [3].

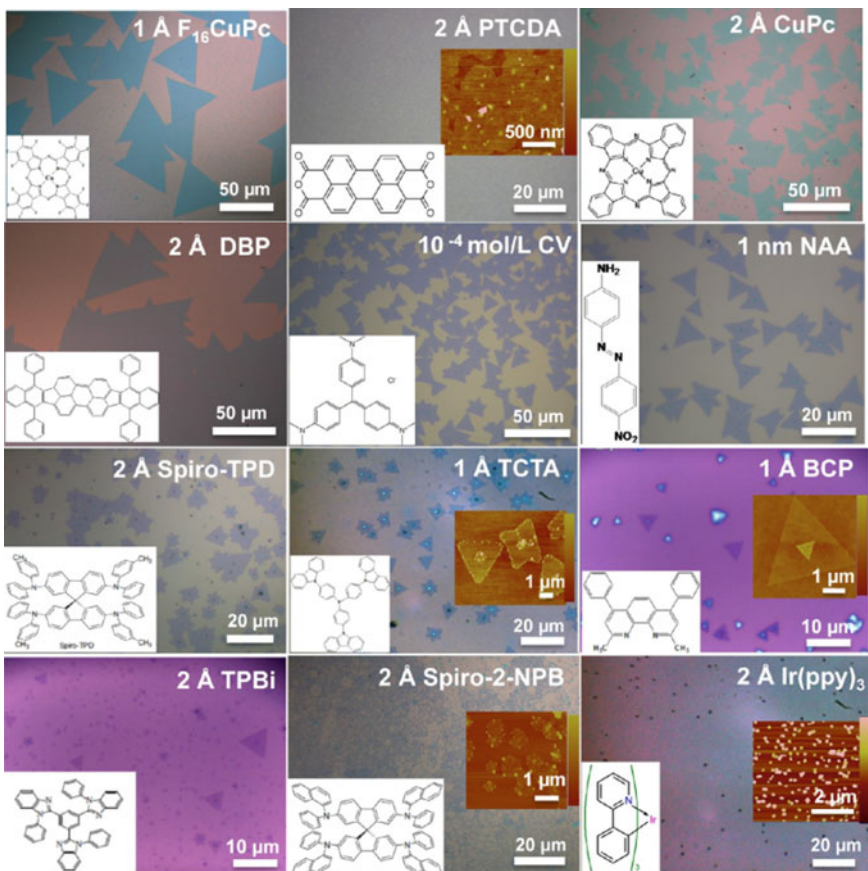


Fig. 4.9 Typical optical images of the surface after the MoS₂ growth using different aromatic molecules as seeding promoters. The names and thicknesses of the seeding promoters are labeled on the images. The insets show the corresponding molecular structures or AFM images of the surface after MoS₂ growth [52]. Copyright 2014 American Chemical Society. Published with permission

Although SiO₂/Si is currently the preferred substrate for growing MX₂ thin layers, insulating single crystals such as sapphire, mica and SrTiO₃ were considered by some as more suitable substrates for the CVD growth of MX₂ based on their ultraflat surfaces, excellent thermal stability, and possible lattice registry with MX₂ adlayers.

Chemical preparation of MoS₂ and MoSe₂ have also been demonstrated using hydrothermal synthesis [64, 65]. This method produces reasonably good-quality material with typical flake sizes of up to a few micrometers, but fabrication of monolayers was not conclusive.

The composition and purity of CVD MoS₂ layers was analyzed by the X-ray photoemission spectra. Figure 4.12a shows the photoelectron spectrum of Mo 3d. Peaks at 233.3 and 230.2 eV corresponds to the binding energy of Mo 3d_{3/2} and Mo

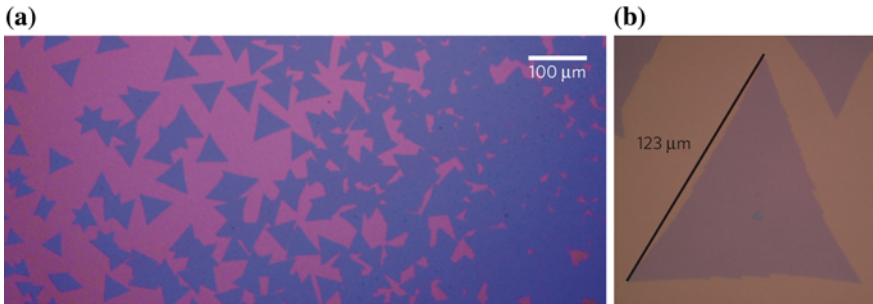


Fig. 4.10 **a** Optical reflection image of a CVD growth of a typical large-grain MoS₂ on a SiO₂ (285 nm)/Si substrate. The image contrast has been increased for visibility; *magenta* is the bare substrate, and *violet* represents monolayer MoS₂. **b** Optical image of a monolayer MoS₂ triangle. The *triangle* is 123 μm from tip to tip [55]. Reprinted by permission from Macmillan Publishers Ltd., copyright (2013)

$3d_{5/2}$, respectively [66]. The spin energy separation of Mo 3d doublet is 3.1 eV and in good agreement with the previous reports [39]. The S 2p spectrum (Fig. 4.12b) contains spin-orbit doublets of S $2p_{3/2}$ centered at 162.9 eV whereas the S $2p_{1/2}$ is found at 164.1 eV with a spin energy separation of 1.2 eV for S [39]. The obtained results are closely matched with the bulk MoS₂ crystal [66].

4.2.4 Growth of TMDC Alloys

The CVD synthesis of ternary MoS_{2(1-x)}Se_{2x} nanosheets with tunable compositions has been achieved [67]. In this case, two chalcogen powders (selenium and sulphur) were placed at upstream, with a temperature gradient along the quartz tube then applied to enable control over the composition and spatial separation. Thus, by simply changing the position of the boat filled with MoO₃ and the SiO₂/Si substrate above, the constituent stoichiometries of the resulting nanosheets can be varied from pure MoS₂ to pure MoSe₂.

Selenization of CVD MoS₂ and sulfurization of CVD MoSe₂ (Fig. 4.13) are alternative possibilities to produce TMDC alloys [68, 69].

4.2.5 Van der Waals Epitaxy

Homo- and heteroepitaxy is one of the most important methods in thin film technology. However, in order to obtain high-quality overlayers in heteroepitaxy one has to overcome the problem of lattice matching between the substrate and the grown layer. The lattice-matching requirement is especially severe in such tetrahedrally bonded

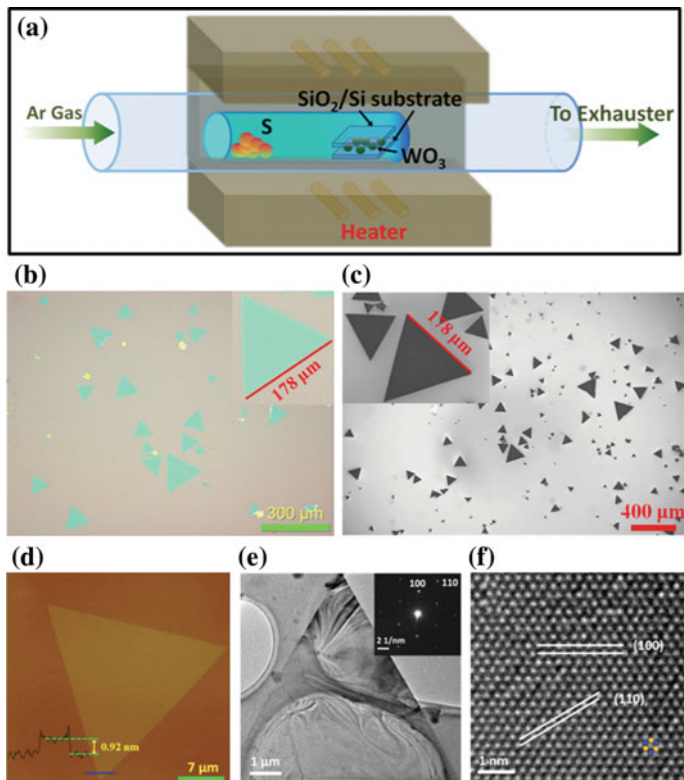


Fig. 4.11 **a** Schematic diagram of the CVD system used for the growth of WS₂. **b** Optical image of as-grown WS₂ on SiO₂ (300 nm)/Si substrate. Inset shows a triangular monolayer WS₂. **c** SEM image of the area shown in **(b)**. **d** AFM image of a monolayer WS₂. The height profile demonstrates the as-grown WS₂ flakes are monolayers. **e,f** Low- and high-magnification TEM images of triangular WS₂ monolayer, respectively. Optical, SEM, AFM, and TEM images show the perfect triangular shape and sharp edges (at the microscale) of the as-grown WS₂ monolayers [56]. Reproduced with permission from Wiley-VCH Verlag GmbH

covalent semiconducting materials as GaAs and Si. This arises from the fact that dangling bonds on the surface of a substrate can be connected only to the atoms of well-lattice-matched materials, since the length and the angle of the covalent bonds cannot be changed easily.

An interesting observation was made by Koma [70] that the lattice-matching requirement is relaxed drastically when the heteroepitaxial growth proceeds with a vdW interaction in case of the growth of a layered material on a cleaved face of the other layered material having no dangling bonds. This type of epitaxy was termed vdW epitaxy. It was demonstrated that epitaxial growth by vdW epitaxy is possible even under the existence of lattice mismatch as large as 50% [71]. Moreover, because of the non-existence of the dangling bonds, atomically abrupt interfaces

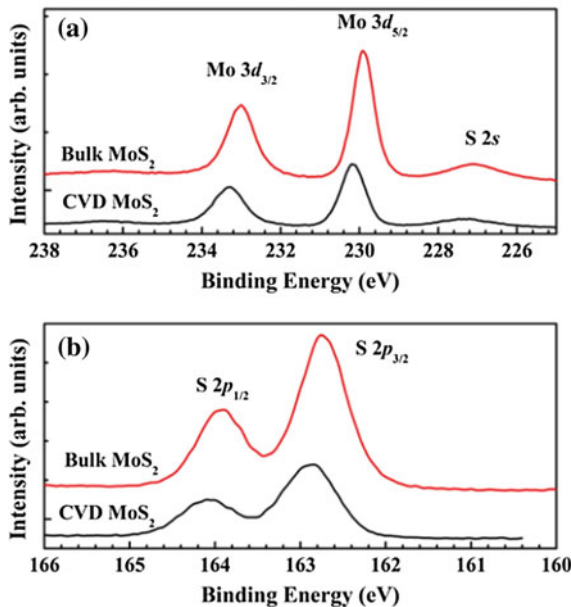


Fig. 4.12 X-ray photoemission spectroscopy scans for **a** Mo and **b** S binding energies of the MoS₂ monolayer [66]. Reproduced with permission from Springer

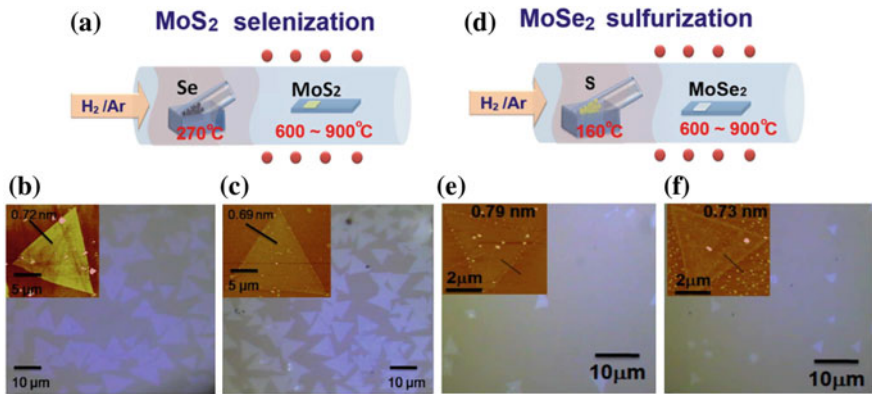


Fig. 4.13 Schematic illustration of the experimental set-up for the selenization/sulfurization process, where the inlet gas carries the vaporized selenium (sulfur) to the heated MoS₂ (MoSe₂) flakes and optical micrographs for the **b**, **e** as-synthesized MoS₂/MoSe₂, and **c**, **f** selenized (sulfurized) MoS₂/MoSe₂ (at 800 °C) on sapphire substrates. AFM images for the MoS₂/MoSe₂ flakes before and after selenization (sulfurization) (at 800 °C) are shown as insets in optical microscopy images. Reproduced from [69]

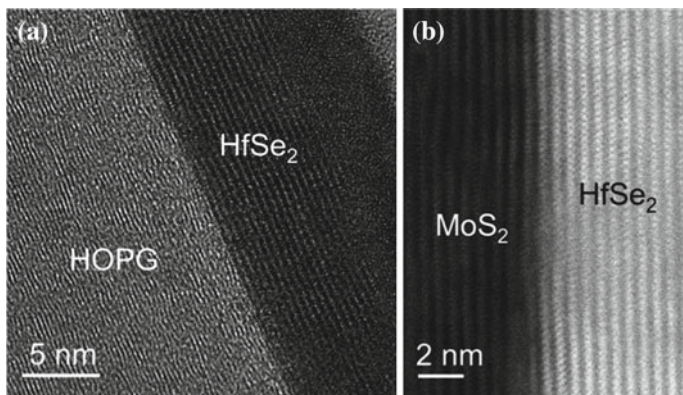


Fig. 4.14 **a** TEM image of grown HfSe₂ on HOPG and **b** HADDF-STEM image of grown HfSe₂ on MoS₂ showing abrupt interfaces and layered crystalline films [78]. Copyright 2014 American Chemical Society. Published with permission

can be fabricated [72–74]. In case of a 3D substrate, the dangling bonds must be first terminated, e.g. by sulphur. Successful growth of epitaxial TMDCs on sulphur-terminated GaAs(111) was reported back in 1990 [75]. Interested readers may also check a review on epitaxial growth of 3D topological insulators [76]. Since both TMDC and 3D topological insulators are vdW solids, the growth process has some common features.

The interest in epitaxial growth of TMDC single and few layers using the vdW mode re-emerged in recent years using methods ranging from CVD to MBE and the substrates varying from graphene to SiO₂/Si [77–80]. High epitaxial quality of the grown films can be seen in Fig. 4.14. Single layers of MoS₂ were also successfully grown on other substrates such as SnS₂ and mica [79, 81, 82], as is illustrated in Fig. 4.15.

In [83] (sub)monolayer MoTe₂ was grown by molecular beam epitaxy on a bulk MoS₂ substrate. The film morphology, the thermally induced transformation of structural and compositional phases, as well as the chemical stability upon exposure to atmosphere were studied by scanning tunneling microscopy and photoemission spectroscopy.

Of special interest is the growth by molecular beam epitaxy of heterostructures between TMDC and topological insulators. The first such report was published in [84], where MoSe₂/Bi₂Se₃ heterostructures were successfully fabricated.

Theoretical analysis of single-layer MoS₂ on Cu(111) surface found that there was rather strong chemical interaction between the layer and the substrate [85], which is not surprising considering strong reactivity between copper and chalcogens.

It is interesting to note that even such a technique as pulsed laser evaporation results in the formation of hexagonal MoS₂, which, in combination with the orienting effect of an appropriately chosen substrate, may open way to fabricate atomically thin layers by mass-production methods such as sputtering [86, 87]. Finally it should

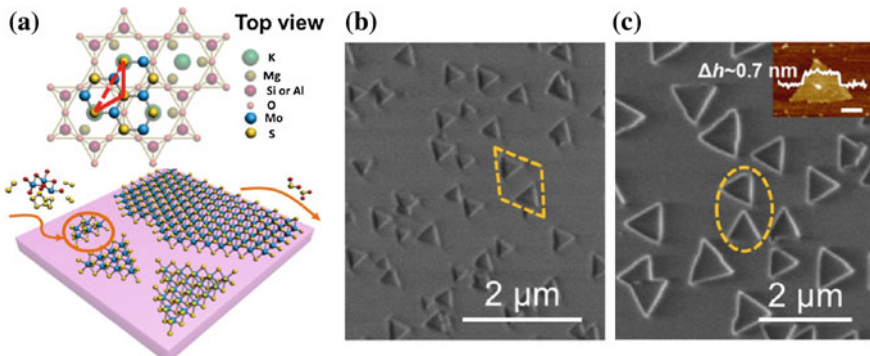


Fig. 4.15 Low-pressure CVD synthesis of MoS₂ nano/microstructures on mica. **a** A schematic view illustrating the surface reaction during epitaxial growth of MoS₂. The upper panel gives probable occupation of MoS₂ on mica. **b–c** SEM images showing the initial growth of MoS₂ on mica. Inset in **c** is the AFM profile of the MoS₂ flake (scale bar 200 nm) [79]. Copyright 2013 American Chemical Society. Published with permission

be mentioned that by appropriately choosing the composition of the substrate material, self-organized vdW epitaxial growth of layered chalcogenides structures was successfully realized using industry-friendly RF-magnetron sputtering [88].

4.3 Layer Transfer

When a thin TMDC layer is synthesized it is important for fundamental and applied research for it to be transferred to an arbitrary substrate [51, 89].

As the growth temperature of TMDC monolayers are relatively high, temperature-sensitive substrates (such as polymer-based substrates) cannot be used in the synthetic process, while their use is essential for flexible electronics. It is thus essential to develop a transfer technique to implement large-area TMDC on different substrates. One such technique that maintains the quality of the as-grown monolayer was described in [51]. The as-grown MoS₂ sample was cut into three pieces and treated for 30 s with DI water, isopropyl alcohol, and acetone, respectively. The surface of the as-grown monolayer is hydrophobic, so that isopropyl alcohol and acetone spreaded out on MoS₂, whereas water remained as a droplet. During the 30 s, the as-grown MoS₂ monolayer started to break into small pieces and floating on the water droplet, which demonstrated that the as-grown MoS₂ monolayer can be easily removed from the substrate with DI water.

In [89] a surface-energy-assisted process has been developed that allowed the authors to perfectly transfer centimeter-scale monolayer and few-layer TMDC films from original growth substrates onto arbitrary substrates with no observable wrinkles, cracks, or polymer residues. The unique strategies used in this process

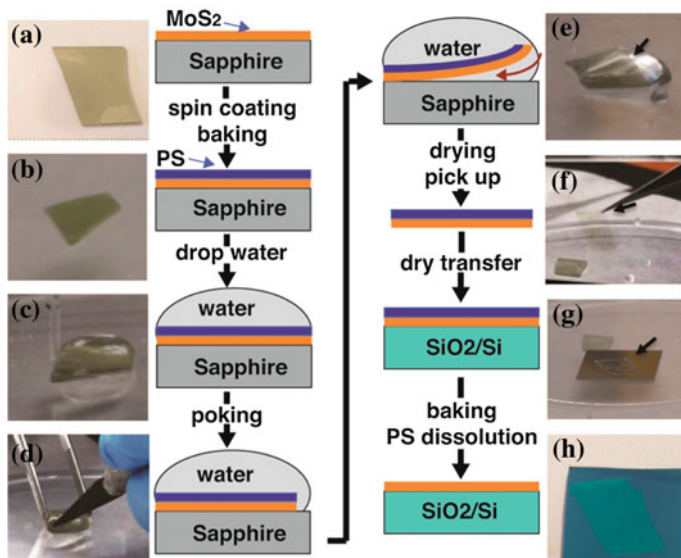


Fig. 4.16 Illustration of the surface-energy-assisted transfer process. **a–h** Typical images of the transfer process. The arrows in **e–g** point toward the MoS₂ film for visual convenience [89]. Copyright 1984 American Chemical Society. Published with permission

included leveraging the penetration of water between hydrophobic TMDC films and hydrophilic growth substrates to lift off the films and dry transferring the film after the lift off. The whole process is schematically illustrated in Fig. 4.16.

Scalable transfer of suspended TMDC layers on nanoscale patterned substrates (varying from polymers to Si to metals) using a capillary-force-free wet-contact printing method was demonstrated in [90]. As a proof-of-concept a photodetector of suspended MoS₂ was fabricated using this method. As an advantage of this approach the authors note a possibility of directly suspending a TMDC layer on nanoscale interdigitated electrodes.

4.4 Analysis of 2D TMDC Layers

4.4.1 Comparison of Exfoliated and CVD-Grown TMDCs

While mono- and few layer sheets can be obtained by both exfoliation and CVD growth, the samples are not perfectly identical. The issue of comparing exfoliated and CVD-grown samples was raised in [91], where MoS₂ single-layer samples obtained along these two pathways were compared using optical spectroscopy.

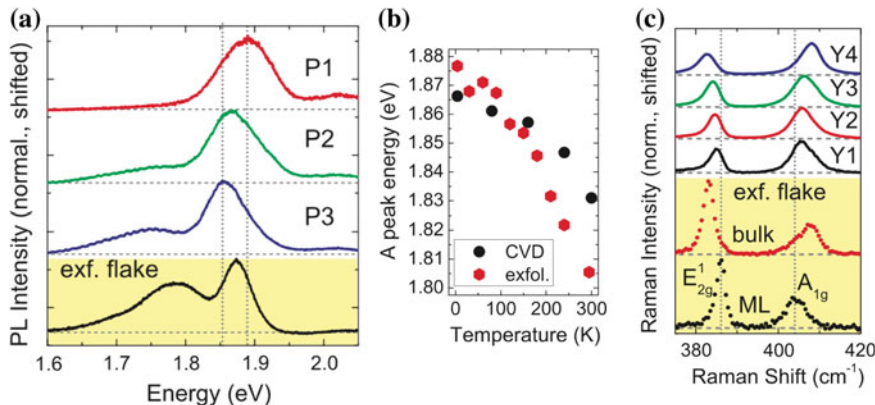


Fig. 4.17 **a** Normalized PL spectra measured on different positions of a CVD film and on an exfoliated flake at liquid-helium temperature; **b** The A exciton peak position as a function of temperature for the CVD-grown sample (black dots) and an exfoliated MoS_2 flake (red hexagons) **c** Raman spectra measured on different positions of the CVD-grown film and on exfoliated monolayer (ML) and bulk-like flakes. All spectra are normalized to the amplitude of the A_{1g} mode. The vertical lines mark the positions of A_{1g} and E_{2g}^1 in an exfoliated monolayer and serve as guide to the eye [91]. Reprinted with permission from IOP Publishing Ltd

In Fig. 4.17a individual spectra measured at different positions of the CVD sample are shown (the positions P1–P3 are separated by $100\ \mu\text{m}$). The vertical lines serve as a guide to the eye to mark maximum and minimum A exciton peak positions. The spectral shift indicates that the growth conditions, and the corresponding microscopic properties of the MoS_2 layer, vary in different parts of the layer, which may be associated with different strains [91].

CVD-grown and exfoliated layer were also compared in [92]. Figure 4.18b shows a comparison of the reflectance spectra for exfoliated and CVD-grown MoS_2 monolayers. Shifts in the A and B excitonic peaks of $\sim 40\ \text{meV}$ are observed, although the overall dielectric function is very similar. For comparison, in Fig. 4.18a, reflectance spectra for two different exfoliated samples of MoS_2 are shown.

In addition to the shift of the A exciton peak position, it was also found that the FWHM of the peaks changed as a function of position, with values between 80 and $60\ \text{meV}$, while in an exfoliated single-layer MoS_2 flake has a significantly lower FWHM of about $37\ \text{meV}$, indicating a larger inhomogeneous broadening of the A exciton transition in the CVD-grown sample. In exfoliated MoS_2 flakes at low temperatures, a second, lower-energy PL peak was observed, which was previously associated with localized excitons bound to surface adsorbates [93].

The difference was also observed in the temperature dependence of the PL emission (Fig. 4.17b). While the maximum of the A exciton emission redshifts by $35\ \text{meV}$ in the temperature range from 4 to $300\ \text{K}$ in CVD samples, in exfoliated MoS_2 flakes, the authors observed a spectral redshift of the A exciton peak by $72\ \text{meV}$ in the same temperature range. It was proposed that the redshift indicates a temperature-induced

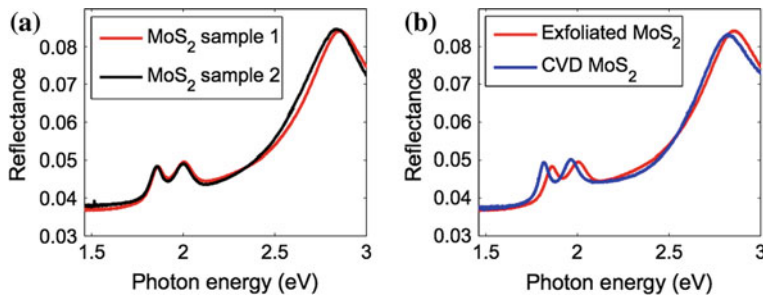


Fig. 4.18 **a** Comparison of the reflectance spectra of two different exfoliated MoS_2 monolayers. **b** Comparison of the reflectance spectra of exfoliated (red) and CVD-grown (blue) MoS_2 monolayers [92]. Copyright 2014 by the American Physical Society. Reprinted with permission

reduction of the band gap due to thermal expansion of the crystal lattice. Hence, the fact that the redshift is far less pronounced in the CVD-grown sample shows that the CVD-grown MoS_2 film strongly adheres to the SiO_2 substrate, which has a very small thermal expansion coefficient [91].

Finally, Fig. 4.17c shows four Raman spectra collected at different positions on the CVD film compared with the Raman spectrum from exfoliated flakes. All spectra were normalized to the A_{1g} mode amplitude. In the CVD-grown sample, the E_{2g}^1 amplitude was lower than the A_{1g} , while in the exfoliated flakes, the opposite was observed. Additionally, the line widths for both Raman modes in the CVD-grown film were larger than in the exfoliated flake, and the E_{2g}^1 mode was asymmetric. It was argued that these results suggest that the carrier density in the CVD-grown film may be significantly smaller than in the exfoliated flake [91].

It should also be noted that stoichiometry variation during the CVD growth may have an effect on optical and electrical properties of the grown layers. This issue was addressed in [94] for the case of MoS_2 .

4.4.2 Thickness Determination

Because properties of single-layer and few-layer TMDC can significantly vary, accurate thickness measurements are crucial. Development of such measurements are especially important for the ultrathin materials. Also important is the determination of the crystal orientation. The problem is complicated by the fact that the samples are usually not uniform in thickness and the same flake may have areas with different thicknesses, as well as domain boundaries. In this section be briefly describe the available methods.

One obvious, accurate, but not very practical method is to use atomic force microscopy (AFM), where the thickness of the sample can be measured directly. Other methods include use of Raman scattering and photoluminescence (Fig. 4.19)

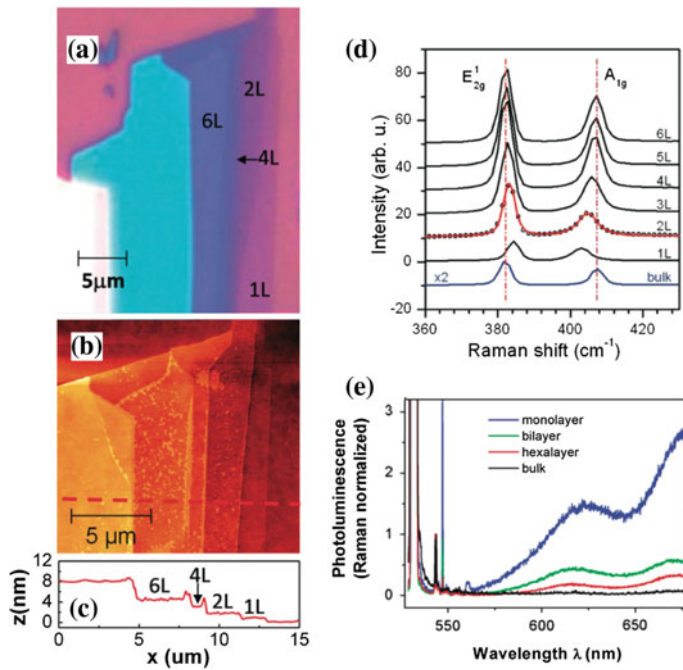


Fig. 4.19 Exfoliated MoS₂ flakes on a Si/SiO₂ substrate. **a** Optical microscope image of the exfoliated MoS₂ sample. The purple background is from the Si/SiO₂ substrate and areas with different contrast correspond to MoS₂ flakes of different thicknesses. **b** Atomic force microscope (AFM) image of the same sample. **c** Sample height along the red line in **b**, which confirms the optical determined thicknesses of areas 1L, 2L, and 4L. It also shows area 6L to be a hexalayer [95] Copyright 2010 American Chemical Society. Published with permission. **d** Raman spectra from MoS₂ flakes with different thicknesses [96] Copyright 2010 American Chemical Society. Published with permission. **e** photoluminescence spectra normalized by Raman intensity for MoS₂ layers with different thickness, showing a dramatic increase of luminescence efficiency in MoS₂ monolayer [95]. Copyright 2010 American Chemical Society. Published with permission

and make use of the facts that Raman peak position and intensities as well as photoluminescence intensity strongly depend on the flake thickness. These methods are described in more detail below in appropriate sections (see Chap. 7).

Second-harmonic generation is also an effective way to determine the thickness due to its strong intensity dependence on the layer thickness and especially between flakes with odd and even number of layers (see Sect. 12.1)

Finally, it was proposed that optical contrast can be a measure of the sample thickness as a fast and non-destructive method [97–99]. In [98] a method has been developed for simple, and reliable identification of thicknesses of 2D nanosheets on 90 and 300 nm SiO₂/Si. By processing the color optical images and the grayscale images of R, G, and B channels, the optical contrast differences between 2D nanosheets and SiO₂/Si were measured and plotted as standard charts to guide the layer number identification. This is exemplified for MoS₂ in Fig. 4.20. It was suggested that transition

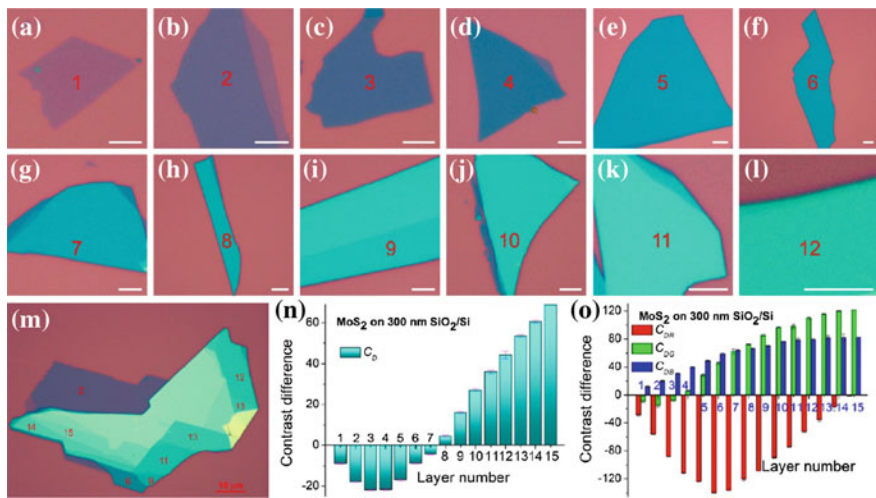


Fig. 4.20 **a–m** Color optical images of 1L–15L MoS₂ on 300 nm SiO₂/Si. The scale bars are 5 μm for images **a–l** and 10 μm for image **m**. The digits shown in **a–m** indicate the layer numbers of the corresponding MoS₂ nanosheets. Plots of (**n**) C_D values and (**o**) C_{DR} , C_{DG} , and C_{DB} values of 1L–15L MoS₂ on 300 nm SiO₂/Si [98]. Copyright 2013 American Chemical Society. Published with permission

of C_D , C_{DR} , C_{DG} , and C_{DB} values can be used as a clear mark for quick identification of the layer number. It was pointed out that since neither complex calculation nor special instrument is required in this method, just a standard optical microscope and a digital camera, it can be widely used for thickness determination. Optical contrast spectroscopy was proposed for identification of layer numbers of atomically thin TMDCs of different compositions [100–104].

4.4.3 Domain Orientation

Crystal orientation and differentiation among different domains in a crystal can be obtained using polarisation dependence of Raman scattering (Sect. 7.6.1) and second harmonic generation (Sect. 12.1).

References

1. H. Nam, S. Wi, H. Rokni, M. Chen, G. Priessnitz, W. Lu, X. Liang, MoS₂ transistors fabricated via plasma-assisted nanoprinting of few-layer MoS₂ flakes into large-area arrays. *ACS Nano* **7**(7), 5870 (2013)
2. P. Browning, S. Eichfeld, K. Zhang, L. Hossain, Y.C. Lin, K. Wang, N. Lu, A. Waite, A. Voevodin, M. Kim et al., Large-area synthesis of WSe₂ from WO₃ by selenium–oxygen ion exchange. *2D Mater.* **2**(1), 014003 (2015)

3. J.K. Huang, J. Pu, C.L. Hsu, M.H. Chiu, Z.Y. Juang, Y.H. Chang, W.H. Chang, Y. Iwasa, T. Takenobu, L.J. Li, Large-area synthesis of highly crystalline WSe₂ monolayers and device applications. *ACS Nano* **8**(1), 923 (2013)
4. Y.H. Lee, X.Q. Zhang, W. Zhang, M.T. Chang, C.T. Lin, K.D. Chang, Y.C. Yu, J.T.W. Wang, C.S. Chang, L.J. Li et al., Synthesis of large-area MoS₂ atomic layers with chemical vapor deposition. *Adv. Mater.* **24**(17), 2320 (2012)
5. X. Li, W. Cai, J. An, S. Kim, J. Nah, D. Yang, R. Piner, A. Velamakanni, I. Jung, E. Tutuc et al., Large-area synthesis of high-quality and uniform graphene films on copper foils. *Science* **324**(5932), 1312 (2009)
6. N. Liu, P. Kim, J.H. Kim, J.H. Ye, S. Kim, C.J. Lee, Large-area atomically thin MoS₂ nanosheets prepared using electrochemical exfoliation. *ACS Nano* **8**(7), 6902 (2014)
7. R.J. Smith, P.J. King, M. Lotya, C. Wirtz, U. Khan, S. De, A. O'Neill, G.S. Duesberg, J.C. Grunlan, G. Moriarty et al., Large-scale exfoliation of inorganic layered compounds in aqueous surfactant solutions. *Adv. Mater.* **23**(34), 3944 (2011)
8. E. Varrla, C. Backes, K.R. Paton, A. Harvey, Z. Gholamvand, J. McCauley, J.N. Coleman, Large-scale production of size-controlled MoS₂ nanosheets by shear exfoliation. *Chem. Mater.* **27**(3), 1129 (2015)
9. H. Wang, L. Yu, Y.H. Lee, W. Fang, A. Hsu, P. Herring, M. Chin, M. Dubey, L.J. Li, J. Kong et al., Large-scale 2D electronics based on single-layer MoS₂ grown by chemical vapor deposition. arXiv preprint [arXiv:1302.4027](https://arxiv.org/abs/1302.4027) (2013)
10. Y. Zhan, Z. Liu, S. Najmaei, P.M. Ajayan, J. Lou, Large-area vapor-phase growth and characterization of MoS₂ atomic layers on a SiO₂ substrate. *Small* **8**(7), 966 (2012)
11. G.Z. Magda, J. Pető, G. Dobrik, C. Hwang, L.P. Biró, L. Tapasztó, Exfoliation of large-area transition metal chalcogenide single layers. *Sci. Rep.* **5** (2015). doi:[10.1038/srep14714](https://doi.org/10.1038/srep14714)
12. K.S. Novoselov, Nobel lecture: graphene: materials in the flatland. *Rev. Mod. Phys.* **83**(3), 837 (2011)
13. H. Li, J. Wu, Z. Yin, H. Zhang, Preparation and applications of mechanically exfoliated single-layer and multilayer MoS₂ and WSe₂ nanosheets. *Acc. Chem. Res.* **47**(4), 1067 (2014)
14. D.M. Tang, D.G. Kvashnin, S. Najmaei, Y. Bando, K. Kimoto, P. Koskinen, P.M. Ajayan, B.I. Yakobson, P.B. Sorokin, J. Lou, D. Golberg, Nanomechanical cleavage of molybdenum disulphide atomic layers. *Nat. Commun.* **5** (2014). doi:[10.1038/ncomms4631](https://doi.org/10.1038/ncomms4631)
15. Z. Lu, M.I.B. Utama, J. Zhang, Y. Zhao, Layer-by-layer thinning of MoS₂ by thermal annealing. *Nanoscale* **5**(19), 8904 (2013)
16. A. Castellanos-Gomez, M. Barkelid, A. Goossens, V.E. Calado, H.S. van der Zant, G.A. Steele, Laser-thinning of MoS₂: on demand generation of a single-layer semiconductor. *Nano Lett.* **12**(6), 3187 (2012)
17. Y.K. Huang, J.D. Cain, L. Peng, S. Hao, T. Chasapis, M.G. Kanatzidis, C. Wolverton, M. Grayson, V.P. Dravid, Evaporative thinning: a facile synthesis method for high quality ultrathin layers of 2D crystals. *ACS Nano* **8**(10), 10851 (2014)
18. M.H. Jeon, C. Ahn, H. Kim, K.N. Kim, T.Z. LiN, H. Qin, Y. Kim, S. Lee, T. Kim, G.Y. Yeom, Controlled MoS₂ layer etching using CF₄ plasma. *Nanotechnology* **26**(35), 355706 (2015)
19. J.N. Coleman, M. Lotya, A. O'Neill, S.D. Bergin, P.J. King, U. Khan, K. Young, A. Gaucher, S. De, R.J. Smith et al., Two-dimensional nanosheets produced by liquid exfoliation of layered materials. *Science* **331**(6017), 568 (2011)
20. V. Nicolosi, M. Chhowalla, M.G. Kanatzidis, M.S. Strano, J.N. Coleman, Liquid exfoliation of layered materials. *Science* **340**(6139), 1226419 (2013)
21. G. Cunningham, M. Lotya, C.S. Cucinotta, S. Sanvito, S.D. Bergin, R. Menzel, M.S. Shaffer, J.N. Coleman, Solvent exfoliation of transition metal dichalcogenides: dispersibility of exfoliated nanosheets varies only weakly between compounds. *ACS Nano* **6**(4), 3468 (2012)
22. P. Joensen, R. Frindt, S.R. Morrison, Single-layer MoS₂. *Mat. Res. Bull.* **21**(4), 457 (1986)
23. M.B. Dines, Lithium intercalation via n-butyllithium of the layered transition metal dichalcogenides. *Mat. Res. Bull.* **10**(4), 287 (1975)
24. G. Eda, H. Yamaguchi, D. Voiry, T. Fujita, M. Chen, M. Chhowalla, Photoluminescence from chemically exfoliated MoS₂. *Nano Lett.* **11**(12), 5111 (2011)

25. H.L. Tsai, J. Heising, J.L. Schindler, C.R. Kannewurf, M.G. Kanatzidis, Exfoliated-restacked phase of WS₂. *Chem. Mater.* **9**(4), 879 (1997)
26. R. Gordon, D. Yang, E. Crozier, D. Jiang, R. Frindt, Structures of exfoliated single layers of WS₂, MoS₂, and MoSe₂ in aqueous suspension. *Phys. Rev. B* **65**(12), 125407 (2002)
27. S. Kirmayer, E. Aharon, E. Dovgolevsky, M. Kalina, G.L. Frey, Self-assembled lamellar MoS₂, SnS₂ and SiO₂ semiconducting polymer nanocomposites. *Philos. Trans. Royal Soc. (London) A* **365**(1855), 1489 (2007)
28. Z. Ding, S.K. Bux, D.J. King, F.L. Chang, T.H. Chen, S.C. Huang, R.B. Kaner, Lithium intercalation and exfoliation of layered bismuth selenide and bismuth telluride. *J. Mater. Chem.* **19**(17), 2588 (2009)
29. G.L. Frey, K.J. Reynolds, R.H. Friend, H. Cohen, Y. Feldman, J. Solution-processed anodes from layer-structure materials for high-efficiency polymer light-emitting diodes. *Amer. Chem. Soc.* **125**(19), 5998 (2003)
30. D. Chakravarty, D.J. Late, Exfoliation of bulk inorganic layered materials into nanosheets by the rapid quenching method and their electrochemical performance. *Europ. J. Inorg. Chem.* **2015**(11), 1973 (2015)
31. Z. Zeng, Z. Yin, X. Huang, H. Li, Q. He, G. Lu, F. Boey, H. Zhang, Single-layer semiconducting nanosheets: high-yield preparation and device fabrication. *Angew. Chem. Int. Ed.* **50**(47), 11093 (2011)
32. Z. Zeng, T. Sun, J. Zhu, X. Huang, Z. Yin, G. Lu, Z. Fan, Q. Yan, H.H. Hng, H. Zhang, An effective method for the fabrication of few-layer-thick inorganic nanosheets. *Angew. Chem. Int. Ed.* **51**(36), 9052 (2012)
33. J. Zheng, H. Zhang, S. Dong, Y. Liu, C.T. Nai, H.S. Shin, H.Y. Jeong, B. Liu, K.P. Loh, High yield exfoliation of two-dimensional chalcogenides using sodium naphthalenide. *Nat. Commun.* **5**, 2995 (2014). doi:[10.1038/ncomms3995](https://doi.org/10.1038/ncomms3995)
34. S. Jeong, D. Yoo, M. Ahn, P. Miró, T. Heine, J. Cheon, Tandem intercalation strategy for single-layer nanosheets as an effective alternative to conventional exfoliation processes. *Nat. Commun.* **6**, 5763 (2015). doi:[10.1038/ncomms6763](https://doi.org/10.1038/ncomms6763)
35. Q. Ji, Y. Zhang, Y. Zhang, Z. Liu, Chemical vapour deposition of group-VIB metal dichalcogenide monolayers: engineered substrates from amorphous to single crystalline. *Chem. Soc. Rev.* **44**, 2587 (2015)
36. Y. Shi, H. Li, L.J. Li, Recent advances in controlled synthesis of two-dimensional transition metal dichalcogenides via vapour deposition techniques. *Chem. Soc. Rev.* **44**(9), 2744 (2015)
37. M. Bosi, RSC growth and synthesis of mono and few-layers transition metal dichalcogenides by vapour techniques: a review. *Adv.* **5**(92), 75500 (2015)
38. X. Wang, H. Feng, Y. Wu, L. Jiao, Controlled synthesis of highly crystalline MoS₂ flakes by chemical vapor deposition. *J. Amer. Chem. Soc.* **135**(14), 5304 (2013)
39. K.K. Liu, W. Zhang, Y.H. Lee, Y.C. Lin, M.T. Chang, C.Y. Su, C.S. Chang, H. Li, Y. Shi, H. Zhang et al., Growth of large-area and highly crystalline MoS₂ thin layers on insulating substrates. *Nano Lett.* **12**(3), 1538 (2012)
40. A. Antonelou, G. Syrrakostas, L. Sygellou, G. Leftheriotis, V. Dracopoulos, S.N. Yannopoulos, Facile, substrate-scale growth of mono-and few-layer homogeneous MoS₂ films on Mo foils with enhanced catalytic activity as counter electrodes in dsscs. *Nanotechnology* **27**(4), 045404 (2015)
41. D. Kong, H. Wang, J.J. Cha, M. Pasta, K.J. Koski, J. Yao, Y. Cui, Synthesis of MoS₂ and MoSe₂ films with vertically aligned layers. *Nano Lett.* **13**(3), 1341 (2013)
42. H. Wang, D. Kong, P. Johanes, J.J. Cha, G. Zheng, K. Yan, N. Liu, Y. Cui, MoSe₂ and WSe₂ nanofilms with vertically aligned molecular layers on curved and rough surfaces. *Nano Lett.* **13**(7), 3426 (2013)
43. Y.C. Lin, W. Zhang, J.K. Huang, K.K. Liu, Y.H. Lee, C.T. Liang, C.W. Chu, L.J. Li, Wafer-scale MoS₂ thin layers prepared by MoO₃ sulfurization. *Nanoscale* **4**(20), 6637 (2012)
44. Y. Li, Y. Bando, D. Golberg, MoS₂ nanoflowers and their field-emission properties. *Appl. Phys. Lett.* **82**, 1962 (2003)

45. L. Chen, B. Liu, A.N. Abbas, Y. Ma, X. Fang, Y. Liu, C. Zhou, Screw-dislocation-driven growth of two-dimensional few-layer and pyramid-like WSe₂ by sulfur-assisted chemical vapor deposition. *ACS Nano* **8**(11), 11543 (2014)
46. C. Yuan, Y. Cao, X. Luo, T. Yu, Z. Huang, B. Xu, Y. Yang, Q. Li, G. Gu, W. Lei, Monolayer-by-monolayer stacked pyramid-like MoS₂ nanodots on monolayered MoS₂ flakes with enhanced photoluminescence. *Nanoscale* **7**(41), 17468 (2015)
47. L. Zhang, K. Liu, A.B. Wong, J. Kim, X. Hong, C. Liu, T. Cao, S.G. Louie, F. Wang, P. Yang, Three-dimensional spirals of atomic layered MoS₂. *Nano Lett.* **14**(11), 6418 (2014)
48. L. Zhou, K. Xu, A. Zubair, A.D. Liao, W. Fang, F. Ouyang, Y.H. Lee, K. Ueno, R. Saito, T. Palacios et al., Large-area synthesis of high-quality uniform few-layer MoTe₂. *J. Am. Chem. Soc.* **137**(37), 11892 (2015)
49. J.C. Park, S.J. Yun, H. Kim, J.H. Park, S.H. Chae, S.J. An, J.G. Kim, S.M. Kim, K.K. Kim, Y.H. Lee, Phase-engineered synthesis of centimeter-scale 1T-and 2H-molybdenum ditelluride thin films. *ACS Nano* **9**(6), 6548 (2015)
50. J.G. Song, J. Park, W. Lee, T. Choi, H. Jung, C.W. Lee, S.H. Hwang, J.M. Myoung, J.H. Jung, S.H. Kim et al., Layer-controlled, wafer-scale, and conformal synthesis of tungsten disulfide nanosheets using atomic layer deposition. *ACS Nano* **7**(12), 11333 (2013)
51. Y.H. Lee, L. Yu, H. Wang, W. Fang, X. Ling, Y. Shi, C.T. Lin, J.K. Huang, M.T. Chang, C.S. Chang et al., Synthesis and transfer of single-layer transition metal disulfides on diverse surfaces. *Nano Lett.* **13**(4), 1852 (2013)
52. X. Ling, Y.H. Lee, Y. Lin, W. Fang, L. Yu, M.S. Dresselhaus, J. Kong, Role of the seeding promoter in MoS₂ growth by chemical vapor deposition. *Nano Lett.* **14**(2), 464 (2014)
53. S. Najmaei, Z. Liu, W. Zhou, X. Zou, G. Shi, S. Lei, B.I. Yakobson, J.C. Idrobo, P.M. Ajayan, J. Lou, Vapour phase growth and grain boundary structure of molybdenum disulphide atomic layers. *Nat. Mater.* **12**(8), 754 (2013)
54. S. Ganorkar, J. Kim, Y.H. Kim, S.I. Kim, Effect of precursor on growth and morphology of MoS₂ monolayer and multilayer. *J. Phys. Chem. Solids* **87**, 32 (2015)
55. A.M. van der Zande, P.Y. Huang, D.A. Chenet, T.C. Berkelbach, Y. You, G.H. Lee, T.F. Heinz, D.R. Reichman, D.A. Muller, J.C. Hone, Grains and grain boundaries in highly crystalline monolayer molybdenum disulphide. *Nat. Mater.* **12**(6), 554 (2013)
56. C. Cong, J. Shang, X. Wu, B. Cao, N. Peimyoo, C. Qiu, L. Sun, T. Yu, Synthesis and optical properties of large-area single-crystalline 2D semiconductor WS₂ monolayer from chemical vapor deposition. *Adv. Opt. Mater.* **2**(2), 131 (2014)
57. S. Wu, C. Huang, G. Aivazian, J.S. Ross, D.H. Cobden, X. Xu, Vapor-solid growth of high optical quality MoS₂ monolayers with near-unity valley polarization. *ACS Nano* **7**(3), 2768 (2013)
58. Y. Kobayashi, S. Sasaki, S. Mori, H. Hibino, Z. Liu, K. Watanabe, T. Taniguchi, K. Suenaga, Y. Maniwa, Y. Miyata, Growth and optical properties of high-quality monolayer WS₂ on graphite. *ACS Nano* **9**(4), 4056–4063 (2015)
59. H.R. Gutiérrez, N. Perea-López, A.L. Elías, A. Berkdemir, B. Wang, R. Lv, F. López-Urías, V.H. Crespi, H. Terrones, M. Terrones, Extraordinary room-temperature photoluminescence in triangular WS₂ monolayers. *Nano Lett.* **13**(8), 3447 (2012)
60. Y. Zhang, Y. Zhang, Q. Ji, J. Ju, H. Yuan, J. Shi, T. Gao, D. Ma, M. Liu, Y. Chen et al., Controlled growth of high-quality monolayer WS₂ layers on sapphire and imaging its grain boundary. *ACS Nano* **7**(10), 8963 (2013)
61. Y.H. Chang, W. Zhang, Y. Zhu, Y. Han, J. Pu, J.K. Chang, W.T. Hsu, J.K. Huang, C.L. Hsu, M.H. Chiu et al., Monolayer MoSe₂ grown by chemical vapor deposition for fast photodetection. *ACS Nano* **8**(8), 8582 (2014)
62. J.C. Shaw, H. Zhou, Y. Chen, N.O. Weiss, Y. Liu, Y. Huang, X. Duan, Chemical vapor deposition growth of monolayer MoSe₂ nanosheets. *Nano Res.* **7**(4), 511 (2014)
63. X. Lu, M.I.B. Utama, J. Lin, X. Gong, J. Zhang, Y. Zhao, S.T. Pantelides, J. Wang, Z. Dong, Z. Liu et al., Large-area synthesis of monolayer and few-layer MoSe₂ films on SiO₂ substrates. *Nano Lett.* **14**(5), 2419 (2014)

64. Y. Peng, Z. Meng, C. Zhong, J. Lu, W. Yu, Y. Jia, Y. Qian, Hydrothermal synthesis and characterization of single-molecular-layer MoS₂ and MoSe₂. *Chem. Lett.* **30**(8), 772 (2001)
65. H.R. Matte, B. Plowman, R. Datta, C. Rao, Graphene analogues of layered metal selenides. *Dalton Trans.* **40**(40), 10322 (2011)
66. V. Senthilkumar, L.C. Tam, Y.S. Kim, Y. Sim, M.J. Seong, J.I. Jang, Direct vapor phase growth process and robust photoluminescence properties of large area MoS₂ layers. *Nano Res.* **7**(12), 1759 (2014)
67. H. Li, X. Duan, X. Wu, X. Zhuang, H. Zhou, Q. Zhang, X. Zhu, W. Hu, P. Ren, P. Guo et al., Growth of alloy MoS_{2x}Se_{2(1-x)} nanosheets with fully tunable chemical compositions and optical properties. *J. Amer. Chem. Soc.* **136**(10), 3756 (2014)
68. S.H. Su, Y.T. Hsu, Y.H. Chang, M.H. Chiu, C.L. Hsu, W.T. Hsu, W.H. Chang, H. He Jr., L.J. Li, Band gap-tunable molybdenum sulfide selenide monolayer alloy. *Small* **10**(13), 2589 (2014)
69. S.H. Su, W.T. Hsu, C.L. Hsu, C.H. Chen, M.H. Chiu, Y.C. Lin, W.H. Chang, K. Suenaga, H. He Jr., L.J. Li, Controllable synthesis of band-gap-tunable and monolayer transition-metal dichalcogenide alloys. *Front. Energ. Res.* **2**, 27 (2014)
70. A. Koma, K. Sunouchi, T. Miyajima, Fabrication of ultrathin heterostructures with van der Waals epitaxy. *J. Vac. Sci. Technol. B* **3**(2), 724 (1985)
71. A. Koma, Van der Waals epitaxy for highly lattice-mismatched systems. *J. Cryst. Growth* **201**, 236 (1999)
72. A. Koma, Van der Waals epitaxy a new epitaxial growth method for a highly lattice-mismatched system. *Thin Solid Films* **216**(1), 72 (1992)
73. A. Koma, K. Yoshimura, Ultrasharp interfaces grown with van der Waals epitaxy. *Surf. Sci.* **174**(1), 556 (1986)
74. F. Ohuchi, T. Shimada, B. Parkinson, K. Ueno, A. Koma, Growth of MoSe₂ thin films with van der Waals epitaxy. *J. Cryst. Growth* **111**(1), 1033 (1991)
75. K. Ueno, T. Shimada, K. Saiki, A. Koma, Heteroepitaxial growth of layered transition metal dichalcogenides on sulfur-terminated gaas {111} surfaces. *Appl. Phys. Lett.* **56**(4), 327 (1990)
76. L. He, X. Kou, K.L. Wang, Review of 3D topological insulator thin-film growth by molecular beam epitaxy and potential applications. *Phys. Status Sol. - RRL* **7**(1–2), 50 (2013)
77. Y. Shi, W. Zhou, A.Y. Lu, W. Fang, Y.H. Lee, A.L. Hsu, S.M. Kim, K.K. Kim, H.Y. Yang, L.J. Li et al., Van der Waals epitaxy of MoS₂ layers using graphene as growth templates. *Nano Lett.* **12**(6), 2784 (2012)
78. R. Yue, A.T. Barton, H. Zhu, A. Azcatl, L.F. Pena, J. Wang, X. Peng, N. Lu, L. Cheng, R. Addou et al., HfSe₂ thin films: 2D transition metal dichalcogenides grown by molecular beam epitaxy. *ACS Nano* **9**(1), 474 (2014)
79. Q. Ji, Y. Zhang, T. Gao, Y. Zhang, D. Ma, M. Liu, Y. Chen, X. Qiao, P.H. Tan, M. Kan et al., Epitaxial monolayer MoS₂ on mica with novel photoluminescence. *Nano Lett.* **13**(8), 3870 (2013)
80. Y. Cheng, K. Yao, Y. Yang, L. Li, Y. Yao, Q. Wang, X. Zhang, Y. Han, U. Schwingenschlögl, Van der Waals epitaxial growth of MoS₂ on SiO₂/Si by chemical vapor deposition. *RSC Adv.* **3**(38), 17287 (2013)
81. K. Ueno, K. Saiki, T. Shimada, A. Koma, Epitaxial growth of transition metal dichalcogenides on cleaved faces of mica. *J. Vac. Sci. Tech. A* **8**(1), 68 (1990)
82. X. Zhang, F. Meng, J.R. Christianson, C. Arroyo-Torres, M.A. Lukowski, D. Liang, J.R. Schmidt, S. Jin, Vertical heterostructures of layered metal chalcogenides by van der Waals epitaxy. *Nano Lett.* **14**(6), 3047 (2014)
83. H.C. Diaz, R. Chaghgi, Y. Ma, M. Batzill, Molecular beam epitaxy of the van der Waals heterostructure MoTe₂ on MoS₂: phase, thermal, and chemical stability. *2D Mater.* **2**(4), 044010 (2015)
84. E. Xenogianopoulos, P. Tsipas, K.E. Aretouli, D. Tsoutsou, S.A. Giannini, C. Bazioti, G. Dimitrakopoulos, P. Komninou, S. Brems, C. Huyghebaert et al., High-quality, large-area MoSe₂ and MoSe₂/Bi₂Te₃ heterostructures on AlN(0001)/Si(111) substrates by molecular beam epitaxy. *Nanoscale* **7**(17), 7896 (2015)

85. D. Le, D. Sun, W. Lu, L. Bartels, T.S. Rahman, Single layer MoS₂ on the Cu (111) surface: first-principles electronic structure calculations. *Phys. Rev. B* **85**(7), 075429 (2012)
86. M. Donley, P. Murray, S. Barber, T. Haas, Deposition and properties of MoS₂ thin films grown by pulsed laser evaporation. *Surf. Coat. Tech.* **36**(1), 329 (1988)
87. M. Donley, N. McDevitt, T. Haas, P. Murray, J. Grant, Deposition of stoichiometric MoS₂ thin films by pulsed laser evaporation. *Thin Solid Films* **168**(2), 335 (1989)
88. Y. Saito, P. Fons, A.V. Kolobov, J. Tominaga, Self-organized van der Waals epitaxy of layered chalcogenide structures. *Phys. Stat. Sol. B* **252**(10), 2151 (2015)
89. A. Gurarslan, Y. Yu, L. Su, Y. Yu, F. Suarez, S. Yao, Y. Zhu, M. Ozturk, Y. Zhang, L. Cao, Surface-energy-assisted perfect transfer of centimeter-scale monolayer and few-layer MoS₂ films onto arbitrary substrates. *ACS Nano* **8**(11), 11522 (2014)
90. B. Li, Y. He, S. Lei, S. Najmaei, Y. Gong, X. Wang, J. Zhang, L. Ma, Y. Yang, S. Hong et al., Scalable transfer of suspended two-dimensional single crystals. *Nano Lett.* **15**(8), 5089 (2015)
91. G. Plechinger, J. Mann, E. Preciado, D. Barroso, A. Nguyen, J. Eroms, C. Schüller, L. Bartels, T. Korn, A direct comparison of CVD-grown and exfoliated MoS₂ using optical spectroscopy. *Semicond. Sci. Tech.* **29**(6), 064008 (2014)
92. Y. Li, A. Chernikov, X. Zhang, A. Rigosi, H.M. Hill, A.M. van der Zande, D.A. Chenet, E.M. Shih, J. Hone, T.F. Heinz, Measurement of the optical dielectric function of monolayer transition-metal dichalcogenides: MoS₂, MoSe₂, WS₂, and WSe₂. *Phys. Rev. B* **90**(20), 205422 (2014)
93. G. Plechinger, F.X. Schrettenbrunner, J. Eroms, D. Weiss, C. Schueller, T. Korn, Low-temperature photoluminescence of oxide-covered single-layer MoS₂. *Phys. Stat. Sol. - RRL* **6**(3), 126 (2012)
94. I.S. Kim, V.K. Sangwan, D. Jariwala, J.D. Wood, S. Park, K.S. Chen, F. Shi, F. Ruiz-Zepeda, A. Ponce, M. Jose-Yacaman et al., Influence of stoichiometry on the optical and electrical properties of chemical vapor deposition derived MoS₂. *ACS Nano* **8**(10), 10551 (2014)
95. A. Splendiani, L. Sun, Y. Zhang, T. Li, J. Kim, C.Y. Chim, G. Galli, F. Wang, Emerging photoluminescence in monolayer MoS₂. *Nano Lett.* **10**(4), 1271 (2010)
96. C. Lee, H. Yan, L.E. Brus, T.F. Heinz, J. Hone, S. Ryu, Anomalous lattice vibrations of single-and few-layer MoS₂. *ACS Nano* **4**(5), 2695 (2010)
97. A. Castellanos-Gomez, N. Agraït, G. Rubio-Bollinger, Optical identification of atomically thin dichalcogenide crystals. *Appl. Phys. Lett.* **96**(21), 213116 (2010)
98. H. Li, J. Wu, X. Huang, G. Lu, J. Yang, X. Lu, Q. Xiong, H. Zhang, Rapid and reliable thickness identification of two-dimensional nanosheets using optical microscopy. *ACS Nano* **7**(11), 10344 (2013)
99. M. Benameur, B. Radisavljevic, J. Heron, S. Sahoo, H. Berger, A. Kis, Visibility of dichalcogenide nanolayers. *Nanotechnology* **22**(12), 125706 (2011)
100. P. Hajiyev, C. Cong, C. Qiu, T. Yu, Contrast and Raman spectroscopy study of single-and few-layered charge density wave material: 2H-TaSe₂. *Sci. Rep.* **3**, 2593 (2013). doi:[10.1038/step02593](https://doi.org/10.1038/step02593)
101. A. Castellanos-Gomez, E. Navarro-Moratalla, G. Mokry, J. Quereda, E. Pinilla-Cienfuegos, N. Agraït, H.S. van der Zant, E. Coronado, G.A. Steele, G. Rubio-Bollinger, Fast and reliable identification of atomically thin layers of TaSe₂ crystals. *Nano Res.* **6**(3), 191 (2013)
102. D.J. Late, B. Liu, H. Matte, C. Rao, V.P. Dravid, Rapid characterization of ultrathin layers of chalcogenides on SiO₂/Si substrates. *Adv. Funct. Mater.* **22**(9), 1894 (2012)
103. Y.Y. Wang, R.X. Gao, Z.H. Ni, H. He, S.P. Guo, H.P. Yang, C.X. Cong, T. Yu, Thickness identification of two-dimensional materials by optical imaging. *Nanotechnology* **23**(49), 495713 (2012)
104. H. Li, G. Lu, Z. Yin, Q. He, H. Li, Q. Zhang, H. Zhang, Optical identification of single-and few-layer MoS₂ sheets. *Small* **8**(5), 682 (2012)

Chapter 5

Structure and Physico-Chemical Properties of Single Layer and Few-Layer TMDCs

Atomically thin two-dimensional crystals such as graphene, TMDCs, and topological insulators, have attracted broad attention due to their scientific significance and also technological potential. Numerous intriguing phenomena stemming from a drastic reduction in dimensionality are not necessarily limited to monolayers; oftentimes they emerge in samples with thicknesses of several monolayers. For instance, the surface Dirac cones in Bi_2Te_3 films are generated in layers thicker than a few quintuple layers [1].

In many cases the structure of single layers is the same as the structure of a triple layer in the corresponding bulk material, however, this is not always the case. Most studies have been focused on MoS_2 and we describe the available results below in this chapter.

5.1 Structure of Single Layers

Monolayers of TMDCs have only two polymorphs, viz., trigonal prismatic and octahedral phases (Fig. 5.1). The former belongs to the D_{3d} point group (honeycomb motif) and the latter belongs to the D_{3d} point group (centered honeycomb motif). Another important change upon 3D to 2D transition is the disappearance of inversion symmetry (present in films with an even number of layers). It is explicitly broken in films with an odd number of layers, with concomitant effects on the material's properties such as second harmonic generation and polarised photoluminescence (see Sects. 12.1 and 11.1.1 below). It should also be noted that, similar to graphene, monolayer TMDCs are not flat but possess ripples that may reach 6–10 Å in height [2].

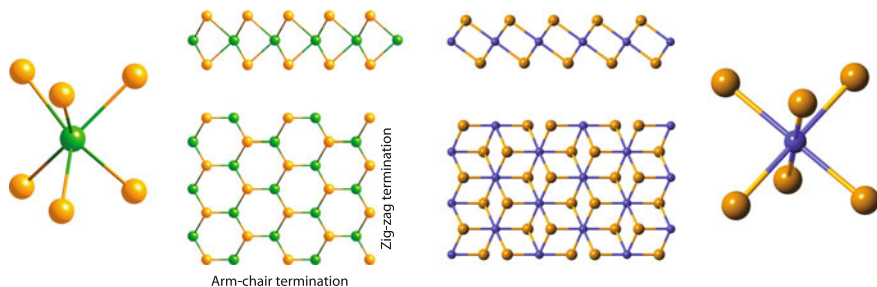


Fig. 5.1 Side and top views of the two polymorphs of monolayer TMDCs. *Left panel* trigonal prismatic (2H); *right panel* octahedral (1T). Chalcogen atoms are shown in orange and metal atoms are shown in green (blue)

5.1.1 2H-Phase

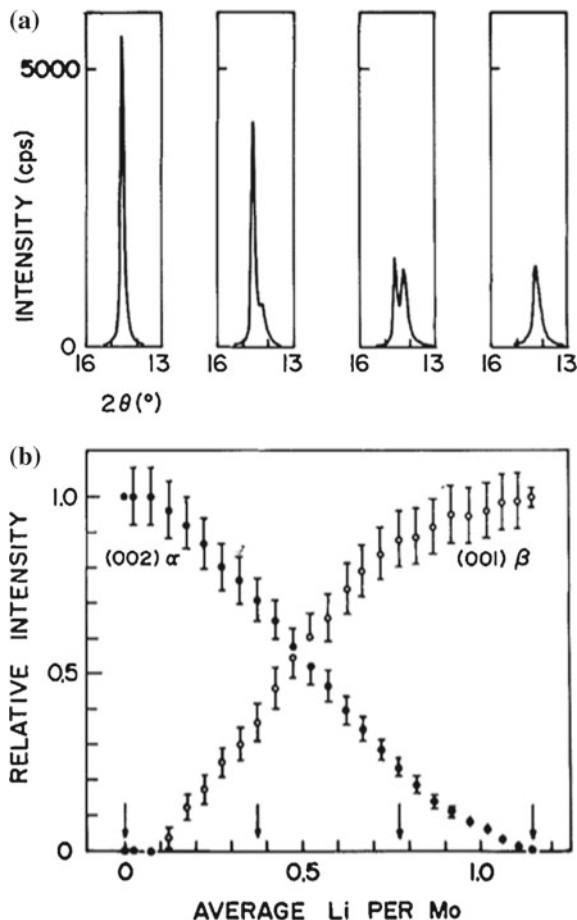
When prepared by dry methods such as Scotch-tape exfoliation or ultrasonication of the bulk material in an appropriate organic solvent, which has also been reported as a simple approach to exfoliation for a number of layered compounds [3], the yield of single layers is typically low, but the crystal structure of the bulk-2H exfoliated layers remains essentially undisturbed during the process, i.e. it is trigonal prismatic. While for single layers the notation 2H does not make much sense, it is usually preserved for consistency, although sometimes the notation H is also used. The structure of the 2H polymorph is shown in Fig. 5.1 (left).

5.1.2 1T-Phase

Layered transition metal dichalcogenides can also be efficiently exfoliated via alkali metal, e.g. lithium, intercalation and subsequent addition of excess water which leads to hydrogen formation and forced separation of the layers [4, 5]. This process results in exfoliated layers being in a metastable phase [6]. It is believed that the electron transfer from Li during intercalation causes a change in the electron count from d^2 to d^3 , leading to destabilization of the original crystal structure resulting in a change in the metal coordination from trigonal prismatic (2H) to octahedral geometry (1T) [7, 8]. It should be noted that no LiS_2 formation was observed at Li concentrations required for the transformation [7]. In [9], the lithiation process of MoS_2 was studied *in situ* using transmission electron microscopy.

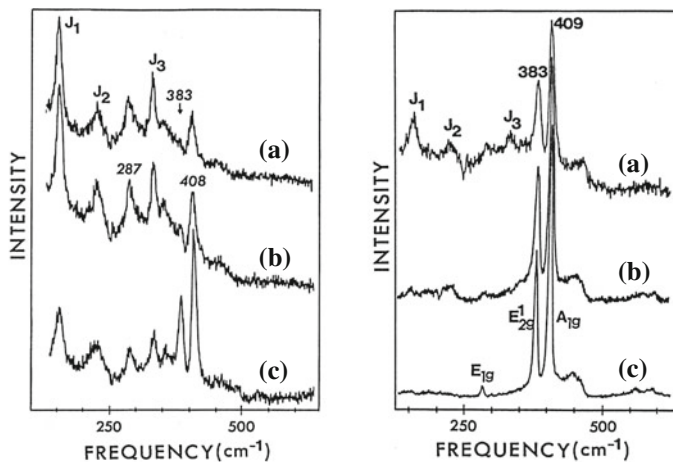
Structural characterization of single layers obtained by Li-exfoliation was initially performed by X-ray diffraction (Fig. 5.2), where an appearance and subsequent growth of a new peak was observed concomitant with a disappearance of the peak characteristic of the bulk 2H phase, which was the first demonstration that the structure of exfoliated layers (using Li-exfoliation) is different from that of the bulk.

Fig. 5.2 Evolution of X-ray diffraction profiles of the cathode during the discharge corresponding to different degrees of Li intercalation. **b** Approximate contributions of the two peaks as a function of the average lithium composition in the cathode. The arrows indicate the compositions at which the profiles shown in **a** were taken. Reproduced from [7], copyright Canadian Science Publishing



Subsequently, the Li-exfoliated single layers were investigated using Raman scattering (Fig. 5.3) [6, 10]. Figure 5.3 (left) shows a typical room-temperature Raman spectrum obtained from a freshly prepared MoS_2 single layer aqueous suspension while the right panel shows the Raman spectra for re-stacked films alongside with those of bulk $2H\text{-MoS}_2$. In the bottom, the calculated frequencies of the vibrational modes at the Γ -point for single molecular layers of MoS_2 with undistorted trigonal prism and octahedral coordinations are shown. The essential difference between the spectra for the single layer and the bulk phase is the disappearance of the 383 cm^{-1} peak and the appearance of new peaks, labelled J_1 , J_2 and J_3 , located at 156, 226, and 333 cm^{-1} , respectively.

From the disappearance of the 383 cm^{-1} peak, it was deduced that the trigonal prismatic phase is transformed into an octahedral phase. As regards the appearance of the new peaks, J_1 , J_2 and J_3 , they were interpreted in terms of the existence of a superlattice associated with a zone-folding mechanism, strongly suggesting that



	Trigonal prism (τ -MoS ₂)				Octahedral (Ω -MoS ₂)			
Mode Activity	E'' R	E' R, IR	A'_1 R	A''_2 IR	E_g R	A_{1g} R	E_u IR	A_{2u} IR
Calculated frequency (cm ⁻¹)	280	384	407	481	290	413	421	483

Fig. 5.3 Left room-temperature Raman spectra of **a** a freshly prepared MoS₂ single layer aqueous suspension, **b** a 12-day-old suspension, and **c** a 1.5-month-old suspension. Right room-temperature Raman spectra of **a** a fresh restacked MoS₂ film, **b** a 2-month-old film, and **c** 2H-MoS₂ powder before exfoliation. The table below shows the calculated frequencies of the vibrational modes at the Γ -point for single molecular layers of MoS₂ with undistorted trigonal prism and octahedral coordinations are shown [6]. Copyright 1991 by the American Physical Society. Reprinted with permission

the octahedral phase is distorted. Similar results and conclusions for Li-intercalated MoS₂ were obtained in [11]. The formation of the distorted phase with a larger lattice parameter was subsequently confirmed by direct measurements of the local structure using extended X-ray absorption fine structure (EXAFS) [12] (see below). The Raman modes for the distorted octahedral phase were simulated in [13] (see Sect. 7.11.1 below) and were in agreement with the experimental data. In [14] it was noted that both A_{1g} and E_{2g}^1 modes exhibited a shift to larger wavenumbers upon Li⁺ intercalation.

The metastable 1T phase remains even in the solid form and the residual negative charge on the nanosheets is passivated by the presence of a water bilayer containing protons or residual Li ions. Chemical analysis suggested that residual Li ions are not present so the excess charge stabilizing the 1T phase is likely to be due to the water bilayer [15]. In [6] it was further noted that as the single molecular layers re-stack with the expulsion of water and the sulfur-sulfur interlayer interaction is recovered, their structure reverts back to the trigonal prismatic coordination as evidenced by the

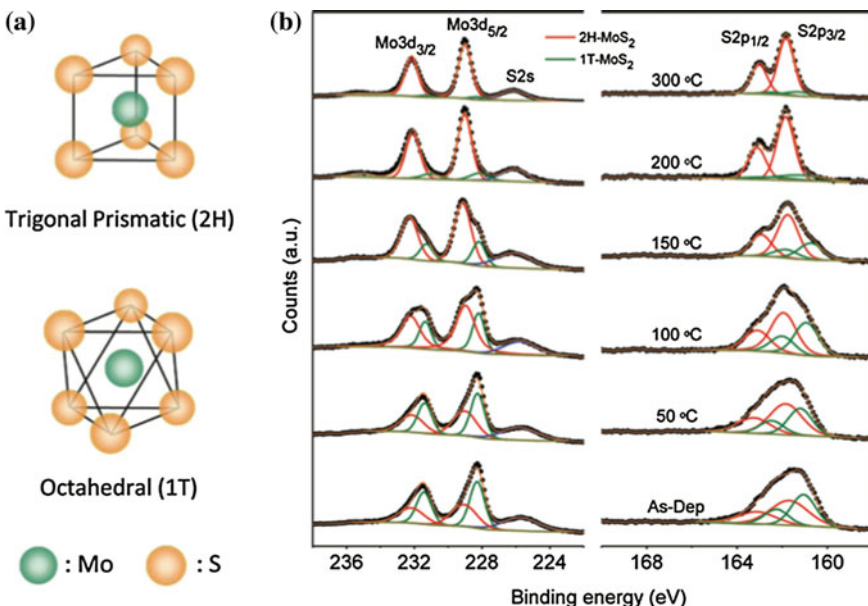


Fig. 5.4 **a** Structure of 2H- and 1T-MoS₂. **b** XPS spectra showing Mo 3d, S 2s, and S 2p core level peak regions for samples annealed at various temperatures. The samples were measured on Pt foil and Pt 4f_{7/2} was taken as a reference. After Shirley background subtraction, the Mo 3d and S 2p peaks were deconvoluted to show the 2H and 1T contributions, represented by red and green plots, respectively [18]. Copyright 2011 American Chemical Society. Published with permission

re-appearance of the 383 cm⁻¹ peak. This observation provides further evidence that the distorted octahedral phase is not due to the presence of the remaining Li ions. At the same time, it also demonstrates that the distorted octahedral phase is not a stable structure (at least when the layers are re-stacked).

The structure modification was proposed to be accompanied by an increase in the Mo-S bond ionicity in agreement with the respective stability of the new atomic arrangement, because the Coulomb repulsion between partially charged ligands favors the octahedral form [16]. Indeed, the transformation between the 2H and 1T phases also manifests itself as a change in XPS spectra [17, 18]. Figure 5.4 shows the evolution of the XPS spectra upon the annealing of exfoliated MoS₂ films. The sample in this case was not purely monolayered but had admixtures of blocks with several layers. The Mo 3d spectra consist of peaks at around 229 and 232 eV that correspond to Mo⁴⁺ 3d_{5/2} and Mo⁴⁺ 3d_{3/2} components of 2H-MoS₂, respectively. Deconvolution of these peaks reveals additional peaks that are shifted to lower binding energies by ca. 0.9 eV with respect to the position of the 2H-MoS₂ peaks. Similarly, in the S 2p region of the spectra, additional peaks were found besides the known doublet peaks of 2H-MoS₂, S 2p_{1/2}, and S 2p_{3/2}, which appear at 163 and 161.9 eV, respectively. From the parallel shift of these additional peaks it was concluded that they arise from the 1T phase [18]. Similar results were reported for

single crystal MoS₂ progressively intercalated by Li where additional peaks appear due to the formation of the 1T phase [17]. Upon annealing, the peaks attributed to the 1T phase gradually disappear.

As regards the origin of the peak shift, based on the results of infrared reflectivity measurements on group IVB and group VIB TMDCs, it was argued [19] that the octahedral group-IVB 1T-MX₂ compounds are purely ionic whereas the trigonal-prismatic group-VIB 2H-MX₂ compounds are covalent, which is also in line with the earlier mentioned proposal presented in [16].

As mentioned above, from the Raman measurements it was proposed that the octahedral phase was distorted and had a larger lattice parameter (superstructure). To confirm this, Bragg diffraction is not an option because it only characterizes long-range order and often misses local distortions [20]. To detect such local distortions, local probes like total scattering with pair-distribution function (PDF) analysis of total scattering or EXAFS have to be used [20–22]. Using EXAFS on single layers of MoS₂, MoSe₂, WS₂ obtained by Li-intercalation (measurements were performed on aqueous suspensions), it was demonstrated that the 1T-phase is locally distorted as shown in Fig. 5.5 with subsets of short, intermediate and long metal-metal distances similar to the structure of triple layers in bulk WTe₂ (cf. Figure 3.5). Qualitatively similar results were obtained for all three compositions studied. The formation of the Mo-Mo zig-zag chains causes the formation of a superstructure as was also supported by AFM and STM studies [23, 24].

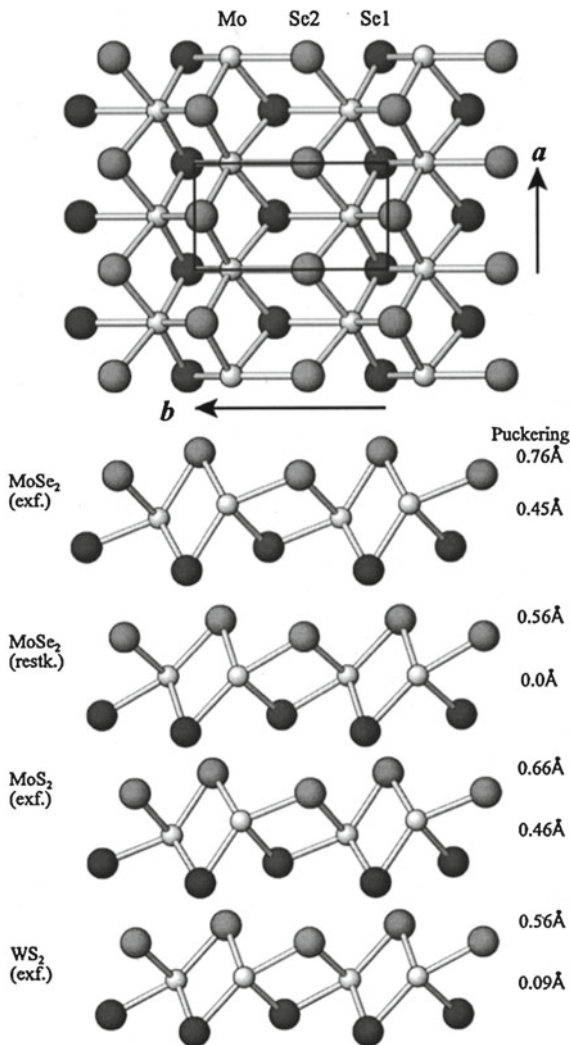
The structure of Li-intercalated MoS₂ (LiMoS₂) was also studied using PDF analysis of total scattering [25] with the result being slightly different. The atomic PDF is a function that gives the number of atoms in a spherical shell of unit thickness at a distance r from a reference atom. It peaks at characteristic distances separating pairs of atoms and thus reflects the structure of materials. The PDF $G(r)$ is defined as

$$G(r) = 4\pi r[\rho(r) - \rho_0] = (2/\pi) \int_{Q=0}^{Q_{max}} Q[S(Q) - 1]\sin(Qr)dQ \quad (5.1)$$

where ρ_0 is the average atomic number density, $\rho(r)$ the atomic pair density, Q the magnitude of the scattering vector, and $S(Q)$ is the corrected and properly normalized powder-diffraction pattern of the material. In other words, $G(r)$ is simply another representation of the diffraction data. An important point is that in total scattering both Bragg peaks as well as diffuse scattering contribute to the PDF, i.e. *all diffracted intensities are considered on the same footing*. By accessing high values of Q , experimental PDFs of high real-space resolution can be obtained that reveal fine structural features. Very important is also the fact that the PDF is obtained with no assumption of periodicity. Thus materials of various degrees of long-range order, ranging from perfect crystals to glasses and liquids, can be studied using the same approach.

Using a PDF analysis, the conclusion was reached that Mo atoms form diamond-shaped chains as shown in Fig. 5.6, a result in agreement with theoretical predictions of [26]. Rather similar conclusions were reached regarding the structure of

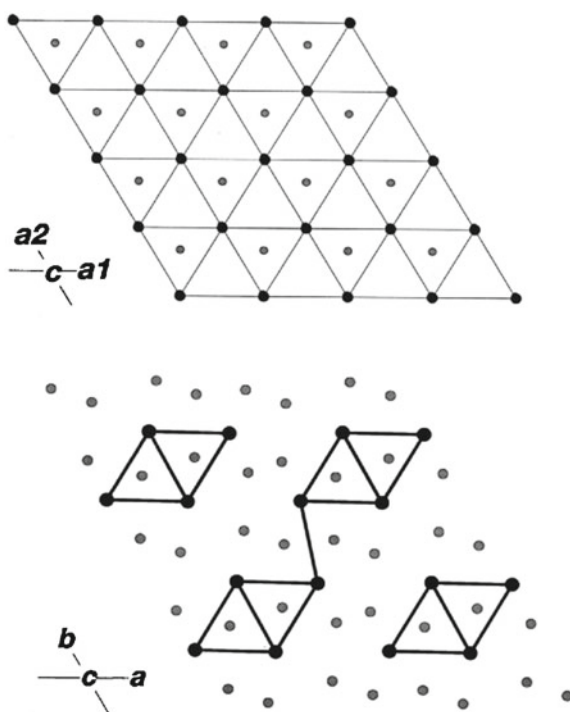
Fig. 5.5 Structural representations for (*upper panel*) exfoliated MoSe₂ single-layer model viewed perpendicular to the layer and (*lower panel*) single-layer MoSe₂ exfoliated, MoSe₂ restacked, MoS₂, and WS₂ viewed along the *a* axis. Small, white spheres are metal atoms. Larger medium and dark gray spheres are chalcogens above and below the plane, respectively [12]. Copyright 2002 by the American Physical Society. Reprinted with permission



intercalation-exfoliated WS₂ [27–30]. Interestingly, while in both Li intercalated and the exfoliated-restacked structures the low-*r* peaks in the PDF of the metastable phase were sharp and resolution limited, testifying to the well-defined order, the oscillations rapidly decreased with increasing *r*, indicating that the extent of the structural order is rather short-range, with the structural coherence being limited to 5 nm or less [20].

Upon re-stacking and annealing the structure reverted to the trigonal prismatic phase according to Raman and diffraction studies but remains partially distorted according to EXAFS results [12].

Fig. 5.6 Projection down the c axis of the crystal structures of hexagonal MoS₂ (*up*) and triclinic LiMoS₂ (*down*). The large black circles are Mo atoms and the small gray circles are the S atoms. Li atoms are not shown for the sake of clarity [25]. Copyright 2002 by the American Physical Society. Reprinted with permission



This issue was further investigated for MoS₂ [13, 31] using DFT simulations. The simulations confirmed that the *H*-phase is most stable. Three metastable phases of MoS₂, namely, the octahedral non-distorted structure, the distorted octahedral structure with zig-zag Mo–Mo chains and also a distorted structure with diamond-shape connected Mo–Mo chains atoms (following the prediction by [26], referring to the two distorted structures as *ZT* and *DT* structures, respectively, were compared. It was found that free-standing *T*-MoS₂ is unstable at 0 K and transforms into *ZT*-MoS₂, which was interpreted as a charge density wave state resulting from a Peierls instability [31]. It was argued that because the Mo atom in an octahedrally coordinated position has a d^2 configuration, each Mo uses only two of the three in-plane t_{2g} orbitals. This fits the two-center two-electron bonding model, which requires each Mo atom to bind with two neighboring Mo atoms to form two bonds, resulting in a relatively stable zig-zag chain configuration.

As regards the *DT*-phase it was found to be unstable for a free-standing layer and transformed to the *ZT* phase spontaneously. At the same time, it was concluded that it could exist in some impure state through the lithium adsorption or charging. Finally, it was found that the *T*-phase was unstable and transformed to the *H*-phase

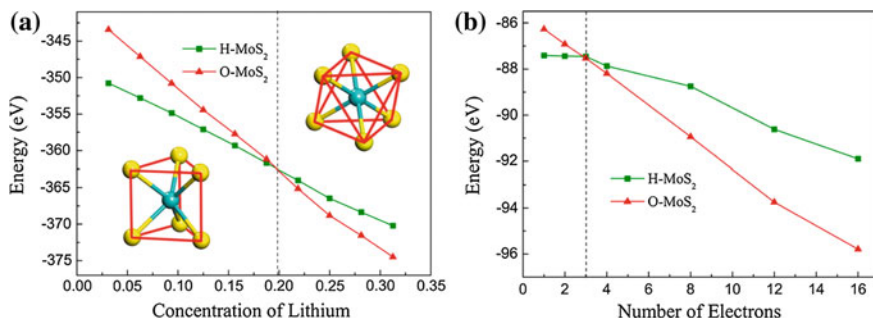


Fig. 5.7 **a** Variation of the energy for *H*-MoS₂ and *T*-MoS₂ (marked *O*-MoS₂ in the figure) as the concentration of Li changes. **b** The variation of the energy for *H*-MoS₂ and *T*-MoS₂ with respect to the number of electrons in the systems [31]. Copyright 2014 American Chemical Society. Published with permission

at a critical temperature of ca. 300 °C. In [13], the Raman modes for the distorted *ZT* phase were simulated (see below), the obtained results being in agreement with the experimental results [6].

Stability of the *T*- and *H*-phases as a function of Li concentration was also investigated. It was found that the *H*-phase is stable for up to 20% of Li. When the concentration of Li atoms exceeds 20%, the octahedral phase becomes more stable (Fig. 5.7, left). This result is in agreement with the conclusion drawn in [7]. An interesting observation was that the phase transition in 1 kg of 2D *H*-MoS₂ can be induced with only 17.5 g of Li [31]. The transition is associated with a charge transfer from the intercalant to the host material (Fig. 5.7, right) and can be explained as follows. The explanation was first offered in [7].

It was proposed that the stabilizing factor for the trigonal prismatic structure comes from a strong *d*-covalent bonding. The major difference between the octahedral and trigonal prismatic coordination is reflected in the splitting of the (mainly) *d*-band manifold. This is illustrated in Fig. 5.8 based on calculation [32] of the *d*-band density of states for the *2H* and *1T* polymorphs of TaS₂. In the octahedral phase, the lower sub-band contains six states and the upper band has four states per transition metal atom. Thus, a hypothetical *1T*-MoS₂ compound would exhibit metallic behaviour since only two of the six states in the lower sub-band would be occupied. In the trigonal prismatic phase, on the other hand, two *d*-bands are split off from the other eight by a gap of about 1 eV. The stabilizing effect responsible for the trigonal prismatic coordination in the group VI compounds is expected to be strongly affected by lithium intercalation since the insertion of each lithium atom is accompanied by the transfer of approximately one electron to the host [33]. As is seen from Fig. 5.8, because of the large bandgap (about 1 eV) between the filled

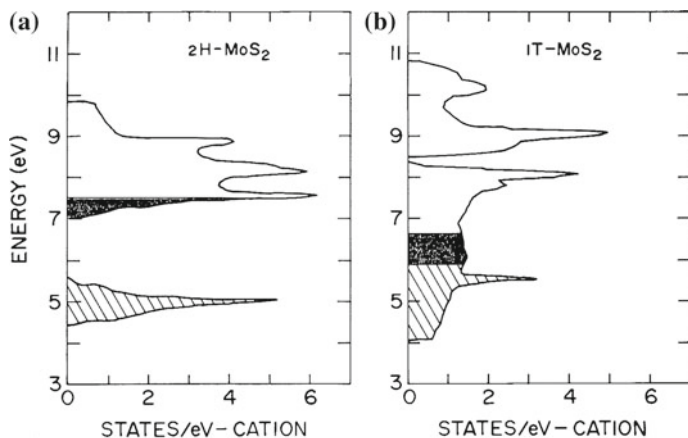


Fig. 5.8 Comparison of the d -band density of states for $2H$ -MoS₂ and hypothetical $1T$ -MoS₂ based on results for the $2H$ and $1T$ polymorphs of TaS₂ [34]. **a** The hatched region shows the occupied states in $2H$ -MoS₂; the shaded region depicts the additional states occupied in $2H$ -Li_xMoS₂. **b** Similar schematic diagram for $1T$ -MoS₂ host. Reproduced from [7], copyright Canadian Science Publishing

and empty states in the original material, the electronic energy of $2H$ -Li_xMoS₂ will be significantly higher than in $2H$ -MoS₂. In contrast, the increase expected for $1T$ -Li_xMoS₂, is much smaller because of the absence of an energy gap in the latter case. Thus, upon lithium intercalation, the host lattice of a group VI compound will tend to adopt the thereafter more stable octahedral coordination. Of special interest is the fact that while the $2H$ -phase is semiconducting, the $1T$ -phase is metallic.

While Li intercalation is one way to change the charge of the layer, an alternative way is by doping [35] MoS₂ with Re, Tc, or Mn, which have more electrons than Mo (or W) and act as donors. The arguments used are very similar to those used earlier to explain the $2H$ - $1T$ transformation under Li intercalation. It was argued that while doping of the semiconducting $2H$ -MoS₂ allotrope, the electrons that are donated to the Mo $4d_{xy,yz,xz}$ orbitals and to the Mo $4d_{x^2-y^2}$ orbitals result in metallic-like character of the electronic structure, and this causes destabilization of the lattice. At the same time, the incomplete occupation of Mo $4d_{xy,yz,xz}$ orbitals in $1T$ -MoS₂ leads to a metallic ground state, but it also decreases the stability of this MoS₂ allotrope (Fig. 5.9). Therefore, by doping the $1T$ -MoS₂ lattice with a donor atom, the additional electrons occupy the Mo $4d_{xy,yz,xz}$ orbitals and increase the stability of the $1T$ -phase [35].

The $2H$ - $1T$ phase transition can be visualised as gliding of the chalcogen planes [36] as illustrated schematically in Fig. 5.10.

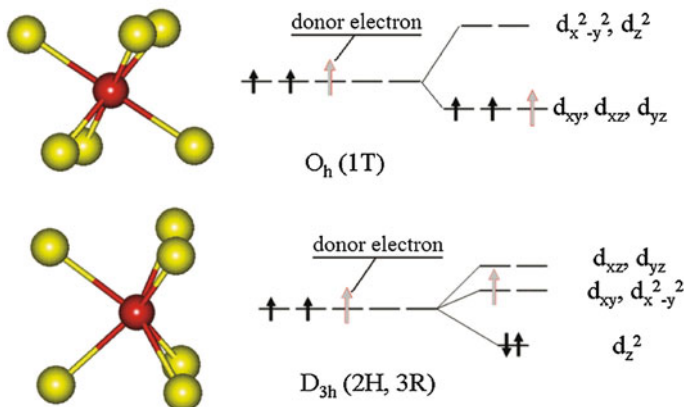


Fig. 5.9 Crystal-field theory used to describe energy levels of octahedral (*top*) and trigonal prismatic (*bottom*) MoS_2 . Adapted after [35]. Copyright 2011 American Chemical Society. Published with permission

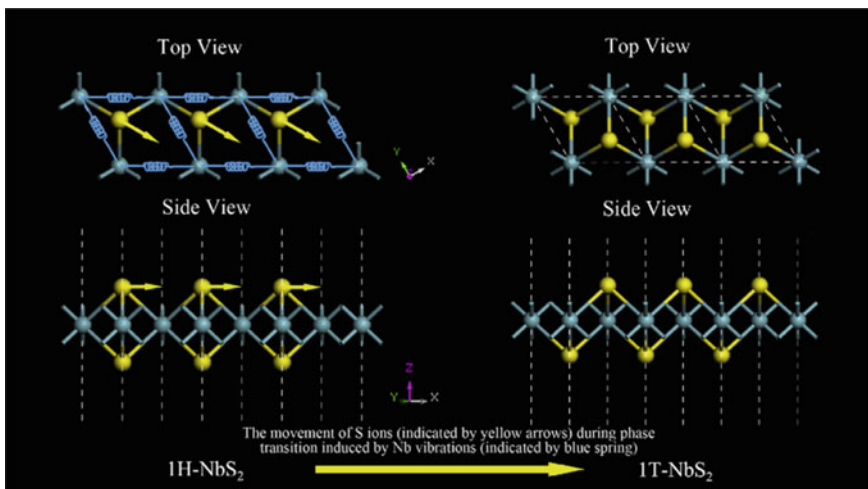


Fig. 5.10 Schematic route of the transformation from 1H to 1T phase for the single-layer NbS_2 [36]. Reprinted with permission from Elsevier

5.2 2H-1T Phase Transition

5.2.1 Phase Stability

Another thermodynamic parameter that can drive a structural transformation is pressure. Pressure induced structural phase transitions in two-dimensional Mo- and W-dichalcogenide monolayers were studied in [37]. Under ambient pressure, the

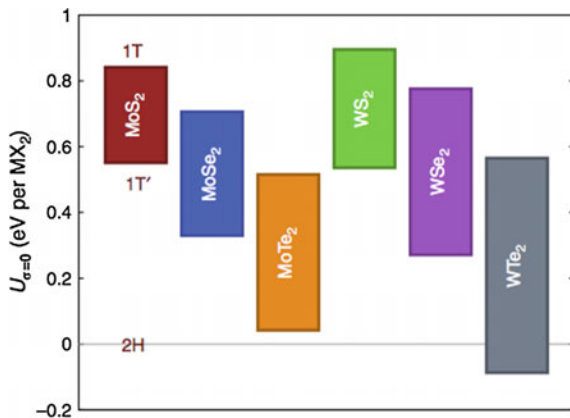


Fig. 5.11 Ground-state energy differences between monolayer phases of the six studied materials. The energy U is given per formula unit MX_2 for the $2H$, $1T'$ and $1T$ phases. Its value is computed at the equilibrium (zero stress, σ) lattice parameters for each phase. Because $\sigma = 0$, these values for U are equivalent to the enthalpy H . Vibrational energy is not included in these values [37]. Reprinted by permission from Macmillan Publishers Ltd., copyright (2014)

high symmetry $1T$ -structure for different group VIB TMDCs is unstable and converts to the lower-symmetry octahedral like phase $1T'$, which is a distorted version of the $1T$ structure. As noted earlier, the $1T'$ phase is observed in bulk WTe_2 under ambient conditions, and MoTe_2 also acquires this phase at high temperature [38]. Ground-state energy differences between monolayer $2H$, $1T$, and $1T'$ phases for six studied compositions (using DFT theory) are shown in Fig. 5.11.

Structural stability under applied (negative) pressure was subsequently studied making use of the fact that by attachment of a monolayer to a substrate large elastic deformations can be reached through tensile strain [39, 40], whereas large elastic deformations in most bulk materials are accessible only under compression. On the other hand, large compressive stresses are problematic in TMDC monolayer materials due to the spontaneous ripple formation [40–42].

Figure 5.12a shows the contours that follow the intersection of the $2H$ and $1T'$ energies in (a, b) space. The changes in the a and b axes required to change the relative energies U of the $2H$ and $1T'$ phase range from 13% (MoS_2) to 3% (MoTe_2). While these threshold values appear to be rather large, it has been experimentally demonstrated that monolayer TMDCs are exceedingly strong. e.g. $2H$ - MoS_2 monolayers were shown to reversibly withstand in-plane tensile stresses up to 15 Nm^{-1} , which corresponds to ca. 10% of the material's in-plane Young's modulus. From Fig. 5.12a, one can also see that WTe_2 , which usually exists in the $1T'$ phase, can be transformed into the $2H$ phase by compression, which is complementary to all the other cases.

Because the energy difference between the two phases is relatively small, vibrational effects could have a role in the energetic ordering of phases. Indeed it was found that temperature has a pronounced effect, which is illustrated in Fig. 5.12b,

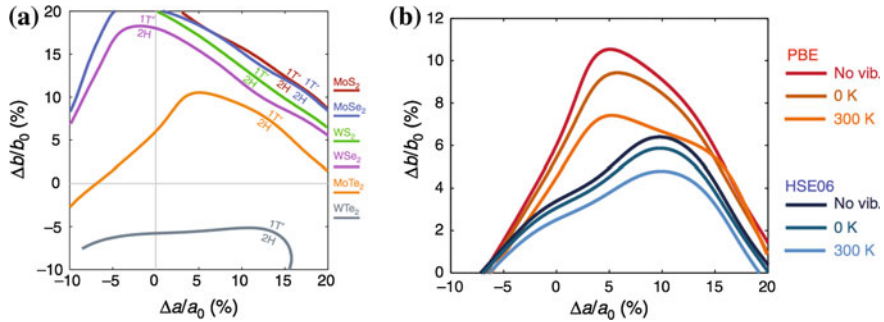


Fig. 5.12 **a** Intersection contours of the 2H and 1T' energy surfaces when varying the rectangular lattice constants a and b . The lattice constants a and b are represented as percent engineering strains, normalized over the equilibrium lattice constants a_0 and b_0 of the lowest energy structure (2H in all cases except WTe₂). The lower-energy (that is, lower- U) phase is labelled on each side of the contours. **b** Vibrational effects and hybrid functionals in MoTe₂. This figure shows the intersections of the MoTe₂ 2H and 1T' free energies $A(a, b, T)$ using different treatments of vibrational (vib.) effects and two exchange-correlation functionals. The top curve (GGA-DFT, no vibrational effects) corresponds to the MoTe₂ contour in panel **a**. Inclusion of vibrational free energy at 0 K (that is, only the vibrational zero-point energy) and at 300 K shifts the onset of the 1T' regime closer to the origin. It can also be seen from this figure that the use of the HSE06 DFT/Hartree-Fock functional in lieu of PBE has a similar effect [37]. Reprinted by permission from Macmillan Publishers Ltd., copyright (2014)

which shows that the required strains decrease at elevated temperatures. The result is shown for the two different functionals used [37], PBE and HSE06, the latter is argued to generally give a better agreement with experiment.

Phase stability with respect to the 2H-1T transformation for MoTe₂ was studied using DFT [43] simulations and stability of different monolayer compounds was analyzed in [44]. A summary of these studies for selected TMDCs is shown in Fig. 5.13.

5.2.2 Atomistic Details of the 2H to 1T Phase Transition

As already mentioned, the net result of the 2H to 1T transition can be viewed as sliding of chalcogen planes (Fig. 5.10). But this is just the net result. How does this transformation proceed on an atomistic scale?

The dynamic process of the atomic motions between 2H and 1T phases in single-layered MoS₂ was investigated using an aberration-corrected scanning transmission electron microscope (STEM) operating at 60 kV to visualize the dynamic process of the atomic motions [45]. In this work, an exfoliated 0.6 at.-% Re-doped MoS₂ was used and the sample was heated to 400–700 °C to promote the phase transition. The results of this work are shown in Fig. 5.14, where the step-by-step progress of MoS₂ phase transformation at $T = 600^\circ\text{C}$ is represented with annular dark-field (ADF)

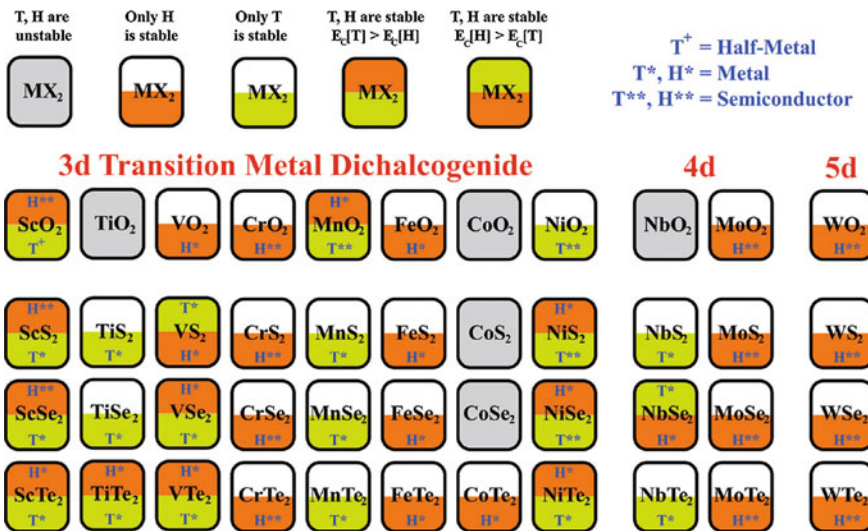


Fig. 5.13 Summary of the results of the stability analysis comprising 44 different MX_2 compounds that can form stable, 2D single-layer H and/or T structures. Transition-metal atoms indicated by M are divided into 3d, 4d and 5d groups. MX_2 compounds shaded light gray form neither stable H nor T structure. In each box, the lower-lying structure (H or T) is the ground state. The resulting structures (T or H) can be half-metallic (+), metallic (*), or semiconducting (***) [44]. Copyright 2012 American Chemical Society. Published with permission

images shown in the top panel, schematics correlating with the ADF images in the middle and a corresponding model of the atomic movements in the 2H-1T phase transition in the bottom panel.

The initial MoS_2 lattice (Fig. 5.14a) exhibits the 2H phase, with a honeycomb structure consisting of three Mo atoms and three overlapped S pairs arranged in a hexagon. At ca. 100 s, two identical band-like structures consisting of three to four constricted MoS_2 zig-zag chains (labelled α in Fig. 5.14b) gradually form along two zig-zag directions. When two non-parallel such bands are in contact, the atoms at the corner formed by the local acute angle are very densely packed, and it was argued that this triggers them to glide towards an area with lower atomic concentration to release the stress with the subsequent formation and growth of the triangular-shaped 1T phase. Further, the formation of two new phase boundaries (β and γ in Fig. 5.14) at the edges of the 1T phase was observed, which demonstrates that the phase transformation in single-layered MoS_2 involves numerous atomic displacements besides the simple atomic plane gliding.

It was concluded that the α phase, in which Mo atoms do not show a trigonal arrangement, but align as zig-zag chains, is a precursor structure. The Mo-Mo distance is locally compressed along these zig-zag chains, resulting in a local strain in the MoS_2 lattice, which is released by changing the Mo-S bond angles. An interesting observation was that the α -phase has a strong tendency to nucleate at the vicinity of

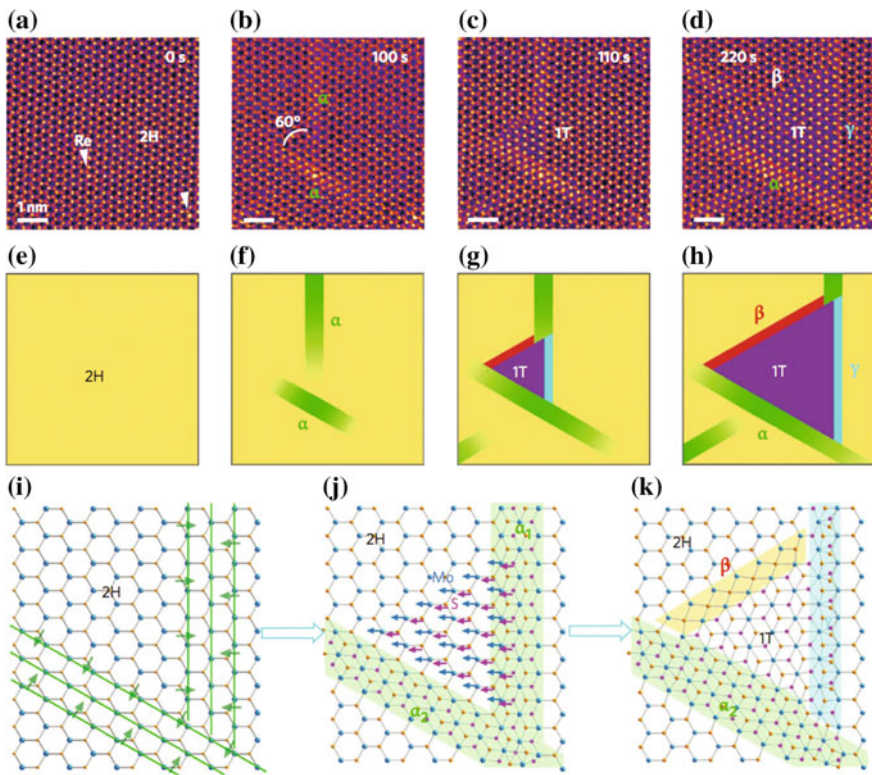


Fig. 5.14 Atomic movements during $2H \rightarrow 1T$ phase transformation in single-layered MoS₂ at $T = 600^{\circ}\text{C}$. **a** Single-layered MoS₂ doped with Re substitution dopants (indicated by arrowheads) has the initial $2H$ phase of a hexagonal lattice structure with a clear hollow center. **b** At $t = 100\text{s}$, two identical intermediate (precursor) phases (denoted α) form with an angle of 60° , and consist of three constricted Mo zig-zag chains. **c** At $t = 110\text{s}$, a triangular shape indicating the $1T$ phase (ca. 1.08 nm^2) appears at the acute corner between the two α -phases. The $1T$ phase provides noticeable contrast because of the S atoms at the hollow center sites. **d** At $t = 220\text{s}$, the area of the transformed $1T$ phase is enlarged to ca. 8.47 nm^2 . Three different boundaries (α , β and γ) are found at the three edges between the $1T$ and $2H$ phases. **e-h** Simple schematic illustrations of the $2H - 1T$ phase transition corresponding to the ADF images in **a-d**, respectively. **i** Atomic model of α -phase formation by the constriction of three Mo zig-zag chains. **j** Nucleation of the $1T$ phase (triangular) with the Mo + S (or S') atoms gliding in the directions indicated by blue and pink arrows. **k** β -boundary formation at the growth frontier side [45]. Reprinted by permission from Macmillan Publishers Ltd., copyright (2014)

Re substitution dopants, which was attributed to the initial out-of-plane protuberance of the Re-S bond that could help the S out-of-plane displacement and thus the formation of the α -phase. Another interesting observation was that the α -phase always consists of three or four MoS₂ zig-zag chains and does not expand in width.

The β -boundary is discussed by analogy with a twin boundary containing Mo-S four-membered rings. Figure 5.15e shows a typical ADF image of MoS₂ in the $2H$

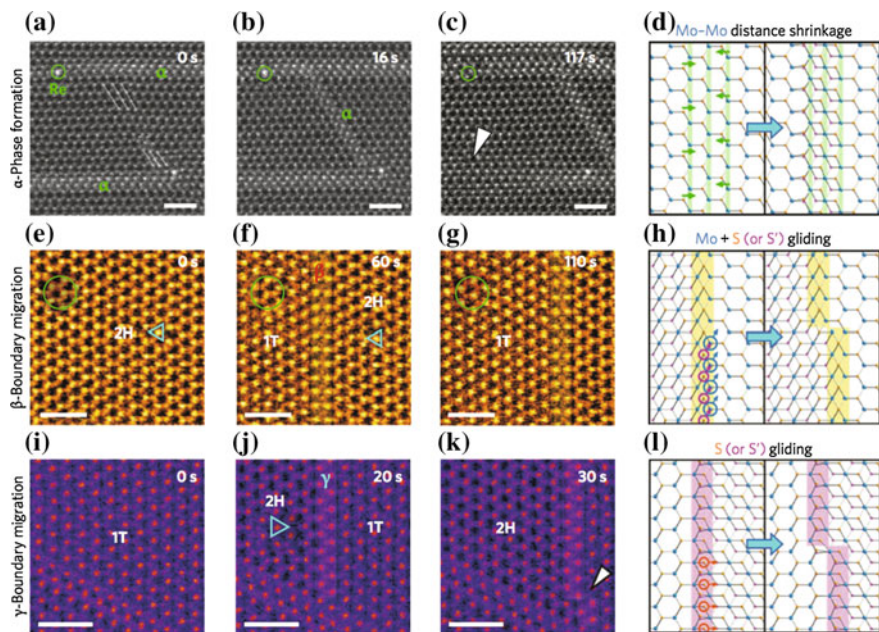


Fig. 5.15 Three elemental steps responsible for phase transitions in single-layered MoS₂ (T = 600 °C). **a–d**, α -Phase (three or four zig-zag chains) formation. **a** Nucleation of an α -phase at an angle of 60° with the other α -phases. The α -phase shows three or four constricted zig-zag MoS₂ chains. Three white lines highlight the distance between the zig-zag chains, with the in-plane constriction in the α -phase being ca. 15% that of the original MoS₂. **b** Growth of the α -phase. **c** At t = 117 s, the α -phase begins to migrate rightward. The left side of the bottom α -phase (indicated by an arrowhead) disappears and reverts to the initial MoS₂ lattice. Re dopants are marked by green circles. **d** Constriction (green arrows) induces strain in-plane (left), and the model α -phase forms with a reduced Mo–Mo distance (right). The S atoms in the α -phase are also misaligned vertically. **e–h** β -Boundary migration. **e** Single-layered MoS₂ with 2H phase. The orientation of the initial 2H phase is indicated by the blue triangle. **f** At t = 60 s, the β -boundary (highlighted by yellow shading) appears in the middle of the 2H-MoS₂. The left-hand side of the β -boundary demonstrates the 1T phase. **g** The β -boundary migrates rightward and the 1T phase is enlarged. **h** Schematic model before (top) and after (bottom) gliding of the Mo + S (or S') atoms, which causes β -boundary migration. In **e–g** the ADF images are filtered by a local two-dimensional Wiener filter to enhance the contrast. **i–l** γ -Boundary (two zig-zag chains) migration. **i** Single-layered MoS₂ with 1T phase (α -phase is also visible). **j** At t = 20 s, a γ -boundary (highlighted by purple shading) appears in the middle. The left-hand side of the γ -boundary demonstrates the nucleated 2H phase. **k** The γ -boundary migrates rightward and has a non-straight structure. **l** Schematic model before (top) and after (bottom) gliding of top S (or S') atoms, which drives γ -boundary migration. Scale bars, 1 nm [45]. Reprinted by permission from Macmillan Publishers Ltd., copyright (2014)

phase with a threefold symmetry (orientation described by a blue triangle). At t = 60 s, the β -boundary (highlighted by yellow shading) appears in the middle of the 2H-MoS₂ (Fig. 5.15f). The left-hand side of the β -boundary becomes the 1T phase. It was noted that the β -boundary shows up when a Mo plane and a S plane both

glide during the 2H-1T transition. A simpler transition from 2H to 1T with only one S-plane gliding results in the formation of a γ -boundary between the phases.

Finally it was noted that there was an incubation period during *e*-beam exposure before the transformation started. From this result, combined with the fact that the Re-concentration was rather low (less than 1 at.%), it was proposed that the continuous electron-beam irradiation may play an electronic role in accumulating negative charge to trigger the phase transition [45].

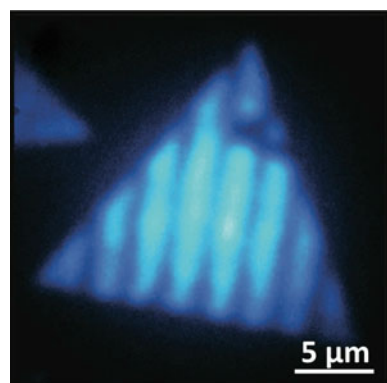
The 2H-1T transition in MoS₂ was also studied in [46] using in-situ transmission electron microscopy. It was concluded that H-MoS₂ transforms to T-LiMoS₂ at the early stages of lithiation, followed by the formation of Mo and Li₂S phases. The transition from H-MoS₂ to T-LiMoS₂ was explained in terms of an interplay between electron doping and electron-phonon coupling.

In [47], structural phase stability of monolayer MoTe₂ was studied with respect to adsorbed atoms and molecules. The simulations included spin-orbit coupling and a variety of vdW correction techniques. It was concluded that atomic adsorption generally induced 1T' metallic phases while molecular adsorption induced 2H phases. In MoS₂ monolayers, the 1T'-2H transformation was considered as a solid-state reaction [48].

5.2.3 Local Phase-Patterning

The local 2H-1T transition in MoS₂, also called phase-patterning, can be achieved in a controllable way. One of such methods used in [49] is based on a chemical treatment. First, using simple lithography to create well ordered masks, the authors locally patterned the surface. Subsequently, by exposing unmasked regions to 1.6 M *n*-butyl lithium for 48 h, it was possible to convert them to the 1T phase while the masked regions remain in the 2H phase. The dark strips in Fig. 5.16 represent the regions exposed to the butyl lithium and therefore converted to the metallic 1T phase.

Fig. 5.16 PL map of a CVD-grown nanosheet patterned with 1T phase strips. The *dark strips* represent the 1T phase, where the PL was quenched. The *bright regions* indicate that the 2H phase is unaffected by the chemical treatment [49]. Reprinted with permission. Copyright 2014 by the American Institute of Physics



The conversion was confirmed by performing PL mapping, where pronounced bright PL could be observed from the $2H$ region whilst no PL was observed from the $1T$ phase region.

In [50], laser-induced phase patterning of MoTe₂ was reported but it is not clear to what extent electronic excitation was important. In the original work only thermal effects were considered and the phase-patterning was attributed to the formation of Te vacancies.

5.2.4 Stability of CDW States and Gate-Tunable Phase Transitions in nm-Thick 1T-TaS₂

Thinning of 1T-TaS₂ was found to have a pronounced effect on the formation of CDW states [51, 52]. Bulk 1T-TaS₂ is a correlated metallic TMDC, whose rich phase diagram includes a series of CDW transitions as the temperature is lowered. It possesses a metallic incommensurate CDW (IC-CDW) phase below 550 K, changing to a textured nearly commensurate CDW (NC-CDW) phase below 350 K and finally acquiring a commensurate CDW (C-CDW) phase below 180 K. In the low-temperature C-CDW phase it is characterized by a 13×13 superlattice of David-stars formed by twelve Ta atoms clustered around a thirteenth Ta atom [53]. The periodic lattice distortion creates energy gaps in the 1T-TaS₂ bandstructure leaving exactly one conduction electron per David-star. The on-site Coulomb repulsion further localizes this conduction electron and produces a Mott insulator state [54, 55]. The neighbouring NC-CDW phase consists of trigonally packed C-CDW domains separated by metallic regions that are not fully distorted [56, 57]. In the high-temperature IC-CDW phase, the CDW aligns with the 1T-TaS₂ lattice and exhibits normal metallic behaviour [56]. Transitions between different CDW states manifest themselves as jumps (or drops) in the temperature dependence of the resistance, as shown in Fig. 5.17a (the lowest curve).

The effect of dimensionality for the CDW phases in 1T-TaS₂ was probed by studying pristine thin flakes with thicknesses varying down to a few nm (2 nm in [52] vs. 7 nm in [51]). It was found that both C-CDW/NC-CDW and NC-CDW/IC-CDW phase transitions are strongly modulated by sample thickness, namely, as the sample thickness was reduced, both transitions were shifted to lower temperatures during cool-down, and suddenly vanished at critical thicknesses of ca. 10 nm and ca. 3 nm, respectively. Samples thinner than 3 nm exhibited insulating behavior (Fig. 5.17b). The obtained results demonstrated the fragility of the CDW phases and pointed the vital role of dimensionality in sustaining long-range charge ordering in 1T-TaS₂.

More importantly, both groups found that in thin flakes the transitions between different CDW states could be electrically controlled [51, 52]. For this purpose, an ionic field-effect transistor structure was used. The strong charge doping induced by the tunable ion intercalation alters the energetics of various charge-ordered states in 1T-TaS₂ and produces a series of phase transitions in thin-flake samples with

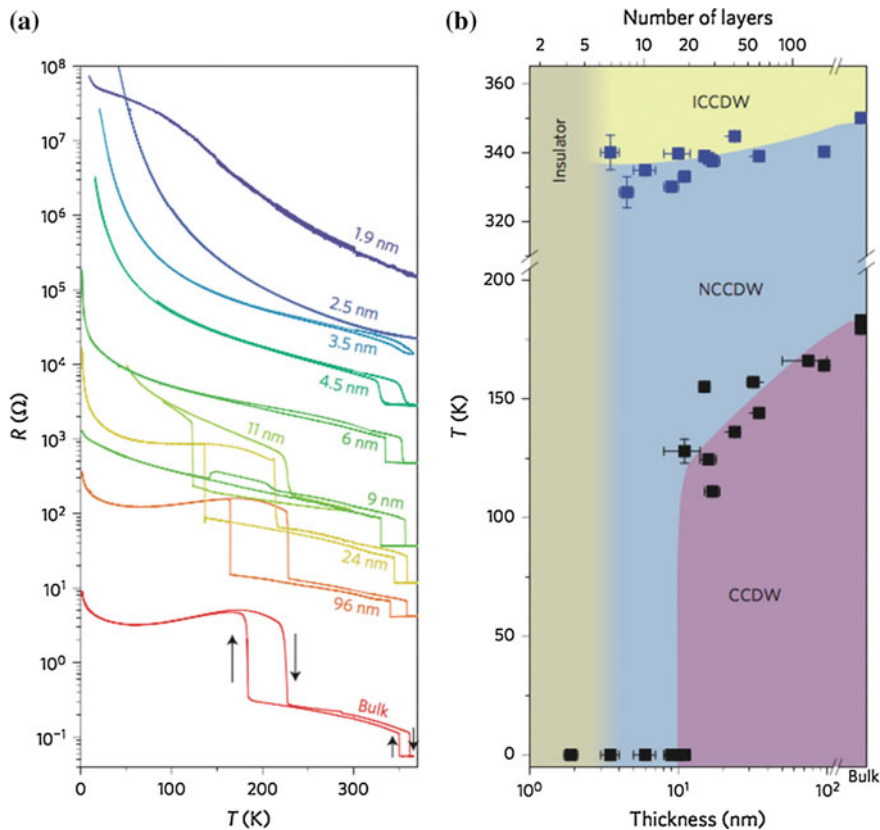


Fig. 5.17 CDW phases in pristine 1T-TaS₂ thin flakes with varying thicknesses. **a** Resistance as a function of temperature for pristine 1T-TaS₂ thin-flake samples with varying thicknesses. Red curve shows typical behaviour of bulk crystal. Arrows indicate the direction of temperature ramping. The first-order IC-CDW/NC-CDW and NC-CDW/C-CDW phase transitions are identified as jumps in sample resistance. **b** Thickness-temperature phase diagram obtained from the measurements in **a**. Blue and black squares mark the IC-CDW/NC-CDW and NC-CDW/C-CDW phase boundaries, respectively. For simplicity, only phase boundaries recorded during cooldown are shown. Horizontal error bars represent the uncertainty in sample thickness determination from AFM and optical measurements. Vertical error bars denote the widths of the phase transitions in temperature [52]. Reprinted by permission from Macmillan Publishers Ltd., copyright (2015)

reduced dimensionality. At low temperatures, the ionic gating induced multiple phase transitions from Mott-insulator to metal in 1T-TaS₂ thin flakes, with five orders of magnitude modulation in resistance, and superconductivity emerged in a textured charge-density wave state induced by ionic gating [52]. A summary of the results in form of phase diagrams is presented in Fig. 5.18.

It was recently found that exposure of bulk 1T-TaS₂ to femtosecond laser pulses resulted in the reversible formation of a stable “hidden” phase with a much lower resistance [58], associated with a different David-star clustering. Switching between

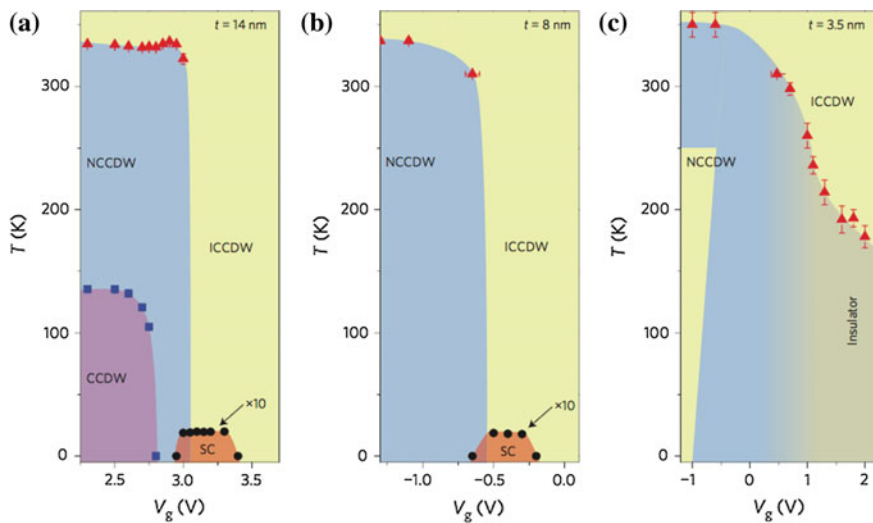


Fig. 5.18 **a–c** Doping-temperature phase diagrams of 1T-TaS₂ thin-flake samples in bulk **a** quasi-two-dimensional **b** and two-dimensional **c** limits, respectively. Boundaries of the C-CDW, NC-CDW and superconducting (SC) phases are marked by blue, red and black symbols, respectively. Only transition temperatures recorded during cool-down are shown for simplicity. The metal-insulator transition temperature in **c** is defined as the temperature where the (initially metallic) sample starts to show insulating behaviour as the temperature is lowered. *Horizontal and vertical error bars* denote the widths of the phase transitions in V_g and temperature, respectively [52]. Reprinted by permission from Macmillan Publishers Ltd., copyright (2015)

different conductivity states in 1T-TaS₂ can also be achieved electronically [59]. No such studies have been reported to date for ultra thin 1T-TaS₂ layers.

A CDW transition in single-layer TiSe₂ was reported in [60] at a critical temperature $T_c = 232 \pm 5$ K, which is higher than that of the bulk phase (~ 200 K).

5.3 Defects, Dislocations, and Grain Boundaries

Defects, dislocations, and grain boundaries occurring in real crystals can have a significant effect on their properties. Thus, point defects introduce states in the band gap of a material affecting the Fermi level and the properties of semiconductors. Similarly, dislocations can also significantly modulate the electronic properties of crystals by introducing states within their band gap [61]. They can also act as nucleation sites for the onset of deformation, when subjected to stress [62]. Furthermore, when exposed to chemical functional groups, defects can behave as highly reactive sites and efficiently trap different molecules[63].

Because of the high surface-to-volume ratio of 2D crystals, dislocations can lead to unique crystal geometries by introducing strain [64]. While in three-dimensional crystals migration of dislocations occurs when a large number of atoms move simultaneously, in 2D crystals this process takes place through the movement of a relatively few number of atoms near the dislocation core. Because of the 2D nature of such crystals, dislocation glides occur by the movement of atoms on the surface, where atomic diffusion usually has a lower-energy barrier compared with the bulk.

5.3.1 Point Defects

Intrinsic point defects in monolayer MoS₂ grown by CVD method were studied in [65] using atomic resolution annular dark field (ADF) imaging on an aberration-corrected scanning transmission electron microscope (STEM) and first-principles calculations. Figure 5.19a shows the STEM-ADF images of six commonly observed point defects, namely, a monosulfur vacancy (V_S), a disulfur vacancy (V_{S2}), a vacancy complex consisting of Mo and three neighbouring sulfur atoms (V_{MoS3}), a vacancy complex of Mo and three disulfur pairs (V_{MoS6}), and antisite defects with a Mo atom substituting a S₂ column (Mo_{S2}) or, vice versa, the S₂ column substituting a Mo atom ($S2_{Mo}$). In this work, the term ‘S₂ column’ corresponds to two S atoms located one on top of the other in the upper and lower sulphur layers. The atom-by-atom chemical analysis capability of STEM-ADF imaging made it possible to distinguish a monosulfur vacancy from a disulfur vacancy, and antisite defects from regular lattice sites.

To explore the energetics of the observed point defects, DFT calculations were performed [65]. The optimized defect structures from DFT calculations (Fig. 5.19b) were in agreement with the experimental images. It was noted that most of the defects maintain the 3-fold symmetry. The structural stability of the defects was explored through their formation energies (Fig. 5.19c). In the whole range of sulphur chemical potential, V_S was found to have the lowest formation energy, consistent with the frequent experimental occurrence of such defects. The chalcogen vacancy formation energies in various TMDCs were studied in [66].

The effects of the point defects on the electronic properties of MoS₂ were further studied. The in-gap defect levels for three types of defects: V_S , V_{S2} , and $S2_{Mo}$ are shown schematically in Fig. 5.19d.

Atomic defects in a monolayered tungsten disulphide nanoribbon was successfully studied by means of time-resolved annular dark-field imaging and spatially resolved electron energy-loss spectroscopy [67].

Defects can be generated during the growth process, or during the monolayer transfer, but can also be generated in the sample under extended electron irradiation. It was found [65] that extended electron irradiation preferentially generates two types of defects: V_S and V_{MoS3} . It was suggested that the preferential generation of V_{MoS3} under electron irradiation could potentially be useful for chemical sensing and hydrogen generation utilizing active edge sites. In addition, filling the metal

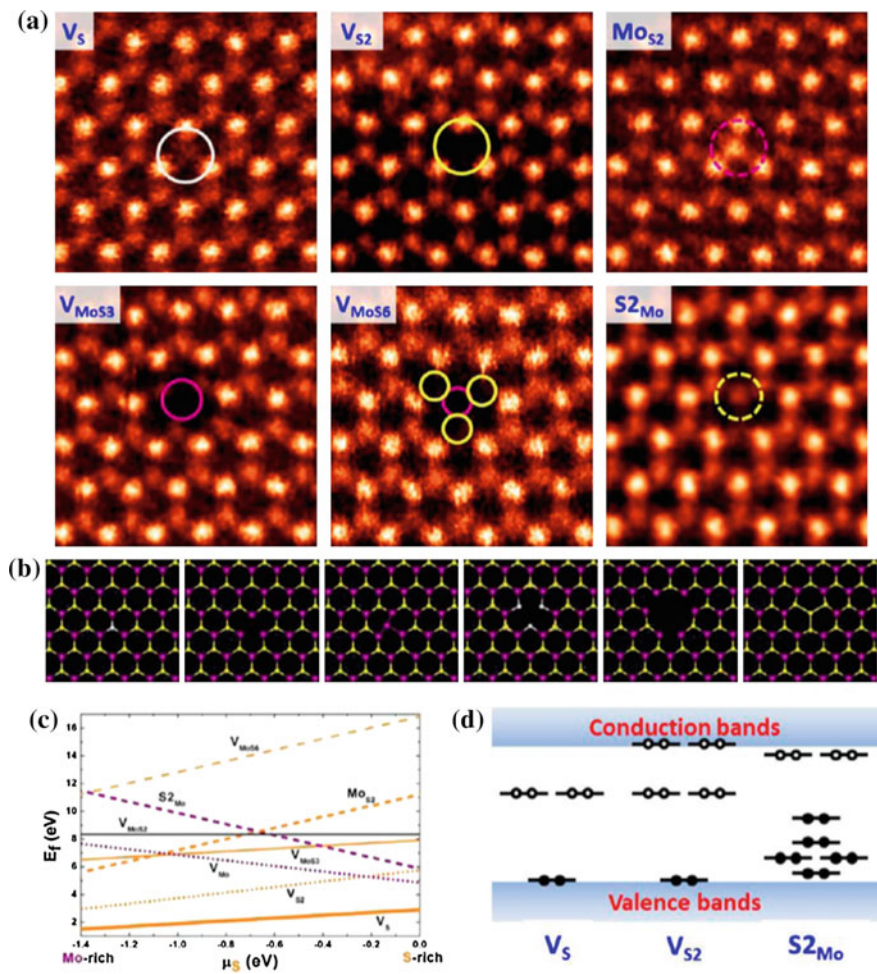


Fig. 5.19 Intrinsic point defects in monolayer MoS₂. **a** Atomic resolution ADF images of various intrinsic point defects present in monolayer CVD MoS₂: V_S, V_{S2}, V_{MoS₃}, V_{MoS₆}, Mo_{S2}, and S_{2Mo}. **b** Fully relaxed structural models of the six types of point defects observed experimentally. From left to right V_S, V_{S2}, V_{MoS₃}, V_{MoS₆}, Mo_{S2}, and S_{2Mo}. Purple, yellow, and white balls represent Mo, top layer S, and bottom layer S, respectively. **c** Formation energies of different point defects as functions of sulfur chemical potential, plotted in the range 1.4 eV < μ_S < 0 eV, where MoS₂ can remain stable with respect to the formation of bulk Mo (μ_S = ca. 1.4 eV) or bulk alpha-S (μ_S = 0 eV). **d** Schematic representation of the defect levels [65]. Copyright 2013 American Chemical Society. Published with permission

vacancy complexes with foreign atoms, such as other transition metals, provides new opportunities to tune the properties of MoS₂ monolayers.

Defect production in 2D TMDCs under electron irradiation was also studied in [68]. The authors calculated displacement threshold energies for atoms in different

TMDC compounds and estimated the corresponding electron energies required to produce defects. For a representative structure of MoS₂, high-resolution transmission electron microscopy experiments were carried out and the formation of vacancies under exposure to an 80 keV electron beam was observed. It was also suggested that TMDCs can be doped by filling the vacancies created by the electron beam with impurity atoms.

The same authors subsequently studied the evolution of point defects to extended defects under electron irradiation [69]. Under extended irradiation, they observed the formation of extended line defects that could be well described by a row of single vacancies, without significant atomic reconstruction. However, the tendency to line up and to remain as a line was not very strong, suggesting that the energy gain is small. It was further found that the line defects were preferentially formed parallel to the sample edges suggesting correlation of these defect agglomerates with strain.

After prolonged exposure to the electron beam and further increase in the vacancy concentration, the nature of the lines changed: the lines extended to span two neighboring rows of the S sublattice. It was noted [69] that during the formation of vacancy lines, the number of single vacancies surrounding the line dropped significantly, suggesting that the lines were formed through agglomeration of vacancies rather than through production of a large number of new vacancies.

In order to determine the underlying atomic structure, the DFT simulations for various atomic models were performed (Fig. 5.20), where panels (a) and (d) show experimental images. The optimized geometries, shown in panels (b), (e), (g), and (i) were used as an input for TEM image simulation [(panels (c), (f), (h), and (j))] (using Cs of 0.02 mm and the corresponding Scherzer focus of -11.2 nm .) The relative formation energies for these structures are shown in panel (k).

In the case of single vacancy (SV) lines, there is only one reasonable choice for the underlying atomic structure, and a good agreement between simulated and experimental images was obtained. The obtained formation energies show that agglomeration to a line leads to an energy gain of ca. 0.05–0.2 eV per S vacancy, agreeing well with the tendency to line up.

For a line of double vacancies, the three models shown in panels (e), (g), and (i) were considered that correspond to (e) two neighboring lines of S vacancies at the same side of the MoS₂. (g) Two lines of vacancies at the opposite sides of MoS₂ thereby forming a line of vacancy columns (subsequently showing Mo-Mo bonds with bond length close to that in bulk Mo). (i) Two lines of vacancies are at the neighboring sites and opposite sides in the staggered configuration. From comparison of the simulated and experimental TEM images, agreement was good only for the staggered model. Furthermore, the only model yielding negative formation energies is the staggered one. Consequently, the double vacancy lines were assigned to the staggered model.

It was noted that for all the line structures discussed above, vacancies along the line were always on the same side of the monolayer, which was attributed to the fact that the formation energies tended to increase whenever the vacancies were on different sides of the sheet, but in the same line. For example, the formation energy of a SV line consisting of four vacancies with all vacancies on the same side showed

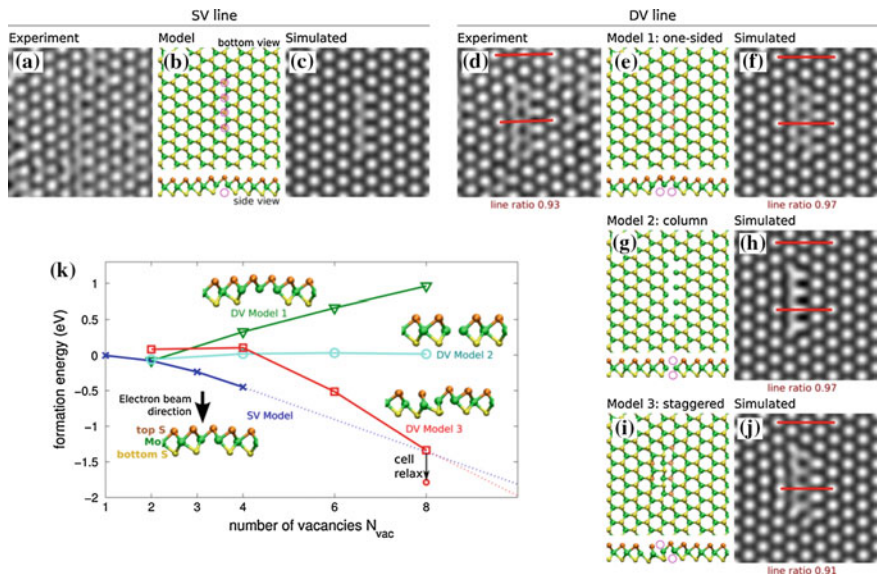


Fig. 5.20 Comparison of experimental and simulated TEM images. **a, d** Examples of experimental high resolution TEM images of the single vacancy (SV) and double vacancy (DV) lines. Various models of the vacancy lines: **b** and **c** a single vacancy line, **e** and **f** two neighboring vacancy lines in the same S layer, **g** and **h** two vacancy lines coinciding in *top* and *bottom layers*, and **i** and **j** two vacancy lines in staggered configuration, The atomic structures (**b**, **e**, **g**, and **i**) were obtained from DFT calculations and used to simulate TEM images (**c**, **f**, **h**, and **j**). Note that the *bottom* and *side views* are shown. In order to distinguish between atoms in the two S layers, they are colored differently: *orange* for the *top layer* and *yellow* for the *bottom layer*. *Magenta circles* denote the initial vacancy positions. For DV lines, the local shrinkage of the lattice is quantified by the ratio of the length of line segments (*solid red lines*) in pristine lattice and around the defect. **k** Formation energies for all considered models as a function of the number of constituting single vacancies (the number of missing S atoms). The DV lines always have an even number of vacancies. The extrapolation to *longer lines* is also shown. The insets are the side views of the atomic models presented in **(b)**, **(e)**, **(g)** and **(i)** [69]. Copyright 2013 by the American Physical Society. Reprinted with permission

a 0.7 eV lower formation energy as compared to the case with the vacancies placed in an up-down-up-down configuration [69].

Looking into the dynamics of the defect line formation, it was found that the SV lines formed fairly slowly, and often via diffusion of single vacancies. In contrast, the formation of the double vacancy (DV) line was usually rapid, often occurring within the time interval of one frame, inconsistent with the simple picture of slow vacancy diffusion. The calculations suggested that the migration barrier is dramatically lowered, and thereby the diffusion rate is enhanced, when the number of vacancies in the nearby S sites was increased [69].

Chalcogen vacancies in monolayer TMDCs were also studied in [66] and it was concluded that vacancy formation energies increase from sulphides to tellurides. Point defects in MoSe₂ bilayer was studied in [70] by scanning tunneling microscopy and spectroscopy.

5.3.2 Dislocations and Grain Boundaries

Dislocations and grain boundaries in monolayers of TMDCs were investigated by several groups [65, 71–74]. In [71], dislocations and grain boundaries were studied by DFT simulations. It was found that in contrast to graphene and h-BN, due to the sandwich structure of individual monolayers in TMDCs, edge dislocations extend in third dimension, forming concave dreidel-shaped polyhedra.¹ An interesting finding was also that grain boundaries under certain circumstances became metallic lines embedded into a semiconducting matrix, which could provide new functionalities and form intrinsic electronic heterostructures in monolayer MoS₂ [71]. Subsequently, dislocations and grain boundaries in monolayers were studied experimentally [65, 72–74].

The structure of a 60° grain boundary was MoS₂ was studied in [65]. The boundary was parallel to the zig-zag direction of the MoS₂ lattice and is composed of 4-fold rings with *point sharing* at a common S₂ site (denoted as a 4|4P structure). The structure of the 4|4P type grain boundary is shown in Fig. 5.21b with the relaxed structure model overlaid. The Mo atoms at this grain boundary retain the regular 6-fold coordination; however, the S atoms at the grain boundary change from the regular 3-fold coordination to 4-fold coordination. This particular grain boundary structure was predicted to be a 1D metallic stripe embedded in the otherwise semiconducting MoS₂ [71].

Grain boundaries are usually not straight but have kinks. The separation of these kinks (white arrows in Fig. 5.21) generates 4|4P segments with different lengths, providing the general description of this particular type of 60° grain boundary in monolayer MoS₂. It was noted that, depending on the precise manner of how the two 60° rotated grains meet, another type of 60° grain boundary consisting of strings of 4-fold rings with *edge sharing* (4|4E) can also form, panel (d). In the extreme case, corresponding to a 4|4P grain boundary with the highest density of kink pairs, it becomes a line of 4|8 grain boundaries as shown in panel (e).

The electronic structures of the experimentally observed grain boundaries was also explored and it was found that both 4|4P grain boundaries and 4|4E grain boundaries serve as perfect 1D metallic quantum wires embedded in the semiconducting MoS₂ matrix with dispersive bands crossing the Fermi level. At the same time, the 4|8 grain boundary only introduces localized mid-gap states right above the top of valence

¹A dreidel is a four-sided spinning top. The dreidel is a Jewish variant on the T-totum, a gambling toy found in many European cultures.

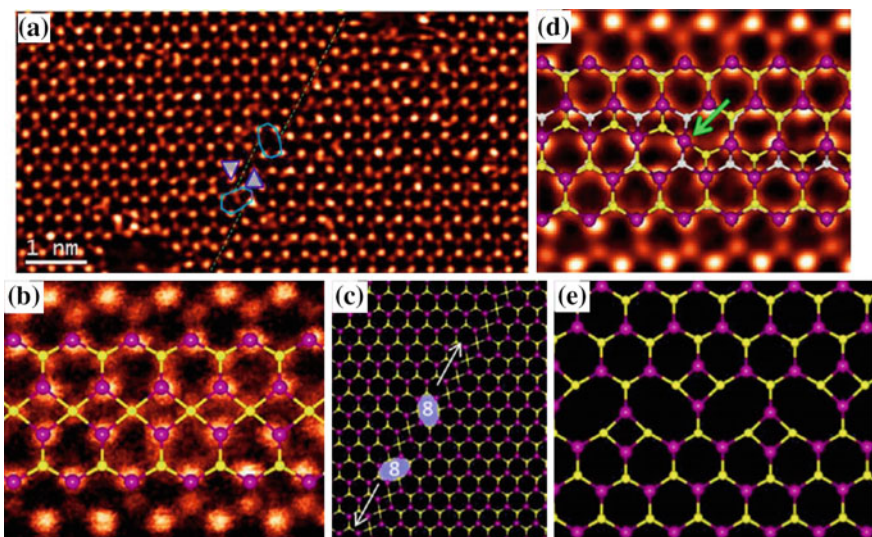


Fig. 5.21 Atomic structure of 60° grain boundaries in monolayer MoS_2 . **a** ADF image of a 4|4P 60° grain boundary. The green dash line highlights the position of the 4|4P grain boundary, and the grain boundary steps are linked by octagons as indicated. The blue triangles illustrate the orientation of the two grains with 60° rotation. **b** ADF image of the 4|4P 60° grain boundary structures with the structural model overlaid. **c** Schematic structure of the grain boundary and grain boundary kinks as shown in panel **a**. **d** ADF image and overlaid structural model of a 4|4E type 60° grain boundary, and the grain boundary steps are linked by 4-fold coordinated Mo atoms as highlighted. **e** Relaxed structure for 4|8 grain boundary, representing a 4|4P grain boundary with the highest kink density [65]. Copyright 2013 American Chemical Society. Published with permission

bands of the MoS_2 matrix, as was demonstrated by comparing the LDOS and band structure [65].

The grain boundary structure is different for the case of smaller angles. Figure 5.22a shows an 18.5° grain boundary composed of 5|7 and 6|8 structures as schematically shown in the STEM-ADF image. The detailed atomic structures for the 5|7 and 6|8 dislocation cores are shown in panels (b, c), respectively. The 5|7 structure can serve as the basic dislocation core structure, and the addition of monosulfur or disulfur into the Mo-Mo bonds generates the 6|8 structures observed at the same grain boundary. A different grain boundary was observed in another area of the continuous MoS_2 film that showed primarily 4|6 structures (panels d, e) with 4- and 6-fold rings joined by 4-fold coordinated S atoms.

The complexity of the grain boundaries is not limited to the above shown cases. Figure 5.23a, b show a mirror twin boundary in a 6-pointed star [72]. Whereas the grain boundary follows the zig-zag direction on the micrometre scale, it exhibits faceting of $\pm 20^\circ$ relative to this direction on the nanometre scale. Figure 5.23b shows the atomic structure of the grain boundary. The overlaid purple and green polygons

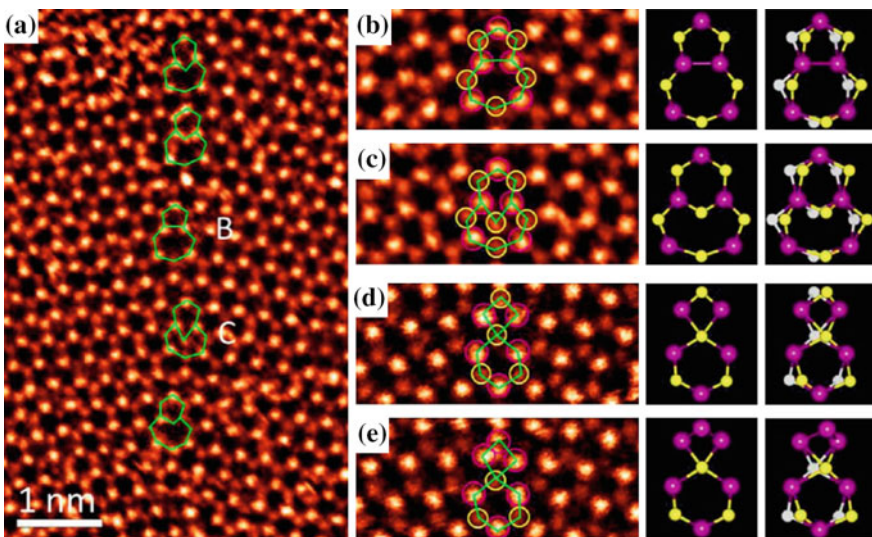


Fig. 5.22 Atomic structure of small-angle grain boundaries in monolayer MoS₂. **a–c** STEM-ADF images of an 18.5° grain boundary consisting of dislocations with five- and seven-fold rings (5|7) and dislocations with six- and eight-fold rings (6|8). Panels **b** and **c** are the zoom-in view of the 5|7 and 6|8 structures from the regions indicated in **a**. **d**, **e** ADF images of a 17.5° grain boundary consisting of dislocations with four- and six-fold rings (4|6), either pristine (**d**) or with Mo-substitution (**e**). The 2D and 3D structural models for the various dislocation structures are placed next to the corresponding ADF images [65]. Copyright 2013 American Chemical Society. Published with permission

show that the boundary is formed primarily from 4- and 8-membered rings, with a recurring periodic 8-4-4 ring motif.²

In the observed 8-4-4 motif, the neighbouring 4-rings meet at a sulphur site, which appears to have four nearest neighbours rather than the usual three. This change in coordination requires either the S atoms to have dangling bonds, or the Mo atoms to change their oxidation state. DFT simulations found that after relaxation, the 8-4-4 boundary structure was at a local energetic minimum (Fig. 5.23c).

Figure 5.23d compares the DFT-calculated density of states (DOS) of defect-free monolayer MoS₂ and a structure that includes a grain boundary. Figure 5.23e shows a spatial plot of the local DOS of pristine + grain boundary in the plane of the Mo atoms, integrated in the energy range of the pristine bandgap; the mid-gap states are spatially localized at the boundary. These localized mid-gap states, typical of defects in semiconductors, also observed in [65] are important because they can affect the optical and transport properties of the material.

The process of grain boundary formation was also studied in [73], where two possible mechanisms of grain boundary formation in MoS₂ were identified. In addition

²We preserve here the notations of the original publication [72], the relationship with the grain boundaries described above is obvious from comparing Figs. 5.21 and 5.23.

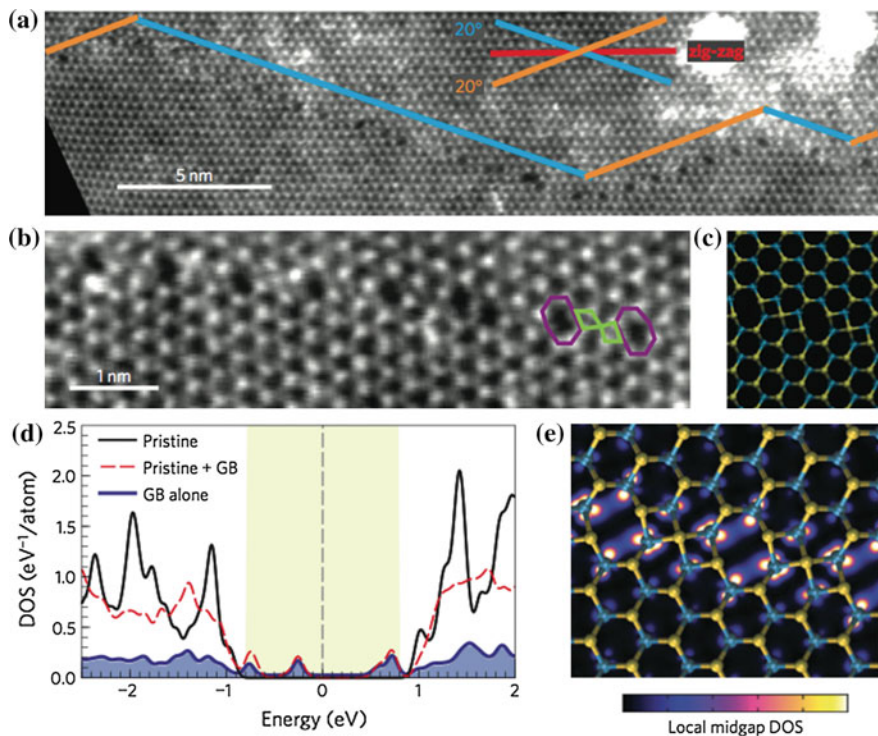


Fig. 5.23 Grain boundary atomic structure. **a** High-resolution ADF-STEM image of a mirror twin boundary. The boundary is visible just below the annotated line. The annotation indicates the nanoscale faceting of the boundary at $\pm 20^\circ$ off the zig-zag direction. **b** Zoomed-in image of the grain boundary shows a periodic line of 8-4-4 ring defects. **c** An atomistic model of the experimental structure shown in **b**. Energy minimization with DFT confirms that this boundary is locally stable. **d** The total DOS of defect-free, that is pristine, MoS₂ (black), the total DOS of MoS₂ with the grain boundary (red dashed) and the projected DOS of the atoms along the grain boundary (blue filled). The dashed grey line denotes the Fermi energy of pristine MoS₂, and the light green shaded area indicates the pristine bandgap. All states have been given a Gaussian broadening of 0.07 eV. **e** A 2D spatial plot of the local mid-gap DOS (integrated in the plane of the Mo over a 1.7 eV range about the Fermi energy of the pristine MoS₂). The colour scale of the density is 0–0.05 states per Bohr³ [72]. Reprinted by permission from Macmillan Publishers Ltd., copyright (2013)

to traditional grain boundaries where chemical bonds between the two single-layered grains are formed and the in-plane growth stops, at times, the growth could proceed with the nucleation of a second layer at the boundaries without forming any in-plane chemical bonds. Consequently, the interaction between these grains at the overlapped junctions could be mediated by weak vdW forces. The formation of conventional grain boundaries and the overlapped junctions were found to be competing processes, but a clear dependence on the degree of lattice orientation mismatch in the two grains was not observed.

Similar studies were done for tilt grain boundaries in a monolayer of WS₂ [74] with 12° and 22° misorientation angles. At the larger tilt angle, a higher dislocation

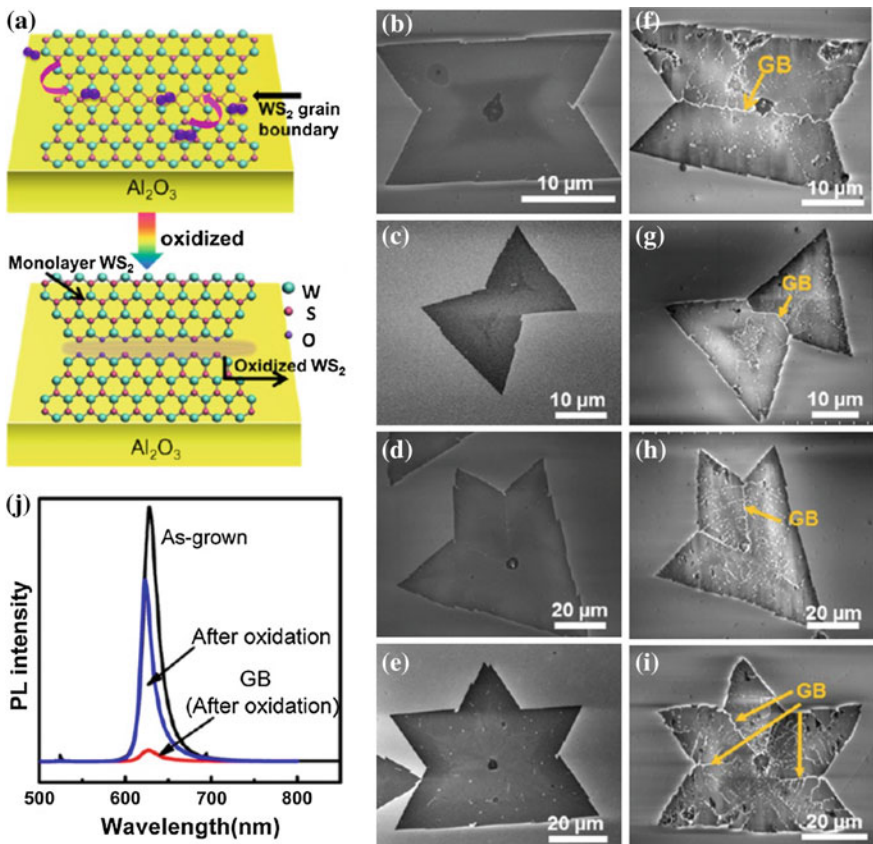


Fig. 5.24 Imaging the grain boundaries of WS_2 by mild oxidation under atmospheric conditions. **a** Schematic model of the surface oxidations. **b–e** SEM images of as-grown monolayer WS_2 . **f–i** SEM images of WS_2 grain structures after a mild oxidation process. **j** PL spectra of the samples with and without an oxidation process (far away and at the grain boundary) [78]. Copyright 2013 American Chemical Society. Published with permission

density was observed along the grain boundary that leads to higher local strain. In both cases, grain boundaries are predominantly comprised of 6|8 edge dislocations, which are derived from 5|7 defects by the insertion of a two-atom column of S between the W-W bonds. Interestingly, the 6|8 dislocations are nonmagnetic, in contrast to the magnetic 5|7 dislocations [75].

In monolayer MoSe_2 , 5|7 and 4|4 rings were reported [76], with two different configurations, namely, point-sharing (4|4P) at Se_2 sites and edge-sharing (4|4E) at Mo-Se bonds [77]. It was further shown that collective evolution of Se vacancies leads to the formation of inversion domains [77]. Line and point defects in MoSe_2 were also studied in bilayers [70].

An interesting observation was made in [78]. The authors noted that after mild oxidation under moisture-rich ambient conditions (as demonstrated with the schematic model in Fig. 5.24a), the grain boundaries could be clearly visualized by SEM,

showing bright line shape contrast (Fig. 5.24f–i). It was argued that for WS₂ on sapphire, the reconstructions at grain boundaries create new states near the Fermi level [65, 79], which may induce a higher reactivity for oxidation or impurity adsorption under the mild oxidation process. PL measurements were also utilized to characterize the mild surface oxidation, since doping or defects can lead to strong PL quenching or enhancement [80]. Indeed, the PL intensity was much reduced on the merging boundary after the oxidation process, as compared with that of the regions far away from the grain boundary and on the as-grown samples (Fig. 5.24j).

Another method of visualisation of grain boundaries in MoS₂, viz., thought molecular decoration, was proposed in [81]. It was shown that spin-coating of MoS₂ with octadecylphosphonic acid monolayers readily revealed grain boundaries at ambient conditions without the need of atomic resolution measurements under vacuum.

5.3.3 Grain Boundary Migration

Due to the unique geometry of 2D crystals, dislocations reside at the crystal surface and can easily interact with surface atoms. Highly mobile S atoms can interact with the dislocation cores and form different derivative dislocation structures with different migration mechanisms involving the rearrangement of the local W and S atoms around the defect [74]. It was found that such dynamics have a strikingly low-energy barrier leading to significant grain boundary reconstruction in TMDCs, despite their complex lattice structure [74]. Figure 5.25 shows an example of dislocation migration in a 12° grain boundary, where selected snapshots from the observed atomic-scale dynamics are shown.

Figure 5.25a, b shows glide of the marked dislocation to the bottom right, along its Burgers vector, while Fig. 5.25c, d reveals the same dislocation several seconds later, which moves to the bottom right again, through a glide along its Burgers vector marked by an arrow in Fig. 5.25c. By comparing individual frames of the movie, S atoms were observed to be very dynamic and mobile around the dislocation cores.

In order to gain a better understanding of the dislocation migration mechanism observed in WS₂ monolayer, DFT calculations were performed. The results are summarized in Fig. 5.25e–j, that depicts the mechanism for the migration of the 6|8-V_S (a 6|8 dislocation with one sulphur vacancy, V_S) and 6|8 dislocations (the orange atoms located at the dislocation core show the S atoms on the bottom layer, whereas the yellow atoms indicate S atoms on the top layer). The calculations suggested that dislocation migration starts when one of the top S atoms at site 2 (red dashed circle) moves to site 1. This movement is accompanied by the circled W atom simultaneously gliding and disconnecting from the S atom at site 2, generating a bond with the S atom at site 1. The concurrent movements of W and S atoms lead to a significant structural distortion in the saddle-point structure (Fig. 5.25f) that results in a migration barrier of about 1.4 eV. It was noted that this energy barrier is considerably lower than the diffusion energy barrier for a single S vacancy (V_S), highlighting the important role of the dislocations and their interaction with S vacancies in mediating

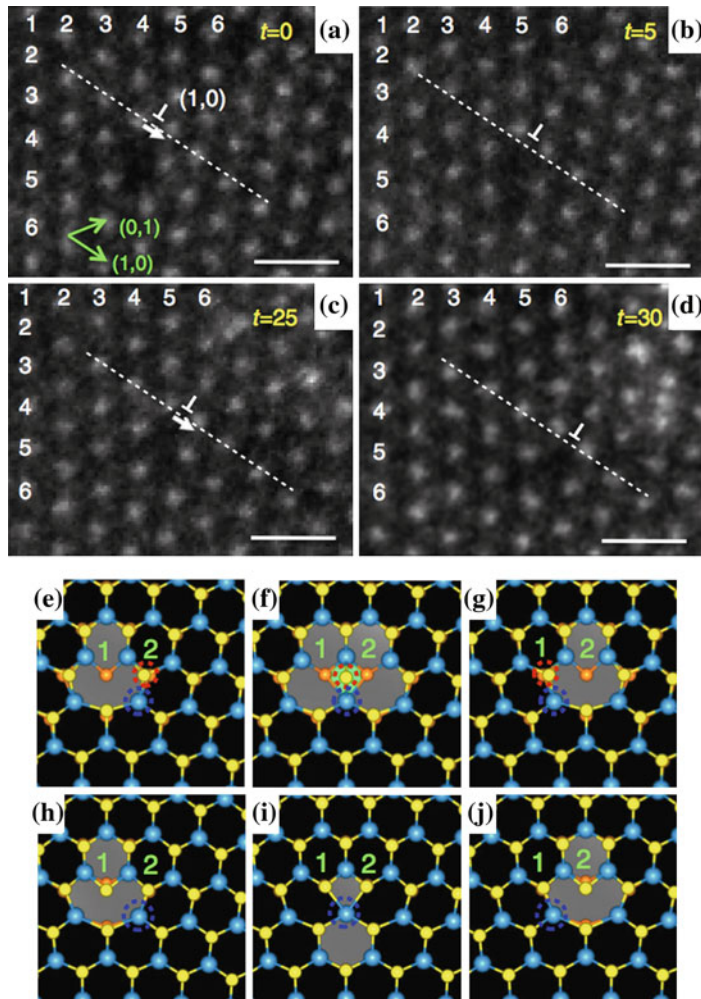


Fig. 5.25 Dislocation migration in a 12° grain boundary. Dislocation glide along its Burgers vector $(1, 0)$ on its glide plane (shown by *dashed lines*) from **a** to **b**. Several seconds later the same dislocation glides again along $(1, 0)$ from **c** to **d**. **e–g** Structural models for the migration of a $6|8$ dislocation with one S vacancy ($6|8-V_S$). **h–j** $6|8$ with initial, saddle-point and final structures in the *left, middle* and *right panels*, respectively [74]. Reprinted by permission from Macmillan Publishers Ltd., copyright (2014)

both the dislocation and S migration in TMDCs through the coupled displacement of W atoms.

It was further found that without the S vacancy in the dislocation core (Fig. 5.25h–j), the dislocation migration barrier further drops to 0.6 eV. Under this condition, the lattice undergoes a much smaller structural distortion, as the S sub-lattice recovers and only a single W atom is involved during the dislocation glide through direct bond breaking and reconnection.

5.3.3.1 Optical and Electronic Properties of Grain Boundaries

Optical properties of grain boundaries in MoS₂ were measured using photoluminescence mapping [72], where a focused excitation laser was stepped over the sample and photoluminescence spectra were recorded at each point. Figure 5.26a, e shows optical images of a mirror twin island and a tilt boundary island. Figure 5.26b–d, f–h shows corresponding maps of integrated photoluminescence intensity, peak position and peak width. At the grain boundaries, the islands showed strong photoluminescence modifications. Several possible mechanisms for these modifications were considered, ranging from photoluminescence quenching arising from defects to doping and strain associated with the presence of the boundaries [72].

Transport across grain boundaries was also investigated [72] using field-effect transistors from islands containing a single grain boundary. The FET channels followed three different configurations: within a grain (pristine), across the grain

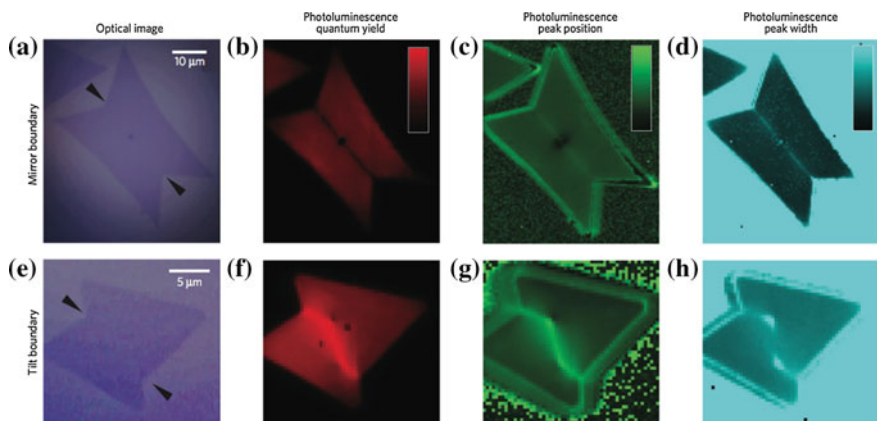


Fig. 5.26 Optical properties of mirror and tilt boundaries. **a–d** Optical measurements of an island containing a mirror twin boundary. **e–h** Corresponding measurements for an island containing a tilt boundary. **a, e** are optical images, **b–d** and **f–h** are colour plots of photoluminescence. In **b, f** red is the relative quantum yield, with colour scale 0–1100 a.u. One can see 50% quenching at the mirror twin boundary and a 100% enhancement at the tilt boundary. In **c, g** green is the peak position, with colour scale 1.82–1.87 eV. There is an upshift of 8 meV at the mirror twin boundary, and a much stronger 26 meV upshift in the tilt boundary. In **d, h** cyan is the peak width with colour scale of 53–65 meV. The peak broadens from 55 to 62 meV at the boundary in both samples [72]. Reprinted by permission from Macmillan Publishers Ltd., copyright (2013)

boundary (perpendicular) and along the grain boundary (parallel). It was found that in the mirror twin devices the perpendicular device showed nearly identical performance to the pristine devices, indicating that the mirror twin boundary had little effect on channel conductivity. At the same time, the electrical characteristics of the parallel devices differed measurably from the pristine devices.

5.4 Doping 2D TMDCs

There exist two essentially different strategies to dope TMDC monolayers, namely, via S/Mo substitution or as adsorbates. In few-layer structures there is an additional possibility for the dopants to be located between the layers.

In [82] substitutional doping and adsorption were studied for MoS₂ using DFT simulations. Among possible substitutional dopants at the Mo site, Nb was identified as a suitable *p*-type dopant, while Re was the donor with the lowest activation energy. When dopants were simply adsorbed on a monolayer it was found that alkali metals shift the Fermi energy into the conduction band, making the system *n*-type. Finally, the adsorption of charged molecules was considered, mimicking an ionic liquid environment, and it was found that molecules adsorption can lead to both *n*- and *p*-type conductivity, depending on the charge polarity of the adsorbed species. Adsorption of various elements and their effect on properties of MoS₂ monolayers was also studied in [83, 84].

Through STEM experiments and DFT studies it was found that the behavior of the dopants can be quite different, thus while Re dopants in concentrations up to 0.6% were dispersed on the MoS₂ monolayer surface, Au atoms at similar concentrations tended to form clusters [85].

DFT simulations were also used to study adsorption of various gas molecules (H₂, O₂, H₂O, NH₃, NO, NO₂, and CO) on monolayer MoS₂ [86]. It was shown that all molecules were weakly adsorbed on the monolayer surface and acted as charge acceptors. NH₃ was found to be a charge donor. It was additionally found that charge transfer between the adsorbed molecule and MoS₂ could be significantly modulated by a perpendicular electric field.

Z-contrast annular dark-field (ADF) imaging by means of STEM was successfully used to identify the atomic positions of individual Re and Au dopants in the host MoS₂ lattice [85]. In combination for DFT simulations, it was possible to correlate the migration behaviors of dopant atoms with their energetics.

Chemical functionalisation of monolayer TMDC can also be achieved by covalent attachment of functional groups [87].

In [88], degenerate *n*-doping of few-layer TMDCs by potassium was reported using FET-structures. It is not clear to what extent the K-doping affected the TMDC structure, because it was also reported [89] that K-doping resulted in the formation of quasi-free MoS₂ layers with K ions acting as intercalants.

Alloying, which is also a kind of doping, was shown to suppress deep levels in TMDCs [90], while maintaining their basic electronic properties. Specifically, it was shown that for MoSe₂ and WSe₂, where anion vacancies are the most abundant

defects that can induce deep levels, the deep levels can be effectively suppressed in $\text{Mo}_{1-x}\text{W}_x\text{Se}_2$ alloys at low W concentrations, which was attributed to the fact that band edge energies can be substantially tuned by the global alloy concentration, whereas the defect levels are controlled locally by the preferred locations of Se vacancies around W atoms.

The effect of doping on properties of TMDCs is discussed in some of the following chapters.

5.5 Order-Disorder Phase Transitions in TMDC Alloys

An interesting question is whether TMDC alloys have ordered or random distribution of metal and chalcogen atoms. This issue was addressed in [91] for $\text{Mo}_{1-x}\text{W}_x\text{X}_2$ (where X = S, Se, and Te) alloys. The authors used a combination of density functional theory, an empirical model, and Monte Carlo simulations to study the evolution of the atomic distribution as a function of the W concentration and temperature. Ordered phases were predicted for $x = 1/3$ and $2/3$ by the empirical model but only existed at low temperature according to the Monte Carlo simulations. At higher temperature the small energetic preference is not sufficient to maximize the number of Mo-X-W interactions. The obtained negative formation energies suggested a good miscibility for all three alloys [91].

5.6 Properties of Two-Dimensional TMDCs

TMDCs have been the subject of study for over half a century. Some of the first examples of what we refer to as 2D crystals today were routinely produced and studied back in the 1960s [92]. Now the subject is revisited with a fresh perspective and inspiration from graphene.

5.6.1 Mechanical Properties

Elastic properties, stretching and breaking of ultra thin freely suspended MoS_2 were investigated in [39, 93]. In both studies an AFM tip was placed on top of a film situated on top of a small (ca. $1 \mu\text{m}$) hole in a pre-patterned SiO_2 substrate and the MoS_2 membrane deflection under the applied force was measured. The same approach was used to determine the mechanical parameters of graphene [94]. The experiment scheme and loading curves for 5–20 layers thick sample are shown in Fig. 5.27. From a least-squares fit of the experimental curves, the pretension σ_0^{2D} and the elastic modulus E^{2D} of the MoS_2 membrane were extracted.

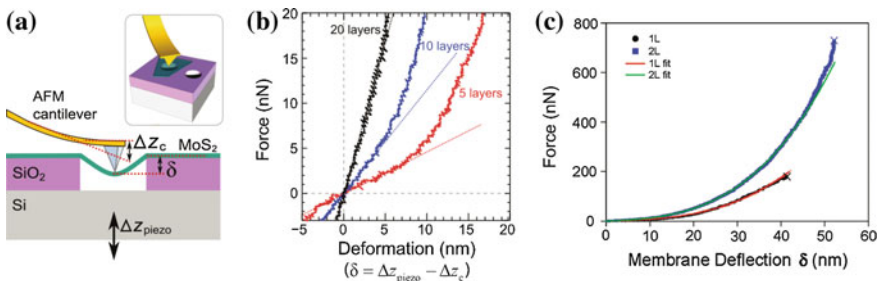


Fig. 5.27 **a** Schematic diagram of the nanoscopic bending test experiment carried out on a freely suspended MoS_2 nanosheet. **b** Force versus deformation traces measured at the center of the suspended part of MoS_2 nanosheets with 5, 10, and 20 layers in thickness [93]. Reproduced with permission from Springer; **c** Loading curves for single and bilayer MoS_2 [39]. Copyright 2011 American Chemical Society. Published with permission

The numerical values somewhat vary between the two studies [39, 93]. Thus, for the 5–20 layer thick samples, the pre-tension was determined to be $0.05 \pm 0.02 \text{ Nm}^{-1}$ and the Young's modulus, E_{Young} , $0.35 \pm 0.02 \text{ TPa}$ [93]. At the same time, for monolayer thin membranes [39], the average value of the elastic modulus E^{2D} of $180 \pm 60 \text{ Nm}^{-1}$ and pre-stress σ_0^{2D} in the $0.02\text{--}0.1 \text{ Nm}^{-1}$ range were obtained. Assuming an effective monolayer thickness of 0.65 nm , the Young's modulus $E_{\text{Young}} = 270 \pm 100 \text{ GPa}$ was obtained, close to the Young's modulus of MoS_2 nanotubes (230 GPa , [95]), or steel (210 GPa) and only ca. 4 time smaller than that of graphene (1 TPa [94]). The Young's modulus of bilayer MoS_2 was found to be $200 \pm 60 \text{ GPa}$, a value a little smaller than that for a monolayer, which was attributed as ‘possibly due to defects or interlayer sliding’ [39].

As regards the breaking of MoS_2 , the averages of maximum stress values were, respectively, $22 \pm 4 \text{ GPa}$ and $21 \pm 6 \text{ GPa}$ for a monolayer and a bilayer. On the average, these values correspond to 8 and 10% of the Young's modulus for monolayer and bilayer MoS_2 . It was noted that these values are at the theoretical upper limit of a material's breaking strength and thus represent the intrinsic strength of interatomic bonds in MoS_2 . It was further noted that the strength of monolayer MoS_2 is exceeded only by carbon nanotubes and graphene [39].

Stretching and breaking of monolayer MoS_2 was also studied using atomistic simulations [96], with the obtained values of $E_{\text{Young}} = 262 \text{ GPa}$ and a breaking stress of 21 GPa being in good agreement with the experimental results. The mechanical properties of monolayer MoS_2 were also studied in [97].

In [98] the mechanical response of various TMDCs to large elastic deformation was studied using first-principles density functional calculations. In Fig. 5.28a–c, the calculated stress-strain relations are shown under arm-chair (x), zig-zag (y), and biaxial tensions, respectively. For small strain, the stress for all MX_2 exhibits linear dependence on the applied strain for all loading directions.

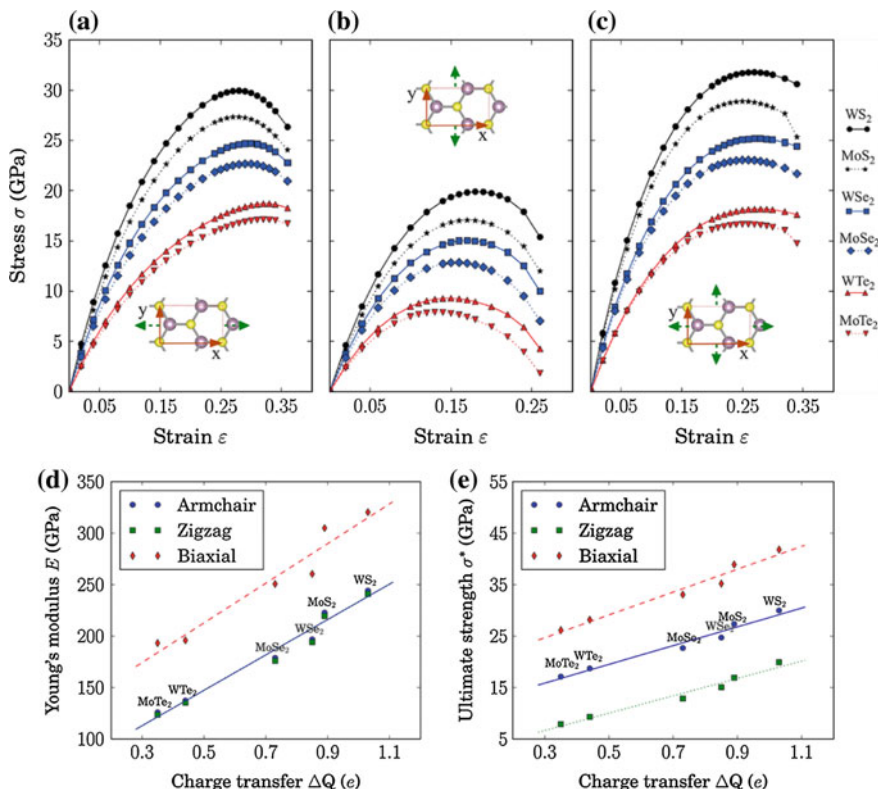


Fig. 5.28 Tensile stress, σ , as a function of uniaxial strain, ϵ , along the **a** arm-chair and **b** zig-zag directions and **c** of biaxial strain, respectively, for monolayer MX₂ ($M = Mo, W; X = S, Se, Te$) TMDCs. *Solid* and *dashed lines* are used for WX₂ and MoX₂, respectively. Variation of **d** the Young's modulus and **e** the ultimate strength of monolayer MX₂ ($M = Mo, W; X = S, Se, Te$) TMDCs with the charge transfer, ΔQ , from transition metal M to chalcogens, X. The Young's modulus and ultimate strength for biaxial strain are shifted rigidly upward for drawing purposes by 50 and 10 GPa, respectively [98]. Copyright 2013 American Chemical Society. Published with permission

As MX₂ monolayers are strained further ($\epsilon > 4\%$), the stress-strain response deviates from the linear behavior. For large strains, the hexagonal symmetry is broken, with the stress developed upon loading in the arm-chair direction (Fig. 5.28a) much larger than in the zig-zag direction (Fig. 5.28b). Upon straining further, the stress continues to increase until it reaches a maximum, termed the ultimate strength σ^* . It was found that in general, the chalcogens of W (WX₂) have larger moduli and tensile strength than those of Mo (MoX₂), while for the same transition metal, sulphides (MS₂) are the strongest and tellurides (MTe₂) are the weakest. The anisotropy in stress response was found to be inversely correlated with the strength of the monolayer sheets: the MX₂ with lower Young's modulus and ultimate strength (for example, tellurides) are characterized by larger anisotropy factors.

A direct correlation between the amount of charge transfer from the transition metal to the chalcogens and material's elastic properties were found. The results are shown in Fig. 5.28d, e, that depict the Young's modulus, E , and ultimate strength, σ^* , as a function of the (Bader) charge transfer, ΔQ and demonstrate that the mechanical properties of TMDCs exhibit a linearly increasing relation with the charge transfer from the transition metal atom to the chalcogen atoms [98].

Local deformations in free-standing MoS₂ sheets were theoretically studied in [99] and it was concluded that the electronic structure was robust with respect to local deformations.

Theoretical studies of the mechanical behavior of TiS₂ and MoS₂ arm-chair and zig-zag nanotubes were performed in [100]. It was found that the Poisson ratio and Young's modulus depend on the tube diameter for smaller tubes (up to 20 Å in radius) and subsequently approach that of infinite monolayers. The Young's moduli for arm-chair and zig-zag nanotubes were different for the 2H phases of both MoS₂ and TiS₂ (the former being larger in case of TiS₂ and smaller for MoS₂) and essentially the same for 1T-TiS₂. The influence of defects on the strain of rupture was also studied and it was found that the presence of various kinds of defects decreased the rupture stress from ca. 29 GPa for defect free zig-zag MoS₂ nanotubes to ca. 19 GPa in nanotubes with defects.

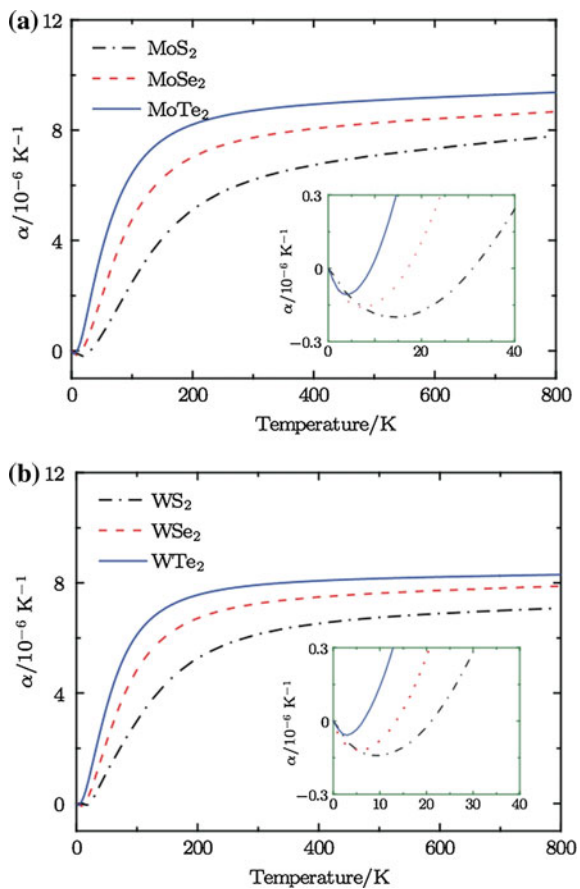
A combined molecular dynamics (MD) density functional-tight binding simulation of the stretching process was performed for single-wall MoS₂ nanotubes in [95]. According to these simulations, the failure of the nanotube is abrupt starting at a single atomic defect and propagating very quickly across its entire circumference. The calculated stress and strain were 40 GPa and 17% for the zig-zag (22, 0) tube, and 34 GPa and 19% for the armchair (14, 14) tube. The calculated strength results are equivalent to 17.4% and 14.7% (for the zig-zag and arm-chair nanotubes, respectively) of Young's modulus of MoS₂ nanotubes (which was calculated to be 230 GPa). Nonlinear elastic behavior of 2D MoS₂ was theoretically investigated in [40].

Besides the Young's modulus, the bending modulus is another fundamental mechanical property. The obtained elastic bending modulus of 9.61 eV in single-layer MoS₂ was significantly higher than the bending modulus of graphene (1.4 eV) [101].

5.6.2 Thermal Expansion

Thermal expansion of MoX₂ and WX₂ monolayers was theoretically studied in [102, 103]. The results generally agree with each other and are shown in Fig. 5.29. Experimentally, values of 8.2×10^{-5} 1/K and 10.5×10^{-5} 1/K were obtained for monolayers of MoS₂ and MoSe₂, respectively [104].

Fig. 5.29 Calculated thermal expansions in monolayers of **a** MoX_2 , and **b** WX_2 [103]. Reprinted with permission

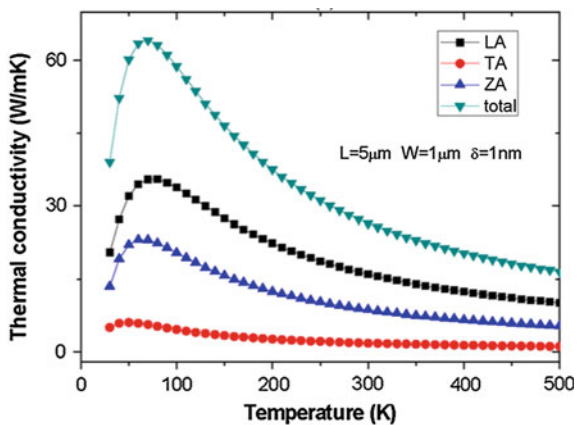


5.6.3 Thermal Conductivity

The thermal conductivity of monolayer MoS_2 was theoretically studied using the phonon Boltzmann transport equation combined with relaxation time approximation for transverse acoustic (*TA*), longitudinal acoustic (*LA*) and out-of-plane acoustic (*ZA*) phonons [105]. The result is shown in Fig. 5.30.

At the same time, using first-principles simulations, the thermal conductivity was determined for samples of different sizes and it was concluded that for a typical sample size of $1 \mu\text{m}$ the thermal conductivity κ should be larger than 83 W/mK at room temperature [106], demonstrating a disagreement with the previous results. On the other hand, in a study of the anharmonic behavior of phonons and the intrinsic thermal conductivity associated with umklapp scattering in monolayer MoS_2 , the room temperature thermal conductivity of monolayer MoS_2 was found to be around 23.2 W/mK [107]. This value is contrasted by the result of [108], where DFT

Fig. 5.30 The thermal conductivity of a monolayer MoS₂ flake as a function of temperature [105]. Reprinted with permission. Copyright 2014 by the American Institute of Physics



simulations yielded the thermal conductivity of a monolayer of MoS₂ to be only 1.35 W/mK.

Thermal conductivity was shown to be anisotropic. In particular, the thermal conductivity at room temperature for the armchair MoS₂ nanoribbon was found to be about 673.6 W/mK, while a value of 841.1 W/mK was obtained for the zig-zag nanoribbon [109].

Experimentally determined values (from temperature dependent Raman scattering) are in the range of 34–52 W/mK for monolayers of both MoS₂ and WS₂ [110–112]. Thermal conductivity decreased with increasing temperature from 62.2 W/mK at 300 K to 7.45 W/mK at 450 K [113].

5.6.4 Thermoelectric Properties

The thermoelectric performance of monolayer transition-metal dichalcogenides, MoS₂, MoSe₂, WS₂, and WSe₂ was studied in [114, 115] using a two-dimensional ballistic transport approach based on the full electronic band structures and phonon energy dispersion relations obtained from first-principles calculations with different crystal orientations and temperatures for *n*-type and *p*-type materials. It was found that figures of merit of these materials are generally low.

The thermoelectric properties of bulk and monolayer MoSe₂ and WSe₂ were also studied by first-principles calculations and semiclassical Boltzmann transport theory [116]. WSe₂ was found to be superior to MoSe₂ for thermoelectric applications.

In [118] analytical results for thermoelectric transport in monolayer MoS₂ and related group-VI dichalcogenides in the presence of off-resonant light were derived. It was shown that an increased intensity of light reduces the direct band gap and results in a strong spin splitting in the conduction band and, therefore, in a dramatic enhancement of thermoelectric transport.

5.6.5 Optical Properties

Dielectric function of monolayer TMDCs was determined by reflectance measurements of the samples at room temperature. The absolute reflectance spectra for the TMDC monolayers on fused silica are presented in Figs. 5.31a–d. For all four TMDC monolayers, the two lowest energy peaks in the reflectance spectra correspond to the excitonic features associated with interband transitions at the $K(K')$ point in the Brillouin zone [117]. The two features, denoted by *A* and *B*, correspond to the splitting of the valence band by spin-orbit coupling. At higher photon energies spectrally broad response from higher-lying interband transitions were observed.

Dielectric functions were obtained from the Kramers–Kronig constrained analysis. In Figs. 5.31e–l, resultant real and imaginary parts are shown for MoSe₂, WSe₂, MoS₂, and WS₂ over the spectral range of 1.5–3.0 eV.

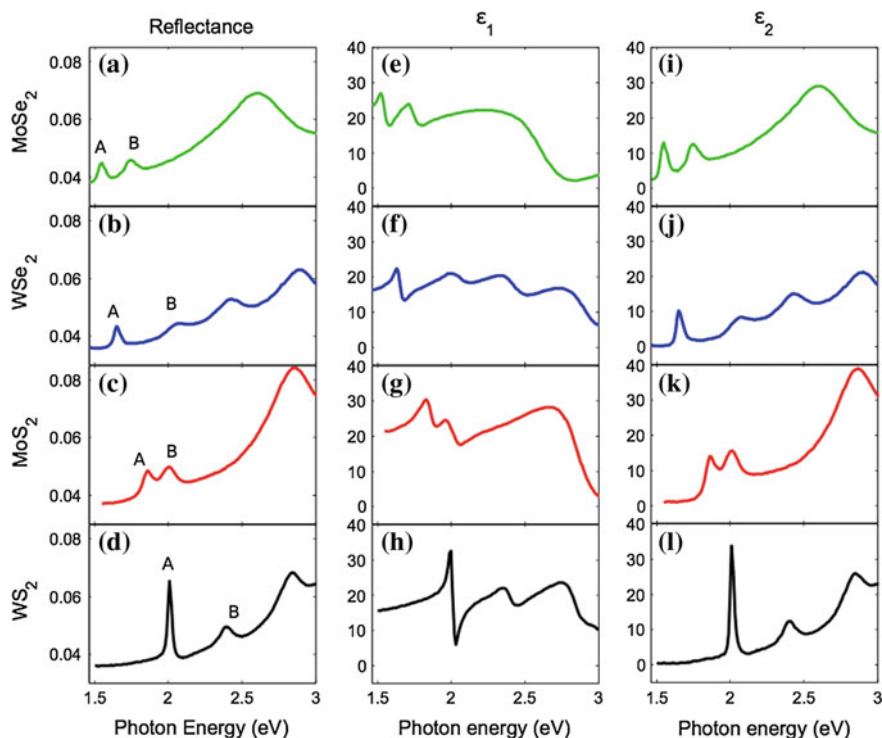


Fig. 5.31 Optical response of monolayers of MoSe₂, WSe₂, MoS₂, and WS₂ exfoliated on fused silica: **a–d** Measured reflectance spectra. **e–h** Real part of the dielectric function, ϵ_1 . **i–l** Imaginary part of the dielectric function, ϵ_2 . The peaks labeled *A* and *B* in **a–d** correspond to excitons from the two spin-orbit split transitions at the K point of the Brillouin zone [119]. Copyright 2014 by the American Physical Society. Reprinted with permission

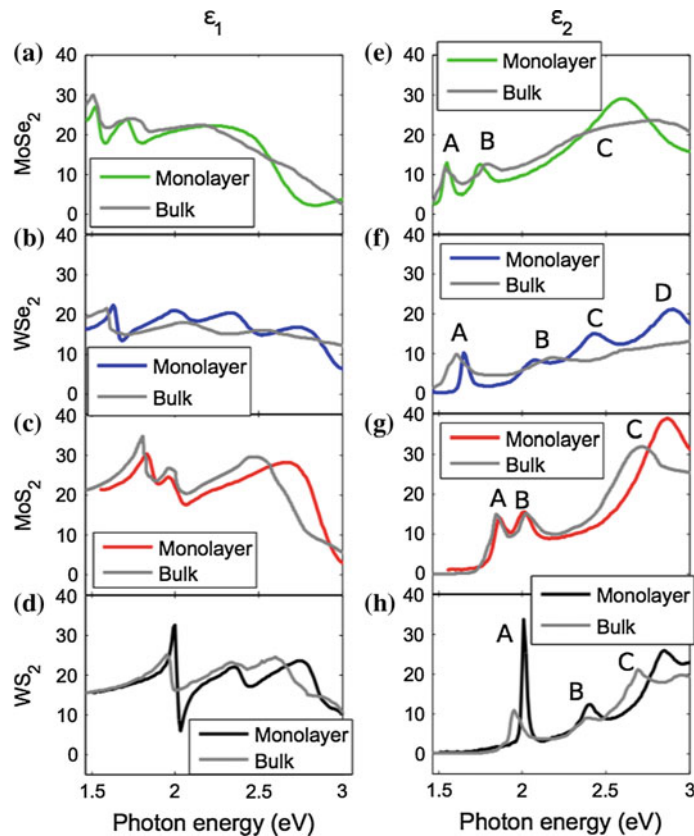


Fig. 5.32 Comparison of the dielectric functions of monolayer TMDC crystals (colored lines) with those of the corresponding bulk materials (gray) [119]. Copyright 2014 by the American Physical Society. Reprinted with permission

The obtained dielectric functions for the monolayer TMDC crystals in comparison with the dielectric functions for the corresponding bulk materials are shown in Fig. 5.32. While the two data sets show an overall similarity, differences in the spectral responses are readily seen, such as broadening of the resonance features in the bulk materials compared to the monolayers, which was attributed to the additional optical transitions and carrier relaxation channels arising from interlayer coupling. Also, the resonance energies in the monolayer dielectric function are modestly shifted from the corresponding bulk material.

Optical properties of monolayer transition metal dichalcogenides were investigated in [120] using spectroscopic ellipsometry. Figure 5.33a–d shows the refractive index, n , and extinction coefficient, k , spectra of monolayer MoS₂, MoSe₂, WS₂, and WSe₂ thin films obtained from these measurements. In all cases, the refractive indices increase with increasing wavelength in the spectral range from 193–550 nm,

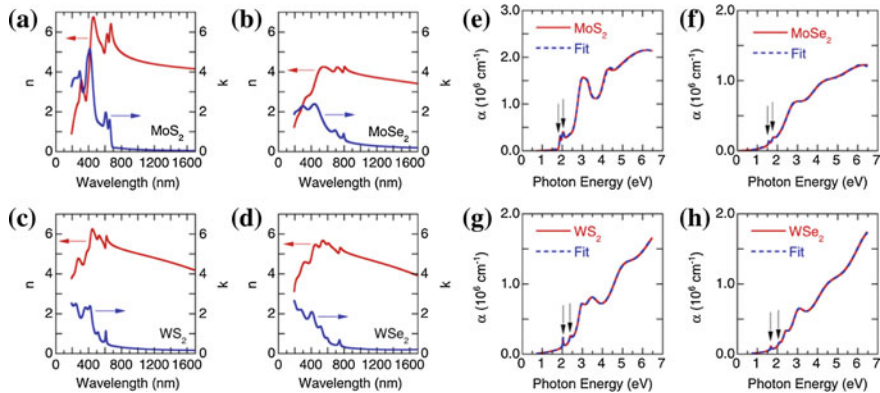


Fig. 5.33 Refractive index n and extinction coefficient k of monolayer **a** MoS₂, **b** MoSe₂, **c** WS₂, and **d** WSe₂ thin films and optical absorption coefficient α of monolayer **e** MoS₂, **f** MoSe₂, **g** WS₂, and **h** WSe₂ thin films [120]. Reprinted with permission. Copyright 2014 by the American Institute of Physics

and then approach the maxima, and decrease with wavelength until 1700 nm. It was noted that (i) the dispersive response in the refractive index exhibits several anomalous dispersion features below 800 nm and approaches a constant value of 3.5–4.0 in the near-infrared frequency range and (ii) monolayer MoS₂ has the extraordinary large value of refractive index about 6.50 at 450 nm. In [121] optical constants, n and k , for ultrathin NbS₂ and MoS₂ crystals have been determined for the visible range.

Non-linear optical properties of TMDC nanosheets were studied in [122].

5.6.6 Electrical Transport

In 2D TMDC layers, transport and scattering of the carriers are confined to the plane of the material. Carrier in-plane mobility is related to the momentum scattering time τ_D by $\mu = e\tau_D/m^*$, where m^* is the in-plane effective mass. The mobility of carriers is affected by (i) acoustic and optical phonon scattering; (ii) Coulomb scattering at charged impurities; (iii) surface interface phonon scattering; and (iv) roughness scattering. The degree to which these scattering mechanisms affect the carrier mobility is influenced by the layer thickness, carrier density, temperature, effective carrier mass, electronic band structure and phonon band structure.

At low temperatures ($T < 100 \text{ K}$), the acoustic component dominates, but at higher temperatures the optical component dominates. Coulomb scattering in 2D TMDCs is caused by random charged impurities located within the 2D TMDC layer or on its surfaces, and is the dominant scattering effect at low temperatures. The effect of surface phonon scattering and roughness scattering can be very important in extremely thin 2D materials. The phonon-limited room-temperature mobility was

calculated [123] for MoS₂ to be ca. 410 cm²/V · s, and similar values are expected for other single-layer TMDCs.

Using first-principle calculations combined with Boltzmann transport equation, mobility of electrons and holes in different structural modifications of MoS₂ was calculated [31]. In 2H-MoS₂, the electron (hole) mobility was found to be 1.2 (3.8) $\times 10^2$ cm²/V · s and was isotropic. On the other hand, in ZT-MoS₂ the electron and hole mobility was 1–2 orders of magnitude larger and anisotropic (the electron (hole) mobility of ZT-MoS₂ was 4.1 (2.1) $\times 10^3$ and 6.4 (5.7) $\times 10^4$ cm²/V · s along the *x* and *y* directions, respectively). The increase in the mobility was attributed to the reduction of electron (hole) effective mass from 0.49 (0.60) m_e to 0.12 (0.05) m_e when 2H-MoS₂ was transformed to ZT-MoS₂. It was noted that the mobility of ZT-MoS₂ is higher than that of silicon and comparable to that of graphene nanoribbons.

Experimentally the room temperature values of mobility were studied using device structures [124–126] with the maximum value determined as up to 700 cm²/V · s for multilayer MoS₂ at room temperature [125]. In [125] MoS₂ field effect transistors on both SiO₂ and polymethyl methacrylate (PMMA) dielectrics were fabricated and charge carrier mobility was measured in a four-probe configuration. For multilayer MoS₂ on SiO₂, the mobility was 30–60 cm²/V · s, relatively independent of thickness (15–90 nm); most devices exhibited unipolar *n*-type behavior. In contrast, multilayer MoS₂ on PMMA showed mobility increasing with thickness, up to 470 cm²/V · s (electrons) and 480 cm²/V · s (holes) at thickness ca. 50 nm [127].

It is interesting to note that the obtained values depend on the measurement conditions. Thus, for a back-gated two-terminal configuration, mobilities in MoS₂ of ca. 90 cm²/V · s were observed, which is considerably smaller than 306 cm²/V · s extracted from the same device when using a four-terminal configuration [126], indicating the important limiting role of non-Ohmic contacts in some measurements. In [128], using contact-less mobility determination based on THz spectroscopy, room temperature intrinsic mobility was determined to be ca. 250 cm²/V · s at room temperature increasing up to 4200 cm²/V · s at 30 K.

5.6.7 Stability

The oxidization characteristics of bulk MoS₂ and MoSe₂ were studied, and they were found to be oxidized in the 500–700 K range [129, 130]. On the other hand, heating single-layer MoSe₂ in air to 500 K does not alter its PL peak intensity and position upon cooling back to room temperature, implying that the single layers are thermally stable up to these temperatures. This might be due to self-limited oxidization and merits further studies [131]. At the same time, WTe₂ was readily oxidised via environmental exposure [132].

In studies of WSe₂ nanosheets adhered on SiO₂/Si substrates [133], optical and Raman data indicated that a major component of the oxidation starts from the nanosheet edges and propagates laterally toward the center.

The surface of monolayer TMDCs was studied by first-principles simulations [134, 135] and it was found that perfect single-layer sheets stay intact when exposed to O₂ due to the weak physical adsorption of O₂. However, O₂ can be chemically adsorbed onto the monolayer of TMDCs (including MoS₂, MoSe₂, MoTe₂, WS₂, WSe₂, and WTe₂) with single vacancies of chalcogen, which are the most common defects in realistic TMDC. It was also found [135] that oxidation significantly influenced the electronic properties of a defective MoS₂ monolayer, while other defective TMDC monolayers (especially MoTe₂ and WTe₂) suffered less from oxidation. Experimentally, the heating of the molybdenite surface in air at 400 °C induced oxidation. Oxidation in the first hour of heating was initially slow and then increased significantly [16]. It was also found that oxidation predominantly proceeds at grain boundaries [78]. While the effect was only reported for WS₂, it is likely to be general.

The effect of intense femtosecond laser excitation on the structure of bulk and monolayer MoS₂, under conditions ranging from lattice heating to material damage was systematically investigated in [136]. Single layers MoS₂ exposed to intense photoexcitation conditions were also studied in [137] with excitation conditions corresponding to the order of one electron-hole pair per unit cell and a transient temperature increase of a few thousand degrees. No photoinduced change in lattice symmetry were observed despite the extreme excitation conditions. In a subsequent work [138], dynamic structural response and deformations in monolayer MoS₂ were studied using femtosecond electron diffraction. It was found that photoexcitation of monolayer MoS₂ films gives rise to large-amplitude in-plane atomic displacements and out-of-plane wrinkling with percent-level peak strains. Intense femtosecond excitation of bulk and monolayer MoS₂ using 800 nm light was also studied in [136] and it was found the single-pulse optical damage threshold was 50 mJ/cm² for the monolayer and 15 mJ/cm² for the bulk.

The structural behavior of bulk WS₂ under high pressure was investigated using synchrotron X-ray diffraction and a diamond anvil cell up to 52 GPa along with high temperature X-ray diffraction and high pressure Raman spectroscopy analysis [139]. The high pressure results obtained from X-ray diffraction and Raman analysis did not show any pressure induced structural phase transformations up to 52 GPa. The high temperature results show that the WS₂ crystal structure is stable upon heating up to 600 °C. Furthermore, the powder X-ray diffraction obtained on shock subjected WS₂ to high pressures up to 10 GPa also did not reveal any structural changes.

The same group also performed in-situ high pressure powder X-ray diffraction experiments using synchrotron radiation on MoS₂ [140] and in addition, diffraction experiments were performed as a function of temperature in the range of 25–500 °C, and samples were shocked to study the crystal structure stability and it was concluded that the 2H_c hexagonal phase of MoS₂ is very stable up to 500 °C and ca. 20 GPa. Structural data on shocked MoS₂ showed no significant changes, which means that MoS₂ is a good shock absorber. The effect of high temperature shock waves on few-layer MoS₂, WS₂, and MoSe₂ was studied in [141].

The stability of few-layer WSe₂ was studied in [142]. It was found that exposure to ozone (O₃) below 100 °C leads to the lateral growth of tungsten oxide selectively along selenium zig-zag edge orientations on WSe₂. With further O₃ exposure, the

oxide regions coalesce and terminate leaving a uniform thickness oxide film on top of unoxidized WSe₂. At higher temperatures (up to 200 °C), oxidation evolves in a layer-by-layer regime up to tri-layers. The oxide films formed on WSe₂ were nearly atomically flat.

5.7 Structures with Lower Dimensionality

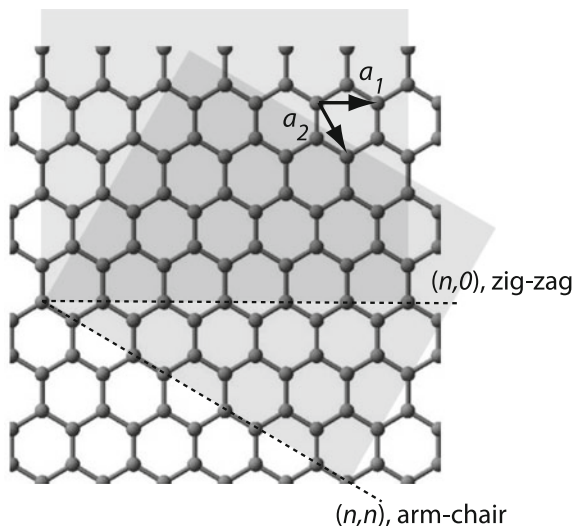
5.7.1 TMDC Nanotubes

The discovery of carbon nanotubes [143] opened a new page in the physics of low dimensional materials. Single-walled carbon nanotubes can be viewed as a rolling up a graphene sheet into a seamless cylinder and have a diameter close to 1 nm. The way the graphene sheet is wrapped is usually represented by a pair of indices (n, m) , where the integers n and m denote the number of unit vectors a_1 and a_2 along two directions in the honeycomb crystal lattice of graphene (Fig. 5.34). If $m = 0$, the nanotubes are called zigzag nanotubes, and if $n = m$, the nanotubes are called armchair nanotubes. Nanotubes with other combinations of n and m are called chiral.

The electronic properties of the single-wall carbon nanotubes are strongly dependent on their chirality, that is, how the graphene sheet is rolled up and this dependence is non-monotonic. In particular, their band gap can vary from zero to about 2 eV and their electrical conductivity can show metallic or semiconducting behavior.

Multi-walled nanotubes consist of multiple rolled layers (concentric tubes) of graphene. There are two models, viz., the Russian doll model and the Parchment

Fig. 5.34 The (n, m) nanotube naming scheme can be thought of as a vector in an infinite graphene sheet that describes how to “roll up” the graphene sheet to make the nanotube. a_1 and a_2 are the unit vectors of graphene in real space



model, that can be used to describe the structures of multi-walled nanotubes. In the former, sheets of graphite are arranged in concentric cylinders, while in the latter, a single sheet of graphite is rolled in around itself, resembling a scroll of parchment.

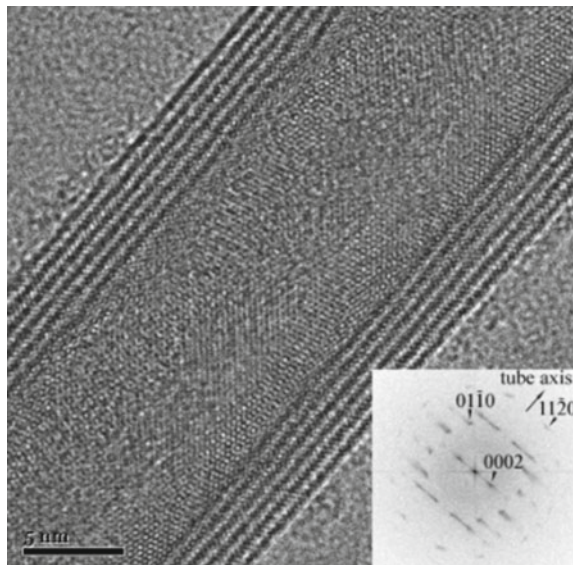
Since the discovery of carbon nanotubes, considerable efforts were devoted to synthesizing inorganic nanotubes based on other 2D materials. Thus boron nitride nanotubes, synthesized shortly after the discovery of carbon nanotubes, can be viewed as rolled up hexagonal boron nitride layers. Different from carbon nanotubes, which can be metallic or semiconducting depending on the rolling direction and radius, BN nanotubes are insulating with a band gap of ca. 5.5 eV, essentially independent of the tube chirality and morphology.

5.7.1.1 TMDC Nanotube Synthesis

The interest in making nanotubes from single and few-layer TMDCs existed well before the exotic properties of 2D TMDCs were discovered. The first report of TMDC nanotubes, which were WS₂ nanotubes, dates back to 1992 [144], followed by the finding of MoS₂ nanotubes [145]. Subsequently, WS₂ [146–148], MoS₂ [147, 149], WSe₂, MoSe₂ [150, 151] and MoTe₂ [151, 152] nanotubes were grown by different groups. In most cases, multi-walled nanotubes were produced (e.g. Figure 5.35) with diameters typically ~20 nm, although single-wall nanotubes were also reported [149].

Methods of preparation of TMDC nanotubes vary. Thus the MoS₂ nanotubes can be prepared using the gas-phase reaction between MoO₃ and H₂S in the presence of

Fig. 5.35 HR-TEM micrograph of a WS₂ nanotube consisting of six layers. Fourier transform of the nanotube is shown in the insert [148]. Reproduced by permission of The Royal Society of Chemistry



argon. The procedure involves heating solid MoO_3 in a stream of forming gas (95% $\text{N}_2 + 5\%$ H_2) to reduce the oxide to some extent, followed by the reaction of the oxide with a stream of H_2S mixed with the forming gas [145]. They could also be prepared by decomposition of MoS_3 at high temperatures in a hydrogen atmosphere and also by hydrogen treatment of ammonium thiomolybdate which is the precursor of MoS_3 [147]. Similar reactions were carried out with ammonium thiotungstate to produce WS_2 nanotubes [147]. Hydrogen reduction of ammonium selenometalates was shown to a useful route to fabricate MoSe_2 and WSe_2 nanotubes. MoTe_2 nanotubes were produced by irradiation with high doses of electrons [151, 152]. A two-step approach to the synthesis of MoTe_2 nanotubes in bulk was developed in [153], with the first step, the sonochemical process, used to synthesize nanoparticles of inorganic materials for which the bulk crystals have layered structures and the second step, heating at 650°C in a nitrogen atmosphere, to transform the nanoparticles to nanosheets, which then automatically rolled up into nanotubular structures.

5.7.1.2 TMDC Nanotubes Properties

Most studies of TMDC nanotube properties are based on first-principles simulations. Strain-tunable electronic and transport properties of MoS_2 nanotubes were studied in [154] and tailoring of electronic and magnetic properties was considered in [155]. Thermoelectric properties of WSe_2 , MoSe_2 , WS_2 , and MoS_2 were investigated in [156]. In [157], TMDC nanotubes were considered for Li and Mg ion battery applications. Single-walled MoTe_2 nanotubes were studied in [158]. Electromechanics of MoS_2 and WS_2 nanotubes was the subject of [159].

Experimentally, defect-controlled electric properties were studied in [160] and nanomechanical behavior of MoS_2 and WS_2 nanotubes was investigated in [161].

Field-effect transistors based on MoS_2 [162, 163] and WS_2 [164] nanotubes were reported, the observed mobility varying from $0.014\text{ cm}^2\text{V}^{-1}\text{s}^{-1}$ [162] to $50\text{ cm}^2\text{V}^{-1}\text{s}^{-1}$ [164].

5.7.2 Nanoribbons

TMDC nanoribbons may have ziz-zag and arm-chair edges, which has a pronounced effect on their properties electronic and magnetic properties (cf. Sect. 10.1.1). Nanoribbons may potentially be produced by nanopatterning. For example, in [165] a nanomanufacturing of 2D TMDCs was developed using self-assembled DNA nanotubes as lithographic templates with subsequent dry etching. As an alternative, laser-induced unzipping of nanotubes was proposed as a method to fabricate WS_2 and MoS_2 nanoribbons [166]. Multi-layer nanoribbons may also be produced by squeezing nanotubes.

5.7.3 Quantum Dots

Reports of zero-dimensional quantum dot structures based on TMDC are very limited. One example is the formation of quantum dots in device structures by changing the back-gate voltage [167].

References

1. K. Park, J. Heremans, V. Scarola, D. Minic, Robustness of topologically protected surface states in layering of Bi_2Te_3 thin films. *Phys. Rev. Lett.* **105**, 186801 (2010)
2. J. Brivio, D.T. Alexander, A. Kis, Ripples and layers in ultrathin MoS_2 membranes. *Nano Lett.* **11**(12), 5148 (2011)
3. J.N. Coleman, M. Lotya, A. O'Neill, S.D. Bergin, P.J. King, U. Khan, K. Young, A. Gaucher, S. De, R.J. Smith, Two-dimensional nanosheets produced by liquid exfoliation of layered materials. *Science* **331**(6017), 568 (2011)
4. D. Yang, R. Frindt, Li-intercalation and exfoliation of WS_2 . *J. Phys. Chem. Solids* **57**(6), 1113 (1996)
5. P. Joensen, R. Frindt, S.R. Morrison, Single-layer MoS_2 . *Mat. Res. Bull.* **21**(4), 457 (1986)
6. S.J. Sandoval, D. Yang, R. Frindt, J. Irwin, Raman study and lattice dynamics of single molecular layers of MoS_2 . *Phys. Rev. B* **44**(8), 3955 (1991)
7. M. Py, R. Haering, Structural destabilization induced by lithium intercalation in MoS_2 and related compounds. *Can. J. Phys.* **61**(1), 76 (1983)
8. M. Kertesz, R. Hoffmann, Octahedral vs. trigonal-prismatic coordination and clustering in transition-metal dichalcogenides. *J. Am. Chem. Soc.* **106**(12), 3453 (1984)
9. M.T. Janish, C.B. Carter, In situ TEM observations of the lithiation of molybdenum disulfide. *Scripta Materialia* **107**, 22 (2015)
10. D. Yang, S.J. Sandoval, W. Dividalpitiya, J. Irwin, R. Frindt, Structure of single-molecular-layer MoS_2 . *Phys. Rev. B* **43**(14), 12053 (1991)
11. T. Sekine, C. Julien, I. Samaras, M. Jouanne, M. Balkanski, Vibrational modifications on lithium intercalation in MoS_2 . *Mater. Sci. Eng. B* **3**(1), 153 (1989)
12. R. Gordon, D. Yang, E. Crozier, D. Jiang, R. Frindt, Structures of exfoliated single layers of WS_2 , MoS_2 , and MoSe_2 in aqueous suspension. *Phys. Rev. B* **65**(12), 125407 (2002)
13. T. Hu, R. Li, J. Dong, A new (2 x 1) dimerized structure of monolayer 1T-molybdenum disulfide, studied from first principles calculations. *J. Chem. Phys.* **139**(17), 174702 (2013)
14. S. Balendhran, J.Z. Ou, M. Bhaskaran, S. Sriram, S. Ippolito, Z. Vasic, E. Kats, S. Bhargava, S. Zhuiykov, K. Kalantar-Zadeh, Atomically thin layers of MoS_2 via a two step thermal evaporation-exfoliation method. *Nanoscale* **4**(2), 461 (2012)
15. M. Chhowalla, H.S. Shin, G. Eda, L.J. Li, K.P. Loh, H. Zhang, The chemistry of two-dimensional layered transition metal dichalcogenide nanosheets. *Nat. Chem.* **5**(4), 263 (2013)
16. C. Ramana, U. Becker, V. Shutthanandan, C. Julien, Oxidation and metal-insertion in molybdenite surfaces: evaluation of charge-transfer mechanisms and dynamics. *Geochem. Trans.* **9**(1), 8 (2008)
17. C. Papageorgopoulos, W. Jaegermann, Li intercalation across and along the van der Waals surfaces of MoS_2 (0001). *Surf. Sci.* **338**(1), 83 (1995)
18. G. Eda, H. Yamaguchi, D. Voiry, T. Fujita, M. Chen, M. Chhowalla, Photoluminescence from chemically exfoliated MoS_2 . *Nano Lett.* **11**(12), 5111 (2011)
19. G. Lucovsky, R. White, J. Benda, J. Revelli, Infrared-reflectance spectra of layered group-IV and group-VI transition-metal dichalcogenides. *Phys. Rev. B* **7**(8), 3859 (1973)
20. T. Egami, S.J.L. Billinge, *Underneath the Bragg Peaks: Structural Analysis of Complex Materials* (Pergamon, Kiddington, 2003)

21. E. Stern, Y. Yacoby, Structural disorder in perovskite ferroelectric crystals as revealed by XAFS. *J. Phys. Chem. Solids* **57**(10), 1449 (1996)
22. P. Fons, A.V. Kolobov, M. Krbař, J. Tominaga, K. Andrikopoulos, S. Yannopoulos, G. Voyatzis, T. Uruga, Phase transitions in crystalline GeTe: Pitfalls of averaging effects. *Phys. Rev. B* **82**(15), 155209 (2010)
23. A. Schumacher, L. Scandella, N. Kruse, R. Prins, Single-layer MoS₂ on mica: studies by means of scanning force microscopy. *Surf. Sci.* **289**(1), L595 (1993)
24. X. Qin, D. Yang, R. Frindt, J. Irwin, Scanning tunneling microscopy of single-layer MoS₂ in water and butanol. *Ultramicroscopy* **42**, 630 (1992)
25. V. Petkov, S.J.L. Billinge, P. Larson, S.D. Mahanti, T. Vogt, K.K. Rangan, M.G. Kanatzidis, Structure of nanocrystalline materials using atomic pair distribution function analysis: Study of LiMoS₂. *Phys. Rev. B* **65**(9), 092105 (2002)
26. X. Rocquefeuille, F. Boucher, P. Gressier, G. Ouvrard, P. Blaha, K. Schwarz, Mo cluster formation in the intercalation compound LiMoS₂. *Phys. Rev. B* **62**(4), 2397 (2000)
27. H.L. Tsai, J. Heising, J.L. Schindler, C.R. Kannewurf, M.G. Kanatzidis, Exfoliated-restacked phase of WS₂. *Chem. Mater.* **9**(4), 879 (1997)
28. J. Heising, M.G. Kanatzidis, Exfoliated and restacked MoS₂ and WS₂: Ionic or neutral species? Encapsulation and ordering of hard electropositive cations. *J. Am. Chem. Soc.* **121**(50), 11720 (1999)
29. J. Heising, M.G. Kanatzidis, Structure of restacked MoS₂ and WS₂ elucidated by electron crystallography. *J. Am. Chem. Soc.* **121**(4), 638 (1999)
30. E. Prouzet, J. Heising, M.G. Kanatzidis, Structure of restacked and pillared WS₂: an X-ray absorption study. *Chem. Mater.* **15**(2), 412 (2003)
31. M. Kan, J. Wang, X.W. Li, S. Zhang, Y. Li, Y. Kawazoe, Q. Sun, P. Jena, Structures and phase transition of a MoS₂ monolayer. *J. Phys. Chem. C* **118**(3), 1515 (2014)
32. L. Mattheiss, Band structures of transition-metal-dichalcogenide layer compounds. *Phys. Rev. B* **8**(8), 3719 (1973)
33. B. Silbernagel, Lithium intercalation complexes of layered transition metal dichalcogenides: an NMR survey of physical properties. *Solid State Commun.* **17**(3), 361 (1975)
34. P. Williams, F. Shepherd, He II photoemission studies of transition metal dichalcogenides. *J. Phys. C* **6**(1), L36 (1973)
35. A.N. Enyashin, L. Yadgarov, L. Houben, I. Popov, M. Weidenbach, R. Tenne, M. Bar-Sadan, G. Seifert, New route for stabilization of 1T-WS₂ and MoS₂ phases. *J. Phys. Chem. C* **115**(50), 24586 (2011)
36. Y. Li, Y.L. Li, W. Sun, R. Ahuja, Dynamic stability of the single-layer transition metal dichalcogenides. *Comp. Mater. Sci.* **92**, 206 (2014)
37. K.A.N. Duerloo, Y. Li, E.J. Reed, Structural phase transitions in two-dimensional Mo-and W-dichalcogenide monolayers. *Nat. Commun.* **5** (2014). doi:[10.1038/ncomms5214](https://doi.org/10.1038/ncomms5214)
38. B.E. Brown, The crystal structures of WTe₂ and high-temperature MoTe₂. *Acta Cryst.* **20**(2), 268 (1966)
39. S. Bertolazzi, J. Brivio, A. Kis, Stretching and breaking of ultrathin MoS₂. *ACS Nano* **5**(12), 9703 (2011)
40. R.C. Cooper, C. Lee, C.A. Marianetti, X. Wei, J. Hone, J.W. Kysar, Nonlinear elastic behavior of two-dimensional molybdenum disulfide. *Phys. Rev. B* **87**(3), 035423 (2013)
41. P. Miró, M. Ghorbani-Asl, T. Heine, Spontaneous ripple formation in MoS₂ monolayers: Electronic structure and transport effects. *Adv. Mater.* **25**(38), 5473 (2013)
42. S.K. Singh, M. Neek-Amal, S. Costamagna, F. Peeters, Rippling, buckling, and melting of single-and multilayer MoS₂. *Phys. Rev. B* **91**(1), 014101 (2015)
43. M. Kan, H.G. Nam, Y.H. Lee, Q. Sun, Phase stability and Raman vibration of the molybdenum ditelluride (MoTe₂) monolayer. *Phys. Chem. Chem. Phys.* **17**(22), 14866 (2015)
44. C. Ataca, H. Sahin, S. Ciraci, Stable, single-layer MX₂ transition-metal oxides and dichalcogenides in a honeycomb-like structure. *J. Phys. Chem. C* **116**(16), 8983 (2012)
45. Y.C. Lin, D.O. Dumcenco, Y.S. Huang, K. Suenaga, Atomic mechanism of the semiconducting-To-metallic phase transition in single-layered MoS₂. *Nat. Nanotech.* **9**(5), 391 (2014)

46. Y. Cheng, A. Nie, Q. Zhang, L.Y. Gan, R. Shahbazian-Yassar, U. Schwingenschlögl, Origin of the phase transition in lithiated molybdenum disulfide. *ACS Nano* **8**(11), 11447 (2014)
47. Y. Zhou, E.J. Reed, Structural phase stability control of monolayer MoTe₂ with adsorbed atoms and molecules. *J. Phys. Chem. B* **119**(37), 21674 (2015)
48. M.R. Ryzhikov, V.A. Slepkov, S.G. Kozlova, S.P. Gabuda, V.E. Fedorov, Solid-state reaction as a mechanism of 1T–2H transformation in MoS₂ monolayers. *J. Comput. Chem* **36**(28), 2131 (2015)
49. R. Kappera, D. Voiry, S.E. Yalcin, W. Jen, M. Acerce, S. Torrel, B. Branch, S. Lei, W. Chen, S. Najmaei et al., Metallic 1T phase source/drain electrodes for field effect transistors from chemical vapor deposited MoS₂. *APL Mater.* **2**(9), 092516 (2014)
50. S. Cho, S. Kim, J.H. Kim, J. Zhao, J. Seok, D.H. Keum, J. Baik, D.H. Choe, K. Chang, K. Sue-naga et al., Phase patterning for ohmic homojunction contact in MoTe₂. *Science* **349**(6248), 625 (2015)
51. M. Yoshida, Y. Zhang, J. Ye, R. Suzuki, Y. Imai, S. Kimura, A. Fujiwara, Y. Iwasa, Controlling charge-density-wave states in nano-thick crystals of 1T-TaS₂. *Sci. Rep.* **4** (2014). doi:[10.1038/srep07302](https://doi.org/10.1038/srep07302)
52. Y. Yu, F. Yang, X.F. Lu, Y.J. Yan, Y.H. Cho, L. Ma, X. Niu, S. Kim, Y.W. Son, D. Feng et al., Gate-tunable phase transitions in thin flakes of 1T-TaS₂. *Nat. Nanotech.* **10**(3), 270 (2015)
53. P. Fazekas, E. Tosatti, Electrical, structural and magnetic properties of pure and doped 1T-TaS₂. *Philos. Mag. B* **39**(3), 229 (1979)
54. P. Fazekas, E. Tosatti, Charge carrier localization in pure and doped 1T-TaS₂. *Physica B+C* **99**(1), 183 (1980)
55. F. Zwick, H. Berger, I. Voborník, G. Margaritondo, L. Forró, C. Beeli, M. Onellion, G. Panaccione, A. Taleb-Ibrahimi, M. Grioni, Spectral consequences of broken phase coherence in 1T-TaS₂. *Phys. Rev. Lett.* **81**(5), 1058 (1998)
56. R.E. Thomson, B. Burk, A. Zettl, J. Clarke, Scanning tunneling microscopy of the charge-density-wave structure in 1T-TaS₂. *Phys. Rev. B* **49**(24), 16899 (1994)
57. A. Spijkerman, J.L. de Boer, A. Meetsma, G.A. Wiegers, S. van Smaleen, X-ray crystal-structure refinement of the nearly commensurate phase of 1T-TaS₂ in (3+2)-dimensional superspace. *Phys. Rev. B* **56**(21), 13757 (1997)
58. L. Stojchevska, I. Vaskivskyi, T. Mertelj, P. Kusar, D. Svetin, S. Brazovskii, D. Mihailovic, Ultrafast switching to a stable hidden quantum state in an electronic crystal. *Science* **344**(6180), 177 (2014)
59. M.J. Hollander, Y. Liu, W.J. Lu, L.J. Li, Y.P. Sun, J.A. Robinson, S. Datta, Electrically driven reversible insulator-metal phase transition in 1T-TaS₂. *Nano Lett.* **15**(3), 1861 (2015)
60. P. Chen, Y.H. Chan, X.Y. Fang, Y. Zhang, M.Y. Chou, S.K. Mo, Z. Hussain, A.V. Fedorov, T.C. Chiang, Charge density wave transition in single-layer titanium diselenide. *Nat. Commun.* **6** (2015). doi:[10.1038/ncomms9943](https://doi.org/10.1038/ncomms9943)
61. P. Batson, Atomic and electronic structure of a dissociated 60° misfit dislocation in Ge_xSi_(1-x). *Phys. Rev. Lett.* **83**(21), 4409 (1999)
62. N. Alem, V.P. David, Correlative deformation mechanisms in Ni_xCo_{1-x}O/ZrO₂ (CaO) directionally solidified eutectic composites with a confined metallic interphase. *Acta Materialia* **56**(16), 4378 (2008)
63. Y. Hajati, T. Blom, S. Jafri, S. Haldar, S. Bhandary, M. Shoushtari, O. Eriksson, B. Sanyal, K. Leifer, Improved gas sensing activity in structurally defected bilayer graphene. *Nanotechnology* **23**(50), 505501 (2012)
64. J.H. Warner, E.R. Margine, M. Mukai, A.W. Robertson, F. Giustino, A.I. Kirkland, Dislocation-driven deformations in graphene. *Science* **337**(6091), 209 (2012)
65. W. Zhou, X. Zou, S. Najmaei, Z. Liu, Y. Shi, J. Kong, J. Lou, P.M. Ajayan, B.I. Yakobson, J.C. Idrobo, Intrinsic structural defects in monolayer molybdenum disulfide. *Nano Lett.* **13**(6), 2615 (2013)
66. Y. Guo, D. Liu, J. Robertson, Chalcogen vacancies in monolayer transition metal dichalcogenides and fermi level pinning at contacts. *Appl. Phys. Lett.* **106**(17), 173106 (2015)

67. Z. Liu, K. Suenaga, Z. Wang, Z. Shi, E. Okunishi, S. Iijima, Identification of active atomic defects in a monolayered tungsten disulphide nanoribbon. *Nat. Commun.* **2** (2011). doi:[10.1038/ncomms1224](https://doi.org/10.1038/ncomms1224)
68. H.P. Komsa, J. Kotakoski, S. Kurasch, O. Lehtinen, U. Kaiser, A.V. Krasheninnikov, Two-dimensional transition metal dichalcogenides under electron irradiation: defect production and doping. *Phys. Rev. Lett.* **109**(3), 035503 (2012)
69. H.P. Komsa, S. Kurasch, O. Lehtinen, U. Kaiser, A.V. Krasheninnikov, From point to extended defects in two-dimensional MoS₂: Evolution of atomic structure under electron irradiation. *Phys. Rev. B* **88**(3), 035301 (2013)
70. H. Liu, H. Zheng, F. Yang, L. Jiao, J. Chen, W. Ho, C. Gao, J. Jia, M. Xie, Line and point defects in MoSe₂ bilayer studied by scanning tunneling microscopy and spectroscopy. *ACS Nano* **9**(6), 6619 (2015)
71. X. Zou, Y. Liu, B.I. Yakobson, Predicting dislocations and grain boundaries in two-dimensional metal-disulfides from the first principles. *Nano Lett.* **13**(1), 253 (2012)
72. A.M. van der Zande, P.Y. Huang, D.A. Chenet, T.C. Berkelbach, Y. You, G.H. Lee, T.F. Heinz, D.R. Reichman, D.A. Muller, J.C. Hone, Grains and grain boundaries in highly crystalline monolayer molybdenum disulphide. *Nat. Mater.* **12**(6), 554 (2013)
73. S. Najmaei, Z. Liu, W. Zhou, X. Zou, G. Shi, S. Lei, B.I. Yakobson, J.C. Idrobo, P.M. Ajayan, J. Lou, Vapour phase growth and grain boundary structure of molybdenum disulphide atomic layers. *Nat. Mater.* **12**(8), 754 (2013)
74. A. Azizi, X. Zou, P. Ercius, Z. Zhang, A.L. Elías, N. Perea-López, G. Stone, M. Terrones, B.I. Yakobson, N. Alem, Dislocation motion and grain boundary migration in two-dimensional tungsten disulphide. *Nat. Commun.* **5** (2014). doi:[10.1038/ncomms5867](https://doi.org/10.1038/ncomms5867)
75. Z. Zhang, X. Zou, V.H. Crespi, B.I. Yakobson, Intrinsic magnetism of grain boundaries in two-dimensional metal dichalcogenides. *ACS Nano* **7**(12), 10475 (2013)
76. X. Lu, M.I.B. Utama, J. Lin, X. Gong, J. Zhang, Y. Zhao, S.T. Pantelides, J. Wang, Z. Dong, Z. Liu et al., Large-area synthesis of monolayer and few-layer MoSe₂ films on SiO₂ substrates. *Nano Lett.* **14**(5), 2419 (2014)
77. J. Lin, S.T. Pantelides, W. Zhou, Vacancy-induced formation and growth of inversion domains in transition-metal dichalcogenide monolayer. *ACS Nano* **9**, 5189 (2015)
78. Y. Zhang, Y. Zhang, Q. Ji, J. Ju, H. Yuan, J. Shi, T. Gao, D. Ma, M. Liu, Y. Chen et al., Controlled growth of high-quality monolayer WS₂ layers on sapphire and imaging its grain boundary. *ACS Nano* **7**(10), 8963 (2013)
79. H.R. Gutiérrez, N. Perea-López, A.L. Elías, A. Berkdemir, B. Wang, R. Lv, F. López-Urías, V.H. Crespi, H. Terrones, M. Terrones, Extraordinary room-temperature photoluminescence in triangular WS₂ monolayers. *Nano Lett.* **13**(8), 3447 (2012)
80. K.F. Mak, K. He, C. Lee, G.H. Lee, J. Hone, T.F. Heinz, J. Shan, Tightly bound trions in monolayer MoS₂. *Nat. Mater.* **12**(3), 207 (2013)
81. M.C. Prado, R. Nascimento, B.E. Faria, M.J. Matos, H. Chacham, B.R. Neves, Nanometre-scale identification of grain boundaries in MoS₂ through molecular decoration. *Nanotechnology* **26**(47), 475702 (2015)
82. K. Dolui, I. Runger, C.D. Pemmaraju, S. Sanvito, Possible doping strategies for MoS₂ monolayers: an ab initio study. *Phys. Rev. B* **88**(7), 075420 (2013)
83. Y. Wang, B. Wang, R. Huang, B. Gao, F. Kong, Q. Zhang, First principles study of transition metal atom adsorption on MoS₂ monolayer. *Physica E* **63**, 276 (2014)
84. C. Ataca, S. Ciraci, Functionalization of single-layer MoS₂ honeycomb structures. *J. Phys. Chem. C* **115**(27), 13303 (2011)
85. Y.C. Lin, D.O. Dumcenco, H.P. Komsa, Y. Niimi, A.V. Krasheninnikov, Y.S. Huang, K. Suenaga, Properties of individual dopant atoms in single-layer MoS₂: Atomic structure, migration, and enhanced reactivity. *Adv. Mater.* **26**(18), 2857 (2014)
86. Q. Yue, Z. Shao, S. Chang, J. Li, Adsorption of gas molecules on monolayer MoS₂ and effect of applied electric field. *Nanoscale Res. Lett.* **8**(1), 425 (2013)
87. D. Voiry, A. Goswami, R. Kappera, C.C.C. Silva, D. Kaplan, T. Fujita, M. Chen, T. Asefa, M. Chhowalla, Covalent functionalization of monolayered transition metal dichalcogenides by phase engineering. *Nat. Chem.* **7**(1), 45 (2015)

88. H. Fang, M. Tosun, G. Seol, T.C. Chang, K. Takei, J. Guo, A. Javey, Degenerate n-doping of few-layer transition metal dichalcogenides by potassium. *Nano Lett.* **13**(5), 1991 (2013)
89. T. Eknapakul, P.D. King, M. Asakawa, P. Buaphet, R.H. He, S.K. Mo, H. Takagi, K.M. Shen, F. Baumberger, T. Sasagawa et al., Electronic structure of a quasi-freestanding MoS₂ monolayer. *Nano Lett.* **14**(3), 1312 (2014)
90. B. Huang, M. Yoon, B.G. Sumpter, S.H. Wei, F. Liu, Alloy engineering of defect properties in semiconductors: suppression of deep levels in transition-metal dichalcogenides. *Phys. Rev. Lett.* **115**(12), 126806 (2015)
91. L.Y. Gan, Q. Zhang, Y.J. Zhao, Y. Cheng, U. Schwingenschlögl, Order-disorder phase transitions in the two-dimensional semiconducting transition metal dichalcogenide alloys Mo_{1-x}W_xX₂ (X = S, Se, and Te). *Sci. Rep.* **4** (2014). doi:[10.1038/srep06691](https://doi.org/10.1038/srep06691)
92. R. Frindt, Single crystals of MoS₂ several molecular layers thick. *J. Appl. Phys.* **37**(4), 1928 (1966)
93. A. Castellanos-Gomez, M. Poot, G.A. Steele, H.S. van der Zant, N. Agrait, G. Rubio-Bollinger, Mechanical properties of freely suspended semiconducting graphene-like layers based on MoS₂. *Nanoscale Res. Lett.* **7**(1), 1 (2012)
94. C. Lee, X. Wei, J.W. Kysar, J. Hone, Measurement of the elastic properties and intrinsic strength of monolayer graphene. *Science* **321**(5887), 385 (2008)
95. I. Kaplan-Ashiri, S.R. Cohen, K. Gartsman, V. Ivanovskaya, T. Heine, G. Seifert, I. Wiesel, H.D. Wagner, R. Tenne, On the mechanical behavior of WS₂ nanotubes under axial tension and compression. *Proc. Nat. Acad. Sci.* **103**(3), 523 (2006)
96. T. Lorenz, J.O. Joswig, G. Seifert, Stretching and breaking of monolayer MoS₂ an atomistic simulation. *2D Mater.* **1**(1), 011007 (2014)
97. Q. Yue, J. Kang, Z. Shao, X. Zhang, S. Chang, G. Wang, S. Qin, J. Li, Mechanical and electronic properties of monolayer MoS₂ under elastic strain. *Phys. Lett. A* **376**(12), 1166 (2012)
98. J. Li, N.V. Medhekar, V.B. Shenoy, Bonding charge density and ultimate strength of monolayer transition metal dichalcogenides. *J. Phys. Chem. C* **117**(30), 15842 (2013)
99. T. Lorenz, M. Ghorbani-Asl, J.O. Joswig, T. Heine, G. Seifert, Is MoS₂ a robust material for 2d electronics? *Nanotechnology* **25**(44), 445201 (2014)
100. T. Lorenz, D. Teich, J.O. Joswig, G. Seifert, Theoretical study of the mechanical behavior of individual TiS₂ and MoS₂ nanotubes. *J. Phys. Chem. C* **116**(21), 11714 (2012)
101. J.W. Jiang, Z. Qi, H.S. Park, T. Rabczuk, Elastic bending modulus of single-layer molybdenum disulfide (MoS₂): finite thickness effect. *Nanotechnology* **24**(43), 435705 (2013)
102. L.F. Huang, P.L. Gong, Z. Zeng, Correlation between structure, phonon spectra, thermal expansion, and thermomechanics of single-layer MoS₂. *Phys. Rev. B* **90**(4), 045409 (2014)
103. W. Zhan-Yu, Z. Yan-Li, W. Xue-Qing, W. Fei, S. Qiang, G. Zheng-Xiao, J. Yu, Effects of in-plane stiffness and charge transfer on thermal expansion of monolayer transition metal dichalcogenide. *Chin. Phys. B* **24**(2), 026510 (2015)
104. D.J. Late, S.N. Shirodkar, U.V. Waghmare, V.P. Dravid, C. Rao, Thermal expansion, anharmonicity and temperature-dependent Raman spectra of single-and few-layer MoSe₂ and WSe₂. *ChemPhysChem* **15**(8), 1592 (2014)
105. X. Wei, Y. Wang, Y. Shen, G. Xie, H. Xiao, J. Zhong, G. Zhang, Phonon thermal conductivity of monolayer MoS₂: A comparison with single layer graphene. *Appl. Phys. Lett.* **105**(10), 103902 (2014)
106. W. Li, J. Carrete, N. Mingo, Thermal conductivity and phonon linewidths of monolayer MoS₂ from first principles. *Appl. Phys. Lett.* **103**(25), 253103 (2013)
107. Y. Cai, J. Lan, G. Zhang, Y.W. Zhang, Lattice vibrational modes and phonon thermal conductivity of monolayer MoS₂. *Phys. Rev. B* **89**(3), 035438 (2014)
108. X. Liu, G. Zhang, Q.X. Pei, Y.W. Zhang, Phonon thermal conductivity of monolayer MoS₂ sheet and nanoribbons. *Appl. Phys. Lett.* **103**(13), 133113 (2013)
109. J.W. Jiang, X. Zhuang, T. Rabczuk, Orientation dependent thermal conductance in single-layer MoS₂. *Sci. Rep.* **3** (2013). doi:[10.1038/srep02209](https://doi.org/10.1038/srep02209)

110. R. Yan, J.R. Simpson, S. Bertolazzi, J. Brivio, M. Watson, X. Wu, A. Kis, T. Luo, A.R. Hight Walker, H.G. Xing, Thermal conductivity of monolayer molybdenum disulfide obtained from temperature-dependent Raman spectroscopy. *ACS Nano* **8**(1), 986 (2014)
111. S. Sahoo, A.P. Gaur, M. Ahmadi, M.J.F. Guinel, R.S. Katiyar, Temperature-dependent Raman studies and thermal conductivity of few-layer MoS₂. *J. Phys. Chem. C* **117**(17), 9042 (2013)
112. N. Peimyoo, J. Shang, W. Yang, Y. Wang, C. Cong, T. Yu, Thermal conductivity determination of suspended mono-and bilayer WS₂ by Raman spectroscopy. *Nano Res.* **8**(4), 1210 (2015)
113. A. Taube, A. Lapinska, J. Judek, M. Zdrojek, Temperature-dependent thermal properties of supported MoS₂ monolayers. *Int. ACS Appl. Mater.* **7**(9), 5061 (2015)
114. W. Huang, H. Da, G. Liang, Thermoelectric performance of MX₂ (M= Mo, W; X= S, Se) monolayers. *J. Appl. Phys.* **113**(10), 104304 (2013)
115. W. Huang, X. Luo, C.K. Gan, S.Y. Quek, G. Liang, Theoretical study of thermoelectric properties of few-layer MoS₂ and WSe₂. *Phys. Chem. Chem. Phys.* **16**(22), 10866 (2014)
116. S. Kumar, U. Schwingenschlögl, Thermoelectric response of bulk and monolayer MoSe₂ and WSe₂. *Chem. Mater.* **27**(4), 1278 (2015)
117. M. Kastner, Bonding bands, lone-pair bands, and impurity states in chalcogenidesemiconductors. *Phys. Rev. Lett.* **28**(6), 355–357 (1972)
118. M. Tahir, U. Schwingenschlögl, Tunable thermoelectricity in monolayers of MoS₂ and other group-VI dichalcogenides. *New J. Phys.* **16**(11), 115003 (2014)
119. Y. Li, A. Chernikov, X. Zhang, A. Rigosi, H.M. Hill, A.M. van der Zande, D.A. Chenet, E.M. Shih, J. Hone, T.F. Heinz, Measurement of the optical dielectric function of monolayer transition-metal dichalcogenides: MoS₂, MoSe₂, WS₂, and WSe₂. *Phys. Rev. B* **90**(20), 205422 (2014)
120. H.L. Liu, C.C. Shen, S.H. Su, C.L. Hsu, M.Y. Li, L.J. Li, Optical properties of monolayer transition metal dichalcogenides probed by spectroscopic ellipsometry. *Appl. Phys. Lett.* **105**(20), 201905 (2014)
121. A. Castellanos-Gomez, N. Agrait, G. Rubio-Bollinger, Optical identification of atomically thin dichalcogenide crystals. *Appl. Phys. Lett.* **96**(21), 213116 (2010)
122. N. Dong, Y. Li, Y. Feng, S. Zhang, X. Zhang, C. Chang, J. Fan, L. Zhang, J. Wang, Optical limiting and theoretical modelling of layered transition metal dichalcogenide nanosheets. *Sci. Rep.* **5** (2015). doi:[10.1038/srep14646](https://doi.org/10.1038/srep14646)
123. K. Kaasbjerg, K.S. Thygesen, K.W. Jacobsen, Phonon-limited mobility in n-type single-layer MoS₂ from first principles. *Phys. Rev. B* **85**(11), 115317 (2012)
124. S. Kim, A. Konar, W.S. Hwang, J.H. Lee, J. Lee, J. Yang, C. Jung, H. Kim, J.B. Yoo, J.Y. Choi, et al., High-mobility and low-power thin-film transistors based on multilayer MoS₂ crystals. *Nat. Commun.* **3** (2012). doi:[10.1038/ncomms2018](https://doi.org/10.1038/ncomms2018)
125. S. Das, H.Y. Chen, A.V. Penumatcha, J. Appenzeller, High performance multilayer MoS₂ transistors with scandium contacts. *Nano Lett.* **13**(1), 100 (2012)
126. N. Pradhan, D. Rhodes, Q. Zhang, S. Talapatra, M. Terrones, P. Ajayan, L. Balicas, Intrinsic carrier mobility of multi-layered MoS₂ field-effect transistors on SiO₂. *Appl. Phys. Lett.* **102**(12), 123105 (2013)
127. W. Bao, X. Cai, D. Kim, K. Sridhara, M.S. Fuhrer, High mobility ambipolar MoS₂ field-effect transistors: substrate and dielectric effects. *Appl. Phys. Lett.* **102**(4), 042104 (2013)
128. J.H. Strait, P. Nene, F. Rana, High intrinsic mobility and ultrafast carrier dynamics in multilayer metal-dichalcogenide MoS₂. *Phys. Rev. B* **90**(24), 245402 (2014)
129. G.D. Moore, A study of the oxidation kinetics of synthetic molybdenum diselenide. *ASLE Trans.* **13**(2), 117 (1970)
130. M.T. Lavik, T.M. Medved, G.D. Moore, Oxidation characteristics of MoS₂ and other solid lubricants. *ASLE Trans.* **11**(1), 44 (1968)
131. S. Tongay, J. Zhou, C. Ataca, K. Lo, T.S. Matthews, J. Li, J.C. Grossman, J. Wu, Thermally driven crossover from indirect toward direct bandgap in 2D semiconductors: MoSe₂ versus MoS₂. *Nano Lett.* **12**(11), 5576 (2012)
132. C.H. Lee, E.C. Silva, L. Calderin, M.A.T. Nguyen, M.J. Hollander, B. Bersch, T.E. Mallouk, J.A. Robinson, Tungsten ditelluride: a layered semimetal. *Sci. Rep.* **5** (2015). doi:[10.1038/srep10013](https://doi.org/10.1038/srep10013)

133. Y. Liu, C. Tan, H. Chou, A. Nayak, D. Wu, R. Ghosh, H.Y. Chang, Y. Hao, X. Wang, J.S. Kim et al., Thermal oxidation of WSe₂ nanosheets adhered on SiO₂/Si substrates. *Nano Lett.* **15**(8), 4979 (2015)
134. K. Santosh, R.C. Longo, R.M. Wallace, K. Cho, Surface oxidation energetics and kinetics on MoS₂ monolayer. *J. Appl. Phys.* **117**(13), 135301 (2015)
135. H. Liu, N. Han, J. Zhao, Atomistic insight into the oxidation of monolayer transition metal dichalcogenides: from structures to electronic properties. *RSC Adv.* **5**(23), 17572 (2015)
136. I. Paradiso, E. Kymakis, C. Fotakis, G. Kioseoglou, E. Stratikis, Intense femtosecond photoexcitation of bulk and monolayer MoS₂. *Appl. Phys. Lett.* **105**(4), 041108 (2014)
137. E.M. Mannebach, K.A.N. Duerloo, L.A. Pellouchoud, M.J. Sher, S. Nah, Y.H. Kuo, Y. Yu, A.F. Marshall, L. Cao, E.J. Reed et al., Ultrafast electronic and structural response of monolayer MoS₂ under intense photoexcitation conditions. *ACS Nano* **8**(10), 10734 (2014)
138. E.M. Mannebach, R. Li, K.A. Duerloo, C. Nyby, P. Zalden, T. Vecchione, F. Ernst, A.H. Reid, T. Chase, X. Shen et al., Dynamic structural response and deformations of monolayer MoS₂ visualized by femtosecond electron diffraction. *Nano Lett.* **15**(10), 6889 (2015)
139. N. Bandaru, R.S. Kumar, J. Baker, O. Tschauner, T. Hartmann, Y. Zhao, R. Venkat, Structural stability of WS₂ under high pressure. *Int. J. Mod. Phys. B* **28**, 1450168 (2014)
140. N. Bandaru, R.S. Kumar, D. Snead, O. Tschauner, J. Baker, D. Antonio, S.N. Luo, T. Hartmann, Y. Zhao, R. Venkat, Effect of pressure and temperature on structural stability of MoS₂. *J. Phys. Chem. C* **118**(6), 3230 (2014)
141. K. Vasu, H. Matte, S.N. Shirodkar, V. Jayaram, K. Reddy, U.V. Waghmare, C. Rao, Effect of high-temperature shock-wave compression on few-layer MoS₂, WS₂ and MoSe₂. *Chem. Phys. Lett.* **582**, 105 (2013)
142. M. Yamamoto, S. Dutta, S. Aikawa, S. Nakaharai, K. Wakabayashi, M.S. Fuhrer, K. Ueno, K. Tsukagoshi, Self-limiting layer-by-layer oxidation of atomically thin WSe₂. *Nano Lett.* **15**(3), 2067 (2015)
143. S. Iijima et al., Helical microtubules of graphitic carbon. *Nature* **354**(6348), 56 (1991)
144. R. Tenne, L. Margulis, M. Genut, G. Hodes, Polyhedral and cylindrical structures of tungsten disulphide. *Nature* **360**(6403), 444 (1992)
145. Y. Feldman, E. Wasserman, D. Srolovitz, R. Tenne, High-rate, gas-phase growth of MoS₂ nested inorganic fullerenes and nanotubes. *Science* **267**(5195), 222 (1995)
146. A. Rothschild, J. Sloan, R. Tenne, Growth of WS₂ nanotubes phases. *J. Am. Chem. Soc.* **122**(21), 5169 (2000)
147. M. Nath, A. Govindaraj, C. Rao, Simple synthesis of MoS₂ and WS₂ nanotubes. *Adv. Mater.* **13**(4), 283 (2001)
148. A. Margolin, R. Rosentsveig, A. Albu-Yaron, R. Popovitz-Biro, R. Tenne, Study of the growth mechanism of WS₂ nanotubes produced by a fluidized bed reactor. *J. Mater. Chem.* **14**(4), 617 (2004)
149. M. Remskar, A. Mrzel, Z. Skraba, A. Jesih, M. Ceh, J. Demšar, P. Stadelmann, F. Lévy, D. Mihailovic, Self-assembly of subnanometer-diameter single-wall MoS₂ nanotubes. *Science* **292**(5516), 479 (2001)
150. M. Nath, C.N.R. Rao, MoSe₂ and WSe₂ nanotubes and related structures. *Chem. Commun.* pp. 2236–2237 (2001)
151. D.H. Galván, R. Rangel, E. Adem, Formation of MoTe₂ nanotubes by electron irradiation. *Fullerene. Sci. Technol.* **7**(3), 421 (1999)
152. E. Flores, A. Tlahuice, E. Adem, D.H. Galvan, Optimization of the electron irradiation in the production of MoTe₂ nanotubes. *Fullerene. Sci. Technol.* **9**(1), 9 (2001)
153. L. Qiu, V.G. Pol, Y. Wei, A. Gedanken, A two-step process for the synthesis of MoTe₂ nanotubes: combining a sonochemical technique with heat treatment. *J. Mater. Chem.* **13**(12), 2985 (2003)
154. W. Li, G. Zhang, M. Guo, Y.W. Zhang, Strain-tunable electronic and transport properties of MoS₂ nanotubes. *Nano Res.* **7**(4), 1 (2014)
155. N. Li, G. Lee, Y.H. Jeong, K.S. Kim, Tailoring electronic and magnetic properties of MoS₂ nanotubes. *J. Phys. Chem. C* **119**(11), 6405 (2015)

156. K.X. Chen, X.M. Wang, D.C. Mo, S.S. Lyu, Thermoelectric properties of transition metal dichalcogenides: from monolayers to nanotubes. *J. Phys. Chem. C* **119**, 26706 (2015)
157. A.O. Pereira, C.R. Miranda, First-principles investigation of transition metal dichalcogenide nanotubes for Li and Mg ion battery applications. *J. Phys. Chem. C* **119**(8), 4302 (2015)
158. X. Wu, Z. Xu, X. Zeng, Single-walled MoTe₂ nanotubes. *Nano Lett.* **7**(10), 2987 (2007)
159. M. Ghorbani-Asl, N. Zibouche, M. Wahiduzzaman, A.F. Oliveira, A. Kuc, T. Heine, Electromechanics in MoS₂ and WS₂: nanotubes vs. monolayers. *Sci. Rep.* **3** (2013). doi:[10.1038/srep02961](https://doi.org/10.1038/srep02961)
160. M. Remskar, A. Mrzel, M. Virsek, M. Godec, M. Krause, A. Kolitsch, A. Singh, A. Seabaugh, The MoS₂ nanotubes with defect-controlled electric properties. *Nanoscale Res. Lett.* **6**(1), 26 (2011)
161. D. Maharaj, B. Bhushan, Nanomechanical behavior of MoS₂ and WS₂ multi-walled nanotubes and carbon nanohorns. *Sci. Rep.* **5** (2015). doi:[10.1038/srep08539](https://doi.org/10.1038/srep08539)
162. M. Strojnik, A. Kovic, A. Mrzel, J. Buh, J. Strle, D. Mihailovic, MoS₂ nanotube field effect transistors. *AIP Adv.* **4**, 097114 (2015)
163. S. Fathipour, M. Remskar, A. Varlec, A. Ajoy, R. Yan, S. Vishwanath, S. Rouvimov, W. Hwang, H. Xing, D. Jena et al., Synthesized multiwall MoS₂ nanotube and nanoribbon field-effect transistors. *Appl. Phys. Lett.* **106**(2), 022114 (2015)
164. R. Levi, O. Bitton, G. Leitus, R. Tenne, E. Joselevich, Field-effect transistors based on WS₂ nanotubes with high current-carrying capacity. *Nano Lett.* **13**(8), 3736 (2013)
165. J. Choi, H. Chen, F. Li, L. Yang, S.S. Kim, R.R. Naik, P.D. Ye, J.H. Choi, Nanomanufacturing of 2d transition metal dichalcogenide materials using self-assembled DNA nanotubes. *Small* **11**(41), 5520 (2015)
166. K. Vasu, S.S. YamiJala, A. Zak, K. Gopalakrishnan, S.K. Pati, C. Rao, Clean WS₂ and MoS₂ nanoribbons generated by laser-induced unzipping of the nanotubes. *Small* **11**, 3916 (2015)
167. X.X. Song, D. Liu, V. Mosallanejad, J. You, T.Y. Han, D.T. Chen, H.O. Li, G. Cao, M. Xiao, G.C. Guo et al., A gate defined quantum dot on the two-dimensional transition metal dichalcogenide semiconductor WSe₂. *Nanoscale* **7**, 16867 (2015)

Chapter 6

Electronic Band Structure of 2D TMDCs

The electronic band structure of monolayers of TMDCs has been intensely investigated both experimentally and using first-principles calculations in the past several years [1–25]. In this chapter we review the existing results starting with theoretical studies. The interested readers are also referred to an excellent review [26].

6.1 Theoretical Studies

Most theoretical studies are based on first-principles calculations but significant efforts have been also placed to develop tight-binding models, which were successfully used for example for prediction and studies of spin-valley interactions in monolayer TMDCs [27, 28] and the indirect-to-direct gap transition in monolayers [29, 30] as well as to study defect states [31]. In many cases a simple $k \cdot p$ model is used to study transport, optical and magnetic properties of mono and few-layer TMDC [32, 33] however, the model is only valid close to the band edges. A more complicated three-band tight-binding model using metal d_{z^2} , d_{xy} and $d_{x^2-y^2}$ orbitals that was developed in [34], was sufficient to capture the band-edge properties in the $\pm K$ valleys, including the energy dispersion and the Berry curvatures. By including up to the third-nearest-neighbour metal-metal hopping, the model could reproduce the energy bands in the entire Brillouin zone [34]. An analytical approach was also used to study spin-orbit effects [28, 35–37], magnetotransport [38], excitonic polarizations [39, 40], etc.

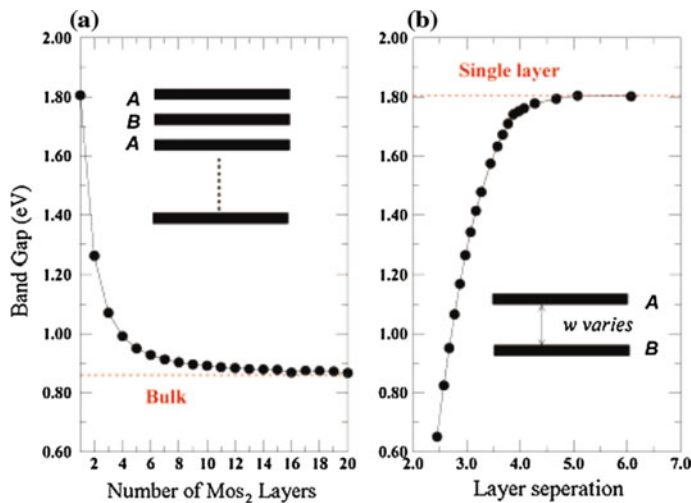


Fig. 6.1 Variations of the band gap in multilayer MoS₂ sheets with respect to (a) the number of sheets n and (b) separation distance w (in Angstroms), where w refers to the z -axis distance between the *upper S* layer of sheet B and the *lower S* layer of sheet A. Note that both sheets A and B contain three atomic layers S-Mo-S [41]. Copyright 2007 American Chemical Society. Published with permission

6.1.1 Indirect-to-Direct Gap Transition

Bulk TMDCs are indirect gap materials. At the same time, when the thickness decreases to a single monolayer, the band gap in MoS₂ and other group VI TMDCs increases and, more importantly, the material becomes a direct gap semiconductor [1, 16, 18, 20, 41–43]. Several authors reported this result at about the same time with, perhaps, one of the first reports being [41]. Band gap opening with decreasing number of layers is illustrated in Fig. 6.1 following this work.

DFT calculations first pointed to a direct band gap in monolayer WSe₂ and MoS₂ located at the corners of the hexagonal Brillouin zone, i.e. at the K -points. Incidentally, the WS₂ monolayer was studied a decade ago both experimentally and using DFT calculations, which identified its valence band maximum at the $\pm K$ points but did not draw the conclusion of a direct band gap [44]. The evolution of the band structure as one goes from the bulk phase to a monolayer for several group VIB TMDCs is shown in Fig. 6.2a–c.

The variation of the band gaps in MoS₂ for the number of layers $n = 1$ to 7 is shown in Fig. 6.3a. All the band gaps decrease monotonically with increasing number of layers and converge rapidly to the bulk values [46]. The $K - K$ gap for $n = 5$ is only 10 meV higher than in the bulk, and it is equal to the bulk value for $n = 7$. For $\Gamma - K$ the difference with the bulk is 70 meV for $n = 5$ and 44 meV for $n = 7$. This variation of the band gap was found to have important consequences for the valley degeneracy. For the conduction band (CB) the degeneracy is 2 for monolayer, and with increasing number of layers the CB edge at A_{min} also becomes important,

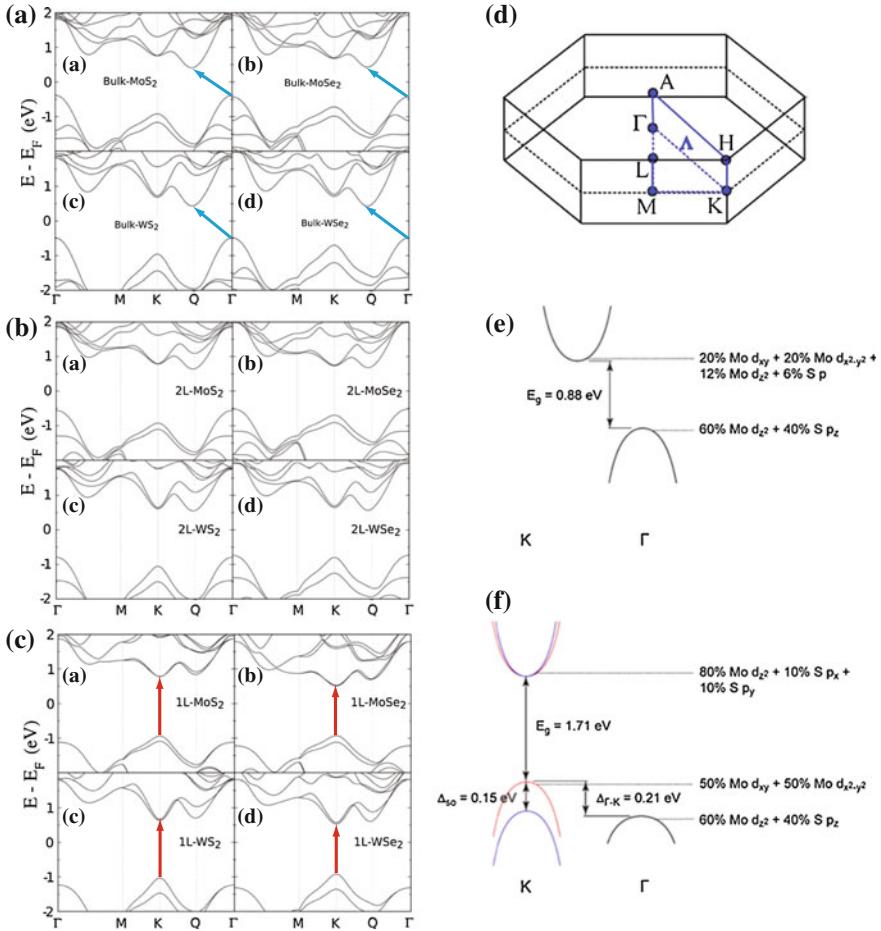


Fig. 6.2 Band structures of (a) bulk, (b) bi-layer, and (c) monolayer MoS₂, MoSe₂, WS₂, and WSe₂. The arrows indicate the fundamental band gap, direct (red) or indirect (blue) for a given system, after [43]. Reproduced with permission from Wiley-VCH Verlag GmbH; (d) the Brillouin zone and the corresponding high-symmetry points, (e) and (f) show schematic drawings of low-energy bands in (e) bulk MoS₂ and (f) monolayer MoS₂ showing the band gaps E_g as well as the valence band spin-orbit splitting Δ_{SO} and the Γ valley band offset $\Delta_{\Gamma-K}$ for the case of monolayer MoS₂. The orbital composition of electronic states at band extrema is also indicated [45]. Reprinted with permission from Elsevier

leading to an additional valley degeneracy of 6.¹ For the valence band (VB) the degeneracy is 2 for monolayer and 1 for all other layers. The band edges were also calculated on an absolute energy scale, i.e., with respect to the vacuum level [46], which not only provides important insight into the physical origins of the band-gap variations but also helps in screening materials for ohmic and Schottky contacts and

¹The notation A used in [46] is not usual. Usually this point is referred to as Q .

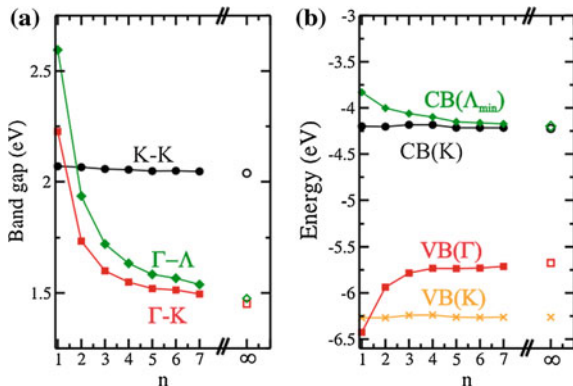


Fig. 6.3 **a** Evolution of the band gaps as a function of the number of layers (n). The *black circles* ($K-K$), *red squares* ($\Gamma-K$), and *green diamonds* ($\Gamma-\Lambda_{\min}$) indicate the magnitude of the different band gaps. (The notation Λ used here is not usual. Usually this point is referred to as Q). Hollow symbols indicate the bulk band gaps. **b** Position of the band edge with respect to the vacuum level for the VB at the K -point (orange crosses), VB at Γ (red squares), CB at the K -point (black circles), and CB at Λ_{\min} (green diamonds) [46]. Copyright 2014 by the American Physical Society. Reprinted with permission (color figure online)

determines band alignments in heterostructures. The evolution of the band edges as a function of the number of layers n is shown in Fig. 6.3b, showing that both the VB and CB edges at the K -point exhibit only small variations (smaller than 50 meV) [46].

All the single-layer compounds of group VIB are direct gap semiconductors, with the gap lying at the two inequivalent K -points of the hexagonal Brillouin zone. The most important orbital contribution at the edge of the valence band at the K -point is due to a combination of d_{xy} and $d_{x^2-y^2}$ of the metal, which hybridize to p_x and p_y orbitals of the chalcogen atoms. On the other hand, the edge of the conduction band has its main contribution from the $d_{3z^2-r^2}$ orbital of the metal, plus minor contributions from p_x and p_y orbitals of chalcogens [29].

The band gap opening, associated with quantum confinement has been explained as follows. The states at the Γ -point originate from a linear combination of p_z orbitals on S atoms and d_{z^2} orbitals on Mo atoms [47], both of which are rather delocalized and have an antibonding nature. An increase in the interlayer distance decreases the layer-layer interaction. As a result, the energy arising from antibonding states is lowered. On the other hand, both the top of the valence band and the bottom of the conduction band near the K -point are primarily composed of orbitals localized in the xy plane, and these basically are unaffected by a change of distance along z . Such a downward energy shift at the Γ -point not only results in an increase of the band gap but also changes its nature from indirect to direct [41].

Experimentally, the increase in the band gap and the conversion of the gap nature from an indirect to direct manifests itself as a shift in photoluminescence peak position to higher energies alongside with a drastic increase in the photoluminescence intensity (cf. e.g. Fig. 8.1 below).

Of interest is also the symmetry of band-edge wavefunctions. This issue was considered in detail in [26]. At the $\pm K$ points, the wave-vector group is C_{3h} whose generators are C_3 and σ_h . C_{3h} is an Abelian group with only one-dimensional irreducible representations. This makes all the Bloch states at the K -points nondegenerate, which have to be eigenstate of both C_3 and σ_h . The σ_h symmetry divides the five metal (M) d -orbitals into two sets: the even set ($d_{x^2-y^2}, d_{xy}, d_{z^2}$) and the odd set (d_{xz}, d_{yz}). Chalcogen (X) p orbitals above and below the M atom plane can also be arranged in terms of linear superpositions with odd and even σ_h symmetry respectively.

A word of warning should be said here. Although, first-principles calculations provide valuable insights into the electronic structures, one must always remember that the exact results depend on the calculation details [43]. We give a few examples here. Thus, it was found that the direct and indirect energy gaps depend on the lattice constant. LDA exchange-correlation functional usually underestimates the lattice constant in the energy minimization process while GGA overestimates it. Turning (or not turning) on spin-orbit coupling (SOC) also modifies the obtained results. GW calculations, that are more typically used to calculate the optical absorption, yield conflicting results about the nature of the gap: both indirect [23, 48] and direct gaps [49, 50] were reported. It was argued that the inclusion of the 4s (for Mo) and 5s (for W) semi-core electrons is crucial to obtain the direct gap [49].

6.1.2 Monolayers Versus Bi-Layers

In monolayers, the conduction band (CB) minimum and the valence band (VB) maximum are both located at the corners of the first Brillioun zone. The six corners belong to two inequivalent groups denoted by K and $-K$ points, respectively, (in some papers the K' notation is used for the latter) where each group has three equivalent corners related to each other by reciprocal lattice vectors. In this volume both $-K$ and K' notations are used interchangeably, following the original publications. The CB also has six local minima at the low symmetry Q points (see Fig. 6.2a-c) [sometimes referred to as Λ (cf. e.g. Fig. 6.3)], although Λ is conventionally used to refer to a direction rather than to a point], while the VB has a local maximum at the Γ point, which are referred to as Q_c and Γ_v , respectively, hereafter. These local extrema are important because they are close in energy to K_c and K_v , respectively, and in certain cases, e.g. under strain or in multilayers, may become global energy extrema.

K and Γ are high symmetry points that are invariant under the C_3 operation (the rotation by $2\pi/3$ around the z axis). The six Q_c valleys can be divided into two groups: Q and $-Q$. The C_3 operation transforms the three Q (or $-Q$) valleys into each other, while Q and $-Q$ are related by time-reversal operation.

In monolayers, similar to bulk materials, the first several bands above the band gap and below the band gap are predominantly built from the M d orbitals and X p orbitals [47]. The band-edge states at K_c and K_v have dominant contributions from the M $d_{x^2-y^2}, d_{xy}, d_{z^2}$ orbitals, with an admixture of the X p orbitals [9, 29, 51]. For wavefunctions at Q_c and Γ_v , the contributions from the X p_z orbitals become

significant. This $X p_z$ contribution at Q_c and Γ_v plays an important role in the crossover from the direct to indirect band gap from monolayer to bulk, because the close distance between $X p_z$ orbitals from neighbouring layers leads to large hopping, which significantly changes the energy of Q_c and Γ_v [29].

For bi-layers, the first-principles calculated band structures, in particular the band edges and band gaps, strongly depend on the parameters and approximations used [26, 43]. Lattice constant and interlayer distance are the two geometry parameters affecting the band edges most. DFT calculations that do not incorporate a vdW correction overestimate the interlayer distance in the GGA calculations [4, 52] and may underestimate it in LDA calculations [8, 53], resulting in too small interlayer interactions to describe the bilayers properly. Other computational details such as the SOC, exchange correlation functional, pseudopotential, and GW may also give different results, e.g. including SOC can change the VB maximum of the WSe₂ bilayer from Γ_v to K_v [3]. The only direct evidence available are ARPES studies, which showed the VB maximum at Γ_v for MoS₂ and MoSe₂ bilayers [6, 54]. More experimental studies are needed for determining the band edges and band gaps in bilayer TMDCs under various conditions.

The crossover from a direct band gap at the monolayer to an indirect band gap at the bilayer and multilayers is a consequence of interlayer hopping [26]. It can be seen from Fig. 6.4a–d that the band extrema K_v , Γ_v , and Q_c all split with the increase of the number of layers, which is evidence of interlayer hopping. The splitting magnitude represents the interlayer hopping strength. A hopping matrix element of ca. 0.1 eV can be extracted from the splitting pattern. The splittings at Γ_v and Q_c are notably larger than at K_v , which is attributed to the fact that the Bloch states at K_v are predominantly from the metal d orbitals, while the Bloch states at Γ_v and Q_c have non-negligible compositions of the chalcogen p_z -orbitals [26].

At the same time, at K_c , there is no visible splitting from interlayer hopping (Fig. 6.4a–d). This is dictated by the rotational symmetry of the 2H bilayer lattice and the Bloch functions of each monolayer, which means that interlayer hopping is allowed between the VB maximum states, but is forbidden between the two CB minimum states at the K -point in the lower and upper layers.

The interlayer hopping integral between the p_z orbitals of the nearest neighbor chalcogen atoms is more significant compared to other orbitals. The interlayer hopping at K_v is then much weaker compared to that at Γ_v and Q_c , because the two metal planes have larger separation compared to the two nearest neighbor chalcogen planes from the two layers. With an increase in the number of layers, the energy of Γ_v is raised and that of Q_c is lowered significantly, while the energies of K_c and K_v do not change much. The band gap crosses over to an indirect one at the bilayer, and further decreases with an increase in thickness.

In [55] electronic structure of dichalcogenide monolayer alloys was studied, such as MoS_{2x}Se_{2(1-x)}. Figure 6.5 (upper panel) shows the atomic structure of the binaries and the alloy (in the center) and a representative band structure for MoS_{2(0.6)}Se_{2(1-0.6)} alloy is shown in the lower panel together with those of the corresponding constituents. The size of the spheres denotes the magnitude of the projection, and the color denotes the weight of each atomic species. The band structure of the alloy is generally very similar to those of its binary end-points, MoS₂ and MoSe₂, with only

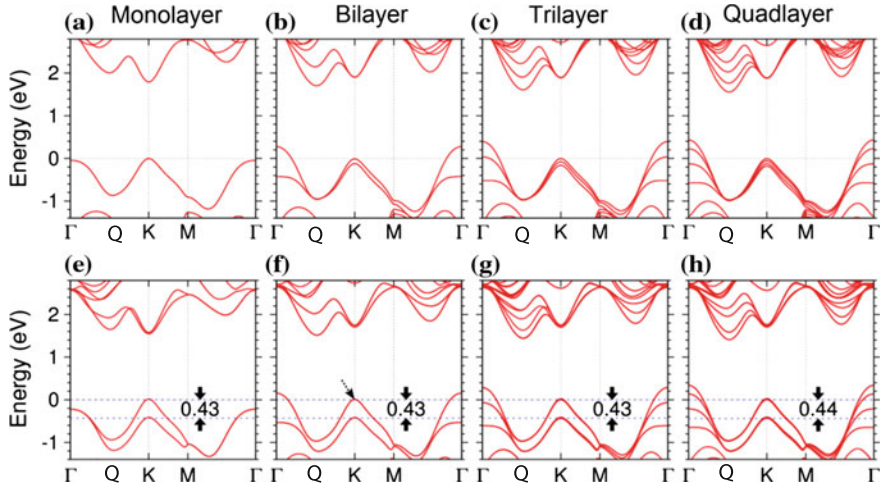


Fig. 6.4 First-principles band structures for WS_2 mono-, bi-, tri-, and quad-layers without SOC (a)–(d) and with SOC (e)–(h). The valence band splittings at the K -points are nearly independent of the number of layers. The experimental bulk lattice constant is used in the calculations. Reproduced from [3]

very minor mixing throughout the Brillouin zone. The gap was found to be direct, and it was concluded that due to the Mo-character of the band edges at the K -point, the effect of chalcogen mixing on these states was small.

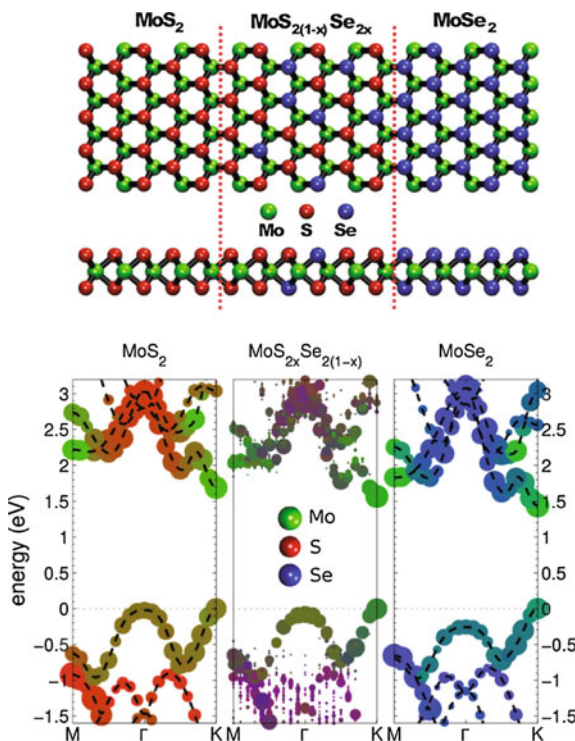
DFT calculations also suggested that the effective hole mass in 2D $\text{Mo}_{1-x}\text{W}_x\text{S}_2$ was nearly isotropic and was predicted to change almost linearly with the tungsten concentration x , while the effective electron mass showed significant spatial anisotropy, which was attributed to orbital symmetry, which is different for the valence and conduction bands [56].

6.1.3 Spin-Orbit Splitting

In the absence of SOC, K_c states in the upper layer and lower layer belong to different irreducible representations of C_3 symmetry, thus interlayer hopping vanishes to all orders between the K_c states in the two layers. This situation is unique to the $2H$ stacking order. A relative translation or rotation of the two layers will change the rotational symmetry, allowing a finite interlayer hopping between the K_c states [26].

When SOC was included, the splitting pattern drastically changed (Fig. 6.4e–h) [3]. In particular, the VB edges split into two degenerate manifolds with a splitting magnitude independent of the film thickness. It was noted that this result is in perfect agreement with the $A - B$ splitting patterns observed in the photoluminescence of mono-, bi-, tri-, and quad-layer WS_2 and WSe_2 . The calculated valence band edge splittings of 0.43 eV in WS_2 and 0.47 eV in WSe_2 also agree with the measured $A - B$

Fig. 6.5 *Upper panel:* Top and side views of the atomic structures of MoS_2 (left), $\text{Mo}_{2x}\text{Se}_{2(1-x)}$ alloy (middle), and MoSe_2 (right) 2D TMDCs. Note that the systems consist of three layers of atoms. *Bottom panel:* The effective band structures of MoS_2 , $\text{Mo}_{2(0.6)}\text{Se}_{2(1-0.6)}$ alloy, and MoSe_2 . The size of the sphere denotes the magnitude of the projection to the corresponding primitive cell k -point. The color denotes the Mo/S/Se weight of the states. For MoS_2 and MoSe_2 , the band structures obtained from primitive cell calculation are overlaid with dashed lines [55]. Copyright 2012 American Chemical Society. Published with permission



splitting of 0.4 eV. It was argued that such splitting patterns in multilayer WS_2 and WSe_2 are manifestations of the giant spin-valley coupling in VB, which suppresses interlayer hopping. As a consequence, the splitting patterns for multi-layers remain the same as that of monolayers, and the valence band Bloch states near the K points are largely localized in individual layers.

It is important to point out that the splitting of the valence-band maximum of the monolayer at the K -point is purely because of the spin-orbit effect and the lack of inversion symmetry which has been studied earlier. The same splitting for the bilayer is caused by the combination of the interlayer interaction and the SOC effect.

The main difference between the Mo- and W- compounds is the larger splitting of the valence band for the latter, which is due to the larger SOC [43]. Thus while the splittings for Mo compounds are typically on the order of 150 meV, for the heavier W compounds they increase to ca. 450 meV [27, 57]. The strong SOC originates from the d orbitals of the metal atoms. The form of SOC induced spin splitting of bands in monolayers has been discussed using a symmetry analysis [26]. It was noted that the first constraint comes from σ_h , the mirror reflection symmetry about the metal atom plane, which requires that a Bloch state and its mirror reflection have identical energy. The σ_h mirror reflection of an in-plane spin vector is its opposite, while the mirror reflection of an out-of-plane spin vector is itself. Thus spin splitting

is only allowed in the out-of-plane z direction, where the spin expectation value of the Bloch states is either along the $+z$ or $-z$ direction. Secondly, the time-reversal symmetry dictates the spin splittings at an arbitrary pair of momentum space points k and $-k$ to have identical magnitude but opposite signs [58]. In the neighborhood of K and $-K$, the SOC then manifests as an effective coupling between the spin and valley pseudospin. It was noted that inversion symmetry would impose a conflicting constraint from that of the time-reversal symmetry, so inversion symmetry breaking in the monolayer is the necessary condition for having spin-valley coupling [26].

Experimental evidence for such a large SOC is reflected in PL measurements where two peaks, attributed to A and B excitons with the holes from the two split-off spin subbands respectively, are seen with an energy separation in agreement with the valence-band spin splitting at $\pm K$ [1]. ARPES measurements of MBE grown MoSe₂ (see Sect. 6.2.4) provide direct evidence of the VB maximum spin-orbit splitting of ca. 0.18 eV [54] in agreement with the calculations.

Because of this giant SOC, the VB maximum in monolayer TMDCs has the spin index locked with the valley index, i.e. valley K ($-K$) has only the spin up (down) holes. Another important consequence of the SOC is that the valley dependent optical selection rules become spin dependent [27]. The spin-valley coupling is the subject of a dedicated chapter (Chap. 11).

The CB at the $\pm K$ -points also has the spin splitting with the same symmetry-dictated form as the VB but with a much smaller magnitude of just a few meV [5, 9, 34, 36, 59, 60]. The small CB SOC was attributed to the fact that the CB Bloch states at $\pm K$ are predominantly formed by the M d_{z^2} orbitals where the intraatomic $\mathbf{L} \cdot \mathbf{S}$ coupling as the dominant contribution to SOC vanishes to leading order [26]. It should also be noted that the overall sign of the CB splitting is different between MoX₂ and WX₂ [34].

For the Q_c valleys of the CB, sizable spin splittings were also found in first-principles calculations [61].

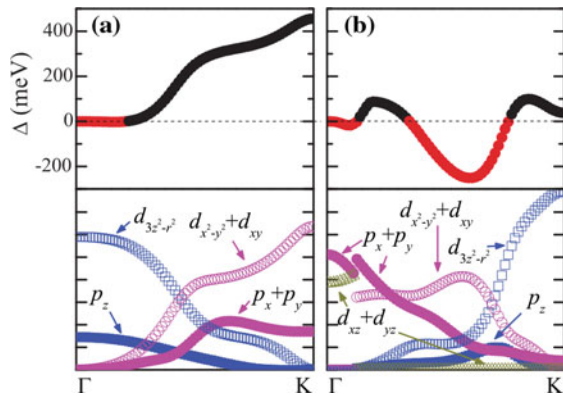
Spin splitting by symmetry arguments was discussed in [51]. It was noted that spin degeneracy at the Γ point results from time-reversal symmetry alone [62]. A combination of time-reversal and translational symmetry results in zero splitting at the M point, whereas the spin splitting of a general k -point is determined by time-reversal and D_{3h} point-group symmetry. The D_{3h} group combines the C_s and C_{3v} symmetry groups, which leads to the spin splitting $\Delta(k_{||}, \theta) = \beta(k_{||}) |\sin 3\theta|$, where β is in-plane potential gradient asymmetry [51].

Further, the $k_{||}$ dependence of the spin splitting Δ for the VB top and the CB bottom was studied using ab-initio simulations. The results are shown in Fig. 6.6.

Both bands exhibit complicated behavior. For the upper VB, $\Delta(k_{||})$ first becomes slightly negative and then rises continuously up to its maximum value (456 meV) at the K -point. For the lower CB, $\Delta(k_{||})$ changes its sign several times, with a steep minimum about midway and a local minimum at the K -point. Similar behaviour was observed for other compounds studied, namely, MoS₂, MoSe₂, and WS₂.

An explanation of the observed $k_{||}$ dependence of Δ was provided by an investigation of the orbital contributions to the upper VB and lower CB [51]. The upper VB reveals hybridization between the Se p_z and W $d_{3z^2-r^2}$ states at the Γ point.

Fig. 6.6 Spin splitting in WSe₂ as a function of $k_{||}$ along the $\Gamma - K$ line: **a** uppermost VB as well as **b** lowermost CB. The sign reflects the spin orientation. Orbitally resolved contributions of Se and W are presented in the bottom panels (in arbitrary units) [51]. Copyright 2011 by the American Physical Society. Reprinted with permission



Toward the K -point, these contributions are gradually replaced by the Se $p_x + p_y$ and W $d_{x^2-y^2} + d_{xy}$ states. Due to their out-of-plane orientations, the Se p_z and W $d_{3z^2-r^2}$ states play no role for the spin splitting. The change of sign in $\Delta(k_{||})$ reflects the opposite effects of the Se $p_x + p_y$ and W $d_{x^2-y^2} + d_{xy}$ states due to the opposite directions of the potential gradient asymmetry on the Se and W sites. The competition is also visible in the spin-splitting behavior of the lower CB. As the lower CB at the K -point is dominated by the W $d_{3z^2-r^2}$ states, Δ is much smaller than for the upper VB.

Band structure calculations for other TMDCs are rather limited but some data are available. Thus, the band structure for ReSe₂ was calculated in [63], although SOC was not included.

6.1.4 Band Gap Tuning

6.1.4.1 Strain Effects

The band structure of TMDC monolayers was found to be strongly affected by strain [64], which is illustrated in Fig. 6.7.

A comprehensive simulational study of the effects of tensile and shear strains on the band structure of group-VIB TMDCs was performed in [65]. The authors investigated a change in the energy separation between the valence and conduction bands for high symmetry points Γ , K , M , L , M' as depicted in Fig. 6.8. The tensile strain was ‘applied’ in three different ways: uniaxial expansion of a monolayer in x -direction (xx), y -direction (yy), and homogeneous biaxial expansion in both x - and y -directions ($xx+yy$), while two types of pure shear strain were applied by expanding and compressing the monolayer in the x - and y -directions ($xx - yy$), respectively, and by compressing it in the x -direction and expanding in the y -direction ($yy - xx$) with the same magnitude of strain. The six panels in Fig. 6.8 present the evolution of the band gaps of monolayers of TMDCs with respect to strain.

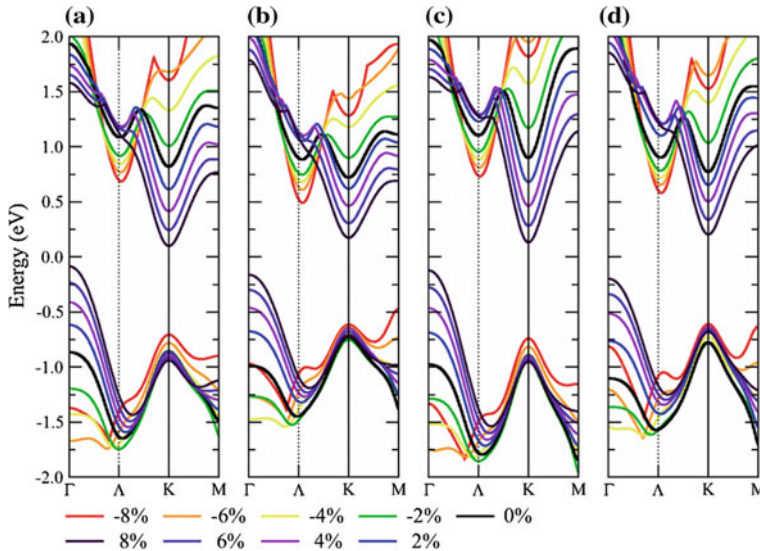


Fig. 6.7 The change of highest valence band and lowest conduction band of TMDC monolayers under compressive and tensile biaxial strains [64]. Copyright 2013 by the American Physical Society. Reprinted with permission

It was noted that the variations in the band gap with respect to strain applied through various approaches do not alter much with the change in transition metal, Mo and W. However, a qualitative as well as quantitative diversity in the trends can be seen with a change in chalcogenides, while moving from MS_2 to MSe_2 to MTe_2 . In sulphides, upon application of tensile strain, the band gap monotonically decreased with strain and the shortest transition that was otherwise a direct band transition for the unstrained system, transformed to an indirect band transition which corresponds to (i) $\Gamma - K$, when the monolayer is stretched in the x -direction; (ii) $\Gamma - L$, when it is stretched in the y -direction; and (iii) $\Gamma - K$ and $\Gamma - L$, when the sheet was homogeneously stretched in both the x - and y -directions. Besides tensile strain, shear strain is also responsible for band gap modifications but the band gap decrease for $xx - yy$ and $yy - xx$ is not as steep as for the case of tensile strain.

For heavier chalcogen atoms, such as Se and Te, the band gap decreased relatively slowly and larger amounts of tensile strain were required to obtain a direct-to-indirect band transition, which was attributed to the ‘diffuse nature’ of these chalcogen atoms. On the application of pure shear strain, materials with heavier chalcogen atoms showed a different behavior as compared to sulphides. While in the former, for both types of shear strains ($xx - yy$ and $yy - xx$) the band gap decreased slowly as compared to tensile strains and almost with the same rate, in MSe_2 and MTe_2 , a split/divergence in the curves (band gap vs. strain) of both types of shear strains was observed, which increased with the size of chalcogen. In contrast to sulphides, the band gap decreased rapidly when the system was stretched in the y -direction

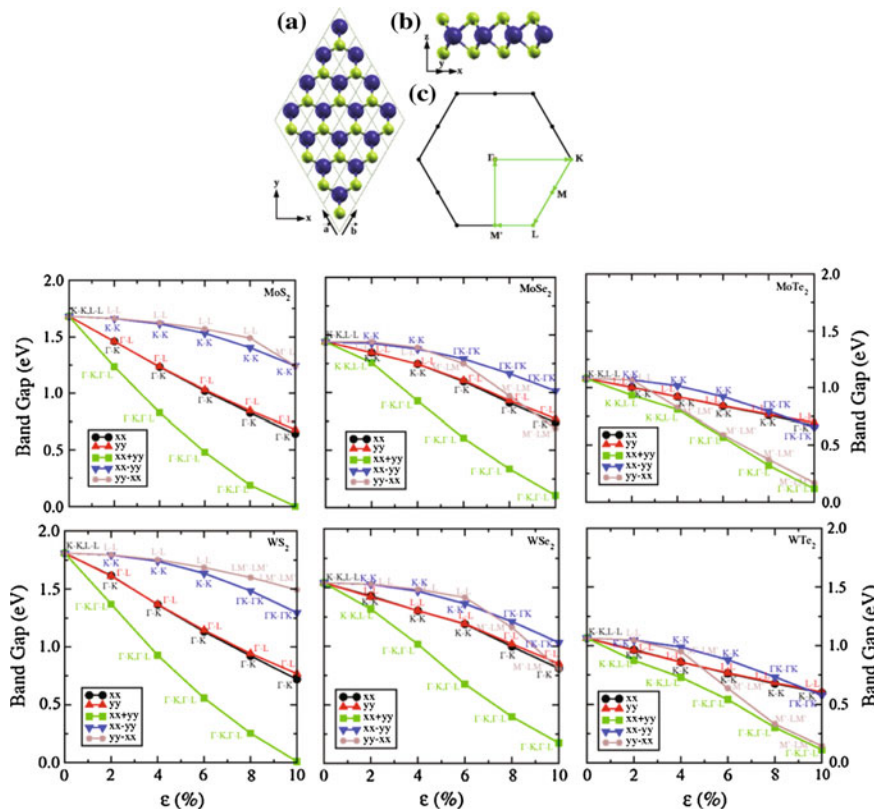


Fig. 6.8 *Upper panel:* **a** top and **b** side view of MX₂, where big and small spheres depict M and X atoms, respectively. **c** Irreducible Brillouin zone of MX₂. *Lower panel:* Band gap of monolayer TMDCs with respect to strain, ϵ , which varies from 0 to 10% [65]. Copyright 2012 American Chemical Society. Published with permission

and compressed in the x -direction ($yy - xx$), as compared to the other case of pure shear strain ($xx - yy$). The different behaviour was attributed to a different degree of overlapping of p_x orbitals for the lighter and heavier chalcogen atoms [65]. Finally the differences in orbital involvement upon application of biaxial tensile strain and shear strain were discussed and it was concluded that the mechanism of the band decrease were different in these two cases. Similar studies were reported in [66].

Indirect-to-direct gap crossover in strained MoSe₂ was also studied in [67, 68]. In [67] it was found that as a consequence of the strain-dependent transition of the valence band edge from the K to Γ point the effective mass of the holes shows significant variations under strain, while the mass of the electrons at the band edge does not change notably (Fig. 6.9). In [68], it was found that the energy valleys drifted far off the K -points of the Brillouin zone (12 time the amount observed in graphene). It was further found that the splitting of the valence bands due to the breaking of

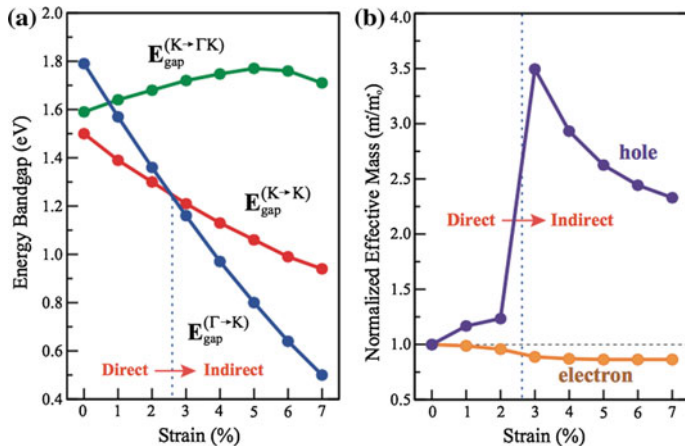


Fig. 6.9 Evolution of (a) direct and indirect energy band gaps, b electron and hole effective mass, normalized to unstrained value, under biaxial tensile strain [67]. Copyright 2013 by the American Physical Society. Reprinted with permission

inversion symmetry and SOC was not sensitive to strain. It was noted that these results were quantitatively different from earlier studies [65], but in better agreement with experiment, due to the inclusion of the SOC into simulations, in particular the system remained a direct-gap semiconductor up to 4% strain while simulations that did not include SOC yielded a smaller value of 1%.

The sensitivity of the band-edge to the lattice constant and interlayer distance results in interesting strain effects. The MoS₂ bilayer under in-plane biaxial strain was found to behave similarly to its monolayer counterpart: (i) band gap decreased with the increase of tensile strain; (ii) under compressive strain the gap first increased and then decreased; (iii) under large enough strain of either tension or compression, the bilayer can become metallic [69]. Under out-of-plane compressive strain, TMDC bilayers can also undergo a semiconductor-to-metal transition [52]. As an example, DFT simulations predicted a semiconductor-metal transition for a single layer or a bi-layer of MoS₂ under a tensile strain of about 8% or a compressive strain of about 15% [70].

Strain was also proposed as a method to engineer the work function in monolayer TMDC [71]. Of special interest is the use of local strain engineering to create an optical funnel, where continuous change in the strain across a sheet of monolayer of TMDC such as MoS₂ leads to a continuous variation of the optical band gap, which allows to capture photons across a wide range of spectrum and concentrate excitons or charge carriers [72, 73].

6.1.4.2 Hydrostatic Pressure

The effect of hydrostatic pressure on monolayer MoS₂ was studied in [74]. Through photoluminescence measurements (see Fig. 8.16) it was found that the direct band gap

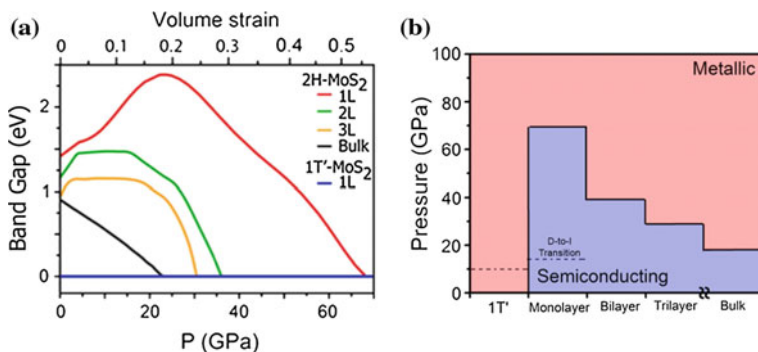


Fig. 6.10 Electronic structures of the MoS₂ polytypes under hydrostatic pressure. **a** Band gap energies of the polytypes as a function of pressure. **a** Below 22.3 GPa, an increase in the direct band gap is observed for the monolayer 2H-MoS₂, whereas for higher pressure, the band gap decreases with strain and closes at 67.9 GPa indicating a metallization transition. A smaller critical pressure of 39.2 and 29.5 GPa is observed for the bilayer and trilayer 2H-MoS₂ respectively. **b** Hydrostatic pressure effects on monolayer, bilayer, trilayer, bulk MoS₂, and 1T'-MoS₂. A metallic state is more easily reached in the bulk state because more interlayer interactions are present [74]. Copyright 2014 American Chemical Society. Published with permission

initially increased and subsequently decreased at higher pressures. DFT calculations were additionally performed with the results being in agreement with the experiment. The ambient theoretical band gap initially was direct until a pressure of 22.3 GPa was reached. At 22.3 GPa, a direct-to-indirect transition took place. Theoretical calculations (Fig. 6.10a) revealed that the band gap of 2H-MoS₂ monolayer first increases until a pressure of ca. 22 GPa is reached. Beyond this pressure, the band gap gradually decreases, eventually leading to the metallization of monolayer 2H-MoS₂ at around 68 GPa [74].

To understand the mechanism of this band gap change and the semiconductor-metal transition under hydrostatic pressure, the contributions from different molecular orbitals were analyzed by performing angular momentum projected density of states (LDOS) calculations [74]. At lower pressures, both VB and CB are mainly composed of Mo $d_{x^2-y^2}$, d_{z^2} and S p_x , p_y orbitals. With increasing pressure, these orbitals move away from the Fermi level, resulting in an increase in the band gap up to 22.3 GPa pressure. At higher pressure, the out-of-plane compression becomes more dominant, making the Mo d_{z^2} , d_{xz} , and p_z orbitals interact strongly with S p -orbitals. This intralayer hybridization leads to a decrease in band gap after ca. 22 GPa pressure and finally the closing of the band gap at higher pressure (68 GPa). It was concluded that for the monolayer 2H-MoS₂, in-plane intralayer interactions play a dominant role in the metallization at 67.9 GPa [74].

In bulk MoS₂ interlayer interactions play a critical role in the metallization [75]. It is therefore natural to expect that the critical pressure or critical volume strain at which the metallization occurs would decrease as the number of layers increases, as was, indeed, observed [74] (Fig. 6.10b).

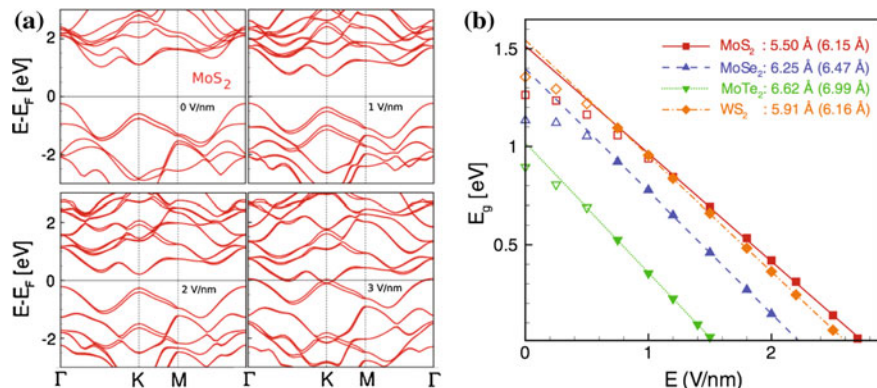


Fig. 6.11 **a** Band structure of MoS₂ along $\Gamma - K - M - \Gamma$ direction in reciprocal space as a function of applied external electric field. **b** Band gap E_g versus applied electric field E for MoS₂, MoSe₂, MoTe₂, and WS₂. The *lines* are fits to the linear portion of the *curve* indicated by *solid* symbols. *Hollow* symbols are within the region of nonlinear response and are excluded from the fits. The giant Stark effect coefficients (magnitudes of the slopes of the linear fits) are indicated; interlayer spacings are in parentheses [4]. Copyright 2011 by the American Physical Society. Reprinted with permission

6.1.4.3 Band Gap Tuning by Electric Field

The interesting possibility of tuning the band gap of bilayer TMDCs by an external electric field was considered in [4]. Using density functional theory, it was shown that with increasing applied electric field, the fundamental band gaps of MoSe₂, MoSe₂, MoTe₂, and WS₂ bilayer structures continuously decreased and eventually closed. As an example, Fig. 6.11a, shows the evolution of the band structures of MoSe₂ bilayers as a function of applied external field. The results were interpreted in light of the giant Stark effect.

It was noted that the critical electric field for the semiconductor-metal transition decreased in going from S to Se to Te, which was attributed to the increasingly diffuse nature of the valence p_z orbitals in going from S to Te, the latter facilitating greater charge transfer from the chalcogen to Mo at the same level of electric field. The effect of changing the transition metal from Mo to W while retaining the chalcogen (S) was very weak. The results for band-gap variation versus applied electric field for the different studied bilayers are shown in Fig. 6.11b.

Detailed studies of the orbital contribution to the electronic states around the Γ point and the K -points under the applied electric field were performed and it was found [4] that while at zero field the upper and lower layers were equivalent (as expected), under the applied electrical field the symmetry of the HOMO and LUMO states changed and they became localised on different layers (Fig. 6.12).

The effect of electric field on bi-layer of MoS₂ was also studied in [76]. A decrease in the band gap was observed and it was found that breaking the inversion symmetry of bilayer MoS₂ by an external field splits the spin degeneracy of the valence band

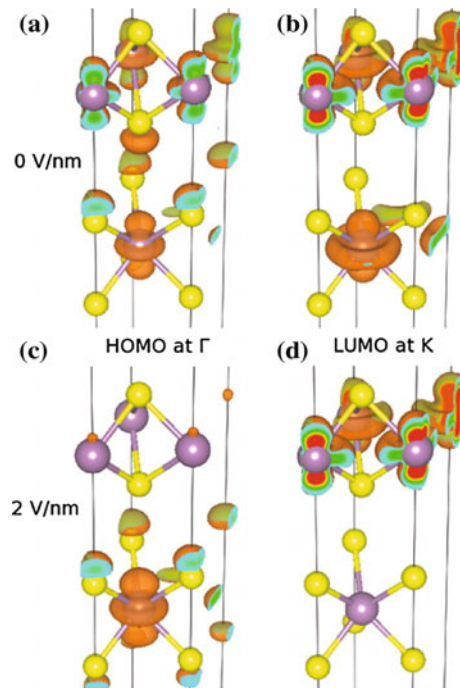


Fig. 6.12 Partial charge density from the HOMO at the Γ -point (a), (c) and the LUMO at the K-point (b), (d) at external fields of 0 V/nm (upper row) and 2 V/nm (lower row). All isosurfaces are at 0.05 e/ \AA^3 . At zero electric field inversion symmetry of the layers is preserved. The HOMO at the Γ -point is primarily of Mo d_{z^2} and Sp_z character with smaller contributions from Mo d_{xy} and $d_{x^2-y^2}$. The LUMO at the K-point is also primarily of Mo d_{z^2} in character with smaller contributions from Mo d_{xy} and $d_{x^2-y^2}$. An external field of 2 V/nm external fields clearly breaks symmetry between the MoSe₂ layers, localizing the HOMO and LUMO on different layers [4]. Copyright 2011 by the American Physical Society. Reprinted with permission

of bilayer MoS₂. The splitting increased linearly from 2 μeV to 152 meV when the electric field was increased from 0 to 0.6 V nm^{-1} .

Electric-field effects on monolayer arm-chair MoS₂ nanoribbons were studied in [77], where it was found that an electric field caused a decrease in the band gap and eventually a semiconductor-metal transition. It was also found that an applied electric field caused magnetism.

6.1.4.4 Twisted Bi-Layers

A way to tune the interlayer interaction in a bi-layer structure is by varying the twist angle between the two layers or by changing the stacking sequence. The effect of the twist angle on the band structure of MoS₂ was studied in several works [78–81], and valley and band structure engineering in differently stacked MoS₂ bilayers was

studied in [79]. There are two aspects of tuning the band structure through a variable twist angle. Firstly, a bi-layer in the $2H$ -phase possesses inversion symmetry, while a bi-layer with an arbitrary twist angle does not. Secondly, when the angle is varied, the interlayer distance varies as is schematically illustrated in Fig. 6.13a. Results of DFT simulations demonstrate that the interlayer distance is minimal for the 0° and 60° twist angles and steeply increases by ca. 0.3 Å for most intermediate angles [78, 80] (Fig. 6.13b).

Figure 6.13c, d show, respectively, the band structure of $2H\text{-MoS}_2$ for two different interlayer distances and the orbital contributions to states 1–3 marked in panel (c). While there is almost no change in the energy of the states near the K -points that determine the onset of the A transitions, the highest occupied state near the Γ -point is substantially downshifted for larger separation. As a result, the onset of the $\Gamma - K$ indirect electronic band gap and optical transition increases by 147 meV.

This is readily understood considering the orbital contributions of the electronic states involved. The valence (State 3 shown in Fig. 6.13) and conduction (State 2) band states related to the direct transition at the K -point involve Mo d states that are localized within the two layers, while the valence state at the Γ point (State 1) has appreciable p_z content of the S atoms between layers, as well as Mo d_{z^2} character. The overlap of the S p_z -orbitals and the resulting band energy of State 1 depend strongly on the interlayer separation. Thus, the interlayer electronic coupling is mainly defined by the orbital overlap of the inner sulfur atoms [78].

The evolution of the direct and indirect band gaps as a function of the twist angle is shown in Fig. 6.13e [81]. Similar results were obtained by other groups [78, 80].

6.1.5 Monolayer-Bilayer Boundary

The difference in the electronic band structure in monolayers and bi-layers can lead to interesting properties of 1L-2L atomic steps. In [82], spin-dependent electronic transport mechanism was proposed, in which a spin-unpolarized electron beam is split into different directions depending on spins at an atomic domain boundary in a nonmagnetic material. The electronic transmission across the boundary between the monolayer and bilayer TMDCs was calculated and it was demonstrated that up-spin and down-spin electrons entering the boundary are refracted and collimated to opposite directions as illustrated in Fig. 6.14. The phenomenon was attributed to the strong spin-orbit interaction, the trigonally warped Fermi surface, and the different crystal symmetries between the monolayer and bilayer systems [82].

6.1.6 Band Structure of the 1T-MoS₂ Phase

Band structures were also calculated for monolayers of the metastable octahedral MoS₂ phase [83] for both undistorted and distorted phases using GGA-PBE along

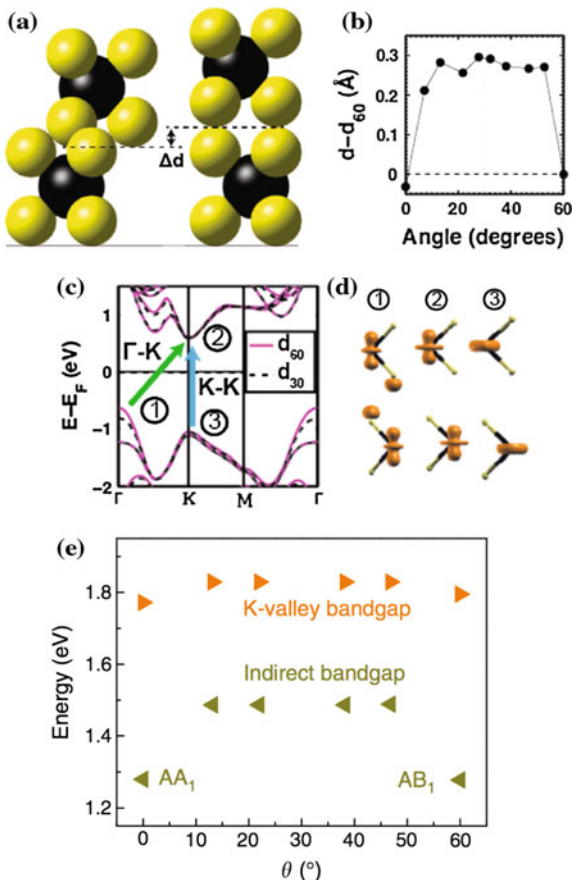
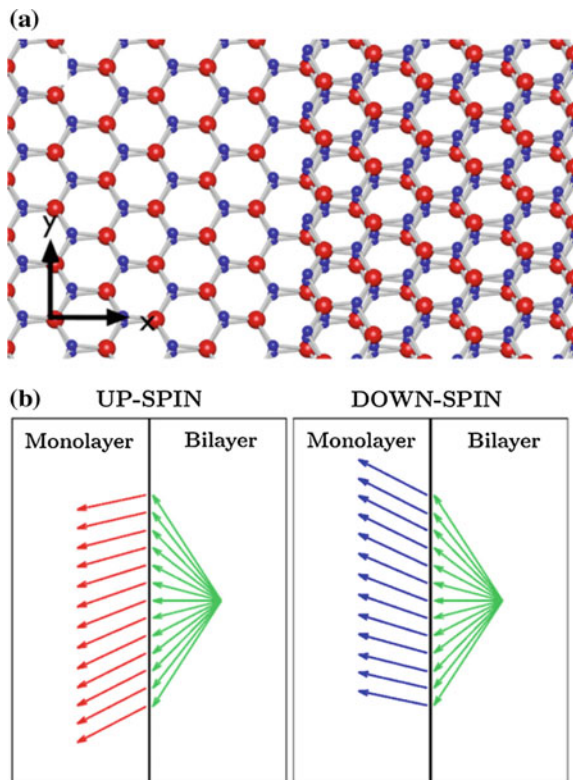


Fig. 6.13 **a** The surface of a MoS₂ monolayer is corrugated because the sulfur atoms (yellow) project out of the plane. As a result, the interlayer separation depends on the relative position of the sulfur atoms in the two layers. **b** Bilayer separation as a function of twist angle θ relative to the 60° separation of $d_0 = 6.23 \text{ \AA}$ determined from dispersion-corrected density functional theory calculations. The bilayer separation for intermediate θ is greater than for the crystallographic orientations (0° and 60°). **c** Electronic structures of a 60° bilayer system with separations corresponding to 60° (solid lines) and 30° (broken lines), highlighting the impact of layer separation. The energy of the valence band at the Γ -point varies strongly with the separation. **d** The partial charge density of states corresponding to the valence band at the Γ -point (State 1), the conduction band at the K -point (State 2), and the valence band at the K -point (State 3). Only State 1 involves inner sulfur atoms, explaining why the indirect transition is affected by twist angle [78]. Copyright 2014 American Chemical Society. Published with permission. **e** Calculated values for the direct and indirect band gaps for the energetically favourable structures at each twist angle [81]. Reprinted by permission from Macmillan Publishers Ltd., copyright (2014)

the lines connecting the high-symmetry points of the Brillouin zone (Fig. 6.15a). Spin-polarized calculations were carried out to see if the ground state could be magnetic, but both 1T-MoS₂ and ZT-MoS₂ remained nonmagnetic. The structural

Fig. 6.14 **a** Atomic structure of the junction between the monolayer and bilayer of TMDC. The large (red) and small (blue) spheres represent the transition-metal and chalcogenide atoms, respectively. **b** Electron refraction at the atomic step between the monolayer and bilayer of MoTe_2 for an incident electron from the bilayer side [82]. Copyright 2015 by the American Physical Society. Reprinted with permission



distortions of monolayer dichalcogenides $ZT\text{-MoS}_2$ lead to the opening of a direct gap of 0.022 eV in the electronic structure as compared to the undistorted metallic $1T\text{-MoS}_2$ phase as shown in Fig. 6.15b.

6.1.7 Strong Light-Matter Coupling and Band Nesting

TMDCs have long been considered for photovoltaic devices due to their large optical absorption (larger than 10^5 cm^{-1} , meaning that 95% of the light can be absorbed by a 300 nm film) with another advantage being their high chemical stability and the band gap in the visible range of the spectrum. Recently it was demonstrated that the strong light-matter interaction in TMDCs can also be extended to monolayers, which allows development of extremely efficient flexible photovoltaic devices with photoresponsivity corresponding to more than 30% [84]. The issue of the very strong light-matter interactions in two-dimensional TMDCs was considered in detail in [85] based on band nesting and in what follows we reproduce the main results starting with the introduction of the band nesting concept.

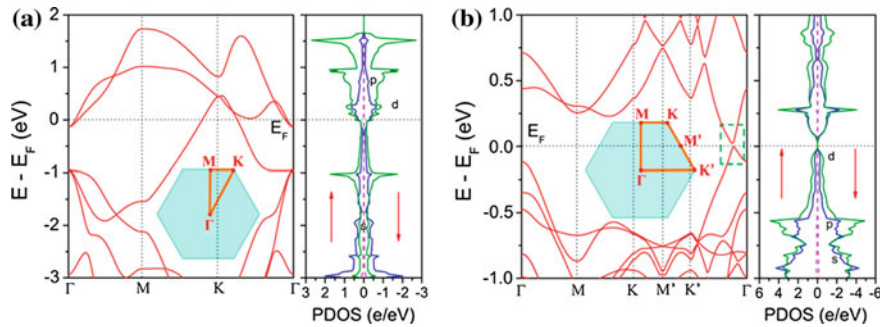


Fig. 6.15 Band structures and PDOS of the optimized (a) (1×1) 1T-MoS₂ and (b) (2×2) ZT-MoS₂ along the *lines* connecting high-symmetry points of the Brillouin zone [83]. Copyright 2014 American Chemical Society. Published with permission

The optical conductivity of a material can be written as

$$\sigma_1(\omega) = \kappa_2(\omega)\omega\epsilon_0 \quad (6.1)$$

where $\kappa_2(\omega)$ is the imaginary part of the relative electric permittivity, ω is the frequency of electromagnetic radiation and ϵ_0 is permittivity of vacuum. Within the dipole approximation:

$$\kappa_2(\omega) = A(\omega) \sum_{v,c} \int_{BZ} \frac{d^2 k}{(2\pi)^2} |d_{vc}|^2 \delta(E_c - E_v - \hbar\omega) \quad (6.2)$$

with the sum over the occupied states in the valence band and the empty states in the conduction band and the intergral over the Brillouin zone, d_{vc} is the dipole matrix element.

The authors consider cuts $S(E)$ of constant energy E such that $E = \hbar\omega = E_c - E_v$ and re-write the integral as [85]:

$$\kappa_2(\omega) = A(\omega) \sum_{v,c} \frac{1}{(2\pi)^2} \int_{S_\omega} \frac{dS}{|\nabla_k(E_c - E_v)|} |d_{vc}|^2 \quad (6.3)$$

It was noted that the strong peaks in optical conductivity come from regions where $|\nabla_k(E_c - E_v)| \approx 0$. If $|d_{vc}|$ varies slowly, the equation can be re-written as

$$\kappa_2(\omega) = A(\omega) \sum_{v,c} |d_{vc}|^2 \rho_{vc}(\omega) \quad (6.4)$$

where

$$\rho_{vc}(\omega) = \frac{1}{(2\pi)^2} \int_{S_\omega} \frac{dS}{|\nabla_k(E_c - E_v)|} \quad (6.5)$$

is the joint density of states (DOS).

The points satisfying the condition $\nabla_k(E_c - E_v) = 0$ are called critical points and they usually occur only at high-symmetry points. The condition $\nabla_k(E_c - E_v) = 0$ with $|\nabla_v| \approx |\nabla_c|$ is called band nesting. This condition is determined by the topographic differences between the valence and conduction bands.

In other words, in the nesting region of the band structure, the conduction and valence bands are “parallel” to each other. As a result, the joint DOS diverges for the resonance energy, generating a giant enhancement in the corresponding optical conductivity. It has been proposed that this divergence in optical conductivity due to band nesting is unique to low-dimensional systems [86] (reference provided after [87]). The absorption is also enhanced for photon energies corresponding to transitions between van Hove singularity peaks in the DOS, which is attributed to heavy effective mass of carriers in MX_2 compounds [47].

Band structure calculations including SOC [85] were performed for a variety of TMDCs and the results are shown in Fig. 6.16 alongside with the corresponding densities of states. Plots of the real part of the optical conductivity are shown in Fig. 6.17. The discussion concentrated on WS_2 and it was noted that the steps at the absorption edges corresponding to the van Hove singularities at the band edges are low compared to the sharp peaks originating from the parallel bands near the conduction band minimum between the Γ and M points (marked G in the Figure), which is not a high symmetry point. It was pointed out that the presence of singularities in the DOS could not explain the high absorption peaks in the optical conductivity (Fig. 6.17).

Based on the analysis of the energy difference between the highest occupied band and the lowest unoccupied band together with the gradients along the high-symmetry lines, a direct correlation was found between the gradient of the $E_c - E_v$ difference and the large optical peak observed at 2.56 eV. Subsequently the entire Brillouin zone was explored in order to determine the extent of band nesting. The result is shown in Fig. 6.18a. The large white areas close to Λ (for the definition of Λ see Fig. 6.16) are the areas where band nesting occurs.

Band nesting in several octahedral compounds was also studied [85], the result for TiS_2 being exemplified in Fig. 6.18b. It was concluded that octahedral compounds TiS_2 and ZrS_2 are among those with the largest band-nesting regions. At the same time, the trigonal prismatic systems, which lack inversion symmetry, also have a strong non-linear optical response, indicating that despite their small thickness they exhibit strong photon-electron coupling [85].

Because absorption is highly efficient in the resonance conditions corresponding to band nesting, understanding the resulting photocarrier relaxation dynamics is crucial for incorporating these materials into light-harvesting devices. Dynamics of photocarriers generated in the band-nesting region are of particular interest as the electrons and holes are expected to relax at the same rate, but with opposite momenta. Such studies were performed in [87], where the authors examined the relaxation processes of photoexcited carriers in mono- and bilayer MX_2 using photoluminescence excitation (PLE) spectroscopy and DFT calculations. The results are summarised below (see Sect. 8.1.3).

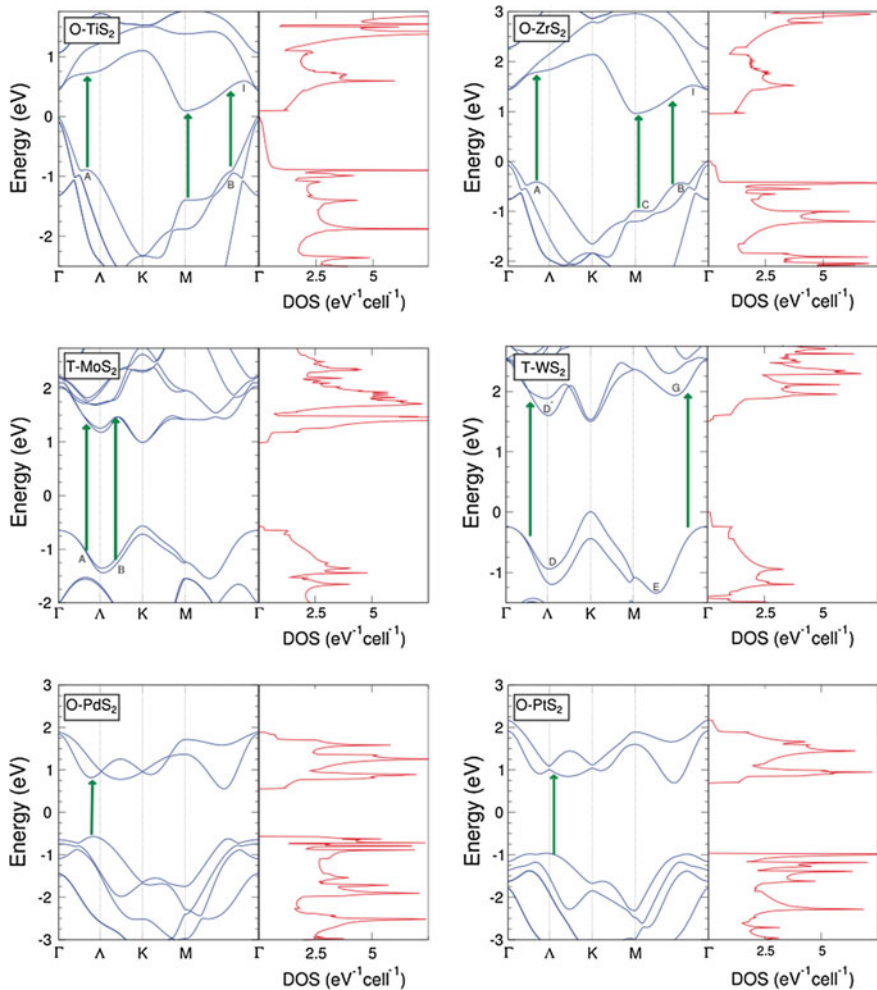
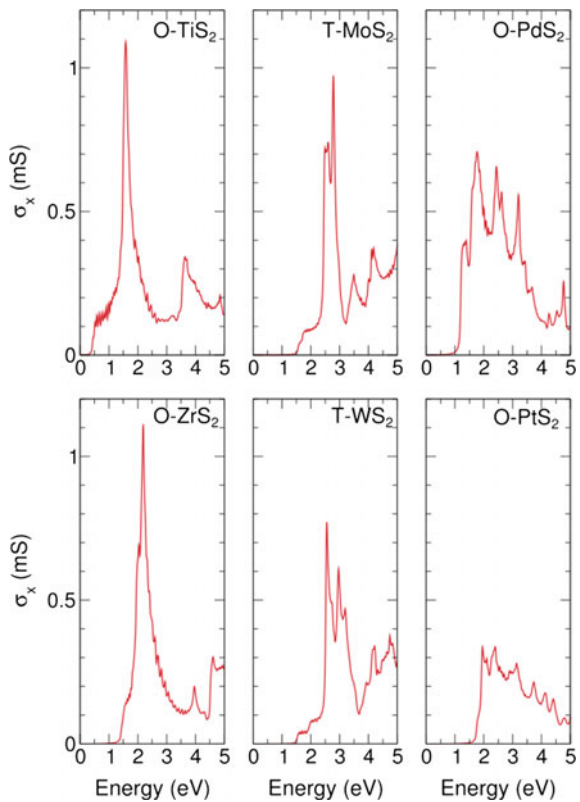


Fig. 6.16 Band structures, and DOS of TiS_2 and ZrS_2 (group 4A sulphides), MoS_2 and WS_2 (group 6A sulphides), and PdS_2 and PtS_2 (group 8 sulphides). The arrows indicate the transitions corresponding to the first prominent peaks in the optical conductivity [85]. Copyright 2013 by the American Physical Society. Reprinted with permission

The issue of extraordinary (sun)light absorption by monolayers of TMDCs was also investigated in [88], where it was shown that a single TMDC monolayer with subnanometer thickness can absorb as much sunlight as 50 nm of Si and generate electrical currents as high as 4.5 mA/cm^{-2} . Figure 6.19a compares the computed absorbance for a monolayer of MoS_2 with experimental measurements [1] demonstrating quantitative agreement observed between the computed and experimental absorbance. Fig. 6.19b shows the absorbance calculated for monolayers of MoS_2 ,

Fig. 6.17 Real part of the optical conductivity of 2D transition metal disulphides. [85]. Copyright 2013 by the American Physical Society. Reprinted with permission



MoSe₂, and WS₂, compared to the absorbance of graphene and to the incident AM1.5G solar spectrum.

It was noted that in addition to the high joint DOS, excitonic effects in TMDCs monolayers resulting from the poor screening of electrons and holes due to the vacuum surrounding the monolayer, give rise to a strong mixing of electron-hole configurations in the excited-state wave function. This results in a constructive superposition of the oscillator strengths for transitions at low energies near the absorption onset [88].

While being extraordinary strong compared to other semiconductors, in absolute terms the absorption in a monolayer thick films is rather weak. Various ways to enhance light-matter interaction in thin films can be considered such as use of localized surface plasmons, surface plasmon polariton states, integrated Si wave guides, reflector microcavities, planar photonic crystals, and quantum dots [89]. The issue of light generating and harvesting using monolayers of TMDCs was also considered in [90].

To complete this section, we would like to note that the term ‘strong light-matter coupling’ is also used to describe a completely different phenomenon, viz., the

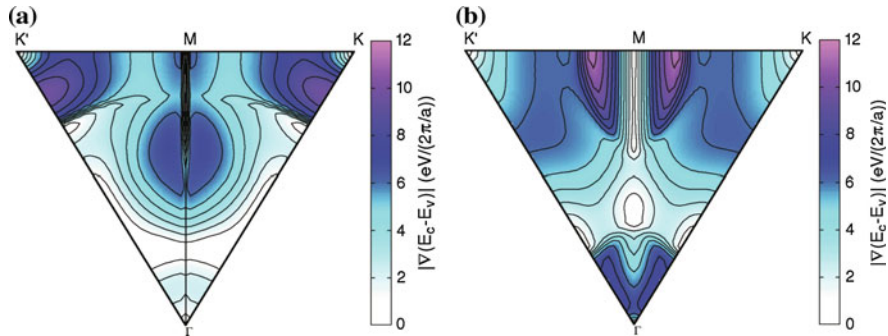
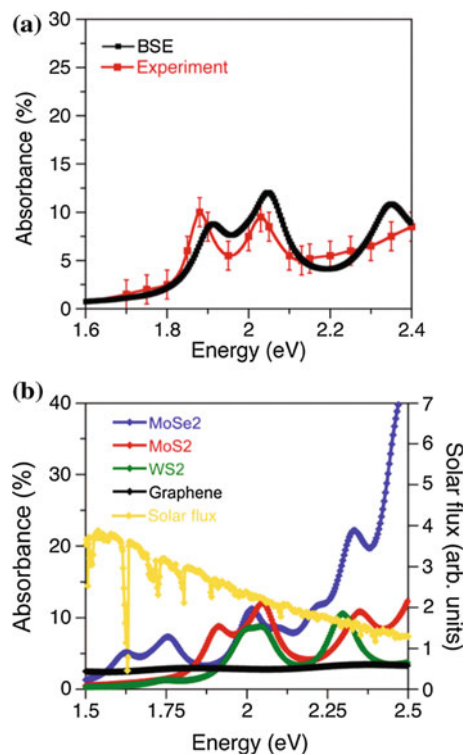


Fig. 6.18 Maps on the Brillouin zone of $|\nabla_k(E_c - E_v)|$ for WS₂ **(a)** and TiS₂ **(b)**, a is the lattice constant [85]. Copyright 2013 by the American Physical Society. Reprinted with permission

Fig. 6.19 Absorbance of TMDC monolayers. **a** Comparison of the computed and experimental absorbance of monolayer MoS₂. The error bars in the experimental curve were taken with an absolute value of $\pm 1.5\%$ due to the presence of a nonzero baseline; **b** Absorbance of three TMDC monolayers and graphene, overlapped to the incident AM1.5G solar flux [88]. Copyright 1984 American Chemical Society. Published with permission



condition when the interaction between the dipole and the cavity photons occurs at a rate that is faster than the average dissipation rates of the cavity photon and dipole, resulting in the formation of new eigenstates that are half-light, half-matter bosonic quasiparticles called cavity polaritons. Incidentally, this phenomenon was also observed in TMDCs [91] (see Sect. 12.6).

6.1.8 Excitonic Effects and Band Gap Renormalization

The term “band gap” generally refers to the energy difference between the CB minimum and VB maximum, which can be determined either by electrical or optical measurements. The band gaps determined from the two types of measurement are usually different because of the excitonic effect. The band gap determined from electrical measurements (sometimes referred to as an electronic band gap) characterizes single-particle excitations and is defined as the sum of the energies needed to separately tunnel an electron and a hole into the system. In optical measurements, on the other hand, the absorption of a photon simultaneously creates an electron in the CB and a hole in the VB, which may bind to form an exciton due to the Coulomb interaction. This means that in optical measurements it is the energy required to create an exciton that is measured (referred to as the optical band gap). The difference between the electronic and optical band gaps corresponds to the binding energy of the exciton, which reflects the strength of the Coulomb interaction. While in conventional semiconductors such as GaAs the exciton binding energy is typically on the order of 10 meV, in TMDCs the exciton binding energy is an order of magnitude larger (see Chap. 9).

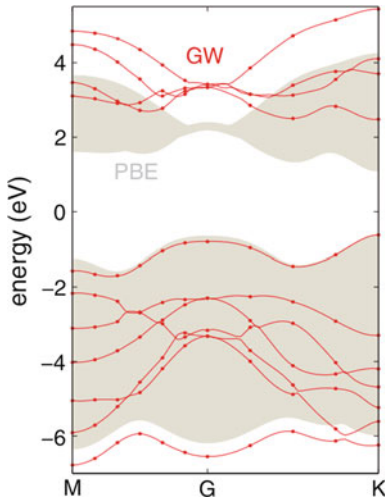
There have been significant efforts to determine band gaps and excitonic effects on TMDC monolayers using first-principles calculations. DFT calculations are known to underestimate the electronic band gap significantly. In order to properly address the issue of exciton using first-principles methods, the GW method that goes beyond DFT and is based on many-body perturbation theory is generally used to obtain the electronic band gap. Here G stands for the one-electron Green’s function and W for the screened Coulomb interaction and their product defines the quasiparticle self-energy corrections. The self-consistent (sc) GW method is usually better than single-shot GW, or G_0W_0 , in obtaining the band structures.

While the quasiparticle picture is generally sufficient to obtain accurate photoemission spectra, it is still inadequate for photoabsorption processes [93] in which electron-hole pairs are created (without actual addition or removal of electrons). This deficiency can be overcome by first treating the quasielectron and quasihole (e.g., within the GW approximation) and then accounting for their interaction by solving the Bethe-Salpeter equation (BSE) for the two-particle Green’s function [93]. The exciton binding energy is obtained by subtracting the optical transition energy from the electronic band gap. Each additional level of theory in the DFT-GW-BSE ladder inevitably increases computational cost [57] (Fig. 6.20).

The issue of quasiparticle band structure calculation and the estimation of large excitonic effects in monolayer TMDCs was first addressed in [5, 57].

As noted earlier, the valence-band edge in TMDCs is split due to SOC, the splitting being largest at the K -point of the Brillouin zone. The conduction-band minimum, which is also at the K -point, is doubly degenerate. Optical transitions between the split valence band and the conduction band give rise to two distinct low-energy peaks in the absorption spectrum, commonly referred to as the A and B excitons [94]. At the PBE level of theory, the valence band in MoS₂ undergoes a spin-orbit splitting

Fig. 6.20 Comparison of the GW (red lines) and the PBE band structures (gray areas) [92]. Copyright 2012 by the American Physical Society. Reprinted with permission



of 146 meV [57]. It was further noted that the spin-orbit splitting is sensitive to the level of theory employed, following the trend $\Delta_{SO}^{PBE} < \Delta_{SO}^{G_0W_0} < \Delta_{SO}^{HSE}$ [57]. Band gaps also vary for various levels of theory and are summarised in Fig. 6.21. The experimentally measured optical gap for MoS₂ is ca. 1.8–1.9 eV.

Absorption spectra from BSE calculations BSE for various TMDC monolayers are displayed in Fig. 9.5. Within the MoX₂ or WX₂ families, one can see a systematic redshift of the *A* and *B* excitonic peaks as the chalcogen species become heavier. While the effective exciton mass increases with heavier chalcogen species, the concomitant increase in dielectric screening is sufficient to lead to a systematic decrease in the exciton binding energy. For a given chalcogen, the choice of metal atom has a smaller influence on the position of the *A* excitonic peak leading to fairly similar transition and exciton binding energies.

The position of the *B* excitonic peak was found to be quite sensitive to the choice of metal atom, which was attributed to much larger SOC effects in W as opposed to Mo. Nevertheless, the *B* excitons are also strongly bound, as may be inferred from Fig. 9.5. Overall, it was concluded that all TMDC monolayers studied universally display the presence of two strongly bound excitons below the direct band gap with excitation energies ranging from 1 to 2 eV. A rather interesting observation is that the GW correction and the exciton binding energy have a comparable value, giving rise to the accidental agreement between the DFT calculated gap and the measured optical gap [48, 50].

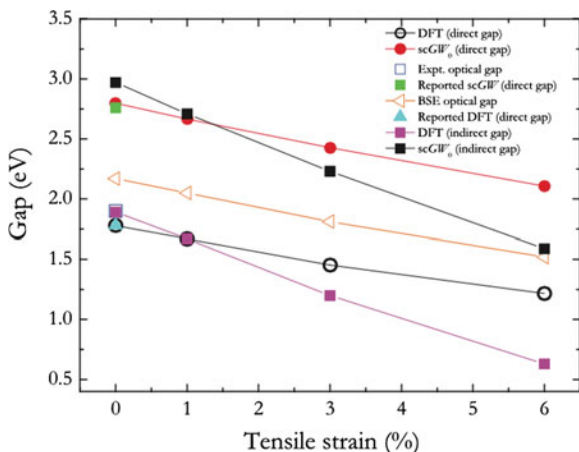
It should be noted that the obtained exciton binding energy depends on the computational details. *k*-sampling not dense enough overestimates the exciton binding energy [13, 23, 48], while finite interlayer separation underestimates the exciton binding energy [23, 92]. It was also noted that a higher energy cut-off and a larger number of bands are needed to obtain better agreement with experiment. Thus,

	Δ_{SO} (meV)			E_g (eV)		
	PBE	HSE	G_0W_0	PBE	HSE	G_0W_0
MoS ₂	146	193	164	1.60	2.05	2.82
MoSe ₂	183	261	212	1.35	1.75	2.41
MoTe ₂	216	344	266	0.95	1.30	1.77
WS ₂	425	521	456	1.56	1.87	2.88
WSe ₂	461	586	501	1.19	1.68	2.42 ^a

^a This direct gap at K is not the lowest quasiparticle gap at the G_0W_0 level; the actual gap is 2.34 eV and is indirect. At the PBE and HSE levels of theory, the gap at K is direct.

Fig. 6.21 Valence-band spin-orbit splitting (Δ_{SO}) at the K -point, and direct electronic band gaps (E_g) at the K -point for various LTMD monolayers at different levels of theory. HSE stands for a hybrid DFT calculation with the Heyd-Scuseria-Ernzerhof exchange correlation potential [57]. Copyright 2012 by the American Physical Society. Reprinted with permission

Fig. 6.22 Band gaps for monolayer MoS₂ obtained by DFT, scGW₀, and BSE together with some of the previously reported data [48]. Copyright 2013 by the American Physical Society. Reprinted with permission



in [50], an excellent agreement with experiment was obtained (1.88 and 2.02 eV for the *A* and *B* excitons in calculations versus 1.88 and 2.03 eV in experiment [1]).

It is also interesting to note that the exciton peak positions only weakly depend on the number of layers, despite the significantly larger band gap in a monolayer, which reflects the significantly smaller exciton binding energy in the bulk (1.1 eV on a monolayer MoS₂ versus 0.13 eV in the bulk [92]).

Quasiparticle band structure and optical properties were also studied in strained monolayers of MoS₂ and WS₂ [48] using self-consistent GW₀ calculations and the BSE equation. It was found that the exciton binding energy was insensitive to the strain while optical band gap decreased with tensile strain, the value of the gap being dependent on the details of the simulations (Fig. 6.22). In addition, it was found that the electron effective masses of monolayer MoS₂, WS₂, MoSe₂, and WSe₂ decreased as the tensile strain increased, with WS₂ possessing the lightest mass among the four monolayer materials at the same strain.

6.1.9 Van der Waals Interaction

Of special interest for TMDCs is computations of vdW interaction. In fact, if the vdW interaction is not taken into account properly, there is no attractive interaction between the layers, i.e. a vdW solid falls apart (in silico) (see e.g. [95]). Despite the recent progress in DFT calculations, inclusion of vdW interactions is not straightforward. In what follows we discuss this issue in more detail following [96].

The problem in describing the vdW interactions is that DFT conventionally applies local approximations, while the vdW interaction is a non-local correlation effect. It was argued that while the local density approximation (LDA) of the exchange-correlation functional sometimes yields reasonably good results for bond lengths and binding energies in layered systems [97], this is accidental and due to the fact that LDA overestimates the range of the exchange interactions, giving rise to an attraction between layers at a larger separation, and not because LDA correctly simulates vdW interactions [98], the latter arise purely from correlation. It was concluded that using the LDA is not the right strategy.

At the same time, the inclusion of vdW interaction is crucial. Without this, using a GGA-PBE level of theory without vdW corrections, one clearly gets unphysical results as illustrated in Fig. 6.23 for hexagonal BN [99]. At the same time, when vdW is taken into account using vdW-DF (see below), the interlayer distance in good agreement with experiment was obtained. Very similar results were obtained for graphite and MoS₂.

In [96], the authors note that the adiabatic-connection fluctuation-dissipation theorem (ACFDT) [100, 101] in principle gives an exact formulation of the exchange-correlation energy within the DFT framework, but requires methods such as the random-phase approximation (RPA) [102], which are computationally very demanding. Several approaches that have been proposed recently to address the issue of vdW

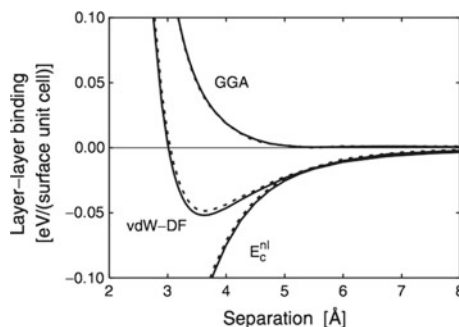


Fig. 6.23 Comparison of the vdW-DF layer-to-layer binding in the staggered bulk hexagonal-BN system (solid lines) and adhesion between two sheets of BN (broken lines) shown as functions of the interlayer separation $d = c/2$. In both descriptions, the GGA gives unphysical results for bond and equilibrium separation. The total adhesion is dominated by the contribution of the vdW interaction E_c^{nl} [99]. Copyright 2003 by the American Physical Society. Reprinted with permission

interactions focusing on methods within DFT that have only moderate additional computational costs were discussed in [96]. One such feasible approach consists of a semi-empirical force-field-based correction to the energy as first proposed by Grimme and is known as DFT-D [103]. The assumption is that the total dispersion interaction can be described as a sum of contributions from all pairs of atoms. The energy contribution is proportional to $C_6 R^{-6}$, where C_6 are the atomic dispersion coefficients. Subsequent improvements are known as DFT-D2 [104] and DFT-D3 [105].

Another approach, called vdW-DF, is based on the ACFDT but makes several approximations. This approach improves traditional density functionals by including, in addition to the LDA correlation energy, a non-local correlation functional that vanishes for uniform electron densities. The choice of exchange functional is not restricted, but it is important that no additional (spurious) attractions are introduced. Generalized-gradient approximation (GGA) functionals are usually used. Recently a functional was proposed that derives the exchange functional using a similar method used to derive the correlation functional. The computational speed of this class of functionals [106–108] is comparable to the empirical schemes.

In [97, 109] a comparative study on a wide variety of layered systems was conducted and it was concluded that among the available schemes ACFDT using RPA gives the best overall results, but at a very high computational cost. The other functionals [102, 104, 110–112], which are computationally less demanding, each has their own advantages and disadvantages, but in general they are not able to provide both good lattice geometries and acceptable binding energies for the entire range of studied materials [97, 109]. This issue must be always kept in mind.

In [113], the most favorable stacking order in bilayer MX₂ was determined within a many-body framework including the RPA, which is the most accurate method to-date, for the structural and energetic properties in comparison with simpler approaches such as DFT-D2, vdW-DF. Five possible high-symmetry stacking orders, which are depicted in Fig. 6.24, were considered. It was found that the most stable configuration was AA', which was by only ≈ 5 meV per formula unit (f.u.) more stable than the AB sequence. The next most stable stacking order was AB', about 20 meV/f.u. less stable than AA'. The remaining high symmetry stackings AA and A'B' were significantly less bounded, by almost 40 meV/f.u. The overall relative stability trend was: AA' \simeq AB > AB' \gg AA \simeq A'B'. The same energy hierarchy was obtained using RPA, DFT-D2, and vdW-DFT. However, the RPA description outperforms the vdW corrected DFT approaches: although the DFT methods with dispersion corrections yielded very good interlayer distances and a correct stability sequence, the values of the binding energy were systematically overestimated [113].

Interestingly, from the calculation of low-frequency Raman modes it was suggested [114] that, although LDA underestimates the interlayer distance in comparison with the vdW-DF functional, the vdW-DF calculation overestimates the phonon frequencies compared with experiment. Considering similar good agreement with experiment that was obtained for LDA calculations on the shear mode in multilayer graphene, it was suggested that, although vdW-DF gives a more accurate descrip-

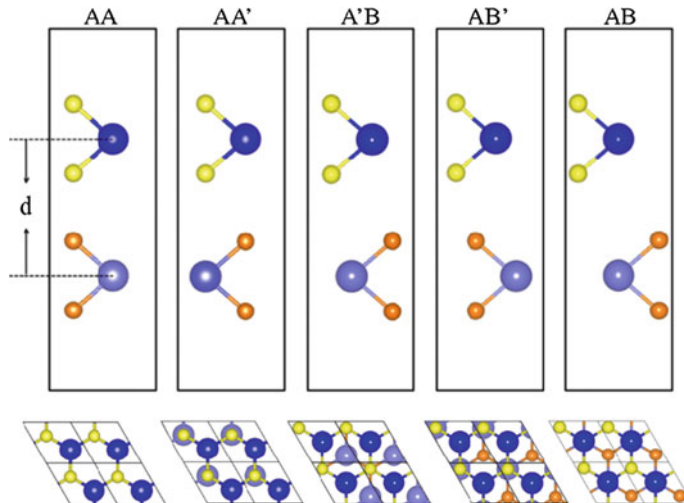


Fig. 6.24 Side (upper panel) and top (lower panel) views of the high-symmetry stacking orders of bilayer MX_2 . Large and small spheres represent the M and X atomic species, respectively. A grayscale (color coding) is used to distinguish the position of the atoms in the two MX_2 layers. The full lines demarcate the unit cell [113]. Copyright 2014 by the American Physical Society. Reprinted with permission

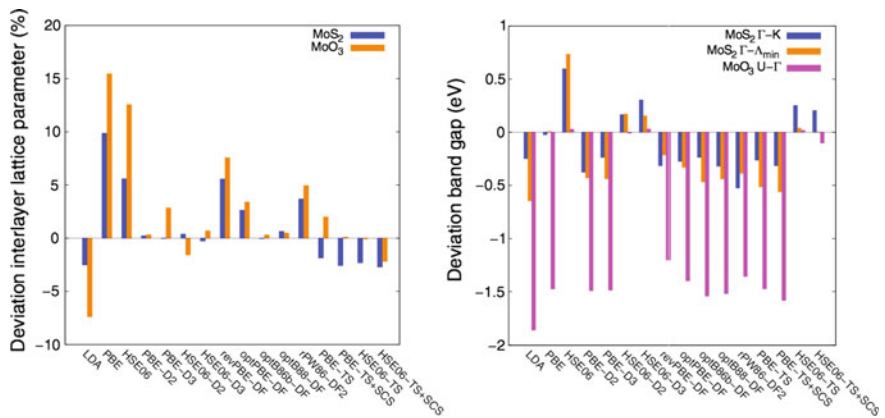


Fig. 6.25 Deviation from the experimental lattice parameter perpendicular to the layers (left) and from the experimentally measured band gaps (right) for MoS_2 and MoO_3 , evaluated using different functionals [96]. Reprinted with permission from IOP Publishing Ltd. The interested readers should see the original work for the description of the functionals

tion of the forces, LDA better describes the derivative of the forces with respect to displacements. In Fig. 6.25 the accuracy of the results obtained by using different functionals are compared.

Apart from the problem of calculating an accurate vdW energy, there is another important issue associated with visualization of vdW interactions. While covalent bonds and lone-pair electrons can be visualized using such methods as maximally localized Wannier functions [115], electron localization function (ELF) [116] or a charge density difference [117], the situation with non-covalent interactions, such as vdW bonding, is more complex and analogous methods for noncovalent interactions are conspicuously missing.

A very appealing approach has been developed in [118–120], using non-covalent interaction (NCI) index plots. This method is based on two parameters: the electron density, ρ , and the reduced-density gradient, s , defined as:

$$s = \frac{1}{2(3\pi)^{1/3}} \frac{|\nabla\rho|}{\rho^{4/3}} \quad (6.6)$$

It was noted that the combination of s and ρ allows a rough partition of real space into bonding regions: high- s low- ρ corresponds to non-interacting density tails, low- s high- ρ to covalent bonds, and low- s low- ρ to non-covalent interactions.

The second ingredient of the NCI index is the classification of interactions as attractive or repulsive according to the sign of the second eigenvalue (λ_2) of the electron-density Hessian matrix. The interested reader is referred to [118] for more details. In brief, the Laplacian of the density, $\nabla^2\rho$ can be decomposed into a sum of contributions along the three principal axes of maximal variation. These components are the three eigenvalues λ_i of the electron-density Hessian (second derivative) matrix, such that $\nabla^2\rho = \lambda_1 + \lambda_2 + \lambda_3$. Analysis of these components has been widely applied to chemical bonding [121]. In particular, the sign of λ_2 distinguishes bonding interactions, where the electron density is locally accumulated with respect to the plane perpendicular to the bond path ($\lambda_2 < 0$) from the non-bonding interactions or steric crowding ($\lambda_2 > 0$). Analysis of the sign of λ_2 thus helps to discern between different types of non-covalent interactions, whereas the density itself provides information about their strength [118].

The convenience of this method is that the only input it requires is the electron density. It was noted that while DFT has a problem in extracting an accurate energy and different computational methods give rather different energetics, they give nearly the same densities, the dominant features of which are quite insensitive to the choice of electronic structure method used in the computations. The NCI method is exemplified in Fig. 6.26a–c, where gradient isosurfaces for a water dimer, a benzene dimer, and graphite are shown. The gradient isosurfaces are colored according to the corresponding values of $\text{sign}(\lambda_2)\rho$, which was found to be a good indicator of interaction strength. Large, negative values of $\text{sign}(\lambda_2)\rho$ (blue) are indicative of attractive interactions (such as dipole-dipole or hydrogen bonding); while if the $\text{sign}(\lambda_2)\rho$ is large and positive, the interaction is non-bonding (red). Values near zero indicate very weak, vdW interactions (green). This approach with respect to TMDCs was first discussed in [122] and is illustrated in Fig. 6.26d.

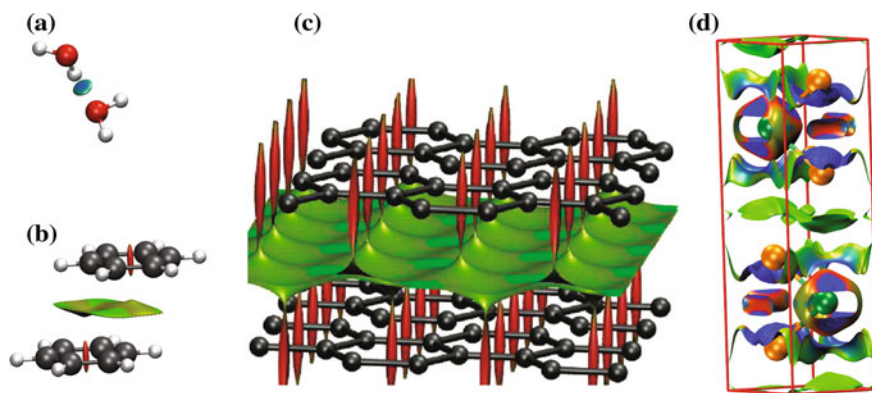


Fig. 6.26 Gradient isosurfaces for (a) water dimer, (b) benzene dimer, and (c) graphite. The surfaces are colored on a *blue-green-red* scale according to values of $\text{sign}(\lambda_2)\rho$. *Blue* indicates strong attractive interactions, *red* indicates strong non-bonded overlap and *green* corresponds to weak vdW interaction. [118]. Copyright 2010 American Chemical Society. Published with permission. Panel (d) shows the application of this approach to MoTe₂ (Mo atoms—*green*, Te atoms—*orange*)

In view of the extreme importance of vdW interactions for TMDCs, we believe that use of NCI index isosurfaces is one of the best methods that has been developed to-date.

6.1.10 Gapless MoS₂ Allotrope

The question may be asked if a MoS₂ monolayer can possess Dirac fermions similar to graphene. This issue was addressed in [123]. The authors constructed a monolayer MoS₂ allotrope, “inspired by recent theoretical and experimental studies of grain boundary atomic structures of monolayer MoS₂” [124–126].

While in the commonly studied monolayer 2H-MoS₂, the transition-metal atoms are located in one sublattice that is sandwiched by two superimposed chalcogenide atomic layers in the other sublattice, at the grain boundaries in addition to six-membered rings, four- and eight-membered rings consisting entirely of heterobonds (S-Mo) were found [125] (see Sect. 5.3.2). Based on the experimentally observed stable grain-boundary structures, a monolayer MoS₂ (Fig. 6.27) was constructed by repeating the square-octagon pairs in a square lattice (abbreviated *so*-MoS₂ to distinguish from the normal hexagonal lattice). The primitive cell of this structure is square with *p4* symmetry, containing four Mo and eight S atoms. The optimized structure of *so*-MoS₂ had a lattice constant of 6.36 Å. The thickness of the monolayer was 3.12 Å, similar to that of 2H-MoS₂. There were structural distortions in *so*-MoS₂ because of the square-octagon topology: the Mo-S bonds that constitute the square (labelled 1 in Fig. 6.27a) were stretched to 2.46 Å, while the Mo-S bonds that link

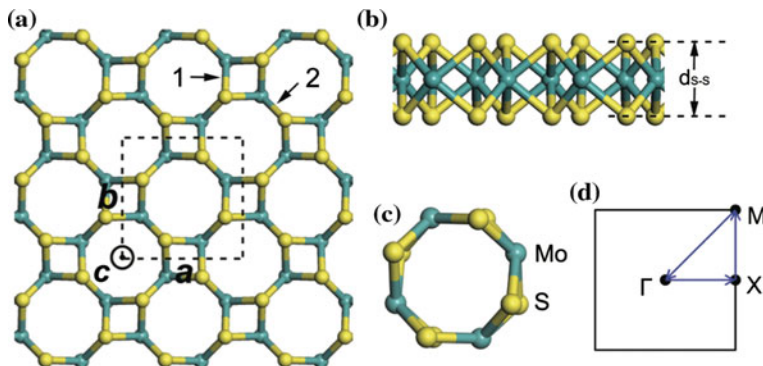


Fig. 6.27 **a** Top view and **b** side view of *so*-MoS₂. The dashed-line square and bold italic text **a**, **b** and **c** in panel (a) indicate the primitive cell, which is also highlighted in panel (c) and the three lattice-vector directions, respectively. **(d)** The first Brillouin zone of *so*-MoS₂ with letters designating special points and the lines for band-structure calculation [123]. Copyright 2014 by the American Physical Society. Reprinted with permission

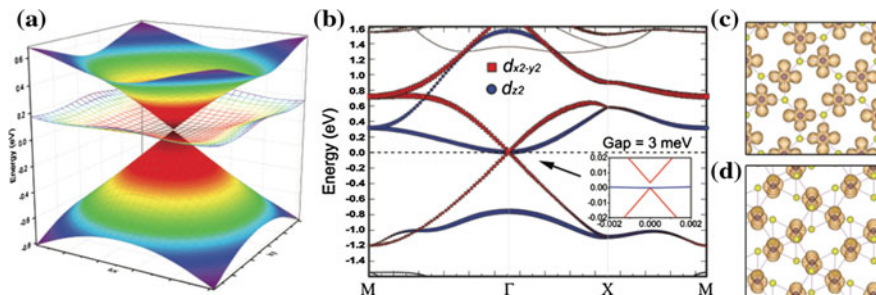


Fig. 6.28 **a** Dirac cone formed in the vicinity of the Dirac point. **b** Electronic band structures of *so*-MoS₂. **c**, **d** Charge-density plots of the $d_{x^2-y^2}$ and d_z^2 orbitals of Mo, respectively (electron orbital isosurface level of 0.01\AA^{-3}) [123]. Copyright 2014 by the American Physical Society. Reprinted with permission

the squares (labelled 2 in Fig. 6.27a) were compressed to a length of 2.39 Å. For comparison, the Mo-S bond in 2H-MoS₂ is 2.42 Å [123].

In order to assess the stability of the *so*-MoS₂-based Dirac fermion system, its formation energy was calculated and it was found to be ca. 0.3 eV/atom less stable than 2H-MoS₂. The thermal stability of the phase was examined by calculating the phonon dispersion relations and it was found that there are no imaginary frequencies in the whole phonon spectrum, indicating that *so*-MoS₂ is structurally stable. It was suggested that a possible approach to realize *so*-MoS₂ could be to use specific substrates.

The electronic band structure of *so*-MoS₂ is shown in Fig. 6.28b. The valence band, conduction band, and conduction band +1 (VB, CB, and CB +1) approach the Γ point at E_F . The slopes of VB are -16.0 eV \AA (X to Γ) and $+15.4 \text{ eV \AA}$ (M to Γ),

respectively. The upper cone (from CB +1) locates 3 meV above E_F at the Γ point. The slopes of the CB +1 branch are +15.6 eV Å (X to Γ) and -15.5 eV Å (M to Γ), respectively. The Fermi velocity (v_F) of the Dirac fermions was also calculated by using v_F , which was about $2.3\text{--}2.4 \times 10^6$ m/s, comparable to that of graphene [127], but an order of magnitude higher than that of hexagonal silicene and germanene monolayers [128]. The CB deviates from the linear slope and is flattened, indicating the coexistence of heavy fermions. The effective mass of the heavy fermion are $1.11 m_e$ (X to Γ) and $1.78 m_e$ (M to Γ), respectively. In panel (a) a three-dimensional (3D) plot of the conduction and valence bands is shown, indicating massless Dirac fermions.

It was found that in real space, the four pear-shaped lobes of in-plane $d_{x^2-y^2}$ orbitals spread in the *so*-MoS₂ plane and have centers on the a and b lattice axes, (Fig. 6.28c), fully compatible with the square lattice symmetry, leading to the formation of a Dirac cone. At the same time, the two more localized pear-shaped regions of out-of-plane d_{z^2} orbitals result in heavy fermions [123].

6.2 Experimental Studies

6.2.1 Optical Gap

Optical band gaps can be determined from either absorption edge or photoluminescence measurements [129]. The choice of the technique is determined by the materials in question. For example, in the case of a large Stokes shift, such as in chalcogenide glasses, the PL peak is located around the middle of the gap [130–132], and is not a reliable method of gap determination. On the other hand, in TMDCs, the PL is usually taken as a measure of the optical gap.

The absorption spectra of monolayer MoS₂, MoSe₂, WS₂, and WSe₂ thin films are displayed in Fig. 5.33e–h. The absorption spectra can be divided into a region at low energy that is dominated by excitonic transitions on a relatively low absorption background and a region of strong absorption at higher energies. For all monolayer TMDCs, excitonic absorption peaks *A* and *B*, originating from the spin-split direct gap transitions at the K -point of the Brillouin zone were clearly observed.

It was proposed that there is a correlation between the exciton binding energy and band gap energy in monolayer TMDCs that can be described as $E_b^{2D} = 0.18$ eV + $6.4 \times 10^{-3} E_g^4$, which was interpreted in terms of the Penn gap [133] where the dielectric constant of a semiconductor is related to the band gap [134]. It was further noted that for monolayer TMDs, the valence-band spin-orbit splitting at the K -point correlates with the average atomic number as $\Delta_{SO} = 115$ eV + $6.0 \times 10^{-4} Z_{av}^4$ [135].

Light absorption by excitons and trions in monolayers of MoS₂ was also studied in [136]. A typical broadband absorption spectrum of MoS₂ monolayers obtained at 5 K is shown in Fig. 6.29a. Two large excitonic resonances, labeled *A* and *B*, are clearly visible at ca. 1.9 and ca. 2.1 eV, respectively. A smaller absorption peak,

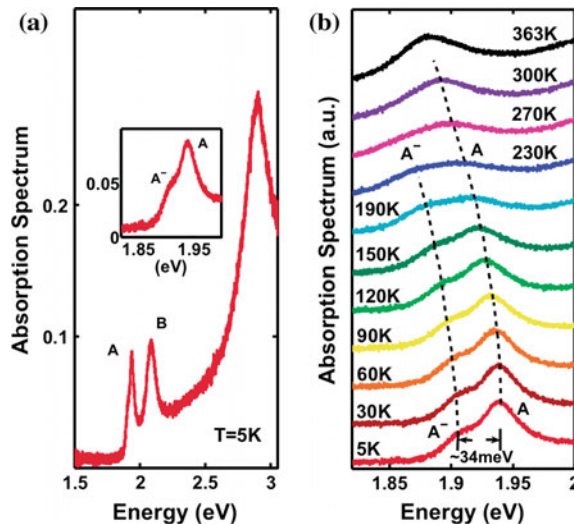


Fig. 6.29 **a** Measured broadband absorption spectrum of a MoS_2 monolayer at $T = 5\text{ K}$ is plotted. Two main absorption resonances, A and B , attributed to excitons are visible together with a smaller A^- attributed to trions. The inset shows the A and A^- peaks in greater detail. **b** Measured absorption spectrum of a MoS_2 monolayer near the A and A^- peaks is plotted for different temperatures. The curves for different temperatures are given offsets in the vertical direction for clarity. The A^- trion absorption peak is clearly visible and distinguishable from the A -exciton absorption peak for all temperatures below 230 K . The dashed lines are guides to eyes showing the evolution of the exciton (A) and trion (A^-) peaks as a function of temperature [136]. Copyright 2014 by the American Physical Society. Reprinted with permission

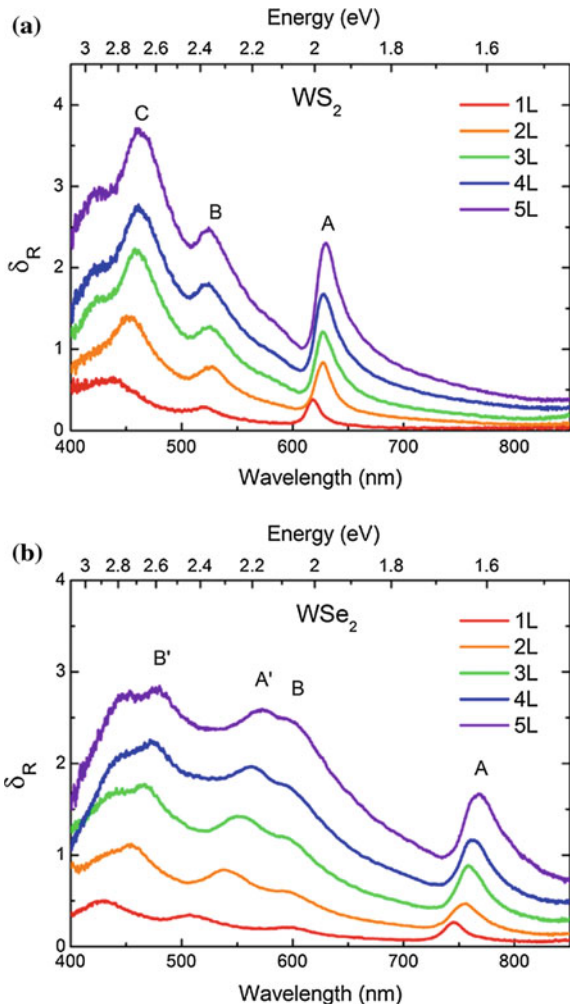
labeled A^- , is also visible near the A peak and is attributed to trion² absorption. Panel (b) shows absorption spectra for a MoS_2 monolayer near the A and A^- peaks for different temperatures in the $5 - 363\text{ K}$ temperature range. The splitting in the exciton and trion absorption peaks is ca. 34 meV at 5 K and does not change much as the temperature is increased to 230 K , at which temperature the two peaks merge.

Individual layers of TMDCs are excellent light absorbers [84, 88] despite being atomically thin. Absorption spectra of MX_2 ($M = \text{Mo}, \text{W}$ and $X = \text{S}, \text{Se}$) consist of characteristic peaks due to excitonic resonance and interband transitions. Recent ab-initio studies attributed the strong light-matter interaction to ‘band nesting’, which gives rise to singularity features in the joint DOS [85].

Absorption features for bulk crystals have been discussed earlier [137, 138] (see Sect. 3.2.1). Measuring absorption directly for samples less than 1 nm in thickness is not possible. For atomically thin layers supported by a transparent substrate, differential reflectance provides an effective measure of absorbance. The fractional change in reflectance δ_R for a thin layer sample relative to the reflectance of a dielectric sub-

²Trions are described later in this volume (Chap. 9).

Fig. 6.30 Differential reflectance spectra of mechanically exfoliated (a) 2H-WS₂ and (b) 2H-WSe₂ flakes consisting of 1–5 monolayers [139]. Copyright 2012 American Chemical Society. Published with permission



strate with refractive index of n_{subs} is related to the absorbance A of the material by

$$\delta_R(\lambda) = \frac{4}{n_{subs}^2 - 1} A(\lambda) \quad (6.7)$$

where n_{subs} is assumed to be wavelength independent in the spectral region of interest.

Figure 6.30 shows the differential reflectance spectra of one to five monolayer thick WS₂ and WSe₂ [139]. General features of the peaks are in good agreement with the previously reported results for the bulk phases [137, 138]. All peaks exhibit a gradual blueshift with decreasing thicknesses. Excitonic absorption peaks A and B , which arise from direct gap transitions at the K -point, are located around 625 and

550 nm for WS₂ and around 760 and 600 nm for WSe₂. The energy difference between the *A* and *B* peaks, which is an indication of the strength of SOC, is approximately 400 meV for both materials in reasonable agreement with earlier simulations [57].

The corresponding value for MoS₂ (ca. 160 meV) is significantly smaller [1, 16].

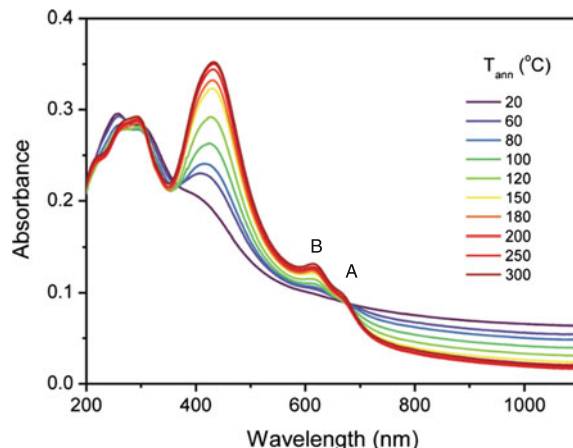
For WS₂, an additional peak, previously labeled as *C*, is observed around 450 nm. This peak was attributed [139] to optical transitions between the density of states peaks in the valence and conduction bands [47]. The WSe₂ spectra show more additional features attributed to greater overlap of Se *p* orbitals with W *d* orbitals as well as those of adjacent layers [137, 138]. The absorption peaks *A'* and *B'* are believed to be excitonic in nature and arise from the splitting of the ground and excited states of *A* and *B* transitions, respectively, due to inter- and intralayer perturbation of the *d* electron band by the Se *p* orbitals [137, 138].

Figure 6.31 shows the evolution of the optical absorption spectrum of chemically exfoliated MoS₂ upon annealing. The as-produced films that have the 1*T'* structure and do not show *A* and *B* excitons peaks characteristic of pristine 2*H*-MoS₂. The free-carrier-like broad absorption that continues toward the near-IR region below the optical gap of 2*H*-MoS₂ reveals the predominantly metallic character of the material. The emergence of the characteristic *A*, *B*, and *C* (not marked in Fig. 6.31) exciton features of 2*H*-MoS₂ upon annealing indicates the gradual restoration of the 2*H* phase [140].

6.2.1.1 Photoluminescence

Photoluminescence was the first technique that experimentally demonstrated the indirect-to-direct gap transition in MoS₂ upon thinning the sample to a monolayer. This conclusion was drawn from a drastic (by more than an order of magnitude) increase in the PL intensity as the sample thickness changed from a bi-layer to a

Fig. 6.31 Absorption spectra of MoS₂ thin films obtained by Li-intercalation and subsequently annealed at various temperatures [140]. Copyright 2011 American Chemical Society. Published with permission



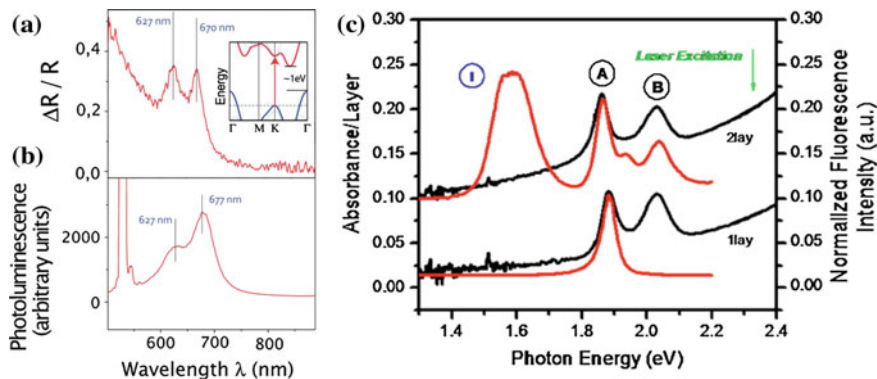


Fig. 6.32 Reflection (a) and photoluminescence (b) spectra of ultrathin MoS₂ layers. The inset schematically shows the bulk MoS₂ band structure [16] Copyright 2010 American Chemical Society. Published with permission; c Absorption spectra (left axis) normalized by the layer number N in the photon energy range from 1.3 to 2.4 eV. The corresponding PL spectra (right axis, normalized by the intensity of the peak A) [1]. Copyright 2010 by the American Physical Society. Reprinted with permission

monolayer and was also confirmed by DFT simulations [1, 16]. PL in monolayer and few-layer TMDCs is discussed in detail in a dedicated chapter (see Chap. 8).

The PL peak positions agree very well with the excitonic peaks obtained in the absorption measurements, as illustrated in Fig. 6.32. In addition to the A and B excitons, a peak C located at higher energy was also observed and attributed to band nesting [87].

6.2.1.2 Photocurrent Spectroscopy

An alternative way to study optical absorption is photocurrent spectroscopy. Since photocurrent is proportional to the number of photo-generated charge carriers, it is directly linked to optical absorption. Photocurrent spectroscopy was applied to characterise excitonic states in various TMDCs. An example of such studies is presented in Fig. 6.33, that shows the photocurrent spectra alongside with the excitonic peak positions and band gap values for variable number of layers of MoS₂ and also compares E_g , E_b , and SOC strengths for different monolayer-TMDCs [141].

In addition to the A and B excitons, a strong peak attributed to C exciton was observed and it was noted that this feature ca. 2.9 eV has been previously observed in the absorption spectrum of MoS₂ [1, 13, 140], but not thoroughly analyzed. This peak was interpreted as coming from an excitonic state associated with the van Hove singularity of 1L-MoS₂. This van Hove singularity is peculiar, as neither the conduction nor the valence bands have singularities in the density of states in the corresponding region of the Brillouin zone. At the same time, the bands are locally parallel in that region [141], a situation known as band nesting (see Sect. 6.1.7). The same interpretation of the C peak has been proposed in [87] (see above).

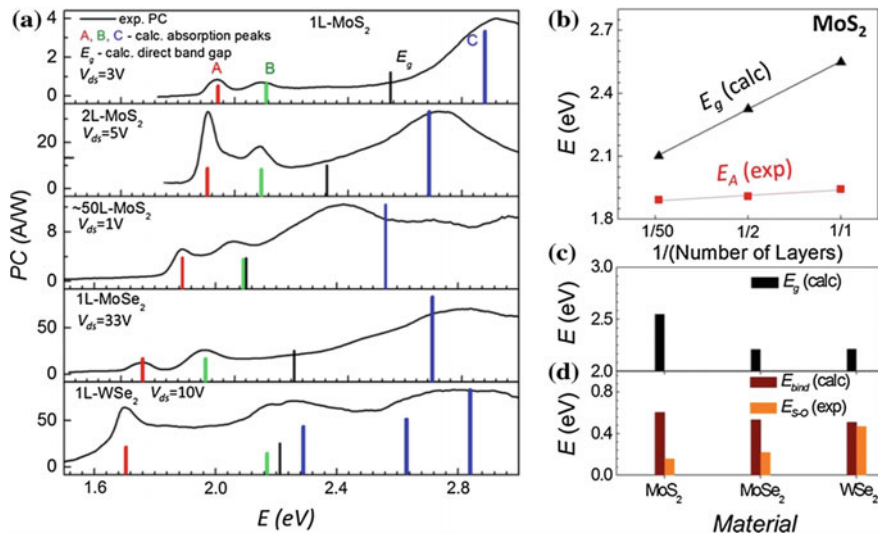


Fig. 6.33 **a** Experimental photocurrent spectra of different TMDC devices. All the devices are suspended and annealed except for the multilayer MoS₂ device, which is supported on a glass substrate. For each device, the bias voltage was chosen to maximize the signal to noise ratio for the photocurrent. *Solid* bars are calculated excitonic peaks and band gap values. *Large* SOC of WSe₂ results in splitting of the valence and the conduction bands even near the *C*-point, which leads to splitting of the *C*-peak. **b** Dependence of excitonic peak positions and band gap values on the number of layers of MoS₂. **c**, **d** Comparison of E_g , E_b and SOC strengths for different 1L-TMDCs. Reproduced from [141]

6.2.2 Electronic Gap

The electronic band gap can be measured using scanning tunneling spectroscopy (STS) and the band structure can be studied using angle-resolved photoemission spectroscopy (ARPES). The available results are summarized below.

6.2.2.1 Scanning Tunneling Spectroscopy

For monolayer MoS₂ on highly ordered pyrolytic graphite (HOPG), STS measurements give an electronic band gap of 2.15 or 2.35 eV at 77 K depending on the choice of threshold value of tunneling current [142]. For comparison, a PL measurement on the same sample gives an optical gap of 1.93 eV at 79 K. For WSe₂ and WS₂ monolayers on HOPG, the STS measurement shows an electronic band gap of 2.51 eV and 2.59 eV respectively at 77 K [143]. For monolayer MoSe₂ grown by molecular beam epitaxy (MBE) on bilayer graphene, the STS-determined electronic band gap is 2.18 eV at 5 K, while PL shows an optical gap of 1.63 eV at 77 K [144]. MoSe₂ grown by MBE on a HOPG substrate shows a similar electronic band gap of

2.1 eV in the STS measurement [145]. For MoTe₂, a gap of 0.96 eV was obtained at 77 K [25].

It is interesting to note that when similar measurements were performed on MoS₂ on gold, the obtained value of the excitonic was 1.8 eV [146], i.e. significantly lower than the value of 2.15 eV on HOPG [142]. The difference was attributed to the presence of Au donor states [146].

Scanning tunnelling microscopy and STS measurements were also performed for monolayer and bilayer WSe₂ [147], where a band gap of ca. 2.21 eV was found in monolayer WSe₂, which is much larger than the energy of the photoluminescence peak, indicating a large excitonic binding energy. Using Fourier transform STS, the energy was mapped versus momentum dispersion relations for monolayer and bilayer WSe₂. Further, by tracking allowed and forbidden scattering channels as a function of energy, the spin texture of both the conduction and valence bands was inferred. A large spin-splitting of the valence band due to strong spin-orbit coupling, and spin-valley-layer coupling in the conduction band of bilayer WSe₂ were observed [147].

For an example of STS measurements and for a comparison of STS and PL gap measurements on the same sample see Fig. 6.42.

In the interpretation of the STS measured gap, a possible complication is that Γ_v and Q_c have much larger weight in the scanning tunneling spectra than K_v and K_c [144] due to the larger density of states as well as the larger tunneling coefficient at Γ_v and Q_c . The latter is due to the fact that the wavefunctions at Γ_v and Q_c have a nonnegligible component from X p orbitals that are closer to the STM tip, which may obscure the attribution of the band edge [26].

It was subsequently noted [148] that using a constant tip-to-sample distance Z makes some critical points difficult to access and a combination of the constant and variable Z spectroscopies was used to analyze the electronic structure including quasiparticle gap, critical-point energy location, and their origins in the Brillouin zone. Using this approach, it was argued that monolayer WSe₂ is in fact an indirect gap material with the CB minimum located at the Q-point (and not at the K point), albeit the two states were found to be nearly degenerate.

STS measurements on samples with a varying number of MoSe₂ layers on top of bi-layer graphene (BLG) found a systematic decrease in the band gap with increasing number of layers [149], the obtained values were 2.18, 1.56, and 1.32 eV, for a monolayer, bi-layer and tri-layer structures, respectively (Fig. 6.34a). A similar result was obtained for MoS₂ [150] (Fig. 6.34b).

Another interesting observation was made in [150] regarding the effect of grain boundaries on the band gap. This is illustrated by a series of STS spectra that were taken across the grain boundary (Fig. 6.35), where in panel (a) triangles mark the positions where the spectra shown in panel (b) were recorded. One can see that the band gap sizes vary with the distance from the grain boundary, decreasing from the intrinsic 2.40 eV at $d > 4$ nm to 1.55 eV at $d = 0$ nm, d being the distance from the grain boundary [panel (c)]. It was further found that the decrease in the gap size depended on the grain misorientation, being as large as 0.85 eV when the

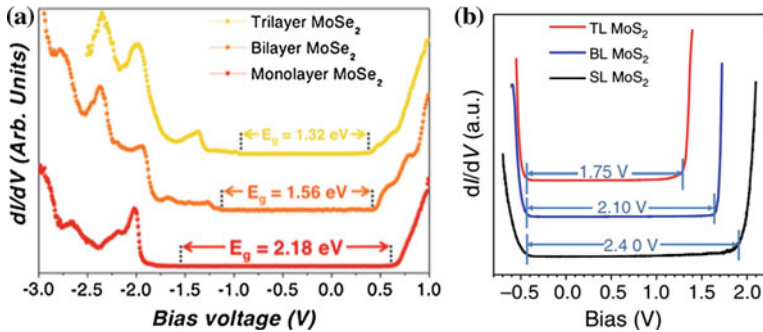


Fig. 6.34 **a** STS spectra ($T = 5$ K) obtained for (a) monolayer MoSe₂/BLG (lock-in wiggle voltage: $\Delta V_{rms} = 4$ mV, $f = 872$ Hz, set point current: $I_t = 5$ nA), **b** bilayer MoSe₂/BLG (lock-in wiggle voltage: $\Delta V_{rms} = 5$ mV, $f = 871$ Hz, set point current: $I_t = 100$ pA), and (c) TL MoSe₂/BLG (lock-in wiggle voltage: $\Delta V_{rms} = 5$ mV, $f = 871$ Hz, set point current: $I_t = 5$ nA) [149]. **(b)** dI/dV spectra taken at the SL, BL and TL MoS₂, respectively, reveal band gap decrease with the increasing thickness (set point: $V_{Tip} = 1.5$ V, $I_{Tip} = 80$ pA) [150]. Reprinted by permission from Macmillan Publishers Ltd., copyright (2015)

misorientation between the two neighbouring grains was 18° , but only 0.17 eV when the misorientation was 3° .

6.2.3 Spin-Orbit Coupling

An effective way of detecting the spin-orbit interaction is magneto-transport measurements. Such experiments were performed on WSe₂ to probe the spin relaxation processes [151] through weak (anti-)localization detection. In a few words, weak localization is a physical effect that occurs in disordered electronic systems at very low temperatures. The effect is quantum-mechanical in nature and has the following origin: in a disordered electronic system, the electron motion is diffusive rather than ballistic, i.e. an electron experiences a series of random scattering off structure imperfections. Of special interest are closed paths, when, as a result of several scattering acts, the electrons return to the same place. Such paths can be neglected in 3D systems but become important in 2D systems. An electron can go along such a path in two opposite directions and because an electron is a quantum-mechanical particle, the contributions are not a simple sum but an interference effect. In case of elastic scattering, the phase is not changed and the interference is constructive, i.e. the probability of an electron to come back is increased. The effect is called weak localization and manifests itself as a positive correction to the resistivity. Application of an external magnetic field breaks the degeneracy between the two paths, decreasing the interference and leading to an increase in conductivity.

In a system with (strong) SOC the spin of a carrier is coupled to its momentum. As a result, the spin of the carrier rotates as it goes around a self-intersecting path,

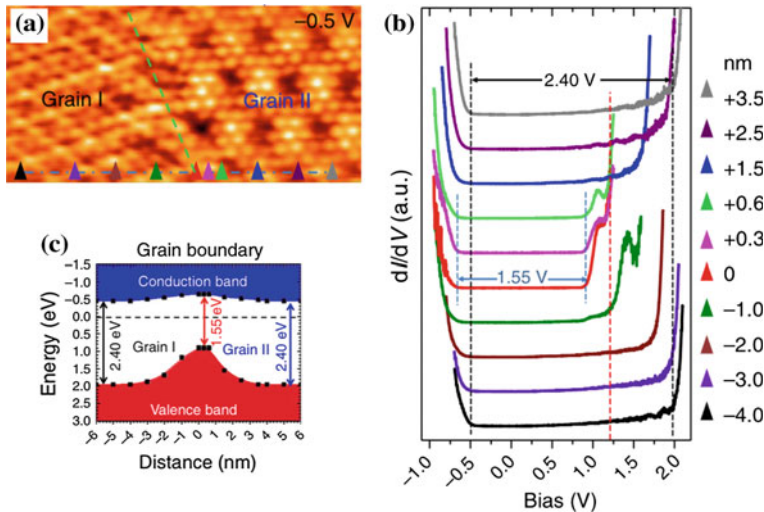


Fig. 6.35 Band-gap tunability at grain boundaries. **a** Bias-dependent image recorded at the grain boundary at $V_{Tip} = -0.5\text{ V}$. **b** dI/dV spectra recorded at the positions denoted by the triangles in panel **a**. The variation of the band gap with distance from the boundary is quite pronounced. **c** Schematic diagram showing the band gap change at the grain boundary. Reproduced from [150]

and the direction of this rotation is opposite for the two directions about the loop. Consequently, the two paths along any loop interfere destructively which leads to a lower net resistivity and called weak *anti*-localization. The external magnetic field has the opposite effect, viz., the conductivity is decreased with magnetic field producing a cusp-like peak.

Experimentally, the effect was studied using an electric-double-layer transistor structure [151] by varying the gate voltage V_G . Figure 6.36 shows the V_G variation of normalized magnetoconductance for a magnetic field applied perpendicular to the interface. For $|V_G| < 3.0\text{ V}$, a positive magnetoconductance, indicating a dominant weak localization, was observed. By changing the gate voltage V_G from -3.5 V to -6 V , a sharp magnetoconductance peak, initially appearing as a spike feature, quickly starts to grow around $H = 0$, which is a characteristic feature of the weak anti-localization regime, where owing to the dominance of SOC, the carriers travelling along the time-reversed closed loops interfere destructively, leading to the quantum enhancement of conductivity.

SOC in monolayer MoS₂ was also revealed using triply resonant Raman scattering [152].

Fig. 6.36 Electric field modulation of magnetoconductance. A clear WL-to-WAL crossover occurs as negative gate voltage V_G increases. The vertical arrows labelled ‘0.01’ indicate the scale of relative conductance [151]. Reprinted by permission from Macmillan Publishers Ltd., copyright (2013)

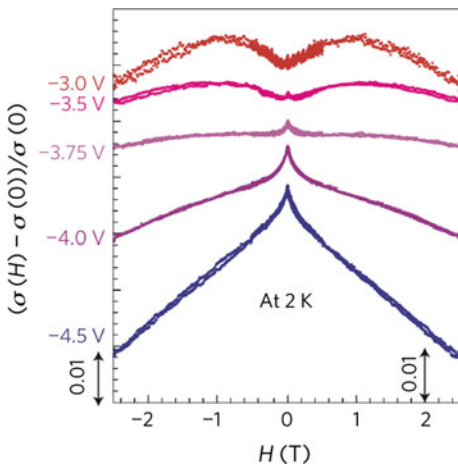
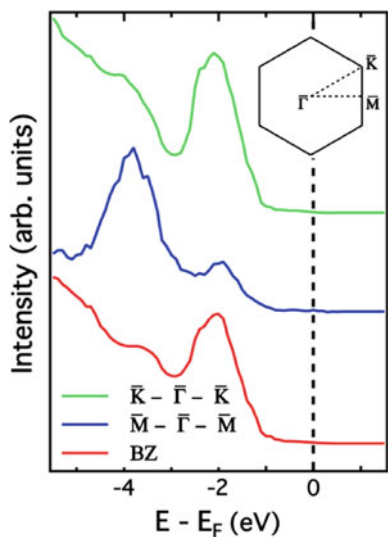


Fig. 6.37 Angle-integrated photoemission spectra of exfoliated monolayer MoS₂ extracted from high-symmetry directions of the Brillouin zone and over the full Brillouin zone. *Inset* shows the Brillouin zone of monolayer MoS₂ [54]. Copyright 2013 by the American Physical Society. Reprinted with permission



6.2.4 ARPES Measurements

Direct measurements of the band structure of few-single layered TMDC can be performed by ARPES. In [54], the evolution of the thickness-dependent electronic band structure of MoS₂ of mechanically exfoliated and CVD-grown crystals was investigated for bulk samples and also for samples ranging in thickness from 3 layers to a single monolayer.

Shown in Fig. 6.37 are angle-integrated photoemission spectra of exfoliated monolayer MoS₂ that were acquired along high-symmetry directions and also over the full

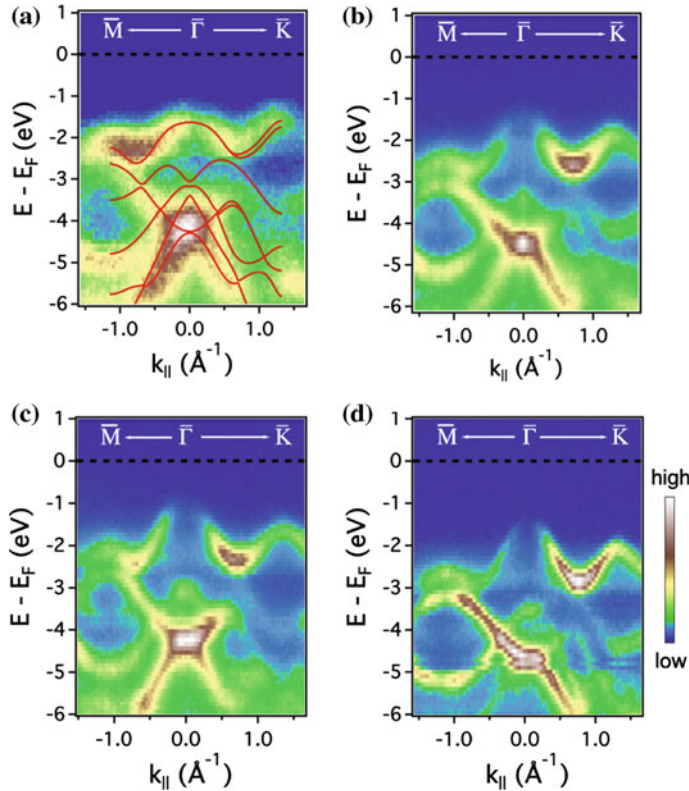


Fig. 6.38 **a** ARPES band map of exfoliated monolayer MoS₂ along the $M - \Gamma - K$ high symmetry lines. DFT band calculations adapted from [51] (solid red lines) are overlaid onto it for comparison. **b–d** ARPES band maps of exfoliated bilayer, trilayer, and bulk MoS₂, respectively [54]. Copyright 2013 by the American Physical Society. Reprinted with permission

Brillouin zone. The strong peaks at binding energies of 2 and 4 eV, i.e., the main states probed here, were assigned to Mo 4d states.

Figure 6.38a–d shows the evolution of band structure along the high-symmetry directions of the Brillouin zone with thickness for exfoliated single layer, bilayer, trilayer, and bulk MoS₂, respectively. The band structure of a monolayer is in agreement with DFT band calculations with spin-orbit interaction taken into account [51]. The most distinct features include the VB maximum at the Γ and M points originating from Mo d_{z^2} orbitals, the VB maximum at the K -point induced by Mo $d_{x^2-y^2}/d_{xy}$ orbitals, and a saddle point at binding energy 4 eV, as derived from $d_{x^2-y^2}/d_{xy}$ orbitals [29, 153]. In the few-layer and bulk MoS₂ the VB maxima at the K -point were found to be all lower than that at the Γ -point, providing experimental support for the indirect-to-direct band gap transition in going from few-layer to monolayer MoS₂.

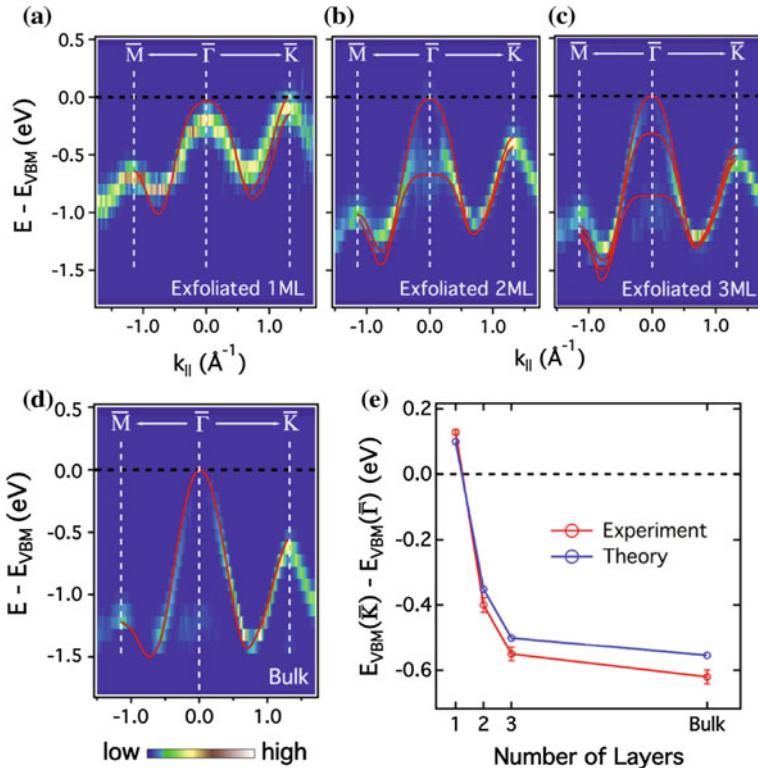


Fig. 6.39 **a–d** 2D curvature intensity plots of the low energy valence band of exfoliated monolayer, bilayer, trilayer, and bulk MoS_2 , respectively. Red curves are the corresponding DFT calculated bands. **e** Thickness dependence of the energy difference between VB maximum at the K and Γ points. The theoretical and experimental results are plotted together for comparison [54]. Copyright 2013 by the American Physical Society. Reprinted with permission

The authors further extract the ARPES features of the upper VB along $M - \Gamma - K$ high-symmetry line using 2D-curvature analysis [154] (Fig. 6.39a–d) [54]. The upper VB of exfoliated 1–3 ML and bulk MoS_2 closely match the corresponding calculated bands. These results provide further experimental evidence that the VB maximum at the K -point and Γ shifts upwards in energy relative to that of the K -point as the number of layers increases. The thickness dependence of the energy difference between the VB maximum at the K and Γ points is shown in Fig. 6.39e.

This evolution in band structure, attributed to changes in quantum confinement as the number of layers increases, was interpreted as follows. The VB maximum at the K -point is derived from the localized in-plane Mo $d_{x^2-y^2}/d_{xy}$ orbitals and is unlikely to be affected by the quantum confinement in the z direction. On the other hand the VB maximum at the Γ -point originates from the rather delocalized out-of-plane Mo d_{z^2} orbitals and S p_z orbitals and is lowered in energy when interlayer interactions decrease in decreasing number of layers.

It was noted that the VB maximum of monolayer MoS₂ at the Γ -point is relatively flat compared with its bulk counterpart, indicating a substantially larger effective mass of holes in the monolayer. The experimental hole effective mass at the Γ -point was estimated to be $(2.4 \pm 0.3)m_e$ (m_e being the electron mass) in monolayer MoS₂, which is in agreement with a theoretical prediction (ca. $2.8 m_e$) [155]. For the bulk, a value of $(0.67 \pm 0.01)m_e$ was obtained, which, again, is very close to the theoretically predicted value of $0.62 m_e$ [155]. At the same time, the hole effective mass at the K -point from bulk to monolayer MoS₂ only slightly increases. It was proposed that this difference evidently explains the relatively poor carrier mobility ($< 10 \text{ cm}^2/\text{V}\cdot\text{s}$) [156] of monolayer MoS₂ compared to that of bulk ($50 - 200 \text{ cm}^2/\text{V}\cdot\text{s}$ at room temperature) [157]. Similar measurements were performed on CVD-grown monolayer MoS₂ and qualitatively similar results were obtained [54].

ARPES measurements on monolayers of MoS₂ on HOPG were subsequently performed by a different group [158], where spin-orbit splitting of the valence band was detected.

ARPES measurements were also performed on atomically thin epitaxial MoSe₂ layers (from a single monolayer to 8 monolayers) [6]. In the studies of the VB maximum it was found that in the spectra from the monolayer MoSe₂ film, the VB maximum at the K -point was significantly higher than the Γ point valence band, while in bilayer and thicker films, the VB maximum switched to the Γ point.

Another interesting observation was a clear band-splitting of the VB maximum at the K -point of the monolayer MoSe₂ film, with a similar band-splitting also observed in bilayer, trilayer and 8 ML MoSe₂ films. Based on DFT calculations, the authors attribute this splitting to the strength of the SOC. For an odd number of layers, there is no inversion symmetry, and each state at the K -point is spin-nondegenerate. At the same time, for an even number of layers, inversion symmetry is restored, and every state becomes spin-degenerate. Each spin split state was predicted to be nearly 100% spin-polarized.

The authors [6] further used potassium doping to raise the chemical potential of the samples, which enabled them to observe how the conduction band (CB minimum) dropped below the Fermi level (Fig. 6.40b). Figure 6.40c, d shows constant energy maps at the CB minimum (Fig. 6.40b) and VB maximum (Fig. 6.40a). One can see that both the CB minimum and VB maximum are located at the K -points in the Brillouin zone with no photoemission intensity observed at the Γ point, a result implying the presence of a direct band gap at the six K -points in monolayer MoSe₂. The measured direct band gap was 1.58 eV, which is very close to the value of 1.55 eV reported by a photoluminescence experiment in mechanically exfoliated monolayer MoSe₂ [159].

We would like to note here that ARPES measurements are supposed to yield the electronic band gap. Hence the obtained value similar to the optical gap in the heavily doped sample can be attributed either to a large band gap renormalization due to screening or the structure could have changed as a result of K-doping.

Figure 6.40e, f shows the second-derivative spectra of undoped and potassium-doped 8 ML MoSe₂ films, respectively. In contrast to the monolayer MoSe₂ film, in the 8 ML MoSe₂ film while the CB minimum is still at the six K -points (Fig. 6.40g),

the VB maximum is located at the Γ point (Fig. 6.40h), i.e., the 8 ML MoSe₂ possesses an indirect band gap of 1.41 eV (Fig. 6.40f).

Bulk MoSe₂ ARPES measurements were also reported in [158], where the authors succeeded in observing trigonal warping near the K -point. They note that trigonal warping has been theoretically predicted for monolayer TMDCs [60, 160].

Potassium doping was subsequently also used to characterize K-intercalated MoS₂ [17]. In this case, potassium was first deposited on the surface and is believed to have subsequently intercalated into the structure of MoS₂ resulting in the formation of a quasi-freestanding MoS₂ monolayer. Due to the shift in the Fermi level caused by potassium doping, it was possible to observe both the VB maximum and CB minimum, both located at the K -point with a direct gap of ca. 1.86 eV (Fig. 6.41). Similar measurements for MoSe₂ were reported in [158], where the authors concluded that adsorption of alkali metals on the surface of bulk MoSe₂ results in the formation of quantum well states due to the formation of a nearly free layer rather than electron doping and providing access to the conduction band, thus challenging the conclusions of [6].

It should be noted here that Li-intercalation causes a transformation of the monolayer structure from 2H to 1T, which is explained by charge transfer (see Sect. 5.1.2). K-doping, that is also very effective for liquid exfoliation [161], would normally be expected to produce the same effect. This issue has not been considered in either [6] or [17], leaving open the question of whether the structure remained unchanged upon K-doping.

Layer-dependent electronic structure in mechanically exfoliated WSe₂ was studied in [162]. ARPES measurements found that the VB maximum is at the K -point for 1 ML WSe₂ and shifts to the Γ -point for multilayer WSe₂, in agreement with theoretical prediction. From analysis of the curvature of the bands from the ARPES measurements the effective masses of monolayer and bilayer WSe₂ were deduced: for monolayer WSe₂ the hole effective mass was $(1.4 \pm 0.6)m_0$ at K and a hole effective mass of $(3.5 \pm 1.8)m_0$ at the Γ -point. For the case of bilayer WSe₂, the experimentally derived hole effective mass was $(0.4 \pm 0.1)m_0$ at the K -point.

At the same time, no spin-orbit splitting could be observed [162]. The reason for this is not clear, it was speculated that this might be due to the sample roughness and the concomitant line width broadening [162]. Spin-splitting of 513 meV was observed by ARPES measurements in monolayer of WSe₂ in a subsequent work [163].

6.2.5 Band Gap Renormalization

Enhanced Coulomb interactions due to low-dimensional effects are expected to increase the quasiparticle band gap as well as to cause electron-hole pairs to form more strongly bound excitons [5, 50, 57, 92]. The electronic band gap (E_g) characterizes single-particle (or quasiparticle) excitations and is defined by the sum of the energies needed to separately tunnel an electron and a hole into monolayer MoSe₂. The optical band gap (E_{opt}) describes the energy required to create an exciton, a

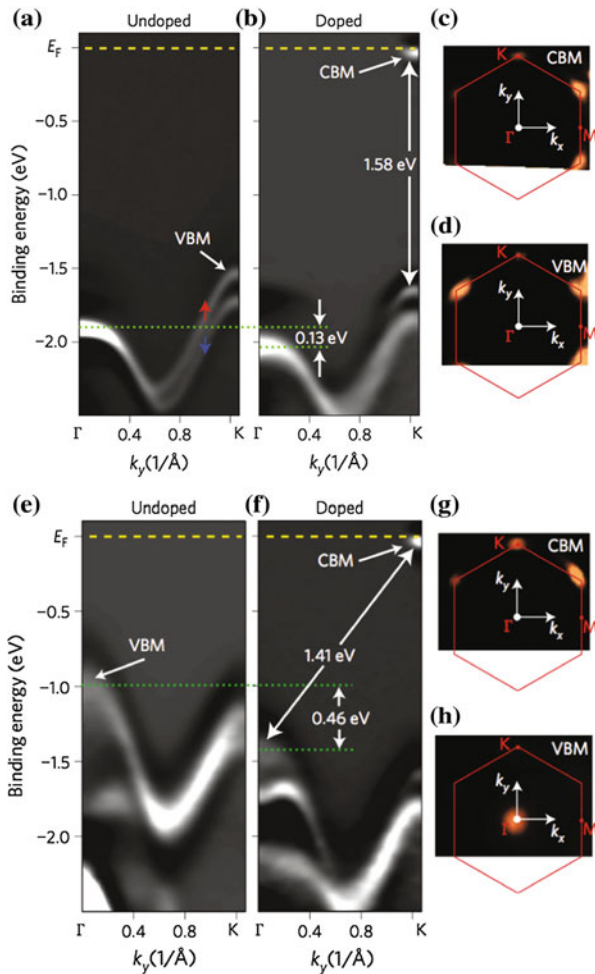


Fig. 6.40 Direct band gap in monolayer and indirect band gap in 8 ML MoSe₂ thin films. **a–d** ARPES data for the monolayer sample. **e–h** ARPES data for the 8 ML sample. **a, e** Second-derivative spectra of undoped monolayer (**a**) and 8 ML MoSe₂ (**e**) films along the Γ –K direction. **b, f** Second-derivative spectra along the Γ –K direction after potassium surface doping to shift the chemical potential and reveal the CB minimum in monolayer and 8 ML MoSe₂ thin films, respectively. Yellow dashed lines are Fermi levels. Blue and red arrows in (**a**) indicate the opposite spin directions of the spin-split states near the K-point in the monolayer MoSe₂ film. Green dotted lines indicate the valence bands in monolayer and 8 ML MoSe₂ films, moved by 0.13 eV and 0.46 eV with potassium doping, respectively. **c, g** Constant energy maps at the CB minimum of potassium-doped monolayer and 8 ML MoSe₂ films, respectively. **d, h** Constant energy maps at the VB maximum of undoped monolayer and 8 ML MoSe₂ films, respectively. Red hexagons indicate the first Brillouin zone of the system. k_x and k_y refer to the momentum along the Γ –K and Γ –M directions [6]. Reprinted by permission from Macmillan Publishers Ltd., copyright (2013)

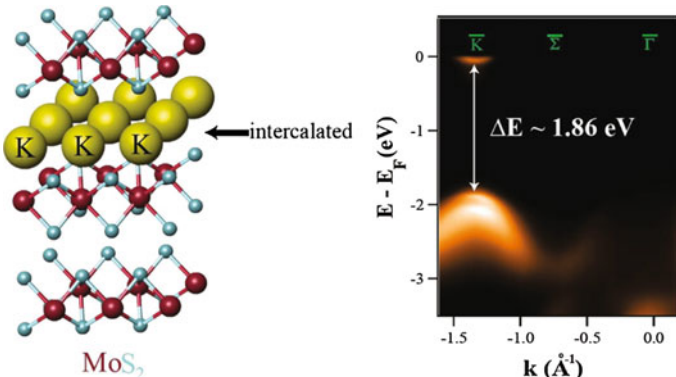


Fig. 6.41 *Left* schematics of the formation of a quasi freestanding MoS_2 layer by K-intercalation. *Right* the corresponding electronic structure measured by ARPES [17]. Copyright 2014 American Chemical Society. Published with permission

correlated two-particle electron-hole pair, via optical absorption. The difference in these energies ($E_g - E_{opt}$) directly yields the exciton binding energy (E_b). Such measurements were performed in [144], where the authors experimentally investigated both the electronic structure and optical transitions in monolayer MoSe_2 by combining STS and PL spectroscopy.

Figure 6.42 (upper panel) shows a typical STM dI/dV spectrum acquired on monolayer MoSe_2 /bi-layer graphene (BLG). The observed electronic structure is dominated by a large electronic band gap surrounded by features labelled V_1 through V_4 in the VB and C_1 in the CB. The STS measurements yield a value for the single-particle electronic band gap for MoSe_2/BLG of $E_g = E_{CBM} - E_{VBM} = 2.18 \pm 0.04$ eV.

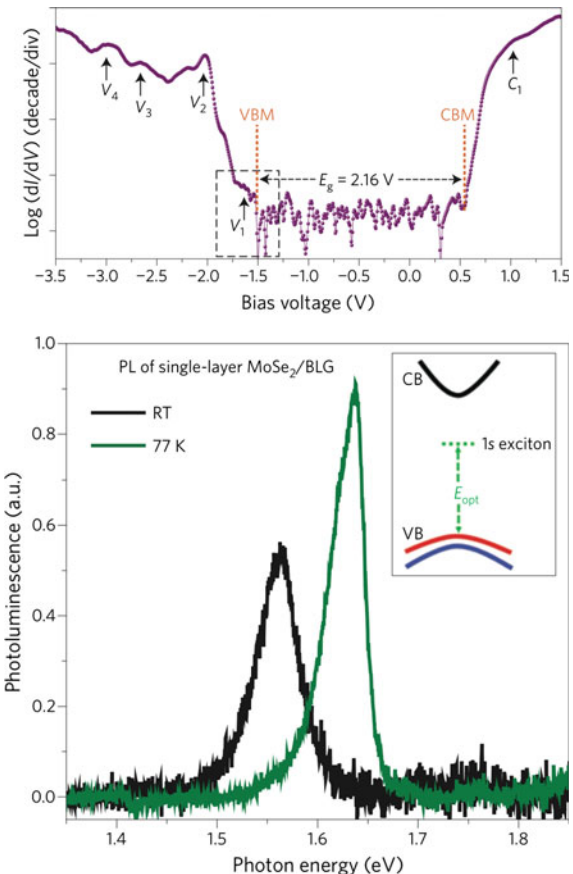
To complement these measurements, measurement of the optical band gap (E_{opt}) was performed using PL spectroscopy from single-layer MoSe_2 . A representative set of data taken at two different temperatures for MoSe_2/BLG is shown in Fig. 6.42, lower panel, where PL at room temperature shows a peak centered at 1.55 eV, while at 77 K, the peak shifted to 1.63 eV.

One immediately notices that the MoSe_2/BLG optical band gap of $E_{opt} = 1.63$ eV differs from the electronic band gap $E_g = 2.18$ eV by the amount 0.55 ± 0.04 eV, which corresponds to the binding energy of the MoSe_2/BLG electron-hole excitation.

To understand the experimental findings, ab-initio GW and GW plus Bethe-Salpeter equation (GW-BSE) calculations were additionally performed. The results are shown in Fig. 6.43 and are in agreement with experiment, demonstrating that many-electron interactions are strong in MoSe_2/BLG and prominently affect the quasiparticle excitations and optical response of this system resulting in a significant band gap van Hove singularity.

The difference between the measured electronic and optical band gaps points to a large exciton binding energy of hundreds of meV in monolayer TMDCs. An exciton

Fig. 6.42 *Upper panel:* Logarithm of a typical dI/dV spectrum used in the statistical analysis to obtain E_g ($f = 873$ Hz, $I_t = 5$ nA, $V_{rms} = 3$ mV, $T = 5$ K). *Lower panel:* Representative photoluminescence spectra acquired at room temperature (RT; black) and at 77 K (green) for 0.8 ML MoSe₂ on a BLG/SiC substrate. The photoluminescence at room temperature is centered at 1.55 eV. The peak shifts to 1.63 eV at 77 K. This photoluminescence peak corresponds to the lowest-energy exciton transition (E_{opt}) in single-layer MoSe₂ (*inset*) [144]. Reprinted by permission from Macmillan Publishers Ltd., copyright (2014)



binding energy in the range of 0.3–0.7 eV was also inferred in the WX_2 monolayer from spectral features in two-photon absorption and reflectance measurement which were attributed as excitonic excited states [164, 165]. The charging energy, i.e. energy difference between the neutral exciton and charged exciton in the PL, was measured to be in the range of 20–40 meV [166, 167], which is consistent with the above binding energy for 2D excitons. These results all point to exceptionally strong Coulomb interaction, due to the large effective masses of both electrons and holes and the reduced screening in the 2D limit [144].

A large band gap van Hove singularity was also reported in atomically thin WS₂ layers under the conditions of intense photoexcitation [168]. It was found that upon exposure to intense excitation pulses, both monolayers and bi-layers of WS₂ exhibited disappearance of the absorption peak associated with exciton along with a concurrent decrease in absorption at energies about 0.3 eV lower than the excitonic peak, accompanied by a band gap renormalization of 500 meV as is exemplified in Fig. 6.44 for a WS₂ bi-layer. Similar results were also obtained for monolayers. The restruc-

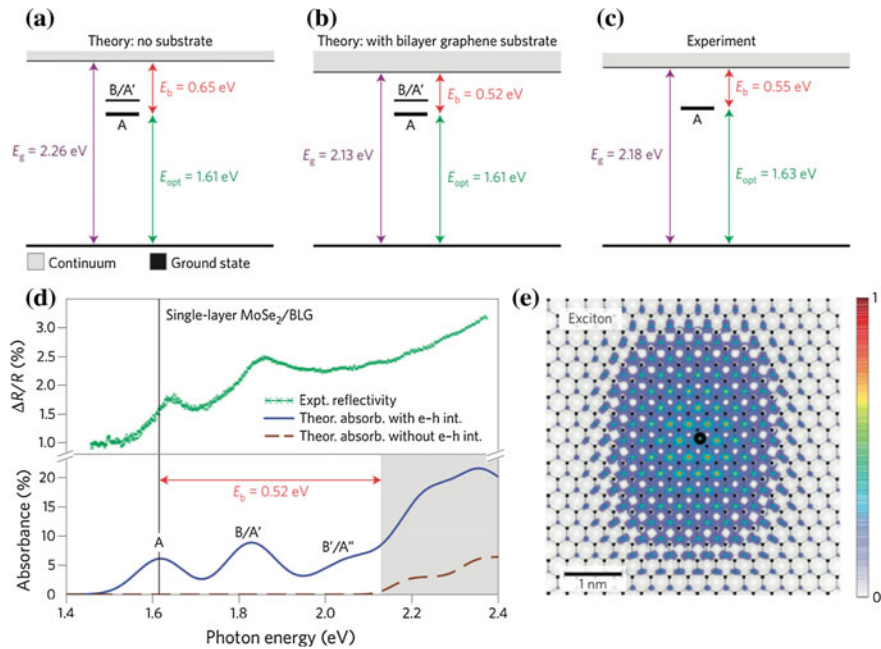


Fig. 6.43 Comparison between ab-initio excited-state calculations and a single-layer MoSe₂ experiment. **a–c** Relevant energy levels sketched for a GW-BSE calculation without a substrate (**a**), GW-BSE calculation with BLG substrate (**b**) and experimental data (**c**). **d** Calculated optical absorbance of single-layer MoSe₂ with and without electron-hole interactions, including BLG screening. A constant Gaussian broadening of ca. 50 meV (30 meV) was used in the curve with (without) electron-hole interactions. The shaded grey area corresponds to energies above the single-particle excitonic gap. The experimental differential reflectivity spectrum measured at 77 K is shown in green. **e** Spatial map of the exciton wavefunction corresponding to the excitonic peak labelled *A* in (**a–d**) (wavefunction is shown with the hole (black circle) fixed in space). Mo atoms are small black squares, Se atoms are not shown [144]. Reprinted by permission from Macmillan Publishers Ltd., copyright (2014)

turing of the band-edge optical response after intense photoexcitation was attributed to a Mott transition. All changes were transient and reversible. It was concluded that these phenomena were intimately related to strong Coulomb interaction between charge carriers. It was also stressed that the observation of these effects at room temperature and at ambient conditions are especially advantageous for applications in optoelectronic and photonic devices [168].

6.2.5.1 Experimental Band Gap Tuning

There have been numerous experimental reports about band gap tuning in single and few-layer TMDCs. These include use of pressure, temperature, uniaxial and biaxial strain, dielectric screening, and interlayer coupling. For example, biaxial compressive strain of tri-layer MoS₂ causes the band gap to blue-shift by 300 meV per 1% strain [169], while application of uniaxial strain to monolayer MoS₂ results in a red-shift

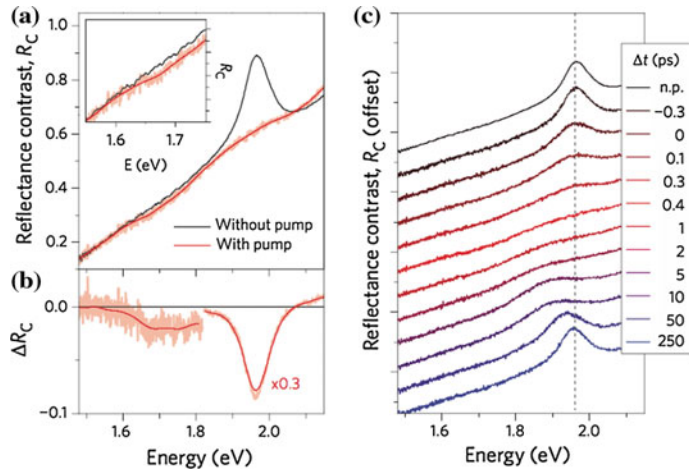


Fig. 6.44 Photoinduced optical response of WS₂ bilayers. **a** Reflectance contrast spectra, shown without pump excitation and 0.4 ps after excitation by a pump pulse with an applied fluence of 840 $\mu\text{J cm}^2$. The sample temperature was $T = 70$ K. The solid red line is a guide to the eye, obtained by smoothing the original data (light red). The low-energy part of the spectra is presented in the inset. **b** Corresponding differential reflectance contrast spectra ΔR_C . The region around 2 eV is scaled by a factor of 0.3. **c** Reflectance contrast spectra at different time delays after excitation, vertically offset for clarity ('n.p.' denotes the spectrum without pump excitation) [168]. Reprinted by permission from Macmillan Publishers Ltd., copyright (2015)

of ca. 70 meV per 1% applied strain [170] (Fig. 6.45a). A strain-induced indirect-to-direct band gap transition in multilayer WSe₂ with a resulting drastic increase in the PL intensity was reported in [171], while thermally driven crossover from indirect

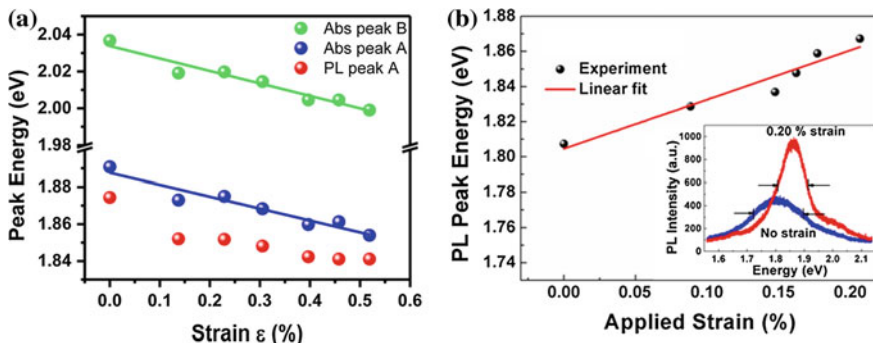


Fig. 6.45 **a** Uniaxial tensile strain dependence of the *A* and *B* peak energies from absorption measurements and the *A* peak energy from PL measurements (symbols) for monolayer MoS₂. Lines are linear fits to the data [170]. **b** PL peak energy as a function of compressive strain in a tri-layer MoS₂. The inset shows the PL spectra of the sample under 0.0% and 0.2% strain [169]. Copyright 2013 American Chemical Society. Published with permission

to direct band gap was observed in MSe_2 [159]. Dielectric screening was also shown to affect the PL peak position, although the absolute shifts were rather small, as well as a significant change in the PL intensity [172]. Changing of interlayer interaction by varying the stacking angle [78] is another way to taylor the electronic structure of bi-layers. These results are described in more detail elsewhere in this volume.

Effect of strain on the electronic gap was also studied through piezoresistivity measurements, where a change in resistivity of the material is observed during mechanical deformation [173] using a setup schematically shown in the upper-left corner of Fig. 6.46. Concurrent measurements of the current and tip deflection allowed the authors to observe the effect of deformation and confirm the mechanical origin of

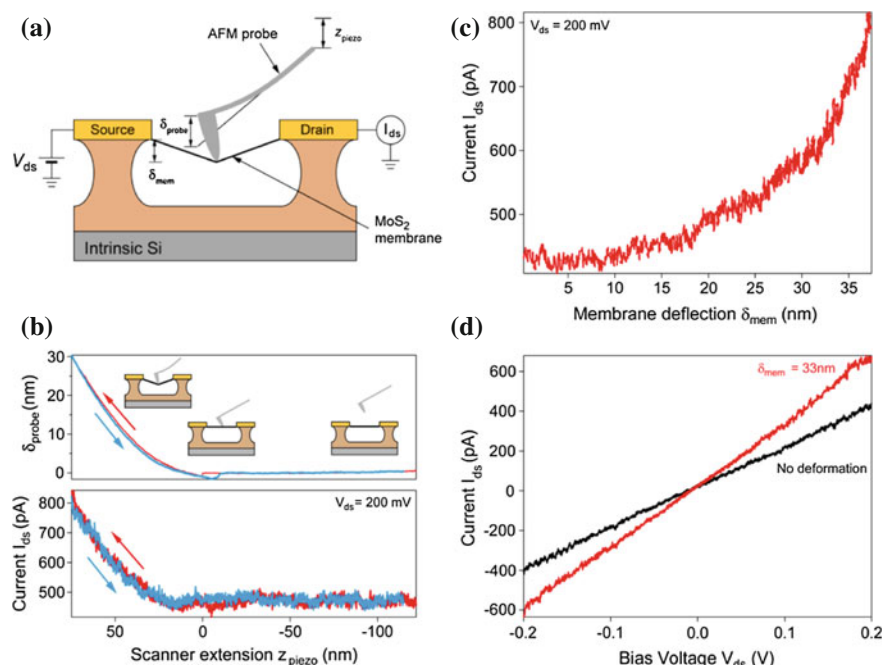


Fig. 6.46 **a** Schematic drawing of the setup for direct current electrical characterization of suspended channel MoS_2 devices under strain. The suspended atomically thin membrane is deformed at the center using an AFM probe attached to a piezo scanner. The vertical displacement of the scanner (z_{piezo}) results in the deflection of the cantilever (δ_{probe}) and the membrane (δ_{mem}). The device is kept under bias voltage V_{ds} , whereas the drain current I_{ds} is monitored **b** Output data from electromechanical experiment on device 1 showing simultaneous measurement of the cantilever deflection (*top panel*) and the drain current (*bottom panel*) as a function of the piezo scanner extension. The electromechanical response is reproducible in both extension (red) and retraction (blue) cycles. **c** Drain current as a function of membrane deflection at the center ($\delta_{\text{mem}} = (z_{\text{piezo}} - \delta_{\text{probe}})$). **d** Output characteristics of the same MoS_2 device. The *black curve* is recorded after the AFM tip has touched the membrane and before indentation. The *red curve* is recorded while the membrane is kept at constant deformation. The modulation of carrier transport under strain is consistent with the extension and retraction experiments in panel **b** and the piezoresistive effect [173]. Copyright 2015 American Chemical Society. Published with permission

the current modulation. Monolayer, bi-layer and three-layer structures were studied. Results of measurements on a monolayer MoS₂ device are presented in Fig. 6.46a. A plot of current, I_{ds} as a function of δ_{mem} is shown in Fig. 6.46b demonstrating that I_{ds} increases with the increased deformation of the membrane, which indicates the modulation of resistance due to the applied deformation. The output characteristics of the device in the relaxed state and under constant deformation are compared in Fig. 6.46c. The observed piezoresistive behavior was interpreted in terms of band gap reduction under tensile strain.

In [174], it was demonstrated that piezoresistivity of TMDCs can be used to fabricate strain sensors.

References

1. K.F. Mak, C. Lee, J. Hone, J. Shan, T.F. Heinz, Atomically thin MoS₂: a new direct-gap semiconductor. *Phys. Rev. Lett.* **105**(13), 136805 (2010)
2. W. Zhao, R. Ribeiro, M. Toh, A.H. Carvalho, C. Kloc, A. Castro Neto, G. Eda, Origin of indirect optical transitions in few-layer MoS₂, WS₂, and WSe₂. *Nano Lett.* **13**(11), 5627 (2013)
3. H. Zeng, G.B. Liu, J. Dai, Y. Yan, B. Zhu, R. He, L. Xie, S. Xu, X. Chen, W. Yao, et al., Optical signature of symmetry variations and spin-valley coupling in atomically thin tungsten dichalcogenides. *Sci. Rep.* **3** (2013). doi:[10.1038/srep01608](https://doi.org/10.1038/srep01608)
4. A. Ramasubramaniam, D. Naveh, E. Towe, Tunable band gaps in bilayer transition-metal dichalcogenides. *Phys. Rev. B* **84**(20), 205325 (2011)
5. T. Cheiwchanchamnangij, W.R. Lambrecht, Quasiparticle band structure calculation of monolayer, bilayer, and bulk MoS₂. *Phys. Rev. B* **85**(20), 205302 (2012)
6. Y. Zhang, T.R. Chang, B. Zhou, Y.T. Cui, H. Yan, Z. Liu, F. Schmitt, J. Lee, R. Moore, Y. Chen et al., Direct observation of the transition from indirect to direct bandgap in atomically thin epitaxial MoSe₂. *Nat. Nanotech.* **9**(2), 111 (2014)
7. Y. Ma, Y. Dai, M. Guo, C. Niu, J. Lu, B. Huang, Electronic and magnetic properties of perfect, vacancy-doped, and nonmetal adsorbed MoSe₂, MoTe₂ and WS₂ monolayers. *Phys. Chem. Chem. Phys.* **13**(34), 15546 (2011)
8. A. Kumar, P. Ahluwalia, Electronic structure of transition metal dichalcogenides monolayers $1H-MX_2$ ($M = Mo, W; X = S, Se, Te$) from ab-initio theory: new direct band gap semiconductors. *Eur. Phys. J. B* **85**(6), 186 (2012)
9. E.S. Kadantsev, P. Hawrylak, Electronic structure of a single MoS₂ monolayer. *Solid State Commun.* **152**(10), 909 (2012)
10. W. Huang, X. Luo, C.K. Gan, S.Y. Quek, G. Liang, Theoretical study of thermoelectric properties of few-layer MoS₂ and WSe₂. *Phys. Chem. Chem. Phys.* **16**(22), 10866 (2014)
11. Y. Ding, Y. Wang, J. Ni, L. Shi, S. Shi, W. Tang, First principles study of structural, vibrational and electronic properties of graphene-like MX₂ ($M = Mo, Nb, W, Ta; X = S, Se, Te$) monolayers. *Phys. B* **406**(11), 2254 (2011)
12. J.K. Ellis, M.J. Lucero, G.E. Scuseria, The indirect to direct band gap transition in multilayered MoS₂ as predicted by screened hybrid density functional theory. *Appl. Phys. Lett.* **99**(26), 261908 (2011)
13. A. Molina-Sánchez, D. Sangalli, K. Hummer, A. Marini, L. Wirtz, Effect of spin-orbit interaction on the optical spectra of single-layer, double-layer, and bulk MoS₂. *Phys. Rev. B* **88**(4), 045412 (2013)
14. H.P. Komsa, A.V. Krasheninnikov, Electronic structures and optical properties of realistic transition metal dichalcogenide heterostructures from first principles. *Phys. Rev. B* **88**(8), 085318 (2013)

15. H. Sahin, S. Tongay, S. Horzum, W. Fan, J. Zhou, J. Li, J. Wu, F. Peeters, Anomalous Raman spectra and thickness-dependent electronic properties of WSe₂. *Phys. Rev. B* **87**(16), 165409 (2013)
16. A. Splendiani, L. Sun, Y. Zhang, T. Li, J. Kim, C.Y. Chim, G. Galli, F. Wang, Emerging photoluminescence in monolayer MoS₂. *Nano Lett.* **10**(4), 1271 (2010)
17. T. Eknakapakul, P.D. King, M. Asakawa, P. Buaphet, R.H. He, S.K. Mo, H. Takagi, K.M. Shen, F. Baumberger, T. Sasagawa et al., Electronic structure of a quasi-free-standing MoS₂ monolayer. *Nano Lett.* **14**(3), 1312 (2014)
18. A. Kuc, N. Zibouche, T. Heine, Influence of quantum confinement on the electronic structure of the transition metal sulfide TS₂. *Phys. Rev. B* **83**(24), 245213 (2011)
19. L. Debbichi, O. Eriksson, S. Lebègue, Electronic structure of two-dimensional transition metal dichalcogenide bilayers from ab initio theory. *Phys. Rev. B* **89**(20), 205311 (2014)
20. S. Lebegue, O. Eriksson, Electronic structure of two-dimensional crystals from ab initio theory. *Phys. Rev. B* **79**(11), 115409 (2009)
21. H. Jiang, Electronic band structures of molybdenum and tungsten dichalcogenides by the GW approach. *J. Phys. Chem. C* **116**(14), 7664 (2012)
22. T. Böker, R. Severin, A. Müller, C. Janowitz, R. Manzke, D. Voß, P. Krüger, A. Mazur, J. Pollmann, Band structure of MoS₂, MoSe₂, and α -MoTe₂: angle-resolved photoelectron spectroscopy and ab initio calculations. *Phys. Rev. B* **64**(23), 235305 (2001)
23. F. Hüser, T. Olsen, K.S. Thygesen, How dielectric screening in two-dimensional crystals affects the convergence of excited-state calculations: Monolayer MoS₂. *Phys. Rev. B* **88**(24), 245309 (2013)
24. C. Espejo, T. Rangel, A. Romero, X. Gonze, G.M. Rignanese, Band structure tunability in MoS₂ under interlayer compression: a DFT and GW study. *Phys. Rev. B* **87**(24), 245114 (2013)
25. I.G. Lezama, A. Ubaldini, M. Longobardi, E. Giannini, C. Renner, A.B. Kuzmenko, A.F. Morpurgo, Surface transport and band gap structure of exfoliated 2H-MoTe₂ crystals. *2D Mater.* **1**(2), 021002 (2014)
26. G.B. Liu, D. Xiao, Y. Yao, X. Xu, W. Yao, Electronic structures and theoretical modelling of two-dimensional group-VIB transition metal dichalcogenides. *Chem. Soc. Rev.* **44**(9), 2643 (2015)
27. D. Xiao, G.B. Liu, W. Feng, X. Xu, W. Yao, Coupled spin and valley physics in monolayers of MoS₂ and other group-VI dichalcogenides. *Phys. Rev. Lett.* **108**(19), 196802 (2012)
28. F. Rose, M. Goerbig, F. Piéchon, Spin-and valley-dependent magneto-optical properties of MoS₂. *Phys. Rev. B* **88**(12), 125438 (2013)
29. E. Cappelluti, R. Roldán, J. Silva-Guillén, P. Ordejón, F. Guinea, Tight-binding model and direct-gap/indirect-gap transition in single-layer and multilayer MoS₂. *Phys. Rev. B* **88**(7), 075409 (2013)
30. E. Ridolfi, D. Le, T.S. Rahman, E.R. Mucciolo, C.H. Lewenkopf, A tight-binding model for MoS₂ monolayers. *J. Phys. Condens. Matter* **27**(36), 365501 (2015)
31. M. Erementchouk, M. Khan, M.N. Leuenberger, Optical signatures of states bound to vacancy defects in monolayer MoS₂. *Phys. Rev. B* **92**, 121401 (2015)
32. X. Li, F. Zhang, Q. Niu, Unconventional quantum hall effect and tunable spin hall effect in dirac materials: application to an isolated MoS₂ trilayer. *Phys. Rev. Lett.* **110**(6), 066803 (2013)
33. F. Parhizgar, H. Rostami, R. Asgari, Indirect exchange interaction between magnetic adatoms in monolayer MoS₂. *Phys. Rev. B* **87**(12), 125401 (2013)
34. G.B. Liu, W.Y. Shan, Y. Yao, W. Yao, D. Xiao, Three-band tight-binding model for monolayers of group-VIB transition metal dichalcogenides. *Phys. Rev. B* **88**(8), 085433 (2013)
35. R.L. Chu, G.B. Liu, W. Yao, X. Xu, D. Xiao, C. Zhang, Spin-orbit-coupled quantum wires and Majorana fermions on zigzag edges of monolayer transition-metal dichalcogenides. *Phys. Rev. B* **89**(15), 155317 (2014)
36. A. Kormányos, V. Zólyomi, N.D. Drummond, G. Burkard, Spin-orbit coupling, quantum dots, and qubits in monolayer transition metal dichalcogenides. *Phys. Rev. X* **4**(1), 011034 (2014)

37. Y. Song, H. Dery, Transport theory of monolayer transition-metal dichalcogenides through symmetry. *Phys. Rev. Lett.* **111**(2), 026601 (2013)
38. C. Wang, X. Lei, Linear magnetotransport in monolayer MoS₂. *Phys. Rev. B* **92**(12), 125303 (2015)
39. A. Thilagam, Excitonic polarons in low-dimensional transition metal dichalcogenides. *Phys. B* **464**, 44 (2015)
40. Y.N. Gartstein, X. Li, C. Zhang, Exciton-polaritons in transition-metal dichalcogenides and their direct excitation via energy transfer. *Phys. Rev. B* **92**, 075445 (2015)
41. T. Li, G. Galli, Electronic properties of MoS₂ nanoparticles. *J. Phys. Chem. C* **111**(44), 16192 (2007)
42. H.S.S.R. Matte, A. Gomathi, A.K. Manna, D.J. Late, R. Datta, S.K. Pati, C.N.R. Rao, MoS₂ and WS₂ analogues of graphene. *Angew. Chem.* **122**(24), 4153 (2010)
43. R. Roldán, J.A. Silva-Guillén, M.P. López-Sancho, F. Guinea, E. Cappelluti, P. Ordejón, Electronic properties of single-layer and multilayer transition metal dichalcogenides MX₂ (M = Mo, W and X = S, Se). *Ann. Phys.* **526**(9–10), 347 (2014)
44. K. Albe, A. Klein, Density-functional-theory calculations of electronic band structure of single-crystal and single-layer WS₂. *Phys. Rev. B* **66**(7), 073413 (2002)
45. O.V. Yazyev, A. Kis, MoS₂ and semiconductors in the flatland. *Mater. Today* **18**(1), 20 (2015)
46. J. Padilha, H. Peelaers, A. Janotti, C. Van de Walle, Nature and evolution of the band-edge states in MoS₂: from monolayer to bulk. *Phys. Rev. B* **90**(20), 205420 (2014)
47. L. Mattheiss, Band structures of transition-metal-dichalcogenide layer compounds. *Phys. Rev. B* **8**(8), 3719 (1973)
48. H. Shi, H. Pan, Y.W. Zhang, B.I. Yakobson, Quasiparticle band structures and optical properties of strained monolayer MoS₂ and WS₂. *Phys. Rev. B* **87**(15), 155304 (2013)
49. Y. Liang, S. Huang, R. Soklaski, L. Yang, Quasiparticle band-edge energy and band offsets of monolayer of molybdenum and tungsten chalcogenides. *Appl. Phys. Lett.* **103**(4), 042106 (2013)
50. D.Y. Qiu, F.H. da Jornada, S.G. Louie, Optical spectrum of MoS₂: many-body effects and diversity of exciton states. *Phys. Rev. Lett.* **111**(21), 216805 (2013)
51. Z. Zhu, Y. Cheng, U. Schwingenschlögl, Giant spin-orbit-induced spin splitting in two-dimensional transition-metal dichalcogenide semiconductors. *Phys. Rev. B* **84**(15), 153402 (2011)
52. S. Bhattacharya, A.K. Singh, Semiconductor-metal transition in semiconducting bilayer sheets of transition-metal dichalcogenides. *Phys. Rev. B* **86**(7), 075454 (2012)
53. Q. Liu, L. Li, Y. Li, Z. Gao, Z. Chen, J. Lu, Tuning electronic structure of bilayer MoS₂ by vertical electric field: a first-principles investigation. *J. Phys. Chem. C* **116**(40), 21556 (2012)
54. W. Jin, P.C. Yeh, N. Zaki, D. Zhang, J.T. Sadowski, A. Al-Mahboob, A.M. van der Zande, D.A. Chenet, J.I. Dadap, I.P. Herman et al., Direct measurement of the thickness-dependent electronic band structure of MoS₂ using angle-resolved photoemission spectroscopy. *Phys. Rev. Lett.* **111**(10), 106801 (2013)
55. H.P. Komsa, A.V. Krasheninnikov, Two-dimensional transition metal dichalcogenide alloys: stability and electronic properties. *J. Phys. Chem. Lett.* **3**(23), 3652 (2012)
56. A. Kutana, E.S. Penev, B.I. Yakobson, Engineering electronic properties of layered transition-metal dichalcogenide compounds through alloying. *Nanoscale* **6**(11), 5820 (2014)
57. A. Ramasubramaniam, Large excitonic effects in monolayers of molybdenum and tungsten dichalcogenides. *Phys. Rev. B* **86**(11), 115409 (2012)
58. Z. Gong, G.B. Liu, H. Yu, D. Xiao, X. Cui, X. Xu, W. Yao, Magnetolectric effects and valley-controlled spin quantum gates in transition metal dichalcogenide bilayers. *Nat. Commun.* **4** (2013). doi:[10.1038/ncomms3053](https://doi.org/10.1038/ncomms3053)
59. H. Ochoa, R. Roldán, Spin-orbit-mediated spin relaxation in monolayer MoS₂. *Phys. Rev. B* **87**(24), 245421 (2013)
60. A. Kormányos, V. Zólyomi, N.D. Drummond, P. Rakytá, G. Burkard, V.I. Fal'ko, Monolayer MoS₂: trigonal warping, the Γ valley, and spin-orbit coupling effects. *Phys. Rev. B* **88**(4), 045416 (2013)

61. H. Yu, Y. Wu, G.B. Liu, X. Xu, W. Yao, Nonlinear valley and spin currents from Fermi pocket anisotropy in 2D crystals. *Phys. Rev. Lett.* **113**(15), 156603 (2014)
62. Y.M. Koroteev, G. Bihlmayer, J. Gayone, E. Chulkov, S. Blügel, P. Echenique, P. Hofmann, Strong spin-orbit splitting on Bi surfaces. *Phys. Rev. Lett.* **93**(4), 046403 (2004)
63. D. Wolverson, S. Crampin, A.S. Kazemi, A. Ilie, S.J. Bending, Raman spectra of monolayer, few-layer, and bulk ReSe_2 : an anisotropic layered semiconductor. *ACS Nano* **8**(11), 11154 (2014)
64. C.H. Chang, X. Fan, S.H. Lin, J.L. Kuo, Orbital analysis of electronic structure and phonon dispersion in MoS_2 , MoSe_2 , WS_2 , and WSe_2 monolayers under strain. *Phys. Rev. B* **88**(19), 195420 (2013)
65. P. Johari, V.B. Shenoy, Tuning the electronic properties of semiconducting transition metal dichalcogenides by applying mechanical strains. *ACS Nano* **6**(6), 5449 (2012)
66. A. Kumar, P.K. Ahluwalia, Mechanical strain dependent electronic and dielectric properties of two-dimensional honeycomb structures of MoX_2 ($\text{X}=\text{S}, \text{Se}, \text{Te}$). *Phys. B* **419**, 66 (2013)
67. S. Horzum, H. Sahin, S. Cahangirov, P. Cudazzo, A. Rubio, T. Serin, F. Peeters, Phonon softening and direct to indirect band gap crossover in strained single-layer MoSe_2 . *Phys. Rev. B* **87**(12), 125415 (2013)
68. Q. Zhang, Y. Cheng, L.Y. Gan, U. Schwingenschlögl, Giant valley drifts in uniaxially strained monolayer MoS_2 . *Phys. Rev. B* **88**(24), 245447 (2013)
69. P. Lu, X. Wu, W. Guo, X.C. Zeng, Strain-dependent electronic and magnetic properties of MoS_2 monolayer, bilayer, nanoribbons and nanotubes. *Phys. Chem. Chem. Phys.* **14**(37), 13035 (2012)
70. E. Scalise, M. Houssa, G. Pourtois, V. Afanasev, A. Stesmans, Strain-induced semiconductor to metal transition in the two-dimensional honeycomb structure of MoS_2 . *Nano Res.* **5**(1), 43 (2012)
71. N.A. Lanzillo, A.J. Simbeck, S.K. Nayak, Strain engineering the work function in monolayer metal dichalcogenides. *J. Phys. Condens. Matter* **27**(17), 175501 (2015)
72. J. Feng, X. Qian, C.W. Huang, J. Li, Strain-engineered artificial atom as a broad-spectrum solar energy funnel. *Nat. Photon.* **6**(12), 866 (2012)
73. A. Castellanos-Gomez, R. Roldán, E. Cappelluti, M. Buscema, F. Guinea, H.S. van der Zant, G.A. Steele, Local strain engineering in atomically thin MoS_2 . *Nano Lett.* **13**(11), 5361 (2013)
74. A.P. Nayak, T. Pandey, D. Voiry, J. Liu, S.T. Moran, A. Sharma, C. Tan, C.H. Chen, L.J. Lee, M. Chhowalla et al., Pressure-dependent optical and vibrational properties of monolayer molybdenum disulfide. *Nano Lett.* **15**(1), 346 (2015)
75. A.P. Nayak, S. Bhattacharyya, J. Zhu, J. Liu, X. Wu, T. Pandey, C. Jin, A.K. Singh, D. Akinwande, J.F. Lin, Pressure-induced semiconducting to metallic transition in multilayered molybdenum disulphide. *Nat. Commun.* **5** (2014). doi:[10.1038/ncomms4731](https://doi.org/10.1038/ncomms4731)
76. J. Xiao, M. Long, X. Li, Q. Zhang, H. Xu, K.S. Chan, Effects of van der waals interaction and electric field on the electronic structure of bilayer MoS_2 . *J. Phys. Condens. Matter* **26**(40), 405302 (2014)
77. K. Dolui, C.D. Pemmaraju, S. Sanvito, Electric field effects on armchair MoS_2 nanoribbons. *ACS Nano* **6**(6), 4823 (2012)
78. A.M. van der Zande, J. Kunstmann, A. Chernikov, D.A. Chenet, Y. You, X. Zhang, P.Y. Huang, T.C. Berkelbach, L. Wang, F. Zhang et al., Tailoring the electronic structure in bilayer molybdenum disulfide via interlayer twist. *Nano Lett.* **14**(7), 3869 (2014)
79. T. Jiang, H. Liu, D. Huang, S. Zhang, Y. Li, X. Gong, Y.R. Shen, W.T. Liu, S. Wu, Valley and band structure engineering of folded MoS_2 bilayers. *Nat. Nanotech.* **9**(10), 825 (2014)
80. S. Huang, X. Ling, L. Liang, J. Kong, H. Terrones, V. Meunier, M.S. Dresselhaus, Probing the interlayer coupling of twisted bilayer MoS_2 using photoluminescence spectroscopy. *Nano Lett.* **14**(10), 5500 (2014)
81. K. Liu, L. Zhang, T. Cao, C. Jin, D. Qiu, Q. Zhou, A. Zettl, P. Yang, S.G. Louie, F. Wang, Evolution of interlayer coupling in twisted molybdenum disulfide bilayers. *Nat. Commun.* **5** (2014). doi:[10.1038/ncomms5966](https://doi.org/10.1038/ncomms5966)

82. M. Koshino, T. Habe, Spin-dependent refraction at the atomic step of transition-metal dichalcogenides. *Phys. Rev. B* **91**, 201407 (2015)
83. M. Kan, J. Wang, X.W. Li, S. Zhang, Y. Li, Y. Kawazoe, Q. Sun, P. Jena, Structures and phase transition of a MoS₂ monolayer. *J. Phys. Chem. C* **118**(3), 1515 (2014)
84. L. Britnell, R.M. Ribeiro, A. Eckmann, R. Jalil, B.D. Belle, A. Mishchenko, Y.J. Kim, R.V. Gorbachev, T. Georgiou, S.V. Morozov et al., Strong light-matter interactions in heterostructures of atomically thin films. *Science* **340**(6138), 1311 (2013)
85. A. Carvalho, R. Ribeiro, A.C. Neto, Band nesting and the optical response of two-dimensional semiconducting transition metal dichalcogenides. *Phys. Rev. B* **88**(11), 115205 (2013)
86. G.F. Bassani, G.P. Parravicini, *Electronic States and Optical Transitions in Solids* (Pergamon Press, Oxford, 1975)
87. D. Kozawa, R. Kumar, A. Carvalho, K.K. Amara, W. Zhao, S. Wang, M. Toh, R.M. Ribeiro, A.C. Neto, K. Matsuda, et al., Photocarrier relaxation pathway in two-dimensional semiconducting transition metal dichalcogenides. *Nat. Commun.* **5** (2014). doi:[10.1038/ncomms5543](https://doi.org/10.1038/ncomms5543)
88. M. Bernardi, M. Palummo, J.C. Grossman, Extraordinary sunlight absorption and one nanometer thick photovoltaics using two-dimensional monolayer materials. *Nano Lett.* **13**(8), 3664 (2013)
89. G. Eda, S.A. Maier, Two-dimensional crystals: managing light for optoelectronics. *ACS Nano* **7**(7), 5660 (2013)
90. O. Lopez-Sanchez, E. Alarcon Llado, V. Koman, A. Fontcuberta i Morral, A. Radenovic, A. Kis. Light generation and harvesting in a van der Waals heterostructure. *ACS Nano* **8**(3), 3042 (2014)
91. X. Liu, T. Galfsky, Z. Sun, F. Xia, E.C. Lin, Y.H. Lee, S. Kéna-Cohen, V.M. Menon, Strong light-matter coupling in two-dimensional atomic crystals. *Nat. Photonics* **9**(1), 30 (2015)
92. H.P. Komsa, A.V. Krasheninnikov, Effects of confinement and environment on the electronic structure and exciton binding energy of MoS₂ from first principles. *Phys. Rev. B* **86**(24), 241201 (2012)
93. G. Onida, L. Reining, A. Rubio, Electronic excitations: density-functional versus many-body Green's-function approaches. *Rev. Mod. Phys.* **74**(2), 601 (2002)
94. R. Coehoorn, C. Haas, J. Dijkstra, C. Flipse, R. De Groot, A. Wold, Electronic structure of MoSe₂, MoS₂, and WSe₂. I. Band-structure calculations and photoelectron spectroscopy. *Phys. Rev. B* **35**(12), 6195 (1987)
95. H. Mirhosseini, G. Roma, J. Kiss, C. Felser, First-principles investigation of the bulk and low-index surfaces of MoSe₂. *Phys. Rev. B* **89**(20), 205301 (2014)
96. H. Peelaers, C.G. Van de Walle, First-principles study of van der Waals interactions in MoS₂ and MoO₂. *J. Phys. Condens. Matter* **26**(30), 305502 (2014)
97. T. Björkman, A. Gulans, A. Krasheninnikov, R. Nieminen, Are we van der Waals ready? *J. Phys. Condens. Matter* **24**(42), 424218 (2012)
98. J. Harris, Simplified method for calculating the energy of weakly interacting fragments. *Phys. Rev. B* **31**(4), 1770 (1985)
99. H. Rydberg, M. Dion, N. Jacobson, E. Schröder, P. Hyldgaard, S. Simak, D.C. Langreth, B.I. Lundqvist, Van der Waals density functional for layered structures. *Phys. Rev. Lett.* **91**(12), 126402 (2003)
100. J. Harris, R. Jones, The surface energy of a bounded electron gas. *J. Phys. F* **4**(8), 1170 (1974)
101. D.C. Langreth, J.P. Perdew, The exchange-correlation energy of a metallic surface. *Solid State Commun.* **17**(11), 1425 (1975)
102. T. Olsen, K.S. Thygesen, Random phase approximation applied to solids, molecules, and graphene-metal interfaces: from van der Waals to covalent bonding. *Phys. Rev. B* **87**(7), 075111 (2013)
103. S. Grimme, Accurate description of van der Waals complexes by density functional theory including empirical corrections. *J. Comput. Chem.* **25**(12), 1463 (2004)
104. S. Grimme, Semiempirical GGA-type density functional constructed with a long-range dispersion correction. *J. Comput. Chem.* **27**(15), 1787 (2006)

105. S. Grimme, J. Antony, S. Ehrlich, H. Krieg, A consistent and accurate ab initio parametrization of density functional dispersion correction (DFT-D) for the 94 elements H-Pu. *J. Chem. Phys.* **132**(15), 154104 (2010)
106. J. Klimeš, D.R. Bowler, A. Michaelides, Van der Waals density functionals applied to solids. *Phys. Rev. B* **83**(19), 195131 (2011)
107. K. Berland, P. Hyldgaard, Exchange functional that tests the robustness of the plasmon description of the van der Waals density functional. *Phys. Rev. B* **89**(3), 035412 (2014)
108. G. Román-Pérez, J.M. Soler, Efficient implementation of a van der Waals density functional: application to double-wall carbon nanotubes. *Phys. Rev. Lett.* **103**(9), 096102 (2009)
109. T. Björkman, A. Gulans, A.V. Krasheninnikov, R.M. Nieminen, Van der Waals bonding in layered compounds from advanced density-functional first-principles calculations. *Phys. Rev. Lett.* **108**(23), 235502 (2012)
110. O.A. Vydrov, T. Van Voorhis, Nonlocal van der Waals density functional: the simpler the better. *J. Chem. Phys.* **133**(24), 244103 (2010)
111. M. Dion, H. Rydberg, E. Schröder, D.C. Langreth, B.I. Lundqvist, Van der Waals density functional for general geometries. *Phys. Rev. Lett.* **92**(24), 246401 (2004)
112. K. Lee, É.D. Murray, L. Kong, B.I. Lundqvist, D.C. Langreth, Higher-accuracy van der Waals density functional. *Phys. Rev. B* **82**(8), 081101 (2010)
113. J. He, K. Hummer, C. Franchini, Stacking effects on the electronic and optical properties of bilayer transition metal dichalcogenides MoS₂, MoSe₂, WS₂, and WSe₂. *Phys. Rev. B* **89**(7), 075409 (2014)
114. Y. Zhao, X. Luo, H. Li, J. Zhang, P.T. Araujo, C.K. Gan, J. Wu, H. Zhang, S.Y. Quek, M.S. Dresselhaus et al., Interlayer breathing and shear modes in few-trilayer MoS₂ and WSe₂. *Nano Lett.* **13**(3), 1007 (2013)
115. N. Marzari, A.A. Mostofi, J.R. Yates, I. Souza, D. Vanderbilt, Maximally localized Wannier functions: theory and applications. *Rev. Mod. Phys.* **84**(4), 1419 (2012)
116. A. Savin, R. Nesper, S. Wengert, T.F. Fässler, The electron localization function. *Angew. Chem. Int. Ed.* **36**(17), 1808 (1997)
117. A.V. Kolobov, P. Fons, J. Tominaga, S.R. Ovshinsky, Vacancy-mediated three-center four-electron bonds in GeTe-Sb₂Te₃ phase-change memory alloys. *Phys. Rev. B* **87**, 165206 (2013)
118. E.R. Johnson, S. Keinan, P. Mori-Sánchez, J. Contreras-Garcia, A.J. Cohen, W. Yang, Revealing noncovalent interactions. *J. Am. Chem. Soc.* **132**(18), 6498 (2010)
119. A. Otero-de-la Roza, E.R. Johnson, J. Contreras-Garcia, Revealing non-covalent interactions in solids: NCI plots revisited. *J. Phys. Chem. Chem. Phys.* **14**, 12165 (2012)
120. A. Otero-de-la Roza, E.R. Johnson, V. Luña, Critic2: A program for real-space analysis of quantum chemical interactions in solids. *Comput. Phys. Commun.* **185**(3), 1007 (2014)
121. R.F.W. Bader, *Atoms in Molecules: A Quantum Theory* (Clarendon Press, Oxford, 1990)
122. E. Kadantsev, MoS₂: materials, physics, and devices, in *Chapter 2: Electronic Structure of Exfoliated MoS₂*, ed. by Z.M. Wang, pp. 37–51 (Springer Science and Business Media, Berlin, 2014)
123. W. Li, M. Guo, G. Zhang, Y.W. Zhang, Gapless MoS₂ allotrope possessing both massless Dirac and heavy fermions. *Phys. Rev. B* **89**(20), 205402 (2014)
124. S. Najmaei, Z. Liu, W. Zhou, X. Zou, G. Shi, S. Lei, B.I. Yakobson, J.C. Idrobo, P.M. Ajayan, J. Lou, Vapour phase growth and grain boundary structure of molybdenum disulphide atomic layers. *Nat. Mater.* **12**(8), 754 (2013)
125. A.M. van der Zande, P.Y. Huang, D.A. Chenet, T.C. Berkelbach, Y. You, G.H. Lee, T.F. Heinz, D.R. Reichman, D.A. Muller, J.C. Hone, Grains and grain boundaries in highly crystalline monolayer molybdenum disulphide. *Nat. Mater.* **12**(6), 554 (2013)
126. X. Zou, Y. Liu, B.I. Yakobson, Predicting dislocations and grain boundaries in two-dimensional metal-disulfides from the first principles. *Nano Lett.* **13**(1), 253 (2012)
127. P. Avouris, Z. Chen, V. Perebeinos, Carbon-based electronics. *Nat. Nanotech.* **2**(10), 605 (2007)
128. C.C. Liu, W. Feng, Y. Yao, Quantum spin Hall effect in silicene and two-dimensional germanium. *Phys. Rev. Lett.* **107**(7), 076802 (2011)

129. W. Zhao, R.M. Ribeiro, G. Eda, Electronic structure and optical signatures of semiconducting transition metal dichalcogenide nanosheets. *Acc. Chem. Res.* **48**(1), 91 (2015)
130. N. Mott, E. Davis, R. Street, States in the gap and recombination in amorphous semiconductors. *Philos. Mag.* **32**(5), 961 (1975)
131. R. Street, T. Searle, I. Austin, The photoluminescence properties of glasses in the As-Se system. *Philos. Mag.* **30**(5), 1181 (1974)
132. R. Street, Luminescence in amorphous semiconductors. *Adv. Phys.* **25**(4), 397 (1976)
133. N. Ravindra, S. Auluck, V. Srivastava, On the Penn gap in semiconductors. *Phys. Status Solidi B* **93**(2), K155 (1979)
134. K. Shimakawa, L. Střížík, T. Wagner, M. Frumar, Penn gap rule in phase-change memory materials: no clear evidence for resonance bonds. *APL Mater.* **3**(4), 041801 (2015)
135. H.L. Liu, C.C. Shen, S.H. Su, C.L. Hsu, M.Y. Li, L.J. Li, Optical properties of monolayer transition metal dichalcogenides probed by spectroscopic ellipsometry. *Appl. Phys. Lett.* **105**(20), 201905 (2014)
136. C. Zhang, H. Wang, W. Chan, C. Manolatou, F. Rana, Absorption of light by excitons and trions in monolayers of metal dichalcogenide MoS₂: experiments and theory. *Phys. Rev. B* **89**(20), 205436 (2014)
137. A. Beal, J. Knights, W. Liang, Transmission spectra of some transition metal dichalcogenides. II. Group VIA: trigonal prismatic coordination. *J Phys. C* **5**(24), 3540 (1972)
138. R. Bromley, R. Murray, A. Yoffe, The band structures of some transition metal dichalcogenides. III. Group VIA: trigonal prism materials. *J. Phys. Condens. Matter* **5**(7), 759 (1972)
139. W. Zhao, Z. Ghorannevis, L. Chu, M. Toh, C. Kloc, P.H. Tan, G. Eda, Evolution of electronic structure in atomically thin sheets of WS₂ and WSe₂. *ACS Nano* **7**(1), 791 (2012)
140. G. Eda, H. Yamaguchi, D. Voiry, T. Fujita, M. Chen, M. Chhowalla, Photoluminescence from chemically exfoliated MoS₂. *Nano Lett.* **11**(12), 5111 (2011)
141. A.R. Klots, A.K.M. Newaz, B. Wang, D. Prasai, H. Krzyzanowska, J. Lin, D. Caudel, N.J. Ghimire, J. Yan, B.L. Ivanov, et al., Probing excitonic states in suspended two-dimensional semiconductors by photocurrent spectroscopy. *Sci. Rep.* **4** (2014). doi:[10.1038/srep06608](https://doi.org/10.1038/srep06608)
142. C. Zhang, A. Johnson, C.L. Hsu, L.J. Li, C.K. Shih, Direct imaging of band profile in single layer MoS₂ on graphite: quasiparticle energy gap, metallic edge states, and edge band bending. *Nano Lett.* **14**(5), 2443 (2014)
143. M.H. Chiu, C. Zhang, H.W. Shiu, C.P. Chuu, C.H. Chen, C.Y.S. Chang, C.H. Chen, M.Y. Chou, C.K. Shih, L.J. Li, Determination of band alignment in the single-layer MoS₂/WSe₂ heterojunction. *Nat. Commun.* **6** (2015). doi:[10.1038/ncomms8666](https://doi.org/10.1038/ncomms8666)
144. M.M. Ugeda, A.J. Bradley, S.F. Shi, H. Felipe, Y. Zhang, D.Y. Qiu, W. Ruan, S.K. Mo, Z. Hussain, Z.X. Shen et al., Giant bandgap renormalization and excitonic effects in a monolayer transition metal dichalcogenide semiconductor. *Nat. Mater.* **13**(12), 1091 (2014)
145. H. Liu, L. Jiao, F. Yang, Y. Cai, X. Wu, W. Ho, C. Gao, J. Jia, N. Wang, H. Fan et al., Dense network of one-dimensional midgap metallic modes in monolayer MoSe₂ and their spatial undulations. *Phys. Rev. Lett.* **113**(6), 066105 (2014)
146. S.G. Sørensen, H.G. Füchtbauer, A.K. Tuxen, A.S. Walton, J.V. Lauritsen, Structure and electronic properties of in situ synthesized single-layer MoS₂ on a gold surface. *ACS Nano* **8**(7), 6788 (2014)
147. M. Yankowitz, D. McKenzie, B.J. LeRoy, Local spectroscopic characterization of spin and layer polarization in WSe₂. *Phys. Rev. Lett.* **115**, 13680 (2015)
148. C. Zhang, Y. Chen, A. Johnson, M.Y. Li, L.J. Li, P.C. Mende, R.M. Feenstra, C.K. Shih, Probing critical point energies of transition metal dichalcogenides: surprising indirect gap of single layer WSe₂. *Nano Lett.* **15**, 6494 (2015)
149. A.J. Bradley, M.M. Ugeda, F.H. da Jornada, D.Y. Qiu, W. Ruan, Y. Zhang, S. Wickenburg, A. Riss, J. Lu, S.K. Mo et al., Probing the role of interlayer coupling and Coulomb interactions on electronic structure in few-layer MoSe₂ nanostructures. *Nano Lett.* **15**(4), 2594 (2015)
150. Y.L. Huang, Y. Chen, W. Zhang, S.Y. Quek, C.H. Chen, L.J. Li, W.T. Hsu, W.H. Chang, Y.J. Zheng, W. Chen, et al., Bandgap tunability at single-layer molybdenum disulphide grain boundaries. *Nat. Commun.* **6** (2015). doi:[10.1038/ncomms7298](https://doi.org/10.1038/ncomms7298)

151. H. Yuan, M.S. Bahramy, K. Morimoto, S. Wu, K. Nomura, B.J. Yang, H. Shimotani, R. Suzuki, M. Toh, C. Kloc et al., Zeeman-type spin splitting controlled by an electric field. *Nat. Phys.* **9**(9), 563 (2013)
152. L. Sun, J. Yan, D. Zhan, L. Liu, H. Hu, H. Li, B.K. Tay, J.L. Kuo, C.C. Huang, D.W. Hewak et al., Spin-orbit splitting in single-layer MoS₂ revealed by triply resonant Raman scattering. *Phys. Rev. Lett.* **111**(12), 126801 (2013)
153. S.W. Han, G.B. Cha, E. Frantzeskakis, I. Razado-Colambo, J. Avila, Y.S. Park, D. Kim, J. Hwang, J.S. Kang, S. Ryu et al., Band-gap expansion in the surface-localized electronic structure of MoS₂ (0002). *Phys. Rev. B* **86**(11), 115105 (2012)
154. P. Zhang, P. Richard, T. Qian, Y.M. Xu, X. Dai, H. Ding, A precise method for visualizing dispersive features in image plots. *Rev. Sci. Instrum.* **82**(4), 043712 (2011)
155. H. Peelaers, C.G. Van de Walle, Effects of strain on band structure and effective masses in MoS₂. *Phys. Rev. B* **86**(24), 241401 (2012)
156. A. Ayari, E. Cobas, O. Ogundadegbe, M.S. Fuhrer, Realization and electrical characterization of ultrathin crystals of layered transition-metal dichalcogenides. *J. Appl. Phys.* **101**(1), 014507 (2007)
157. R. Fivaz, E. Mooser, Mobility of charge carriers in semiconducting layer structures. *Phys. Rev.* **163**(3), 743 (1967)
158. N. Alidoust, G. Bian, S.Y. Xu, R. Sankar, M. Neupane, C. Liu, I. Belopolski, D.X. Qu, J.D. Denlinger, F.C. Chou, et al., Observation of monolayer valence band spin-orbit effect and induced quantum well states in MoX₂. *Nat. Commun.* **5** (2014). doi:[10.1038/ncomms5673](https://doi.org/10.1038/ncomms5673)
159. S. Tongay, J. Zhou, C. Ataca, K. Lo, T.S. Matthews, J. Li, J.C. Grossman, J. Wu, Thermally driven crossover from indirect toward direct bandgap in 2D semiconductors: MoSe₂ versus MoS₂. *Nano Lett.* **12**(11), 5576 (2012)
160. H. Rostami, A.G. Moghaddam, R. Asgari, Effective lattice hamiltonian for monolayer MoS₂: tailoring electronic structure with perpendicular electric and magnetic fields. *Phys. Rev. B* **88**(8), 085440 (2013)
161. J. Zheng, H. Zhang, S. Dong, Y. Liu, C.T. Nai, H.S. Shin, H.Y. Jeong, B. Liu, K.P. Loh, High yield exfoliation of two-dimensional chalcogenides using sodium naphthalenide. *Nat. Commun.* **5** (2014). doi:[10.1038/ncomms3995](https://doi.org/10.1038/ncomms3995)
162. P.C. Yeh, W. Jin, N. Zaki, D. Zhang, J.T. Liou, J.T. Sadowski, A. Al-Mahboob, J.I. Dadap, I.P. Herman, P. Sutter et al., Layer-dependent electronic structure of an atomically heavy two-dimensional dichalcogenide. *Phys. Rev. B* **91**(4), 041407 (2015)
163. D. Le, A. Barinov, E. Preciado, M. Isarraran, I. Tanabe, T. Komatsu, C. Troha, L. Bartels, T.S. Rahman, P.A. Dowben, Spin-orbit coupling in the band structure of monolayer WSe₂. *J. Phys. Condens. Matter* **27**(18), 182201 (2015)
164. A. Chernikov, T.C. Berkelbach, H.M. Hill, A. Rigosi, Y. Li, O.B. Aslan, D.R. Reichman, M.S. Hybertsen, T.F. Heinz, Exciton binding energy and nonhydrogenic Rydberg series in monolayer WS₂. *Phys. Rev. Lett.* **113**(7), 076802 (2014)
165. K. He, N. Kumar, L. Zhao, Z. Wang, K.F. Mak, H. Zhao, J. Shan, Tightly bound excitons in monolayer WSe₂. *Phys. Rev. Lett.* **113**(2), 026803 (2014)
166. K.F. Mak, K. He, C. Lee, G.H. Lee, J. Hone, T.F. Heinz, J. Shan, Tightly bound trions in monolayer MoS₂. *Nat. Mater.* **12**(3), 207 (2013)
167. J.S. Ross, S. Wu, H. Yu, N.J. Ghimire, A.M. Jones, G. Aivazian, J. Yan, D.G. Mandrus, D. Xiao, W. Yao, et al., Electrical control of neutral and charged excitons in a monolayer semiconductor. *Nat. Commun.* **4** (2013). doi:[10.1038/ncomms2498](https://doi.org/10.1038/ncomms2498)
168. A. Chernikov, C. Ruppert, H.M. Hill, A.F. Rigosi, T.F. Heinz, Population inversion and giant bandgap renormalization in atomically thin WS₂ layers. *Nat. Photonics* **9**(7), 466 (2015)
169. Y.Y. Hui, X. Liu, W. Jie, N.Y. Chan, J. Hao, Y.T. Hsu, L.J. Li, W. Guo, S.P. Lau, Exceptional tunability of band energy in a compressively strained trilayer MoS₂ sheet. *ACS Nano* **7**(8), 7126 (2013)
170. K. He, C. Poole, K.F. Mak, J. Shan, Experimental demonstration of continuous electronic structure tuning via strain in atomically thin MoS₂. *Nano Lett.* **13**(6), 2931 (2013)

171. S.B. Desai, G. Seol, J.S. Kang, H. Fang, C. Battaglia, R. Kapadia, J.W. Ager, J. Guo, A. Javey, Strain-induced indirect to direct bandgap transition in multilayer WSe₂. *Nano Lett.* **14**(8), 4592 (2014)
172. Y. Lin, X. Ling, L. Yu, S. Huang, A.L. Hsu, Y.H. Lee, J. Kong, M.S. Dresselhaus, T. Palacios, Dielectric screening of excitons and trions in single-layer MoS₂. *Nano Lett.* **14**(10), 5569 (2014)
173. S. Manzeli, A. Allain, A. Ghadimi, A. Kis, Piezoresistivity and strain-induced band gap tuning in atomically thin MoS₂. *Nano Lett.* **15**(8), 5330 (2015)
174. M.Y. Tsai, A. Tarasov, Z.R. Hesabi, H. Taghinejad, P.M. Campbell, C. Joiner, A. Adibi, E.M. Vogel. Flexible MoS₂ field-effect transistors for gate-tunable piezoresistive strain sensors. *ACS Appl. Mater. Interfaces* **7**, 12850 (2015)

Chapter 7

Raman Scattering of 2D TMDCs

Raman scattering is a powerful tool to obtain information about the lattice vibrations of a crystal and it has been widely applied for the characterization of 2D TMDCs. This chapter provides a detailed description of the symmetry of odd- and even-layered structures, non-resonant and resonant Raman scattering, as well as polarisation effects with a special accent on features that are only observed in few-layer systems. The effects of hydrostatic pressure, strain, temperature, interlayer coupling and other factors are also covered.

7.1 Symmetry of Odd- and Even-Layer Structures

Symmetry analysis of vibrational modes in bulk TMDCs has been performed in [1] and was summarized earlier (see Sect. 3.1.6). In few-layer TMDCs, the symmetry along the z -axis is reduced due to the lack of translation in this direction. Below we discuss the symmetry of odd- and even-layer structures for both 2H and 1T phases, starting with the 2H phase.

7.1.1 2H-Polytype

In the 2D case of the 2H phase, the number of symmetry operations is decreased from 24 in the bulk phase to 12 each in structures with even- and odd number of layers, with symmetry groups different from that of the bulk 2H materials (D_{6h}^4). The symmetry operations in few-layer structures are illustrated in Fig. 7.1, using single-layer and bi-layer structures as examples for odd- and even-layered structures, respectively, following the analysis presented in [2]. There are 12 symmetry operations in odd-layer structures, namely, E (identity symmetry), $2C_3$ (the axis of the clockwise and anticlockwise rotations is shown in Fig. 7.1a), $3C'_2$ (the three rotation axes are shown

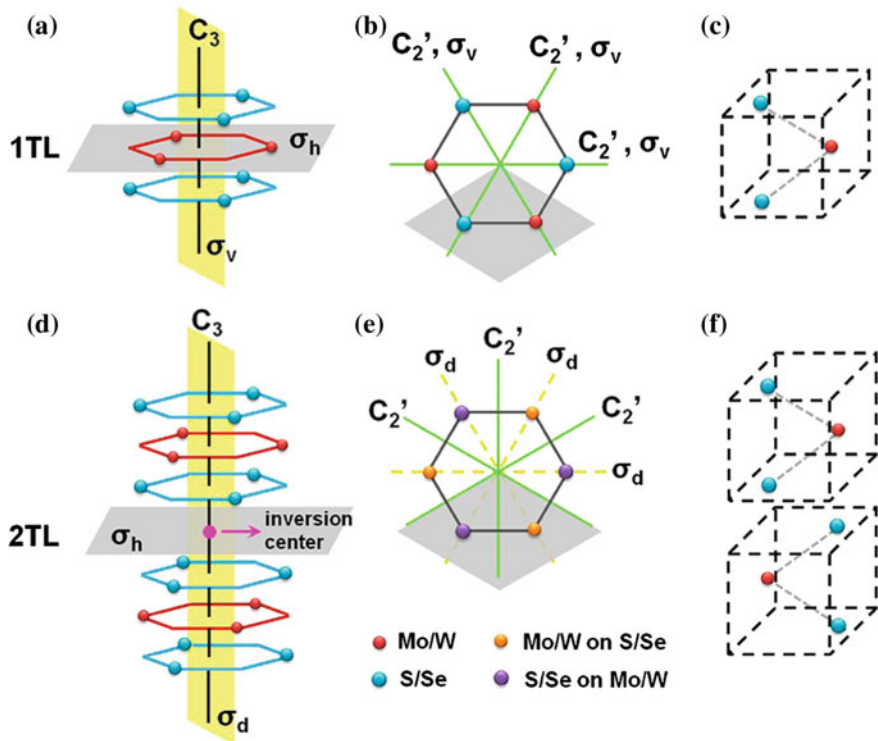


Fig. 7.1 Symmetry operations in a monolayer and bilayer of group VIB TMDCs. **a** Side view of a monolayer. The axis of the two C_3 operations (clockwise and anticlockwise) is denoted as the black line. The horizontal (σ_h) and vertical (σ_v) reflection operations are shown as the gray and yellow planes, respectively. **b** Top view of a monolayer. The axes of the three C_2' operations are denoted as the green lines, which are lying in the σ_h plane. The top view of the σ_v planes are also demonstrated as the green lines. The gray diamond shows the unit cell from a top view. **c** Side view of the monolayer unit cell, where one Mo atom and two S atoms are contained. **d** Side view of bi-layer with /AbA BaB/ stacking. The axis of the C_3 operations is denoted as the black line. The inversion center is demonstrated by the pink solid circle. The horizontal (σ_h) and dihedral (σ_d) reflection operations are shown as the gray and yellow planes, respectively. Note that σ_h is not one of the operations in the space group for the bi-layer. **e** Top view of bi-layer. The purple spheres represent the sites where two S atoms (of the top layer) sit on top of one Mo atoms (of the bottom layer). The orange spheres represent the sites where one Mo atom (top layer) sits on top of two S atoms (bottom layer). The axes of the three C_2' operations are denoted as the green lines, which are lying in the σ_h plane. The top view of the σ_d planes are shown as the yellow dashed lines. The gray diamond shows the unit cell. **f** Side view of the bi-layer unit cell, which contains four S atoms and two Mo atoms. The two layers are represented by two dashed boxes [2]. Copyright 2013 American Chemical Society. Published with permission

in Fig. 7.1b and lie in the σ_h plane), σ_h (the horizontal reflection plane is represented by the gray plane in Fig. 7.1a), $2S_3$ (two C_3 rotations followed by a σ_h reflection), $3\sigma_v$ (one of the vertical reflection planes is represented as the yellow plane in Fig. 7.1a, and the top views are shown as the green solid lines in Fig. 7.1b). In a similar way, the 12 symmetry operations in even-layer structures are: E , $2C_3$, $3C_2'$ (the three

rotation axes are shown in Fig. 7.1e and lie in the σ_h plane), i (the inversion center is shown as the pink solid circle in Fig. 7.1d), $3\sigma_d$ (one of the dihedral reflection planes is represented as the yellow plane in Fig. 7.1d, and the top views are shown as the yellow dashed lines in Fig. 7.1e), $2S_6$ (clockwise and anti-clockwise C_6 rotations followed by a σ_h reflection).

Consequently, odd-layer structures belong to the symmorphic space group D_{3h}^1 ($P\bar{6}m2$), which has no inversion symmetry; the irreducible representations of the zone-center phonons can be written as [2]:

$$\Gamma_{odd} = ((3N - 1)/2)(A'_1 + E'') + ((3N + 1)/2)(A''_2 + E') \quad (7.1)$$

where $N = 1, 3, 5$, etc.

The even-layer structures belong to the symmorphic space group D_{3d}^3 ($P\bar{3}m1$) with inversion symmetry; the irreducible representations for the zone-center phonons are:

$$\Gamma_{even} = (3N/2)(A_{1g} + A_{2u} + E_g + E_u) \quad (7.2)$$

where, $N = 2, 4, 6$, etc.

7.1.2 1T-Polytype

Figure 7.2a, d shows the monolayer and bi-layer structures, respectively, of the 1T polytype. The structure has the D_{3d}^3 ($P\bar{3}m1$) space group. The symmetry operations of a monolayer are E , $2C_3$, $3C'_2$ (the C'_2 rotation axes are in the reflection plane, between the two chalcogen atoms, dividing in half the transition metal atom, as shown in the black lines in Fig. 7.2c), inversion i (red dot in the transition metal atom), $3\sigma_d$ (dihedral vertical mirror planes represented by red lines in Fig. 7.2b), and $2S_6$ (clockwise and anticlockwise rotations by 60° followed by a σ_h reflection). In the bi-layer case, the same operations are still valid, but now the inversion and the reflection planes (Fig. 7.2f) for the S_6 operation are located in the van der Waals gap [3].

The presence or absence of inversion symmetry is an important aspect of few-layered TMDCs from several perspectives, e.g. (i) it opens the possibility of coupled spin and valley physics in monolayers (Chap. 11) and (ii) is also important for optics, e.g., second-harmonic generation (see Sect. 12.1).

Table 7.1 summarises the space groups and groups of the wave vectors for the high-symmetry points and directions in the Brillouin zone for an odd and even number of layers for the 2H polytype. The data for the 1T polytype are given in Table 3.3, where the same description applies for the bulk and odd/even layers.

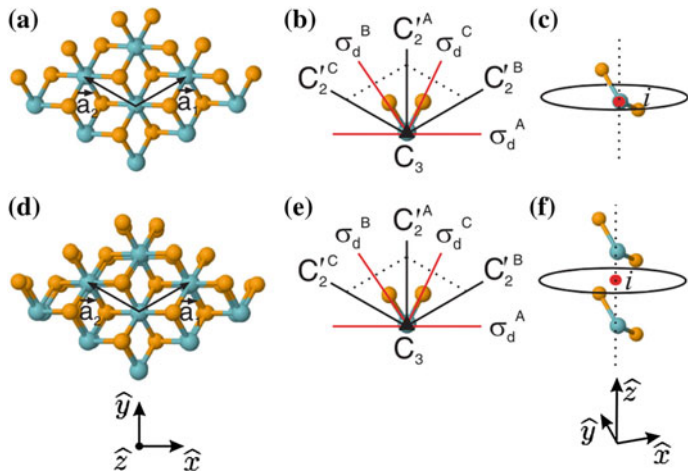


Fig. 7.2 Primitive unit cells and symmetry operations of the 1T TMDCs polytype. **a** and **d** show the *top views* of a monolayer and a bi-layer. In (**d**), chalcogen atoms are on *top* of chalcogen atoms, and transition metal atoms are on *top* of transition metal atoms, giving a similar *top view* to that observed for 1TL. In (**b**) and (**e**), the C_3 rotation axes (represented as *black triangles*) are perpendicular to the basal plane. The *red lines* represent σ_d mirror planes, while the *black lines* stand for C'_2 rotation axes that lie in the σ_h plane. The primitive unit cells for the monolayer (and bulk) and for bilayer are shown in (**c**) and (**f**), respectively, and the *red dot* in their centers denotes the inversion operations. Notice that σ_h is not a symmetry operation for a monolayer (or N -odd), bi-layer (or N -even), or bulk, but the reflection plane shown to indicate the reflection in the two S_6 operations [3]. Copyright 2014 by the American Physical Society. Reprinted with permission

Table 7.1 Space group and group of the wave vector for the high-symmetry points and directions in the Brillouin zone for odd and even number of layers in the 2H polytype

Number of layers	Space group	Γ	$K(K')$	M	$T(T')$	Σ
Odd	$D_{3h}^1 (P\bar{6}m2)$	$D_{3h}^1 (P\bar{6}m2)$	$C_{3h}^1 (P\bar{6})$	$C_{2v}^{14} (Amm2)$	C_s^{xy} (or C_s^1 , Pm)	$C_{2v}^{14} (Amm2)$
Even	$D_{3d}^3 (P\bar{3}m1)$	$D_{3d}^3 (P\bar{3}m1)$	$D_3^2 (P321)$	$C_{2h}^3 (C2/m)$	$C_2^3 (C2)$	C_s^{xz} (or C_s^3 , Cm)

7.1.3 Raman Tensors

The Raman scattering intensity is proportional to $|e_i \cdot \tilde{R} \cdot e_s|^2$, where e_i is the polarization vector of the incident light and e_s is that of the scattered light. \tilde{R} is the Raman tensor. A given phonon mode can be observed by Raman scattering spectroscopy only when $|e_i \cdot \tilde{R} \cdot e_s|^2$ has a nonzero value. Raman tensors of the Raman-active interlayer vibrational modes were analysed in several works [2–5]. Following [3], the Raman tensors for the 2H polytype with N-odd layers can be written as:

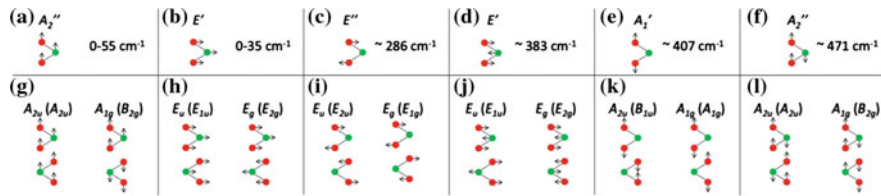


Fig. 7.3 **a–f** Normal mode vibration patterns and symmetries of single-layer MoS₂ (*top*). The frequencies denote the typical range found in few-layer MoS₂. **g–l** The corresponding in-phase and antiphase combination normal modes for bilayer (bulk) MoS₂ (*bottom*) [7]. Copyright 2015 by the American Physical Society. Reprinted with permission

$$\begin{aligned} \Gamma_1^+(A'_1) &: \begin{pmatrix} a & 0 & 0 \\ 0 & a & 0 \\ 0 & 0 & b \end{pmatrix}, \\ \Gamma_3^+(E')_{(x)} &: \begin{pmatrix} 0 & d & 0 \\ d & 0 & 0 \\ 0 & 0 & 0 \end{pmatrix}, \quad \Gamma_3^+(E')_{(y)} : \begin{pmatrix} d & 0 & 0 \\ 0 & -d & 0 \\ 0 & 0 & 0 \end{pmatrix} \\ \Gamma_3^-(E'') &: \begin{pmatrix} 0 & 0 & 0 \\ 0 & 0 & c \\ 0 & c & 0 \end{pmatrix}, \quad \begin{pmatrix} 0 & 0 & -c \\ 0 & 0 & 0 \\ -c & 0 & 0 \end{pmatrix} \end{aligned}$$

For the 2H polytype with N-even and for both N-even and N-odd for the 1T polytype, the Raman tensors are the same as for the bulk 1T phase (see Sect. 3.1.6).

As follows from the above description, the symmetry of odd-layer and even-layer structures are different and, strictly speaking, different notations should be used for the Raman modes in these structures. While some authors use the correct notations, in most original papers, however, this difference is ignored and the notations used are often those for the bulk phase. In particular, it has become customary to associate the A'_1 and E' optical phonon modes of the single layer with the A_{1g} and E_{2g} modes of the bulk. In what follows, the notations used in the original publications are usually preserved. The correspondence between the notations for the bulk, odd-layer and even-layer TMDC structures was discussed in several papers (e.g. [6, 7]) and is shown in Fig. 7.3. Figure 7.4 additionally shows the correlation of the symmetries of the normal modes between bulk, single-, and bilayer MoS₂.

7.2 Non-resonant Raman Scattering

7.2.1 Unusual Behaviour of the E_{2g}^1 and A_{1g} Modes

Raman scattering was first applied for the characterization of single layer MoS₂ in [8]. These results are reproduced in Fig. 7.5 that shows representative Raman spectra for single- and few-layer MoS₂ samples. Among the four Raman-active modes of the

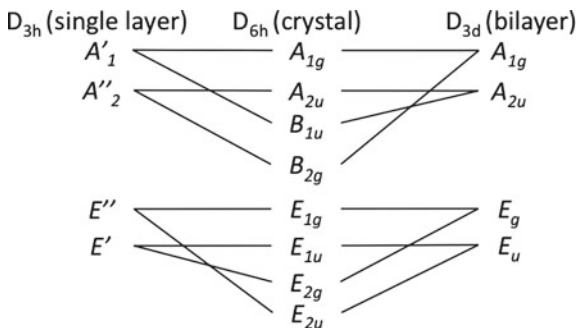


Fig. 7.4 Correlation diagram of the symmetries of the normal modes for bulk ($2H$), single-, and bilayer MoS_2 [7]. Copyright 2015 by the American Physical Society. Reprinted with permission

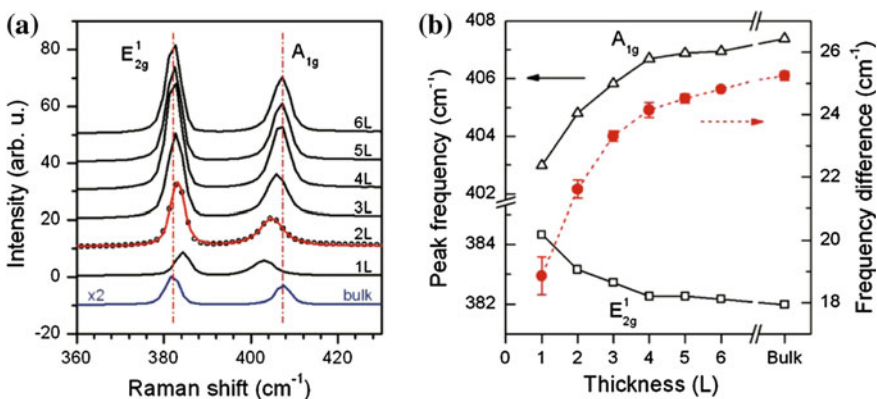


Fig. 7.5 **a** Raman spectra of thin (n layers) and bulk MoS_2 films. The solid line for the 2L spectrum is a double Voigt fit through data (circles for 2L, solid lines for the rest). **b** Frequencies of E_{2g}^1 and A_{1g} Raman modes (left vertical axis) and their difference (right vertical axis) as a function of layer thickness [8]. Copyright 2010 American Chemical Society. Published with permission

bulk $2H$ - MoS_2 crystal, the E_{2g}^1 and A_{1g} modes near 400 cm^{-1} were clearly observed. The other two Raman active modes expected from group analysis of the structure could not be detected due to the selection rules for the used back-scattering geometry and the limited rejection of Rayleigh scattered radiation.

The main finding (Fig. 7.5a, b) was that the E_{2g}^1 vibration softened (red shifted), while the A_{1g} vibration stiffened (blue shifted) with increasing sample thickness. For films of four or more layers, the frequencies of both modes converged to bulk values. The rate of frequency change was twice as large for the A_{1g} as for the E_{2g}^1 mode.

It was noted that the observed shift in the frequency of the A_{1g} mode as a function of thickness was consistent with a transition from surface to bulk layers [9]. As regards the opposite trend for the E_{2g}^1 mode, it was proposed that it may reflect the influence of stacking-induced structural changes, or, alternatively, could be attributed to long-range Coulomb interlayer interactions [10].

In addition to the peak energies, the intensities and widths of the peaks also varied with the number of layers [8]. The authors further studied Raman scattering on supported and suspended films but found no meaningful difference [8].

It was noted that the strong vibrational mode at ca. 384 cm^{-1} , corresponding to the E_{2g}^1 mode of bulk $2H$ -MoS₂, indicates that exfoliated single layers maintain the trigonal prismatic coordination of bulk MoS₂ and suggests that the absence of this mode (associated with octahedral coordination) found in single layers obtained using Li intercalation (cf. Fig. 5.3) resulted from an intercalation-assisted phase transformation [8]. The difference in the position and intensities of the A_{1g} and E_{2g}^1 peaks was proposed as an efficient method to identify the MoS₂ thickness with a monolayer precision.

The issue of the opposite shift of the A_{1g} and E_{2g}^1 modes was further addressed in [11] using DFT simulations. It was found that the interlayer distance c noticeably increased upon the reduction of the number of layers, while changes in the intralayer lattice parameters a and b were much smaller. Derivatives of the modes frequency with respect to the lattice parameters were further calculated and it was found that while the $\frac{\partial\omega}{\partial a}$ and $\frac{\partial\omega}{\partial b}$ values were both negative and had rather similar values for A_{1g} and E_{2g}^1 modes, the sign of $\frac{\partial\omega}{\partial c}$ was negative for A_{1g} while it was positive for E_{2g}^1 . As a result, the total frequency shift $\Delta\omega = \frac{\partial\omega}{\partial a} \cdot \Delta a + \frac{\partial\omega}{\partial b} \cdot \Delta b + \frac{\partial\omega}{\partial c} \cdot \Delta c$ was mainly determined by the last term, which has a different sign for the two modes. It was [11] concluded that this is a consequence of the reduced interlayer coupling with decreasing slab thickness.

It should be noted that upon application of hydrostatic pressure to bulk MoS₂, both peaks shift *in the same direction* (stiffened) [12], indicating that the difference in the trend is not simply related to the interlayer distance (and hence coupling) alone, the situation is more complicated.

Interatomic distances and atomic charges for bi-layer MoSe₂ were also investigated [11] and it was found that for increasing interlayer distance, the S–S distance across the layer increased, concomitant with an increase in the distance between a Mo atom and the S atom located at the interface. At the same time, the Mo–S distance to the S atom located at the outermost plane remained essentially unchanged. In parallel with the changes in distances, the charge on the Mo atom decreased, while the charge on the S atoms located at the interface increased. The charge on the outermost S atom remained unchanged. This result demonstrates that interlayer coupling strongly affects the electron distribution among the S atoms at interfaces and Mo atoms, with subsequent effects on the electronic properties.

Similar trends for the E_{2g}^1 mode were found in other transition TMDCs such as MoSe₂ [13, 14], WS₂ [15] and WSe₂ [2, 16, 17]. The results for WS₂ and WSe₂ are shown in Fig. 7.6.

In a subsequent work on MoSe₂ [13], similar Raman spectra were obtained but it was noted that the intensity ratio between the A_{1g} and E_{2g}^1 modes ($I_{A_{1g}}/I_{E_{2g}^1}$) changed significantly as a function of the layer number, namely from 4.9 for few-layer (ca. 10 layers) to 23.1 for the single-layer MoSe₂, in contrast to MoS₂, where this ratio remained nearly constant (ca. 1.2).

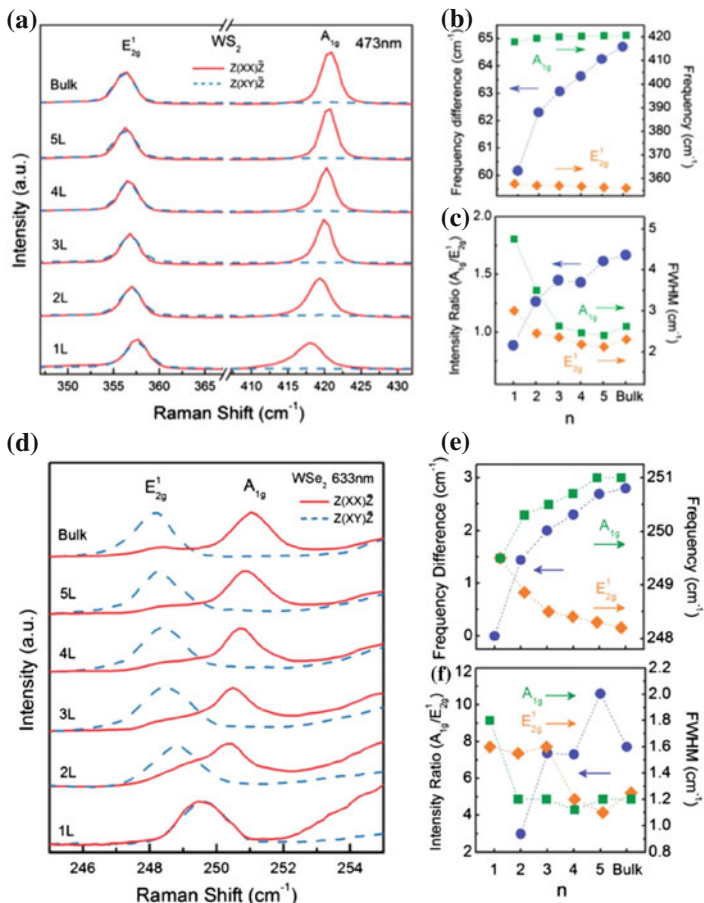


Fig. 7.6 Raman spectra of 1–5L and bulk WS₂ (**a**) and WSe₂ (**d**) flakes obtained in the parallel and cross polarization conditions. The spectra are normalized and vertically offset for clarity. **b, e** Position of the A_{1g} and E_{2g}¹ modes (right vertical axis) and their difference (left vertical axis) as a function of the number of layers (n). **c, f** Intensity ratio (left vertical axis) and FWHM (right vertical axis) of A_{1g} and E_{2g}¹ modes as a function of the number of layers. The excitation wavelengths are marked in panels (**a**) and (**d**) [17]. Reproduced by permission of The Royal Society of Chemistry

Experimental and theoretical papers discussed that the anomalous trend reflects the presence of additional interactions, and possible explanations for this trend are stacking-induced structural changes [8] or long-range Coulomb interactions [18]. In [19] through a combination of Raman scattering experiment and theoretical studies the unusual trend was attributed to surface effects competing with the thickness effects (Fig. 7.7). This approach was successfully extended to WSe₂ [4].

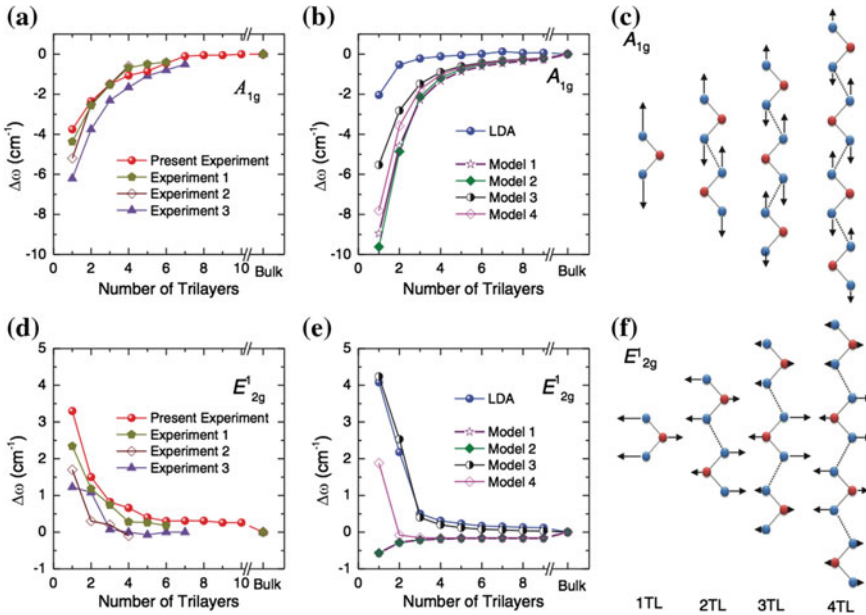


Fig. 7.7 Frequency evolutions of the high-frequency (**a–c**) A_{1g} and (**d–f**) E_{2g}^1 modes showing the frequency differences with respect to their corresponding bulk values. Data marked as experiments 1, 2, and 3 in the figure are from the literature. The force constants model results for the A_{1g} and E_{2g}^1 modes are shown in (**b**) and (**e**), where model 1 uses parameters from the bulk, model 2 uses parameters from the interior of the thin films, model 3 is the same as model 2 but takes into account modified surface force constants on both surfaces, and model 4 is like model 3 but with surface force constants on one surface only [19]. Copyright 2013 by the American Physical Society. Reprinted with permission

A theoretical study of lattice dynamics of 3D and 2D MoSe₂ was performed in [20], where cohesive energy, phonon dispersion curves, and corresponding density of states and related properties, such as Born-effective charges, dielectric constants, Raman and infrared active modes were calculated for 3D layered as well as 2D single-layer MoSe₂ using their optimized structures.

A specific behavior was observed in WSe₂ [21]. While the E_{2g}^1 and A_{1g} modes were degenerate in bulk WSe₂ yielding a single Raman peak, as the dimensionality was lowered, the experimentally observed peak splitted into two. In contrast, the ab-initio calculations predicted that the degeneracy should be retained even for WSe₂ monolayers. It was further found that for minuscule biaxial strain, the degeneracy was preserved, but once the crystal symmetry was broken by a small uniaxial strain, the degeneracy was lifted. It was speculated that the experimentally observed peak splitting may be related to the roughness of the SiO₂ substrate onto which the monolayer was transferred, which would generate both biaxial and uniaxial strain components or, alternatively, strain may be induced by the exfoliation process.

7.2.2 Davydov Splitting

Davydov splitting is typically observed in layered crystals. The Raman-infrared mutual exclusion implied by the bulk crystal symmetry means that there is no symmetry-induced coincidence between frequencies observed in the infrared and Raman spectra. At the same time, the layer symmetry suggests the appearance in Raman scattering of the same eigenfrequencies that occur in infrared absorption, in marked contrast to the mutual exclusion dictated by the crystal symmetry [22]. The splitting of the Raman and IR frequencies due to intermolecular or interlayer interactions is known as Davydov splitting [23].

This issue for TMDC few-layers was addressed in [18]. The Raman-active E_{2g}^1 and infra-red active E_{1u} modes were considered and it was noted that in the bulk phase they are almost degenerate, the latter having 1 cm^{-1} higher frequency [24]. Since bulk MoS₂(2H) possesses a center of inversion, infrared- and Raman-active modes are mutually exclusive [24]. Possibly the degeneracy is due to the fact that the E_{2g}^1 and E_{1u} modes differ only by an interlayer phase shift of π . The authors have pointed out in their earlier paper [25] that if the interlayer interaction is assumed to be weak in comparison with the forces within layers, the E_{2g}^1 and E_{1u} modes will be degenerate.

The authors of [18] note that the fact that splitting between the E_{2g}^1 and E_{1u} modes is such that the E_{1u} has a higher frequency is unusual [26]. Indeed, for the E_{2g}^1 mode, the sulfur atoms of different layers move in opposite direction and thus the additional ‘spring’ between sulfur atoms of the neighboring layers should increase the frequency of the E_{2g}^1 mode with respect of that of the E_{1u} mode, where sulfur atoms of the neighboring sheets are moving in phase (Fig. 7.8).

In a single layer, the high-frequency Γ modes E_{1u} and E_{2g}^1 collapse into a single mode E' . It was noted [18] that the bulk E_{2g}^1 mode is lower in frequency than the single-layer E' mode. This contradicts the expectation that the additional interlayer interaction should increase the frequency but is in line with the anomalous sign of the Davydov splitting between the bulk E_{2g}^1 and E_{1u} modes. It was finally concluded that the unusual behaviour of the E_{2g}^1 mode is caused by an increase in the dielectric screening which reduces the long-range Coulomb interaction between the effective charges and thus reduces the overall restoring force on the atoms [18].

Davydov splitting of mid-frequency modes in N -layer MoTe₂ in the range of 100 to 200 cm^{-1} was studied in [28].

7.2.3 Low-Frequency Modes

In [29, 30], low frequency Raman modes were studied and the results essentially agree with each other. Similar to the case of the A_{1g} and E_{2g}^1 modes, it was found [30] that in the low-frequency range, two modes can be clearly seen, with one of them (E_{2g}^2) undergoing a blueshift with increasing thickness, from 22 cm^{-1} in the

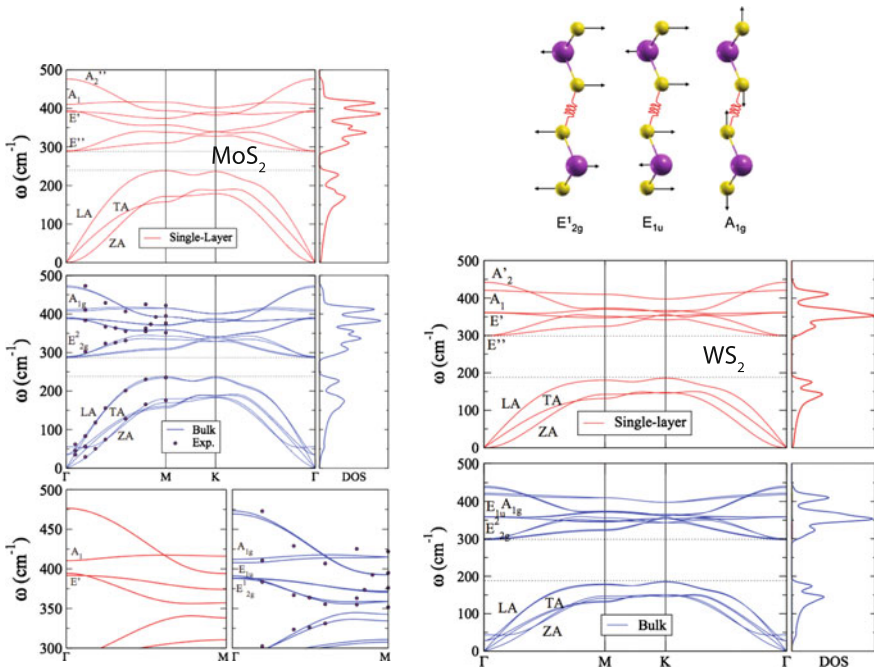


Fig. 7.8 Phonon dispersion curves and density of states of single-layer and bulk MoS₂ (left) and WS₂ (right). For MoS₂, points are experimental data from [27]. Bottom left panel branches in the region of the E_{2g}^1 and A_{1g} modes of MoS₂ [18]. Copyright 2011 by the American Physical Society. Reprinted with permission

bilayer to 32 cm⁻¹ in bulk form, while the other mode, characterised by a broad bandwidth, undergoes an opposite evolution from 42 cm⁻¹ in a bi-layer to 15 cm⁻¹ in a seven-layer sample. A very similar result was obtained for the E_{2g}^2 mode in [29], despite the absolute value being consistently smaller (by ca. 3 cm⁻¹). The E_{2g}^2 mode was identified as the interlayer shear mode [2, 5].

The other mode has been described as a compression mode (see Fig. 7.9a). It follows a $1/N$ thickness dependence (Fig. 7.9c), from which it was concluded that it can be viewed as a standing wave in a multilayer attached to a substrate [31]. An alternative reference proposed for this mode is a layer-breathing mode [2, 5].

Low-frequency interlayer shear and layer breathing modes were studied in detail in [2, 5]. The approaches used and the results obtained were very similar. Below we concentrate on the results reported in [2].

Considering the Raman tensors of the Raman active modes and using the Porto notations (see Sect. 3.2.2), the interlayer shear modes E' and E_g can be observed for both the $\bar{z}(xx)z$ and $\bar{z}(xy)z$ polarization configurations, while the interlayer breathing modes A'_1 and A_{1g} can only be observed for the $\bar{z}(xx)z$ configuration.

Evolution of the polarized low-frequency Raman spectra as a function of number of layers is shown in Fig. 7.10 for MoS₂ and WSe₂ [2]. The Raman-active bulk mode

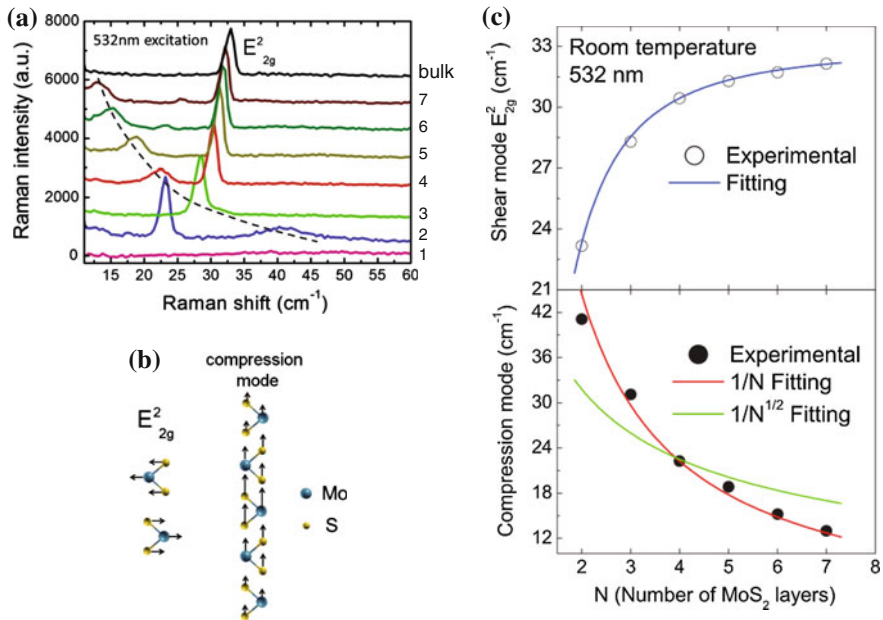


Fig. 7.9 **a** Low-wave-number Raman spectra of atomically thin MoS₂ flakes with different thicknesses under 532 nm excitation. The dashed line denotes the evolution of the weaker low frequency mode. **b** Schematics of Raman-active modes. **c** The thickness dependence of frequencies of the E_{2g}^2 shear mode (upper panel) and of the compression mode (lower panel). The red and green curves are produced with least-squares fitting [30]. Copyright 2012 by the American Physical Society. Reprinted with permission

E_{2g}^2 (labeled *S1*) corresponds to an interlayer shear mode, where the adjacent layers are vibrating out-of-phase. For MoS₂, the *S1* peak moves to lower frequencies as the thickness changes from bulk (ca. 32 cm^{-1}) to a bi-layer (ca. 22 cm^{-1}). Based on DFT calculations, it was concluded that the *S1* peak corresponds to the highest frequency shear mode. The other (broader) peak (labeled as *B1*), was assigned to the lowest frequency interlayer out-of-plane breathing mode. This assignment is consistent with the disappearance of *B1* in the $\bar{z}(xy)z$ polarization configuration, in accordance with the Raman selection rule.

For samples with a thickness larger than 3 layers, additional peaks, labeled *S2* and *B2*, were observed showing similar thickness trends as *S1* and *B1*. Based on DFT calculations it was concluded that *B2* corresponds to the breathing mode with the third lowest frequency, while the *S2* peaks corresponds to the shear mode with the third highest frequency for the *N*-layer system. The atomic displacements corresponding to these modes are shown in Fig. 7.11.

In Fig. 7.12 frequency evolution of the measured and simulated (using a linear chain model) frequencies of the shear and breathing modes of MoSe₂ and WSe₂ as a function of the number of layers.

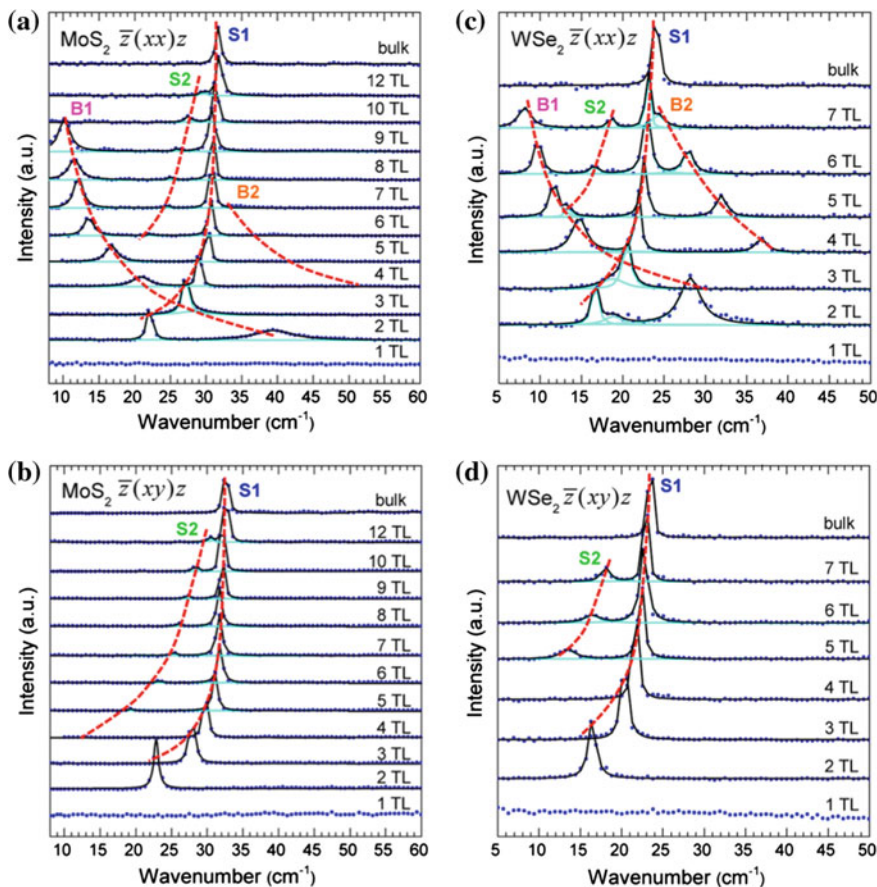


Fig. 7.10 Low-frequency Raman spectrum evolutions as a function of the number of layers in MoS₂ and WSe₂. **a, b** Low-frequency Raman spectra of 1–12 layer structures of MoS₂ measured using (a) the $\bar{z}(xx)z$ polarization configuration, and (b) the $\bar{z}(xy)z$ polarization configuration. **c, d** Low-frequency Raman spectra of 1–7 layer samples of WSe₂ measured under the (c) $\bar{z}(xx)z$ polarization configuration and (d) $\bar{z}(xy)z$ polarization configuration. The blue dots are experimental data points, while the black solid curves are Lorentzian fittings to the data. The Rayleigh scattering background has been subtracted for all of the spectra using a polynomial baseline treatment. The spectra are normalized by the intensity of the E_{2g}^1 peak of the bulk phase [2]. Copyright 2013 American Chemical Society. Published with permission

Very similar conclusions were independently drawn in [5] where the same modes were identified by polarization measurements and symmetry analysis and also using the chain model. It was additionally found that the peak positions change with different scaling for odd and even numbers of layers.

The low frequency modes were demonstrated to be an efficient means to determine not only the number of layers but also their stacking configurations (e.g. 2H vs. 3R) [32].

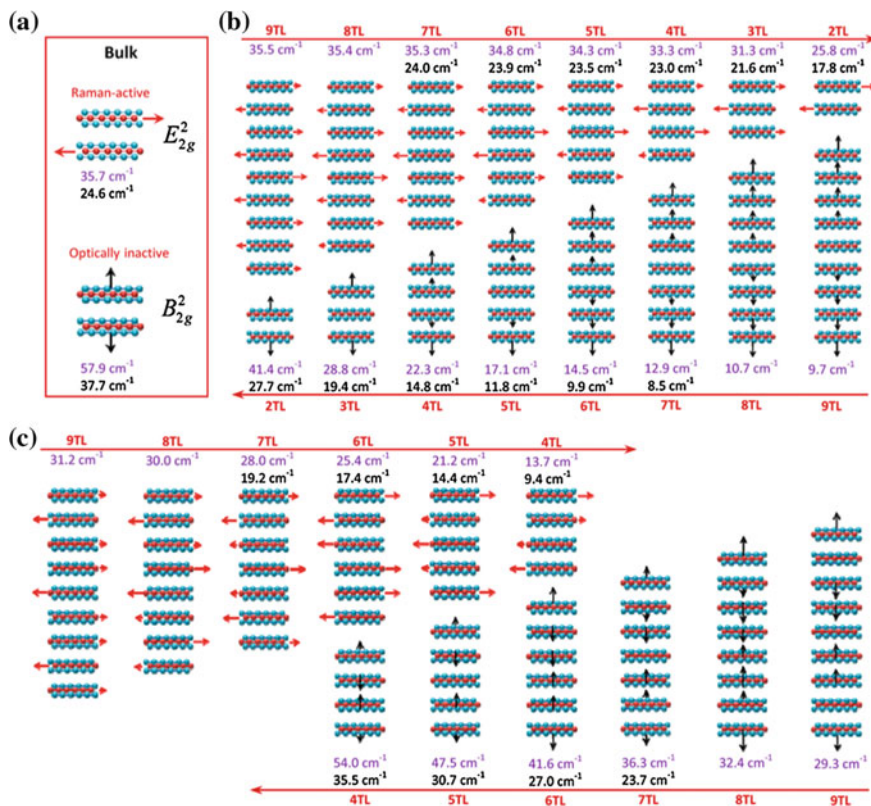


Fig. 7.11 Vibrational normal modes of the interlayer shear and breathing modes in MoS₂/WSe₂. **a** The vibrational normal modes of the interlayer shear (E_{2g}^2) and breathing modes (B_{2g}^2) in bulk 2H-MoS₂/WSe₂. The shear mode is Raman-active, and the breathing mode is optically inactive. **b** Vibrational normal modes of the highest frequency shear mode *S1* (*top*) and the lowest frequency breathing mode *B1* (*bottom*) from 2 layers to 9 layers. **c** Vibrational normal modes of the minor shear mode *S2* (*top*) and the minor breathing mode *B2* (*bottom*) from 4L to 9L. The arrows indicate the direction of motion of the whole (triple) layer, and the length of the arrows represents the magnitude. The denoted frequencies are results of the first principles calculations for both MoS₂ (in purple) and WSe₂ (in black) [2]. Copyright 2013 American Chemical Society. Published with permission

7.2.4 Peaks Associated with Decreased Dimensionality

Most studies concentrate on differences between the Raman scattering of bulk phases and the corresponding monolayers. At the same time, in few layer-systems additional first-order Raman peaks may appear associated with the different symmetry of the structure. A detailed study of the new Raman peaks in few-layered TMDCs such as MoS₂, MoSe₂, WS₂, and WSe₂, was performed in [33]. The authors start by noting that the symmetry of a few-layers system depends on the number of layers. Thus a monolayer is non-centrosymmetric and its vibrational modes belong to the D_{3h} point

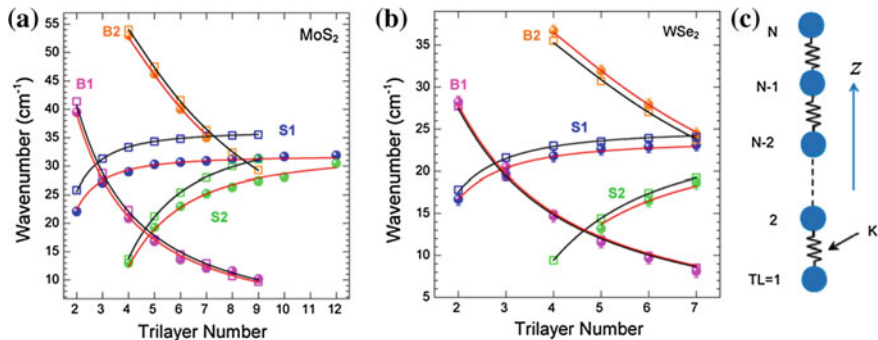


Fig. 7.12 Frequency evolution of measured and computed interlayer shear and breathing modes and the linear chain model interpretation. **a**, **b** Plot of shear and breathing mode frequencies as a function of the layer number in **(a)** MoS₂ and **(b)** WSe₂. The experimental data (*solid dots*) and first-principles calculation results (*open squares*) match very well. **c** Schematic of the linear chain model for N layers of MoS₂/WSe₂. One *blue sphere* stands for a monolayer (a three-layer sandwich). The force constant is K between nearest neighbor layers [2]. Copyright 2013 American Chemical Society. Published with permission

group and, in agreement with the irreducible representations of this point group, the symbols A'_1 and E' , are used for the out of plane and in-plane vibrations, respectively. The same is true for all odd-number systems. At the same time, in systems with an even number of layers the modes belong to the D_{3d} point group, which exhibits a center of inversion, and hence the out-of-plane Raman-active modes possess the A_{1g} irreducible representation.

In the case of monolayer WSe₂ the experimental Raman spectrum exhibits the presence of the perpendicular mode A'_1 and the in-plane E' mode that are located at around 250 cm⁻¹ [4, 14, 17] and are almost degenerate. As the number of layers is increased, the out-of-plane modes A'_1 (A_{1g}) shift to higher frequencies and the E' (E_g) move to lower frequencies, in line with other studies. In bulk crystals these modes are associated with the A_{1g} (located at 251 cm⁻¹) and the E_{2g}^1 (around 247 cm⁻¹) irreducible representations of the D_{6h} point group, exhibiting inversion symmetry.

It was further noted that using the laser line of 514.5 nm a new peak located at 310.4 cm⁻¹ appears for the bilayer, tri-layer, tetra-layer and penta-layer (Fig. 7.13), which were compared with the observation by others (308 cm⁻¹ [17], 309 cm⁻¹ [14] and 310 cm⁻¹ [4]). It was noted that this peak was previously assigned to a combination of shear modes and the E_{2g}^1 mode [17], while another publication related this peak to the inactive B_{2g} mode of the bulk phase [14]. The simulations predicted an appearance of new Raman-active modes around 306 cm⁻¹. These new Raman-active modes, which were labelled as A'^2_1 and A'^2_{1g} , involve the vibrations of the chalcogen and the transition metal atoms, belonging to the A'_1 or A_{1g} irreducible representations for odd and even number of layers, respectively, and do not appear in the monolayer. While for the bi-layer (306.97 cm⁻¹) and tri-layer (306.57 cm⁻¹) samples, only one Raman-active mode appears around this frequency, for the tetra-layer (305.57 and

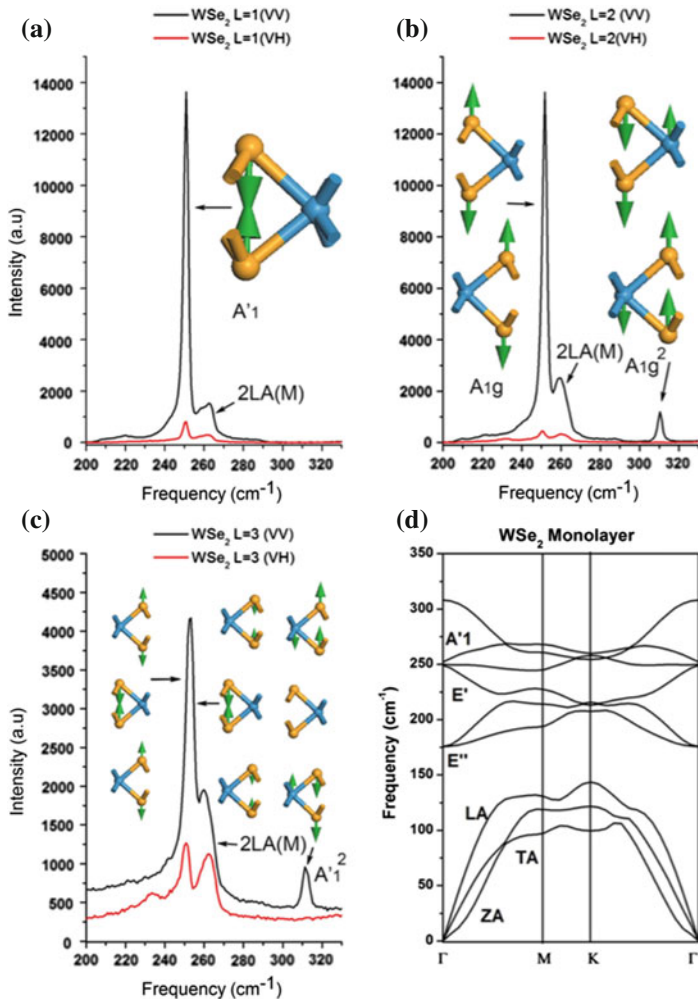


Fig. 7.13 Experimental Raman spectra of WSe₂ taken with a 514 nm laser under conventional geometry (VV) and cross polarization (VH). **a** Monolayer (L = 1). **b** Bilayer (L = 2). **c** Trilayer (L = 3). Insets show models of the out of plane vibrational modes present in each case. **d** Calculated phonon dispersion of a WSe₂ monolayer. Reproduced from [33]

306.62 cm^{-1}) and penta-layer (305.29 and 306.84 cm^{-1}), two modes appear that are very close in frequency, which were related to exterior and interior layer vibrations (Fig. 7.14). Experimentally, these features vanished completely in the cross-polarized Raman configuration (xy), demonstrating that these first order high frequency modes belong to vibrations perpendicular to the lattice plane.

It was further noted [33] that these new modes have also been reported experimentally in MoSe₂ at ca. 353 cm^{-1} [14] but were not properly identified. In par-

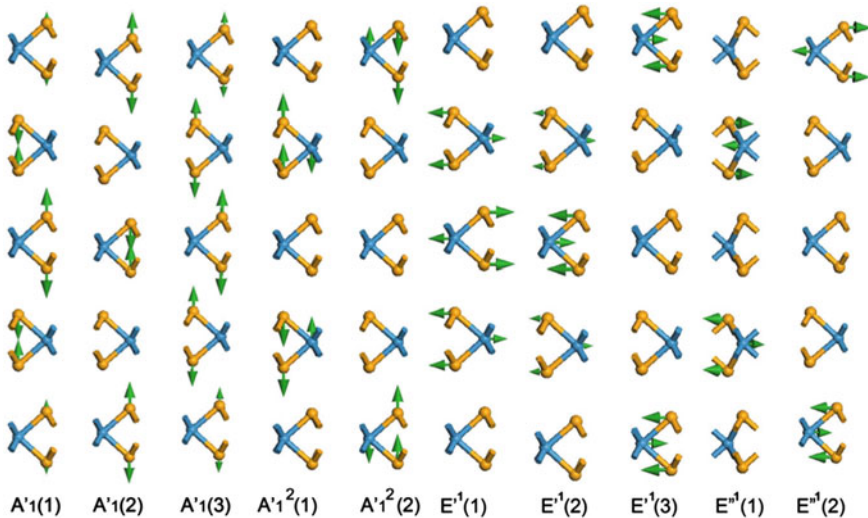


Fig. 7.14 Models showing the vibrations of A'_1 , E' and E'' Raman-active modes for penta-layer WSe₂: $A'_1(1)$ at 248.83 cm^{-1} ; $A'_1(2)$ at 250.15 cm^{-1} ; $A'_1(3)$ at 251.21 cm^{-1} ; $A'_1^2(1)$ at 305.29 cm^{-1} ; $A'_1^2(2)$ at 306.84 cm^{-1} ; $E'^1(1)$ at 247.55 cm^{-1} ; $E'^1(2)$ at 247.65 cm^{-1} ; $E'^1(3)$ at 248.55 cm^{-1} ; $E''^1(1)$ at 247.59 cm^{-1} and $E''^1(2)$ at 248.54 cm^{-1} . Reproduced from [33]

ticular, it was noted that for MoSe₂, the observed mode at 464 cm^{-1} is close to the $2LA(M)$ mode located at 455 cm^{-1} and it is often confused with it, and sometimes it is assigned to the Raman inactive A_{2u} mode of the bulk crystal, but no further discussion or analysis was made [5, 34].

Simulations further suggested [33] that the modes should split, although this was not observed experimentally, possibly, as the authors suggested, due to limited resolution.

Finally, it was proposed that the new in-plane modes can differentiate between interior and exterior layers, and should also appear in hetero-bilayered systems formed by stacking different layers of TMDCs. In particular, for a bilayered system made of one layer of WSe₂ and another layer of WS₂, calculations demonstrated that, besides the A_1 (C_{3v} symmetry) vibrational modes at 251.7 cm^{-1} for WSe₂ and at 415.4 cm^{-1} for WS₂, two other perpendicular Raman-active modes should appear at different frequencies, one at 311.1 cm^{-1} for WSe₂ and another at 427.9 cm^{-1} for WS₂.

Raman spectra for few-layered MoSe₂ and WSe₂ [14] as well as MoTe₂ [35] are shown on Fig. 7.15, although the interpretation of the few-layer peaks are different. In the case of MoTe₂, Raman scattering was measured using two different wavelengths of 532 and 633 nm [35]. It was noted that the B_{2g}^1 mode, inactive in the bulk, appears for few-layer MoTe₂. A similar result was obtained in [6]. The peak intensity was enhanced largely with decreasing thickness, but the peak vanished in a single layer. Using group theory and DFT calculations within the LDA, the observed peak was assigned as the bulk-Raman inactive B_{2g}^1 mode. The activation of the B_{2g}^1 peak in few-layer samples was attributed to breaking of the translation symmetry along the

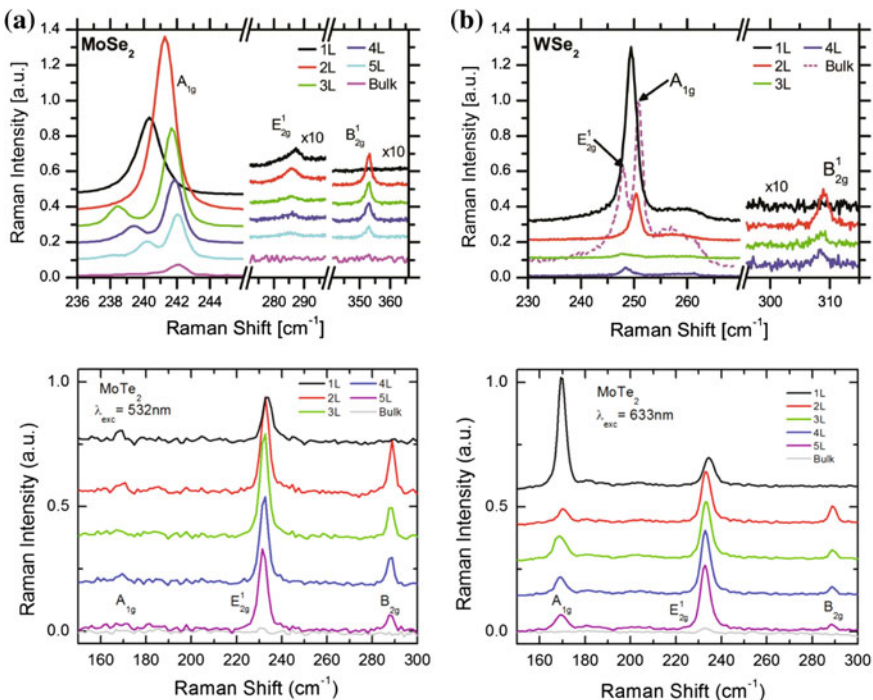


Fig. 7.15 Raman spectra of bulk and few-layer MoSe₂ and WSe₂ [14] (with permission from OSA) and MoTe₂ [35] (copyright 2014 American Chemical Society; published with permission). For the latter, two different excitation energies were used

c-axis direction. The appearance of the B_{2g}^1 peak in few-layer samples was also observed for WSe₂ [4].

It was further noted that mono- and few-layer Raman responses differ strikingly for excitation at 633 nm compared to that for 532 nm excitation. In the former case, the A_{1g} mode was found to be unusually strong. For the monolayer, the A_{1g} mode has by far the strongest Raman response; for few-layer samples (except the bilayer) this mode is stronger than B_{2g}^1 . For 532 nm excitation, on the other hand, the A_{1g} mode was consistently weak. While it is common for few-layer TMDCs systems to analyze the relative shift and amplitudes of the E_{2g}^1 and B_{2g}^1 Raman modes in order to determine sample thickness, it was proposed that for 633 nm excitation, the Raman spectra of single-layer and bi-layer samples exhibit such different A_{1g} and B_{2g}^1 mode intensities compared with thicker layers that they can be used for identification of the sample thickness [35].

The appearance of new modes in few-layer structures was also reported for MoS₂ [7], which is illustrated in Fig. 7.16 for two different excitation energies. It was noted that the newly observed modes start to appear only at relatively high excitation energy, typically above 2.4 eV, with their relative enhancement towards the C absorption peak being stronger than that of the other Raman modes. At 3.8 eV excitation energy, the

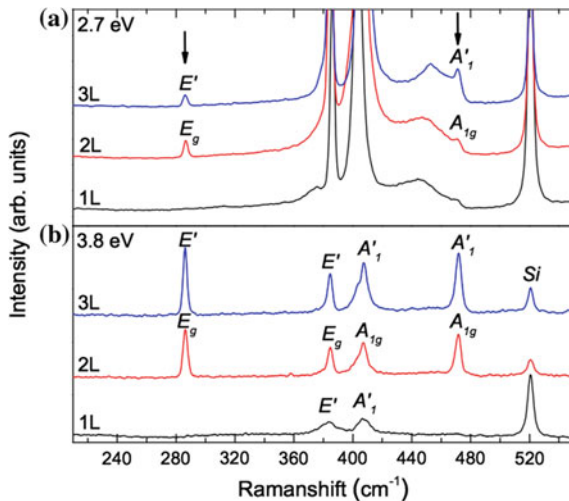


Fig. 7.16 Raman spectra of single (1L), bi- (2L), and trilayer (3L) MoS₂ on Si/SiO₂ excited with (a) 2.7 and (b) 3.8 eV. Two additional Raman modes appear in few-layer MoS₂: an E'/E_g mode around 286 cm^{-1} and an A_{1g}/A'_1 mode around 471 cm^{-1} , which is related to the A''_2 single-layer mode [7]. Copyright 2015 by the American Physical Society. Reprinted with permission

“new” peaks exhibited even higher intensity than the other, typically observed modes [see also Fig. 7.16 (lower panel)].

In order to understand the distinct resonance behavior of the newly observed Raman modes, the spatial distribution of the excitonic wave functions in few-layer MoS₂ were considered. While the wave function of the A exciton in few-layer MoS₂ and MoSe₂ are strongly confined to a single layer with only small overlap to the neighboring layers [36–38], it was proposed that the C exciton instead extends over the entire few-layer thickness. It was remarked that this proposal is in agreement with the significantly larger blueshift of the C absorption peak compared to the A and B absorption peaks when the number of layers is reduced [39].

It was argued that spatial confinement of the wave functions has strong implications on the Raman scattering process. If the Raman excitation is in resonance with the A or B exciton in few-layer MoS₂ the excitation is still confined mainly to a single layer as illustrated in Fig. 7.17. As a result, the N -layer system reacts rather like an independent superposition of N single layers from a selection-rule point of view. In the single layer, the vibrations at 286 and 471 cm^{-1} are symmetry-forbidden in backscattering geometry, and therefore their corresponding symmetry-allowed Raman signal in the few-layer system is still vanishingly small in resonance with the A or B exciton. Only when the optical excitation creates an exciton that is extended over the entire number of layers, as in resonance with the C transition, the symmetry of the few-layer system becomes dominant and determines the selection

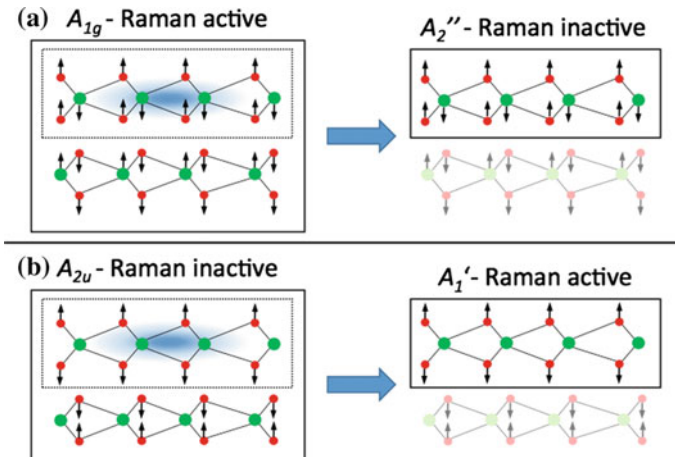


Fig. 7.17 In resonance with the A exciton, the Raman active A_{1g} mode of 2L MoS₂ can be “seen” like the Raman inactive A_2'' mode of 1L MoS₂ **(a)**. The Raman inactive A_{2u} mode of 2L MoS₂ can be “seen” like a A_{1g} symmetry mode of 1L MoS₂ **(b)** and starts to become observable [7]. Copyright 2015 by the American Physical Society. Reprinted with permission

rules, allowing the newly observed Raman modes and bringing them into resonance [7].

In [40] it was noted that the out-of-plane A'_1 mode of WS₂ splits into several peaks in few-layer structures, the effect being much more strongly pronounced in case of resonance excitation (Fig. 7.18). While the monolayer and bulk spectra showed a single peak, for two or more layers there was at least another mode appearing as a low-energy shoulder of the dominant Raman feature.

The spectra were fitted with Lorentzian profiles (Fig. 7.19). The bilayer A_{1g} mode spectrum possessed a low-energy shoulder that was not previously observed. In the four-layer spectrum the dominant A_{1g} mode shifted up with respect to the bilayer, and a prominent shoulder was observed at almost the same frequency as the shoulder in the bilayer spectrum. The 4L spectrum was best fitted with four Lorentzians to account for the Raman intensity between the two stronger Raman features. A similar pattern was observed for odd-layer structures. Thus the tri-layer (3L) spectrum consisted of the A'_1 peak as the most significant contribution and a pronounced low-energy shoulder, with a third Lorentzian fitting the plateau between the main peaks. Finally, the five-layer spectrum was fitted with five Lorentzians, two of which fill up the region between the main A'_1 peak and the two low-energy shoulders. From these results it was proposed that there are always N components to the out-of-plane A mode, where N is the number of layers.

Additionally, it was found that with an increasing number of layers not only the main Raman-active component with A symmetry stiffened, but also other components followed the same trend, as is illustrated in Fig. 7.20a, where the frequencies are plotted against the number of layers.

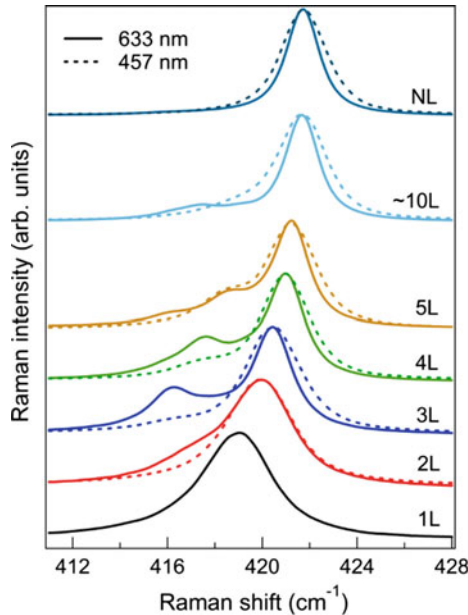


Fig. 7.18 Experimental resonance Raman spectra (excitation wavelength 633 nm) of the A-mode region in few-layer-WS₂ from the bilayer (2L) to five layers (5L) and the bulk (NL). The monolayer spectrum (1L) is only shown with an excitation wavelength of 457 nm, as the Raman features are dominated by strong photoluminescence at 633-nm excitation spectrum (not shown). For few-layer-WS₂, spectra of the same region taken with the 457-nm excitation wavelength are overlaid and depicted with *dashed lines*. Spectra are normalized to the main Raman peak and are offset for clarity [40]. Copyright 2015 by the American Physical Society. Reprinted with permission

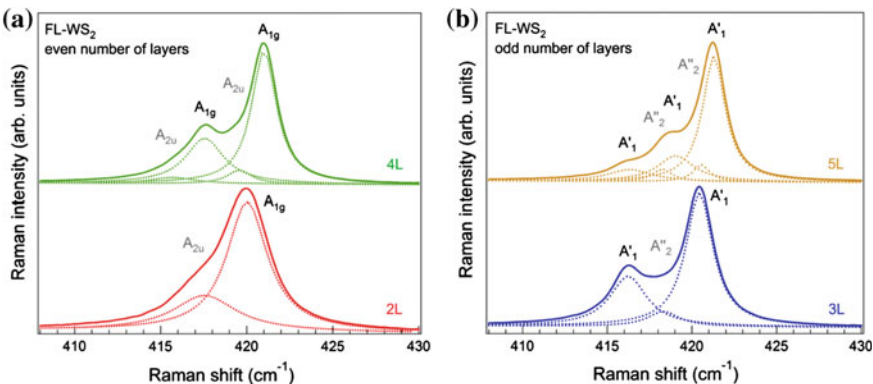


Fig. 7.19 Experimental resonance Raman spectra of few-layer-WS₂. The Lorentzian fit curves are shown as well as the symmetry attributed to the individual modes. In general, there are N components for an N -layer spectrum. **a** For an even number of layers, Raman-active A_{1g} modes alternate with infrared-active A_{2u} modes. **b** For an odd number of layers, Raman-active A'_1 modes alternate with infrared A''_2 modes. For both even and odd N , the Raman-active modes are more intense than the rather weak infrared-active modes [40]. Copyright 2015 by the American Physical Society. Reprinted with permission

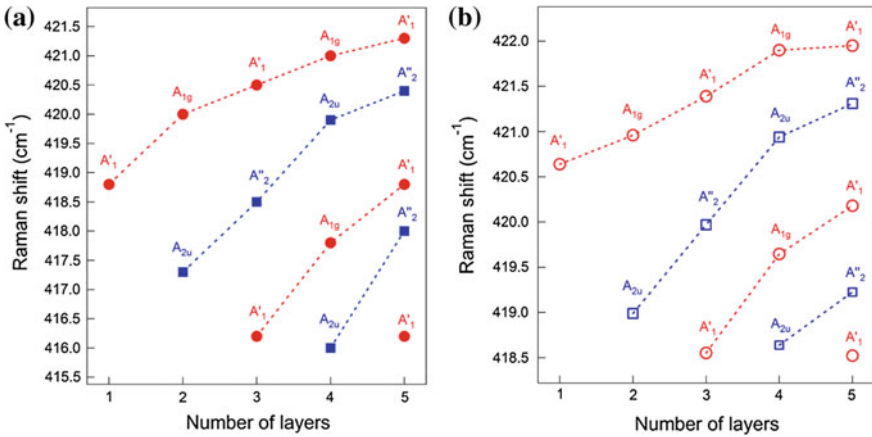


Fig. 7.20 **a** Raman frequencies of the A-type modes in few-layer-WS₂. Red circles mark the Raman-active modes; blue squares denote the infrared-active modes also seen in the Raman spectra. Dashed lines are used to guide the eye. Starting from one layer, the splitting of the modes for few-layer-WS₂ produces a fanlike shape of the possible vibrational frequencies. **b** Theoretical calculations with DFT reproduce the observed trends. Raman-active modes are denoted with open red circles; infrared-active modes are marked with open blue squares [40]. Copyright 2015 by the American Physical Society. Reprinted with permission

To obtain insights into the origin of the peak splitting, DFT simulations were performed considering full sets of phonon modes that exist in few-layers structures and based on the obtained results the splitting of the out-of-plane mode was attributed to the fact that for monolayer and bulk WS₂ there is only one Raman-active A'_1 (A_{1g}) mode, while for a few layers, more than one Raman mode becomes allowed. In particular, the modes that are infrared-active in the bulk become Raman-active in few-layer structures. Using this model, a good agreement with experiment was obtained (Fig. 7.20b).

Optical phonon modes in N -layer MoTe₂ were studied in [28], where the authors observed series of N -dependent low-frequency interlayer shear and breathing modes and well-defined Davydov splittings of the mid-frequency modes, which solely involve displacements of the chalcogen atoms, while the high-frequency modes, arising from displacements of both the metal and chalcogen atoms, exhibited considerably smaller splittings. The manifold of phonon modes associated with the in-plane and out-of-plane displacements were quantitatively described by a force constant model, including interactions up to the second nearest neighbor and surface effects as fitting parameters.

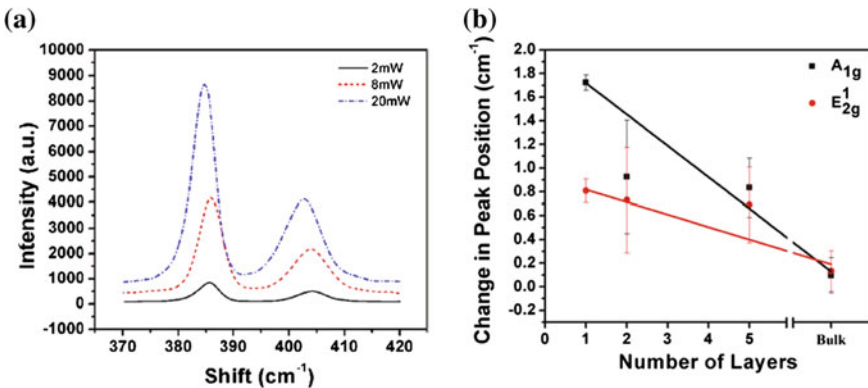


Fig. 7.21 **a** Characteristic *red* shift observed in the Raman spectra of single-layered MoS₂ at varying laser powers. **b** The change in peak positions of MoS₂ samples of different thicknesses represented by the difference in the peak position for A_{1g} and E_{2g}^1 modes as the laser power is increased from 2 to 20 mW [41]. Reprinted with permission. Copyright 2012 by the American Institute of Physics

7.3 Laser Power Effects

7.3.1 Temperature Dependence of Raman Scattering

In most cases, the effect of temperature (i.e. the laser power) on the Raman spectra is ignored. At the same time, it is known that temperature has a strong effect on the Raman peak position (as well as the line width). This issue was first looked into in [41] for monolayers of MoS₂. A noticeable dependence of the peak position on the laser power and also on the number of layers in the system (Fig. 7.21) was demonstrated. A similar result for the laser-power dependence was obtained in [42].

Temperature-dependent Raman studies on few-layer MoS₂ prepared by high-temperature vapour-phase method were further carried out by varying the temperature over a range of 83–523 K [42]. For all temperatures, there were strong scattering intensities from both the E_{2g}^1 and A_{1g} modes. As seen from Fig. 7.22a, both E_{2g}^1 and A_{1g} modes follow a systematic red shift with increase in temperature. The FWHM of both peaks increased with increasing temperature. The change in peak position of the E_{2g}^1 and A_{1g} modes with increasing temperature are plotted in Fig. 7.22b, c, respectively. The experimental results were fitted using the following equation:

$$\omega(T) = \omega_0 + \chi \cdot T \quad (7.3)$$

where ω_0 is the frequency of vibration of the E_{2g}^1 and A_{1g} modes at absolute zero temperature and χ is the first-order temperature coefficient of the E_{2g}^1 and A_{1g} modes.

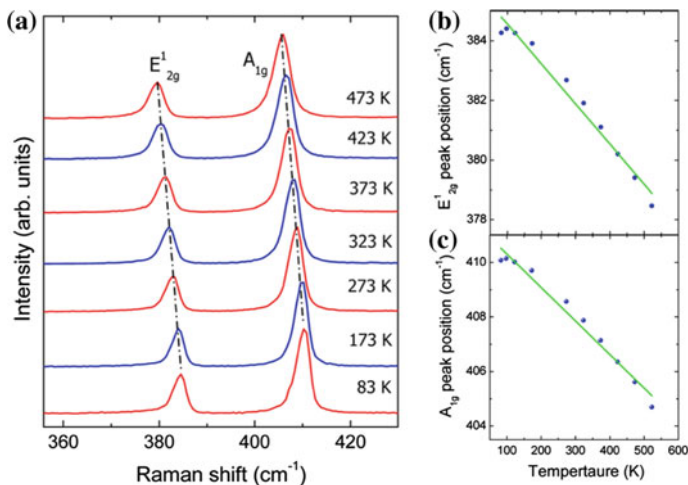


Fig. 7.22 **a** Raman spectra of few-layer MoS₂ recorded at different temperatures. **b, c** temperature dependence of the frequencies of Raman active E_{2g}^1 and A_{1g} modes, respectively [42]. Copyright 2013 American Chemical Society. Published with permission

The slope of the fitted straight line represents the value of χ , which was found to be $\chi_{E_{2g}^1} = -1.32 \times 10^{-2} \text{ cm}^{-1}/\text{K}$ and $\chi_{A_{1g}} = -1.23 \times 10^{-2} \text{ cm}^{-1}/\text{K}$ for the E_{2g}^1 and A_{1g} modes, respectively.

It was found that the frequency of the low frequency interlayer shear E_{2g}^2 mode was not affected much by an increase in temperature; only a small shift of ca. 0.6 cm^{-1} in the peak position was noticed for the whole temperature range (83–523 K). However, the intensity of the E_{2g}^2 mode increased with increasing temperature.

From these measurements, an estimate for the thermal conductivity of the suspended few-layer MoS₂ at room temperature was made with the obtained value of $\kappa = 52 \text{ W/m}\cdot\text{K}$ [42].

An identical approach was used in [43] for exfoliated monolayer-thick MoS₂. The value of the thermal conductivity from these results was $34.5 \text{ W/m}\cdot\text{K}$ at room temperature. It is not clear whether the numerical differences stem from different flake thicknesses or from different fabrication techniques.

Subsequently, the temperature dependence of Raman scattering in MoS₂ and some other TMDCs was studied by various groups and the results are summarised in Table 7.2. In [44] it was noted that the temperature dependence of the peak positions was non-linear deviating from the linear dependence at lower temperatures (<100 K). Possible reasons for this deviations could be (i) contribution from thermal expansion and (ii) anharmonicity [45, 46]. In [47] polynomial fitting to the experimental data was performed up to third-order terms but the obtained numbers for the linear term was significantly larger than in most other studies.

Table 7.2 Linear temperature coefficients of the A_{1g} and E_{2g}^1 Raman modes of selected TMDCs

Material	$\chi_{A_{1g}} \times 10^2$	$\chi_{E_{2g}^1} \times 10^2$	Reference
MoS ₂ , 1L, exf., sup.	1.43	1.24	[44]
MoS ₂ , 1L, exf., susp.	1.3	1.1	[43]
MoS ₂ , 1L, exf., sup.	1.3	1.7	[43]
MoS ₂ , 1L, exf., sup.	6.26	2.41	[47]
MoS ₂ , 1L, CVD, sup.	3.01	2.17	[47]
MoS ₂ , 1L, CVD, sup.	1.1	1.6	[46]
MoS ₂ , 2L, CVD, sup.	1.89	1.37	[48]
MoS ₂ , few-L, exf., sup.	1.23	1.32	[42]
MoS ₂ , few-L, hydro, sup	1.6	1.3	[45]
MoS ₂ , 1L CVD., sup	1.43	1.79	[48]
MoS ₂ , bulk (<100 nm)	1.3	1.5	[46]
MoS ₂ , bulk	1.23	1.47	[49]
MoS ₂ , bulk	1.97	2.21	[47]
MoS ₂ , bulk	1.23	1.47	[50]
MoSe ₂ , 1L, exf	0.54	0.86 (A_{2u}^2 mode)	[51]
MoSe ₂ , 3L, exf	0.45	0.85 (A_{2u}^2 mode)	[51]
WS ₂ , 1L, exf., sup.	0.6	0.6	[52]
WS ₂ , 1L, CVD, sup.	1.49	1.25	[53]
WS ₂ , 1L, CVD, susp.	1.44	1.17	[53]
WS ₂ , 2L, CVD, sup.	1.21	1.33	[53]
WS ₂ , 2L, CVD, susp.	1.14	1.28	[53]
WSe ₂ , 1L, exf	0.32	0.48	[51]

Notations used: 1L—monolayer, nL— n layers, exf—exfoliated, hydro—hydrothermal method, susp—suspended, sup—supported

From temperature dependent Raman measurements, the thermal conductivities around room temperature was determined to be 32 and 53 W/m·K for suspended single layer and bi-layer of (CVD grown) WS₂, respectively [53].

Lateral and interfacial thermal conductivity of single- and bilayer MoS₂ and MoSe₂ was studied in [54] using refined optothermal Raman technique. The room-temperature values obtained were the following: for 1L MoS₂ and MoSe₂, 84±17 and 59±18 W/m·K, respectively. For 2L MoS₂ and MoSe₂, 77±25 W and 42±13 W/m·K. The interfacial thermal conductance was found to be on the order of 0.1–1 MW/m²K, substantially smaller than previously assumed [54].

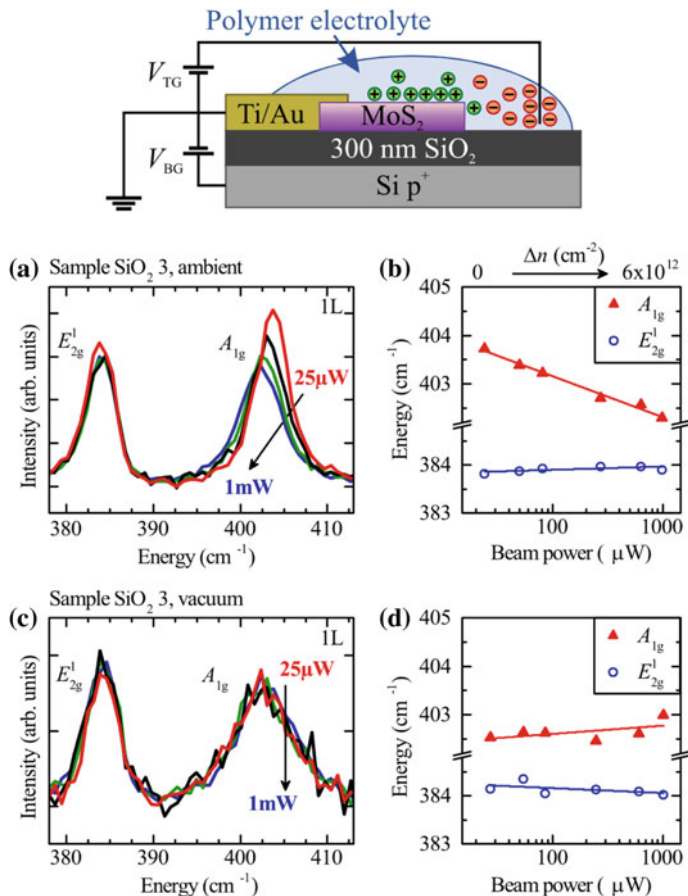


Fig. 7.23 Raman spectra of monolayer MoS₂ for different laser powers ranging from 25 to 1000 μW **a** on Si/SiO₂ taken in ambient conditions and **c** on in vacuum, and **b**, **d** are logarithmic plots of the related A_{1g} and the E_{2g}^l mode energies as a function of the laser power. The solid lines are linear fits to the data points [55]. Reprinted with permission. Copyright 2015 by the American Institute of Physics

7.3.2 Photogating

Exposure of a semiconductor to light results in photogeneration of charge carriers. In addition, photo-excitation may change the number and state of the absorbed species, also influencing the properties. These issues were addressed in [55]. The structure of the sample is shown in Fig. 7.23 (upper panel). Micromechanically exfoliated MoS₂ flakes were transferred onto sapphire or Si/SiO₂ substrates. The latter consisted of p^+ -doped silicon with a 300 nm thick SiO₂ layer. The doped Si substrate served

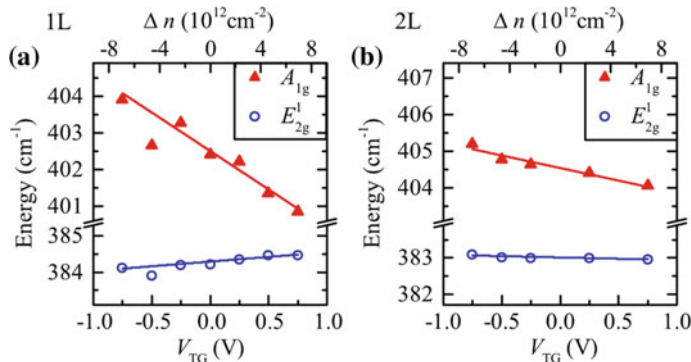


Fig. 7.24 Energy of the A_{1g} and the E_{2g}^1 modes in dependence of the applied top gate voltage for mono-layer (a) and bilayer MoS₂ (b). The solid lines are linear fits to the data points [55]. Reprinted with permission. Copyright 2015 by the American Institute of Physics

as a back gate electrode. A solid polymer electrolyte composed of a mixture of polyethylene-oxide and CsClO₄ acted as a transparent top gate electrode.

Figure 7.23a, c compares the dependence of the Raman spectra on laser power for pristine monolayer MoS₂ on SiO₂ in ambient conditions and in vacuum. It was found that for ambient conditions, the A_{1g} mode shifted towards lower energies and the peak broadened with increasing laser power, while the E_{2g}^1 mode remained almost unaffected. Figure 7.23b, d show the energies of the A_{1g} and E_{2g}^1 modes versus the laser power in a semilogarithmic representation demonstrating the exponential dependence of the A_{1g} mode energy on the laser power for the sample measured in ambient conditions. From the fact that the energy of the E_{2g}^1 phonon mode was unaffected by the laser power, it was concluded that light-induced heating of the MoS₂ flake can be ruled out. Consequently, the redshift of the A_{1g} mode was attributed to phonon renormalization induced by an increase of free charge carriers, which is consistent with an earlier report on an electrostatically doped monolayer MoS₂ [56].

To corroborate this interpretation, Raman measurements on electrostatically gated MoS₂ mono- and bi-layer field-effect devices were additionally performed. It was found (Fig. 7.24) that the A_{1g} mode energy was linearly dependent on the applied gate voltage and hence on the change in charge carrier density Δn for both MoS₂ mono- and bi-layer flakes. The E_{2g}^1 mode was unaffected by the gate voltage. Consequently, the light induced change Δn could be deduced from a direct comparison with gate-voltage dependent measurements.

It was found that the described photogating effect was not persistent and it was independent of the substrate used. It was reversible and tunable by the power of the light. Interestingly, photogating was not observable for measurements in vacuum (Fig. 7.23c, d), suggesting that the interface between MoS₂ and the gaseous environment causes the laser power dependent change in the charge carrier density. Additionally, the A_{1g} mode was found to significantly broaden and red-shift for

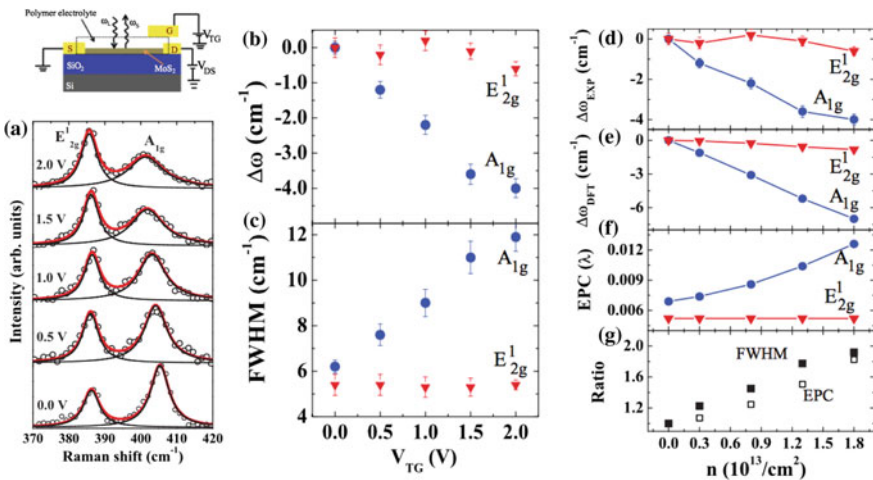


Fig. 7.25 **a** Raman spectra of monolayer MoS₂ at different top-gate voltages V_{TG} . Open circles are experimental data points, the gray (red) lines are Lorentzian fits to the total spectrum, and the black lines are the Lorentzian fit to individual peak. Change in the (b) phonon frequency $\Delta\omega$ and (c) FWHM of A_{1g} and E_{2g}^1 modes as a function of V_{TG} . Change in zone center phonons $\Delta\omega$ of (d) from experiment and (e) from DFT calculations as a function of electron concentration n . **f** Electron-phonon coupling of A_{1g} and E_{2g}^1 modes as a function of n . **g** Ratio of EPC shown by open squares and phonon linewidth shown by solid squares as a function of n [56]. Copyright 2012 by the American Physical Society. Reprinted with permission

measurements in vacuum compared to measurements in ambient conditions, suggesting a large charge carrier density of MoS₂ in vacuum, which is independent of the laser power. The enhanced doping in vacuum was entirely reversible. The photo-gating was explained by photodesorption of environmental molecules, such as H₂O and O₂, that leads to a reduction of the charge carrier density in MoS₂ [57, 58].

7.4 Effect of Carrier Concentration

Strong electron-phonon interaction that limits the electronic mobility of semiconductors can also have significant effects on phonon frequencies. The effect of carrier concentration on Raman scattering was studied in [56] using a single-layer MoS₂ electrochemically top-gated field-effect transistor, whose structure is schematically shown in Fig. 7.25. Figure 7.25a shows the evolution of zone-center phonon E_{2g}^1 and A_{1g} modes of the MoS₂ monolayer at different top-gate voltages. Figure 7.25b, c show the shift of the mode frequencies and the corresponding full width at half maximum (FWHM), respectively, as a function of gate voltage. The dependence of the change in mode frequencies on the carrier concentration (n) is shown in Fig. 7.25d. It was noted that the A_{1g} peak position could be used as an in-situ readout of the carrier concentration in MoS₂ devices.

The first-principles simulated results [56] (Fig. 7.25e) were in good agreement with experiment. The results for electron-phonon coupling (Fig. 7.25f) show that the A_{1g} mode couples much more strongly with electrons than the E_{2g}^1 mode. This result is discussed using a group theoretical analysis. The A_{1g} mode has the symmetry of the lattice. As a result, all electronic states can have a nonzero expectation value for the perturbation of the A_{1g} mode, giving a large electron-phonon coupling. In contrast, the matrix element vanishes for the E_{2g}^1 mode and its coupling with electrons is weakly dependent on doping. In other words, the electron doping results in the occupation of the antibonding states in the conduction band of MoS₂, making the bonds weaker, and the A_{1g} mode, which preserves the symmetry of the lattice, softens [56].

7.5 Effect of Substrate

The effect of substrate material was studied in [59] and the results are summarized in Fig. 7.26. The position of the E_{2g}^1 mode was found insensitive to the substrate material. At the same time, the A_{1g} mode showed a sizeable stiffening of up to ca. 2 cm^{-1} .

Several possible mechanism to account for the observed result were proposed, such as (i) the stiffening of the A_{1g} mode can be associated with reduced electron density in 1L MoS₂ and (ii) a change in the strength of the dipolar interaction between the MoS₂ layer and the fixed charges in different substrates. Since the A_{1g} mode is the out-of-plane motion of the negatively charged S atoms with respect to the Mo atoms, a different electrostatic environment will provide a change in the potential landscape where the motion takes place. While this should not induce intrinsic doping in the 1L MoS₂ it should affect the A_{1g} frequency. It may also be possible that the change in the Raman frequency is associated with the vdW interaction between the monolayer and the substrate (see below in this chapter).

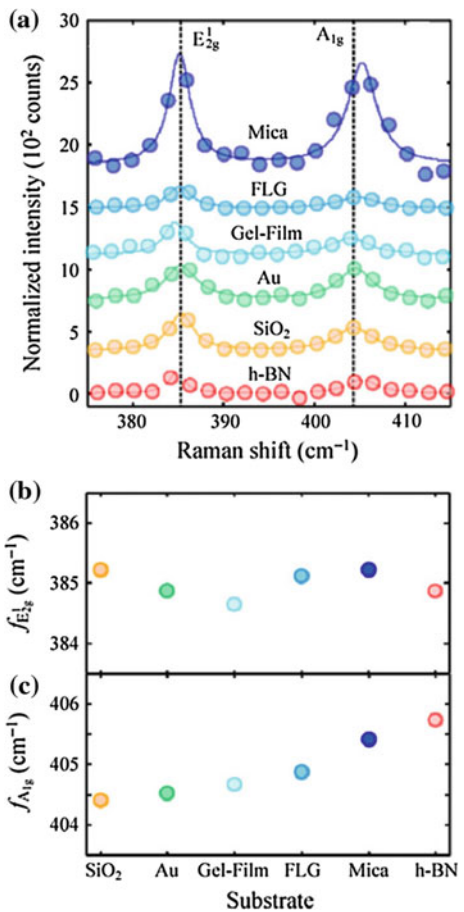
7.6 Effect of Pressure and Strain on Raman Scattering

7.6.1 Uniaxial Strain

As with bulk semiconductors, Raman scattering is an efficient tool to detect strain in few layer and monolayer samples [60]. This is exemplified in Fig. 7.27 where Raman spectra for a bi-layer WSe₂ flake [61] and a monolayer of MoS₂ [62] under different uniaxial tensile strain are shown. One can see that the degeneracy of the E_{2g}^1 mode is broken and the peak splits into two peaks, E_{2g}^{1+} and E_{2g}^{1-} , with the peak positions moving in opposite directions from the original peak, corresponding to the vibrational modes parallel and perpendicular to the direction of strain. The peak

Fig. 7.26 Effect of the substrate on the Raman modes of 1L MoS₂. **a** Normalized Raman spectra for 1L MoS₂ on mica, FLG, Gel-Film, Au, SiO₂ and h-BN (shifted vertically for clarity). The dots are the experimental points; the solid lines are Lorentzian fits. The dashed solid lines correspond to the E_{2g}¹ and A_{1g} frequencies on SiO₂. Frequencies of the E_{2g}¹ (**b**) and A_{1g} (**c**) Raman-active modes as a function of the substrate material [59].

Reproduced with permission from Springer



splitting increases as strain is increased. At the same time the A₁ peak position (for MoS₂) was essentially unchanged [62]. From the strain dependence of the Raman E_{2g}¹ mode the Grüneisen parameter, γ (1.1 ± 0.2), and the shear deformation potential of monolayer MoS₂, β (0.8 ± 0.1) were extracted [62].

The E_{2g}¹ and A_{1g} modes have different polarization dependencies [63]. As shown in Fig. 7.28a, the A_{1g} mode exhibits remarkable polar dependence almost vanishing when the polarizations of the incident light and scattered light are orthogonal, while the intensities of the E_{2g}¹ mode vary very slightly. The fitting results (Fig. 7.28b) further reveal the nature of polar behaviour of these two modes, which could be perfectly explained by the Raman selection rules as given by their Raman tensors.

In contrast to the non-polar dependence of the E_{2g}¹ mode for an unstrained monolayer MoS₂ (Fig. 7.28b), the split E_{2g}¹⁺ and E_{2g}¹⁻ modes induced by uniaxial strain were sensitive to the polarization (Fig. 7.28c) [63] (also in agreement with the prediction of [64]), with the E_{2g}¹⁺ mode almost vanishing when the polarization of the scattered light is perpendicular to that of the incident laser and also

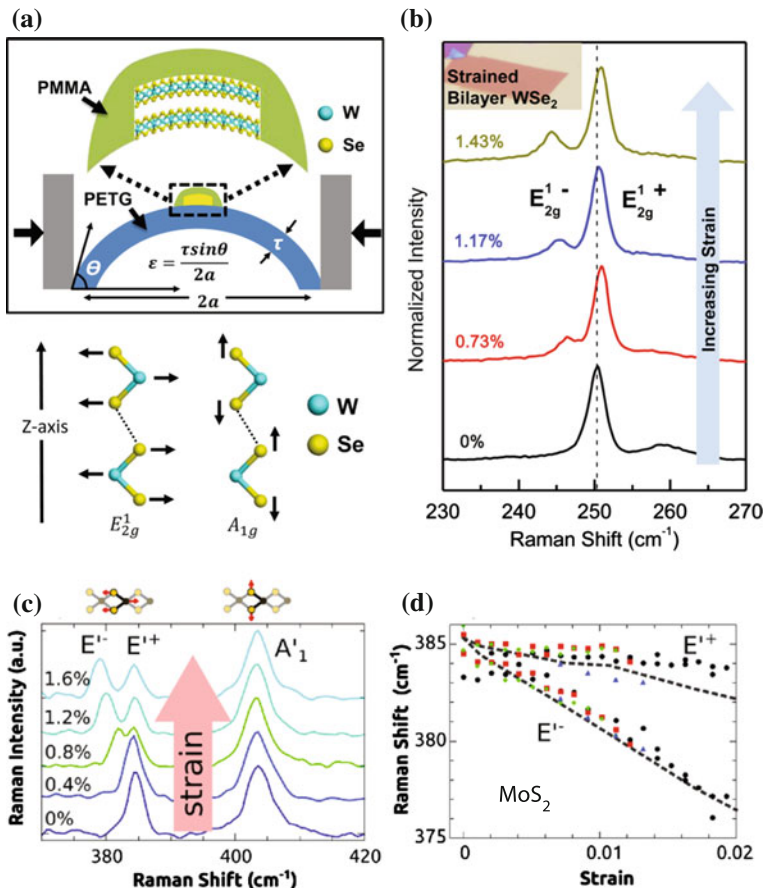


Fig. 7.27 **a** Schematic of the two-point bending apparatus along with the method to compute strain. **b** Raman spectra for bilayer WSe_2 at different strain. E_{2g}^1 degeneracy breaks under strain and the mode splits into E_{2g}^{1-} and E_{2g}^{1+} which show a *left* and *right* shift from the original Raman peak. The *inset* shows the optical microscope image of the bilayer WSe_2 flake used in this study [61]. Copyright 2014 American Chemical Society. Published with permission **(c)** Evolution of the Raman spectrum as a device is strained from 0 to 1.6%. **d** The peak location of the E_{2g}^{1+} and E_{2g}^{1-} Raman modes, extracted by fitting the peaks to a Lorentzian, as their degeneracy is broken by straining MoS₂. Different colors represent individual devices. *Dashed lines* are the results of first-principles calculations after subtraction of 9 cm^{-1} to account for underestimating phonon energies [62]. Copyright 2013 American Chemical Society. Published with permission

to the strain axis ($\phi = 90^\circ$), whereas the intensity of E_{2g}^{1-} mode reached maximum. On the other hand, further rotating the analyzer by 90° ($\phi = 180^\circ$), one can find the maximum of the E_{2g}^{1+} and the minimum of the E_{2g}^{1-} . This indicates that the linear polarizations of the scattered light from E_{2g}^{1+} and E_{2g}^{1-} are orthogonal. Their intensities can be written as [63]:

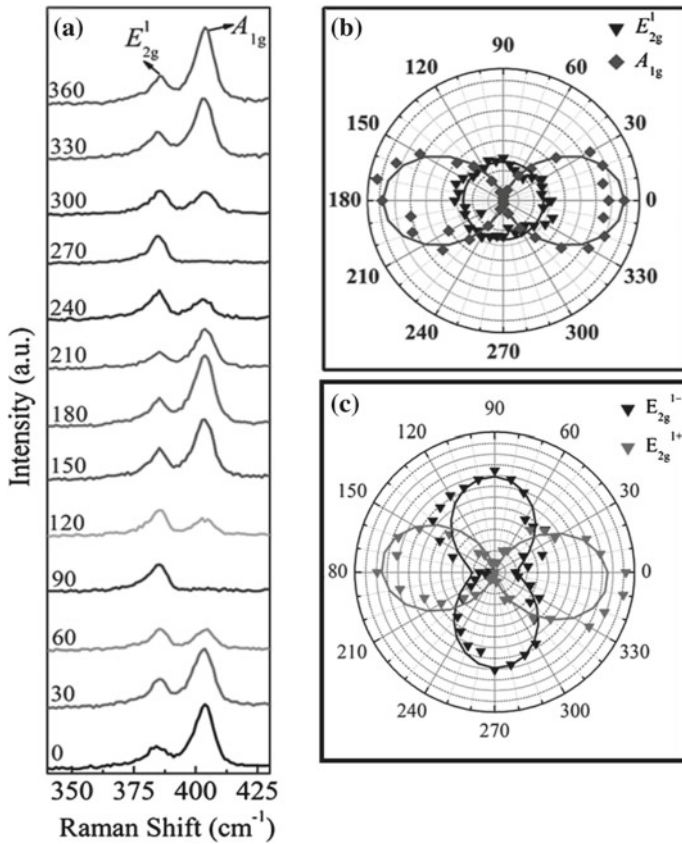


Fig. 7.28 **a** Raman spectra of E_{2g}^1 and A_{1g} modes of the as-prepared monolayer MoS₂ on a PET substrate as a function of the angle between the polarizations of the incident and the scattered lights. **b** Polar plot of the fitted intensities of E_{2g}^1 and A_{1g} modes as a function of angles between the polarizations of the incident and scattered beams **c** polar plots of the fitted peak intensities of E_{2g}^{1+} and E_{2g}^{1-} modes as a function of angle between polarizations of the incident and scattered beams for a uniaxially strained monolayer [63]. Reproduced with permission from Wiley-VCH Verlag GmbH

$$I_{E_{2g}^{1+}} \propto d^2 \cos^2(\varphi + \psi + 3\theta) \quad (7.4)$$

$$I_{E_{2g}^{1-}} \propto d^2 \sin^2(\varphi + \psi + 3\theta) \quad (7.5)$$

where the notations used for the angles are indicated in Fig. 7.29. It was proposed that this polarization dependence can be used to determine the orientation of monolayer MoS₂, as exemplified in Fig. 7.29.

An interesting observation was made in [65]. It was found that during the preparation of layered MoS₂ materials via a vapor-solid growth route using MoS₂ as the

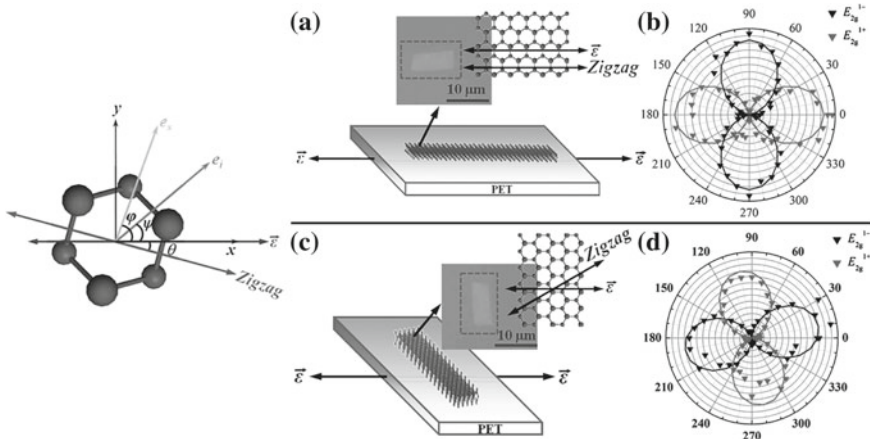


Fig. 7.29 *Left panel:* Schematic diagram of the configuration of the measurements. ϵ is the strain direction which is fixed along to the horizontal direction (x-axis) and with an angle of θ to the zig-zag direction of the crystal lattice. e_i and e_s indicate the polarization of the incident and scattered light, which deviate from the direction of strain by angles of ψ and φ , respectively. *Right panel:* **a** and **c** Schematic diagrams and optical images of the same piece of monolayer MoS₂ on PET by applying uniaxial strain along different directions. **b** and **d** Polar plots of the fitted peak intensities of E_{2g}^{1+} , and E_{2g}^{1-} modes as a function of angle φ . Note for **c** and **d** the sample including both PET and monolayer MoS₂ flake was remounted by rotating by ca. 90° with respect to the fixed strain axis after fully releasing the strain [63]. Reproduced with permission from Wiley-VCH Verlag GmbH

only source, in addition to the common monolayer and bilayer MoS₂, 1+ α L MoS₂ structures are formed that appear to be an intermediate transition from monolayer to bilayer. The upper panel of Fig. 7.30 illustrates schematically the various MoS₂ structures. It was found that the areas corresponding to such 1+ α L exhibited splitting of the E_{2g}^1 peak, which was attributed to self-induced uniaxial strain at the boundary between monolayers and bi-layers.

Local strain manifesting itself as the splitting of the E_{2g}^1 peak was also observed at the MoS₂ (WS₂)—Ag (Au) nanodot boundaries with the splitting being the largest for monolayer TMDCs and decreasing as the number of layers was increased. In addition, the E_{1g} peak could be detected, that is inactive in back-scattering geometry. The appearance of the E_{1g} mode was attributed to the development of an out-of-plane electric field component in samples with metallic nanoislands [66].

7.6.2 Hydrostatic Pressure

The pressure dependence of Raman scattering in monolayers of different phases of MoS₂ (2H and 1T') was studied in [67] by means of hydrostatic pressure experiments using a diamond anvil cell and DFT simulations for both 2H and 1T' polytypes.

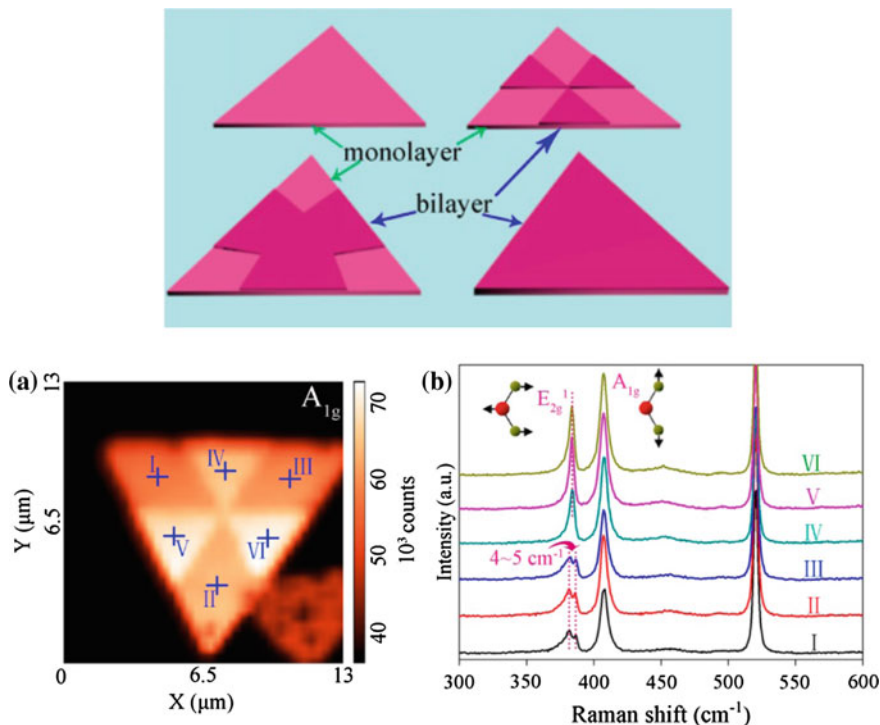


Fig. 7.30 Upper panel: Schematic illustration of a bi-layer growth on a monolayer. Regions IV, V, and VI of the sample shown in panel (a) are bilayers. Panel (b) shows Raman spectra taken on all six regions. The spectra from regions I, II, and III show splitting of the E_{2g}^1 peak [65]. Copyright 2015 American Chemical Society. Published with permission

For monolayers of the 2H-MoS₂ polytype, the intensity of the in-plane Raman mode (E_{2g}^1) decreased at pressures above 16 GPa (Fig. 7.31a), concomitant with an increase in the intensity ratio of A_{1g}/E_{2g}^1 . The diminishing intensity of the E_{2g}^1 mode was attributed to the dominance of normal compressive strain on the monolayer 2H-MoS₂ under large hydrostatic pressures, which hinders the in-plane E_{2g}^1 movement. The A_{1g} out-of-plane vibrational mode remained strong up to 30 GPa.

Both modes stiffened with pressure with the rate of change being higher for the A_{1g} mode. This difference was explained as follows. The A_{1g} mode originates from transverse vibrations of the S–S atom, while the E_{2g}^1 mode emerges from the longitudinal vibrations of Mo and S atoms in opposite directions. The change in the Mo–S bond length (in-plane movement of atoms) plays a significant role in determining the behavior of the E_{2g}^1 mode. As the hydrostatic pressure increases, the out-of-plane (A_{1g}) compression becomes more favorable than the in-plane (E_{2g}^1)

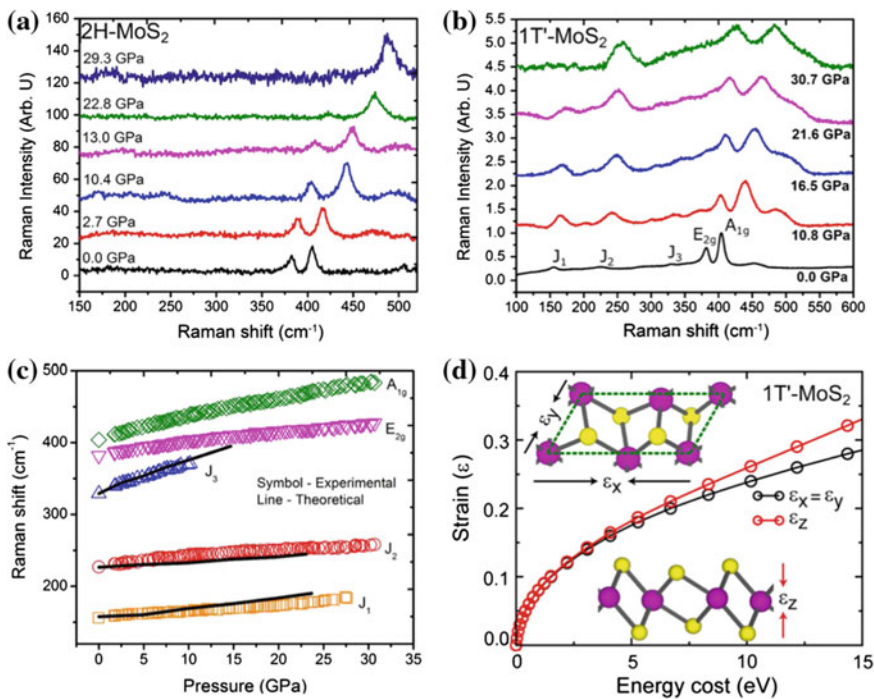


Fig. 7.31 Pressure-dependent lattice vibrational properties of monolayer 1T'- and 2H-MoS₂. Representative Raman spectra of the monolayer **a** 2H-MoS₂ and **b** 1T'-MoS₂ at high pressures. For the 2H-MoS₂ polytype, the E_{2g}^1 mode diminishes, whereas the dominant Raman modes are J_2 , E_{2g}^1 , and A_{1g} for 1T'-MoS₂ at pressures above 27 GPa. **c** Raman frequencies with variation in pressure for the five Raman active modes. The J_3 merges with the E_{2g}^1 mode at around 10 GPa, whereas the J_1 diminishes at 27 GPa. The solid line indicates the theoretical agreement with the J_1 , J_2 , and J_3 modes and further supports the phonon merging of the J_3 and E_{2g}^1 modes. **d** The applied strain is plotted with respect to the energy required to compress the in-plane and out-of-plane bonds, suggesting that the in-plane mode vibration is suppressed at higher pressures. Inset schematic representing the application of strain in the in-plane direction (ϵ_x , ϵ_y) (upper inset) and out-of-plane (ϵ_z) directions [67]. Copyright 2014 American Chemical Society. Published with permission

compression, indicating that at higher pressures, the transverse moment of the S–S atom is faster than the in-plane movement of the Mo–S atom.¹

The distorted 1T' phase shows three Raman active modes that are not present in the trigonal prismatic 2H-MoS₂ polytype, namely, J_1 , J_2 , and J_3 , observed at 150, 225, and 325 cm⁻¹, respectively, at ambient pressure (see Sect. 5.1.2). As the hydrostatic pressure increases, J_3 becomes indistinguishable from the E_{2g}^1 mode at ca. 10 GPa, whereas J_1 and J_2 are still prominent at higher pressures. The J_1 mode also diminished at pressures above 22 GPa, with only J_2 , A_{1g} , and E_{2g}^1 modes remaining

¹The terminology in the original publication [67], i.e. ‘S–S atom’ and ‘Mo–S atom’, is somewhat inaccurate but it was preserved here.

above 27 GPa (Fig. 7.31b). The pressure-dependent rate of increase for the J_1 and J_2 Raman mode was found to be $0.9 \text{ cm}^{-1}/\text{GPa}$, whereas the J_3 mode increased at $3.90 \text{ cm}^{-1}/\text{GPa}$. The Raman shift with pressure for the A_{1g} mode was $2.6 \text{ cm}^{-1}/\text{GPa}$, and the E_{2g}^1 mode increases at a rate of $1.7 \text{ cm}^{-1}/\text{GPa}$, with the separation between A_{1g} and E_{2g}^1 modes increasing at a rate of $1.2 \text{ cm}^{-1}/\text{GPa}$.

Unlike bulk 2H-MoS₂, no intermediate phase region between the semiconducting and metallic region was observed, indicating that the monolayer MoS₂ does not undergo metallization or a structural transition at pressures up to 30 GPa. Theoretically, the metallization of 2H-MoS₂ was predicted to occur at much higher pressures of ca. 68 GPa [67].

Pressure effects on monolayer MoS₂ were also studied in [68], where the appearance of two new peaks located at 200 and 240 cm^{-1} was observed. It was proposed that the new high-pressure structure has a distorted unit with the S atoms sliding within a single layer like the case for metastable 1T'-MoS₂.

7.7 Twisted and Folded Structures

A way to change interaction in a bi-layer structure is to stack two layers at variable twist angles. The change in the interlayer interaction can be directly monitored by measuring Raman spectra [69, 70], with the difference between the A_{1g} and E_{2g}^1 modes being the largest for 0 and 60° twist angle. The results obtained by the two groups are shown in Fig. 7.32.

An interesting proof-of-principle experiment was reported in [71]. In order to see how the interlayer coupling affects the Raman modes the authors studies folded layers of MoS₂, where the interlayer interaction was expected to be weaker than in properly stacked layers. It was found that, indeed, for the structure consisting of two folded layers the Raman peak positions were intermediate with respect to a single layer and two properly stacked layers. Similar results were found for other combinations of folded layers (Fig. 7.33).

7.8 Helicity-Resolved Raman Scattering

While Raman scattering is usually measured using linearly polarised light, the presence of spin-valley coupling in TMDCs (cf. a dedicated Chap. 11) makes it interesting to perform similar measurements using circularly polarised light. Such measurements are reported in [72]. The results of helicity-resolved Raman spectra of MoS₂ are shown in Fig. 7.34. The out-of-plane scattered photons (labelled OC) have the same $\sigma+$ helicity as the incident photon while the in-plane phonon band (labelled IMC) is observed only in the opposite $\sigma-$ polarization. For further confirmation, the half-waveplate in the collection path was rotated and the angular dependence of the

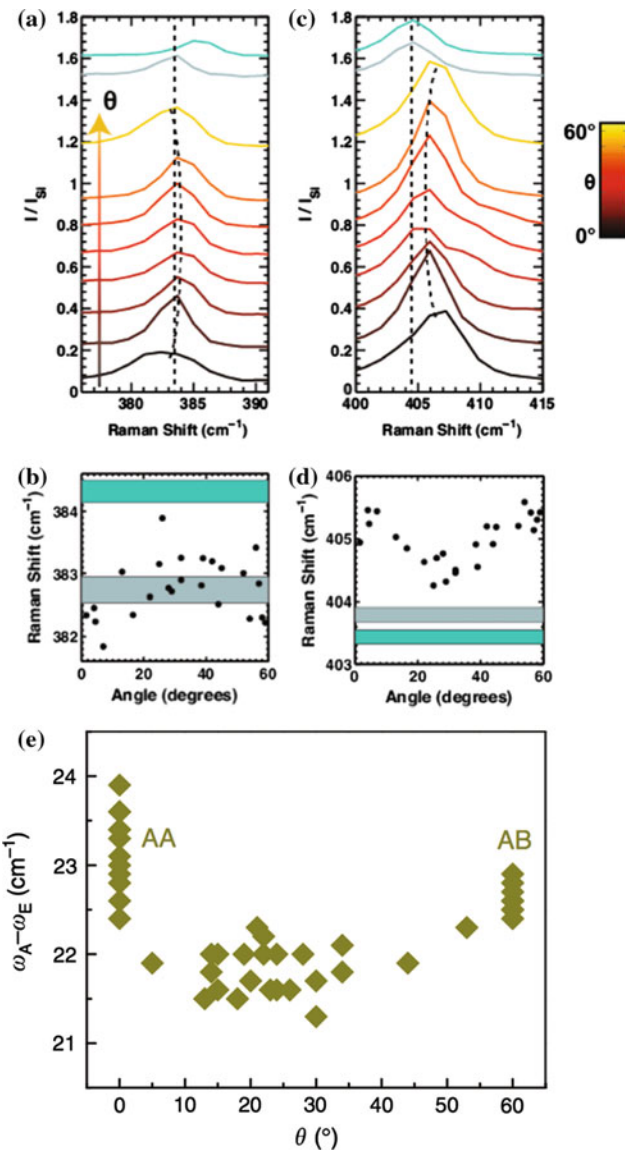


Fig. 7.32 **a** Tuning of the Raman E_{2g} mode with twist angle θ and **b** extracted peak positions (black points). **c** Tuning of the Raman A_{1g} mode with θ and **d** the extracted peak positions (black points). The spectra are offset for clarity and color-coded by twist angle, as indicated, with black corresponding to 0° and yellow corresponding to 60° . Black dashed lines highlight relevant tuning features. The green and gray bars indicate the standard deviation in the extracted peak positions for the bottom and top layers, respectively [70]. Copyright 2014 American Chemical Society. Published with permission **e** Raman peak separation between the A_{1g} and E_{2g}^1 in MoS₂ bilayers with different twist angles [69]. Reprinted by permission from Macmillan Publishers Ltd., copyright (2014)

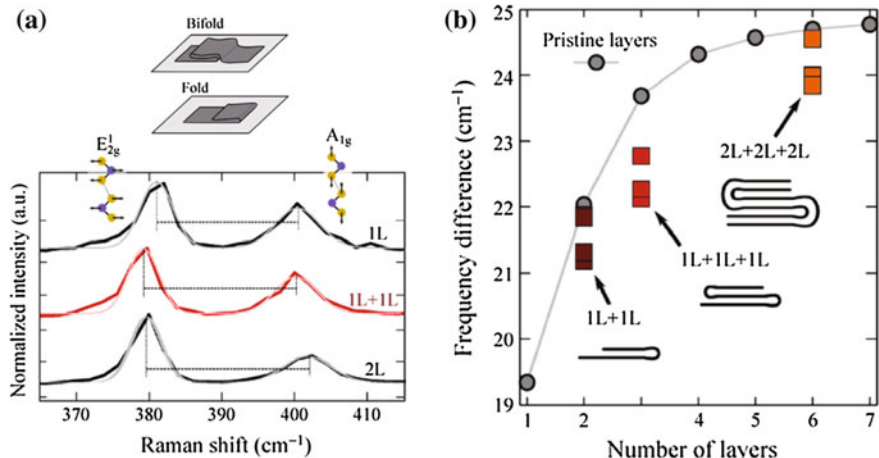


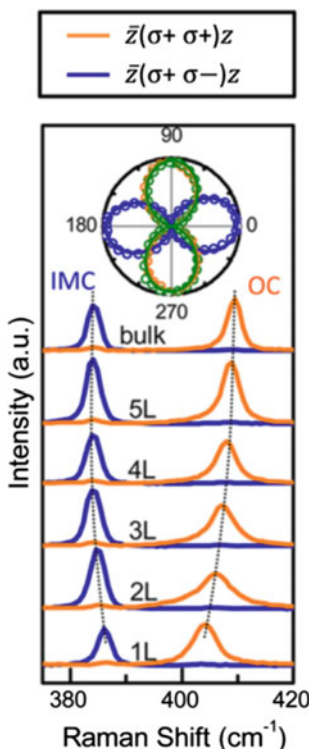
Fig. 7.33 **a** Raman spectrum measured for folded single-layer (1L+1L, in red) MoS₂ layers. The Raman spectra measured for pristine 1L and 2L have been included for comparison. The frequency difference between the E_{2g}^1 and A_{1g} Raman modes is indicated with dashed horizontal lines. The thin light lines are Lorentzian fits to the experimental data. **b** Frequency difference between the E_{2g}^1 and A_{1g} Raman modes as a function of the number of layers measured for: pristine layers (gray circles), folded and bi-folded single-layer (1L+1L and 1L+1L+1L, dark and light red squares respectively) and bi-folded bilayer MoS₂ (2L+2L+2L, orange squares) [71]. Reproduced with permission from Springer (color figure online)

spectra was measured. The normalized intensities of the IMC (blue), OC (orange), and Rayleigh (green) scattered light of 1L-MoS₂ are plotted as a function of detection angle in the inset of Fig. 7.34. The OC scattered photon has exactly the same polarization as Rayleigh scattered light, while IMC scattered photon has the exact opposite polarization.

To test the robustness of the observed helicity selectivity, the helicity of the scattered photons in multilayers and with different laser excitations were examined. The photon helicity was found to be independent of the number of layers and incident photon energy: the IMC mode always switched the photon helicity, in drastic contrast to luminescence spectra where the percentage of photons that maintain the incident photon polarization depended sensitively on the incident photon energy as well as on the number of TMDC layers. It was concluded that the helicity selection rules are robust and do not rely on the spin splitting of valence bands nor the orbital character of specific electron states. An explanation of this effect was proposed by considering the symmetry of relevant phonon modes [72].

It was further argued that the use of circularly polarised light may be more advantageous in distinguishing and assigning phonon modes, as well as allowing for more accurate measurements especially in the presence of accidental mode degeneracy.

Fig. 7.34 Helicity-resolved Raman spectra of 1L–5L and bulk MoS₂. The excitation wavelength is 488 nm with $\sigma+$ polarization. Inset : normalized angular dependence of the Rayleigh (green), IMC (blue), and OC phonon (orange) scattering intensities for 1L-MoS₂ [72]. Copyright 1984 American Chemical Society. Published with permission



7.9 Resonant Raman Scattering

The non-resonant Raman scattering of single and few-layer TMDCs was discussed in detail above. More complex is the Raman spectrum due to resonant excitation. In this case second-order Raman scattering processes, which are enhanced by the coupling of phonon modes to electronic states excited optically in the crystal, become as effective as the modes related to the first-order Raman scattering. In TMDCs, the excitation of Raman modes can easily be tuned to coincide with one of the direct optical transitions, such as the *A*, *B*, and *C* excitons, which are often close to the laser lines commonly used. This means that Raman data are often taken close to resonant conditions. This is an advantage when one needs information about modes that are usually not Raman-active. Resonant Raman scattering creates an important avenue to study band/excitonic excitations in diverse nanomaterials and also offers unique insights into multi-phonon processes due to the relaxation of selection rules and a huge amplification of Raman intensity under the resonance condition. Such resonant vibrational spectra can provide significant additional information concerning the electronic properties. For example, it was suggested that the observation of a strong second-order Raman resonance involving the longitudinal acoustic phonons

($2LA$) in monolayer WS_2 is a signature of the single-layer nature of the sample [73]. Furthermore, because the intervalley scattering process involving the $2LA$ phonon may be the main source of valley depolarization [74], understanding the resonant Raman processes in TMDCs is of great importance. At the same time, the presence of second-order peaks may also be a disadvantage when Raman scattering is simply used to determine the sample thickness, especially in cases where the first-order and second-order peaks are located close to each other because it may complicate the spectra analysis.

Resonant Raman spectra are composed of both first- and second-order Raman excitations and were extensively studied for bulk and nanostructured TMDC [75–77]. The first-order peaks do not show an excitation energy dependence, hence only the second-order peaks vary with excitation energy. Recently, second-order Raman modes have been reported in various single-layer TMDCs such as MoS_2 [78–81] and WS_2 [73, 82] and below in this section we summarise the main results.

7.9.1 MoS_2

7.9.1.1 From Bulk to a Monolayer

In [80], resonant Raman spectra from bulk as well as the 3ML, 2ML, and 1ML flakes were measured at room temperature and also at 4.2 K (Fig. 7.35). The following changes in the spectra were noticed. Firstly, the peaks due to second-order processes observed at energies higher than 500 cm^{-1} are hardly present in the spectrum from the 1ML flake. Another remarkable effect of decreasing MoS_2 thickness was the change in the line shape of the peaks at 465 and 643 cm^{-1} . While the peak at 465 cm^{-1} had a bimodal structure with the low-energy component of the peak assigned to a combined $2LA(M)$ process [76] with the high-energy component of the peak at 465 cm^{-1} usually related to an IR-active process of A_{2u} symmetry from the Γ point of the MoS_2 Brillouin zone, a different assignment of the high-energy component was proposed in [83], namely, it was suggested that the peak is rather due to a combined $E_{1g}(M) + XA(M)$ process. It was noted that the E_{1g} mode is a Raman-active mode that is forbidden in the backscattering geometry [24] employed in this experiment, which explains its absence in the spectrum. The $XA(M)$ is a transverse acoustical phonon (TA or ZA) from the vicinity of the high-symmetry M point of the Brillouin zone with energy equal to 179 cm^{-1} . It was argued that although the $E_{1g}(\Gamma)$ process is forbidden in the backscattering geometry, the combined $E_{1g}(M) + XA(M)$ process should be allowed by the crystal-momentum conservation principle. The bimodal structure of the peak at 465 cm^{-1} is unveiled by its evolution with decreasing number of layers. It was proposed that the observed evolution is due to relative changes of the $E_{1g}(M) + XA(M)$ and $2LA(M)$ line intensities with decreasing number of layers.

It was noticed that the behavior of the 643 cm^{-1} peak with decreasing layer thickness is rather similar [80]. According to the original work, this peak also comprises two components: the high-energy one due to $E_{1g}(M) + 2XA(M)$ and the low-energy

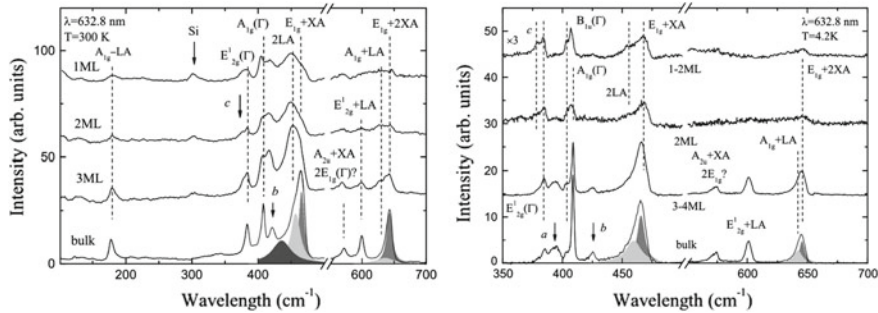


Fig. 7.35 The evolution of resonant Raman spectra as a function of layer thickness measured at room temperature (*left*) and at 4.2 K (*right*). The background photoluminescence was removed for more clarity. The broadened peaks were deconvoluted to show Lorentzian waveform contributions. The attributed phonons originate from the M -point of the Brillouin zone unless stated otherwise [80]. Reprinted with permission from Elsevier

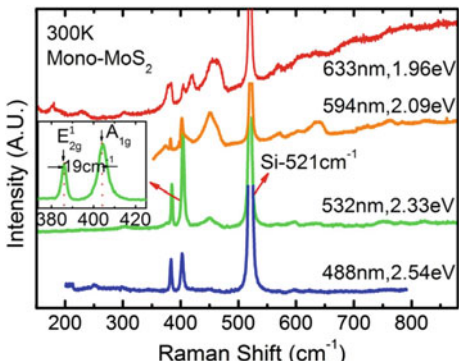
component due to the $A_{1g}(M) + LA(M)$ process. Contrary to the previous suggestion [34] it was proposed that the observed evolution of the peak with decreasing number of layers is due to changes in relative intensities of its both components rather than due to an “emerging new peak” in the spectrum [34].

The observed evolution of both peaks with the decreasing layer thickness suggests that the electron-phonon interactions with transverse acoustic phonons become less effective in few-layer structures. It was proposed that this is due to the effect of the substrate on the long-range acoustic modes by additional forces provided by the substrate. The results suggest that the processes involving transverse acoustic phonons are affected more strongly than those with longitudinal acoustic phonons.

Another result of the room-temperature resonant Raman measurements was the observation that the so-called dispersive mode *b* at 420 cm^{-1} seems to be still present in the 1ML sample. The peak has been previously [50] interpreted as a result of a resonant process involving subsequent emission of a dispersive, low frequency, quasi-acoustical phonon at a finite wavevector in the $(\Gamma - A)$ direction and the following emission of a dispersionless optical E_{1u}^2 phonon with the opposite wavevector. Finally a change of the E_{2g}^1 peak line shape as a function of the layer thickness was noted.

In order to obtain more information on the electron-phonon interactions in MoS_2 additional measurements at 4.2 K were performed. Similar to the room-temperature data, the second-order processes that give rise to peaks at energies higher than 500 cm^{-1} become less effective in few-layer structures. The evolution of the line shape of the peaks at 465 and 643 cm^{-1} was explained in terms of changes in relative intensities of their components. Additional changes were observed at low energies. The peak *b* at 420 cm^{-1} disappeared from the spectrum in few-layer flakes, the behavior being consistent with its assignment to the combined process involving phonons with wavevectors parallel to the *c*-axis. Similar to the peak *b*, the peak *a* observed at 395 cm^{-1} also disappeared from the spectrum in few-layer samples. From its sensitivity to the sample thickness its assignment was suggested to be related processes involving phonons of wavevectors parallel to the *c*-axis of the crystal. The peaks

Fig. 7.36 Room-temperature Raman spectra of monolayer MoS₂ under different excitation wavelengths. The inset shows the frequency separation between the E_{2g}^1 and A_{1g} modes, which demonstrates that the sample is monolayer MoS₂ [79]. Reprinted with permission. Copyright 2014 by the American Institute of Physics



observed at 378 and 404 cm⁻¹ become more pronounced in few-layer samples. The peak *c* at 378 cm⁻¹ was previously assigned to a dispersionless optical E_{1u}^2 Raman-inactive phonon with a finite wavevector from the vicinity of the Γ point [34, 50]. The peak at 404 cm⁻¹ is due to another Raman-inactive B_{1u} mode, which is the Davydov couple of the A_{1g} [24]. Both peaks were previously observed [34] in thin samples. The present results show that at low temperature the Raman peaks due to inactive processes become as pronounced as the peaks corresponding to Raman-active modes. This can be due to the symmetry-breaking resulting from the interaction of the MoS₂ atoms with the substrate [80].

7.9.1.2 Wavelength Dependence

Resonance Raman scattering in single-layer MoS₂ measured using different excitation wavelengths [79] is shown in Fig. 7.36. Like in the bulk, despite the gap opening and a transition to a direct gap, the resonance still occurs at 633 nm (1.96 eV) and 594 nm (2.09 eV). It was proposed that the resonance is always dominated by the excitonic excitations at K/K' in both bulk and single-layer MoS₂. One difference between the resonance spectra of the bulk and single-layer is the gradual lift-up of background towards high frequencies in monolayer MoS₂, which was attributed to the tail of the extremely strong photoluminescence in monolayer MoS₂. A significant difference between bulk and monolayer MoS₂ in resonance Raman spectra is that almost all the first-order and multi-phonon modes were greatly broadened and their relative intensities were substantially changed in monolayer MoS₂. The sharp multi-phonon modes above 550 cm⁻¹ in the resonance spectra of the bulk were strongly suppressed and almost invisible in the monolayer case, in agreement with the results of [80].

Several possible reasons for the suppression of Raman modes above 550 cm⁻¹ in monolayer MoS₂ were considered. One reason could be a change of the electronic band structures with the transition from bulk to monolayer. Another possibility could be a change of phonon band structures. The third possibility is that the acoustic branches in monolayer are strongly affected by the substrate. It was argued that the

third mechanism is more relevant, where the modification of the acoustic modes by the substrate causes the suppression of most multi-phonon process [79].

The Raman resonance profiles of the A_{1g} phonon for single-layer MoS₂ as well as the corresponding photoluminescence were studied in [84]. It was found that at both transitions, A and B , the Raman signal was enhanced. The FWHMs for the Raman resonance profiles were slightly narrower than for photoluminescence. In addition, the amplitude of the B transition relative to the A transition was 3.6 times stronger in the Raman resonance profiles, which could indicate either that the exciton-phonon coupling is stronger for the B exciton than for the A exciton or could be a result of different radiative lifetimes. It was further found that the Raman intensity of the A_{1g} mode in bilayer MoS₂ was, when in resonance with the A exciton, approximately six times higher than in the single layer, possibly indicating a stronger exciton-phonon coupling in bilayer MoS₂ [84].

In [85], where the authors used as many as 30 different excitation energies, it was confirmed that the A_{1g} phonon mode is enhanced by the A and B excitons; the enhancement decreased with a decreasing number of layers, which was interpreted as being due to the dependence of the lifetime of the intermediate excitonic states on the number of layers. In addition, it was observed that the E_{2g}^1 phonon mode is strongly enhanced around 2.7 eV, in a region of the optical spectrum that exhibits a broad band associated with a diversity of excitons. It was proposed that the high energy C exciton is responsible for the enhancement of the E_{2g}^1 phonon mode, due to symmetry-dependent exciton-phonon interaction in MoS₂.

Resonant Raman scattering in few-layered MoS₂ (up to 14 layers) using 6 different excitation energies was studied in [81].

7.9.2 WS₂

7.9.2.1 Wavelength Dependence

Figure 7.37a, b show typical Raman spectra of monolayer WS₂ regions using 514.5 and 488 nm excitations [73]. For $\lambda_{exc} = 488$ nm, the Raman spectrum is dominated by the first-order modes: $LA(M)$ at 176 cm^{-1} , $E_{2g}^1(\Gamma)$ at 356 cm^{-1} and $A_{1g}(\Gamma)$ at 418 cm^{-1} . However, when monolayer WS₂ is excited at 514.5 nm, the Raman spectrum becomes very rich, revealing many second-order peaks that are stronger than those observed in the bulk material. Figure 7.37a, b gives symmetry assignments for several peaks according to previous reports in bulk and fullerene-like WS₂ nanostructures. For $\lambda_{exc} = 514$ nm, it is remarkable that the intensity of the strongest second-order Raman peak, the $2LA(M)$ mode at 352 cm^{-1} , is approximately twice the intensity of the first-order $A_{1g}(\Gamma)$. Although the $2LA(M)$ mode overlaps with the first-order $E_{2g}^1(\Gamma)$ mode at 356 cm^{-1} , multi-peak Lorentzian fitting clearly separates their individual contributions. The interplay of these two components was also studied in [86] and is described below.

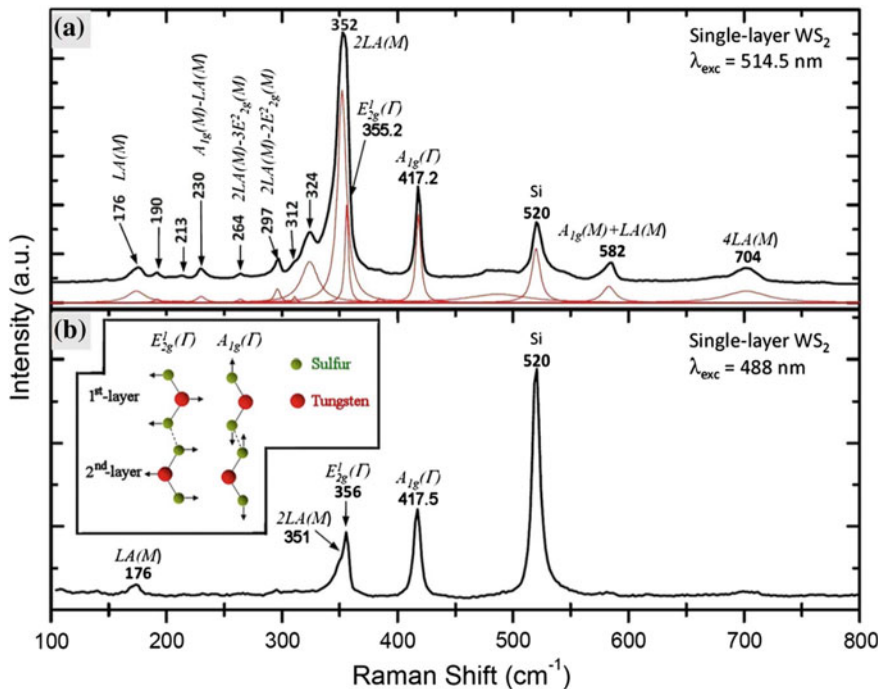


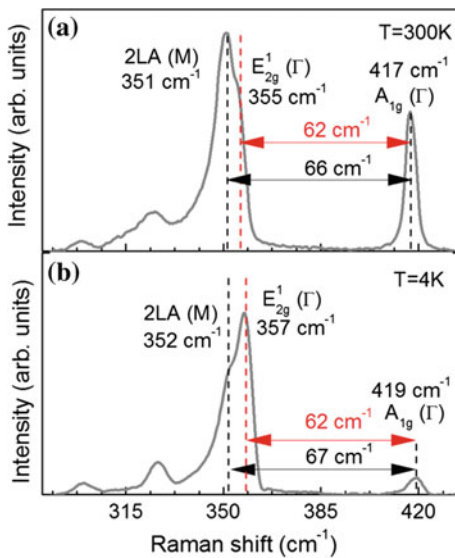
Fig. 7.37 **a** and **b** Room-temperature Raman spectra from a monolayer WS₂ region, using the 514.5 and 488 nm laser excitation, respectively, including Lorentzian peak fits for 514.5 nm data. The *inset* in **b** shows the atomic displacements for the in-plane phonon mode $E_{2g}^1(\Gamma)$ and the out-of-plane phonon mode $A_{1g}(\Gamma)$ for two adjacent layers, the *dashed line* represents the weak inter-layer van der Waals interaction. Reproduced from [73]

7.9.2.2 Temperature Dependence

A typical resonant Raman spectrum taken at 300 K is shown in Fig. 7.38a. Two strong features are observed: a single resonance peak at 417 cm⁻¹, which corresponds to the A_{1g} mode in a single-layer of WS₂ and a more complicated feature around 353 cm⁻¹ that is composed of two peaks: a peak at 351 cm⁻¹ accompanied by a weaker peak at 355 cm⁻¹. The latter corresponds to the E_{2g}^1 mode in single-layer WS₂ and the low-energy feature was assigned to a second-order Raman resonance involving longitudinal acoustic phonons (2LA) [73]. The peak at 351 cm⁻¹ corresponds well to such a second-order Raman resonance. At room temperature, the 2LA mode is stronger than E_{2g}^1 mode for single-layer material.

Further proof of the 2LA character of the peak at 351 cm⁻¹ is provided by measurements at low temperature ($T = 4 \text{ K}$) presented in Fig. 7.38b. In addition to a small blue shift of the resonance frequencies observed with decreasing temperature due to the anharmonic vibrations of the lattice within the interatomic potential energy

Fig. 7.38 a and b Typical Raman spectra measured at $T = 300$ and 4 K. The dashed lines indicate the position of three Raman modes: 2LA, E_{2g}^1 , and A_{1g} [86]. Copyright 2014 by the American Physical Society. Reprinted with permission



mediated by phonon-phonon interactions, the dominant effect of the temperature was the radical change in the intensity ratio between the E_{2g}^1 and 2LA modes. While at room temperature the 2LA mode dominates over the E_{2g}^1 mode, at low temperature, the situation is reversed.

7.9.3 Raman Excitation Profiles

In Raman studies, usually only one or a few laser excitation lines are used preventing the determination of the excitation profile of the Raman features and the dependence on the number of atomic layers. In [87], a complete resonant Raman scattering study of 1L, 2L, 3L, and bulk WSe₂ using up to 20 excitation energies in the visible range was reported. The excitation spectrum of the most intense Raman features were measured, which made it possible to distinguish the behavior of the first- and second-order Raman bands. From the position of the maxima of the Raman excitation profile, it was also possible to obtain the energies of the (A' , B') exciton pair as a function of the number of atomic layers, which were in good agreement with absorption and photoluminescence studies.

Figure 7.39a, b shows, respectively, the excitation profile of the first-order band around 250 cm^{-1} and the second-order band around 260 cm^{-1} . It was first noted that the excitation profiles of the first- and second-order features are different. While for monolayer WSe₂, the excitation profile of the first-order peaks exhibit only one large maximum around 2.4 eV, the Raman excitation profile of the second-order bands, additionally exhibit a second maximum at lower energies, around 2.1 eV. The energy

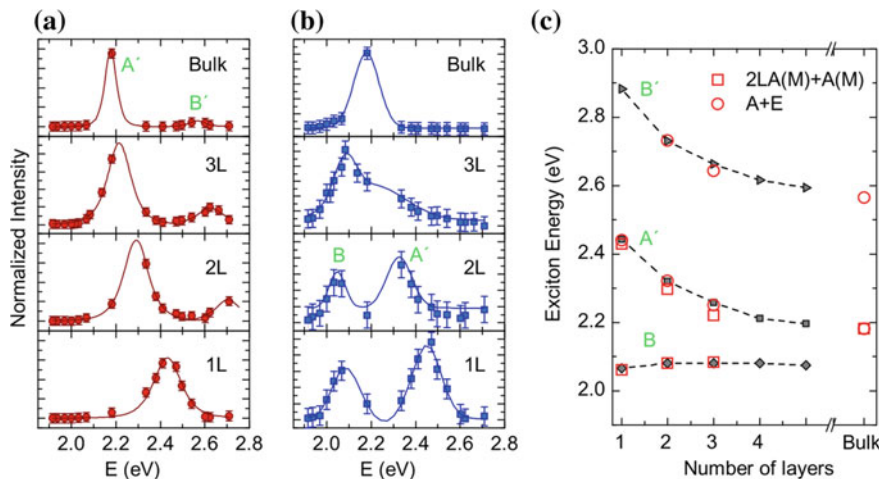


Fig. 7.39 Evolution of the Raman excitation profile with the number of layers for (a) the first-order modes ($A + E$) and (b) the second-order bands ($2LA(M) + A(M)$). **c** Comparison between the position of the Raman signal enhancement obtained in this work (open symbols) and the absorption data derived from literature (solid symbols) [87]. Copyright 2014 American Chemical Society. Published with permission

separation of these two maxima for the second-order features decreases with the number of layers and the two peaks converge to a single maximum for bulk WSe₂.

The optical absorption spectra of WSe₂ exhibited four peaks that were ascribed to two pairs of excitons, (A, B) and (A', B'). For monolayer WSe₂, these four peaks appear, respectively, at 1.65, 2.05, 2.40, and 2.80 eV. An important result was the fact that the first-order ($A + E$) Raman features are not enhanced (or very weakly enhanced) using laser energies corresponding to the B exciton (the A exciton was out of the range of laser energies used in this work). At the same time, the Raman excitation profile of this first-order band exhibits a strong enhancement for laser energies near the A' and B' exciton energies, which indicates that coupling of these first-order phonons is stronger for the (A', B') pair. It was argued that this is an advantage of resonant Raman scattering over optical absorption and photoluminescence experiments, where the latter cannot provide information about electron-phonon coupling.

The dependence of the maxima in the excitation profiles on the number of layers was also discussed and comparison was made with previous results of optical studies in WSe₂. Figure 7.39c compares the B , A' , and B' exciton energy variation with the number of layers, obtained from optical absorption [88] and from the Raman results, which demonstrates good agreement between the resonant Raman and optical data.

7.10 Thickness Determination

Since the pioneering work [8], where strong differences among Raman spectra from flakes with different number of layers were reported, Raman scattering has been widely used to determine layer thicknesses.

The authors of [78] compared the use of various parameters obtained from Raman measurements to characterize the number of layers (Fig. 7.40) and concluded that peak position is a more accurate method to determine the number of layers, as opposed to peak intensity and/or width.

A comprehensive study of reliable thickness identification of atomic layers of TMDCs using Raman scattering was performed in [89]. The authors performed systematic measurements for thicknesses varying from a monolayer to 120 layers and found that the peak intensity changed in a non-monotonic way (Fig. 7.41), in particular a new enhancement peak appeared at ca. 85 layers. The increased intensity of the peaks was accounted for by interference effects. Various modellings were performed considering multiple scattering effects and the simulated results were in good agreement with experiment. It was concluded that the intensity ratios of the

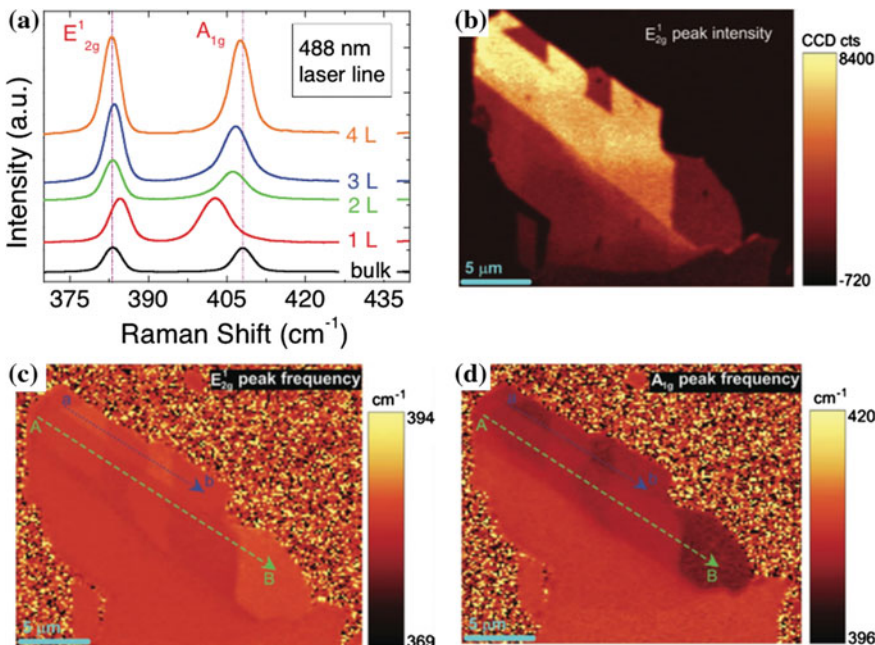


Fig. 7.40 Raman characterizations of a MoS_2 sample using 488 nm laser line. **a** Raman spectra of different locations with various thicknesses on the sample. **b** Raman mapping image with the E_{2g}^1 peak intensity, **c** the E_{2g}^1 peak frequency, and **d** the A_{1g} peak frequency. Inset color bars. The scale bars represent 5 μm [78]. Reproduced with permission from Wiley-VCH Verlag GmbH

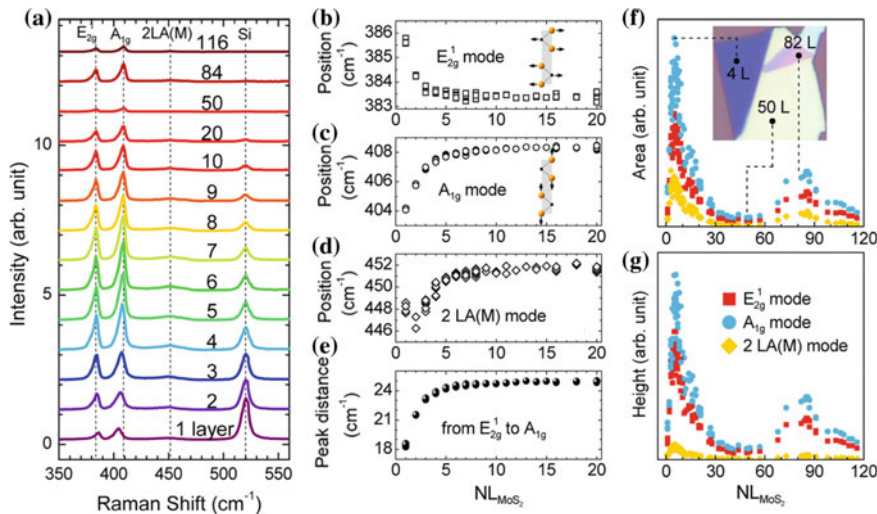


Fig. 7.41 Raman spectra for MoS₂ flakes and evolution of spectral features with thickness. **a** Typical Raman spectra of MoS₂ flakes for different numbers of layers (NL) varying from 1 to 116. **b–d** Position evolution for the three Raman modes E_{2g}^1 , A_{1g} , and 2 LA(M) as a function of NL. **e** Peak distance between the E_{2g}^1 and A_{1g} modes. **f** Area and **g** height plots for the three modes as a function of NL. The *inset* of (f) is an optical image for an MoS₂ flake of three typical NL values (4, 50, and 82) [89]. Copyright 2012 American Chemical Society. Published with permission

E_{2g}^1 and A_{1g} modes to that of the Si substrate is a very accurate way to determine thickness (Fig. 7.42).

In [73] a method to identify single layers of WS₂ was proposed based on the fact that in the case of a monolayer a strong resonant 2LA(M) peaks appears at excitations close to 514.7 nm. The appearance of this peak was interpreted in terms of a double resonance process, which is active only in a monolayer.

Since the shift in the low-frequency range is significantly larger than that in the higher-frequency range, it was argued that use of the E_{2g}^2 mode may be more efficient than using the A_{1g} and E_{2g}^1 modes at higher frequencies. This proposal is substantiated in Fig. 7.43, where maps for a sample with variable thickness have been made using the A_{1g} – E_{2g}^1 mode difference (left) and the position of the E_{2g}^2 (right). One can see that the latter approach produces a larger contrast, i.e. is more accurate.

While it is common for few-layer TMDCs systems to analyze the relative shift and amplitudes of the E_{2g}^1 and B_{2g}^1 Raman modes in order to determine sample thickness, for MoTe₂ it was proposed that when using 633 nm excitation, the Raman spectra of single-layer and bi-layer samples exhibit such different A_{1g} and B_{2g}^1 mode intensities compared with thicker layers that they can be used for identification of the sample thickness [35].

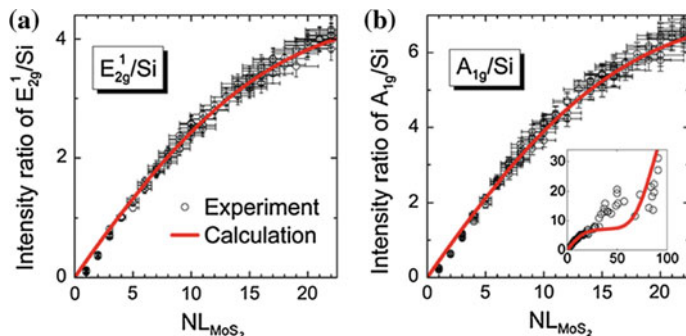


Fig. 7.42 Comparison between calculation and experiment for the intensity ratio of the MoS_2 E_{2g}^1 (383 cm^{-1}) and A_{1g} (408 cm^{-1}) modes to that of the Si substrate (520 cm^{-1}) [89]. Copyright 2012 American Chemical Society. Published with permission

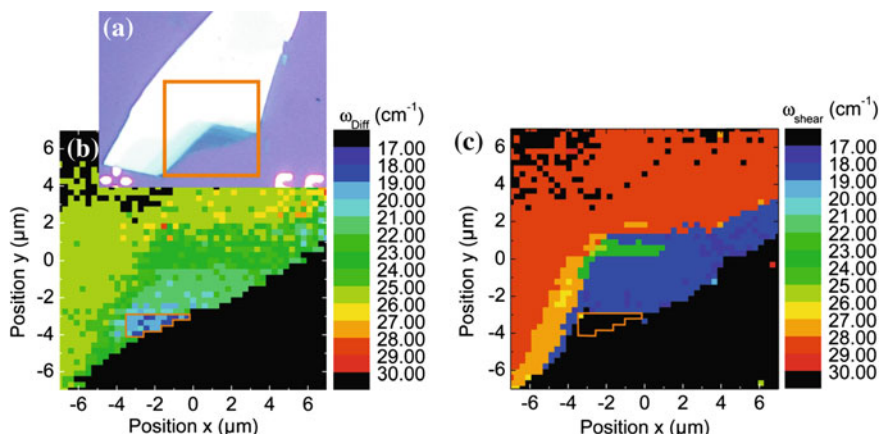


Fig. 7.43 **a** Optical micrograph of a few-layer MoSe_2 flake. The square marks the scan region for the false color plots in **b** and **c**. **b** False color plot of the frequency difference between the A_{1g} and E_{2g}^1 modes. The outline of the single-layer area of the flake is marked by the *solid line*. **c** False color plot of the shear mode (B_{2g}^2) position. The scan region is identical to **(b)** [29]. Reprinted with permission. Copyright 2012 by the American Institute of Physics

For ReS_2 [90], it was noted that measuring the ratio of two peaks located at different wave numbers, such as $r = I_{124}/I_{158}$ may be a useful measure for mapping single crystal domains in the crystal [91].

The thickness dependence of the position of the A_{1g} and E_{2g}^1 modes of Raman scattering was also demonstrated to be a useful method for thickness determination for TaSe_2 [92].

7.11 Raman Scattering of Specific Materials

7.11.1 Raman Modes of the $1T'$ -Phase

As already mentioned, the distorted $1T'$ phase (also referred to as the ZT phase) shows three Raman active modes that are not present in the trigonal prismatic $2H$ -MoS₂ polytype, namely, J_1 , J_2 , and J_3 , observed at 150, 225, and 325 cm⁻¹, respectively (see Sect. 5.1.2 above). In [93], the Raman modes for the distorted ZT phase of MoS₂ were simulated (Fig. 7.44), the obtained results being in agreement with the experimental results [94].

Raman vibrations of $1T$ - and $1T'$ -MoTe₂ were studied in [95] and Raman modes of $1T'$ -WTe₂ were measured in [96].

7.11.2 Rhenium Dichalcogenides: A 2D Response from 3D Samples

An interesting exception to the trends discussed above is ReS₂, where the Raman peaks do not change as one goes from the bulk phase to a monolayer (Fig. 7.45) [90].

The vibrational spectra of ReS₂ were further studied in [97], where the authors successfully observed all 18 first-order Raman-active modes from bulk to monolayer

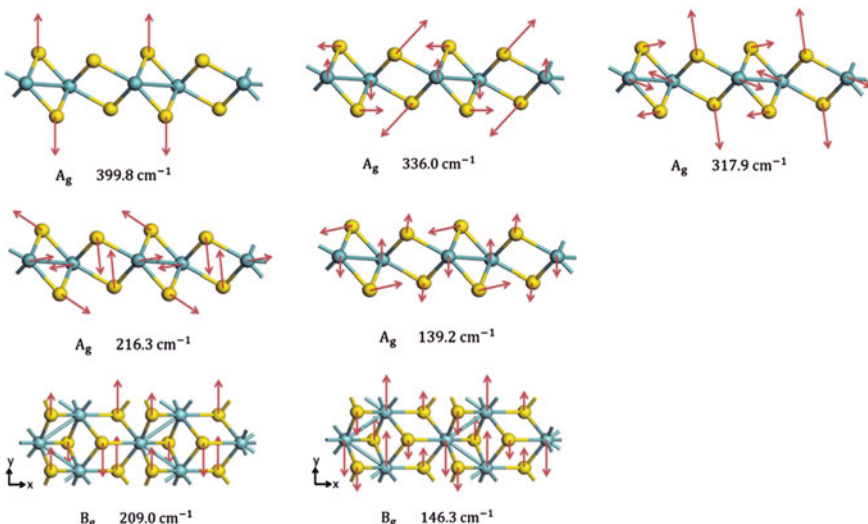


Fig. 7.44 The vibrational vectors of Raman-active modes for $1T'$ -MoS₂. The A_g modes are viewed in the xz plane while the B_g modes are viewed in the xy plane [93]. Reprinted with permission. Copyright 2013 by the American Institute of Physics

Fig. 7.45 Raman spectrum taken on bulk (blue) and monolayer (red) ReS_2 [90]. Reprinted by permission from Macmillan Publishers Ltd., copyright (2014)

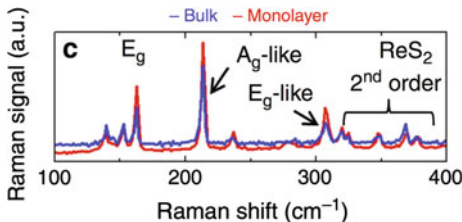
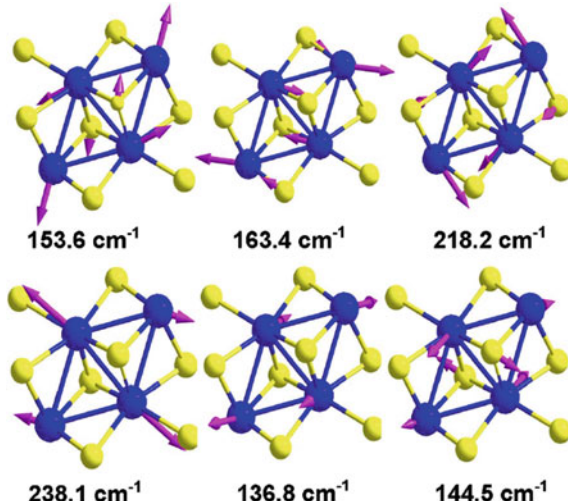


Fig. 7.46 E_g -like vibration modes at 153.6, 163.4, 218.2, 238.1 cm^{-1} and two A_g -like vibration at 136.8 and 144.5 cm^{-1} for bulk ReS_2 , from LDA theoretical calculations and analysis of the vibration eigenvectors. The lengths of the arrows are proportional to the modular of the phonon eigenvectors, with the length weights less than 15% ignored [97]. Copyright 2015 by the American Physical Society. Reprinted with permission



samples.² It was also confirmed that there are no peak shifts between bulk and monolayers of ReS_2 [97]. The E_g -like and A_g -like modes for ReS_2 are shown in Fig. 7.46.

Similar results were obtained for ReSe_2 [91]. The authors note that because ReSe_2 has 12 atoms per unit cell, 36 normal modes are expected. Given the unit cell only has identity and inversion symmetry elements, and since all atoms are displaced from the inversion center, all normal modes are non-degenerate. There are 18 Raman-active A_g modes, 15 infrared active A_u modes, and 3 zero-frequency A_u modes. Experimentally, it was found that up to 16 modes were required to fit the measured spectra for samples with different thicknesses [91].

The polarization dependence was studied by rotating the plane of polarization of the incident light in the layer plane. No analyzer was used before the detector in this experiment. The Raman peaks of ReSe_2 showed a clear variation of intensity with the angle of rotation of the excitation polarization for all modes. The observed angle dependences was attributed to the structure of the Raman signal [91]. To analyze this

²There is a discrepancy between peak assignments between [90] and [97]. While in the former the peaks located between 300 and 400 cm^{-1} are referred to as second-order, in the latter, they are believed to be first-order.

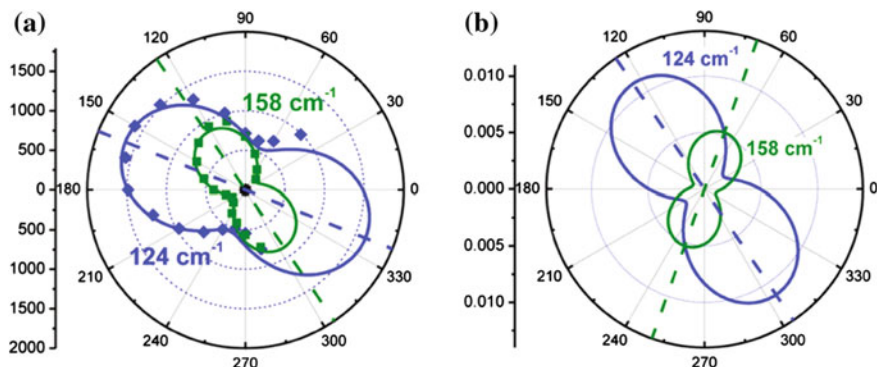


Fig. 7.47 **a** Measured and **b** calculated angle dependence of the peak intensities of ReSe_2 using the 124 and 158 cm^{-1} modes (blue circles and green squares respectively) [91]. Copyright 2014 American Chemical Society. Published with permission

behavior in detail, a group of overlapping bands was considered from 110 to 124 cm^{-1} and the peak at 158 cm^{-1} which exhibit a good signal-to-noise at all orientations.

This angular dependence was proposed to be useful for determination of the crystal orientation. For the particular case of unpolarized detection where the incident polarization makes an angle θ to the crystal a axis, the total recorded intensity $I_T(\theta)$ is the sum of the scattered intensities in the polarization directions parallel and perpendicular to the excitation polarization and can be written as [91]:

$$I_T(\theta) \propto u^2 \cos^2 \theta + w^2 \sin^2 \theta + v^2 + 2v(u+w) \sin \theta \cdot \cos \theta \quad (7.6)$$

where u , v , and w form the Raman tensor.

It was noted that by comparing of the angular dependences of the Raman mode predicted from the Raman tensor and the experimental tensor R' (Fig. 7.47), one can determine the absolute rotation of the crystal with respect to the laboratory axes and hence the crystal orientation. For the particular case shown in Fig. 7.47, the sample orientation was found to be ca. 42° .

It was further noted that there was no observed (or predicted) shift in the frequencies of any Raman bands from their bulk values, so that no indication of sample thickness can be obtained from peak shifts alone, a result in agreement with the recent observations on ReS_2 [90]. While the peak intensities vary among samples with different thicknesses, they cannot be a reliable measure of the thickness because of the polarization dependence. At the same time it was noted that measuring a ratio of two peaks, such as $r = I_{124}/I_{158}$ may be a useful measure for mapping single crystal domains in the crystal [91].

The different behavior of ReS_2 and ReSe_2 compared with Mo- and W- dichalcogenides comes from the different interlayer coupling strength [90]. As shown in Fig. 7.48, interlayer bonding between adjacent layers in ReS_2 is much weaker compared to that of MoS_2 , namely the coupling energy of $\approx 18\text{ meV}$ per unit cell was

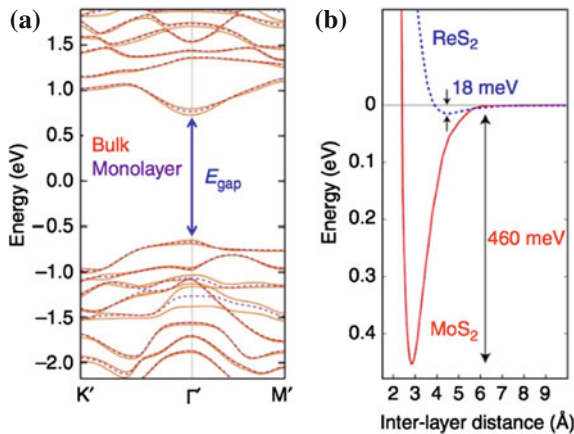


Fig. 7.48 **a** DFT calculated electronic band structure of bulk (orange solid curves) and monolayer (purple dashed curves) ReS₂. Both are predicted to be a direct bandgap semiconductor with nearly identical bandgap values at the Γ point. **b** The calculated total energy of the system as a function of interlayer separation. The significantly shallower depth of the well in ReS₂ implies much weaker interlayer coupling energy in ReS₂ as compared with MoS₂ [90]. Reprinted by permission from Macmillan Publishers Ltd., copyright (2014)

obtained, which is ca. 8% of that of MoS₂ (460 meV for the corresponding 2×2 conventional cell).³ The weak interlayer interaction results in the bulk and monolayer ReS₂ having nearly identical band structures, both being direct-bandgap semiconductors with predicted GGA bandgaps of 1.35 eV (bulk) and 1.43 eV (monolayer), in contrast to conventional TMDCs, where the band structure is strongly dependent on the number of layers.

7.11.3 Raman Signatures as a Fingerprint of VdW Interaction in Heterostructures

Raman scattering was also found to be an important tool to characterize vdW interaction in TMDC heterostructures that are held together by vdW interactions [100, 101].

³It should be noted that the details of the calculations are not sufficiently described in the original publication, which poses several questions. According to the description provided, the calculations were performed using GGA-PBE (Perdew–Burke–Ernzerhof) functional and it is well established that at the GGA-PBE level of theory the interaction between layers is much weaker than in cases when vdW interaction is properly accounted for; repulsive interlayer interaction can be obtained even for MoS₂ [98, 99]. At the same time, the vdW energy obtained for MoS₂ in the cited work [90] is the same as the one obtained in [98] with vdW-DFT functional used. Hence, calculations that explicitly include vdW interaction have to be performed before this issue can be definitively answered.

A comprehensive study of MoS₂-graphene, MoS₂-mica and MoS₂-WS₂ nanostructures was done in [100], being complemented by a study of MoS₂-WSe₂ [101]. It was found that when a layer of MoS₂ was capped by graphene, or vice versa, both the MoS₂ and graphene Raman modes slightly shifted. Thus, for n G/mMo heterostructures on Si/SiO₂ ($n = 1, 2; m = 1, 2$), where G refers to graphene and Mo to MoS₂, the G peak position is 1583–1584 cm⁻¹ in all cases, showing no remarkable difference between graphene on MoS₂ and Si/SiO₂. At the same time, the second-order Raman peak of graphene shows a blue shift from 2685 cm⁻¹ for bare graphene to 2699 cm⁻¹ when transferred on MoS₂. This shift was independent of the number of MoS₂ layers beneath graphene.

For MoS₂, both the E and A peaks shifted when the layer is encapsulated. In particular, the additional layer of graphene caused the E_{2g}^1 peak to slightly shift from 385 to 384 cm⁻¹ (green region in Fig. 7.49c) and the A_{1g} to shift from 403 to 405 cm⁻¹. These positions did not change when a second layer of graphene was transferred on top. This indicates that the shifts of E_{2g}^1 and A_{1g} are caused only by

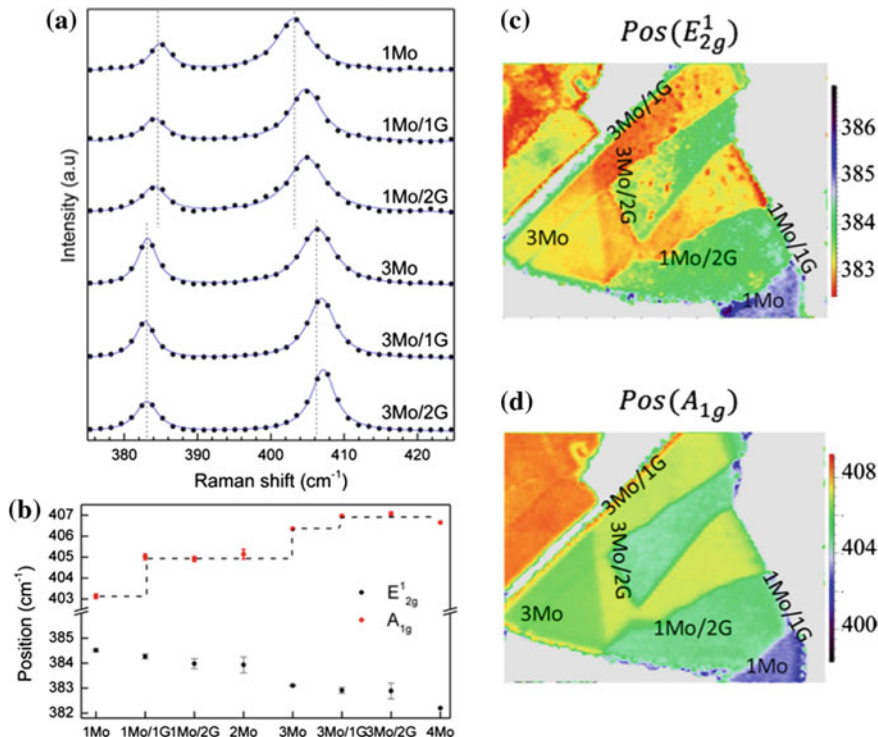


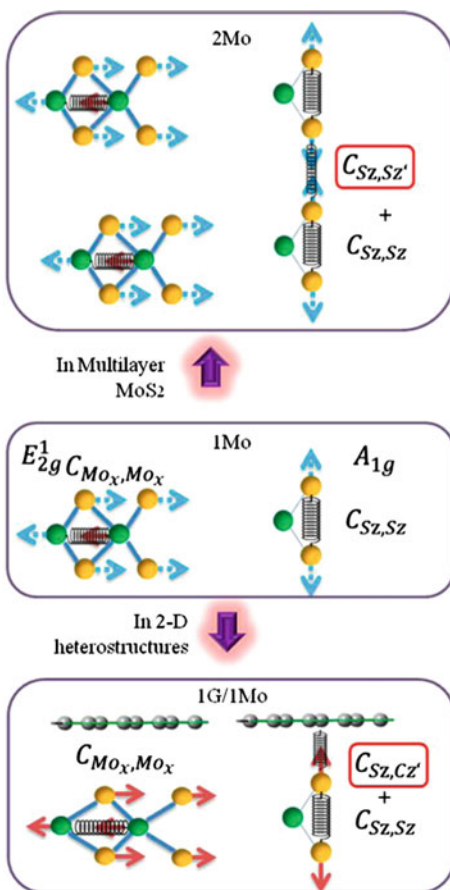
Fig. 7.49 **a** Raman spectra of MoS₂ in nMo/mG heterostructures. The dots correspond to the experimental data, while the solid lines are the fits obtained by using a Lorentzian line shape. **b** MoS₂ peak positions extracted from the spectra in (a). The Raman maps of the position of the **c** E_{2g}^1 and **d** A_{1g} modes for the heterostructure [100]. Copyright 2014 American Chemical Society. Published with permission

the direct contact with graphene and not by the number of graphene layers placed on top of MoS₂. Similarly, for bilayer MoS₂, its encapsulation in one or two layers of graphene caused a blue shift of A_{1g} from 405 to 406.5 cm⁻¹; also, in this case, the effect did not depend on the number of graphene layers used as a top layer.

In order to understand these results, it was noted that the changes in the E_{2g}¹ and A_{1g} positions observed in encapsulated MoS₂ are similar to the shift in the positions observed when increasing the thickness from single-layer MoS₂ to few-layer MoS₂ [8, 78]. The process was modelled using different interaction terms as shown in Fig. 7.50, where the term C_{Sz,Cz'} fingerprints the vdW interaction of the neighboring layers.

Several other effects that may cause the peak shift were considered, such as laser-induced thermal effect and/or doping and it was concluded that such factors can be excluded as possible causes. It was finally concluded that the shift of 2 cm⁻¹ of the A_{1g} mode can be taken as a fingerprint of the vdW contact.

Fig. 7.50 Schematic of the interaction between graphene and MoS₂ in a heterostructure 1G/1Mo (bottom panel), as compared to 1Mo (middle panel) and 2Mo (top panel). The green, gold, and gray balls represent molybdenum, sulfur, and carbon atoms, respectively. The arrows indicate the direction of atom displacement (*x* or *z*). The dominating interaction terms for the E_{2g}¹ and A_{1g} mode are modeled by springs [100]. Copyright 2014 American Chemical Society. Published with permission



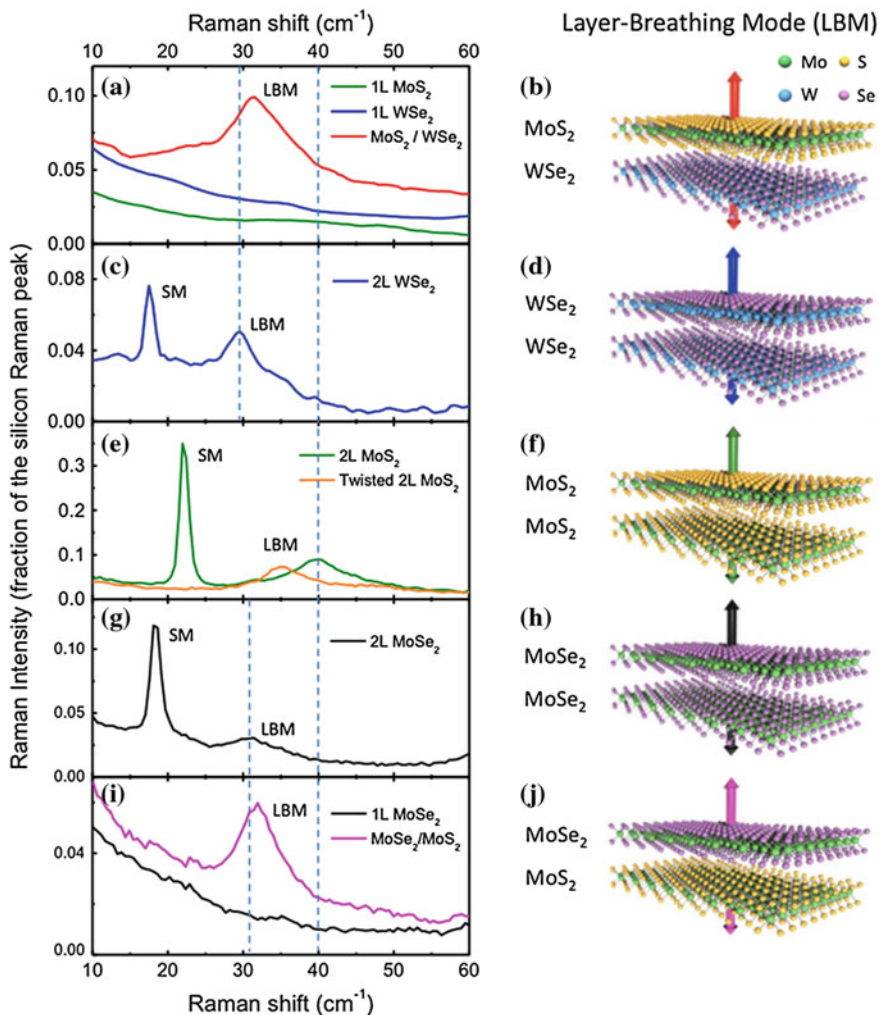


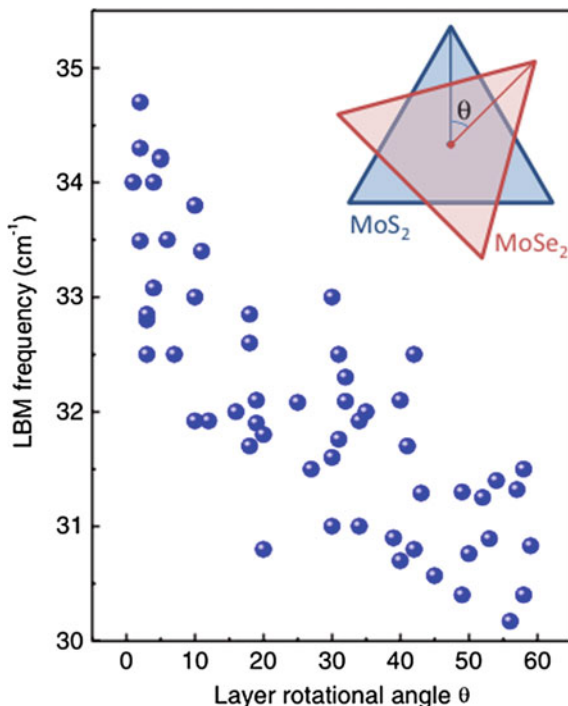
Fig. 7.51 Low-frequency Raman spectra (left column) and schematics of the vibrations (right column). **a** and **b** MoS₂/WSe₂ heterobilayer, and monolayers of MoS₂ and WSe₂; **c** and **d** Bernal-stacked WSe₂ bi-layer; **e** and **f** Bernal-stacked and twisted MoS₂ bi-layer; **g** and **h** Bernal-stacked MoSe₂ bi-layer; and **i** and **j** MoSe₂/MoS₂ heterobilayer and MoSe₂ monolayer [102]. Copyright 2015 by the American Physical Society. Reprinted with permission

It was concluded that in the heterostructure a 0.3% lattice expansion occurred for MoS₂ while graphene was compressed by 0.1%.

Similar analyses were made for other heterostructures, such as MoS₂-mica and MoS₂-WS₂ [100].

In [32], low frequency mode were demonstrated to be an efficient means to determine the stacking configurations (e.g. 2H vs. 3R) [32]. Layer-breathing modes were also shown to be an effective probe in heterostructures [102]. Figure 7.51 shows the

Fig. 7.52 The low-frequency breathing mode of $\text{MoSe}_2/\text{MoS}_2$ heterobilayers as a function of the layer rotational angle (θ). The inset shows the schematic rotational angle between the monolayers [102]. Copyright 2015 by the American Physical Society. Reprinted with permission



Raman response of heterobilayer samples. A pronounced Raman peak emerges at $\sim 32 \text{ cm}^{-1}$ for both $\text{MoS}_2/\text{WSe}_2$ and $\text{MoSe}_2/\text{MoS}_2$ heterobilayers [102], while this feature was not observed in any monolayers, which indicates that it arises from the interaction between the two adjacent TMDC layers. Use of low-frequency modes for identification of polytypism and stacking sequences was also proposed in [103].

The dependence of the observed low frequency mode on the relative orientation of the layers in the heterostructures is shown in Fig. 7.52, where shows the mode frequency of all is presented as a function of the twist angle θ [102], demonstrating the sensitivity of this mode to the layer stacking.

7.11.4 Raman Scattering in 2D Group IVB TMDCs

Raman scattering was also used to characterize monolayers and few-layer flakes of group IVB chalcogenides such as $2H\text{-TaSe}_2$ [104]. $2H\text{-TaSe}_2$ in bulk has a transition from the normal (metallic) phase to the incommensurate charge-density-wave (I-CDW) phase at 123 K, followed by a commensurate charge-density-wave (C-CDW) phase transition at ca. 90 K [105].

Atomically thin layers of TaSe_2 on 300 nm SiO_2/Si substrates were prepared by mechanical exfoliation. Figure 7.53 shows Raman spectra of TaSe_2 samples sup-

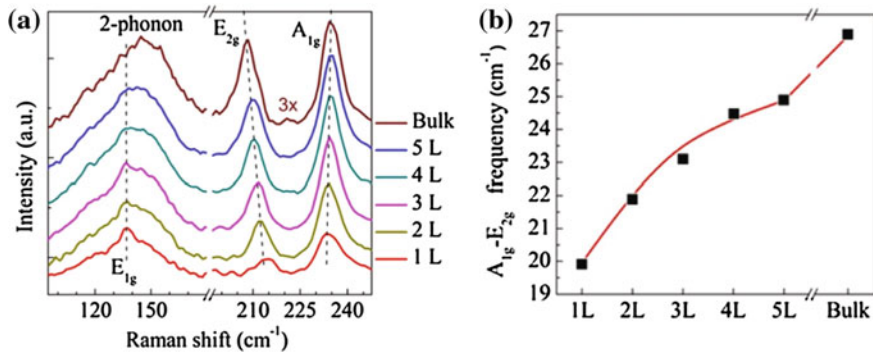


Fig. 7.53 **a** Raman spectra of TaSe₂ samples, ranging from single layer to bulk at room temperature (in a backscattering Raman configuration). As the number of layers decreases, the E_{2g}^1 and the A_{1g} peaks approach each other. The E_{1g} peak is easily observed at 137 cm^{-1} for samples below 4 layers in thickness. **b** Energy difference between the A_{1g} and the E_{2g}^1 modes saturates to the bulk value in an inversely exponential manner. Reproduced from [104]

ported on a 300 nm SiO₂/Si substrate with thicknesses varying from single layer to bulk obtained in a backscattering configuration. There are three prominent Raman features, which are A_{1g} , E_{2g}^1 and two-phonon modes for TaSe₂ samples from single layer to bulk. Moreover, the E_{1g} mode which is usually forbidden in the backscattering Raman configuration was observed in thin (less than 4 layers) TaSe₂ samples. Similar to MoS₂, the energy difference of the A_{1g} and the E_{2g}^1 is the smallest for the single layer, however, increment for this energy difference decreases with increasing layer number.

As mentioned before, bulk 2H-TaSe₂ possesses a CDW phase transition at low temperatures within the liquid nitrogen temperature region [105]. To investigate the CDW-influenced Raman scattering response together with the Raman feature evolution with temperature, the authors performed temperature-dependent Raman measurements on TaSe₂ samples from single layer to bulk. Figure 7.54a shows representative temperature-dependent Raman spectra of a bilayer TaSe₂ sample in the temperature range of 80–300 K. It can be seen that both the A_{1g} and E_{2g}^1 modes blue shift with decreasing temperature. Moreover, in the low temperature measurements, it was noticed that the intensities of the E_{2g}^1 mode and the broad two-phonon peak diminished with decreasing temperature. In contrast, the intensity of the E_{1g} mode, that is forbidden in the bulk, increased with decreasing temperatures.

The results of the temperature-dependent Raman measurements on TaSe₂ samples from single layer to bulk are summarized in Fig. 7.54. It clearly shows that the energies of both the A_{1g} and the E_{2g}^1 modes increase with decreasing temperature (Fig. 7.54c, d). This effect could be also observed through laser heating at different laser powers. Temperature-dependent-shifts in phonon energy are related to anharmonic terms in the lattice potential energy. This shift in one-phonon modes depends on anharmonic coupling of the phonons and the thermal expansion of the crystal. In addition, for

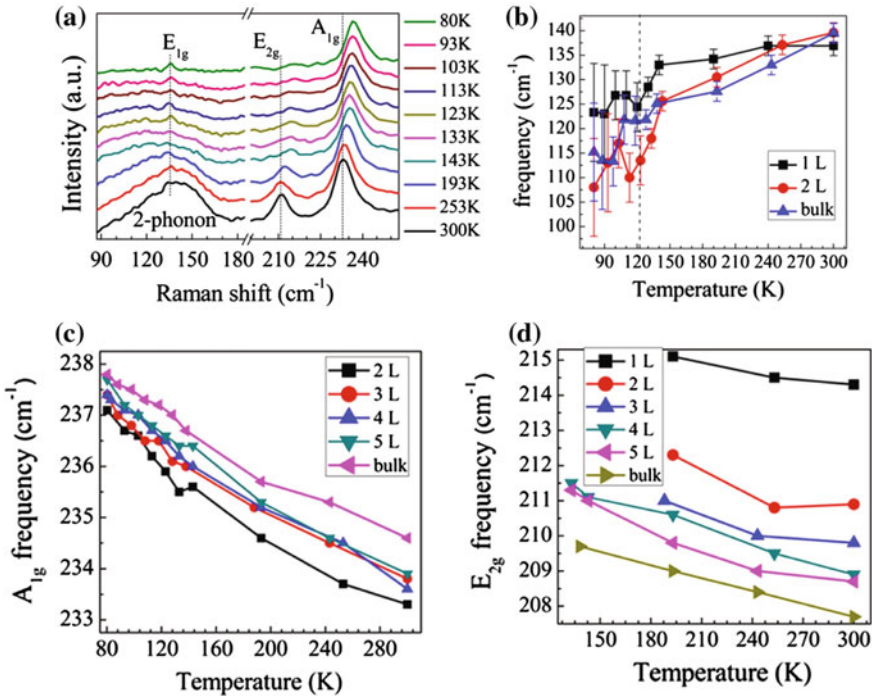


Fig. 7.54 **a** In-situ low temperature micro-Raman spectra of bilayer TaSe_2 sample. **b** Observation of a phase transition through the sudden softening of two-phonon peaks. In bulk samples, upon reaching I-CDW phase transition temperatures, the broad peak due to the two-phonon process broadens, softens in energy and intensity also decreases (*black dashed line* represents the I-CDW phase transition point for bulk at ca. 123 K). This broad peak is fitted by a Lorenz function to obtain the frequency corresponding to the center of the peak (the data below 120 K has a large error due to severely diminished Raman signal). As the temperature approaches the Peierls phase transition point, the two-phonon peak of the single layer and bilayer samples softens similar to the bulk sample. The layer dependent behavior of the A_{1g} (**c**) and the E_{2g}^1 (**d**) modes at low temperatures. Reproduced from [104]

the case of TaSe_2 , the energy of the A_{1g} and the E_{2g}^1 modes is also related to the electronic susceptibility. The CDW phase transition is accompanied by an increase in electronic susceptibility which can be observed through the relatively sudden stiffening of phonons below critical phase transition temperature (ca. 123 K).

The second-order Raman peak is a very unique optical feature of CDW materials like TaSe_2 and carries rich physics. The Kohn anomaly is an anomaly in the dispersion curve of a phonon branch in a metal. As discussed earlier, the second-order broad Raman peak arises from a two-phonon scattering process involving longitudinal acoustic (*LA*) phonons. The *LA* phonons in 2H-TMDC compounds exhibit a Kohn anomaly which results in large two-phonon density of states. The presence of a Kohn anomaly in a *LA* mode is due to Fermi surface nesting and the strong electron-phonon coupling required for a CDW transition [106].

Bulk TaSe₂ has a Peierls phase transition from metallic to the I-CDW phase at ca. 123 K and another transition into C-CDW phase at ca. 90 K. In the C-CDW phase, 2H-TaSe₂ has superlattice with $3a \times 3a \times c$ unit cell and the same hexagonal D_{6h}^4 symmetry. Below 90 K, four new Raman modes appear at energies lower than 85 cm^{-1} in the Raman spectrum which are directly associated with the creation of a CDW superlattice over the underlying crystal lattice [106]. As depicted in Fig. 7.54b, an overall softening of the two-phonon peak can be clearly seen for single, bilayer and bulk TaSe₂. More importantly, a sudden drop of the frequency of this two-phonon mode appeared for all the three samples at ca. 120 K, close to the critical temperature for the phase transition from normal metallic to I-CDW as previously reported [107]. This clearly demonstrates the existence of the I-CDW phase in the atomic thin layers of TaSe₂. Recent theoretical studies suggest that the CDW distortion for TaSe₂ might be stronger in thin layers than in the bulk, however, the critical transition temperature is expected to be similar to the bulk [108].

The commensurate-incommensurate CDW transition in 1T-TaSe₂ thin films using Raman scattering was also studied in [109], where it was found that the transition temperature decreased from 473 to 413 K as the film thickness decreased from 150 to 35 nm. The peak at 154 cm^{-1} observed in the commensurate phase was attributed in this work to zone-folded phonons [109].

7.11.5 TMDC Alloys

Raman scattering was also applied to study few-layer structures of TMDC alloys, such as Mo_{1-x}W_xS₂ [110, 111] and Mo_{1-x}W_xSe₂ [112]. In both works, polarized Raman measurements were used to identify the peak symmetries.

Figure 7.55a, b shows unpolarized Raman spectra of Mo_{1-x}W_xSe₂ monolayers with different W compositions x and the corresponding composition-dependent Raman frequencies. The out-of-plane A_{1g} and in-plane E_{2g}^1 modes showed one-mode and two-mode behaviors, respectively. The A_{1g} mode continuously shifted from 240.1 to 249.3 cm^{-1} when the W composition x increased from 0 to 1, which is close to a linear dependence on the W composition. At the same time, the MoSe₂-like E_{2g}^1 shifted to lower frequency as the W composition increased. In addition, when the W composition x increased, all MoSe₂-like second-order Raman peaks slightly shifted to lower frequencies. WSe₂-like Raman peaks showed different shift directions: WSe₂-like A_{1g} -LA(M) and $2E_{1g}$ modes upshifted, 3LA(M) downshifted, and the E_{2g}^1 -LA(M) mode had almost no shift. Figure 7.55c, d shows Raman spectra and the Raman frequency shift of Mo_{1-x}W_xSe₂ bi-layers with different W composition.

Similar results were obtained for Mo_{1-x}W_xS₂ [110]. In both cases the modified random element isodisplacement (MREI) model was used, based on the assumption of isodisplacement of the same atoms and the random distribution of Mo/W atoms,

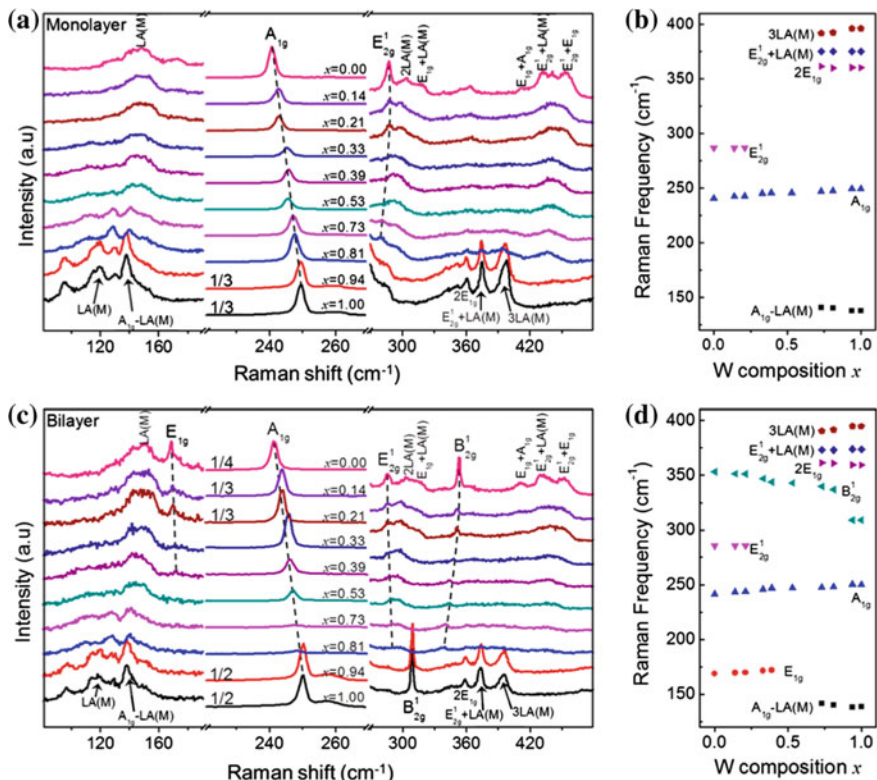


Fig. 7.55 **a** Raman spectra of $\text{Mo}_{1-x}\text{W}_x\text{Se}_2$ monolayers with different W composition x in the range $80\text{--}480\text{ cm}^{-1}$. **b** Composition-dependent Raman frequencies of $\text{Mo}_{1-x}\text{W}_x\text{Se}_2$ monolayer alloys. **c** Raman spectra of $\text{Mo}_{1-x}\text{W}_x\text{Se}_2$ bilayers with different W composition x . **d** Composition-dependent Raman frequencies of $\text{Mo}_{1-x}\text{W}_x\text{Se}_2$ bilayer alloys. All the spectra were calibrated with the 520 cm^{-1} Raman peak from the Si substrate. The *black dashed lines* in (a) and (c), guides for the eye, show the frequency shift of the first-order Raman modes with different W compositions x . For clarity, the intensity of spectra in the range $220\text{--}270\text{ cm}^{-1}$ is magnified by a factor labeled on the corresponding spectra. The excitation laser wavelength was 514.5 nm [112]. Copyright 2014 American Chemical Society. Published with permission

and good agreement with experiment was achieved. An example is shown in Fig. 7.56. The observed trend is similar to the changes in the bulk phase of the same alloys [113].

$\text{MoS}_{2(1-x)}\text{Se}_{2x}$ monolayers were studied in [114]. The authors measured Raman spectra of films of different compositions (Fig. 7.57) using a 352 nm excitation wavelength. The experimental Raman spectra of the $\text{MoS}_{2(1-x)}\text{Se}_{2x}$ monolayer films show two distinct sets of features, with one set related to MoS_2 -like E_{2g} and A_{1g} modes at around 400 cm^{-1} and the other set related to the corresponding MoSe_2 -like features near 240 cm^{-1} . Unlike the band-gap, which varies smoothly with composition, the vibrational behavior of the alloys is more complex than that of the stoichiometric compounds. The spectra represent ‘two-mode behavior’ that occurs when the

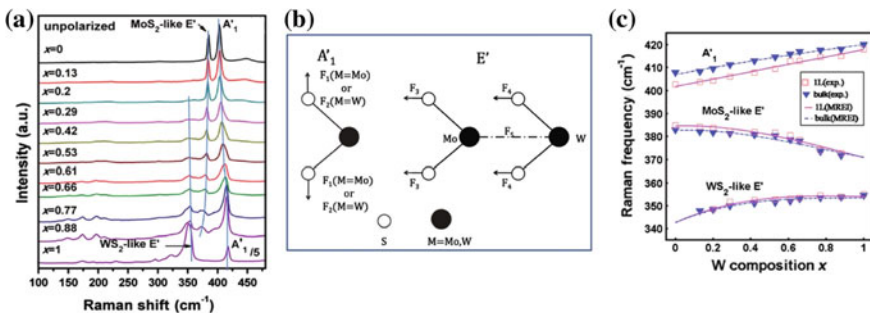


Fig. 7.56 **a** Raman spectra of $\text{Mo}_{0.47}\text{W}_{0.53}\text{S}_2$ monolayers with different W content x . The three solid (blue) lines show frequency shift of E' and A'_1 peaks with W composition x . **b** The schematics of force constants used in MREI model. **c** Composition-dependent Raman frequencies of E' and A'_1 (E_{2g}^1 and A_{1g} for bulk) modes in $\text{Mo}_{1-x}\text{W}_x\text{S}_2$. The solid and dashed lines are the MREI fits of $\text{Mo}_{1-x}\text{W}_x\text{S}_2$ monolayers and bulks, respectively and the scattered square and triangle points are the experimental data of $\text{Mo}_{1-x}\text{W}_x\text{S}_2$ monolayers and bulks [110]. Reproduced by permission of The Royal Society of Chemistry (color figure online)

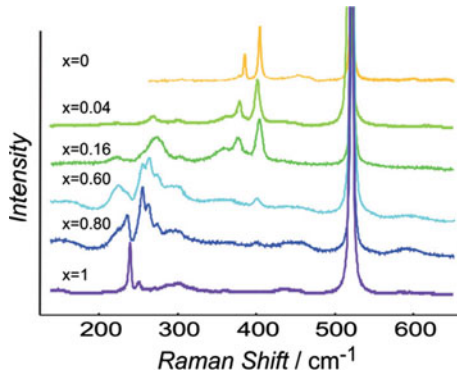


Fig. 7.57 Raman spectra measured for $\text{MoS}_{2(1-x)}\text{Se}_{2x}$ films of different selenium content x . The pronounced feature near 520 cm^{-1} arises from the SiO_2 substrate vibrations. While the peak patterns for the pure materials are simple and sharp, the patterns for alloy films are broader and more complex. The evolution is understood in terms of two-mode behavior [114]. Reproduced with permission from Wiley-VCH Verlag GmbH

frequencies of phonon modes in the pure binary compounds differ sufficiently in frequency from one another [114]. This is opposed to the case of $\text{Mo}_{(1-x)}\text{W}_x\text{S}_2$ alloys, for which the corresponding difference is less than 50 cm^{-1} , and one observes ‘one-mode behavior’ with a continuous shift of phonon frequencies with composition.

References

1. G. Lucovsky, R. White, J. Benda, J. Revelli, Infrared-reflectance spectra of layered group-IV and group-VI transition-metal dichalcogenides. *Phys. Rev. B* **7**(8), 3859 (1973)
2. Y. Zhao, X. Luo, H. Li, J. Zhang, P.T. Araujo, C.K. Gan, J. Wu, H. Zhang, S.Y. Quek, M.S. Dresselhaus et al., Interlayer breathing and shear modes in few-trilayer MoS₂ and WSe₂. *Nano Lett.* **13**(3), 1007 (2013)
3. J. Ribeiro-Soares, R. Almeida, E. Barros, P. Araujo, M. Dresselhaus, L. Cançado, A. Jorio, Group theory analysis of phonons in two-dimensional transition metal dichalcogenides. *Phys. Rev. B* **90**(11), 115438 (2014)
4. X. Luo, Y. Zhao, J. Zhang, M. Toh, C. Kloc, Q. Xiong, S.Y. Quek, Effects of lower symmetry and dimensionality on Raman spectra in two-dimensional WSe₂. *Phys. Rev. B* **88**(19), 195313 (2013)
5. X. Zhang, W. Han, J. Wu, S. Milana, Y. Lu, Q. Li, A. Ferrari, P. Tan, Raman spectroscopy of shear and layer breathing modes in multilayer MoS₂. *Phys. Rev. B* **87**(11), 115413 (2013)
6. M. Yamamoto, S.T. Wang, M. Ni, Y.F. Lin, S.L. Li, S. Aikawa, W.B. Jian, K. Ueno, K. Wakabayashi, K. Tsukagoshi, Strong enhancement of Raman scattering from a bulk-inactive vibrational mode in few-layer MoTe₂. *ACS Nano* **8**(4), 3895 (2014)
7. N. Scheuschner, R. Gillen, M. Staiger, J. Maultzsch, Interlayer resonant Raman modes in few-layer MoS₂. *Phys. Rev. B* **91**(23), 235409 (2015)
8. C. Lee, H. Yan, L.E. Brus, T.F. Heinz, J. Hone, S. Ryu, Anomalous lattice vibrations of single-and few-layer MoS₂. *ACS Nano* **4**(5), 2695 (2010)
9. P. Bertrand, Surface-phonon dispersion of MoS₂. *Phys. Rev. B* **44**(11), 5745 (1991)
10. T. Wieting, J. Verble, Interlayer bonding and the lattice vibrations of β -GaSe. *Phys. Rev. B* **5**(4), 1473 (1972)
11. Y. Cheng, Z. Zhu, U. Schwingenschlögl, Role of interlayer coupling in ultra thin MoS₂. *RSC Adv.* **2**(20), 7798 (2012)
12. A. Bagnall, W. Liang, E. Marseglia, B. Welber, Raman studies of MoS₂ at high pressure. *Phys. B+C* **99**(1), 343 (1980)
13. S. Tongay, J. Zhou, C. Ataca, K. Lo, T.S. Matthews, J. Li, J.C. Grossman, J. Wu, Thermally driven crossover from indirect toward direct bandgap in 2D semiconductors: MoSe₂ versus MoS₂. *Nano Lett.* **12**(11), 5576 (2012)
14. P. Tonndorf, R. Schmidt, P. Böttger, X. Zhang, J. Börner, A. Liebig, M. Albrecht, C. Kloc, O. Gordan, D.R. Zahn et al., Photoluminescence emission and Raman response of monolayer MoS₂, MoSe₂, and WSe₂. *Opt. Express* **21**(4), 4908 (2013)
15. H.R. Gutiérrez, N. Perea-López, A.L. Elfas, A. Berkdemir, B. Wang, R. Lv, F. López-Urías, V.H. Crespi, H. Terrones, M. Terrones, Extraordinary room-temperature photoluminescence in triangular WS₂ monolayers. *Nano Lett.* **13**(8), 3447 (2012)
16. H. Li, G. Lu, Y. Wang, Z. Yin, C. Cong, Q. He, L. Wang, F. Ding, T. Yu, H. Zhang, Mechanical exfoliation and characterization of single-and few-layer nanosheets of WSe₂, TaS₂, and TaSe₂. *Small* **9**(11), 1974 (2013)
17. W. Zhao, Z. Ghorannevis, K.K. Amara, J.R. Pang, M. Toh, X. Zhang, C. Kloc, P.H. Tan, G. Eda, Lattice dynamics in mono- and few-layer sheets of WS₂ and WSe₂. *Nanoscale* **5**(20), 9677 (2013)
18. A. Molina-Sánchez, L. Wirtz, Phonons in single-layer and few-layer MoS₂ and WS₂. *Phys. Rev. B* **84**(15), 155413 (2011)
19. X. Luo, Y. Zhao, J. Zhang, Q. Xiong, S.Y. Quek, Anomalous frequency trends in MoS₂ thin films attributed to surface effects. *Phys. Rev. B* **88**(7), 075320 (2013)
20. C. Ataca, M. Topsakal, E. Akturk, S. Ciraci, A comparative study of lattice dynamics of three- and two-dimensional MoS₂. *J. Phys. Chem. C* **115**(33), 16354 (2011)
21. H. Sahin, S. Tongay, S. Horzum, W. Fan, J. Zhou, J. Li, J. Wu, F. Peeters, Anomalous Raman spectra and thickness-dependent electronic properties of WSe₂. *Phys. Rev. B* **87**(16), 165409 (2013)

22. R. Zallen, M. Slade, A. Ward, Lattice vibrations and interlayer interactions in crystalline As_2S_3 and As_2Se_3 . *Phys. Rev. B* **3**(12), 4257 (1971)
23. A.S. Davydov, Theory of absorption spectra of molecular crystals. *Zh. Exper. Teor. Fiz.* **18**, 210 (1948)
24. T. Wieting, J. Verble, Infrared and Raman studies of long-wavelength optical phonons in hexagonal MoS_2 . *Phys. Rev. B* **3**(12), 4286 (1971)
25. J. Verble, T. Wieting, Lattice mode degeneracy in MoS_2 and other layer compounds. *Phys. Rev. Lett.* **25**(6), 362 (1970)
26. P.N. Ghosh, C. Maiti, Interlayer force and Davydov splitting in 2H- MoS_2 . *Phys. Rev. B* **28**(4), 2237 (1983)
27. N. Wakabayashi, H.G. Smith, R.M. Nicklow, Lattice dynamics of hexagonal MoS_2 studied by neutron scattering. *Phys. Rev. B* **12**(2), 659 (1975)
28. G. Froehlicher, E. Lorchat, F. Fernique, C. Joshi, A. Molina-Sánchez, L. Wirtz, S. Berciaud, Unified description of the optical phonon modes in N-layer MoTe_2 . *Nano Lett.* **15**(10), 6481 (2015)
29. G. Plechinger, S. Heydrich, J. Eroms, D. Weiss, C. Schüller, T. Korn, Raman spectroscopy of the interlayer shear mode in few-layer MoS_2 flakes. *Appl. Phys. Lett.* **101**(10), 101906 (2012)
30. H. Zeng, B. Zhu, K. Liu, J. Fan, X. Cui, Q. Zhang, Low-frequency Raman modes and electronic excitations in atomically thin MoS_2 films. *Phys. Rev. B* **86**(24), 241301 (2012)
31. A. Bera, A.K. Sood, Insights into vibrational and electronic properties of MoS_2 using Raman, photoluminescence and transport studies, in *MoS_2 : Materials, Physics, and Devices*, ed. by Z.M. Wang (Springer Science & Business Media, Berlin, 2014), pp. 155–215
32. A.A. Puretzky, L. Liang, X. Li, K. Xiao, K. Wang, M. Mahjouri-Samani, L. Basile, J.C. Idrobo, B.G. Sumpter, V. Meunier et al., Low-frequency Raman fingerprints of two-dimensional metal dichalcogenide layer stacking configurations. *ACS Nano* **9**(6), 6333 (2015)
33. H. Terrones, E. Del Corro, S. Feng, J.M. Poumirol, D. Rhodes, D. Smirnov, N. Pradhan, Z. Lin, M. Nguyen, A. Elias et al., New first order Raman-active modes in few layered transition metal dichalcogenides. *Sci. Rep.* **4** (2014). doi:[10.1038/srep04215](https://doi.org/10.1038/srep04215)
34. B. Chakraborty, H. Matte, A. Sood, C. Rao, Layer-dependent resonant Raman scattering of a few layer MoS_2 . *J. Raman Spectrosc.* **44**(1), 92 (2013)
35. C. Ruppert, O.B. Aslan, T.F. Heinz, Optical properties and band gap of single- and few-layer MoTe_2 crystals. *Nano Lett.* **14**(11), 6231 (2014)
36. A. Molina-Sánchez, D. Sangalli, K. Hummer, A. Marini, L. Wirtz, Effect of spin-orbit interaction on the optical spectra of single-layer, double-layer, and bulk MoS_2 . *Phys. Rev. B* **88**(4), 045412 (2013)
37. J.A. Schuller, S. Karaveli, T. Schiros, K. He, S. Yang, I. Kymissis, J. Shan, R. Zia, Orientation of luminescent excitons in layered nanomaterials. *Nat. Nanotech.* **8**(4), 271 (2013)
38. A.J. Bradley, M.M. Ugeda, F.H. da Jornada, D.Y. Qiu, W. Ruan, Y. Zhang, S. Wickenburg, A. Riss, J. Lu, S.K. Mo et al., Probing the role of interlayer coupling and Coulomb interactions on electronic structure in few-layer MoSe_2 nanostructures. *Nano Lett.* **15**(4), 2594 (2015)
39. K.P. Dhakal, D.L. Duong, J. Lee, H. Nam, M. Kim, M. Kan, Y.H. Lee, J. Kim, Confocal absorption spectral imaging of MoS_2 : optical transitions depending on the atomic thickness of intrinsic and chemically doped MoS_2 . *Nanoscale* **6**(21), 13028 (2014)
40. M. Staiger, R. Gillen, N. Scheuschner, O. Ochedowski, F. Kampmann, M. Schleberger, C. Thomsen, J. Maultzsch, Splitting of monolayer out-of-plane A'_1 Raman mode in few-layer WS_2 . *Phys. Rev. B* **91**(19), 195419 (2015)
41. S. Najmaei, Z. Liu, P. Ajayan, J. Lou, Thermal effects on the characteristic Raman spectrum of molybdenum disulfide (MoS_2) of varying thicknesses. *Appl. Phys. Lett.* **100**(1), 013106 (2012)
42. S. Sahoo, A.P. Gaur, M. Ahmadi, M.J.F. Guinel, R.S. Katiyar, Temperature-dependent Raman studies and thermal conductivity of few-layer MoS_2 . *J. Phys. Chem. C* **117**(17), 9042 (2013)
43. R. Yan, J.R. Simpson, S. Bertolazzi, J. Brivio, M. Watson, X. Wu, A. Kis, T. Luo, A.R. Hight Walker, H.G. Xing, Thermal conductivity of monolayer molybdenum disulfide obtained from temperature-dependent Raman spectroscopy. *ACS Nano* **8**(1), 986 (2014)

44. A. Taube, J. Judek, C. Jastrzebski, A. Duzynska, K. Switkowski, M. Zdrojek, Temperature-dependent nonlinear phonon shifts in a supported MoS₂ monolayer. *ACS Appl. Mater. Interface* **6**(12), 8959 (2014)
45. M. Thripuranthaka, R.V. Kashid, C.S. Rout, D.J. Late, Temperature dependent Raman spectroscopy of chemically derived few layer MoS₂ and WS₂ nanosheets. *Appl. Phys. Lett.* **104**(8), 081911 (2014)
46. N.A. Lanzillo, A.G. Birdwell, M. Amani, F.J. Crowne, P.B. Shah, S. Najmaei, Z. Liu, P.M. Ajayan, J. Lou, M. Dubey et al., Temperature-dependent phonon shifts in monolayer MoS₂. *Appl. Phys. Lett.* **103**(9), 093102 (2013)
47. L. Su, Y. Zhang, Y. Yu, L. Cao, Dependence of coupling of quasi 2D MoS₂ with substrates on substrate types, probed by temperature dependent Raman scattering. *Nanoscale* **6**(9), 4920 (2014)
48. S. Najmaei, P.M. Ajayan, J. Lou, Quantitative analysis of the temperature dependency in Raman active vibrational modes of molybdenum disulfide atomic layers. *Nanoscale* **5**(20), 9758 (2013)
49. J. Wilson, A. Yoffe, The transition metal dichalcogenides discussion and interpretation of the observed optical, electrical and structural properties. *Adv. Phys.* **18**(73), 193 (1969)
50. T. Livneh, E. Sterer, Resonant Raman scattering at exciton states tuned by pressure and temperature in 2H-MoS₂. *Phys. Rev. B* **81**(19), 195209 (2010)
51. D.J. Late, S.N. Shirodkar, U.V. Waghmare, V.P. Dravid, C. Rao, Thermal expansion, anharmonicity and temperature-dependent Raman spectra of single- and few-layer MoSe₂ and WSe₂. *ChemPhysChem* **15**(8), 1592 (2014)
52. D.J. Late, Temperature dependent phonon shifts in single-layer WS₂. *ACS Appl. Mater. Interfaces* **6**(2), 1158 (2014)
53. N. Peimyoo, J. Shang, W. Yang, Y. Wang, C. Cong, T. Yu, Thermal conductivity determination of suspended mono- and bilayer WS₂ by Raman spectroscopy. *Nano Res.* **8**(4), 1210 (2015)
54. X. Zhang, D. Sun, Y. Li, G.H. Lee, Xu Cui, D. Chenet, Y. You, T. Heinz, J. Hone, Measurement of lateral and interfacial thermal conductivity of single- and bi-layer MoS₂ and MoSe₂ using refined optothermal Raman technique. *ACS Appl. Mater. Interfaces* **7**, 25923 (2015)
55. B. Miller, E. Parzinger, A. Vernickel, A.W. Holleitner, U. Wurstbauer, Photogating of mono- and few-layer MoS₂. *Appl. Phys. Lett.* **106**(12), 122103 (2015)
56. B. Chakraborty, A. Bera, D. Muthu, S. Bhowmick, U. Waghmare, A. Sood, Symmetry-dependent phonon renormalization in monolayer MoS₂ transistor. *Phys. Rev. B* **85**(16), 161403 (2012)
57. S. Tongay, J. Zhou, C. Ataca, J. Liu, J.S. Kang, T.S. Matthews, L. You, J. Li, J.C. Grossman, J. Wu, Broad-range modulation of light emission in two-dimensional semiconductors by molecular physisorption gating. *Nano Lett.* **13**(6), 2831 (2013)
58. H. Nan, Z. Wang, W. Wang, Z. Liang, Y. Lu, Q. Chen, D. He, P. Tan, F. Miao, X. Wang et al., Strong photoluminescence enhancement of MoS₂ through defect engineering and oxygen bonding. *ACS Nano* **8**(6), 5738 (2014)
59. M. Buscema, G.A. Steele, H.S. van der Zant, A. Castellanos-Gomez, The effect of the substrate on the Raman and photoluminescence emission of single-layer MoS₂. *Nano Res.* **7**(4), 561 (2014)
60. E. Scalise, M. Houssa, G. Pourtois, V. Afanas, A. Stesmans et al., First-principles study of strained 2D MoS₂. *Phys. E* **56**, 416 (2014)
61. S.B. Desai, G. Seol, J.S. Kang, H. Fang, C. Battaglia, R. Kapadia, J.W. Ager, J. Guo, A. Javey, Strain-induced indirect to direct bandgap transition in multilayer WSe₂. *Nano Lett.* **14**(8), 4592 (2014)
62. H.J. Conley, B. Wang, J.I. Ziegler, R.F. Haglund Jr., S.T. Pantelides, K.I. Bolotin, Bandgap engineering of strained monolayer and bilayer MoS₂. *Nano Lett.* **13**(8), 3626 (2013)
63. Y. Wang, C. Cong, C. Qiu, T. Yu, Raman spectroscopy study of lattice vibration and crystallographic orientation of monolayer MoS₂ under uniaxial strain. *Small* **9**(17), 2857 (2013)
64. C. Rice, R. Young, R. Zan, U. Bangert, D. Wolverson, T. Georgiou, R. Jalil, K. Novoselov, Raman-scattering measurements and first-principles calculations of strain-induced phonon shifts in monolayer MoS₂. *Phys. Rev. B* **87**(8), 081307 (2013)

65. K. Zhang, S. Hu, Y. Zhang, T. Zhang, X. Zhou, Y. Sun, T. Li, H.J. Fan, G. Shen, X. Chen et al., Self-induced uniaxial strain in MoS₂ monolayers with local van der Waals-stacked interlayer interactions. *ACS Nano* **9**(3), 2704 (2015)
66. Y. Sun, K. Liu, X. Hong, M. Chen, J. Kim, S. Shi, J. Wu, A. Zettl, F. Wang, Probing local strain at MX₂-metal boundaries with surface plasmon-enhanced Raman scattering. *Nano Lett.* **14**(9), 5329 (2014)
67. A.P. Nayak, T. Pandey, D. Voiry, J. Liu, S.T. Moran, A. Sharma, C. Tan, C.H. Chen, L.J. Lee, M. Chhowalla et al., Pressure-dependent optical and vibrational properties of monolayer molybdenum disulfide. *Nano Lett.* **15**(1), 346 (2015)
68. F. Li, Y. Yan, B. Han, L. Li, X. Huang, M. Yao, Y. Gong, X. Jin, B. Liu, C. Zhu et al., Pressure confinement effect in MoS₂ monolayers. *Nanoscale* **7**(19), 9075 (2015)
69. K. Liu, L. Zhang, T. Cao, C. Jin, D. Qiu, Q. Zhou, A. Zettl, P. Yang, S.G. Louie, F. Wang, Evolution of interlayer coupling in twisted molybdenum disulfide bilayers. *Nat. Commun.* **5** (2014). doi:[10.1038/ncomms5966](https://doi.org/10.1038/ncomms5966)
70. A.M. van der Zande, J. Kunstmann, A. Chernikov, D.A. Chenet, Y. You, X. Zhang, P.Y. Huang, T.C. Berkelsbach, L. Wang, F. Zhang et al., Tailoring the electronic structure in bilayer molybdenum disulfide via interlayer twist. *Nano Lett.* **14**(7), 3869 (2014)
71. A. Castellanos-Gomez, H.S. van der Zant, G.A. Steele, Folded MoS₂ layers with reduced interlayer coupling. *Nano Res.* **7**(4), 572 (2014)
72. S.Y. Chen, C. Zheng, M.S. Fuhrer, J. Yan, Helicity-resolved Raman scattering of MoS₂, MoSe₂, WS₂, and WSe₂ atomic layers. *Nano Lett.* **15**(4), 2526 (2015)
73. A. Berkdemir, H.R. Gutiérrez, A.R. Botello-Méndez, N. Perea-López, A.L. Elías, C.I. Chia, B. Wang, V.H. Crespi, F. López-Urías, J.C. Charlier et al., Identification of individual and few layers of WS₂ using Raman spectroscopy. *Sci. Rep.* **3** (2013). doi:[10.1038/srep01755](https://doi.org/10.1038/srep01755)
74. G. Kioseoglou, A. Hanbicki, M. Currie, A. Friedman, D. Gunlycke, B. Jonker, Valley polarization and intervalley scattering in monolayer MoS₂. *Appl. Phys. Lett.* **101**(22), 221907 (2012)
75. J. Chen, C. Wang, Second order Raman spectrum of MoS₂. *Solid State Commun.* **14**(9), 857 (1974)
76. G.L. Frey, R. Tenne, M.J. Matthews, M. Dresselhaus, G. Dresselhaus, Raman and resonance Raman investigation of MoS₂ nanoparticles. *Phys. Rev. B* **60**(4), 2883 (1999)
77. C. Sourisseau, F. Cruege, M. Fouassier, M. Alba, Second-order Raman effects, inelastic neutron scattering and lattice dynamics in 2H-WS₂. *Chem. Phys.* **150**(2), 281 (1991)
78. H. Li, Q. Zhang, C.C.R. Yap, B.K. Tay, T.H.T. Edwin, A. Olivier, D. Baillargeat, From bulk to monolayer MoS₂: evolution of Raman scattering. *Adv. Funct. Mater.* **22**(7), 1385 (2012)
79. J.H. Fan, P. Gao, A.M. Zhang, B.R. Zhu, H.L. Zeng, X.D. Cui, R. He, Q.M. Zhang, Resonance Raman scattering in bulk 2H-MX₂ (M= Mo, W; X= S, Se) and monolayer MoS₂. *J. Appl. Phys.* **115**(5), 053527 (2014)
80. K. Gołas, M. Grzeszczyk, R. Bożek, P. Leszczyński, A. Wysmołek, M. Potemski, A. Babiński, Resonant Raman scattering in MoS₂: from bulk to monolayer. *Solid State Commun.* **197**, 53 (2014)
81. J.U. Lee, J. Park, Y.W. Son, H. Cheong, Anomalous excitonic resonance Raman effects in few-layer MoS₂. *Nanoscale* **7**(7), 3229 (2015)
82. J.G. Song, J. Park, W. Lee, T. Choi, H. Jung, C.W. Lee, S.H. Hwang, J.M. Myoung, J.H. Jung, S.H. Kim et al., Layer-controlled, wafer-scale, and conformal synthesis of tungsten disulfide nanosheets using atomic layer deposition. *ACS Nano* **7**(12), 11333 (2013)
83. K. Gołas, M. Grzeszczyk, P. Leszczyński, C. Faugeras, A. Nicolet, A. Wysmołek, M. Potemski, A. Babiński, Multiphonon resonant Raman scattering in MoS₂. *Appl. Phys. Lett.* **104**(9), 092106 (2014)
84. N. Scheuschner, O. Ochedowski, M. Schleberger, J. Maultzsch, Resonant Raman profiles and μ -photoluminescence of atomically thin layers of molybdenum disulfide. *Phys. Stat. Sol. B* **249**(12), 2644 (2012)
85. B.R. Carvalho, L.M. Malard, J.M. Alves, C. Fantini, M.A. Pimenta, Symmetry-dependent exciton-phonon coupling in 2D and bulk MoS₂ observed by resonance Raman scattering. *Phys. Rev. Lett.* **114**(13), 136403 (2015)

86. A. Mitioglu, P. Plochocka, G. Deligeorgis, S. Anghel, L. Kulyuk, D. Maude, Second-order resonant Raman scattering in single-layer tungsten disulfide WS₂. *Phys. Rev. B* **89**(24), 245442 (2014)
87. E. del Corro, H. Terrones, A. Elias, C. Fantini, S. Feng, M.A. Nguyen, T.E. Mallouk, M. Terrones, M.A. Pimenta, Excited excitonic states in 1L, 2L, 3L, and bulk WSe₂ observed by resonant Raman spectroscopy. *ACS Nano* **8**(9), 9629 (2014)
88. W. Zhao, Z. Ghorannevis, L. Chu, M. Toh, C. Kloc, P.H. Tan, G. Eda, Evolution of electronic structure in atomically thin sheets of WS₂ and WSe₂. *ACS Nano* **7**(1), 791 (2012)
89. S.L. Li, H. Miyazaki, H. Song, H. Kuramochi, S. Nakaharai, K. Tsukagoshi, Quantitative Raman spectrum and reliable thickness identification for atomic layers on insulating substrates. *ACS Nano* **6**(8), 7381 (2012)
90. S. Tongay, H. Sahin, C. Ko, A. Luce, W. Fan, K. Liu, J. Zhou, Y.S. Huang, C.H. Ho, J. Yan et al., Monolayer behaviour in bulk ReS₂ due to electronic and vibrational decoupling. *Nat. Commun.* **5** (2014). doi:[10.1038/ncomms4252](https://doi.org/10.1038/ncomms4252)
91. D. Wolverson, S. Crampin, A.S. Kazemi, A. Ilie, S.J. Bending, Raman spectra of monolayer, few-layer, and bulk ReSe₂: an anisotropic layered semiconductor. *ACS Nano* **8**(11), 11154 (2014)
92. A. Castellanos-Gomez, E. Navarro-Moratalla, G. Mokry, J. Quereda, E. Pinilla-Cienfuegos, N. Agrait, H.S. van der Zant, E. Coronado, G.A. Steele, G. Rubio-Bollinger, Fast and reliable identification of atomically thin layers of TaSe₂ crystals. *Nano Res.* **6**(3), 191 (2013)
93. T. Hu, R. Li, J. Dong, A new (2 x 1) dimerized structure of monolayer 1T-molybdenum disulfide, studied from first principles calculations. *J. Chem. Phys.* **139**(17), 174702 (2013)
94. S.J. Sandoval, D. Yang, R. Frindt, J. Irwin, Raman study and lattice dynamics of single molecular layers of MoS₂. *Phys. Rev. B* **44**(8), 3955 (1991)
95. M. Kan, H.G. Nam, Y.H. Lee, Q. Sun, Phase stability and Raman vibration of the molybdenum ditelluride (MoTe₂) monolayer. *Phys. Chem. Chem. Phys.* **17**(22), 14866 (2015)
96. C.H. Lee, E.C. Silva, L. Calderin, M.A.T. Nguyen, M.J. Hollander, B. Bersch, T.E. Mallouk, J.A. Robinson, Tungsten ditelluride: a layered semimetal. *Sci. Rep.* **5** (2015). doi:[10.1038/srep10013](https://doi.org/10.1038/srep10013)
97. Y. Feng, W. Zhou, Y. Wang, J. Zhou, E. Liu, Y. Fu, Z. Ni, X. Wu, H. Yuan, F. Miao et al., Raman vibrational spectra of bulk to monolayer ReS₂ with lower symmetry. *Phys. Rev. B* **92**, 054110 (2015)
98. H. Rydberg, M. Dion, N. Jacobson, E. Schröder, P. Hyldgaard, S. Simak, D.C. Langreth, B.I. Lundqvist, Van der Waals density functional for layered structures. *Phys. Rev. Lett.* **91**(12), 126402 (2003)
99. E. Kadantsev, Electronic structure of exfoliated MoS₂, in *MoS₂: Materials, Physics, and Devices*, ed. by Z.M. Wang (Springer Science & Business Media, Berlin, 2014), pp. 37–51
100. K.G. Zhou, F. Withers, Y. Cao, S. Hu, G. Yu, C. Casiraghi, Raman modes of MoS₂ used as fingerprint of van der Waals interactions in 2-D crystal-based heterostructures. *ACS Nano* **8**(10), 9914 (2014)
101. M.H. Chiu, M.Y. Li, W. Zhang, W.T. Hsu, W.H. Chang, M. Terrones, H. Terrones, L.J. Li, Spectroscopic signatures for interlayer coupling in MoS₂-WSe₂ van der Waals stacking. *ACS Nano* **8**(9), 9649 (2014)
102. C.H. Lui, Z. Ye, C. Ji, K.C. Chiu, C.T. Chou, T.I. Andersen, C. Means-Shively, H. Anderson, J.M. Wu, T. Kidd et al., Observation of interlayer phonon modes in van der Waals heterostructures. *Phys. Rev. B* **91**(16), 165403 (2015)
103. X. Lu, M. Utama, J. Lin, X. Luo, Y. Zhao, J. Zhang, S.T. Pantelides, W. Zhou, S.Y. Quek, Q. Xiong, Rapid and nondestructive identification of polytypism and stacking sequences in few-layer molybdenum diselenide by raman spectroscopy. *Adv. Mater.* **27**(30), 4502 (2015)
104. P. Hajiyev, C. Cong, C. Qiu, T. Yu, Contrast and Raman spectroscopy study of single- and few-layered charge density wave material: 2H-TaSe₂. *Sci. Rep.* **3** (2013). doi:[10.1038/srep02593](https://doi.org/10.1038/srep02593)
105. S. Sugai, K. Murase, Generalized electronic susceptibility and charge-density waves in 2H-TaSe₂ by Raman scattering. *Phys. Rev. B* **25**(4), 2418 (1982)

106. D.E. Moncton, J.D. Axe, F.J. DiSalvo, Study of superlattice formation in 2H-NbSe₂ and 2H-TaSe₂ by neutron scattering. *Phys. Rev. Lett.* **34**(12), 734 (1975)
107. H. Myron, J. Rath, A. Freeman, Generalized electronic susceptibility and charge-density waves in 1T-TaS₂ and 1T-TaSe₂. *Phys. Rev. B* **15**(2), 885 (1977)
108. Y. Ge, A.Y. Liu, Effect of dimensionality and spin-orbit coupling on charge-density-wave transition in 2H-TaSe₂. *Phys. Rev. B* **86**(10), 104101 (2012)
109. R. Samnakay, D. Wickramaratne, T. Pope, R.K. Lake, T.T. Salguero, A.A. Balandin, The zone-folded phonons and the commensurate-incommensurate charge-density-wave transition in 1T-TaSe₂ thin films. *Nano Lett.* **15**(5), 2965 (2015)
110. Y. Chen, D.O. Dumcenco, Y. Zhu, X. Zhang, N. Mao, Q. Feng, M. Zhang, J. Zhang, P.H. Tan, Y.S. Huang et al., Composition-dependent Raman modes of Mo_{1-x}W_xS₂ monolayer alloys. *Nanoscale* **6**(5), 2833 (2014)
111. L. Liang, V. Meunier, First-principles Raman spectra of MoS₂, WS₂ and their heterostructures. *Nanoscale* **6**(10), 5394 (2014)
112. M. Zhang, J. Wu, Y. Zhu, D.O. Dumcenco, J. Hong, N. Mao, S. Deng, Y. Chen, Y. Yang, C. Jin et al., Two-dimensional molybdenum tungsten diselenide alloys: photoluminescence, Raman scattering, and electrical transport. *ACS Nano* **8**(7), 7130 (2014)
113. D. Dumcenco, K. Chen, Y. Wang, Y. Huang, K. Tiong, Raman study of 2H-Mo_{1-x}W_xS₂ layered mixed crystals. *J. Alloys Compd.* **506**(2), 940 (2010)
114. J. Mann, Q. Ma, P.M. Odenthal, M. Isarraraz, D. Le, E. Preciado, D. Barroso, K. Yamaguchi, G. von Son Palacio, A. Nguyen et al., 2-dimensional transition metal dichalcogenides with tunable direct band gaps: MoS_{2(1-x)}Se_{2x} monolayers. *Adv. Mater.* **26**(9), 1399 (2014)

Chapter 8

Luminescence of 2D TMDC

The direct-indirect gap transition accompanying thickness change has a strong effect on luminescence. The present chapter covers various aspects of luminescence such as strain and electrical gating effects but excludes spin-valley coupling (which is the subject of a dedicated chapter). Of special interest is the observation of single photon emission from monolayers.

In this chapter we concentrate on the general features of photoluminescence (PL) in 2D TMDC. Various other aspects of PL are also described in Chap. 9, which is dedicated to excitons.

8.1 Intrinsic PL from Monolayers Versus Few-Layer Structures

8.1.1 *Effect of the Number of Layers*

As discussed in Chap. 6, a decrease in the number of layers leads to an indirect-direct gap transformation and results in a pronounced change in the PL signal [1–3]. An important point to notice is the drastic increase in the PL intensity as the thickness is decreased to a single layer associated with the formation of a direct gap. This is illustrated in Fig. 8.1 (upper panel) for mechanically exfoliated MoS₂ and MoTe₂. Concomitantly, the peak position shifts to higher energies [Fig. 8.1 (lower panel)].¹

¹Conflicting results for MoTe₂ were obtained in [4], where low-temperature measurements were performed and it was found that the PL yield was identical for mono and bilayer samples, decreased slightly for trilayer, and was significantly lower in the tetralayer, from which it was concluded that both mono and bilayer MoTe₂ are direct band gap semiconductors with tetralayer MoTe₂ being an indirect gap semiconductor and with trilayers having nearly identical direct and indirect gaps. This discrepancy was interpreted in terms of a small differences in the size of the indirect and direct

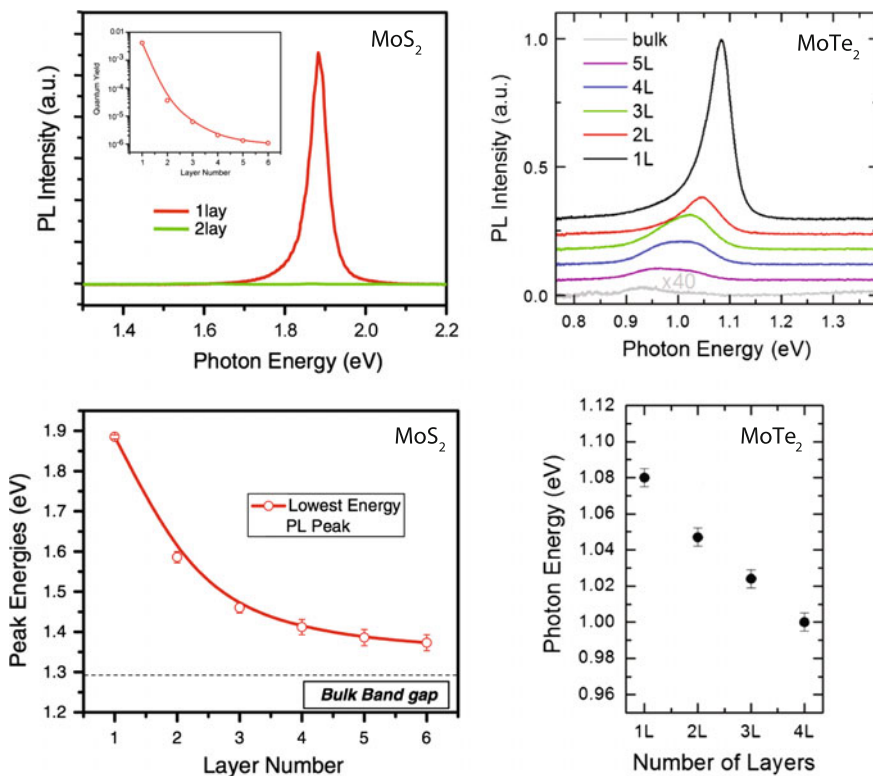


Fig. 8.1 PL intensity dependence (*upper panel*) and PL energies (*lower panel*) for different thicknesses of MoS_2 [1] (Copyright 2010 by the American Physical Society. Reprinted with permission) and MoTe_2 [3] (Copyright 2014 American Chemical Society. Published with permission)

Qualitatively similar results were also obtained for WS_2 and WSe_2 (Fig. 8.2), where the emission from monolayers were found to be 100–1000 times stronger than from the bulk materials [5] with the difference being smaller for WSe_2 . At the same time, while the change between the bulk sample and the monolayers was more modest than that observed for MoS_2 , the absolute emission intensity of the WS_2 and WSe_2 monolayers was 20–40 times higher than that of monolayer MoS_2 exfoliated from a natural crystal. The much stronger PL intensity in WS_2 compared to MoS_2 was also reported in [6].

While this difference in intensity may be determined by the material composition it may also arise due to various intrinsic and extrinsic factors. For example, in annealed chemically exfoliated (using Li intercalation) MoS_2 single layers [7], the observed PL was in good agreement with the results for mechanically exfoliated samples [1]. At the same time, the PL intensity gradually decreased with increasing film thickness,

(Footnote 1 continued)

gaps in layers of different thickness, comparable to kT at room temperature, which can account for different results at different temperatures.

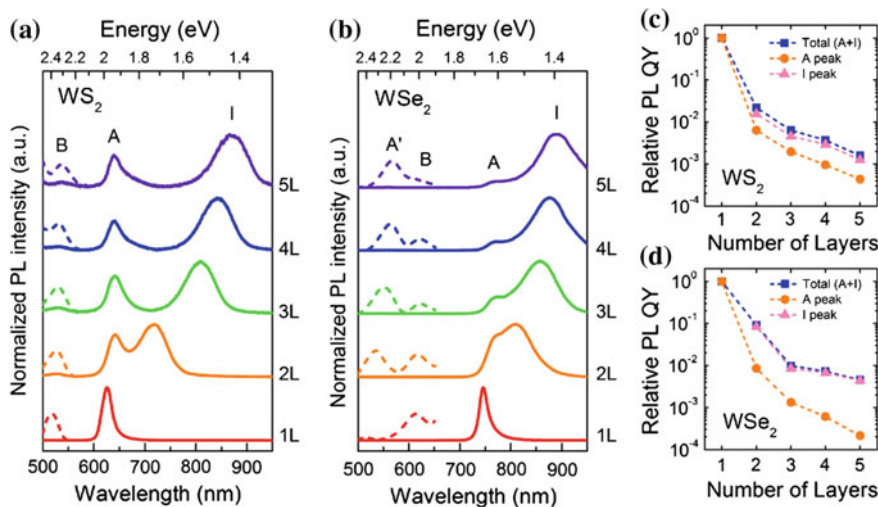


Fig. 8.2 **a, b** Normalized PL spectra of mechanically exfoliated **a** 2H- WS_2 and **b** 2H- WSe_2 flakes consisting of 1–5 layers. Peak *I* is an indirect gap emission. The total emission intensity becomes significantly weaker with increasing number of layers. **c, d** Relative decay in the PL quantum yield with the number of layers for **c** WS_2 and **d** WSe_2 . The values are relative to the PL quantum yield of a monolayer flake. The plots are shown for *A* and *I* peaks and their sum (*A* + *I*). Reproduced after [5]. Copyright 2012 American Chemical Society. Published with permission

in contrast to that in mechanically exfoliated MoS_2 where the quantum yield dropped rapidly from monolayer to bilayer. The authors [7] propose that this difference may be due to the fact that there may be monolayered regions within the multi-layered films or, alternatively, weaker interlayer coupling between the restacked MoS_2 sheets due to rotational stacking disorder could be responsible for the gradual decrease in PL.

A specific PL behaviour was observed in MoSe_2 [8]. While the change in PL intensity significantly increased for a monolayer MoSe_2 sample (Fig. 8.3a) similar to MoS_2 and other studied TMDCs, the temperature dependence was fundamentally different. For a single layer MoS_2 sample the intensity decreased with temperature but for a few-layer sample it, very unexpectedly, increased with temperature (Fig. 8.3b). The decrease of PL of semiconductors with increasing temperature is normal and typically attributed to the exponential enhancement in non-radiative electron–hole recombination processes, reducing the probability of radiative transition.

The unusual behavior of the few-layer samples was attributed to almost degenerate indirect and direct gaps in MoSe_2 . To address further the unusual temperature dependence of PL in MoSe_2 , which is opposite to that observed in MoS_2 , [8] band structure simulations for varying interlayer distances were performed. It was found that a small increase in the interlayer distances (used to mimic thermal expansion) was sufficient to change the gap from indirect to direct, while to achieve the same effect in MoS_2 a much larger increase was needed. It was concluded that the observed PL enhancement with temperature was driven by thermally decoupling neighboring layers via interlayer thermal expansion.

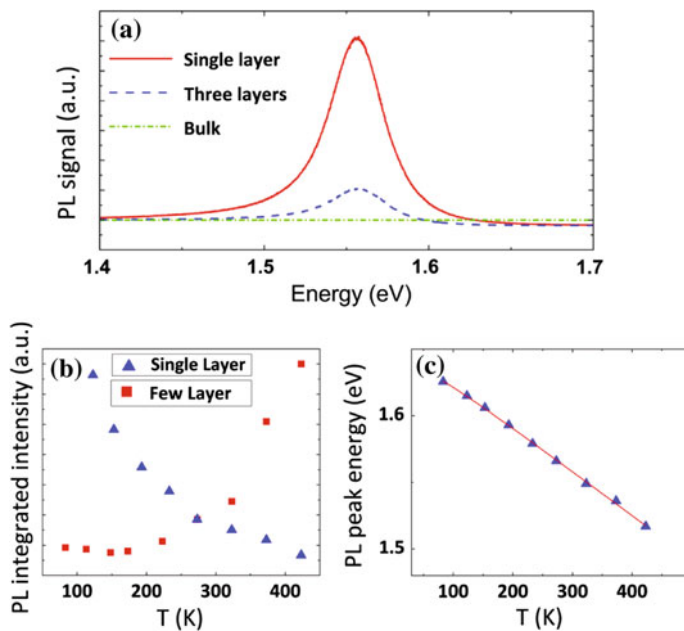


Fig. 8.3 **a** Measured room-temperature PL on a single-layer (red), three-layer (blue dashed), and bulk (green dotted dashed) MoSe_2 . **b** Temperature dependence of PL intensity measured on a single-layer (blue triangles) and nine-layer (red squares) MoSe_2 flakes. **c** Variation of the single-layer MoSe_2 bandgap values (PL peak energy) in the 87–450 K range [8]. Copyright 2012 American Chemical Society. Published with permission (color figure online)

In contrast to most other studied TMDCs, where the PL intensity is increased as one goes from the bulk to a monolayer, in ReS_2 , the PL intensity *decreased* (Fig. 8.4a, b) [9]. The DFT simulations showed that the energy gap is direct for both the bulk and monolayer forms of ReS_2 (Fig. 8.4c). It was concluded that the weak dependence of the band structure on the number of layers is a consequence of a very weak interlayer coupling so that bulk ReS_2 effectively behaves as a 2D material. (Cf. also Sect. 7.11.2, where Raman scattering from ReS_2 and its pressure dependence are discussed.)

8.1.2 Effect of Interlayer Coupling (Twisted Layers)

To develop a good photonic device, the tunability of the optical features of the material is important. Considering the transformation of the direct to indirect band gap from monolayer to bilayer MoS_2 , the interlayer coupling between the two MoS_2 layers should play an important role in the change of the band structure, and, consequently, the change of the PL emission. This argument implies that twisted bilayer MoS_2 , where the two layers are arranged at an arbitrary angle, is a promising system for tuning the PL emission. Such twisted bi-layer systems were a subject of several studies [10–13]. The main findings are summarized below.

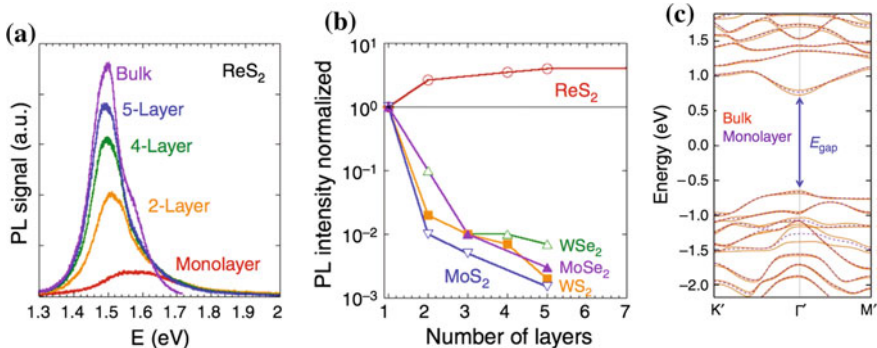


Fig. 8.4 **a** PL spectrum of ReS₂ flakes with different numbers of layers. **b** Integrated PL intensity as a function of number of layers (normalized to that of monolayer) in ReS₂, MoS₂, MoSe₂, WS₂ and WSe₂. **c** DFT calculated electronic band structure of bulk (orange solid curves) and monolayer (purple dashed curves) ReS₂. Both are predicted to be a direct band gap semiconductor with nearly identical bandgap value at the Γ point [9]. Reprinted by permission from Macmillan Publishers Ltd., copyright (2014)

It was found [10] that the variation of the PL from bilayer MoS₂ depends on the twist angle. The results of a systematic investigation are shown in Fig. 8.5. In Fig. 8.5a, the intensity ratio of the A^- -trion² and A -exciton peaks in the bilayer region is normalized by the value for the bottom layer region, which eliminated the influence of the variation of the A and A^- peak ratio introduced from the CVD growth process itself. As can be seen, the ratio exhibits an oscillatory behavior as a function of the twist angle, being approximately symmetric with respect to the twist angle of 60°, in line with the D_{3h} symmetry of monolayer MoS₂. The maximum intensity ratio peaks appear at $\theta = 0^\circ$, 60°, and 120°, and minima at 30° and 90°. The interlayer separation, trion binding energy, peak energy difference between the A and B excitons show similar behavior, suggesting that the interlayer couplings for 30° and 90° may be distinctly different from the interlayer couplings at 0° and 60°. Based on the experimental observations and DFT calculations, it was concluded that at a twist angle of 0° or 60°, the interlayer coupling is maximized mainly due to the minimized interlayer separation, and the change of the A^-/A PL intensity ratio is mainly attributed to the change of trion binding energy with the twist angle [10]. Similar results were obtained in [12, 13].

The effect of stacking in few-layer MoS₂ on interlayer coupling using PL was studied in detail in [14].

Enhanced PL was observed in pyramidal MoS₂ nanoflakes [15] where, due to the screw-dislocation-driven growth mechanism, the stacking is different from $2H$, which can be considered as a kind of layer twisting compared to the standard material.

² A trion is a charged quasiparticle consisting of one electron and two holes (or two electrons and one hole) bound together. see Chap. 9 for a more detailed description.

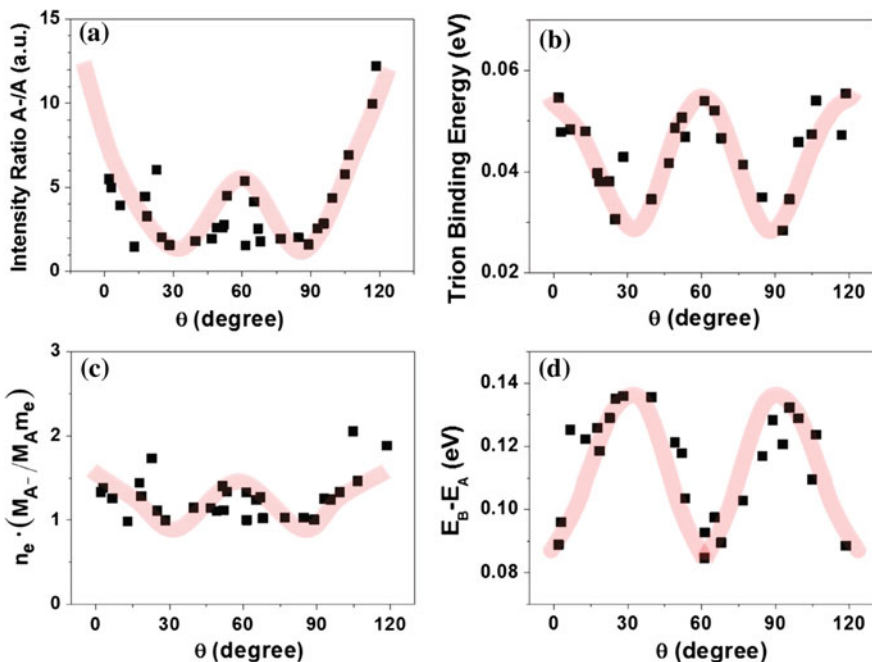


Fig. 8.5 Twist angle dependence of the: **a** A trion to *A* exciton PL intensity ratio, **b** trion binding energy ϵ_{A^-} , **c** $n_e \cdot [M_A - (M_A m_e)]$ normalized by the value at $\theta = 30^\circ$, **d** PL peak energy difference between the *B* and *A* excitons. The black solid squares are experimental data points and the pink solid lines show the changing trend of each parameter [10]. Copyright 2014 American Chemical Society. Published with permission (color figure online)

8.1.3 Band Nesting Effects

In [16], effect of band nesting (cf. also Sect. 6.1.7) on photocarrier relaxation pathway was investigated. For monolayer MX₂, the conduction band minimum and the valence band maximum are both located at the *K*/*K'*-point of the Brillouin zone (Fig. 8.6b). The conduction band valley at the *Λ*-point³ and the valence band hill at the Γ point play a dominant role in the direct to indirect gap crossover. Band-nesting regions in MoS₂ and WS₂ monolayers occur midway between the Γ and *Λ* points [17]. Such a band structure suggests that excited electrons and holes in the nesting region relax to their immediate band extrema, which corresponds to the *Λ* valley for electrons and the Γ hill for holes.

The effect of band nesting on the behaviour of photoexcited electron–hole pairs in monolayer MX₂ was studied by using excitation-dependent PL quantum yield. It was noted that the intraband relaxation in mono- and few-layer MoS₂ is very fast

³The *Λ*-point was not shown in the original work and was added to Fig. 8.6b by the present authors.

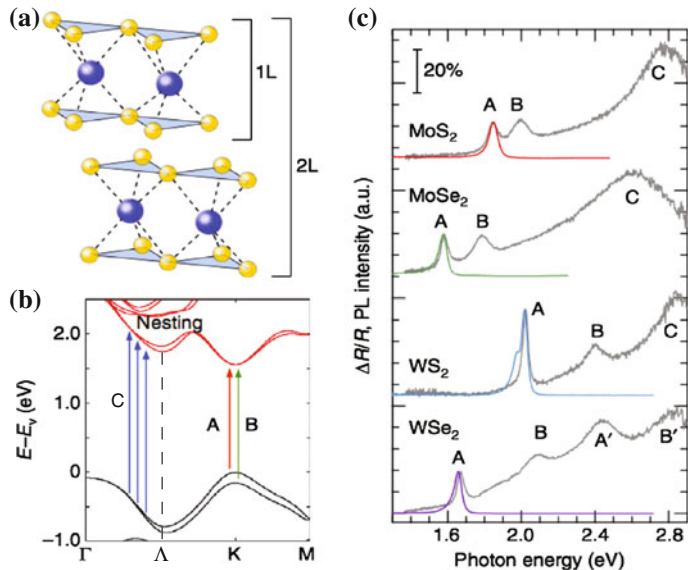


Fig. 8.6 **a** Lattice structures of monolayer and bilayer MX_2 . **b** The band structure of monolayer MoS_2 with the label of C calculated by DFT. The arrows indicate the transition in A , B and the band nesting (C). **c** PL spectra (red, green, blue and purple curves) from excitation at the C (A' for WSe_2) peak and differential reflectance spectra (grey curves) of monolayer MX_2 flakes on quartz substrates. The scale bar indicates 20% absorption based on the differential reflectance spectra. The PL intensity is normalized by the A exciton peak of the differential reflectance spectra for each material and the spectra are displaced along the vertical axis for clarity [16]. Reprinted by permission from Macmillan Publishers Ltd., copyright (2014)

(ca. 500 fs) and is the dominant relaxation process [18–20]. Radiative recombination of the electron–hole pairs separated in k -space requires emission or absorption of a phonon, which is a slow process, typically resulting in low yield emission. The carrier lifetime in the indirect emission process was estimated to be on the order of 1 ns based on previous studies [18, 21]. On the other hand, direct excitons exhibit lifetime on the order of 100 ps with correspondingly higher quantum yield [18].

Figures 8.7 and 8.8 show the PL excitation intensity map of monolayer MoS_2 , WS_2 , MoSe_2 and WSe_2 flakes and comparisons between the PL excitation spectra (red plots), relative quantum yield of emission (blue dots) and the differential reflectance spectra (grey lines). The relative quantum yield was estimated by dividing the integrated PL intensity by the absorption at the excitation energy. It can be seen that the PL excitation intensity is enhanced when the excitation is in resonance with the B exciton absorption. At the same time, the PL excitation intensity at the C absorption peak was suppressed or only weakly enhanced. In all cases, the relative quantum yield drops consistently for excitation energies above the B peak resonance.

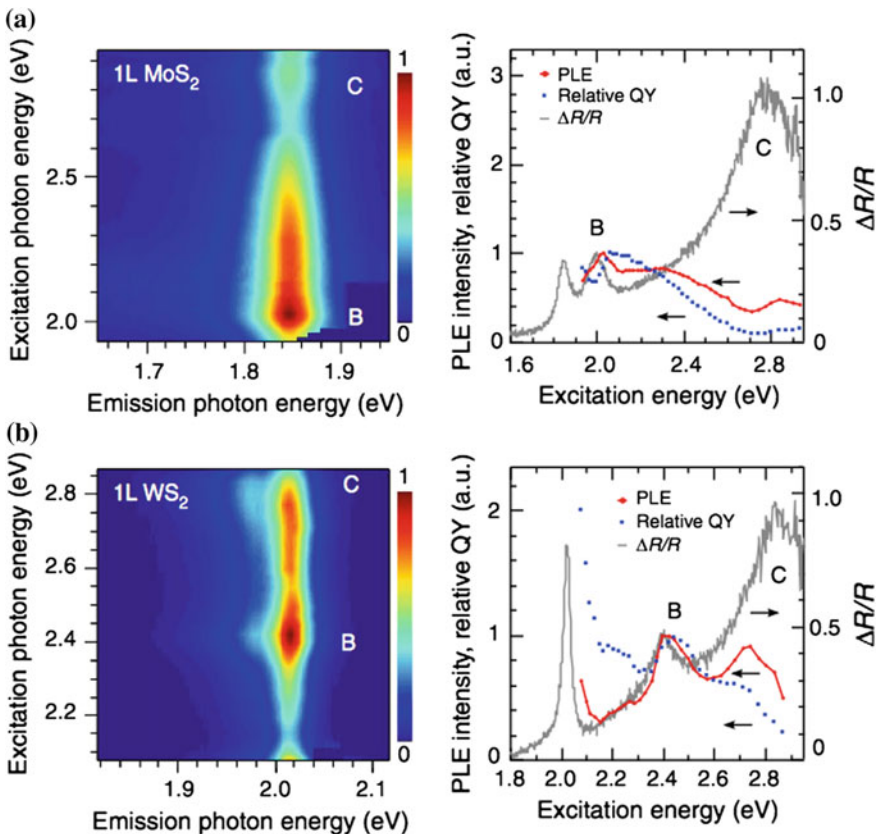


Fig. 8.7 PL excitation spectra of monolayer MS₂. PL excitation intensity map (*left panel*), PL excitation spectra and relative quantum yield of emission (*right panel*) for band gap emission for monolayer **a** MoS₂ and **b** WS₂ flakes. Differential reflectance spectra are also shown for comparison. The PL excitation spectra are based on the integrated intensity of the *A* peak in the PL spectra at each excitation energy. Each PL excitation spectrum is normalized by the *B* exciton peak of each material [16]. Reprinted by permission from Macmillan Publishers Ltd., copyright (2014)

This result was compared with the PL excitation spectra of bi-layer MoS₂ (Fig. 8.9a). The absorption features of bilayer samples are similar to those of monolayers, exhibiting excitonic resonance peaks *A* and *B* and strong *C* peak absorption due to band nesting (Fig. 8.6b). Because bilayer MoS₂ and WS₂ exhibit indirect band gap emission involving the Λ valley in the conduction band and the Γ point in the valence band an enhancement in the band gap indirect emission when the carriers are excited in the band-nesting region can be expected. The PL excitation spectrum of the indirect peak (*I*) indeed shows a distinct enhancement at the *C* absorption peak (Fig. 8.9b). On the other hand, the *A* emission peak shows relatively weaker enhancement in this energy range.

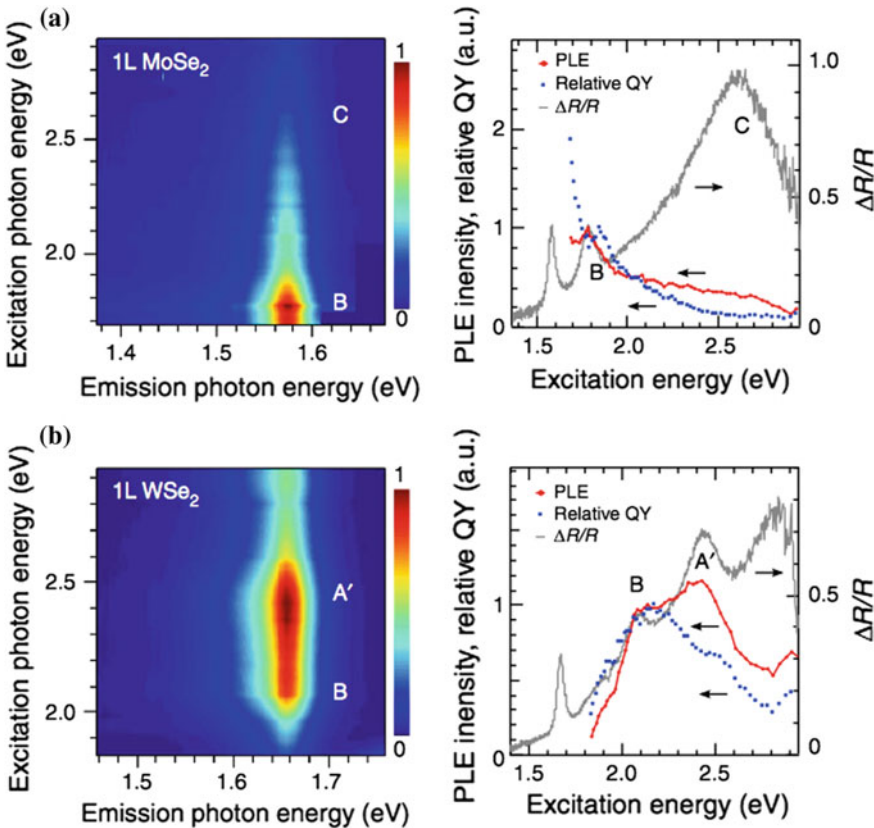


Fig. 8.8 PL excitation spectra of monolayer MSe₂. PL excitation intensity map (*left panel*), PL excitation spectra and relative quantum yield of emission (*right panel*) for band gap emission for monolayer **a** MoSe₂ and **b** WSe₂ flakes. Differential reflectance spectra are also shown for comparison. The PL excitation spectra are based on the integrated intensity of the *A* peak in the PL spectra at each excitation energy. Each PL excitation spectrum is normalized by the *B* exciton peak of each material [16]. Reprinted by permission from Macmillan Publishers Ltd., copyright (2014)

The results were analyzed in terms of band nesting, radiative recombination, non-radiative decay (which is a very fast process, ca. 2–4 ps [18]), and intervalley scattering and it was concluded that photoexcited electron–hole pairs in the nesting region spontaneously separate in *k*-space, relaxing towards immediate band extrema with opposite momenta which suggested that direct exciton recombination is suppressed for excitation in resonance with band nesting. It was proposed that these results may be useful for efficient hot carrier collection using these materials as the absorbers in optoelectronic devices.

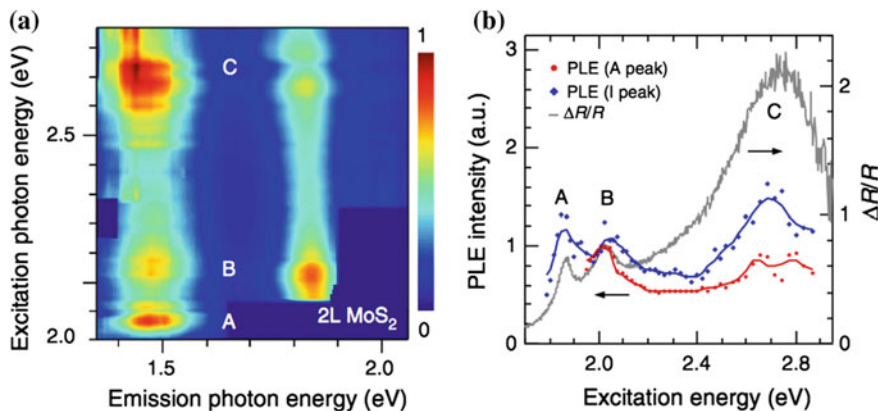


Fig. 8.9 PL excitation spectra of bi-layer MoS₂. **a**, **b** The PL excitation intensity map and PL excitation spectra for bilayer MoS₂. The PL excitation spectra are based on the integrated intensity of the *A* and *I* peak in the PL spectra at each excitation energy. The differential reflectance spectrum is also shown for comparison. The PL excitation spectrum of the *A* peak is normalized by the *B* exciton peak of the differential reflectance and the PL excitation of the *I* peak is multiplied by the same factor as the PL excitation spectrum of the *A* peak [16]. Reprinted by permission from Macmillan Publishers Ltd., copyright (2014)

8.2 Defect-Related Photoluminescence

8.2.1 Defect-Enhanced PL Yield

In [22], defect-induced PL in monolayer TMDCs was reported. The authors intentionally created atomic-scale defects in the hexagonal lattice of pristine WS₂ and MoS₂ monolayers using plasma treatment, whose formation was confirmed by high-resolution transmission electron microscopy. It was found that while the Raman spectra of semiconducting transition metal dichalcogenides (at 532 nm excitation) were insensitive to defects, their PL revealed a distinct defect-related spectral feature located ca. 0.1 eV below the neutral free *A*-exciton peak (Fig. 8.10), which was associated with defect-bound neutral excitons. Defect-activated PL in TMDCs was also studied in [23], where it was found that defect-related PL was pronounced in gas environments (such as N₂) and absent in a vacuum.

An interesting observation was reported in [6]. While mechanically exfoliated 1L WS₂ flakes from synthetic crystals exhibit uniform PL [5], in triangular-shaped samples grown by CVD, highly non-uniform PL with a drastic increase (up to 25 times) in intensity towards the edges was observed [6] but no explanation was offered. The authors of [6] tried to create edges using an ultrasharp tungsten needle, however, the edges created mechanically did not show any significant PL enhancement (Fig. 8.11), suggesting that the edge structure and chemistry of as-grown monolayer WS₂ islands were crucial for localized PL enhancement.

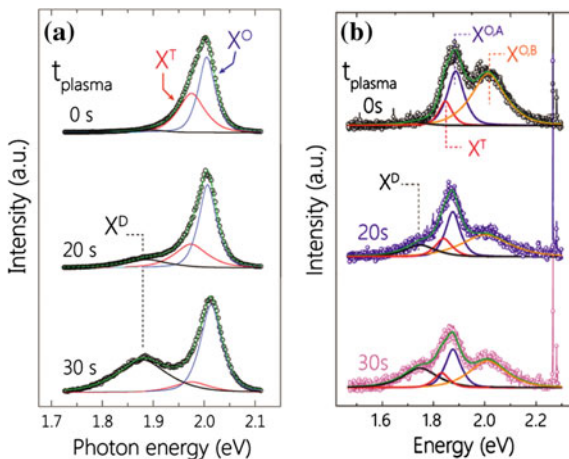


Fig. 8.10 **a** Representative PL spectra (normalized to the total integrated PL intensity) from exfoliated WS₂ monolayers as a function of plasma treatment time. Curve fitting reveals neutral (X^O), charged (X^T), and defect-related (X^D) spectral contributions. **b** Representative PL spectra ($P_{\text{laser}} = 5 \pm 1 \mu\text{W}$) for the exfoliated MoS₂ monolayer (normalized to the total integrated PL intensity) for various plasma treatment times with curve-fitting results. Curve fitting reveals contributions from the B-exciton ($X^{O,B}$), A-exciton ($X^{O,A}$), charged exciton (X^T), and defect-related (X^D) spectral contributions [22]. Copyright 2015 American Chemical Society. Published with permission

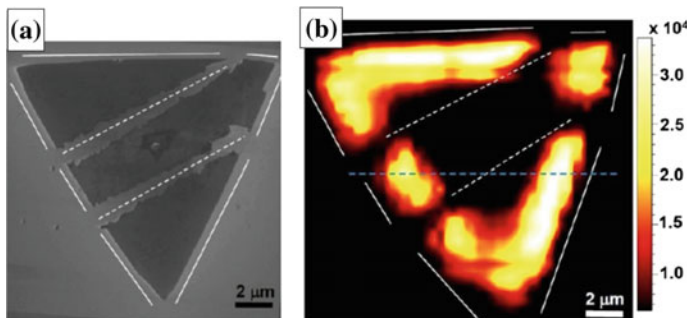


Fig. 8.11 **a** SEM image of a mechanically scratched island (mechanical scratches are along the dashed lines) and the corresponding PL map **(b)**. The ‘new’ edges created mechanically do not exhibit PL enhancement [6]. Copyright 2012 American Chemical Society. Published with permission

In a follow-up work [24], a different group succeeded in CVD growth of WS₂ islands that show highly uniform PL and argued that the existence of non-uniform PL was associated with structural defects and defect-related doping.

Photoluminescence associated with surface impurities in monolayer WS₂ was studied in [25].

It should be kept in mind that the presence of defects is not always beneficial for the PL signal. Thus typically observed room-temperature PL quantum yield is

usually extremely low. The prototypical 2D material MoS₂ quantum yield values ranging from 0.01 to 6% were reported and the origin of the low quantum yield observed was attributed to defect-mediated nonradiative recombination and biexcitonic recombination at higher excitation powers [1, 26, 27]. In a recent study [28], air-stable, solution-based chemical treatment by an organic superacid was reported, which uniformly enhanced the photoluminescence and minority carrier lifetime of MoS₂ monolayers by more than two orders of magnitude. It was argued that this treatment eliminates defect-mediated nonradiative recombination, thus resulting in a final quantum yield of more than 95%, with a longest-observed lifetime of over 10 ns.

8.2.2 Quantum Light Emission

Four groups independently reported (in the same issue of *Nature Nanotechnology*) photoluminescence due to single-phonon emission in WSe₂ structures. The obtained results were in excellent agreement among the published papers [29–32].

It was found that excitation of certain region of WSe₂ resulted in photoluminescence with very intense and narrow lines on the order of 100 μeV, with the smallest reported value of 58 μeV [30]. For comparison, a characteristic width of typical exciton emission is on the order of 10 meV. An example of such PL is shown in Fig. 8.12.

The narrow emission lines exhibited pronounced photon antibunching [29–32] as is exemplified in Fig. 8.13, where the dip reaching ca. 0.2 at zero time delay is a signature of the photon antibunching, from which it was concluded that the emission is associated with single photons emitted by isolated quantum dots. The narrow emission peaks were characterised by a rather long life time on the order of a 2–3 ns [29–32], which is also characteristic of three-dimensional confinement.

Fig. 8.12 PL spectrum of localized emitters. The *left inset* is a high-resolution spectrum of the highest intensity peak. The *right inset* is a zoom-in of the monolayer valley exciton emission, integrated for 60 s. The emission of the localized emitters exhibits a red shift and much sharper spectral lines [30]. Reprinted by permission from Macmillan Publishers Ltd., copyright (2015)

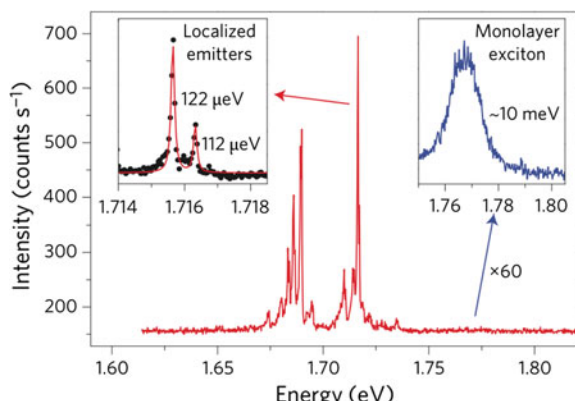
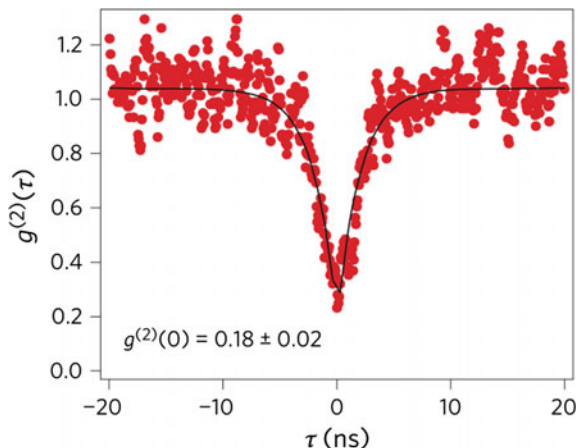


Fig. 8.13 Second-order photon correlation function, $g^2(\tau)$, of PL showing a pronounced dip (antibunching) at zero time delay for emission lines from a quantum dot, confirming that they originate from zero-dimensional emitters [31]. Reprinted by permission from Macmillan Publishers Ltd., copyright (2015)



As regards the origin of the quantum dot emitters, there are some disagreements among the groups. Thus in [29, 32] it was argued that the single photon emitters were located at the edges of WSe₂ monolayers or at interface between monolayers and multilayers (Fig. 8.14a–d). At the same time, in [30], the bright spots were observed also from the surface of monolayers at a distance of a few microns away from the edge (Fig. 8.14e). All groups agree that the sharp emission lines are associated with crystal imperfections [29–32].

Also controversial are the results regarding the stability of the single photon emitters. Thus in [29] it was noted that while overall, the light emitters at the edges of WSe₂ flakes appeared to be robust on a long timescale, and survive many temperature cycles (room to helium temperature), including prolonged exposures to ambient (air) conditions, practically all of them showed clear fluctuation effects on a short timescale: jittering of centres of lines of the order of the linewidth, on a millisecond timescale, as well as larger jumps of lines on a timescale of seconds or minutes. The stability could be improved on decreasing the laser excitation power, when using resonant excitation, and when working with freshly exfoliated structures. It was also improved upon raising the temperature. In contrast, in [31] no blinking was observed, although the authors do note that this observation pertains to a rather small set of the brightest localized emitters in the two flakes that exhibited sharp emission peaks.

Of special interest is the fact that the emission energy can be controlled by an external magnetic field applied perpendicular to the layer (Faraday geometry) [29–32] as is illustrated in Fig. 8.15. At the same time, when the magnetic field was applied in the Voigt geometry (parallel to the layer), the effect was not detected [31]. The relative separation of the magnetic field split transitions can be described as $\Delta = \sqrt{[(g\mu_B B)^2 + \Delta_0^2]}$, where g is the g -factor, μ_B is the Bohr magneton, and Δ_0 is the zero-field splitting. In all four papers, the g -factor was found to be very large, ca. 10 [29–32]. In [32] it was additionally noted that single photon emission from quantum dots could be controlled by an electric field.

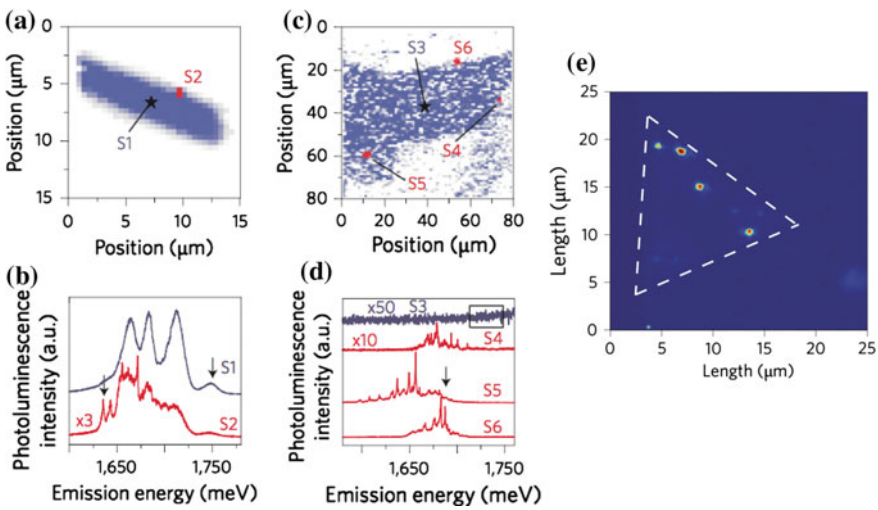
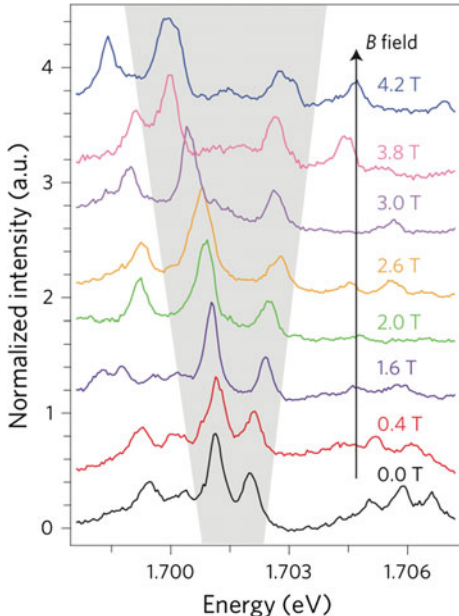


Fig. 8.14 **a** A contour plot (*violet* contrast) of the WSe₂ monolayer showing the intensity of the micro-PL detected at the selected emission energy of ≈ 1.75 eV (free-exciton resonance of a WSe₂ monolayer). **b** Micro-PL spectra measured at two selected spots (S1 and S2) on the WSe₂ monolayer. **c** A contour map for a thicker flake. Even though the thicker flake shows a suppressed photoluminescence, **d** narrow emission lines are found at specific edge positions (S4–S6) on the thick WSe₂ flake [29]. **e** PL-intensity map of narrow emission lines from a WSe₂ monolayer grown using physical vapour transport within a spectral width of 12 meV centred at 1.719 eV, over a $25\text{ }\mu\text{m} \times 25\text{ }\mu\text{m}$ area. The *dashed triangle* indicates the position of the monolayer [30]. Reprinted by permission from Macmillan Publishers Ltd., copyright (2015)

Fig. 8.15 Magnetic field dependence of quantum dot emission spectra in the Faraday configuration [32]. Reprinted by permission from Macmillan Publishers Ltd., copyright (2015)



8.3 PL Tuning by External Stimuli

8.3.1 Pressure and Strain Effects

8.3.1.1 Hydrostatic Pressure

PL in monolayer 2H-MoS₂ exhibits a (reversible) blue shift under applied hydrostatic pressure at a rate of 30 meV/GPa at pressures below 5 GPa [33] (Fig. 8.16a). At higher pressures, the direct band gap gradually increases to 2.08 eV at ca. 12 GPa, showing a significant (11.7%) change in band gap (Fig. 8.16b), while increasing the PL full width half-maximum.

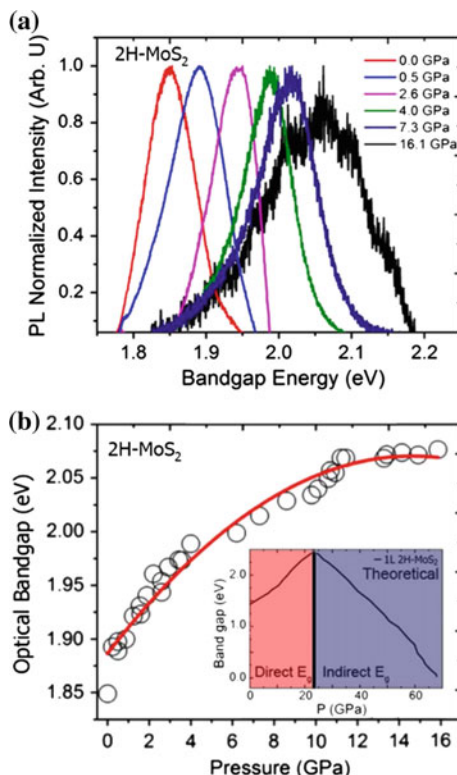


Fig. 8.16 Pressure modulated photoluminescent properties of monolayer 2H-MoS₂. **a** Representative PL spectra as a function of pressure. An increase in the band gap with increasing pressure and then the diminishing of the PL signals at ca. 16 GPa indicates a direct-to-indirect band gap transformation. **b** Derived band gap at high pressures. Extracted from the Lorentzian fit from the PL peaks, the band gap is shown to increase as a function of pressure. Red solid line a polynomial fit to the experimental data described by $E_g = 1.88 + 0.03P - 8.59 \times 10^{-4}P^2$ where E_g is optical band gap and P is pressure. *Inset:* The theoretical prediction of the direct-to indirect band gap transition [33]. Copyright 2014 American Chemical Society. Published with permission

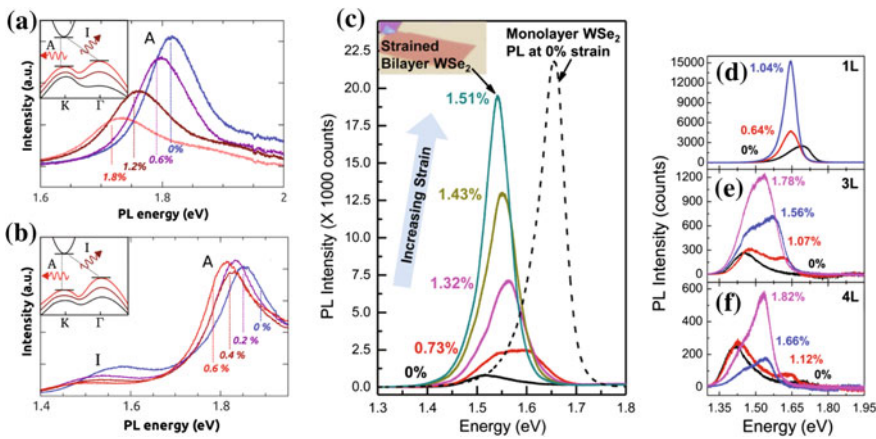


Fig. 8.17 *Left:* Photoluminescence spectra of strained MoS₂. **a** PL spectra of a representative monolayer device as it is strained from 0 to 1.8%. Strain independent PL background was subtracted. **b** PL spectra of a representative bi-layer device as strain is increased from 0 to 0.6% [35]. Copyright 2013 American Chemical Society. Published with permission. **c** Bilayer WSe₂ PL spectra at different strain. PL of unstrained monolayer WSe₂ on SiO₂ is shown for comparison. The inset shows an optical microscope image of the bilayer WSe₂ flake used in this study. *Right:* PL spectra at different strain for **(d)** Monolayer, **(e)** Trilayer and **(f)** Quadlayer WSe₂ [34]. Copyright 2014 American Chemical Society. Published with permission

8.3.1.2 Uniaxial Strain

A strain-induced indirect-to-direct bandgap transition was observed in few-layers WSe₂ [34]. The evolution of the bilayer WSe₂ PL with strain is shown in Fig. 8.17, middle panel. A drastic ($\times 35$) enhancement in PL intensity for bilayer WSe₂ is clearly seen as the uniaxial tensile strain is increased. The peak at zero strain is broad and the PL peak intensity is more than an order of magnitude less than that for unstrained monolayer WSe₂ under identical conditions, which are also shown for reference. At the same time, the PL signal from the strained bilayer WSe₂ was comparable to that from the unstrained monolayer WSe₂ measured under identical laser power and acquisition time conditions.

The effect of strain on different thicknesses of WSe₂ was examined [Fig. 8.17 (right panel)] using PL and Raman spectroscopy. PL for monolayer WSe₂ showed a drastic increase with strain, indicating that monolayer WSe₂ remains direct bandgap even under uniaxial tensile strain and the difference between the indirect and direct CB minima increases further. Based on these observations and the results of DFT simulations, the drastic PL enhancement for the strained bilayer was attributed to an indirect-to-direct band transition [34].

A different behavior was observed in MoS₂ under rather similar conditions [35], where a monolayer exhibited a decrease in the PL intensity indicating a direct-to-indirect transition under uniaxial tensile strain, in agreement with the prediction of [36, 37]. At the same time, a few-layer structure did not show a noticeable strain dependence (Fig. 8.17, left panel).

Similar studies were also performed in [38] for both monolayer and bilayer samples and it was found that the *A* and *B* exciton resonance peaks, associated with the direct gap transitions, redshift under tensile strains with similar rates, with a larger redshift rate being observed for the indirect band gap transitions in bilayer MoS₂. The effect of mechanical strain on the electronic structure and properties of MoS₂ was also studied in [39–41].

Exceptional tunability of band energy in a compressively strained trilayer MoS₂ sheet was reported in [42], where it was shown that the direct band gap can be blue-shifted by ca. 300 meV per 1% strain, which the authors claim to be the highest value ever reported for strained semiconductors.

These observations demonstrate that strain engineering may be an enabling tool to both explore novel physics of TMDCs and to tune their optical and electronic properties. The authors of [35] suggested that an interesting avenue of research may be to explore the regime of degenerate direct and indirect bands that play key roles in a plethora of spin-related properties of MoS₂.

8.3.2 Electrical Gating

In [43] electrical gating of PL and optical absorption in monolayers and bi-layers of MoS₂ configured in a field-effect transistor geometry was investigated. The authors observed a hundred-fold increase in PL intensity in the monolayer devices when an external gate voltage was varied from –50 to 50 V, while the PL wavelength remained nearly constant. In contrast, in bilayer MoS₂ devices, almost no changes could be observed in PL with gate voltage (Fig. 8.18).

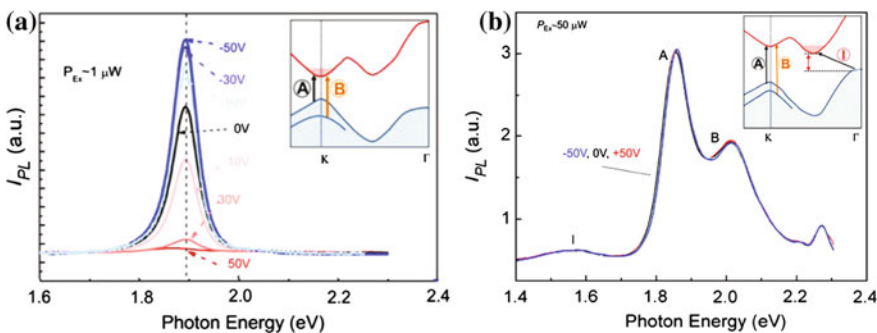


Fig. 8.18 **a** PL spectra of a monolayer device taken at different gate voltages ($V_G = -50, -30, -10, 0, 10, 30, 50$ V) at low excitation power (1 mW). The *inset* shows the band diagram of monolayer MoS₂; direct band-gap exciton transitions *A* and *B* are indicated by arrows. **b** PL spectra of a bilayer MoS₂ device recorded at $V_G = -50, 0, 50$ V under 50 mW laser excitation power. Spectra at different V_G are very similar and collapse onto the same curve. The *inset* shows the band structure of bilayer MoS₂. Along with *A* and *B* transitions, the momentum violating transition *I* across the indirect band gap of bilayer MoS₂ is indicated [43]. Reprinted with permission from Elsevier

The authors [43] proposed that the different responses of the monolayer and bilayer devices are related to the phase-space filling effect [44], where an increase of the carrier density renders part of a phase space unavailable for exciton formation due to the Pauli exclusion principle, causing a reduction in the exciton oscillator strength and a corresponding decrease of PL intensity and excitonic absorption. It was noted that this mechanism is consistent with the absence of gate-dependent changes in PL in bilayer MoS₂. For bi-layer MoS₂, the excitons and the conduction electrons occupy different regions of phase space with one-particle states participating in the formation of A and B excitons having momenta near the K-point, whereas conduction electrons reside across the indirect gap, away from the K-point (Fig. 8.18b, inset). Therefore, changes in the carrier density should not affect the excitonic absorption and PL intensity for the bi-layer MoS₂ sample.

Photoluminescent properties under a lateral electric field in monolayer and bilayer WS₂ were studied in [45]. It was shown that monolayer and bilayer structures have opposite responses to lateral electric fields, with PL substantially reduced in the monolayer and increased in bilayers with increasing lateral electric field strength (Fig. 8.19). Temperature-dependent PL measurements showed behavior distinctly different than that of the lateral electric field effect, ruling out heating as the cause of the PL changes. The PL variation in both monolayer and bilayer WS₂ was attributed to the transfer of photoexcited electrons from one conduction band extremum to another, made possible due to the small energy difference between the two conduction band extrema, modifying the resultant recombination pathways.

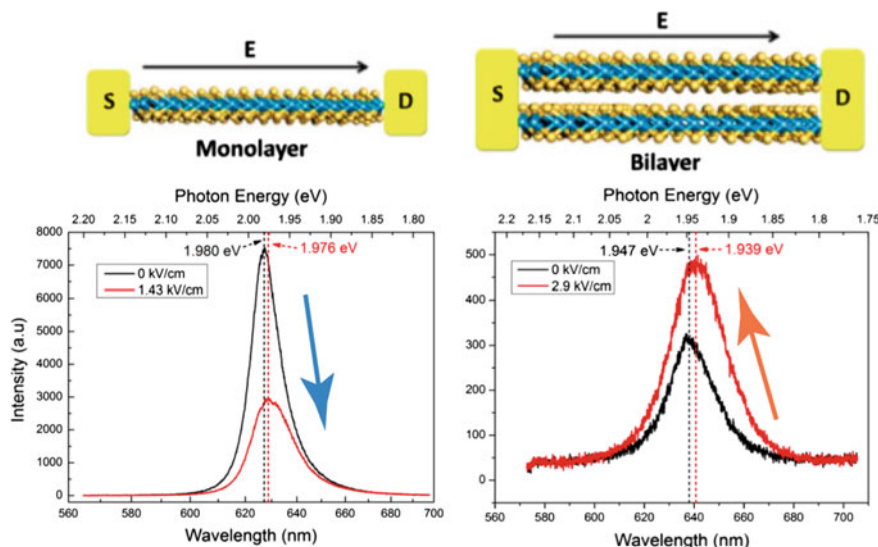


Fig. 8.19 PL signals from monolayer (*left*) and bilayer (*right*) WS₂ without and with lateral electric field [45]. Copyright 2015 American Chemical Society. Published with permission

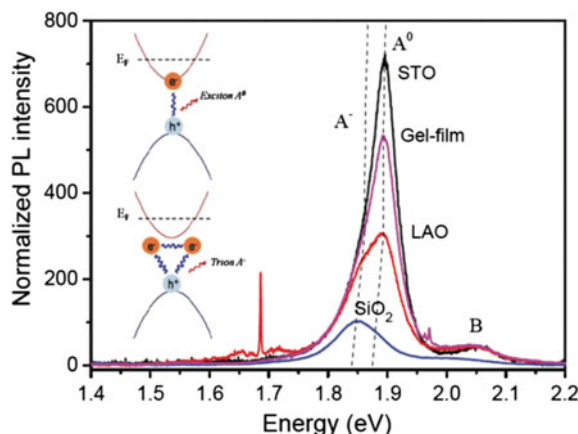
8.3.3 Effect of Doping

In [46] it was demonstrated that the PL properties of monolayer MoS₂ can be tuned via a solution-based chemical doping technique. The PL intensity could be drastically enhanced when *p*-type dopants cover its surface. This enhancement was understood as a consequence of switching the dominant PL process from the recombination of negative trions to the recombination of excitons through extraction of the unintentionally high-doped electrons in the as-prepared sample. In contrast, the PL intensity reduced when MoS₂ was covered with *n*-type dopants, which was interpreted as being due to the suppression of exciton PL by the injection of excess electrons.

8.3.4 Substrate Effects

PL strongly depends on the substrate material, as is exemplified in Fig. 8.20, where PL from a monolayer MoS₂ on SiO₂, LaAlO₃, gel-film and SrTiO₃ substrates is shown [47]. Significant differences in the PL spectra were observed for these four kinds of substrates. Firstly, the normalized peak *A* intensity indicates an evident difference. Monolayer MoS₂ on a SrTiO₃ substrate has the highest emission intensity, while monolayer MoS₂ on SiO₂ substrate has the lowest emission intensity. In addition, the positions and shapes of peak *A* also show obvious differences. In these substrates, the position of peak *A* for MoS₂/SiO₂ is at the lowest energy and there is a large blue-shift (>40 meV) for the other three kinds of substrates compared to that of MoS₂/SiO₂. When the substrates changed from SiO₂ to LaAlO₃ to a gel-film to SrTiO₃, the variation of the intensity, position and shape of peak *A* were very similar to those seen as a result of chemical doping and electrical doping [46, 48], from which it was suggested that charge transfer is occurring between monolayer MoS₂ and the

Fig. 8.20 Normalized PL spectra of monolayer MoS₂ on SiO₂, LaAlO₃, gel-film and SrTiO₃ substrates [47]. Reproduced by permission of The Royal Society of Chemistry



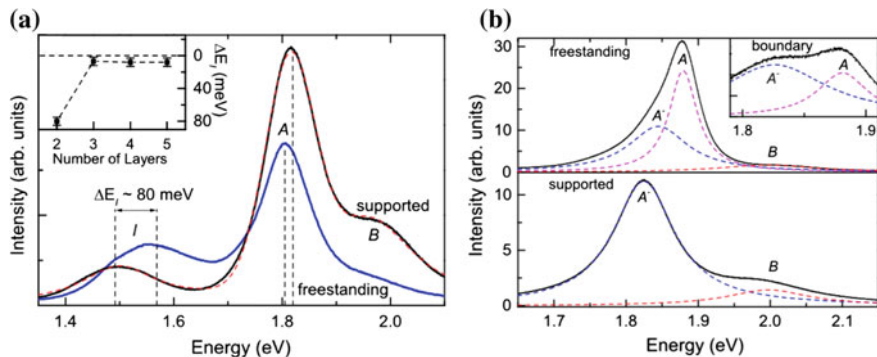


Fig. 8.21 **a** PL spectra of free-standing and supported bilayer MoS₂. The *inset* shows the difference of the indirect transition energy between supported and freestanding areas as a function of the layer number. **b** PL of freestanding and supported single-layer MoS₂ (*solid lines*). *Dotted lines* show fit functions of the *A*, *B*, and *A*[−] peaks. The *inset* shows PL from the boundary region between supported and freestanding areas, showing an overlap of both types of spectra [49]. Copyright 2014 by the American Physical Society. Reprinted with permission

substrates since the excitons will change their charge states and present different optical responses when additional charges are introduced into system [47].

In line with this, PL was found to be different in free standing and supported films [49] for both monolayers and bi-layers. Figure 8.21b shows PL spectra from free-standing and supported monolayers as well as from the boundary between the supported and freestanding areas (inset). The maximum of the PL emission shows a blueshift of ca. 65 meV in the freestanding single layer compared to the supported one; the emission peak becomes asymmetric. At the boundary between supported and free-standing areas, the emission showed double-peak structures, attributed to the simultaneous observation of the *A* and *A*[−] peaks. The *A*[−] peak was assigned to negatively charged trions. While the emission intensity of the trions (*A*[−]) showed no dependence on the charge-carrier concentration, the exciton *A* emission was strongly reduced for *n*-type doped MoS₂. It was proposed that observed changes in the PL of freestanding single-layer MoS₂ can be understood when assuming *n*-type doping of the MoS₂ by charge-transfer effects from the substrate. Therefore, the emission of the exciton *A* is suppressed on the substrate; instead, the observed PL of single-layer MoS₂ on Si/SiO₂ substrate is primarily from the trion (*A*[−]). In the freestanding areas, the MoS₂ layer is less doped, and the emission of the exciton becomes dominant. A similarly strong PL difference between free-standing and supported bi-layers is illustrated in Fig. 8.21a [49].

Charge transfer between the TMDC and the substrate, or a material deposited on top, can also lead to complete quenching of PL, as was observed in gold-MoS₂ hybrid nanoflakes, which was interpreted as being due to *p*-type doping of MoS₂ [50]. It is interesting to note that *p*-doping (by oxygen) was also named as a reason

for a huge enhancement of PL of monolayer MoS₂ [51]. Chemically tunable light emission of charged and neutral excitons in monolayer WS₂ was observed in [52], where electron-withdrawing molecules absorbed on WS₂ strongly enhanced the PL intensity.

In [53] a strong effect of water on the PL of monolayer MoS₂ was reported, with the PL being quenched in presence of water, which was attributed to *n*-type doping.

8.4 Electroluminescence

While most of the reported data refer to PL, electroluminescence (EL) was also observed from a single layer MoS₂ field-effect transistor [54]. The adopted design allowed the measurement of both PL and EL (Fig. 8.22a) and from comparison of the absorption, PL, and EL spectra (Fig. 8.22b) it was concluded that the EL involves the same states as PL.

The result for MoS₂ was reconfirmed in [55] and electroluminescence in WSe₂ [56] and WS₂ [57] was also demonstrated albeit, with a low efficiency (typically less than 1%). Light emission was subsequently observed in electrically tunable p-n diodes in monolayers of WSe₂ [58, 59].

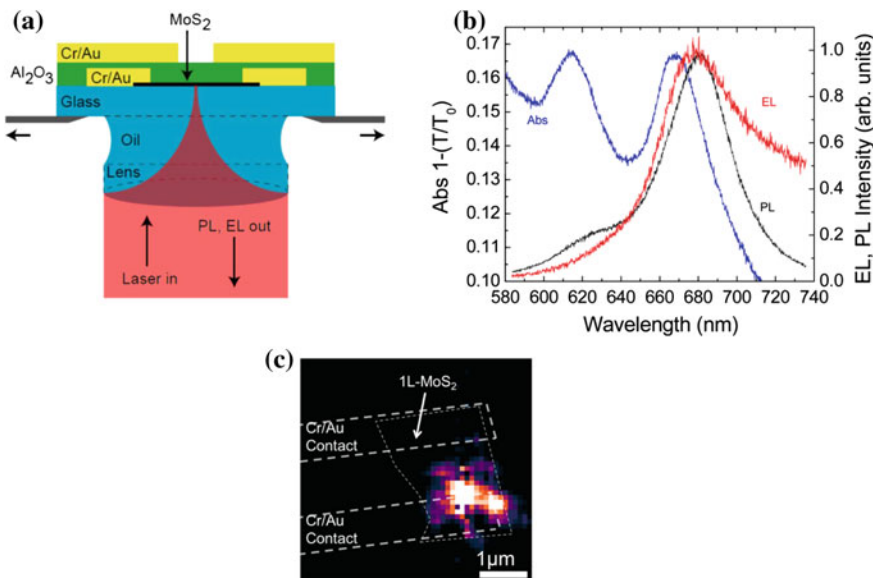


Fig. 8.22 **a** Schematic of a top-gated MoS₂ FET and the optical setup. **b** Absorption (Abs), EL, and PL spectra on the same 1L-MoS₂. The EL spectrum is measured at $V_D = 8\text{ V}$ and $I_D = 164\text{ }\mu\text{A}$ [54]. Copyright 2013 American Chemical Society. Published with permission

Subsequently, electrically switchable chiral EL was reported in [60]. In this work, p-i-n junctions were formed using an electric-double-layer transistor (EDLT) structure with WSe₂ thin flakes having thicknesses of 0.6–2.6 nm as the channel material. When the p-i-n junction was forward-biased, clear EL was observed. The EL spectra showed net circular polarization. The circular polarization was reversed when the source-drain bias was exchanged.

Electric-field induced enhancement of EL in multilayer MoS₂ was reported in [61] and was attributed to carrier redistribution from the lowest energy points (indirect band gap) to higher energy points (direct gap) in k -space.

8.5 PL from TMDC Alloys

PL from few-layer samples of Mo_{1-x}W_xS₂ was studied in [62] and the results are shown in Fig. 8.23. As in single-metal TMDC, the PL intensity drastically increased for monolayer samples (Fig. 8.23f).

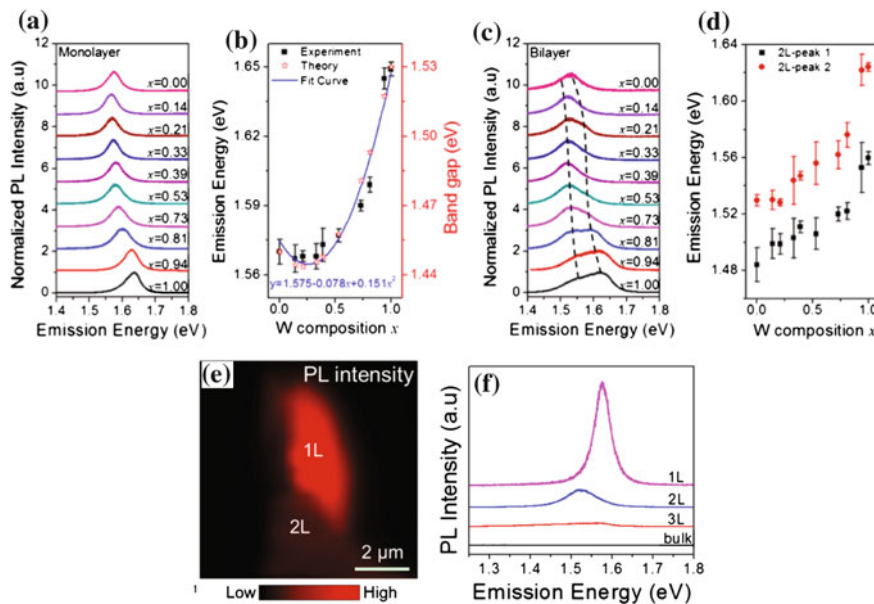


Fig. 8.23 Composition-dependent PL spectra and PL emission energies of Mo_{1-x}W_xS₂ monolayer alloys (**a**, **b**) and similar plots (**c**, **d**) for bilayers. The black dashed lines in **c** show the emission energy shift of the two peaks. The excitation laser wavelength was 514.5 nm. **e** A mapping image of PL intensity of a Mo_{0.67}W_{0.33}Se₂ sheet and its PL spectrum (**f**) [62]. Copyright 2014 American Chemical Society. Published with permission

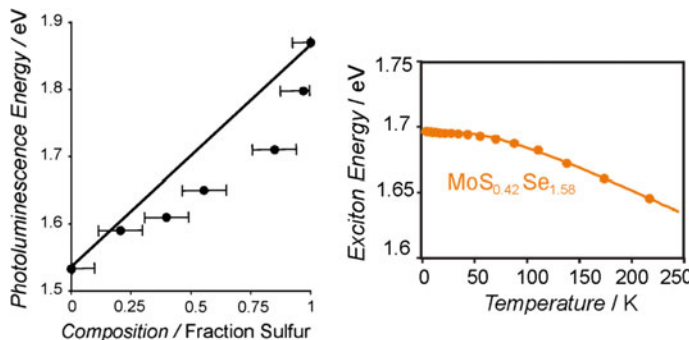


Fig. 8.24 Left variation of the photon energy of the PL emission peak as a function of sample composition for $\text{MoS}_{2(1-x)}\text{Se}_{2x}$ monolayers. Right the exciton emission energy as a function of the temperature of the $\text{MoS}_{0.42}\text{Se}_{1.58}$ film [63]. Reproduced with permission from Wiley-VCH Verlag GmbH

PL was also studied in $\text{MoS}_{2(1-x)}\text{Se}_{2x}$ monolayers [63]. Variation of the photon energy of the PL emission peak as a function of sample composition and the exciton emission energy as a function of the temperature of the $\text{MoS}_{0.42}\text{Se}_{1.58}$ film are examples shown in Fig. 8.24.

References

1. K.F. Mak, C. Lee, J. Hone, J. Shan, T.F. Heinz, Atomically thin MoS_2 : a new direct-gap semiconductor. *Phys. Rev. Lett.* **105**(13), 136805 (2010)
2. A. Splendiani, L. Sun, Y. Zhang, T. Li, J. Kim, C.Y. Chim, G. Galli, F. Wang, Emerging photoluminescence in monolayer MoS_2 . *Nano Lett.* **10**(4), 1271 (2010)
3. C. Ruppert, O.B. Aslan, T.F. Heinz, Optical properties and band gap of single-and few-layer MoTe_2 crystals. *Nano Lett.* **14**(11), 6231 (2014)
4. I.G. Lezama, A. Arora, A. Ubaldini, C. Barreteau, E. Giannini, M. Potemski, A.F. Morpurgo, Indirect-to-direct band gap crossover in few-layer MoTe_2 . *Nano Lett.* **15**(4), 2336 (2015)
5. W. Zhao, Z. Ghorannevis, L. Chu, M. Toh, C. Kloc, P.H. Tan, G. Eda, Evolution of electronic structure in atomically thin sheets of WS_2 and WSe_2 . *ACS Nano* **7**(1), 791 (2012)
6. H.R. Gutiérrez, N. Perea-López, A.L. Elías, A. Berkdemir, B. Wang, R. Ly, F. López-Urias, V.H. Crespi, H. Terrones, M. Terrones, Extraordinary room-temperature photoluminescence in triangular WS_2 monolayers. *Nano Lett.* **13**(8), 3447 (2012)
7. G. Eda, H. Yamaguchi, D. Voiry, T. Fujita, M. Chen, M. Chhowalla, Photoluminescence from chemically exfoliated MoS_2 . *Nano Lett.* **11**(12), 5111 (2011)
8. S. Tongay, J. Zhou, C. Ataca, K. Lo, T.S. Matthews, J. Li, J.C. Grossman, J. Wu, Thermally driven crossover from indirect toward direct bandgap in 2D semiconductors: MoSe_2 versus MoS_2 . *Nano Lett.* **12**(11), 5576 (2012)
9. S. Tongay, H. Sahin, C. Ko, A. Luce, W. Fan, K. Liu, J. Zhou, Y.S. Huang, C.H. Ho, J. Yan et al., Monolayer behaviour in bulk ReS_2 due to electronic and vibrational decoupling. *Nat. Commun.* **5** (2014). doi:[10.1038/ncomms4252](https://doi.org/10.1038/ncomms4252)
10. S. Huang, X. Ling, L. Liang, J. Kong, H. Terrones, V. Meunier, M.S. Dresselhaus, Probing the interlayer coupling of twisted bilayer MoS_2 using photoluminescence spectroscopy. *Nano Lett.* **14**(10), 5500 (2014)

11. T. Jiang, H. Liu, D. Huang, S. Zhang, Y. Li, X. Gong, Y.R. Shen, W.T. Liu, S. Wu, Valley and band structure engineering of folded MoS₂ bilayers. *Nat. Nanotech.* **9**(10), 825 (2014)
12. A.M. van der Zande, J. Kunstmann, A. Chernikov, D.A. Chenet, Y. You, X. Zhang, P.Y. Huang, T.C. Berkelbach, L. Wang, F. Zhang et al., Tailoring the electronic structure in bilayer molybdenum disulfide via interlayer twist. *Nano Lett.* **14**(7), 3869 (2014)
13. K. Liu, L. Zhang, T. Cao, C. Jin, D. Qiu, Q. Zhou, A. Zettl, P. Yang, S.G. Louie, F. Wang, Evolution of interlayer coupling in twisted molybdenum disulfide bilayers. *Nat. Commun.* **5** (2014). doi:[10.1038/ncomms5966](https://doi.org/10.1038/ncomms5966)
14. J. Yan, J. Xia, X. Wang, L. Liu, J.L. Kuo, B.K. Tay, S. Chen, W. Zhou, Z. Liu, Z. Shen, Stacking-dependent interlayer coupling in trilayer MoS₂ with broken inversion symmetry. *Nano Lett.* **15**(12), 8155 (2015). doi:[10.1021/acs.nanolett.5b03597](https://doi.org/10.1021/acs.nanolett.5b03597)
15. C. Yuan, Y. Cao, X. Luo, T. Yu, Z. Huang, B. Xu, Y. Yang, Q. Li, G. Gu, W. Lei, Monolayer-by-monolayer stacked pyramid-like MoS₂ nanodots on monolayered MoS₂ flakes with enhanced photoluminescence. *Nanoscale* **7**(41), 17468 (2015)
16. D. Kozawa, R. Kumar, A. Carvalho, K.K. Amara, W. Zhao, S. Wang, M. Toh, R.M. Ribeiro, A.C. Neto, K. Matsuda et al., Photocarrier relaxation pathway in two-dimensional semiconducting transition metal dichalcogenides. *Nat. Commun.* **5** (2014). doi:[10.1038/ncomms5543](https://doi.org/10.1038/ncomms5543)
17. A. Carvalho, R. Ribeiro, A.C. Neto, Band nesting and the optical response of two-dimensional semiconducting transition metal dichalcogenides. *Phys. Rev. B* **88**(11), 115205 (2013)
18. H. Shi, R. Yan, S. Bertolazzi, J. Brivio, B. Gao, A. Kis, D. Jena, H.G. Xing, L. Huang, Exciton dynamics in suspended monolayer and few-layer MoS₂ 2D crystals. *ACS Nano* **7**(2), 1072 (2013)
19. S. Sim, J. Park, J.G. Song, C. In, Y.S. Lee, H. Kim, H. Choi, Exciton dynamics in atomically thin MoS₂: Interexcitonic interaction and broadening kinetics. *Phys. Rev. B* **88**(7), 075434 (2013)
20. R. Wang, B.A. Ruzicka, N. Kumar, M.Z. Bellus, H.Y. Chiu, H. Zhao, Ultrafast and spatially resolved studies of charge carriers in atomically thin molybdenum disulfide. *Phys. Rev. B* **86**(4), 045406 (2012)
21. N. Kumar, J. He, D. He, Y. Wang, H. Zhao, Charge carrier dynamics in bulk MoS₂ crystal studied by transient absorption microscopy. *J. Appl. Phys.* **113**(13), 133702 (2013)
22. P.K. Chow, R.B. Jacobs-Gedrim, J. Gao, T.M. Lu, B. Yu, H. Terrones, N. Koratkar, Defect-induced photoluminescence in monolayer semiconducting transition metal dichalcogenides. *ACS Nano* **9**(2), 1520 (2015)
23. S. Tongay, J. Suh, C. Ataca, W. Fan, A. Luce, J.S. Kang, J. Liu, C. Ko, R. Raghunathanan, J. Zhou et al., Defects activated photoluminescence in two-dimensional semiconductors: interplay between bound, charged, and free excitons. *Sci. Rep.* **3** (2013). doi:[10.1038/srep02657](https://doi.org/10.1038/srep02657)
24. N. Peimyoo, J. Shang, C. Cong, X. Shen, X. Wu, E.K. Yeow, T. Yu, Nonblinking, intense two-dimensional light emitter: Monolayer WS₂ triangles. *ACS Nano* **7**(12), 10985 (2013)
25. T. Kato, T. Kaneko, Optical detection of a highly localized impurity state in monolayer tungsten disulfide. *ACS Nano* **8**(12), 12777 (2014)
26. L. Yuan, L. Huang, Exciton dynamics and annihilation in WS₂ 2D semiconductors. *Nanoscale* **7**(16), 7402 (2015)
27. H. Wang, C. Zhang, F. Rana, Ultrafast dynamics of defect-assisted electron-hole recombination in monolayer MoS₂. *Nano Lett.* **15**(1), 339 (2015)
28. M. Amani, D.H. Lien, D. Kiriya, J. Xiao, A. Azcatl, J. Noh, S.R. Madhvapathy, R. Addou, S. KC, M. Dubey, K. Cho, R.M. Wallace, S.C. Lee, J.H. He, J.W. Ager, X. Zhang, E. Yablonovitch, A. Javey, Near-unity photoluminescence quantum yield in MoS₂. *Science* **350**(6264), 1065 (2015)
29. M. Koperski, K. Nogajewski, A. Arora, V. Cherkez, P. Mallet, J.Y. Veuillet, J. Marcus, P. Kossacki, M. Potemski, Single photon emitters in exfoliated WSe₂ structures. *Nat. Nanotech.* **10**, 503 (2015)
30. Y.M. He, G. Clark, J.R. Schaibley, Y. He, M.C. Chen, Y.J. Wei, X. Ding, Q. Zhang, W. Yao, X. Xu et al., Single quantum emitters in monolayer semiconductors. *Nat. Nanotech.* **10**, 497 (2015)

31. A. Srivastava, M. Sidler, A.V. Allain, D.S. Lembke, A. Kis, A. Imamoğlu, Optically active quantum dots in monolayer WSe₂. *Nat. Nanotech.* **10**, 491 (2015)
32. C. Chakraborty, L. Kinnischtzke, K.M. Goodfellow, R. Beams, A.N. Vamivakas, Voltage-controlled quantum light from an atomically thin semiconductor. *Nat. Nanotech.* **10**, 507 (2015)
33. A.P. Nayak, T. Pandey, D. Voiry, J. Liu, S.T. Moran, A. Sharma, C. Tan, C.H. Chen, L.J. Lee, M. Chhowalla et al., Pressure-dependent optical and vibrational properties of monolayer molybdenum disulfide. *Nano Lett.* **15**(1), 346 (2015)
34. S.B. Desai, G. Seol, J.S. Kang, H. Fang, C. Battaglia, R. Kapadia, J.W. Ager, J. Guo, A. Javey, Strain-induced indirect to direct bandgap transition in multilayer WSe₂. *Nano Lett.* **14**(8), 4592 (2014)
35. H.J. Conley, B. Wang, J.I. Ziegler, R.F. Haglund Jr., S.T. Pantelides, K.I. Bolotin, Bandgap engineering of strained monolayer and bilayer MoS₂. *Nano Lett.* **13**(8), 3626 (2013)
36. T. Li, Ideal strength and phonon instability in single-layer MoS₂. *Phys. Rev. B* **85**(23), 235407 (2012)
37. E. Scalise, M. Houssa, G. Pourtois, V. Afanasev, A. Stesmans, Strain-induced semiconductor to metal transition in the two-dimensional honeycomb structure of MoS₂. *Nano Res.* **5**(1), 43 (2012)
38. K. He, C. Poole, K.F. Mak, J. Shan, Experimental demonstration of continuous electronic structure tuning via strain in atomically thin MoS₂. *Nano Lett.* **13**(6), 2931 (2013)
39. S. Ahmad, S. Mukherjee et al., A comparative study of electronic properties of bulk MoS₂ and its monolayer using DFT technique: Application of mechanical strain on MoS₂ monolayer. *Graphene* **3**(4), 52 (2014)
40. L. Yang, X. Cui, J. Zhang, K. Wang, M. Shen, S. Zeng, S.A. Dayeh, L. Feng, B. Xiang, Lattice strain effects on the optical properties of MoS₂ nanosheets. *Sci. Rep.* **4** (2014). doi:[10.1038/srep05649](https://doi.org/10.1038/srep05649)
41. H. Peelaers, C.G. Van de Walle, Effects of strain on band structure and effective masses in MoS₂. *Phys. Rev. B* **86**(24), 241401 (2012)
42. Y.Y. Hui, X. Liu, W. Jie, N.Y. Chan, J. Hao, Y.T. Hsu, L.J. Li, W. Guo, S.P. Lau, Exceptional tunability of band energy in a compressively strained trilayer MoS₂ sheet. *ACS Nano* **7**(8), 7126 (2013)
43. A. Newaz, D. Prasai, J. Ziegler, D. Caudel, S. Robinson, R. Haglund Jr., K. Bolotin, Electrical control of optical properties of monolayer MoS₂. *Solid State Commun.* **155**, 49 (2013)
44. S. Schmitt-Rink, D. Chemla, D. Miller, Theory of transient excitonic optical nonlinearities in semiconductor quantum-well structures. *Phys. Rev. B* **32**(10), 6601 (1985)
45. Z. He, Y. Sheng, Y. Rong, G.D. Lee, J. Li, J.H. Warner, Layer-dependent modulation of tungsten disulfide photoluminescence by lateral electric fields. *ACS Nano* **9**(3), 2740 (2015)
46. S. Mouri, Y. Miyachi, K. Matsuda, Tunable photoluminescence of monolayer MoS₂ via chemical doping. *Nano Lett.* **13**(12), 5944 (2013)
47. Y. Li, Z. Qi, M. Liu, Y. Wang, X. Cheng, G. Zhang, L. Sheng, Photoluminescence of monolayer MoS₂ on LaAlO₃ and SrTiO₃ substrates. *Nanoscale* **6**(24), 15248 (2014)
48. K.F. Mak, K. He, C. Lee, G.H. Lee, J. Hone, T.F. Heinz, J. Shan, Tightly bound trions in monolayer MoS₂. *Nat. Mater.* **12**(3), 207 (2013)
49. N. Scheuschner, O. Ochedowski, A.M. Kaulitz, R. Gillen, M. Schleberger, J. Maultzsch, Photoluminescence of freestanding single-and few-layer MoS₂. *Phys. Rev. B* **89**(12), 125406 (2014)
50. U. Bhanu, M.R. Islam, L. Tetard, S.I. Khondaker, Photoluminescence quenching in gold-MoS₂ hybrid nanoflakes. *Sci. Rep.* **4**, 5575 (2014). doi:[10.1038/srep05575](https://doi.org/10.1038/srep05575)
51. H. Nan, Z. Wang, W. Wang, Z. Liang, Y. Lu, Q. Chen, D. He, P. Tan, F. Miao, X. Wang et al., Strong photoluminescence enhancement of MoS₂ through defect engineering and oxygen bonding. *ACS Nano* **8**(6), 5738 (2014)
52. N. Peimyoo, W. Yang, J. Shang, X. Shen, Y. Wang, T. Yu, Chemically driven tunable light emission of charged and neutral excitons in monolayer WS₂. *ACS Nano* **8**(11), 11320 (2014)

53. J.O. Varghese, P. Agbo, A.M. Sutherland, V.W. Brar, G.R. Rossman, H.B. Gray, J.R. Heath, The influence of water on the optical properties of single-layer molybdenum disulfide. *Adv. Mater.* **27**, 2734 (2015)
54. R. Sundaram, M. Engel, A. Lombardo, R. Krupke, A. Ferrari, P. Avouris, M. Steiner, Electroluminescence in single layer MoS₂. *Nano Lett.* **13**(4), 1416 (2013)
55. Y. Ye, Z. Ye, M. Gharghi, H. Zhu, M. Zhao, Y. Wang, X. Yin, X. Zhang, Exciton-dominant electroluminescence from a diode of monolayer MoS₂. *Appl. Phys. Lett.* **104**(19), 193508 (2014)
56. J.S. Ross, P. Klement, A.M. Jones, N.J. Ghimire, J. Yan, D. Mandrus, T. Taniguchi, K. Watanabe, K. Kitamura, W. Yao et al., Electrically tunable excitonic light-emitting diodes based on monolayer WSe₂ p-n junctions. *Nat. Nanotech.* **9**(4), 268 (2014)
57. S. Jo, N. Ubrig, H. Berger, A.B. Kuzmenko, A.F. Morpurgo, Mono-and bilayer WS₂ light-emitting transistors. *Nano Lett.* **14**(4), 2019 (2014)
58. A. Pospischil, M.M. Furchi, T. Mueller, Solar-energy conversion and light emission in an atomic monolayer p-n diode. *Nat. Nanotech.* **9**(4), 257 (2014)
59. B.W. Baugher, H.O. Churchill, Y. Yang, P. Jarillo-Herrero, Optoelectronic devices based on electrically tunable p-n diodes in a monolayer dichalcogenide. *Nat. Nanotech.* **9**(4), 262 (2014)
60. Y. Zhang, T. Oka, R. Suzuki, J. Ye, Y. Iwasa, Electrically switchable chiral light-emitting transistor. *Science* **344**(6185), 725 (2014)
61. D. Li, R. Cheng, H. Zhou, C. Wang, A. Yin, Y. Chen, N.O. Weiss, Y. Huang, X. Duan, Electric field induced strong enhancement of electroluminescence in multi-layer MoS₂. *Nat. Commun.* **6** (2015). doi:[10.1038/ncomms8509](https://doi.org/10.1038/ncomms8509)
62. M. Zhang, J. Wu, Y. Zhu, D.O. Dumcenco, J. Hong, N. Mao, S. Deng, Y. Chen, Y. Yang, C. Jin et al., Two-dimensional molybdenum tungsten diselenide alloys: Photoluminescence, raman scattering, and electrical transport. *ACS Nano* **8**(7), 7130 (2014)
63. J. Mann, Q. Ma, P.M. Odenthal, M. Isarraraz, D. Le, E. Preciado, D. Barroso, K. Yamaguchi, G. von Son Palacio, A. Nguyen et al., 2-dimensional transition metal dichalcogenides with tunable direct band gaps: MoS_{2(1-x)Se_{2x}} monolayers. *Adv. Mater.* **26**(9), 1399 (2014)

Chapter 9

Excitons

The 2D nature of mono- and few-layer TMDCs plays a very important role in exciton behaviour. The extraordinary large exciton binding energy in 2D TMDCs forms a platform for both fundamental studies and novel applications. Various aspects of 2D excitons in TMDCs are described in this Chapter.

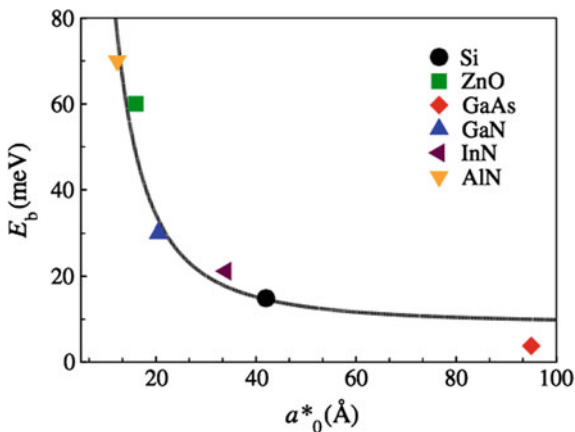
9.1 Excitons in 2D

An exciton is a bound state formed by an excited electron and hole due to Coulomb attraction [1]. Depending on the exciton radius and the strength of the Coulomb interaction between the electron and the hole, excitons in solids can be divided into two types. In materials with a small dielectric constant, such as ionic crystals, the electron and the hole are tightly bound to each other within the same or nearest-neighbor unit cells. Such excitons are called Frenkel excitons and have a typical binding energy on the order of 0.1–1 eV. Frenkel excitons are typically found in ionic crystals and in organic molecular crystals composed of aromatic molecules.

In semiconductors, on the other hand, the dielectric constant is generally large. Consequently, electric field screening by the valence electrons reduces the Coulomb interaction between electrons and holes, resulting in the exciton radius (much) larger than the lattice spacing. As a result, the effect of the lattice potential can be incorporated into the effective masses of the electron and hole. Such excitons are usually called Wannier (or Wannier-Mott) excitons. Because of the lower masses and the screened Coulomb interaction, the binding energy of the Wannier excitons is typically on the order of 0.01 eV (Fig. 9.1).

As the concentration of excitons is increased, four-particle complexes such as bi-excitons can also be formed (Fig. 9.2a) [3, 4] and are characterised in 2D TMDCs by binding energy that is more than an order of magnitude greater than that found in conventional quantum-well structures.

Fig. 9.1 Exciton binding energy (E_b) versus exciton Bohr radius [2]. Copyright 2013 by the American Physical Society. Reprinted with permission



In addition to neutral quasiparticles, charged quasiparticles (trions) can also be formed. The latter term refers to a three-particle complex, e.g. two electrons and a hole can form a negatively charged trion. Schematically excitons and trions are illustrated in Fig. 9.2b.

9.1.1 Exciton Binding Energy

In addition to the dielectric constant of the material, the binding energy of excitons also strongly depends on dimensionality α of the system. In a general case of α D space, the exciton binding energy is given by the following equation [6]:

$$E_n = -\frac{E_0}{(n + \frac{\alpha-3}{2})^2} \quad (9.1)$$

where n is the principal quantum number and E_0 is the exciton Rydberg.

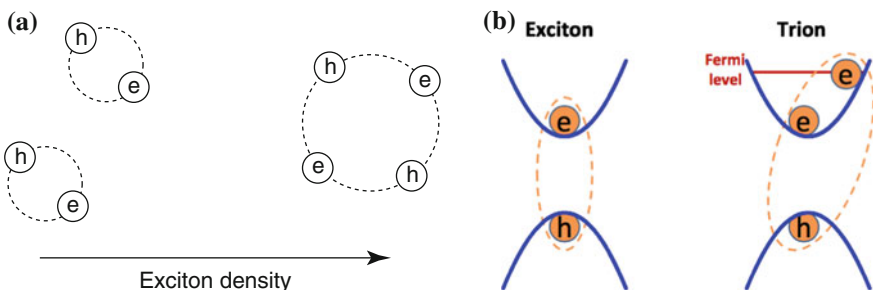


Fig. 9.2 **a** Schematics of the formation of bi-excitons. **b** Schematic representation of the quasiparticles, exciton (left) and trion (right), in the two-band model [5]. Copyright 2014 by the American Physical Society. Reprinted with permission

In the absence of dielectric effects, this yields an exciton binding energy that is a factor of 4 larger in 2D than in 3D. In the limit of atomically thin materials, however, the dielectric screening is additionally reduced because the electric field lines joining the electron and hole extend outside of the sample (Fig. 9.3a), which may lead to an even larger enhancement factor. Experimentally, enhancement of the exciton binding energy in monolayer TMDCs due to the very different dielectric environment outside the sample was observed e.g. in [7], based on optical investigation of monolayer and bulk WSe₂ in high magnetic fields.

Basic excitonic properties of a thin 2D layer differ fundamentally from those of three-dimensional bulk semiconductor of the same material. The real-space origin of this behavior in TMDCs is illustrated schematically in Fig. 9.3a. In contrast to the bulk phase, the electron and hole forming an exciton in a monolayer are strongly confined within the plane and additionally experience reduced screening due to the change in the dielectric environment. As noted in [8], these effects have two major implications on the electronic and excitonic properties of the material (Fig. 9.3b), namely, the quasiparticle band gap is expected to increase for the monolayer and also the enhanced electron-hole interaction is expected to increase the exciton binding energy.

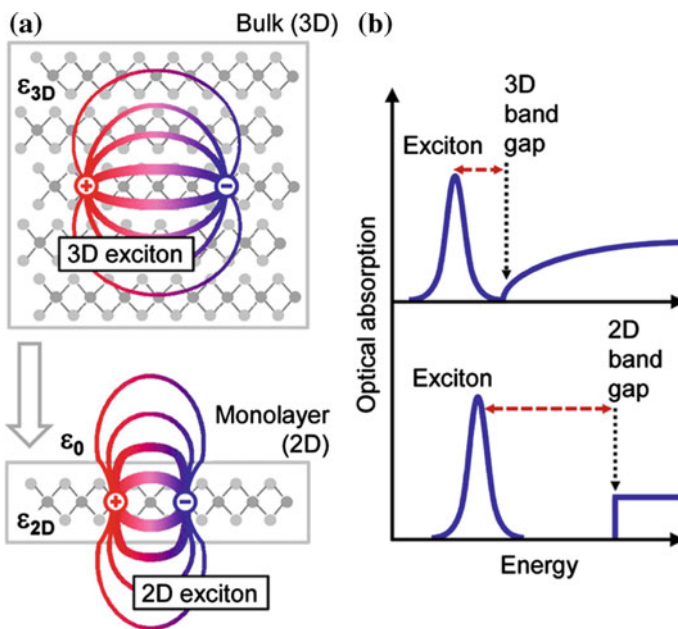


Fig. 9.3 **a** Real-space representation of electrons and holes bound into excitons for the three-dimensional bulk and a quasi-two-dimensional monolayer. The changes in the dielectric environment are indicated schematically by different dielectric constants ϵ_{3D} and ϵ_{2D} and by the vacuum permittivity ϵ_0 . **b** Impact of the dimensionality on the electronic and excitonic properties, schematically represented by optical absorption. The transition from 3D to 2D is expected to lead to an increase of both the band gap and the exciton binding energy (indicated by the *dashed red line*). The excited excitonic states and Coulomb correction for the continuum absorption have been omitted for clarity [8]. Copyright 2014 by the American Physical Society. Reprinted with permission

As a consequence, in low-dimensional materials, such as carbon nanotubes or 2D TMDCs, excitons have both Wannier-Mott and Frenkel character, i.e. the excitons are rather large (Wanner type) but strongly bound (Frenkel type). The exciton Bohr radius calculated by the GW-BSE method is on the order of 1 nm [9–11]. In [12], MoS₂ was studied and the effective Bohr radii of 9.3 Å for monolayer and 13.0 Å for bilayer were obtained with the effective binding energies of 0.224 and 0.106 eV for monolayer and bilayer, respectively, leading to the ground-state binding energy of 0.897 eV for monolayer and 0.424 eV for bilayer. Significantly larger values of 65 Å were reported in [13].

This is because the dielectric function is large enough to allow for the spatial extent of the wave function to extend over a few to several nanometers, while poor screening in the vacuum or dielectric environment allows for large binding energies. Excitonic bound states often play an important role in the optical properties of low-dimensional materials [14], owing to their strong spatial confinement and reduced screening effects compared to 3D solids. Correspondingly, the exciton wave function is well localized in momentum space.

In a two-dimensional (2D) gapped system with dipole-allowed interband transitions, the optical absorption spectrum in the non-interacting limit (i.e. ignoring the Coulomb interaction) acts like a step function. Strong electron-hole interaction red-shifts a large amount of the spectral weight, resulting in a qualitatively different spectrum with a series of new excitonic levels below the quasiparticle bandgap (Fig. 9.3b).

In quasi-2D quantum wells of conventional semiconductors, the electron-hole interaction is rather weak. Therefore, by measuring the energy difference between the first excitonic peak and the band-edge absorption step, the exciton binding energy can be unambiguously determined; it usually has an energy of tens of meV and is vulnerable to environment screening and temperature broadening. At the same time, experiments on a single-layer TMDCs such as MoS₂ found no absorption step [15, 16]. Instead, two absorption peaks resulting from spin-orbit splitting were detected around the Kohn-Sham band-gap energy, as given by density functional theory (DFT) within the local density approximation. The peaks were initially interpreted as direct band edge transitions. More accurate first-principles calculations on MoS₂ monolayer using the GW method [17] predicted a quasiparticle bandgap that was larger than the initial experimental reported value by nearly one electronvolt [11, 12, 18]. Relevant calculations based on first-principles GW-BSE theory [19] showed this energy gap discrepancy to originate from strong excitonic effects. It is therefore critical to uncover the underlying physics of the strong light-matter interaction in such 2D systems.

As mentioned in Chap. 6 there were significant efforts to determine band gaps and excitonic effects in TMDC monolayers using first-principles calculations. The state of the art approach to compute quasiparticle band structure and optical response including electron-electron interactions and excitonic contributions is the GW plus Bethe-Salpeter equation (GW-BSE). It was further noted that accurate description of excitonic states requires fine k -space sampling, since the excitonic states are correlated bound states in real space [11], as well a higher energy cut-off than is generally

used. Also, a much larger number of bands was required to obtain better agreement with experiment. By using a $72 \times 72 \times 1 k$ grid, a 476 eV energy cutoff and 6000 bands, excellent agreement with experiment was obtained [11] and it was predicted that the optical spectrum between 2.2 and 2.8 eV is not featureless, but contains many bright and dark excitonic states, which are broadened by electron-phonon interactions.

A theory of neutral and charged excitons in monolayer TMDCs based on an effective mass model of excitons and trions, parameterized by ab-initio calculations and incorporating a proper treatment of screening in two dimensions was developed in [9]. The calculated exciton binding energies are in good agreement with high-level many-body computations based on the Bethe-Salpeter equation. An analytical approach to study optical properties of TMDC, using MoS₂ as an example, was developed in [20].

Exciton band structure was also studied from the perspective of mirror, threefold rotational, and time-reversal discrete symmetries [21]. It was proposed that, due to the possible presence of low-energy exciton states that appear both near the Brillouin-zone center and near the Brillouin-zone corners (e.g. excitons that have electrons and holes in opposite valleys (K and K'), or excitons that have holes in the Γ valley and electrons in either the K or K' valley), a monolayer MoS₂ may appear to be an indirect gap material when judged by its excitation spectra.

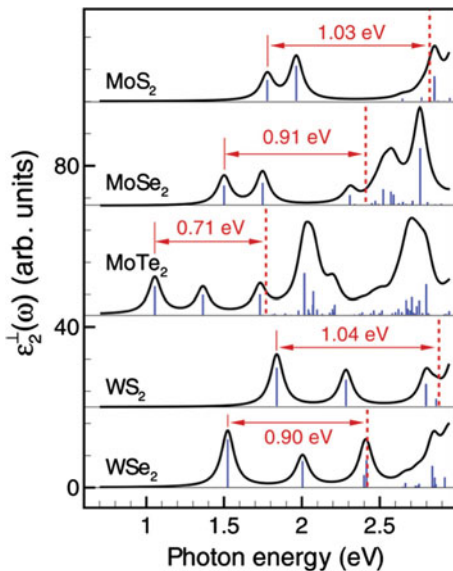
The optical spectrum of the monolayer group VIB TMDCs is characterized by the presence of two low-energy exciton peaks that arise from vertical transitions at the K point of the Brillouin zone from a spin-orbit-split valence band to a doubly degenerate conduction band. These excitons are confined to a (near) 2D geometry and are strongly bound due to poor dielectric screening in the monolayer.

One of the first papers to address the issue of excitons in few-layer TMDCs was [12], where the author used the quasi-particle self-consistent GW method. The obtained splittings of 146 meV in the monolayer and 174 meV in the bilayer agree very well with the energy difference between the A and B exciton peaks in the absorption spectrum reported in [15].

The Mott-Wannier effective-mass theory within the plane was used, assuming that at the length scale of the exciton Bohr radius, the electron and hole are both confined to $z = 0$ in the plane. The Coulomb interaction in the plane is screened by an effective dielectric constant $\kappa = \sqrt{\epsilon_{||}\epsilon_{\perp}}$ with $\epsilon_{||}$ and ϵ_{\perp} being the dielectric tensor components parallel and perpendicular to the c axis, respectively. The values of $\epsilon_{||} = 2.8$ (4.2) and $\epsilon_{\perp} = 4.2$ (6.5) were obtained for a mololayer (bi-layer). It was noted that the obtained values were much smaller than the bulk values. These values somewhat differ from those reported in [22] that were obtained using a different approach. Both calculations however agree on a strong reduction of the dielectric screening in the monolayer compared to the bulk.

Large excitonic effects in MoS₂ and WS₂ were also considered in [18], where it was noted that DFT is ill equipped to describe photoemission as the Kohn-Sham energies do not formally correspond to quasiparticle energies, which are required to correctly describe electron addition or removal events. To overcome this problem, the GW approximation was used, which goes beyond the mean-field,

Fig. 9.4 Imaginary part of the transverse dielectric constant $\epsilon_2^\perp(\omega)$ as a function of photon energy for MoX_2 and WX_2 monolayers. Vertical (blue) bars represent the relative oscillator strengths for the optical transitions. Red dashed lines indicate the G_0W_0 band gap. The binding energies of the A exciton are indicated in each case [18]. Copyright 2012 by the American Physical Society. Reprinted with permission. (Color figure online)



independent-particle DFT approach and properly accounts for many-body electron-electron interactions, subsequently accounting for the electron-hole interaction for their interaction by solving the Bethe-Salpeter equation (BSE) for the two-particle Green's function. It was noted that the spin-orbit splitting is sensitive to the level of theory employed, following the trend $\Delta^{PBE} < \Delta^{G_0W_0} < \Delta^{HSE}$.

Fig. 9.4 shows the absorption spectra calculated from BSE. Overall, the absorption spectra of all monolayers studied indicate the presence of two strongly bound excitonic peaks arising from vertical transitions at the K point from a spin-orbit-split valence band to a doubly degenerate conduction band. The exciton binding was found to become weaker as the chalcogen becomes heavier, which was interpreted in terms of the increased dielectric screening by the more diffuse orbitals of heavier chalcogens. At the same time, the exciton splitting was found to be larger in WX_2 compounds, compared to their MoX_2 counterparts [18].

9.1.2 Non-Rydberg Excitonic Series

The challenge in experimental determination of the exciton binding energy in 2D TMDCs by linear optical methods, commonly used for bulk semiconductors or conventional semiconductor QWs, lies in the identification of the onset of band-to-band transitions in the optical absorption or emission spectrum. As noted in [23] such an onset of band-to-band transitions has not been observed in 2D TMDCs presumably due to the significant transfer of oscillator strengths from the band-to-band transitions to the fundamental exciton states, lifetime broadening, and potential overlap in energy with exciton states originated from higher energy bands and/or different

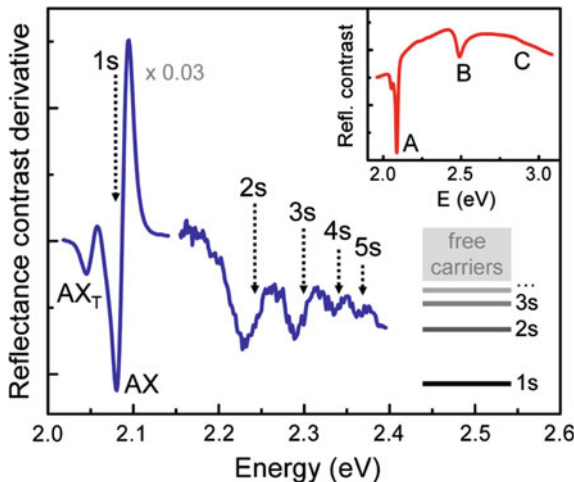


Fig. 9.5 The derivative of the reflectance contrast spectrum ($d/dE(\Delta R/R)$) of the WS_2 monolayer. The exciton ground state and the higher excited states are labeled by their respective quantum numbers (schematically shown at the bottom right). The spectral region around the $1s$ transition (AX) and the trion peak (AX_T) of the A exciton is scaled by a factor of 0.03 for clarity. The inset shows the as-measured reflectance contrast $\Delta R/R$ for comparison, allowing for the identification of the A , B , and C transitions [8]. Copyright 2014 by the American Physical Society. Reprinted with permission

parts of the Brillouin zone. An alternative is to determine the exciton excited states and evaluate the binding energy from the level spacing based on a model. In the simple 2D hydrogenic model, where an electron-hole pair in 2D interacts through a Coulomb potential, the energy spectrum is known as the Rydberg series. Measurements of the $1s$ and $2s/2p$ states allow one to determine the exciton binding energy in the 2D hydrogenic model.

The properties of excitons in mono- and few-layer WS_2 were experimentally and theoretically investigated in [8], where not only the ground-state exciton but the full sequence of excited (Rydberg) exciton states was characterized. The choice of WS_2 was determined by its large spin-orbit splitting between the A and B excitons of about 0.4 eV, allowing for a study of the low-energy excitons unobscured by features from higher-lying transitions.

To access these exciton properties experimentally, excitonic Rydberg series was studied, i.e., the excited states of the bound electron-hole pairs, labeled in analogy to the hydrogen series as $2s$, $3s$, and so on. The energy separation of these resonances corresponds to a hydrogenic progression for Wannier-like excitons. In addition, the coupling of the excited states to light is reduced compared to the main transition, so that their spectral weight decreases with increasing quantum number.

Experimentally, the reflectance contrast $\Delta R/R = (R_{\text{sample}} - R_{\text{substrate}})/R_{\text{substrate}}$ of the WS_2 mono-layer sample at a temperature of 5 K was measured. The $\Delta R/R$ spectrum (inset of Fig. 9.5), exhibits several pronounced peaks that cor-

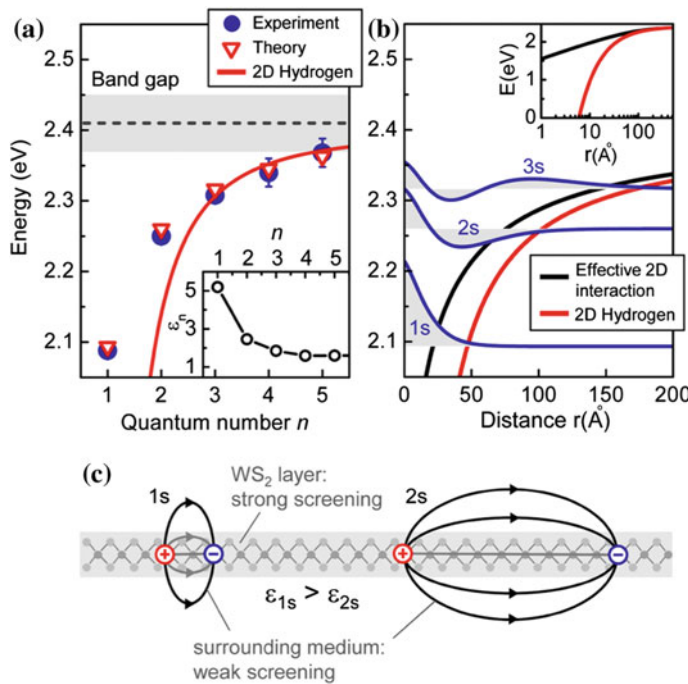


Fig. 9.6 **a** Experimentally and theoretically obtained transition energies for the exciton states as a function of the quantum number n . The fit of the $n = 3, 4, 5$ data to the 2D hydrogen model for Wannier excitons is shown for comparison. Gray bands represent uncertainty in the quasiparticle band gap from the fitting procedure. The corresponding effective dielectric constants are shown in the inset. **b** Screened 2D interaction used in the model Hamiltonian (black lines) compared to the 2D hydrogen interaction $1/r$ (red lines); a semilogarithmic plot is given in the inset. Also shown are the corresponding energy levels and radial wave functions up to $n = 3$. **c** Schematic representation of electron-hole pairs forming 1s and 2s excitonic states in a nonuniform dielectric environment [8]. Copyright 2014 by the American Physical Society. Reprinted with permission

respond to A , B , and C excitons. A small additional feature on the low-energy side of the A peak is interpreted as a charged exciton, or trion, with a binding energy on the order of 20–30 meV.

The authors focus on the properties of the A exciton, related to the fundamental band gap of the material [8]. In order to highlight the weak signatures of the higher-lying excitonic transitions, the derivative of the reflectance contrast $(d/dE)(\Delta R/R)$ in the energy range of interest was plotted (Fig. 9.5). On the high-energy side of the exciton 1s ground state, multiple additional peaks are clearly observed, which were identified as the 2s, 3s, 4s, and 5s states of the A exciton. The peak positions extracted by taking the respective points of inflection are shown in Fig. 9.6a.

To calculate the exciton binding energy, one must first determine the quasiparticle band gap corresponding to the energy of a separated electron-hole pair. At the simplest level, if an electron-hole pair interacts through a Coulomb attractive central potential,

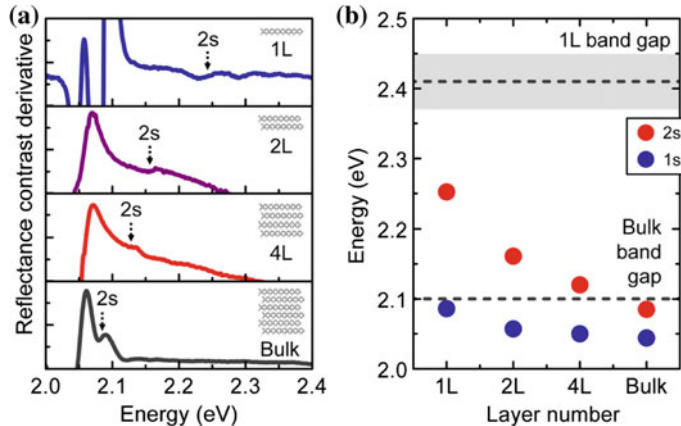


Fig. 9.7 **a** The derivative of the reflectance contrast spectra for 1L, 2L, 4L, and bulk WS₂. The positions of the 2s exciton resonance are indicated by *dotted arrows*. **b** Energies of the 1s and 2s states for various layer thicknesses. Band gaps of the bulk and the monolayer are represented by the *dashed lines* [8]. Copyright 2014 by the American Physical Society. Reprinted with permission

it will form a series of excitonic Rydberg-like states with definite parity, similar to the hydrogen model. It was found that in the 2D case the exciton energies exhibited a much weaker scaling with the quantum number n , precluding a simple fit to the data based on the hydrogen model. Only the $n = 3\text{--}5$ peaks were reasonably hydrogenic, and by fitting to these data points only, a quasiparticle band gap of E_g of ca. 2.41 eV was extracted from which an exciton binding energy of ca. 0.32 eV was obtained.

To understand the nonhydrogenic physics of the lower state excitons, the effective dielectric constant in the hydrogenic Hamiltonian was considered and the n -dependent dielectric constant ϵ_n required to reproduce the experimental binding energy of the n th exciton was determined. The results plotted in the inset of Fig. 9.6a show a strong decrease in the effective dielectric constant with increasing quantum number n . It was proposed that this can be understood in terms of a nonuniform dielectric environment schematically illustrated in Fig. 9.6c: the electric field between an electron and a hole forming an exciton permeates both the thin layer of material with comparably strong screening and the surrounding medium with much weaker screening. As the spatial separation between the charges increases, a larger portion of the electric field is located in the surrounding low-dielectric medium and the effective screening is reduced. This experimental observation is in line with the theoretical prediction that excitons in 2D semiconductors have a non-Rydberg series arising from the nonlocal character of screening of the Coulomb interactions [11, 24]. It may also be interesting to note that in bulk MoS₂ a proper Rydberg series for the exciton energy spectrum was observed [25, 26].

The influence of the material thickness on the higher resonances by monitoring the spectral position of the 2s resonance for varying thickness of the WS₂ sample was further studied. Individual derivatives of the reflection contrast are shown in Fig. 9.7a.

for the monolayer (1L), bilayer (2L), tetralayer (4L), and bulk. The corresponding energies of the 1s and 2s transitions are shown in Fig. 9.7b, with higher excited states masked by additional spectral broadening. As the layer thickness decreases, the 2s resonance shifts to higher energies, while the 1s resonance remains relatively unchanged, implying a strong increase in both the exciton binding energy and the quasiparticle band gap. The two shifts were found to be large in absolute energies but opposite in sign [8].

9.1.3 ‘Dark’ Excitonic States

Excitonic effects in monolayer WS₂ were also probed in [27], using two-photon excitation spectroscopy. It was noted that while the breaking of rotational and inversion symmetry owing to the crystal structure and the spatial dependence of screening will modify the energy and symmetry of the states from those of the 2D Rydberg series, for exciton states with an electron-hole wavefunction that is large compared to the unit cell size, specific parity may still be assigned to each excitonic state.

Incident photons can excite the electronic system from the ground state to one of these excitonic states (Fig. 9.8a). It was noted that in addition to energy conservation, the selection rules of such a transition depend on the symmetry of the final state: for systems with dipole-allowed interband transitions, one-photon transitions can only reach excitonic states with even parity (the case studied above [8]), while two-photon transitions reach states with odd parity. It was mentioned that two-photon resonances are sometimes called excitonic dark states because they do not appear in the linear optical spectrum.

The two-photon absorption induced luminescence (TPL) was monitored and a complete two-photon spectrum was obtained by scanning the excitation laser energy. Two important resonances of similar line widths occurring at 2.28 and 2.48 eV, corresponding to two excitonic dark excited states (Fig. 9.8b) were observed. The absorption spectrum of a WS₂ monolayer is also plotted for comparison, where the A exciton (the 1s state) and its trion result in two absorption peaks at 2.04 and 2 eV, respectively. It was noted that near these one-photon resonances, TPL is negligible, consistent with the 1s nature of these states, while no significant one-photon absorption is observed near the excitonic dark states, except for the B exciton (the other 1s state) at 2.45 eV which results from the spin-orbit splitting in the valence band. Such a complementary behaviour reflects the symmetry of the observed excitonic states.

The TPL peaks were labeled as the 2p and 3p state of the A exciton series. Accordingly, the 1s – 2p and 1s – 3p separations are 0.24 and 0.44 eV, respectively. The extraordinarily large 1s – np ($n = 2, 3$) separations suggest that the exciton binding energy, defined as the separation between the 1s exciton ground state and the conduction band edge, is larger than 0.44 eV, which also indicates a significant self-energy contribution to the quasiparticle band gap. Based on this result, it was concluded that the previously claimed band-to-band transition mechanism in the optical response of monolayer WS₂ is inaccurate: the optical response is dominated

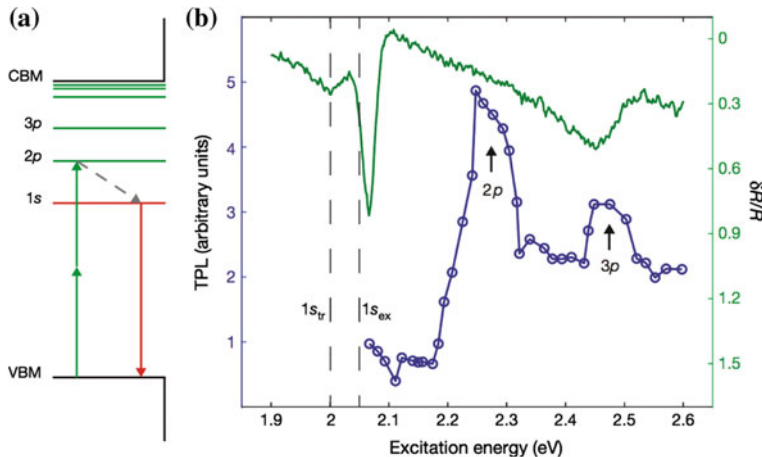


Fig. 9.8 **a** Schematic of the TPL process in single-layer WS₂. Under two-photon excitation, electrons transition to one of the excitonic dark states with odd parity (*double green arrow*). Following the excitation, the exciton experiences a fast relaxation to the excitonic ground state (*grey arrow*) and emits a photon (*red arrow*). The two-photon selection rule completely eliminates the one-photon transition background and reveals the excitonic excited states. States are labelled *s* (*red*) or *p* (*green*) according to the excitonic envelope wave function character. CBM and VBM represent respectively the conduction band minimum and the valence band maximum. **b** Extraordinarily strong excitonic effect in monolayer WS₂. Two-photon absorption (*blue*) and one-photon absorption (*green*) spectra are measured in single-layer WS₂ at 10K. In the two-photon absorption spectrum, 2*p* and 3*p* resonances are observed at 2.28 and 2.48 eV, respectively, on top of a plateau background. For comparison, the one-photon absorption spectrum, measured as the relative reflectance signal ($\delta R/R$), exhibits no corresponding features except a *B* exciton (*1s*) related absorption resonance at 2.45 eV. Additionally, the *A* exciton ($1s_{ex}$) and trion ($1s_{tr}$) absorption peaks are detected consistently with the TPL emission peaks, with a 20 meV Stokes shift, and are marked at 2.04 and 2 eV, respectively, by *black dashed lines*. The energy difference between the *A* exciton 1s state emission peak and the 3*p* state absorption peak is 0.44 eV, which yields the lower bound for the exciton binding energy in monolayer WS₂. This binding energy is extraordinarily large for a Wannier exciton, and implies that an excitonic mechanism is dominant for the intense light-matter interaction in 2D TMDCs [27]. Reprinted by permission from Macmillan Publishers Ltd., copyright (2014)

by excitonic states within the bandgap, in agreement with the GW-BSE calculation of MoS₂ [11]. It was further concluded that real quasiparticle bandgap is much larger than previously reported [27] and proposed that this result may be general for other TMDC monolayers with similar structure.

The quasiparticle band structure was also studied using the ab-initio GW-BSE approach to calculate the excitonic states and optical spectrum of a WS₂ monolayer. In spite of its Wannier character, it was found that the exciton series in monolayer WS₂ deviates significantly from a 2D hydrogen model, in agreement with the findings of [8, 11]. An interesting finding from the GW-BSE calculations was that states in the same shell but of higher orbital angular momentums are at lower energy levels, that is, $E_{3d} < E_{3p} < E_{3s}$. It was proposed that these two exotic energy-level behaviours are caused by a strong spatial-dependent dielectric screening: in an atomically thin

semiconductor, the screening effect at more than a certain distance is weaker when the separation between the electron and hole is bigger, which is known as the dielectric confinement effect in 2D quantum wells [27]. Since the wavefunction of excitonic states with higher principal or higher orbital quantum number features a larger nodal structure near the hole (that is, a larger average electron-hole separation), weaker screening at larger separation leads to enhanced Coulomb attraction in the excited states and therefore a lowering of their excitation energies as compared with those of the hydrogen model [27].

Finally, by measuring two-photon spectra of monolayer WS₂ with different dielectric capping layers, including water, immersion oil and aluminium oxide, it was demonstrated that the excitonic ground state and low-energy excited states with large binding energy were robust to environmental perturbations [27], which was attributed to the opposite effects of the dielectric screening on the exciton binding energy and the quasiparticle self-energy [28, 29].

The exciton binding energy was determined to be 0.71 eV in a monolayer of WS₂ using a combination of transmission spectroscopy and two-photon photoluminescence excitation [30] while the lower bound for the binding energy in this material was determined to be 0.83 eV based on reflectivity measurements [31].

A combined linear and nonlinear optical study on the exciton excited states and binding energy was also performed for monolayers of WSe₂ [23]. The linear absorption measurement revealed up to five *s* states from the *A* exciton series even at room temperature. Two-photon photoluminescence excitation spectroscopy was employed to probe the *p*-states and measure the band edge energy directly. A band gap energy of 2.02 eV and an exciton binding energy of 0.37 eV were determined for monolayer WSe₂ from the experimental results without relying on any specific exciton models. (For comparison, from reflectivity measurements the lower bound for the exciton binding energy was found to be 0.79 eV in a monolayer of WSe₂ [31]). As in the results discussed above, the measured exciton excitation spectrum with much more evenly spaced energy levels is very distinct from the simple 2D hydrogenic model. Also in agreement with the discussion above, it was found that with increasing energies, the states are expected to be more Rydberg-like and provide a better basis for the estimation of the exciton binding energy based on the 2D hydrogenic model.

In addition to the dielectric screening issue responsible for the deviation from the Rydberg series, the hypothetical possibility of the effect of non-parabolic band dispersion was also considered and ruled it out based on the obtained results [9, 32].

The dark spin-singlet excitons have also been investigated and found to exhibit another deviation from the hydrogen model, in the form of a broken angular momentum degeneracy [33].

It was proposed that the unique spectrum of exciton states with differing optical activities may present new opportunities for the study and control of the spin/valley polarization in 2D TMDCs through inter-excitonic and intra-excitonic processes.

The excitonic Rydberg states in monolayers of MoS₂ and WS₂ were also studied using photoluminescence excitation spectroscopy [34] where excited exciton transitions were detected. Based on the obtained results, the exciton binding energies were determined to be 0.32 eV in WS₂ and 0.44 eV in MoS₂.

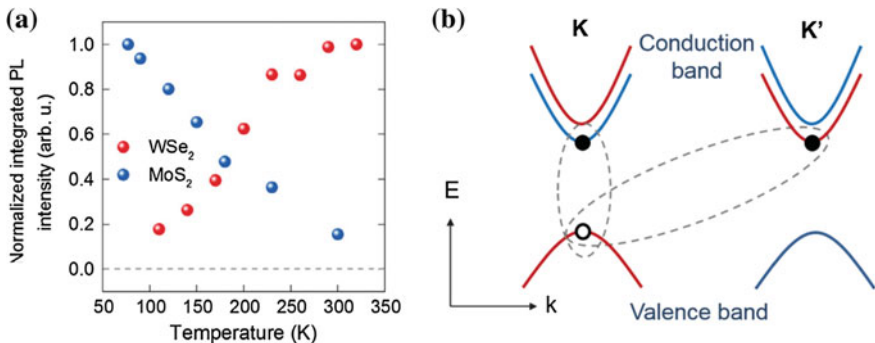


Fig. 9.9 **a** Comparison of temperature dependence of the time-integrated PL intensity of WSe₂ and MoS₂. **b** A schematic representation of the valence and conduction band structure predicted for monolayer WSe₂, with blue and red corresponding to the two spin states of electrons. The conduction band splitting is responsible for the dark exciton states. Shown by dotted lines are the lowest energy excitons: the intravalley dark excitons, i.e., $|K_{e\uparrow}K_{h\uparrow}\rangle$ and $|K'_{e\downarrow}K_{h\downarrow}\rangle$, and the intervalley dark excitons, i.e., $|K_{e\uparrow}K'_{h\downarrow}\rangle$ and $|K'_{e\uparrow}K_{h\uparrow}\rangle$ [37]. Copyright 2015 by the American Physical Society. Reprinted with permission

Excitonic resonances in 2D TMDCs was studied in detail for WSe₂ [35] and MoSe₂ [36] from monolayers to the bulk limit. An interesting observation was the fact that PL intensity *increased* with temperature for monolayer WSe₂ [35]. It was speculated that this unusual behaviour was caused by the presence of dark excitonic states located below the bright exciton state. The same observation was subsequently reported in [37] and is illustrated in Fig. 9.9a.

The authors of [37] consider the physical origin of this dark state in detail starting with the character of the relevant electronic bands in monolayer WSe₂ and taking into account the fact that conduction band splitting varies among different TMDCs. Specifically, for WX₂ (X = S, Se), electrons in the lower conduction band are expected to have spin polarization opposite to those in the upper valence band; in contrast, for MoX₂ (X = S, Se), electrons in the lower conduction band are expected to have spin polarization that matches that in the upper valence band [38–40]. They further examine the energies of the different possible excitonic states, taking into account the spin and valley degrees of freedom at the K/K' points. Because of the large spin splitting in the valence band, for the A exciton emission, we need only to consider photoexcited holes as residing in the upper valence band. At the same time, for the photoexcited electrons, there are four possible states (two valleys and two spins). Consequently, there is a total of eight different species of excitons. Among them, there are two bright excitons, i.e., the singlet-like intravalley exciton, and six dark excitons, i.e., the triplet-like intravalley excitons and all intervalley excitons. For WSe₂, with the conduction band ordering described above, the triplet-like intravalley excitons and the singlet-like intervalley excitons are degenerate and have the lowest energy, as depicted schematically in Fig. 9.9b. The discussion also considers

the influence of $e-h$ exchange interactions, which would lead to a more complex spectrum of states [37].

Variation in the magnitude and sign of spin-orbit splitting among different TMDCs was the basis of spin-orbit-engineering in $\text{Mo}_{1-x}\text{W}_x\text{S}_2$ alloy monolayers proposed in [41]. In this work, the impact of the tuning of the conduction band spin-orbit spin-splitting on the bright versus dark exciton population was also studied.

9.1.4 *Excitonic Collapse*

While the above ascription of the excitonic states (those probed by linear processes to s -states and those probed by two-photon processes to p -states) seems to be generally accepted, it should be noted that using the formalism of relativistic quantum mechanics, strong Coulomb coupling can lead in extreme cases to an excitonic collapse accompanied by merging of the $1s$ states into the band structure continuum [42, 43]. Simple selection rules show that only s -like excitonic states couple to the light field, resulting in the well-known excitonic Rydberg series, and the assignment of the lowest optical active state to the $1s$ exciton resonance is based on these selection rules. However, the s -type optical selection rules follow from the implicit assumption that the system is excited from the non-interacting ground state. In a strongly interacting system, the ground state itself may be excitonic [43] in which case the optical transitions correspond to intra-excitonic transitions, that are governed by fundamentally different optical selection rules and, correspondingly, to different peak assignments, making p -states bright and s -states dark.

While this possibility seems rather exotic and should be further investigated, it should be noted that the energy positions of the various observed features assigned using this approach agrees much better (within the Rydberg model) with experiment than the conventional assignment (Fig. 9.10). It also provides a natural explanation of the resonant increase of second harmonic generation for energies corresponding to $1s$ resonances of A and B excitons (see Sect. 12.1).

9.1.5 *Effect of Surrounding Dielectric Media*

As mentioned above, variation of the dielectric media surrounding WS_2 did not have an effect on the excitonic energy [27]. A different result was obtained in [44], where the influence of the dielectric constant of the environments on the exciton behavior of single-layer MoS_2 was systematically investigated. To prevent doping or strain effects that may be induced by the fabrication process or the lattice mismatch between MoS_2 and the dielectrics, nonionic organic solvents were used as the environmental dielectrics, having the relative dielectric constants in a very large range varying from 2 to 33.

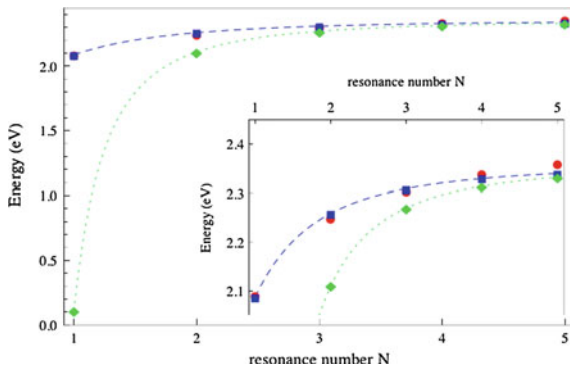


Fig. 9.10 Spectral position of the energetically lowest bright excitonic transitions with $j = \pm 3/2$ in WS_2 . The blue squares are the computed results assuming bright p -type excitons, the red dots show the experimental data taken from [8], and the green diamonds indicate the theoretical predictions if one assumes s -type bright states, respectively. The dashed and dotted lines are guides to the eye. The x -axis label denotes the number N of the experimentally observed bright exciton resonances and is related to the principle quantum number via $n = N - 1$. The inset to the figure shows the results for the energetically higher states with a finer energy resolution [43]. Reprinted with permission from IOP Publishing Ltd

In Fig. 9.11a, a typical PL spectrum in one of the solvents (anisole) was fitted with three peaks, which were assigned to originate from the radiative combination of the A^- trion (ca. 1.85 eV), A exciton (ca. 1.90 eV), and B exciton (ca. 2.03 eV), respectively. It was noted that the intensity of the A^- trion peak (black curve) is comparable with the intensity of the A exciton (red curve). The peak positions and accumulated intensities normalized by the A_{1g} Raman peak intensities as a function of the dielectric constant of the solvents are plotted in Fig. 9.11b, c. The energy positions of all three peaks increased as the dielectric constant of the solvent increased, whereas these blue shifts started to saturate when the dielectric constant exceeded 18. The A^- trion peak shifted faster than the A exciton peak.

The intensities of the PL peaks were enhanced approximately exponentially as a function of the dielectric constant of the solvent. The A^- trion peak was enhanced by ca. 4 times, while the A exciton peak by ca. 20 times, and the B exciton peak by less than 2 times.

Special care was taken to exclude other possible environmental factors that may have also influenced the electron-to-photon transition energies, such as temperature, mechanical strain, doping or interference effects.

Figure 9.11e shows the relative binding energies of the A and B excitons and of the A^- trion as a function of the effective dielectric constant. Both the electronic band gap and the exciton binding energies are relatively large when MoS_2 is in vacuum and decrease rapidly with the effective dielectric constant.

It was finally noted that the intensity ratio of trions and excitons can also be tuned by the environmental dielectric constant [44]. As shown in Fig. 9.11f, the A^-/A

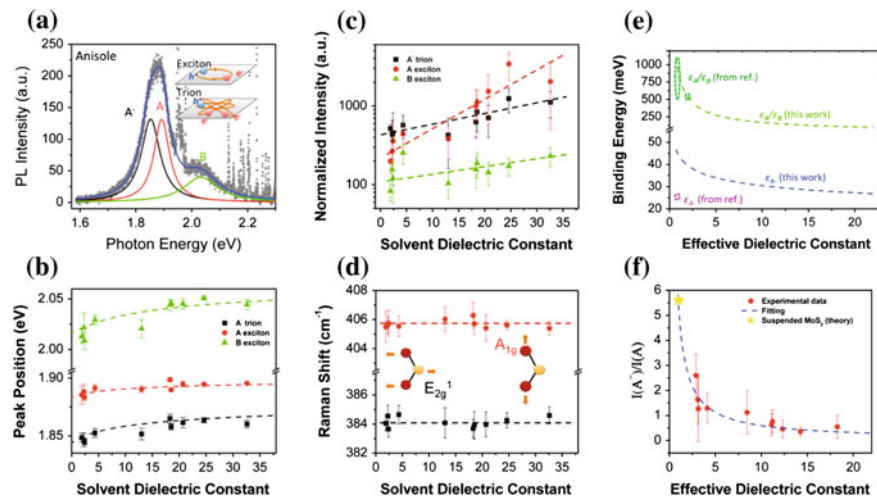


Fig. 9.11 **a** A typical PL spectrum of single-layer MoS₂ that is immersed in anisole. The gray dots are experimental data, and the black, red, and green lines are the three fitted peaks by Lorentzian functions. The blue line is the summation of the fitting peaks, which matches the experimental data very well. The inset schematics demonstrate the classical pictures of a trion and an exciton, which are bound states of 2 electrons with 1 hole, and 1 electron with 1 hole, respectively. **b** The PL peak positions as a function of the solvent dielectric constant. The dots with error bars are experimental data, and the dashed curves are fitting curves from the scaling relationship. **c** Accumulated PL intensities normalized to the A_{1g} Raman peak intensities with the dots together with their error bars showing experimental data and the dashed lines are the guides to the eye. **d** Raman shifts of the E_{2g}^1 and A_{1g} vibrational modes as a function of the solvent dielectric constant. The inset schematics indicate the directions of the vibration of each atom for each mode. **e** Dependence of the binding energies of the A/B exciton (green) and A^- trion (blue) on the effective dielectric constant. **f** Dependence of the A^-/A intensity ratio on the effective dielectric constant. The red dots with error bars are experimental data, and the blue dotted line is the fitting results from the mass action model [44]. Copyright 2014 American Chemical Society. Published with permission

intensity ratio decreased from 2.5 to 0.4 as the effective dielectric constant varied from 3 to 20.

A related effect was reported for folded monolayer MoS₂, where a blue-shift of the A^- exciton peak was reported [45], which was explained in terms of exciton screening.

It is interesting to note that reduced dielectric screening also affects the energy transfer between semiconductor nanodots in contact with few-layer TMDCs [46], where PL from CdSe and InAs quantum dots was studied (Fig. 9.12). For the former, the PL energy was located above the absorption edge of MoS₂, while for the latter the bandgap energy was smaller than that of MoS₂. Strong quenching of fluorescence from CdTe dots was observed when the latter were placed on top of MoS₂, the quenching being faster for thinner layers. In contrast, the photoluminescence lifetime of InAs quantum dots remained unchanged when placed on top of a MoS₂ surface.

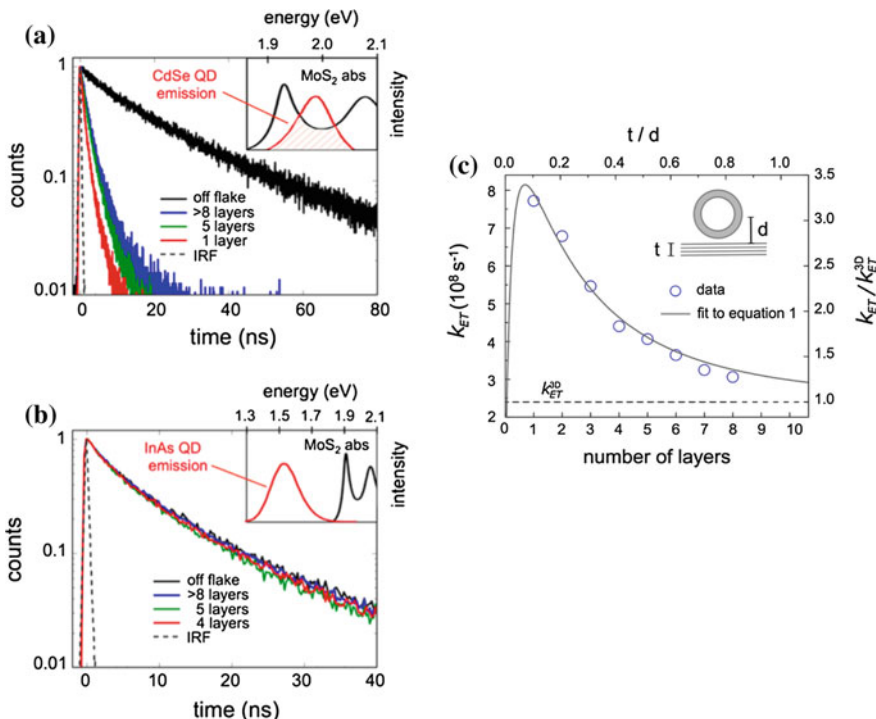


Fig. 9.12 **a** Fluorescence lifetime histograms of CdSe quantum dots placed on MoS₂ of different thicknesses. The *black curve* is obtained from quantum dots on top of SiO₂. The *dashed gray curve* represents the instrument's response function. Inset: spectral overlap between CdSe quantum dot emission and MoS₂ absorption spectra. **b** Same as (a) but for InAs quantum dots with a bandgap energy below the MoS₂ bandgap. **c** Energy transfer rate as a function of the number of MoS₂ layers. The *dashed line* represents the energy transfer rate to thick, bulk-like MoS₂. *Blue circles* indicate experimental data with associated uncertainty that is smaller than the size of the symbols. The *solid line* is a theoretical fit [46]. Copyright 2014 American Chemical Society. Published with permission

It was further shown that, as a result of reduced dielectric screening in thin layers, the energy transfer rate was significantly enhanced compared to the bulk [46].

9.1.6 Intra-Excitonic Transition

Intra-excitonic transitions between different exciton quantum states in monolayer WSe₂ were studied in [47]. In this work, in contrast to the interband absorption that is used to measure the ability to generate bound electron-hole pairs, intra-excitonic absorption probes existing excitons through transitions from the 1s ground state to higher relative-momentum states, such as 2p, by absorption of mid-infrared phonons. In this scheme, the exciton 1s ground state was photogenerated by a 90-fs pulsed laser centered at $\lambda = 742 \text{ nm}$. After a variable delay time t_{pp} , the low-energy dielectric

response was probed by a phase-locked mid-infrared pulse as illustrated in Fig. 9.13a. The measurements revealed a clear absorption resonance for an infrared photon energy of 165 meV, which was attributed to the $1s - 2p$ resonance, in agreement with earlier data for interband spectroscopy [48].

Once excitons are optically created at $K \sim 0$ they may either recombine radiatively (Fig. 9.13b) or scatter with phonons or background carriers into dark states outside the light cone. Large-momentum states are still visible to the probe pulse, but their radiative annihilation is blocked and the fastest remaining decay channel is given by Auger recombination (Fig. 9.13c). The utilised methodology provides access to the entire exciton population in momentum space, including excitons that appear ‘dark’ in standard interband spectroscopy (Fig. 9.13b, c) [47, 49].

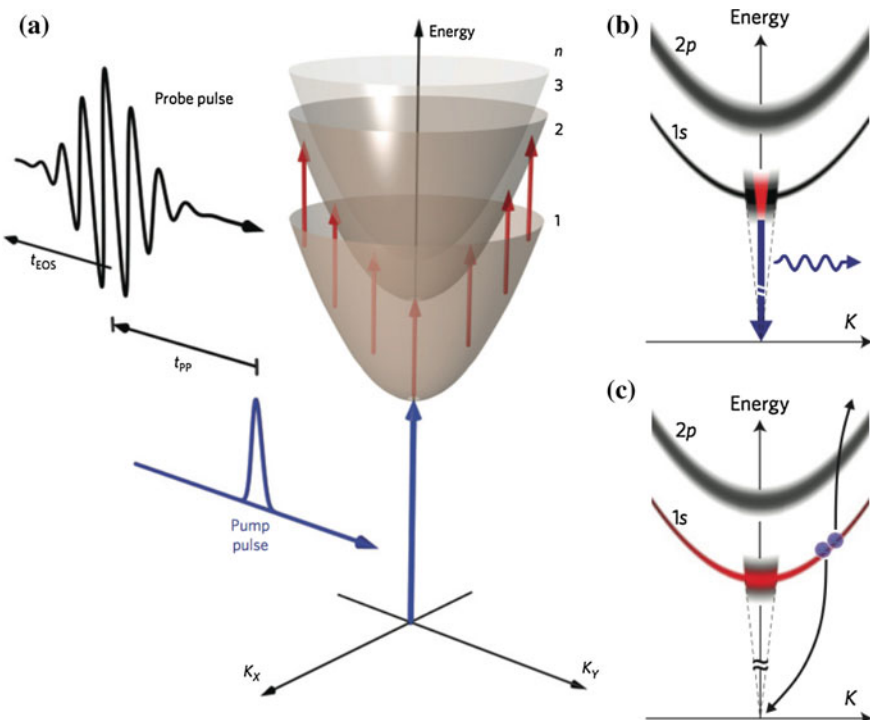


Fig. 9.13 **a** Schematic dispersion (paraboloids) of excitons with different principal quantum numbers n , as a function of the centre-of-mass momentum $K = \sqrt{K_x^2 + K_y^2}$. In the time-resolved pump-probe experiment, $1s$ A excitons are resonantly generated at $K \sim 0$ by a 90-fs near-infrared pump pulse (blue) while a mid-infrared transient (black waveform) delayed by t_{pp} probes the internal $1s - 2p$ transition (red arrows) of all pre-existing excitons, irrespective of K . **b** Schematic of the ultrafast radiative interband recombination (blue arrow) of optically bright $1s$ excitons (red area) at $K \sim 0$ within the light cone (black dashed lines). **d** Non-radiative exciton annihilation by Auger recombination (black arrows) of a dark population (red area) of excitons (blue spheres) with large centre-of-mass momenta [47]. Reprinted by permission from Macmillan Publishers Ltd., copyright (2015)

9.2 Exciton Dynamics

Exciton dynamics in 2D TMDCs was a subject of various studies and the main results are reviewed below. In this chapter we do not discuss processes associated with spin-valley coupling, which is the subject of a dedicated chapter.

Exciton dynamics in atomically thin MoS₂ was studied using ultrafast pump-probe spectroscopy [50]. Spectrally and temporally resolved measurements were performed to investigate the interaction dynamics of two important direct-gap excitons (*A* and *B*) and their associated broadening kinetics. The two excitons showed strongly correlated inter-excitonic dynamics, in which the transient blue-shifted excitonic absorption was attributed to the internal *A*-*B* excitonic interaction. The complex spectral response was interpreted in terms of the exciton collision-induced line width broadening, where the broadening of the *B*-exciton line width in turn lowered the peak spectral amplitude of the *A* exciton. Resonant excitation at the *B*-exciton energy revealed that inter-excitonic scattering played a more important role in determining the broadening kinetics than free-carrier scattering.

In [51] the authors observed the appearance of a low-energy PL peak at low sample temperatures, which was attributed to a bound exciton state. Time-resolved PL showed that the PL decays on the ps timescale at low temperatures, but develops a long-lived component at higher temperatures, and was explained by exciton-phonon scattering.

Exciton dynamics in suspended monolayers and few-layers of MoS₂ was studied in [52] in comparison with bulk samples. Kinetics taken at different wavelengths (in the 660–690 nm range) for both monolayer and few-layer samples exhibited an instantaneous rise within the pulse width of 500 fs followed by multiexponential decays that could be fitted with three decay time constants, namely $\tau_1 = 2.6$ ps, $\tau_2 = 74$ ps and $\tau_3 = 850$ ps. It was noted that the dynamics of the thick crystal were remarkably different from those of the monolayer and the few-layer cases, namely the thick crystal exhibited a biexponential rise with time constants of 1.8 and 20 ps, contrary to the instantaneous (< 500 fs) rise observed in monolayers and few-layers. After the initial rise, the dynamics in the bulk decayed with a single exponential decay of ca. 2600 ps. The experimental results are shown in Fig. 9.14.

The multiexponential nature implies that more than one relaxation process is involved. Because the fast decay was extremely rapid and did not exhibit a strong dependence on pump fluence, exciton–exciton annihilation was ruled out and the fast decay time τ_1 was attributed to trapping of the excitons by surface trap states. The intermediate decay time constant τ_2 was similar to the interband carrier-phonon scattering time observed in photoluminescence lifetime measurements, which was found to be strongly dependent on temperature [52] in both monolayer and few-layer structures. Finally, the slowest decay component τ_3 observed in monolayer and few-layer cases on the order of hundreds of picoseconds was assigned to a direct interband electron-hole recombination, that is significantly faster than the indirect recombination time in the bulk. Charge carrier dynamics in bulk MoS₂ using transient absorption microscopy was also studied in [53], where three characteristic times

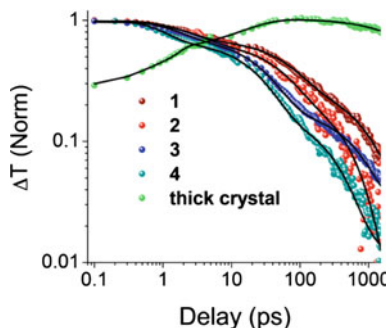


Fig. 9.14 Transient absorption dynamics of MoS₂ with pump wavelength of 387 nm and a probe wavelength of 670 nm for various sample positions presented in a log-log scale (*1*—suspended monolayer, *2*—supported monolayer, *3*—suspended few-layer, *4*—supported few-layer). Exciton dynamics in the bulk is probed at 690 nm. The *solid lines* are fits of a triexponential decay function convoluted with a Gaussian response function [52]. Copyright 2013 American Chemical Society. Published with permission

were found: 0.35 ps associated with intervalley transfer, 50 ps related to hot carrier relaxation, and 180 ps that characterises carrier life time.

In an ultrafast pump-probe differential reflectance measurements study [54] of atomically thin MoS₂, a decay time of ca. 100 ps was found using a pump energy of 3.179 eV (much higher than the exciton energy).

Using near-resonance conditions a fast exciton decay time of ca. 4 ps was observed in MoS₂, which was essentially unchanged in the temperature range of 4–300 K [55]. It was further noted that upon increasing the temperature, in addition to the ps exciton decay, a longer-lived (ca. 125 ps) component was observed. When discussing the origin of the fast decay, nonradiative processes and the intrinsic exciton lifetime were considered as possible mechanisms, noting that systems with large exciton binding energies have intrinsic exciton radiative lifetimes on the order of a few ps.

In [56] the possible important role of Auger recombination in 2D TMDCs resulting from strong Coulomb interaction and abrupt boundaries was highlighted. Auger processes were also discussed with respect to defect-assisted electron-hole recombination [57].

Exciton dynamics were also studied for monolayers and bilayers of WSe₂ [58, 59]. In monolayers, a rather complicated behavior was observed. Two individual components were deduced from results of the time-resolved PL response that could be well fitted with a biexponential decay function. Both time constants increased with rising temperature and drop with further increase of temperature above 260 K. The short-lived component varied from 20 ps at 130 K to 60 ps at 260 K, while the long-lived component varied from 70 ps at 130 K to 250 ps at 260 K.

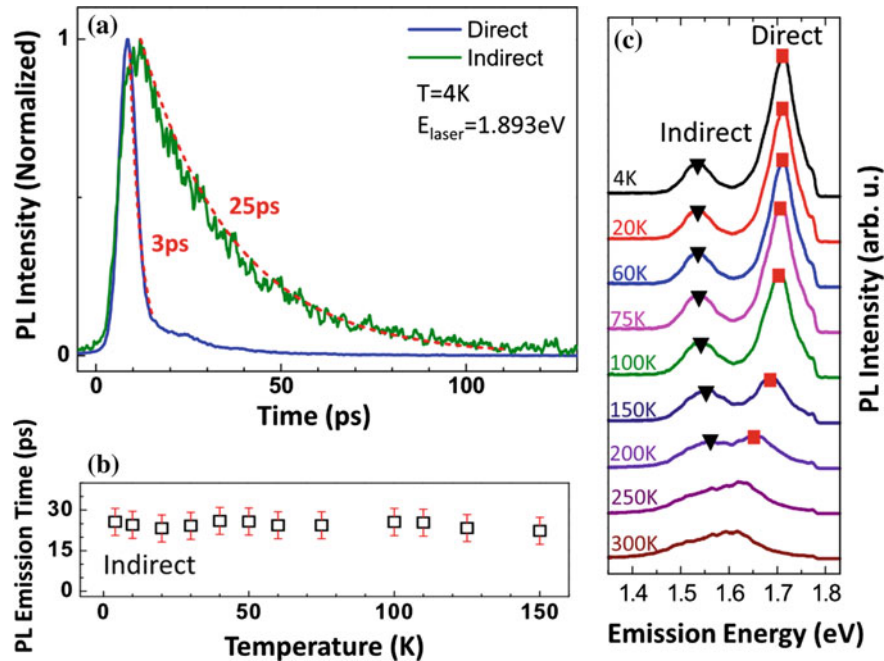


Fig. 9.15 **a** Normalized PL intensity in WSe₂ bilayers as a function of time for the indirect (green line) and direct (blue line) transitions at $E = 1.535$ eV and $E = 1.711$ eV, respectively. The picosecond laser energy is $E_{\text{laser}} = 1.893$ eV. The red dotted lines correspond to mono-exponential fits. **b** Temperature dependence of the PL emission time of the indirect transition. **c** PL spectra of both the direct and indirect transitions as a function of temperature. The fitted direct (indirect) peak energy is indicated by red squares (black triangles) [58]. Reprinted with permission. Copyright 2014 by the American Institute of Physics

In WSe₂ bilayers, excitons associated with direct and indirect transitions could be detected by PL [58] that had very different recombination times. In Fig. 9.15a, the exciton kinetics for both optical transitions are shown for $T = 4$ K. The indirect transition is characterized by a PL decay time (ca. 25 ps) about one order of magnitude longer than the direct one, which was attributed to the fact that an indirect transition requires in addition absorption or emission of a phonon. The indirect transition decay time was independent of the temperature (Fig. 9.15b) up to 150 K. At higher temperatures the two peaks merge (Fig. 9.15c) and unambiguous life time determination becomes impossible.

Exciton dynamics in monolayers and bulk MoSe₂ was studied in [60] where the exciton life times of 130 and 210 ps were determined for the monolayer and bulk samples respectively.

Exciton dynamics in TMDC monolayers and bi-layers (and also in TMDC heterostructures) were also studied from first principles [61].

9.2.1 Exciton–Exciton Interaction

9.2.1.1 Exciton–Exciton Annihilation

Several groups independently reported exciton–exciton annihilation (EEA) in TMDC monolayers [62–64]. In [64] it was noted that PL in WSe₂ was strongly nonlinear with an appearance of a strong fast component at higher excitation densities. In particular, strong nonlinear saturation behavior of exciton PL with increasing excitation power density and long-distance exciton diffusion, reaching several micrometers was observed. Figure 9.16a shows the normalized PL spectra of 1L-WSe₂ on a quartz substrate, obtained by increasing the excitation power density, where each PL spectrum is normalized by the corresponding excitation power density. It was noted that while the PL intensity increased with increasing excitation power density, the relative intensity of the normalized PL spectrum gradually decreased, which suggests strong saturation behavior of the PL spectra as a function of the excitation power density. At the same time, the shape of the PL spectra was unchanged between the weak ($0.006 \mu\text{J}/\text{cm}^2$) and strong ($12 \mu\text{J}/\text{cm}^2$) excitation power densities (Fig. 9.16b), suggesting that the formation of trions or defect-trapped excitons can be neglected. Figure 9.16c shows the integrated PL intensity of 1L-WSe₂ as a function of excitation power density demonstrating strong nonlinear PL behavior. This strong nonlinear PL response in

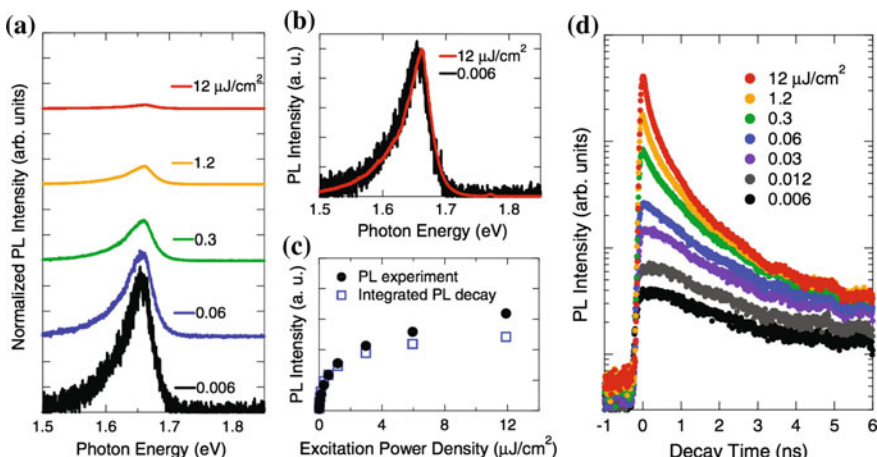


Fig. 9.16 **a** PL spectra of 1L-WSe₂, with varying excitation power densities. PL spectra are normalized by the corresponding excitation power density. **b** PL spectra of 1L-WSe₂ normalized by their peak values with excitation power densities of 12 and $0.006 \mu\text{J}/\text{cm}^2$. **c** PL intensity as a function of excitation power density (black circles). Calculated PL intensity deduced from the integration of the PL decay profile over the whole time range as a function of excitation power density (blue squares). **d** PL decay profiles of 1L-WSe₂, with varying excitation power densities. The vertical axis for the PL intensity has a logarithmic scale [64]. Copyright 2014 by the American Physical Society. Reprinted with permission

WSe₂ was contrasted to the previously reported linear response in MoS₂ [51] but this comparison should be taken with care because in the latter work only the intensities but not the power densities were reported.

To understand the origin of the strong nonlinear PL behavior, the time-resolved PL decay in 1L-WSe₂ was measured at various excitation power densities (Fig. 9.16d). It was noticed that under low-excitation conditions (<0.03 μJ/cm²), the shape of PL decay profile did not change but under higher-excitation conditions, a rapid PL decay component noticeably appeared with increasing excitation power density, so that the PL decay curves were composed of two components with time constants of 4 and 12 ns, respectively. The fast component and the resulting nonlinearity were attributed to exciton–exciton annihilation [64].

The diffusion-assisted EEA scheme was proposed as a possible mechanism for the emergence of the rapid exciton decay component with increasing excitation power density. Figure 9.17a shows a schematic of diffusion-assisted EEA, i.e., EEA occurs with the probability P_{EEA} , and one of the excitons is nonradiatively relaxed to the ground state when two excitons are encountered after long-distance exciton diffusion. A computational simulation of multiexciton decay dynamics was performed with consideration of the diffusion-assisted EEA process based on the Monte Carlo simulation method. Figure 9.17b shows that the simulated exciton decay curves are proportional to the PL intensity at various initial exciton densities obtained by the Monte Carlo method. The inset shows the comparison between the half-decay time of the rapid decay component estimated from the simulation (red circles) and that from the experimental result (black squares). The simulated half-decay time is consistent with the experimentally obtained half-decay time, which supports the validity of this simulation. The EEA rate was estimated as ~0.35 cm²/s. The exciton diffusion coefficient of 2.2 cm²/s was obtained [64].

Similar conclusions were drawn in [62, 63, 65] for MoS₂ and MoSe₂ based on femtosecond transient absorption measurements, where strong nonlinearity in the optical response was observed. The experimental curves were well fitted if one includes a quadratic term in the rate equation so that

$$\frac{dN}{dt} = -\frac{1}{\tau}N - \frac{1}{2}\gamma N^2 \quad (9.2)$$

where the quadratic term describes exciton–exciton annihilation, with τ being the exciton lifetime and γ being the exciton–exciton annihilation rate.

The obtained values for the exciton–exciton annihilation rate were $\gamma_{MoS_2} = 4.3 \times 10^{-2}$ cm²/s [63] and $\gamma_{MoSe_2} = 0.33$ cm²/s [62]. Interestingly, no signature of exciton–exciton annihilation could be seen when similar measurements were performed on bulk MoSe₂ [62].

As mentioned in [63], exciton–exciton annihilation is also important as the time-reversed image of the process of multiple-exciton generation because the high efficiency of the exciton–exciton annihilation process suggests that TMDCs may be particularly well suited for multiple-exciton generation and, correspondingly, as candidate materials for advanced photovoltaic devices.

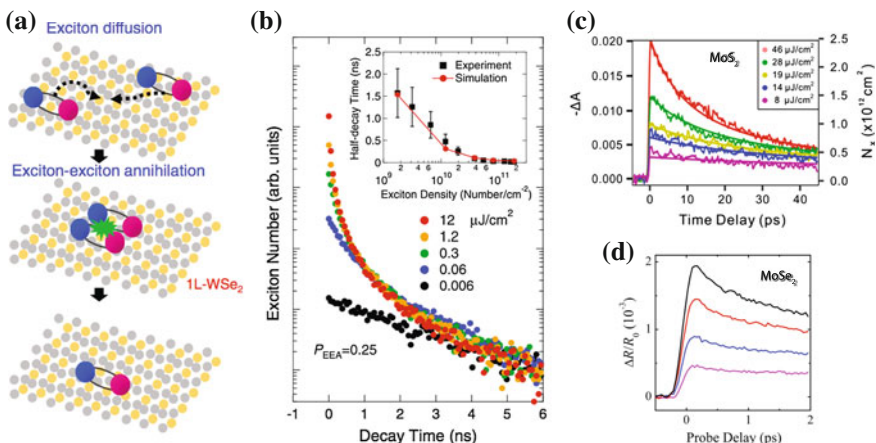


Fig. 9.17 **a** Schematic of the diffusion-assisted EEA process in an atomically thin layered material. **b** PL decay curves of atomically thin WSe₂ with varying excitation power densities obtained from Monte Carlo simulations using EEA probability $P_{EEA} = 0.25$ and diffusion coefficient $D_{ex} = 2 \text{ cm}^2/\text{s}$. The vertical axis for the PL intensity has a logarithmic scale. The inset shows the half-decay time estimated from experimental PL decay curves (black squares) and from calculated exciton decay curves (red circles) as a function of estimated exciton density [64]. Copyright 2014 by the American Physical Society. Reprinted with permission **c** Transient reflectivity of monolayer MoS₂ at room temperature measured at two pump fluences of 22 and 3 $\mu\text{J}/\text{cm}^2$ with a time scale of 600 ps [63]. Copyright 2014 American Chemical Society. Published with permission; **d** Differential reflection of a MoSe₂ monolayer measured with a probe wavelength of 810 nm and a pump wavelength of 750 nm with pump fluences of (from bottom to top) 10, 20, 40, and 55 $\mu\text{J}/\text{cm}^2$, respectively [62]. Copyright 2014 by the American Physical Society. Reprinted with permission

In most studies, the TMDCs layers are on a substrate. The presence of a substrate may induce unwanted effects such as screening and disorder. In [66] suspended TMDCs were studied. Robust (photogain > 1,000) and fast (response time < 1 ms) photoresponse allowed the authors to study the formation, binding energies, and dissociation mechanisms of excitons in TMDCs through photocurrent spectroscopy. By analyzing the spectral positions of peaks in the photocurrent and by comparing them with first-principles calculations, they obtain binding energies, band gaps and spin-orbit splitting in monolayer TMDCs. For monolayer MoS₂, in particular, a rather large binding energy for band-edge excitons, $E_{bind} \approx 570 \text{ meV}$ was obtained. We note in passing that in MoS₂ two mechanisms have been proposed to contribute to photoconductivity, namely, photovoltaic and photothermoelectric effects [67].

Comparison of exciton–exciton annihilation in mono and few-layer WS₂ demonstrated that exciton–exciton annihilation rates for monolayered, bilayered, and trilayered WS₂ were ca. 0.4, 0.006 and 0.002 cm^2/s , respectively, i.e. the exciton–exciton annihilation rate was two orders of magnitude faster in the monolayer than in the bilayer and trilayer [68].

9.2.1.2 Bi-Excitons

As an alternative to exciton–exciton annihilation, two excitons can bind together and form a bi-exciton. The formation of bi-excitons in WSe₂ was reported in [4]. The binding energy of bi-excitons was estimated as 52 meV. The bi-exciton emission intensity exhibited a plateau at low temperature, and then decreased significantly for temperature $T > 70$ K. While the observed bi-exciton binding energy was very large in absolute terms, exceeding the value found in III-V quantum wells by almost two orders of magnitude [69], it was found to scale with the exciton binding energy, and was also attributed to the overall strength of the Coulomb interaction [4].

It was further found that the bi-exciton consisted of two distinct excitons, each with a Bohr radius equal to that of a single exciton (1 nm), separated by a distance three to four times larger. It was argued [4] that because of the large separation between charges, the screening of the Coulomb interaction should be strongly influenced by that of the external media, rather than the intrinsic screening of the monolayer and proposed the bi-exciton states to be particularly sensitive to the nature of the surrounding media.

Bi-excitons were also observed in monolayers of MoS₂, with the binding energy in a 35–60 meV range [70].

9.2.2 “Excitons in a Mirror”

An interesting observation was made in [71]. The authors found that the optical properties of MoS₂ can be strongly influenced when placed in close proximity to a gold-coated surface. Figure 9.18 compares dark field images and scattering spectra from monolayers MoS₂ on quartz and on gold.

Images taken with a CCD camera revealed dramatically different scattering colours of MoS₂ crystals on the different substrates. While scattering on quartz had a blue colour, scattering on Au was green. In general, the scattered light intensity for MoS₂ on quartz was twice as strong as for MoS₂ on Au. In both systems, light was scattered more strongly from the edges of the monolayer than from their centre, however the spectral shape was not altered. In both cases, the two K -excitonic states A and B , split in energy due to strong spin-orbit coupling, were clearly visible as peaks at 663 and 620 nm. The apparent colour of the material in the optical images was dominated by strong (and different) scattering at higher energies compared to the K -excitonic resonances.

At shorter wavelengths, the resonant scattering amplitude was approximately four times as strong as scattering from the K -excitons. Most interestingly, while for a quartz substrate, only one scattering peak was seen, centred at 439 nm for light scattered from the edge of the crystal, for MoS₂ on gold, a second strong scattering peak (labelled C') appeared at 502 nm giving the crystals a green appearance. This peak was associated with an exciton associated with band nesting near the Γ -point, where the valence and conduction band dispersions are parallel thus providing a van Hove singularity with excitonic features [11, 13]. Based on this assignment,

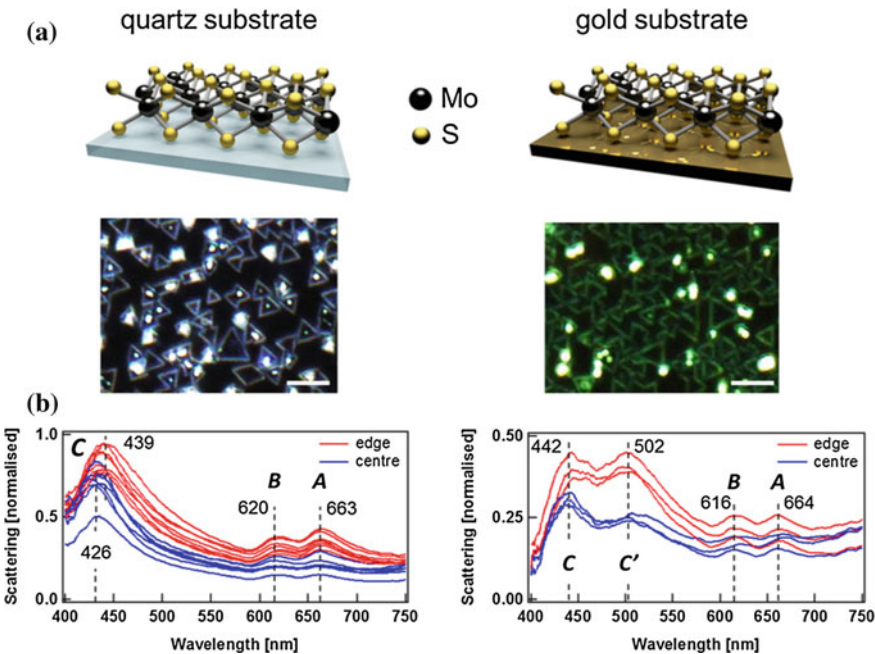


Fig. 9.18 Light scattering from MoS₂ crystals on quartz (*left*) and on gold (*right*) substrates. **a** Dark field images of MoS₂ on both substrates; Scale bars are 4 μm. **b** Scattering spectra from the edge (red) and centre (blue) of different monolayer crystals. Data are normalised to the maximum light scattering amplitude of the quartz sample. Resonances are denoted by *A*, *B*, *C*, and *C'* [71]. Reprinted with permission. Copyright 2014 by the American Institute of Physics

these resonances were referred to as *C*-excitons (noting that their origin remains under discussion). The *C*-excitons have a six-fold symmetry in *k*-space close to the Γ -point and are strongly localised in real space with calculated radii of 30 to 50 Å [11, 13]. At the same time, the *A* and *B* excitons at the *K*-point extend over 65–100 Å [11, 13].

It was proposed that the splitting of the *C*-exciton observed on gold substrates is due to the interaction with its image exciton within the metal. The 350 meV red-shift of the *C'*-exciton can be estimated from the interaction of a dipole-emitter with its reflected field from the Au surface. The frequency shift $\Delta\omega_s$ from the complex dielectric functions of Au (ϵ_{Au}) and MoS₂ (ϵ) was estimated to be [72]:

$$\Delta\omega_s = -\frac{3}{32}qb_\infty d^{-3}\Re e \left(\frac{\epsilon_{Au} - \epsilon}{\epsilon_{Au} + \epsilon} \right) \quad (9.3)$$

Here, q is the quantum yield of the emitter (around 10%), b_∞ is its decay rate (for which the 24 nm line width of the *C*-exciton on quartz was used), and d is the distance of the emitter from the surface. Estimating the complex in-plane dielectric function for MoS₂ the frequency shifts of 350 meV were obtained, corresponding to

$d = 0.6\text{ nm}$, which agrees well with the thickness of a monolayer of MoS₂. It was concluded that the C' -exciton arises from exciton–exciton coupling of a C -exciton in MoS₂ with its image in the gold surface leading to the formation of a “mirror-bi-exciton”.

9.3 Excitons and Trions

As already mentioned earlier, quasiparticles can be either neutral (excitons) or charged (trions). While excitons in 2D TMDCs have binding energies of a few hundreds of meV, the trion binding energies are typically an order of magnitude smaller, which is, nonetheless, an order of magnitude larger than in conventional semiconductor quantum wells [73]. In many cases both exciton and trion peaks are observed in photoluminescence experiments.

The neutral exciton is the ground state of a charge neutral system and trions are only formed in the presence of excess charge, which therefore directly controls the intensity of the trion emission. Thus, trion emission is usually not observed in exfoliated samples of MoS₂ and WS₂ unless a gate is used. Gated samples can exhibit an additional line 20–35 meV below the excitonic line which is attributed to the emission from charged excitons (X^\pm) [74, 75].

Tightly bound trions in monolayer MoS₂ were observed in [74]. In Fig. 9.19 the behaviour of the low-energy (A) exciton is shown over the spectral range of 1.8–2.0 eV under gate voltages from -100 to 80 V, with -100 V corresponding to a nearly undoped sample and $+80$ V corresponding to a doping density of ca. 10^{13} cm^2 . One can see an overall suppression of the optical absorbance with increasing electron doping. The prominent A exciton peak evolves into two resonances, with the emergence of a lower energy resonance (labelled as A^-). For $V_g > 0$, the absorbance of feature A diminishes rapidly and disappears into the background. The A^- feature, on the other hand, broadens gradually, while approximately preserving its spectral weight. Similarly, in the photoluminescence spectra, both resonances can be identified for negative gate voltages. The photoluminescence intensity of the A exciton, like its absorbance, can be switched off by doping. In addition, red-shifts in the photoluminescence peak energies from the corresponding absorption energies (Stokes shifts) were observed for both features; the magnitude of Stokes shift was found to increase with doping level. A and A^- features were ascribed to neutral and charged excitons, respectively.

Trions emerge, accompanied by a reduction of exciton absorption and photoluminescence, when excess electrons are introduced to bind to photoexcited electron-hole pairs, where the exciton spectral weight is transferred to the trion [74].

It was found that when the Fermi energy was varied from 0 to 30 meV, the exciton energy blue-shifted monotonically, whereas the trion energy remained largely unchanged, after a slight initial red-shift (Fig. 9.19b). The splitting between the exciton and trion energy is expected to be linearly dependent on the Fermi energy [76]:

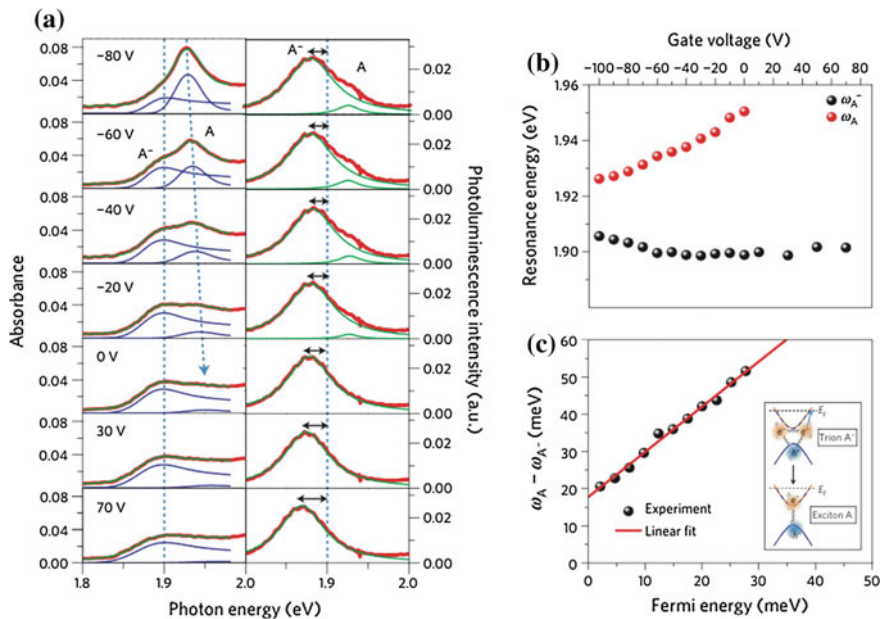


Fig. 9.19 Doping dependence of the optical properties of a monolayer MoS₂ FET. **a** Absorption and photoluminescence spectra (red lines) in the range of 1.8–2.0 eV for the indicated back-gate voltages. The exciton (A) and trion (A^-) resonances behave differently with gate voltage. *Left*: absorption spectra, with the *dashed blue lines* as a guide to the eye for the threshold energies of A and A^- features. The *green lines* are power-law fits to the experimental results, as described in the main text, with the A and A^- components shown as the *blue lines*. *Right*: the photoluminescence spectra of the A and A^- features are fit to Lorentzians (*green lines*). The *dashed blue line* indicates the absorption peak of the A^- resonance and the *arrows* show the doping-dependent Stokes shift of the trion photoluminescence. **b** Threshold energies of the trion ω_{A^-} (*black symbols*) and the neutral exciton ω_A (*red symbols*), determined from the absorption spectra, as a function of gate voltage (*upper axis*) and Fermi energy E_F (*lower axis*). **c** The difference in the exciton and trion energies, $\omega_A - \omega_{A^-}$ (*symbols*), as a function of Fermi energy E_F . The *red line*, a linear fit to the E_F -dependence, has a slope of 1.2 and an intercept of 18 meV. The latter determines the binding energy. *Inset* illustrates the dissociation of a trion into an exciton and an electron at the Fermi level [74]. Reprinted by permission from Macmillan Publishers Ltd., copyright (2013)

$$\omega_A - \omega_{A^-} = E_{A^-} + E_F \quad (9.4)$$

where E_{A^-} is the trion binding energy. From the linear fit (Fig. 9.19c) it was determined to be 18.0 ± 1.5 meV. The large trion binding energy observed in monolayer MoS₂ suggests the importance of trions even at elevated temperatures. The absorption and especially photoluminescence were found to be highly dependent on doping: while the exciton photoluminescence varied by nearly two orders of magnitude, the trion photoluminescence was gate independent.

In [75], excitonic features of MoSe₂ were investigated by differential reflectance and micro PL measurements. At low temperature, two pronounced peaks were

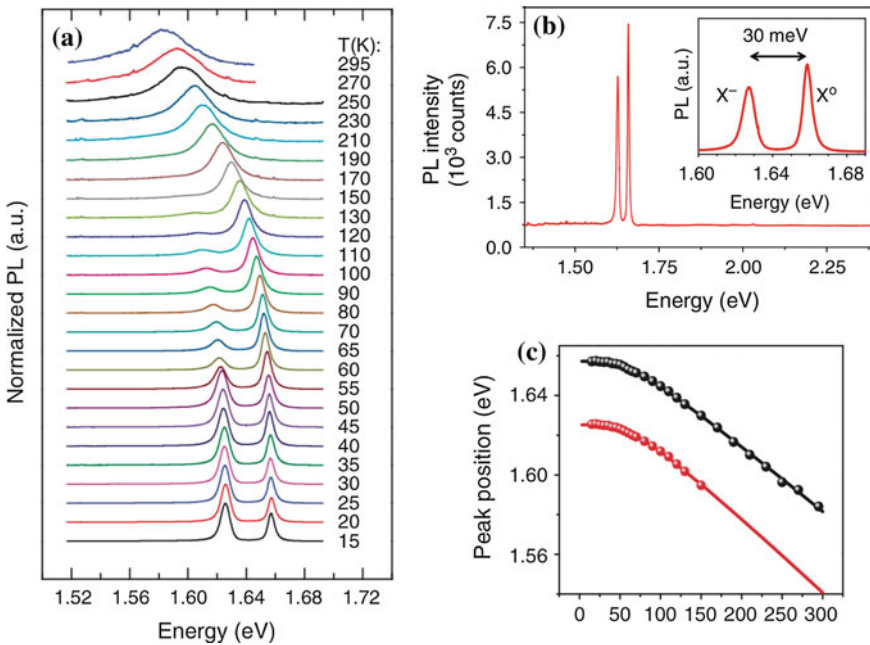


Fig. 9.20 **a** Normalized PL of monolayer MoSe₂ versus temperature. **b** PL excited by a 2.33 eV laser shows a neutral exciton (X^0) and a lower-energy charged exciton (X^-). PL from the B exciton has not been observed. *Inset:* PL of the exciton peaks. The X^- shows a binding energy of about 30 meV. **c** Neutral exciton (black) and trion (red) peak position versus temperature with fits (solid lines) [75]. Reprinted by permission from Macmillan Publishers Ltd., copyright (2013)

observed at 1.659 and 1.627 eV (separated by 30 meV) in the vicinity of the A exciton (Fig. 9.20a, b), with the lower one attributed to a trion. Figure 9.20a shows the evolution of X^- and X^0 (normalized PL) as a function of temperature under 1.96 eV laser excitation. As the temperature increased, the X^- signal dropped significantly at about 55 K. The X^- and X^0 peak positions are shown in (Fig. 9.20c). The peak positions were well fitted using a standard semiconductor band gap dependence:

$$E_g(T) = E_g(0) - S\langle\hbar\omega\rangle \left[\coth\left(\frac{\langle\hbar\omega\rangle}{2k_B T}\right) - 1 \right] \quad (9.5)$$

where $E_g(0)$ is the emission energy at $T = 0$, S is a coupling constant, and $\langle\hbar\omega\rangle$ is the average phonon energy. From the fits, for X^0 (X^-) the values of $E_g = 1.657$ (1.625) eV, $S = 1.96$ (2.24) and $\langle\hbar\omega\rangle = 15$ meV for both quasiparticles were extracted [75].

Similar studies of temperature effects on optical spectra of monolayer MoS₂ were reported in [77, 78].

Gate-dependent PL measurements using monolayer MoSe₂ FETs were also performed using a 1.73 eV excitation laser for better resonance with the luminescent

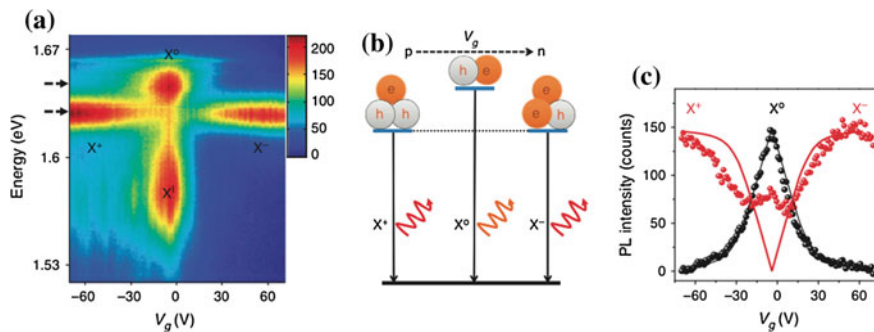


Fig. 9.21 Electrostatic control of exciton charge. **a** MoSe₂ PL (colour scale in counts) is plotted as a function of back-gate voltage. Near zero doping, mostly neutral and impurity-trapped excitons are observed. With large electron (hole) doping, negatively (positively) charged excitons dominate the spectrum. **b** Illustration of the gate-dependent trion and exciton quasi-particles and transitions. **c** Trion and exciton peak intensity versus gate voltage at dashed arrows in (a). Solid lines are fits based on the mass action model [75]. Reprinted by permission from Macmillan Publishers Ltd., copyright (2013)

states. Figure 9.21a shows a colour map of the PL spectrum at 30 K as a function of back-gate voltage, V_g , in which four spectral features were clearly observed whose intensities strongly depend on V_g . Near zero V_g , the spectrum shows a broad low-energy feature around 1.57 eV and a narrow high-energy peak at 1.647 eV. With large V_g of either sign, these peaks disappear and a single-emission peak dominates the spectrum. Both peaks (at negative or positive V_g) have similar energies and intensities with the latter increasing with the magnitude of V_g .

From the gate dependence, the peaks near 1.627 eV were identified as the X^- and X^+ trions, when V_g is positive and negative, respectively. An interesting observation was that they exhibited a nearly identical binding energy, which was associated with similar effective masses of electrons and holes. These measurements demonstrate the electrical control of exciton species in a 2D semiconductor, as illustrated in Fig. 9.21b. By setting V_g negative, the sample is p -doped, favouring excitons to form lower-energy-bound complexes with free holes. As V_g decreases, more holes are injected into the sample, and all X^0 turn into X^+ to form a positively charged hole-trion gas. With positive V_g , a similar situation occurs with free electrons to form an electron-trion gas.

Figure 9.21c shows the extracted X^0 (black) and trion (red) peak intensities as a function of V_g where the negative V_g data were adjusted due to background. The plot shows that the maximum X^0 intensity is about equal to the saturated trion PL when X^0 vanishes. This observation suggests the conservation of the total number of X^0 and trions in the applied voltage range and similar radiative decay rates for both quasi-particles.

A similar behavior, namely an anticorrelation between the peak intensities of the neutral exciton X^0 and positively and negatively charged trions, X^\pm , was observed

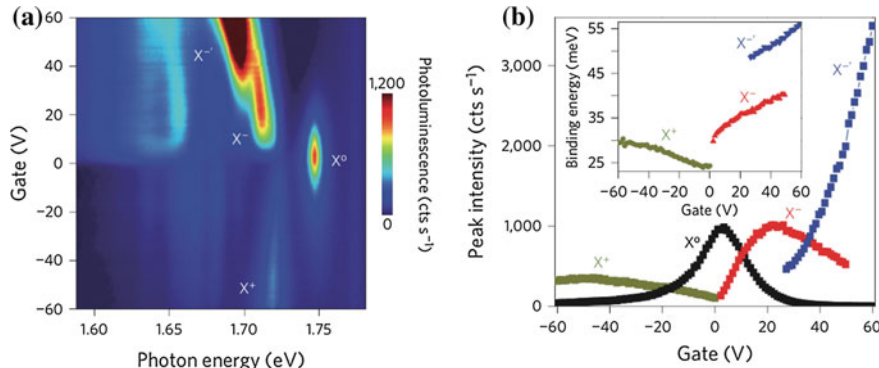


Fig. 9.22 Electrical control of valley excitons in monolayer WSe₂. **a** Photoluminescence intensity map as a function of gate voltage and photon energy showing neutral exciton (X^0), negative trion (X^-) and its fine structure (X^-'), and positive trion (X^+) states. **b** Peak intensity of exciton and trion photoluminescence as a function of gate voltage. Inset: trion binding energy as a function of gate voltage [82]. Reprinted by permission from Macmillan Publishers Ltd., copyright (2013)

for monolayer MoTe₂ [79], with the binding energies for the exciton and trions being ~ 0.58 eV and $\sim 0.24\text{--}0.27$ eV, respectively.

Excitonic fine structure, including both neutral excitons and trions under gating conditions and also under varying excitation power in WS₂ monolayers was studied in detail in [80]. From the observed superlinear emission, a conclusion about the formation of bi-excitons was made.

The situation is somewhat different in WSe₂ monolayers [81]. In the latter case, positive and negative trions behave asymmetrically and, in addition, at higher positive gate voltages a new feature labelled X^-' emerges and rapidly increases in intensity (Fig. 9.22). Based on its polarisation dependence it was attributed to the fine structure of a X^- trion.

Optical manipulation of the exciton charge state in single-layer WS₂ was demonstrated in [83]. Figure 9.23a shows typical micro-PL spectra measured on a single-layer region at $T = 4$ K. Under these conditions, a second emission line on the low-energy side of the neutral exciton emission was observed at around 1980 meV. This line became much stronger as the excitation power was increased. It was found that the behavior of the low-energy line had all the characteristics of a trion: with increasing excitation power, the intensity increased linearly (bi-excitons have a quadratic dependence), the binding energy varied linearly, while the ratio of the trion and neutral exciton emission intensities was not constant.

It was noted that trion emission is usually not observed in exfoliated samples of MoS₂ and WS₂ unless a gate is used. Hence, in the ungated samples, the low-energy line was attributed to emission from charged excitons (trions) which was associated the *n*-type nature of the bulk crystals. It was proposed that laser illumination, in addition to creating electron-hole pairs, is expected to dynamically photoionize carriers trapped on the donors at low temperature, creating a nonequilibrium excess electron

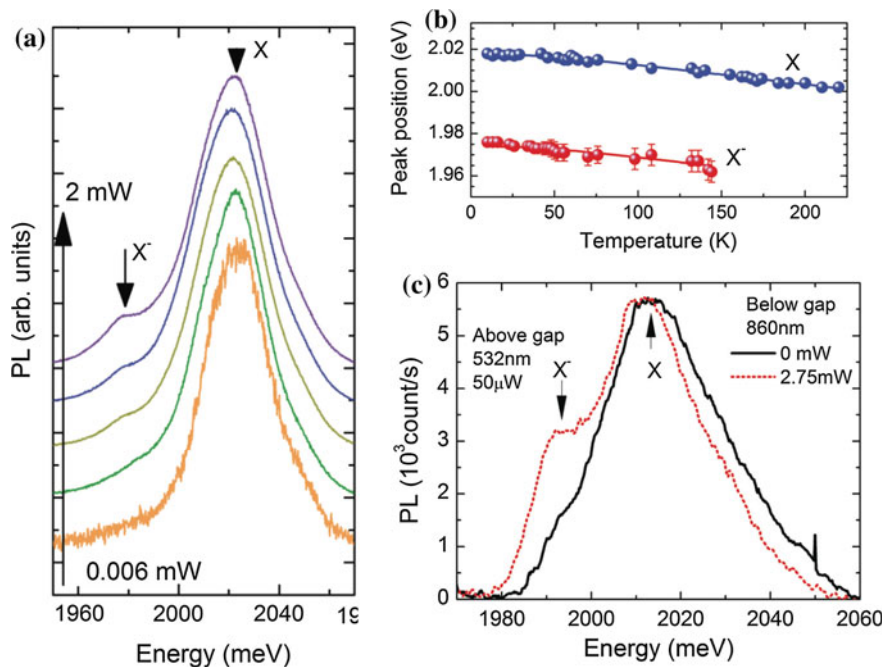


Fig. 9.23 **a** Typical micro-PL spectra of single-layer WS₂ measured as a function of the 532 nm excitation power at 4 K. **b** Emission energy of the neutral and charged exciton as a function of temperature. **c** Typical micro-PL spectra measured with and without additional below gap illumination. All spectra are measured with a low constant power of a green (532 nm) laser (50 μ W). The difference between emission energy of the neutral and charged exciton [83]. Copyright 2013 by the American Physical Society. Reprinted with permission

density in the conduction band. Therefore, it was suggested that the intensity ratio between a neutral and charged exciton can simply be tuned by varying the power of the laser.

The temperature dependence of the emission is presented in Fig. 9.23b. Both exciton lines red-shifted as the temperatures increases and the charged exciton emission vanished around 140 K. Using the standard expression for the temperature dependence of the semiconductor band gap (see above), the best fit was obtained for $E_0 = 2.017$ eV, $S = 0.56$, and $\langle \hbar\omega \rangle = 10.4$ meV. The charged exciton was fitted using the same parameters except for the zero temperature emission energy $E_0 = 1.973$ eV [83].

The possibility to tune the trion and neutral exciton emission by means of two color excitation using a low power above-gap excitation in order to generate a constant density of electron hole pairs was also demonstrated. Additional below-gap excitation was provided by a laser centered at 860 nm (1441 meV). Photons with this energy, which is well below the gap, do not generate electron-hole pairs but their energy is sufficient to photoionize electrons from the donor level which is a few hundred meV below the indirect conduction band in bulk crystals. Representative two

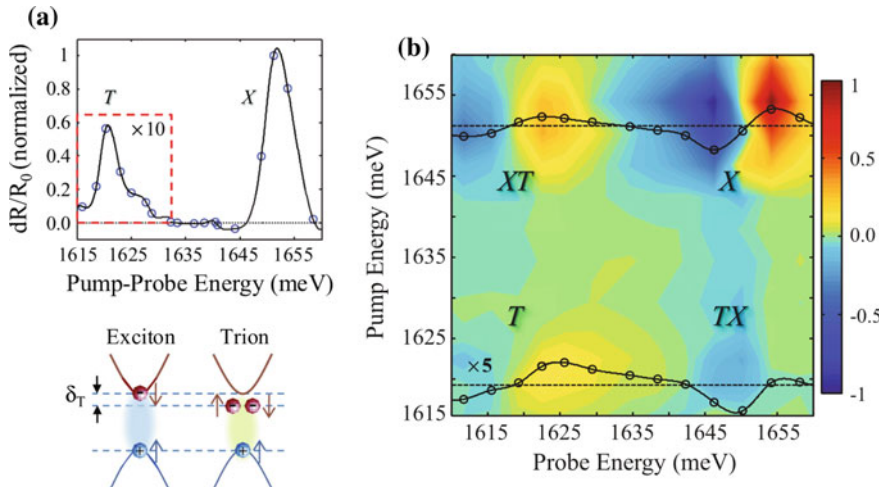


Fig. 9.24 **a** Degenerate pump-probe spectrum (points) for delay $t_D = 0.7$ ps. The curve serves as a guide to the eye. Optical excitation generates either excitons (X) or trions (T) red-shifted from the exciton by an energy δ_T . **b** Normalized two-dimensional differential reflectivity spectrum featuring exciton (X) and trion (T) peaks and their coupling (XT and TX). Differential probe spectra (points) are shown for the pump resonant with the exciton (top) and trion (bottom). The curves serve as a guide to the eye [85]. Copyright 2014 by the American Physical Society. Reprinted with permission

color PL spectra are presented Fig. 9.23c. It was found that in the absence of below gap illumination, the trion line was very weak but its intensity increased while the (integrated) intensity of the neutral exciton emission decreased when additionally illuminated using a laser at 860 nm.

In addition to playing an important role in photoluminescence trions were also argued to result in negative photoconductivity in monolayer MoS₂ [84].

Excitons and trions in atomically thin MoSe₂ were demonstrated to be coherently coupled [85]. In Fig. 9.24a the degenerate pump-probe spectrum is shown for $t_D = 0.7$ ps, that was used to identify exciton (X) and trion (T) resonances at ca. 1650 and ca. 1619 meV, respectively. The transition energies and trion binding energy of $\delta_T \approx 30$ meV are consistent with values obtained from photoluminescence spectra of similarly prepared samples. To look into coupling between resonances, two-color pump-probe spectra were taken (Fig. 9.24b), that feature four peaks: two diagonal peaks corresponding to the exciton (X) and trion (T), respectively, a cross-peak when pumping at the exciton and probing at the trion (XT), and vice versa (TX). The appearance of cross-peaks is an unambiguous sign of exciton-trion coupling.

To elucidate the nature of the coupling density matrix calculations were performed and the obtained results suggested that coherent exciton-trion coupling leads to the formation of a correlated state with a remarkably large binding energy [85].

Time-dependent density-matrix functional theory for exciton and trion excitations for the case example of MoS₂ was developed in [5]. Three different types of exchange-

correlation kernels were used and their validity was evaluated through comparison with available experimental data. For excitons, it was found that the local kernels, from the local density approximation and its gradient-corrected form, led to much smaller binding energy than that extracted from experimental data, while those based on long-range interactions fared much better. The same result was obtained for the trion binding energy when screening effects were taken into account.

Excited carriers also have a different effect. By solving the semiconductor Bloch equations, using ab initio band structures and Coulomb interaction matrix elements, spectra for excited carrier densities up to 10^{13} cm^{-2} were calculated [86] and revealed a red-shift of the excitonic ground-state absorption, whereas higher excitonic lines were found to disappear successively due to Coulomb-induced band gap shrinkage of more than 500 meV and a corresponding binding-energy reduction.

The effect of Coulomb interaction on optical properties of monolayer TMDCs and on exciton–exciton interaction was theoretically studied in [87] by solving the Bethe-Salpeter equation.

Excitons and trions were also studied in [9] based on an effective mass model of excitons and trions, parameterized by ab initio calculations and incorporating a proper treatment of screening in two dimensions. The obtained exciton and trion energies were in good agreement with experiment.

In [80] effects of both doping and photoexcitation were studied that revealed unconventional emission and excitonic fine structure in monolayer WS₂, which reflects the interplay of exciton, trion and other excitonic states. Of interest was the superposition effect of electrical doping and optical excitation and tunable excitonic emission in a 1L WS₂ field-effect device that were demonstrated in a controllable manner.

In [88] it was argued that in monolayers of TMDC strong coupling of the valley pseudospin with the exciton center of mass motion through electron-hole exchange results in a number of interesting phenomena, including the formation of a massless Dirac cone.

9.4 Excitons in Heterostructures

In MoS₂ and MoSe₂ theory predicts the exciton wave function extent to be of the order of several nm [13, 89]. Therefore, it is interesting to study excitons on a nanometer scale, below the wavelength of light emitted by these excitons. Standard optical techniques, such as photoluminescence, cannot probe excitons at the subwavelength limit due to the diffraction limit. In [90], it was demonstrated that mapping excitons in sub-wave-length scales is possible using electron-energy-loss spectroscopy (EELS). Schematic of the experiment is shown in Fig. 9.25a. As an example, spatial variation of excitons in MoS₂–MoSe₂ interfaces in single two-dimensional heterogeneous layers of MoS_{2(1-x)}Se_{2x} ($0 < x < 1$) were measured.

In Fig. 9.25b the electron-energy-loss (EEL) spectra of pure single-layer MoS₂ and MoSe₂ measured with a monochromated electron beam are shown. Losses below

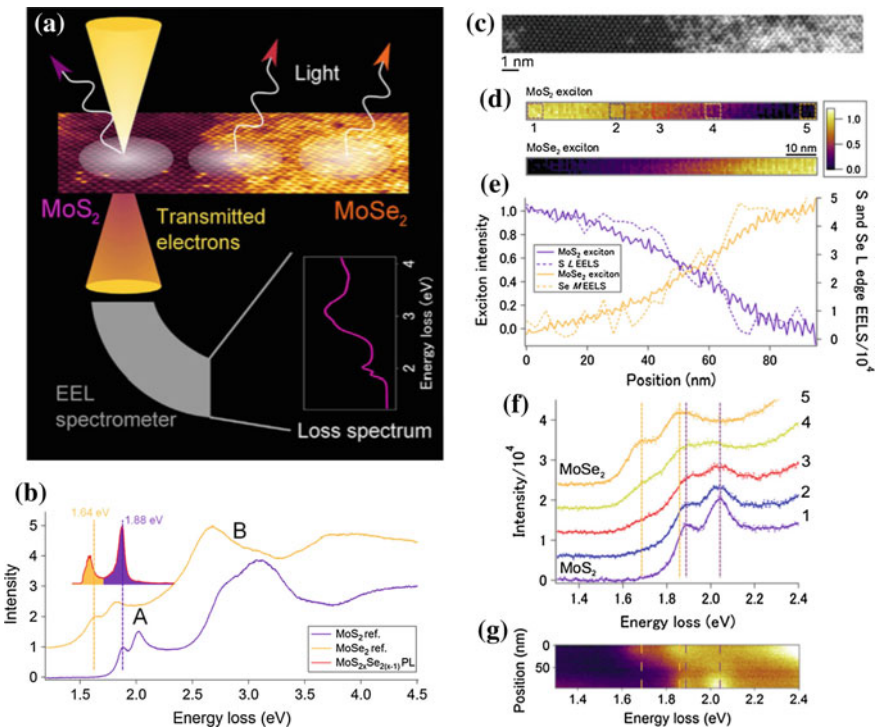


Fig. 9.25 **a** EELs experiments were performed in scanning transmission mode where a narrow electron beam (yellow cone, width $R \sim 1$ nm) was used to probe excitons across a diffuse interface. For the pure regions, the area probed was limited by the size of the exciton wave function (represented by ellipses), as it was larger than R , and delocalization effects. Interestingly, using a narrow electron probe allows access to the energy-loss spectrum of materials at scales far below the wavelength of the emitted light (*arrows* in the drawing). **b** Low loss EELs spectra of MoS₂ (purple) and MoSe₂ (orange). Two main features are seen. The first one, marked *A*, is associated with excitons. It is split in two energy-loss peaks due to spin-orbit coupling. The second feature, marked *B*, is also associated with an exciton. The red curve is a PL spectrum taken from the heterogeneous sample. **c** Typical high angle annular dark field (HAADF) image of MoS₂-MoSe₂ interfaces, showing a diffuse chemical profile. **d** Maps of the fitting coefficients for MoS₂ (*above*) and MoSe₂ (*below*). **e** Comparison of the fitting coefficient profiles from with the chemical profiles measured from core-loss EELS of the S *L*- and Se *M*-edges. **f** Five spectra integrated at different positions across the interface, with positions marked by colored squares and numbers in **(d)**. **g** Projection of the EELS map in the spatial direction perpendicular to the interface. The change from MoS₂ to MoSe₂ is followed by peak broadening but no apparent spectral shift [90]. Copyright 2015 by the American Physical Society. Reprinted with permission

2 eV were clearly resolved without deconvolution. Two sharp peaks between 1.5 and 2.1 eV were labelled as *A* exciton and a broader peak at around 3.0 eV as *B* exciton. Here we preserve the original notations in the description of the results but it should be noted that these notations are not conventional: in most cases the two sharp features at the lower energy are associated with *A* and *B* excitons and the peak around 3 eV is known as a *C* exciton (see e.g. [91]). The position of the first *A* exciton peak and the

splitting to the second peak (usually referred to as *B* exciton) were 1.88 eV (1.64 eV) and 0.14 eV (0.19 eV) for MoS₂ (MoSe₂). These values agree well with the MoS₂ and MoSe₂ excitons measured using photoluminescence (1.93 eV [20] and 1.63 eV [21] at 77 K). For a thin anisotropic system, such as a two-dimensional monolayer, an EEL spectrum is directly related to the parallel (relative to the surface of the monolayer) component of the dielectric function, hence low loss EELS measures the optical absorption of the system [90]. It was noted that EELS based on scanning electron microscopy has the ability to detect spatial variations in the excitations. In a typical EELS experiment, the electron beam is scanned over the sample and a spectrum of the energy loss by electrons provides information about various excitations and, in the low loss range, reflects the local density of optical states [90].

The authors of [90] measured a 112×6 EEL spectra with a 0.9 nm increment across a MoS₂-MoSe₂ interface in a single-layer MoS_{2(1-x)}Se_{2x} sample. An atomically resolved image of a typical interface is shown in Fig. 9.25c. Across the interface the spectra did not show abrupt changes but changed gradually, which was interpreted by the diffuse chemical profile of the interface and also by delocalization effects. The dotted profiles in Fig. 9.25e show the intensities of the S *L*- and Se *M*-edges (purple and orange, respectively) measured in the same region, which are proportional to the chemical composition.¹

Interestingly, in the EELS maps a continuous shift of the exciton energy following the chemical changes was not observed. In other words, the exciton peak in MoS₂ did not continuously shift to the exciton peak in MoSe₂. In Fig. 9.25f, five spectra taken from the EELS map are shown (measured at positions marked in the map in Fig. 9.25d). Even if an intermediate chemical composition existed in a narrow interface, the exciton did not show an intermediate energy. This was explained as due to the fact that EELS experiments measure directly the energy lost, in which case, one can probe the local states within the interface, which make EELS measurements different from PL measurements.

Indirect excitons in vertical TMDC heterostructures have been studied in several publications [92–94]. In [92], the MoSe₂-WSe₂ monolayers and heterostrcutures were studied using PL measurements. Figure 9.26a shows PL spectra taken at 20 K using 1.88 eV excitation, where both intralayer neutral (X^0) and charged (X^-) excitons are resolved and are also preserved in the heterostructure region. In addition there is a rather strong new feature located at ca. 1.35 eV (labelled X_I). Figure 9.26b shows an intensity plot of X_I emission as a function of photoexcitation energy, where the enhancement of the emission is seen when the excitation energy is resonant with intralayer exciton states. Since this feature was not observed in either monolayers or bi-layers of pure TMDCs, it was attributed to an interlayer exciton in the MoSe₂-WSe₂ heterostructure, which has the type-II band alignment (Fig. 9.26c), analogous to spatially indirect excitons in coupled quantum wells.

The emission energy of the indirect exciton was found to be electrically tunable. Figure 9.27 shows the interlayer exciton PL intensity as V_g is varied from +100

¹Note that the authors of the original paper use notations that are different from the *A*, *B*, and *C* excitons used in other publications

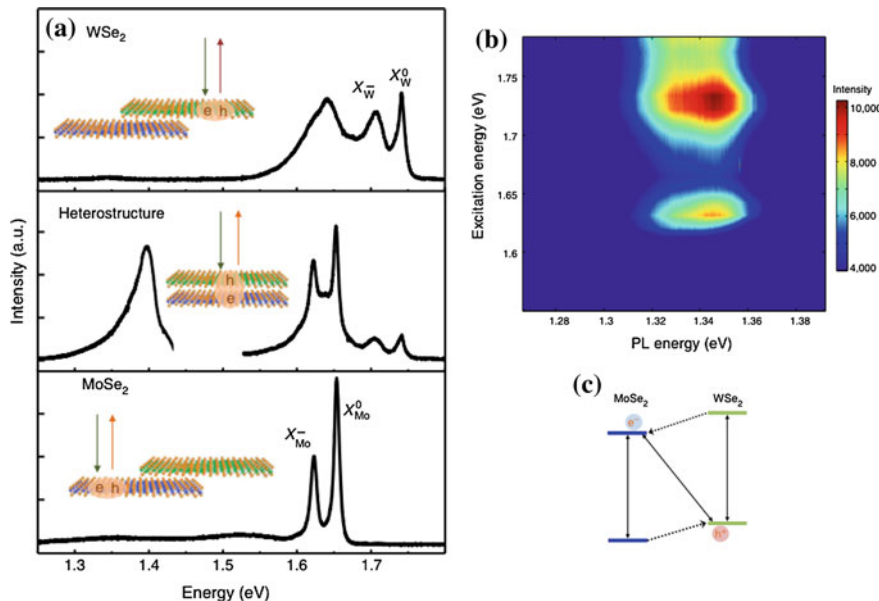


Fig. 9.26 **a** Photoluminescence of individual monolayers and the heterostructure at 20 K under 20 mW excitation at 1.88 eV (plotted on the same scale) **b** PL excitation intensity plot of the heterostructure region with an excitation power of 30 mW and 5 s charge-coupled device CCD integration time. **c** Type-II semiconductor band alignment diagram for the 2D MoSe₂-WSe₂ heterojunction [92]. Reprinted by permission from Macmillan Publishers Ltd., copyright (2014)

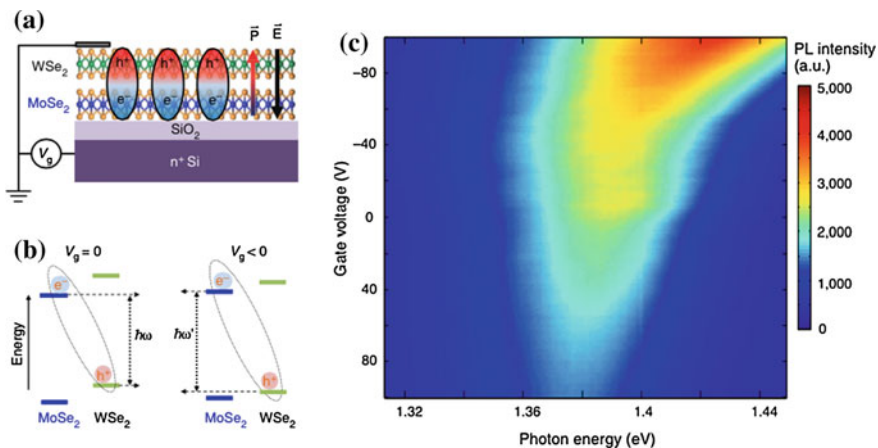


Fig. 9.27 Gate control of the interlayer exciton and band alignment. **a** Device geometry. The interlayer exciton has a permanent dipole, corresponding to an out-of-plane electric polarization. **b** Electrostatic control of the band alignment and the interlayer exciton resonance. **c** Colourmap of interlayer exciton photoluminescence as a function of applied gate voltage under 70 μ W excitation at 1.744 eV, 1 s integration time [92]. Reprinted by permission from Macmillan Publishers Ltd., copyright (2014)

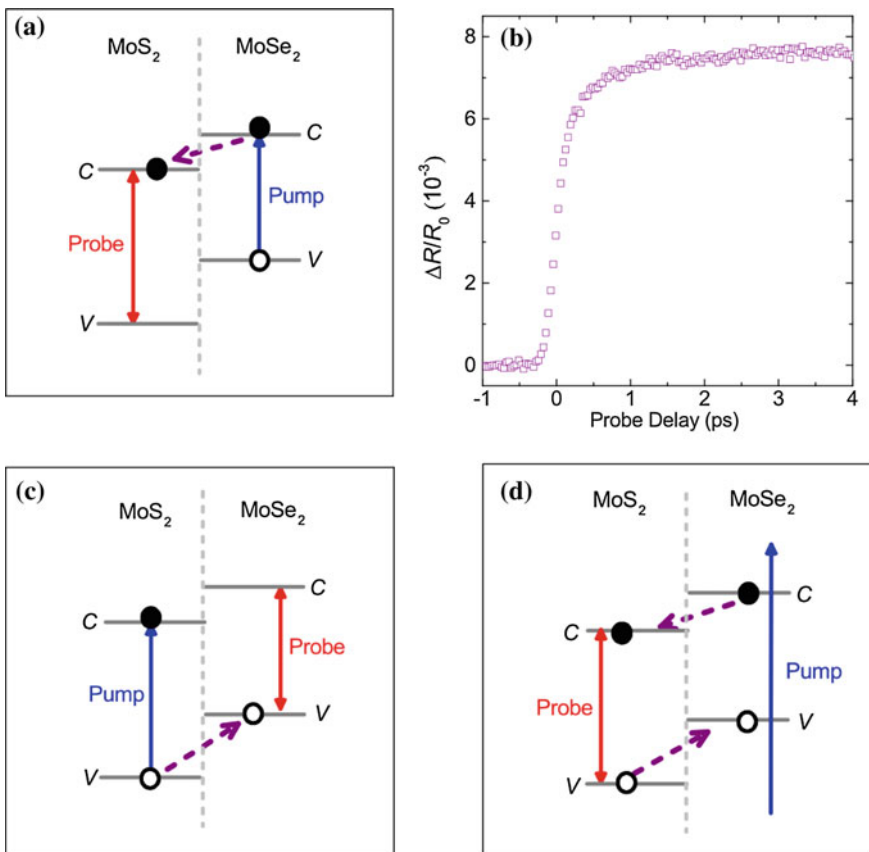


Fig. 9.28 **a** Schematics of the pump-probe configuration used to study the transfer of electrons from MoSe₂ to MoS₂ in the heterostructure. **b** Differential reflection signal near zero probe delay. **c** Schematics of the pump-probe configuration used to study the transfer of holes from MoS₂ to MoSe₂; **d** Schematics of the pump-probe configuration with a 395 nm pump exciting both layers of the heterostructure (blue vertical arrow) and a 655 nm probe at the MoS₂ resonance (red vertical arrow) [93]. Copyright 2014 American Chemical Society. Published with permission

to -100 V. Over this range, the peak centre blue-shifted by about 45 meV. The gate dependence of X_I was consistent with that expected for the interlayer exciton, which maintains a dipole direction from MoSe₂ to WSe₂.

Further experiments showed that the X_I peak is a doublet with both peaks of the doublet displaying a consistent blue shift with increased laser intensity. The spectrally integrated intensity of X_I also exhibited strong saturation as a function of laser power at rather low intensities, which suggests a much longer lifetime than that of intralayer excitons. The long lifetime of the interlayer exciton was explained by it being the lowest energy configuration and where its spatially indirect nature leads to a reduced optical dipole moment [92].

Charge separation and indirect exciton formation was also studied in MoS₂-MoSe₂ heterostructures by selectively exciting one or both materials using light with different wavelengths as illustrated in Fig. 9.28. By selectively injecting excitons in the MoSe₂ layer and probing the MoS₂ layer (panel a), it was found [93] that the electrons in the excitons injected in MoSe₂ transfer to MoS₂ on a subpicosecond time scale (panel b). Similarly, holes in the excitons resonantly injected in MoS₂ (panel c) were found to transfer to MoSe₂ on the same time scale. It was further found that, once transferred, the electrons and holes form spatially indirect excitons with recombination lifetimes longer than the excitons in individual monolayers, in agreement with the results of [92].

Interlayer interaction in TMDC heterostructures was also studied by optical spectroscopy [95]. In the heterostructure spectra, a significant broadening of the excitonic transitions was observed compared to the corresponding features in the isolated layers. The broadening was interpreted as a lifetime effect arising from decay of excitons initially created in either layer through charge transfer processes expected for a staggered band alignment. From the measured spectral broadening of 20–35 meV, lifetimes for charge separation of the near band-edge A and B excitons was estimated to be in the range of 20–35 fs. Higher-lying transitions exhibited still greater broadening [95].

It is interesting to note that the interlayer exciton relaxation was found to be equally efficient in epitaxial and randomly stacked MoS₂-WS₂ [94] heterostructures, which can be probably generalized to other combinations of TMDCs.

References

1. R.S. Knox, *Theory of Excitons*, vol. 5 (Academic Press, New York, 1963)
2. M. Dvorak, S.H. Wei, Z. Wu, Origin of the variation of exciton binding energy in semiconductors. Phys. Rev. Lett. **110**(1), 016402 (2013)
3. A. Thilagam, Exciton complexes in low dimensional transition metal dichalcogenides. J. Appl. Phys. **116**(5), 053523 (2014)
4. Y. You, X.X. Zhang, T.C. Berkelbach, M.S. Hybertsen, D.R. Reichman, T.F. Heinz, Observation of biexcitons in monolayer WSe₂. Nat. Phys. **11**, 477 (2015)
5. A. Ramirez-Torres, V. Turkowski, T.S. Rahman, Time-dependent density-matrix functional theory for trion excitations: application to monolayer MoS₂ and other transition-metal dichalcogenides. Phys. Rev. B **90**(8), 085419 (2014)
6. X.F. He, Excitons in anisotropic solids: the model of fractional-dimensional space. Phys. Rev. B **43**(3), 2063 (1991)
7. A. Mitioglu, P. Plochocka, Á. Granados del Aguilera, P. Christianen, G. Deligeorgis, S. Anghel, L. Kulyuk, D. Maude, Optical investigation of monolayer and bulk tungsten diselenide (WSe₂) in high magnetic fields. Nano Lett. **15**(7), 4387 (2015)
8. A. Chernikov, T.C. Berkelbach, H.M. Hill, A. Rigosi, Y. Li, O.B. Aslan, D.R. Reichman, M.S. Hybertsen, T.F. Heinz, Exciton binding energy and nonhydrogenic Rydberg series in monolayer WS₂. Phys. Rev. Lett. **113**(7), 076802 (2014)
9. T.C. Berkelbach, M.S. Hybertsen, D.R. Reichman, Theory of neutral and charged excitons in monolayer transition metal dichalcogenides. Phys. Rev. B **88**(4), 045318 (2013)
10. J. Feng, X. Qian, C.W. Huang, J. Li, Strain-engineered artificial atom as a broad-spectrum solar energy funnel. Nat. Photon. **6**(12), 866 (2012)

11. D.Y. Qiu, F.H. da Jornada, S.G. Louie, Optical spectrum of MoS₂: many-body effects and diversity of exciton states. *Phys. Rev. Lett.* **111**(21), 216805 (2013)
12. T. Cheiwchanwathanij, W.R. Lambrecht, Quasiparticle band structure calculation of monolayer, bilayer, and bulk MoS₂. *Phys. Rev. B* **85**(20), 205302 (2012)
13. A. Molina-Sánchez, D. Sangalli, K. Hummer, A. Marini, L. Wirtz, Effect of spin-orbit interaction on the optical spectra of single-layer, double-layer, and bulk MoS₂. *Phys. Rev. B* **88**(4), 045412 (2013)
14. G.D. Scholes, G. Rumbles, Excitons in nanoscale systems. *Nat. Mater.* **5**(9), 683 (2006)
15. K.F. Mak, C. Lee, J. Hone, J. Shan, T.F. Heinz, Atomically thin MoS₂: a new direct-gap semiconductor. *Phys. Rev. Lett.* **105**(13), 136805 (2010)
16. A. Splendiani, L. Sun, Y. Zhang, T. Li, J. Kim, C.Y. Chim, G. Galli, F. Wang, Emerging photoluminescence in monolayer MoS₂. *Nano Lett.* **10**(4), 1271 (2010)
17. M.S. Hybertsen, S.G. Louie, Electron correlation in semiconductors and insulators: band gaps and quasiparticle energies. *Phys. Rev. B* **34**(8), 5390 (1986)
18. A. Ramasubramaniam, Large excitonic effects in monolayers of molybdenum and tungsten dichalcogenides. *Phys. Rev. B* **86**(11), 115409 (2012)
19. M. Rohlfing, S.G. Louie, Electron-hole excitations and optical spectra from first principles. *Phys. Rev. B* **62**(8), 4927 (2000)
20. G. Berghäuser, E. Malic, Analytical approach to excitonic properties of MoS₂. *Phys. Rev. B* **89**(12), 125309 (2014)
21. F. Wu, F. Qu, A. MacDonald, Exciton band structure of monolayer MoS₂. *Phys. Rev. B* **91**, 075310 (2015)
22. A. Molina-Sánchez, L. Wirtz, Phonons in single-layer and few-layer MoS₂ and WS₂. *Phys. Rev. B* **84**(15), 155413 (2011)
23. K. He, N. Kumar, L. Zhao, Z. Wang, K.F. Mak, H. Zhao, J. Shan, Tightly bound excitons in monolayer WSe₂. *Phys. Rev. Lett.* **113**(2), 026803 (2014)
24. P. Cudazzo, I.V. Tokatly, A. Rubio, Dielectric screening in two-dimensional insulators: implications for excitonic and impurity states in graphane. *Phys. Rev. B* **84**(8), 085406 (2011)
25. B. Evans, P. Young, Exciton spectra in thin crystals: the diamagnetic effect. *Proc. Phys. Soc.* **91**(2), 475 (1967)
26. A. Beal, J. Knights, W. Liang, Transmission spectra of some transition metal dichalcogenides. II. Group-VIA: trigonal prismatic coordination. *J Phys. C* **5**(24), 3540 (1972)
27. Z. Ye, T. Cao, K. O'Brien, H. Zhu, X. Yin, Y. Wang, S.G. Louie, X. Zhang, Probing excitonic dark states in single-layer tungsten disulphide. *Nature* **513**(7517), 214 (2014)
28. F. Wang, G. Dukovic, L.E. Brus, T.F. Heinz, The optical resonances in carbon nanotubes arise from excitons. *Science* **308**(5723), 838 (2005)
29. J. Maultzsch, R. Pomraenke, S. Reich, E. Chang, D. Prezzi, A. Ruini, E. Molinari, M. Strano, C. Thomsen, C. Lienau, Exciton binding energies in carbon nanotubes from two-photon photoluminescence. *Phys. Rev. B* **72**(24), 241402 (2005)
30. B. Zhu, X. Chen, X. Cui, Exciton binding energy of monolayer WS₂. *Sci. Rep.* **5** (2014). doi:[10.1038/srep09218](https://doi.org/10.1038/srep09218)
31. A. Hanbicki, M. Currie, G. Kioseoglou, A. Friedman, B. Jonker, Measurement of high exciton binding energy in the monolayer transition-metal dichalcogenides WS₂ and WSe₂. *Solid State Commun.* **203**, 16 (2015)
32. Y. Song, H. Dery, Transport theory of monolayer transition-metal dichalcogenides through symmetry. *Phys. Rev. Lett.* **111**(2), 026601 (2013)
33. T.C. Berkelbach, M.S. Hybertsen, D.R. Reichman, Bright and dark singlet excitons via linear and two-photon spectroscopy in monolayer transition metal dichalcogenides. *Phys. Rev. B* **92**, 085413 (2015)
34. H.M. Hill, A.F. Rigos, C. Roquelet, A. Chernikov, T.C. Berkelbach, D.R. Reichman, M.S. Hybertsen, L.E. Brus, T.F. Heinz, Observation of excitonic Rydberg states in monolayer MoS₂ and WS₂ by photoluminescence excitation spectroscopy. *Nano Lett.* **15**(5), 2992 (2015)
35. A. Arora, K. Nogajewski, M. Molas, M. Koperski, M. Potemski, Exciton band structure in layered MoSe₂: from a monolayer to the bulk limit. *Nanoscale* **7**(48), 20769 (2015)

36. A. Arora, M. Koperski, K. Nogajewski, J. Marcus, C. Faugeras, M. Potemski, Excitonic resonances in thin films of WSe₂: from monolayer to bulk material. *Nanoscale* **7**, 10421 (2015)
37. X.X. Zhang, Y. You, S.Y.F. Zhao, T.F. Heinz, Experimental evidence for dark excitons in monolayer WSe₂. *Phys. Rev. Lett.* **115**(25), 257403 (2015)
38. G.B. Liu, W.Y. Shan, Y. Yao, W. Yao, D. Xiao, Three-band tight-binding model for monolayers of group-VIB transition metal dichalcogenides. *Phys. Rev. B* **88**(8), 085433 (2013)
39. K. Kośmider, J. Fernández-Rossier, Electronic properties of the MoS₂-WS₂ heterojunction. *Phys. Rev. B* **87**(7), 075451 (2013)
40. A. Kormányos, G. Burkard, M. Gmitra, J. Fabian, V. Zólyomi, N.D. Drummond, V. Fal'ko, kp theory for two-dimensional transition metal dichalcogenide semiconductors. *2D Mater.* **2**(2), 022001 (2015)
41. G. Wang, C. Robert, A. Suslu, B. Chen, S. Yang, S. Alamdar, I.C. Gerber, T. Amand, X. Marie, S. Tongay, et al., Spin-orbit engineering in transition metal dichalcogenide alloy monolayers. *Nat. Commun.* **6** (2015). doi:[10.1038/ncomms10110](https://doi.org/10.1038/ncomms10110)
42. A. Rodin, A.C. Neto, Excitonic collapse in semiconducting transition-metal dichalcogenides. *Phys. Rev. B* **88**(19), 195437 (2013)
43. T. Stroucken, S.W. Koch, Optically bright p-excitons indicating strong Coulomb coupling in transition-metal dichalcogenides. *J. Phys., Cond. Matter* **27**, 345003 (2015)
44. Y. Lin, X. Ling, L. Yu, S. Huang, A.L. Hsu, Y.H. Lee, J. Kong, M.S. Dresselhaus, T. Palacios, Dielectric screening of excitons and trions in single-layer MoS₂. *Nano Lett.* **14**(10), 5569 (2014)
45. F.J. Crowne, M. Amani, A.G. Birdwell, M.L. Chin, T.P. O'Regan, S. Najmaei, Z. Liu, P.M. Ajayan, J. Lou, M. Dubey, Blueshift of the A-exciton peak in folded monolayer 1h-MoS₂. *Phys. Rev. B* **88**(23), 235302 (2013)
46. F. Prins, A.J. Goodman, W.A. Tisdale, Reduced dielectric screening and enhanced energy transfer in single-and few-layer MoS₂. *Nano Lett.* **14**(11), 6087 (2014)
47. C. Poellmann, P. Steinleitner, U. Leierseder, P. Nagler, G. Plechinger, M. Porer, R. Bratschitsch, C. Schüller, T. Korn, R. Huber, Resonant internal quantum transitions and femtosecond radiative decay of excitons in monolayer WSe₂. *Nat. Mater.* **14**(9), 889 (2015)
48. G. Wang, X. Marie, I. Gerber, T. Amand, D. Lagarde, L. Bouet, M. Vidal, A. Balocchi, B. Urbaszek, Giant enhancement of the optical second-harmonic emission of WSe₂ monolayers by laser excitation at exciton resonances. *Phys. Rev. Lett.* **114**(9), 097403 (2015)
49. X. Marie, B. Urbaszek, 2D materials: ultrafast exciton dynamics. *Nat. Mater.* **14**(9), 860 (2015)
50. S. Sim, J. Park, J.G. Song, C. In, Y.S. Lee, H. Kim, H. Choi, Exciton dynamics in atomically thin MoS₂: interexcitonic interaction and broadening kinetics. *Phys. Rev. B* **88**(7), 075434 (2013)
51. T. Korn, S. Heydrich, M. Hirmer, J. Schmutzler, C. Schüller, Low-temperature photocarrier dynamics in monolayer MoS₂. *Appl. Phys. Lett.* **99**(10), 102109 (2011)
52. H. Shi, R. Yan, S. Bertolazzi, J. Brivio, B. Gao, A. Kis, D. Jena, H.G. Xing, L. Huang, Exciton dynamics in suspended monolayer and few-layer MoS₂ 2D crystals. *ACS Nano* **7**(2), 1072 (2013)
53. N. Kumar, J. He, D. He, Y. Wang, H. Zhao, Charge carrier dynamics in bulk MoS₂ crystal studied by transient absorption microscopy. *J. Appl. Phys.* **113**(13), 133702 (2013)
54. R. Wang, B.A. Ruzicka, N. Kumar, M.Z. Bellus, H.Y. Chiu, H. Zhao, Ultrafast and spatially resolved studies of charge carriers in atomically thin molybdenum disulfide. *Phys. Rev. B* **86**(4), 045406 (2012)
55. D. Lagarde, L. Bouet, X. Marie, C. Zhu, B. Liu, T. Amand, P. Tan, B. Urbaszek, Carrier and polarization dynamics in monolayer MoS₂. *Phys. Rev. Lett.* **112**(4), 047401 (2014)
56. O. Salehzadeh, N.H. Tran, X. Liu, I. Shih, Z. Mi, Exciton kinetics, quantum efficiency, and efficiency droop of monolayer MoS₂ light-emitting devices. *Nano Lett.* **14**(7), 4125 (2014)
57. H. Wang, C. Zhang, F. Rana, Ultrafast dynamics of defect-assisted electron-hole recombination in monolayer MoS₂. *Nano Lett.* **15**(1), 339 (2015)

58. G. Wang, X. Marie, L. Bouet, M. Vidal, A. Balocchi, T. Amand, D. Lagarde, B. Urbaszek, Exciton dynamics in WSe₂ bilayers. *Appl. Phys. Lett.* **105**(18), 182105 (2014)
59. T. Yan, X. Qiao, X. Liu, P. Tan, X. Zhang, Photoluminescence properties and exciton dynamics in monolayer WSe₂. *Appl. Phys. Lett.* **105**(10), 101901 (2014)
60. N. Kumar, Q. Cui, F. Ceballos, D. He, Y. Wang, H. Zhao, Exciton diffusion in monolayer and bulk MoSe₂. *Nanoscale* **6**(9), 4915 (2014)
61. M. Palummo, M. Bernardi, J.C. Grossman, Exciton radiative lifetimes in two-dimensional transition metal dichalcogenides. *Nano Lett.* **15**, 2794 (2015)
62. N. Kumar, Q. Cui, F. Ceballos, D. He, Y. Wang, H. Zhao, Exciton-exciton annihilation in MoSe₂ monolayers. *Phys. Rev. B* **89**(12), 125427 (2014)
63. D. Sun, Y. Rao, G.A. Reider, G. Chen, Y. You, L. Brézin, A.R. Harutyunyan, T.F. Heinz, Observation of rapid exciton-exciton annihilation in monolayer molybdenum disulfide. *Nano Lett.* **14**(10), 5625 (2014)
64. S. Mouri, Y. Miyauchi, M. Toh, W. Zhao, G. Eda, K. Matsuda, Nonlinear photoluminescence in atomically thin layered WSe₂ arising from diffusion-assisted exciton-exciton annihilation. *Phys. Rev. B* **90**(15), 155449 (2014)
65. M.J. Shin, D.H. Kim, D. Lim, Photoluminescence saturation and exciton decay dynamics in transition metal dichalcogenide monolayers. *J. Korean Phys. Soc.* **65**(12), 2077 (2014)
66. A.R. Klots, A.K.M. Newaz, B. Wang, D. Prasai, H. Krzyzanowska, J. Lin, D. Caudel, N.J. Ghimire, J. Yan, B.L. Ivanov, et al., Probing excitonic states in suspended two-dimensional semiconductors by photocurrent spectroscopy. *Sci. Rep.* **4** (2014). doi:[10.1038/srep06608](https://doi.org/10.1038/srep06608)
67. Y. Zhang, H. Li, L. Wang, H. Wang, X. Xie, S.L. Zhang, R. Liu, Z.J. Qiu, Photothermoelectric and photovoltaic effects both present in MoS₂. *Sci. Rep.* **5** (2015). doi:[10.1038/srep07938](https://doi.org/10.1038/srep07938)
68. L. Yuan, L. Huang, Exciton dynamics and annihilation in WS₂ 2D semiconductors. *Nanoscale* **7**(16), 7402 (2015)
69. C.F. Klingshirn, *Semiconductor Optics*, vol. 3 (Springer Science and Business Media, 2007)
70. E.J. Sie, Y.H. Lee, A.J. Frenzel, J. Kong, N. Gedik, Biexciton formation in monolayer MoS₂ observed by transient absorption spectroscopy. arXiv preprint [arXiv:1312.2918](https://arxiv.org/abs/1312.2918) (2013)
71. J. Mertens, Y. Shi, A. Molina-Sánchez, L. Wirtz, H.Y. Yang, J.J. Baumberg, Excitons in a mirror: formation of optical bilayers using MoS₂ monolayers on gold substrates. *Appl. Phys. Lett.* **104**(19), 191105 (2014)
72. R. Chance, A. Prock, R. Silbey, Frequency shifts of an electric-dipole transition near a partially reflecting surface. *Phys. Rev. A* **12**(4), 1448 (1975)
73. K. Kheng, R. Cox, M.Y. d'Aubigné, F. Bassani, K. Saminadayar, S. Tatarenko, Observation of negatively charged excitons X⁻ in semiconductor quantum wells. *Phys. Rev. Lett.* **71**(11), 1752 (1993)
74. K.F. Mak, K. He, C. Lee, G.H. Lee, J. Hone, T.F. Heinz, J. Shan, Tightly bound trions in monolayer MoS₂. *Nat. Mater.* **12**(3), 207 (2013)
75. J.S. Ross, S. Wu, H. Yu, N.J. Ghimire, A.M. Jones, G. Aivazian, J. Yan, D.G. Mandrus, D. Xiao, W. Yao, et al., Electrical control of neutral and charged excitons in a monolayer semiconductor. *Nat. Commun.* **4** (2013). doi:[10.1038/ncomms2498](https://doi.org/10.1038/ncomms2498)
76. V. Huard, R. Cox, K. Saminadayar, A. Arnoult, S. Tatarenko, Bound states in optical absorption of semiconductor quantum wells containing a two-dimensional electron gas. *Phys. Rev. Lett.* **84**(1), 187 (2000)
77. R. Soklaski, Y. Liang, L. Yang, Temperature effect on optical spectra of monolayer molybdenum disulfide. *Appl. Phys. Lett.* **104**(19), 193110 (2014)
78. L.Y. Gan, Q. Zhang, Y.J. Zhao, Y. Cheng, U. Schwingenschlögl, Order-disorder phase transitions in the two-dimensional semiconducting transition metal dichalcogenide alloys Mo_{1-x}W_xX₂ (X= S, Se, and Te). *Sci. Rep.* **4** (2014). doi:[10.1038/srep06691](https://doi.org/10.1038/srep06691)
79. J. Yang, T. Lü, Y.W. Myint, J. Pei, D. Macdonald, J.C. Zheng, Y. Lu, Robust excitons and trions in monolayer MoTe₂. *ACS Nano* **9**(6), 6603 (2015)
80. J. Shang, X. Shen, C. Cong, N. Peimyoo, B. Cao, M. Eginligil, T. Yu, Observation of excitonic fine structure in a 2D transition metal dichalcogenide semiconductor. *ACS Nano* (2015)

81. A.M. Jones, H. Yu, J.S. Ross, P. Klement, N.J. Ghimire, J. Yan, D.G. Mandrus, W. Yao, X. Xu, Spin-layer locking effects in optical orientation of exciton spin in bilayer WSe₂. *Nat. Phys.* **10**(2), 130 (2014)
82. A.M. Jones, H. Yu, N.J. Ghimire, S. Wu, G. Aivazian, J.S. Ross, B. Zhao, J. Yan, D.G. Mandrus, D. Xiao et al., Optical generation of excitonic valley coherence in monolayer WSe₂. *Nat. Nanotech.* **8**(9), 634 (2013)
83. A. Mitioglu, P. Plochocka, J. Jadczak, W. Escoffier, G. Rikken, L. Kulyuk, D. Maude, Optical manipulation of the exciton charge state in single-layer tungsten disulfide. *Phys. Rev. B* **88**(24), 245403 (2013)
84. C. Lui, A. Frenzel, D. Pilon, Y.H. Lee, X. Ling, G. Akselrod, J. Kong, N. Gedik, Trion-induced negative photoconductivity in monolayer MoS₂. *Phys. Rev. Lett.* **113**(16), 166801 (2014)
85. A. Singh, G. Moody, S. Wu, Y. Wu, N.J. Ghimire, J. Yan, D.G. Mandrus, X. Xu, X. Li, Coherent electronic coupling in atomically thin MoSe₂. *Phys. Rev. Lett.* **112**(21), 216804 (2014)
86. A. Steinhoff, M. Rösner, F. Jahnke, T.O. Wehling, C. Gies, Influence of excited carriers on the optical and electronic properties of MoS₂. *Nano Lett.* **14**(7), 3743 (2014)
87. S. Konabe, S. Okada, Effect of Coulomb interactions on optical properties of monolayer transition-metal dichalcogenides. *Phys. Rev. B* **90**(15), 155304 (2014)
88. H. Yu, G.B. Liu, P. Gong, X. Xu, W. Yao, Dirac cones and Dirac saddle points of bright excitons in monolayer transition metal dichalcogenides. *Nat. Commun.* **5** (2014). doi:[10.1038/ncomms4876](https://doi.org/10.1038/ncomms4876)
89. M.M. Ugeda, A.J. Bradley, S.F. Shi, H. Felipe, Y. Zhang, D.Y. Qiu, W. Ruan, S.K. Mo, Z. Hussain, Z.X. Shen et al., Giant bandgap renormalization and excitonic effects in a monolayer transition metal dichalcogenide semiconductor. *Nat. Mater.* **13**(12), 1091 (2014)
90. L.H. Tizei, Y.C. Lin, M. Mukai, H. Sawada, A.Y. Lu, L.J. Li, K. Kimoto, K. Suenaga, Exciton mapping at subwavelength scales in two-dimensional materials. *Phys. Rev. Lett.* **114**(10), 107601 (2015)
91. J. Wilson, A. Yoffe, The transition metal dichalcogenides discussion and interpretation of the observed optical, electrical and structural properties. *Adv. Phys.* **18**(73), 193 (1969)
92. P. Rivera, J.R. Schaibley, A.M. Jones, J.S. Ross, S. Wu, G. Aivazian, P. Klement, N.J. Ghimire, J. Yan, D. Mandrus et al., Observation of long-lived interlayer excitons in monolayer MoSe₂-WSe₂ heterostructures. *Nat. Commun.* **6**, 6242 (2015). doi:[10.1038/ncomms7242](https://doi.org/10.1038/ncomms7242)
93. F. Ceballos, M.Z. Bellus, H.Y. Chiu, H. Zhao, Ultrafast charge separation and indirect exciton formation in a MoS₂-MoSe₂ van der Waals heterostructure. *ACS Nano* **8**(12), 12717 (2014)
94. Y. Yu, S. Hu, L. Su, L. Huang, Y. Liu, Z. Jin, A.A. Purezky, D.B. Geohegan, K.W. Kim, Y. Zhang et al., Equally efficient interlayer exciton relaxation and improved absorption in epitaxial and non-epitaxial MoS₂/WS₂ heterostructures. *Nano Lett.* **15**(1), 486 (2015)
95. A.F. Rigos, H.M. Hill, Y. Li, A. Chernikov, T.F. Heinz, Probing interlayer interactions in transition metal dichalcogenide heterostructures by optical spectroscopy: MoS₂/WS₂ and MoSe₂/WSe₂. *Nano Lett.* **15**(8), 5033 (2015)

Chapter 10

Magnetism in 2D TMDC

This chapter discusses magnetism in few-layer transition metal dichalcogenides associated with the presence of edges, defects, dislocations and grain boundaries as well as dopants.

Defect-free pristine TMDCs are nonmagnetic because there are no unsaturated bonds and no magnetic elements. In [1] it was additionally noted that 2H-MoS₂ is macroscopically nonmagnetic, because the Mo⁴⁺ ions are in a trigonal prismatic local coordination in which the two 4d electrons are spin-antiparallel and the net magnetic moment is zero, although it is not clear to what extent this is significant.

At the same time, in real materials there are always edges, dislocations, grain boundaries and other imperfections that may have an effect on magnetic properties. One of the first reports of magnetism in TMDC was [2], where ferromagnetism (FM) was observed in polycrystalline MoS₂ films (Fig. 10.1), while it was not observed in single crystals,¹ which was attributed to the presence of imperfections, such as grain boundaries. In addition, magnetism may be induced by doping with magnetic elements. Finally, in TMDC there exists a specific possibility of controlling magnetism by application of strain. These issues form the subject of the present chapter.

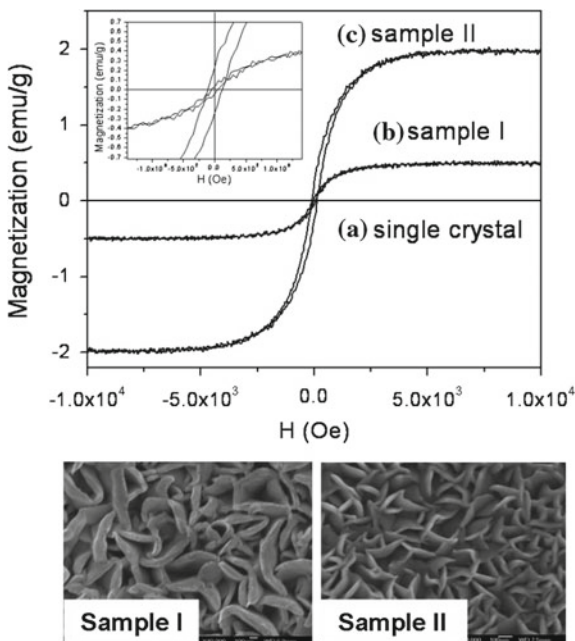
10.1 Ferromagnetism Associated with Crystal Imperfections

10.1.1 Magnetic States at Edges

Magnetic response from TMDC was initially studied theoretically [3–5]. In [3], electronic and magnetic properties of MoS₂ nanoribbons were studied. Two kinds

¹No trace corresponding to the single crystal seems to be shown in the figure. We preserved the original figure caption.

Fig. 10.1 Hysteresis curves recorded at room temperature from two MoS₂ samples (I and II) of varying morphology (scanning electron micrographs below) using a magnetic field of 2000 Oe. The MoS₂ single crystal is nonmagnetic and shows a flat line [2]. Copyright 2007 American Chemical Society. Reprinted with permission

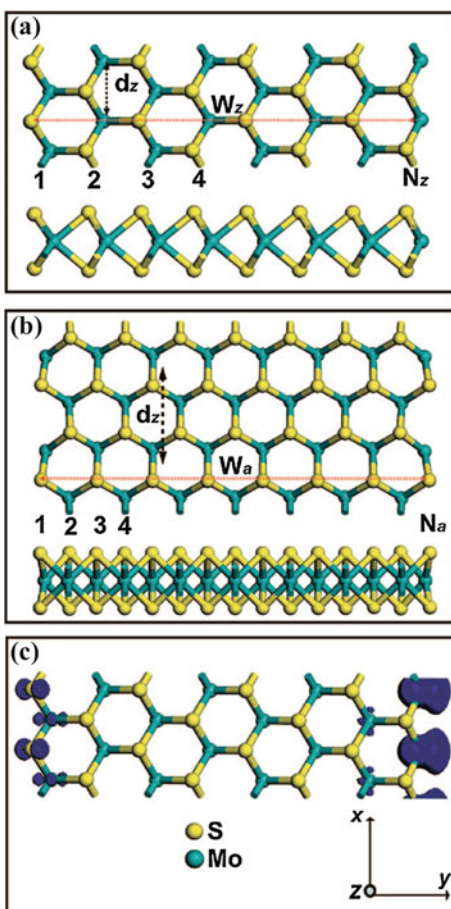


of MoS₂ nanoribbons can be distinguished according to the different directions of their termination: zig-zag (Z) and arm-chair (A) (Fig. 10.2). The author's DFT simulations demonstrated that for arm-chair MoS₂ nanoribbons, spin-polarized total energies are less favorable than spin-unpolarized ones, indicating that arm-chair MoS₂ nanoribbons had a nonmagnetic ground state. At the same time, for zig-zag MoS₂ nanoribbons spin-polarized total energies were more favorable, demonstrating their magnetic ground state. As shown in Fig. 10.2c, the unpaired spin mainly concentrates on the edge Mo and S atoms, while the inner Mo atoms also contribute a small amount of unpaired spin. It was proposed that unsaturated edge atoms should be responsible for the magnetic behavior of zig-zag MoS₂ nanoribbons since the coordination of these atoms is different from that of the inner atoms. It was further argued that the magnetism of the zig-zag MoS₂ ribbons arises from both edges that are ferromagnetically coupled.

The unit magnetic moment of MoS₂ nanoribbons (magnetic moment per MoS₂ molecular formula) decreased gradually with increasing ribbon width, implying that the magnetism of MoS₂ zig-zag nanoribbons became weaker and weaker as the ribbon width increased and disappeared in the infinitely single-layered MoS₂ and bulk.

The band structure of the two kinds of nanoribbons were further studied. In zig-zag ribbons, for both spin orientations up to two energy levels in each spin channel cross the Fermi level and close the band gap. This metallic behavior was found independent of the ribbon width. Metallic edge states in MoS₂ were also observed

Fig. 10.2 Top and side views of geometric structures of **a** 8-zig-zag (Z)-MoS₂ nanoribbons and **b** 15-arm-chair (A)-MoS₂. The ribbon width and 1-D unit cell distance are denoted by W_z (W_a) and d_z (d_a), respectively. **c** Spatial spin distribution (*up-down*) of 8Z-MoS₂. MoS₂ nanoribbons are extended periodically along the x direction [3]. Copyright 2008 by the American Chemical Society. Reprinted with permission



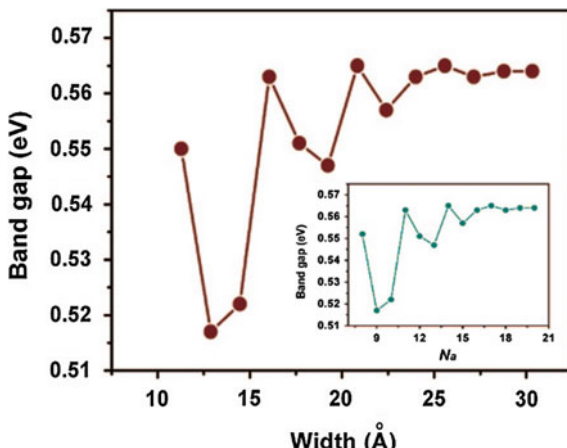
in [6–8]. It was further argued that zig-zag edges of monolayer TMDC can host a well isolated single edge band with strong spin-orbit-coupling energy. Combining with proximity induced *s*-wave superconductivity and in-plane magnetic fields, the zig-zag edges support robust topological Majorana bound states at the edge ends, although the two-dimensional bulk itself is not a topological insulator [9].

In contrast, arm-chair MoS₂ nanoribbons possess semiconducting character, and their electronic properties are weakly dependent on the ribbon width. Band gap oscillations were observed for the narrow ribbons, and those ribbons of $N_a = 3p - 1$ (where p is an integer) had larger band gaps than the neighboring two ribbons (Fig. 10.3). However, as the width increases, the band gaps finally converge to a constant value of ca. 0.56 eV [3].

For comparison, the magnetic properties of bulk MoS₂ and a single layer were also computed, which were both nonmagnetic [3].

In [10], the magnetic response from 10 to 100 μm thick MoS₂ single crystals was studied. While in principle, single crystals of semiconducting MoS₂ are expected to be

Fig. 10.3 Variation of energy band gaps for a series of arm-chair MoS₂ nanoribbons ($8 \leq N_a \leq 20$) as a function of the ribbon width. The inset is the relationship of band gaps of arm-chair MoS₂ nanoribbons as a function of N_a [3]. Copyright 2008 by the American Chemical Society. Reprinted with permission



diamagnetic just like any other semiconductor, in [10] it was found that even though the magnetic response was dominated by diamagnetism as shown in Fig. 10.4a, the diamagnetic background was superimposed onto a FM loop (Fig. 10.4b) implying that the total magnetic susceptibility is comprised of both diamagnetic and FM parts.

The FM component was determined after subtracting the diamagnetic part and is shown in Fig. 10.4c, where the FM response at different temperatures is plotted versus the magnetic field applied parallel to the *c*-axis. It was noted that the saturation magnetization (M_s) remained unchanged with respect to the temperature while the coercive field slightly increased from 100 Oe to 400 Oe. To exclude the presence of magnetic impurities in the sample XPS spectra were measured and there was no sign of magnetic impurities present [10].

Magnetism in exfoliated freestanding nanosheets of MoS₂ was subsequently investigated in [11]. After deducting the diamagnetic signal, the measured saturation magnetizations for the MoS₂ nanosheets (10 h) were 0.0025 and 0.0011 emu/g at 10 and 300 K, respectively. It was also found that M_s of the obtained MoS₂ nanosheets increased as the size of the nanosheets decreased in agreement with the theoretical results [3]. The Curie temperature was determined to be at least 300 K. The presence of intrinsic room-temperature FM was attributed to the presence of edge spins on the edges of the nanosheets.

Ferromagnetism was also reported for MoS₂ and WS₂ grown by CVD [12] with the Curie temperatures of 865 and 820 K, respectively. Experimentally observed FM in exfoliated WS₂ nanosheets (Fig. 10.5) was also attributed to zig-zag edges at grain boundaries [13]. Clear *S*-shaped saturated open curves were observed at all the measured temperatures with $M_s = 0.002$ emu/g at room temperature. Both M_s and the coercivity decreased as the temperature increased from 10 to 330 K. Zig-zag-edge related ferromagnetism was also observed in MoSe₂ nanoflakes [14].

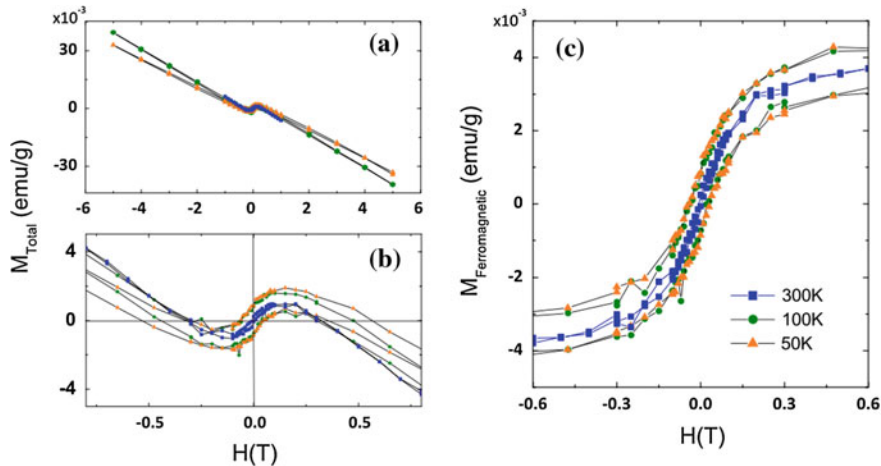


Fig. 10.4 **a** Magnetization (M) of MoS_2 single crystal versus applied field (H) data taken at different temperatures in the field parallel to the c-axis direction. **b** $M - H$ curves displayed at lower magnetic fields. **c** M_{ferro} versus H curves after subtracting the diamagnetic background [10]. Reprinted with permission. Copyright 2012 by the American Institute of Physics

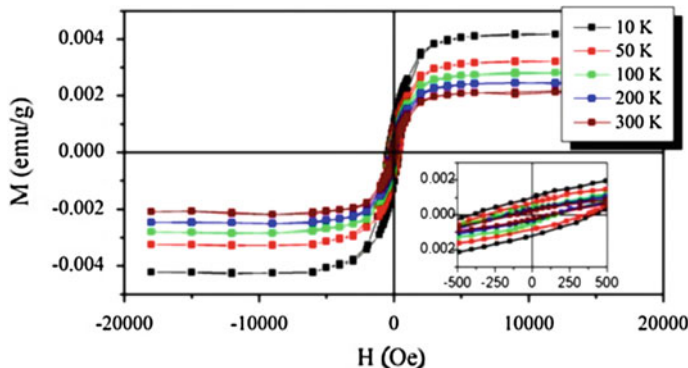


Fig. 10.5 $M - H$ curves for the WS_2 nanosheets measured at different temperatures after subtraction of the diamagnetic signal [13]. Reproduced with permission from Springer

The edge-states FM of WS_2 nanosheets was studied in [15]. In Fig. 10.6a, magnetization hysteresis loops measured at room temperature in the field range of $-5 \text{ kOe} < H < +5 \text{ kOe}$ are shown, where M_S , remanent magnetization (M_R), and H_c are 0.0058 emu/g , 0.002 emu/g , and 92 Oe , respectively. It was noted that these values are comparable to and even larger than those for other 2D materials. The magnetization of the WS_2 nanosheets was also measured at 3 K (Fig. 10.6b). It was found that hysteresis loops became broader with a significantly increased H_c (1115 Oe).

By checking the total DOS of the modeled nanosheets, it was found that the spin-up and spin-down components were asymmetric near the Fermi level, as shown in

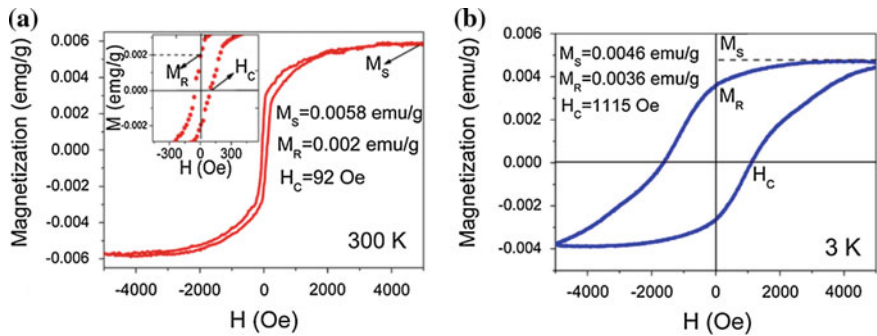


Fig. 10.6 Hysteresis loops of WS_2 nanosheets at **a** room temperature (300 K), the *inset* is an enlarged view, and **b** low temperature (3 K) after subtracting the diamagnetic background [15]. Reprinted with permission. Copyright 2014 by the American Institute of Physics

Fig. 10.7a. In panels (b) and (c), the spin-polarized partial DOS of edge S and W atoms of the nanosheets are shown, respectively, from which one can see that the spin-up and spin-down components of S $3p$ orbitals and W $5d$ states are strongly localized and polarized near the Fermi level. The calculated magnetic moments of edge S and W atoms were 0.19 and $0.13 \mu_B$, respectively, while the net magnetic moments of the inner atoms were zero.

10.1.2 Magnetism at Grain Boundaries

Grain boundaries and dislocations can be viewed as grain edges and hence they are naturally expected to generate magnetism. In [16], where the authors focus on MoS_2 , it was demonstrated that, in addition to this simplistic understanding, there exists a specific mechanism that determines magnetism of grain boundaries.

A dislocation can be created in MX_2 by removing half of an arm-chair atomic line and reconnecting seamlessly all of the resultant dangling bonds, which yields a $5|7$ core as shown in Fig. 10.8 for a -9° tilt angle. It was noted that the strain energy is proportional to the square of the Burgers vector $|\vec{b}|^2$, which is lowest for the $5|7$ core. Bielemental MX_2 can have two types of $5|7$ dislocations: an M-rich dislocation with an M-M bond and $\vec{b} = (1, 0)$, called \perp in the original work [16], and an X-rich dislocation with an X-X bond and $\vec{b} = (0, 1)$, called \top . Figure 10.8b, c present the ground-state magnetization densities of isolated Mo-rich \perp and S-rich \top dislocations. It was found that the spin polarization was highly localized at the dislocations, embedded within an ambient 2D semiconducting host. In the Mo-rich \perp the spin was mainly on the Mo-Mo bond and its four nearest-neighbor Mo atoms. In the S-rich \top dislocation the spin was found to be mostly on the three Mo atoms of the heptagon, particularly on the two atoms adjacent to the S-S pair. Both dislocation types had

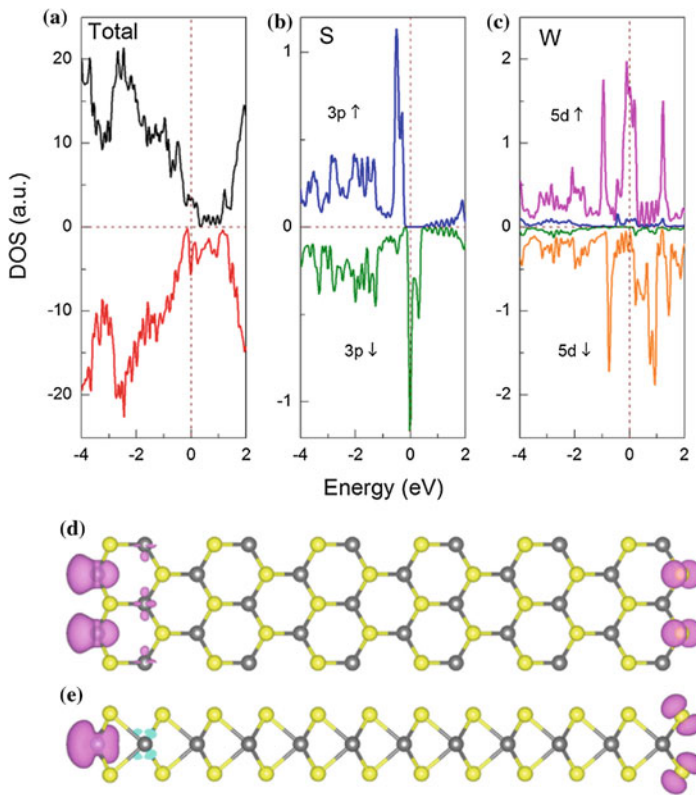


Fig. 10.7 **a** Total DOS of rectangular zig-zag-edge WS₂ nanosheets. Partial DOS of edge **b** S and **c** W atoms. **d** Top and **e** side views of spin density distributions (up-down) of rectangular zig-zag-edge WS₂ nanosheets. The magnetic moments are mainly concentrated on the edge S and W atoms. (The magnetic moment is 1.69 μ_B per unit cell) [15]. Reprinted with permission. Copyright 2014 by the American Institute of Physics

total magnetic moments of $\mu = 1.0 \mu_B$. The energy difference between nonmagnetic and magnetic states was found to be rather substantial, namely, 36 meV per dislocation. It was argued that magnetism of dislocations, as robust defects imbedded in the 2D material, is novel and distinctly different from magnetic edge states along bare zig-zag edges or at some special vacancies.

It was further found that magnetic moment of grain boundaries per unit length M was proportional to the tilt angle θ below $\theta = 32^\circ$ (Fig. 10.9). Above 32° the number of 5/7 dislocations declined and hexagons with homoelemental bonds appeared instead (symmetric “s-hexagons”), which resulted in a further increase in the magnetic moment up to about $\theta = 47^\circ$. At higher angles the magnetism rapidly decreased

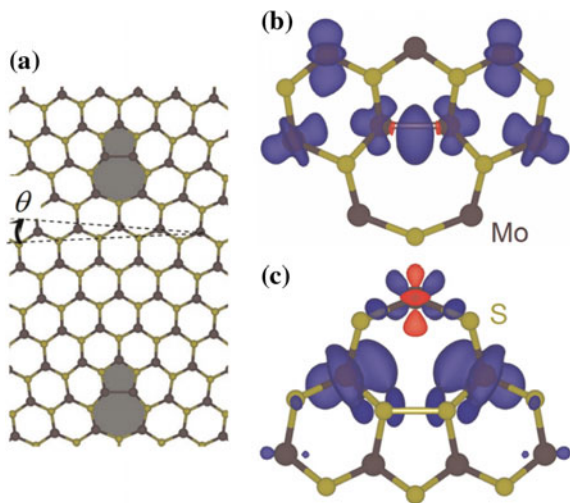


Fig. 10.8 Structure of grain boundary in single-layer MoS₂. **a** Symmetric GB with a tilt angle $\theta = 9^\circ$. Each repeat cell includes a Mo-rich \perp with a homoelemental Mo-Mo bond, tagged as Mo-rich \perp . Reversing the grain tilt to -9° creates a S-rich T with two S-S bonds. Isosurface plots ($2 \times 10^{-3} \text{ e}/\text{\AA}^3$) show the magnetization densities of **b** Mo-rich \perp and **c** S-rich T. Blue and red colors denote positive and negative values of the magnetization density, respectively [16]. Copyright 2013 American Chemical Society. Published with permission

as the grain boundaries approached a state of pure s-hexagons at $\theta = 60^\circ$. Above $\theta = 47^\circ$ the 4|8 core becomes more favorable than the 5|7 core [16]. The magnetic moment of these 4|8 grain boundaries sharply increased reaching $2.1 \mu\text{B}/\text{nm}$ at $\theta = 60^\circ$ [16].

The energies of grain boundaries with FM or anti-FM order between adjacent dislocations were also compared. In grain boundaries composed of 5|7s, the FM structure was energetically preferred, while, grain boundaries with 4|8 cores favored an anti-FM structure. It was proposed that this distinction may be related to carrier-mediated FM, where the 5|7 defects support free charge carriers at these doping levels, while the 4|8 defects do not. Another important difference between the 5|7 and 4|8 configurations is the presence of homoelemental bonds in the former but not the latter [16].

10.1.3 Vacancy-Induced Magnetism

Vacancy-induced magnetism in MoS₂ was studied [5] using DFT calculations for two types of S vacancies (Fig. 10.10). It was found that a vacancy on the S-edge with 50% coverage intensifies the magnetization of the edge of the MoS₂ nanoribbon, but such a vacancy on S-edge with 100% coverage causes this magnetic property to

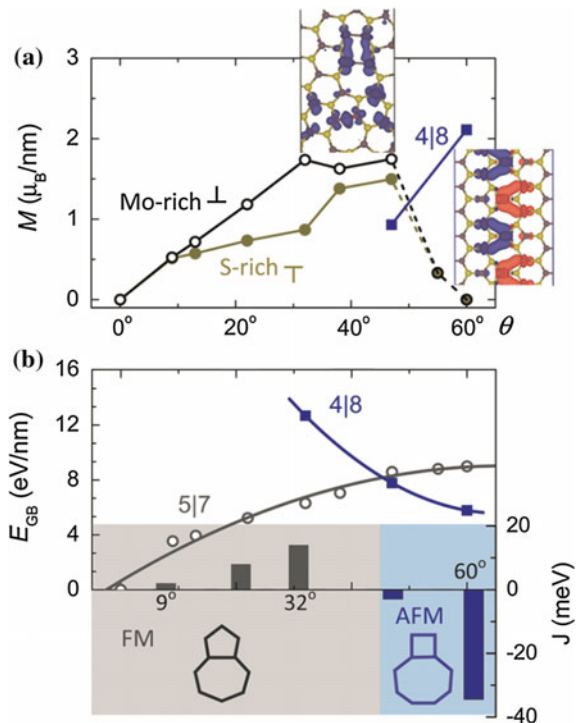


Fig. 10.9 Tilt-dependent magnetism of grain boundaries in MoS_2 . **a** Magnetic moment M per unit length of grain boundary as a function of tilt angle. All values are obtained from grain boundaries with FM order. *Insets* show magnetization densities (isovalue $2 \times 10^{-3} \text{ e}\text{\AA}^3$) of a 38° grain boundary composed of Mo-rich \perp and a 60° grain boundary composed of 4|8s. **b** Top left axis: energies of grain boundaries as a function of θ , with gray circles for grain boundaries composed of 5|7s and blue squares for grain boundaries composed of 4|8s. Bottom right axis: exchange coupling parameter J for several typical grain boundaries composed of Mo-rich \perp or 4|8s [16]. Copyright 2013 American Chemical Society. Published with permission

disappear. It was also found in [17] that in the presence of a vacancy defect, such as MoS -divacancy, S_2 -divacancy, Mo -vacancy and S -vacancy, the spin-polarization of the zig-zag nanoribbons was suppressed. In contrast, the creation of a MoS_2 triple vacancy resulted in a significant magnetic moment in the system [18].

The role of vacancies in FM of MoS_2 was also considered in [1], where magnetism in mixed $2H$ - $1T$ phases was studied (see also 10.5). It was concluded that magnetism of $1T$ - MoS_2 incorporated in the $2H$ phase originated from exchange interactions between S vacancies and Mo^{4+} ions.

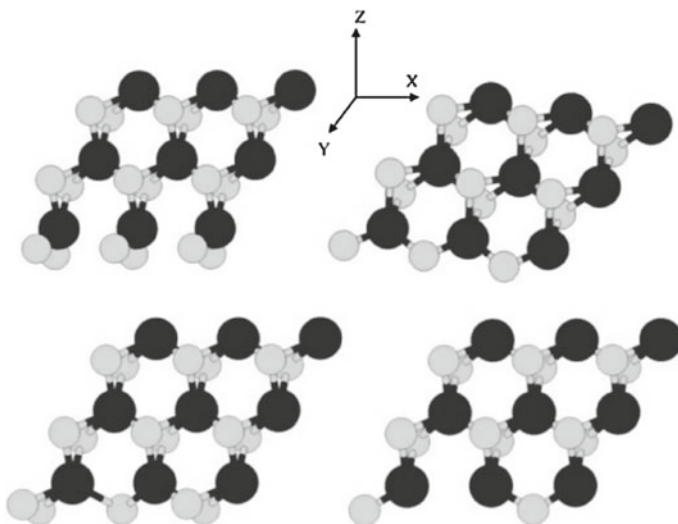


Fig. 10.10 *Upper panel:* ribbon-like structure with various edges structure of S edge with 100% coverage of S atoms (*left*) and with 50% S coverage (*right*). *Lower panel:* a S vacancy at the S edge with a 100% S coverage containing an S vacancy (*left*) and with 50% S coverage (*right*). S and Mo atoms are shown by bright and dark circles, respectively [5]. Reproduced by permission of The Royal Society of Chemistry

10.1.4 Disorder-Induced Magnetism

In [19] MoS_2 nanosheets with different degree of crystalline order were synthesized by the hydrothermal method using different annealing temperatures and it was found that the samples with lower degree of crystallinity had larger saturation magnetisation.

Magnetism could also be induced in pristine MoS_2 by proton irradiation [20]. It was proposed that the appearance of magnetism observed in proton-irradiated MoS_2 samples could be due to a combination of defect moments arising from vacancies, interstitials, deformation and partial destruction of the lattice structure, i.e. the formation of edge states and reconstructions of the lattice.

10.2 Doping-Induced Magnetism

While magnetism associated with edges, grain boundaries and vacancies opens interesting possibilities, it is also associated with certain problems such as the stability

of these entities. An alternative way to fabricate TMDC with a magnetic response is to dope the latter. Doping can be performed either by magnetic or non-magnetic impurities [21]. The former are usually incorporated into the material's structure, while the latter are absorbed on the surface.

10.2.1 *Magnetism Due to Magnetic Dopants*

Magnetism due to magnetic dopants was first considered theoretically in [22]. In this work, using ab-initio calculations, a two-dimensional diluted magnetic semiconductor, namely, monolayer MoS₂ doped by transition metals, was proposed. While doping by transition metal atoms from the IIIB to VIB groups resulted in nonmagnetic states, magnetism was observed for Mn, Fe, Co, Zn, Cd, and Hg doping. Analysis of the binding energies and magnetic properties suggested that (Mo, X)S₂ (X = Mn, Fe, Co, and Zn) were promising systems to explore two-dimensional diluted magnetic semiconductors.

FM ordering in Mn-doped 2D TMDCs was studied in [23] using DFT simulations. It was concluded that the long-range FM of Mn spins is mediated by an anti-FM exchange between the localized Mn *d* states and the delocalized *p* states of the S, Se, and Te atoms. In contrast, transition metals like Fe, Co, and Ni showed a FM exchange with the S, Se, and Te atoms, resulting in a very weak FM (even slightly anti-FM) coupling for transition-metal defects with large separations.

Doping of WSe₂ with transition metals was also studied in [24]. In this work, in order to account for the electron correlations of *d* electrons in the transition metal dopants, the DFT + *U* scheme [25] was used. The obtained results were in partial disagreement with those of [23]. It was found that only Mn, Fe, and Ni generated nontrivial magnetic interactions, with Mn and Fe being the best candidates to generate long-range room temperature FM within their high spin states. The magnetic exchange interaction between Mn and Fe ions was found to oscillate between strong FM to strong anti-FM depending on the spatial positions, distances, and concentrations of the dopants. It was further found that the long-range interaction for Fe requires a percolation threshold, while Mn doping generated long-range room temperature interaction even at a very low doping concentrations. It was argued that the long-range interaction between Mn and Fe ions is mediated by the delocalized 4*p* states of Se coupled antiferromagnetically with the Mn and ferromagnetically with the *d* states of Fe [24].

In [26] dependence of the geometry and stability of Fe dopants in MoS₂ on the chemical potential and the layer number of sheets was reported based upon *ab-initio* simulations. Figure 10.11 shows the formation energies of different doping

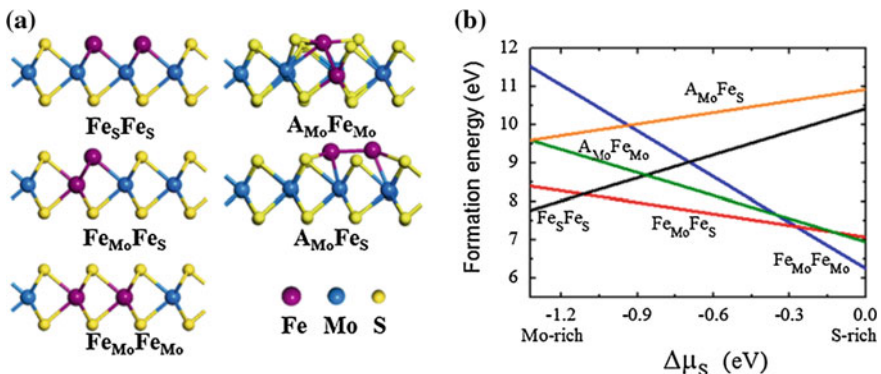


Fig. 10.11 **a** Optimized doping atomic configurations (side view) and **b** formation energies of two Fe impurities in monolayer MoS₂. Five potential doping configurations are Fe_{Mo}Fe_{Mo}, Fe_{Mo}Fe_S, and Fe_SFe_S, respectively. Mo, S, and Fe atoms are colored by blue, yellow, and purple balls, respectively [26]. Copyright 2015 American Chemical Society. Published with permission

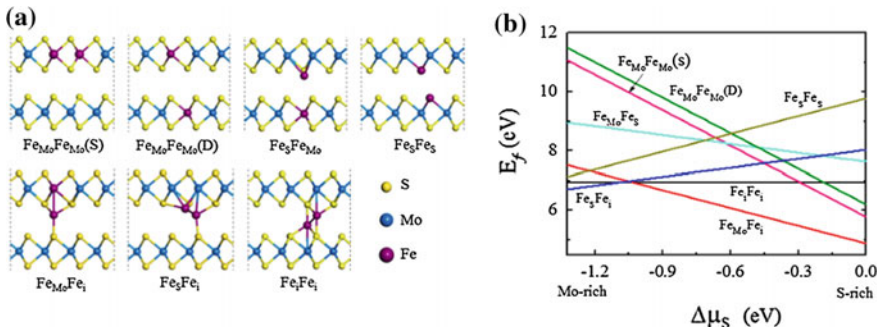


Fig. 10.12 **a** Doping atomic configurations and **b** formation energies of Fe-doped bilayer MoS₂. Mo, S, and Fe atoms are colored by blue, yellow, and purple balls, respectively [26]. Copyright 2015 American Chemical Society. Published with permission

configurations as a function of S chemical potential. It was found that Fe_SFe_S was stable under Mo-rich conditions, while Fe_{Mo}Fe_{Mo} became the most stable configuration in the S-rich regime. The magnetic exchange coupling of Fe-doped MoS₂ monolayer was evaluated by the energy comparison of FM and anti-FM states. The obtained results indicated that the Fe_{Mo}Fe_{Mo}, Fe_{Mo}Fe_S, and Fe_SFe_S doping configurations had the FM ground states that were, respectively, 202, 247, and 20 meV lower in energy than the corresponding anti-FM state. The calculated magnetic moments were 3.78 μ_B , 5.98 μ_B , and 6.56 μ_B for Fe_{Mo}Fe_{Mo}, Fe_{Mo}Fe_S, and Fe_SFe_S, respectively.

In a bi-layer, doping configurations that involve interstitial Fe become most stable (Fig. 10.12). It was argued that the formation of Fe-Fe bonds in these configurations enhances the layer interactions and contributes to the reduction of total energy of the

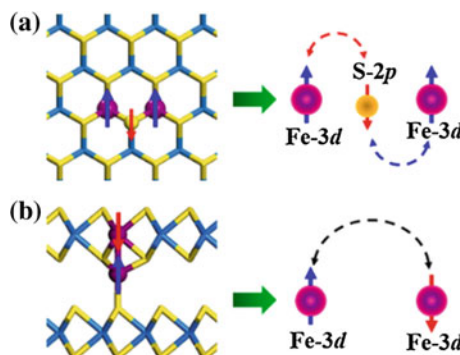
system. It was found that $\text{Fe}_\text{S}\text{Fe}_\text{i}$ and $\text{Fe}_\text{Mo}\text{Fe}_\text{i}$ had an anti-FM ground state, while the ground state of $\text{Fe}_\text{i}\text{Fe}_\text{i}$ is FM.

Double-exchange interaction and superexchange interaction between the Fe dopants were further studied and it was concluded that in monolayer MoS_2 , the substitutional Fe dopants at Mo sites are coupled ferromagnetically via the double-exchange mechanism with the FM coupling being mediated by the hybridization between Fe $3d$ states and S $2p$ states, which results in the anti-FM coupling between the Fe dopants and the nearest neighboring S atoms (Fig. 10.13a). In contrast, for Fe-doped bilayer and multilayer MoS_2 nanosheets, the formation of $\text{Fe}_\text{Mo}\text{Fe}_\text{i}$ structures leads to mediated bonding interaction between dopants with the d -electrons interaction among Fe dopants follows the superexchange mechanism, resulting in an antiparallel spin polarization among neighboring Fe dopants (Fig. 10.13b). It was concluded that the anti-FM coupling is favored in MoS_2 sheets with two and more layers [26].

A possibility of using more complicated complexes for doping, such as $\text{Fe}-X_6$ clusters ($X = \text{S}, \text{C}, \text{N}, \text{O}, \text{F}$) was studied in [27], where it was concluded that cluster doping can be an efficient strategy for exploring two-dimensional diluted magnetic semiconductors, although it is not clear how this doping can be realised experimentally.

Experimental data on magnetic doping of 2D TMDC are rather limited. In [28] room temperature FM was reported in Co-doped MoS_2 sheets. In this work, MoS_2 nanosheets with varying Co dopant concentrations of 0, 3, 7% synthesized using a hydrothermal method were studied and it was found that the magnetic moments decreased with an increase in the Co concentration. This result was interpreted in terms of coupling with magnetic moments localised at the edges.

Fig. 10.13 Schematic models of **a** double-exchange mechanism and **b** superexchange mechanism in Fe-doped MoS_2 nanosheets [26]. Copyright 2015 American Chemical Society. Published with permission



We also mention here that magnetic properties were studied (using DFT simulations) in MnX_2 monolayers, where X = S, Se, and O) and in all cases strong FM was found with a magnetic moment of $3\mu_B$ per unit cell [29, 30].

10.2.2 *Magnetism of Non-metal Adsorbates*

The magnetic properties of MoS_2 monolayers resulting from absorption of non-metal atoms such as H, B, C, N, and F were studied from first-principle simulations [31] and magnetic ordering in MoS_2 nanosheets resulting from fluorine adsorption was experimentally observed in [32].

10.3 Controlling Ferromagnetic Easy Axis

In [33], two methods to induce the FM order, which persists up to room temperature, from a diamagnetic MoS_2 single crystal by either employing proton irradiation or annealing the material in the hydrogen ambient condition were compared. It was found that while the former method enables the layered MoS_2 to have the easy axis in plane, the latter enables it to have the easy axis out of plane, resulting in improved transport properties. The hydrogenated samples were annealed at several different temperatures of 200 °C (*Ha*), 300 °C (*Hb*), and 400 °C (*Hc*) for 1 h. For the case of the proton irradiation, the doses of 1×10^{13} proton/cm² (*Pa*) and 1×10^{14} proton/cm² (*Pa*) were used.

While the pristine MoS_2 shows a negative slope of the hysteresis loop, it changes upon hydrogenation and proton irradiation and further becomes positive for a certain condition. Figure 10.14 clearly demonstrates the anisotropic behaviors between the two methods. In the case of the hydrogenated samples, the hysteresis loops of the *Ha* and *Hb* samples displayed s-type of FM hysteresis along the out-of-plane direction (Fig. 10.14b), while the hysteresis loops along the in-plane still remained diamagnetic (Fig. 10.14a), despite the slope change of the loop and the very weak rectangular hysteresis between ± 1 kOe.

In the case of proton irradiation, the hysteresis loop of the *Pa* sample, in particular, showed FM behavior along the in-plane direction. It was noted that the hysteresis loop of the *Pa* sample along the out-of-plane direction exhibited enhanced coercivity (300 Oe). In contrast, the *Pb* and *Hc* samples did not show anisotropic behavior [33].

In [34], using first-principles simulations, it was proposed that the direction of the easy axis can be rotated by charging.

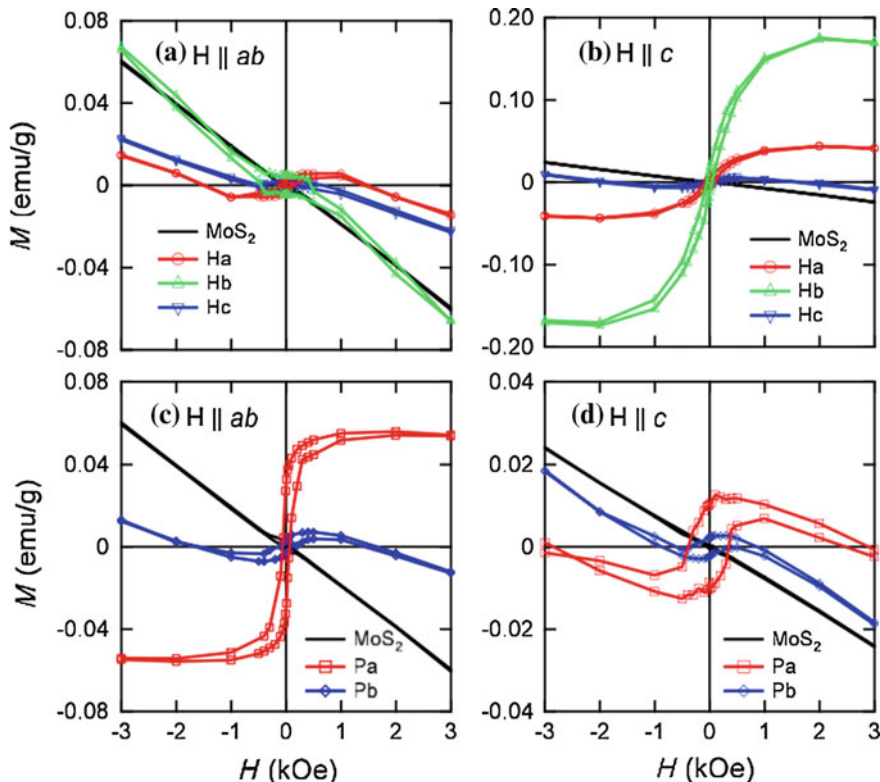


Fig. 10.14 Magnetic hysteresis loops at room temperature (300K) in the presence of applied magnetic field H parallel (a), (c) and perpendicular (b), (d) to the hydrogenated (a), (b) and proton irradiated (c), (d) samples, respectively. Note that the diamagnetic background of the pristine MoS_2 was not subtracted [33]. Copyright 2013 by the American Physical Society. Reprinted with permission

10.4 Strain-Induced Tunable Magnetism

Earlier in this volume, application of strain was demonstrated to be an efficient means to control electronic properties of 2D TMDC. The possibility to use strain for tuning TMDC magnetic properties was also investigated, predominantly using ab-initio simulations [35–43]. The main results are summarised below.

The possibility to tune magnetic properties of MoS_2 nanoribbons using strain was studied in [37, 38]. The FM properties of metallic zig-zag MoS_2 nanoribbons were found to improve under tensile strain resulting in an increase of ca. 5 times of the energy difference between the non-magnetic and magnetic states, and the magnetic moments increased up to 2 times under a strain of 10% [38]. In [37] it was additionally found that the simultaneous application of tensile strain and electric field increased the modulation of magnetic properties in zig-zag nanoribbons.

Defects were found to play a significant role in strain-tuning of magnetism. Thus while pristine MoS₂ was diamagnetic under applied strain, the presence of S and/or Mo vacancies had a strong effect on magnetism (Fig. 10.15). It was found that under a small value of strain (< 10% for V_{S₂} and < 7% for V_{Mo}), the energy gain had a global minimum at zero spin moment, showing that MoS₂ with both V_{Mo} and V_{S₂} vacancies is nonmagnetic. However, as strain goes beyond some critical value (10% for V_{S₂}, 7% for V_{Mo}), the energy gain achieved a global minimum at a finite spin moment, suggesting that spontaneous magnetism appeared in both V_{S₂} and V_{Mo} systems [42].

An interesting observation was made in [41]. When the tensile strain was applied to 1L-MoS₂ with a vacancy it became ferroelectric, in particular, 1L-MoS₂ with a two-sulfur vacancy (V_{2S}) showed the largest magnetic moment at ca. 14% strain among various vacancy types. Most intriguingly, the magnetic moment underwent a spin reorientation transition from out-of-plane to in-plane magnetization at ca. 13% strain (Fig. 10.16).

Strain also affects magnetism in doped TMDCs, as was demonstrated for hydrogenated [39] and Mn-doped [36] MoS₂ monolayers.

Strain effects on magnetic properties of some other TMDCs were also studied, e.g. in SnSe₂ [43], NbS₂ and NbSe₂ [40] and in pristine VS₂ and VSe₂ [35]. Figure 10.17 shows the variation in the magnetic moment per V atom (M_V) and the magnetic moment per X atom (M_X) of the VX₂ monolayers with strain. It is found that the magnetic moments M_V and M_X increase monotonically with increasing isotropic strain from -5 to 5% for VX₂ monolayers. At the same time, the magnetic moment M_V of the strained VX₂ monolayers with $\epsilon = 5\%$ increased by approximately 187% and 235% for the VS₂ and VSe₂ monolayers, respectively. The magnetic moment M_X of the VS₂ and VSe₂ monolayers with $\epsilon = 5\%$ also shows a 315% and 244%

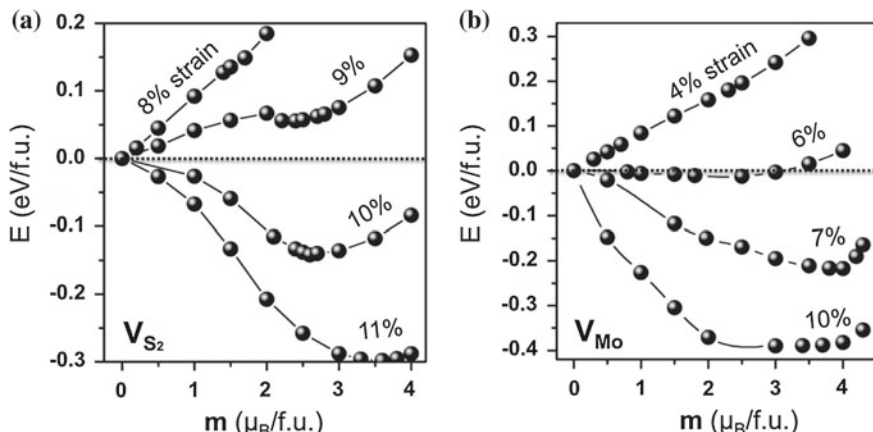


Fig. 10.15 The energy gain $E - E_0$ (in eV) as a function of magnetic moment m per formula unit (in μ_B) of **a** V_{S₂}- and **b** V_{Mo}-MoS₂ systems under a series of biaxial tensile strains. E and E_0 are the total energies under the same strain with nonzero and zero moment, respectively [42]. Reprinted with permission. Copyright 2014 by the American Institute of Physics

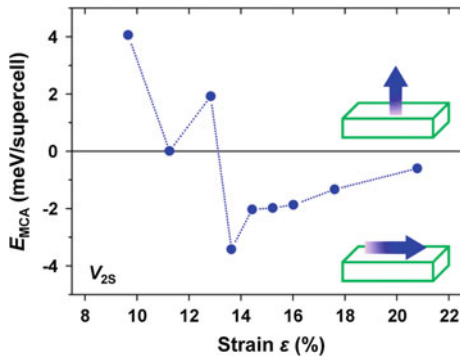


Fig. 10.16 Magnetocrystalline anisotropy energy E_{MCA} as a function of the tensile strain for the V_{2S} -defective 1L-MoS₂. The blue arrow indicates the magnetization direction with respect to the surface [41]. Copyright 2015 American Chemical Society. Published with permission (colorfigure online)

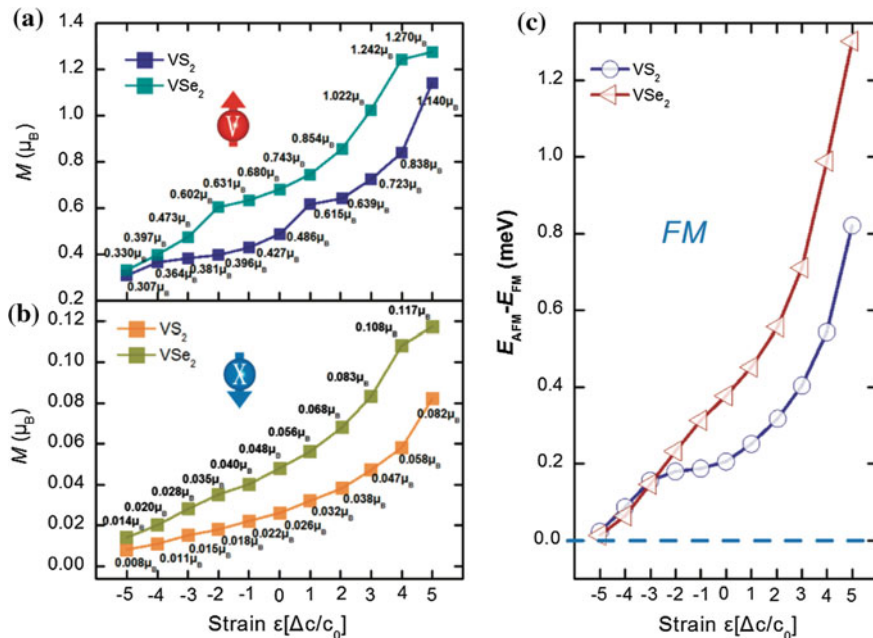


Fig. 10.17 Strain dependence of the magnetic moment per V atom M_V (a), the magnetic moment per X atom M_X (b), and the energy difference between FM and anti-FM order (c) of VX₂ monolayers [35]. Copyright 2012 American Chemical Society. Published with permission

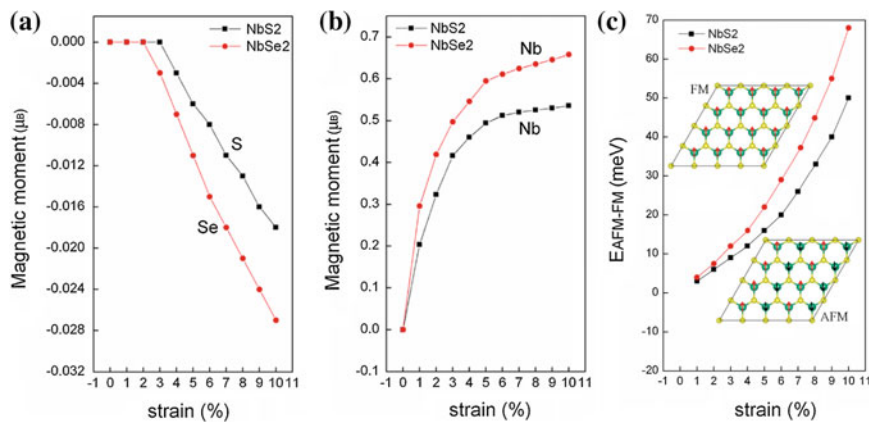


Fig. 10.18 Strain dependence of the magnetic moment **a** per S and Se atoms in NbS₂ and NbSe₂ structures, respectively, **b** per Nb atom in NbS₂ and NbSe₂ structures, and **c** the energy difference per unit cell between FM and anti-FM coupling [40]. Copyright 2012 American Chemical Society. Published with permission

enhancement, respectively, over their undeformed values. The obtained results were interpreted in terms of co-existence of ionic and covalent interactions between the V and X atoms [35]. Similar results for NbX₂ are shown in Fig. 10.18.

10.5 Magnetism Associated with the 2H-1T Phase Transition

Magnetism was also studied in monolayer samples prepared by ultrasonication of Li-intercalated MoS₂ [44]. Both 1T and 2H phases were found to be present in the exfoliated sheets, i.e. only part of MoS₂ sheets underwent a phase transition. The magnetic properties changed compared to the pristine sample. As shown in Fig. 10.19, the pristine MoS₂ exhibited typical diamagnetism, while after exfoliation, the magnetic response of MoS₂ markedly changed.

The concentration of the 1T phase was determined from XPS measurements and Fig. 10.20 shows the field-dependent magnetizations of the samples with different 1T-phase concentration at 2 K.

Figure 10.20b, c shows the fitted results of the paramagnetic component and diamagnetic components. It can be seen that with increasing 1T phase concentration, paramagnetism increases, while with increasing 2H phase concentration, diamagnetism increases. The dependences of magnetization as a function of phase are plotted in Fig. 10.20d. It can be seen that there is a clear linear relationship between the 1T/2H concentration and paramagnetism/diamagnetism.

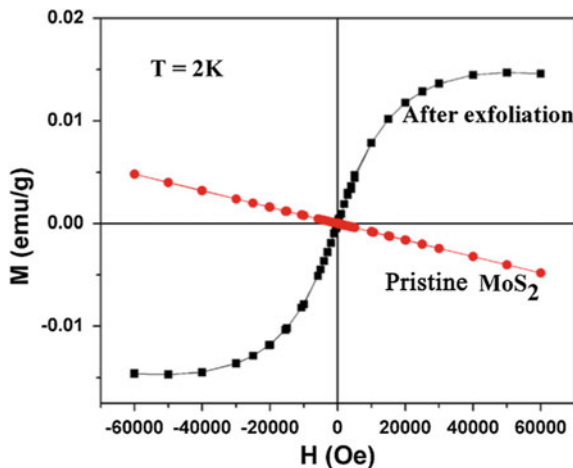


Fig. 10.19 $M - H$ curves of pristine $2H$ - MoS_2 and exfoliated MoS_2 (a mixture of $2H$ and $1T$ phases) at 2 K [44]. Reprinted with permission. Copyright 2015 by the American Institute of Physics

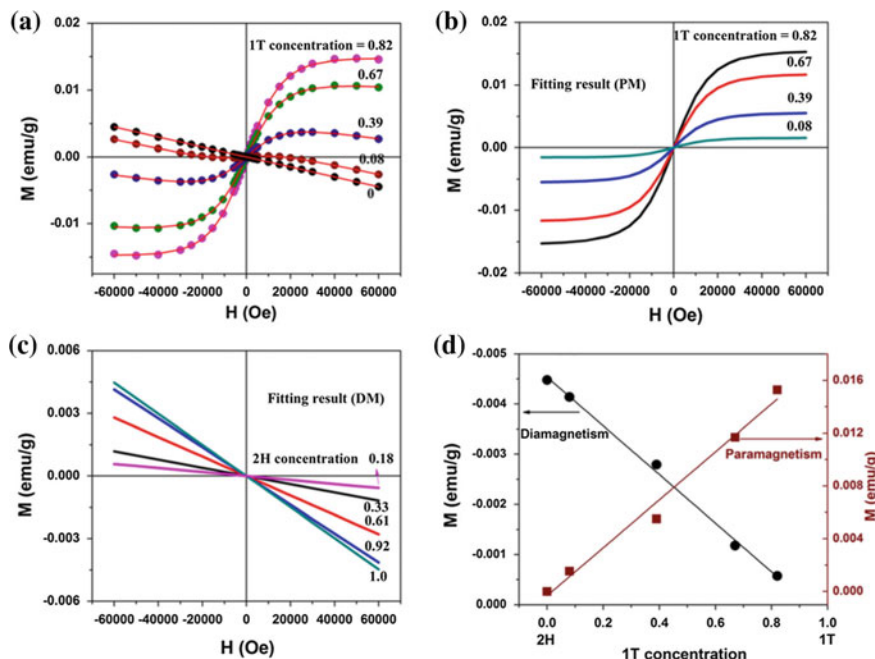


Fig. 10.20 **a** $M - H$ curves for the samples with various $1T$ concentrations. Dots indicate the experimental data, lines indicate the fitting results. **b** $M - H$ curves of PM components for the samples with various $1T$ concentrations. **c** $M - H$ curves of DM components for the samples with various $1T$ concentrations. **d** Magnetization as a function of phase concentration. A linear fit of the plot is shown as the solid line [44]. Reprinted with permission. Copyright 2015 by the American Institute of Physics

To confirm the correlation between the magnetism and the structure of MoS₂, DFT calculations were performed. Figure 10.21a shows the magnetic moment distribution obtained by spin polarized calculations. The magnetic moments were found to mainly localize on the Mo atoms of the 1T phase.

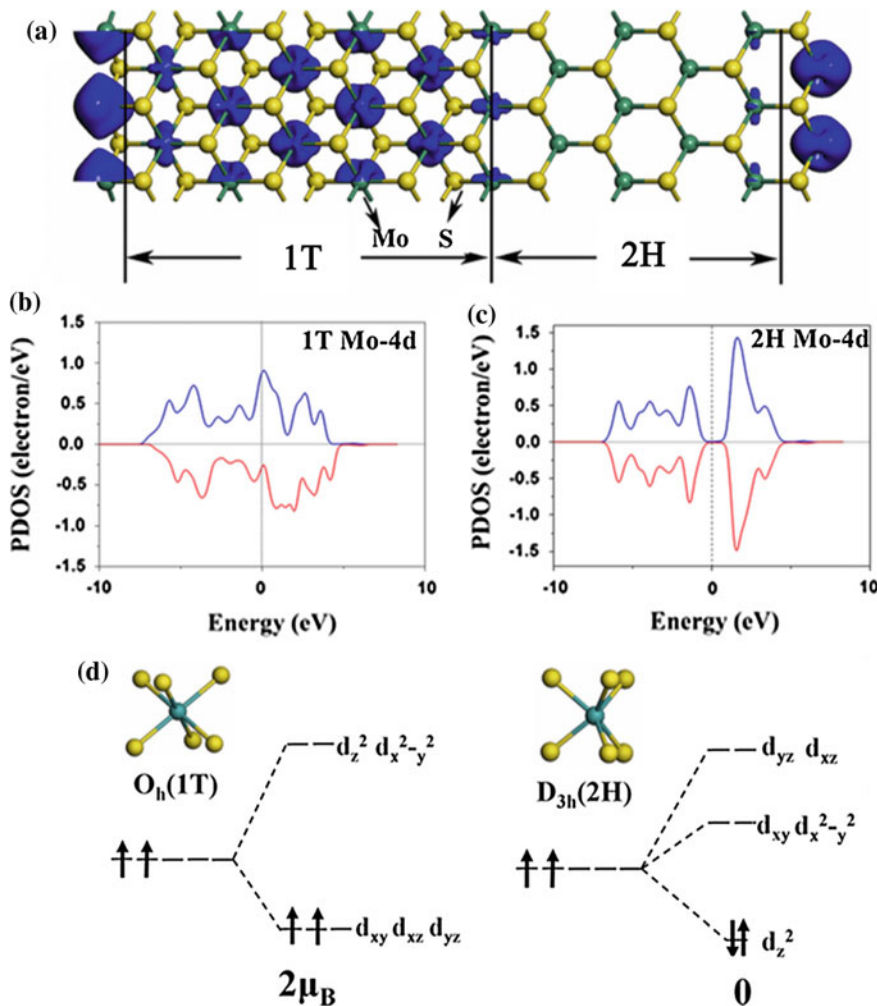


Fig. 10.21 **a** Top views of the isosurface plot of the spin density. The blue iso-surface represents the spin density. The dark cyan and yellow balls represent Mo, S, respectively. Calculated partial DOSs of the 4d states of Mo for **b** 1T phase, **c** 2H phase. **d** The occupation of electrons in Mo 4d orbitals under the crystal fields of 1T phase and 2H phase [44]. Reprinted with permission. Copyright 2015 by the American Institute of Physics

For transition metal atoms, the splitting of the d orbitals is determined by the crystal field. Thus, Mo atoms in 2H-MoS₂ have trigonal prismatic coordination and the 4d electrons are divided into three sets of orbitals: $d_{x^2-y^2}/d_{xy}$, d_{yz}/d_{xz} , and d_{z^2} (see also Sect. 3.1.7), with the d_{z^2} orbital being the lowest (Fig. 10.21d, right). When the crystal-field splitting energy is larger than the correlation energy, the two 4d electrons are paired on the d_{z^2} orbital and the 2H-MoS₂ phase is diamagnetic.

The situation is different for the 1T-MoS₂, where Mo atoms are octahedrally coordinated. Under this crystal field, the 4d electrons states split into two energy levels: (d_{xy} , d_{yz} , and d_{xz}), located lower in energy and (d_{z^2} and $d_{x^2-y^2}$), located higher in energy (Fig. 10.21d, left). As a consequence, the two d electrons occupy two different orbitals, resulting in a net magnetic moment $2\mu_B$ on each Mo atom. It was concluded that the enhanced magnetism originates from the Mo atoms in the 1T phase of MoS₂.

A mixed 1T-2H phase, referred to as 1T@2H-MoS₂, was also studied in [1] (the presence of the 1T phase incorporated in to the 2H phase was confirmed by Raman scattering and XANES measurements as well as by HR-TEM) and similar experimental results were obtained. As regards the explanation, It was noted that in spite of the atomic moment of $2\mu_B$ per Mo⁴⁺ in 1T-MoS₂, the electron spin exchange interactions between Mo⁴⁺ ions remains anti-FM in the 1T phase. Therefore, the 1T phase alone is not able to lead to significant FM at room temperature. It was proposed that the FM response is caused by electronic interactions between Mo⁴⁺ ions in the 1T and 2H phases [1].

Based on ESR experiments and DFT simulations, it was argued that the bound magnetic polaron model is best suited to explain the magnetic origin. According to the average size (2 nm) and concentration (ca. 25%) of the 1T-MoS₂ phase in the 1T@2H-MoS₂ nanosheets, the distances between two neighboring 1T-MoS₂ regions have the highest distribution probability at 1–3 nm, which is smaller than the size of a polaron. Then the spins of the localized defects (S vacancy) align those of the nearby Mo ions in the 1T phase, which provides the magnetic moments, producing an effective magnetic field and activating the FM interactions between Mo ions within the polaron radius (Fig. 10.22b). It was pointed out that the 1T phase incorporated in the 2H-MoS₂ host could not be simply regarded as a secondary phase as commonly observed in diluted magnetic semiconductors, because the 1T-MoS₂ phase alone cannot cause the robust ferromagnetism, but just provides a magnetic moment. Only those Mo⁴⁺ ions located within the effective radius of a same polaron (around a sulfur vacancy center) can interact with each other in a FM manner and give rise to the observed FM of the 1T@2H-MoS₂ nanosheets [1].

Effect of the 2H-1T phase transition accompanying exfoliation was also considered in [45].

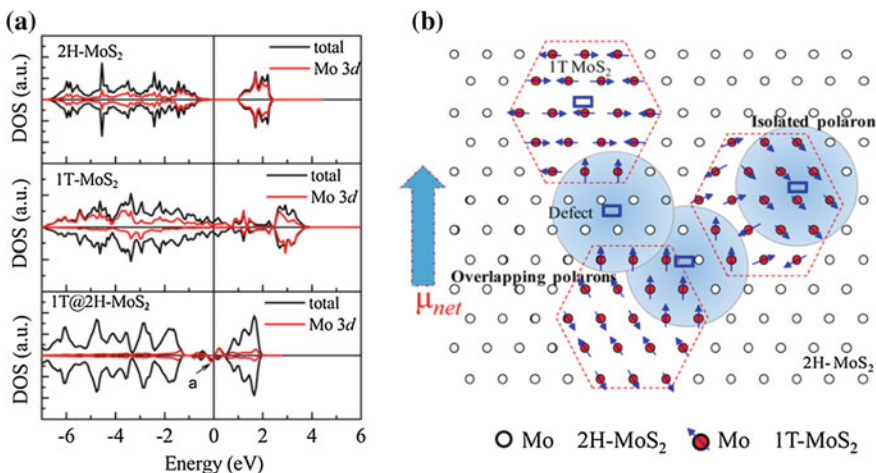


Fig. 10.22 **a** Calculated DOS for various model structures: 2H-MoS₂, 1T-MoS₂, and 1T@2H-MoS₂ nanosheets. **b** Representation of magnetic polarons [1]. Copyright 2015 American Chemical Society. Published with permission

10.6 Non-saturating Magnetoresistance in WTe₂

Large and non-saturating magnetoresistance in bulk WTe₂ was reported in [46], followed by several other experimental and theoretical papers (see Sect. 3.3.2 for details), where the effect was associated with the perfect electron-hole charge compensation. As regards the existence of this effect in mono-and few-layer WTe₂, at the moment of writing there were no experimental reports but there was a theoretical paper [47] arguing that the monolayer and bilayer WTe₂ preserve the equal hole and electron carrier concentrations. In combination with the high carrier mobilities found in WTe₂ monolayer, this result suggested monolayer WTe₂ would also exhibit the extraordinary magnetoresistance effect.

References

1. L. Cai, J. He, Q. Liu, T. Yao, L. Chen, W. Yan, F. Hu, Y. Jiang, Y. Zhao, T. Hu et al., Vacancy-induced ferromagnetism of MoS₂ nanosheets. *J. Amer. Chem. Soc.* **137**(7), 2622 (2015)
2. J. Zhang, J.M. Soon, K.P. Loh, J. Yin, J. Ding, M.B. Sullivan, P. Wu, Magnetic molybdenum disulfide nanosheet films. *Nano Lett.* **7**(8), 2370 (2007)
3. Y. Li, Z. Zhou, S. Zhang, Z. Chen, MoS₂ nanoribbons: high stability and unusual electronic and magnetic properties. *J. Am. Chem. Soc.* **130**(49), 16739 (2008)
4. A.R. Botello-Méndez, F. Lopez-Urias, M. Terrones, H. Terrones, Metallic and ferromagnetic edges in molybdenum disulfide nanoribbons. *Nanotechnology* **20**(32), 325703 (2009)
5. R. Shidpour, M. Manteghian, A density functional study of strong local magnetism creation on MoS₂ nanoribbon by sulfur vacancy. *Nanoscale* **2**(8), 1429 (2010)

6. M. Bollinger, J. Lauritsen, K.W. Jacobsen, J.K. Nørskov, S. Helveg, F. Besenbacher, One-dimensional metallic edge states in MoS₂. *Phys. Rev. Lett.* **87**(19), 196803 (2001)
7. D. Davelou, G. Kopidakis, G. Kioseoglou, I.N. Remediakis, MoS₂ nanostructures: semiconductors with metallic edges. *Solid State Commun.* **192**, 42 (2014)
8. J.V. Lauritsen, M. Nyberg, R.T. Vang, M. Bollinger, B. Clausen, H. Topsøe, K.W. Jacobsen, E. Lægsgaard, J. Nørskov, F. Besenbacher, Chemistry of one-dimensional metallic edge states in MoS₂ nanoclusters. *Nanotechnology* **14**(3), 385 (2003)
9. R.L. Chu, G.B. Liu, W. Yao, X. Xu, D. Xiao, C. Zhang, Spin-orbit-coupled quantum wires and Majorana fermions on zigzag edges of monolayer transition-metal dichalcogenides. *Phys. Rev. B* **89**(15), 155317 (2014)
10. S. Tongay, S.S. Varanoosfaderani, B.R. Appleton, J. Wu, A.F. Hebard, Magnetic properties of MoS₂: existence of ferromagnetism. *Appl. Phys. Lett.* **101**(12), 123105 (2012)
11. D. Gao, M. Si, J. Li, J. Zhang, Z. Zhang, Z. Yang, D. Xue, Ferromagnetism in freestanding MoS₂ nanosheets. *Nanoscale Res. Lett.* **8**(1), 1 (2013)
12. Z. Yang, D. Gao, J. Zhang, Q. Xu, S. Shi, K. Tao, D. Xue, Realization of high Curie temperature ferromagnetism in atomically thin MoS₂ and WS₂ nanosheets with uniform and flower-like morphology. *Nanoscale* **7**(2), 650 (2015)
13. X. Mao, Y. Xu, Q. Xue, W. Wang, D. Gao, Ferromagnetism in exfoliated tungsten disulfide nanosheets. *Nanoscale Res. Lett.* **8**(1), 1 (2013)
14. B. Xia, D. Gao, P. Liu, Y. Liu, S. Shi, K. Tao, Zigzag-edge related ferromagnetism in MoSe₂ nanoflakes. *Phys. Chem. Chem. Phys.* **17**(48), 32505 (2015)
15. N. Huo, Y. Li, J. Kang, R. Li, Q. Xia, J. Li, Edge-states ferromagnetism of WS₂ nanosheets. *Appl. Phys. Lett.* **104**(20), 202406 (2014)
16. Z. Zhang, X. Zou, V.H. Crespi, B.I. Yakobson, Intrinsic magnetism of grain boundaries in two-dimensional metal dichalcogenides. *ACS Nano* **7**(12), 10475 (2013)
17. C. Ataca, H. Sahin, E. Akturk, S. Ciraci, Mechanical and electronic properties of MoS₂ nanoribbons and their defects. *J. Phys. Chem. C* **115**(10), 3934 (2011)
18. C. Ataca, S. Ciraci, Functionalization of single-layer MoS₂ honeycomb structures. *J. Phys. Chem. C* **115**(27), 13303 (2011)
19. R. Zhang, Y. Li, J. Qi, D. Gao, Ferromagnetism in ultrathin MoS₂ nanosheets: from amorphous to crystalline. *Nanoscale Res. Lett.* **9**(1), 1 (2014)
20. S. Mathew, K. Gopinadhan, T. Chan, X. Yu, D. Zhan, L. Cao, A. Rusydi, M. Breese, S. Dhar, Z. Shen et al., Magnetism in MoS₂ induced by proton irradiation. *Appl. Phys. Lett.* **101**(10), 102103 (2012)
21. Y. Ma, Y. Dai, M. Guo, C. Niu, J. Lu, B. Huang, Electronic and magnetic properties of perfect, vacancy-doped, and nonmetal adsorbed MoSe₂, MoTe₂ and WS₂ monolayers. *Phys. Chem. Chem. Phys.* **13**(34), 15546 (2011)
22. Y. Cheng, Z. Guo, W. Mi, U. Schwingenschlögl, Z. Zhu, Prediction of two-dimensional diluted magnetic semiconductors: doped monolayer MoS₂ systems. *Phys. Rev. B* (2013)
23. R. Mishra, W. Zhou, S.J. Pennycook, S.T. Pantelides, J.C. Idrobo, Long-range ferromagnetic ordering in manganese-doped two-dimensional dichalcogenides. *Phys. Rev. B* **88**(14), 144409 (2013)
24. C.J. Gil, A. Pham, A. Yu, S. Li, An ab initio study of transition metals doped with WSe₂ for long-range room temperature ferromagnetism in two-dimensional transition metal dichalcogenide. *J. Phys.: Cond. Matter* **26**(30), 306004 (2014)
25. S. Dudarev, G. Botton, S. Savrasov, C. Humphreys, A. Sutton, Electron-energy-loss spectra and the structural stability of nickel oxide: An LSDA+U study. *Phys. Rev. B* **57**(3), 1505 (1998)
26. H. Shu, P. Luo, P. Liang, D. Cao, X. Chen, Layer-dependent dopant stability and magnetic exchange coupling of iron-doped MoS₂ nanosheets. *ACS Appl. Mater. Int.* **7**(14), 7534 (2015)
27. N. Feng, W. Mi, Y. Cheng, Z. Guo, U. Schwingenschlögl, H. Bai, First principles prediction of the magnetic properties of Fe-X₆ (X= S, C, N, O, F) doped monolayer MoS₂. *Sci. Rep.* **4** (2014). doi:[10.1038/srep03987](https://doi.org/10.1038/srep03987)
28. Z. Xiang, Z. Zhang, X. Xu, Q. Zhang, Q. Wang, C. Yuan, Room-temperature ferromagnetism in Co doped MoS₂ sheets. *Phys. Chem. Chem. Phys.* **17**, 15822 (2015)

29. M. Kan, J. Zhou, Q. Sun, Y. Kawazoe, P. Jena, The intrinsic ferromagnetism in a MnO₂ monolayer. *J. Phys. Chem. Lett.* **4**(20), 3382 (2013)
30. M. Kan, S. Adhikari, Q. Sun, Ferromagnetism in MnX₂ (X= S, Se) monolayers. *Phys. Chem. Chem. Phys.* **16**(10), 4990 (2014)
31. J. He, K. Wu, R. Sa, Q. Li, Y. Wei, Magnetic properties of nonmetal atoms absorbed MoS₂ monolayers. *App. Phys. Lett.* **96**(8), 082504 (2010)
32. D. Gao, S. Shi, K. Tao, B. Xia, D. Xue, Tunable ferromagnetic ordering in MoS₂ nanosheets with fluorine adsorption. *Nanoscale* **7**(9), 4211 (2015)
33. S.W. Han, Y.H. Hwang, S.H. Kim, W.S. Yun, J. Lee, M.G. Park, S. Ryu, J.S. Park, D.H. Yoo, S.P. Yoon et al., Controlling ferromagnetic easy axis in a layered MoS₂ single crystal. *Phys. Rev. Lett.* **110**(24), 247201 (2013)
34. E. Torun, H. Sahin, C. Bacaksiz, R. Senger, F. Peeters, Tuning the magnetic anisotropy in single-layer crystal structures. *Phys. Rev. B* **92**(10), 104407 (2015)
35. Y. Ma, Y. Dai, M. Guo, C. Niu, Y. Zhu, B. Huang, Evidence of the existence of magnetism in pristine VX₂ monolayers (X = S, Se) and their strain-induced tunable magnetic properties. *ACS Nano* **6**(2), 1695 (2012)
36. J. Qi, X. Li, X. Chen, K. Hu, Strain tuning of magnetism in Mn doped MoS₂ monolayer. *J. Phys: Cond. Matter* **26**(25), 256003 (2014)
37. L. Kou, C. Tang, Y. Zhang, T. Heine, C. Chen, T. Frauenheim, Tuning magnetism and electronic phase transitions by strain and electric field in zigzag MoS₂ nanoribbons. *J. Phys. Chem. Lett.* **3**(20), 2934 (2012)
38. H. Pan, Y.W. Zhang, Tuning the electronic and magnetic properties of MoS₂ nanoribbons by strain engineering. *J. Phys. Chem. C* **116**(21), 11752 (2012)
39. H. Shi, H. Pan, Y.W. Zhang, B.I. Yakobson, Strong ferromagnetism in hydrogenated monolayer MoS₂ tuned by strain. *Phys. Rev. B* **88**(20), 205305 (2013)
40. Y. Zhou, Z. Wang, P. Yang, X. Zu, L. Yang, X. Sun, F. Gao, Tensile strain switched ferromagnetism in layered NbS₂ and NbSe₂. *ACS Nano* **6**(11), 9727 (2012)
41. W.S. Yun, J. Lee, Strain-induced magnetism in single-layer MoS₂: origin and manipulation. *J. Phys. Chem. C* **119**(5), 2822 (2015)
42. P. Tao, H. Guo, T. Yang, Z. Zhang, Strain-induced magnetism in MoS₂ monolayer with defects. *J. Appl. Phys.* **115**(5), 054305 (2014)
43. Y. Huang, C. Ling, H. Liu, S. Wang, B. Geng, Versatile electronic and magnetic properties of SnSe₂ nanostructures induced by the strain. *J. Phys. Chem. C* **118**(17), 9251 (2014)
44. S. Yan, W. Qiao, X. He, X. Guo, L. Xi, W. Zhong, Y. Du, Enhancement of magnetism by structural phase transition in MoS₂. *Appl. Phys. Lett.* **106**(1), 012408 (2015)
45. J. Luxa, O. Jankovský, D. Sedmidubský, R. Medlín, M. Maryško, M. Pumera, Z. Sofer, Origin of exotic ferromagnetic behavior in exfoliated layered transition metal dichalcogenides MoS₂ and WS₂. *Nanoscale* (2016). doi:[10.1039/c5nr05757d](https://doi.org/10.1039/c5nr05757d)
46. M.N. Ali, J. Xiong, S. Flynn, J. Tao, Q.D. Gibson, L.M. Schoop, T. Liang, N. Haldolaarachchige, M. Hirschberger, N. Ong et al., Large, non-saturating magnetoresistance in WTe₂. *Nature* **514**(7521), 205 (2014)
47. H.Y. Lv, W.J. Lu, D.F. Shao, Y. Liu, S.G. Tan, Y.P. Sun, Perfect charge compensation in WTe₂ for the extraordinary magnetoresistance: from bulk to monolayer. *Europhys. Lett.* **110**(3), 37004 (2015)

Chapter 11

Spin-Valley Coupling

In 2D TMDCs, spin and valley indices of charge carriers are coupled. This coupling, which is one the most interesting areas of TMDC research and forms the basis of potential TMDC applications in valleytronics, is the subject of the present Chapter.

11.1 Valley Degree of Freedom

In monolayer TMDCs, the conduction and valence-band edges are located at the corners (K and K') of the 2D hexagonal Brillouin zone. These two inequivalent valleys constitute a binary index for low energy charge carriers. Because of the large valley separation in momentum space, the valley index in TMDCs is expected to be robust against scattering by smooth deformations and long wavelength phonons, as first proposed in [1].

The most-studied example of an external degree of freedom of electrons is the electron spin, associated with the magnetic moment, which led to the vast field of spintronics. Similar to spin, other binary quantum degrees of freedom, which may be viewed as pseudospins, have been searched for. An example of this is valley pseudospin, which labels the degenerate energy extrema in momentum space, and, in analogy with spintronics, a parallel concept of valleytronics emerged, which aims to use the valley index of charge carriers as an information carrier [2].

In order to manipulate the valley degree of freedom, one need measurable physical quantities that distinguish the $\pm K$ valleys. For example, the spin up and down states are time-reversed images of one another and are distinguished by opposite values of the magnetic moment. The latter is a pseudovector, possessing odd parity under time reversal. This quantity allows spin to couple to magnetic fields and spin polarization to be detected as magnetization, demonstrating that physical quantities that have odd parity under time reversal are good candidates to distinguish valley pseudospin states [2].

Several important differences between TMDCs, such as MoS₂ monolayers, and graphene were noted [1]. First, inversion symmetry is explicitly broken in monolayer

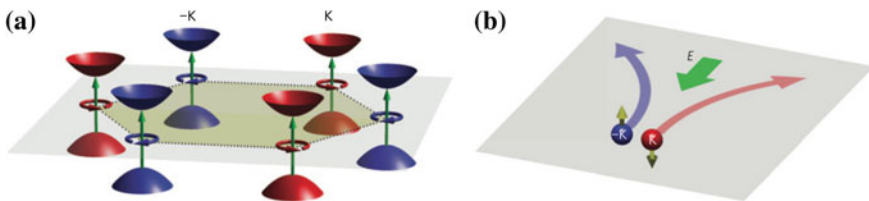


Fig. 11.1 **a** Valley contrasting optical selection rules in a 2D hexagonal lattice with broken inversion symmetry. The interband transition in valley K ($-K$) couples to σ^+ (σ^-) circularly polarized light only (*circular arrows*). **b** Valley Hall effect. *Blue* (*red*) denotes the electron in valley K ($-K$). The *yellow arrows* indicate the pseudo-vector quantities (Berry curvature or orbital magnetic moment) of the electron, while the *green arrow* indicates the applied electric field [2]. Reprinted by permission from Macmillan Publishers Ltd., copyright (2014)

MoS_2 , which can give rise to the valley Hall effect (Fig. 11.1b) where carriers in different valleys flow to opposite transverse edges when an in-plane electric field is applied. Second, the inversion symmetry breaking can lead to valley-dependent optical selection rules for interband transitions at K points. And, third, MoS_2 has a strong spin-orbit coupling (SOC) originating from the d -orbitals of the heavy metal atoms.

Important concepts for understanding valley physics are the Berry curvature (Ω) and orbital magnetic moment (m), two physical quantities that characterize the effect of the Berry phase of electrons in the Bloch bands. Ω gives rise to an anomalous velocity perpendicular to an applied electric field, while m , which arises from the self-rotating motion of the electron wavepacket, leads to an energy shift in a magnetic field. Both Ω and m are pseudovectors, and the $\pm K$ valleys are allowed to have opposite values of these quantities. At the same time, when spatial inversion symmetry is present, the spatial inversion operation transforms K and K' valleys into one another. Therefore, inversion symmetry breaking, such as in monolayers of TMDCs, is a necessary condition for the $\pm K$ valleys to exhibit valley contrast for Ω and m [2]. In bi-layers, the spin-valley interaction leads to spin-layer locking, which results in interesting magnetoelectric effects [3].

It may be interesting to note that in conventional semiconductors, such as GaAs, excitons and trions form at the Brillouin zone centre. However, in monolayer TMDCs, confinement of electrons and holes to the $\pm K$ valleys gives rise to valley excitons and trions, formed at an energy-degenerate set of non-central points in momentum space.

It should also be mentioned that in the presence of Landau-level quantization such selection rules are taken over by selection rules between the Landau levels, which are not necessarily valley contrasting. Using MoS_2 as an example [4] it was shown that the spatial inversion-symmetry breaking results in unusual valley-dependent inter-Landau level selection rule, which is controlled by the sign of the magnetic field and directly locks the polarization to a given valley. Landau levels were also studied with respect to quantum Hall effect [5] and quantum spin Hall effect [6] in TMDCs.

11.1.1 Optical Control of Valley Polarization

Experimentally, valley polarisation in monolayers of MoS₂ using circularly polarized light was reported simultaneously by different groups [7–9]. Figure 11.2a shows the circularly polarized luminescence spectra of a pristine MoS₂ monolayer, which peak around 1.9 eV with right- and left-handed circularly polarized excitation (He-Ne laser, 1.96 eV) at a near-resonant condition at T = 10 K. The luminescence corresponds to a direct inter-band transition at the K (K') valley. The helicity of the luminescence exactly follows that of the excitation light. In other words, the right-handed circularly polarized excitation generates right-handed luminescence, and the left-handed circularly polarized excitation generates left-handed luminescence. To characterize the circular component in the luminescence spectra, the degree of circular polarization $P = \frac{I(\sigma+) - I(\sigma-)}{I(\sigma+) + I(\sigma+)}$ was defined, where $I(\sigma\pm)$ is the intensity of the left (right)-handed circular component. For perfectly circularly polarized light, $P = 1$. Luminescence spectra of symmetric polarization for excitation with opposite helicities, with $P \approx \pm 0.32$ were observed. A similar result was obtained in [9], except that in this work the degree of polarization close to 1.0 was reported.

In both studies [8, 9], it was found that the polarisation had a resonant behavior: the degree of polarisation dropped rapidly for excitation energies below 1.8 eV and above 2.33 eV. In [9] this phenomenon was explained by the relaxation of the optical selection rules, where off-resonance excitation simultaneously populates both K and K' valleys.

A decrease of polarization at higher excitation energies was also reported in [10], where it was attributed to scattering by longitudinal acoustic phonons. It was also noted that different degrees of polarisation obtained in different studies may be due to the fact that the energy of the A exciton is sample dependent [10].

In many semiconductor systems such as GaAs bulk and heterostructures, the circular polarization of luminescence from circularly polarized excitation originates from electron (hole) spin polarization as a result of the spin-dependent optical selection rules [11, 12]. In this case, the degree of polarisation can be reduced by an application of an in-plane magnetic field, which is a well known Hanle effect. In [8] it was shown that an application of an in-plane magnetic field of 0.65 T had no effect on the degree of polarization. It was subsequently demonstrated that the polarization of emission is robust even for much higher fields up to 8.5 T and the polarization of 40% remained even at 300 K [13]. These results demonstrate that the observed circular polarisation of PL is not due to spin-dependent optical selection rules.

Of interest is a pronounced difference between PL from a monolayer and bi-layer. While the intensity of the luminescence in bilayers is insignificantly weaker than that of monolayers, the circular polarization of luminescence from bilayers was negligible (Fig. 11.2b). This difference can be easily understood by the presence of inversion symmetry that is preserved in the bilayer unit cell, so the valley-dependent selection rule is not allowed. It was found that if the excitation power is increased above $1 \times 10^5 \text{ W} \cdot \text{cm}^{-2}$, circularly polarized photoluminescence could also be observed in bilayers, which was interpreted in terms of heating induced structural anisotropy and consequently the breaking of inversion symmetry in the bi-layer [8].

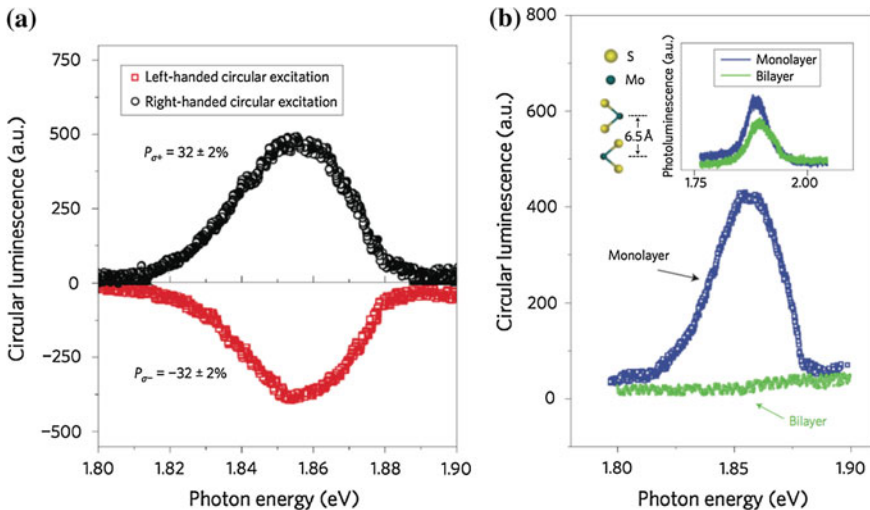


Fig. 11.2 **a** Polarization resolved luminescence spectra under circularly polarized excitation from a He-Ne laser at 1.96 eV and 10 K. Circular polarizations are observed along the out-of-plane direction of a MoS₂ monolayer with right- and left-handed circular excitation, respectively. **b** Circularly polarized components of luminescence spectra from MoS₂ bilayers (green) and monolayers (blue) under circular excitation at 1.96 eV and 10 K. Negligible circular polarization is observed for the MoS₂ bilayers. *Inset:* photoluminescence spectra of monolayer (blue) and bilayer (green) MoS₂ under the same conditions (base temperature, 10 K; 0.2 mW linearly polarized excitation at 1.96 eV). The intensity of the bilayer luminescence is slightly weaker than that of the monolayer [8]. Reprinted by permission from Macmillan Publishers Ltd., copyright (2012)

In [9], a hole valley-spin lifetime of more than 1 ns in monolayer MoS₂ was found while in a bilayer the exciton emission had a much shorter lifetime, which was interpreted to be a result of very slow intervalley scattering in monolayers, where scattering from the K to K' point requires a simultaneous spin flip. The authors provide a detailed discussion of spin relaxation mechanism, including (i) the Elliot-Yafet mechanism [14, 15], (ii) the Dyakonov–Perel mechanism [16], (iii) the Bir-Aronov–Pikus mechanism [17], and (iv) the hyperfine interaction [18]. It was noted that the hyperfine interaction is unimportant for the d_{xy} and $d_{x^2-y^2}$ orbitals because of the small overlap of the hole wavefunction with the nucleus. It was further noted that as a result of the coupled valley and spin degrees of freedom in monolayer MoS₂, the Elliot-Yafet relaxation, which is operative during each scattering event due to spin-orbit coupling, is strongly suppressed. The authors provided a detailed discussion of the Dyakonov–Perel and Bir–Aronov–Pikus mechanisms and concluded that the Bir–Aronov–Pikus process could be a relevant spin relaxation mechanism for MoS₂ monolayers. The interested reader is referred to the supplementary information of [9] for more details.

The circular polarization in MoS₂ had a flat plateau at ~31% below 90 K, then dramatically drops with increasing temperature [8], which is an indicator of phonons dominating the intervalley scattering at high temperatures. A similar temperature dependence of circular polarization in MoS₂ was reported in [19] but a different

interpretation was proposed. It was argued that because the A -exciton transition energy redshifted as the temperature is increased, the A -exciton energy moved away from the photoexcitation energy, resulting in a decrease in the degree of circular polarization.

Polarised photoluminescence was also studied in some other TMDCs. While the main features were the same there were some interesting differences. In WSe_2 , it was found that the degree of polarisation changed very little when the excitation energy was changed from 1.79 to 2.33 eV, or ~ 80 times the exciton linewidth above the valley exciton emission energy (Fig. 11.3) [20], in stark contrast to monolayer MoS_2 , where valley polarization was generated only when the photo-excitation energy was within the line width of the exciton emission. In addition, it was found that in monolayer WSe_2 both neutral exciton and trion had strong polarization. In MoSe_2 monolayers very low circular polarization was reported, increasing from $\simeq 0$ for $3 \mu\text{W}$ excitation to $\simeq 4$ for $200 \mu\text{W}$ excitation [21].

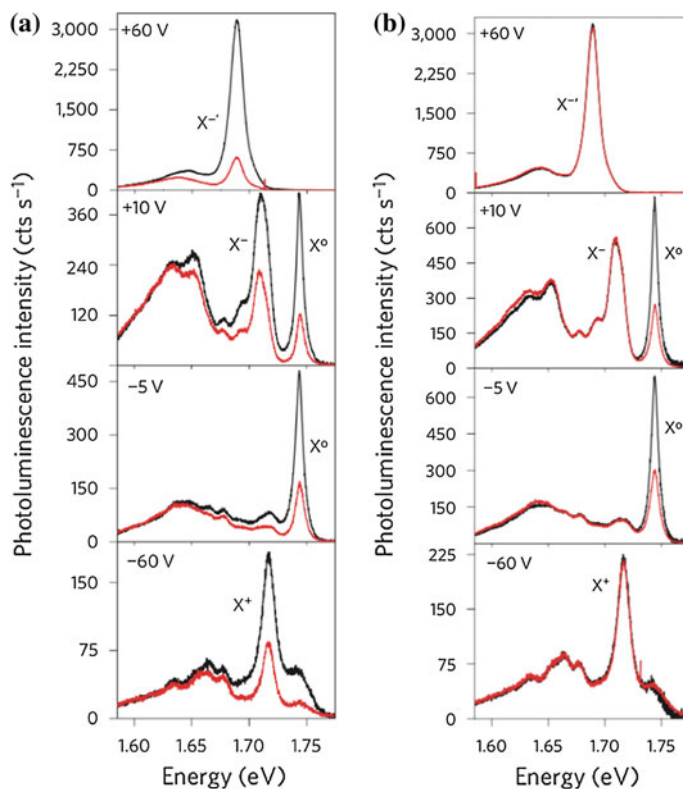


Fig. 11.3 **a** Polarization-resolved photoluminescence spectra at selected gate voltages for $\sigma(+)$ (black curve) and $\sigma(-)$ (red curve) detection. Incident laser is $\sigma(+)$ polarized. Excitonic peaks are labelled. **b** Polarization-resolved photoluminescence spectra at selected gate voltages for horizontally (H , black curve) and vertically (V , red curve) polarized detection. Incident laser is horizontally polarized [22]. Reprinted by permission from Macmillan Publishers Ltd., copyright (2014)

In WS₂, circularly polarised photoluminescence was observed from both monolayers and bi-layers [23]. Intriguingly, the degree of polarisation was larger (0.95 vs. 0.4 at 10 K) in bi-layers. In both cases the degree of polarisation exhibited a plateau at temperatures below 150 K and then decreased approaching 0.1 and 0.6 at 300 K for monolayers and bi-layers, respectively. Various scenarios of the spin-flip process were discussed but no clear conclusion regarding the observed results was reached.

Because the presence of valley polarisation in TMDC monolayers is associated with the breaking of inversion symmetry, one might expect it to be present in the bulk 3R polymorph of MoS₂, as indeed, was observed experimentally [24]. The authors compared valley polarisation for 2H and 3R stacking for different number of layers and found that while it changed as $1/N$ (N is the number of layers) for the 2H polymorph (Fig. 11.4), it stayed constant for the 3R polymorph, indicating the important role of the 3R stacking. The observed $1/N$ dependence is in agreement with the simulation results of [25] where the thickness dependence of the spin polarization of TMDCs was studied, except that the theoretical values for an even number of layers was zero, i.e.:

$$\rho(N) = \begin{cases} 0 & \text{if } N = 2, 4, 6 \\ 1/N & \text{if } N = 1, 3, 5 \end{cases} \quad (11.1)$$

The appearance of valley polarisation in inversion-symmetric bilayer in quadlayer flakes with 2H stacking was attributed to symmetry breaking associated with the substrate. Valley engineering in folded MoS₂ bilayers with different stacking was also studied in [26].

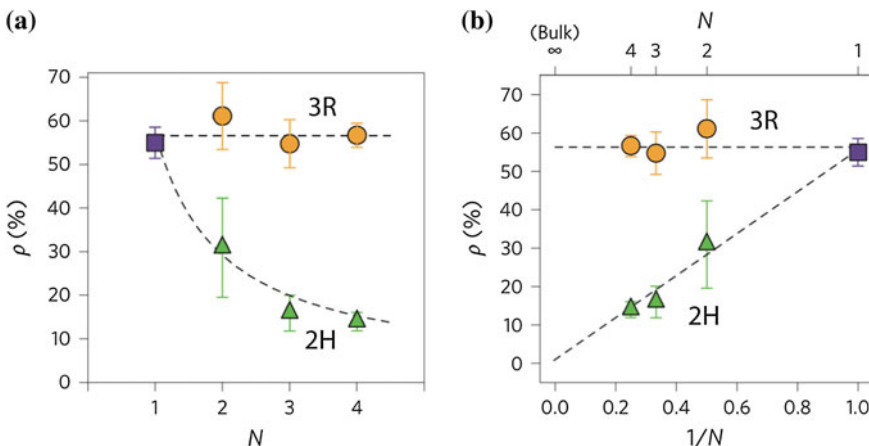
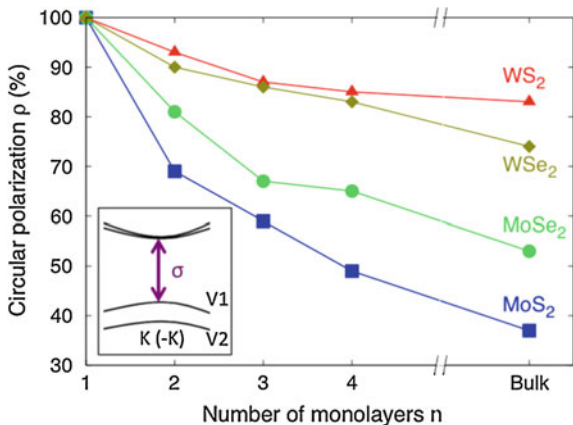


Fig. 11.4 Layer number (a) and inverse layer number (b) dependences of polarization ρ for 2H- and 3R-stackings with error bars of experimental standard deviation for several samples [24]. Reprinted by permission from Macmillan Publishers Ltd., copyright (2014)

Fig. 11.5 Calculated circular polarization ρ for different MX_2 materials as a function of the number of monolayers n . The inset shows a schematic band structure of bilayer MX_2 [27]. Copyright 2015 by the American Physical Society. Reprinted with permission



It appears, however, that the issue of measurable valley polarization for samples with even number of layers is more complicated. While such results are typically interpreted as being due to the substrate charging, heating, and sample imperfection, it was also argued that it could be explained based on fundamental spin-orbit physics [27]. The authors consider spin-orbit physics as a local effect, building on the recent finding that SOC-induced spin polarization can exist not only when inversion symmetry is absent, but also in systems where inversion symmetry is present (i.e., globally centrosymmetric systems) while its individual sectors (e.g., monolayers) lack inversion [28], such as TMDCs. It was demonstrated that such hidden spin polarization can lead to circular polarization for even number of layers in the stack. The results of their first-principles calculated polarization, ρ , for the emission from the direct band states at the K and $-K$ valley as a function of the number of monolayers in shown in Fig. 11.5, approaching the bulk value for a large n . One can see that the circular polarization decreases monotonically with increasing n without odd-even oscillations, in contrast to the expectation based on valley symmetries [8, 25] but in agreement with the experimental observation of [24] (cf. Fig. 11.4).

11.1.2 Electrical Control of Valley Polarisation

Electrically switchable chiral electroluminescence was reported in [29] using WSe₂ p-i-n junctions. When the p-i-n junction was forward-biased, circularly polarised EL was observed with the degree of circular polarization reaching values as high as 45%, which is comparable with that of PL from monolayers. Furthermore, the circular polarization was reversed (Fig. 11.6) when the source-drain bias was exchanged, demonstrating the possibility of electrical control of circularly polarized luminescence.

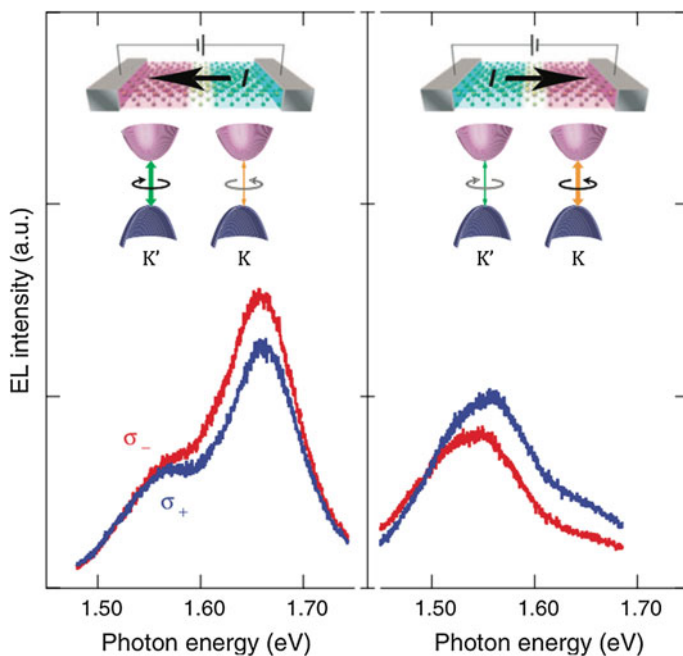


Fig. 11.6 Circularly polarized EL spectra for two opposite current directions schematically indicated in the top illustration. Bottom illustrations represent the contribution to EL from two valleys [29]. Reprinted with permission from AAAS

11.1.3 Valley Coherence

Circularly polarised luminescence was the first demonstration that structural inversion asymmetry present in monolayer transition-metal dichalcogenides gives rise to valley-dependent circularly polarized optical selection rules. More challenging is to realize quantum coherence between the two well-separated band extrema in momentum space, that is, valley quantum coherence. One of the first experimental reports of valley coherence in TMDCs was for a WSe₂ monolayer [20].

It was found that for linearly polarized light excitation, the X⁰ emission was also highly linearly polarized ($r = 0.4$), while trion photoluminescence was not. Figure 11.3b shows the photoluminescence spectra at selected gate voltages V_g under horizontally (H) polarized light excitation at 1.88 eV. One can see that the H component of X⁰ (black curve) is much stronger than the vertically polarized (V) photoluminescence component (red curve), while trions have equal photoluminescence intensity for both H and V detection. It was found that the observed X⁰ polarization was independent of the crystal orientation. It was also noted that linearly polarized X⁰ emission can arise from crystal anisotropy but in systems that lack crystal anisotropy, the isotropic linear polarization can be generated if excitonic coherence is maintained for longer than the exciton recombination time. Because monolayer

WSe_2 has three-fold rotational symmetry, the observed linearly polarised luminescence was attributed to the generation of excitonic quantum coherence between opposite valleys by linearly polarized light [20].

As demonstrated above, with $\sigma(+)$ ($\sigma(-)$) polarized laser excitation, X^0 is highly polarized at the $\pm K$ valleys due to the circularly polarized valley optical selection rule. Because linear polarization is a coherent superposition of $\sigma(+)$ and $\sigma(-)$, it will simultaneously excite both K and $-K$ valleys and transfer the optical coherence to valley quantum coherence; that is, the photoexcited electron-hole pair is a linear superposition in the valley subspace [20]. It was concluded that the observation of linearly polarized X^0 photoluminescence parallel to the arbitrarily oriented linearly polarized excitation light implies that the intervalley coherence has been preserved in the exciton formation. Key to the preservation of valley quantum coherence is the equivalence of quantum trajectories for the photoexcited electron (hole) on states $|K + q\rangle$ and $| -K + q\rangle$ so that their relative phase remains unchanged in exciton formation.

The absence of polarisation for trions was further discussed. For the X^+ trion, there are only two possible configurations because the holes at the valley $+K$ ($-K$) only have spin-down (-up) states due to the giant spin-valley coupling and time-reversal symmetry. Upon electron-hole recombination, one X^+ configuration becomes a $\sigma(+)$ photon plus a spin-down hole, and the other becomes a $\sigma(-)$ photon plus a spin-up hole. It was argued that linearly polarized photons as a superposition of $\sigma(+)$ and $\sigma(-)$ are always forbidden for X^+ emission, because the hole states associated with $\sigma(+)$ and $\sigma(-)$ are orthogonal. The explanation for the absence of linearly polarised luminescence associated with X^- trions was rather speculative [20].

Valley coherence in monolayer and bilayer WS_2 was reported in [23]. It was found that the degree of linear polarisation was as high as 80% at 10 K for a bilayer, while it was much smaller (4% under identical experimental conditions) in a monolayer. The degree of the linear polarization in bilayer WS_2 slightly decreases with the increasing temperature (to 50% at room temperature).

In contrast to the rather large linear polarization in tungsten chalcogenides, in MoS_2 , linear polarization was found to be negligibly small in monolayers and increased with an increasing number of layers. Interestingly, it also increased with increasing temperature [19].

11.2 Zeeman-Type Splitting by an Electric Field

Spin-orbit coupling can be efficiently measured using magnetoelectric measurements [30]. By using a WSe_2 electric double layer transistor structure, it was shown that an application of an external electric field caused a transition from a weak localization to a weak anti-localization regime, the latter being associated with the spin-orbit interaction.

As the Γ -point and K -point have different symmetry properties, a set of first-principles calculations was performed for sufficiently thick slabs of WSe_2 , exposed

to a perpendicular electric field E_{ex} , in order to determine how their corresponding Fermi pockets are spin-polarized by the applied field. It was found that E_{ex} induced a huge spin splitting among the top valence bands with an energy order up to ca. 270 meV in the vicinity of the K -points, while no significant spin splitting could be seen around the Γ -point. The reason why the spin splitting is absent at the Γ -point whereas it is large and out-of-plane at the K -point was explained by the group theory [30]. Despite the strong spin-orbit interaction of W ions, without gating the whole structure remains centrosymmetric and nonpolar and, thus, the electronic states cannot be intrinsically spin-polarized. In the presence of E_{ex} , the centrosymmetry of electronic wavefunctions is disturbed and thus each monolayer can retain part of its intrinsic spin polarization vector without any cancellation from the adjacent monolayer. As a result, E_{ex} can controllably produce an out-of-plane Zeeman-like spin polarization among the electronic states at (and in the vicinity of) the K -points.

11.3 Magnetic Control of Valley Pseudospin in Monolayers

As described earlier, in TMDC monolayers there is a valley pseudospin which describes the two inequivalent but energy-degenerate band edges (the $\pm K$ valleys) at the corners of the hexagonal Brillouin zone. With broken inversion symmetry, electrons in the two valleys can have finite orbital contributions to their magnetic moments which are equal in magnitude but opposite in sign due to time-reversal symmetry. The orbital magnetic moment in turn has two parts: a contribution from the parent atomic orbitals, and a ‘valley magnetic moment’ contribution from the lattice structure. The latter leads to the valley-dependent optical selection rule in TMDC monolayers.

In a 2D material such as a monolayer, the current circulation from the orbitals can only be within the plane; as a consequence, the corresponding orbital magnetic moment can only point out-of-plane. A magnetic field (B) along z distinguishes the sense of circulation in 2D, causing opposite energy shifts (μB) in $\pm K$ valleys as a result of opposite magnetic moments. The lifting of degeneracy between the two valleys in the presence of a magnetic field would represent a valley analogue of the spin-Zeeman effect [31].

At the same time, the optical excitation spectra of TMDCs are strongly modified by Coulomb interactions, leading to strongly bound neutral and charged exciton (trion) resonances with non-hydrogenic excited states (cf. Sect. 9.1.2). Hence a question arises to what extent predictions about circular dichroism or orbital magnetic moments based on a non-interacting particle picture remain valid in optical measurements probing exciton or trion resonances.

Three different groups independently demonstrated the possibility of controlling excitonic valley pseudospin via the Zeeman effect in an external magnetic field [32–34].

Figure 11.7b shows the normalized PL spectra from a WSe₂ monolayer for the neutral exciton peak at selected values of the magnetic field B . Excitation was with

circularly polarised (1.88 eV) light. For $B = 0$, the PL from the $+K$ valley exciton (blue, $\sigma+$) is identical to that from the $-K$ valley (red, $\sigma-$), as expected from time-reversal symmetry. In contrast, at high fields the $\sigma+$ and $\sigma-$ components split. The splitting was found to be proportional to B with a slope of $-0.11 \pm 0.01 \text{ meV} \cdot \text{T}^{-1}$ (or ca. $-1.9 \mu_B$) (Fig. 11.7c) [33].

In a similar experiment, when the detection was in a circularly polarised basis but the excitation light was linearly polarised (and detuned by over 200 meV from the X^0 resonance) [32], the splitting was found to increase with a slope that was ca. twice as large: $0.25 \text{ meV} \cdot \text{T}^{-1}$. For trions, the splitting also scaled linearly with B but with a slope of ca. $0.32\text{--}0.36 \text{ meV} \cdot \text{T}^{-1}$, which is more than 25% larger than the value obtained for the X^0 peak. It is also interesting to note that the measurement of the magnetic-field dependence of PL in the Voigt geometry ($B \perp z$) showed no observable splitting up to the highest B . This extreme anisotropy in the magnetic response of the monolayer was interpreted as a direct consequence of the fact that the orbital magnetic moment of a strictly 2D material points out-of-plane and thus can couple only to B_z [32].

The observed magnetic spectral splitting can be explained [33] by the combination of the magnetic moment of the transition metal d -orbitals and the valley magnetic moment m_τ , the latter being the lattice contribution associated with the Berry curvature. The bottom part of Fig. 11.7a shows the Zeeman shift of the band edges from each of these two contributions as well as that from the bare spin. The dashed (solid) lines are the conduction and valence band edges at zero (positive) magnetic field, with blue and red denoting spin up and down, respectively. Because of the very large spin splitting in the valence band (ca. 0.4 eV), the valence band edge in the $+K$ ($-K$) valley has only spin-up (down) states. For the conduction band edge, on the other hand, the spin splitting is rather small (0.03 eV), with opposite signs in the two valleys, hence both spin states are relevant. The overall Zeeman shift of each band is determined by the sum of these three contributions to magnetic moment as shown in the figure.

The authors note [33] that the Zeeman shift due to the spin magnetic moment ($\Delta_s = 2s_z\mu_B B$) does not affect the optical resonances because optical transitions conserve spin so that the effect on the initial and final states is the same. The atomic orbital contribution, however, does affect them because the conduction band edges are mainly composed of d -orbitals with $m = 0$, whereas the valence band edges are mainly d -orbitals with $m = 2$ in the $+K$ valley and $m = -2$ in the $-K$ valley. This contributes no shift to the conduction band and a shift of $\Delta_\alpha = 2\tau\mu_B B$ to the valence band edge (purple arrows in the figure). Here $\tau = \pm 1$ is the index for the $\pm K$ valleys. Finally, the Zeeman shift due to the valley magnetic moment is $\Delta_v = \alpha_i \tau \mu_B B$ (green arrows), where α_i is the valley g -factor for the i band ($i = c, v$). The net effect is a valley-dependent linear shift of the exciton resonance.

The splitting in the applied magnetic field breaks the valley degeneracy, enabling control of the valley polarization [33, 34]. In [33], this was demonstrated by measuring the degree of PL polarization for both helicities of incident circular polarization. Figure 11.8a shows the degree of PL polarization for both $\sigma+$ (blue) and $\sigma-$ (red) excitation as a function of B between -7 T and $+7 \text{ T}$ for the neutral exciton peak.

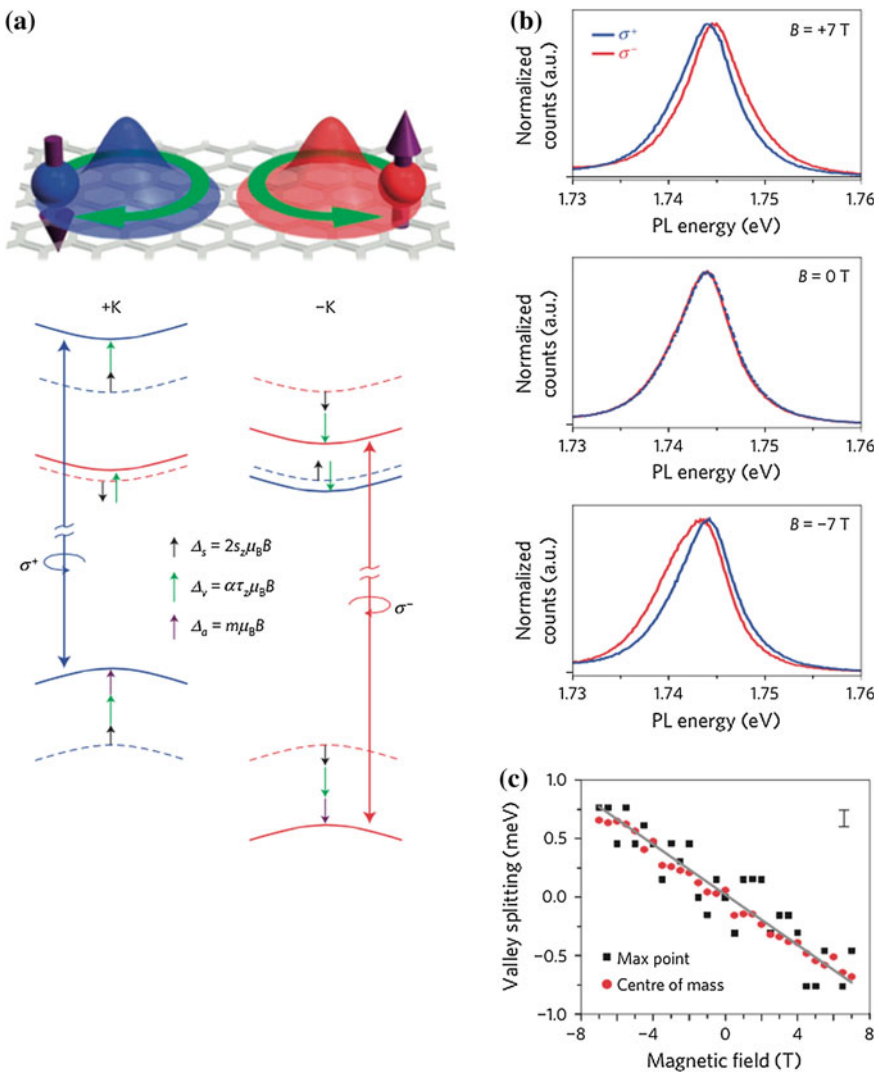


Fig. 11.7 Valley Zeeman splitting. **a** Top cartoon depicting the valley magnetic moments. Blue (red) represents spin up (down) in $+K$ ($-K$) valleys. The self-rotation of the wave packet indicated by green arrows gives rise to the valley magnetic moment. For holes, the magnetic moment also has a contribution from the atomic orbital (purple arrow), which has opposite sign in the K and $-K$ valleys. Bottom: energy level diagram showing the three contributions to the valley Zeeman shifts (black for spin, green for valley, purple for atomic orbital). **b** Polarization-resolved valley-exciton photoluminescence (PL) at selected magnetic fields. Blue and red curves represents PL when exciting and detecting with a single helicity, corresponding to the $+K$ and $-K$ valleys, respectively. **c** Valley-exciton Zeeman splitting as a function of magnetic field extracted using two different methods. The solid line is a linear fit (to the black squares) using the equation described in the text. The bar at the top right indicates the spectral resolution of the detection system [33]. Reprinted by permission from Macmillan Publishers Ltd., copyright (2014)

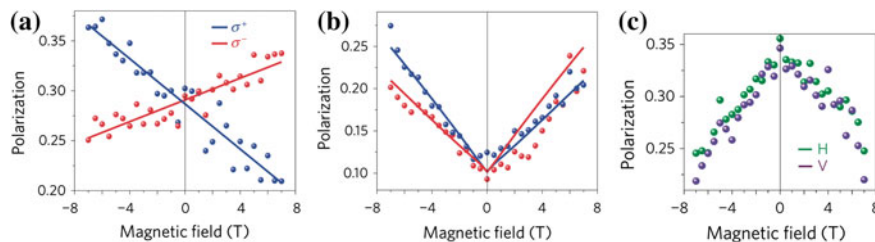


Fig. 11.8 Degree of photoluminescence polarization for exciton (a) and trion (b) peaks, when excited by circularly polarised light. c Degree of linear polarization as a function of magnetic field [33]. Reprinted by permission from Macmillan Publishers Ltd., copyright (2014)

The degree of polarisation was linear in B , with a negative (positive) slope. This X -shaped pattern implies that the valley Zeeman splitting induces an asymmetry in the intervalley scattering. In contrast, the PL polarization of the negative trion peak increases for either sign of B and shows a V -shaped pattern (Fig. 11.8b).

The difference between the X and V patterns for excitons and trions was attributed to different dominant valley depolarization processes. If depolarization occurs during exciton formation, one sees an X pattern because exciton formation favours the upper exciton branch. If, on the other hand, depolarization occurs predominantly after reaching the ground state, one sees a V shape because either sign of magnetic field suppresses the ground-state inter-valley relaxation [33].

Finally, the magnetic field dependence of valley coherence was investigated [33]. As the magnetic field increased, the degree of linear polarization decreased showing a Λ pattern (Fig. 11.8c), demonstrating that valley coherence is suppressed by the magnetic field.

The breaking of the valley degeneracy by a magnetic field in monolayer MoSe₂ was studied in [34]. While the results are qualitatively similar to those reported for WSe₂, there were some differences. Thus, in contrast to WSe₂, in MoS₂ for both the exciton and trion peaks, the valley splitting showed a linear magnetic-field dependence with the *same* slope of $-0.22 \text{ meV} \cdot \text{T}^{-1}$. It was further found that the trion valley splitting and the resulting luminescence polarization both depend on the applied back-gate voltage. It was proposed that application of magnetic and electric fields can, therefore, provide an effective strategy for manipulating the valley degree of freedom in TMDC monolayers [34].

In MoSe₂, both neutral excitons and trions shifted linearly with field at a rate of $\mp 0.12 \text{ meV} \cdot \text{T}^{-1}$ for fields up to 10 T, while at higher fields the trion Zeeman shift increases to $\mp 0.18 \text{ meV} \cdot \text{T}^{-1}$ [35]. The increase in the shift rate was attributed to many-body effects on the binding energy of trions.

Interestingly, spontaneous circularly polarised light emission from a single layer WS₂ excited by linearly polarised light at zero magnetic field was reported in [36]. The authors attributed it to spin-valley locking and strong electron-electron interactions, pointing out that other possibilities such as defects or grain boundaries cannot be excluded.

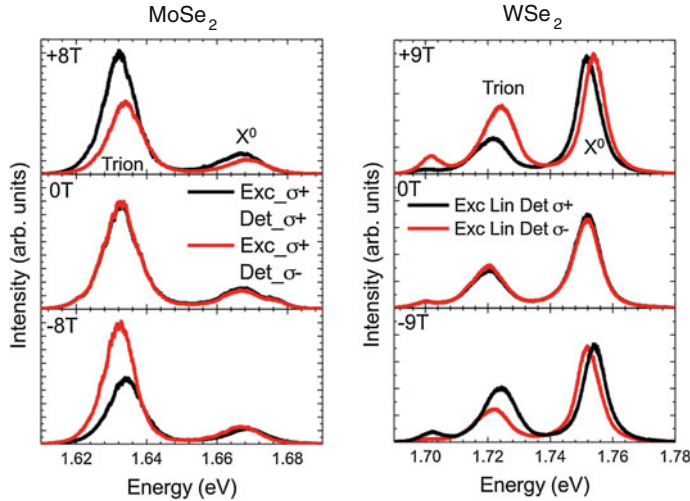


Fig. 11.9 PL of monolayer MoSe_2 (left) and monolayer WSe_2 (right); excitation energy $E_{\text{Laser}} = 1.96 \text{ eV}$. Middle panel PL spectra at $B_z = 0 \text{ T}$; upper panel $B_z = +8(+9) \text{ T}$; lower panel $B_z = -8(-9) \text{ T}$ [37]. Reprinted with permission from IOP Publishing Ltd.

A comparative study of MoSe_2 and WSe_2 monolayers was carried out in [37]. It was found that while the Zeeman energy evolution of both monolayer materials shows close similarities (Fig. 11.9), the evolution of the valley polarization as a function of the applied magnetic field was completely different.

Figure 11.10a, c show X^0 PL polarization for MoSe_2 and WSe_2 monolayers as a function of the applied magnetic field. For WSe_2 , using circular excitation, the X^0 polarization was essentially independent of the applied field, while for a linearly polarized excitation laser, P_c was close to zero for all applied fields. For $\sigma+$ circularly polarized excitation, $P_c \approx 40\%$, remained practically unchanged for applied fields from -9 T to $+9 \text{ T}$, indicating that over the entire magnetic field range, the X^0 emission polarization was determined by the initially, optically created valley polarization rather than induced by the magnetic field. Excitation with $\sigma-$ polarized light yielded $P_c \approx 40\%$, also independent of the applied magnetic field. This behaviour for the X^0 in monolayer WSe_2 was in stark contrast to the observations for MoSe_2 monolayers: while for the former, the optical valley initialization determined the PL polarization, for the latter the applied magnetic field direction and amplitude allowed for control of the valley polarization.

Contrary to the X^0 , the trion polarization in WSe_2 could be controlled via an applied magnetic field, shown in Fig. 11.10d. This is in contrast to the trion polarization evolution in MoSe (Fig. 11.10b): whereas application of a positive magnetic field results in a strong *positive* P_c in MoSe_2 , also strong but *negative* polarization was created in WSe_2 .

The difference between optical transitions in monolayer MoSe_2 and monolayer WSe_2 was also addressed in [38], where it was argued that indirect excitons in the

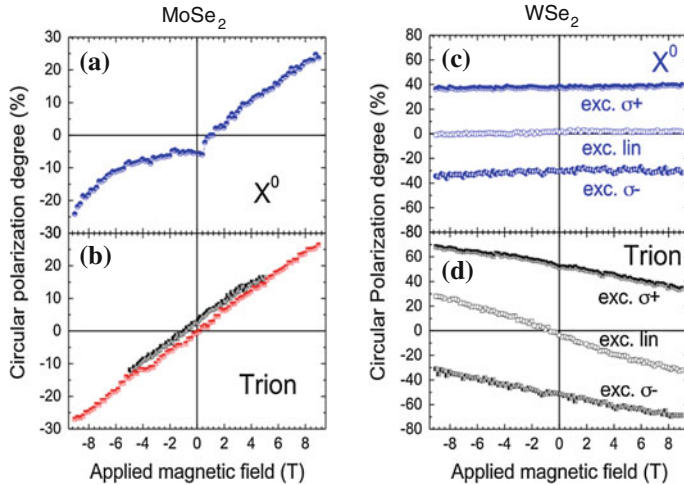


Fig. 11.10 PL polarization of monolayer MoSe₂ (left) and monolayer WSe₂ (right). **a** Emission of the X^0 as a function of B_z . **b** Emission of the trion as a function of B_z using $\sigma+$ (black squares) and $\sigma-$ excitation (red squares). **c** PL emission of the X^0 as a function of B_z for three different laser polarizations. **d** PL emission of the trion as a function of B_z for three different laser polarizations [37]. Reprinted with permission from IOP Publishing Ltd.

latter correspond to several low-energy optical transitions that so far were attributed to excitons bound to impurities. A possible mechanism that can explain the vanishing polarization in MoSe₂ was proposed as follows. The authors note that the energy splitting between dark and bright exciton branches in this material resonates with the energy of the phonon that couples these branches. This resonance condition, not met in other TMDCs, can result in vanished polarization due to polaron-induced Rabi oscillations between dark and bright excitons. The effect of an out-of-plane electric field was also considered and it was proposed that it can reduce the initial polarization of bright excitons due to a Rashba-type coupling with dark excitons.

It was also proposed that valley polarisation in TMDC monolayers can be controlled by the use of magnetic dopants [39]. In [40] it was proposed to use proximity-induced Zeeman effect to generate valley splitting. First-principle simulations of monolayer MoTe₂ on an insulating ferromagnetic EuO substrate revealed that valley splitting over 300 meV could be generated. It was further found that this valley splitting could be continuously tuned by changing the substrate magnetisation direction.

11.4 Valley Hall Effect

Because of the broken inversion symmetry in the crystal structure, electrons in the two valleys experience effective magnetic fields (proportional to the Berry curvature) with equal magnitudes but opposite signs. Such a magnetic field not only defines the

optical selection rules that allow optical pumping of valley-polarized carriers by circularly polarized photons but also generates an anomalous velocity for the charge carriers: when the semiconductor channel is biased, electrons from different valleys experience opposite Lorentz-like forces and hence move in opposite directions perpendicular to the drift current. This phenomenon is called the valley Hall effect and originates from the coupling of the valley degree of freedom to the orbital motion of the electrons, analogous to the spin Hall effect with the spin-polarized electrons replaced by valley-polarized carriers.

Under time-reversal symmetry, equal Hall currents from each valley flow in opposite directions so that no net Hall voltage is produced. To measure the valley Hall effect, time-reversal symmetry was broken by shining circularly polarized light onto a Hall bar device [41]. The presence of a photoinduced anomalous Hall effect driven by a net valley polarization was interpreted as an experimental manifestation of the valley Hall effect. Measurements were performed on monolayers and bilayers on MoS₂ at 77 K.

Fig. 11.11 The valley Hall effect. **a** The source-drain bias (V_x) dependence of the Hall voltage (V_H) for the monolayer device under R-L (red solid line), L-R (red dashed line), and half-wave s-p modulations (red dotted line). Results from the bilayer device under R-L modulation (blue solid line) are also shown. **b** The anomalous Hall resistance of the monolayer device as a function of the incidence angle θ under quarter-wave ($\Delta\lambda = 1/4$, solid red circles) and half-wave ($\Delta\lambda = 1/2$, open red circles) modulations. Results for the bilayer device under quarter-wave modulation are also shown (blue circles) [41]. Reprinted with permission from AAAS

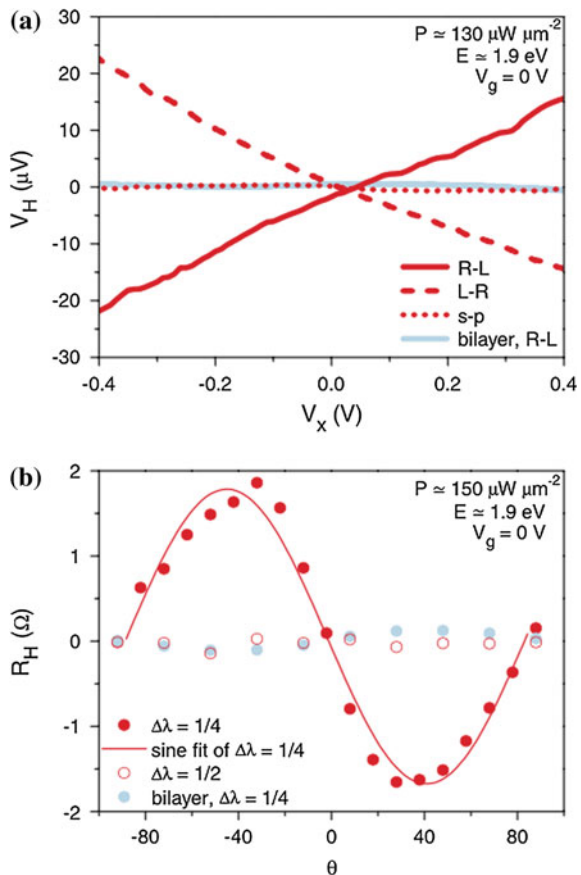


Figure 11.11a shows the V_x -dependence of the anomalous Hall voltage (V_H) at $V_g = 0$ V where a small but finite V_H that scales linearly with V_x is observed under a quarter-wave $R-L$ modulation, in which the polarization is modulated from right-to left-handed, (solid red line), which is the signature of a photo-induced anomalous Hall effect, driven by a net valley polarization. The sign of the signal was reversed when the excitation was changed to $L-R$ modulation (dashed red line). No net Hall voltage could be seen using a linear ($s-p$) modulation (dotted red line), or when a MoS₂ bi-layer was used.

The Hall resistance R_H exhibited a sine dependence on θ under quarter-wave modulation, with the maximum Hall resistance of $\sim 2\Omega$ measured under an excitation intensity of $150\mu\text{W/mm}^2$. Zero Hall resistance was observed under half-wave modulation and also in bi-layers. From the contrast between mono- and bilayer devices it was concluded that an intervalley population imbalance is required to drive the anomalous Hall effect. Such imbalance cannot be produced in a bilayer because the latter possesses inversion symmetry [41].

Valley Hall effect in disordered monolayer MoS₂ was also studied from first principles [42].

11.4.1 Nonlinear Valley and Spin Currents

The effect of the anisotropy of Fermi pockets on valley and spin currents were investigated in [43]. It was demonstrated that such valley and spin currents can be generated by an electric bias only and appear in the second order to the electric field. It was proposed that this quadratic dependence on field makes possible current rectification for generation of dc spin and valley currents by means of an ac electric field, with the absence of net charge current. It was predicted that, at a p-n junction in monolayer TMDCs, the nonlinear valley current will result in a unique circular polarization pattern of electroluminescence depending on the orientation of the junction relative to the crystalline axis. Nonlinear valley and spin Seebeck effects were further predicted, where a temperature gradient can play the same role as the electric field in giving rise to valley and spin currents, where the quadratic dependence of the valley (spin) thermopower on the temperature gradient implies a simple way to generate pure valley (spin) flow with zero charge current by an inhomogeneous temperature distribution.

11.5 Spin-Valley Physics in Bi-Layers

11.5.1 Electrical Control of Valley Magnetic Moment

As discussed above, the Dirac-valley degree of freedom manifests itself when the inversion symmetry is broken. As a result, in monolayer TMDCs the magnetic moment m and Berry curvature \mathcal{Q} are non-zero, having equal magnitude but opposite

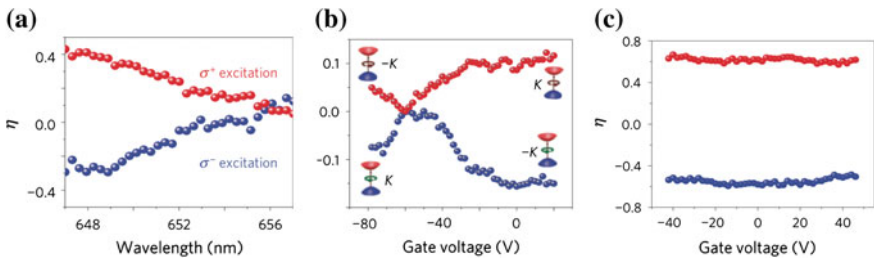


Fig. 11.12 Degree of photoluminescence polarization as a function of wavelength (a) and gate voltage at 648 nm (b) for a MoS₂ bi-layer, compared with the gate-voltage dependence for a monolayer (c) [44]. Reprinted by permission from Macmillan Publishers Ltd., copyright (2013)

signs in the two $\pm K$ valleys owing to time-reversal symmetry. Unlike monolayers with the structural inversion asymmetry, pristine bilayers of TMDC are inversion symmetric, requiring that m , Ω and the consequent valley-contrasting dichroism vanish. Is this, indeed, always the case?

In [44], it was proposed that inversion symmetry can be broken by applying an electric field perpendicular to the bilayer, which leads to a potential difference between the two layers. Polarization-resolved photoluminescence measurements on bilayers of MoS₂ were performed at 30 K. It was found that in contrast to the expectation, the photoluminescence at 650 nm, which is from direct transitions in the $\pm K$ valleys showed circular polarization that exhibited a wavelength dependence (Fig. 11.12a), “implying the existence of broken inversion symmetry in the as-prepared bilayer”. It was further found that the degree of polarization η changed markedly as a function of the applied voltage V_g (Fig. 11.12b), showing an X -shaped pattern, completely disappearing at $V_c = -60$ V and becoming finite on either decreasing or increasing V_g , and seemed to saturate for larger or smaller voltages.

At the same time, the spectra of monolayer MoS₂ devices exhibited no appreciable V_g dependence of polarisation, that reached reaches 0.8 in some devices [44].

The observed X -shaped pattern was interpreted by the relation between inversion symmetry and orbital magnetic moment. When inversion symmetry is present in the bilayer at $V_g = V_c$, m and the associated valley-contrasting optical dichroism disappear. For all other values of V_g , inversion symmetry is broken and consequently non-zero m and valley circular dichroism appear near the band edge, which leads to finite photoluminescence polarization. The bilayer configurations at the two gate voltages $V_g = V_c \pm \Delta V$ is expected to be equivalent by spatial inversion.

11.5.2 Spin-Layer Locking

Bilayer two-dimensional materials possess a distinct degree of freedom known as the layer pseudospin. An electronic state localized to the upper or lower layer can be labelled with pseudospin up or down, respectively, which corresponds to electrical

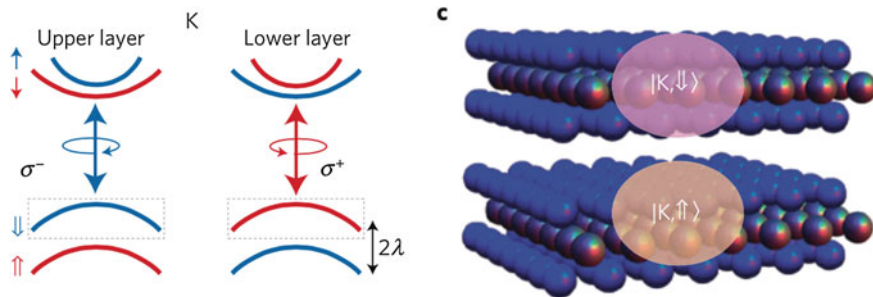


Fig. 11.13 *Left:* a cartoon depicting excitation/emission processes in the K valley of bilayer WSe_2 . Spin configuration is indicated by \downarrow (\uparrow) for holes (electrons). The same for the $-K$ valley is obtained by time reversal. *Right:* depiction of spin-down (-up) hole states localized in the *upper* (*lower*) layer in the K valley [22]. Reprinted by permission from Macmillan Publishers Ltd., copyright (2014)

polarization. In a layered material with spin-valley coupling and AB stacking, such as bilayer TMDCs, both spin and valley are coupled to the layer pseudospin. Because the lower layer is rotated by 180° with respect to the upper layer, the out-of-plane spin splitting has a sign that depends on both valley and layer pseudospins. As a result, interlayer hopping has an energy cost equal to twice the spin-orbit coupling strength λ . When 2λ is larger than the hopping amplitude t_\perp , a carrier is localized in either the upper or lower layer depending on its valley and spin state, i.e. the spin configuration is locked to the layer index. This is schematically illustrated in Fig. 11.13. Experimental signatures of coupling between this layer pseudospin and the spin and valley degrees of freedom were demonstrated in bilayers of WSe_2 [22]. Although bi-layer WSe_2 is an indirect-bandgap semiconductor, the near degeneracy between indirect and direct transitions made it possible to monitor direct-gap photoluminescence from the K valleys.

Both circularly and linear polarised excitation and detection were used. It was found that in both cases, the photoluminescence was polarised and at high V_g (above 60 V), a doublet structure emerged for the X^- trion (Fig. 11.14a, b). Since the second harmonic generation measurements showed more than two orders of magnitude suppression compared to a monolayer, it was concluded that the structure possessed inversion symmetry. Therefore, it was concluded that it was not possible that the circularly polarized photoluminescence near $V_g = 0$ stems from valley polarization, as demonstrated in single-layer materials but rather, it originates from exciton spin polarization, a consequence of the spin optical selection rules present for both inversion-symmetric and asymmetric bilayers with large SOC [22].

For the case of circular polarisation, the following explanation was offered. The large exciton spin polarization, together with the emergence of an X^- doublet at high electric field, was attributed to the spin-layer locking effect, which leads to an enhanced spin lifetime and electrically induced spin splitting. Figure 11.15 (upper panel) shows the energy level diagram of AB -stacked bi-layer WSe_2 without an applied electric field. Single and double arrows denote the spin configurations of

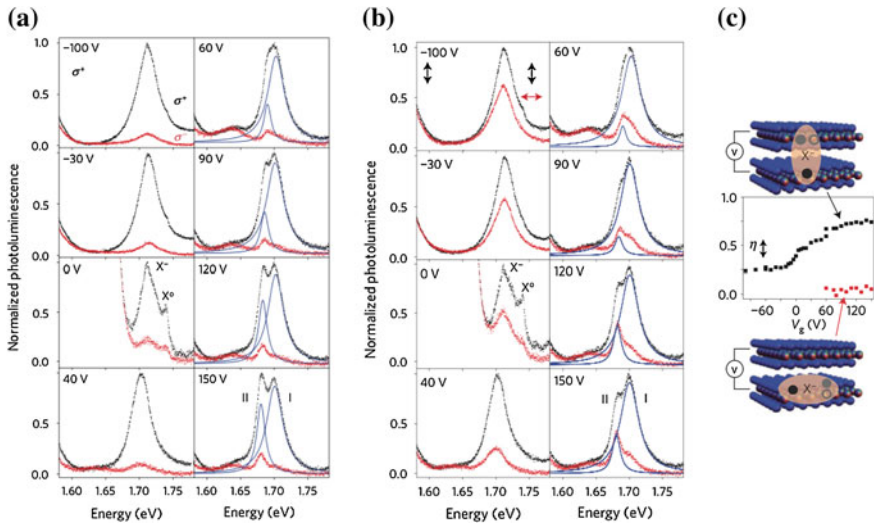


Fig. 11.14 **a** Normalized photoluminescence spectra versus photon energy at selected gate voltages for circularly (**a**) and linearly (**b**) polarised excitation and detection. *Blue lines* in plots for $V_g > 50$ V show Lorentzian fits. **c** Trion linear polarization as a function of gate voltage for vertically polarized excitation (*centre*), with corresponding depictions of interlayer (*top*) and intralayer (*bottom*) trions. For $V_g > 50$ V, the trion peak splits. *Black* and *red data* correspond to polarisations of peak I (interlayer trions) and peak II (intralayer trions), respectively [22]. Reprinted by permission from Macmillan Publishers Ltd., copyright (2014)

electrons and holes, respectively. Only those electron-hole pairs that emit significant photoluminescence are shown. Under σ^+ excitation, the transition involving spin-up hole states is excited in both $+K$ and $-K$ valleys with equal strength and no valley polarization is generated. Intra-valley spin flips are suppressed because the spin-up and spin-down states are localized in opposite layers. Consequently, the spin relaxation time is long compared to the exciton lifetime, resulting in large exciton spin orientation.

A perpendicular electric field creates a potential difference between upper and lower layers, which lifts the energy degeneracy between spin-up and spin-down states localized in opposite layers for a given valley. The result is an electrically induced spin Zeeman splitting, with the spin splitting for electrons, Δ_c , being slightly larger than that for holes, Δ_v [22], leading to the splitting of the trion emission peak (Fig. 11.15, lower panel).

A similar splitting was also observed for excitation and detection using linearly polarised light (Fig. 9.23b). It was argued that this splitting arises from the presence of both intralayer and interlayer trions (Fig. 9.23c).

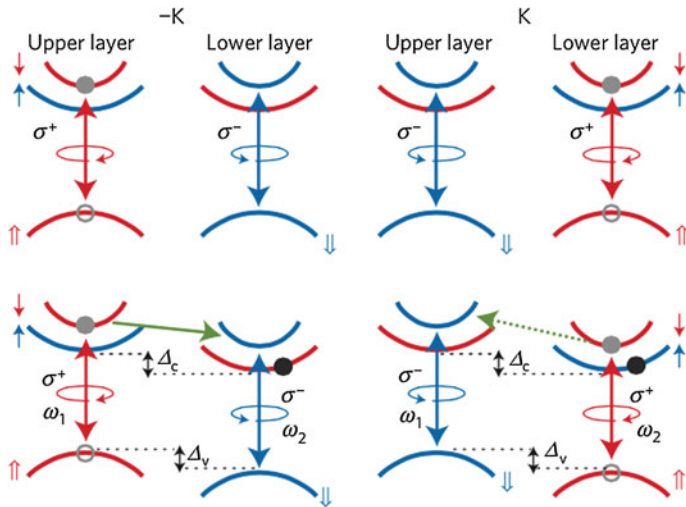


Fig. 11.15 *Upper panel:* schematic depiction of the formation of excitons in both K and $-K$ valleys under $\sigma+$ excitation in unbiased bilayer WSe₂, resulting in no net valley polarization. Hollow (solid) circles denote holes (electrons). Grey circles denote photo-excited electron-hole pairs. *Lower panel:* schematic of electric-field-induced band shifts and electron spin relaxation pathways (green arrows). Emission from the *upper* and *lower layers* is at ω_1 and ω_2 , respectively, whose splitting originates in the difference between the conduction (Δ_c) and valence (Δ_v) band energy shifts with gate electric field [22]. Reprinted by permission from Macmillan Publishers Ltd., copyright (2014)

11.6 Spin Polarisation in Inversion-Symmetric Structures

It is commonly believed that in order for the Dresselhous or Rashba effects to be observed, crystal bulk inversion symmetry must be broken and hence spin splitting in a 3D material that has bulk inversion symmetry should not be expected, precluding the observation of spin splitting effects in centrosymmetric structures. This consensus was challenged in [28], where it was argued that because the SOC is a relativistic effect, anchored on particular nuclear sites in the solid, it is *the symmetry of individual atomic sites in the solid* that forms a good starting point to describe the SOC-induced spin polarization effect, rather than the global symmetry of the unit cell. This formulation provides a natural explanation to the observation of spin polarization in bi-layer TMDC structures [27].

The combination of inversion symmetry $E(k, \uparrow) = E(-k, \uparrow)$ with time-reversal symmetry $E(k, \uparrow) = E(-k, \downarrow)$ ensures that electronic states of non-magnetic centrosymmetric materials must be doubly spin-degenerate. If inversion symmetry is broken, spin-orbit interaction can induce a momentum-dependent spin splitting via an effective magnetic field imposed by spatially-varying potentials.

In [45], it was experimentally demonstrated through the combined use of spin- and angle-resolved photoemission spectroscopy (ARPES) that 2H-WSe₂, a material

which retains bulk inversion symmetry, exhibited a large spin polarization of its bulk electronic states.

The spin-resolved photoemission measurements revealed a strong spin polarization of the upper pair of valence band states at the K point of the Brillouin zone (Fig. 11.16). The measured polarization was entirely out of the surface plane within experimental error, with up (down) orientation for the upper (lower) valence band, respectively. From fitting the measured energy distribution curves, the magnitude of the spin polarization was estimated to exceed 90%, suggestive of an almost fully spin-polarized band. Moreover, the signs of all polarizations were reversed at the K' point, confirming that time-reversal symmetry remains unbroken, and thus there is no net magnetic moment, which was attributed to the local inversion asymmetry of individual WSe₂ layers, leading to spin-polarized states whose texture is strongly

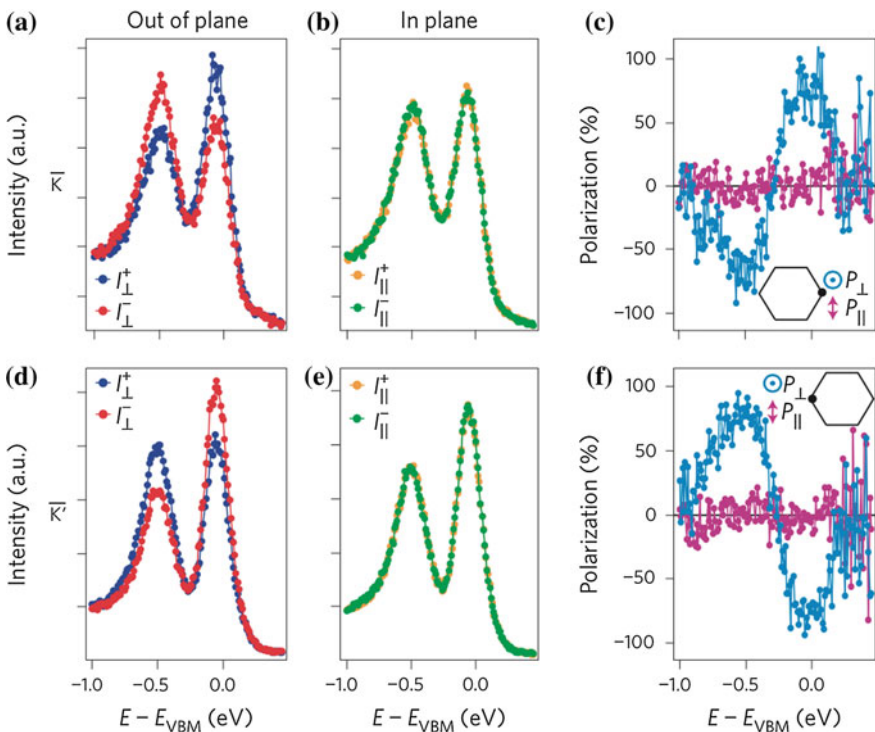


Fig. 11.16 Observation of spin-polarized bulk bands in an inversion-symmetric host. **a, b** Energy distribution curves (in arbitrary units (a.u.)) from spin-resolved ARPES measurements ($h\nu = 25$ eV, $T = 300$ K) at the K point measured by the out-of-plane (a) and in-plane (b) detectors in the Mott scattering chamber. **c** The extracted polarizations show a strong out-of-plane spin polarization, opposite for the two valence band peaks. **d–f**, Plots as for (a–c), but for the K' point, showing that the signs of all components are reversed [45]. Reprinted by permission from Macmillan Publishers Ltd., copyright (2014)

modulated in both real and momentum space despite the global inversion symmetry of the unit cell.

A recent theory established general grounds by which such a lack of inversion symmetry of the crystal site point group can lead to a macroscopic spin polarization, driven by the local nature of spin-orbit coupling [28]. Photoemission, being extremely surface sensitive, can be expected to predominantly probe the top layer of this material. The strong measured spin polarization was attributed to be a direct observation of a layer-localized spin-polarization of bulk electronic states in WSe₂.

The evolution of spin polarised states along different directions was further studied both experimentally and using ab-initio simulations. Figure 11.17 reveals how the underlying spin-polarized states evolve along the $K - \Gamma - K'$ direction, where a marked suppression of the out-of-plane spin polarization approximately half-way along this line was found, with negligible polarization observed around the zone centre.

This observation was explained by considering the orbital character of the underlying states [45]. Close to K , the electronic states are derived mostly from d_{xy} and $d_{x^2-y^2}$ orbitals. There is thus a significant orbital overlap within the surface plane, which, together with the net in-plane dipole, favours strong out-of-plane spin polarization [30]. Around Γ , on the other hand, the orbital character becomes dominantly d_{z^2}/p_z -like, causing this component to be strongly suppressed. A small in-plane spin

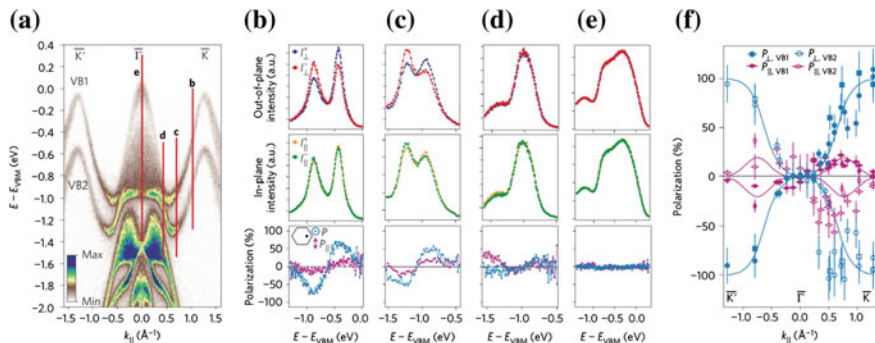


Fig. 11.17 Evolution of spin texture along $K' - \Gamma - K$ in bulk WSe₂ **a** Dispersion measured by ARPES ($h\nu = 125$ eV, $T = 30$ K) along the $K' - \Gamma - K$ direction. **b-e** Energy distribution curves (EDCs) in arbitrary units measured using spin-resolved photoemission ($h\nu = 25$ eV, $T = 300$ K) and corresponding extracted spin polarizations, measured at the locations labelled by the corresponding vertical lines in panel (a). **f** The out-of-plane (P_{\perp}) and in-plane ($P_{||}$) spin polarizations determined from fitting these and additional EDCs ($h\nu = 25$ eV, $T = 80$ K (squares and vertical diamonds, respectively) and $T = 300$ K (circles and horizontal diamonds, respectively)) reveal some canting of the spin into the surface plane away from the K points, and a total suppression of the measured spin polarization around the zone centre. Error bars reflect an approximate estimate of the uncertainty in extracting the polarization from the experimental measurements, incorporating statistical errors in peak fitting, systematic errors and uncertainty in sample alignment. The lines in (f) are provided as guides to the eye [45]. Reprinted by permission from Macmillan Publishers Ltd., copyright (2014)

component that emerged along $K' - \Gamma - K$, which switched sign on either side of Γ , was also found.

A suppression of this out-of-plane spin polarization along the entire $M - \Gamma$ direction was found, which was attributed to the degeneracy of two oppositely polarized bands within a single layer. It was noted that while at the M -point itself, this is a natural consequence of time-reversal symmetry, as M is a time-reversal invariant momentum, along the $M - \Gamma$ line, such degeneracies are enforced by the combination of time-reversal with the rotational D_{3h} symmetry of a single monolayer within the unit cell, ensuring that the out-of-plane component of the spin must have opposite sign in neighbouring sextants of the Brillouin zone [45].

11.7 Optical Stark Effect

The optical Stark effect was observed in WS₂ [46] and WSe₂ [47] monolayers. Before we proceed to the description of the results, we briefly describe the physics of the optical Stark effect following [46].

Coherent interaction between light and matter can modify the energy level spectrum of a given electronic system. The simplest example of this is a two-level atomic system in the presence of monochromatic light. It can be described by the semi-classical Hamiltonian:

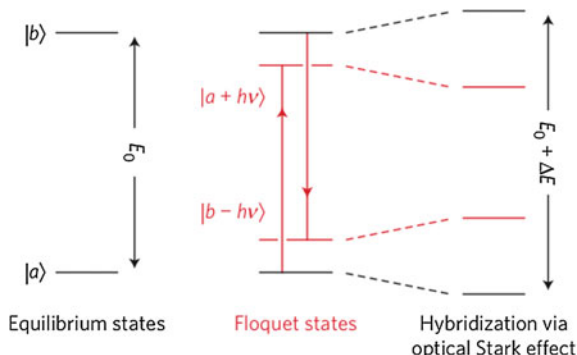
$$\hat{H}(t) = \hat{H}_0 + \hat{p}\mathcal{E}(t) \quad (11.2)$$

where \hat{H}_0 is the equilibrium Hamiltonian describing a two-level atom with eigenstates $|a\rangle$ and $|b\rangle$, \hat{p} is the electric dipole moment operator of the atom, and $\mathcal{E}(t) = \mathcal{E}_0\cos 2\pi\nu t$ is the oscillating electric field of light with amplitude \mathcal{E}_0 and frequency ν . The perturbation term in the Hamiltonian contains a time-dependent factor $\cos 2\pi\nu t$ that enables the coherent absorption of light by the ground $|a\rangle$ state resulting in the formation of the photon-dressed state $|a + h\nu\rangle$ and also the stimulated emission of light by the $|b\rangle$, which leads to the formation of another photon-dressed state $|b - h\nu\rangle$, which is schematically shown in Fig. 11.18. The series of photon-dressed states formed in this way are called the Floquet states [46].

The Floquet states can hybridize with the equilibrium states $|a\rangle$ and $|b\rangle$ through the electric field term \mathcal{E} in (11.2) similar to the hybridization between two atomic orbitals by the Coulomb interaction to form the bonding and anti-bonding molecular orbitals in quantum chemistry, which results in a wider energy level separation. Through the simultaneous energy repulsion of these pairs, the optical transition between states $|a\rangle$ and $|b\rangle$ shifts to a larger energy, which is known as the optical Stark effect [48, 49]. The energy shift (ΔE) is given by

$$\Delta E = \frac{\mathcal{M}_{ab}^2 \langle \mathcal{E}^2 \rangle}{\Delta} \quad (11.3)$$

Fig. 11.18 The optical Stark effect: Energy level diagram of two-level $|a\rangle$ and $|b\rangle$ atoms showing that the equilibrium and Floquet states $|a + h\nu\rangle$ and $|b - h\nu\rangle$ can hybridize, resulting in shifted energy levels [46]. Reprinted by permission from Macmillan Publishers Ltd., copyright (2014)



where \mathcal{M}_{ab}^2 is the polarization matrix element between $|a\rangle$ and $|b\rangle$, and $\langle \mathcal{E}^2 \rangle$ is the time-averaged value of the electric field squared, proportional to the light intensity. In solids, the optical Stark effect has been observed in a rather limited number of materials, e.g. Cu₂O, GaAs and Ge [46].

In [47] the authors provide an interesting observation that using non-resonant circularly polarised light (pump) with energies below the bandgap induces a coherent and dissipationless valley selective optical Stark effect that can be used for spin manipulation. The authors used WSe₂ monolayers for the demonstration of the effect focusing on the lowest energy A-exciton. It was noted that the A-exciton is well separated from other excited states in energy thanks to strong electron-hole interaction, which allows one to approximate the ground state and the A-exciton as a two-level system and neglect the effect from other excited states. In monolayer WSe₂, the A-exciton states at the K and K' valleys are time-reversal pairs and have degenerate energy levels that have distinct optical selection rules and couple to photons of opposite helicity [1]. As a result, the A-exciton in the K -valley couples exclusively to left circularly polarised light while the A-exciton in the K' valley couples to the right circularly polarised light.

It was noted that in order to manipulate the valley polarization using nonresonant coupling based on the optical Stark effect has an advantage because it avoids the dissipation and dephasing naturally accompanying real excitations. The optical Stark effect using the dressed-atom picture [50] (Fig. 11.19a) was considered within a two-level system composed of the ground state and A-exciton state at the K (or K') valley in a monolayer WSe₂ exposed to left circularly polarized ($\sigma+$) pump with photon energies below the exciton resonance (red arrow). In the dressed-atom picture, the dressed-ground state (with N $\sigma+$ photons), and the K valley A-exciton (with $N - 1$ $\sigma+$ photons) are coupled by the dipole transition, which leads to wave function hybridization and energy-level repulsion, which effectively shifts down the ground-state energy and shifts up the K valley exciton energy. The A-exciton at the K' valley, on the other hand, cannot couple to the ground state with an extra $\sigma+$ photon because of the optical selection rule, and the related states are not shifted by $\sigma+$ polarized light. As a result, the energy degeneracy between K and K' valley states is lifted

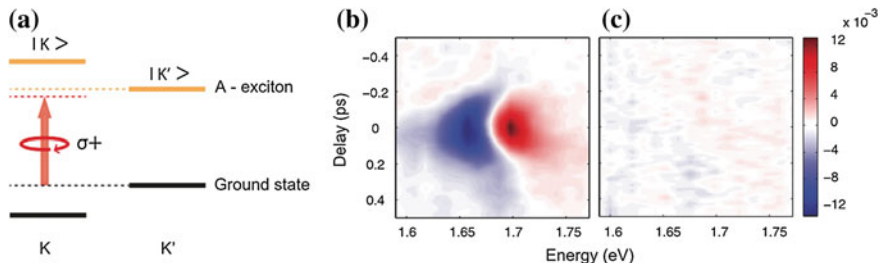


Fig. 11.19 **a** The valley-dependent optical Stark effect with a nonresonant circularly polarized pump. **a** Schematic of the optical Stark effect for valley transitions with a nonresonant, left circularly polarized $\sigma+$ pump. The dashed black and yellow lines denote the unperturbed ground and exciton states, respectively, and the pump photon energy is lower than the exciton resonance energy (red arrow). In the dressed atom picture, the dressed ground state (with $N \sigma+$ photons) and the K valley A-exciton (with $N - 1 \sigma+$ photons) are coupled by dipole transition, which results in energy-level repulsion (left, solid black and yellow lines) and an increased exciton transition energy. On the other hand, $\sigma+$ pump does not affect K' valley A-exciton resonance because of the optical selection rule (right). **b, c** Transient reflection spectra of A-exciton resonance at 77 K. The color scale, horizontal axis, and vertical axis represent the relative reflectivity change $\Delta R/R$, the probe photon energy, and the pump-probe time delay, respectively. For atomically thin WSe₂ on a sapphire substrate, $\Delta R/R$ is proportional to the absorption change. A nonresonant $\sigma+$ pump of photon energy at 1.53 eV leads to **(b)** a strong transient absorption signal for probes with the same polarization $\sigma+$, but **(c)** produces no transient response for probes with the opposite polarization $\sigma-$ [47]. Reprinted with permission from AAAS

by the valley-selective optical Stark effect, which can be characterized by a valley pseudo-magnetic field.

The valley-selective optical Stark shift in WSe₂ monolayers was measured with nonresonant circularly polarized excitation using pump-probe spectroscopy. Displayed in Fig. 11.19b, c are two-dimensional plots of transient reflection spectra in a monolayer WSe₂ with $\sigma+$ and $\sigma-$ polarized probe light, respectively, upon $\sigma+$ polarized pump excitation. Here, the non-resonant pump photons are at 1.53 eV, which is 150 meV below the exciton resonance and do not excite any real transitions. The color scale in Fig. 11.19b, c, represents the pump-induced change of the probe beam reflectivity $\Delta R/R$, the horizontal axis shows the probe photon energy, and the vertical axis shows the pump-probe time delay. It is apparent that strong changes in the exciton absorption are present only for $\sigma+$ probe pulses (Fig. 11.19b), and no pump-induced signals can be detected above the noise level for $\sigma-$ probe pulses (Fig. 11.19c).

The authors further examined how the valley-selective optical Stark shift varies with the pump laser intensity and detuning [47]. It was found that the optical Stark shift was inversely proportional to the pump detuning and scales linearly with the laser intensity. It was noted that such scaling matches well with the theoretical prediction of optical Stark shift.

Similar results were reported in [46] for WS₂. The fluence dependence of $\Delta\alpha$ and the spectral weight transfer is shown in Fig. 11.20. The observed linear dependence

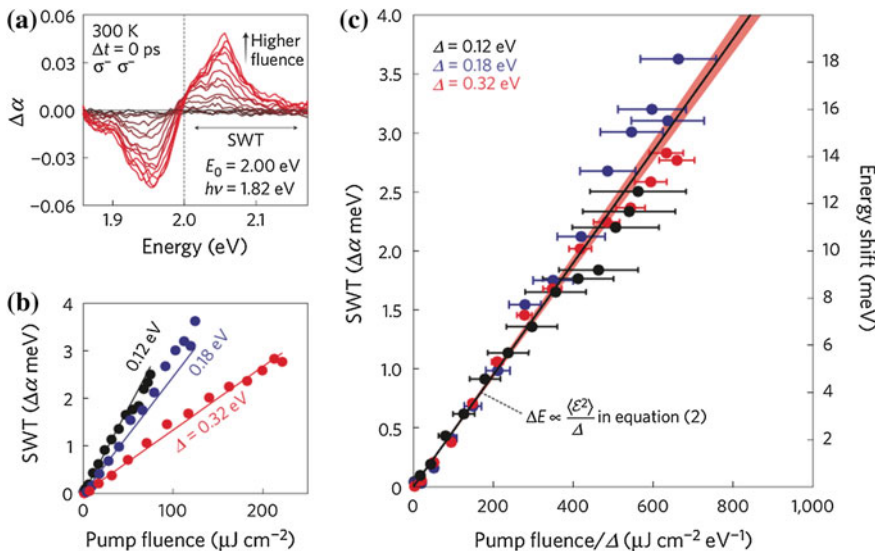


Fig. 11.20 Fluence and detuning dependences of the optical Stark shift in a WS_2 monolayer. **a** Fluence dependence of the $\Delta\alpha$ spectra with fluences up to $120 \mu\text{J}/\text{cm}^2$ measured with the same pump and probe helicities. **b** Fluence and detuning dependences of the spectral weight transfer with the integration range shown in (a). **c** Spectral weight transfer plotted as a function of fluence/ Δ , showing that all of the data points fall along a common slope (black line). The fitting slope (black line) and the 95% confidence band (red shading) show an excellent agreement with the characteristic dependences of the optical Stark shift in (11.3) ((2) in the original publication) [46]. Reprinted by permission from Macmillan Publishers Ltd., copyright (2014)

on fluence is in agreement with (11.3). It was noted that, for a given fluence and energy detuning, WS_2 exhibits the largest optical Stark shift in any materials reported so far [46].

The ability to create valley-specific Floquet-Bloch bands in monolayer TMDCs allowed the authors to consider it as a means to induce new topological phases with valley-specific edge states as illustrated in Fig. 11.21 [46]. The coherent absorption of light (red line) from the valence band creates a Floquet-Bloch band close to the conduction band edge (dashed curves) and induces hybridization that results in energy repulsion (solid curves). When the pump detuning is set at $\Delta < 0$, band inversion should occur at the K' valley, which is accompanied by an avoided crossing away from the symmetry point ($k = K' + \delta k$). It was argued that this gap opening should allow the creation of topological edge states (red) [51]. The pump helicity breaks time-reversal symmetry, inducing chiral edge states along the boundary of the laser-exposed region where the topological order changes [52], offering an exciting possibility to generate valley-selective topological phases in monolayer TMDCs [46].

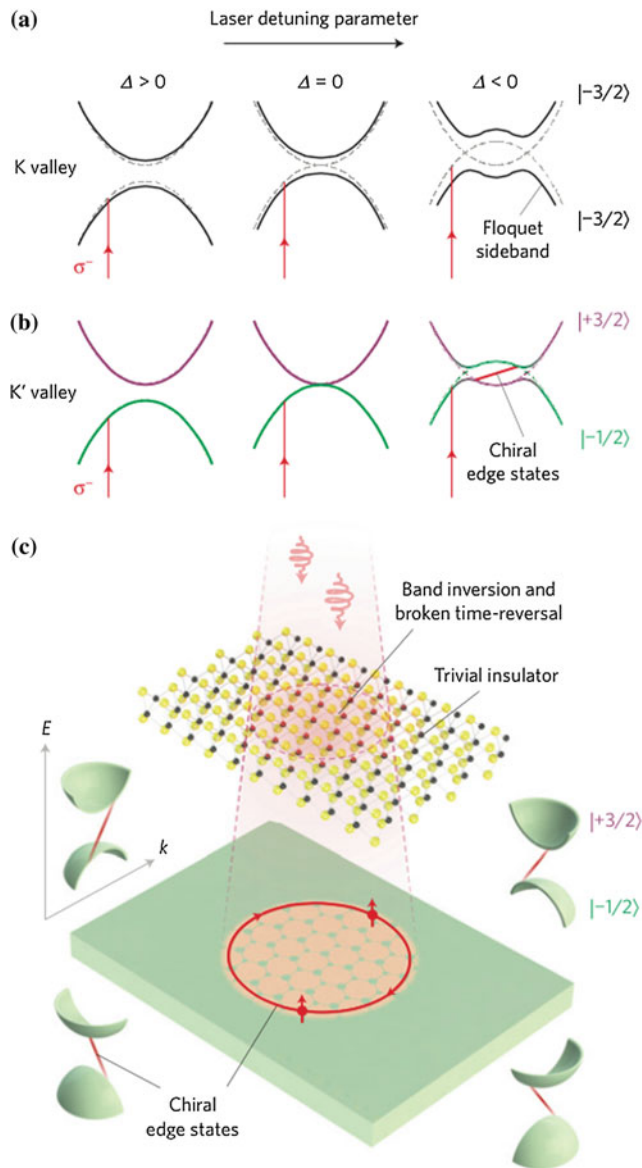


Fig. 11.21 The valley-specific Floquet topological phase. **a, b** hybridization between the Floquet-Bloch band and the conduction band when Δ is varied, which gives rise to the avoided crossing at the K valley (**a**) and the band inversion at the K' valley (**b**). The crossing straight line (red) at the K' valley is the anticipated chiral edge states due to the band inversion. **c** Schematic of the Floquet-driven chiral edge state along the boundary of the laser-exposed region [46]. Reprinted by permission from Macmillan Publishers Ltd., copyright (2014)

11.8 Valley Depolarisation Dynamics

Valley depolarisation in mono and few-layer TMDCs was studied both theoretically and experimentally, mainly using ultrafast pump-probe spectroscopy [21, 53–61]. In most studied materials, exciton dephasing time was found to be in the picosecond range. Kerr rotation measurements were argued to be more accurate [59]. Using this technique, the exciton valley depolarization time of 6 ps at 4 K was obtained for WSe₂ monolayers, and decreased to 1.5 ps at 125 K. The temperature dependence was explained considering the exchange interaction and fast exciton scattering time for the short-range potential [59].

For single-layer WS₂, very short (<1 ps) electron valley relaxation was measured [60], while the hole valley lifetime was at least two orders of magnitude longer and exhibited a temperature dependence that could be explained by single-carrier spin/valley relaxation mechanisms. It was suggested that two potential processes should be considered, namely, direct scattering of excitons from K to K' valleys with a spin flip-flop interaction and scattering through the spin-degenerate Γ valley, the second process being thermally activated due to the energy barrier between the Γ and K valleys.

For MoS₂, the polarisation anisotropy was found to be lost in about 10 ps seconds in monolayers and much faster (ca. 600 fs) in bi-layers [55].

Exciton spin decoherence in TMDC monolayers was also studied theoretically [62], where exciton spin or valley decoherence due to the long-range exchange interaction was predicted and the obtained results were in good agreement with experiment.

References

1. D. Xiao, G.B. Liu, W. Feng, X. Xu, W. Yao, Coupled spin and valley physics in monolayers of MoS₂ and other group-VI dichalcogenides. *Phys. Rev. Lett.* **108**(19), 196802 (2012)
2. X. Xu, W. Yao, D. Xiao, T.F. Heinz, Spin and pseudospins in layered transition metal dichalcogenides. *Nat. Phys.* **10**(5), 343 (2014)
3. Z. Gong, G.B. Liu, H. Yu, D. Xiao, X. Cui, X. Xu, W. Yao, Magnetoelectric effects and valley-controlled spin quantum gates in transition metal dichalcogenide bilayers. *Nat. Commun.* **4** (2013). doi:[10.1038/ncomms3053](https://doi.org/10.1038/ncomms3053)
4. R.L. Chu, X. Li, S. Wu, Q. Niu, W. Yao, X. Xu, C. Zhang, Valley-splitting and valley-dependent inter-Landau-level optical transitions in monolayer MoS₂ quantum Hall systems. *Phys. Rev. B* **90**(4), 045427 (2014)
5. X. Li, F. Zhang, Q. Niu, Unconventional quantum Hall effect and tunable spin Hall effect in Dirac materials: application to an isolated MoS₂ trilayer. *Phys. Rev. Lett.* **110**(6), 066803 (2013)
6. M.A. Cazalilla, H. Ochoa, F. Guinea, Quantum spin Hall effect in two-dimensional crystals of transition-metal dichalcogenides. *Phys. Rev. Lett.* **113**(7), 077201 (2014)
7. T. Cao, G. Wang, W. Han, H. Ye, C. Zhu, J. Shi, Q. Niu, P. Tan, E. Wang, B. Liu et al., Valley-selective circular dichroism of monolayer molybdenum disulphide. *Nat. Commun.* **3**, 887 (2012). doi:[10.1038/ncomms1882](https://doi.org/10.1038/ncomms1882)

8. H. Zeng, J. Dai, W. Yao, D. Xiao, X. Cui, Valley polarization in MoS₂ monolayers by optical pumping. *Nat. Nanotech.* **7**(8), 490 (2012)
9. K.F. Mak, K. He, J. Shan, T.F. Heinz, Control of valley polarization in monolayer MoS₂ by optical helicity. *Nat. Nanotech.* **7**(8), 494 (2012)
10. G. Kioglou, A. Hanbicki, M. Currie, A. Friedman, D. Gunlycke, B. Jonker, Valley polarization and intervalley scattering in monolayer MoS₂. *Appl. Phys. Lett.* **101**(22), 221907 (2012)
11. F. Meier, B.P. Zakharchenya, *Optical Orientation* (Elsevier, Amsterdam, 2012)
12. M. Dyakonov, Introduction to spin physics in semiconductors. *Phys. E* **35**(2), 246 (2006)
13. G. Sallen, L. Bouet, X. Marie, G. Wang, C. Zhu, W. Han, Y. Lu, P. Tan, T. Amand, B. Liu et al., Robust optical emission polarization in MoS₂ monolayers through selective valley excitation. *Phys. Rev. B* **86**(8), 081301 (2012)
14. R.J. Elliott, Theory of the effect of spin-orbit coupling on magnetic resonance in some semiconductors. *Phys. Rev.* **96**(2), 266 (1954)
15. Y. Yafet, Conduction electron spin relaxation in the superconducting state. *Phys. Lett. A* **98**(5), 287 (1983)
16. M. Dyakonov, V. Perel, Spin relaxation of conduction electrons in noncentrosymmetric semiconductors. *Sov. Phys. Solid State* **13**(12), 3023 (1972)
17. G. Bir, A. Aronov, G. Pikus, Spin relaxation of electrons due to scattering by holes. *Sov. J. Exp. Theor. Phys.* **42**, 705 (1976)
18. M. D'yakonov, V. Perel, Optical orientation in a system of electrons and lattice nuclei in semiconductors. Theory. *Sov. J. Exp. Theor. Phys.* **38**, 177 (1974)
19. D.H. Kim, M.J. Shin, D. Lim, Excitonic valley polarization and coherence in few-layer MoS₂. *J. Korean Phys. Soc.* **66**(5), 806 (2015)
20. A.M. Jones, H. Yu, N.J. Ghimire, S. Wu, G. Aivazian, J.S. Ross, B. Zhao, J. Yan, D.G. Mandrus, D. Xiao et al., Optical generation of excitonic valley coherence in monolayer WSe₂. *Nat. Nanotech.* **8**(9), 634 (2013)
21. G. Wang, E. Palleau, T. Amand, S. Tongay, X. Marie, B. Urbaszek, Polarization and time-resolved photoluminescence spectroscopy of excitons in MoSe₂ monolayers. *Appl. Phys. Lett.* **106**(11), 112101 (2015)
22. A.M. Jones, H. Yu, J.S. Ross, P. Klement, N.J. Ghimire, J. Yan, D.G. Mandrus, W. Yao, X. Xu, Spin-layer locking effects in optical orientation of exciton spin in bilayer WSe₂. *Nat. Phys.* **10**(2), 130 (2014)
23. B. Zhu, H. Zeng, J. Dai, Z. Gong, X. Cui, Anomalously robust valley polarization and valley coherence in bilayer WS₂. *Proc. Natl. Acad. Sci.* **111**(32), 11606 (2014)
24. R. Suzuki, M. Sakano, Y. Zhang, R. Akashi, D. Morikawa, A. Harasawa, K. Yaji, K. Kuroda, K. Miyamoto, T. Okuda et al., Valley-dependent spin polarization in bulk MoS₂ with broken inversion symmetry. *Nat. Nanotech.* **9**(8), 611 (2014)
25. T.R. Chang, H. Lin, H.T. Jeng, A. Bansil, Thickness dependence of spin polarization and electronic structure of ultra-thin films of MoS₂ and related transition-metal dichalcogenides. *Sci. Rep.* **4** (2014). doi:[10.1038/srep06270](https://doi.org/10.1038/srep06270)
26. T. Jiang, H. Liu, D. Huang, S. Zhang, Y. Li, X. Gong, Y.R. Shen, W.T. Liu, S. Wu, Valley and band structure engineering of folded MoS₂ bilayers. *Nat. Nanotech.* **9**(10), 825 (2014)
27. Q. Liu, X. Zhang, A. Zunger, Intrinsic circular polarization in centrosymmetric stacks of transition-metal dichalcogenide compounds. *Phys. Rev. Lett.* **114**(8), 087402 (2015)
28. X. Zhang, Q. Liu, J.W. Luo, A.J. Freeman, A. Zunger, Hidden spin polarization in inversion-symmetric bulk crystals. *Nat. Phys.* **10**(5), 387 (2014)
29. Y. Zhang, T. Oka, R. Suzuki, J. Ye, Y. Iwasa, Electrically switchable chiral light-emitting transistor. *Science* **344**(6185), 725 (2014)
30. H. Yuan, M.S. Bahramy, K. Morimoto, S. Wu, K. Nomura, B.J. Yang, H. Shimotani, R. Suzuki, M. Toh, C. Kloc et al., Zeeman-type spin splitting controlled by an electric field. *Nat. Phys.* **9**(9), 563 (2013)
31. H. Rostami, R. Asgari, Valley Zeeman effect and spin-valley polarized conductance of monolayer MoS₂ in perpendicular magnetic field. *Phys. Rev. B* **91**, 075433 (2015)

32. A. Srivastava, M. Sidler, A.V. Allain, D.S. Lembke, A. Kis, A. Imamoğlu, Valley Zeeman effect in elementary optical excitations of monolayer WSe₂. *Nat. Phys.* **11**, 141 (2015)
33. G. Aivazian, Z. Gong, A.M. Jones, R.L. Chu, J. Yan, D.G. Mandrus, C. Zhang, D. Cobden, W. Yao, X. Xu, Magnetic control of valley pseudospin in monolayer WSe₂. *Nat. Phys.* **11**, 148 (2015)
34. D. MacNeill, C. Heikes, K.F. Mak, Z. Anderson, A. Kormányos, V. Zólyomi, J. Park, D.C. Ralph, Breaking of valley degeneracy by magnetic field in monolayer MoSe₂. *Phys. Rev. Lett.* **114**(3), 037401 (2015)
35. Y. Li, J. Ludwig, T. Low, A. Chernikov, X. Cui, G. Arefe, Y.D. Kim, A.M. van der Zande, A. Rigosi, H.M. Hill et al., Valley splitting and polarization by the Zeeman effect in monolayer MoSe₂. *Phys. Rev. Lett.* **113**(26), 266804 (2014)
36. T. Scrase, Y. Tsai, B. Barman, L. Schweidenback, A. Petrou, G. Kioseoglou, I. Ozfidan, M. Korkusinski, P. Hawrylak, Magnetoluminescence and valley polarized state of a two-dimensional electron gas in WS₂ monolayers. *Nat. Nanotech.* **10**, 603 (2015)
37. G. Wang, L. Bouet, M. Glazov, T. Amand, E. Ivchenko, E. Palleau, X. Marie, B. Urbaszek, Magneto-optics in transition metal diselenide monolayers. *2D Mater.* **2**(3), 034002 (2015)
38. H. Dery, Y. Song, Polarization analysis of excitons in monolayer and bilayer transition-metal dichalcogenides. *Phys. Rev. B* **92**(12), 125431 (2015)
39. Y. Cheng, Q. Zhang, U. Schwingenschlögl, Valley polarization in magnetically doped single-layer transition-metal dichalcogenides. *Phys. Rev. B* **89**(15), 155429 (2014)
40. J. Qi, X. Li, Q. Niu, J. Feng, Giant and tunable valley degeneracy splitting in MoTe₂. *Phys. Rev. B* **92**, 121403 (2015)
41. K.F. Mak, K.L. McGill, J. Park, P.L. McEuen, The valley Hall effect in MoS₂ transistors. *Science* **344**(6191), 1489 (2014)
42. T. Olsen, I. Souza, Valley Hall effect in disordered monolayer MoS₂ from first principles. *Phys. Rev. B* **92**(12), 125146 (2015)
43. H. Yu, Y. Wu, G.B. Liu, X. Xu, W. Yao, Nonlinear valley and spin currents from Fermi pocket anisotropy in 2D crystals. *Phys. Rev. Lett.* **113**(15), 156603 (2014)
44. S. Wu, J.S. Ross, G.B. Liu, G. Aivazian, A. Jones, Z. Fei, W. Zhu, D. Xiao, W. Yao, D. Cobden et al., Electrical tuning of valley magnetic moment through symmetry control in bilayer MoS₂. *Nat. Phys.* **9**(3), 149 (2013)
45. J. Riley, F. Mazzola, M. Dendzik, M. Michiardi, T. Takayama, L. Bawden, C. Granerød, M. Leandersson, T. Balasubramanian, M. Hoesch et al., Direct observation of spin-polarized bulk bands in an inversion-symmetric semiconductor. *Nat. Phys.* **10**(11), 835 (2014)
46. E.J. Sie, J.W. McIver, Y.H. Lee, L. Fu, J. Kong, N. Gedik, Valley-selective optical stark effect in monolayer WS₂. *Nat. Mater.* **14**, 290 (2015)
47. J. Kim, X. Hong, C. Jin, S.F. Shi, C.Y.S. Chang, M.H. Chiu, L.J. Li, F. Wang, Ultrafast generation of pseudo-magnetic field for valley excitons in WSe₂ monolayers. *Science* **346**(6214), 1205 (2014)
48. S.H. Autler, C.H. Townes, Stark effect in rapidly varying fields. *Phys. Rev.* **100**(2), 703 (1955)
49. J.S. Bakos, AC Stark effect and multiphoton processes in atoms. *Phys. Rep.* **31**(3), 209 (1977)
50. C. Cohen-Tannoudji, S. Reynaud, Dressed-atom description of resonance fluorescence and absorption spectra of a multi-level atom in an intense laser beam. *J. Phys. B* **10**(3), 345 (1977)
51. B.A. Bernevig, T.L. Hughes, S.C. Zhang, Quantum spin Hall effect and topological phase transition in HgTe quantum wells. *Science* **314**(5806), 1757 (2006)
52. P. Perez-Piskunow, G. Usaj, C. Balseiro, L.F. Torres, Floquet chiral edge states in graphene. *Phys. Rev. B* **89**(12), 121401 (2014)
53. Q. Wang, S. Ge, X. Li, J. Qiu, Y. Ji, J. Feng, D. Sun, Valley carrier dynamics in monolayer molybdenum disulfide from helicity-resolved ultrafast pump-probe spectroscopy. *ACS Nano* **7**(12), 11087 (2013)
54. T. Yu, M. Wu, Valley depolarization due to intervalley and intravalley electron-hole exchange interactions in monolayer MoS₂. *Phys. Rev. B* **89**(20), 205303 (2014)
55. C. Mai, A. Barrette, Y. Yu, Y.G. Semenov, K.W. Kim, L. Cao, K. Gundogdu, Many-body effects in valleytronics: direct measurement of valley lifetimes in single-layer MoS₂. *Nano Lett.* **14**(1), 202 (2013)

56. D. Lagarde, L. Bouet, X. Marie, C. Zhu, B. Liu, T. Amand, P. Tan, B. Urbaszek, Carrier and polarization dynamics in monolayer MoS₂. Phys. Rev. Lett. **112**(4), 047401 (2014)
57. G. Wang, X. Marie, L. Bouet, M. Vidal, A. Balocchi, T. Amand, D. Lagarde, B. Urbaszek, Exciton dynamics in WSe₂ bilayers. Appl. Phys. Lett. **105**(18), 182105 (2014)
58. G. Wang, L. Bouet, D. Lagarde, M. Vidal, A. Balocchi, T. Amand, X. Marie, B. Urbaszek, Valley dynamics probed through charged and neutral exciton emission in monolayer WSe₂. Phys. Rev. B **90**(7), 075413 (2014)
59. C. Zhu, K. Zhang, M. Glazov, B. Urbaszek, T. Amand, Z. Ji, B. Liu, X. Marie, Exciton valley dynamics probed by Kerr rotation in WSe₂ monolayers. Phys. Rev. B **90**(16), 161302 (2014)
60. C. Mai, Y.G. Semenov, A. Barrette, Y. Yu, Z. Jin, L. Cao, K.W. Kim, K. Gundogdu, Exciton valley relaxation in a single layer of WS₂ measured by ultrafast spectroscopy. Phys. Rev. B **90**(4), 041414 (2014)
61. Y.T. Wang, C.W. Luo, A. Yabushita, K.H. Wu, T. Kobayashi, C.H. Chen, L.J. Li, Ultrafast multi-level logic gates with spin-valley coupled polarization anisotropy in monolayer MoS₂. Sci. Rep. **5** (2015). doi:[10.1038/srep08289](https://doi.org/10.1038/srep08289)
62. M. Glazov, T. Amand, X. Marie, D. Lagarde, L. Bouet, B. Urbaszek, Exciton fine structure and spin decoherence in monolayers of transition metal dichalcogenides. Phys. Rev. B **89**(20), 201302 (2014)

Chapter 12

Miscellaneous Phenomena

In this Chapter we describe phenomena, observed in 2D TMDCs, that are not sufficiently broad or well studied to form individual chapters, namely, second-harmonic generation, piezoelectric effect, Burstein-Moss effect, superconductivity, and the formation of polaritons.

12.1 Second Harmonic Generation

12.1.1 SHG from Odd- and Even-Layer Structures

Strong second-harmonic generation (SHG) in few-layers of MoS₂ was independently reported by two groups [1, 2]. The approaches, obtained results and conclusions were very similar.

Bulk 2H-MoS₂ possesses a trigonal prismatic structure with Bernal stacking,¹ and is characterized by D_{6h}^4 nonsymmorphic space group with an inversion symmetry operation in the middle of the two MoS₂ monolayers. Consequently its second-order non-linear response is vanishingly small (a value of 10^{-14} m/V was reported for the second-order susceptibility [4]).

At the same time, the symmetry of a monolayer is D_{3h} , and hence the inversion symmetry of the bulk phase is lost. On the other hand, in bilayer MoS₂ the inversion symmetry operation is again present. As a consequence, one would expect SHG for an odd MoS₂ layer number, while it should not be generated in samples with an even number of layers.

The electric field of the generated second-harmonic light, $E(2\omega)$, along a given direction, $\hat{\epsilon}_{2\omega}$ in terms of the second-harmonic tensor χ^2 and input light polarization vector $\hat{\epsilon}_\omega$ can be written as [1]:

¹This stacking pattern refers to layered structures where half of the atoms in the upper layer lie directly over the center of a hexagon in the lower layer, and half of the atoms lie over an atom. First described by J.D. Bernal for the case of graphite [3].

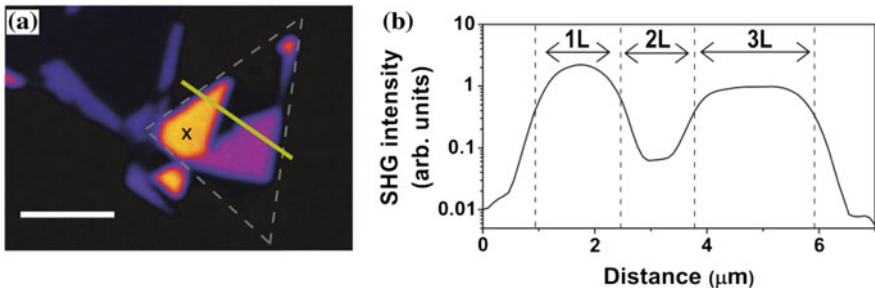


Fig. 12.1 **a** Second-harmonic image collected from a MoS_2 thin film, pump-laser wavelength at 800 nm, 1.55 eV. Brighter colors mean stronger SHG intensity, and the scale bar is 5 μm . **b** Intensity profile of the SHG image from left to right at the yellow line shown in panel (a) [1]. Copyright 2013 by the American Physical Society. Reprinted with permission

$$E(2\omega) \cdot \hat{\epsilon}_{2\omega} = C \hat{\epsilon}_{2\omega} \cdot \chi^2 : \hat{\epsilon}_\omega \hat{\epsilon}_\omega \quad (12.1)$$

where ω is the laser frequency, 2ω is the second harmonic frequency, and C is a proportionality constant which contains local-field factors determined by the local dielectric environment.

For odd-layer MoS_2 with D_{3h} point-group symmetry, the second-order susceptibility tensor has a single nonzero element: $\chi^{(2)} \equiv \chi_{xxx}^{(2)} = -\chi_{xyy}^{(2)} = -\chi_{yyx}^{(2)} = -\chi_{xxy}^{(2)}$, where x corresponds to the arm-chair direction and y is along the zig-zag direction [1].

Hence the resulting dependence of the generated second-harmonic electric field as a function of the sample angle for a pump-laser polarization $\hat{\epsilon}_\omega$ parallel to the analyzer $\hat{\epsilon}_{2\omega}$, can be expressed as [1]:

$$E(2\omega) = C \chi_{\text{MoS}_2}^{(2)} \cos(3\phi + \phi_0) \quad (12.2)$$

where ϕ is the angle between the input laser polarization and the x direction and ϕ_0 is the initial crystallographic orientation of the MoS_2 sample.

Figure 12.1a shows the intensity of the second harmonic signal from a sample that contains areas with one, two and three monolayers of MoS_2 and Fig. 12.1b shows the intensity profile on a log scale along the yellow line shown in panel (a). Indeed, a stronger signal is present for monolayer MoS_2 when compared to trilayer MoS_2 , for the pump wavelength at 800 nm, considering that less material is present in the former case. At the same time, the bilayer MoS_2 shows very low SHG, almost two orders of magnitude lower than the monolayer. It was suggested that the small observed signal may come from the boundary between the layers [1].

To confirm that the strong optical emission is due to the optical second-harmonic generation, its intensity dependence on pump-laser power was measured. In both studies [1, 2] the log scale plot showed a linear dependence with a slope equal to 2.

In absolute terms, the surface nonlinear susceptibility of monolayer MoS_2 was determined to be $d_{\text{MoS}_2}^s = 8.8 \times 10^{-31} \text{ m}\cdot\text{C}/\text{V}^2$, which corresponds to the effective volume second-order nonlinear susceptibility of $d_{\text{MoS}_2} = 1.4 \times 10^{-21} \text{ C}/\text{V}^2$ [5].

The authors of both papers [1, 2] propose that due to the sensitivity of the SHG to the crystal symmetry, polarization-resolved SHG measurements provide

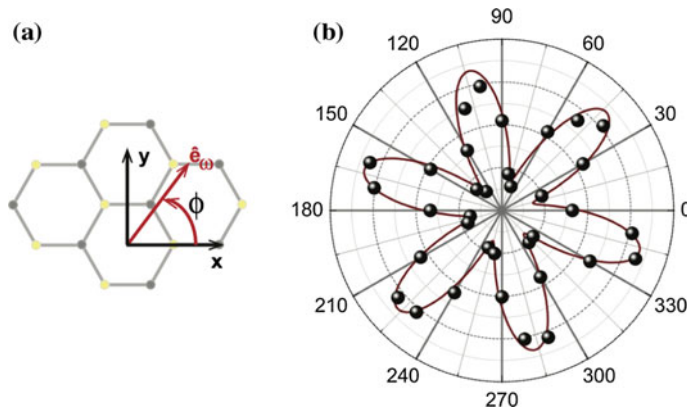


Fig. 12.2 **a** Top view of the MoS₂ crystallographic orientation with respect to the incident laser polarization (\hat{e}_ω) **b** Polar plot of the second-harmonic intensity from monolayer MoS₂ as a function of the sample angle [1]. Copyright 2013 by the American Physical Society. Reprinted with permission

important crystallographic information of MoS₂ atomic layers. In [1], it is noted that for measurements with the analyzer at crossed polarization with the input laser, the second-harmonic electric field is proportional to $\sin(3\phi + \phi_0)$ (see Fig. 12.2a for the experimental geometry showing a top view of the MoS₂ crystallographic orientation with respect to the incident laser polarization \hat{e}_ω). The intensity of the generated second-harmonic light as a function of the sample angle can be written as [1]:

$$I_{2\omega} \propto \cos^2(3\phi + \phi_0) \quad (12.3)$$

where ϕ is the angle between the input laser polarization and the x direction and ϕ_0 is the initial crystallographic orientation of the MoS₂ sample.

This is exemplified in Fig. 12.2b that shows the experimental results of the SHG polarization dependence for monolayer of MoS₂, where the second-harmonic intensity is plotted as a function of the sample rotation angle. A clear sixfold pattern could be observed.

This approach has been successfully used to determine both absolute and relative orientations of the MoS₂ flakes (Fig. 12.3).

In [2] this method was specifically used to determine the orientation of triangular MoS₂ flakes grown by CVD. The edges of these triangular flakes are expected to be along zig-zag directions since these are lowest energy configurations and the experimental results were consistent with this prediction [2].

Similar results were obtained for WS₂ and WSe₂ flakes, namely, strong SHG for samples with an odd number of layers and a drastic decrease for samples with an even number of layers, with a maximum strength for monolayer samples (samples with up to 7 monolayers were measured) [6]. Measurements in this case were performed using a pulsed laser beam of 800 nm wavelength at normal incidence and 130 fs pulse duration (Fig. 12.4). In [5] it was noted the second harmonic intensity from odd

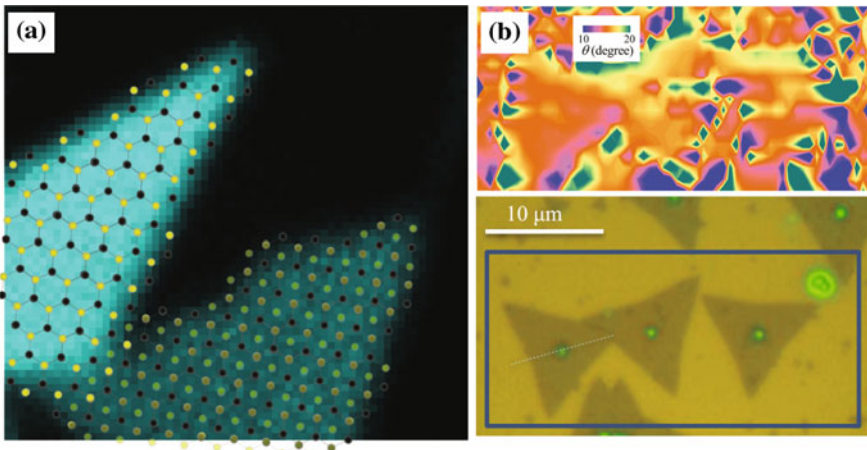


Fig. 12.3 **a** Second harmonic image showing the crystallographic direction of the monolayer and trilayer MoS₂ sample determined by the polarization measurements [1]. Copyright 2013 by the American Physical Society. Reprinted with permission. **b** *Top* map of θ calculated from second harmonic intensity measurements from the rectangular region of a substrate containing flakes grown by CVD, shown in the optical microscopy photograph (*bottom panel*). θ is the angle between the arm-chair direction of the layer and the light polarization (*horizontal*) direction [2]. Copyright 2013 by the American Physical Society. Reprinted with permission

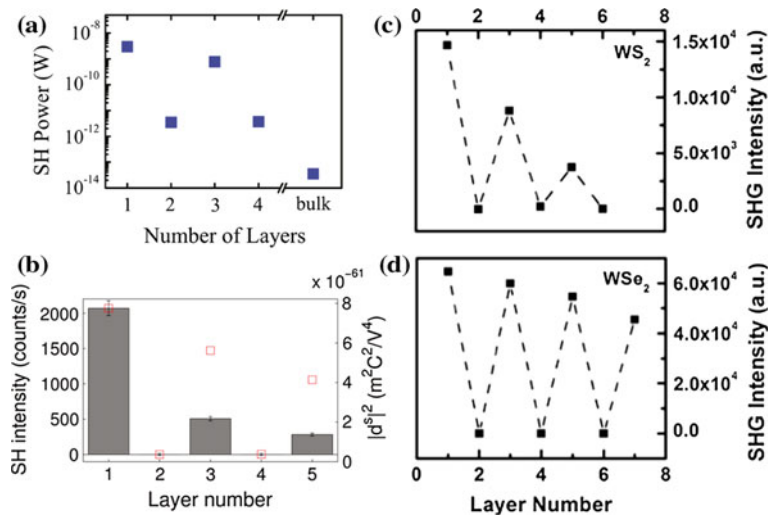


Fig. 12.4 The intensity of SHG as a function of the number of monolayers in MoS₂ **a**—[2]. Copyright 2013 by the American Physical Society. Reprinted with permission; **b**—[5] Copyright 2013 American Chemical Society. Published with permission and WS₂ **c** and WSe₂ **d**. Reproduced from [6]

numbers of layers, however, decreases significantly from one layer to five layers, in contrast to the nearly constant response for h-BN [5]. This dependence was attributed to light absorption in TMDC and also to interlayer coupling, which modifies the electronic structure of few-layer MoS₂ and may induce further changes in the linear and nonlinear susceptibilities [5].

In line with these results was the observation made in the 1998 that strong SHG could be detected in bulk 3R-MoS₂, while the signal was unmeasurably small in 2H-MoS₂ [4].

12.1.2 SHG and Edge States

It was further found that the SHG response was different from the central area of the flake and from its edges [7]. The ratio of the central region and edge second-harmonic responses had a pronounced spectral dependence with a maximum at about 1310 nm (~ 0.95 eV), a slightly higher photon energy than the half transition energy of the A exciton complex, which was interpreted as being due to electronic structure variations between the sharp crystalline edges and the bulk monolayer crystals.

12.1.3 Resonant SHG

In [8] SHG in monolayer WS₂ was studied and the authors found an unusually large second order nonlinear susceptibility nearly three orders of magnitude larger than in other common nonlinear crystals. In order to quantitatively characterize the nonlinear susceptibility of two-dimensional (2D) materials, they developed a formalism to model SHG based on the Green's function with a 2D nonlinear sheet source. Their analysis suggested the origin of the large nonlinear susceptibility is in resonance enhancement and the large joint density of states as illustrated in Fig. 12.5.

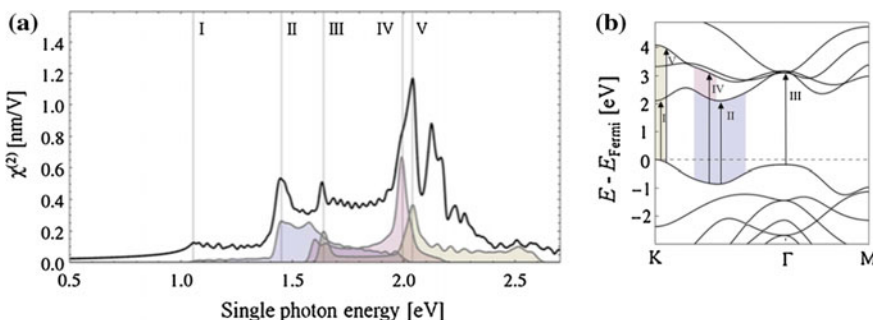


Fig. 12.5 **a** The nonlinear susceptibility $\chi^{(2)}$ of monolayer WS₂. Also shown is the colour-coded joint density states contributions from the highest valence band to the first, second, and third conduction bands, aligned to the calculated spectra at the appropriate second-order resonant frequencies and following the colour scheme shown in **(b)**. Reproduced from [8] (colour figure online)

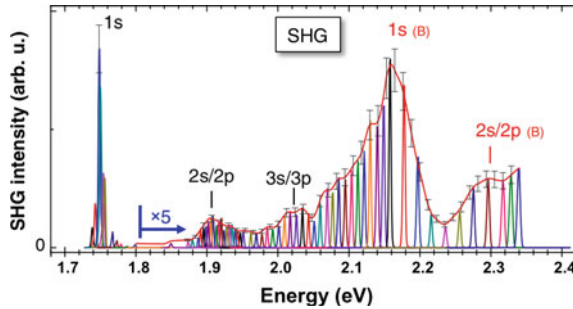


Fig. 12.6 Results of SHG spectroscopy at $T = 4$ K as a function of $2\hbar\omega$. Typical error bars are shown, based on the standard deviation of the measured laser pulse width (for each wave-length) as a direct measure of the fluctuation of the peak power during the experiment [10]. Copyright 2015 by the American Physical Society. Reprinted with permission

12.1.4 Excitonic Effects

The theory of excitonic SHG in monolayer MoS₂ was developed in [9]. In [10] SHG spectroscopy was performed and it was found that by tuning the optical excitation on and off resonance with respect to the ground ($1s$) and excited ($2s$, $2p$...) exciton states a variation over several orders of magnitude of the nonlinear and linear optical response of monolayer WSe₂ could be achieved. The results are shown in Fig. 12.6. To clarify the exact origin of these transitions and to investigate their excitonic nature and symmetry, 2-photon and 1-photon PL excitation experiments were additionally performed.

A particularly surprising feature was the strong SHG signal when the 2-photon laser energy was in resonance with $1s\ A$ exciton (1.75 eV) and the $1s\ B$ exciton (2.17 eV), whose energies were determined in the same sample through PL and reflectivity. In contrast to the SHG results, the $1s$ transitions were not observed in 2-photon PL excitation experiments, as they are dipole forbidden. PL emission and SHG could be clearly distinguished due to the different emission line-width and polarization selection rules. It was concluded that the clear SHG resonances observed indicate that contributions beyond the usual electric-dipole coupling of the light-matter interaction are involved, which was attributed to magnetic dipole interactions [10].

12.1.5 SHG in Twisted Bi-layers

Of special interest is SHG in artificially stacked bi-layers when the two layers can be twisted by an arbitrary angle. This issue was addressed in [11–13] and the obtained results are in good agreement with each other. The authors of [13] performed the most detailed study and in what follows we concentrate on their results.

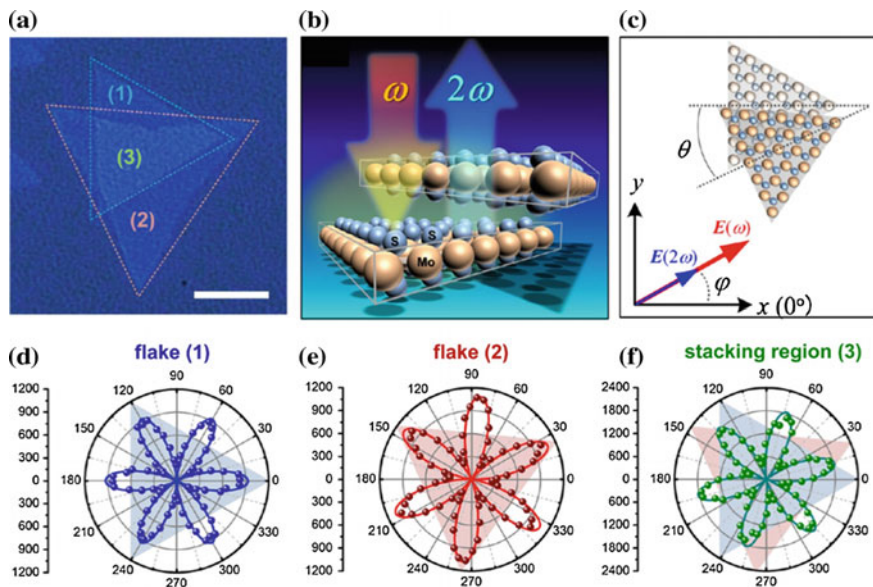


Fig. 12.7 **a** An optical microscopy image of a particular MoS₂ bilayer with a stacking angle of $\theta \approx 25^\circ$. The scale is 5 μm . **b** and **c** Schematics showing (**b**) the measurement geometry and (**c**) the polarization directions of the incident laser and the measured SHG. The azimuthal angle j defines the angle between the laser polarization and the x -axis, which is aligned with the armchair direction of the flake (*1*). **d–f** Polar plots of the polarization-resolved second harmonic intensity as a function of azimuthal angle θ measured from (**d**) the monolayer region (*1*), **e** the monolayer region (*2*), and **f** the stacking region (*3*) [13]. Copyright 2014 American Chemical Society. Published with permission

To illustrate the twist angle effect on polarization-resolved SHG, a bilayer with a stacking angle of $\theta = 25^\circ$ between two monolayers was measured (Fig. 12.7a). The SHG experiment was performed in a back-reflection geometry using a pump laser normally incident on the sample (Fig. 12.7b). The incident pump laser was linearly polarized along the x direction aligned with the armchair direction of one of the monolayers (Fig. 12.7c). For the monolayer MoS₂ crystal with a three-fold rotational symmetry, the second harmonic response for the case of the polarization parallel (perpendicular) to the incident laser polarization is known to exhibit six-fold rotational symmetry (see above), with a second harmonic intensity varying as $I_{||} = \cos^2 3\varphi (I_{\perp} + \sin^2 3\varphi)$, where φ is the azimuthal angle between the incident laser polarization and the arm-chair direction. Consequently, the second harmonic response from individual monolayers should exhibit an intensity maximum when the incident laser polarization aligns with the arm-chair (zig-zag) direction for the parallel (perpendicular) polarization configuration, in agreement with the experiment (Fig. 12.7d, e) where the polarization-resolved SHG shows a six-petal pattern, with petals lying along the perpendicular bisectors of each flake. An interesting finding was that the second harmonic light from the twisted bi-layer region did not appear

as a sum of the individual flakes but also showed a six-petal polarization pattern (Fig. 12.7f), however, with petals lying along a direction between the two nearest perpendicular bisectors of the two monolayers.

The authors model the artificially stacked MoS₂ bilayers as two electrically decoupled layers of atomically thin sheet dipole moments driven coherently by the fundamental laser field [13]. In this case, the second harmonic fields generated from the two layers interfere coherently with a phase difference depending on the stacking angle, which explains the fact that SHG from the stacked region retained the six-fold rotational symmetry with petals lying between the two flakes. The coherent superposition of second harmonic fields can be either constructive or destructive, leading to an enhanced or suppressed second harmonic intensity in the stacking region.

The total second harmonic intensity in the stacked region can be expressed as [13]:

$$I_s = I_1 + I_2 + \sqrt{I_1 I_2} \cos 3\theta \quad (12.4)$$

where I_s and $I_{1,2}$ correspond for the second harmonic intensity in the stacking region, and the individual monolayer flakes and θ is the stacking angle, which is defined as the angle between two nearest perpendicular bisectors of the two triangular flakes (Fig. 12.8b). According to (12.4), interference is completely constructive for $\theta = 0^\circ$ and completely destructive for $\theta = 60^\circ$.

The second harmonic response of the artificially stacked bilayers (also using different material combinations) with different stacking angles was subsequently examined. In order to avoid the effect on the angular dependence due to the presence of second harmonic intensity variation among different flakes, a dimensionless parameter $\kappa(\theta) \equiv (I_s - I_1 - I_2)/2(I_1 I_2)^{1/2}$ was introduced and its angular dependence was examined (Fig. 12.8c–e). One can clearly see that the second harmonic intensity in the bilayer region indeed changes from maximum to minimum as the twist angle changes from $\theta = 0^\circ$ to $\theta = 60^\circ$. The best fit was obtained when the propagating effects of the electromagnetic waves were included into analysis.

An impressive example of the interference effect from two twisted monolayers is shown in Fig. 12.9, where in the optical image two layers with opposite orientations are indistinguishable, while in the SHG map a drastic contrast is observed.

Enhanced SHG was observed in three-dimensional pyramidal spirals of MoS₂, where, due to the sample structure, the stacking sequence is different from 2H [14].

12.1.6 Electrical Control of SHG

As mentioned above, SHG is enhanced when excited in resonance with excitonic states. Is it possible to make use of this effect to electrically control SHG in TMDC monolayers? The issue was addressed in [15], where the authors provided a positive answer to this question. The authors used a monolayer WSe₂ field-effect transistor (Fig. 12.10a), where the tunable SHG was observed from the resonant responses of neutral and charged excitons. After confirming that the strong SHG signal was from

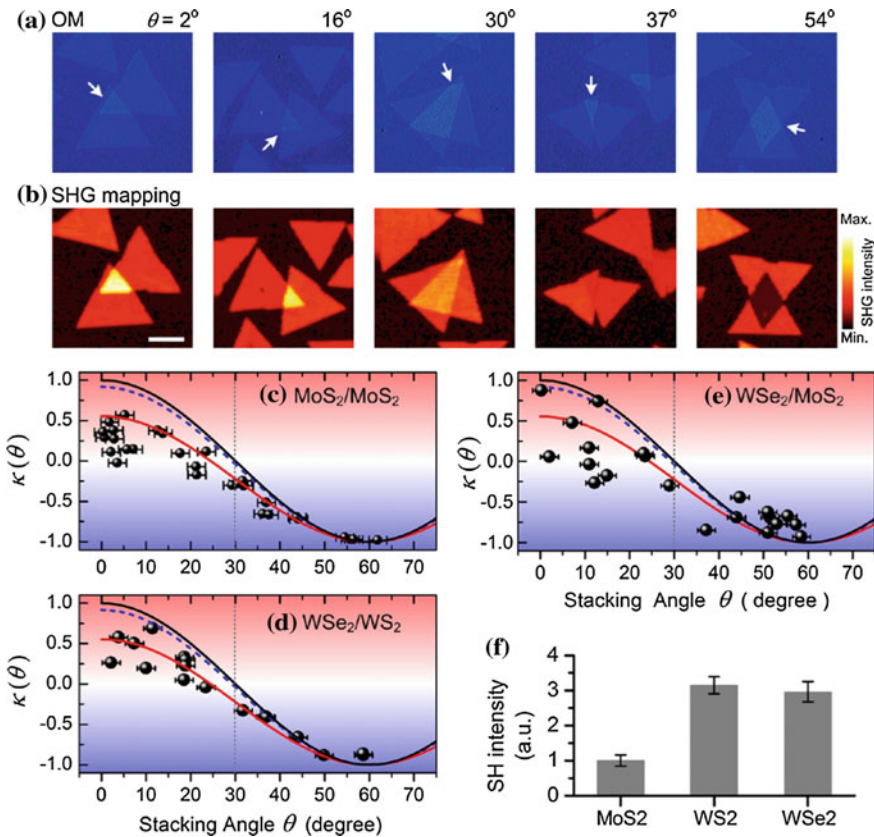


Fig. 12.8 **a** Optical microscopy images for a series of MoS₂ bilayers with a stacking angle changing from 0° to 60°. **b** The corresponding false color-coded second harmonic intensity mappings of flakes shown in (a). The scale bar is 5 μm. **c–e** The measured angular dependence of $\kappa(\theta)$ for (**c**) homogeneous MoS₂/MoS₂ bilayers, **d** heterogeneous WSe₂/WS₂ bilayers, and **e** heterogeneous WSe₂/MoS₂ bilayers. Curves are calculated $\kappa(\theta)$: black solid curves, $\kappa(\theta) = \cos 3\theta$; red (blue dashed) curves, calculations considering the propagation effects of electromagnetic waves with (without) including material absorption. Symbols are data points collected from all the investigated bilayers. **f** The measured second harmonic intensities for MoS₂, WS₂, and WSe₂ monolayers [13]. Copyright 2014 American Chemical Society. Published with permission

resonant coupling to the A exciton, it was demonstrated that the resonant SHG can be tuned by electrostatic doping, where a nearly fourfold reduction in the resonant SHG intensity was observed when the d.c. gate voltage V_g was swept from -80 to 80 V (Fig. 12.10b).

Figure 12.10c, d illustrate the tunability of the SHG by gate bias. The electrostatic doping tunes the strength of the neutral and charged excitonic resonances, and hence the strength and frequencies of the SHG response. Specifically, X^0 SHG decreased by over an order of magnitude from -30 to 70 V. For the trions, the SHG tuned opposite to the exciton signal.

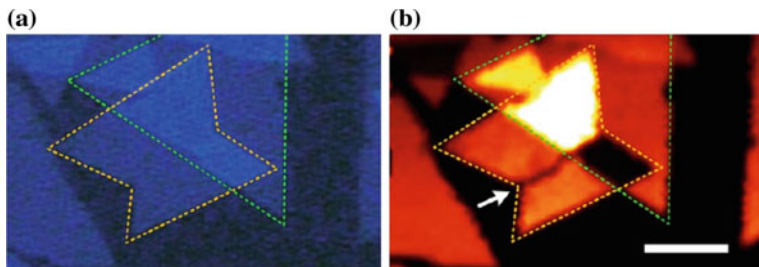


Fig. 12.9 **a** An optical microscopy image for a triangular MoS₂ monolayer overlapped with a butterfly-shaped MoS₂ monolayer. **b** The corresponding false color-coded second harmonic intensity obtained by pixel-to-pixel spatial mappings of flakes in (a). The *butterfly-shaped* MoS₂ monolayer consists of two mirror-twin domains with a twin boundary located at the intersection of the two wings (indicated by arrow) [13]. Copyright 2014 American Chemical Society. Published with permission

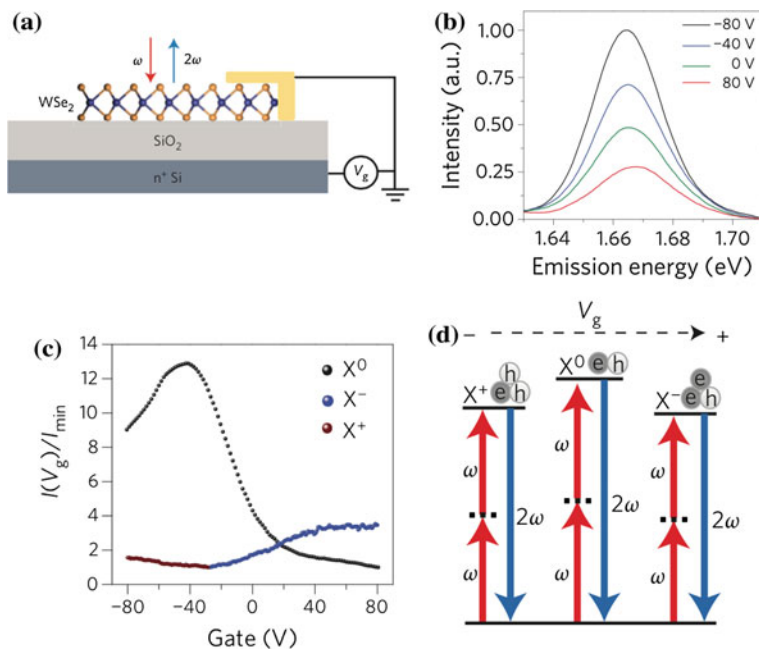


Fig. 12.10 **a** Schematic of gated monolayer WSe₂. Excitation at ω (red arrow) generates second-harmonic radiation at 2ω (blue arrow) **b** SHG spectra on resonance with the exciton at selected gate voltages, **c** Normalized peak intensity of exciton and trion SHG as a function of gate voltage. Laser excitation is fixed at the corresponding resonance **d** Illustration of gate-dependent exciton- and trion-enhanced SHG [15]. Reprinted by permission from Macmillan Publishers Ltd., copyright (2015)

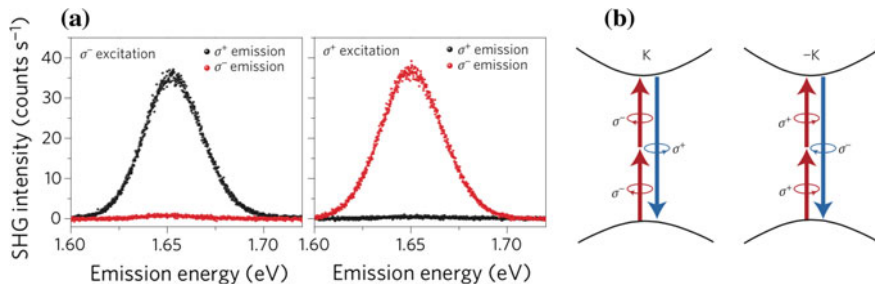


Fig. 12.11 Valley-dependent SHG selection rules. **a** Circular polarization-resolved SHG spectra showing the generation of counter-circular SHG. **b** Interband valley optical selection rules for SHG [15]. Reprinted by permission from Macmillan Publishers Ltd., copyright (2015)

Finally, an interesting remark was made on the two-photon optical selection rules of the exciton-enhanced SHG. Figure 12.11 shows how two left-circular (σ^-) photons at the fundamental frequency (ω) generate a single right-circular (σ^+) photon at the second-harmonic frequency (2ω) with near-unity polarization. The opposite holds for σ^+ excitation. It was noted that this is the expected SHG selection rule from D_{3h} crystal symmetry, where the production of a counter-rotating second harmonic is a general feature of materials with both broken inversion and three-fold rotational symmetry, where the lattice supplies the angular momentum mismatch of the absorbed and emitted photons [15]. The role of valley contrasting absorption to the microscopic origin of the SHG selection rule was further considered. While the one-photon emission process from the valleys reproduced the circular polarisation of the excitation light, for the two-photon interband transition a flip in the selection rule was found where two σ^- (σ^+) photons could be simultaneously absorbed at $+K$ ($-K$) resulting in the expected counter-circular SHG selection rule (Fig. 12.11b) [15].

Charge-induced SHG was observed in bilayer WSe₂ [16], where, based on the observed threshold and asymmetry of the process, it was concluded that it was the charge and not the electric field that was causing the SHG.

12.1.7 SHG Dynamics

Dynamical response of single layer MoS₂ to intense above-bandgap photoexcitation using the nonlinear-optical second order susceptibility as a direct probe of the electronic and structural dynamics was studied in [17]. Excitation conditions corresponding to the order of one electron-hole pair per unit cell and transient temperature increase of a few thousand degrees generated unexpected increases in the second harmonic from monolayer films, occurring on few picosecond time-scales. These large amplitude changes recovered on tens of picosecond time-scales and were reversible at megahertz repetition rates with no photoinduced change in lattice symmetry observed despite the extreme excitation conditions.

12.2 Piezoelectricity in Monolayer MoS₂

For a material to be piezoelectric, it must not be centrosymmetric. Bulk 2H-TMDCs are centrosymmetric and hence no piezoelectric response is expected. At the same time, their single layers do not possess an inversion center. Piezoelectricity in monolayer TMDCs was theoretically predicted in [18], where it was found that some of these materials exhibited stronger piezoelectric coupling than traditionally employed bulk wurtzite structures. Their piezoelectric coefficients spanned more than 1 order of magnitude, and exhibited monotonic periodic trends.

Experimentally, two groups independently reported piezoelectric response from monolayer MoS₂ [19, 20]. They used different approaches to study the effect but obtained essentially very similar results. In [20], a free-standing monolayer MoS₂ was studied using a setup shown in Fig. 12.12a, which combined a laterally applied electric field and nanoindentation in an atomic force microscope. Due to the D_{3h} symmetry of the crystal, the electromechanical coupling in monolayer MoS₂ can be described by a single piezoelectric coefficient ϵ_{11} . Within the MoS₂ structure, each rhombic prismatic unit cell is asymmetrically occupied by two S atoms on the left site and one Mo atom on the right, such that an external electric field pointing from the S site to the Mo site in the hexagonal lattice (arm-chair direction) can deform the unit cell by stretching the Mo-S bond and cause internal piezoelectric stress (Fig. 12.12b).

The thickness dependence of the piezoelectric coefficient of two-dimensional membranes exfoliated from natural 2H-MoS₂ crystals was studied and a piezoelectric response could only be observed for odd-layer membranes, in agreement with the lack of inversion symmetry (Fig. 12.12c), whereas in even-layer membranes, the contributions to piezoelectricity from alternating orientations of adjacent layers cancelled.

The angular dependence of piezoelectricity was also studied with θ (see Fig. 12.12d) ranging from 0° to 60°. The obtained piezoelectric coupling fit well to a cosine curve (red solid line) with a period of 120° as shown in Fig. 12.12e [20].

A different approach was used in [19], where piezoelectric response was studied by applying strain to a device coupled to an external load resistor (Fig. 12.13a). In this configuration, strain-induced polarization charges at the sample edges can drive the flow of electrons in external circuit. When the substrate is released, electrons flow back in the opposite direction. Figure 12.13b shows the piezoelectric current and voltage responses of a single-layer MoS₂. When strain is applied in the x ('arm-chair') direction, positive voltage and current outputs were observed with increasing strain, and negative outputs were observed with decreasing strain, directly demonstrating the conversion of mechanical energy into electricity. Both responses increased with the magnitude of the applied strain with voltage and current responsivities of 55.1 ± 12.3 pA and 32.8 ± 4.5 mV, respectively, for each 1% change in strain. The output reversed sign when the strain was rotated from the x to the y ('zigzag') direction (Fig. 12.13b) in agreement with the crystal symmetry.

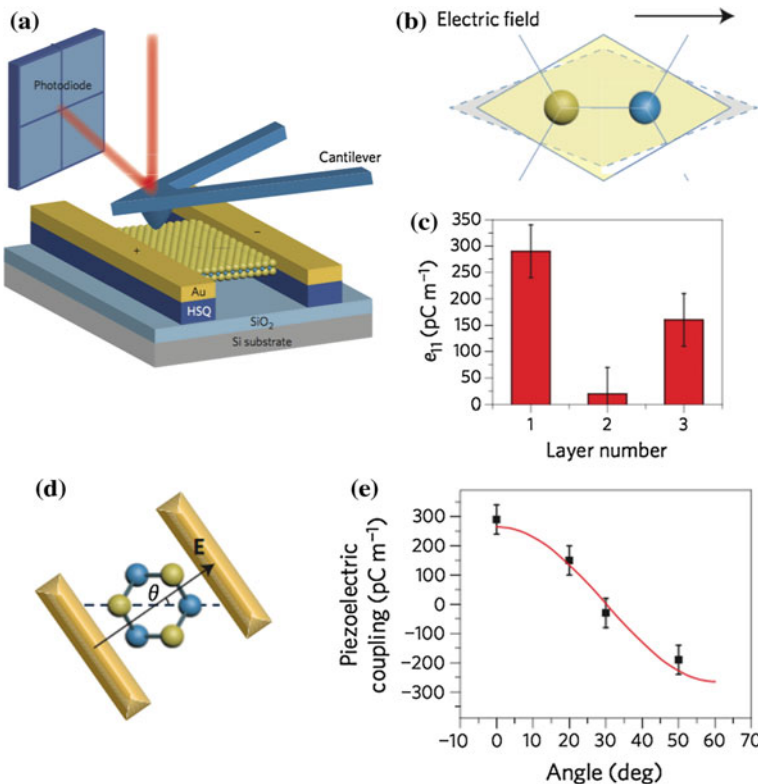


Fig. 12.12 **a** Schematic of the experiment. To measure the in-plane piezoelectric stress, the MoS₂ film was suspended on two HSQ (hydrogen silsesquioxane) posts, clamped underneath by two Au electrodes. The film was indented with a scanning AFM probe. The induced stress changed the load on the cantilever, which was observed by the deflection of a laser beam. **b** With an external electric field pointing from the S site to the Mo site, the Mo-2S dipole² is stretched and the unit cell is elongated, creating compressive stress in the x direction and tensile stress in the y direction. **c** Measured piezoelectric coefficient in one-, two- and three-layer MoS₂ membranes, showing that only odd numbers of layers exhibit a significant coupling strength due to their broken inversion symmetry. **d** The rotation of the crystal with respect to the electric field and mechanical boundary was achieved by patterning the electrodes at different angles θ . **e** Measured piezoelectric coupling strength (square data points) followed the $\cos(\theta)$ dependence (the red fitting curve) predicted from the crystalline three-fold symmetry [20]. Reprinted by permission from Macmillan Publishers Ltd., copyright (2015)

The conversion efficiency of the single-layer MoS₂ nanogenerator, which is the ratio of the electric power delivered to the load to the total mechanical deformation energy stored in the single-layer MoS₂ after being strained was estimated as $\sim 5.08\%$ and was stable over time (Fig. 12.13c).

²It is not exactly clear what “the Mo-2S dipole” means. In the caption we preserved the notation from the original publication.

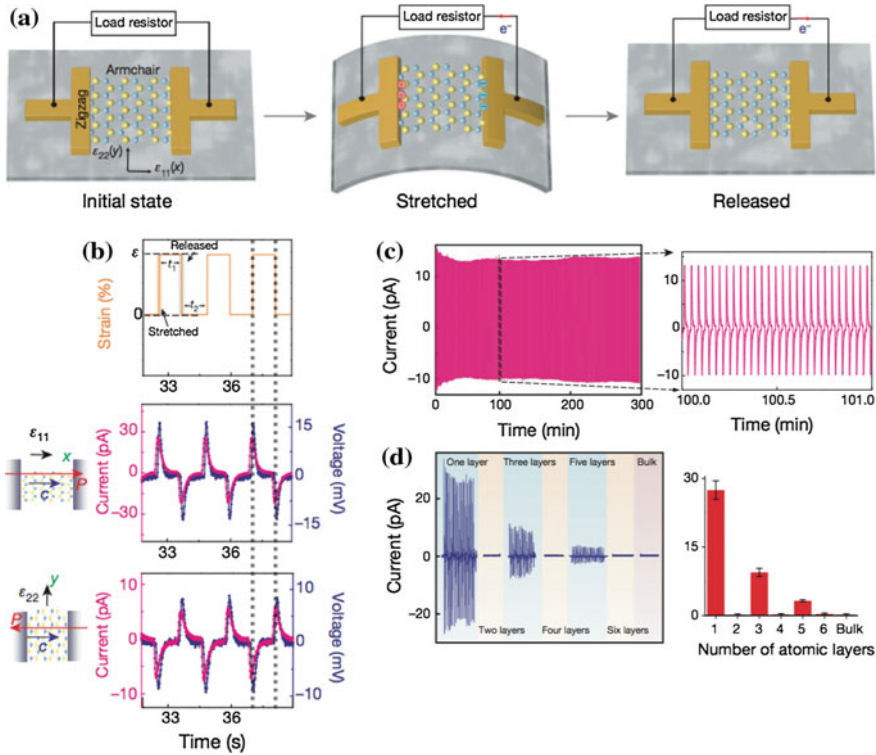


Fig. 12.13 **a** Operation scheme of the single-layer MoS₂ piezoelectric device. When the device is stretched, piezoelectric polarization charges of opposite polarity (plus and minus symbols) are induced at the zigzag edges of the MoS₂ flake. Periodic stretching and releasing of the substrate can generate piezoelectric outputs in external circuits with alternating polarity (as indicated by the red arrows). **b** Voltage response with 1 GOhm external load and short-circuit current response of a single-layer MoS₂ device under periodic strain in two different principal directions. *Top* applied strain as a function of time. *Middle* corresponding piezoelectric outputs from single-atomic-layer MoS₂ when strain is applied in the *x* direction (armchair direction). *Bottom* corresponding piezoelectric outputs from the same device when strain is applied in the *y* direction (zigzag direction). The phase difference highlighted by black dashed lines is obtained by theoretical derivation and has been intentionally exaggerated for clarity. Red, blue and black arrows represent the directions of polarization, the polar axis of MoS₂ and principal strains, respectively. **c** Cyclic test showing the stability of a single-layer MoS₂ device for a prolonged period. **d** Evolution of the piezoelectric outputs with increasing numbers of atomic layers (n) in MoS₂ flakes [19]. Reprinted by permission from Macmillan Publishers Ltd., copyright (2014)

Figure 12.13d shows the measured piezoelectric output for MoS₂ flakes with $n = 1, 2, 3, 4, 5$ and 6, and for a bulk MoS₂ flake with a thickness of more than 100 nm. Almost no detectable output could be seen for the bulk flake and the even-layer samples. For the odd-layer samples, the piezoelectric output was large and decreased roughly as the inverse of n , confirming that single-layer MoS₂ with broken inversion symmetry has a strong intrinsic piezoelectric response, whereas centrosymmetric bilayers and bulk crystals are non-piezoelectric. A similar dependence on the number of layers was observed for SHG (see above).

12.3 Quantum Spin Hall Effect

Quantum spin Hall (QSH) insulators are insulators in the bulk but possess conducting edge states that are topologically protected from back-scattering by time-reversal symmetry and have been claimed to be very promising for device applications. However, as noted in [21], the realization of such QSH-based devices for practical applications is impeded by three critical factors: (i) band gaps of existing QSH insulators are too small, which limits the operating regime to low temperatures; (ii) the small number of conducting channels results in a small signal-to-noise ratio; and (iii) efficient methods of fast on/off switching are lacking. Hence search of new QSH materials is a very hot subject. The issue of quantum spin Hall effect in two-dimensional TMDC has been addressed by several groups [21–23]. Here we concentrate on the results of [21].

It was noted that the structure of the T' phase may be particularly suitable for QSH applications. Figure 12.14a shows the band structure of $1T'$ -MoS₂ as an example (other group VI TMDCs had similar electronic structure [21]). Unlike the $2H$ phase, $1T'$ -MoS₂ is a semiconductor with a fundamental gap (E_g) of about 0.08 eV, located at $\Lambda = \pm 0.0146$ Å [red dots in panel (b)]. The conduction and valence showed a camelback shape near Γ , suggesting band inversion with a large inverted gap (2δ) of about 0.6 eV.

The Z_2 index (0 or 1, indicating a trivial or nontrivial topology, respectively) was further calculated based on the parity criterion of the valence bands and $Z_2 = 1$ was obtained, indicating that 2D $1T'$ -MX₂ materials are in the QSH insulator phase [21]. To understand the origin of the inverted band structure near Γ , the orbital character of the bands was analyzed and it was found that the valence band mainly consists of metal d -orbitals and the conduction band mainly consists of chalcogenide p -orbitals, as expected. The observed band inversion arises from the period doubling of the metal chain in the $1T'$ structure, which lowers the metal d -orbital below the chalcogen p -orbital around Γ .

It was noted that the band inversion at Γ (ca. 0.6 eV) is an intrinsic characteristic of the $1T'$ structure that takes place even without the inclusion of spin-orbit interaction in the calculations. This band inversion leads to the appearance of two Dirac cones at the Λ points in 2D Brillouin zone. Spin-orbit coupling opens up a fundamental gap of 0.08 eV at the Dirac points. It was found that other group VI TMDCs also have Z_2 nontrivial band topology.

The QSH insulator phase in 2D $1T'$ -MX₂ leads to helical edge states that are protected from localization and elastic backscattering by time-reversal symmetry (Fig. 12.14c).

It was proposed that the inverted bands between chalcogen p - and metal d -orbitals located on well-separated planes might offer a simple means to control topological electronic properties by an external electric field. Based on first-principles calculations, it was found that a vertical electric field indeed induced a topological phase transition. First, the electric field breaks inversion symmetry and introduces a strong Rashba splitting of the doubly degenerate bands near the fundamental gap E_g at the

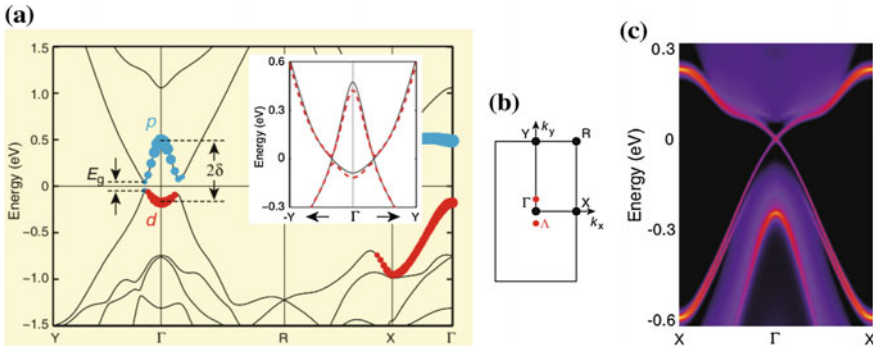


Fig. 12.14 **a** Band structure and **b** Brillouin zone of 1T'-MoS₂. (E_g —fundamental gap; 2δ —inverted gap). The inset compares band structures with (red dashed line) and without (black solid line) spin-orbit coupling. Four time-reversal invariant momenta are marked by black dots and labeled as Γ , X, Y, and R. The locations of the fundamental gap are marked by red dots and labeled by Λ . **c** Edge density of states at the Γ point [21]. Reprinted with permission from AAAS

Λ points. As the field increases, E_g first decreased to zero and then reopened, which was accompanied by a topology change to a trivial phase [21].

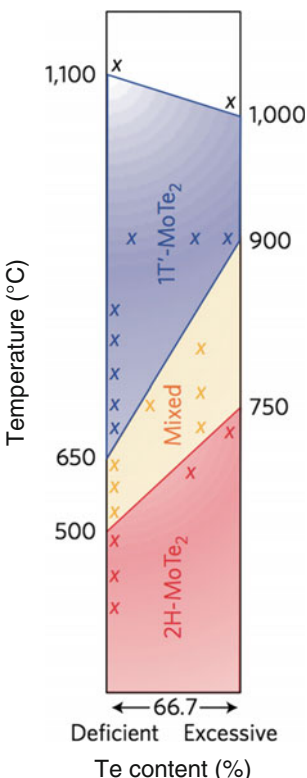
It was noted [21] that while the 1T' phase in monolayer MoS₂ is not the ground state, this phase was recently experimentally observed in high-resolution transmission electron microscopy experiments [24] and ab-initio calculations demonstrated that there was a barrier of more than 1 eV between the 1T' and 2H phases. It was further noted that another TMDC, namely, WTe₂ naturally exists in the 1T' phase [25], which makes it potentially the most promising 2D TMDC for realizing the QSH effect and related vdW devices. Although monolayer WTe₂ is a semimetal, it was proposed that a small negative fundamental gap can be created by a tensile strain [21].

In this connection, it is interesting to note that a reversible structural phase transition between the 2H and 1T' phases in bulk single-crystalline MoTe₂ was reported in [26]³ with the phase diagram shown in Fig. 12.15. Bulk 1T'-MoTe₂ crystals exhibited a maximum carrier mobility of 4,000 cm²/V·s and a giant magnetoresistance of 16,000% in a magnetic field of 14 T at 1.8 K. As the structure was changed from bulk to few-layers, a bandgap opening of up to 60 meV was observed, which was attributed to strong interband spin-orbit coupling.

Photo-induced quantum spin and valley Hall effects in monolayer MoS₂ were also studied in [28], where it was proposed to use off-resonant circularly polarised light to enable valley-polarised nanoelectronics in TMDC.

³It was subsequently argued [27] that the conclusion about the ‘reversible phase transition’ stemmed from misinterpretation of the experimental results.

Fig. 12.15 Phase diagram of MoTe₂ [26]. Reprinted by permission from Macmillan Publishers Ltd., copyright (2015)



12.4 Burstein–Moss Effect

The Burstein–Moss effect was discovered independently by Burstein [29] and Moss [30] and consists in an apparent increase of the fundamental optical band gap with an increasing concentration of electrons. The effect typically occurs in degenerate semiconductors when the Fermi level lies inside the conduction band. In this case, an electron from the top of the valence band can only be excited into conduction band above the Fermi level (which lies in the conduction band) since all the states below the Fermi level are occupied. The Pauli exclusion principle forbids excitation into the occupied states. As a result, with increased doping, when the Fermi level moves deeper (higher) into the valence (conduction) band, one observes an apparent increase in the optical band gap.

Rhenium-doped inorganic fullerene-like (IF) nanoparticles (Re:MoS₂) provide an interesting physical platform for the investigation of *n*-doping effects in confined TMDC systems. Rhenium centers act as substitutional dopants rather than interstitial impurities, which, in addition to changing the carrier concentration allows for an additional tunability of the electronic structure with strain. Such studies were

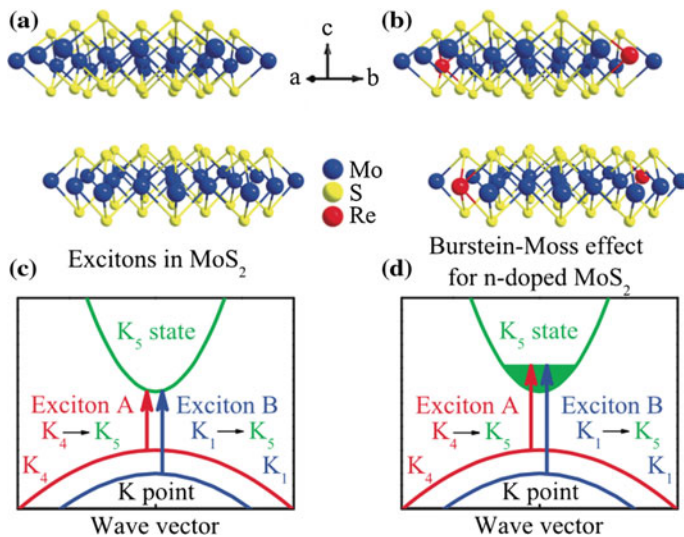


Fig. 12.16 **a,b** Schematic views of the characteristic MoS₂ double layers along with an example of how the Re centers go into the lattice as substitutional impurities (rather than interstitial impurities), introduce extra electrons, making *n*-doped material. **c** Schematic view of the transitions corresponding to excitons *A* and *B* in pristine 2*H*- and *IF*-MoS₂. **d** Schematic view of the Burstein–Moss effect in electron doped MoS₂. In both panels, excitons *A* and *B* are associated with optically allowed K₄ → K₅ and K₁ → K₅ transitions [31]. Copyright 2013 by the American Chemical Society. Reprinted with permission

performed in [31]. The differences between MoS₂ and Re:MoS₂ are illustrated in Fig. 12.16.

Figure 12.17a, b shows the optical conductivities of the Re:MoS₂ nanoparticles at two characteristic doping levels (panel (b) zooms into the exciton region). As expected, the optical conductivity of Re:MoS₂ is larger than that of pristine *IF*-MoS₂, and the effective number of electrons $n_{eff}(E)$ increases systematically with doping well above the band gap. Since Re:MoS₂ is an electron-rich system with a partially filled conduction band, this trend was interpreted as a Burstein–Moss shift. Plotting the difference between the exciton position in the substituted sample and that in the pristine nanoparticles with increasing doping level (Fig. 12.17c, d), a systematic shift was observed.

According to parabolic band theory (see e.g. [32]), the Burstein–Moss shift is given as:

$$\Delta E_{BM} = \frac{\hbar^2}{2m^*} (3\pi^2 n)^{2/3} \quad (12.5)$$

Here, ΔE_{BM} is Burstein–Moss shift, n is the carrier density, m^* is the effective electron mass, and \hbar is the reduced Planck constant. A good agreement between the measured data and the theoretical prediction was obtained, as shown in Fig. 12.17e, f.

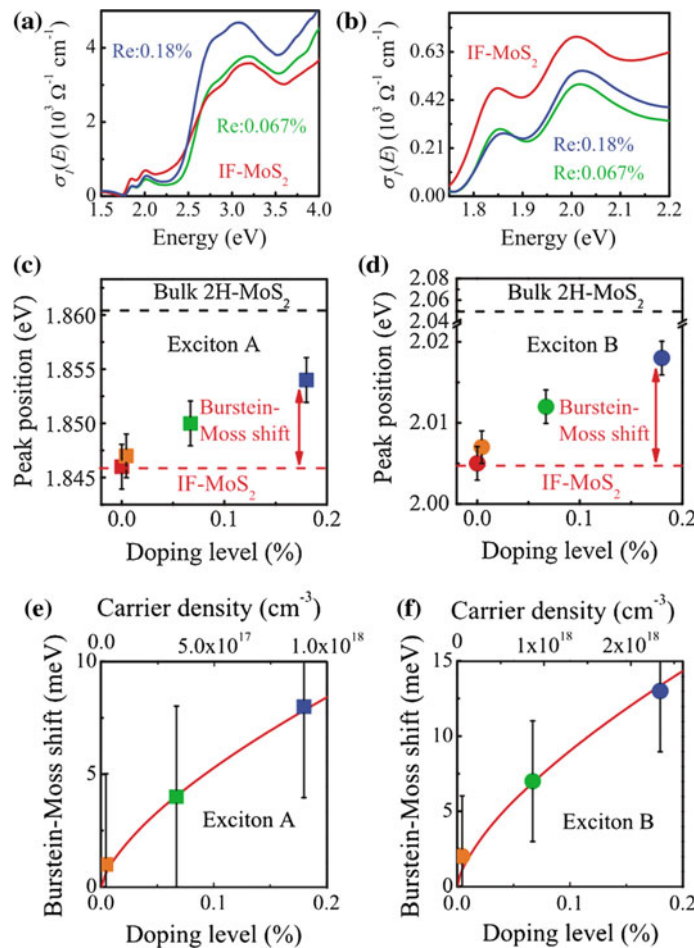


Fig. 12.17 **a, b** 300 K optical conductivity of nanoscale MoS_2 calculated from a Kramers–Kronig analysis of the measured reflectance for different levels of Re doping. **c, d** *A* and *B* exciton energies as a function of Re doping level. Black and red dashed lines indicate 2H- and IF-values, which represent the two limiting cases. **e, f** Burstein–Moss shift as a function of Re doping. Red solid curves denote simulated shifts [31]. Copyright 2013 by the American Chemical Society. Reprinted with permission

12.5 Gate-Tuned Superconductivity

In unconventional superconductors, the transition temperature T_c often has a maximum as a function of external parameters such as chemical doping or pressure [33, 34], a so-called superconductivity dome. In band insulators the observation of superconductivity dome is less common. In recent years, electrostatic carrier doping has been effectively implemented by using ionic liquids (IL) to form an electrical

double layer (EDL) of high capacitance [35], which allowed one to generate carrier densities quasicontinuously and precisely that span the superconductivity dome [36].

Recently, this method was applied to investigate superconductivity in few-layered TMDCs [37, 38]. The device structure is shown in Fig. 12.18 (inset) and DEME-TFSI was used as ionic liquid. MoS₂ and MoSe₂ exhibited rather similar behaviours. As an illustration, Fig. 12.18a shows gate-induced superconductivity in MoSe₂, which emerged at $V_G = 2.4$ V and developed further with further increase in V_G . Figure 12.18b shows the temperature dependence of the normalized sheet resistance of the MoSe₂ device at various V_G , demonstrating that the superconducting transition can be controlled via electrostatic ionic gating. The T_c value increased with increasing V_G , reaching a maximum of $T_c = 7.1$ K.

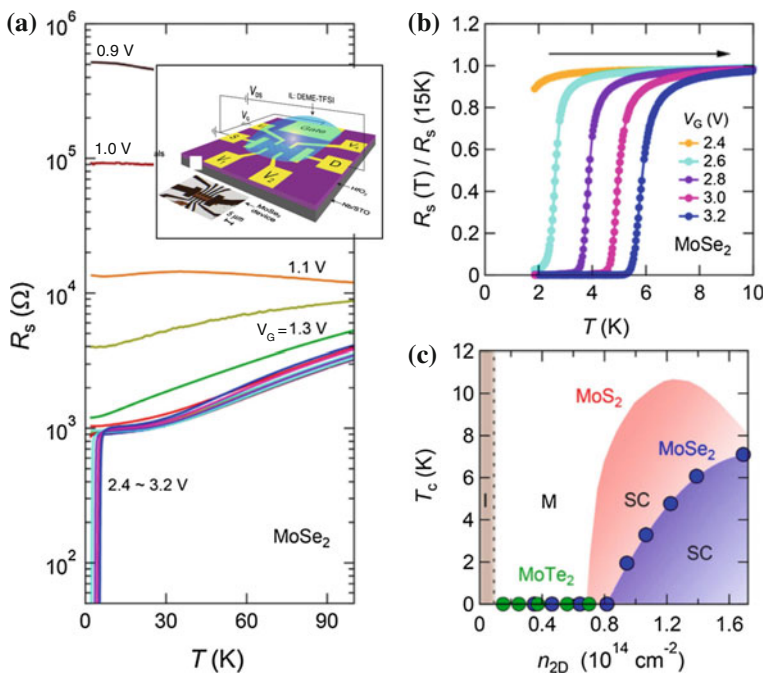


Fig. 12.18 Superconductivity induced by electrostatic IL gating and the phase diagram of electron-doped MoSe₂. **a** The temperature dependence of the channel sheet resistance R_s at various liquid gate voltages for a MoSe₂ EDLT device using DEME-TFSI as ionic media. The *inset* shows the EDLT device and measurement configuration. **b** Normalized channel sheet resistance $R_s/R_s(15\text{K})$ of the same MoSe₂ EDLT device as a function of temperature for various liquid gate voltages from 2.4 V to 3.2 V. **c** T_c versus n_{2D} phase diagram of electron-doped MoSe₂. The MoS₂ phase diagram (red shade) is shown for comparison. Here, sheet carrier density n_{2D} is obtained from Hall effect measurements and T_c is defined as the position corresponding to 90% of the total resistance drop. MoTe₂ data are also presented in (c), showing no evidence of superconductivity down to 2 K ($T_c = 0$) because of the insufficient maximum carrier density achieved through electrostatic IL gating. Reproduced from [38]

The relationship between T_c and n_{2D} is shown Fig. 12.18c. In MoS₂, the superconductivity sharply appeared at $n_{2D} = 6.8 \times 10^{13} \text{ cm}^{-2}$, then saturated after reaching a maximum $T_c = 10.8 \text{ K}$ at $n_{2D} = 1.2 \times 10^{14} \text{ cm}^{-2}$, followed by a decrease in T_c at larger n_{2D} , resulting in a dome-like superconducting state [37]. In a similar manner to MoS₂, the superconductivity in MoSe₂ abruptly emerged above a critical carrier density. Subsequently, T_c increased with increasing n_{2D} until a maximum was reached. These similarities suggest that the dome-shaped phase diagram is a universal feature of gate-induced superconductivity in TMDC systems [38].

Superconductivity TMDC was theoretically investigated in [39], where the electron-phonon interaction in electron-doped single-layer MoS₂ was investigated using first-principles calculations. The electron-phonon coupling was found to be very weak at low doping levels. It then grew rapidly to a maximum of $\lambda \approx 1.7$, after which it began to decrease with additional doping. This behavior was attributed to the growth and shrinkage of Fermi sheets with different orbital character [39] and it was predicted that the superconducting transition temperature is expected to follow the same trends.

No superconducting transition was observed in MoTe₂ up to $V_G = 2.5 \text{ V}$. Figure 12.18c also shows n_{2D} values for MoTe₂ devices (denoted by green symbols) with $T_c = 0$, indicating that no superconducting transitions were observed down to 2 K. When the ionic liquid was replaced with a KClO₄/PEG electrolyte, the electron doping could be significantly enhanced through a crossover to an electrochemical regime beyond the electrostatic limit. As a result, superconductivity in MoTe₂ was enabled with observed T_c value of approximately 2.8 K, which was additionally confirmed by the magnetic field dependence of the resistivity [38].

Insulator-metal transitions also occurred when negative V_G was applied, but no hole superconductivity could be observed down to 2 K for all MoX₂ [38].

WS₂ is another member of the semiconducting TMDCs, in which bulk superconductivity can be induced by conventional chemical doping of Sr [40] and also by ionic gating [41]. In [38], few-layer WS₂ was investigated. Figure 12.19a presents the results for R_S as a function of temperature at various V_G from 6 V to 12 V. Good metallic conduction was observed followed by a superconducting transition *at the same* onset transition temperature (the dashed vertical line in Fig. 12.19a) for V_G at 9 V, 10 V and 12 V. The transition could be completely destroyed by applying a magnetic field of 2 T as indicated by the dashed curves in Fig. 12.19a, providing further evidence of superconductivity. Superconductivity disappeared at higher doping levels. The phase diagram for T_c versus n_{3D} and doping concentration x is shown in Fig. 12.19b.

To explain the observed unusual carrier concentration dependence, the superconducting phase was argued to be a line-phase compound in terms of potassium concentration that is a mixture of superconducting and non-superconducting phases whose fraction varies as the K-intercalation proceeds [38].

Superconductivity in gated MoS₂ was also studied in [42] and it was concluded that two-dimensional Ising superconductivity was established, where spins of electrons in the Cooper pairs are strongly pinned by an effective Zeeman field.

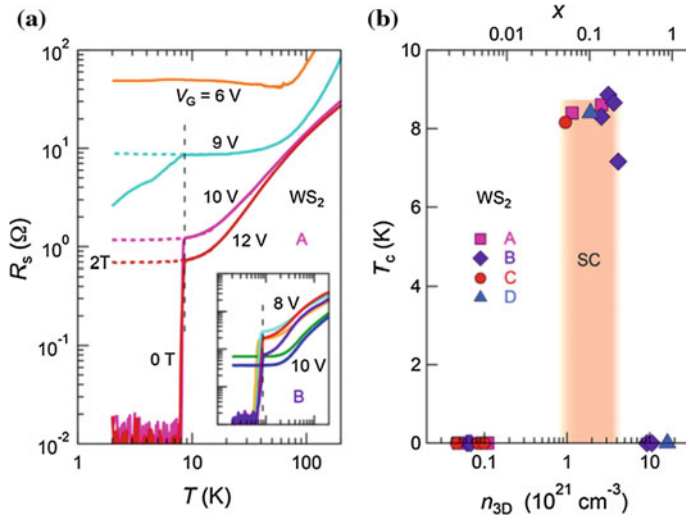


Fig. 12.19 **a** Temperature dependence of R_s on a log scale at various V_G from 6 V to 12 V. The solid and dashed curves represent the data for magnetic fields at 0 T and 2 T, respectively. The inset shows R_s versus T in the same log scale for another WS₂ device at various V_G from 8 V to 10 V. The vertical dashed line indicates that the same onset T_c was observed for different V_G , implying the existence of a line-phase K_xWS₂ compound. **b** Phase diagram of electron-doped WS₂ as a function of bulk carrier density n_{3D} (bottom horizontal axis) and doping concentration x (upper horizontal axis). The superconducting transition temperature T_c is defined as the position corresponding to 90% of the total resistance drop. n_{3D} and x were calculated from Hall effect results assuming that the whole flake was uniformly doped. Different filled symbols represent different devices and the shaded area defines a complete superconducting (SC) region reaching “zero resistance”. Reproduced from [38]

12.6 Strong Light-Matter Coupling and Polaritons

When the interaction between the dipole and the cavity photons occurs at a rate that is faster than the average dissipation rates of the cavity photon and dipole, one enters the strong coupling regime, resulting in the formation of new eigenstates that are half-light, half-matter bosonic quasiparticles called cavity polaritons. The first observation of strongly coupled two-dimensional exciton-polaritons using a MoS₂ monolayer embedded in a dielectric microcavity was reported in [43]. The microcavity consisted of a monolayer of MoS₂, sandwiched between two MoS₂ layers to form the cavity layer, which was placed between SiO₂/Si₃N₄ distributed Bragg reflector mirrors grown via plasma-enhanced chemical vapour deposition (Fig. 12.20a).

To confirm the formation of polariton states in the active spot of the microcavity, angle-resolved reflectivity measurements were performed. The results for TM polarization are shown in Fig. 12.20b. At small angles ($<20^\circ$), two prominent modes were observed, that were identified as the lower polariton branch and the upper polariton branch. The lower polariton branch blueshifted with increasing angle and approached ex_A , while the upper polariton branch shifted away from the exciton energy, ex_A , with

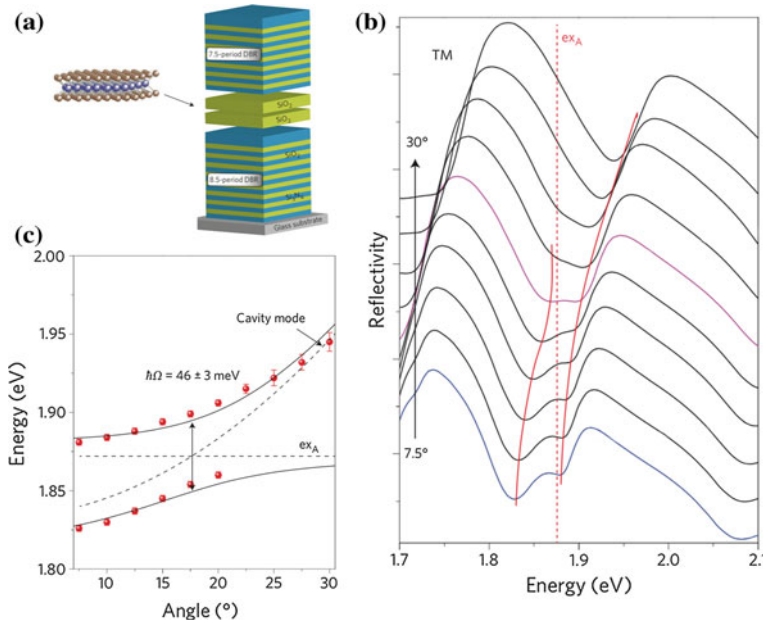


Fig. 12.20 **a** Schematic of the microcavity structure, **b** Angle-resolved reflectivity spectra for TM polarization from 7.5° to 30°. The vertical red dashed line represents the MoS₂ ex_A energy. Red curves trace the dispersion of microcavity polariton modes. **c** Dispersion relation extracted from the angle-resolved reflectivity spectra. Red spheres with error bars are the polariton energies obtained from the reflectivity spectra. The horizontal black dashed line represents the ex_A energy. The black short-dashed curve represents the cavity modes. The two black solid curves correspond to theoretical fits of the polariton branches using a coupled oscillator model [43]. Reprinted by permission from Macmillan Publishers Ltd., copyright (2015)

increasing angle. The red solid lines trace the dispersion of both branches, showing the anticrossing around 20°. The dispersion extracted from the reflectivity minima is shown in Fig. 12.20c as well as the fit to a coupled oscillator model (solid black lines) with a detuning of -40 meV and a Rabi splitting of $\hbar\Omega_{\text{Rabi}} = 46 \pm 3\text{ meV}$. Using the experimental halfwidths for ex_A ($\hbar\Gamma_{\text{ex}} = 30\text{ meV}$) and the cavity phonon ($\hbar\Gamma_{\text{cav}} = 9\text{ meV}$), it was deduced the light-matter interaction potential $V_A = 25 \pm 2\text{ meV}$, which results in $V_A^2 > ((\hbar\Gamma_{\text{ex}})^2 + (\hbar\Gamma_{\text{cav}})^2)/2$, a necessary condition for the formation of strongly coupled polariton states [43].

References

1. L.M. Malard, T.V. Alencar, A.P.M. Barboza, K.F. Mak, A.M. de Paula, Observation of intense second harmonic generation from MoS₂ atomic crystals. Phys. Rev. B **87**(20), 201401 (2013)
2. N. Kumar, S. Najmaei, Q. Cui, F. Ceballos, P.M. Ajayan, J. Lou, H. Zhao, Second harmonic microscopy of monolayer MoS₂. Phys. Rev. B **87**(16), 161403 (2013)
3. J.D. Bernal, The structure of graphite. Proc. R. Soc. Lond. A **106**(740), 749 (1924)

4. G. Wagoner, P. Persans, E. Van Wagenen, G. Korenowski, Second-harmonic generation in molybdenum disulfide. *J. Opt. Soc. Am. B* **15**(3), 1017 (1998)
5. Y. Li, Y. Rao, K.F. Mak, Y. You, S. Wang, C.R. Dean, T.F. Heinz, Probing symmetry properties of few-layer MoS₂ and h-BN by optical second-harmonic generation. *Nano Lett.* **13**(7), 3329 (2013)
6. H. Zeng, G.B. Liu, J. Dai, Y. Yan, B. Zhu, R. He, L. Xie, S. Xu, X. Chen, W. Yao, et al., Optical signature of symmetry variations and spin-valley coupling in atomically thin tungsten dichalcogenides. *Sci. Rep.* **3** (2013). doi:[10.1038/srep01608](https://doi.org/10.1038/srep01608)
7. X. Yin, Z. Ye, D.A. Chenet, Y. Ye, K. O'Brien, J.C. Hone, X. Zhang, Edge nonlinear optics on a MoS₂ atomic monolayer. *Science* **344**(6183), 488 (2014)
8. C. Janisch, Y. Wang, D. Ma, N. Mehta, A.L. Elías, N. Perea-López, M. Terrones, V. Crespi, Z. Liu, Extraordinary second harmonic generation in tungsten disulfide monolayers. *Sci. Rep.* **4** (2014). doi:[10.1038/srep05530](https://doi.org/10.1038/srep05530)
9. M.L. Trolle, G. Seifert, T.G. Pedersen, Theory of excitonic second-harmonic generation in monolayer MoS₂. *Phys. Rev. B* **89**(23), 235410 (2014)
10. G. Wang, X. Marie, I. Gerber, T. Amand, D. Lagarde, L. Bouet, M. Vidal, A. Balocchi, B. Urbaszek, Giant enhancement of the optical second-harmonic emission of WSe₂ monolayers by laser excitation at exciton resonances. *Phys. Rev. Lett.* **114**(9), 097403 (2015)
11. K. Liu, L. Zhang, T. Cao, C. Jin, D. Qiu, Q. Zhou, A. Zettl, P. Yang, S.G. Louie, F. Wang, Evolution of interlayer coupling in twisted molybdenum disulfide bilayers. *Nat. Commun.* **5** (2014). doi:[10.1038/ncomms5966](https://doi.org/10.1038/ncomms5966)
12. A.M. van der Zande, J. Kunstmann, A. Chernikov, D.A. Chenet, Y. You, X. Zhang, P.Y. Huang, T.C. Berkelbach, L. Wang, F. Zhang et al., Tailoring the electronic structure in bilayer molybdenum disulfide via interlayer twist. *Nano Lett.* **14**(7), 3869 (2014)
13. W.T. Hsu, Z.A. Zhao, L.J. Li, C.H. Chen, M.H. Chiu, P.S. Chang, Y.C. Chou, W.H. Chang, Second harmonic generation from artificially stacked transition metal dichalcogenide twisted bilayers. *ACS Nano* **8**(3), 2951 (2014)
14. L. Zhang, K. Liu, A.B. Wong, J. Kim, X. Hong, C. Liu, T. Cao, S.G. Louie, F. Wang, P. Yang, Three-dimensional spirals of atomic layered MoS₂. *Nano Lett.* **14**(11), 6418 (2014)
15. K.L. Seyler, J.R. Schaibley, P. Gong, P. Rivera, A.M. Jones, S. Wu, J. Yan, D.G. Mandrus, W. Yao, X. Xu, Electrical control of second-harmonic generation in a WSe₂ monolayer transistor. *Nat. Nanotech.* **10**, 407 (2015)
16. H. Yu, D. Talukdar, W. Xu, J.B. Khurgin, Q. Xiong, Charge-induced second-harmonic generation in bilayer WSe₂. *Nano Lett.* **15**(8), 5653 (2015)
17. E.M. Mannebach, K.A.N. Duerloo, L.A. Pellouchoud, M.J. Sher, S. Nah, Y.H. Kuo, Y. Yu, A.F. Marshall, L. Cao, E.J. Reed et al., Ultrafast electronic and structural response of monolayer MoS₂ under intense photoexcitation conditions. *ACS Nano* **8**(10), 10734 (2014)
18. K.A.N. Duerloo, M.T. Ong, E.J. Reed, Intrinsic piezoelectricity in two-dimensional materials. *J. Phys. Chem. Lett.* **3**(19), 2871 (2012)
19. W. Wu, L. Wang, Y. Li, F. Zhang, L. Lin, S. Niu, D. Chenet, X. Zhang, Y. Hao, T.F. Heinz et al., Piezoelectricity of single-atomic-layer MoS₂ for energy conversion and piezotronics. *Nature* **514**(7523), 470 (2014)
20. H. Zhu, Y. Wang, J. Xiao, M. Liu, S. Xiong, Z.J. Wong, Z. Ye, Y. Ye, X. Yin, X. Zhang, Observation of piezoelectricity in free-standing monolayer MoS₂. *Nat. Nanotech.* **10**(2), 151 (2015)
21. X. Qian, J. Liu, L. Fu, J. Li, Quantum spin Hall effect in two-dimensional transition metal dichalcogenides. *Science* **346**(6215), 1344 (2014)
22. X. Li, F. Zhang, Q. Niu, Unconventional quantum Hall effect and tunable spin Hall effect in dirac materials: application to an isolated MoS₂ trilayer. *Phys. Rev. Lett.* **110**(6), 066803 (2013)
23. A. Cazalilla, M.H. Ochoa, F. Guinea, Quantum spin Hall effect in two-dimensional crystals of transition-metal dichalcogenides. *Phys. Rev. Lett.* **113**(7), 077201 (2014)
24. G. Eda, T. Fujita, H. Yamaguchi, D. Voiry, M. Chen, M. Chhowalla, Coherent atomic and electronic heterostructures of single-layer MoS₂. *ACS Nano* **6**(8), 7311 (2012)

25. J. Wilson, A. Yoffe, The transition metal dichalcogenides discussion and interpretation of the observed optical, electrical and structural properties. *Adv. Phys.* **18**(73), 193 (1969)
26. D.H. Keum, S. Cho, J.H. Kim, D.H. Choe, H.J. Sung, M. Kan, H. Kang, J.Y. Hwang, S.W. Kim, H. Yang et al., Bandgap opening in few-layered monoclinic MoTe₂. *Nat. Phys.* **11**(6), 482 (2015)
27. K. Ueno, K. Fukushima, Changes in structure and chemical composition of α -MoTe₂ and β -MoTe₂ during heating in vacuum conditions. *Appl. Phys. Express* **8**(9), 095201 (2015)
28. M. Tahir, A. Manchon, U. Schwingenschlögl, Photoinduced quantum spin and valley Hall effects, and orbital magnetization in monolayer MoS₂. *Phys. Rev. B* **90**(12), 125438 (2014)
29. E. Burstein, Anomalous optical absorption limit in InSb. *Phys. Rev.* **93**(3), 632 (1954)
30. T. Moss, The interpretation of the properties of indium antimonide. *Proc. Phys. Soc. B* **67**(10), 775 (1954)
31. Q.C. Sun, L. Yadgarov, R. Rosentsveig, G. Seifert, R. Tenne, J.L. Musfeldt, Observation of a burstein-moss shift in rhodium-doped MoS₂ nanoparticles. *ACS Nano* **7**(4), 3506 (2013)
32. C.M. Wolfe, N. Holonyak Jr, G.E. Stillman, *Physical Properties of Semiconductors* (Prentice-Hall, Inc., Upper Saddle River, 1988)
33. P.A. Lee, N. Nagaosa, X.G. Wen, Doping a mott insulator: Physics of high-temperature superconductivity. *Rev. Mod. Phys.* **78**(1), 17 (2006)
34. Y. Takabayashi, A.Y. Ganin, P. Jeglič, D. Arčon, T. Takano, Y. Iwasa, Y. Ohishi, M. Takata, N. Takeshita, K. Prassides et al., The disorder-free non-BCS superconductor Cs₃C₆₀ emerges from an antiferromagnetic insulator parent state. *Science* **323**(5921), 1585 (2009)
35. K. Ueno, S. Nakamura, H. Shimotani, A. Ohtomo, N. Kimura, T. Nojima, H. Aoki, Y. Iwasa, M. Kawasaki, Electric-field-induced superconductivity in an insulator. *Nat. Mater.* **7**(11), 855 (2008)
36. A.T. Bollinger, G. Dubuis, J. Yoon, D. Pavuna, J. Misewich, I. Božović, Superconductor-insulator transition in La_{2-x}Sr_xCuO₄ at the pair quantum resistance. *Nature* **472**(7344), 458 (2011)
37. J.T. Ye, Y.J. Zhang, R. Akashi, M.S. Bahramy, R. Arita, Y. Iwasa, Superconducting dome in a gate-tuned band insulator. *Science* **338**(6111), 1193 (2012)
38. W. Shi, J. Ye, Y. Zhang, R. Suzuki, M. Yoshida, J. Miyazaki, N. Inoue, Y. Saito, Y. Iwasa, Superconductivity series in transition metal dichalcogenides by ionic gating. *Sci. Rep.* **5** (2015). doi:[10.1038/srep12534](https://doi.org/10.1038/srep12534)
39. Y. Ge, A.Y. Liu, Phonon-mediated superconductivity in electron-doped single-layer MoS₂: a first-principles prediction. *Phys. Rev. B* **87**(24), 241408 (2013)
40. G.V.S. Rao, M.W. Shafer, S. Kawarazaki, A.M. Toxen, Superconductivity in alkaline earth metal and Yb intercalated group VI layered dichalcogenides. *J. Sol. State Chem.* **9**(4), 323 (1974)
41. S. Jo, D. Costanzo, H. Berger, A.F. Morpurgo, Electrostatically induced superconductivity at the surface of WS₂. *Nano Lett.* **15**(2), 1197 (2015)
42. J.M. Lu, O. Zheliuk, I. Leermakers, N.F.Q. Yuan, U. Zeitler, K.T. Law, J.T. Ye, Evidence for two-dimensional ising superconductivity in gated MoS₂. *Science* (2015). doi:[10.1126/science.aab2277](https://doi.org/10.1126/science.aab2277)
43. X. Liu, T. Galfsky, Z. Sun, F. Xia, E.c. Lin, Y.H. Lee, S. Kéna-Cohen, V.M. Menon, Strong light-matter coupling in two-dimensional atomic crystals. *Nat. Photon.* **9**(1), 30 (2015)

Chapter 13

TMDC Heterostructures

Semiconductor heterostructures and superlattices are the fundamental platform for many important device applications such as lasers, light-emitting diodes, solar cells, high-electron-mobility transistors, etc. Conventional heterostructures, mainly based on group IV, III–V, or II–VI semiconductors with covalent bonding between atoms at the heterointerface, are usually fabricated using epitaxial growth. As a result, the choice of material components is strongly limited by lattice mismatch. Furthermore, due to atomic interdiffusion during growth, the resulting atomic-scale interface roughness and composition gradients at the interface compromise the performance of such heterostructures, especially as the thicknesses are reduced toward a single atomic layer.

TMDC, where covalently bonded individual layers are held together by week vdW forces, *without surface dangling bonds*, have a unique advantage because in this case heterostructures can be built by assembling individual layers into functional multilayer structures, with atomically sharp interfaces, no interdiffusion of atoms, digitally controlled layered components, and no lattice parameter constraints.

The idea was first suggested by Koma [1–5] who pointed out the possibility to use vdW epitaxy to grow high quality ultrathin layers on substrates with a large lattice mismatch and atomically flat interfaces. Epitaxial growth of MoS₂ using vdW forces was demonstrated back in the early 1990s [5, 6]. In addition to epitaxial growth, monolayers of the same or different TMDCs can also be mechanically assembled by bringing together individual layers [7]. The resulting stack, sometimes referred to as a vertical heterostructure, represents an artificial material assembled in a chosen sequence as in building with Lego blocks [8] with atomic precision (Fig. 13.1). Using this approach, various 2D materials can be combined together alongside with graphene and h-BN. Such structures have been extensively studied both theoretically and experimentally. Among the existing problems are the stability of single layers with respect to oxygen and surface (interfacial) contamination.

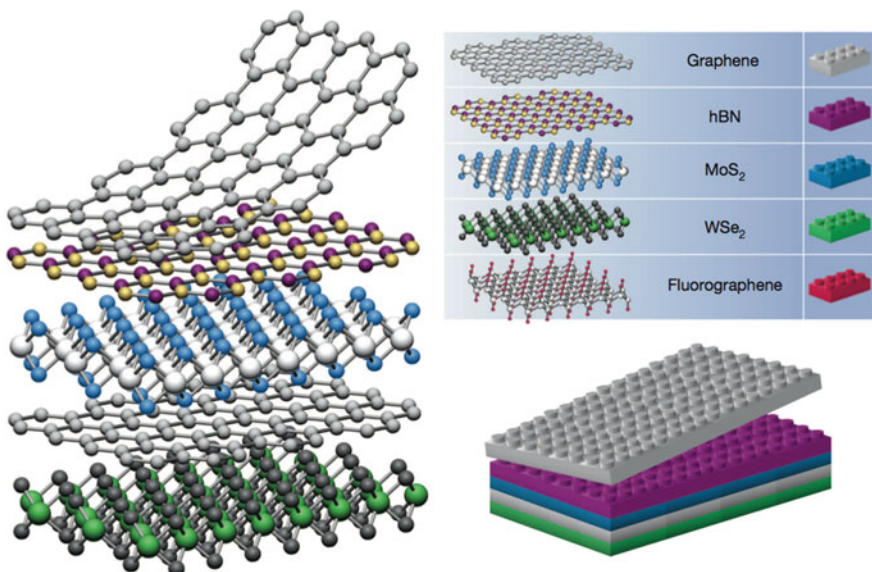


Fig. 13.1 Building van der Waals heterostructures. If one considers 2D crystals to be analogous to Lego blocks (*right panel*), the construction of a huge variety of layered structures becomes possible. Conceptually, this atomic-scale Lego resembles molecular beam epitaxy but employs different ‘construction’ rules and a distinct set of materials [8]. Reprinted by permission from Macmillan Publishers Ltd., copyright (2013)

An alternative way to make a heterostructure is a horizontal heterostructure when the composition changes in a controllable way *within the same monolayer*. Finally, heterostructures between TMDCs and other materials can be envisaged. In what follows we describe the progress achieved.

13.1 Vertical Heterostructures

13.1.1 Lattice-Matched Simulations

In early theoretical works lattice-matched heterostructures were considered. In [9] a systematic study of several heterostructure was performed for the two different stacking sequences, shown in Fig. 13.2, namely the stacking sequence of the bulk phase when the transition metal of one layer is on top of the chalcogen atom of the other layer (B) and another stacking sequence with chalcogen atoms of the two planes across the gap are on top each other (A). While this is not explicitly mentioned in the original paper, it should be noted that this building strategy necessarily results in generating strain in layers with different lattice constants, which may have a drastic effect on the results.

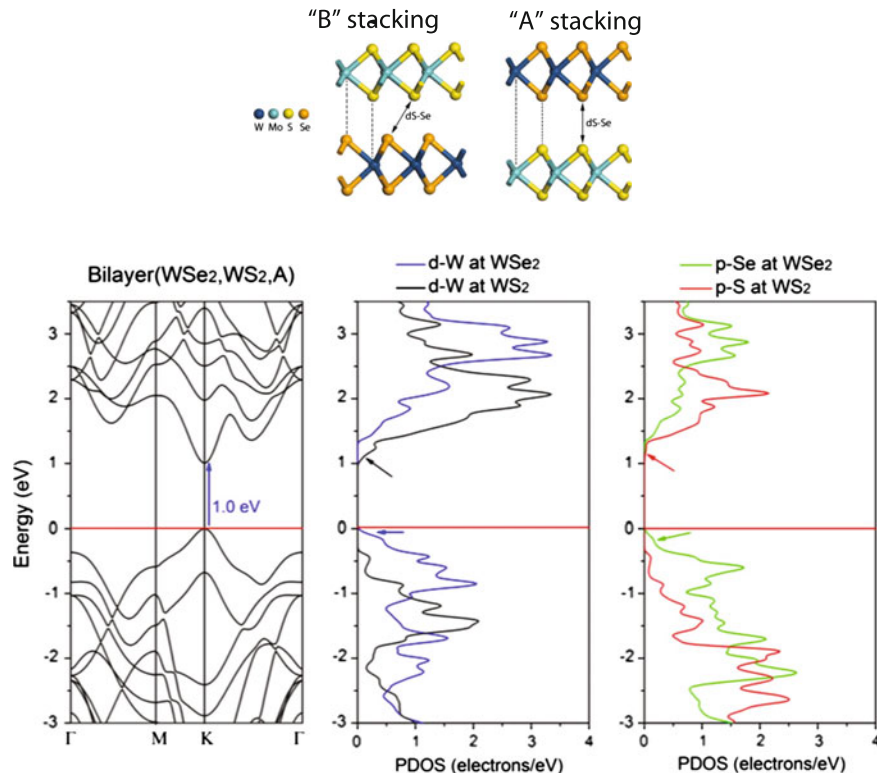


Fig. 13.2 *Upper panel* Atomic models representing bilayer heterostructures of semiconducting TMDCs with different stackings A and B. The dotted lines indicate the alignment of atoms between layers, and the arrows correspond to the distance d_{S-Se} between chalcogen atoms of different layers. *Lower panel* Type 2 Bilayer (WSe₂, WS₂, A): **a** band structure showing the direct band gap; **b** PDOS showing the *d*-electrons of W at each of the layers. The blue arrow indicates the states at the top of the VB originating from W in the WSe₂ layer, and the black arrow shows the states at bottom of the CB due to W in the WS₂ layer; **c** PDOS showing the *p*-electrons of the chalcogen atoms. The green arrow exhibits the states at the top of the VB of Se in the WSe₂ layer, and the red arrow reveals the states at the bottom of the CB of the S atoms in the WS₂ layer. Reproduced from [9]

The authors use the notation of the type “bilayer (MoS₂, WS₂, B)”. This particular example corresponds to a bilayer made of MoS₂ and WS₂ with B stacking. They also investigated bulk crystals made of alternating layers, such as “crystal (MoS₂, MoSe₂, A)”, where MoS₂ and MoSe₂ are repeatedly alternated with A stacking.

Based on the obtained results, various heterostructures were divided into 4 types. Type 1 is represented by WS₂/MoS₂ hybrids and is characterised by an indirect gap for both A and B stackings, the latter being energetically more favorable. At the same time, the difference between the direct and indirect gaps was rather small and it is not clear to what extent this result was effected by the choice of the functional in DFT simulations.

At the same time, bilayers of WS_2/WSe_2 and $\text{MoS}_2/\text{WSe}_2$ (type 2) hybrids exhibited a direct gap behavior at K for both A and B bilayer stackings. Interestingly, the bulk crystal formed by an infinite number of stacked layers with A stacking, crystal ($\text{WS}_2, \text{WSe}_2, \text{A}$), also exhibited a direct band gap at K (ca. 1 eV), which the authors claimed to be the first case of a multilayer TMDC system with a direct band gap [9]. At the same time, the crystal formed by alternating layers with the stacking type B, crystal ($\text{WS}_2, \text{WSe}_2, \text{B}$), exhibited an indirect gap.

The obtained results indicated that the states at the top of the VB, for the bilayer case ($\text{WS}_2/\text{WSe}_2, \text{A}$), were due to the W and Se atoms of the WSe_2 layer, and those at the bottom of the CB originated from the W and S atoms of the WS_2 layer, meaning that electrons and holes are spatially separated. It may be interesting to note that a similar behavior was found in bilayers of TMDCs, where inversion symmetry was broken under an applied external electric field [10, 11] (see Sect. 6.1.4). Local Mulliken charges for the atoms in different layers were calculated and it was found that, e.g. in the bilayer ($\text{WS}_2/\text{WSe}_2, \text{A}$), the W atoms of the WS_2 layer possessed a positive net charge (+0.16e), whereas the W atoms of the WSe_2 layer were negatively charged (-0.09e). Similarly, the S atoms of the WS_2 layer exhibited a negative net charge, and the Se showed a positive net charge. It is worth noting that this behavior was only observed when the different layers possess different chalcogen species. It was concluded that an intrinsic electric field might be the cause of the electron–hole separation and the presence of the direct band gap but it is not clear which one is the cause and which one is the consequence.

The hybrid cases consisting of $\text{WS}_2/\text{MoSe}_2$ layers and $\text{MoS}_2/\text{MoSe}_2$ layers (type 3) are both direct gap materials when stacked in the A fashion but an indirect gap for the B stacking. $\text{WSe}_2/\text{MoSe}_2$ hybrids (type 4) possess an indirect gap.

MoS_2/WS_2 heterostructures were also studied in [12]. Comparing the heterostructure with bi-layers of pure materials, it was concluded that in the case of the heterojunction the interlayer coupling competes with the energy difference of the monolayer states. It was found that the VB at the Γ point is almost degenerate and the “optically active” K -point states are localised on different monolayers making the lowest energy electron–hole pairs spatially separated.

At the same time it should be noted that the band structure can depend on the calculation details. This is demonstrated in Fig. 13.3, where the band structure for the MoS_2/WS_2 heterojunction is shown. While the use of LDA and projector-augmented waves method yields very similar energies of the VB at the K - and Γ -points [12], the K -point becomes significantly lower when the GW method [13] was used.

An interesting observation made in [14] was that in heterostructures the electron transfer only occurred at the adjacent two layers of the interface, whereas other layers were almost unaffected (Fig. 13.4, upper panel) (($\text{MoS}_2)_3 - (\text{MoSe}_2)_3$ and $(\text{MoSe}_2)_3 - (\text{MoTe}_2)_3$ interfaces were studied). From a Mulliken population analysis, it was found that the S atom of the L4 layer MoS_2 in the six-layer structure gains only 0.01e, while the Se atom of L3 MoSe_2 losses only 0.03e, which also replicates closely the trend of electron affinity of the chalcogen atoms. It was further found

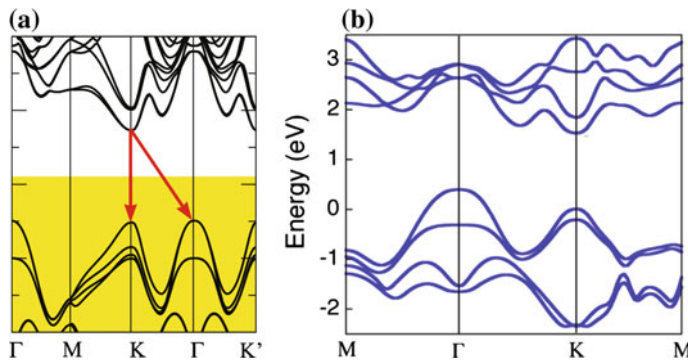
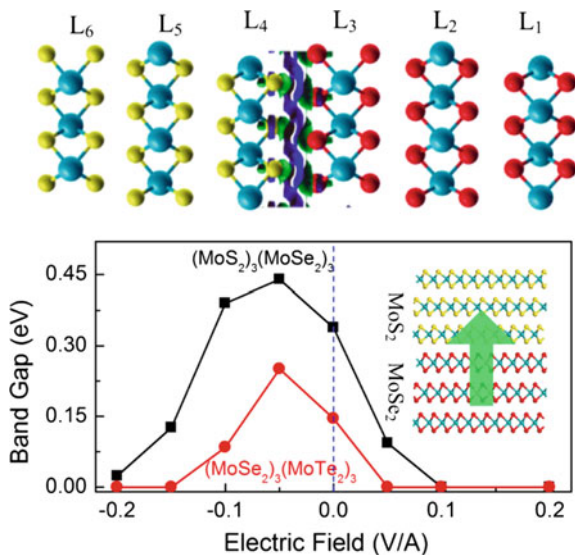


Fig. 13.3 DFT bandstructure of the MoS₂/WS₂ bilayer calculated using different functionals: **a** LDA and augmented waves [12] and **b** the GW method [13]. Copyright 2013 American Chemical Society. Published with permission

Fig. 13.4 *Upper panel* electron transfer when stacking three-layer MoS₂ on three-layer MoSe₂, where the isosurface value is $5 \times 10^{-4} \text{ e}/\text{\AA}^3$. *Lower panel* band gap of TMDC as a function of external vertical electric field. The inset indicates the positive direction of the electric field, pointing from MoSe₂ to MoS₂ (MoTe₂ to MoSe₂) [14]. Copyright 2013 American Chemical Society. Published with permission



that the band gap of the heterostructures can be almost continuously tuned under the external vertical electric field, eventually achieving a semiconductor-metal transition at critical fields. The response of the electronic properties to positive and negative fields was different (Fig. 13.4, lower panel), which was explained by asymmetrical structures along the thickness direction and the intrinsic polarization. Under a positive electric field, the band gap of (MoS₂)₃ – (MoSe₂)₃ [(MoSe₂)₃ – (MoTe₂)₃] continuously decreased with increasing applied electric field, eventually achieving a semiconductor–metal transition at $\sim 0.1 \text{ V}/\text{\AA}$ [$0.05 \text{ V}/\text{\AA}$]. In contrast, when a negative field was applied, the band gap first increased until $-0.05 \text{ V}/\text{\AA}$, reaching values up to 0.45 eV [0.28 eV] for (MoS₂)₃ – (MoSe₂)₃ [(MoSe₂)₃ – (MoTe₂)₃] and then decreased linearly. The initial increase of the band gap is likely arising from the

gradual neutralization of the intrinsic polarization of heterogeneous TMDCs under a negative electric field [14]. It was noticed that the critical electric field for the semiconductor–metal transition in $(\text{MoSe}_2)_3(\text{MoTe}_2)_3$ was noticeably lower than that of $(\text{MoS}_2)_3 - (\text{MoSe}_2)_3$. This result was related to the fact that besides the smaller band gap, the increasingly diffuse nature of the valence p_z -orbitals from S to Te facilitates more charge transfer from the chalcogen to Mo atoms at the same electric field.

13.1.2 Minimized-Strain Calculations

It was subsequently noted that perfect layer alignment with lattice matching generates strong strains resulting in a situation when it is difficult to distinguish between superlattice effects and strain effects [15]. The authors took special care to build bilayer models in such a way that the strain was minimized by constructing supercells with twisted layers leading to a strain of less than 1%. Their approach is illustrated in Fig. 13.5. Band structures were subsequently calculated using G_0W_0 (Fig. 13.6).

Building heterostructures is a way to engineer the band structure and tune the material's optical properties. Optical absorption of a MoS_2/WS_2 heterostructure was simulated in [13, 15] using either lattice matched or strain-minimized approaches. The results are shown in Fig. 13.7. One immediately notices that the results are different. While for the perfectly stacked (and strained) heterostructure (Fig. 13.7b)

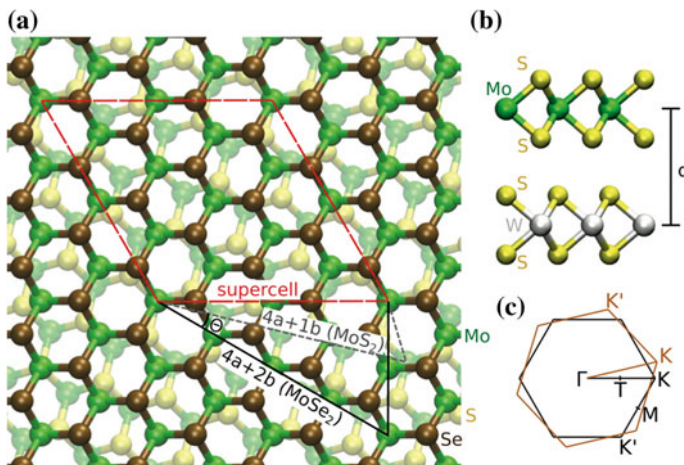


Fig. 13.5 **a** Top view of $\text{MoS}_2/\text{MoSe}_2$ bilayer heterostructure as modeled in the supercell approach. The construction of the supercell basis vectors ($n_i a_i + m_i b_i$) is also illustrated. **b** Side view of the MoS_2/WS_2 heterostructure showing the adopted stacking similar to the 2H polytype of MoS_2 . The definition for layer distance d is indicated. **c** Schematic demonstration of the overlap of the primitive-cell Brillouin zones from the $\text{MoS}_2/\text{MoSe}_2$ system [15]. Copyright 2013 by the American Physical Society. Reprinted with permission

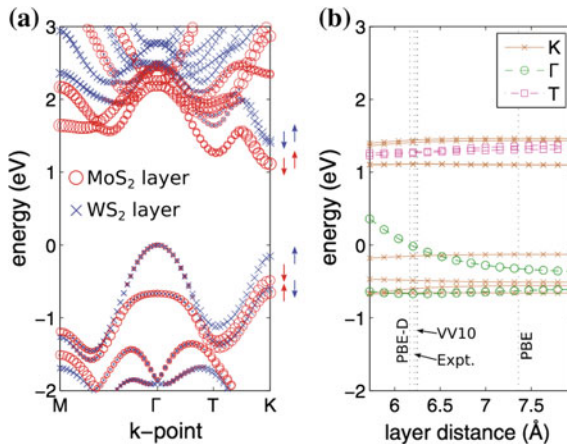


Fig. 13.6 **a** Band structure of MoS₂/WS₂ heterostructure. Projection to MoS₂ layer is denoted by red (circles) and to WS₂ by blue (crosses). The spin orientations of the wave functions at the K/K' point are also denoted. **b** The energies for the band-edge states as a function of the interlayer distance d [cf. Fig. 13.5b]. The vertical dotted lines denote distances calculated with various functionals (the two VV10-type functionals give nearly identical results) and experimental value evaluated from the average of bulk MoS₂ and WS₂ [15]. Copyright 2013 by the American Physical Society. Reprinted with permission

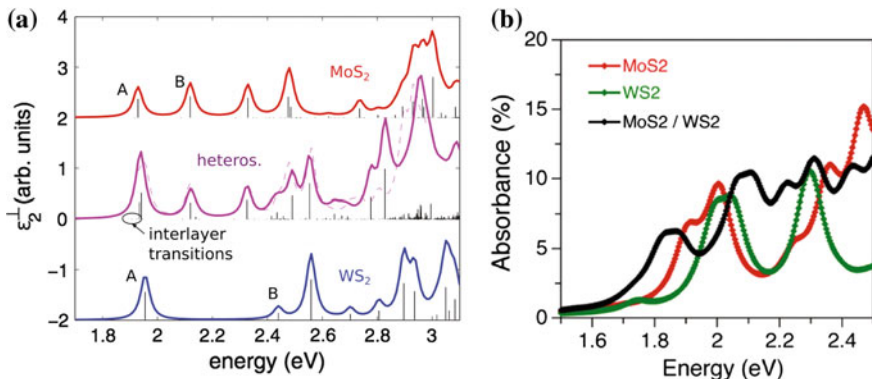


Fig. 13.7 **a** The optical absorption spectrum of a MoS₂/WS₂ heterostructure with minimised strain (middle) together with the spectra from monolayer MoS₂ (top) and WS₂ (bottom). The vertical lines denote the actual calculated transition energies and intensities. Overlaid with the explicitly calculated heterostructure spectrum, the sum of the monolayer spectra is also plotted (dashed line) [15]. Copyright 2013 by the American Physical Society. Reprinted with permission. **b** Absorbance spectra of lattice-matched MoS₂/WS₂ heterostructure and of the individual composing layers, computed using BSE [13]. Copyright 2013 American Chemical Society. Published with permission

the absorption edge shifts to lower energy compared to those of the constituent materials (right), it seems more like a sum of weakly interacting monolayers for the switched bilayer with minimized stress (Fig. 13.7a). This comparison demonstrates that the issue of optical properties of TMDCs heterostructures requires further studies (alongside with the important role played by strain).

Strain-free bilayers of MoS₂/MoSe₂ were studied in [16]. It was found that the interlayer vdW interaction is not strong enough to form a lattice-matched coherent heterostructure. Instead, nanometer-scale Moiré pattern structures are formed. Two possible Moiré patterns A and B, as shown in Fig. 13.8 were considered, namely, with their in-plane hexagonal edges aligned in the same orientation and with a 4.4% lattice mismatch. In each Moiré pattern, the local stacking geometry was classified into six different types as I^A to VI^A (I^B to VI^B) respectively, as shown in Fig. 13.8. In the I^A configuration, the Mo and Se atoms in the MoSe₂ layer are on top of the Mo and S atoms in the MoS₂ layer, respectively, while in the I^B configuration, the Mo and Se atoms in the MoSe₂ layer are on top of the S and Mo atoms in the MoS₂ layer, respectively. Starting from the I^A (I^B) configuration, other configurations (before relaxation) can be obtained by translating the top MoSe₂ layer along the (*n*, *n*) (hexagonal primary cell direction index) direction (downward direction in Fig. 13.8) in a step of $3(a/6)^{1/2}$ for each translation (where *a* is the lateral lattice constant). The most stable configuration was found to be III^A, with an adsorption energy per formula unit (each MoSe₂/MoS₂) of 195 meV, followed by I^B (194 meV) and V^A (191 meV). In these configurations, the Se atoms are on top of the hollow sites of the MoS₂ layer. Configurations with Se atoms on top of the S atoms, namely, I^A and III^B, have the lowest adsorption energies. It was found that the Se and S atom interlayer vertical height difference in different configurations varied from 3.08 to 3.77 Å and had a reverse linear relationship with respect to the adsorption energy.

The electronic structures of the different stacking patterns were further calculated. The overall band structures of all the stacking configurations were rather similar, and those of I^A and III^A are illustrated in Fig. 13.9 (upper panel). Due to the absence of inversion symmetry, the band structure shows significant spin-orbit splitting that does not appear in pure MoS₂ or MoSe₂ bilayers. The heterostructures have a direct band gap at the *K*-point, much like in the single-layer structure with the highest VB state at the *K*-point (V1) being contributed only by the MoSe₂ layer, while the lowest CB state (C1) being contributed only by the MoS₂ layer. It was noted that the highest VB at the point (V2) has significant contributions from both the MoS₂ and MoSe₂ layers (green color), which indicates that there is a strong interlayer electron-coupling effect for the V2 state. Through an analysis of the electronic structure with various stackings, it was concluded that the V2 state in the III^A region represents the top of VB of the whole system, i.e. the top of the VB is strongly localised. At the same time, the situation of the CB minimum state was found to be quite different: it was distributed in the MoS₂ layer and only weakly localized (Fig. 13.9, lower panel).

In [17] vdW trilayers and superlattices were studied from first-principles. In this work, a monolayer of BN, MoS₂, WS₂, or WSe₂ was inserted between two MoS₂ monolayers to form various MoS₂/ML/MoS₂ sandwich trilayers. It was found that the BN monolayer was the most effective sheet to decouple the interlayer vdW

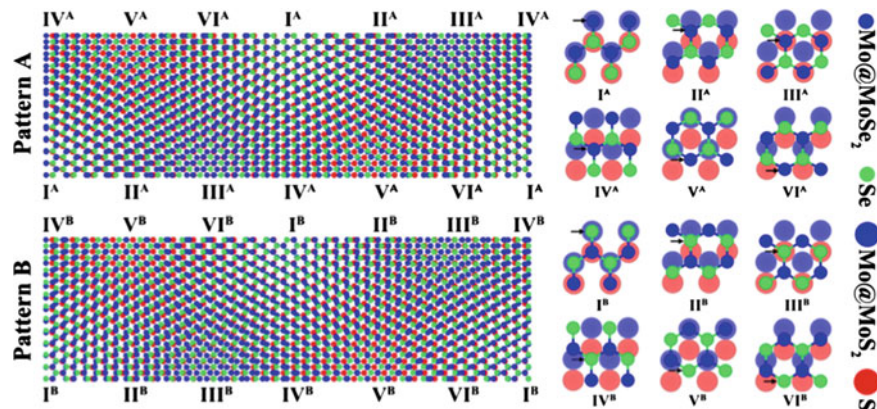


Fig. 13.8 Moiré patterns A and B with 4.4% lattice mismatch corresponding to 24×24 MoS₂ and 23×23 MoSe₂ supercells along the primary cell lattice vectors. Only half (in the $(n, 0)$ direction) of the rectangular periodic supercell is shown above to denote different stacking regions. (Right) The 12 different stacking configurations considered (with MoSe₂ on top of MoS₂). Between consecutive configurations within I^A/VI^A or I^B/VI^B, the MoSe₂ layer is translated along the (n, n) direction in steps of $3(a/6)^{1/2}$, where a is the lattice constant, which is fixed at the average of the values for the MoS₂ and MoSe₂ monolayers. The arrows indicate the same atom in the MoSe₂ layer in I^A/VI^A or I^B/VI^B. Configurations I^A/VI^A cover the A pattern, and configurations I^B/VI^B cover the B pattern [16]. Copyright 2013 American Chemical Society. Published with permission

coupling of the MoS₂ bilayer, where the resulting sandwich trilayer could recover the electronic structures of the MoS₂ monolayer, particularly the direct-gap character. It was also found that the intercalation of MoSe₂ or WSe₂ sheet makes the sandwich trilayer undergo an indirect-gap to direct-gap transition due to the newly formed heterogeneous S/Se interfaces, i.e. interfaces with two different kinds of chalcogen species, the result being in agreement with the findings of [9], where MS₂/MSe₂ bilayers were studied.

At the same time, the MoS₂/WS₂/MoS₂ sandwich trilayer still retains the indirect-gap character of the MoS₂ bilayer due to the lack of the heterogeneous S/Se interfaces. Finally, it was found that the 3D superlattice heterostructures containing S/Se interfaces also exhibits a direct gap, albeit with a slight decrease of the bandgap compared to the trilayers, again being an agreement with earlier studies [9].

A continuously tunable electronic structure of TMDC superlattices was reported in [18] for an example of MoS₂/WSe₂ superlattices. The band gap was found to be direct and the VB and CB being spatially separated.

A summary of simulated band alignments in various TMDCs [19] is shown in Fig. 13.10. Similar studies using different functionals were reported in [20, 21]. Experimentally, band-offsets were determined in the MoS₂/WSe₂ heterojunction using microbeam X-ray photoelectron spectroscopy and scanning tunnelling microscopy/spectroscopy [22], where a valence band offset value of 0.83 eV and a conduction band offset of 0.76 eV were obtained.

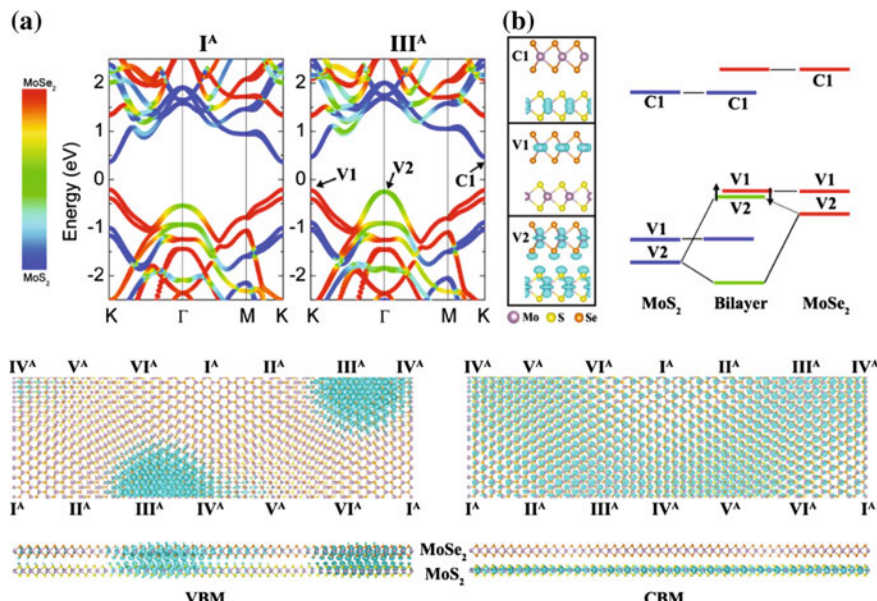
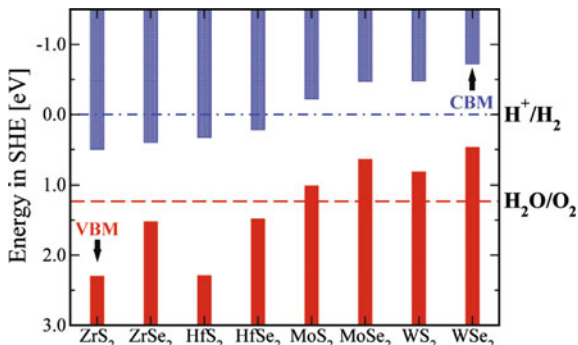


Fig. 13.9 *Top panel a* Band structures of the I^A and III^A bilayers. Blue and red denote the contributions from MoS₂ and MoSe₂ layers, respectively. The partial charge densities of C1, V1, and V2 states of III^A are also shown. **b** Schematic of the band alignment between MoS₂ and MoSe₂ and the coupling effect for the V2 state in III^A. The arrows denote the eigenenergy shift of the V1 and V2 states when MoS₂ and MoSe₂ layers relax to their natural lattice constants from the average lattice constant. *Bottom panel* top view and side view of the spatial distribution of the VBM, VBM-1 (left), and CBM (right) states for the Moiré structure A [16]. Copyright 2013 American Chemical Society. Published with permission

Fig. 13.10 Theoretical band positions of MX₂ (M = Zr, Hf, Mo, and W; X = S and Se) in the standard hydrogen electrode (SHE) scale obtained from the GW-BGC scheme. The redox potentials for water reduction (H⁺/H₂) and oxidation H₂O/O₂ are also shown for comparison [19]. Copyright 2012 American Chemical Society. Published with permission



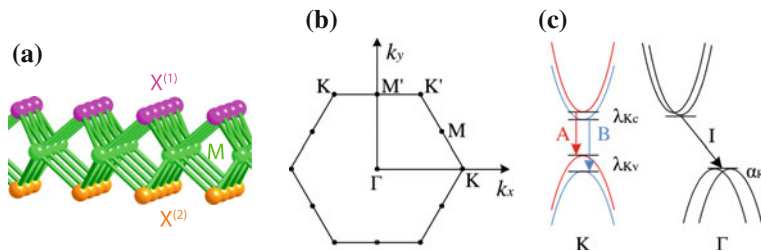


Fig. 13.11 **a** Schematic representation of a $\text{MX}_1^{(1)}\text{X}_1^{(2)}$ monolayer heterostructure. **b** Corresponding first Brillouin zone. **c** Schematic view of the electronic band structure around the K and Γ -points. While band splittings at the K -point occur due to the SOC, at the Γ -point, Rashba spin splitting of the uppermost VB is observed [23]. Reprinted with permission

13.1.3 Single Layer Vertical Heterostructures

An interesting variation of vertical heterostructures was investigated in [23], where the electronic structures and the lattice dynamics of $\text{MX}_1^{(1)}\text{X}_1^{(2)}$ monolayer heterostructures with the upper and lower planes formed by different chalcogenide species $\text{X}^{(1)}$ and $\text{X}^{(2)}$ (Fig. 13.11a) were studied, using a plane-wave approach and the DFT/PBE level of theory. It was found that in contrast to non-polar systems with $\text{X}^{(1)} = \text{X}^{(2)}$, in the polar systems with $\text{X}^{(1)} \neq \text{X}^{(2)}$ the Rashba splitting occurred at the Γ -point for the uppermost valence band, which was interpreted in terms of the broken mirror symmetry.

The Rashba coupling parameters (α_R) were determined to be 2, 12, 4, 5, 14, and $10 \text{ meV}\cdot\text{\AA}$, for MoSSe, MoSTe, MoSeTe, WSSe, WSTe, and WSeTe structures, respectively. i.e. the Rashba splitting was enhanced by stronger SOC (M: from Mo to W and $\text{X}^{(1)}, \text{X}^{(2)}$: from S to Te). The Rashba effect was found to be more sensitive to the difference in the distances of chalcogen atoms from the transition metal planes than to the atomic species.

13.1.4 Re-Stacked TMDCs

When monolayers of MoS_2 are obtained using Li-intercalation, the structure changes from trigonal prismatic to distorted octahedral (see Sect. 5.1.2). What happens when such monolayers are re-stacked? Raman scattering and x-ray diffraction studies indicate that the T' -structure of the re-stacked material is metastable and reverts to the $2H$ phase [24], at ca. 90°C for MoS_2 and ca. 210°C for WS_2 [25]. Fitting the position of exothermic DSC peaks shift to an Arrhenius type equation yielded the activation energy of the transformation of 82.4 kJ/mol for WS_2 [25], being, according to the cited work, significantly higher than the value for MoS_2 .

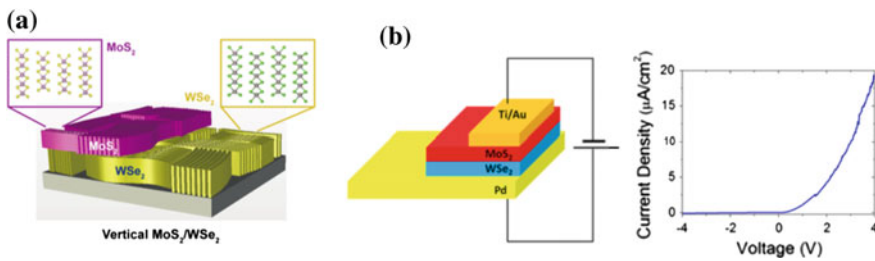


Fig. 13.12 **a** The heterostructure consists of the MoS₂ and WSe₂, in which their van der Waals layers are aligned perpendicular to the substrate. **b** Schematic of the MoS₂/WSe₂ heterostructure diode. The heterostructure was sandwiched between Pd and Ti/Au, which were defined as positive and negative electrodes, respectively. **c** Current–voltage characteristic of the MoS₂/WSe₂ heterostructure diode [30]. Copyright 2015 American Chemical Society. Published with permission

At the same time, some studies suggested that the recovery is incomplete [26]. Even after heating to 800 °C, there is remaining disorder and the material cannot be described as 2H-MoS₂. It was proposed that 2H- and 3R-like stacking may be randomly mixed in the re-stacked phase.

Based on the results of diffraction and EXAFS studies it was concluded that restacked MoS₂ and WS₂ were of WTe₂ type [27]. The re-stacked WS₂ structure was subsequently studied by EXAFS [28] and it was concluded that it presents two types of distorted octahedral sites for the two nonequivalent W atoms. These octahedra are linked together to build a zig-zag chain. Moreover, the local shift of the W atoms was found to be in tandem with a periodic shift of the S atoms along the stacking axis, causing the layer to deviate from full planarity. A similar conclusion was drawn earlier for re-stacked MoSe₂ [29] (see also Fig. 5.5).

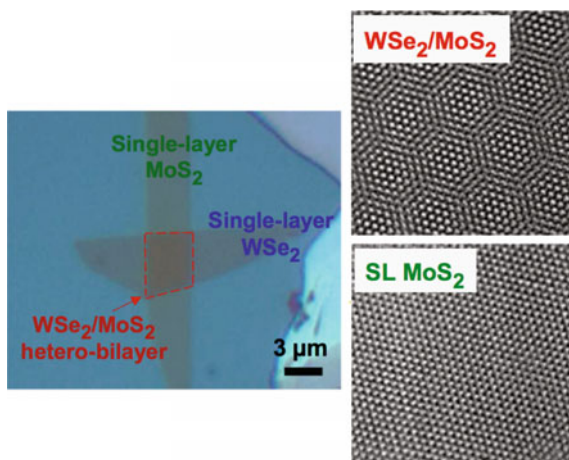
13.1.5 Heterostructures with Vertically Aligned Layers

In [30], scalable synthesis of vertical MoS₂/WSe₂ heterostructures with vertically aligned layers was demonstrated and using this structure in a diode configuration rectification behavior was demonstrated (Fig. 13.12).

13.1.6 Experimental Studies

Artificially stacked atomic TMDC layers as a way to fabricate artificial vdW solids also attracted significant interest from an experimental perspective [8, 31–37]. The fabrication of WSe₂/MoS₂ heterobilayers was realized in [36] by stacking individual monolayers on top of each other. Figure 13.13 shows an optical image of the heterobilayer, and the corresponding high-resolution transmission electron microscopy

Fig. 13.13 Optical microscope image of a WSe₂/MoS₂ hetero-bilayer on a Si/SiO₂ substrate (260-nm SiO₂) and HRTEM images of a boundary region of SL MoS₂ and the hetero-bilayer, showing the resulting Moiré pattern [36]. Reproduced with permission by National Academy of Sciences, USA



(HRTEM) images. Owing to the 3.8% lattice mismatch, estimated from the bulk lattice constants, as well as the unregulated, but in principle controllable, angular alignment between the constituent layers, the heterostructure lattice forms a Moiré pattern clearly visible in the HRTEM image.

To shed light on the electronic structure of the WSe₂/MoS₂ heterostack, X-ray photoelectron spectroscopy was performed, using a photoemission electron microscope (PEEM) as illustrated in Fig. 13.14a. A peak shift of about -220 meV in binding energy (or $+220\text{ meV}$ in kinetic energy) was observed for the W 4f core levels of the hetero-bilayer compared with the WSe₂ single layer (Fig. 13.14b). The direction of the peak shift is consistent with a negative net charge on the WSe₂ in the WSe₂/MoS₂ hetero-bilayer. At the same time, a shift of $+190\text{ meV}$ was observed for the Mo 3d core levels of the WSe₂/MoS₂. These results therefore indicate that the WSe₂ layer has a negative net charge, whereas the MoS₂ layer has a positive net charge as a result of contact potential. It was suggested that the hetero-bilayer can essentially be interpreted as being a 2D dipole, an atomically thin parallel plate capacitor with vdW gap with a built-in potential up to 400 meV , originating from the work function difference induced charge transfer between the two constituent single layers. The latter interpretation is also consistent with the *p*- and *n*-type character of WSe₂ and MoS₂, respectively [38, 39].

In order to investigate the optoelectronic properties of the WSe₂/MoS₂ heterobilayer, photoluminescence (PL) and absorption spectroscopy [36] were additionally used. For single-layer WSe₂ and MoS₂, strong excitonic PL peaks were observed at 1.64 and 1.87 eV , with single-layer WSe₂ showing a 10–20 times higher PL intensity than single-layer MoS₂, which is in agreement with previous work [40]. For the WSe₂/MoS₂ hetero-bilayer, a peak at 1.55 eV , lying at a lower energy than for the two constituent single layers, was observed (Fig. 13.15a, b).

An interesting feature of the photoluminescence of the WSe₂/MoS₂ heterobilayer was pointed out [36], namely, the first absorption peak at 1.65 eV and the

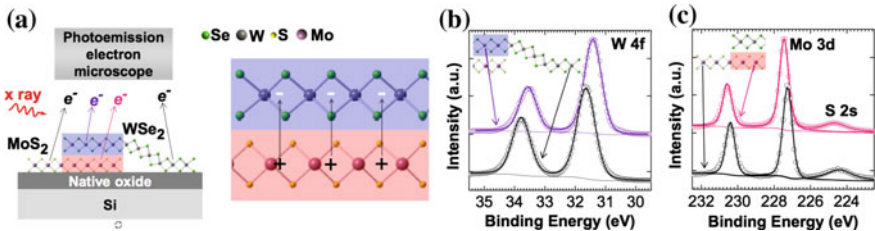


Fig. 13.14 XPS core level shift analyses of WSe₂/MoS₂ heterostructures. **a** Sketch of the spatially resolved PEEM experiment. **b** Comparison of W 4f core level doublet from WSe₂ and WSe₂/MoS₂ indicating a 220 meV shift to lower binding energy, corresponding to a negative net charge on the WSe₂ top layer. **c** Comparison of Mo 3d core level doublet and S 2s singlet from MoS₂ and WSe₂/MoS₂ indicating a shift of 190 meV to higher binding energy, corresponding to a positive net charge on MoS₂. The single peak at 224.4–224.6 eV is identified as S 2s, which shows the same shift as Mo 3d, as expected [36]. Reproduced with permission by National Academy of Sciences, USA

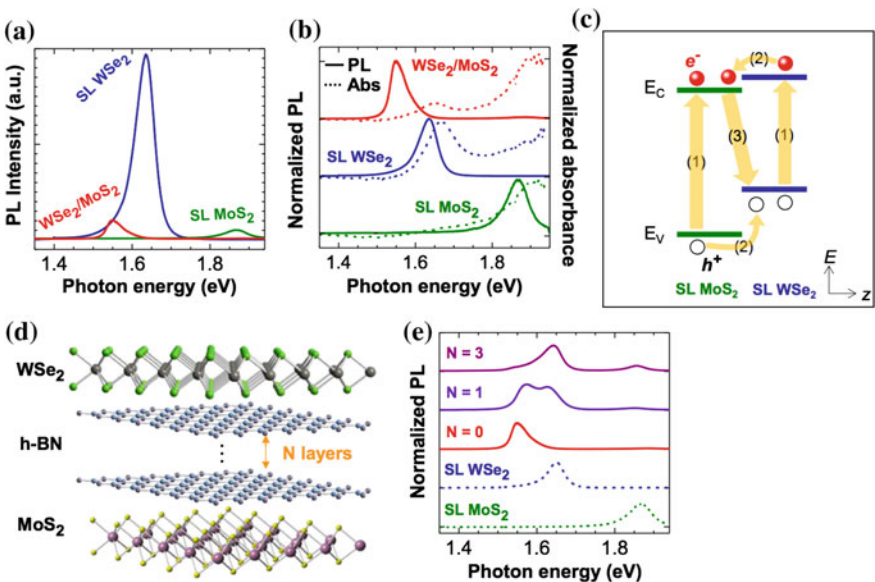


Fig. 13.15 Photoluminescence and absorption from WSe₂/MoS₂ hetero-bilayers. **a** PL spectra of single-layer WSe₂, MoS₂, and the corresponding hetero-bilayer. **b** Normalized PL (solid lines) and absorbance (dashed lines) spectra of single-layer WSe₂, MoS₂, and the corresponding hetero-bilayer, where the spectra are normalized to the height of the strongest PL/absorbance peak. **c** Band diagram of a WSe₂/MoS₂ hetero-bilayer under photo excitation, depicting 1 absorption and exciton generation in WSe₂ and MoS₂ single layers, 2 relaxation of excitons at the MoS₂/WSe₂ interface driven by the band offset, and 3 radiative recombination of spatially indirect excitons. **d** An atomistic illustration of the heterostructure of single-layer WSe₂/single-layer MoS₂ with few-layer h-BN spacer in the vdW gap. **e** Normalized PL spectra from single-layer WSe₂/single-layer MoS₂ heterostructure with n layers of h-BN ($n = 0, 1$, and 3) [36]. Reproduced with permission by National Academy of Sciences, USA

second peak at 1.91 eV essentially coincide with the absorption peaks of single-layer WSe₂ and MoS₂, respectively. At the same time, the hetero-bilayer exhibits a \sim 100 meV shift between the PL and absorbance peaks. The authors propose that this large Stokes-like shift arises from a spatially indirect transition in a staggered gap (type II) heterostructure.

Certain similarities between WSe₂/MoS₂ hetero-bilayer and organic semiconductor hetero-structures in which donor and acceptor layers are also bound by weak intermolecular vdW forces were noticed. Similar to the optical processes in organic heterostructures, photons are absorbed in single-layer WSe₂ and single-layer MoS₂, generating excitons in both layers. Photo-excited excitons then relax at the MoS₂/WSe₂ interface, driven by the band offset as shown in Fig. 13.15c. The obtained band offset is consistent with the measured built-in electric field from PEEM. As a consequence of the band offset, the PL excitonic peak energy is lower than the excitonic band gaps of either material component.

Finally, in order to fine-tune the interlayer interaction in the WSe₂/MoS₂ heterobilayer, single- and few-layer sheets of hexagonal BN (h-BN) spacer layers were inserted into the vdW gap (Fig. 13.15d) using the same transfer technique. Figure 13.15e shows the normalized PL of heterostacks with single- and trilayer h-BN spacers. The results demonstrate that the interlayer coupling can be readily tuned by intercalation of dielectric layers and provide yet another degree of control in the vdW heterostructure properties [36]. We note here that in order to characterize the interlayer interaction in TMDC junctions, Raman spectroscopy can be efficiently used [33, 41, 42] (see Sect. 7.11.3).

Photoluminescence from TMDC heterostructures was also studied in [41]. While all monolayer spectra exhibited strong PL signals, the PL intensity was strongly reduced in the overlapping MoS₂/WSe₂ and MoSe₂/MoS₂ regions. The reduction of PL intensity varied from a few tens of percent to two orders of magnitude for different heterobilayer samples (which was attributed to their different quality). Similar PL quenching has also been observed in various TMDC heterostructures [43–45] and the underlying mechanism was proposed to be the interlayer charge transfer.

As mentioned above, the MoS₂/WS₂ heterostructure forms a type II heterojunction, with the CB minimum residing in MoS₂ and the VB maximum in WS₂, respectively, i.e. electrons and holes residing in two layers are separated. This leads to two important questions [45] regarding charge transfer processes in the atomically thin vdW-coupled MoS₂/WS₂ heterostructure: (1) How do strong electron-electron interaction and excitonic effects affect charge transfer processes? and (2) How fast can charge transfer take place between the vdW-coupled layers? (as was mentioned earlier, electron-electron interaction is enhanced in two-dimensional materials due to size confinement and inefficient screening)

The charge transfer process and its dynamics were probed using transient absorption resonant pump-probe spectroscopy [45]. Since MoS₂ and WS₂ monolayers have distinctly different exciton transitions, the MoS₂ or WS₂ layers were selectively excited using specific resonant optical excitations and probed the accumulation of electrons and holes in different layers through photo-induced changes in their respective exciton transitions. Specifically, pump photon energy at 1.86 eV was used to

excite exclusively the *A*-exciton transition of MoS₂ (this pump cannot excite WS₂ directly because the photon energy is far below the absorption threshold of WS₂) and examined the photo-induced changes of both WS₂ and MoS₂ exciton resonances in transient absorption spectra from 2.0 to 2.5 eV to probe the charge distribution in the heterostructures.

From these measurements, it was concluded that optical excitation in MoS₂ leads to strong modification of exciton transitions in WS₂, which has a larger optical bandgap, which provides direct evidence of efficient charge separation in photoexcited MoS₂/WS₂ heterostructures: electron-hole pairs that are initially created in the MoS₂ layer, but holes quickly transfer to the WS₂ layer due to the type II band alignment, while electrons stay in the MoS₂ layer. The photoexcited electrons in MoS₂ and holes in WS₂ lead to a strong transient absorption signal for exciton transitions in both MoS₂ and WS₂.

It was further found that holes are transferred from the MoS₂ layer to the WS₂ layer within 50 fs after optical excitation of the MoS₂/WS₂ heterostructure, which is much shorter than the exciton lifetime and most other dynamic processes in MX₂ monolayers, which are on the order of several to tens of picoseconds [46]. It was concluded that electrons and holes can be efficiently separated into different layers immediately after their generation. It was proposed that one factor contributing to the ultrafast charge transfer rate in atomically thin heterostructures is the close proximity of the two heterolayers, because electrons or holes only need to move less than 1 nm vertically for the charge transfer process to happen.

In [44] epitaxial and non-epitaxial MoS₂/WS₂ heterostructures were compared. Through photoluminescence and absorption studies it was concluded that the efficiency of interlayer coupling was essentially non-dependent on whether the two layers were grown epitaxially or stacked manually (in the latter case annealing at 200–250 °C for 10–30 min was performed).

The undoped *n*-type—Nb-doped *p*-type MoSe₂ junction, which exhibited ideal p-n diode behavior [47], may also be mentioned here.

13.2 Lateral Heterostructures

13.2.1 Theoretical Studies

In [20] calculations on MoX₂/WX₂ lateral heterostructures were performed. The authors note that MoX₂ and WX₂ have very similar lattice parameters, allowing one to create these heterostructures without inducing structural defects. Based on the distribution of charge densities (Fig. 13.16), they observed that the electrons were confined in the MoX₂, while the holes were confined in the WX₂ side. The authors speculate that spontaneous charge separation occurs when excitons diffuse to the WX₂/MoX₂ junction, a process that should be useful for photovoltaics.

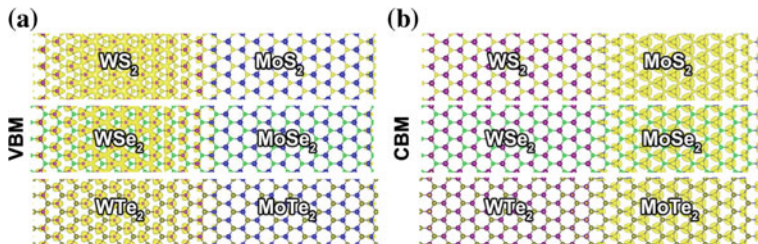


Fig. 13.16 Charge densities at the VB maximum (a) and the CB minimum (b) states for monolayer WX_2/MoX_2 lateral heterostructures with common chalcogen species [20]. Reprinted with permission. Copyright 2013 by the American Institute of Physics

13.2.2 Experimental Results

Alongside with vertical heterostructures where two different materials are located across the vdW gap, lateral heterostructures where the composition changes in-plane were also experimentally studied for different combinations of materials [48–52]. The results for two different TMDCs located within the same layer essentially agree among different groups and can be summarized as follows: (i) the grown samples have a macroscopic triangular shape and (ii) the concentration of the two different metallic species varies monotonically from the center to the edge as illustrated in Fig. 13.17.

This is further illustrated in Fig. 13.18 for a case of MoS₂/MoSe₂ heterostructures, where panel (a) shows Raman spectra taken in the central and edge regions and panel (b) shows the corresponding PL spectra. Panel (c) shows the opposite concentrational trends for S and Se species.

Different from atomically sharp interfaces in vertical heterostructures, lateral heterostrucures typically had the interfaces a few lattice constants wide [49, 52] (Fig. 13.19a), although occasionally observed sharp boundaries (Fig. 13.19b–d) suggest that the interface quality may be improved. It was additionally found that all atoms lie on a single MX₂ honeycomb lattice, implying negligible distortions at interfaces (Fig. 13.19b) as was observed by different groups [49, 52].

Various combinations of TMDCs were studied. For the MS₂/MSe₂ systems (M = Mo, W), the central region is formed by sulphide and the edge region is formed by selenide [48]. For the MoX₂/WX₂ systems (X = S, Se), the central region is formed by molybdenum chalcogenide and the edge region by tungsten chalcogenide [49, 50]. Electrical studies showed current rectification at the (WSe₂/WS₂) boundary [48].

Two-step epitaxial growth of lateral p-n junctions was reported in [53], where after the initial growth of WSe₂, edge epitaxy was used for the growth of MoS₂ along the W growth front. Despite the large lattice mismatch, the grown heterostructure possessed atomically sharp interfaces. In a different work [54], two-step heterostructures with monolayer MoS₂ core wrapped by multilayer WS₂ were reported.

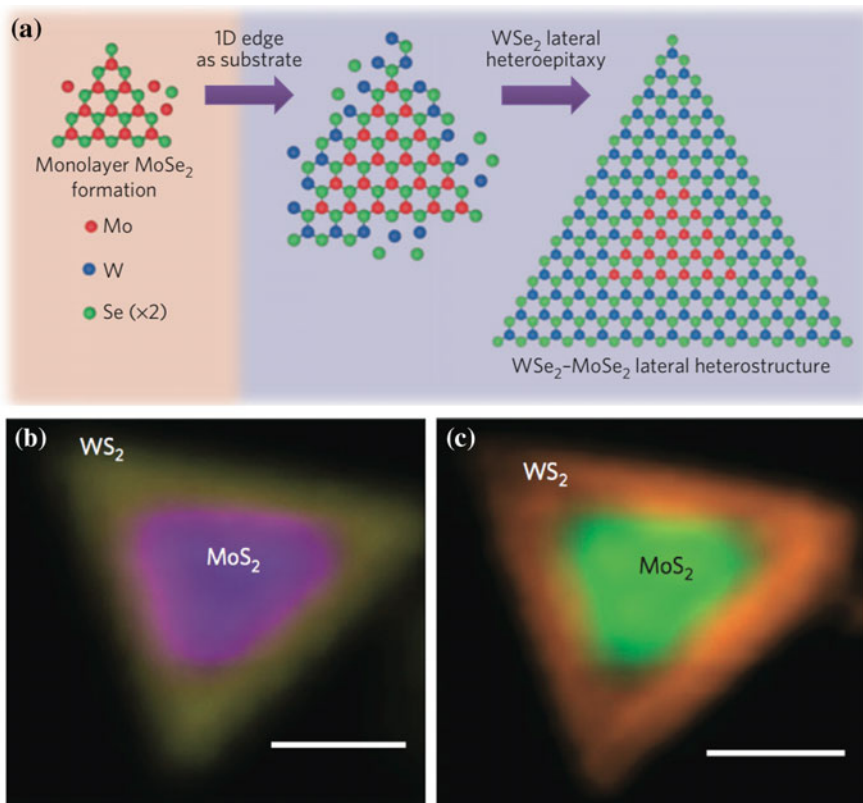


Fig. 13.17 **a** Schematic illustration of the process of in-plane epitaxial growth of lateral heterostructures [49]. **b** Combined Raman intensity mapping at 351 cm⁻¹ (yellow) and 381 cm⁻¹ (purple), showing the core-shell structure with WS₂ as the shell and MoS₂ as the core. **c** Combined PL intensity mapping at 630 nm (orange) and 680 nm (green). The scale bars in (b, c) are 10 μm [52]. Reprinted by permission from Macmillan Publishers Ltd., copyright (2014)

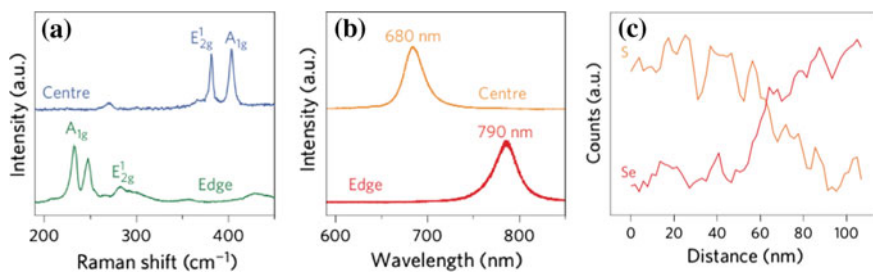


Fig. 13.18 **a** Raman spectra taken from the centre (MoS₂) and peripheral (MoSe₂) areas of a triangular heterostructure domain. **b** Photoluminescence emission spectra obtained from the centre (MoS₂) and peripheral (MoSe₂) areas of a triangular heterostructure domain. **c** EDS linescan profiles across the MoS₂/MoSe₂ heterostructure interface, demonstrating the opposite modulations of S and Se concentrations [48]. Reprinted by permission from Macmillan Publishers Ltd., copyright (2014)

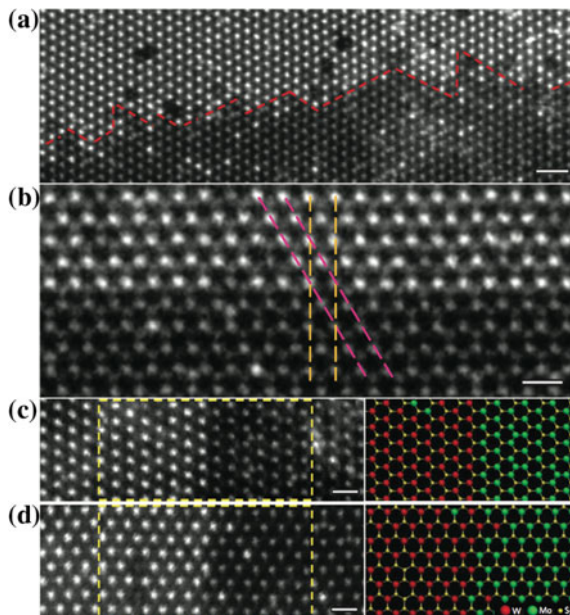


Fig. 13.19 Atomic structure of the lateral heterojunctions between WS₂ and MoS₂ monolayers. **(a, b)** Atomic-resolution Z-contrast STEM images of the in-plane interface between WS₂ and MoS₂ domains. A small roughness resulting from interfacial steps can be seen in **(a)**. The *red dashed lines* highlight the atomically sharp interface along the zig-zag-edge direction. The *orange and pink dashed lines* in **(b)** depict the atomic planes along the armchair and zig-zag directions, respectively, indicating the WS₂ and MoS₂ domains share the same crystal orientation. **(c, d)** Atomic-resolution Z-contrast images of the atomically sharp lateral interfaces along the zig-zag (**c**) and armchair (**d**) directions. The atomic models on the right correspond to the structure in the highlighted regions. Scale bars: **a** 1 nm; **b-d** 0.5 nm [52]. Reprinted by permission from Macmillan Publishers Ltd., copyright (2014)

Using *e*-beam lithography and selective patterning of monolayer MoSe₂ with SiO₂ and subsequent sulfurization using laser vaporization of sulfur, lateral MoSe₂/MoS₂ heterojunctions with pre-defined patterns were obtained with the interface quality similar to that obtained using heteroepitaxy [55].

Chemically exfoliated layers of MoS₂ form a different kind of heterostructures with 2H and 1T phases of the same chemical composition. The interfaces between the two phases were shown to be coherent [51].

13.3 Heterostructures Containing TMDC

13.3.1 TMDC/2D Heterostructures

The electronic structures of TMDC/graphene, BN, germanene and silicene were studied in [15, 56] and the results are shown in Fig. 13.20.

The effect of interlayer hybridisation on the electronic structure of MoS₂/graphene heterostructure was studied in [37] using high-spatial resolution ARPES (nanoARPES) capable of combining multi- and single-grain imaging. The studied sample was polycrystalline CVD-grown graphene that has been transferred to freshly air-cleaved MoS₂ substrates. NanoARPES data of the π -band close to the Fermi level in the $\Gamma-K$ direction showed that the Dirac cone intersects with the Fermi level

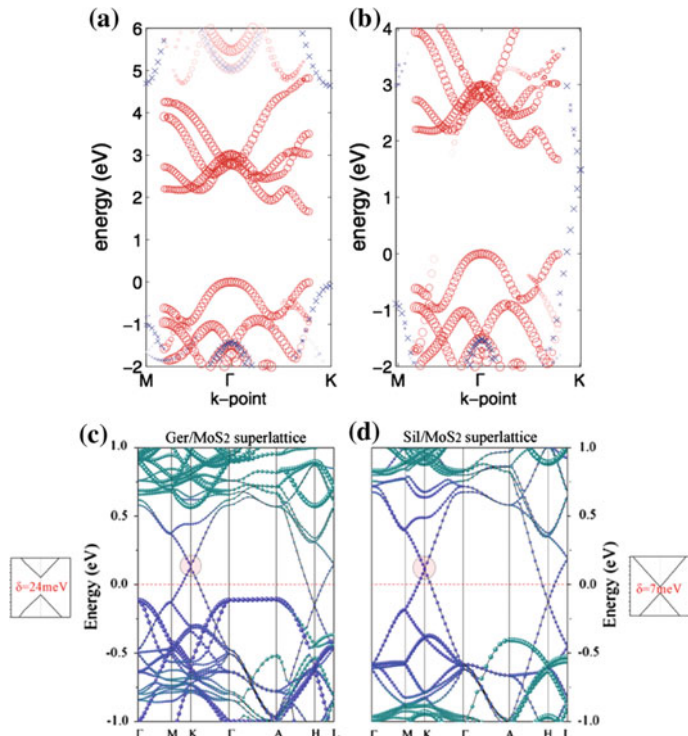


Fig. 13.20 Top panel **a** MoS₂/BN and **b** MoS₂/graphene heterostructures [15]. Bottom panel the band structures of Germanene/MoS₂ and Silicene/MoS₂ superlattices, respectively. The contributions from the germanene/silicene and MoS₂ layers to the band structures of the superlattices are shown with blue and green dots, respectively. The detailed band structures in the vicinity of the opened band gap are inserted. Red dashed lines represent the Fermi level [56]. Reproduced with permission from Springer

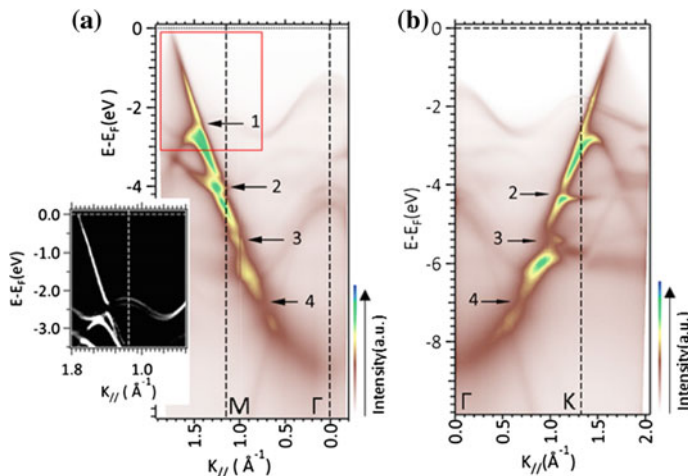


Fig. 13.21 Modification of graphene π -band through hybridization with MoS_2 bands. ARPES with 100 eV p -polarized light along the $(\Gamma - M)_{\text{MoS}_2}$ **(a)** and $(\Gamma - K)_{\text{MoS}_2}$ **(b)** directions. Observed band gaps are labeled 1–4. The inset in **a** shows a zoom-in of the second derivative of ARPES data, which allows better identification of band gap [37]. Copyright 2015 American Chemical Society. Published with permission

directly at the K -point, i.e. the graphene on MoS_2 is undoped and exhibits no band gap at the Dirac-point.

In contrast, the π -band of graphene at higher binding energies is significantly altered by the interaction with the MoS_2 substrate. Results of ARPES measurements with $h\nu = 100$ eV are shown in Fig. 13.21. Along the $(\Gamma - M)_{\text{MoS}_2}$ and $(\Gamma - K)_{\text{MoS}_2}$ directions, four and three distinctive gaps are observed, respectively, labeled in sequential order in the figure. It was noted that the gaps are of significant size of up to 0.8 eV and occur where certain MoS_2 bands intersect the graphene π -band. By performing nano-ARPES, it was found that the electronic interaction between graphene and MoS_2 is independent of the stacking register of the two heterolayers [37].

13.3.2 Miscellaneous TMDC-Based Heterostructures

In [57] ferromagnet/semiconductor contacts formed by transition metal dichalcogenide monolayers, focusing on semiconducting TMDCs such as MoS_2 and WS_2 and ferromagnetic TMDC, VS_2 were studied.

In [58] the electronic band structure of the TMDC/Bi(111) heterostructures (TMDC = MoS_2 , MoSe_2 , WS_2 , and WSe_2) were studied using the first-principles calculations incorporating the band unfolding technique [59, 60], wherein the effective primitive cell projected to TMDC was recovered from the supercell calculation

of the heterostructure using the technique. Giant Rashba-type splitting in Mo-driven bands at the Γ point of the TMDC/Bi(111) heterostructure was found.

It was also shown that a combination of few-layer MoS₂ with a ferroelectric material generates interesting optoelectrical properties that can potentially be used for memory applications [61].

Vertically stacked MoS₂/graphene heterostructures were suggested for fabrication of logic transistors and complementary inverters [35] and MoS₂/h-BN heterostructures were studied in [62].

References

1. A. Koma, K. Sunouchi, T. Miyajima, Fabrication of ultrathin heterostructures with van der Waals epitaxy. *J. Vac. Sci. Technol. B* **3**(2), 724 (1985)
2. A. Koma, K. Yoshimura, Ultrasharp interfaces grown with van der Waals epitaxy. *Surf. Sci.* **174**(1), 556 (1986)
3. A. Koma, Van der Waals epitaxy a new epitaxial growth method for a highly lattice-mismatched system. *Thin Solid Films* **216**(1), 72 (1992)
4. A. Koma, Van der Waals epitaxy for highly lattice-mismatched systems. *J. Cryst. Growth* **201**, 236 (1999)
5. F. Ohuchi, T. Shimada, B. Parkinson, K. Ueno, A. Koma, Growth of MoSe₂ thin films with van der Waals epitaxy. *J. Cryst. Growth* **111**(1), 1033 (1991)
6. K. Ueno, K. Saiki, T. Shimada, A. Koma, Epitaxial growth of transition metal dichalcogenides on cleaved faces of mica. *J. Vac. Sci. Tech. A* **8**(1), 68 (1990)
7. D.M. Tang, X. Wei, M.S. Wang, N. Kawamoto, Y. Bando, C. Zhi, M. Mitome, A. Zak, R. Tenne, D. Golberg, Revealing the anomalous tensile properties of WS₂ nanotubes by in situ transmission electron microscopy. *Nano Lett.* **13**(3), 1034 (2013)
8. A. Geim, I. Grigorieva, Van der Waals heterostructures. *Nature* **499**(7459), 419 (2013)
9. H. Terrones, F. López-Urías, M. Terrones, Novel hetero-layered materials with tunable direct band gaps by sandwiching different metal disulfides and diselenides. *Sci. Rep.* **3**(2013). doi:[10.1038/srep01549](https://doi.org/10.1038/srep01549)
10. A. Ramasubramaniam, D. Naveh, E. Towe, Tunable band gaps in bilayer transition-metal dichalcogenides. *Phys. Rev. B* **84**(20), 205325 (2011)
11. J. Xiao, M. Long, X. Li, Q. Zhang, H. Xu, K.S. Chan, Effects of van der Waals interaction and electric field on the electronic structure of bilayer MoS₂. *J. Phys: Cond. Matter* **26**(40), 405302 (2014)
12. K. Kośmider, J. Fernández-Rossier, Electronic properties of the MoS₂-WS₂ heterojunction. *Phys. Rev. B* **87**(7), 075451 (2013)
13. M. Bernardi, M. Palummo, J.C. Grossman, Extraordinary sunlight absorption and one nanometer thick photovoltaics using two-dimensional monolayer materials. *Nano Lett.* **13**(8), 3664 (2013)
14. L. Kou, T. Frauenheim, C. Chen, Nanoscale multilayer transition-metal dichalcogenide heterostructures: Band gap modulation by interfacial strain and spontaneous polarization. *J. Phys. Chem. Lett.* **4**(10), 1730 (2013)
15. H.P. Komsa, A.V. Krasheninnikov, Electronic structures and optical properties of realistic transition metal dichalcogenide heterostructures from first principles. *Phys. Rev. B* **88**(8), 085318 (2013)
16. J. Kang, J. Li, S.S. Li, J.B. Xia, L.W. Wang, Electronic structural Moiré pattern effects on MoS₂/MoSe₂ 2d heterostructures. *Nano Lett.* **13**(11), 5485 (2013)
17. N. Lu, H. Guo, L. Wang, X. Wu, X.C. Zeng, van der Waals trilayers and superlattices: modification of electronic structures of MoS₂ by intercalation. *Nanoscale* **6**(9), 4566 (2014)

18. Y.H. Zhao, F. Yang, J. Wang, H. Guo, W. Ji, Continuously tunable electronic structure of transition metal dichalcogenides superlattices. arXiv preprint (2013). [arXiv:1310.7285](https://arxiv.org/abs/1310.7285)
19. H. Jiang, Electronic band structures of molybdenum and tungsten dichalcogenides by the GW approach. *J. Phys. Chem. C* **116**(14), 7664 (2012)
20. J. Kang, S. Tongay, J. Zhou, J. Li, J. Wu, Band offsets and heterostructures of two-dimensional semiconductors. *Appl. Phys. Lett.* **102**(1), 012111 (2013)
21. C. Gong, H. Zhang, W. Wang, L. Colombo, R.M. Wallace, K. Cho, Band alignment of two-dimensional transition metal dichalcogenides: application in tunnel field effect transistors. *Appl. Phys. Lett.* **103**(5), 053513 (2013)
22. M.H. Chiu, C. Zhang, H.W. Shiu, C.P. Chu, C.H. Chen, C.Y.S. Chang, C.H. Chen, M.Y. Chou, C.K. Shih, L.J. Li, Determination of band alignment in the single-layer MoS₂/WSe₂ heterojunction. *Nat. Commun.* **6** (2015). doi:[10.1038/ncomms8666](https://doi.org/10.1038/ncomms8666)
23. Y. Cheng, Z. Zhu, M. Tahir, U. Schwingenschlögl, Spin-orbit-induced spin splittings in polar transition metal dichalcogenide monolayers. *Europhys. Lett.* **102**(5), 57001 (2013)
24. P. Joensen, E. Crozier, N. Alberding, R. Frindt, A study of single-layer and restacked MoS₂ by x-ray diffraction and x-ray absorption spectroscopy. *J. Phys. C* **20**(26), 4043 (1987)
25. H.L. Tsai, J. Heising, J.L. Schindler, C.R. Kannewurf, M.G. Kanatzidis, Exfoliated-restacked phase of WS₂. *Chem. Mater.* **9**(4), 879 (1997)
26. A.S. Goloveshkin, I.S. Bushmarinov, N.D. Lenenko, M.I. Buzin, A.S. Golub, M.Y. Antipin, Structural properties and phase transition of exfoliated-restacked molybdenum disulfide. *J. Phys. Chem. C* **117**(16), 8509 (2013)
27. J. Heising, M.G. Kanatzidis, Structure of restacked MoS₂ and WS₂ elucidated by electron crystallography. *J. Am. Chem. Soc.* **121**(4), 638 (1999)
28. E. Prouzet, J. Heising, M.G. Kanatzidis, Structure of restacked and pillared WS₂: an x-ray absorption study. *Chem. Mater.* **15**(2), 412 (2003)
29. R. Gordon, D. Yang, E. Crozier, D. Jiang, R. Frindt, Structures of exfoliated single layers of WS₂, MoS₂, and MoSe₂ in aqueous suspension. *Phys. Rev. B* **65**(12), 125407 (2002)
30. J.H. Yu, H.R. Lee, S.S. Hong, D. Kong, H.W. Lee, H. Wang, F. Xiong, S. Wang, Y. Cui, Vertical heterostructure of two-dimensional MoS₂ and WSe₂ with vertically aligned layers. *Nano Lett.* **15**(2), 1031 (2015)
31. Y.C. Lin, N. Lu, N. Perea-Lopez, J. Li, Z. Lin, X. Peng, C.H. Lee, C. Sun, L. Calderin, P.N. Browning et al., Direct synthesis of van der Waals solids. *ACS Nano* **8**(4), 3715 (2014)
32. G. Gao, W. Gao, E. Cannuccia, J. Taha-Tijerina, L. Balicas, A. Mathkar, T. Narayanan, Z. Liu, B.K. Gupta, J. Peng et al., Artificially stacked atomic layers: toward new van der Waals solids. *Nano Lett.* **12**(7), 3518 (2012)
33. M.H. Chiu, M.Y. Li, W. Zhang, W.T. Hsu, W.H. Chang, M. Terrones, H. Terrones, L.J. Li, Spectroscopic signatures for interlayer coupling in MoS₂-WSe₂ van der Waals stacking. *ACS Nano* **8**(9), 9649 (2014)
34. E.M. Mannebach, K.A.N. Duerloo, L.A. Pellouchoud, M.J. Sher, S. Nah, Y.H. Kuo, Y. Yu, A.F. Marshall, L. Cao, E.J. Reed et al., Ultrafast electronic and structural response of monolayer MoS₂ under intense photoexcitation conditions. *ACS Nano* **8**(10), 10734 (2014)
35. W.J. Yu, Z. Li, H. Zhou, Y. Chen, Y. Wang, Y. Huang, X. Duan, Vertically stacked multi-heterostructures of layered materials for logic transistors and complementary inverters. *Nat. Mater.* **12**(3), 246 (2013)
36. H. Fang, C. Battaglia, C. Carraro, S. Nemsak, B. Ozdol, J.S. Kang, H.A. Bechtel, S.B. Desai, F. Kronast, A.A. Unal et al., Strong interlayer coupling in van der Waals heterostructures built from single-layer chalcogenides. *Proc. Natl. Acad. Sci.* **111**(17), 6198 (2014)
37. H. Coy-Diaz, J. Avila, C. Chen, R. Addou, M.C. Asensio, M. Batzill, Direct observation of interlayer hybridization and dirac relativistic carriers in graphene/MoS₂ van der Waals heterostructures. *Nano Lett.* **15**(2), 1135 (2015)
38. B. Radisavljevic, A. Radenovic, J. Brivio, V. Giacometti, A. Kis, Single-layer MoS₂ transistors. *Nat. Nanotech.* **6**(3), 147 (2011)
39. H. Fang, S. Chuang, T.C. Chang, K. Takei, T. Takahashi, A. Javey, High-performance single layered WSe₂ p-FETs with chemically doped contacts. *Nano Lett.* **12**(7), 3788 (2012)

40. W. Zhao, Z. Ghorannevis, L. Chu, M. Toh, C. Kloc, P.H. Tan, G. Eda, Evolution of electronic structure in atomically thin sheets of WS₂ and WSe₂. *ACS Nano* **7**(1), 791 (2012)
41. C.H. Lui, Z. Ye, C. Ji, K.C. Chiu, C.T. Chou, T.I. Andersen, C. Means-Shively, H. Anderson, J.M. Wu, T. Kidd et al., Observation of interlayer phonon modes in van der Waals heterostructures. *Phys. Rev. B* **91**(16), 165403 (2015)
42. A.A. Puretzky, L. Liang, X. Li, K. Xiao, K. Wang, M. Mahjouri-Samani, L. Basile, J.C. Idrobo, B.G. Sumpter, V. Meunier et al., Low-frequency Raman fingerprints of two-dimensional metal dichalcogenide layer stacking configurations. *ACS Nano* **9**(6), 6333 (2015)
43. P. Rivera, J.R. Schaibley, A.M. Jones, J.S. Ross, S. Wu, G. Aivazian, P. Klement, N.J. Ghimire, J. Yan, D. Mandrus et al., Observation of long-lived interlayer excitons in monolayer MoSe₂-WSe₂ heterostructures. *Nat. Commun.* **6**, 6242 (2015). doi:[10.1038/ncomms7242](https://doi.org/10.1038/ncomms7242)
44. Y. Yu, S. Hu, L. Su, L. Huang, Y. Liu, Z. Jin, A.A. Puretzky, D.B. Geohegan, K.W. Kim, Y. Zhang et al., Equally efficient interlayer exciton relaxation and improved absorption in epitaxial and non-epitaxial MoS₂/WS₂ heterostructures. *Nano Lett.* **15**(1), 486 (2015)
45. X. Hong, J. Kim, S.F. Shi, Y. Zhang, C. Jin, Y. Sun, S. Tongay, J. Wu, Y. Zhang, F. Wang, Ultrafast charge transfer in atomically thin MoS₂/WS₂ heterostructures. *Nat. Nanotech.* **9**, 682 (2014)
46. H. Shi, R. Yan, S. Bertolazzi, J. Brivio, B. Gao, A. Kis, D. Jena, H.G. Xing, L. Huang, Exciton dynamics in suspended monolayer and few-layer MoS₂ 2d crystals. *ACS Nano* **7**(2), 1072 (2013)
47. Y. Jin, D.H. Keum, S.J. An, J. Kim, H.S. Lee, Y.H. Lee, A van der Waals homojunction: Ideal p-n diode behavior in MoSe₂. *Adv. Mater.* **27**(37), 5534 (2015)
48. X. Duan, C. Wang, J.C. Shaw, R. Cheng, Y. Chen, H. Li, X. Wu, Y. Tang, Q. Zhang, A. Pan et al., Lateral epitaxial growth of two-dimensional layered semiconductor heterojunctions. *Nat. Nanotech.* **9**(12), 1024 (2014)
49. C. Huang, S. Wu, A.M. Sanchez, J.J. Peters, R. Beanland, J.S. Ross, P. Rivera, W. Yao, D.H. Cobden, X. Xu, Lateral heterojunctions within monolayer MoSe₂-WSe₂ semiconductors. *Nat. Mater.* **13**(12), 1096 (2014)
50. S. Zheng, L. Sun, T. Yin, A.M. Dubrovkin, F. Liu, Z. Liu, Z.X. Shen, H.J. Fan, Monolayers of W_xMo_{1-x}S₂ alloy heterostructure with in-plane composition variations. *Appl. Phys. Lett.* **106**(6), 063113 (2015)
51. G. Eda, T. Fujita, H. Yamaguchi, D. Voiry, M. Chen, M. Chhowalla, Coherent atomic and electronic heterostructures of single-layer MoS₂. *ACS Nano* **6**(8), 7311 (2012)
52. Y. Gong, J. Lin, X. Wang, G. Shi, S. Lei, Z. Lin, X. Zou, G. Ye, R. Vajtai, B.I. Yakobson et al., Vertical and in-plane heterostructures from WS₂/MoS₂ monolayers. *Nat. Mater.* **13**(12), 1135 (2014)
53. M.Y. Li, Y. Shi, C.C. Cheng, L.S. Lu, Y.C. Lin, H.L. Tang, M.L. Tsai, C.W. Chu, K.H. Wei, J.H. He et al., Epitaxial growth of a monolayer WSe₂-MoS₂ lateral pn junction with an atomically sharp interface. *Science* **349**(6247), 524 (2015)
54. K. Chen, X. Wan, J. Wen, W. Xie, Z. Kang, X. Zeng, H. Chen, J.B. Xu, Electronic properties of MoS₂-WS₂ heterostructures synthesized with two-step lateral epitaxial strategy. *Acs Nano* **9**(10), 9868 (2015)
55. M. Mahjouri-Samani, M.W. Lin, K. Wang, A.R. Lupini, J. Lee, L. Basile, A. Boulesbaa, C.M. Rouleau, A.A. Puretzky, I.N. Ivanov et al., Patterned arrays of lateral heterojunctions within monolayer two-dimensional semiconductors. *Nat. Commun.* **6** (2015). doi:[10.1038/ncomms8749](https://doi.org/10.1038/ncomms8749)
56. X. Li, S. Wu, S. Zhou, Z. Zhu, Structural and electronic properties of germanene/MoS₂ monolayer and silicene/MoS₂ monolayer superlattices. *Nanoscale Res. Lett.* **9**(1), 1 (2014)
57. L.Y. Gan, Q. Zhang, Y. Cheng, U. Schwingenschlögl, Two-dimensional ferromagnet/semiconductor transition metal dichalcogenide contacts: p-type schottky barrier and spin-injection control. *Phys. Rev. B* **88**(23), 235310 (2013)
58. K. Lee, W.S. Yun, J. Lee, Giant rashba-type splitting in molybdenum-driven bands of MoS₂/Bi (111) heterostructure. *Phys. Rev. B* **91**(12), 125420 (2015)

59. P.V. Medeiros, S. Stafström, J. Björk, Effects of extrinsic and intrinsic perturbations on the electronic structure of graphene: Retaining an effective primitive cell band structure by band unfolding. *Phys. Rev. B* **89**(4), 041407 (2014)
60. V. Popescu, A. Zunger, Extracting E versus k effective band structure from supercell calculations on alloys and impurities. *Phys. Rev. B* **85**(8), 085201 (2012)
61. A. Lipatov, P. Sharma, A. Gruverman, A. Sinitskii, Optoelectrical molybdenum disulfide (MoS_2)-ferroelectric memories. *ACS Nano* **9**(8), 8089 (2015)
62. S. Wang, X. Wang, J.H. Warner, All chemical vapor deposition growth of MoS_2 : h-BN vertical van der Waals heterostructures. *ACS Nano* **9**(5), 5246 (2015)

Chapter 14

Emerging Applications of 2D TMDCs

In this chapter we review the emerging applications of 2D TMDC. Some of the interesting features of few-layer MoS₂ and the associated device applications were discussed in [1].

14.1 Transistors

A transistor is a semiconductor device composed of a semiconductor material with typically three terminals for connection to an external circuit. The invention of the transistor revolutionized the electronics industry, allowing the Information Age to occur. In 1956, its inventors, John Bardeen, Walter Brattain, and William Shockley were jointly awarded the Nobel Prize in Physics.

The usefulness of a transistor comes from its ability to use a small signal applied between one pair of its terminals to control a much larger signal at another pair of terminals. This property is called gain. A transistor can be used to produce a stronger output signal, a voltage or current, which is proportional to a weaker input signal, i.e. they can act as an amplifier. Alternatively, the transistor can be used to turn current ON or OFF in a circuit as an electrically controlled switch.

The main kind of modern transistors is the field-effect transistor (FET). A typical FET is composed of source and drain regions that serve as contacts for the thin area connecting them, called the channel. It may be covered with a thin dielectric material, the gate dielectric, and capped with a metal electrode, the top gate. This latter is used to electrostatically control the conductivity of the channel by changing the charge carrier concentration. If the transistor is to be used as a switch, the conductivity should be changed between a value with high resistance, corresponding to the open position of the switch and called the OFF state, to a highly conductive ON state, corresponding to the closed position of the switch. An ideal switch should also be able to instantly switch between the ON and OFF states.

14.1.1 Single- and Few-Layer Field-Effect Transistors

Even though the electrical properties of bulk semiconducting TMDCs have been studied since the middle of the 20th century [2, 3] their use in electronics was very limited. The interest in monolayer semiconducting TMDC FETs was renewed after the success of graphene and it exploded in 2011 after the pioneering paper [4] where a top-gated monolayer MoS₂ FET was demonstrated at room temperature. In this device, 6.5 Å thick exfoliated MoS₂ layer served as the semiconducting channel. It was deposited on SiO₂ and covered by a 30 nm thick layer of HfO₂, which served as the top-gate dielectric. A mobility of at least 200 cm²V⁻¹s⁻¹ was obtained. The transfer curves of the device are shown in Fig. 14.1. The transistor exhibited a current ON/OFF ratio exceeding 10⁸ at room temperature. Besides the very high ON/OFF ratio, the device exhibited off-state currents smaller than 100 fA (25 fA/μm). The high degree of electrostatic control is also reflected by the subthreshold slope $S = (d(\log I_{ds})/dV_{tg})^{-1}$, which was as low as 74 mV/dec.

The encapsulation of MoS₂ using insulating HfO₂ was crucial to achieve high mobility. A complementary approach to achieve high mobility consists in vacuum annealing to remove adsorbates. Using this approach, intrinsic (field-effect) mobility as high as 1000 cm²V⁻¹s⁻¹ was obtained at low temperature in both monolayers and bi-layers [5]. Intrinsic mobility and conductivity of single-layer MoS₂ in single and dual-gated geometry was also studied in [6]. It was found that at charge carrier densities n_{2D} below $\sim 1 \times 10^{13} \text{ cm}^{-2}$, the MoS₂ single-layer exhibits decreasing conductance as the temperature is decreased. For n_{2D} larger than 10^{13} cm^{-2} , the conductance increased with decreasing temperature, which is the hallmark of a metal-insulator transition.

In a later study [7], high-performance single-layer MoS₂ transistors with improved performance due to full-channel gating were demonstrated. The measured transconductance curves are shown in Fig. 14.2a with a maximum of 34 μS/μm (at 4 V), The drain-source bias ($I_{ds} - V_{ds}$) characteristics are shown in Fig. 14.2b. For these measurements, the back-gate voltage V_{bg} was kept at 0 V. At the relatively low drain voltages of V_{ds} of 1 V, the current-carrying capacity of the MoS₂ charge-carrying channel exhibited saturation, making this the first observation of drain current saturation in mono-layer MoS₂ FETs.

It was proposed that with relatively high values of transconductance ($g_m = 20 \mu\text{S}/\mu\text{m}$ for $V_{ds} = 1 \text{ V}$ and $g_m = 34 \mu\text{S}/\mu\text{m}$ for $V_{ds} = 4 \text{ V}$) and observed current saturation ($g_{ds} < 2 \mu\text{S}/\mu\text{m}$), MoS₂ could be interesting not only for applications in digital electronics but also for analog applications where it could offer a gain > 10 [7]. The observed saturation is also important for achieving the maximum possible operating speeds. Breakdown current density in MoS₂ was also studied, which was close to $5 \times 10^7 \text{ A/cm}^2$, that is a value 50 times larger than current carrying capacity of copper [7].

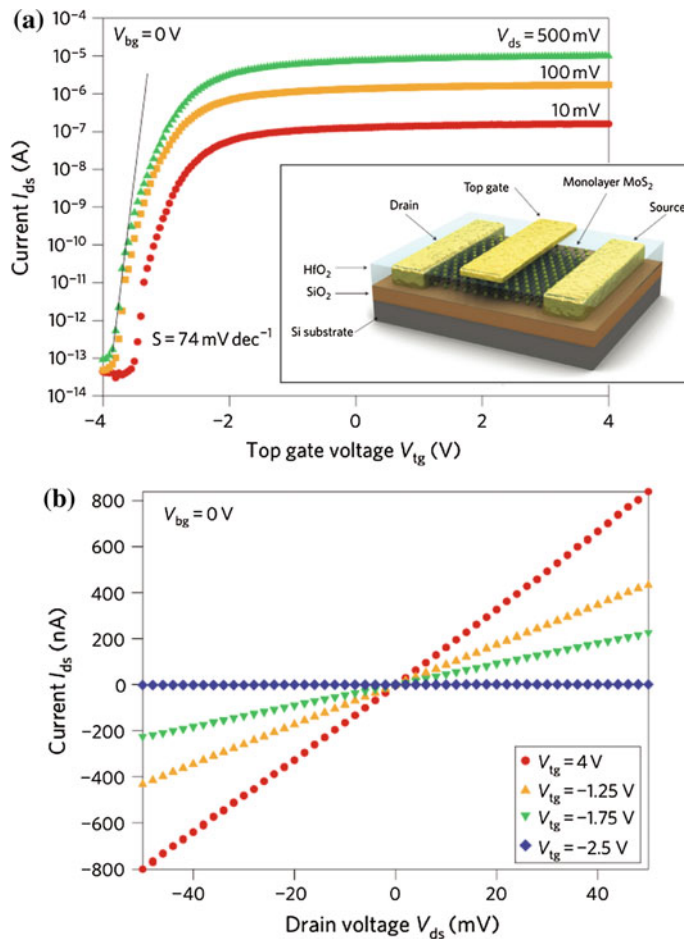


Fig. 14.1 Local gate control of the MoS_2 monolayer transistor. **a** $I_{ds} - V_{tg}$ curves recorded for a bias voltage ranging from 10 to 500 mV. Measurements were performed at room temperature with the back gate grounded. *Inset* Three-dimensional schematic view of one of the transistors. **b** $I_{ds} - V_{ds}$ curves recorded for different values of V_{tg} [4]. Reprinted by permission from Macmillan Publishers Ltd., copyright (2011)

Monolayer MoS_2 FET was also fabricated using CVD on various substrates [8, 9] and the ultimate performance limit of MoS_2 transistors using nonequilibrium Green's function-based quantum transport simulations was studied in [10].

In [11], effects of the ambient atmosphere and illumination on the performance of single-layer MoS_2 FETs was studied. An increasing $I - V$ hysteresis with increasing humidity was clearly observed, which allowed the authors to attribute the hysteresis to absorbed water molecules on MoS_2 (Fig. 14.3a). Interestingly, the hysteresis also increased when the device was cycled under illumination (Fig. 14.3b), demonstrating the important role of the ambient atmosphere and light on the FET performance.

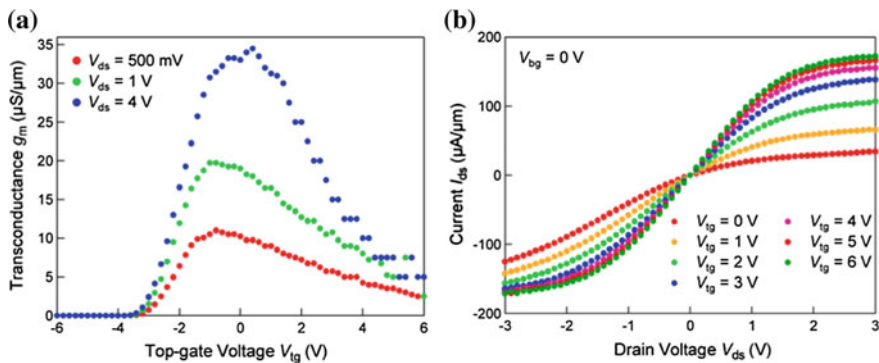


Fig. 14.2 **a** Transconductance $g_m = dI_{ds}/dV_{tg}$ derived from $I_{ds} - V_{tg}$ characteristics. The peak transconductance for $V_{ds} = 4 \text{ V}$ is $g_{m,\max} = 34 \mu\text{S}/\mu\text{m}$. **b** $I_{ds} - V_{ds}$ characteristics measured for different top-gate voltages V_{tg} for drain voltages V_{ds} reaching 3 V [7]. Copyright 2012 American Chemical Society. Published with permission

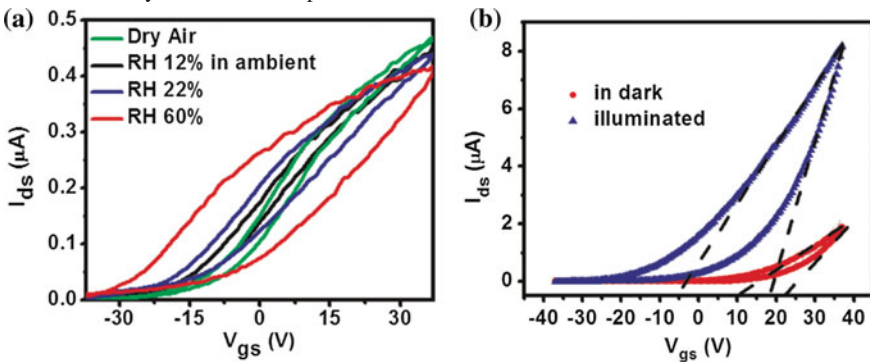


Fig. 14.3 **a** Hysteresis evolution of same device under different humidity. In dry air, small but finite hysteresis is likely due to the residual moisture at the interface between MoS₂ and substrate. Here, the current at $V_{gs} = 37 \text{ V}$ is the largest, which indicates relatively slow decay and smaller density of charge trapping states. With an increase in relative humidity (RH), the hysteresis grows larger and steadily from 4 V (12 % RH, black curve) to 15 V (22 % RH, blue curve) and finally to 25 V (60 % RH, red curve); the current at $V_{gs} = 37 \text{ V}$ steadily decreases, which indicates the growing decay rate and higher density of charge trapping states. **b** Hysteresis with different illumination conditions in a single-layer MoS₂ transistor. Blue dots are under global white illumination ($0.7 \text{ mW}/\text{cm}^2$), and red dots are in the dark. The intersections between the dashed lines and $y = 0$ show the threshold voltages [11]. Copyright 2012 American Chemical Society. Published with permission

Another factor that can limit the performance is flicker noise. Flicker noise is a type of electronic noise with a $1/f$ density spectrum and, therefore, is often referred to as $1/f$ noise. It occurs in almost all electronic devices, and can show up with a variety of other effects, such as impurities in a conductive channel, generation and recombination noise in a transistor due to base current, and so on. In particular, the all-surface structure of ultrathin TMDCs makes them sensitive to random perturbations in the environment. The lowest Hooge parameter (a parameter that characterises the $1/f$ noise), in high-mobility single-layer MoS₂ was found to be 0.005 in vacuum but

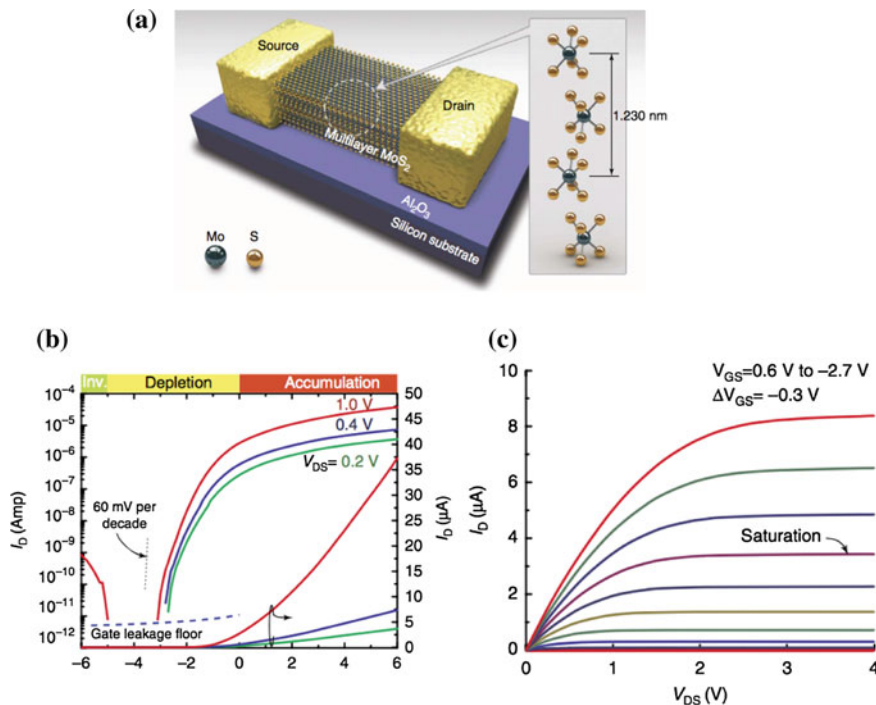


Fig. 14.4 **a** Schematic perspective view of a MoS₂ TFT with a multilayer MoS₂ crystal. **b** Drain current versus back gate bias showing $\sim 10^6$ ON/OFF ratio and 80mV per decade subthreshold slope. **c** Drain current versus drain bias showing current saturation [15]. Reprinted by permission from Macmillan Publishers Ltd., copyright (2012)

increases by more than an order of magnitude under ambient conditions, underscoring the sensitivity of MoS₂ to adsorbates and trapped charges [12]. It was subsequently suggested that the $1/f$ noise originates from the TMDC conducting channel, rather than from the contact barriers [13], where it was also proposed to use this result for development of a new sensing functionality.

FETs were also fabricated on Mo_{1-x}W_xSe₂ monolayers [14]. All Mo_{1-x}W_xSe₂ monolayer FETs exhibited *n*-type semiconducting transport behavior with high ON/OFF ratios ($> 10^5$).

FETs were also fabricated using few-layer TMDCs. High-mobility and low-power thin film transistors based on multilayer MoS₂ crystals were reported in [15, 16] with a large ON/OFF ratio ($\sim 10^6$), the mobility exceeding $100 \text{ cm}^2 \text{V}^{-1} \text{s}^{-1}$, near-ideal subthreshold swings ($\sim 70 \text{ mV/dec}$) and robust current saturation (Fig. 14.4).

An interesting question is whether current flows uniformly or nonuniformly through a multilayered structure. To answer this question, a model was developed in [17]. The model took each layer in a stacked layered material as a resistor. The vdW gap between the layers was also treated as a resistor, and the current tunneled through layers to travel across layers. The simulation predicted the presence of a

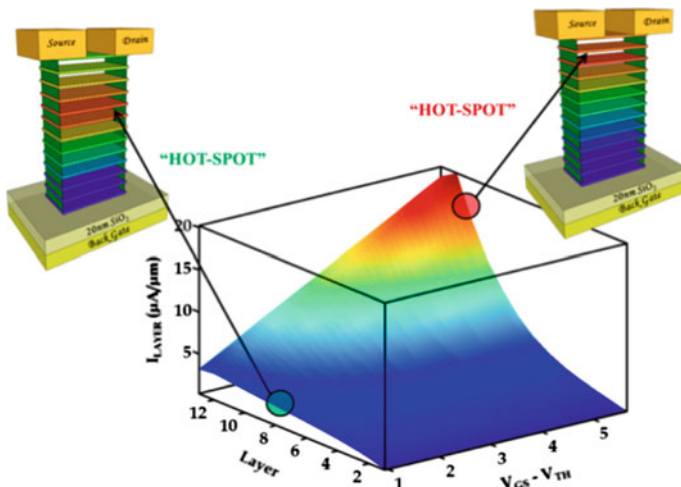


Fig. 14.5 Current distribution among the individual layers of a 13 monolayers thick MoS₂ at different gate bias conditions derived using the resistor network model. The cartoons show the location of the ‘HOT-SPOT’ and the associated current spread schematically corresponding to two different gate bias conditions [17]. Copyright 2013 American Chemical Society. Published with permission

‘hot spot’, that is, a particular layer or set of adjacent layers through which most of the flowing current was concentrated as the gate voltage was varied (see Fig. 14.5). It was predicted that the ‘hot spot’ moved toward the upper layers of the stacked structure and farther away from the back gate as the gate voltage was increased.

The intrinsic carrier mobility of multi-layered MoS₂ field-effect transistors on SiO₂ was studied in [18] and a comparative study of chemically synthesized and exfoliated multilayer MoS₂ FETs was performed in [19]. While MoS₂ is the most studied material, FETs using few-layered exfoliated MoSe₂ [20], MoTe₂ [21, 22], ReS₂ [23], and ReSe₂ [24] were also reported.

In one of the latest publications, a MoS₂ FET with an intrinsic gain over 30, an intrinsic cut-off frequency f_T up to 42 GHz and a maximum oscillation frequency f_{max} up to 50 GHz was reported [25].

It may be interesting to note that in a theoretical study of quantum transport in monolayer WTe₂ tunneling field effect transistors for a proper choice of the doping, gate and supply voltages a giant negative differential resistance with a peak to valley ratio as large as 10³ was reported [26]. Band-to-band tunnelling in double-gated WSe₂ FETs and Schottky barrier tunnelling of holes in back-gated MoS₂ FETs was studied in [27] and it was found that by scaling the flake thickness and the thickness of the gate oxide, the tunnelling current can be increased by several orders of magnitude.

Another interesting observation was made from careful measurements of the source-drain current (in a WSe₂-based device) at different back-gate voltages [28]. It was found that when changing the back gate voltage from 41.5 to 45.5 V, over 40 consecutive Coulomb diamonds with a charging energy of approximately 2 meV

were observed, showing the formation of quantum dots. The size of the quantum dots could be tuned over a factor of 2 by changing the voltages applied to the top gates. Subsequently, it was reported using a different material (WS_2) that the FWHM of the Coulomb peaks increases linearly with temperature while the height of the peaks remains nearly independent of temperature [29].

FETs based on TMDC nanotubes were reported in [30–32].

14.1.2 Ambipolar Transistors

Ambipolar TMDC FETs were fabricated by several groups. In [33], the fabrication of an electric double layer transistor (EDLT, a FET gated by ionic liquids) using a thin flake of MoS_2 was reported. The EDLT of a thin flake of MoS_2 clearly displayed ambipolar operation, in contrast to its commonly known bulk property as an n -type semiconductor. Figure 14.6 shows the transfer curve of the thin flake MoS_2 EDLT (red curve). For comparison, the authors also measured a transfer curve of the bulk single crystal (blue curve) on a device fabricated on the surface of a cleaved bulk single crystal.

For both bulk and thin flake MoS_2 EDLTs, the source-drain current I_{DS} increased as a function of applied gate voltage V_G when V_G was positive, being consistent with the behavior of n -type bulk crystal and electron conductivity found in thin flake solid-state devices. No saturation was observed in I_{DS} , even when V_G is as high as 3 V, indicating high-performance transistor operation. The ON/OFF ratio was over 200 in thin flake EDLT, indicating a highly tunable MoS_2 channel. At the same time, when the gate voltage was biased toward the negative side, significant differences were found between the thin flake and bulk devices: a clear hole current was switched

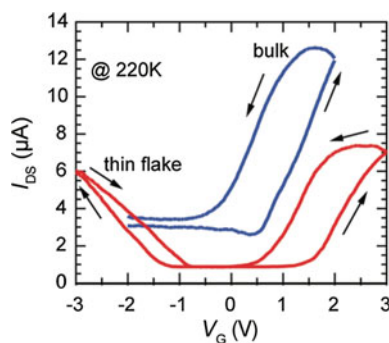


Fig. 14.6 Change in the channel current I_{DS} as a function of gate voltage V_G . V_{DS} is 0.2 V for both samples. Ambipolar transistor operation is only observed in thin flake devices, showing an increase in the channel current with an increase in the gate voltage $|V_G|$ for both hole and electron conductivities [33]. Copyright 2012 American Chemical Society. Published with permission

on at $|V_G| > 1$ V in the thin flake devices, whereas no clear increase in the channel current could be observed in the bulk devices, indicating that the device property in the hole conduction channel was comparable to that of the electron conduction channel [33]. The rather large hysteresis observed was attributed to the slow motion of the ions at low (220 K) temperature.

A sufficiently high ON/OFF ratio of $>10^2$ was observed for both hole and electron transport and the mobilities of 44 and $86 \text{ cm}^2 \text{V}^{-1} \text{s}^{-1}$ for electrons and holes, respectively, were obtained using Hall measurements [33].

Substrate and dielectric effects in ambipolar MoS₂ FETs were studied in [34]. In [35] ambipolar MoTe₂ transistors were fabricated with a current ON/OFF ratio of 5×10^2 for *n*-type and 10^3 for *p*-type regimes. Ambipolar transport was also observed in WS₂ and MoSe₂-based FETs [36–38].

By using low-resistance ionic-liquid-gated graphene contacts both *n*- and *p*-type WSe₂ field-effect transistors with a high ON/OFF ratio of $>10^7$ at 170 K, and large electron and hole mobility of $\mu \approx 200 \text{ cm}^2 \text{V}^{-1} \text{s}^{-1}$ at 160 K [39] were fabricated. Decreasing the temperature to 77 K increased the mobility of electrons to $\sim 330 \text{ cm}^2 \text{V}^{-1} \text{s}^{-1}$ and that of holes to $\sim 270 \text{ cm}^2 \text{V}^{-1} \text{s}^{-1}$. The ability to observe the intrinsic, phonon-limited conduction in both the electron and hole channels was attributed to the drastic reduction of the Schottky barriers between the channel and the graphene contact electrodes using ion liquid gating.

Transistor operations with electrostatically controlled transistor polarity in a dual-top-gated device with an α -MoTe₂ channel were reported in [40]. The transistor structure is shown in Fig. 14.7a, b. Operations in both *p*- and *n*-FET modes were performed in a single transistor by controlling the polarity of the bias voltage applied to one (V_{tgS}) of the two equivalent top gates. The device operation is illustrated in Fig. 14.7e, f, with panels (c-d) showing the band configurations for the two operation modes.

Ambipolar behaviour was also observed in MoX₂ using ionic gating in electrical double layer transistors [41].

14.1.3 Vertical Heterostructure Devices

Vertical heterostructure devices were also fabricated [42–44]. In [43] vertical FETs using MoS₂ and graphene were reported with a room temperature ON/OFF ratio over 10^3 and a high current density of up to $5,000 \text{ A/cm}^2$. The output characteristics of the vertical transistor are shown in Fig. 14.8.

In [42], fabrication of a vertical FET based on graphene-WS₂ heterostructures for flexible and transparent electronics was reported with an ON/OFF ratio exceeding 10^6 even at room temperature.

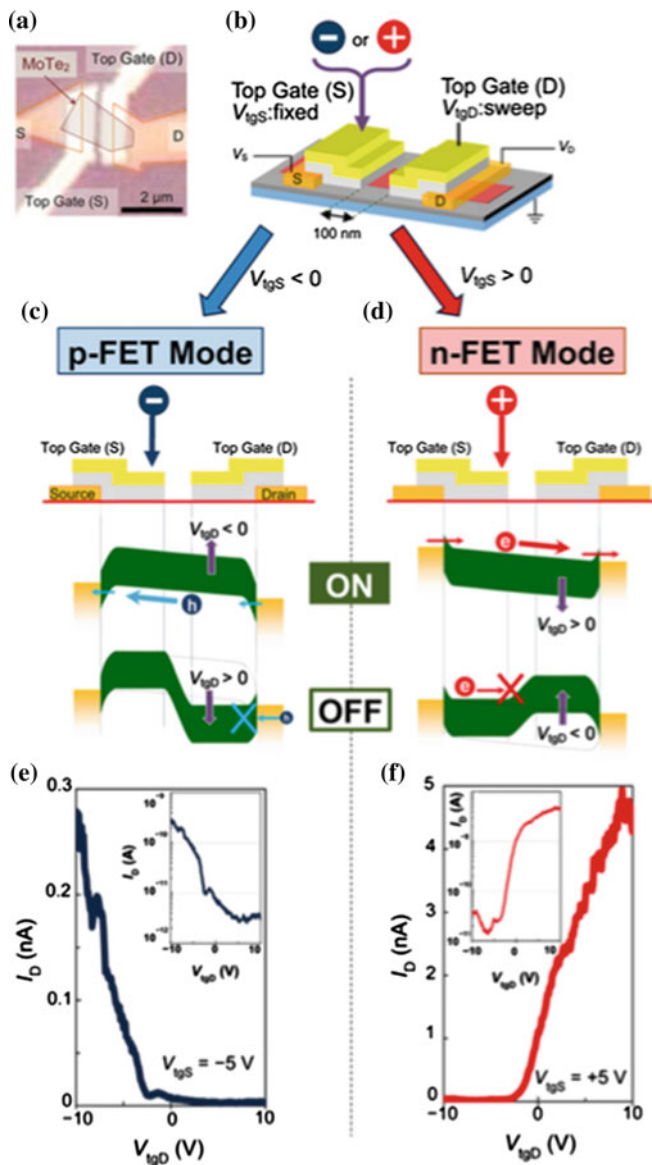
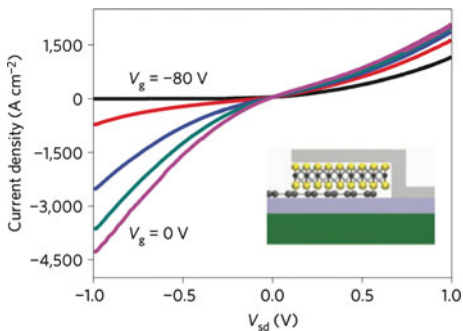


Fig. 14.7 **a** Optical micrograph of a dual-top-gate transistor. The *broken line* shows the region of the $\alpha\text{-MoTe}_2$ flake. **b** Schematic of the transistor structure. The gap between the two top gates is 100 nm. **c** Band configurations of ON and OFF states in the *p*-FET mode at $V_{tgS} < 0$. The ON state occurred at $V_{tgD} < 0$ and the OFF state at $V_{tgD} > 0$. **d** Band configurations of ON and OFF states in the *n*-FET mode at $V_{tgS} > 0$. The on and off states were given by $V_{tgD} > 0$ and $V_{tgD} < 0$, respectively. **e** Experimental results for ON/OFF operation in the *p*-FET mode ($V_{tgS} = -5$ V). The inset is a logarithmic plot. **f** Experimental results of an ON/OFF operation in the *n*-FET mode ($V_{tgS} = +5$ V), with a logarithmic plot provided in the inset [40]. Copyright 2015 American Chemical Society. Published with permission

Fig. 14.8 $I_{sd} - V_{sd}$ output characteristics of a vertical transistor. The current is normalized by the area [43]. Reprinted by permission from Macmillan Publishers Ltd., copyright (2013)



14.2 Integrated Circuits

14.2.1 Amplifiers

After the demonstration of FETs based on single-layer MoS₂, the latter were successfully used to demonstrate the operation of an analog small-signal amplifier based on single-layer MoS₂ [45]. This circuit consisted of two transistors connected in series, where one acted as a “switch” while the other one acted as an active “load” (Fig. 14.9a). The gate of one of the transistors (“switch” transistor) served as input, while the gate of the “load” transistor was connected with the central lead and acted as the output (Fig. 14.9b). The DC transfer characteristics of the amplifier are shown in Fig. 14.9c. When a small AC signal V_{in-AC} was superimposed on a DC bias V_{gs} at the input, the transistor circuit acted as a linear amplifier. The transistor was first biased at a certain DC gate voltage to establish the desired current in the circuit, shown as the Q-point in Fig. 14.9c. A small sinusoidal AC signal V_{in-AC} was then superimposed on the gate bias on the input, causing the output voltage V_{out} to oscillate synchronously with a phase difference of 180° with respect to V_{in-AC} . The small-signal amplification is demonstrated in Fig. 14.9d, e. The gain of the amplifier was $|G| > 4$ decreasing for higher frequencies, which was associated with the influence of high parasitic capacitances [45].

In [25] few-layer MoS₂ FETs were fabricated on both quartz and flexible substrates and integrated to construct functional circuits, including a logic inverter and a RF amplifier, operating in the gigahertz regime. High gain inverters (a DC voltage gain of >12 was measured for the complementary WSe₂ inverter) were obtained using exfoliated WSe₂ flakes FETs [46]. Due to extremely small thickness of such devices, the power consumption of TMDC nanosheet-based inverters is in the sub-nanowatt range [47].

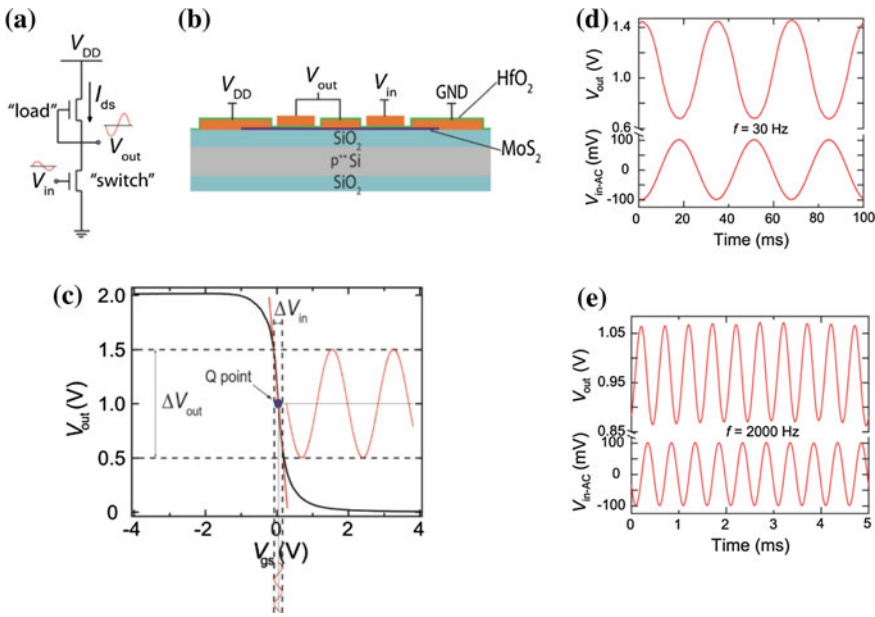


Fig. 14.9 Transfer characteristics of an integrated MoS₂ amplifier. **a** Schematic drawing of integrated amplifier in common-source configuration. The lower transistor acts as a “switch” and upper as a “load”. **b** Vertical cross-section of the amplifier device with appropriate wire connections. **c** Transfer characteristic of the integrated amplifier realized with two transistors on the same MoS₂ flake. The “switch” transistor is first biased at a certain DC gate bias to establish a desired drain current, shown as the “Q”-point (quiescent point). At that point the “load” transistor has a certain constant resistance and acts as an active resistor. A small AC signal of amplitude $\Delta V_{in}/2$ is then superimposed on the gate bias of the “switch” transistor, causing the output voltage to oscillate synchronously with a phase difference of π . **d**, **e** Demonstration of the small-signal amplifier operation. On the input terminal of the amplifier, a sinusoidal signal V_{in-AC} of amplitude $\Delta V_{in} = 100 \text{ mV}$ and frequencies of **d** 30 Hz and **e** 2000 Hz is applied with DC bias of $V_{gs} = 0 \text{ V}$, resulting in an amplified sinusoidal signal on the output. The output signal is shifted in phase by 180° with respect to the input signal, in agreement with the standard characteristic of common-source amplifiers [45]. Reprinted with permission. Copyright 2012 by the American Institute of Physics

14.2.2 Logic Circuits

The amplifiers described in the previous section are simple integrated circuits using monolayer and few-layer TMDC FETs. More complicated devices for logic circuits were also envisaged [48, 49]. An example of such a circuit, a five-stage ring oscillator, leading to operating frequencies up to 1.6 MHz with stage delays of $\sim 60 \text{ ns}$, is shown in Fig. 14.10. While this performance is inferior to ring oscillators based on conventional silicon, graphene, or carbon nanotubes, it is superior to the current generation organics and amorphous oxide semiconductors [50].

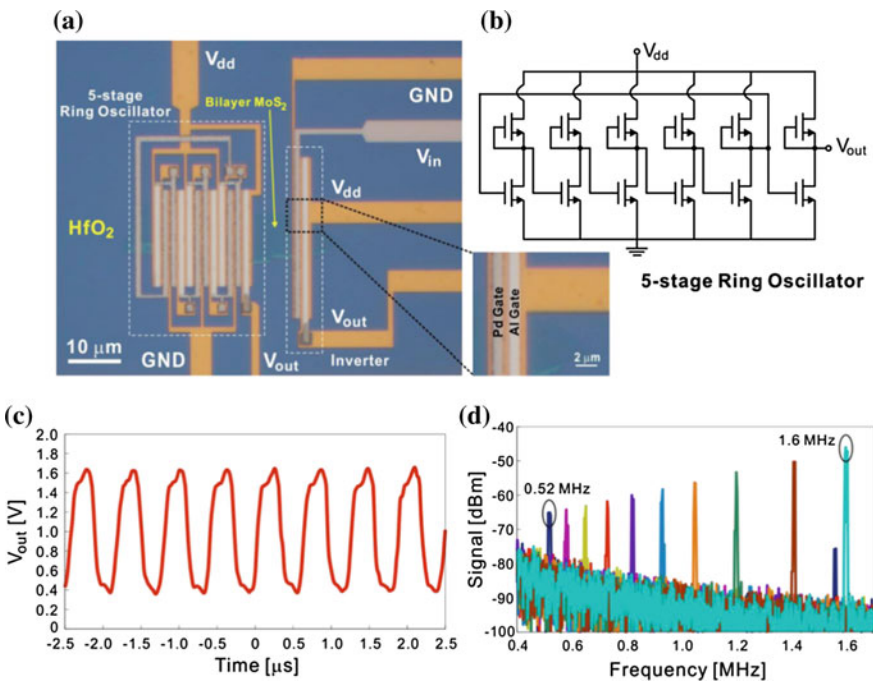


Fig. 14.10 A five-stage ring oscillator based on bilayer MoS_2 . **a** Optical micrograph of a ring oscillator constructed on a bilayer MoS_2 thin film. **b** Schematic of the electronic circuit of the five-stage ring oscillator. The first five inverter stages form a positive feedback loop, which leads to oscillations in the circuit. The last inverter serves as the synthesis stage. **c** Output voltage as a function of time for the ring oscillator at $V_{dd} = 2$ V. The fundamental oscillation frequency is at 1.6 MHz. The corresponding propagation delay per stage is 62.5 ns. **d** The power spectrum of the output signal as a function of V_{dd} . From left to right, $V_{dd} = 1.15$ V and 1.2 to 2.0 V in step of 0.1 V. The corresponding fundamental oscillation frequency increases from 0.52 to 1.6 MHz [49]. Copyright 2012 American Chemical Society. Published with permission

14.3 Optoelectronic Devices

Optoelectronic devices are electronic devices that can generate, detect, interact with or control light. Devices that are flexible and transparent are expected to become increasingly important in solar arrays, wearable electronics and transparent displays. The direct band gap of single-layer semiconducting TMDCs makes them particularly suitable for optoelectronic applications. Several classes of optoelectronic devices have been demonstrated from ultra-thin semiconducting TMDCs including photodetectors, photovoltaic and light-emitting devices.

14.3.1 Photodetectors and Solar Cells

When photons of energy greater than the band gap are incident on a semiconductor, they create bound electron-hole pairs (excitons) or free carriers depending on the exciton binding energy in the semiconductor. Bound excitons separated by an applied or built-in electric field generate a photocurrent. Two major categories of semiconductor-based photodetectors are photodiodes and phototransistors, the former are usually faster but the latter possess higher sensitivities.

Heterojunctions of *p*-type Si with *n*-type MoS₂ were realized [51] with rise and fall times of about 0.3 ms and a photoresponsivity of 210 mA/W measured with green light. Electrically tunable p-n junctions based on monolayer WSe₂ were reported in [52, 53] with an identical photoresponsivity value under optical excitation [52]. Using two-pulse photovoltage correlation technique, intrinsic response times from monolayer MoS₂ photodetectors as short as 3 ps were obtained implying photodetection bandwidths as wide as 300 GHz [54].

First, single-layer mechanically exfoliated MoS₂ phototransistors exhibited a photoresponsivity of 7.5 mA/W at the gate voltage of \sim 50 V [55]. Phototransistors based on CVD MoS₂ monolayer and WS₂ multilayers were also reported [56, 57]. Subsequently, an ultrasensitive single-layer MoS₂ photodetector due to improved mobility and contact quality was demonstrated [58]. The output curves depicted in Fig. 14.11 show an increase of drain current by several orders of magnitude as the device is illuminated, proving photoresponse. The device photoresponsivity reached a value of 880 A/W.

By using MoS₂ layers of different thicknesses, photodetection of different wavelengths can be tuned [59] to absorb light of different wavelength, alternatively the use of multilayer MoS₂ phototransistors allowed photodetection of light from ultraviolet to infra-red [60]. These devices showed a photoresponsivity of \sim 100 mA/W, which is comparable to that of Si-based photodetectors [61]. Figure 14.12 shows a schematic diagram of the device and the different energy gaps of MoS₂ with different number of layers. Engineering of optical and electronic properties by varying the number of layers was also considered for WS₂ [62]. In [63], a photovoltaic effect in MoS₂/WSe₂ heterostructures was reported.

Highly efficient gate-tunable photocurrent generation was demonstrated in vertical heterostructures such as graphene/MoS₂/graphene and graphene/MoS₂/metal where a maximum external quantum efficiency of 55 % and an internal quantum efficiency up to 85 % was achieved [64]. Photodetectors with gate-tunable photoresponsivity and high external quantum efficiency were also fabricated using few-layer ReS₂ [23].

Enhancement of the performance of TMDC photodetectors, such as field-effect mobility, responsivity, and detectivity can be enhanced through doping, in particular, self-assembled monolayer doping [65]. It was also shown that reduction of the Schottky barrier in devices with 1T contacts (see Sect. 14.6.3.2) enhances photoresponsivity by more than an order of magnitude [66].

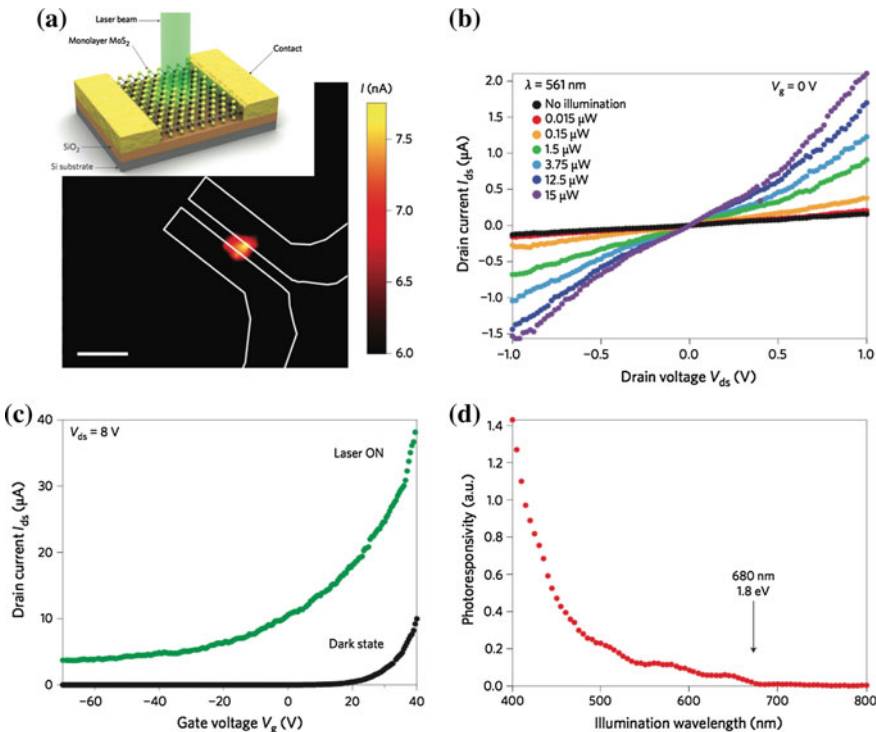


Fig. 14.11 **a** Three-dimensional schematic view of a single-layer MoS₂ photodetector and spatial map of the photocurrent recorded as a focused laser beam was raster-scanned over the surface of the photodetector using a nanopositioning stage. Scale bar, 5 μm. $V_{ds} = 1 \text{ V}$, $V_g = 0 \text{ V}$, $P_{inc} = 0.425 \mu\text{W}$. The spatial profile shows that light detection is confined to a small area centred on the MoS₂ flake. **b** Drain-source ($I_{ds} - V_{ds}$) characteristic of the device in the dark and under different illumination intensities. The device operates as an enhancement-mode transistor. Increasing illumination levels result in enhanced current due to electron-hole pair generation by light absorption in the direct bandgap of monolayer MoS₂. **c** Gating response ($I_{ds} - V_g$) of the MoS₂ photodetector in dark and illuminated states, acquired with a backgate voltage V_g between -70 and $+40$ V. The illumination power was $0.15 \mu\text{W}$. **d** Photoresponsivity of a similar monolayer MoS₂ device as a function of illumination wavelength. The device shows a uniformly increasing response as the illumination wavelength is reduced from 680 to 400 nm and indicates that monolayer MoS₂ photodetectors can be used over a broad range of wavelengths [58]. Reprinted by permission from Macmillan Publishers Ltd., copyright (2013)

It should be noted that despite intense efforts to understand the mechanism of photoresponse in TMDC-based devices, its origin remains a subject of debate. While in some studies the effect was predominately attributed to the photovoltaic effect [66–68], other groups argued that photothermoelectric effect may also play a non-negligible role [69, 70] and large values of Seebeck coefficient were reported.

In [71], MoS₂ transistor with a ferroelectric gate was used as a photodetector, wherein the few-layer MoS₂ served as the photosensitive semiconducting channel while the remnant polarization of polyvinylidene fluoride-trifluoroethylene was

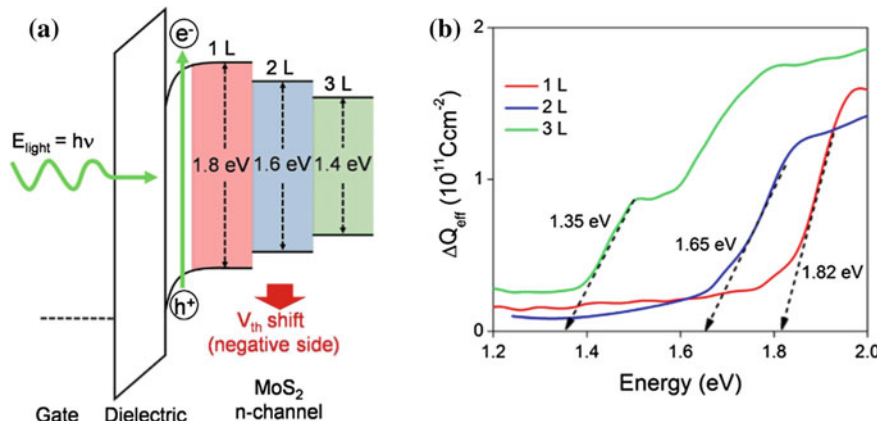


Fig. 14.12 **a** The schematic band diagrams of ITO (gate)/Al₂O₃ (dielectric)/single (1L)-, double (2L)-, triple (3L)-layer MoS₂ (*n*-channel) under light illustrate the photoelectric effects for band gap measurements. **b** Photon energy-dependent ΔQ_{eff} plots indicate the approximate optical energy gaps to be 1.35, 1.65, and 1.82 eV for triple-, double-, and single-layer MoS₂ nanosheets, respectively [59]. Copyright 2012 American Chemical Society. Published with permission

employed to depress the dark current of the MoS₂ semiconducting channel. The authors made use of the ability of stable remnant polarization to provide an ultrahigh local electro-static field ($\approx 10^9$ V/m), which is larger than that produced by gate bias in traditional FETs, maintaining the few-layer MoS₂ channel in a fully depleted state and significantly increasing the sensitivity of the detector even at zero gate voltage. As a result, a photodetector with high detectivity of 2.2×10^{12} Jones and photoresponsivity up to 2570 A/W was achieved. In addition, the spectral sensitivity of the detector was from the visible to the near-infrared (0.85–1.55 μm).

The photovoltaic cell is one of the most widespread applications of a p-n junction. Single-layer semiconducting TMDCs are well-positioned here in terms of both direct band gap and mobility values, making them promising candidates for photovoltaic applications [53, 64, 72–75]. However, thickness-limited absorption poses a challenge for high efficiency. To overcome this issue, light-trapping techniques such as plasmon-enhanced absorption, strain engineering, and/or vertical stacks of atomically thin cells were suggested [50, 76, 77].

14.3.2 Light-Emitting Devices

14.3.2.1 Light-Emitting Diodes

The light-emitting diode (LED) making use of electroluminescence, where photons are emitted in response to electrical stimulus, is another ubiquitous application of

the p-n junction. The direct bandgaps of monolayer semiconducting TMDCs make them ideal candidates for active light-emitting layers in future flexible optoelectronics. An early example of electroluminescence in TMDCs includes MoS₂ emitting light by electrical excitation through Au nano-contacts [78] stimulated by scanning microscopy.

In [79] it was demonstrated that single-layer MoS₂ can be used as a light emitter (see Fig. 8.22). While this study served as a proof-of-principle, the device was limited by its relatively high power threshold for light emission. Light emission was subsequently observed in electrically tunable p-n diodes fabricated from monolayers of WSe₂ [52, 53] with electroluminescence efficiency reaching 1% [52]. Mono-and bi-layers of WS₂ were used to fabricate light-emitting transistors [38]. Excitonic electroluminescence was also observed from SL-MoS₂ and crystalline *p*-type Si heterojunctions [80].

However, the efficiency obtained so far remains low. With commercial organic LEDs approaching 20% emission efficiencies, significant improvements in technology are needed [50].

Of interest is the study in which light-emitting diodes were fabricated by stacking metallic graphene, insulating hexagonal boron nitride and various semiconducting monolayers into complex but carefully designed sequences. The devices already exhibited an extrinsic quantum efficiency of nearly 10% and the emission could be tuned over a wide range of frequencies by appropriately choosing and combining 2D TMDCs [81].

14.3.2.2 Lasers

Spontaneous emission from TMDC monolayers can be enhanced through integration with photonic crystals [82, 83] and distributed Bragg reflector microcavities [84, 85]. Both strategies were used to develop monolayer MoS₂-based lasers.

Figure 14.13a shows a schematic of a monolayer excitonic laser in a microdisk resonator [86], where embedding a monolayer in-between two dielectric layers in a Si₃N₄/WS₂/HSQ structure resulted in strong optical confinement leading to a larger modal gain, particularly crucial for an atomically thin monolayer gain medium. The resonant wavelength matched the dominant peak of the measured lasing spectrum of a WS₂ monolayer embedded 3.3 μm diameter microdisk at 612.2 nm (Fig. 14.13b), with a measured quality factor $Q = \lambda/\Delta\lambda$ of about 2,604 [86]. It was noted that the lasing performance did not decay even after several months, which was attributed to the sandwich Si₃N₄/WS₂/HSQ (hydrogen silsesquioxane) structure that protects the monolayer from direct exposure to air. The quantum yields of various TMDCs, such as MoS₂, WS₂ and WSe₂ monolayers, are compared in Fig. 14.13c.

Using the second strategy, an atomically thin crystalline semiconductor (WSe₂) was introduced as a gain medium at the surface of a pre-fabricated photonic crystal cavity as shown in Fig. 14.14a [87]. A continuous-wave nanolaser operating in the visible regime was thereby achieved with an optical pumping threshold as low as 27 nanowatts at 130 K. It was noted that the key to the lasing action lies in the

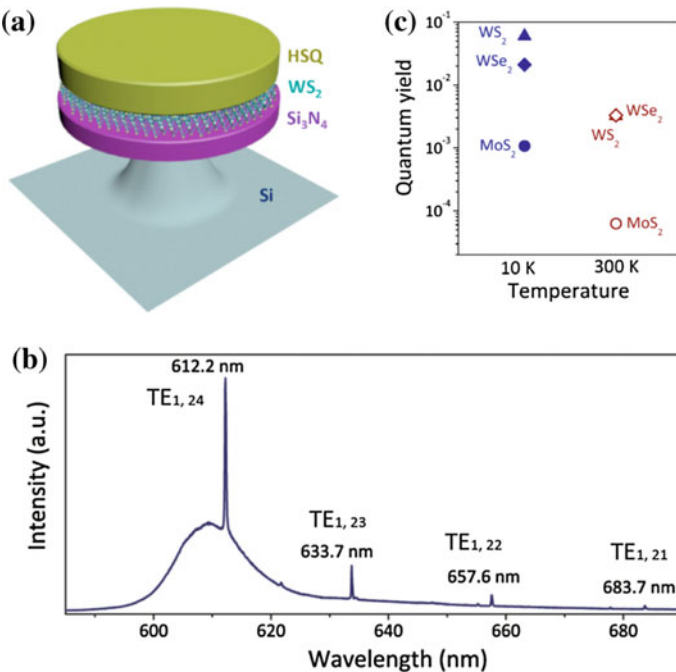


Fig. 14.13 **a** Schematic image of a monolayer WS_2 microdisk laser. The sandwich structure of $\text{Si}_3\text{N}_4/\text{WS}_2/\text{HSQ}$ ensures a higher confinement factor and leads to a larger modal gain. **b** Experimental photoluminescence (PL) spectrum taken at 10 K when the pump intensity is above lasing threshold, showing whispering gallery modes at 612.2, 633.7, 657.6 and 683.7 nm. **c** PL quantum yield of monolayer MoS_2 , WS_2 and WSe_2 at 300 and 10 K [86]. Reprinted by permission from Macmillan Publishers Ltd., copyright (2015)

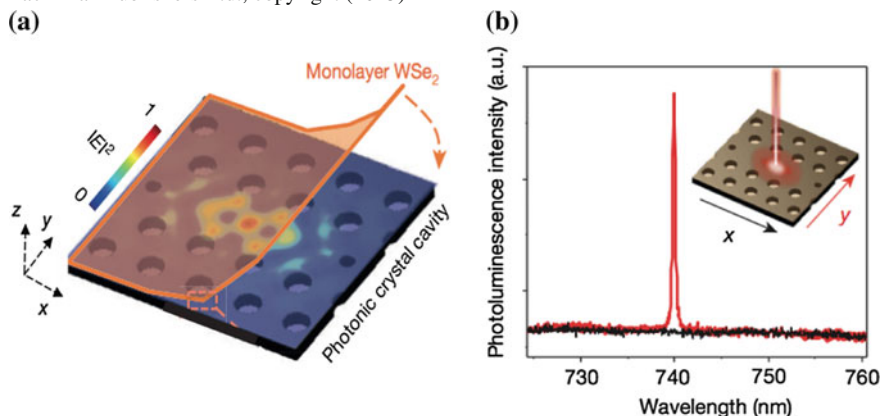


Fig. 14.14 **a** Cartoon depiction of a laser architecture with a photonic crystal. **b** Polarization-resolved photoluminescence spectrum of a device taken at 80 K, showing a completely polarized narrow emission at $\sim 740 \text{ nm}$. The black (red) line corresponds to the detected linear polarization in the x (y) direction [87]. Reprinted by permission from Macmillan Publishers Ltd., copyright (2015)

monolayer nature of the gain medium, which confines direct-gap excitons to within one nanometre of the cavity surface. The surface-gain geometry allows the tailoring of gain properties via external controls such as electrostatic gating and current injection, enabling electrically pumped operation. It was argued that this fabrication method is scalable and compatible with integrated photonics for on-chip optical communication technologies [87].

14.4 Valleytronics

Spin-valley coupling is one of the most exciting phenomena in 2D TMDCs. This effect has been utilised for the fabrication of WSe₂-based electrically switchable chiral light-emitting transistor [88] (see Fig. 11.6).

14.5 Memory Devices

After the demonstration of TMDC-based FETs researchers started integrating them into more complex, functional digital circuitry, where NAND gates and static random access memory cells containing 3 and 4 FETs, respectively, were demonstrated with ultrathin MoS₂ [49].

2D TMDCs can also be used to fabricate memory devices proper. In [89] a nonvolatile memory cell based on a MoS₂/graphene heterostructure was demonstrated. The device architecture resembles that of a floating gate FET and is shown in Fig. 14.15a, b. Monolayer MoS₂ acts as the transistor channel, and graphene electrodes are used to inject and collect the charge carriers. A piece of multilayer graphene, ~4 nm thick, was employed as the charge trapping layer (floating gate) and was separated from the semiconducting channel by a 6 nm thick HfO₂ layer, serving as the tunnel oxide.

Thanks to the atomic scale thickness of single-layer MoS₂ and its large bandgap, the transistor operation was found to be very sensitive to the presence of charges in the floating gate. The device showed a program/erase current ratio as high as 10⁴, which is higher than what was reported for memory devices employing graphene as the active material. The observed memory window (>8 V, Fig. 14.15c) revealed the possibility for engineering 2D memory cells with multilevel data storage capability. The mechanism of the memory effect was discussed in terms of the band diagram shown in Fig. 14.15d.

A somewhat similar design was proposed in [90], where graphene and MoS₂ were employed as both channel and charge-trapping layers, and hexagonal BN was used as a tunnel barrier. In these ultrathin heterostructured memory devices, the atomically thin MoS₂ or graphene-trapping layer stored charge tunnelled through hexagonal boron nitride, serving as a floating gate to control the charge transport in the graphene or MoS₂ channel. By varying the thicknesses of the two-dimensional

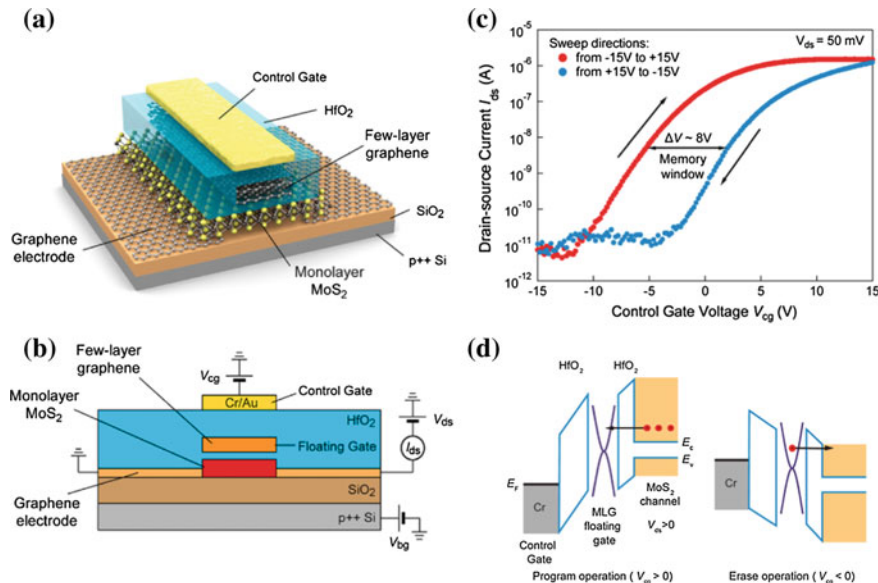


Fig. 14.15 **a** Three-dimensional schematic view of a memory device based on single-layer MoS_2 . **b** Schematics of a heterostructure memory cell with a single-layer MoS_2 semiconducting channel, graphene contacts and a multilayer graphene (MLG) floating gate. The MLG floating gate was separated from the channel by a thin tunneling oxide (ca. 1 nm Al_2O_3 + 6 nm HfO_2) and from the control gate by a thicker blocking oxide (1 nm Al_2O_3 + 30 nm HfO_2). **c** Transfer characteristic (drain-source current I_{ds} vs control-gate voltage V_{cg}) of the floating gate transistor, acquired along two different control-gate voltage sweep directions. The large hysteresis of ~ 8 V is related to accumulation of charge in the MLG floating gate. The voltage sweep rate was 1.4 V/s. **d** A simplified band diagram of the memory device in the program and erase states. Application of a positive control gate voltage V_{cg} programs the device. Electrons tunnel from the MoS_2 channel through the 6 nm thick HfO_2 and accumulate on the multilayer graphene floating gate. Application of a negative control gate voltage V_{cg} depletes the floating gate and resets the device [89]. Copyright 2013 American Chemical Society. Published with permission

materials and modifying the stacking order, the hysteresis and conductance polarity of the field-effect transistor could be controlled.

Use of top-gate MoS_2 transistors for fabrication of nonvolatile memory was reported in [91] and a graphene/ MoS_2 hybrid structure was proposed for multi-functional photoresponsive memory devices [92].

MoS_2 combined with other materials, such as oxides, polymers, and organic small molecules was also used to demonstrate the possibility of fabricating memory devices [93–95]. For example, in [95] it was demonstrated that solution-processed $\text{MoO}_x/\text{MoS}_2$ and WO_x/WS_2 heterostructures sandwiched between two printed silver electrodes exhibited a large and tunable electrical resistance range from 10^2 to 10^8 Ohm combined with the low programming voltages of 0.1–0.2 V. These structures were proposed for use in layered memristive and memcapacitive switches for printable electronics.

The combination of MoS₂ with a ferroelectric (Pb(Zr, Ti)O₃, PZT) was considered in [96]. The device structure is shown in Fig. 14.16a. In addition to the presence of a memory window (Fig. 14.16b) and a pronounced ON/OFF ratio (Fig. 14.16c), the authors made use of the semiconductor nature of MoS₂ to use its photoresponse as an extra degree of freedom to increase the device functionality. It was noted that if a MoS₂-PZT structure is illuminated with visible light, the photogenerated charge carriers in molybdenum disulfide can produce an electric field that affects the polarization of PZT underneath the MoS₂ flake, opening the possibility of eliminating the difference between ON and OFF states by exposure of the device to light. The implementation of this effect in a MoS₂-PZT memory device is illustrated in Fig. 14.16d, which shows that after 5 min of light exposure, the ON and OFF states became completely indistinguishable, and when the light was turned off, the original ON and OFF states were not restored, i.e. a MoS₂-PZT memory can be completely erased simply by exposure to light.

Based on this finding, two different schemes of optoelectrical operation of MoS₂-PZT memories were proposed as illustrated in Fig. 14.16e, where panel (i) shows an array of MoS₂-PZT FeFETs where individual devices are in either ON ("1") or OFF ("0") states. The entire array can be simultaneously erased optically by setting all devices to the ON state via light illumination (ii). Once the array is optically erased, data can be written electrically by individually accessing the devices (iii). Alternatively, starting with the same array of pre-recorded MoS₂-PZT FeFETs (i), it is possible to erase it electrically (iv) by polarizing the entire PZT substrate upward using the global back gate. The data can be subsequently written optically by individually illuminating the devices that need to be in the ON state using, for example, a focused laser beam (v) [96].

It should be noted that while the reported results demonstrate the promise of 2D TMDCs for fabricating memory devices, their present performance is still premature compared to another class of chalcogenides, called phase-change alloys. The latter, typically based on GeTe-Sb₂Te₃ quasibinary alloys, demonstrate switching rates on the order of nanoseconds, reliability of up to 10^8 cycles and retention of more than 10 years at room temperature [97]. The latest modification, where GeTe and Sb₂Te₃ are spatially separated in so-called interfacial phase-change memory, exhibits even better performance [98].

14.6 Contacts for 2D TMDC Devices

A major challenge for developing TMDC-based electronic devices is that they tend to form a substantial Schottky barrier with most metals commonly used for making electrical contacts. This is a serious problem, because low-resistance ohmic contacts are needed for both exploring the intrinsic transport properties of the channel material and also they limit the performance of realistic devices. Thus using a contactless method based on THz spectroscopy, an intrinsic mobility as high as $4200 \text{ cm}^2/\text{V}\cdot\text{s}$

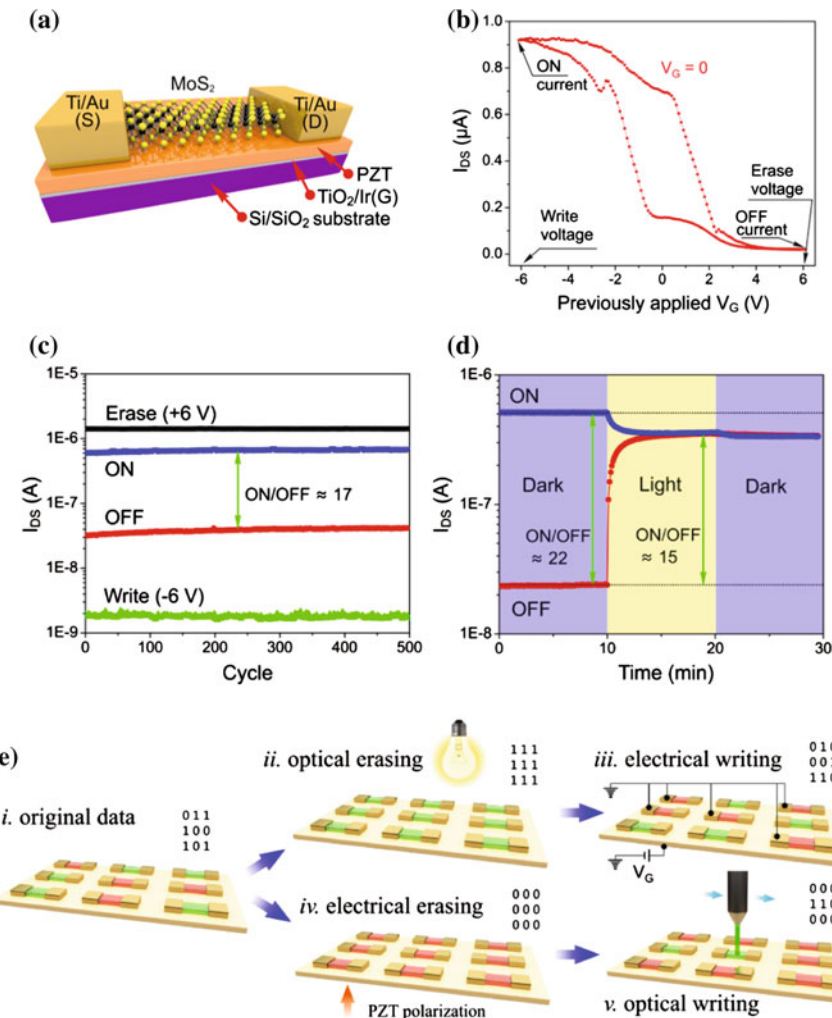


Fig. 14.16 **a** Scheme of a MoS₂-based FeFET. **b** Polarization-dependent hysteresis of electronic transport in a MoS₂-PZT FeFET. Arrows show write and erase voltages and the corresponding ON and OFF currents. **c** Cyclic endurance of the device: 1 ms pulses of -6 and 6 V were used for writing and erasing, respectively. After each write/erase operation, the I_{DS} current was read after $\tau_{wait} = 16$ s at $V_G = 0$. **d** Effect of visible light illumination on the data retention characteristics of a MoS₂-PZT FeFET. **e** “Optical erase—electrical write” and “electrical erase—optical write” operation of MoS₂-PZT memories [96]. Copyright 2015 American Chemical Society. Published with permission

was obtained at 30 K [99], which is significantly higher than any other value reported to-date using structures with contacts.

In some cases the nature of contacts can play a more important role for device performance than the semiconductor itself [100]. There are two basic approaches

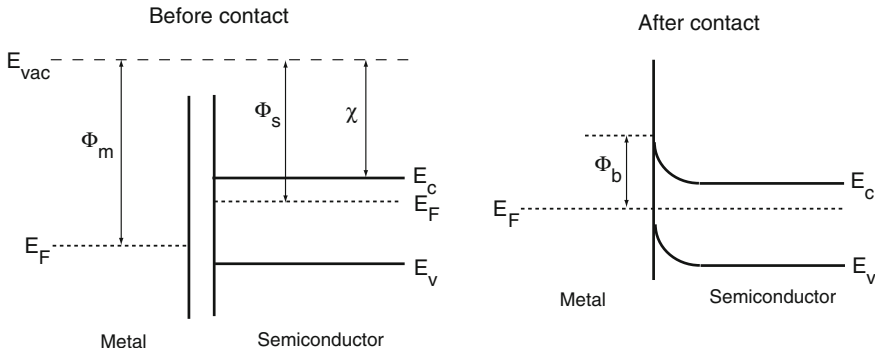


Fig. 14.17 Band alignments of a metal and a semiconductor for $\Phi_M > \chi$ before (left) and after (right) establishing a contact

to achieve low resistance contacts between a semiconductor and a metal, namely (i) thinning the Schottky width by degenerately doping the contact regions and (ii) lowering the barrier height by selecting contact materials with an extremely high (for *p*-type semiconductors) or low (for *n*-type semiconductors) work function.

The formation of a Schottky barrier is illustrated in Fig. 14.17. The upper panel illustrates the electronic band alignment of the metal and TMDC for the case of $\Phi_M > \chi$ (in the example case, the Φ_M of metal is larger than χ), before the metal and TMDC are brought into contact. When the metal and the semiconductor are brought in a contact, the semiconductor bands bend in order to achieve equilibrium between the metal Fermi level and the TMDC chemical potential. In this case, the electrons diffuse from the semiconductor to the lower energy states of the metal in order to achieve a constant Fermi level throughout the system in thermal equilibrium. This results in upward band bending within TMDC (e.g. MoS₂) at the interface concomitant with the formation of a potential barrier against electron migration into the semiconductor, the Schottky barrier. A higher Φ_M results in a higher barrier. Significant theoretical and experimental efforts were made to solve the issue of reducing the Schottky barrier in devices [100–109].

14.6.1 Basic Principles

Contacts to a 2D material can be of three major types: top, edge and combined (Fig. 14.18, upper panel), with top contacts being used in most cases. There are several criteria that should be considered when choosing a good contact, such as fundamental physical properties (melting point and electrical and thermal conductances) as well as chemical properties (stability and toxicity) of the metal, its work function, lattice mismatch, and the orbital overlap between the semiconductor and the metal [101]. Thus Ti, with just a 1 % lattice mismatch, was suggested as a good contact to MoS₂ [100].

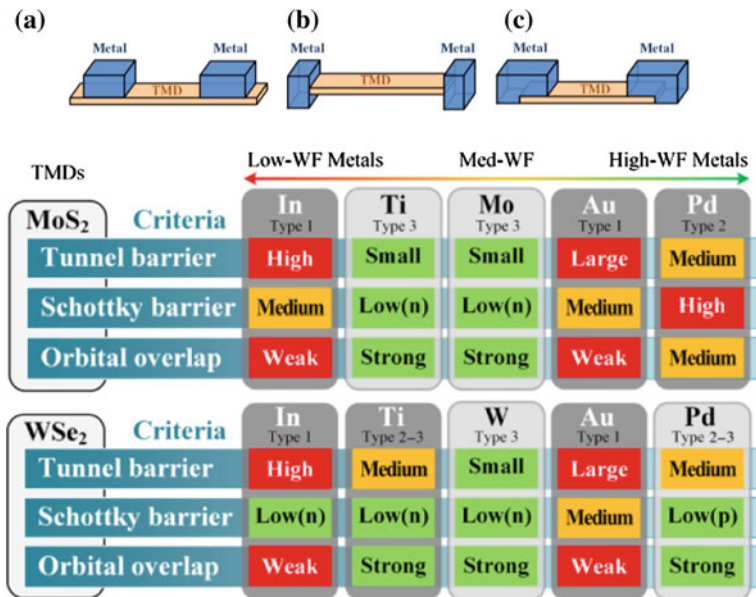


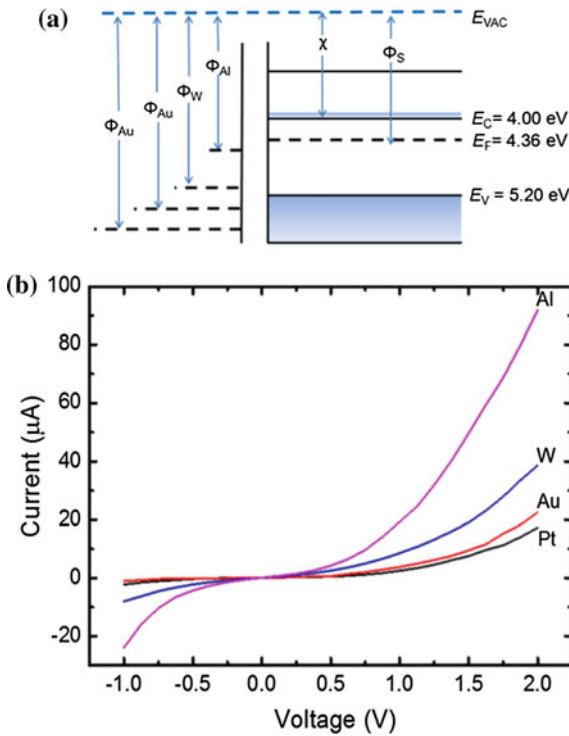
Fig. 14.18 Top panel schematic of metal-TMDC **a** top contact, **b** edge contact, and **c** combined contact. Bottom panel summary of metal-TMDC top-contact electron injection efficiency, in terms of orbital overlap, Schottky barrier, and tunnel barrier. Reproduced from [101]

A comprehensive computational study of metal contacts to monolayer TMDCs was reported in [101]. It was found that Ti and Mo are the best top-contact metals for monolayer intrinsic MoS₂ and are *n*-type contact metals. Pd was considered the best *p*-type top-contact metal for monolayer intrinsic WSe₂, while W can achieve high-quality *n*-type top contacts with WSe₂ due to the strong orbital overlaps and the vanishing of Schottky barriers. These findings are summarized in Fig. 14.18 (lower panel).

It was also argued that edge-contacted configurations can improve the contact by lowering tunnel barriers and strengthening orbital overlap. With the right metal and a certain contact area, in order to achieve the lowest contact resistance, it was proposed to combine edge contacts with top contacts for monolayer TMDCs (Fig. 14.18c). It was further noted that the use of edge contacts can be more significant for multi-layer TMDCs [101], where it becomes necessary to ensure that all of the edges are contacted to the metal, e.g. using the tilt deposition technique [110].

In [111] it was found that despite vdW bonding characteristic of TMDCs many metals form strong covalent bonds to TMDC, but without disturbing the strong intralayer bonding of TMDC itself. Lateral Schottky contacts in MoS₂ and WSe₂ FETs was studied in [112] using scanning photocurrent spectroscopy.

Fig. 14.19 **a** Band diagram illustrations of a metal and MoS₂. χ is the MoS₂ electron affinity, E_F is the Fermi level of MoS₂, E_{vac} is the reference vacuum level, E_v and E_c are the valence and the conduction band levels, respectively. **b** $I - V$ characteristics for different metal/MoS₂ contacts under identical bias conditions [104]. Reprinted with permission. Copyright 2013 by the American Institute of Physics



14.6.2 Role of Metal Contacts: Experiments

As already mentioned, the choice of the metal, and in particular its work function, determine the height of the Schottky barrier. This is illustrated in Fig. 14.19, where the upper panel shows a band diagram illustration and the lower panel shows the $I - V$ characteristics for different MoS₂/metal contacts, where the current is progressively higher for lower work function metals such as Al and W under identical bias conditions indicating their superior room temperature charge injection capabilities for an interface with MoS₂, compared to commonly used contact metals such as Au and Pt [104].

The role of metal contacts was also studied for the FET configuration [113] (Fig. 14.20). The observed linear behavior of the $I_{ds} - V_{ds}$ curve of In-WSe₂ FET indicates that the In-WSe₂ contact is ohmic in nature. Consequently, back-gated In-WSe₂ FETs attained a large ON-current of $210 \mu\text{A}/\mu\text{m}$, whereas an electron mobility of $142 \text{ cm}^2\text{V}^{-1}\text{s}^{-1}$ (with an ON/OFF current ratio exceeding 10^6) was achieved at room temperature. Based on DFT simulations, It was argued that the d -orbitals of the contact metal play a key role in forming low resistance ohmic contacts with monolayer WSe₂. At the same time, it was noted that a good contact material should have a high electrical conductivity and must simultaneously be chemically and thermally stable. Though In exhibited low contact resistance with WSe₂, it has a poor adhesion

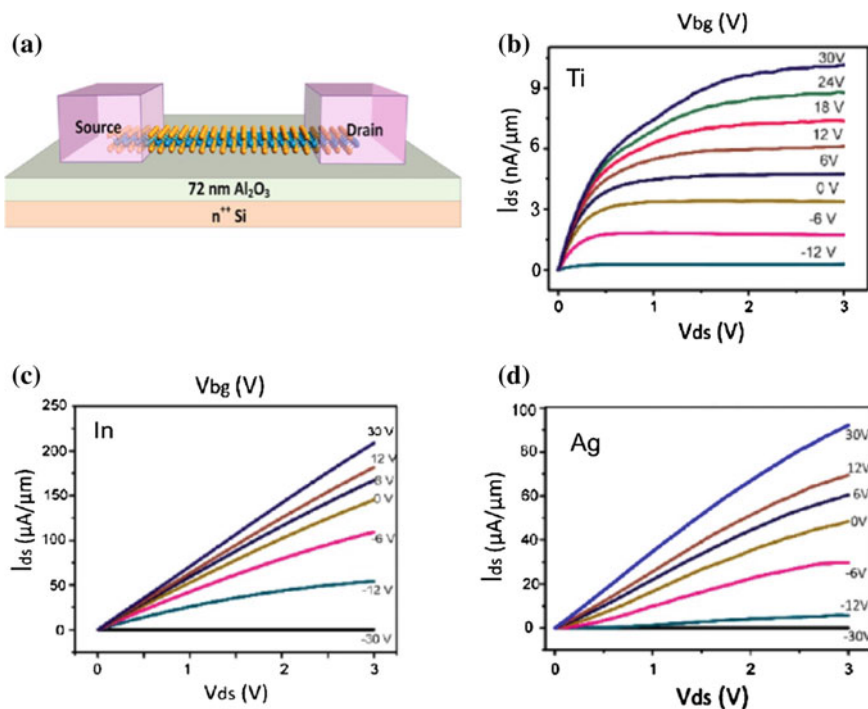


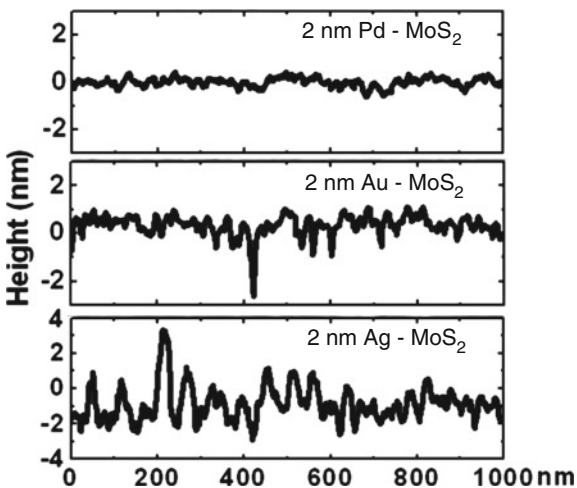
Fig. 14.20 **a** Schematic of back-gated WSe₂ monolayer FET, highly *n*-doped silicon serves as back gate. I_{ds} – V_{ds} curves from devices with **b** Ti (10 nm)/Au (100 nm), **c** In (10 nm)/Au (100 nm), and **d** Ag (10 nm)/Au (100 nm) [113]. Copyright 2013 American Chemical Society. Published with permission

with the substrate as well as a low melting point (156 °C), which may limit its usage as a contact metal [113].

In [102], the formation of metal contacts on MoS₂ was studied. Different metals (Pd, Au, Ag) were *e*-beam-evaporated with an average thickness of 2 nm. It was found (Fig. 14.21) that Pd wets MoS₂ with root-mean-square (rms) roughness of ~0.18 nm forming a uniform contact, while Au assembles in ordered clusters with rms roughness of ~0.36 nm and Ag produces the roughest morphology with a random distribution of islands/clusters of varying sizes with rms roughness of ~0.78 nm.

Graphene electrodes were also used and showed low-resistance contacts [39]. The authors note the following advantages of graphene as a contact: graphene is mechanically strong, flexible, and thermally stable, which is desirable for flexible electronics applications. Furthermore, its work function can be tuned by chemical or electrostatic doping to minimize the Schottky barrier height at the graphene/TMDC interface [39]. Electric-field modulation of Schottky barrier height in graphene/MoS₂ heterostructures was studied in [114, 115]. The possibility to exploit the tunability of the graphene work function by means of chemical functionalization or electrostatic

Fig. 14.21 Roughness of metal-MoS₂ structures for different deposited metals **a** Pd, **b** Au, and **c** Ag [102]. Copyright 2013 American Chemical Society. Published with permission



doping to develop efficient contacts and highly conducting graphene interconnects in advanced electronic circuits was also discussed in [89].

In [116], FET structures with ferromagnetic (Co) contacts to single-layer MoS₂ were studied with the ultimate goal to realize spin injection and spin transport. With the same purpose, gate-voltage controllable Schottky barriers between MoS₂ and permalloy were studied in [117].

The issue of vacancies in TMDCs and their effect on the contact quality was studied in [105]. It was predicted that Schottky barriers of the transition metal dichalcogenides MoSe₂, MoTe₂, WS₂, WSe₂, and WTe₂ would suffer less from Fermi level pinning by chalcogen vacancies than does MoS₂, because their vacancy formation energies are larger. The reduction in vacancy numbers was argued to allow a greater degree of Schottky barrier height tuning by varying the metal work function of the contacts in these compounds.

14.6.3 Ways to Better Contacts

14.6.3.1 Doping

High performance *p*-type FETs based on monolayer WSe₂ as the active channel with chemically doped source/drain contacts and high-*k* gate dielectrics were reported in [103]. Figure 14.22a shows a schematic illustration of a top-gated ML-FET after NO₂ source/drain (S/D) doping. The exposed (underlapped) regions are heavily *p*-doped, while the gated region remains nearly intrinsic due to the protection of the active channel by the gate stack. Figure 14.22b shows the transfer characteristics of a WSe₂ ML-FET before and after NO₂ contact doping. In the figure, the back-gate voltage is fixed at -40 V to electrostatically dope the underlapped regions for both before and after NO₂ exposure. As a result, the difference in the current-voltage characteristics for the two measurements arises from the change of the metal-WSe₂

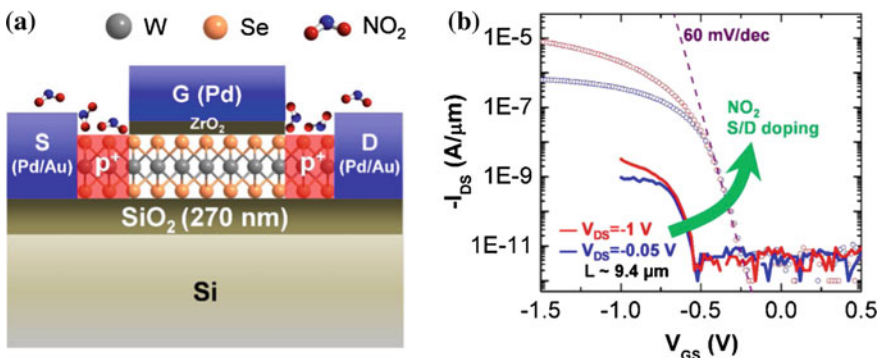


Fig. 14.22 Top-gated WSe₂ ML-FETs with chemically doped contacts. **a** Schematic of a top-gated WSe₂ ML-FET with chemically doped S/D contacts doped by NO₂ exposure. Here the top-gate acts as the mask for protecting the active channel from NO₂ doping. **b** Transfer characteristics of a device with L of $\sim 9.4 \mu\text{m}$ before and after NO₂ patterned doping of the S/D contacts [103]. Copyright 2012 American Chemical Society. Published with permission

contact resistance only, rather than the resistance of the underlapped regions. A drastic enhancement of $\sim 1000\times$ improvement in the ON current was observed in the device after surface doping of the contacts by NO₂, without a change in I_{OFF} . The ML-FET with doped contacts exhibited an ON/OFF ratio of $>10^6$ arising from the large band gap of WSe₂ combined with the monolayer-thick body which minimizes OFF state leakage currents. It was further noted that the transfer characteristics at room temperature show a perfect subthreshold swing, reaching the theoretical limit of $\ln(10) \times kT/q = 60 \text{ mV/dec}$ for a MOSFET [103].

Chloride doping was also successfully used to achieve high performance of MoS₂ FETs with low contact resistance [118].

14.6.3.2 Phase-Patterning

In this approach, one makes use of the fact that TMDCs can exist in two different phases, namely, the stable semiconducting 2H phase and a metastable metallic 1T phase, which differ in their bonding geometry (see Sect. 5.1.2).

In [106, 107], the authors used a chemical approach to induce the 2H – 1T transformation. To perform the phase transformation, samples were immersed into 5 ml of 1.6 M *n*-butyl lithium for 48 hours. Using simple lithography to create well ordered masks, the patterned 1T phase was obtained in the contact regions, while masked regions remained as the 2H phase. Figure 14.23a, b compares $I_d - V_{ds}$ characteristics of back-gated FETs, showing Schottky behaviour for gold deposited directly onto the 2H phase (a) and linear behaviour for the 1T electrodes (b). It was further found that the deposition of different metals had limited influence on FET performance, suggesting that the 1T/2H interface controls carrier injection into the channel [107]. FETs with 1T phase electrodes fabricated and tested in air exhibited mobility values of $\sim 50 \text{ cm}^2 \text{ V}^{-1} \text{ s}^{-1}$, subthreshold swing values below 100 mV per decade, ON/OFF ratios of $>10^7$, drive currents approaching $100 \mu\text{A} \mu\text{m}^{-1}$, and good

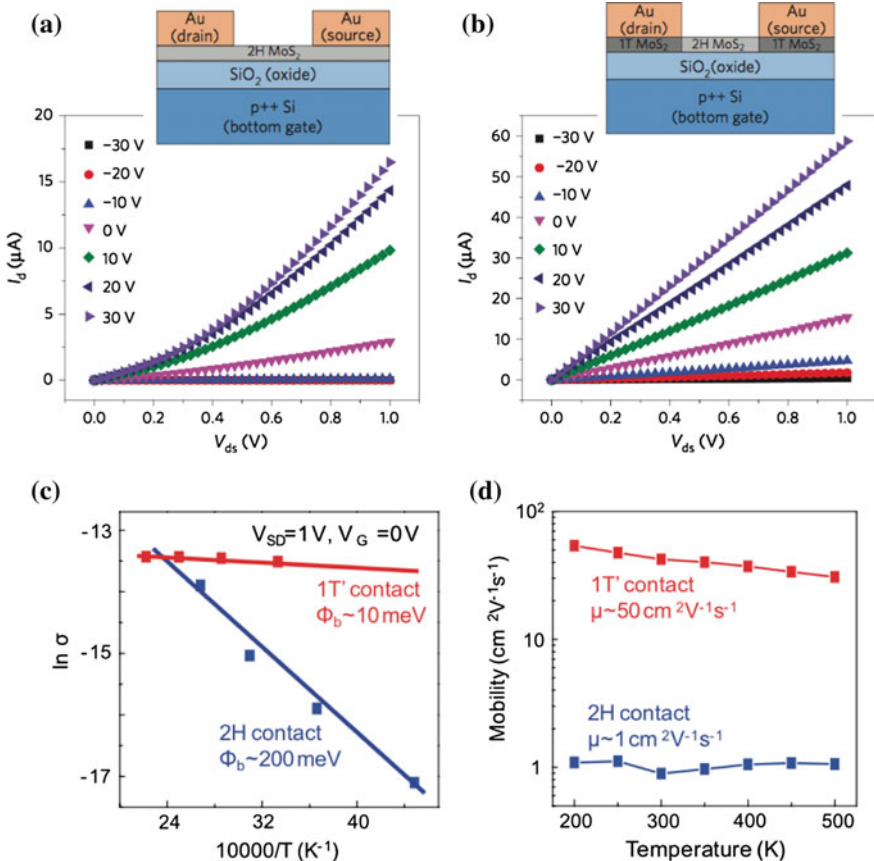


Fig. 14.23 Drain current (I_d) characteristics of back-gated MoS₂ FETs for 0–1 V drain-source voltages (V_{ds}) and gate-source voltages V_{gs} ranging from –30 to 30 V, showing Schottky behaviour for gold directly onto the 2H phase (a) and linear behaviour for the 1T electrodes (b) [107]. Reprinted by permission from Macmillan Publishers Ltd., copyright (2014) c Arrhenius plots of the conductance. (d) Field-effect mobility as a function of temperature [109]. Reprinted with permission from AAAS

current saturation [107]. This approach was subsequently used for fabrication FETs based on monolayer WSe₂ [119] and it was proposed that it can be a generic strategy to fabricate contacts.

In [109], it was noted that since the energy difference between the 2H and 1T phases is the smallest for MoTe₂ (~35 meV [120, 121]), this material may be especially suitable for this approach. In this work, laser-induced phase-patterning was used to induce local phase patterning. The formation of 1T/2H contacts in MoTe₂ resulted in a substantial decrease in the barrier height, concomitant with carrier mobility increase by about a factor of 50, while retaining a high ON/OFF ratio (Fig. 14.23c, d).

14.7 Miscellaneous Applications

14.7.1 Sensors

The high surface-to-volume ratio is a natural asset for applications of 2D TMDCs as chemical sensors, where perturbations to the surface resulting in charge redistribution are readily manifested in the transport characteristics. Several groups demonstrated the applicability of single monolayer and few-layer MoS₂ structures as effective chemical sensors, exhibiting highly selective reactivity to a range of analytes and providing sensitive transduction of transient surface physisorption events to the conductance of the monolayer channel [122–126].

Using a structure with a single monolayer of MoS₂ supported on a SiO₂/Si substrate and contacted with Au contact pads [122] shown in Fig. 14.24a, a strong response upon exposure to triethylamine, a decomposition product of the V-series nerve gas agents, was observed as illustrated in Fig. 14.24b. A highly selective response to electron donors and little response to electron acceptors was observed, consistent with the weak *n*-type character of MoS₂. In Fig. 14.24c, the responses of MoS₂ and carbon nanotube-based sensors to various analytes are compared [122]. Sensitivity of MoS₂ thin films to NO_x and NH₃ was demonstrated in [123, 126, 127].

In [13] it was suggested that the environmental dependence of low-frequency noise can also be used for sensing applications.

Thin-layers MoS₂ transistors and transistor arrays were also used to fabricate NO_x and NH₃ sensors [124–126]. It was shown that compared to the single-layer counterpart, transistors of few MoS₂ layers exhibit excellent sensitivity, recovery, and have the ability to be manipulated by a gate bias. In [125] it was additionally noted that the recovery time can be reduced by exposure to green light and in [124] an increase in sensitivity by up to 3 times through functionalization of MoS₂ with Pt nanoparticles was reported.

A number of biosensing applications were also proposed (see e.g. [128] for a review). Thus, it was demonstrated that single-layer MoS₂ nanosheets could be used as a sensing platform for detection of DNA [129]. Atomistic and quantum simulations showed that single-layer MoS₂ is highly suitable for sequencing of double-stranded DNA (dsDNA) through a MoS₂ nanopore. Time-averaged maximum lengths of dsDNA in the presence of an applied bias were simulated, and it was found that the stretching of the dsDNA increases with the bias (Fig. 14.25a). The snapshots of dsDNA modalities for $V = 0.1$ and 3.0 V revealed that dsDNA knotting occurred frequently in lower biases in the nanopore. The significance of using MoS₂ as a DNA FET (Fig. 14.25b) for nucleobase detection was demonstrated by computing the electronic structure changes induced due to the presence of DNA bases inside the nanopore using DFT [130].

MoS₂ was also used as the channel material for fabricating a new FET-based biosensor for the detection of pH and biomolecules [131]. For the biosensing procedure, the dielectric layer covering the MoS₂ channel was initially modified with biotin to capture streptavidin. With this biosensing procedure the sensitivity, defined

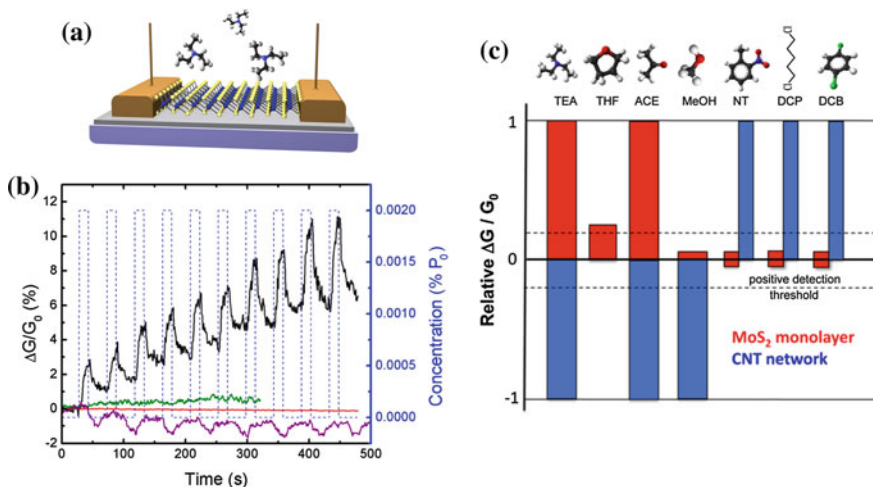


Fig. 14.24 **a** Schematic of the MoS₂ monolayer sensor. **b** Response of sensors to triethylamine (TEA) exposure. Change in conductivity of the monolayer MoS₂ sensor channel upon exposure to a sequence of 0.002 % P_0 TEA pulses (black line). The dashed blue lines show the pulse timing (15 s on/30 s off) and concentration. The solid red line shows the response to exposure of nitrogen only and serves as a control experiment. The solid green and purple lines show the response of the MoS₂ and graphene sensors to water vapor pulses (0.025 % P_0), respectively. **c** Histogram of MoS₂ and carbon nanotube (CNT)-network sensor responses to various analytes. A qualitative summary of the response of the sensors to the analytes tested. The responses are broadly categorized as high, low, or null. The MoS₂ sensor exhibits a much higher selectivity and a complementary response to the CNT-network sensor. The analytes from left to right are triethylamine (TEA), tetrahydrofuran (THF), acetone (ACE), methanol, nitrotoluene (NT), 1,5-dichloropentane (DCP), and 1,4-dichlorobenzene (DCB). Ball-and-stick models of the analyte molecules are shown, in which nitrogen atoms are blue, oxygen atoms are red, carbon atoms are black, chlorine atoms are green, and hydrogen atoms are light gray [122]. Copyright 2013 American Chemical Society. Published with permission

as the ratio of the difference in current before and after biomolecule binding to the lower of the two currents, of 196 even at 100 femtomolar concentration was achieved, showing that that 2D MoS₂ can be good candidate for the next-generation of low-cost FET-based biosensors.

While the majority of sensor application are based on MoS₂, other TMDCs also show promise. Thus, WS₂ biosensors to detect oligonucleotides and proteins were established [132] alongside with a WS₂-based biosensor to detect microRNAs with a detection limit of 300 fM [133].

14.7.2 Nanomechanical Systems

Nanoelectromechanical systems (NEMS) based on atomically thin 2D crystals, such as graphene, have attractive potential for novel actuators and sensors, owing to the ultralow weight and ultrahigh mechanical flexibility of these materials and other

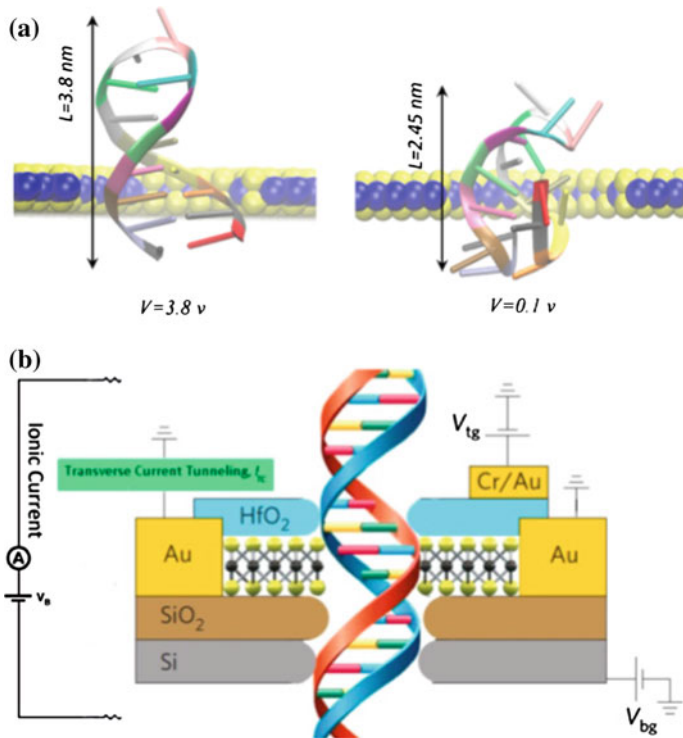


Fig. 14.25 **a** dsDNA modalities for two different applied voltages. The average length of dsDNA during translocation is shown for the two cases. **b** Schematic view of a potential DNA sensing device [130]. Copyright 2014 American Chemical Society. Published with permission

2D attributes that are inaccessible in bulk. In [134] it was demonstrated that MoS_2 NEMS resonators with resonances in the high and very high frequency (HF and VHF) bands, achieve displacement sensitivity of $30.2\text{ fm}/\text{Hz}^{1/2}$, and with fundamental-mode frequency-quality factor product up to $f_0 \times Q \approx 2 \times 10^{10}\text{ Hz}$, a figure of merit that surpasses values reported for graphene-based NEMS counterparts [135, 136]. Nanoresonators based on single-layer MoS_2 were also discussed in [137, 138].

The piezoelectric properties of TMDC monolayers [139, 140] can potentially be used in mechano-electric generators, which can be used, for example, to convert human muscle stretching power to support wearable electronics [141].

14.7.3 Catalysis and Energy Application

Catalytic applications of 2D TMDCs were reported by various groups. Some of the representative publications are [142–151]. As was noted in [152], controlling surface structure at the atomic scale is paramount to developing effective catalysts,

because the edge sites of, e.g. MoS₂ are highly catalytically active and are thus preferred at the catalyst surface over basal planes, which are inert. At the same time, thermodynamics favours the presence of the basal plane, limiting the number of active sites at the surface. To address this issue, vertically aligned layers can be used [153, 154], alternatively contiguous large-area thin films of a highly ordered double-gyroid MoS₂ bicontinuous network with nanoscaled pores was proposed in [152]. A possibility of potential applications of the single-layer MoS₂ as a photocatalyst was considered in [155]. It was also noted that single-layers of the 1T-MoS₂, being metallic, show extraordinary catalytic activity [156].

Nanostructured TMDCs also have potential in energy storage and conversion, e.g. for use as lithium-ion battery electrodes. Reviews can be found in [157–160]. Few-layered TMDC nanosheets were also proposed for use as an advanced electrode material for supercapacitors [161].

14.7.4 Biomedical Applications

2D TMDC may also be used for biomedical applications, including photothermal therapy [162], drug delivery, synergistic therapy, diagnostic imaging, tissue engineering, etc. For a review of these applications the interested reader is referred to recent reviews [128, 163, 164]. Antibacterial activity of two-dimensional MoS₂ sheets was reported in [165].

References

1. R. Ganatra, Q. Zhang, Few-layer MoS₂: a promising layered semiconductor. *ACS Nano* **8**(5), 4074 (2014)
2. R. Fivaz, E. Mooser, Mobility of charge carriers in semiconducting layer structures. *Phys. Rev.* **163**(3), 743 (1967)
3. A. Grant, T. Griffiths, G. Pitt, A. Yoffe, The electrical properties and the magnitude of the indirect gap in the semiconducting transition metal dichalcogenide layer crystals. *J. Phys. C* **8**(1), L17 (1975)
4. B. Radisavljevic, A. Radenovic, J. Brivio, V. Giacometti, A. Kis, Single-layer MoS₂ transistors. *Nat. Nanotech.* **6**(3), 147 (2011)
5. B.W. Baugher, H.O. Churchill, Y. Yang, P. Jarillo-Herrero, Intrinsic electronic transport properties of high-quality monolayer and bilayer MoS₂. *Nano Lett.* **13**(9), 4212 (2013)
6. B. Radisavljevic, A. Kis, Mobility engineering and a metal-insulator transition in monolayer MoS₂. *Nat. Mater.* **12**(9), 815 (2013)
7. D. Lembke, A. Kis, Breakdown of high-performance monolayer MoS₂ transistors. *ACS Nano* **6**(11), 10070 (2012)
8. M. Amani, M.L. Chin, A.G. Birdwell, T.P. O'Regan, S. Najmaei, Z. Liu, P.M. Ajayan, J. Lou, M. Dubey, Electrical performance of monolayer MoS₂ field-effect transistors prepared by chemical vapor deposition. *Appl. Phys. Lett.* **102**(19), 193107 (2013)
9. A. Sanne, R. Ghosh, A. Rai, H. Movva, A. Sharma, R. Rao, L. Mathew, S. Banerjee, Top-gated chemical vapor deposited MoS₂ field-effect transistors on Si₃N₄ substrates. *Appl. Phys. Lett.* **106**(6), 062101 (2015)

10. Y. Yoon, K. Ganapathi, S. Salahuddin, How good can monolayer MoS₂ transistors be? *Nano Lett.* **11**(9), 3768 (2011)
11. D.J. Late, B. Liu, H.R. Matte, V.P. Dravid, C. Rao, Hysteresis in single-layer MoS₂ field effect transistors. *ACS Nano* **6**(6), 5635 (2012)
12. V.K. Sangwan, H.N. Arnold, D. Jariwala, T.J. Marks, L.J. Lauhon, M.C. Hersam, Low-frequency electronic noise in single-layer MoS₂ transistors. *Nano Lett.* **13**(9), 4351 (2013)
13. Y.F. Lin, Y. Xu, C.Y. Lin, Y.W. Suen, M. Yamamoto, S. Nakaharai, K. Ueno, K. Tsukagoshi, Origin of noise in layered MoTe₂ transistors and its possible use for environmental sensors. *Adv. Mater.* **27**, 6612 (2015)
14. M. Zhang, J. Wu, Y. Zhu, D.O. Dumcenco, J. Hong, N. Mao, S. Deng, Y. Chen, Y. Yang, C. Jin et al., Two-dimensional molybdenum tungsten diselenide alloys: photoluminescence, Raman scattering, and electrical transport. *ACS Nano* **8**(7), 7130 (2014)
15. S. Kim, A. Konar, W.S. Hwang, J.H. Lee, J. Lee, J. Yang, C. Jung, H. Kim, J.B. Yoo, J.Y. Choi et al., High-mobility and low-power thin-film transistors based on multilayer MoS₂ crystals. *Nat. Commun.* **3** (2012). doi:[10.1038/ncomms2018](https://doi.org/10.1038/ncomms2018)
16. W. Wu, D. De, S.C. Chang, Y. Wang, H. Peng, J. Bao, S.S. Pei, High mobility and high on/off ratio field-effect transistors based on chemical vapor deposited single-crystal MoS₂ grains. *Appl. Phys. Lett.* **102**(14), 142106 (2013)
17. S. Das, J. Appenzeller, Where does the current flow in two-dimensional layered systems? *Nano Lett.* **13**(7), 3396 (2013)
18. N. Pradhan, D. Rhodes, Q. Zhang, S. Talapatra, M. Terrones, P. Ajayan, L. Balicas, Intrinsic carrier mobility of multi-layered MoS₂ field-effect transistors on SiO₂. *Appl. Phys. Lett.* **102**(12), 123105 (2013)
19. W.S. Hwang, M. Remskar, R. Yan, T. Kosel, J.K. Park, B.J. Cho, W. Haensch, H.G. Xing, A. Seabaugh, D. Jena, Comparative study of chemically synthesized and exfoliated multilayer MoS₂ field-effect transistors. *App. Phys. Lett.* **102**(4), 043116 (2013)
20. S. Larentis, B. Fallahazad, E. Tutuc, Field-effect transistors and intrinsic mobility in ultra-thin MoSe₂ layers. *Appl. Phys. Lett.* **101**(22), 223104 (2012)
21. S. Fathipour, N. Ma, W. Hwang, V. Protasenko, S. Vishwanath, H. Xing, H. Xu, D. Jena, J. Appenzeller, A. Seabaugh, Exfoliated multilayer MoTe₂ field-effect transistors. *App. Phys. Lett.* **105**(19), 192101 (2014)
22. N.R. Pradhan, D. Rhodes, S. Feng, Y. Xin, S. Memaran, B.H. Moon, H. Terrones, M. Terrones, L. Balicas, Field-effect transistors based on few-layered α -MoTe₂. *ACS Nano* **8**(6), 5911 (2014)
23. E. Zhang, Y. Jin, X. Yuan, W. Wang, C. Zhang, L. Tang, S. Liu, P. Zhou, W. Hu, F. Xiu, ReS₂-based field-effect transistors and photodetectors. *Adv. Funct. Mater.* **25**, 4076 (2015)
24. S. Yang, S. Tongay, Y. Li, Q. Yue, J.B. Xia, S.S. Li, J. Li, S.H. Wei, Layer-dependent electrical and optoelectronic responses of ReSe₂ nanosheet transistors. *Nanoscale* **6**(13), 7226 (2014)
25. R. Cheng, S. Jiang, Y. Chen, Y. Liu, N. Weiss, H.C. Cheng, H. Wu, Y. Huang, X. Duan, Few-layer molybdenum disulfide transistors and circuits for high-speed flexible electronics. *Nat. Commun.* **5** (2014). doi:[10.1038/ncomms6143](https://doi.org/10.1038/ncomms6143)
26. F. Liu, J. Wang, H. Guo, Negative differential resistance in monolayer WTe₂ tunneling transistors. *Nanotechnology* **26**(17), 175201 (2015)
27. S. Das, A. Prakash, R. Salazar, J. Appenzeller, Toward low-power electronics: tunneling phenomena in transition metal dichalcogenides. *ACS Nano* **8**(2), 1681 (2014)
28. X.X. Song, D. Liu, V. Mosallanejad, J. You, T.Y. Han, D.T. Chen, H.O. Li, G. Cao, M. Xiao, G.C. Guo et al., A gate defined quantum dot on the two-dimensional transition metal dichalcogenide semiconductor WSe₂. *Nanoscale* **7**, 16867 (2015)
29. X.X. Song, Z.Z. Zhang, J. You, D. Liu, H.O. Li, G. Cao, M. Xiao, G.P. Guo, Temperature dependence of Coulomb oscillations in a few-layer two-dimensional WS₂ quantum dot. *Sci. Rep.* **5** (2015). doi:[10.1038/srep16113](https://doi.org/10.1038/srep16113)
30. R. Levi, O. Bitton, G. Leitus, R. Tenne, E. Joselevich, Field-effect transistors based on WS₂ nanotubes with high current-carrying capacity. *Nano Lett.* **13**(8), 3736 (2013)

31. M. Strojnik, A. Kovic, A. Mrzel, J. Buh, J. Strle, D. Mihailovic, MoS₂ nanotube field effect transistors. *AIP Adv.* **4**, 097114 (2015)
32. S. Fathipour, M. Remskar, A. Varlec, A. Ajoy, R. Yan, S. Vishwanath, S. Rouvimov, W. Hwang, H. Xing, D. Jena et al., Synthesized multiwall MoS₂ nanotube and nanoribbon field-effect transistors. *Appl. Phys. Lett.* **106**(2), 022114 (2015)
33. Y. Zhang, J. Ye, Y. Matsushashi, Y. Iwasa, Ambipolar MoS₂ thin flake transistors. *Nano Lett.* **12**(3), 1136 (2012)
34. W. Bao, X. Cai, D. Kim, K. Sridhara, M.S. Fuhrer, High mobility ambipolar MoS₂ field-effect transistors: substrate and dielectric effects. *Appl. Phys. Lett.* **102**(4), 042104 (2013)
35. Y.F. Lin, Y. Xu, S.T. Wang, S.L. Li, M. Yamamoto, A. Aparecido-Ferreira, W. Li, H. Sun, S. Nakaharai, W.B. Jian et al., Ambipolar MoTe₂ transistors and their applications in logic circuits. *Adv. Mater.* **26**(20), 3263 (2014)
36. D. Braga, I. Gutiérrez, Lezama, H. Berger, A.F. Morpurgo, Quantitative determination of the band gap of WS₂ with ambipolar ionic liquid-gated transistors. *Nano Lett.* **12**(10), 5218 (2012)
37. N.R. Pradhan, D. Rhodes, Y. Xin, S. Memaran, L. Bhaskaran, M. Siddiq, S. Hill, P.M. Ajayan, L. Balicas, Ambipolar molybdenum diselenide field-effect transistors: field-effect and hall mobilities. *ACS Nano* **8**(8), 7923 (2014)
38. S. Jo, N. Ubrig, H. Berger, A.B. Kuzmenko, A.F. Morpurgo, Mono-and bilayer WS₂ light-emitting transistors. *Nano Lett.* **14**(4), 2019 (2014)
39. H.J. Chuang, X. Tan, N.J. Ghimire, M.M. Perera, B. Chamlagain, M.M.C. Cheng, J. Yan, D. Mandrus, D. Tománek, Z. Zhou, High mobility WSe₂ p-and n-type field-effect transistors contacted by highly doped graphene for low-resistance contacts. *Nano Lett.* **14**(6), 3594 (2014)
40. S. Nakaharai, M. Yamamoto, K. Ueno, Y.F. Lin, S. Li, K. Tsukagoshi, Electrostatically reversible polarity of ambipolar α -MoTe₂ transistors. *ACS Nano* **9**(6), 5976 (2015)
41. W. Shi, J. Ye, Y. Zhang, R. Suzuki, M. Yoshida, J. Miyazaki, N. Inoue, Y. Saito, Y. Iwasa, Superconductivity series in transition metal dichalcogenides by ionic gating. *Sci. Rep.* **5** (2015). doi:[10.1038/srep12534](https://doi.org/10.1038/srep12534)
42. T. Georgiou, R. Jalil, B.D. Belle, L. Britnell, R.V. Gorbachev, S.V. Morozov, Y.J. Kim, A. Gholinia, S.J. Haigh, O. Makarovsky et al., Vertical field-effect transistor based on grapheme-WS₂ heterostructures for flexible and transparent electronics. *Nat. Nanotech.* **8**(2), 100 (2013)
43. W.J. Yu, Z. Li, H. Zhou, Y. Chen, Y. Wang, Y. Huang, X. Duan, Vertically stacked multi-heterostructures of layered materials for logic transistors and complementary inverters. *Nat. Mater.* **12**(3), 246 (2013)
44. Y. Deng, Z. Luo, N.J. Conrad, H. Liu, Y. Gong, S. Najmaei, P.M. Ajayan, J. Lou, X. Xu, P.D. Ye, Black phosphorus-monolayer MoS₂ van der Waals heterojunction p-n diode. *ACS Nano* **8**(8), 8292 (2014)
45. B. Radisavljevic, M.B. Whitwick, A. Kis, Small-signal amplifier based on single-layer MoS₂. *App. Phys. Lett.* **101**(4), 043103 (2012)
46. M. Tosun, S. Chuang, H. Fang, A.B. Sachid, M. Hettick, Y. Lin, Y. Zeng, A. Javey, High-gain inverters based on WSe₂ complementary field-effect transistors. *ACS Nano* **8**(5), 4948 (2014)
47. P.J. Jeon, J.S. Kim, J.Y. Lim, Y. Cho, A. Pezeshki, H.S. Lee, S. Yu, S.W. Min, S. Im, Low power consumption complementary inverters with n-MoS₂ and p-WSe₂ dichalcogenide nanosheets on glass for logic and light emitting diode circuits. *ACS Appl. Mater. Interfaces* **7**, 22333 (2015)
48. B. Radisavljevic, M.B. Whitwick, A. Kis, Integrated circuits and logic operations based on single-layer MoS₂. *ACS Nano* **5**(12), 9934 (2011)
49. H. Wang, L. Yu, Y.H. Lee, Y. Shi, A. Hsu, M.L. Chin, L.J. Li, M. Dubey, J. Kong, T. Palacios, Integrated circuits based on bilayer MoS₂ transistors. *Nano Lett.* **12**(9), 4674 (2012)
50. D. Jariwala, V.K. Sangwan, L.J. Lauhon, T.J. Marks, M.C. Hersam, Emerging device applications for semiconducting two-dimensional transition metal dichalcogenides. *ACS Nano* **8**(2), 1102 (2014)
51. M.R. Esmaeili-Rad, S. Salahuddin, High performance molybdenum disulfide amorphous silicon heterojunction photodetector. *Sci. Rep.* **3** (2013). doi:[10.1038/srep02345](https://doi.org/10.1038/srep02345)

52. B.W. Baugher, H.O. Churchill, Y. Yang, P. Jarillo-Herrero, Optoelectronic devices based on electrically tunable pn diodes in a monolayer dichalcogenide. *Nat. Nanotech.* **9**(4), 262 (2014)
53. A. Pospischil, M.M. Furchi, T. Mueller, Solar-energy conversion and light emission in an atomic monolayer pn diode. *Nat. Nanotech.* **9**(4), 257 (2014)
54. H. Wang, C. Zhang, W. Chan, S. Tiwari, F. Rana, Ultrafast response of monolayer molybdenum disulfide (MoS_2) photodetectors. *Nat. Commun.* **6** (2015). doi:[10.1038/ncomms9831](https://doi.org/10.1038/ncomms9831)
55. Z. Yin, H. Li, H. Li, L. Jiang, Y. Shi, Y. Sun, G. Lu, Q. Zhang, X. Chen, H. Zhang, Single-layer MoS_2 phototransistors. *ACS Nano* **6**(1), 74 (2011)
56. W. Zhang, J.K. Huang, C.H. Chen, Y.H. Chang, Y.J. Cheng, L.J. Li, High-gain phototransistors based on a CVD MoS_2 monolayer. *Adv. Mater.* **25**(25), 3456 (2013)
57. N. Perea-López, A.L. Elfas, A. Berkdemir, A. Castro-Beltran, H.R. Gutiérrez, S. Feng, R. Lv, T. Hayashi, F. López-Urías, S. Ghosh et al., Photosensor device based on few-layered WS_2 films. *Adv. Funct. Mater.* **23**(44), 5511 (2013)
58. O. Lopez-Sanchez, D. Lembke, M. Kayci, A. Radenovic, A. Kis, Ultrasensitive photodetectors based on monolayer MoS_2 . *Nat. Nanotech.* **8**(7), 497 (2013)
59. H.S. Lee, S.W. Min, Y.G. Chang, M.K. Park, T. Nam, H. Kim, J.H. Kim, S. Ryu, S. Im, MoS_2 nanosheet phototransistors with thickness-modulated optical energy gap. *Nano Lett.* **12**(7), 3695 (2012)
60. W. Choi, M.Y. Cho, A. Konar, J.H. Lee, G.B. Cha, S.C. Hong, S. Kim, J. Kim, D. Jena, J. Joo et al., High-detectivity multilayer MoS_2 phototransistors with spectral response from ultraviolet to infrared. *Adv. Mater.* **24**(43), 5832 (2012)
61. D. Lembke, S. Bertolazzi, A. Kis, Single-layer MoS_2 electronics. *Acc. Chem. Res.* **48**(1), 100 (2015)
62. H.C. Kim, H. Kim, J.U. Lee, H.B. Lee, D.H. Choi, J.H. Lee, W.H. Lee, S.H. Jhang, B.H. Park, H. Cheong et al., Engineering optical and electronic properties of WS_2 by varying the number of layers. *ACS Nano* **9**(7), 6854 (2015)
63. M.M. Furchi, A. Pospischil, F. Libisch, J. Burgdo rfer, T. Mueller, Photovoltaic effect in an electrically tunable van der Waals heterojunction. *Nano Lett.* **14**(8), 4785 (2014)
64. W.J. Yu, Y. Liu, H. Zhou, A. Yin, Z. Li, Y. Huang, X. Duan, Highly efficient gate-tunable photocurrent generation in vertical heterostructures of layered materials. *Nat. Nanotech.* **8**(12), 952 (2013)
65. D.H. Kang, M.S. Kim, J. Shim, J. Jeon, H.Y. Park, W.S. Jung, H.Y. Yu, C.H. Pang, S. Lee, J.H. Park, High-performance transition metal dichalcogenide photodetectors enhanced by self-assembled monolayer doping. *Adv. Funct. Mater.* **25**, 4219 (2015)
66. H. Yamaguchi, J.C. Blancon, R. Kappera, S. Lei, S. Najmaei, B.D. Magnum, G. Gupta, P.M. Ajayan, J. Lou, M. Chhowalla et al., Spatially resolved photo-excited charge carrier dynamics in phase-engineered monolayer MoS_2 . *ACS Nano* **14**(11), 6456–6462 (2014)
67. M.M. Furchi, D.K. Polyushkin, A. Pospischil, T. Mueller, Mechanisms of photoconductivity in atomically thin MoS_2 . *Nano Lett.* **14**(11), 6165 (2014)
68. C.C. Wu, D. Jariwala, V.K. Sangwan, T.J. Marks, M.C. Hersam, L.J. Lauhon, Elucidating the photoresponse of ultrathin MoS_2 field-effect transistors by scanning photocurrent microscopy. *J. Phys. Chem. Lett.* **4**(15), 2508 (2013)
69. M. Buscema, M. Barkelid, V. Zwiller, H.S. van der Zant, G.A. Steele, A. Castellanos-Gomez, Large and tunable photothermoelectric effect in single-layer MoS_2 . *Nano Lett.* **13**(2), 358 (2013)
70. Y. Zhang, H. Li, L. Wang, H. Wang, X. Xie, S.L. Zhang, R. Liu, Z.J. Qiu, Photothermoelectric and photovoltaic effects both present in MoS_2 . *Sci. Rep.* **5** (2015). doi:[10.1038/srep07938](https://doi.org/10.1038/srep07938)
71. X. Wang, P. Wang, J. Wang, W. Hu, X. Zhou, N. Guo, H. Huang, S. Sun, H. Shen, T. Lin et al., Ultrasensitive and broadband MoS_2 photodetector driven by ferroelectrics. *Adv. Mater.* **27**(42), 6575 (2015)
72. M. Fontana, T. Deppe, A.K. Boyd, M. Rinzan, A.Y. Liu, M. Paranjape, P. Barbara, Electron-hole transport and photovoltaic effect in gated MoS_2 Schottky junctions. *Sci. Rep.* **3** (2013). doi:[10.1038/srep01634](https://doi.org/10.1038/srep01634)

73. M. Shanmugam, T. Bansal, C.A. Durcan, B. Yu, Molybdenum disulphide/titanium dioxide nanocomposite-poly 3-hexylthiophene bulk heterojunction solar cell. *Appl. Phys. Lett.* **100**(15), 153901 (2012)
74. M. Thomalla, H. Tributsch, Photosensitization of nanostructured TiO₂ with WS₂ quantum sheets. *J. Phys. Chem. B* **110**(24), 12167 (2006)
75. O. Lopez-Sanchez, E. Alarcon, Llado, V. Koman, A. Fontcuberta i Morral, A. Radenovic, A. Kis, Light generation and harvesting in a van der Waals heterostructure. *ACS Nano* **8**(3), 3042 (2014)
76. A. Polman, H.A. Atwater, Photonic design principles for ultrahigh-efficiency photovoltaics. *Nat. Mater.* **11**(3), 174 (2012)
77. J. Lin, H. Li, H. Zhang, W. Chen, Plasmonic enhancement of photocurrent in MoS₂ field-effect-transistor. *Appl. Phys. Lett.* **102**(20), 203109 (2013)
78. A. Carladous, R. Coratger, F. Ajustron, G. Seine, R. Péchou, J. Beauvillain, Light emission from spectral analysis of Au/MoS₂ nanocontacts stimulated by scanning tunneling microscopy. *Phys. Rev. B* **66**(4), 045401 (2002)
79. R. Sundaram, M. Engel, A. Lombardo, R. Krupke, A. Ferrari, P. Avouris, M. Steiner, Electroluminescence in single layer MoS₂. *Nano Lett.* **13**(4), 1416 (2013)
80. Y. Ye, Z. Ye, M. Gharghi, H. Zhu, M. Zhao, Y. Wang, X. Yin, X. Zhang, Exciton-dominant electroluminescence from a diode of monolayer MoS₂. *Appl. Phys. Lett.* **104**(19), 193508 (2014)
81. F. Withers, O. Del Pozo-Zamudio, A. Mishchenko, A. Rooney, A. Gholinia, K. Watanabe, T. Taniguchi, S. Haigh, A. Geim, A. Tartakovskii et al., Light-emitting diodes by band-structure engineering in van der Waals heterostructures. *Nat. Mater.* **14**(3), 301 (2015)
82. S. Wu, S. Buckley, A.M. Jones, J.S. Ross, N.J. Ghimire, J. Yan, D.G. Mandrus, W. Yao, F. Hatami, J. Vučković et al., Control of two-dimensional excitonic light emission via photonic crystal. *2D Mater.* **1**(1), 011001 (2014)
83. X. Gan, Y. Gao, K.F. Mak, X. Yao, R.J. Shiue, A. van der Zande, M.E. Trusheim, F. Hatami, T.F. Heinz, J. Hone et al., Controlling the spontaneous emission rate of monolayer MoS₂ in a photonic crystal nanocavity. *App. Phys. Lett.* **103**(18), 181119 (2013)
84. X. Liu, T. Galfsky, Z. Sun, F. Xia, E.-C. Lin, Y.-H. Lee, S. Kéna-Cohen, V.M. Menon, Strong light-matter coupling in two-dimensional atomic crystals. *Nat. Photon.* **9**(1), 30–34 (2015)
85. S. Schwarz, S. Dufferwiel, P. Walker, F. Withers, A. Trichet, M. Sich, F. Li, E. Chekhovich, D. Borisenko, N.N. Kolesnikov et al., Two-dimensional metal-chalcogenide films in tunable optical microcavities. *Nano Lett.* **14**(12), 7003 (2014)
86. Y. Ye, Z.J. Wong, X. Lu, H. Zhu, X. Chen, Y. Wang, X. Zhang, Monolayer excitonic laser. *Nat. Photon.* **9**, 733 (2015)
87. S. Wu, S. Buckley, J.R. Schaibley, L. Feng, J. Yan, D.G. Mandrus, F. Hatami, W. Yao, J. Vučković, A. Majumdar et al., Monolayer semiconductor nanocavity lasers with ultralow thresholds. *Nature* **520**(7545), 69 (2015)
88. Y. Zhang, T. Oka, R. Suzuki, J. Ye, Y. Iwasa, Electrically switchable chiral light-emitting transistor. *Science* **344**(6185), 725 (2014)
89. S. Bertolazzi, D. Krasnozhon, A. Kis, Nonvolatile memory cells based on MoS₂/graphene heterostructures. *ACS Nano* **7**(4), 3246 (2013)
90. M.S. Choi, G.H. Lee, Y.J. Yu, D.Y. Lee, S.H. Lee, P. Kim, J. Hone, W.J. Yoo, Controlled charge trapping by molybdenum disulphide and graphene in ultrathin heterostructured memory devices. *Nat. Commun.* **4** (2013). doi:[10.1038/ncomms2652](https://doi.org/10.1038/ncomms2652)
91. H.S. Lee, S.W. Min, M.K. Park, Y.T. Lee, P.J. Jeon, J.H. Kim, S. Ryu, S. Im, MoS₂ nanosheets for top-gate nonvolatile memory transistor channel. *Small* **8**(20), 3111 (2012)
92. K. Roy, M. Padmanabhan, S. Goswami, T.P. Sai, G. Ramalingam, S. Raghavan, A. Ghosh, Graphene-MoS₂ hybrid structures for multifunctional photoresponsive memory devices. *Nat. Nanotech.* **8**(11), 826 (2013)
93. J. Liu, Z. Zeng, X. Cao, G. Lu, L.H. Wang, Q.L. Fan, W. Huang, H. Zhang, Preparation of MoS₂-polyvinylpyrrolidone nanocomposites for flexible nonvolatile rewritable memory devices with reduced graphene oxide electrodes. *Small* **8**(22), 3517 (2012)

94. Z. Yin, Z. Zeng, J. Liu, Q. He, P. Chen, H. Zhang, Memory devices using a mixture of MoS₂ and graphene oxide as the active layer. *Small* **9**(5), 727 (2013)
95. A.A. Bessonov, M.N. Kirikova, D.I. Petukhov, M. Allen, T. Ryhänen, M.J. Bailey, Layered memristive and memcapacitive switches for printable electronics. *Nat. Mater.* **14**(2), 199 (2015)
96. A. Lipatov, P. Sharma, A. Gruverman, A. Sinitskii, Optoelectrical molybdenum disulfide (MoS₂)-ferroelectric memories. *ACS Nano* **9**(8), 8089 (2015)
97. S. Raoux, M. Wuttig (eds.), *Phase Change Materials: Science and Applications* (Springer Science & Business Media, New York, 2010)
98. R.E. Simpson, P. Fons, A.V. Kolobov, T. Fukaya, M. Krbal, T. Yagi, J. Tominaga, Interfacial phase-change memory. *Nat. Nanotech.* **6**, 501 (2011)
99. J.H. Strait, P. Nene, F. Rana, High intrinsic mobility and ultrafast carrier dynamics in multilayer metal-dichalcogenide MoS₂. *Phys. Rev. B* **90**(24), 245402 (2014)
100. I. Popov, G. Seifert, D. Tománek, Designing electrical contacts to MoS₂ monolayers: a computational study. *Phys. Rev. Lett.* **108**(15), 156802 (2012)
101. J. Kang, W. Liu, D. Sarkar, D. Jena, K. Banerjee, Computational study of metal contacts to monolayer transition-metal dichalcogenide semiconductors. *Phys. Rev. X* **4**(3), 031005 (2014)
102. C. Gong, C. Huang, J. Miller, L. Cheng, Y. Hao, D. Cobden, J. Kim, R.S. Ruoff, R.M. Wallace, K. Cho et al., Metal contacts on physical vapor deposited monolayer MoS₂. *ACS Nano* **7**(12), 11350 (2013)
103. H. Fang, S. Chuang, T.C. Chang, K. Takei, T. Takahashi, A. Javey, High-performance single layered WSe₂ p-FETs with chemically doped contacts. *Nano Lett.* **12**(7), 3788 (2012)
104. S. Walia, S. Balendhran, Y. Wang, R. Ab, Kadir, A.S. Zoolfakar, P. Atkin, J.Z. Ou, S. Sriram, K. alantar-zadeh, M. Bhaskaran, Characterization of metal contacts for two-dimensional MoS₂ nanoflakes. *Appl. Phys. Lett.* **103**(23), 232105 (2013)
105. Y. Guo, D. Liu, J. Robertson, Chalcogen vacancies in monolayer transition metal dichalcogenides and fermi level pinning at contacts. *Appl. Phys. Lett.* **106**(17), 173106 (2015)
106. R. Kappera, D. Voiry, S.E. Yalcin, W. Jen, M. Acerce, S. Torrel, B. Branch, S. Lei, W. Chen, S. Najmaei et al., Metallic 1T phase source/drain electrodes for field effect transistors from chemical vapor deposited MoS₂. *APL Mater.* **2**(9), 092516 (2014)
107. R. Kappera, D. Voiry, S.E. Yalcin, B. Branch, G. Gupta, A.D. Mohite, M. Chhowalla, Phase-engineered low-resistance contacts for ultrathin MoS₂ transistors. *Nat. Mater.* **13**(12), 1128 (2014)
108. D. Jena, K. Banerjee, G.H. Xing, 2D crystal semiconductors: intimate contacts. *Nat. Mater.* **13**(12), 1076 (2014)
109. S. Cho, S. Kim, J.H. Kim, J. Zhao, J. Seok, D.H. Keum, J. Baik, D.H. Choe, K. Chang, K. Sue-naga et al., Phase patterning for ohmic homojunction contact in MoTe₂. *Science* **349**(6248), 625 (2015)
110. H. Li, W. Liu, A.M. Cassell, F. Kreupl, K. Banerjee, Low-resistivity long-length horizontal carbon nanotube bundles for interconnect applications—part I: process development. *IEEE Trans. Electron Devices* **60**(9), 2862 (2013)
111. Y. Guo, J. Robertson, Schottky barrier heights and band alignments in transition metal dichalcogenides. *Microelectron. Eng.* **147**, 184 (2015)
112. Y. Yi, C. Wu, H. Liu, J. Zeng, H. He, J. Wang, A study of lateral Schottky contacts in WSe₂ and MoS₂ field effect transistors using scanning photocurrent microscopy. *Nanoscale* **7**(38), 15711 (2015)
113. W. Liu, J. Kang, D. Sarkar, Y. Khatami, D. Jena, K. Banerjee, Role of metal contacts in designing high-performance monolayer n-type WSe₂ field effect transistors. *Nano Lett.* **13**(5), 1983 (2013)
114. Y. Sata, R. Moriya, S. Morikawa, N. Yabuki, S. Masubuchi, T. Machida, Electric field modulation of Schottky barrier height in graphene/MoS₂ van der Waals heterointerface. *Appl. Phys. Lett.* **107**(2), 023109 (2015)

115. D. Qiu, E.K. Kim, Electrically tunable and negative Schottky barriers in multi-layered graphene/MoS₂ heterostructured transistors. *Sci. Rep.* **5** (2015). doi:[10.1038/srep13743](https://doi.org/10.1038/srep13743)
116. J.R. Chen, P.M. Odenthal, A.G. Swartz, G.C. Floyd, H. Wen, K.Y. Luo, R.K. Kawakami, Control of Schottky barriers in single layer MoS₂ transistors with ferromagnetic contacts. *Nano Lett.* **13**(7), 3106 (2013)
117. W. Wang, Y. Liu, L. Tang, Y. Jin, T. Zhao, F. Xiu, Controllable Schottky barriers between MoS₂ and permalloy. *Sci. Rep.* **4** (2014). doi:[10.1038/srep06928](https://doi.org/10.1038/srep06928)
118. L. Yang, K. Majumdar, Y. Du, H. Liu, H. Wu, M. Hatzistergos, P. Hung, R. Tieckelmann, W.R. Tsai, C. Hobbs et al., High-performance MoS₂ field-effect transistors enabled by chloride doping: record low contact resistance, in *Symposium on VLSI Technology, Digest of Technical Papers* (IEEE, 2014), pp. 1–2
119. Y. Ma, B. Liu, A. Zhang, L. Chen, M. Fathi, C. Shen, A.N. Abbas, M. Ge, M. Mecklenburg, C. Zhou, Reversible semiconducting-to-metallic phase transition in chemical vapor deposition grown monolayer WSe₂ and applications for devices. *ACS Nano* **9**(7), 7383 (2015)
120. K.A.N. Duerloo, Y. Li, E.J. Reed, Structural phase transitions in two-dimensional Mo-and W-dichalcogenide monolayers. *Nat. Commun.* **5** (2014). doi:[10.1038/ncomms5214](https://doi.org/10.1038/ncomms5214)
121. D.H. Keum, S. Cho, J.H. Kim, D.H. Choe, H.J. Sung, M. Kan, H. Kang, J.Y. Hwang, S.W. Kim, H. Yang et al., Bandgap opening in few-layered monoclinic MoTe₂. *Nat. Phys.* **11**(6), 482 (2015)
122. F.K. Perkins, A.L. Friedman, E. Cobas, P. Campbell, G. Jernigan, B.T. Jonker, Chemical vapor sensing with monolayer MoS₂. *Nano Lett.* **13**(2), 668 (2013)
123. K. Lee, R. Gatensby, N. McEvoy, T. Hallam, G.S. Duesberg, High-performance sensors based on molybdenum disulfide thin films. *Adv. Mater.* **25**(46), 6699 (2013)
124. Q. He, Z. Zeng, Z. Yin, H. Li, S. Wu, X. Huang, H. Zhang, Fabrication of flexible MoS₂ thin-film transistor arrays for practical gas-sensing applications. *Small* **8**(19), 2994 (2012)
125. D.J. Late, Y.K. Huang, B. Liu, J. Acharya, S.N. Shirodkar, J. Luo, A. Yan, D. Charles, U.V. Waghmare, V.P. Dravid, C. Rao, Sensing behavior of atomically thin-layered MoS₂ transistors. *ACS Nano* **7**(6), 4879 (2013)
126. H. Li, Z. Yin, Q. He, H. Li, X. Huang, G. Lu, D.W.H. Fam, A.I.Y. Tok, Q. Zhang, H. Zhang, Fabrication of single-and multilayer MoS₂ film-based field-effect transistors for sensing no at room temperature. *Small* **8**(1), 63 (2012)
127. B. Cho, M.G. Hahn, M. Choi, J. Yoon, A.R. Kim, Y.J. Lee, S.G. Park, J.D. Kwon, C.S. Kim, M. Song et al., Charge-transfer-based gas sensing using atomic-layer MoS₂. *Sci. Rep.* **5** (2015). doi:[10.1038/srep08052](https://doi.org/10.1038/srep08052)
128. G. Yang, C. Zhu, D. Du, J. Zhu, Y. Lin, Graphene-like two-dimensional layered nanomaterials: applications in biosensors and nanomedicine. *Nanoscale* **7**(34), 14217 (2015)
129. C. Zhu, Z. Zeng, H. Li, F. Li, C. Fan, H. Zhang, Single-layer MoS₂-based nanoprobe for homogeneous detection of biomolecules. *J. Am. Chem. Soc.* **135**(16), 5998 (2013)
130. A.B. Farimani, K. Min, N.R. Aluru, DNA base detection using a single-layer MoS₂. *ACS Nano* **8**(8), 7914 (2014)
131. D. Sarkar, W. Liu, X. Xie, A.C. Anselmo, S. Mitragotri, K. Banerjee, MoS₂ field-effect transistor for next-generation label-free biosensors. *ACS Nano* **8**(4), 3992 (2014)
132. Y. Yuan, R. Li, Z. Liu, Establishing water-soluble layered WS₂ nanosheet as a platform for biosensing. *Anal. Chem.* **86**(7), 3610 (2014)
133. Q. Xi, D.M. Zhou, Y.Y. Kan, J. Ge, Z.K. Wu, R.Q. Yu, J.H. Jiang, Highly sensitive and selective strategy for microrna detection based on WS₂ nanosheet mediated fluorescence quenching and duplex-specific nuclease signal amplification. *Anal. Chem.* **86**(3), 1361 (2014)
134. J. Lee, Z. Wang, K. He, J. Shan, P.X.L. Feng, High frequency MoS₂ nanomechanical resonators. *ACS Nano* **7**(7), 6086 (2013)
135. J.S. Bunch, A.M. Van Der Zande, S.S. Verbridge, I.W. Frank, D.M. Tanenbaum, J.M. Parpia, H.G. Craighead, P.L. McEuen, Electromechanical resonators from graphene sheets. *Science* **315**(5811), 490 (2007)
136. C. Chen, S. Rosenblatt, K.I. Bolotin, W. Kalb, P. Kim, I. Kymissis, H.L. Stormer, T.F. Heinz, J. Hone, Performance of monolayer graphene nanomechanical resonators with electrical read-out. *Nat. Nanotech.* **4**(12), 861 (2009)

137. H.J. Chen, K.D. Zhu, Coherent optical responses and their application in biomolecule mass sensing based on a monolayer MoS₂ nanoresonator. *J. Opt. Soc. Am. B* **31**(7), 1684 (2014)
138. A. Castellanos-Gomez, R. van Leeuwen, M. Buscema, H.S. van der Zant, G.A. Steele, W.J. Venstra, Single-layer MoS₂ mechanical resonators. *Adv. Mater.* **25**(46), 6719 (2013)
139. W. Wu, L. Wang, Y. Li, F. Zhang, L. Lin, S. Niu, D. Chenet, X. Zhang, Y. Hao, T.F. Heinz et al., Piezoelectricity of single-atomic-layer MoS₂ for energy conversion and piezotronics. *Nature* **514**(7523), 470 (2014)
140. H. Zhu, Y. Wang, J. Xiao, M. Liu, S. Xiong, Z.J. Wong, Z. Ye, Y. Ye, X. Yin, X. Zhang, Observation of piezoelectricity in free-standing monolayer MoS₂. *Nat. Nanotech.* **10**(2), 151 (2015)
141. S. Yu, K. Eshun, H. Zhu, Q. Li, Novel two-dimensional mechano-electric generators and sensors based on transition metal dichalcogenides. *Sci. Rep.* **5** (2015). doi:[10.1038/srep12854](https://doi.org/10.1038/srep12854)
142. T.F. Jaramillo, K.P. Jørgensen, J. Bonde, J.H. Nielsen, S. Horch, I. Chorkendorff, Identification of active edge sites for electrochemical H₂ evolution from MoS₂ nanocatalysts. *Science* **317**(5834), 100 (2007)
143. M.A. Lukowski, A.S. Daniel, F. Meng, A. Forticaux, L. Li, S. Jin, Enhanced hydrogen evolution catalysis from chemically exfoliated metallic MoS₂ nanosheets. *J. Am. Chem. Soc.* **135**(28), 10274 (2013)
144. J. Xie, H. Zhang, S. Li, R. Wang, X. Sun, M. Zhou, J. Zhou, X.W.D. Lou, Y. Xie, Defect-rich MoS₂ ultrathin nanosheets with additional active edge sites for enhanced electrocatalytic hydrogen evolution. *Adv. Mater.* **25**(40), 5807 (2013)
145. D. Voiry, M. Salehi, R. Silva, T. Fujita, M. Chen, T. Asefa, V.B. Shenoy, G. Eda, M. Chhowalla, Conducting MoS₂ nanosheets as catalysts for hydrogen evolution reaction. *Nano Lett.* **13**(12), 6222 (2013)
146. J. Xie, J. Zhang, S. Li, F. Grote, X. Zhang, H. Zhang, R. Wang, Y. Lei, B. Pan, Y. Xie, Controllable disorder engineering in oxygen-incorporated MoS₂ ultrathin nanosheets for efficient hydrogen evolution. *J. Am. Chem. Soc.* **135**(47), 17881 (2013)
147. Y. Yu, S.Y. Huang, Y. Li, S.N. Steinmann, W. Yang, L. Cao, Layer-dependent electrocatalysis of MoS₂ for hydrogen evolution. *Nano Lett.* **14**(2), 553 (2014)
148. N. Singh, G. Jabbour, U. Schwingenschlögl, Optical and photocatalytic properties of two-dimensional MoS₂. *Eur. Phys. J. B* **85**(11), 1 (2012)
149. K. Chang, Z. Mei, T. Wang, Q. Kang, S. Ouyang, J. Ye, MoS₂/graphene cocatalyst for efficient photocatalytic H₂ evolution under visible light irradiation. *ACS Nano* **8**(7), 7078 (2014)
150. L.T.L. Lee, J. He, B. Wang, Y. Ma, K.Y. Wong, Q. Li, X. Xiao, T. Chen, Few-layer MoSe₂ possessing high catalytic activity towards iodide/tri-iodide redox shuttles. *Sci. Rep.* **4** (2014). doi:[10.1038/srep04063](https://doi.org/10.1038/srep04063)
151. C.S. Lim, S.M. Tan, Z. Sofer, M. Pumera, Impact electrochemistry of layered transition metal dichalcogenides. *ACS Nano* **9**(8), 8474 (2015)
152. J. Kibsgaard, Z. Chen, B.N. Reinecke, T.F. Jaramillo, Engineering the surface structure of MoS₂ to preferentially expose active edge sites for electrocatalysis. *Nat. Mater.* **11**(11), 963 (2012)
153. D. Kong, H. Wang, J.J. Cha, M. Pasta, K.J. Koski, J. Yao, Y. Cui, Synthesis of MoS₂ and MoSe₂ films with vertically aligned layers. *Nano Lett.* **13**(3), 1341 (2013)
154. H. Wang, D. Kong, P. Johanes, J.J. Cha, G. Zheng, K. Yan, N. Liu, Y. Cui, MoSe₂ and WSe₂ nanofilms with vertically aligned molecular layers on curved and rough surfaces. *Nano Lett.* **13**(7), 3426 (2013)
155. Y. Li, Y.L. Li, C.M. Araujo, W. Luo, R. Ahuja, Single-layer MoS₂ as an efficient photocatalyst. *Catal. Sci. Technol.* **3**(9), 2214 (2013)
156. U. Maitra, U. Gupta, M. De, R. Datta, A. Govindaraj, C. Rao, Highly effective visible-light-induced H₂ generation by single-layer 1T-MoS₂ and a nanocomposite of few-layer 2H-MoS₂ with heavily nitrogen-doped graphene. *Angew. Chem. Int. Ed.* **52**, 13057 (2013)
157. T. Stephenson, Z. Li, B. Olsen, D. Mitlin, Lithium ion battery applications of molybdenum disulfide (MoS₂) nanocomposites. *Energy Environ. Sci.* **7**(1), 209 (2014)

158. M.R. Gao, Y.F. Xu, J. Jiang, S.H. Yu, Nanostructured metal chalcogenides: synthesis, modification, and applications in energy conversion and storage devices. *Chem. Soc. Rev.* **42**(7), 2986 (2013)
159. H. Wang, H. Feng, J. Li, Graphene and graphene-like layered transition metal dichalcogenides in energy conversion and storage. *Small* **10**(11), 2165 (2014)
160. D. Chen, W. Chen, L. Ma, G. Ji, K. Chang, J.Y. Lee, Graphene-like layered metal dichalcogenide/graphene composites: synthesis and applications in energy storage and conversion. *Mater. Today* **17**(4), 184 (2014)
161. S.K. Balasingam, J.S. Lee, Y. Jun, Few-layered MoSe₂ nanosheets as an advanced electrode material for supercapacitors. *Dalton Trans.* **44**(35), 15491 (2015)
162. S. Wang, X. Li, Y. Chen, X. Cai, H. Yao, W. Gao, Y. Zheng, X. An, J. Shi, H. Chen, A facile one-pot synthesis of a two-dimensional MoS₂/Bi₂S₃ composite theranostic nanosystem for multi-modality tumor imaging and therapy. *Adv. Mater.* **27**(17), 2775 (2015)
163. Y. Chen, C. Tan, H. Zhang, L. Wang, Two-dimensional graphene analogues for biomedical applications. *Chem. Soc. Rev.* **44**(9), 2681 (2015)
164. K. Kalantar-zadeh, J.Z. Ou, T. Daeneke, M.S. Strano, M. Pumera, S.L. Gras, Two-dimensional transition metal dichalcogenides in biosystems. *Adv. Funct. Mater.* **25**(32), 5086 (2015)
165. X. Yang, J. Li, T. Liang, C. Ma, Y. Zhang, H. Chen, N. Hanagata, H. Su, M. Xu, Antibacterial activity of two-dimensional MoS₂ sheets. *Nanoscale* **6**(17), 10126 (2014)

Chapter 15

The Neverending Story

As noted in a recent editorial in Nature [1], “2D TMDCs now generate six publications each day”. With this volume of existing publications and such a pace, it is virtually impossible to keep this book up to-date. After this manuscript was submitted, numerous new publications appeared, which deserve to be included into this volume. Since it was difficult to incorporate them into the main text at this stage, the authors have chosen to summarise them in this Afterword as additions to the earlier Chapters. When the new publications provide additional information to that already described in the main body of this monograph, only the references with (self-explanatory) titles are given. In cases when the reported results are novel, a brief summary is also provided. For more information, the readers are referred to the original publications.

Chapter 3: Bulk TMDCs: Review of Structure and Properties

Y. Luo, H. Li, Y.M. Dai, H. Miao, Y.G. Shi, H. Ding, A. Taylor, D. Yarotski, R. Prasankumar, J. Thompson, Hall effect in the extremely large magnetoresistance semimetal WTe₂. *Appl. Phys. Lett.* **107**(18), 182411 (2015)

Y. Wang, L. Thoutam, Z. Xiao, J. Hu, S. Das, Z. Mao, J. Wei, R. Divan, A. Luican-Mayer, G. Crabtree et al., Origin of the turn-on temperature behavior in WTe₂. *Phys. Rev. B* **92**(18), 180402 (2015)

T.R. Chang, S.Y. Xu, G. Chang, C.C. Lee, S.M. Huang, B. Wang, G. Bian, H. Zheng, D.S. Sanchez, I. Belopolski, et al., Prediction of an arc-tunable Weyl Fermion metallic state in Mo_xW_{1-x}Te₂. *Nat. Commun.* **7** (2016). doi:[10.1038/ncomms10639](https://doi.org/10.1038/ncomms10639)

P.K. Das, D. Di Sante, I. Vobornik, J. Fujii, T. Okuda, E. Bruyer, A. Gyenis, B. Feldman, J. Tao, R. Ciancio, et al., Layer-dependent quantum cooperation of electron and hole states in the anomalous semimetal WTe₂. *Nat. Commun.* **7** (2016). doi:[10.1038/ncomms10847](https://doi.org/10.1038/ncomms10847)

M. Annamalai, K. Gopinadhan, S.A. Han, S. Saha, H.J. Park, E.B. Cho, B. Kumar, A. Patra, S.W. Kim, T. Venkatesan, Surface energy and wettability of van der Waals structures. *Nanoscale* **8**(10), 5764 (2016)

S. Duwal, C.S. Yoo, Shear-induced isostructural phase transition and metallization of layered tungsten disulfide under nonhydrostatic compression. *J. Phys. Chem. C* **120**(9), 5101 (2016)

R. Ang, Z. Wang, C. Chen, J. Tang, N. Liu, Y. Liu, W. Lu, Y. Sun, T. Mori, Y. Ikuhara, Atomistic origin of an ordered superstructure induced superconductivity in layered chalcogenides. *Nat. Commun.* **6** (2015). doi:[10.1038/ncomms7091](https://doi.org/10.1038/ncomms7091)

Y. Wang, K. Wang, J. Reutt-Robey, J. Paglione, M.S. Fuhrer, Breakdown of compensation and persistence of nonsaturating magnetoresistance in gated WTe₂ thin flakes. *Phys. Rev. B* **93**(12), 121108 (2016)

In Y. Wang et al., it is argued that the extremely large nonsaturating magnetoresistance in WTe₂ persists even when electrons and holes are not compensated, as determined by the Hall effect and electrolyte gating effect, which suggests that perfect electron-hole compensation is not the mechanism for the extremely large nonsaturating magnetoresistance.

Chapter 4: From 3D to 2D: Fabrication Methods

G.S. Bang, S. Cho, N. Son, G.W. Shim, B.K. Cho, S.Y. Choi, DNA-assisted exfoliation of tungsten dichalcogenides and their antibacterial effect. *ACS Appl. Mater. Interfaces* **8**, 1943 (2016)

P.V. Sarma, P.D. Patil, P.K. Barman, R.N. Kini, M.M. Shajumon, Controllable growth of few-layer spiral WS₂. *RSC Adv.* **6**(1), 376 (2016)

Y. Sun, Y. Wang, D. Sun, B.R. Carvalho, C.G. Read, C.h. Lee, Z. Lin, K. Fujisawa, J.A. Robinson, V.H. Crespi, et al., Low-temperature solution synthesis of few-layer 1T'-MoTe₂. Nanostructures Exhibiting Lattice Compression. *Angew. Chem. Int. Ed.* **55**(8), 2830 (2016)

D. Wang, Y. Wang, X. Chen, Y. Zhu, K. Zhan, H. Cheng, X. Wang, Layer-by-layer thinning of two-dimensional MoS₂ film by focused ion beam. *Nanoscale* **8**, 4107 (2016)

Z. Liu, L. Zhang, R. Wang, S. Poyraz, J. Cook, M.J. Bozack, S. Das, X. Zhang, L. Hu, Ultrafast microwave nano-manufacturing of fullerene-like metal chalcogenides. *Sci. Rep.* **6** (2016). doi:[10.1038/srep22503](https://doi.org/10.1038/srep22503)

M. Annamalai, K. Gopinadhan, S.A. Han, S. Saha, H.J. Park, E.B. Cho, B. Kumar, A. Patra, S.W. Kim, T. Venkatesan, Surface energy and wettability of van der Waals structures. *Nanoscale* **8**(10), 5764 (2016)

G. Zhao, Y. Wu, Y. Shao, X. Hao, Large-quantity and continuous preparation of two-dimensional nanosheets. *Nanoscale* **8**(10), 5407 (2016)

Y. Kim, J.G. Song, Y.J. Park, G.H. Ryu, S.J. Lee, J.S. Kim, P.J. Jeon, C.W. Lee, W.J. Woo, T. Choi, et al., Self-limiting layer synthesis of transition metal dichalcogenides. *Sci. Rep.* **6** (2016). doi:[10.1038/srep18754](https://doi.org/10.1038/srep18754)

- D. Gerchman, A.K. Alves, Solution-processable exfoliation and suspension of atomically thin WSe₂. *J. Colloid Interface Sci.* **468**, 247 (2016)
- G. Deokar, D. Vignaud, R. Arenal, P. Louette, J. Colomer, Synthesis and characterization of MoS₂ nanosheets. *Nanotechnology* **27**(7), 075604 (2016)
- M.B. Alemayehu, M. Falmbigl, K. Ta, J. Ditto, D.L. Medlin, D.C. Johnson, Designed synthesis of van der Waals heterostructures: The power of kinetic control. *Angew. Chem. Int. Ed.* **127**(51), 15688–15692 (2015)
- A. Roy, H.C. Movva, B. Satpati, K. Kim, R. Dey, A. Rai, T. Pramanik, S. Guchhait, E. Tutuc, S.K. Banerjee, Structural and Electrical Properties of MoTe₂ and MoSe₂ Grown by Molecular Beam Epitaxy. *ACS Appl. Mater. Interfaces* **8**, 7396 (2016)

Chapter 5: Structure and Physico-Chemical Properties of Single Layer and Few-layer TMDCs

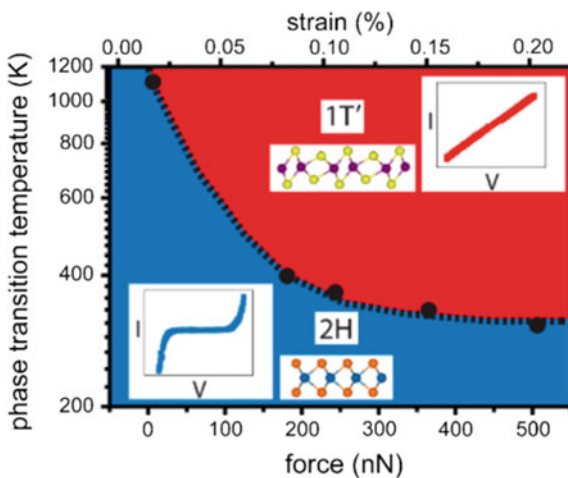
- S. Xiong, G. Cao, Bending response of single layer MoS₂. *Nanotechnology* **27**(10), 105701 (2016)
- C. González, B. Biel, Y.J. Dappe, Theoretical characterisation of point defects on a MoS₂ monolayer by scanning tunnelling microscopy. *Nanotechnology* **27**(10), 105702 (2016)
- E. Kim, C. Ko, K. Kim, Y. Chen, J. Suh, S.G. Ryu, K. Wu, X. Meng, A. Suslu, S. Tongay et al., Site selective doping of ultrathin metal dichalcogenides by laser-assisted reaction. *Adv. Mater.* **28**, 341 (2016)
- F. Ersan, G. Gökoğlu, E. Aktürk, Adsorption and diffusion of lithium on monolayer transition metal dichalcogenides (MoS_{2(1-x)Se_{2x}}) Alloys. *J. Phys. Chem. C* **119**(51), 28648 (2015)
- O.V. Yazyev, Y.P. Chen, Polycrystalline graphene and other two-dimensional materials. *Nat. Nanotech.* **9**(10), 755 (2014)
- A. Kandemir, H. Yapıcıoglu, A. Kinaci, T. Çağın, C. Sevik, Thermal transport properties of MoS₂ and MoSe₂ monolayers. *Nanotechnology* **27**(5), 055703 (2016)
- M. Velický, M.A. Bissett, C.R. Woods, P.S. Toth, T. Georgiou, I.A. Kinloch, K.S. Novoselov, R.A.W. Dryfe, Photoelectrochemistry of pristine mono- and few-layer MoS₂. *Nano Letters* **16**(3), 2023–2032 (2016)

A large fraction of recent papers is dedicated to the phase stability and the 2H-1T' transition

- S. Song, D. Keum, S. Cho, D.J. Perello, Y. Kim, Y.H. Lee, Room-temperature semiconductor-metal transition of MoTe₂ thin film engineered by strain. *Nano Lett.* **16**, 188 (2015)

In S. Song et al. a room-temperature semiconductor-metal transition in thin film MoTe₂ engineered by strain was demonstrated, where reduction of the 2H-1T' phase transition temperature of MoTe₂ to room temperature was realized by introducing a tensile strain of 0.2 % (Fig. 15.1).

Fig. 15.1 Temperature-force phase diagram for semiconducting 2H and metallic 1T' MoTe₂. Copyright 2015 American Chemical Society. Published with permission from Song et al. [2]



Y. Guo, D. Sun, B. Ouyang, A. Raja, J. Song, T.F. Heinz, L.E. Brus, Probing the dynamics of the metallic-to-semiconducting structural phase transformation in MoS₂ crystals. *Nano Lett.* **15**(8), 5081 (2015)

Y. Kang, S. Najmaei, Z. Liu, Y. Bao, Y. Wang, X. Zhu, N.J. Halas, P. Nordlander, P.M. Ajayan, J. Lou et al., Plasmonic hot electron induced structural phase transition in a MoS₂ monolayer. *Adv. Mater.* **26**(37), 6467 (2014)

H. Huang, X. Fan, D.J. Singh, H. Chen, Q. Jiang, W. Zheng, Phys. Chem. Chem. Phys. Controlling phase transition for single-layer MTe₂ (M= Mo and W): modulation of the potential barrier under strain. **18**, 4086 (2016)

B. Ouyang, G. Lan, Y. Guo, Z. Mi, J. Song, Phase engineering of monolayer transition-metal dichalcogenide through coupled electron doping and lattice deformation. *Appl. Phys. Lett.* **107**(19), 191903 (2015)

M. Pandey, P. Bothra, S.K. Pati, Phase transition of MoS₂ bilayer structures. *J. Phys. Chem. C* **120**(7), 3776 (2016)

Q. Tang, D. Jiang, Stabilization and band-gap tuning of the 1T-MoS₂ monolayer by covalent functionalization. *Chem. Mater.* **27**(10), 3743 (2015)

W. Li, J. Li, Ferroelasticity and domain physics in two-dimensional transition metal dichalcogenide monolayers. *Nat. Commun.* **7** (2016). doi:[10.1038/ncomms10843](https://doi.org/10.1038/ncomms10843)

Y. Li, K.A.N. Duerloo, K. Wauson, E.J. Reed, Structural semiconductor-to-semimetal phase transition in two-dimensional materials induced by electrostatic gating. *Nat. Commun.* **7** (2016). doi:[10.1038/ncomms10671](https://doi.org/10.1038/ncomms10671)

K.A.N. Duerloo, E.J. Reed, Structural phase transitions by design in monolayer alloys. *ACS Nano* **10**, 289 (2016)

Chapter 6: Electronic Band Structure of 2D TMDCs

- E.A. Pogna, M. Marsili, D. De Fazio, S. Dal, C. Conte, D. Manzoni, D. Sangalli, A. Yoon, A.C. Lombardo, A. Marini, Ferrari et al., Photo-induced bandgap renormalization governs the ultrafast response of single-layer MoS₂. ACS Nano **10**, 1182 (2016)
- C. Zhang, Y. Chen, J.K. Huang, X. Wu, L.J. Li, W. Yao, J. Tersoff, C.K. Shih, Visualizing band offsets and edge states in bilayer-monolayer transition metal dichalcogenides lateral heterojunction. Nat. Commun. **7** (2016). doi:[10.1038/ncomms10349](https://doi.org/10.1038/ncomms10349)
- J.O. Island, A. Kuc, E.H. Diependaal, R. Bratschitsch, H.S. van der Zant, T. Heine, A. Castellanos-Gomez, Precise and reversible band gap tuning in single-layer MoSe₂ by uniaxial strain. Nanoscale **8**, 2589 (2016)
- X. Dou, K. Ding, D. Jiang, X. Fan, B. Sun, Probing spin-orbit coupling and interlayer coupling in atomically thin molybdenum disulfide using hydrostatic pressure. ACS Nano **10**, 1619 (2016)
- W. Li, T. Wang, X. Dai, X. Wang, C. Zhai, Y. Ma, S. Chang, Bandgap engineering of different stacking WS₂ bilayer under an external electric field. Solid State Commun. **225**, 32 (2016)
- H. Terrones, M. Terrones, Electronic and vibrational properties of defective transition metal dichalcogenide Haecelites: new 2D semi-metallic systems. 2D Materials **1**(1), 011003 (2014)
- L. Zhu, T. Zhang, Suppressing band gap of MoS₂ by the incorporation of four-and eight-membered rings. J. of Nanoparticle Res. **17**(5), 220 (2015)
- Y. Sun, C. Felser, B. Yan, Graphene-like dirac states and quantum spin Hall insulators in square-octagonal MX₂ (M= Mo, W; X= S, Se, Te) isomers. Phys. Rev. B **92**(16), 165421 (2015)
- S. Nie, Z. Song, H. Weng, Z. Fang, Quantum spin Hall effect in two-dimensional transition-metal dichalcogenide haecelites. Phys. Rev. B **91**(23), 235434 (2015)
- B. Li, T. Liu, D.W. Hewak, Z. Shen, Q.J. Wang, Ultrastrong light-matter coupling of cyclotron transition in monolayer MoS₂. Phys. Rev. B **93**(4), 045420 (2016)
- H.L. Zhu, C. Zhou, X.J. Huang, X.L. Wang, H.Z. Xu, Y. Lin, W. Yang, Y. Wu, W. Lin, F. Guo, Evolution of band structures in MoS₂-based homo-and heterobilayers. J. Phys. D: Appl. Phys. **49**(6), 065304 (2016)

Chapter 7: Raman Scattering of 2D TMDCs

- J. Ji, A. Zhang, J. Fan, Y. Li, X. Wang, J. Zhang, E. Plummer, Q. Zhang, Giant magneto-optical Raman effect in a layered transition metal compound. Proc. Nat. Acad. Sci. **113**(9), 2349 (2016)

In J. Ji et al., the authors report a dramatic change in the intensity of Raman modes with applied magnetic field, displaying a gigantic magneto-optical effect as illustrated in Fig. 15.2.

Otherwise, the new publications provide details on Raman scattering in specific materials:

- J.U. Lee, K. Kim, S. Han, G.H. Ryu, Z. Lee, H. Cheong, Raman signatures of polytypism in molybdenum disulfide. ACS Nano **10**, 1948 (2016)
- E. Lorchat, G. Froehlicher, S. Berciaud, Splitting of interlayer shear modes and photon energy dependent anisotropic Raman response in N-layer ReSe₂ and ReS₂. ACS Nano **10**, 2752 (2016)
- A.A. Puretzky, L. Liang, X. Li, K. Xiao, B.G. Sumpter, V. Meunier, D.B. Geohegan, Twisted MoSe₂ bilayers with variable local stacking and interlayer coupling revealed by low-frequency raman spectroscopy. ACS Nano **10**, 2736 (2016)

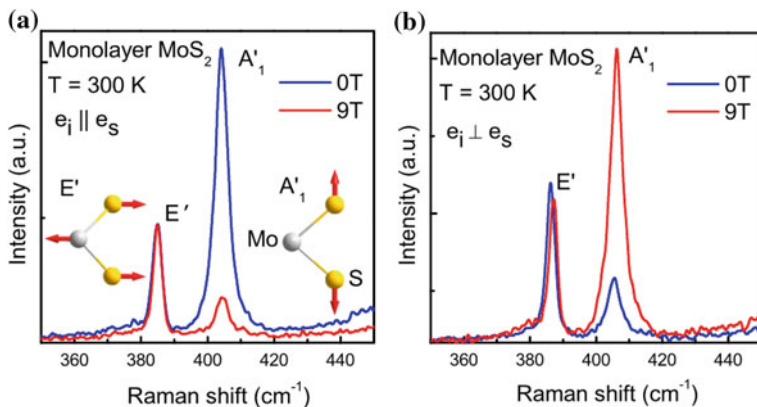


Fig. 15.2 Raman spectra of monolayer MoS_2 of **a** parallel and **b** perpendicular polarization configurations with and without the magnetic field. Reproduced with permission by National Academy of Sciences, USA, from Ji et al. [3]

S. Huang, L. Liang, X. Ling, A.A. Puretzky, D. Geohegan, B.G. Sumpter, J. Kong, V. Meunier, M.S. Dresselhaus, Low-frequency interlayer raman modes to probe interface of twisted bilayer MoS_2 . *Nano Lett.* **16**, 1435 (2016)

Y. Kim, Y.I. Jhon, J. Park, J.H. Kim, S. Lee, Y.M. Jhon, Anomalous raman scattering and lattice dynamics in mono-and few-layer WTe_2 . *Nanoscale* **8**, 2309 (2016)

Y. Jiang, J. Gao, L. Wang, Raman fingerprint for semi-metal WTe_2 evolving from bulk to monolayer. *Sci. Rep.* **6** (2016). doi:[10.1038/srep19624](https://doi.org/10.1038/srep19624)

M. O'Brien, N. McEvoy, D. Hanlon, J.N. Coleman, G.S. Duesberg, Mapping of low-frequency raman modes in CVD-grown transition metal dichalcogenides: layer number, stacking orientation and resonant effects. *Sci. Rep.* **6** (2016). doi:[10.1038/srep19476](https://doi.org/10.1038/srep19476)

X.L. Li, X.F. Qiao, W.P. Han, X. Zhang, Q.H. Tan, T. Chen, P.H. Tan, Determining layer number of two-dimensional flakes of transition-metal dichalcogenides by the raman intensity from substrates. *Nanotechnology* **27**(14), 145704 (2016)

Q. Song, Q. Tan, X. Zhang, J. Wu, B. Sheng, Y. Wan, X. Wang, L. Dai, P. Tan, Physical origin of Davydov splitting and resonant Raman spectroscopy of Davydov components in multilayer MoTe_2 . *Phys. Rev. B* **93**(11), 115409 (2016)

Chapter 8: Luminescence of 2D TMDC

A.M. Jones, H. Yu, J.R. Schaibley, J. Yan, D.G. Mandrus, T. Taniguchi, K. Watanabe, H. Dery, W. Yao, X. Xu, Excitonic luminescence upconversion in a two-dimensional semiconductor. *Nat. Phys. (advance online publication)* (2016)

In A. Jones et al., luminescence upconversion from a negatively charged exciton to a neutral exciton resonance in monolayer WSe_2 , producing spontaneous anti-Stokes emission with an energy gain of 30 meV (Fig. 15.3), was reported. Polarization-resolved measurements found this process to be valley selective, unique to monolayer

semiconductors. The observed result was interpreted in terms of doubly resonant Raman scattering.

Y. Rong, Y. Sheng, M. Pachios, X. Wang, Z. He, H. Bhaskaran, J.H. Warner, Electroluminescence dynamics across grain boundary regions of monolayer tungsten disulfide. *ACS Nano* **10**, 1093 (2015)

T.T. Tran, K. Bray, M.J. Ford, M. Toth, I. Aharonovich, Quantum emission from hexagonal boron nitride monolayers. *Nat. Nanotech.* **11**(1), 37 (2016)

W. Yang, J. Shang, J. Wang, X. Shen, B. Cao, N. Peimyoo, C. Zou, Y. Chen, Y. Wang, C. Cong et al., Electrically tunable valley-light emitting diode (vLED) based on CVD-grown monolayer WS₂. *Nano Lett.* **16**(3), 1560 (2016)

This paper by W. Yang et al. reports a demonstration of electrically tunable chiral electroluminescence from CVD-grown monolayer WS₂ by constructing a p-i-n heterojunction. It is shown that the chirality contrast of the overall electroluminescence reaches as high as 81 % and can be effectively modulated by forward current (Fig. 15.4).

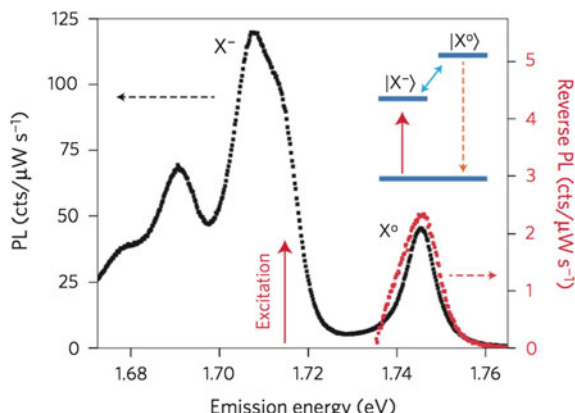
T.T. Tran, K. Bray, M.J. Ford, M. Toth, I. Aharonovich, Quantum emission from hexagonal boron nitride monolayers. *Nat. Nanotech.* **11**(1), 37 (2016)

In this paper, room-temperature, strongly polarized and ultra-bright single-photon emission from a colour center in 2D boron nitride was reported (Fig. 15.5). The result suggest that single-photon emission may be a characteristic feature of vdW crystals. While in the previous work on single-photon emission in WSe₂ [4–7] no microscopic mechanism was suggested, in T. Tran et al., the anti-site nitrogen vacancy (Fig. 15.5d) was identified as the source of quantum emission

Chapter 9: Excitons

S. Cha, J.H. Sung, S. Sim, J. Park, H. Heo, M.H. Jo, H. Choi, 1s-intraexcitonic dynamics in monolayer MoS₂ probed by ultrafast mid-infrared spectroscopy. *Nat. Commun.* **7** (2016). doi:10.1038/ncomms10768

Fig. 15.3 Photoluminescence spectra for 1.96 eV excitation (black) and 1.715 eV excitation (red), indicated by the red arrow. Inset: upconversion scheme. Reprinted by permission from Macmillan Publishers Ltd. from Jones et al. [8]



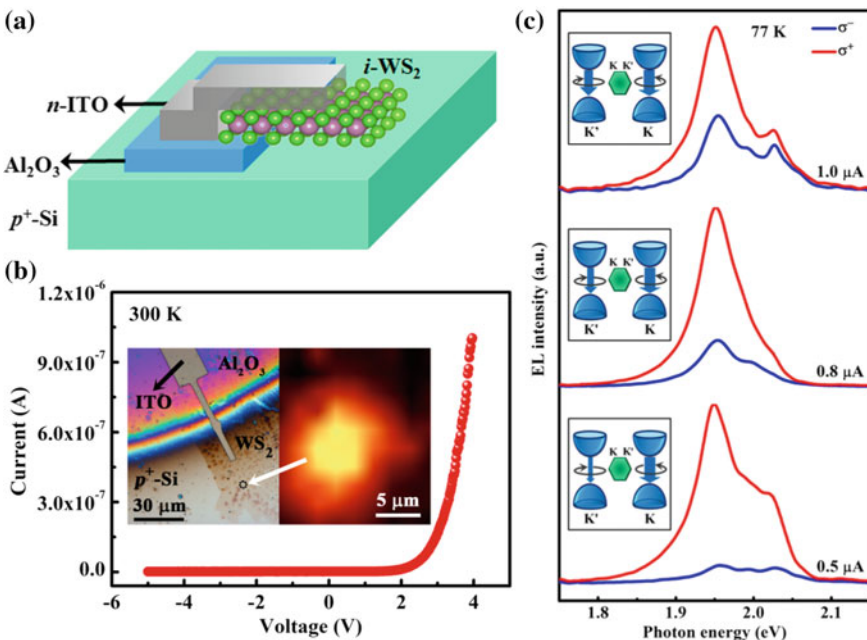


Fig. 15.4 **a** Geometry and **b** room-temperature I-V characteristic of the p^+ -Si/ i -WS₂/n-ITO heterojunction LED device. Inset shows the high-magnification optical images of the device and electroluminescence mapping image as indicated by the white arrow. **c** The current-dependent circularly polarized electroluminescence spectra of the device at 77 K normalized to the right handed circular (σ^+) component at each injection current. *Inset:* Schematic illustration of valley-contrasting circular dichroism under different current injection. Copyright 2016 American Chemical Society. Published with permission from Yang et al. [9]

J. Huang, T.B. Hoang, M.H. Mikkelsen, Probing the origin of excitonic states in monolayer WSe₂. *Scientific reports* **6** (2016). doi:[10.1038/srep22414](https://doi.org/10.1038/srep22414)

A.V. Stier, K.M. McCreary, B.T. Jonker, J. Kono, S.A. Crooker, Exciton diamagnetic shifts and valley zeeman effects in monolayer WS₂ and MoS₂ to 65 tesla. *Nat. Commun.* **7** (2016). doi:[10.1038/ncomms10643](https://doi.org/10.1038/ncomms10643)

P. Cudazzo, L. Sponza, C. Giorgetti, L. Reining, F. Sottile, M. Gatti, Exciton band structure in two-dimensional materials. *Phys. Rev. Lett.* **116**, 066803 (2016)

A. Singh, G. Moody, K. Tran, M.E. Scott, V. Overbeck, G. Berghäuser, J. Schaibley, E.J. Seifert, D. Pleskot, N.M. Gabor et al., Trion formation dynamics in monolayer transition metal dichalcogenides. *Phys. Rev. B* **93**(4), 041401 (2016)

P. Rivera, K.L. Seyler, H. Yu, J.R. Schaibley, J. Yan, D.G. Mandrus, W. Yao, X. Xu, Valley-polarized exciton dynamics in a 2D semiconductor heterostructure. *Science* **351**(6274), 688 (2016)

Z. He, W. Xu, Y. Zhou, X. Wang, Y. Sheng, Y. Rong, S. Guo, J. Zhang, J.M. Smith, J.H. Warner, Biexciton formation in bilayer tungsten disulfide. *ACS Nano* **10**, 2176 (2016)

M.S. Kim, S.J. Yun, Y. Lee, C. Seo, G.H. Han, K.K. Kim, Y.H. Lee, J. Kim, Biexciton emission from edges and grain boundaries of triangular WS₂ monolayers. *ACS Nano* **10**, 2399 (2016)

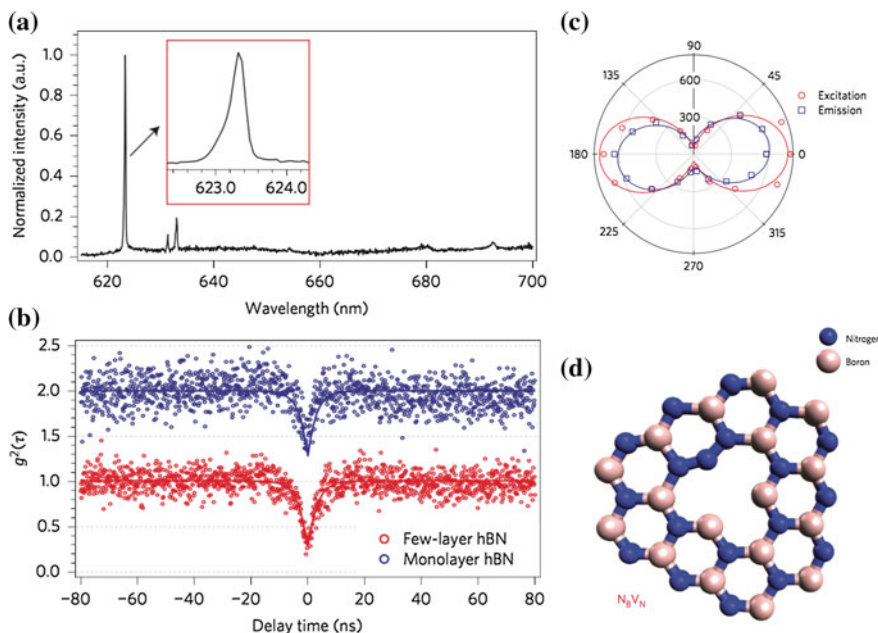


Fig. 15.5 **a** Photoluminescence spectrum taken at 77 K of a defect centre in multilayer h-BN. Inset: the zero phonon line. **b** Antibunching curves from an individual defect centre in h-BN monolayer (blue open circles) and multilayer (red open circles). **c** Excitation (red open circles) and emission (blue open squares) polarization curves from a single defect. **d** The anti-site nitrogen vacancy $N_B V_N$ responsible for single-photon emission. Reprinted by permission from Macmillan Publishers Ltd. from Tran et al. [10]

F. Tseng, E. Simsek, D. Gunlycke, Using dark states for exciton storage in transition-metal dichalcogenides. *J. Phys. Cond. Matter* **28**(3), 034005 (2015)

Chapter 10: Magnetism in 2D TMDC

H. Li, S. Liu, S. Huang, D. Yin, C. Li, Z. Wang, Impurity-induced ferromagnetism and metallicity of WS₂ monolayer. *Ceramics International* **42**(2), 2364 (2016)

C.Y. Yang, K.C. Chiu, S.J. Chang, X.Q. Zhang, J.Y. Liang, C.S. Chung, H. Pan, J.M. Wu, Y.C. Tseng, Y.H. Lee, Phase-driven magneto-electrical characteristics of single-layer MoS₂. *Nanoscale* **8**(10), 5627 (2016)

D. Cao, H. Shu, T. Wu, Z. Jiang, Z. Jiao, M. Cai, W. Hu, First-principles study of the origin of magnetism induced by intrinsic defects in monolayer MoS₂. *Appl. Surf. Sci.* **361**, 199 (2016)

M. Tahir, P. Vasilopoulos, F.M. Peeters, Quantum magnetotransport properties of a MoS₂ monolayer. *Phys. Rev. B* **93**(3), 035406 (2016)

X.L. Fan, Y.R. An, W.J. Guo, Ferromagnetism in transitional metal-doped MoS₂ monolayer. *Nanoscale Res. Lett.* **11**, 154 (2016)

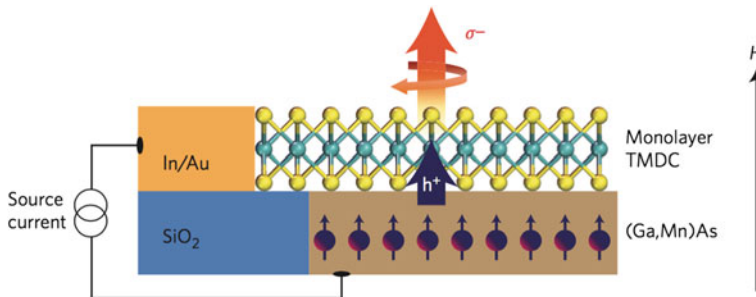


Fig. 15.6 Schematic of the monolayer TMDC/(Ga,Mn)As heterojunction for electrical valley polarization devices. (Ga,Mn)As was used as a spin aligner under an external magnetic field. The valley polarization can be directly determined from the helicity of the emitted electroluminescence as a result of the recombination between the electrically injected spin-polarized holes and the selected degenerate electrons in TMDC monolayers. Reprinted by permission from Macmillan Publishers Ltd. from Ye et al. [11]

Chapter 11: Spin-Valley Coupling

T. Brumme, M. Calandra, F. Mauri, Determination of scattering time and of valley occupation in transition-metal dichalcogenides doped by field effect. Phys. Rev. B **93**(8), 081407 (2016)

W. Yang, J. Shang, J. Wang, X. Shen, B. Cao, N. Peimyoo, C. Zou, Y. Chen, Y. Wang, C. Cong et al., Electrically tunable valley-light emitting diode (vLED) based on CVD-grown monolayer WS₂. Nano Lett. **16**(3), 1560 (2016)

Q. Zhang, S.A. Yang, W. Mi, Y. Cheng, U. Schwingenschlögl, Large spin-valley polarization in monolayer MoTe₂ on Top of EuO (111). Adv. Mater. **28**, 959 (2015)

L. Yang, N.A. Sinitsyn, W. Chen, J. Yuan, J. Zhang, J. Lou, S.A. Crooker, Long-lived nanosecond spin relaxation and spin coherence of electrons in monolayer MoS₂ and WS₂. Nat. Phys. **11**, 830 (2015)

K. Hao, G. Moody, F. Wu, C.K. Dass, L. Xu, C.H. Chen, M.Y. Li, L.J. Li, A.H. MacDonald, X. Li, Direct measurement of exciton valley coherence in monolayer WSe₂. Nat. Phys. (advance online publication) (2016)

Y. Ye, J. Xiao, H. Wang, Z. Ye, H. Zhu, M. Zhao, Y. Wang, J. Zhao, X. Yin, X. Zhang, Electrical generation and control of the valley carriers in a monolayer transition metal dichalcogenide. Nat. Nanotech. (advance online publication) (2016). doi:[10.1038/NNANO.2016.49](https://doi.org/10.1038/NNANO.2016.49)

In Y. Ye et al., using a device based on a heterojunction between a heavily doped *p*-type ferromagnetic semiconductor (Ga,Mn)As and *n*-type monolayer WS₂ (Fig. 15.6), electrical valley polarization with spin injection from a ferromagnetic semiconductor was demonstrated, which was confirmed through the observed valley-polarized light emission.

Chapter 12: Miscellaneous Phenomena

B. Li, T. Liu, D.W. Hewak, Z. Shen, Q.J. Wang, Ultrastrong light-matter coupling of cyclotron transition in monolayer MoS₂. Phys. Rev. B **93**(4), 045420 (2016)

S.H. Rhim, Y.S. Kim, A. Freeman, Strain-induced giant second-harmonic generation in monolayered 2H-MoX₂(X= S, Se, Te). *Appl. Phys. Lett.* **107**(24), 241908 (2015)

Negative electronic compressibility in 2D TMDC

J. Riley, W. Meevasana, L. Bawden, M. Asakawa, T. Takayama, T. Eknapakul, T. Kim, M. Hoesch, S.K. Mo, H. Takagi et al., Negative electronic compressibility and tunable spin splitting in WSe₂. *Nat. Nanotech.* **10**(12), 1043 (2015)

B. Fallahazad, H.C.P. Movva, K. Kim, S. Larentis, T. Taniguchi, K. Watanabe, S.K. Banerjee, E. Tutuc, Shubnikov-de Haas oscillations of high-mobility holes in monolayer and bilayer WSe₂: Landau level degeneracy, effective mass, and negative compressibility. *Phys. Rev. Lett.* **116**(8), 086601 (2016)

Using angle-resolved photoemission (ARPES), the authors demonstrated that doping electrons at the surface of the prototypical strong spin-orbit TMDC bulk WSe₂, akin to applying a gate voltage in a transistor-type device, induces a counter-intuitive *lowering* of the surface chemical potential concomitant with the formation of a multivalley 2D electron gas, which is a direct spectroscopic signature of negative electronic compressibility, the latter being a result of electron-electron interactions.

Charge-density waves in 2D TMDC

X. Xi, L. Zhao, Z. Wang, H. Berger, L. Forró, J. Shan, K.F. Mak, Strongly enhanced charge-density-wave order in monolayer NbSe₂. *Nat. Nanotech.* **10**, 765 (2015)

A combined optical and electrical transport study on the many-body collective-order phase diagram of NbSe₂ down to a thickness of one monolayer. Both the charge density wave and the superconducting phase have been observed down to the monolayer limit. The superconducting transition temperature decreases on lowering the layer thickness, but the newly observed charge-density-wave transition temperature increases from 33 K in the bulk to 145 K in the monolayer (Fig. 15.7). Such highly unusual enhancement of charge density waves in atomically thin samples was interpreted to be a result of significantly enhanced electron-phonon interactions in two-dimensional NbSe₂.

Superconductivity in 2D TMDC

X. Xi, Z. Wang, W. Zhao, J.H. Park, K.T. Law, H. Berger, L. Forró, J. Shan, K.F. Mak, Ising pairing in superconducting NbSe₂ atomic layers. *Nat. Phys.* **11**, 139 (2016)

Y. Saito, Y. Nakamura, M.S. Bahramy, Y. Kohama, J. Ye, Y. Kasahara, Y. Nakagawa, M. Onga, M. Tokunaga, T. Nojima et al., Superconductivity protected by spin-valley locking in ion-gated MoS₂. *Nat. Phys.* **11**, 144 (2016)

Superconductivity in 2T TMDCs was studied in monolayer NbSe₂ and in ion-gated MoS₂ (Fig. 15.8), which effectively behaved as a monolayer, as evidenced by

Fig. 15.7 Thickness-temperature phase diagram for NbSe_2 . Reprinted by permission from Macmillan Publishers Ltd. from Xi et al. [12]

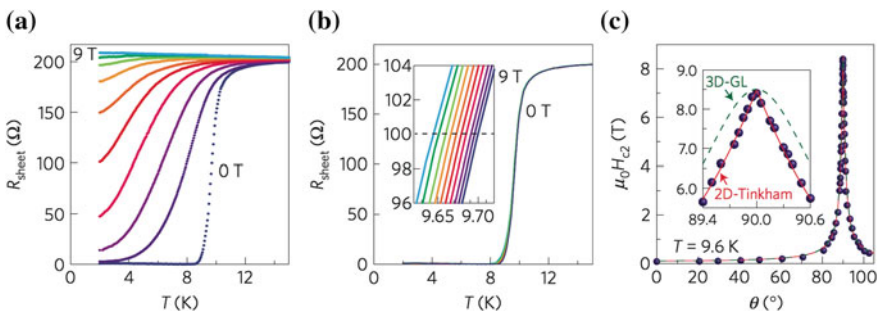
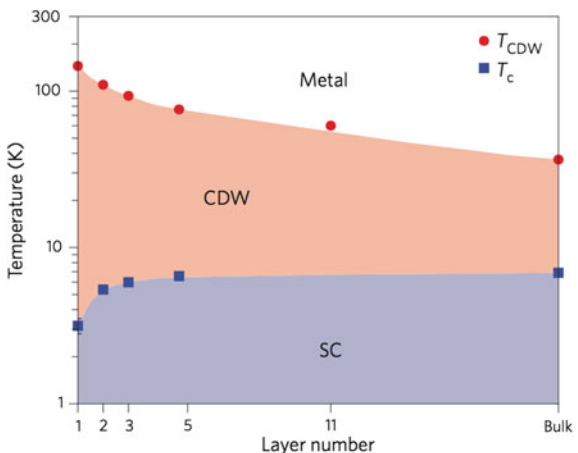


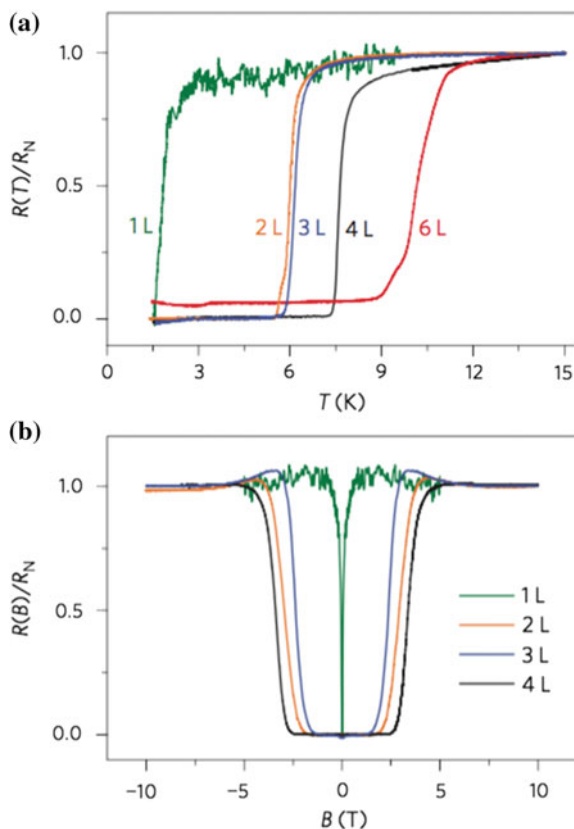
Fig. 15.8 Sheet resistance of a MoS_2 -based electric-double-layer transistor as a function of temperature at $V_G = 6.5$ V, for perpendicular magnetic fields, $\mu_0 H_{c2}^{\perp}$ (a), and parallel magnetic fields, $\mu_0 H_{c2}^{\parallel}$ (b), varying in 1 T steps from 0 to 9 T. The inset of (c) shows a close-up of the resistive transition near the midpoint of the normal state sheet resistance (black dashed line). (c), Angular dependence of the upper critical field, $\mu_0 H_{c2}(\theta)$, where θ is the angle between the magnetic field and the direction perpendicular to the surface of MoS_2 . The inset shows a magnified view of the region around $\theta = 90^\circ$. Reprinted by permission from Macmillan Publishers Ltd. from Saito et al. [13]

the characteristic 2D Tinkham [14] angular dependence of the upper critical field. In both cases it was found that in order to break Cooper's pairs extraordinary large in-plane magnetic fields were required. The observed result was explained in terms of strong out-of-plane spin orientation in monolayers with the resulting unconventional Ising pairing protected by spin-momentum locking.

D. Costanzo, S. Jo, H. Berger, A.F. Morpurgo, Gate-induced superconductivity in atomically thin MoS_2 crystals. Nat. Nanotech. **11**, 339 (2016)

In D. Costanzo et al., superconductivity measurements in MoS_2 down to individual monolayers were performed and it was found that T_c and B_c exhibited a pronounced

Fig. 15.9 Evolution of superconductivity in MoS₂ on decreasing the thickness to the atomic scale from 1 to 6 ML, as a function of temperature (*upper panel*) and magnetic field (*lower panel*) at $T = 1.5$ K.
Reprinted by permission from Macmillan Publishers Ltd. from Costanzo et al. [15]



reduction when going from bilayers to monolayers (Fig. 15.9). Several possible microscopic mechanism for this reduction were proposed such as the physical thickness of the gate-induce accumulation layer, Coulomb interaction between electrons, and specific quantum mechanical states that are occupied by the electrostatically accumulated electrons.

Chapter 13: TMDC Heterostructures

J. Zhang, J. Wang, P. Chen, Y. Sun, S. Wu, Z. Jia, X. Lu, H. Yu, W. Chen, J. Zhu et al., Observation of strong interlayer coupling in MoS₂/WS₂ heterostructures. *Adv. Mater.* **28**, 1950 (2016)

J.P. Xu, M.X. Wang, Z.L. Liu, J.F. Ge, X. Yang, C. Liu, Z.A. Xu, D. Guan, C.L. Gao, D. Qian et al., Experimental detection of a majorana mode in the core of a magnetic vortex inside a topological insulator-superconductor Bi₂Te₃/NbSe₂ heterostructure. *Phys. Rev. Lett.* **114**(1), 017001 (2015)

Chapter 14: Emerging applications of 2D TMDCs

H. Zhong, Z. Ni, Y. Wang, M. Ye, Z. Song, Y. Pan, R. Quhe, J. Yang, L. Yang, J. Shi, et al., Interfacial properties of monolayer and bilayer MoS₂ contacts with metals: beyond the energy band calculations. *Sci. Rep.* **6** (2016). doi:[10.1038/srep21786](https://doi.org/10.1038/srep21786)

- H.J. Chuang, B. Chamlagain, M. Koehler, M.M. Perera, J. Yan, D. Mandrus, D. Tománek, Z. Zhou, Low-resistance 2D/2D ohmic contacts: A universal approach to high-performance WSe₂, MoS₂, and MoSe₂ transistors. *Nano Lett.* **16**(3), 1896 (2016)
- T. Paul, S. Ghatak, A. Ghosh, Percolative switching in transition metal dichalcogenide field-effect transistors at room temperature. *Nanotechnology* **27**, 125706 (2016)
- W. Yang, J. Shang, J. Wang, X. Shen, B. Cao, N. Peimyoo, C. Zou, Y. Chen, Y. Wang, C. Cong et al., Electrically tunable valley-light emitting diode (vLED) based on CVD-grown monolayer WS₂. *Nano Lett.* **16**(3), 1560 (2016)
- H.C. Cheng, G. Wang, D. Liu, H. Wu, M. Ding, Y. Huang, Y. Liu, A. Yin, X. Duan, Q. He, Van der Waals heterojunction devices based on organohalide perovskites and two-dimensional materials. *Nano Lett.* **16**, 367 (2015)
- J. Choi, H. Zhang, J.H. Choi, Modulating optoelectronic properties of two-dimensional transition metal dichalcogenide semiconductors by photoinduced charge transfer. *ACS Nano* **10**(1), 1671 (2016)
- M. Massicotte, P. Schmidt, F. Vialla, K. Schädler, A. Reserbat-Plantey, K. Watanabe, T. Taniguchi, K. Tielrooij, F. Koppens, Picosecond photoresponse in van der Waals heterostructures. *Nat. Nanotech.* **11**(1), 42 (2016)
- J. Feng, K. Liu, R.D. Bulushev, S. Khlybov, D. Dumcenco, A. Kis, A. Radenovic, Identification of single nucleotides in MoS₂ nanopores. *Nat. Nanotech.* **10**(12), 1070 (2015)
- P.M. Campbell, A. Tarasov, C.A. Joiner, M.Y. Tsai, G. Pavlidis, S. Graham, W.J. Ready, E.M. Vogel, Field-effect transistors based on wafer-scale, highly uniform few-layer p-type WSe₂. *Nanoscale* **8**(4), 2268 (2016)
- Y. Wang, R.X. Yang, R. Quhe, H. Zhong, L. Cong, M. Ye, Z. Ni, Z. Song, J. Yang, J. Shi et al., Does p-type ohmic contact exist in WSe₂-metal interfaces?. *Nanoscale* **8**(2), 1179 (2016)

References

1. E. Gibney, 2D or not 2D. *Nature* **522**, 274 (2015)
2. S. Song, D. Keum, S. Cho, D.J. Perello, Y. Kim, Y.H. Lee, Room-temperature semiconductor-metal transition of MoTe₂ thin film engineered by strain. *Nano Lett.* **16**, 188 (2015)
3. J. Ji, A. Zhang, J. Fan, Y. Li, X. Wang, J. Zhang, E. Plummer, Q. Zhang, Giant magneto-optical Raman effect in a layered transition metal compound. *Proc. Nat. Acad. Sci.* **113**(9), 2349 (2016)
4. M. Koperski, K. Nogajewski, A. Arora, V. Cherkez, P. Mallet, J.Y. Veuillen, J. Marcus, P. Kossacki, M. Potemski, Single photon emitters in exfoliated WSe₂ structures. *Nat. Nanotech.* **10**, 503 (2015)
5. Y.M. He, G. Clark, J.R. Schaibley, Y. He, M.C. Chen, Y.J. Wei, X. Ding, Q. Zhang, W. Yao, X. Xu et al., Single quantum emitters in monolayer semiconductors. *Nat. Nanotech.* **10**, 497 (2015)
6. A. Srivastava, M. Sidler, A.V. Allain, D.S. Lembke, A. Kis, A. Imamoğlu, Optically active quantum dots in monolayer WSe₂. *Nat. Nanotech.* **10**, 491 (2015)
7. C. Chakraborty, L. Kinnischitzke, K.M. Goodfellow, R. Beams, A.N. Vamivakas, Voltage-controlled quantum light from an atomically thin semiconductor. *Nat. Nanotech.* **10**, 507 (2015)
8. A.M. Jones, H. Yu, J.R. Schaibley, J. Yan, D.G. Mandrus, T. Taniguchi, K. Watanabe, H. Dery, W. Yao, X. Xu, Excitonic luminescence upconversion in a two-dimensional semiconductor. *Nat. Phys.* (advance online publication) (2016)
9. W. Yang, J. Shang, J. Wang, X. Shen, B. Cao, N. Peimyoo, C. Zou, Y. Chen, Y. Wang, C. Cong et al., Electrically tunable valley-light emitting diode (vLED) based on CVD-grown monolayer WS₂. *Nano Lett.* **16**(3), 1560 (2016)

10. T.T. Tran, K. Bray, M.J. Ford, M. Toth, I. Aharonovich, Quantum emission from hexagonal boron nitride monolayers. *Nat. Nanotech.* **11**(1), 37 (2016)
11. Y. Ye, J. Xiao, H. Wang, Z. Ye, H. Zhu, M. Zhao, Y. Wang, J. Zhao, X. Yin, X. Zhang, Electrical generation and control of the valley carriers in a monolayer transition metal dichalcogenide. *Nat. Nanotech.* (advance online publication) (2016). doi:[10.1038/NNANO.2016.49](https://doi.org/10.1038/NNANO.2016.49)
12. X. Xi, L. Zhao, Z. Wang, H. Berger, L. Forró, J. Shan, K.F. Mak, Strongly enhanced charge-density-wave order in monolayer NbSe₂. *Nat. Nanotech.* **10**, 765 (2015)
13. Y. Saito, Y. Nakamura, M.S. Bahramy, Y. Kohama, J. Ye, Y. Kasahara, Y. Nakagawa, M. Onga, M. Tokunaga, T. Nojima et al., Superconductivity protected by spin-valley locking in ion-gated MoS₂. *Nat. Phys.* **11**, 144 (2016)
14. M. Tinkham, Introduction to superconductivity, 2nd edn. (Dover, 2004)
15. D. Costanzo, S. Jo, H. Berger, A.F. Morpurgo, Gate-induced superconductivity in atomically thin MoS₂ crystals. *Nat. Nanotech.* **11**, 339 (2016)

Chapter 16

Chalcogenides Nanoelectronics: Hype and Hope

Much hope (and hype) rides on graphene and other 2D crystals as ‘post-silicon’ materials for fabricating next-generation nanoelectronic devices. For the first few years, graphene received almost all the attention, but now scientists are beginning to turn to these other 2D crystals, particularly the TMDCs. Recent years have witnessed an unprecedented progress in both fundamental and applied studies of these materials. Transistors, photovoltaic devices, light emitting devices including lasers, memory cells, sensors, NEMS, and integrated circuits were fabricated using 2D TMDCs, demonstrating the rapid advance of TMDCs.

One should not forget other important functional chalcogenides such as phase-change memory alloys, primarily GeTe-Sb₂Te₃ quasibinary alloys, that are currently widely used in optical memories such as digital versatile discs (DVD) and phase-change random-access memories (PC-RAM) [1, 2], and also intensely investigated for use in cognitive (or neuromorphic) computing [3–5]. The ability of phase-change memory alloys to alter properties in a controllable way was also used to fabricate flexible displays [6]. Of interest is the observation that spatial separation of GeTe and Sb₂Te₃ atomically thick layers making a superlattice resulted in a significant improvement of the PC-RAM [7] and also in the appearance of unusual magnetic properties [8].

In recent years materials called topological insulators, of which typical representatives are vdW solids such as Sb₂Te₃ or Bi₂Te₃ that possess a bulk gap but have topologically protected metallic surface states [9–12], entered the scene and applications including quantum computing were suggested [10, 13].

Chalcogenide glasses [14, 15], another class of chalcogenides, are excellent ultrahigh-resolution photoresists [16], whose use with Si and III-V semiconductors was limited because of unintentional doping, may become materials of choice for lithographic processes that include TMDCs and topological insulators. The high

sensitivity of chalcogenide glasses to x-rays paved their way to applications such as highly sensitive medical x-ray detectors [17]. Chalcogenide glasses also show great promise in photonics [18], e.g. for fabrication of flexible photonic devices such as waveguides, microdisk resonators, add-drop filters and photonic crystals [19] that can be potentially coupled with TMDC- or topological-insulator-based devices.

Can one say that era of chalcogenide (nano)electronics is just a few blocks away? While this is an intriguing possibility, especially for those of us who have been involved in chalcogenide research for years, this is probably not possible, nor needed, immediately. At the same time, considering the pace with which the field is developing, it is indeed very likely that in the near future the term ‘chalcogenide electronics’ may enter scene.

It is difficult to predict the exact ways the field will develop, but it seems that one of the real potentials of two-dimensional crystals comes not from using them separately but combining them together to form vertical heterostructures. While the use of TMDCs with graphene and/or h-BN has been intensely studied, no reports have been published so far about heterostructures between TMDCs and topological insulators or GeTe. The latter is not a 2D material but has a pronounced bonding energy hierarchy along the (111) direction and high-quality layered $\text{GeTe}_m[\text{Sb}_2\text{Te}_3]_n$ structures were successfully fabricated. By joining together TMDCs, topological insulators, and phase-change alloys one can obtain materials that do not exist in nature and may possess very interesting properties. One of the major challenges will be finding methods to produce such materials at large scales.

If one wants to dream, one can actually easily imagine an all-chalcogenide personal computer. The electronic components of this computer, such as transistors and integrated circuits, will be made of TMDCs. The memory will be PC-RAM utilizing $\text{GeTe}-\text{Sb}_2\text{Te}_3$, with the same material also used for the display. The battery of this computer will be a lithium-ion battery with nanostructured TMDC used as electrodes. To increase the data transfer rate, chalcogenide glass-based optical fibers will be used and a couple of topological insulator chips will enable the quantum computing mode.

This is a dream. The reality is that to achieve this dream plenty of efforts are needed to better understand the underlying physics of these exciting materials and to develop the technology that will be able to compete with existing technologies. We hope that this monograph will also contribute to make chalcogenide nanoelectronics a reality.

References

1. A.V. Kolobov, J. Tominaga, *Chalcogenides: Metastability and Phase Change Phenomena* (Springer, Berlin, 2012)
2. S. Raoux, M. Wuttig (eds.), *Phase Change Materials: Science and Applications* (Springer, Berlin, 2010)
3. S.R. Ovshinsky, Optical cognitive information processing: a new field. *Jpn. J. Appl. Phys.* **43**(7S), 4695 (2004)

4. Y. Li, Y. Zhong, J. Zhang, L. Xu, Q. Wang, H. Sun, H. Tong, X. Cheng, X. Miao, Activity-dependent synaptic plasticity of a chalcogenide electronic synapse for neuromorphic systems. *Sci. Rep.* **4** (2014). doi:[10.1038/srep04906](https://doi.org/10.1038/srep04906)
5. C.D. Wright, Y. Liu, K.I. Kohary, M.M. Aziz, R.J. Hicken, Arithmetic and biologically-inspired computing using phase-change materials. *Adv. Mater.* **23**(30), 3408 (2011)
6. P. Hosseini, C.D. Wright, H. Bhaskaran, An optoelectronic framework enabled by low-dimensional phase-change films. *Nature* **511**(7508), 206 (2014)
7. R.E. Simpson, P. Fons, A.V. Kolobov, T. Fukaya, M. Krbał, T. Yagi, J. Tominaga, Interfacial phase-change memory. *Nat. Nanotech.* **6**, 501 (2011)
8. D. Bang, H. Awano, J. Tominaga, A.V. Kolobov, P. Fons, Y. Saito, K. Makino, T. Nakano, M. Hase, Y. Takagaki, A. Giussani, R. Calarco, S. Murakami, Mirror-symmetric magneto-optical Kerr rotation using visible light in $[(\text{GeTe})_2(\text{Sb}_2\text{Te}_3)_1]_n$ topological superlattices. *Sci. Rep.* **4** (2014). doi:[10.1038/srep05727](https://doi.org/10.1038/srep05727)
9. J. Moore, Topological insulators: the next generation. *Nat. Phys.* **5**(6), 378 (2009)
10. J. Moore, The birth of topological insulators. *Nature* **464**(7286), 194 (2010)
11. Y. Xia, D. Qian, D. Hsieh, L. Wray, A. Pal, H. Lin, A. Bansil, D. Grauer, Y. Hor, R. Cava et al., Observation of a large-gap topological-insulator class with a single dirac cone on the surface. *Nat. Phys.* **5**(6), 398 (2009)
12. Y. Zhang, K. He, C.Z. Chang, C.L. Song, L.L. Wang, X. Chen, J.F. Jia, Z. Fang, X. Dai, W.Y. Shan et al., Crossover of the three-dimensional topological insulator Bi_2Se_3 to the two-dimensional limit. *Nat. Phys.* **6**(8), 584 (2010)
13. D. Hsieh, Y. Xia, L. Wray, D. Qian, A. Pal, J. Dil, J. Osterwalder, F. Meier, G. Bihlmayer, C. Kane et al., Observation of unconventional quantum spin textures in topological insulators. *Science* **323**(5916), 919 (2009)
14. M.A. Popescu, *Non-Crystalline Chalcogenides* (Kluwer Academic Publishers, Dordrecht, 2000)
15. K. Tanaka, K. Shimakawa, *Amorphous Chalcogenide Semiconductors and Related Materials* (Springer, Berlin, 2011)
16. V. Lyubin, Chalcogenide glassy photoresists: history of development, properties, and applications. *Phys. Stat. Sol. B* **246**(8), 1758 (2009)
17. J. Rowlands, S. Kasap, Amorphous semiconductors usher in digital x-ray imaging. *Phys. Today* **50**(11), 24 (1997)
18. B.J. Eggleton, B. Luther-Davies, K. Richardson, Chalcogenide photonics. *Nat. Photon.* **5**(3), 141 (2011)
19. L. Li, H. Lin, S. Qiao, Y. Zou, S. Danto, K. Richardson, J.D. Musgraves, N. Lu, J. Hu, Integrated flexible chalcogenide glass photonic devices. *Nat. Photon.* **8**(8), 643 (2014)

Index

Symbols

- Z_2 index, 435
- 1/f noise, 475
- 8 – N rule, 10, 11

A

- Alloys, 52, 93, 142, 170, 286, 287, 316
- Annealing, 36, 80, 81, 87, 88, 90, 113–115, 201, 374, 378, 462, 474
- Anti-ferromagnetism, 372, 375–377, 385
- Arm-chair direction, *see* Edge termination, arm-chair
- ARPES, 36, 44, 170, 173, 203, 207, 209–211, 409–411, 466
- Aufbau principle, 17

B

- Band alignment, 167, 455, 456, 462, 494
- Band gap
 - direct, 2, 165, 168, 169, 183, 198, 200, 211, 268, 295, 297, 311, 316, 450
 - electronic, 189, 203, 210
 - indirect, 2, 24, 165, 297, 300, 312, 316, 325, 449, 450
- Kohn-Sham, 324, 325
- optical, 189, 190, 198, 201, 203, 210, 213, 437
- quasiparticle, 204, 211, 323, 330
- renormalization, 189, 210, 211
- Band inversion, 435
- Band nesting, 35, 36, 183, 185, 199, 202, 285, 300–303, 345

- Band structure, 42, 44, 62, 134, 147, 150, 268, 279, 297–301, 311, 324, 325, 331, 334, 354, 366, 395, 435, 436, 449, 450, 452, 454, 457, 467, *see also* Electronic structure
- quasiparticle, 189, 191
- Berry curvature, 59, 165, 390, 399, 403, 405
- Berry phase, 390
- Bethe-Salpeter equation, 189–191, 213
- Bi-exciton, 321, 345, 351
 - “mirror”, 347
- Binding energy
 - exciton, 189–191, 198, 213, 321–324, 326–332, 344, 345, 354
 - dimensionality dependence, 322
 - trion, 348–351, 353, 354, 401
- Birch-Murnaghan equation of state, 68
- Bloch state, 169, 170, 172, 173
- Bohr radius, 322, 324, 325, 345
- Boltzmann transport theory, 146, 147
- Bond
 - covalent, 8–10, 13–16, 18, 19, 22, 31, 34, 44, 67, 117, 195
 - dangling, 11, 13, 15, 29, 30, 94, 135, 447
 - dative, 13, 15, 19, 20
 - ionic, 44, 114
 - multicenter, 14
 - resonant, 8, 13, 14, 67
- Boundary
 - domain, 100, 181
 - grain, 48, 128, 133–135, 138, 196, 204, 372, 373
 - tilt, 136, 140
 - twin, 123, 134, 140, 141, 430

- Bragg peak, 67, 114
 Brillouin scattering, 55
 Brillouin zone, 39–41, 44, 50, 54, 165–168, 170, 176, 182, 184, 185, 188, 189, 197, 198, 202, 204, 207, 208, 210, 212, 229, 230, 266, 267, 300, 325, 327, 389, 390, 398, 410, 412, 435, 436, 452, 457
 Burgers vector, 138, 139, 370
 Burstein-Moss effect, 437, 438
- C**
 C-exciton, 201, 202, 245, 265, 301, 302, 327, 328, 346, 355, 356
 Chalcogenide (nano)electronics, 530
 Chalcogenide glass, 10, 16, 529
 Charge density difference, 9, 13, 15, 16, 30, 31
 Charge density wave, 34–36, 52, 54, 57, 116, 126
 commensurate, 36, 126, 283, 286
 incommensurate, 36, 126
 Charge transfer, 117, 141, 144, 145, 179, 211, 313, 314, 461
 Chemical vapour deposition, 85, 86, 91–93, 96, 98–100, 129, 130, 207, 210, 251, 299, 304, 305, 368, 423, 424, 466, 474, 485
 Coercive field, 368
 Cognitive computing, 529
 Continuous random network, 11
 Cooper’s pairs, 525
 Coordination
 number, 10, 13, 18
 octahedral, 14, 18–20, 30, 109
 trigonal prismatic, 18, 30, 32, 34, 42, 43, 81, 109–112, 115, 117, 185, 233, 261, 276, 365, 385, 457
 Coordination bond, *see* Bond, dative
 Coulomb diamond, 479
 Coulomb interaction, 113, 126, 150, 189, 211, 214, 215, 234, 321, 324, 325, 329, 340, 345, 354, 398, 412
 Curie temperature, 368
 CVD, *see* Chemical vapour deposition
- D**
 Degeneracy, 21, 39, 41, 166, 173, 179, 205, 235, 236, 255, 257, 264, 412
 Dirac cone, 109, 197, 198, 354, 435, 466
 Dislocation, 133, 134, 136, 138, 140, 370–372
- Distributed Bragg reflector, 442, 488
 Doping, 210, 211, 254, 255, 281, 334, 335, 347, 348, 354, 365, 372, 375–377, 429, 437–439, 494, 497–499
 DVD, 529
- E**
 Edge states, 366, 369, 371, 374, 425
 Edge termination
 arm-chair, 110, 143, 144, 180, 365, 367, 370, 422, 427, 432
 zig-zag, 110, 122, 133, 134, 143, 144, 259, 366, 368, 371, 373, 379, 422, 423, 427
 Electric field, 141, 179, 180, 259, 307, 312, 321, 322, 329, 379, 389, 390, 397, 401, 405–408, 412, 413, 421–423, 432, 433, 435, 450, 461, 485, 492
 Electroluminescence, 315, 395, 405, 487, 488
 Electromechanical coupling, 432
 Electron irradiation, 129–131
 Electron spin resonance, 11
 Electron-electron interaction, 523
 Electron-hole interaction, 323, 324, 326
 Electron-hole pair, 189, 211, 300, 303, 327, 328, 337, 347, 351, 352, 408, 450, 462
 Electronic structure, 29, 39, 42–44, 118, 133, 145, 169, 170, 195, 211, 213, 217, 311, 454, 455, 457, 459, 466, *see also* Band structure
 Even/odd layer number, *see* Odd/even layer number
 EXAFS, 112, 114
 Exciton
 dark, 330, 334, 338, 403
 non-Rydberg series, 329
 Rydberg series, 327, 329, 330, 332, 334
 Exciton–exciton annihilation, 342–345
 Exciton-trion coupling, 353
 Excitonic collapse, 334
 Exfoliation, 38, 98, 110, 112, 235, 382
 chemical, 79, 81, 82, 201, 296
 electrochemical, 84, 85
 liquid, 81
 mechanical, 79, 110, 207, 283, 295, 296, 351, 368
 Extinction coefficient, 149
- F**
 Faraday geometry, 307

Fermi

- arc, 59
 - level, 11, 35, 36, 57, 128, 133, 138, 178, 210–212, 366, 369, 370, 437, 466, 494, 496, 498
 - pocket, 57, 64, 398, 405
 - surface, 35, 36, 57, 59, 64, 181, 285
- Ferromagnetic easy axis, 378
- Ferromagnetism, 365, 368, 369, 372, 375–379, 385
- FET, *see* Field-effect transistor
- Field-effect transistor, 126, 140, 311, 428, 473, 474, 477, 478, 480, 482, 490, 496, 498, 499, 501, 502
- Floquet state, 412
- Frenkel exciton, 321, 324

G

- Grüneisen parameter, 256
- Graphene, 1, 17, 29, 38, 79, 81, 82, 85, 96, 109, 133, 142, 143, 151, 176, 187, 188, 193, 196, 198, 203, 204, 213, 280–282, 389, 447, 466–468, 474, 480, 483, 485, 490, 491, 497, 498, 502

H

- Hall effect
- anomalous, 405
 - photoinduced, 404, 405, 436
 - quantum, 1, 390
 - quantum spin, 390, 435
 - spin, 404
 - valley, 389, 390, 404
- Hanle effect, 391
- Heterostructure, 280
- lateral, 462, 463, 465
 - vertical, 35, 279, 282, 283, 356, 359, 447, 463, 480, 491, 530
 - lattice-matched, 448, 450
 - single-layer, 457
 - with minimized strain, 452
 - with vertically aligned layers, 458
- Hidden spin polarization, 395
- Hopping integral, 170
- Hund's rule, 17
- Hybridization, 18, 19, 25, 30, 31, 54, 67, 173, 178, 412, 413, 415, 416
- Hyperfine interaction, 392

I

- Insulator, 17, 36, 96, 109, 128, 435
- topological, 14, 17, 59, 67, 367, 529
- Intercalation, 30, 31, 44, 79, 81–84, 110–112, 114, 115, 117, 118, 126, 201, 211, 213, 233, 296
- Interlayer coupling, 39, 44, 47, 61, 170, 172, 178, 180, 209, 215, 217, 232, 233, 236, 262, 278, 279, 296, 298, 299, 425, 450, 461, 462
- Interlayer distance, 45, 168, 170, 177, 181, 192, 193, 233, 297
- Irreducible representation, 46, 229, 241
- Ising pairing, 525

J

- Jahn–Teller effect, 22, 35, 36

K

- Kerr rotation, 417
- Kohn anomaly, 36, 285

L

- Landau level, 390
- Lifshitz transition, 58
- Ligand, 15, 17–23, 29, 30, 113
- Light-matter coupling, 183, 187, 199
- Lithiation, 82
- Lone-pair electrons, 8, 9, 11

M

- Magnetic field, 57, 205, 206, 307, 308, 366, 368, 379, 385, 390, 391, 398, 399, 401–403, 409, 436
- Magnetic impurity, 368, 375, 376
- Magnetic susceptibility, 368
- Magneto-optical effect, 517
- Magnetoresistance, 63, 64
- Majorana fermion, 367
- Melting, 39, 86
- Memory device, 490, 492, 529
- Metal-metal chain, 34, 35, 114, 116, 122, 123
- Mobility, 150, 474, 476–478, 480, 485, 487, 496, 500, 501
- Mode
- compression, 237
 - interlayer breathing, 237, 238, 240, 241, 282, 283
 - interlayer shear, 237, 238, 240, 241, 275

low-frequency, 236, 238, 239, 282, 283
 multophonon, 268
 Raman-active, 46, 231, 235–237, 241, 243, 261, 266, 268, 276
 rigid-layer, 46, 47, 71
 vibrational, 46, 47, 54, 227, 230, 233, 240, 242, 243, 255, 260, 265
 Moiré pattern, 454, 459
 Monte Carlo method, 142, 343
 Monte Carlo simulations, 142
 Mott insulator, 36, 126, 127
 Mott rule, 10
 Mott transition, 215

N

Nanoelectromechanical system, 503, 529
 Nanoribbon, 155, 365, 366
 Nanotube, 143, 145, 153–155
 Negative electronic compressibility, 523
 Negative-U centres, 11
 NEMS, *see* Nanoelectromechanical system
 Neuromorphic computing, 529
 Non-covalent interaction, 195

O

Odd/even layer number, 40, 41, 101, 109, 210, 227, 229–231, 239, 241, 246, 395, 421–423, 432, 434
 Ohmic contact, 167, 492, 496
 Oxidation, 84, 152, 153

P

Pair-distribution function analysis, 114
 Pauli exclusion principle, 312, 437
 PC-RAM, 529
 Peierls distortion, 35, 36, 57, 116, 285, 286
 Penn gap, 198
 Phase-change alloys, 17, 492, 529
 Phase-space filling, 312
 Photodetector, 485
 Photogating, 252, 253
 Photon antibunching, 306
 Photoresist, 529
 Photothermoelectric effect, 486
 Piezoelectricity, 432
 Piezoresistivity, 217, 218
 Point defects, 128, 129, 131, 137
 Polariton, 188, 442
 Polaron, 36, 37, 385
 Polymorph, 31, 32, 39–41, 178, 227, 229–231, 259, 261, 276, 452

Polytype, *see* Polymorph
 Pressure, 2, 32, 50, 61, 62, 66–70, 91, 119, 120, 152, 177, 178, 215, 233, 261, 298, 309
 Pseudospin, 173, 389, 398, 406, 407

Q

Quantum computing, 529
 Quantum confinement, 168, 209
 Quantum dot, 479
 Quantum yield, 296, 297, 300, 301, 304, 346, 485, 488

R

Rabi oscillations, 403
 Raman
 1T-phase, 111, 261, 276
 Porto notations, 48, 237
 pressure, 66, 68, 70, 71, 259, 260, 262
 scattering, from alloys, 52, 286, 287
 scattering, polarised, 48, 242, 262, 277, 286
 circularly, 262, 264
 scattering, resonant, 48, 265, 271, 272
 scattering, second-order, 50, 52, 265, 266, 269–271, 280, 285, 286
 temperature dependence, 249–251
 tensor, 41, 230, 237, 256, 278
 Random-element isodisplacement model, 286
 Rayleigh scattering, 264
 Recombination, 297, 301, 303, 313, 339, 340, 359, 396, 397, 460, 476
 Auger, 338, 340
 Reflectivity, 43, 55, 215, 332, 344, 353
 Refractive index, 149
 Rietveld refinement, 67

S

Saturation magnetisation, 368, 374
 Schottky barrier, *see* Schottky contact
 Schottky contact, 167, 480, 492, 494–499
 Screening, 2, 210, 215, 321–326, 329–332, 336, 337, 344, 345, 354
 Second harmonic generation, 101, 109, 407, 421, 431
 Seebeck effect
 spin, 405
 valley, 405
 Selection rule
 optical, 330, 331, 334, 391, 396, 397, 407

- valley-dependent, 390, 391, 398, 413
 Sensors, 501
 SHG, *see* Second harmonic generation
 Shubnikov-de Haas oscillations, 59, 63
 Single-phonon emission, 306
 Space group, 35, 39–41, 228, 229
 Spin relaxation mechanism
 Bir-Aronov-Pikus, 392
 Dyakonov-Perel, 392
 Elliot-Yafet, 392
 Spin-layer locking, 390, 407
 Spin-orbit coupling, 125, 169–174, 177, 185,
 189, 190, 201, 202, 205, 206, 210,
 345, 355, 390, 392, 397, 407, 411,
 435, 436, 457
 Spin-valley coupling, 397, 407, 489
 Splitting
 crystal-field, 21, 42, 385
 Davydov, 236
 Rabi, 443
 Rashba, 409, 435, 457
 spin-orbit, 167, 171, 173, 189, 191, 198,
 210, 211, 324–327, 330, 344
 Stacking, 31, 32, 39, 40, 71, 171, 180, 217,
 228, 232, 234, 239, 243, 282, 283,
 394, 407, 448–452, 454, 455, 458,
 467
 Bernal, 282, 421
 Stark effect
 giant, 179
 optical, 412, 413
 Strain, 61, 121, 122, 124, 129, 131, 140, 143,
 145, 169, 174, 175, 177, 178, 191,
 255, 256, 259, 310, 311, 334, 335,
 365, 370, 379, 380, 432, 434, 437,
 448, 453, 454, 487
 biaxial, 174–177, 215, 235
 compressive, 120, 175, 177, 215, 216,
 260, 311, 433
 shear, 174, 175
 tensile, 120, 174, 175, 177, 191, 216, 255,
 310, 311, 379–381, 433, 436
 uniaxial, 144, 215, 216, 235, 255, 256,
 258, 259, 310, 432
 Superconductivity, 66, 439
 Superlattice, 111, 126, 447, 452, 454, 455,
 529
 Superstructure, 114
 Symmetry
 crystal, 129, 196, 198, 286, 422, 431–433
 inversion, 2, 109, 172, 173, 177, 179–
 181, 185, 210, 229, 241, 277, 330,
 389–391, 394–396, 398, 403, 405–407,
 409–411, 421, 432–435, 450, 454
 mirror, 325, 457
 of orbitals, 23, 171
 of state, 21, 171, 173, 330
 of wavefunctions, 168
 operations, 227, 229
 rotational, 170, 397, 427
 time-reversal, 169, 173, 325, 397–399,
 404, 406, 409, 410, 412, 415, 435
 translational, 54, 243
 Symmetry operations, 227
- T**
- Theory
 crystal-field, 20, 22, 23
 density-functional, 25
 group, 39, 41, 243
 ligand-field, 23, 24
 valence bond, 18, 20, 23
- Thermal conductivity, 146, 251
- Thermal expansion, 145
- Tight-binding model, 165
- Tinkham dependence, 525
- Topological defects, 11
- Topological insulator, *see* Insulator, topological
- Total scattering, 114
- Transition
 2H–1T, 110, 114, 119–121, 126, 499
 charge-density wave, 36, 126, 286
 indirect-to-direct gap, 165, 168–170,
 175, 178, 181, 201, 208, 216, 298, 391,
 407
 order-disorder, 142
 semiconductor-metal, 61, 63, 450
- Twist angle, 180, 181, 262, 283, 298, 299
- Two-photon process, 330, 332, 334, 431
- U**
- Ultrasonication, 79, 81, 82
- Unit magnetic moment, 366
- V**
- Vacancy, 2, 14, 16, 129–133, 138–140, 372,
 380, 385, 498
- Valence-alternation pairs, 11, 12
- Valley coherence, 396, 397, 401
- Valley depolarisation, 401, 417
- Valley polarisation, 390, 393–395, 399, 402–
 404, 408, 413

- van-der-Waals
 bond, 39, 67, 71
 correction, 61, 62, 170, 192
 energy, 38, 195
 epitaxy, 94
 gap, 459–461, 463
 interaction/force, 8, 17, 26, 29, 37–39,
 61, 69, 82, 94, 192, 193, 195, 196, 255,
 279, 281, 447, 454, 461
 van Hove singularity, 185, 202, 213, 214, 345
 Voigt geometry, 307, 399
- W**
 Wannier-Mott exciton, 321, 324, 327, 328,
 331
 Weak (anti-)localization, 205, 206
 Weyl point, 59
 Weyl semimetal, 59
- X**
 X-ray diffraction, 110
- Y**
 Young's modulus, 143–145
- Z**
 Zeeman effect
 proximity-induced, 403
 spin, 398
 valley, 398, 400
 Zeeman splitting, 397, 401, 408
 Zig-zag direction, *see* Edge termination, zig-zag
 Zone folding, 111, 286